polymers

Bio-Based Polymers for Engineered Green Materials

Edited by
Gianluca Tondi and Thomas Schnabel

Printed Edition of the Special Issue Published in *Polymers*

www.mdpi.com/journal/polymers

Bio-Based Polymers for Engineered Green Materials

Bio-Based Polymers for Engineered Green Materials

Special Issue Editors

Gianluca Tondi
Thomas Schnabel

MDPI • Basel • Beijing • Wuhan • Barcelona • Belgrade • Manchester • Tokyo • Cluj • Tianjin

Special Issue Editors
Gianluca Tondi
University of Padua
Italy

Thomas Schnabel
Salzburg University of Applied Sciences
Austria

Editorial Office
MDPI
St. Alban-Anlage 66
4052 Basel, Switzerland

This is a reprint of articles from the Special Issue published online in the open access journal *Actuators* (ISSN 2076-0825) (available at: https://www.mdpi.com/journal/polymers/special_issues/bio_polymers_for_engineered_green_materials).

For citation purposes, cite each article independently as indicated on the article page online and as indicated below:

LastName, A.A.; LastName, B.B.; LastName, C.C. Article Title. *Journal Name* **Year**, *Article Number*, Page Range.

ISBN 978-3-03928-925-7 (Pbk)
ISBN 978-3-03928-926-4 (PDF)

Cover image courtesy of Thomas Schnabel.

Contents

About the Special Issue Editors

Gianluca Tondi (Prof. Dr.) is a chemist specialized in bio-based materials. After the master degree in Italy he studied in Switzerland, France and Austria where he developed tannin-based biopolymers for wood adhesive, preserving and building insulation purposes. The objective of his research is to extend the field of use for natural bio-sourced materials and to carry them into large scale production.

Thomas Schnabel (Prof. Dr.) studied timber constructions and wood sciences and technology in Austria and Germany. His's research focus is on characterization and processing of bio-based materials and the fostering of the transformation from sustainable raw materials to high added-value products.

polymers

MDPI

Editorial

Bio-Based Polymers for Engineered Green Materials

Gianluca Tondi [1,*] and Thomas Schnabel [2]

[1] Department of Land, Environment, Agriculture and Forestry, University of Padova, Viale dell'Università 16, 35020 Legnaro, Italy

[2] Forest Products Technology & Timber Constructions Department, Salzburg University of Applied Sciences, Marktstrasse 136a, 5431 Kuchl, Austria; thomas.schnabel@fh-salzburg.ac.at

* Correspondence: gianluca.tondi@unipd.it; Tel.: +39-043-8272776

Received: 27 March 2020; Accepted: 28 March 2020; Published: 1 April 2020

Every. Single. Carbon atom oxides to CO_2 at the end. Every. Single. One.

The more we pump petroleum-fixed carbon into the carbon cycle, the higher will be the concentration of CO_2 in the atmosphere. The higher the CO_2, the greater will be the temperature of the planet. This increase in temperature will also raise the concentration of water in air. Water and CO_2 are the molecules that contribute the most to the greenhouse effect. The planet is subject to daily warming, and the later we take account of it and act, the more difficult will the battle against global warming be.

It is time to change our views and make this problem a priority. Consumer demands need to care about the carbon neutrality of products so that the market and industry are forced to offer alternative and more sustainable solutions.

In polymer science, this message means that we have to exploit as much as possible the materials that nature synthesizes, process them in a sustainable way, and eventually modify them to give the new materials the high-performing properties we are used to. We aim to jealously maintain the carbon atoms that are fixed in solid phase.

This is what our scientific community is trying to do on a daily basis—taking important steps to produce carbon-neutral, bio-based, high-performing materials.

Content of This Issue

The current research on bio-based polymers is summarized in Figure 1.

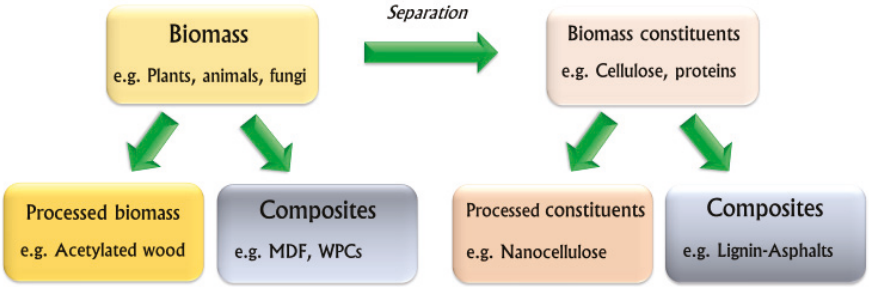

Figure 1. Diagram showing research topics in the field of bio-based polymers.

Among the different kind of biomasses, plants derivatives are the most widely investigated because they are by far the more abundant and are easy to source.

In this special issue, wood is treated to enhance its durability with alkali lignin at high temperature [1] and improve its transparency for the preparation of bleached thin translucent veneer [2]. This sustainable harvested biomass is also considered a source of molecules: a broad number of

extractives such as taxifolin and larixol [3] were extracted by simple extraction, but organic oils could also be gained by applying thermal pyrolysis [4] for further applications.

With regard to biomass constituents, cellulose is certainly the more investigated subject in bio-polymer science. Despite pulping and paper-making having been used for centuries, there is a strong interest in improving the process and applying it to other biomasses, in an effort to enhance yield and pulp quality [5,6].

In recent years, scientific interest has moved to nano-fibrillated cellulose. In this issue, many research groups have proposed interesting technologic solutions [7]. Jiang et al. proposed an efficient method for obtaining NFC from Artemisia Vulgaris bast [8]. Kang et al. found a one-pot method to oxide it and use the product in cosmetic and biomedical applications [9], while other researchers have found attractive ways to modify the cellulose membrane by adding graphene oxide or grafting it to enhance its adsorption properties [10,11].

Cellulosic fibres were combined with various materials to enhance mechanical properties, not only in thermoplastics as polyamides, but also other bio-polymers such as polylactic acid and pectines [12–17].

Cellulose was also used as support for metals and other polymers such as polycaprolactone through electrospinning deposition [18,19].

Other research groups have exploited polysaccharides such as hemicelluloses, starch, and alginate to produce hydrogels, microparticles, and sponges for methylene blue removal [20–22]. Furthermore, bioplastics have been characterized, highlighting that starch has a higher recycle sensibility, while PLA is subject to a decrease in its molecular mass during reprocessing [23].

In spite of their extreme variability, proteins are a consistent subject of study in material science. In this volume, the growing mechanism of silkworm cocoons produced in confined spaces and the use of the silver coated peptone for anti-bacterial effects are presented [24,25].

We present three studies on polyhydroxyalkanoate produced by bacterial fermentation. These macromolecules are biodegradable polyesters and their synthesis is affected by several parameters, of which concentration of substrate and cycle length are fundamental [26]. These promising bio-material often have an unpleasant smell and limited mechanical properties, which can be reduced by adding organoclays [27,28].

Several interesting bio-based polymers from other resources and processes are also presented. Polyesters and NIPU were synthesized using vegetal oils, offering products with enhanced mechanical properties and high thermal stability, respectively [29,30]. Latex was exposed to photodegradation catalyzed by TiO_2 to obtain easy-to-manage low molecular weight rubber [31]. In a study by Yu et al., the possibility to include heavy bio-oils in asphalt rubber to improve the rutting and fatigue resistance of the paving material is shown [32].

The polymerization of natural monomers such as tannins and dopamine were also exploited to produce high-absorbing materials and more mechanically stable explosives [33,34].

In summary, sustainably produced bio-based polymers can be studied from many aspects: We can consider the bio-materials, their constituents obtained by various processes, modifications, and their combinations in composites. Every time a researcher finds new ways to replace fossil-based resources to produce materials, the chances of keeping carbon atoms fixed to the material increases. We will, thus, soon be able to offer high-performing bio-based engineered products and trigger a green revolution.

References

1. Zhou, H.; Li, J.; Ma, E. Multiscale Modification of Populus cathayana by Alkali Lignin Combined with Heat Treatment. *Polymers* **2018**, *10*, 1240. [CrossRef] [PubMed]
2. Wu, Y.; Wu, J.; Yang, F.; Tang, C.; Huang, Q. Effect of H2O2 Bleaching Treatment on the Properties of Finished Transparent Wood. *Polymers* **2019**, *11*, 776. [CrossRef] [PubMed]

3. Wagner, K.; Musso, M.; Kain, S.; Willför, S.; Petutschnigg, A.; Schnabel, T. Larch Wood Residues Valorization through Extraction and Utilization of High Value-Added Products. *Polymers* **2020**, *12*, 359. [CrossRef] [PubMed]
4. Ben, H.; Wu, Z.; Han, G.; Jiang, W.; Ragauskas, A. Pyrolytic behavior of major biomass components in waste biomass. *Polymers* **2019**, *11*, 324. [CrossRef] [PubMed]
5. Abushammala, H.; Mao, J. A Review on the Partial and Complete Dissolution and Fractionation of Wood and Lignocelluloses Using Imidazolium Ionic Liquids. *Polymers* **2020**, *12*, 195. [CrossRef] [PubMed]
6. Bian, H.; Wu, X.; Luo, J.; Qiao, Y.; Fang, G.; Dai, H. Valorization of alkaline peroxide mechanical pulp by metal chloride-assisted hydrotropic pretreatment for enzymatic saccharification and cellulose nanofibrillation. *Polymers* **2019**, *11*, 331. [CrossRef]
7. Balea, A.; Blanco, A.; Negro, C. Nanocelluloses: Natural-based materials for fiber-reinforced cement composites. A critical review. *Polymers* **2019**, *11*, 518. [CrossRef]
8. Nie, K.; Song, Y.; Liu, S.; Han, G.; Ben, H.; Ragauskas, A.J.; Jiang, W. Preparation and Characterization of Microcellulose and Nanocellulose Fibers from Artemisia Vulgaris Bast. *Polymers* **2019**, *11*, 907. [CrossRef]
9. Jun, S.H.; Park, S.G.; Kang, N.G. One-Pot Method of Synthesizing TEMPO-Oxidized Bacterial Cellulose Nanofibers Using Immobilized TEMPO for Skincare Applications. *Polymers* **2019**, *11*, 1044. [CrossRef]
10. Ślusarczyk, C.; Fryczkowska, B. Structure–Property Relationships of Pure Cellulose and GO/CEL Membranes Regenerated from Ionic Liquid Solutions. *Polymers* **2019**, *11*, 1178. [CrossRef]
11. Kim, Y.; Jeong, D.; Park, K.H.; Yu, J.H.; Jung, S. Efficient adsorption on benzoyl and stearoyl cellulose to remove phenanthrene and pyrene from aqueous solution. *Polymers* **2018**, *10*, 1042. [CrossRef] [PubMed]
12. Zhang, W.; Gu, J.; Tu, D.; Guan, L.; Hu, C. Efficient Hydrophobic Modification of Old Newspaper and Its Application in Paper Fiber Reinforced Composites. *Polymers* **2019**, *11*, 842. [CrossRef] [PubMed]
13. Bátori, V.; Lundin, M.; Åkesson, D.; Lennartsson, P.R.; Taherzadeh, M.J.; Zamani, A. The Effect of Glycerol, Sugar, and Maleic Anhydride on Pectin-Cellulose Thin Films Prepared from Orange Waste. *Polymers* **2019**, *11*, 392. [CrossRef] [PubMed]
14. Wang, X.; Jia, Y.; Liu, Z.; Miao, J. Influence of the lignin content on the properties of poly (lactic acid)/lignin-containing cellulose nanofibrils composite films. *Polymers* **2018**, *10*, 1013. [CrossRef]
15. Sousa, S.; Costa, A.; Silva, A.; Simões, R. Poly (lactic acid)/cellulose films produced from composite spheres prepared by emulsion-solvent evaporation method. *Polymers* **2019**, *11*, 66. [CrossRef]
16. Park, J.W.; Shin, J.H.; Shim, G.S.; Sim, K.B.; Jang, S.W.; Kim, H.J. Mechanical strength enhancement of polylactic acid hybrid composites. *Polymers* **2019**, *11*, 349. [CrossRef]
17. Kabir, A.; Dunlop, M.J.; Acharya, B.; Bissessur, R.; Ahmed, M. Polymeric composites with embedded nanocrystalline cellulose for the removal of iron (II) from contaminated water. *Polymers* **2018**, *10*, 1377. [CrossRef]
18. Root, W.; Wright, T.; Caven, B.; Bechtold, T.; Pham, T. Flexible Textile Strain Sensor Based on Copper-Coated Lyocell Type Cellulose Fabric. *Polymers* **2019**, *11*, 784. [CrossRef]
19. Ng, K.; Azari, P.; Nam, H.Y.; Xu, F.; Pingguan-Murphy, B. Electrospin-Coating of Paper: A Natural Extracellular Matrix Inspired Design of Scaffold. *Polymers* **2019**, *11*, 650. [CrossRef]
20. Al-Rudainy, B.; Galbe, M.; Arcos Hernandez, M.; Jannasch, P.; Wallberg, O. Impact of lignin content on the properties of hemicellulose hydrogels. *Polymers* **2019**, *11*, 35. [CrossRef]
21. Paiva, D.; Pereira, A.M.; Pires, A.L.; Martins, J.; Carvalho, L.H.; Magalhães, F.D. Reinforcement of thermoplastic corn starch with crosslinked starch/chitosan microparticles. *Polymers* **2018**, *10*, 985. [CrossRef] [PubMed]
22. Shen, X.; Huang, P.; Li, F.; Wang, X.; Yuan, T.; Sun, R. Compressive Alginate Sponge Derived from Seaweed Biomass Resources for Methylene Blue Removal from Wastewater. *Polymers* **2019**, *11*, 961. [CrossRef] [PubMed]
23. Shojaeiarani, J.; Bajwa, D.S.; Rehovsky, C.; Bajwa, S.G.; Vahidi, G. Deterioration in the Physico-Mechanical and Thermal Properties of Biopolymers Due to Reprocessing. *Polymers* **2019**, *11*, 58. [CrossRef] [PubMed]
24. Cheng, L.; Tong, X.; Li, Z.; Liu, Z.; Huang, H.; Zhao, H.; Dai, F. Natural Silkworm Cocoon Composites with High Strength and Stiffness Constructed in Confined Cocooning Space. *Polymers* **2018**, *10*, 1214. [CrossRef] [PubMed]

25. Kim, M.; Jee, S.C.; Shinde, S.K.; Mistry, B.M.; Saratale, R.G.; Saratale, G.D.; Ghodake, G.S.; Kim, D.Y.; Sung, J.S.; Kadam, A.A. Green-Synthesis of anisotropic peptone-silver nanoparticles and its potential application as anti-bacterial agent. *Polymers* **2019**, *11*, 271. [CrossRef]
26. Cabrera, F.; Torres, Á.; Campos, J.L.; Jeison, D. Effect of Operational Conditions on the Behaviour and Associated Costs of Mixed Microbial Cultures for PHA Production. *Polymers* **2019**, *11*, 191. [CrossRef]
27. García-Quiles, L.; Valdés, A.; Cuello, Á.F.; Jiménez, A.; Garrigós, M.D.C.; Castell, P. Reducing off-Flavour in Commercially Available Polyhydroxyalkanoate Materials by Autooxidation through Compounding with Organoclays. *Polymers* **2019**, *11*, 945. [CrossRef]
28. García-Quiles, L.; Fernández Cuello, Á.; Castell, P. Sustainable materials with enhanced mechanical properties based on industrial polyhydroxyalkanoates reinforced with organomodified sepiolite and montmorillonite. *Polymers* **2019**, *11*, 696. [CrossRef]
29. Liu, C.; Wu, Q.; An, R.; Shang, Q.; Feng, G.; Hu, Y.; Jia, P.; Zhou, Y.; Lei, W. Synthesis and Properties of Tung Oil-Based Unsaturated Co-Ester Resins Bearing Steric Hindrance. *Polymers* **2019**, *11*, 826. [CrossRef]
30. He, X.; Xu, X.; Wan, Q.; Bo, G.; Yan, Y. Solvent-and Catalyst-free Synthesis, Hybridization and Characterization of Biobased Nonisocyanate Polyurethane (NIPU). *Polymers* **2019**, *11*, 1026. [CrossRef]
31. Ibrahim, S.; Othman, N.; Sreekantan, S.; Tan, K.S.; Mohd Nor, Z.; Ismail, H. Preparation and Characterization of Low-Molecular-Weight Natural Rubber Latex via Photodegradation Catalyzed by Nano TiO_2. *Polymers* **2018**, *10*, 1216. [CrossRef] [PubMed]
32. Yu, J.; Ren, Z.; Gao, Z.; Wu, Q.; Zhu, Z.; Yu, H. Recycled heavy bio oil as performance enhancer for rubberized bituminous binders. *Polymers* **2019**, *11*, 800. [CrossRef] [PubMed]
33. Sepperer, T.; Neubauer, J.; Eckardt, J.; Schnabel, T.; Petutschnigg, A.; Tondi, G. Pollutant Absorption as a Possible End-Of-Life Solution for Polyphenolic Polymers. *Polymers* **2019**, *11*, 911. [CrossRef] [PubMed]
34. Lin, C.; Gong, F.; Yang, Z.; Zhao, X.; Li, Y.; Zeng, C.; Li, J.; Guo, S. Core-Shell Structured HMX@ Polydopamine Energetic Microspheres: Synergistically Enhanced Mechanical, Thermal, and Safety Performances. *Polymers* **2019**, *11*, 568. [CrossRef]

polymers

MDPI

Article

Multiscale Modification of *Populus cathayana* by Alkali Lignin Combined with Heat Treatment

Haizhen Zhou, Jingyu Li and Erni Ma *

Beijing Key Laboratory of Wood Science and Engineering, MOE Key Laboratory of Wooden Material Science and Application, Beijing Forestry University, Qinghua Eastroad 35#, Haidian, Beijing 100083, China; zhzbjfu@163.com (H.Z.); ljyemma@163.com (J.L.)

* Correspondence: maerni@bjfu.edu.cn; Tel.: +86-010-6233-6225

Received: 15 September 2018; Accepted: 5 November 2018; Published: 9 November 2018

Abstract: Chemical modification of wood with green modifiers is highly desirable for sustainable development. With the aim of enhancing the water resistance and dimensional stability of fast growing wood, modifications were conducted using renewable and toxicity-free industrial lignin combined with heat treatment. Poplar (*Populus cathayana*) samples first underwent impregnation with alkali lignin solution and were then subjected to heat treatment at 140–180 °C for two hours. The results indicated that the modified wood showed excellent leaching resistance. The alkali lignin treatment improved surface hydrophobicity and compression strength, and decreased moisture and water uptake, thereby reducing the dimensional instability of modified wood. These changes became more pronounced as the heat-treating temperature increased. Scanning electron microscopy, confocal laser scanning microscopy, and Fourier transform infrared spectroscopy evidenced that a multiscale improvement of the alkali lignin occurred in the cell lumen and cell wall of wood fibers and vessels, with small alkali lignin molecules reacting with the wood matrix. This study paves the way for developing an effective modification approach for fast growing wood, as well as promoting the reuse of industrial lignin for high-value applications, and improves the sustainable development of the forestry industry.

Keywords: wood modification; alkali lignin; water resistance; dimensional stability; heat treatment

1. Introduction

As the second richest polymer from biomass after cellulose, lignin is usually accepted as biomass waste in the pulping industry. The lack of use of lignin has led to a massive waste of resources and pulping emissions have become an issue of environmental concern [1]. Only about 100 kt (less than 2%) can be sold commercially as kraft or alkali lignins [2].

Lignin is regarded as a natural raw material that can modify or replace other materials because of its unique chemical structure and abundance in nature. Peng et al. found that polypropylene composites reinforced with alkali lignin showed higher surface hydrophobicity after a weathering treatment [3]. Directly using industrial lignin and modified lignin as fillers was found to lead to a significant reduction in water absorption in thermoplastic starch [4]. Composites mixed by wood flour, lignin (extracted from kraft black liquor) and polypropylene showed decreased hydroscopicity and corresponding swell rate with increasing lignin content [5]. Therefore, lignin is thought to make the composites repellent to water and deformation. However, few studies in the literature examined lignin as an alternative to enhance the hydrophobicity and dimensional stability of solid wood whose hygroscopic nature of the cell wall polymers is a dominating obstacle to the application of usual hydrophobic modifiers. The poor reaction capacity of lignin at room temperature also limits the modification effect of wood.

The problem may be solved by heat treatment. Studies have shown that lignin chemical reactivity increased during heat treatment, since a number of reactions including radical oxidation, molecular transposition, dehydrogenation, and polycondensation occurred, resulting in cross-links between lignin molecules [6–8]. Due to oxidation and condensations, a further self-crosslinking occurs between lignin and the cell wall components of wood when heating [9]. On the other hand, the porosity of wood cell wall increases after heat treatment due to the degradation of hemicellulose [10], which provides the possibility of improving permeability for lignin. Heat treatment has been proven to boost water repellency and dimensional stability of wood caused by decreasing free hydroxyl [11,12]. Therefore, heat treatment could be a good consideration to combine with lignin modification. And according to the previous research [13], heat treatment with lower temperature or short heating time did not adversely affect the mechanical properties of wood.

The objective of this study was to take industrial lignin as a modifier to enhance the water resistance and dimensional stability of fast growing wood. Heat treatment was introduced to facilitate a redistribution of the impregnated lignin and cross-links between it and wood matrix. The effects of this combined treatment, including water resistance and dimensional stability, were investigated. Morphological and chemical characteristics were analyzed by scanning electron microscopy (SEM), confocal laser scanning microscopy (CLSM), and Fourier transform infrared (FTIR) spectroscopy, with high expectation of multiscale modifying both the cell cavity and cell wall levels. Results from this study expand the application field and resolve the bottleneck for the use of fast growing wood, and enable the high-valued reuse of industrial lignin, therefore contributing to more environmentally friendly and sustainable development of the forestry industry.

2. Materials and Methods

2.1. Materials

The test species was Poplar (*Populus cathayana*), which belongs to the fast growing species, and is quite common in North China. The 20 × 20 × 20 mm^3 (L × T × R) samples were oven-dried at 103 °C until they reached a constant weight m_0 (g) (labelled as Control). Alkali lignin extracted from pulping black liquor (average size of 180 nm detected by a laser particle size analyzer, MASTERSIZE 2000, Malvern Panalytical Ltd., Malvern, England and number-average molecular weight of 1336 g/mol obtained by gel permeation chromatography, Agilent 1200, Agilent Technologies Inc., Santa Clara, CA, USA), was purchased from Shan Feng Chemical Co., Ltd., Changzhou, China.

2.2. Sample Treatment Methods

The alkali lignin particles were dispersed in 1,4-dioxane to the maximum concentration followed by filtration for later use. The samples were impregnated with alkali lignin solution using a vacuum-pressure process. In this study, the samples were subjected to a vacuum at −0.1 MPa for 30 min, then they were immersed in alkali lignin solution at 0.5 MPa for 1 h. After impregnation, the excess liquid in the wood surface was wiped with tissue paper and oven-dried at 103 °C to constant weight m_1 (g) (labelled as AL). Finally, the AL samples were subjected to three temperatures of 140, 160, and 180 °C for 2 h (labelled as AL 140 °C, AL 160 °C, and AL 180 °C, respectively), and the weight m_2 (g) after heat treatment was recorded. The weight percent gain (WPG) for the impregnation treatment and mass loss (ML) for the heat treatment were evaluated according to the following equations:

$$\mathrm{WPG}(\%) = 100(m_1 - m_0)/m_0 \quad (1)$$

$$\mathrm{ML}(\%) = 100(m_1 - m_2)/m_1 \quad (2)$$

2.3. SEM Analysis

To characterize structural details and the alkali lignin location of the modified wood, transverse and tangential sections of the samples were placed in conductive glue and sputter-coated with gold. Then, the microstructure of the samples was observed by SEM (Hitachi S-3400, Hitachi Ltd., Tokyo, Japan) with a voltage of 15 KV.

2.4. CLSM Analysis

To further qualitatively and quantitively investigate the spatial distribution of alkali lignin within the samples, transverse sectional samples 10–20 μm thick from the microtome were subsequently inspected with a Leica TCS SP5 confocal microscope (Leica Microsystems Inc., Wetzlar, Germany) with a krypton/argon laser emitting at wavelengths of 488 nm. The same gain setting (115) was used for the samples so the emission intensities could be directly compared in the images.

2.5. FTIR Spectroscopy Analysis

To explore the changes in the functional groups in the wood after treatment, flour of the samples (100 mesh) was pressed into KBr pellets and tested by FTIR (Bruker VERTEX 70V, Bruker Ltd., Karlsruhe, Germany) with a resolution of 4 cm^{-1} and 32 scans per sample in the 4000–400 cm^{-1} interval.

2.6. Leachability Test

The treated samples were tested for leaching resistance according to the E11-06 American Wood Protection Association (AWPA) standard. For each group, three replicates were leached in 300 mL of deionized water at 22–28 °C. The samples were completely submerged and stirred with a magnetic stir bar in flask bottles. The water was replaced after 6, 24, and 48 h, and thereafter at 48-h intervals. The leachability test lasted for 14 days, and the weights of the samples (dried at 103 °C) before and after the leaching treatment were recorded.

2.7. Contact Angle

All the samples were conditioned at 25 °C and 72% relative humidity (RH) to a constant mass before measurement. The time-dependent contact angles were measured according to sessile drop method by Dataphysics OCA20 contact angle analyzer (DataPhysics Instruments GmbH, Filderstadt, Germany). Data were gathered stochastically from three sites on the transverse section of every sample with each group containing three replicates. The dispense process was completed by an automatic microsyringe with approximately 3 μL of distilled water.

2.8. Water Resistance and Dimensional Stability

Water resistance and dimensional stability were tested according to Chinese standard GB/T 1934.1-2009 and GB/T 1934.2-2009, respectively. Oven-dried samples were exposed separately to 3 different RH of 45%, 55%, and 72% at 25 °C for adsorption. The 3 RH conditions were created by applying saturated salt solutions of K_2CO_3, NaBr, and NaCl, respectively [14]. The remaining oven-dried samples were submerged in deionized water at approximately 25 °C for water absorption. The water used in the experiment was replaced daily to ensure the container stayed clean. Weights and dimensions (tangential, radial, and longitudinal direction) were examined at particular intervals during the adsorption and absorption processes. The moisture content (MC), water absorption rate (WAR), tangential swelling rate (α_w and α_{max}), and volumetric swelling rate (α_{Vw} and α_{Vmax}) of the samples were calculated from three replicates as follows:

$$MC(\%) = 100(M_n - M_0)/M_0 \quad (3)$$

$$WAR(\%) = 100(W_n - M_0)/M_0 \quad (4)$$

$$\alpha_w(\%) = 100(L_w - L_0)/L_0 \quad (5)$$

$$\alpha_{max}(\%) = 100(L_{max} - L_0)/L_0 \quad (6)$$

$$\alpha_{Vw}(\%) = 100(V_w - V_0)/V_0 \quad (7)$$

$$\alpha_{Vmax}(\%) = 100(V_{max} - V_0)/V_0 \quad (8)$$

where the subscript w represents the adsorption process; max refers to the absorption process; M_0, M_n, and W_n are weights of over-dried samples and samples after n hours of adsorption and n hours of water absorption (g), respectively; L_0, L_w, and L_{max} are the tangential dimensions of over-dried samples and samples after n hours of adsorption and n hours of water immersion (mm), respectively; and V_0, V_w, and V_{max} are volumes of over-dried samples and samples after n hours of adsorption and n hours of water immersion (mm^3).

The adsorption behavior of the modified samples was analyzed using the Hailwood–Horrobin (H–H) sorption model [15]. According to this theory, the MC corresponding to the total hydration of the available sorption sites (–OH) in wood was 18/W.

2.9. Compression Test

The samples were conditioned over a NaCl saturated solution (75% RH) at 25 °C before mechanical tests. The axial compressive strength was determined with a universal mechanical machine (Universal Mechanical Testing Machine, Beijing, China) at a test speed of 1 $mm \cdot min^{-1}$ according to GB/T 1935-2009. Each group included 6 replicates in the tests. The axial compressive strength (σ) was calculated as follows:

$$\sigma = P_{max}/bt \quad (9)$$

where P_{max} is failure load (N), and b and t are the radial and tangential length of the samples (mm), respectively.

3. Results and Discussion

3.1. General Description of Treated Wood

As listed in Table 1, the WPG of the samples after impregnation ranged from approximately 11% to 13%. The mass loss increased with heat treatment temperature, since an increase in temperature promoted the degradation of hemicellulose. After the leachability test, all treated samples showed considerable leaching resistance, especially the AL 180 °C, for which the leaching rate was only 1.4%. This is ascribed to the hydrophobicity of alkali lignin and the formation of chemical bonds between alkali lignin and the wood matrix during heat treatment, which caused the fixation of alkali lignin in wood.

Table 1. Weight percent gain (WPG), mass loss, leaching rate, initial contact angle, 18/W, and compression strength (σ) of the samples. Number in parenthesis represents standard deviation from several replicates.

Sample	WPG (%)	Mass Loss (%)	Leaching Rate (%)	18/W (%)	σ (MPa)
Control	-	-	-	5.4 (0.1)	41.9 (1.3)
AL	12.3 (0.3)	-	3.3 (0.7)	5.3 (0.1)	42.5 (1.2)
AL 140 °C	12.4 (1.0)	0.8 (0.1)	2.3 (0.2)	5.2 (0.1)	43.8 (1.4)
AL 160 °C	11.2 (0.9)	1.2 (0.1)	1.9 (0.3)	5.1 (0.1)	45.4 (1.2)
AL 180 °C	11.8 (0.7)	2.2 (0.2)	1.4 (0.1)	4.9 (0.0)	45.6 (1.1)

3.2. SEM Analysis of Treated Wood

Figure 1 shows the SEM images of transverse and tangential sections of the samples. Compared with the Control, a portion of the cell cavity of wood fibers and vessels were totally or partially filled

with alkali lignin after alkali lignin impregnation for the AL (Figure 1c). The fillers hinder water passage and may lead to further improvement in mechanical properties. The pits were covered by alkali lignin film (Figure 1d), which blocks the water paths in cell cavities and obstructs the possible hydrogen bonding contact between water molecules and hydroxyl groups in cell walls. After the heat treatment at 180 °C, granular sediments were found near the pits (Figure 1f), which may be associated with the self-condensation of alkali lignin caused by high temperature treatment. The cell wall of AL 180 °C showed no visible difference compared to the Control and the AL, implying that low heat treatment temperature would have little effect on the mechanical properties of wood.

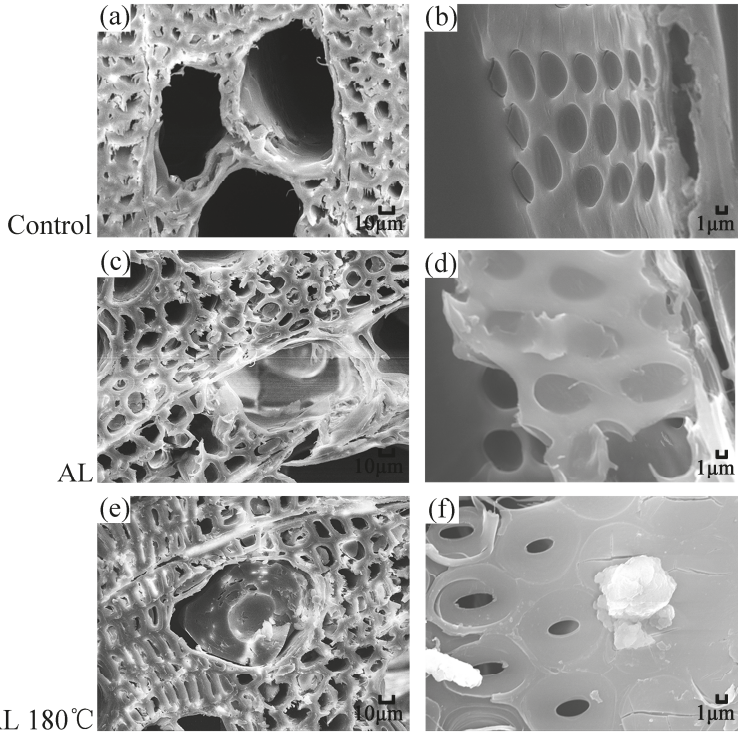

Figure 1. Scanning electron microscopy (SEM) images of (**a**,**c**,**e**) transverse-sections at magnification 500 and (**b**,**d**,**f**) tangential sections at magnification 3000 of the samples.

3.3. CLSM Analysis of Treated Wood

Brighter areas represent higher lignin concentration. As shown in Figure 2, green light fluorescence was found in the cell wall of the Control with brighter fluorescence occurring in the compound middle lamella (CML), suggesting a higher lignin concentration in the CML [16]. The average fluorescence intensity was estimated by randomly calculating various area of the cell wall or cell cavity from five replicates, which also shown in Figure 2. The average intensity of the cell wall of the Control was 38.4, whereas that of the cell cavity was only 2.5. For AL and AL 180 °C, both the brightness of the image and fluorescence signal intensity increased significantly compared with the Control. The intensity values were higher than 130 for the cell wall and 25 for the cell cavity, which indicates that alkali lignin was not only deposited in the cell cavity, but also entered the cell wall after immersion. Further compared to the AL, we found from the signal intensity curve that the fluorescence intensity distribution was more homogeneous for AL 180 °C, suggesting a uniform dispersion of alkali lignin after heat treatment,

which may have resulted from the increasing fusibility of alkali lignin caused by high temperature treatment [17].

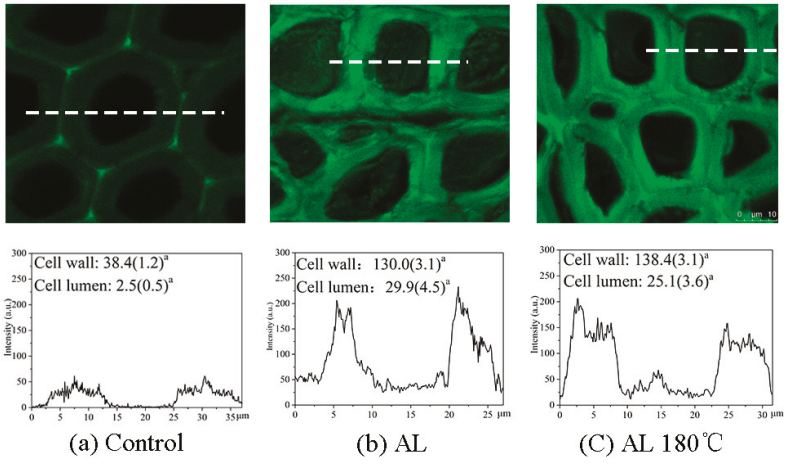

Figure 2. Confocal laser scanning microscopy (CLSM) images showing the lignin distribution over transverse sections of the (**a**) Control, (**b**) AL, and (**c**) AL 180 °C and corresponding varieties of fluorescence signal intensity across the wood cell along the white dotted lines. [a] Average values (standard deviation) from five replicates are shown.

3.4. FTIR Spectroscopy Analysis

Taking the Control, AL, and AL 180 °C as examples, Figure 3 displays the FTIR spectra for the alkali lignin-heat treated samples, which were all normalized based on the highest peak assigned to O–H stretching around 3430 cm^{-1}. Generally, analysis of changes in wood chemical components by O–H stretching absorption bands and C–H absorption bands (around 2923 cm^{-1}) is limited, which is due to the fact that the three main chemical components (cellulose, hemicellulose, and lignin) of wood all contain hydroxyl and methylene moieties [18].

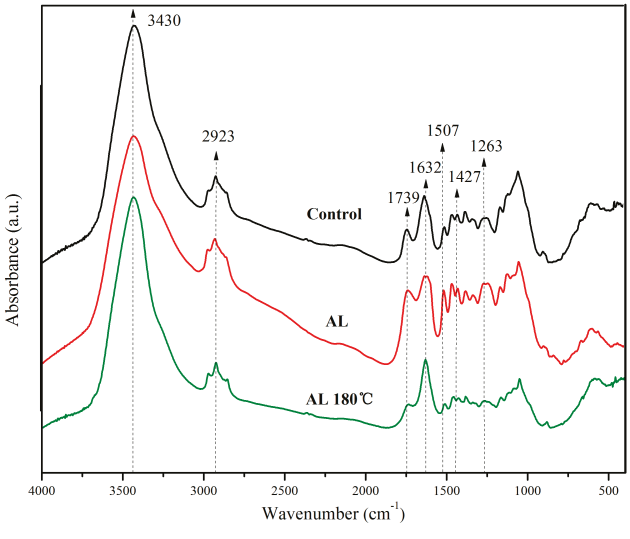

Figure 3. Fourier transform infrared (FTIR) spectra for the Control, AL, and AL 180 °C samples.

From Figure 3, it could be found that the peak intensity in AL at 1632 and 1427 cm^{-1} increased significantly compared with the Control. The peaks were assigned to aromatic conjugated C=O and benzene ring vibration respectively, which originated mainly from lignin [19]. Another characteristic peak of lignin at 1507 cm^{-1} (C=C stretching vibration) [20] also increased after alkali lignin impregnation treatment, which is due to the infusion of alkali lignin in wood. Therefore, the relative amount of lignin for AL increased. The absorbance at 1263 cm^{-1} is the characteristic peak of Ar–O stretching or α- or β-aryl ether in lignin [21,22]. The rising intensity of this peak indicates new ethers formed between the alkali lignin or between alkali lignin and polysaccharide in AL (Figure 4), which also explains the low leaching rate of the treated samples because of the fixation of alkali lignin in wood (Table 1). The subdued signal at 1739 cm^{-1} assigned to C=O stretching, attributed primarily to hemicellulose [23], showed a decrease in the relative amount of hemicellulose for the AL 180 °C due to hemicellulose degradation caused by high temperature treatment.

Because the 1263, 1427, 1507, 1632 cm^{-1} wave numbers were attributed to the functional groups of lignin, to quantitatively estimate the change in lignin content or lignin functional groups after treatment, the lignin index (LI) was calculated according to Equation (10) based on the intensity of the peak at 1049 cm^{-1}, which corresponds to the oxygen-containing functional groups of cellulose in wood [24], usually serving as a reference band.

$$LI = 100(I_{1263,1427,1507,1632}/I_{1049}) \quad (10)$$

where I is band intensity.

As shown in Table 2, the LI_{1263}, LI_{1427}, and LI_{1507} of AL and AL 180 °C increased compared to the Control, again confirming the increase in the lignin content in treated wood. However, the values of LI_{1263}, LI_{1427}, and LI_{1507} of AL 180 °C were lower than those of AL, with an opposite trend for LI_{1632}, which belongs to the aromatic conjugated C=O in lignin. This may be due to the degradation of alkali lignin after heat treatment (Figure 4), followed by the formation of aromatic organics [25,26].

Table 2. Lignin index (LI) for the Control, AL, and AL 180 °C samples.

Sample	LI_{1263}	LI_{1427}	LI_{1507}	LI_{1632}
Control	49.0%	52.8%	39.3%	73.2%
AL	78.6%	73.2%	72.1%	86.0%
AL 180 °C	55.2%	60.6%	48.8%	139.4%

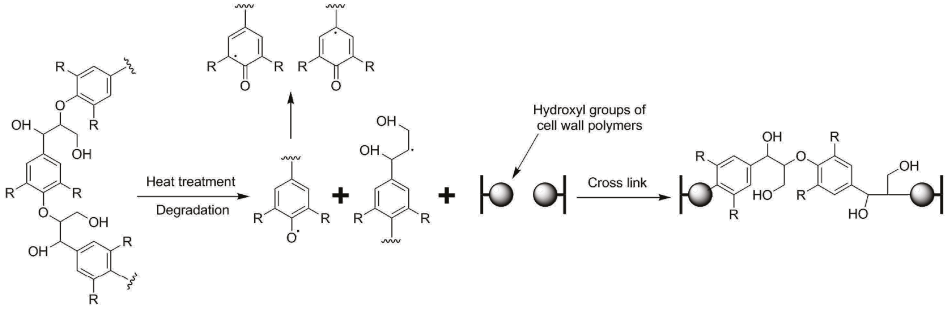

Figure 4. Schematic illustration and chemical reactions showing the bonding mechanism between lignin and the wood matrix.

3.5. Contact Angle

The initial contact angle and change in contact angle with time for the samples is demonstrated in Figure 5. The contact angle of the Control was less than 90°, corresponding to a hydrophilic surface,

and all the treated samples had contact angles greater than 90°, which indicated a hydrophobic surface. It is clear that the contact angle of the Control decreased rapidly during the first three seconds compared with the treated samples, and eventually approached a relatively stable value around 2–3°. In addition, the contact angles of treated wood were much larger, even after 60 s without a significant reduction, which suggests that alkali lignin improves the surface hydrophobicity of wood due to its hydrophobic property. Another reason for this effect could be that the alkali lignin existing on the wood surface may create wood roughness. The contact angle increased with increasing heating temperature at a given testing time. Specifically, the contact angle of AL 180 °C exceeded 140°, which almost corresponds to a super-hydrophobic surface with a water contact angle greater than 150° [27]. The surface active functional groups of the wood probably reduced after heat treatment [28], and high temperature may promote the reactions between surface functional groups and alkali lignin.

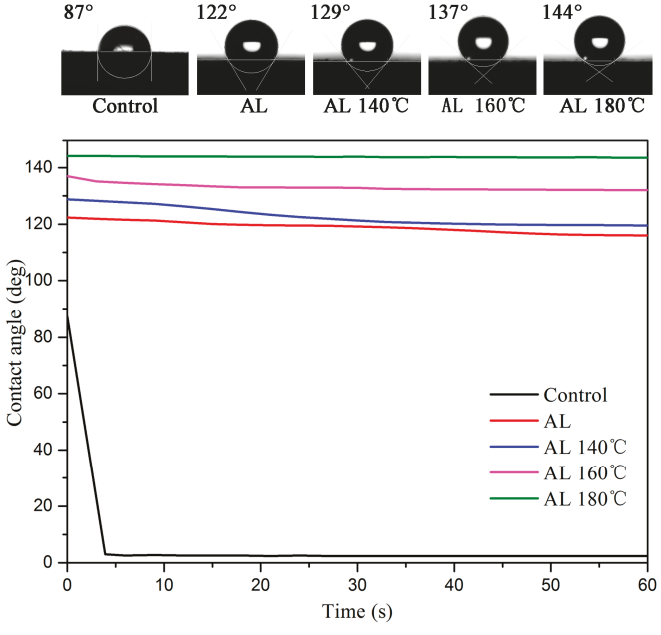

Figure 5. Initial contact angle and contact angle as a function of time for the samples.

3.6. Moisture Adsorption and Water Absorption

Figure 6 presents the adsorption processes at three RH conditions for the samples. Hygroscopicity of samples subjected to heat treatment at 180 °C for 2 h without lignin impregnation was also investigated as a reference, but the results indicated a very limited improvement and are not discussed here. Among the five groups in the Figure 6, the Control exhibited the highest MC, followed by AL, AL 140 °C, AL 160 °C, and AL 180 °C. Taking the 72% RH as an example, the equilibrium MC of AL, AL 140 °C, AL 160 °C, and AL 180 °C dropped by 13.2%, 15.2%, 15.4%, and 20.0% compared with the Control, respectively, which suggests that alkali lignin impregnation combined with heat treatment can reduce wood hygroscopicity. This can be explained by the small molecular alkali lignin reacting with –OH in the wood cell wall (Figure 3) and heat treatment led to a lower moisture adsorption due to the reduced hygroscopicity resulting from hemicellulose degradation.

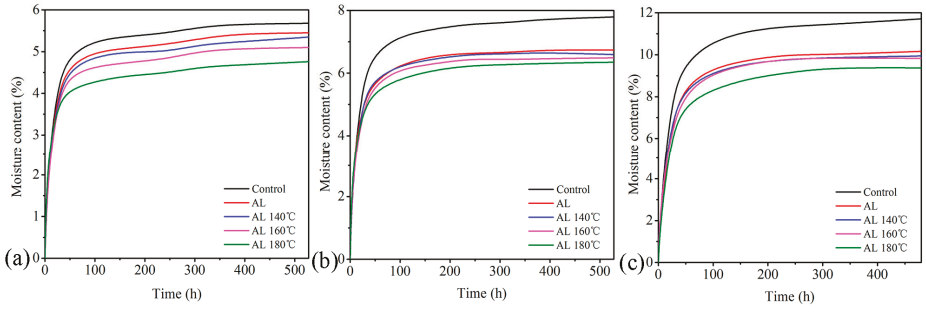

Figure 6. Moisture adsorption processes under (**a**) 45% relative humidity (RH), (**b**) 55% RH, and (**c**) 72% RH at 25 °C for the samples.

The 18/W calculated by the H–H sorption model is listed in Table 1. All the values of 18/W for the samples fell in the range of 4% to 6%. When the effective –OH of the sample reacted with the monolayer adsorbed water, the MC should be limited to 4% to 6%. This result is consistent with previous research [29]. A comparison of 18/W among different samples shows that the value of the modified samples decreases compared with the Control. It also verifies a reduction in available sorption sites after alkali lignin plus heat treatment.

The moisture adsorption rate of the samples was evaluated by taking the first derivative according to Figure 6. The corresponding results of the first 24 h during the adsorption processes are shown in Figure 7. From the figure, the adsorption rate of the samples increased with increasing RH. The adsorption rate of alkali lignin-heat treated samples declined compared with the Control. Specifically, the values of AL, AL 140 °C, AL 160 °C, and AL 180 °C dropped by 16.9%, 17.1%, 25.7%, and 42.2%, respectively, under the 55% RH condition compared with the Control. This implies that alkali lignin plus heat treatment decreases not only moisture adsorption amount but also adsorption rate for the samples, which may due to the blocking of water pathways caused by alkali lignin (Figure 1).

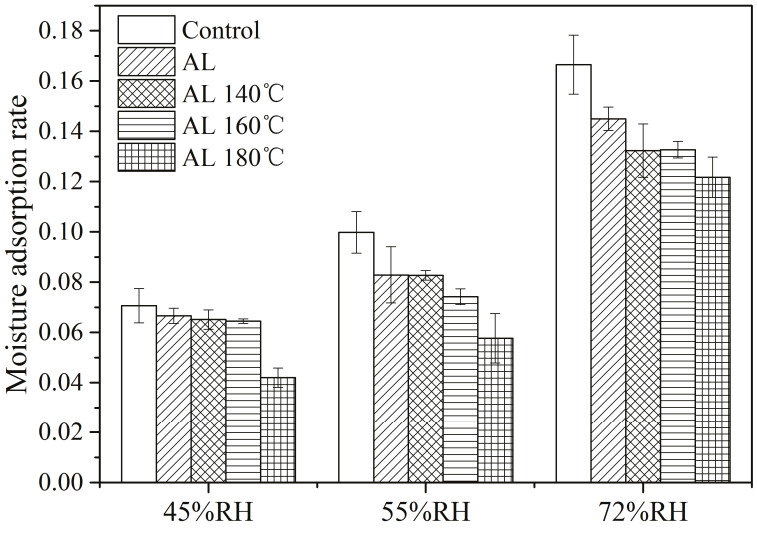

Figure 7. Moisture adsorption rate of the samples during the first 24 h.

As shown in Figure 8, the WAR increased with immersion time. The rate of alkali lignin-modified samples showed an apparent reduction compared with the Control. After 192 hours' immersion, the

WAR of the alkali lignin-modified sample was 65–75% lower than that of the Control. This result indicates that alkali lignin has a remarkable waterproofing effect, owing to the filling effect in the cell cavity of wood fibers or vessels and the blockage effect in the pit caused by alkali lignin (Figure 1). Therefore, water transportation was inhibited. High temperature treatment further decreased WAR slightly, and the degradation of hydrophilic hemicelluloses during thermal treatment could be responsible for this phenomenon, as stated above.

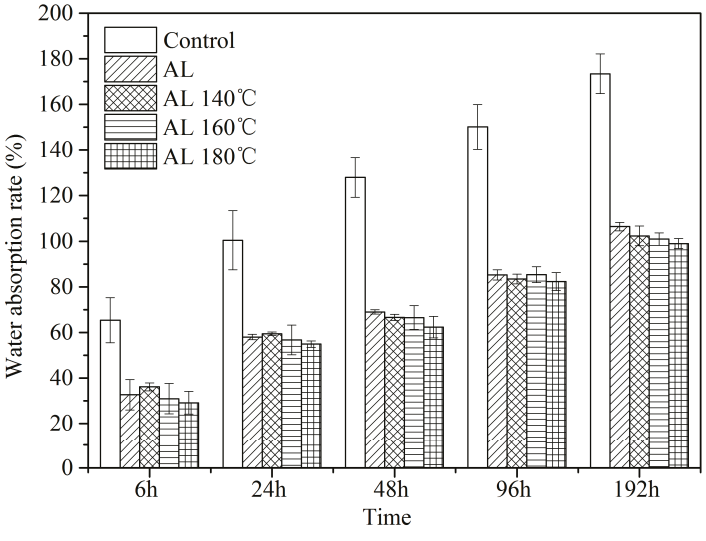

Figure 8. Water absorption rate of the samples as a function of immersion time.

3.7. Dimensional Stability

Figure 9 presents the difference in swelling rate between moisture adsorption and water absorption. In Figure 9a, both the tangential and volumetric swelling rates of AL-treated wood decreased compared with the Control, and the swelling rate reduced more apparently as heat temperature increased. Concerning the tangential swelling rate through moisture adsorption, for example, the values for AL, AL 140 °C, AL 160 °C, and AL 180 °C dropped by 13.8%, 23.8%, 26.4%, and 32.6% compared with the Control, respectively. For swelling rate through water absorption (Figure 9b), the alkali lignin penetration with heat-treatment clearly lowered the tangential and volumetric swelling rates. These results were predictable as both hygroscopicity and WAR decrease as mentioned above (Figures 6 and 8). The swelling of wood could be restrained by alkali lignin plus heat treatment so that the dimensional stability improved. When hydrophobic material like alkali lignin bulks the cell, the water affinity of wood reduces, and the space available for the water molecules to enter the cell wall decreases, which leads to reduced swelling. The results can also be related to the fact that heat treatment at high temperature reduces wood hygroscopicity so as to the long-term dimensional stability improved [30].

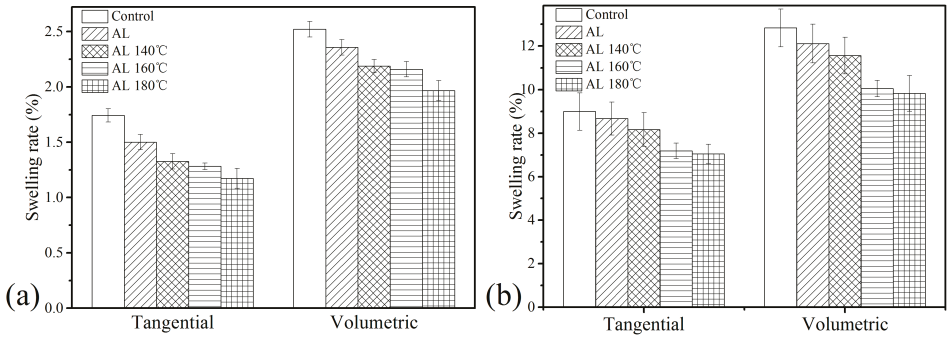

Figure 9. Tangential and volumetric swelling rate of the samples: (**a**) through moisture adsorption (54% RH) and (**b**) through water absorption after 20 days' immersion.

3.8. Compressive Strength

Compression strength values of the samples listed in Table 1 illustrate that the σ value for AL increased slightly compared with the Control and a more obvious improvement was observed as heat treatment temperature increased. This could be interpreted as an enhancement in the mechanical performance achieved by the combined modification. Alkali lignin acts as a stiffener while filling the pore spaces of wood [31], accounting for the increase in compressive strength after impregnation. A negative effect on the mechanical properties of the samples was not found for heat treatment samples. Conversely, the redistribution of alkali lignin and new chemical bonds formed between the alkali lignin and wood matrix benefited from high temperature treatment would further support the improvement in mechanical properties.

4. Conclusions

In this study, we reported an effective, low cost, and sustainable modification method for fast growing wood. The samples modified by alkali lignin combined with heat treatment produced obvious improvement both in hydrophobic properties and dimensional stability, without adversely changing the mechanical properties of the wood. Based on a multiscale modification of the cell cavity as well as cell wall levels, a novel wood with enhanced performance can be used as a fully green product, which can be easily disposed of and used as an ecologically friendly material. Since most chemical modifications are often hindered by ecological drawbacks, such as lack of sustainability, ecoefficiency, and recyclability of the products, this process promotes the efficient and sustainable development of the forestry industry.

Author Contributions: Conceptualization, E.M. and H.Z.; Data curation, H.Z. and J.L.; Formal analysis, H.Z.; Funding acquisition, E.M.; Investigation, H.Z. and J.L.; Resources, E.M.; Supervision, E.M. and H.Z.; Validation, H.Z. and J.L.; Writing—original draft, H.Z.; Writing—review & editing, E.M., J.L. and H.Z.

Funding: This research was funded by Fundamental Research Funds for the Central Universities of China (No. 2017ZY47, No. 2015ZCQ-CL-01).

Conflicts of Interest: The authors declare no conflict of interest.

References

1. Nandanwar, R. Utilization of industrial waste lignin in polymer systems. *Int. J. Knowl. Eng.* **2012**, *31*, 1323–1330.
2. Strassberger, Z.; Tanase, S.; Rothenberg, G. The pros and cons of lignin valorisation in an integrated biorefinery. *RSC Adv.* **2014**, *4*, 25310–25318. [CrossRef]
3. Peng, Y.; Liu, R.; Cao, J.; Chen, Y. Effects of UV weathering on surface properties of polypropylene composites reinforced with wood flour, lignin, and cellulose. *Appl. Surf. Sci.* **2014**, *317*, 385–392. [CrossRef]

4. Kaewtatip, K.; Thongmee, J. Effect of kraft lignin and esterified lignin on the properties of thermoplastic starch. *Mater. Des.* **2013**, *49*, 701. [CrossRef]
5. Behrooz, R.; Kordkheili, H.Y.; Najafi, S.K. Physical properties of lignin added wood flourpolypropylene composites: A comparison of direct and solvent mixing techniques. *Asian. J. Chem.* **2012**, *24*, 157.
6. Braun, J.L.; Holtman, K.M.; Kadla, J.F. Ligninbased carbon fibers: Oxidative thermostabilization of kraft lignin. *Carbon* **2005**, *43*, 385–394. [CrossRef]
7. Dallmeyer, I.; Chowdhury, S.; Kadla, J.F. Preparation and characterization of kraft lignin based moisture-responsive films with reversible shape-change capability. *Biomacromolecules* **2013**, *14*, 2354–2363. [CrossRef] [PubMed]
8. Jian, L. Preparation and characterization of softwood lignin-based carbon fibers. *J. Tribol.* **2013**, *97*, 656. [CrossRef]
9. Wagenführ, A.; Scholz, F. *Taschenbuch der Holztechnik*; Hanser Fachbuch: München, Germany, 2007.
10. Andersson, S.; Serimaa, R.; Väänänen, T.; Paakkari, T.; Jämsä, S.; Viitaniemi, P. X-ray scattering studies of thermally modified Scots pine (*Pinus sylvestris* L.). *Holzforschung* **2005**, *35*, 155–427. [CrossRef]
11. Kavyashree, S.; Krishna, K.P. Effect of heat treatment on color changes, dimensional stability, and mechanical properties of wood. *J. Wood. Chem. Technol.* **2012**, *32*, 304–316. [CrossRef]
12. Zhang, Y.; Xu, D.; Ma, L.; Wang, S.; Liu, X. Influence of Heat Treatment on the Water Uptake Behavior of Wood. *Bioresources* **2017**, *12*, 1697–1705. [CrossRef]
13. Metsä-Kortelainen, S.; Antikainen, T.; Viitaniemi, P. The water absorption of sapwood and heartwood of Scots pine and Norway spruce heat-treated at 170 °C, 190°C, 210 °C and 230 °C. *Holz Roh-Werkst* **2006**, *64*, 192–197. [CrossRef]
14. Macromolecule Academy. *Physical Properties of Macromolecules*; Kyoritsu Press: Tokyo, Japan, 1958.
15. Hailwood, A.J.; Horrobin, S. Absorption of water by polymers: Analysis in terms of a simple model. *J. Chem. Soc. Faraday Trans.* **1946**, *42*, B084–B092. [CrossRef]
16. Ma, J.F.; Yang, G.H.; Mao, J.Z.; Xu, F. Characterization of anatomy, ultrastructure and lignin microdistribution in Forsythia suspensa. *Ind. Crop. Prod.* **2011**, *33*, 358–363. [CrossRef]
17. Sudo, K.; Shimizu, K.; Nakashima, N.; Yokoyama, A. A new modification method of exploded lignin for the preparation of a carbon fiber precursor. *J. Appl. Polym. Sci.* **1993**, *48*, 1485–1491. [CrossRef]
18. Zhang, F.D.; Xu, C.H.; Li, M.Y.; Huang, A.; Sun, S. Rapid identification of Pterocarpus santalinus, and Dalbergia louvelii, by FTIR and 2D correlation IR spectroscopy. *J. Mol. Struct.* **2014**, *1069*, 89–95. [CrossRef]
19. Huang, Y.X.; Ma, E.N.; Zhao, G.J. Thermal and structure analysis on reaction mechanisms during the preparation of activated carbon fibers by KOH activation from liquefied wood-based fibers. *Ind. Crop. Prod.* **2015**, *69*, 447–455. [CrossRef]
20. Moniruzzaman, M.; Ono, T. Separation and characterization of cellulose fibers from cypress wood treated with ionic liquid prior to laccase treatment. *Bioresour. Technol.* **2013**, *127*, 132–137. [CrossRef] [PubMed]
21. Cheng, X.B. *The Influence of Incipient Brown Rot on the Properties of Chinese Fir at Macroscopic and Tissue Level*; Chinese Academy of Forestry: Beijing, China, 2011.
22. Sui, X.J. Study on the Catalytic Liquefaction of Industrial Kraft Lignin for the Production of Phenols. Ph.D. Thesis, South China University of Technology, Guangzhou, China, 2011.
23. Labbé, N.; Rials, T.G.; Kelley, S.S.; Cheng, Z.; Li, Y. FT-IR imaging and pyrolysis-molecular beam mass spectrometry: New tools to investigate wood tissues. *Wood. Sci. Technol.* **2005**, *39*, 61–77. [CrossRef]
24. Müller, G.; Schöpper, C.; Vos, H.; Kharazipou, A.; Polle, A. FTIR-ATR spectroscopic analyses of changes in wood properties during particle-and fibreboard production of hard-and softwood trees. *BioResources* **2008**, *4*, 49–71. [CrossRef]
25. Zhang, Y.; Wu, J.Q.; Li, H.; Yuan, T.Q.; Wang, Y.Y.; Sun, R. Heat treatment of industrial alkaline lignin and its potential application as adhesive for green wood-lignin composites. *ACS Sustain. Chem. Eng.* **2017**, *5*, 7269–7277. [CrossRef]
26. Zhu, X.; Wang, D.; Li, N.; Sun, X. Bio-Based Wood Adhesive from Camelina Protein (a Biodiesel Residue) and Depolymerized Lignin with Improved Water Resistance. *ACS Omega* **2017**, *2*, 7996–8004. [CrossRef]
27. Crick, C.R.; Parkin, I.P. Preparation and characterisation of super-hydrophobic surfaces. *Chemistry* **2010**, *16*, 3568–3588. [CrossRef] [PubMed]
28. Gao, W.; Luo, J.J.; Shi, S.H.; Li, R.; Lu, P.; Guo, X. Effects of steam heat treatment on the surface contact angle of Chinese fir. *Agric. Sci. Technol.* **2014**, *15*, 127.

29. Zhou, H.; Xu, R.; Ma, E. Effects of Removal of Chemical Components on Moisture Adsorption by Wood. *Bioresources* **2016**, *11*, 3110–3122. [CrossRef]
30. Bakar, B.; Hiziroglu, S.; Tahir, P. Properties of some thermally modified wood species. *Mater. Des.* **2013**, *43*, 348–355. [CrossRef]
31. Saidan, M. Improvement of linerboard compressive strength by hot-pressing and addition of recovered lignin from spent pulping liquor. *Chem. Ind. Chem. Eng. Q.* **2014**, *21*, 12. [CrossRef]

polymers

MDPI

Article

Effect of H_2O_2 Bleaching Treatment on the Properties of Finished Transparent Wood

Yan Wu [1,*], Jiamin Wu [1], Feng Yang [2,*], Caiyun Tang [1] and Qiongtao Huang [3]

1 College of Furnishings and Industrial Design, Nanjing Forestry University, Nanjing 210037, China; wujiamin012@163.com (J.W.); tangcaiyun012@163.com (C.T.)
2 Fashion Accessory Art and Engineering College, Beijing Institute of Fashion Technology, Beijing 100029, China
3 Department of Research and Development Center, Yihua Lifestyle Technology Co., Ltd., Shantou 515834, China; huangqt@yihua.com
* Correspondence: wuyan@njfu.edu.cn (Y.W.); yangfeng@bift.edu.cn (F.Y.)

Received: 11 March 2019; Accepted: 25 April 2019; Published: 1 May 2019

Abstract: Transparent wood samples were fabricated from an environmentally-friendly hydrogen peroxide (H_2O_2) bleached basswood (*Tilia*) template using polymer impregnation. The wood samples were bleached separately for 30, 60, 90, 120 and 150 min to evaluate the effects on the changes of the chemical composition and properties of finished transparent wood. Experimental results showed decreases in cellulose, hemicellulose, and lignin content with an increasing bleaching time and while decreasing each component to a unique extent. Fourier transform infrared spectroscopy (FT-IR) and scanning electron microscope (SEM) analysis indicated that the wood cell micro-structures were maintained during H_2O_2 bleaching treatment. This allowed for successful impregnation of polymer into the bleached wood template and strong transparent wood products. The transparent wood possessed a maximum optical transmittance up to 44% at 800 nm with 150 min bleaching time. Moreover, the transparent wood displayed a maximum tensile strength up to 165.1 ± 1.5 MPa with 90 min bleaching time. The elastic modulus (E_r) and hardness (H) of the transparent wood samples were lowered along with the increase of H_2O_2 bleaching treatment time. In addition, the transparent wood with 30 min bleaching time exhibited the highest E_r and H values of 20.4 GPa and 0.45 GPa, respectively. This findings may provide one way to choose optimum degrees of H_2O_2 bleaching treatment for transparent wood fabrication, to fit the physicochemical properties of finished transparent wood.

Keywords: transparent wood; chemical composition; H_2O_2 bleaching treatment; physicochemical properties

1. Introduction

Wood-based materials are widely used in our living environments, such as for housing construction, interior decoration, and furniture manufacturing, etc. [1]. As a novel wood-based material, transparent wood has attracted increasing research interest due to its renewable raw material heritage, outstanding optical transmittance and haze, strong durability as well as its mechanical properties, and finally, its low thermal conductivity [2,3]. The multifunctional transparent wood material not only possessed similar mechanical characteristics to wood in engineering applications, but its unique optical properties can also be beneficially utilized across new fields to expand the applications of the wood. Some examples of these applications include the use of transparent wood as an illuminable structural medium, as a planar light source in luminescent buildings, or as a component of energy efficient smart building, and transparent wood materials are also suitable for application in electronic devices such as conductive substrate, etc. [4–8].

Lignin plays a key role in the visual properties of wood and wood-derived materials, serving as the primary contributor to the opaque color of native wood [9]. To make transparent wood, a crucial step involves beginning with a delignified wood. The superstructure of wood after delignification is then filled with a polymer (or combination of polymers) with a desired refractive index. The finished visual properties of transparent wood is therefore primarily driven by the degree of delignification, as well as the void-filling polymer system chosen.

Recent literature on this specific topic is full of various delignification approaches used to render transparent wood templates (and eventually transparent wood). Fink (1992) developed transparent wood materials based on placing the wood samples for 1–2 days of submersion in a 5% aqueous solution of sodium hypochlorite to remove colored components, including lignin [10]. Li et al. (2016) reported that their delignified transparent wood templates were also prepared using submersion in sodium chlorite ($NaClO_2$), which successfully lowered the lignin content from 24.9% to 2.9% [11]. Qiu et al. (2019) also used 1.5 wt% $NaClO_2$ with an acetate buffer solution (pH 4.6) as a lignin removal solution to impregnate wood samples, and lignin content decreased from 23.5 ± 1.8% for the untreated wood to 1.6 ± 0.2% for the delignified wood after 8 h delignification [12]. Using a different approach, Zhu et al. (2016) reported a means of delignification using a boiling aqueous solution of NaOH and Na_2SO_3, to which additional H_2O_2 was added. In this case, lignin content in the template woods was less than 3% [13]. Liu et al. (2018) also obtained delignified wood by using a 5 g NaOH and 15 g Na_2SO_3 mixing 400 mL methanol (20% volume fraction) water solution to extract wood samples, then the samples were placed in the 1.5 mol/L H_2O_2 solution until the wood yellow color disappeared and the removal rate of lignin reached up to 99.2% [14]. Generally, there are harmful components, such as methyl mercaptan, dimethyl sulfide, and hydrogen sulfide, generated during the delignification process [15]. As can be surmised, these sorts of delignification processes are time-consuming and not necessarily environmentally friendly. In addition, the severity of such processes weakens the mechanical properties of the wood template due to excessive lignin removal. Therefore, it is imperative to optimize the wood template preparation process along the lines of achieving as much lignin retention as possible, and finished transparent wood possessed high light transmittance without significantly sacrificing mechanical properties.

The purpose of this work was to develop a better understanding of how extent of bleaching treatment in transparent wood templates relates to the properties of finished transparent wood materials. An environmentally friendly H_2O_2 bleaching process was adopted, which includes H_2O_2 as a bleaching agent and trisodium citrate dihydrate as a pH stabilizer (used in place of more harmful pH stabilizers). The effect of varying delignification time on the chemical composition and morphological, optical, and macromechanical properties of transparent wood was investigated. In addition, the micromechanical properties of the finished transparent wood were also observed using nanoindentation techniques. The goal of these analyses was to promote the utilization of transparent wood as a novel bio-based material that is both visually appealing and mechanically functional.

2. Experimental

2.1. Materials

Basswood (Tilia) with dimensions of 20 mm long × 20 mm wide × 0.4 mm thick (the depth of the lumina is as long as the length of the wood samples) and ultrapure water were supplied by Yihua Lifestyle Technology Co., Ltd., (Guangdong, China). Trisodium citrate dihydrate was purchased from Sinopharm Chemical Reagent Co., Ltd., (Shanghai, China). Sodium hydroxide (NaOH), Hydrogen peroxide (H_2O_2, 30% solution) and methyl methacrylate (MMA) were provided by Xilong Scientific Co., Ltd., (Guangdong, China). Ethanol was supplied from Tianjin Fuyu Fine Chemical Co., Ltd., (Tianjin, China). 2,2′-Azobis (2-methylpropionitrile) (AIBN) was obtained from Tianjin Benchmark Chemical Reagent Co., Ltd., (Tianjin, China).

2.2. Fabrication of Transparent Wood

Natural wood (NW) samples were first dried at 103 °C for 24 h prior to further bleaching treatment. The bleaching solution was prepared through mixing 6 wt % H_2O_2, 1 wt % trisodium citrate dihydrate, 1 wt % NaOH, and 92 wt % ultrapure water [16]. Afterwards, the bleached wood (BW) samples were prepared from the dried NW by treating it with this bleaching solution at 60 °C for different bleaching times. The Alkaline H_2O_2 bleaching treatment is an environmentally friendly method where the chromophore structures in lignin were removed or selectively reacted and most of lignin was preserved [17]. Because trisodium citrate dihydrate is a safe, non-toxic and biodegradable reagent, it has good PH regulation and buffering performance and could be used as a stabilizer in the process of H_2O_2 bleaching [18]. The bleached wood samples produced were labeled as BW-30, BW-60, BW-90, BW-120, BW-150 samples. These samples correspond to the BW samples produced from NW samples treated for 30, 60, 90, 120 and 150 min, respectively. After treatment, the BW samples were thoroughly washed with ultrapure water and then suspended in ethanol prior to preparation of transparent wood. To begin transparent wood production, pure MMA monomer was uniformly mixed with AIBN initiator (0.5 wt % solution) and pre-polymerized at 75 °C for 15 min [11]. After the designated pre-polymerization time, the impregnation solution was cooled to room temperature. The BW samples were immersed in cooled prepolymerized solution under vacuum for 30 min. Later, the vacuum pump was turned off and the polymer solution was allowed to continue to fill the wood templates for an additional 1 h. Finally, the polymer-infiltrated wood was sandwiched between two pieces of glass and transparent wood (TW) samples were obtained by heated at 70 °C for 5 h. As far as sample labeling is concerned, TW-1, TW-2, TW-3, TW-4 and TW-5 were (respectively) produced from the BW-30, BW-60, BW-90, BW-120 and BW-150 templates. An illustration of the entire preparation process and the finished samples are provided as Figure 1.

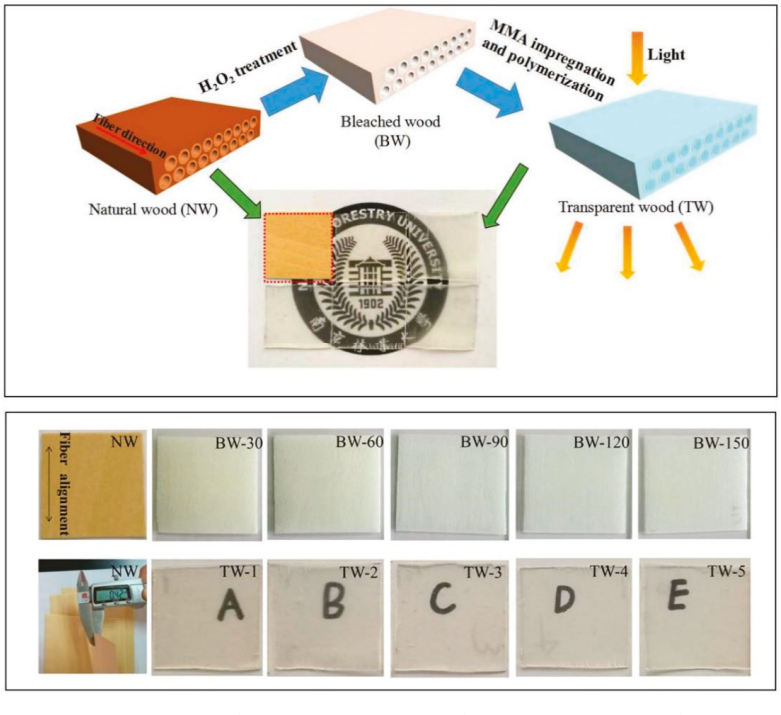

Figure 1. Schematic illustration of the preparation processes for transparent wood and finished samples.

2.3. Chemical Composition Content Analysis

The cellulose, hemicellulose and lignin contents (including acid-insoluble lignin plus acid-soluble lignin) of NW and BW samples were tested by the Laboratory Analytical Procedure (LAP) written by the National Renewable Energy Laboratory (Determination of Structural Carbohydrates and Lignin in Biomass). The main methods were as follows [19]: First, samples were processed into 20–80 meshes of wood powder and dried at 105 °C for 24 h. Then 0.3 ± 0.01 g dried wood powder were put into the hydrolytic flask. The 3.00 ± 0.01 mL 72 wt % concentrated sulfuric acid was added to the hydrolytic flask, and all wood powder samples were infiltrated at the same time. The hydrolysate flasks were all covered and placed in water bath at 30 °C for 1 h. Then the 84.00 mL ± 0.04 mL water was added in the flask. Then flasks were placed into the sterilizer at 121 °C for 1 h and opened after cooling. The hydrolyzed samples were filtered by a constant weight G3 funnel, and 50 mL filtrate was retained for the determination of acid-soluble lignin (measured within 6 h) and sugar concentration. The filtered residue was rinsed with hot deionized water to neutral, and then placed in an oven at 105 °C until constant weight, and the weight was recorded. After constant weight, it was transferred to the muffle furnace and dried at 575 ± 25 °C for 24 ± 6 h. Later, the G3 funnel was taken out and the weight was recorded. The filtrate was diluted with the corresponding multiple, and the UV absorption value was determined by UV spectrophotometer at 205 nm. The filtrate was diluted by a certain multiple, and then the sugar content was analyzed by High performance liquid chromatography (HPLC).

In addition, the content and removing rate of the chemical composition in Table 1 and Figure 2 can be determined by Formulas (1) and (2), respectively [20].

$$\text{Content } (\%) = \frac{M_B}{M_W} \times 100\% \quad (1)$$

$$\text{Removal percentage}(\%) = \frac{M_{NW} - M_{BW}}{M_{NW}} \times 100\% \quad (2)$$

where M_B is the mass of each chemical composition content in samples, M_W is the total mass of the samples, M_{NW} is the mass of each chemical composition content in NW samples, and M_{BW} is the mass of each chemical composition content in BW samples.

2.4. Fourier Transform Infrared Analysis

The attenuated total reflection (ATR) Fourier transform infrared spectroscopy (FT-IR) spectra of NW, BW and TW samples were analyzed using a VERTEX 80 V spectrometer. Spectra were collected over the range from 400 cm^{-1} to 4000 cm^{-1} by 16 scans at a resolution of 4 cm^{-1}. The dimensions of samples were 20 mm long × 20 mm wide × 0.4 mm thick and all samples were dried before analysis.

2.5. Scanning Electron Microscopy

The dried NW, BW and TW samples were coated with gold particles, and then observed with a FEI Quanta 200 scanning electron microscope (SEM) at an accelerating voltage of 20 kV. The cross sections of samples that perpendicular to the direction of the wood fiber alignment were observed.

2.6. Optical Properties

The optical transmittance of NW and TW samples were collected by a *Shanghai youke* UV1900PC spectrophotometer with a wavelength ranging from 350 nm to 800 nm.

2.7. Mechanical Properties

The tensile strength of NW and TW samples were performed in a SANS-CMT6104 electromechanical universal testing machine. The tensile speed was set at 2 mm/min. The dimensions of samples were 20 mm long × 20 mm wide × 0.4 mm thick and stretched in the direction of the fiber alignment.

2.8. Nanoindentation

The nanoindentation test method, the reduced elastic modulus (MOE) (E_r) and hardness (H) measurements upon TW samples, and calculation methods (Formulas (3) and (4)) were all performed according to our previously described research methods [21,22]. The nanoindentation test performed by a Hysitron TriboIndenter system (Hysitron, Inc., Eden Prairie, MN, USA) with scanning probe microscope (SPM) and a three-sided Berkovich type indenter. About 30 valid indents on the wood cell wall were analyzed when the peak load was 400 μN based on a load-controlled mode (the loading time was 5 s, the holding time was 5 s and the unloading time was 5 s). The calculation methods of reduced elastic modulus (MOE) (E_r) and hardness (H) were as follows: Formulas (3) and (4), respectively.

$$E_r = \frac{\sqrt{\pi}}{2\beta}\frac{S}{\sqrt{A}} \quad (3)$$

$$H = P_{max}/A \quad (4)$$

where S is the initial unloading stiffness and β is a correction factor correlated to indenter geometry (β = 1.034), P_{max} is the peak load, and A is the projected contact area of the indents at peak load.

3. Results and Discussion

3.1. Chemical Composition Content Analysis

The NW samples was treated by H_2O_2 bleaching solution and the changes of wood cell wall components as shown in Table 1 and Figure 2. The key components of wood cell wall are linear polysaccharide cellulose, heterogeneous hemicellulose, structurally variable lignin, linkage with each other via hydrogen bond network (between cellulose and hemicellulose) and covalent linkage (between lignin and hemicellulose) [23,24]. Natural lignin is a three-dimensional amorphous polymer with a dark color comprising three types of lignin units, termed syringyl units (S), guaiacyl units (G), and p-hydroxyphenyl units (H) [25]. As can be seen in Table 1 and Figure 2, increasing H_2O_2 bleaching times resulted in increasing removal rates of cellulose, hemicellulose, and lignin. It was found that lignin was the most affected by H_2O_2 bleaching treatment. Regarding lignin removal, the lignin content decreased from 24.3% (NW) to 14.9% (BW-150), translating to a 38.7% delignification in BW-150 compared to NW. A slight decline of cellulose and hemicellulose content took place, decreasing from 48.3% (NW) and 17.2% (NW) to 43.5% (BW-150) and 15.7% (BW-150), respectively. In addition, neither cellulose nor hemicellulose had a removal percentage of more than 10%. One interesting observation was found, in that the removal of cellulose, hemicellulose, and lignin was greatest in the first 30 min of bleaching time. As time was prolonged, the additional removal rates decreased. However, a slightly linear relationship can be visually assessed for lignin removal and the prolonged bleaching times of BW samples. The chromophore structures of lignin were destroyed by oxidizing the carbonyl structure and quinoid structure of lignin side chain during H_2O_2 bleaching [26]. Furthermore, H_2O_2 may react with the benzoquinone structure of lignin to change the solubility of lignin, or react with the side chain carbonyl and carbon-carbon double bond of lignin to further oxidative degradation, leading to lignin removal [27]. Also, during the H_2O_2 bleaching treatment with the existence of alkali, the carbohydrate may be oxidized and degradation of carbohydrate would have occurred [28,29]. The effect of the H_2O_2 bleaching treatment on the wood samples was as expected.

Table 1. Chemical composition content changes of various degrees of H_2O_2 bleaching treatment.

Sample Name	Cellulose Content (%)	Hemicellulose Content (%)	Lignin Content (%)
NW	48.3	17.2	24.3
BW-30	45.0	16.8	19.5
BW-60	44.4	16.5	18.4
BW-90	44.0	16.4	16.6
BW-120	43.9	15.9	15.2
BW-150	43.5	15.7	14.9

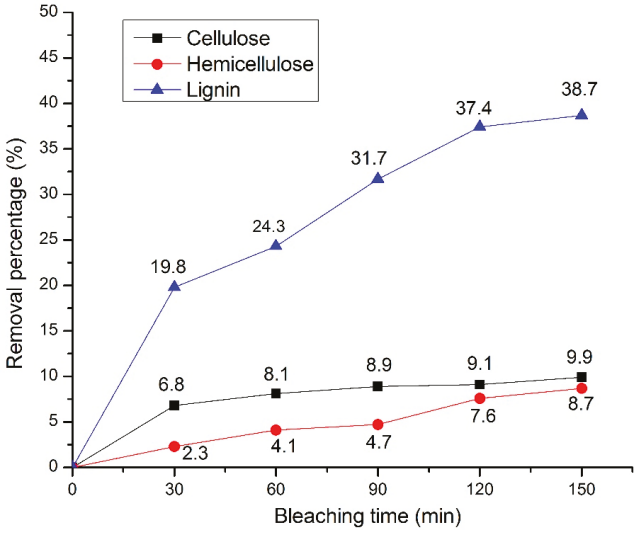

Figure 2. The removal percentage of cellulose, hemicellulose and lignin in wood samples at increasing H_2O_2 bleaching times.

3.2. Fourier Transform Infrared Analysis

Figure 3 shows the FTIR spectra of NW compared against each BW and TW sample. In Figure 3a, characteristic absorption bands of NW samples are marked in the regions of 3330 cm^{-1} (O–H stretch), 2900 cm^{-1} (C–H stretch), 1730 cm^{-1} (C=O stretch in hemicellulose), 1590 cm^{-1} and 1500 cm^{-1} (C=C stretching vibration from lignin), 1370 cm^{-1} (C–H deformation vibration in cellulose and hemicellulose), 1240 cm^{-1} (C–O stretching in lignin and hemicellulose) in Figure 3a [30,31]. The band at 1500 cm^{-1} remained almost unchanged after bleaching treatment as the aromatic lignin had resistance to the hydrogen peroxide treatment [32]. Also after bleaching treatment, the bands at 1240 cm^{-1} and 1370 cm^{-1} in BW samples were shown to be smaller than what is observed in NW samples. In addition, the band at 1730 cm^{-1} (attributed to acetyl groups in hemicelluloses) also weakened and eventually disappeared as the bleaching time increased. The observed changes to the bands were consistent with chemical composition content changes in Table 1, where removal of all three components was observed at increasing treatment times [33]. The spectrum of transparent wood (Figure 3b) showed peaks at 2990 cm^{-1} and 2950 cm^{-1} (C–H stretching of the methyl group), 1720 cm^{-1} (C=O stretching of the ester carbonyl), 1190 cm^{-1} and 1150 cm^{-1} (C–O–C stretching of the ester group), all of which were characteristic of the impregnation polymer PMMA [34]. This observation confirms successful impregnation of MMA solution into the wood template.

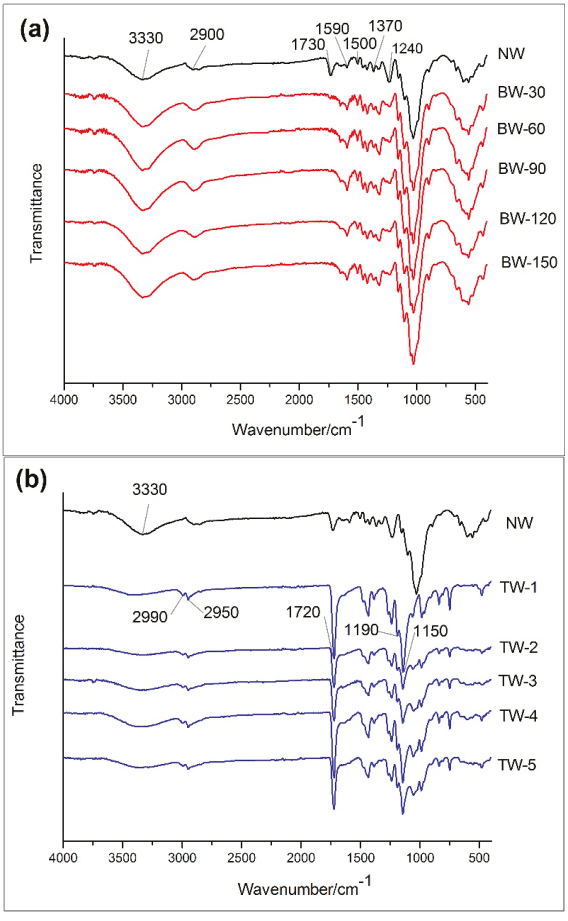

Figure 3. (**a**) FTIR spectra for natural wood (NW) and bleached wood (BW) samples. (**b**) FTIR spectra for natural wood (NW) and transparent wood (TW) samples.

3.3. Scanning Electron Microscopy

As intended, both H_2O_2 bleaching treatment and polymer impregnation resulted in structural changes on the wood surfaces. SEM images acquired of NW, BW and TW samples are each shown in Figure 4 to provide a qualitative assessment of the microstructures of each sample. In addition, simple photographs of NW, BW (BW-150) and TW (TW-5) samples are also shown in Figure 4. As can be seen, the BW (BW-150) sample (Figure 4b) was colorless relative to the NW sample (Figure 4a). This is expected, as we have already established that bleaching removed a fair quantity of color-providing lignin. Speaking to the favorable transparent properties of the TW, the grid lines underneath the TW (TW-5) sample can be clearly seen in Figure 4c. This transparency is also an additional demonstration of successful polymer impregnation. Moving on to microstructural considerations, the microscale pores and their aligned channels can be observed in the SEM images of the BW samples (Figure 4b). This shows that such pores were preserved (comparing Figure 4a,b) in spite of the bleaching treatment while removing color. The main observable difference between the NW and BW microstructures includes the changes to the structure of the cell walls. In NW, the cell wall appears less uniform, while the uniformity increases in the BW samples despite the apparent pore diameters decreasing.

We attribute this difference to removal of both lignin and hemicellulose, biopolymers which are often collectively thought of as binding agents in plant cell wells. By chemically removing a healthy quantity of these binding agents, we are forcing the micromolecular structure to adopt more uniform conformations [35]. As such, we have demonstrated that the bleaching treatment is not severe enough to collapse the lumens of the plant cells, but is selective enough to reduce the visual color of the material itself. Figure 4c shows the SEM images of the TW samples. The displayed TW (TW-5) micrographs show that almost of the cell lumens were successfully filled with the polymer. Furthermore, effective bonding between the interfaces of the wood template surfaces and PMMA polymer and the wood cell walls can be observed. This observation is consistent with similar images and observations reported by Wang et al [36].

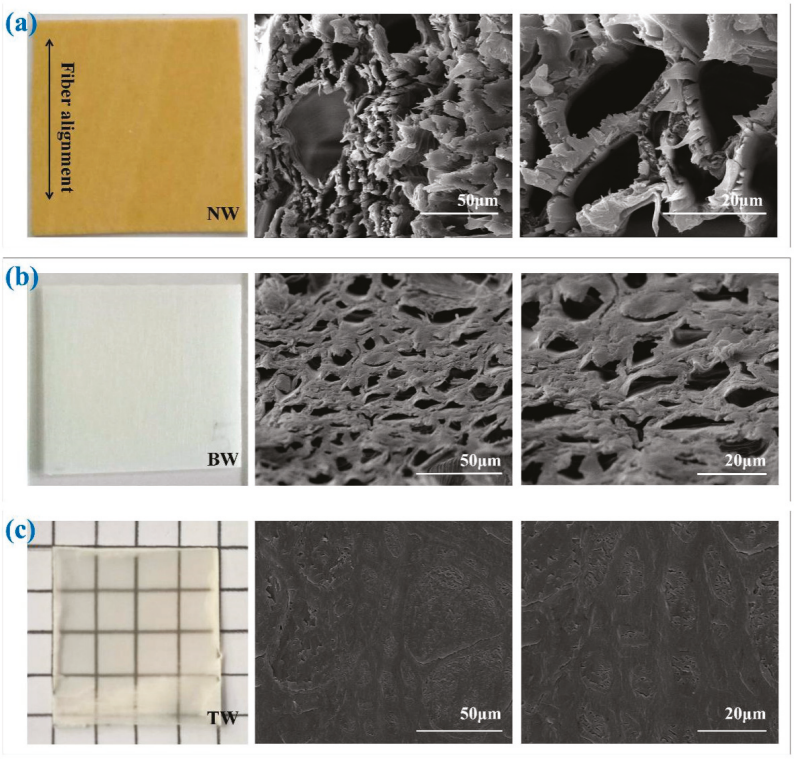

Figure 4. Photographs and SEM images of (**a**) natural wood (NW), (**b**) bleached wood (BW-150) and (**c**) transparent wood (TW-5) samples.

3.4. Optical Properties

Figure 5 shows the optical transmittance of the TW samples with the NW transmittance shown as a control. As a control, the NW sample (24.3% lignin content) exhibited almost 0% optical transmittance due to both light absorption by lignin and light scattering by the porous wood structure [37]. In contrast, it can be seen that TW-5 samples exhibited optical transmittance as high as 44%. The optical transmittance was also found to slightly increase as a function of the template's bleaching time. This finding is congruent to our previous studies, which showed that increasing lignin removal in transparent wood templates contributes to an increase of an optical transmittance value of the finished transparent wood [20]. Specifically, when the lignin content (Table 1) decreased from 19.5% (BW-30) to 14.9% (BW-150), the optical transmittance slightly increased from 38% (TW-1) to 44% (TW-5) at 800 nm.

Beyond lignin removal, each TW sample's transmittance could also be influenced by the viscosity, refractive indices, and shrinkage properties of the PMMA impregnated within [38]. Finally, Figure 5 shows that the optical transmittance of each TW sample increases with measured wavelength (from 350 to 800 nm).

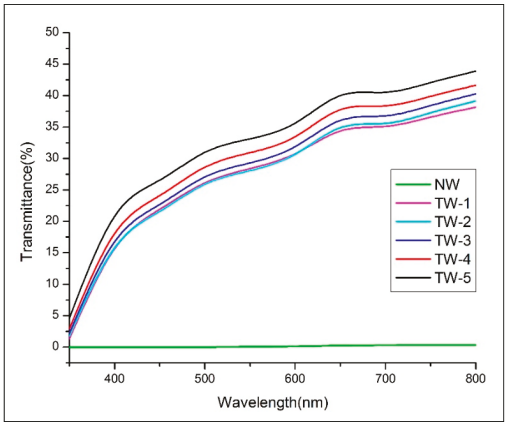

Figure 5. Optical transmittance of natural wood (NW) and transparent wood (TW) samples.

3.5. Mechanical Properties

Figure 6 shows the comparison of tensile strength for NW and a series of TW samples. The tensile strength of TW samples were related to their compositions and chemical structures [39]. All TW samples exhibited stronger tensile strength than NW samples (121.9 ± 6.12 MPa). These results demonstrated that not only was the transparency significantly increased by polymer infiltration, but that mechanical properties could also be improved compared to NW samples [40]. The longitudinally oriented cellulose nanofiber structure and the interaction between wood cellulose nanofibers and PMMA were favorable to the strength of TW samples [41]. It was interesting to find that out of all the TW samples, TW-3 exhibited the greatest tensile strength (165.1 ± 1.5 MPa). An overall pattern of the TW tensile strengths increasing first and then decreasing was observed. This could be due to the wood templates at longer bleaching times being mechanically weaker than the templates produced at shorter bleaching times [42].

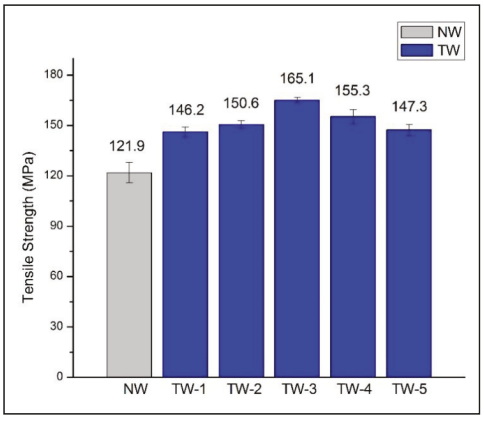

Figure 6. Tensile strength of natural wood (NW) and transparent wood (TW) samples.

3.6. Nanoindentation

The reduced elastic modulus (MOE) (E_r) and hardness (H) of TW cell walls were summarized in Figure 7. It is shown that as the bleaching time increased, both E_r and H of the TW samples obtained showed a downward trend that is concurrent with the removal of lignin, hemicellulose, and cellulose. The TW made from the template with the shortest bleaching time, TW-1, samples exhibited the highest E_r and H values of 20.4 and 0.45 GPa. In comparison, the TW-5 samples exhibited the lowest E_r and H values of 16.4 and 0.37 GPa. With the removal of the wood cell's structural biopolymers at extended bleaching times, the interaction between the main components of the cell wall was weakened, which destroyed the integrity of the cell wall to a certain extent and decreased the E_r of the cell wall [43]. Concerning hemicellulose, its function as an interface coupling agent between cellulose and lignin was increasingly damaged at prolonged bleaching times. Therefore the removal of hemicellulose observed likely also provided significant effect on the E_r of the cell wall in the finished TW materials [43]. Another metric, the cellulose microfibril angle, has also been found to be correlated to the E_r of the wood cell wall [44]. However, the other property measured, H, is governed by the yielding of the cell wall matrix (lignin and hemicelluloses), instead of the property of the microfibrils (or their alignment) [45]. Therefore extraction of hemicellulose and migration of lignin from the matrix surrounding cellulose microfibrils creates pores in the matrix that decrease the density and hardness of the material [46]. The lignin is a dimensional phenolic polymer which imparts rigidity and hydrophobicity to biomass and has a greater effect than hemicellulose on the H of the cell wall [43,47]. The results of nanoindentation were not correlate with the tensile strength. This could be that E_r and H of the TW samples were influenced by the surrounding PMMA polymer, the interface between wood and PMMA polymer, the position of obtained wood sample, and so on.

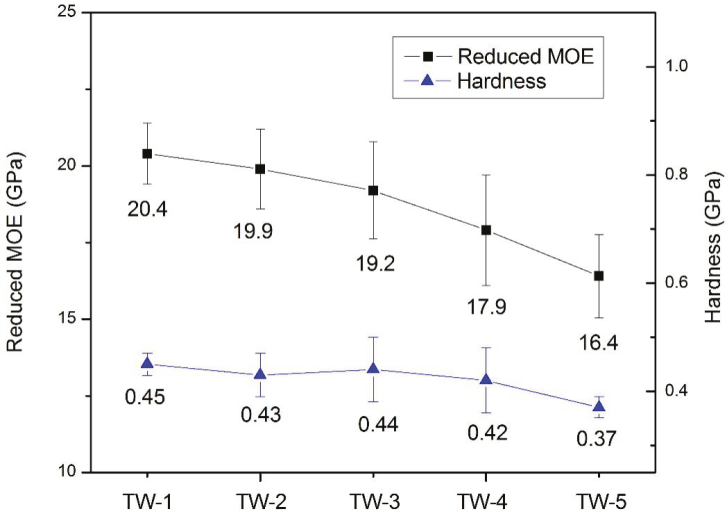

Figure 7. The reduced elastic modulus (MOE) (E_r) and hardness (H) of transparent wood (TW) samples.

4. Conclusions

An environmentally friendly H_2O_2 bleaching treatment method was successfully used to make TW samples. FT-IR and SEM observations showed that the microstructure of the wood cells was still well preserved after bleaching treatment and the MMA was successfully impregnated into the wood template. The optical transmittance and tensile strength of TW samples produced from these templates was superior to NW samples, in spite of the severe chemical compositional changes imparted by the bleaching treatment. The transparent wood possessed a maximum optical transmittance of up to 44 %

at 800 nm and displayed a maximum tensile strength of up to 165.1 ± 1.5 MPa. The E_r and H of the cell wall templates present in the TW sample was also found to be related to the removal of chemical components, as they both decreased at increasing bleaching times. Also, they exhibited the highest E_r and H values of 20.4 and 0.45 GPa. These findings will provide a knowledge base for the further application of transparent wood as a novel home material in various fields of interior decoration.

Author Contributions: Y.W., J.W. and C.T. contributed to synthesis, testing, data analysis, and wrote the manuscript. F.Y. and Q.H. suggested and supervised the work and revised the manuscript.

Funding: This research was funded by the project funded by Jiangsu Government Scholarship for Overseas Studies, Postgraduate Research & Practice Innovation Program of Jiangsu Province (KYCX17-0828), Yihua Lifestyle Technology Co. Ltd. Projects funded (YH-NL-201507) and the Special Scientific Research Fund of Construction of High-level teachers Project of Beijing Institute of Fashion Technology (BIFTQG201805).

Acknowledgments: The authors gratefully acknowledgement the financial support from P.R. China and would like to thank Shang Huang for helping us prepare for the samples.

Conflicts of Interest: The authors declare no conflict of interest.

References

1. Zhao, Z.; Miao, Y.; Yang, Z.; Wang, H.; Sang, R.; Fu, Y.; Huang, C.; Wu, Z.; Zhang, M.; Sun, S.; et al. Effects of sulfuric acid on the curing behavior and bonding performance of tannin-sucrose adhesive. *Polymers* **2018**, *10*, 651. [CrossRef] [PubMed]
2. Li, Y.; Vasileva, E.; Sychugov, I.; Popov, S.; Berglund, L. Optically Transparent Wood: Recent Progress, Opportunities, and Challenges. *Adv. Opt. Mater.* **2018**, *6*, 1800059. [CrossRef]
3. Yaddanapudi, H.S.; Hickerson, N.; Saini, S.; Tiwari, A. Fabrication and characterization of transparent wood for next generation smart building applications. *Vacuum* **2017**, *146*, 649–654. [CrossRef]
4. Vasileva, E.; Li, Y.; Sychugov, I.; Mensi, M.; Berglund, L.; Popov, S. Lasing from organic dye molecules embedded in transparent wood. *Adv. Opt. Mater.* **2017**, *5*, 1700057. [CrossRef]
5. Li, Y.; Yu, S.; Veinot, J.G.C.; Linnros, J.; Berglund, L.; Sychugov, I. Luminescent transparent wood. *Adv. Opt. Mater.* **2017**, *5*, 1600834. [CrossRef]
6. Lang, A.W.; Li, Y.; Keersmaecker, M.D.; Shen, D.E.; Österholm, A.M.; Berglund, L.; Reynolds, J.R. Transparent Wood Smart Windows: Polymer Electrochromic Devices Based on Poly(3,4-Ethylenedioxythiophene):Poly(Styrene Sulfonate) Electrodes. *ChemSusChem* **2018**, *11*, 854–863. [CrossRef] [PubMed]
7. Li, T.; Zhu, M.; Yang, Z.; Song, J.; Dai, J.; Yao, Y.; Luo, W.; Pastel, G.; Yang, B.; Hu, L. Wood Composite as an Energy Efficient Building Material: Guided Sunlight Transmittance and Effective Thermal Insulation. *Adv. Energy Mater.* **2016**, *6*, 1601122. [CrossRef]
8. Tang, Q.; Fang, L.; Wang, Y.; Zou, M.; Guo, W. Anisotropic flexible transparent films from remaining wood microstructures for screen protection and AgNW conductive substrate. *Nanoscale* **2018**, *10*, 4344–4353. [CrossRef]
9. Zhu, M.; Li, T.; Davis, C.S.; Yao, Y.; Dai, J.; Wang, Y.; AlQatari, F.; Gilman, J.W.; Hu, L. Transparent and haze wood composites for highly efficient broadband light management in solar cells. *Nano Energy* **2016**, *26*, 332–339. [CrossRef]
10. Fink, S. Transparent wood—A new approach in the functional study of wood structure. *Holzforschung* **1992**, *46*, 403–408. [CrossRef]
11. Li, Y.; Fu, Q.; Yu, S.; Yan, M.; Berglund, L. Optically transparent wood from a nanoporous cellulosic template: Combining functional and structural performance. *Biomacromolecules* **2016**, *17*, 1358–1364. [CrossRef]
12. Qiu, Z.; Xiao, Z.; Gao, L.; Li, J.; Wang, H.; Wang, Y.; Xie, Y. Transparent wood bearing a shielding effect to infrared heat and ultraviolet via incorporation of modified antimony-doped tin oxide nanoparticles. *Compos. Sci. Technol.* **2019**, *172*, 43–48. [CrossRef]
13. Zhu, M.; Song, J.; Li, T.; Gong, A.; Wang, Y.; Dai, J.; Yao, Y.; Luo, W.; Henderson, D.; Hu, L. Highly anisotropic, highly transparent wood composites. *Adv. Mater.* **2016**, *28*, 5181–5187. [CrossRef]
14. Liu, Y.; Chen, G.; Zhu, J.; Chen, W.; Hu, W.; Liu, Y.; Fang, Z. Preparation, structure and properties of strong, transparent cellulose materials. *Chem. J. Chin. Univ.* **2018**, *39*, 196–201. [CrossRef]

15. Wang, M.; Li, R.; Chen, G.; Zhou, S.; Feng, X.; Chen, Y.; He, M.; Liu, D.; Song, T.; Qi, H. Highly stretchable, transparent and conductive wood fabricated by in-situ photopolymerization with polymerizable deep eutectic solvents. *ACS Appl. Mater. Interfaces* **2019**, *11*, 14313–14321. [CrossRef] [PubMed]
16. Qian, X.; Yu, G.; Liu, H.; An, X. A new way to increase the pulp bleaching efficiency of hydrogen peroxide. Trans. *China Pulp Pap.* **2002**, *17*, 36–39. [CrossRef]
17. Li, Y.; Fu, Q.; Rojas, R.; Yan, M.; Lawoko, M.; Berglund, L. A new perspective on transparent wood: Lignin-retaining transparent wood. *ChemSusChem* **2017**, *10*, 3445–3451. [CrossRef]
18. Yan, D.; Liu, M. Hydrogen peroxide bleaching of AS-AQ wheat straw pulp after oxygen delignification. *China Pulp Pap. Ind.* **2008**, *9*, 38–41. [CrossRef]
19. Sluiter, A.; Hames, B.; Ruiz, R.; Scarlata, C.; Sluiter, J.; Templeton, D.; Crocker, D. *Determination of Structural Carbohydrates and Lignin in Biomass: Laboratory Analytical Procedure (LAP)*; Technical Report NREL/TP-510-42618; National Renewable Energy Laboratory: Golden, CO, USA, 2011.
20. Wu, J.; Wu, Y.; Yang, F.; Tang, C.; Huang, Q.; Zhang, J. Impact of delignification on morphological, optical and mechanical properties of transparent wood. *Compos. Part A* **2019**, *117*, 324–331. [CrossRef]
21. Wu, Y.; Wang, S.; Zhou, D.; Xing, C.; Zhang, Y. Use of Nanoindentation and Silviscan to Determine the Mechanical Properties of 10 Hardwood Species. *Wood Fiber Sci.* **2009**, *41*, 64–73.
22. Wang, X.; Chen, X.; Xie, X.; Wu, Y.; Zhao, L.; Li, Y.; Wang, S. Effects of thermal modification on the physical, chemical and micromechanical properties of Masson pine wood (Pinus massoniana Lamb.). *Holzforschung* **2018**. [CrossRef]
23. Zhang, N.; Li, S.; Xiong, L.; Hong, Y.; Chen, Y. Cellulose-hemicellulose interaction in wood secondary cell-wall. *Model. Simul. Mater. Sci. Eng.* **2015**, *23*, 085010. [CrossRef]
24. Huang, C.; Su, Y.; Shi, J.; Yuan, C.; Zhai, S.; Yong, Q. Revealing the effects of centuries ageing on the chemically structural features of lignin in archaeological fir woods. *New J. Chem.* **2019**, *43*, 3520–3528. [CrossRef]
25. Huang, C.; He, J.; Du, L.; Min, D.; Yong, Q. Structural Characterization of the Lignins from the Green and Yellow Bamboo of Bamboo Culm (Phyllostachys pubescens). *J. Wood Chem. Technol.* **2016**, *36*, 157–172. [CrossRef]
26. Pang, J.; Liu, Z.; Hui, L.; Jiang, H. Recent Developments of Hydrogen Peroxide Bleaching Technology. *Pap. Pap. Mak.* **2013**, *32*, 28–32. [CrossRef]
27. Wang, L.; Ouyang, T.; Dai, X.; Lu, X.; Liang, H.; Deng, R.; Cheng, F. Preparation of Transparent Cellulose Membrane by Hydrogen Peroxide Bleaching of Cellulose-Rich Materials. *For. Eng.* **2018**, *34*, 41–45.
28. Qu, L.; Zhu, S.; Liu, M.; Wang, S. The mechanism and technology parameters optimization of alkali-H_2O_2 one-bath cooking and bleaching of hemp. *J. Appl. Polym. Sci.* **2010**, *97*, 2279–2285. [CrossRef]
29. Wang, X.; Chen, J.; Pang, Z.; Yang, G. The Technology of Chlorine Dioxide and Hydrogen Peroxide Bleaching. *Shanghai Pap. Mak.* **2011**, *42*, 55–61. [CrossRef]
30. Li, C.; Knierim, B.; Manisseri, C.; Arora, R.; Scheller, H.V.; Auer, M.; Vogel, K.P.; Simmons, B.A.; Singh, S. Comparison of dilute acid and ionic liquid pretreatment of switchgrass: Biomass recalcitrance, delignification and enzymatic saccharification. *Bioresour. Technol.* **2010**, *101*, 4900–4906. [CrossRef]
31. Xiong, X.; Bao, Y.; Liu, H.; Zhu, Q.; Lu, R.; Miyakoshi, T. Study on mechanical and electrical properties of cellulose nanofibrils/graphene-modified natural rubber. *Mater. Chem. Phys.* **2019**, *223*, 535–541. [CrossRef]
32. Wójciak, A.; Kasprzyk, H.; Sikorska, E.; Khmelinskii, I.; Krawczyk, A.; Oliveira, A.S.; Ferreira, L.F.V.; Sikorski, M. Changes in chromophoric composition of high-yield mechanical pulps due to hydrogen peroxide bleaching under acidic and alkaline conditions. *J. Photochem. Photobiol. A* **2010**, *215*, 157–163. [CrossRef]
33. Gierlinger, N.; Goswami, L.; Schmidt, M.; Burgert, I.; Coutand, C.; Rogge, T.; Schwanninger, M. In Situ FT-IR Microscopic Study on Enzymatic Treatment of Poplar Wood Cross-Sections. *Biomacromolecules* **2008**, *9*, 2194–2201. [CrossRef] [PubMed]
34. Yap, M.G.S.; Que, Y.T.; Chia, L.H.L. FTIR characterization of tropical wood-polymer composites. *J. Appl. Polym. Sci.* **1991**, *43*, 2083–2090. [CrossRef]
35. Yang, W.; Feng, Y.; He, H.; Yang, Z. Environmentally-Friendly Extraction of Cellulose Nanofibers from Steam-Explosion Pretreated Sugar Beet Pulp. *Materials* **2018**, *11*, 1160. [CrossRef] [PubMed]
36. Wang, X.; Zhan, T.; Liu, Y.; Shi, J.; Pan, B.; Zhang, Y.; Cai, L.; Shi, S. Large-Size Transparent Wood for Energy-Saving Building Applications. *Chem. Sus. Chem.* **2018**. [CrossRef]

37. Gan, W.; Xiao, S.; Gao, L.; Gao, R.; Li, J.; Zhan, X. Luminescent and transparent wood composites fabricated by PMMA and γ-Fe_2O_3@YVO_4:Eu^{3+} nanoparticles impregnation. *ACS Sustain. Chem. Eng.* **2017**, *5*, 3855–3862. [CrossRef]
38. Li, Y.; Fu, Q.; Yang, X.; Berglund, L. Transparent wood for functional and structural applications. Phil. *Trans. R. Soc. A* **2018**, *376*, 20170182. [CrossRef]
39. Yadav, M.; Chiu, F.-C. Cellulose nanocrystals reinforced-carrageenan based UV resistant transparent bionanocomposite films for sustainable packaging applications. *Carbohydr. Polym.* **2019**, *211*, 181–194. [CrossRef]
40. Jiang, F.; Li, T.; Li, Y.; Zhang, Y.; Gong, A.; Dai, J.; Hitz, E.; Luo, W.; Hu, L. Wood-Based Nanotechnologies toward Sustainability. *Adv. Mater.* **2017**, *30*, 1703453. [CrossRef]
41. Yu, Z.; Yao, Y.; Yao, J.; Zhang, L.; Chen, Z.; Gao, Y.; Luo, H. Transparent wood containing $CsxWO_3$ nanoparticles for heat-shielding window applications. *J. Mater. Chem. A* **2017**, *5*, 6019–6024. [CrossRef]
42. Yano, H.; Hirose, A.; Collins, P.J.; Yazaki, Y. Effects of the removal of matrix substances as a pretreatment in the production of high strength resin impregnated wood based materials. *J. Mater. Sci. Lett.* **2001**, *20*, 1125–1126. [CrossRef]
43. Wang, C.; Jiang, Z.; Fei, B.; Yu, Y.; Zhang, S. Effects of chemical components on longitudinal MOE and hardness of wood cell wall. *J. Beijing For. Univ.* **2012**, *34*, 107–110.
44. Konnerth, J.; Gierlinger, N.; Keckes, J.; Gindl, W. Actual versus apparent within cell wall variability of nanoindentation results from wood cell walls related to cellulose microfibril angle. *J. Mater. Sci.* **2009**, *44*, 4399–4406. [CrossRef]
45. Tze, W.T.Y.; Wang, S.; Rials, T.G.; Pharr, G.M.; Kelley, S.S. Nanoindentation of wood cell walls: Continuous stiffness and hardness measurements. *Compos. Part A* **2007**, *38*, 945–953. [CrossRef]
46. Hosseinaei, O.; Wang, S.; Rials, T.G.; Xing, C.; Zhang, Y. Effects of decreasing carbohydrate content on properties of wood strands. *Cellulose* **2011**, *18*, 841–850. [CrossRef]
47. Huang, C.; Tang, S.; Zhang, W.; Tao, Y.; Lai, C.; Li, X.; Yong, Q. Unveiling the structural properties of lignin–carbohydrate complexes in bamboo residues and its functionality as antioxidants and immunostimulants. *ACS Sustain. Chem. Eng.* **2018**, *6*, 12522–12531. [CrossRef]

polymers

MDPI

Article

Larch Wood Residues Valorization through Extraction and Utilization of High Value-Added Products

Kerstin Wagner [1,2], Maurizio Musso [3], Stefan Kain [1], Stefan Willför [4], Alexander Petutschnigg [1,5] and Thomas Schnabel [1,*]

1 Department of Forest Products Technology & Timber Constructions, Salzburg University of Applied Sciences, Marktstraße 136a, 5431 Kuchl, Austria; kerstin.wagner@stud.sgb.ac.at (K.W.); stefan.kain@fh-salzburg.ac.at (S.K.); alexander.petutschnigg@fh-salzburg.ac.at (A.P.)

2 Salzburg Center for Smart Materials, c/o Department of Chemistry and Physics of Materials, Paris Lodron University of Salzburg, Jakob-Haringer-Strasse 2A, 5020 Salzburg, Austria

3 Department of Chemistry and Physics of Materials, Paris Lodron University of Salzburg, Jakob-Haringer-Strasse 2A, 5020 Salzburg, Austria; maurizio.musso@sbg.ac.at

4 Laboratory of Natural Materials Technology, Åbo Akademi University, Porthasgatan 3, 20500 Turku/Åbo, Finland; stefan.willfor@abo.fi

5 Department of Material Sciences and Process Engineering, BOKU University of Natural Resources and Life Sciences, Konrad Lorenz-Straße 24, 3340 Tulln, Austria

* Correspondence: thomas.schnabel@fh-salzburg.ac.at; Tel.: +43-50-2211-2403

Received: 29 November 2019; Accepted: 13 January 2020; Published: 6 February 2020

Abstract: Many of current bio-based materials are not fully or partly used for material utilization, as the composition of their raw materials and/or possible applications are unknown. This study deals with the analysis of the wood extractives from three different tissue of larch wood: Sapwood mainly from outer part of the log, and sound knotwood as well as dead knotwood. The extractions were performed with an accelerated solvent extractor (ASE) using hexane and acetone/water. The obtained extracts were analyzed by gas chromatography coupled to mass spectrometry (GC-MS). Three various vibrational spectroscopy (FT-RAMAN, FT-IR and FT-NIR) methods reflect the information from the extracts to the chemical composition of the types of wood before the extraction processes. Multivariate data analysis of the spectra was used to obtain a better insight into possible classification methods. Taxifolin and kaempferol were found in larger amount in sound knotwood samples compared to larch wood with high percentage of sapwood and dead knotwood samples. While the extractions of dead knotwood samples yielded more larixol and resin acids than the other larch wood samples used. Based on the chemical composition, three lead compounds were defined for the classification of the different wood raw materials. The vibrational spectroscopy methods were applied to show their potential for a possible distinction of the three types of larch wood tissue. This new insight into the different larch wood extracts will help in the current efforts to use more environmentally friendly raw materials for innovative applications. The connection between the raw materials and extraction yields of the target values is important to transform the results from the laboratory to industry and consumer applications.

Keywords: GC-MS; kaempferol; knotwood; larixol; taxifolin; vibrational spectroscopy

1. Introduction

Regarding the bio-economy and bio-refinery approach, not all substances in the wood are currently used. New thinking and techniques are helpful to exploit the huge potential of bio-based products for innovative applications from the laboratory to industry. Different gaps exist and bridges are necessary to use the by-products (e.g., bark) for new applications (e.g., bio-based polymers) and not only for

energy generation [1–4]. This study deals with the analysis of wood chips from an industrial Austrian sawmill for the potential uses of wood extractives.

The European larch (*Larix decidua* Mill.) is a commercially important species in the European Alpine areas and larch wood chips are normally produced as one of the by-products during the sawing process of wood. The outer part (mostly of it is sapwood) of the timber round wood cannot be used for the sawn wood and it is chopped to wood chips and used as thermal energy resources in larger part. As larch wood is not a preferred pulpwood species [5], since the amounts of resin and other extractives are large [6,7]. Furthermore, there is a non-negligible amount of knots in the fraction of these wood chips, which are sorted out during the pulp and paper process. However, knots contain exceptionally large amounts of secondary plant metabolites (e.g., phenolic compounds). The amount of knot wood extracts is often higher than in the stemwood for many tree species [8–10], and the hydrophilic compounds exhibit strong bioactivity against oxidation, bacteria and fungi exploitable for various new applications (e.g., dietary supplements and cosmetic products) [8,11–13].

A knot or knotwood is indicated as the part of the branch which starts to grow from the pith and is hidden inside the stem. Two different types of knots can be distinguished, based on their function (Figure 1). Sound knots are connected with the stem wood and intact branches of the tree. If the lifetime of the branch is over then the tree loses the branches; however, the knot will be protected against bacteria and fungi by the wood extractives [14]. This knot is called a dead knot. As the stem grows further, it will gradually grow over the stump of lost branches, and finally the knot will be completely embedded in the stem wood (cf. Figure 1b).

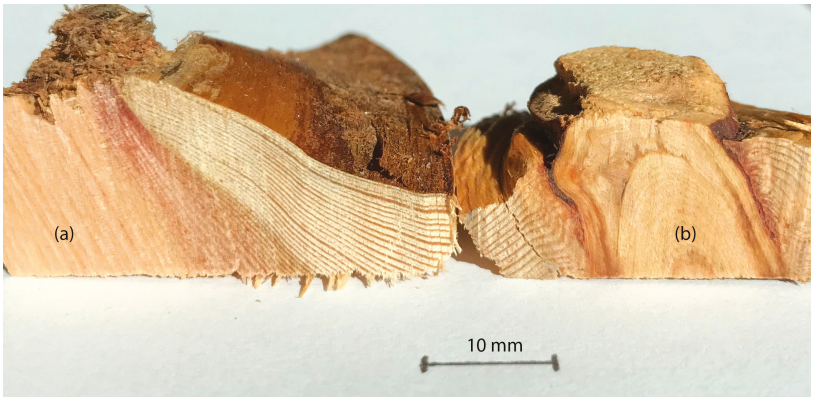

Figure 1. (**a**) One example of a larch wood chip with a sound knot and the intact connection between knot and stem wood; (**b**) a larch wood chip with a dead knot and the inclusion of bark as well as oxidized resin.

The chemical composition of sound and dead knots of different larch wood species has been analyzed by Nisula [15]. As polyphenols are responsible for different functions of wood extracts (e.g., antimicrobial activities) [8,12,13], the results of chemical analysis of different parts of the trees are interesting for discovering wood tissues with a large extraction yield. The difference between both knot types was not focused upon in various studies of extractives and material properties [8–10,13]. GC-MS analyses are often applied to determine the chemical composition of wood extractives [6,8–10,12,13]. This method gives reliable results and is used for the detection of single components of natural extracts. However, in some processes less time-consuming analytical methods are important for the identification of different materials. Vibrational spectroscopy methods have much potentials for the sensitive and selective determination of organic compounds in wood and wood extractives [16–18]. These methods are also relatively inexpensive to implement and easy to apply; furthermore, they are non-destructive techniques [19].

In this study, the qualitative and quantitative chemical differences of sound and dead knots extracts were analyzed using a GC-MS method. New insight into the different extracts contents of bio-based polymers in natural resources will help in the current efforts to use more environmentally friendly raw materials for innovative applications. Based on the chemical composition, three lead compounds were defined for the classification of the different wood raw materials. Furthermore, FT-RAMAN, FT-IR and FT-NIR vibrational spectroscopy methods were applied for development of classification between sound and dead knots, which is also needed for the transformation of the results from the laboratory to the industry. The connection between raw materials and extraction yields of the target values is important for the utilization of different current unused wood tissues.

2. Materials and Methods

2.1. Wood Material

The wood chips of heart and sapwood from the outer part of the timber round wood as well as sound and dead knots from European larch (*Larix decidua* Mill.) trees were collected from an Austrian larch sawmill and ground with a cut mill (Retsch) using solid carbon dioxide to pass a mesh of 500 µm. The wood powder was then freeze-dried.

2.2. Chemicals

Taxifolin and kaempferol were produced by Alfa Aesar and Cayman, respectively, were used as reference.

2.3. Solid-Liquide Extraction

The extraction was done with an ASE (Accelerated Solvent Extractor) according to Willför [10]. The larch was first extracted with hexane (solvent temperature 90 °C, pressure 13.8 MPa, 2 × 5 min static cycles) and then with acetone (VWR) and water in a ratio 95/5 mixture (100 °C, 13.8 MPa, 2 × 5 min).

2.4. GC-MS Characterization

Before GC-MS analysis, the different extractives were evaporated using nitrogen gas and silylated to enhance volatility. For silylation, the evaporated extractives were first dried in a vacuum oven at 40 °C (Binder, Herbertshausen, Germany) and then silylation solvents (80 µL bis-(trimethylsilyl)-trifluoroacetamide, 20 µL pyridine and 20 µL trimethylsilyl-chloride) were added. Finally, the samples were incubated at 70 °C for 45 min. Measurements were performed using a Perkin Elmer Auto-System XL gas chromatograph (GC; PerkinElmer Inc., Waltham, MA, USA) and a GC-MS (HP 6890-5973 from Agilent Technologies Inc., Santa Clara, CA, USA). The GC was equipped with a HP-5 column (length: 25 m; ID: 0.20 mm; film thickness 0.11 µm) and a flame ionization detector (FID). The carrying gas was nitrogen at a flow rate of 0.8 mL/min. Furthermore, other conditions were: internal oven 120 °C with an increasing rate at 6 °C/min to 320 °C (15 min hold); a split injection with a ratio of 25:1 and a temperature of 250 °C; the detector temperature 310 °C and injection volume of 1 µL. The data were analysed based on the mass spectra library created at the Laboratory of Natural Materials Tehcnology at Åbo Akademi University.

2.5. Fourier Transform-RAMAN Spectroscopy

The wood powders (cf. Section 2.1) of different materials were examined in the NIR spectral region by FT-RAMAN using an IFS 66 FT-IR spectrometer (Bruker, Ettlingen, Germany) equipped with a Raman module FRA 106 and having a laser source at 1064 nm and a maximum power of 100 mW. The spectra were taken in the wavenumber range of 3500–100 cm^{-1} with a FWHM-resolution of 4 cm^{-1} and 400 cumulated scans.

2.6. Fourier Transform Infrared Spectroscopy

Small thin sliced samples of the various parts of the wood were produced and measured. The FT-IR spectra of different solid wood parts were recorded between 4000 and 600 cm^{-1} with 32 scans at a resolution of 4 cm^{-1} using a Frontier FT-IR spectrometer (PerkinElmer, Waltham, MA, USA) equipped with a Miracle diamond ATR accessory with a 1.8 mm round crystal surface. All spectra were ATR corrected and two single spectra per sample were averaged. The spectra were baseline corrected in the wavenumber range between 4000 and 600 cm^{-1}.

2.7. Fourier Transform Near-Infrared Spectroscopy

The FT-NIR spectra were obtained from the different surfaces of the wood chips, and from pre-selected sound and dead knots, by an MPA spectrometer (Bruker) equipped with a fibre probe (4 mm measurement diameter) at a resolution of 8 cm^{-1} (32 scans). For every type of wood (e.g., sound and dead knots), a minimum of five samples were selected. Two single spectra of each sample were averaged to minimize the influence of variation on different material surfaces.

2.8. Data Analysis

The Unscrambler X 10.3 software (CAMO, Norway) was used for the data analysis. The FT-NIR spectra were managed without data treatment, and also a second derivative method with 17 smoothing points for the presentation of the NIR data was applied. Principal component analysis (PCA) is a linear project method to reduce the multidimensional data to only few orthogonal features (principal components (PCs)) and was used to show the potential of a possible assignment of chemical information of the various wood types.

3. Results and Discussion

3.1. GC-MS Characterization

Table 1 shows the total amounts of characterized component groups in acetone/water extracts in mg/g of freeze-dried powder of larch wood mixture (heart wood and sapwood), sound knots and dead knots. The amount of total extraction gravimetric yields of the acetone/water solution differed in a range from 3.38 mg/g of dried mixture wood (sapwood and heart wood), 27.13 mg/g of dried sound knotwood and 1.53 mg/g of dried dead knotwood. The hydrophilic extracts of the different wood parts contained various component groups. Based on results of the qualitative analysis all component groups (e.g., carboxylic acids) were found in each material. Nevertheless, there exist high differences in the quantitative results for the group of polyphenols.

Table 1. Main component groups in acetone/water extracts of different larch wood materials by GC-MS.

Component Groups	Larch Wood Mixture (mg/g)	Sound Knotwood (mg/g)	Dead Knotwood (mg/g)
Carboxylic acids	0.026	0.139	0.011
Phenolic acids	0.116	1.666	0.081
Sugar	0.206	0.472	0.045
Fatty acids	0.140	0.483	0.047
Resin acids	0.079	0.186	0.014
Polyphenols	2.726	23.766	1.305
Sterols	0.016	0.235	0.011

The taxifolin and kaempferol amounts in acetone/water extracts of the sound knotwood were higher compared to the larch wood and dead knotwood (Figure 2). Both compounds have an antioxidative potency and/or antimicrobial activities [8,12,13]. Compared to the results of other studies, the determined amount of taxifolin and kaemperol were lesser in this study. Zule et al. [6] used

only larch heartwood for their study, which has a larger total amount of flavonoids compared to sapwood [15]. The used wood chips for this study were from the outer part of the logs and were mostly sapwood. Nevertheless, the samples of the sound knotwood showed the largest amount of taxifolin and kaempferol compared with the larch wood (Figure 2).

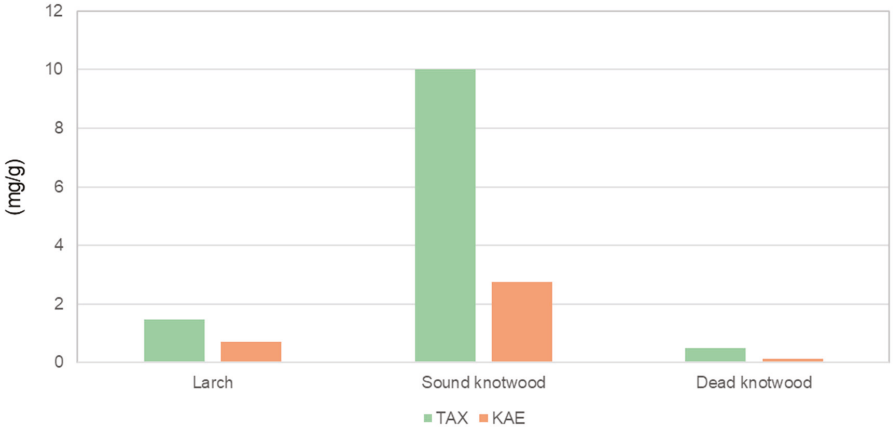

Figure 2. Content and composition of two main phenolic compounds of wood, sound knot and dead knot of larch trees (TAX—taxifolin, KAE—kaempferol).

The results of the hexane extracts of the different tree sections showed differences compared to the acetone/water extracts. The amount of total extraction yields from the dead knotwood was the highest for 7.06 mg/g of dried material, followed by the sound knotwood with 5.05 mg/g and larch wood with an amount of 2.46 mg/g of dried materials. Larixol and resin acids (e.g., isopimaric acid) were the main compounds of dead knot and sound knotwood.

3.2. Univariate Analyis Method of Different Vibrational Spectrosocpy Methods

The wood powder was also analyzed by an FT-RAMAN spectroscopy method. Based on the results from the GC-MS analysis, small differences for the identification of larch wood, sound and dead knotwood know wood should be characterized. The spectra of the various samples presented almost the same peak profile (Figure 3), while the bands at 2930 and 2895 cm^{-1} changed the ratio to each other, which correspond to the CH groups (e.g., CH_2 and CH_3) [20,21] and assigned to different wood compounds (e.g., cellulose and extractives).

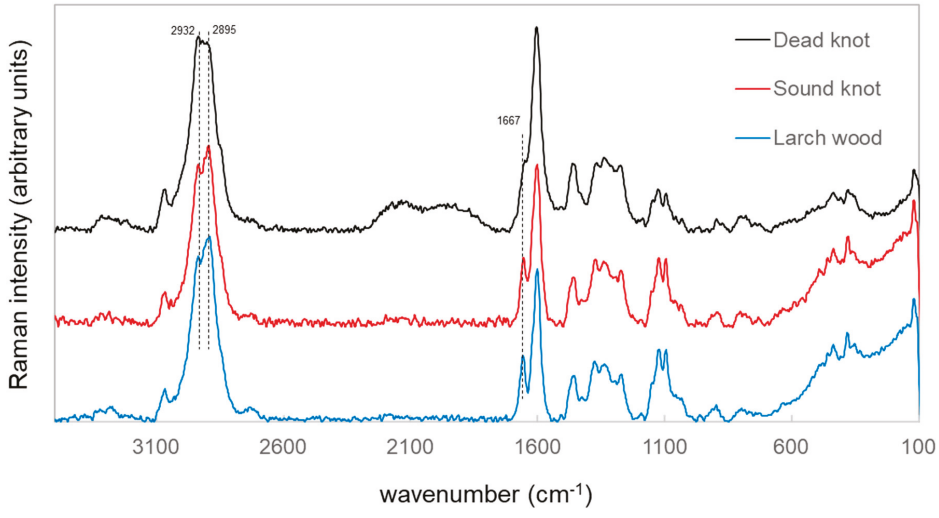

Figure 3. FT-RAMAN spectra of larch wood, sound knotwood and dead knotwood powders, obtained with 1064 nm laser excitation.

Lignin molecules can be observed in the peak at around 1667 and 1660 cm^{-1}, corresponding to an unsaturated molecule (C=C) with a carbonyl group (C=O), which overlaps with the vibration of flavonoid aromatic molecules [18,20]. Furthermore, some resin acids of wood have RAMAN vibrational activity in the range of 1666 to 1638 cm^{-1} [20,22]. A slight Raman shift at around 1667 cm^{-1} can be seen by comparison of the spectrum of dead knotwood materials with the other samples. Therefore, a vibration superimposition of lignin, flavonoids and resin acids may have happened in this range. It can be also assumed that the wood extractives are not homogeneously distributed in the different sample types (e.g., wood and knots) and the used samples preparation method did not support a differentiation between different wood and knotwood samples.

A similar study was run using FT-IR spectroscopy with an ATR unit and the different larch wood types as well as taxifolin and kaempferol as references to analyze the chemical differences (Figure 4), which were found as predominant polyphenols in the GC-MS characterization. The spectrum of larch wood differs significantly in some peak profiles from the knotwood spectra. This tendency is detected for all peaks at 2919, 2880, 1734, 1694, 1630, 1506, 1451, 1316 and 1264 cm^{-1}, although the differences cannot be explained in all cases by the consideration of the spectra of taxifolin and kaemperol compounds. The bands around 1736 and 1694 cm^{-1} did not show any IR signal of the references used and can correspond to carbonyl groups in different molecule arrangements [23].

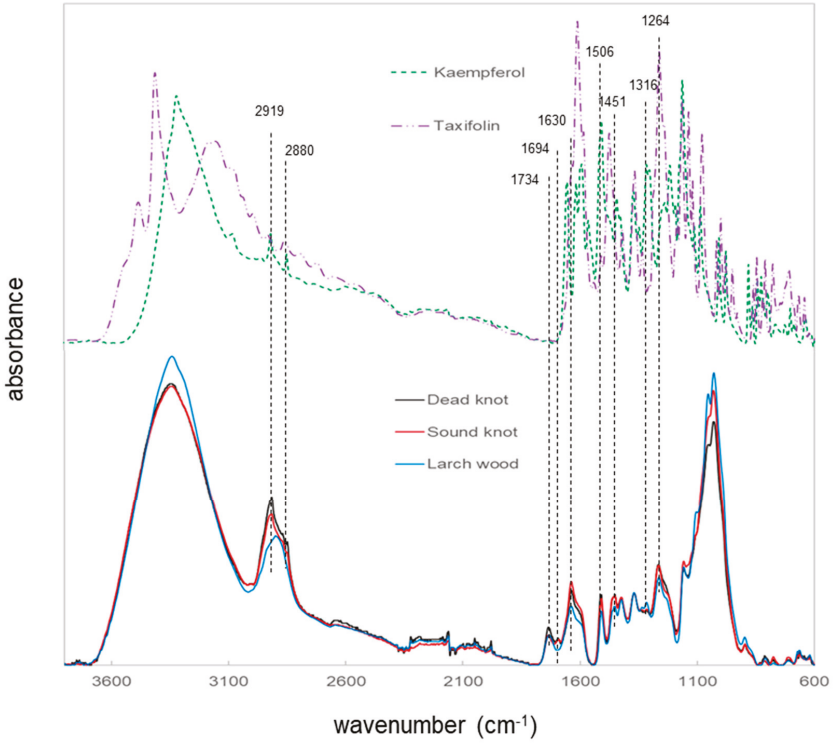

Figure 4. ATR FT-IR spectra of larch wood, sound and dead knotwood as well as kaempferol and taxifolin.

Furthermore, larixol shows vibrational infrared activities in the range of wavenumber between 1750 and 1660 cm^{-1} [24]. Larixol and resin acids were predominantly observed in the different knotwood samples and can correspond to the observed bands in the spectra. The IR absorbance bands at 2919 and 2880 cm^{-1} changed significantly to each other, which correspond to differences in the amount of CH groups (e.g., CH_2 and CH_3) [17]. This fact could be assigned to higher amount of bio-polymers in knotwood samples. The infrared spectra depicted that there is a possible differentiation between the larch wood samples and the knotwood samples. The direct measurements on the various wood samples gave more detailed information about the chemical differences compared to the wood powder, which was used for the RAMAN spectroscopy. With respect to these results, a method for classification of different wood samples with vibrational spectroscopy can be further developed. FT-NIR spectroscopy is very often used for this process [17–20].

The chemical information relating to three various larch wood types was obtained by using the FT-NIR spectroscopy (NIRS). Figure 5 shows the original spectra in the region between the wavenumber range 12,500–4000 cm^{-1} of the larch wood, sound knotwood and dead knotwood samples. The original spectra present differences in the wavenumber range between 6000 and 5300 cm^{-1}, which are associated with wood extractives mainly from the polyphenols (e.g., taxifolin) [20,25]. The band at around 5970 cm^{-1} is corresponded to the aromatic groups in lignin and wood extractives [26] (Figure 6). Furthermore, a difference in the band at around 4640 cm^{-1} can be observed and could be associated with the combination of C_{aryl}-H stretching and C=C stretching [20,27].

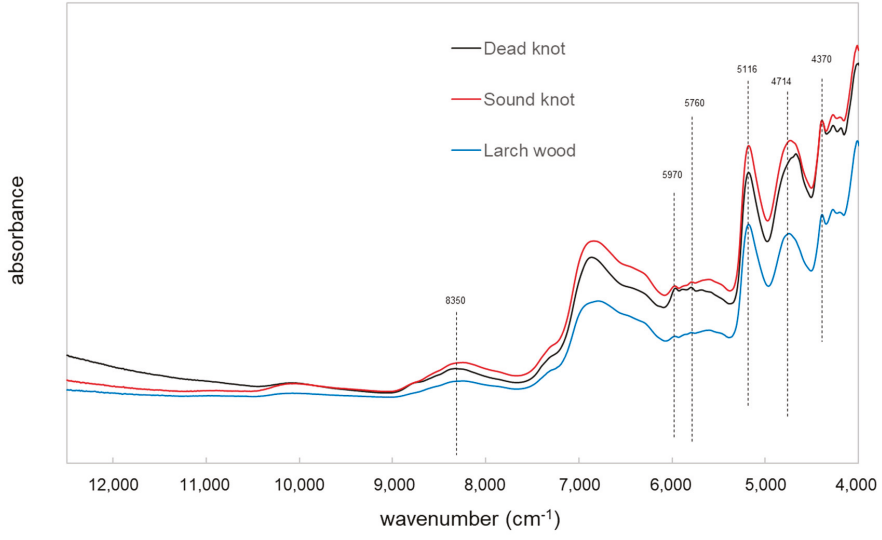

Figure 5. NIR spectra of larch wood, sound and dead knotwood.

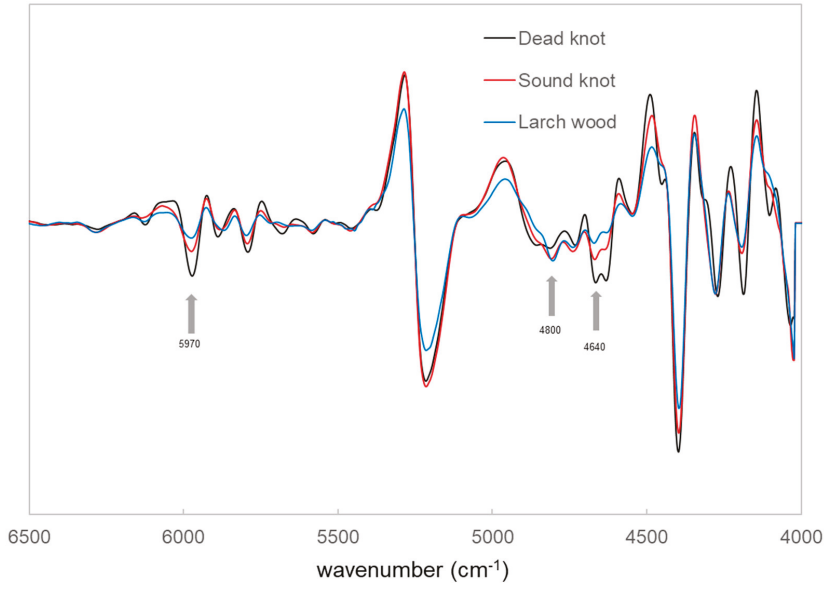

Figure 6. Second derivate FT-NIR spectra of larch wood, sound and dead knotwood.

For the C-H stretching vibration the NIR spectroscopy presents tree principal bands at around 4370 cm^{-1} the C-H stretch combination, around 5760 cm^{-1} the C-H stretch first overtone, and around 8350 cm^{-1} the C-H stretch second overtone, which have significant correlations for the major C-H stretching bands at 2919 and 2854 cm^{-1} of mid-infrared spectroscopy of lipophilic extractives [28].

The results of the NIR measurement showed the higher absorbance of these bands for the sound and dead knotwood samples. Therefore, it seems that the two types of knots may be distinguished

from the larch wood by the univariate analysis of the NIR spectra. Further analysis should be done to show the potential of NIRS for the classification of the various types of wood materials.

3.3. Multivariate Data Analysis of FT-NIR Spetra

The data of the NIRS were used for the classification via principal components analysis (PCA). Figure 7 shows the distribution of two significant factors of the NIRS data. The two principal components explain the highest value of variance within these data and have a great impact on the differentiation of the various wood types used.

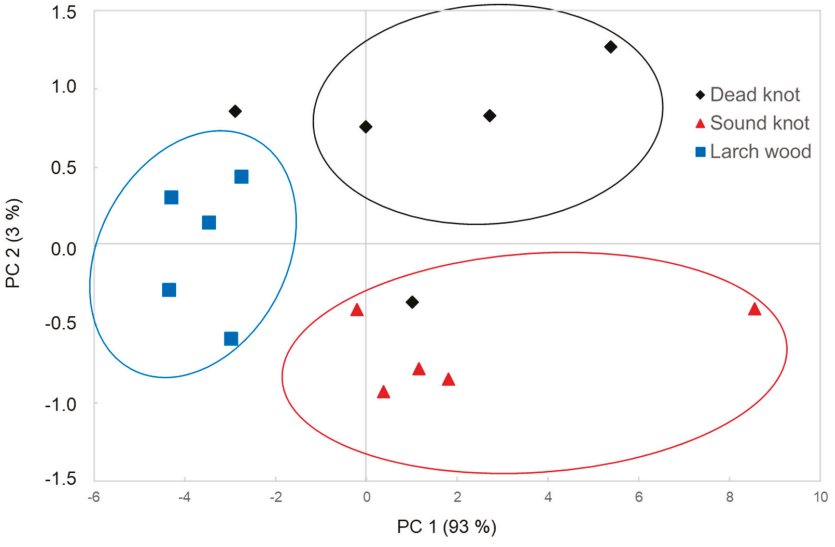

Figure 7. Principal component (PC) analysis score plot of untreated NIR spectra of various larch wood types (e.g., mixture wood, sound and dead knotwood).

Even though the PC 1 explained 93% of the variance, whereas the PC 2 describes only 3% of the variance, the combination of these two components was influenced by the two most important chemical substance groups: polyphenols and lipophilic extractives.

The mixture wood has a lower amount of polyphenols and fatty acids compared to the different knotwood types. The measured samples are clearly separated from the other materials (Figure 6). The sound knotwood samples presented a higher amount of taxifolin and kaempferol, whereas a lower amount of larixol than in the dead knotwood samples can be observed. Therefore, the score plot of the PCA shows also differences between sound and dead knotwood samples. Nevertheless, there are some areas without direct assignment of the samples (e.g., dead knotwood samples). The NIR measurements were performed on different surfaces from various selected samples of the larch wood, sound and dead knotwood. It can be assumed that the wood extractives distribution is not homogeneous. Therefore, some areas have a high amount of wood extractives, whereas some areas have a low amount.

The loadings of the PC 1 state high positive values for the wavenumbers 6870, 5970, 4640 and 4370 cm^{-1}, which are mainly corresponded to the phenolic compounds in wood extractives (Figure 8). The results of principal component analysis showed that the loadings of the PC 2 are contrary to the loadings of the PC 1 at the same NIR band at around 5116 cm^{-1} (water band of NIR signal), while the loadings of the PC 2 contribute to other wood extractives (e.g., lipophilic compounds) with lower moisture content within the samples.

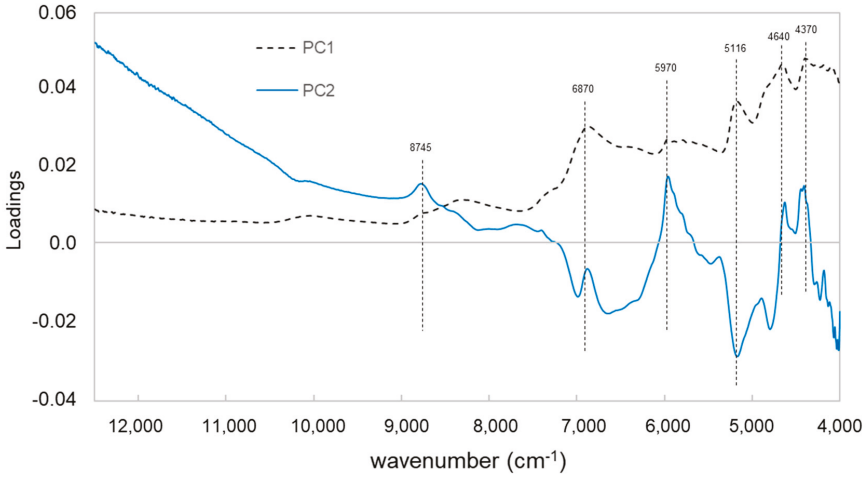

Figure 8. Loadings of the first two principal components (PCs) of near infrared spectra of various wood types.

4. Conclusions

Differences in wood extractives from various resources of larch wood, sound and dead knotwood were observed by a GC-MS method. Sound knotwood can provide a greater extraction yield than dead knotwood and larch wood, mainly sapwood with a small amount of heartwood, from the outer part of the logs, while more resin acids and larixol can be extracted from dead knotwood samples compared to the sound knotwood and larch wood samples.

The results from the GC-MS were used to analyze three various spectroscopy methods for the potential of the characterization of wood extractives and identification of the three wood types. With all vibrational spectroscopy used, chemical differences between the wood and knotwood were observed and can be used to fulfil various research tasks. Moreover, the methods of multivariate statistics were applied to analyze materials by using the score plot and loadings of the PC analysis. These results demonstrate that a classification of various wood tissues based on the different chemical components (e.g., polyphenols and lipophilic substances) is possible with fast, non-destructive measurement methods. The current unused wood chips for material use can be separated into different fractions, where the extraction yields of the target substance (e.g., taxifolin) are higher compared to the other fractions. This method may serve as basis to establish guidelines for quality assurance control systems of this new approach for material use to obtain the huge potential of bio-based products for innovative applications and for further efforts in the upscale from laboratory to industrial conditions.

Author Contributions: Conceptualization, K.W. and S.T.; methodology, K.W., M.M. and S.K.; software, K.W. and S.K.; investigation, K.W., M.M., S.K. and S.W.; resources, M.M., S.W. and A.P.; writing—original draft preparation, K.S.; writing—review and editing, M.M., S.W. and T.S.; supervision, M.M. and S.W.; project administration, A.P. and T.S.; funding acquisition, A.P. All authors have read and agreed to the published version of the manuscript.

Funding: This research was funded by EFRE (European Funds for Regional Development), AWS (Austria Wirtschafts Service) and the region of Salzburg for the support in the development of the Salzburg Center for Smart Materials.

Acknowledgments: Kerstin Wagner thanks the COST Action FP 1407 and the Johan Gadolin Process Chemistry Centre—Åbo Akademi University for the funding received through the Short Term Scientific Mission (STSM). In this section you can acknowledge any support given which is not covered by the author contribution or funding sections. This may include administrative and technical support, or donations in kind (e.g., materials used for experiments).

Conflicts of Interest: The authors declare no conflict of interest. The funders had no role in the design of the study; in the collection, analyses, or interpretation of data; in the writing of the manuscript, or in the decision to publish the results.

References

1. Pieratti, E.; Paletto, A.; Atena, A.; Bernardi, S.; Palm, M.; Patzelt, D.; Romagnoli, M.; Teston, F.; Voglar, G.E.; Grebenc, T.; et al. Environmental and climate change impacts of eighteen biomass-based plants in the alpine region: A comparative anaylsis. *J. Clean. Prod.* **2019**, 242. [CrossRef]
2. Chen, M.; Luo, J.; Shi, R.; Zhang, J.; Gao, Q.; Li, J. Improved adhesion performance of soy protein-based adhesives with a larch tannin-based resin. *Polymers* **2017**, *9*, 408. [CrossRef] [PubMed]
3. Jarre, M.; Petit-Boix, A.; Priefer, C.; Meyer, R.; Leipold, S. Transforming the bio-based sector towards a circular economy–What can we learn from wood cascading? *For. Policy Econ.* **2020**, 101872. [CrossRef]
4. Keegan, D.; Kretschmer, B.; Elbersen, B.; Panoutsou, C. Cascading use: A systematic approach to biomass beyond the energy sector. *Biofuels Bioprod. Biorefin.* **2013**, *7*, 193–206. [CrossRef]
5. Fengel, D.; Wegener, G. *Wood Chemistry Ultrastruture Rections*; Verlag Kessel: Remagen, Germany, 2003.
6. Zule, J.; Čufar, K.; Tišler, V. Hydrophilic extractives in heartwood of European larch (*Larix decidua* Mill.). *Drvna Ind.* **2016**, *67*, 363–370. [CrossRef]
7. Hörhammer, H.; van Heiningen, A. A larch biorefinery: Influence of washing and PS charge on pre-extraction PSAQ pulping. *BioResources* **2012**, *7*, 3539–3554.
8. Willför, S.M.; Ahotupa, M.O.; Hemming, J.E.; Reunanen, M.H.T.; Eklund, P.C.; Sjöholm, R.E.; Eckerman, C.S.E.; Pohjamo, S.P.; Holmbom, B.R. Antioxidant activity of knotwood extractives and phenolic compounds of selected tree species. *J. Agric. Food Chem.* **2003**, *51*, 7600–7606. [CrossRef]
9. Willför, S.M.; Hemming, J.; Reunanen, M.; Eckerman, C.; Holmbom, B. Lignans and lipophilic extractives in Norway spruce knots and steamwood. *Holzforschung* **2003**, *57*, 27–36. [CrossRef]
10. Willför, S.M.; Hemming, J.; Reunanen, M.; Holmbom, B. Phenolic and lipophilic extractives in Scots pine knots and stemwood. *Holzforschung* **2003**, *57*, 359–372. [CrossRef]
11. Laireiter, C.M.; Schnabel, T.; Köck, A.; Stalzer, P.; Petutschnigg, A.; Oostingh, G.J.; Hell, M. Active anti-microbial effects of larch and pine wood on four bacterial strains. *BioRescources* **2013**, *9*, 273–281. [CrossRef]
12. Wagner, K.; Roth, C.; Willför, S.; Musso, M.; Petutschnigg, A.; Oostingh, G.J.; Schnabel, T. Identification of antibmicrobial compounds in different hydrophilic larch bark extracts. *BioRescources* **2019**, *14*, 5807–5815.
13. Välimaa, A.-L.; Honkalampi-Hämäläinen, U.; Pietarinen, S.; Willför, S.; Holmbom, B.; von Wright, A. Antimicrobial and cytotoxic knotwood extracts and related pure compounds and their effects on food-associated microorganisms. *Int. J. Food Microbiol.* **2007**, *115*, 235–243. [CrossRef] [PubMed]
14. Bowyer, J.L.; Shmulsky, R.; Haygreen, J.G. *Forest Products and Wood Science: An Introduction*; Iowa State Press: Ames, IA, USA, 2003.
15. Nisula, L. Wood extractives in conifers. A Study of Stemwood and Knots of Industrially Important Species. Ph.D. Thesis, Åbo Akademi University, Turku, Finland, 2018.
16. Faix, O. Classification of lignins from different botanical origins by FT-IR spectroscopy. *Holzforschung* **1991**, *45*, 21–27. [CrossRef]
17. Schwanninger, M.; Hinterstoisser, B.; Gradingler, C.; Messner, K.; Fackler, K. Examination of spruce wood biodegradaed by Ceriporisopsis subvermispora using near and mid infrared spectroscopy. *J. Near Infrared Spectrosc.* **2004**, *12*, 397–409. [CrossRef]
18. Schnabel, T.; Musso, M.; Tondi, G. Univariate and multivariate analysis of tannin-impregnated wood species using vibrational spectroscopy. *Appl. Spectroc.* **2014**, *68*, 488–494. [CrossRef]
19. Wagner, K.; Schnabel, T.; Barbu, M.-C.; Petutschigg, A. Analysis of selected properties of fibreboard panels manufactured from wood and leather using the near infrared spectroscopy. *Int. J. Spectrosc.* **2015**. [CrossRef]
20. Agarwal, U.P.; Atalla, R.H. Vibrational spectroscopy. In *Lignin and Lignans. Advances in Chemistry*; Heiter, C., Dimmel, D.R., Schmidt, J.A., Eds.; CRC Press: Boca Raton, FL, USA, 2010; pp. 103–136.
21. Musso, M.; Oehem, K.L. Raman spectroscopy. In *Lasers in Chemistry: Probing and Influencing Matter*; Lackner, M., Ed.; Wiley-VCM: Weinheim, Germany, 2008; pp. 531–591.

22. Belt, T.; Keplinger, T.; Hänninen, T.; Rautkari, L. Cellular level distributions of Scots pine heartwood and knot heartwood extractives revealed by Raman spectroscopy imaging. *Ind. Crop. Prod.* **2017**, *108*, 327–335. [CrossRef]
23. Pretsch, E.; Bühlmann, P.; Badertscher, M. *Structure Determination of Organic Compounds*, 4th ed.; Springer: Berling/Heidlberg, Germany, 2009; pp. 207–335.
24. Wienhaus, H.; Pilz, W.; Seibt, H.; Dässler, H.-G. Die Diterpene Larixylacetat and Larixol. *Chem. Berichte* **1960**, *93*, 2625–2630. [CrossRef]
25. Gierlinger, N.; Schwanninger, M.; Hnterstoisser, B.; Wimmer, R. Rapid determination of heartwood extractives in Larix sp. by means of Fourier transform near infrared spectroscopy. *J. Near Infrared Spectrosc.* **2002**, *10*, 203–214. [CrossRef]
26. Schwanninger, M.; Rodrigues, J.C.; Facker, K. A review of band assignsments in near infrared spectra of wodo and wood components. *J. Near Infrared Spectrosc.* **2011**, *19*, 287–308. [CrossRef]
27. Michell, A.J.; Schimleck, L.R. NIR spectroscopy of wood from Eucalyptus globulus. *Appita J.* **1996**, *49*, 23–26.
28. Barton II, F.E.; Himmelbach, D.S.; Duckworth, J.H.; Smith, M.J. Two-dimensional vibration spectroscopy: Correlation of Mid- and Near-Infrared region. *Appl. Spectrosc.* **1992**, *46*, 420–429. [CrossRef]

polymers

MDPI

Article

Pyrolytic Behavior of Major Biomass Components in Waste Biomass

Haoxi Ben [1,2,*], Zhihong Wu [1,2], Guangting Han [3,4], Wei Jiang [3,4] and Arthur Ragauskas [5,6]

1 Southeast University, Nanjing 210096, China; 18915408402@163.com
2 Key Laboratory of Energy Thermal Conversion and Control of Ministry of Education, Nanjing 210096, China
3 Qingdao University, Qingdao 266071, China; hanguangting@gmail.com (G.H.); jiangwei@gmail.com (W.J.)
4 State Key Laboratory of Bio-Fibers and Eco-Textiles, Qingdao University, Qingdao 266071, China
5 Joint Institute for Biological Sciences, Biosciences Division, Oak Ridge National Lab, Oak Ridge, TN 37831, USA; aragausk@utk.edu
6 Department of Chemical and Biomolecular Engineering, University of Tennessee, Knoxville, TN 37996, USA
* Correspondence: benhaoxi@gmail.com

Received: 21 January 2019; Accepted: 5 February 2019; Published: 12 February 2019

Abstract: The pyrolytic behavior of several biomass components including cellulose, hemicellulose, lignin, and tannin, from two sources of waste biomass (i.e., pine bark and pine residues) were examined. Compared to the two aromatic-based components in the biomass, carbohydrates produced much less char but more gas. Surprisingly, tannin produced a significant amount of water-soluble products; further analysis indicated that tannin could produce a large amount of catechols. The first reported NMR chemical shift databases for tannin and hemicellulose pyrolysis oils were created to facilitate the HSQC analysis. Various C–H functional groups (>30 different C–H bonds) in the pyrolysis oils could be analyzed by employing HSQC-NMR. The results indicated that most of the aromatic C–H and aliphatic C–H bonds in the pyrolysis oils produced from pine bark and pine residues resulted from the lignin and tannin components. A preliminary study for a quantitative application of HSQC-NMR on the characterization of pyrolysis oil was also done in this study. Nevertheless, the concepts established in this work open up new methods to fully characterize the whole portion of pyrolysis oils produced from various biomass components, which can provide valuable information on the thermochemical mechanisms.

Keywords: tannin; hemicellulose; waste biomass; HSQC-NMR; pyrolysis mechanism

1. Introduction

Growing concerns about increasing global energy consumption [1] and the effects of growing carbon dioxide emissions from fossil fuels has reinvigorated interest in sustainable energy and chemical sources. Biomass is a promising renewable resource for the sustainable production of fuels and chemicals that, to date, are made primarily from fossil resources [2,3]. Lignocellulosic biomass contains three major constituents: cellulose, hemicelluloses, and lignin. Several reviews summarized the distribution of these major biopolymers in several hardwoods, softwoods, and agricultural residue species [4,5]. However, in softwood select tissues, including leaves, needles, and barks, there is another type of biopolymer—tannins—which could be even more abundant than lignin occasionally [6]. There are two types of tannins; hydrolyzable tannins are derivatives of gallic acid, which are esterified to polyols such as glucose (left structure in Figure 1), and condensed tannins (right structure in Figure 1), which are polymers of flavonoids, and are much more complicated than hydrolyzable tannins. Hernes et al. [6] conducted very detailed research on tannin signatures of 117 tissues from 77 different biomass species at the molecular level. Surprisingly, compared to the pyrolysis of cellulose and lignin, there are only very limited references which investigated the pyrolysis of tannins. Ohara et al. [7] examined the pyrolysis of several tannin model compounds,

including catechin and epicatechin. The authors indicated that catechol and 4-methylcatechol are the major products of pyrolysis of catechin and epicatechin model compounds, and they proposed possible formation pathways for these two products. Gaugler et al. [8] used thermogravimetric analysis (TGA) to analyze the thermal degradation of various condensed tannins and tannin model compounds. The highest weight loss of catechin occurred at 197 °C, while that of sulfited tannin occurred at 159 °C, that of tannin acetate occurred at 189 °C, and that of Quebracho tannin (commercial tannin extracted from Quebracho) occurred at 271 °C. Reported [7] pyrolysis products from tannins are summarized in Table S11 (Supplementary Materials).

The current annual stock of waste biomass is estimated as ~46 exajoules (EJ) from agricultural biomass and ~37 EJ from forestry biomass on a worldwide basis, totaling approximately 83 EJ, which represents approximately 20% of total worldwide energy consumption. Economic and practical limitations, including collection and transportation, are still holding up the price for the applications of these waste bioresources. Based on the United States (US) billion-ton update, the currently (2012) available forestry waste at <$60 per dry ton is estimated to be ~90 million dry tons in the US. In the meanwhile, the currently available agricultural residues and other waste resources at the same cost are suggested to be ~240 million dry tons in the US [9]. Thermal deconstruction is a promising approach to convert these sources of waste biomass to chemicals and precursors of biofuel [10]. Loblolly pine (*Pinus taeda*) is one of the abundant softwood species in the southeastern US and is widely used in various industries [5]. Harvesting operations leave a large amount of residues (e.g., stumps, limbs, tops, and dead trees, which are usually referred to as slash) and bark, which represent an important source of energy and chemicals [11]. Various researchers examined the thermal decomposition process for barks and residues [11–16].

For example, Pakdel et al. [11] pyrolyzed a mixture of spruce, fir, and pine, and maple barks and residues at different temperatures (450–525 °C). They found that the highest yield of pyrolysis oil was 73.6% for softwood residue and 57.1% for softwood bark at 525 °C. The yield of pyrolysis products for the hardwood was found to be similar to that of softwood. Ingram et al. [12] fast pyrolyzed pine wood and bark, and oak wood and bark in a continuous auger reactor at 450 °C. They used GC–MS to analyze pyrolysis products, which indicated that furfural, phenol, 3-methylphenol, catechol, 3-methylcatechol, and levoglucosan were the major products in the pine bark pyrolysis oil. Arpiainen et al. [13] used a fluidized-bed reactor to pyrolyze pine bark from 400–800 °C. They found that the highest yields of pyrolysis oil (~50%) were obtained at 500 °C. The secondary reactions were reported to occur at higher treatment temperature, which lead to a decreasing yield of pyrolysis oil. Lomax et al. [14,15] examined the pyrolysis of two different pine barks (i.e., *Pinus contorta* and *Pinus radiata*) from 505–840 °C. Using GC–MS analysis, the qualitative characterization for pyrolysis oils indicated that furfural, catechol, guaiacol, 2-ethylphenol, and 2-hydroxy-5-methyl phenol were the major components [16].

Due to the limitation of volatility of high-molecular-weight components in the pyrolysis oil, it was reported that only about 40% of pyrolysis oil could be detected by GC [10]. Therefore, many researchers have tried finding alternative characterization methods, which could analyze the whole portion of pyrolysis oil. Characterizations of pyrolysis products using high-resolution mass spectrometry, including both quadrupole time-of-flight mass spectrometry (Q-TOF MS) and Fourier-transform ion cyclotron resonance mass spectrometry (FT-ICR MS), were proposed by several researchers [17–21]. Several different pyrolysis oils produced from different whole sources of biomass, such as eucalyptus, eucalyptus bark, cellulosic mud, water hyacinth, pine wood, birch wood, algae, and switchgrass, using different thermochemical processes including fast pyrolysis, slow pyrolysis, and hydrothermal liquefaction, were analyzed by employing high-resolution mass spectrometry. FT-ICR MS was reported to be a promising method to analyze pyrolysis oil due to its unsurpassed resolution and accuracy [17]. However, the extremely complicated components in the pyrolysis oil (~2000–5000 peaks can be detected using FT-ICR MS) bring many barriers for this method [20]. The results from characterization of pyrolysis oil using FT-ICR MS can be presented

as C_x, N_x, and O_x species. However, a detailed investigation of different chemical functional groups in the pyrolysis oils calls for other analytical methods. In a recent study, quantitative ^{13}C-NMR combined with comprehensive two-dimensional gas chromatography (GC × GC) was used to characterize fast pyrolysis bio-oils, which provided new information on the chemical composition of bio-oils for further upgrading [22]. The use of different NMR techniques to characterize pyrolysis oils can accomplish this task, and is also a rapidly growing field of study [23–29]. The usage of HSQC-NMR (heteronuclear multiple quantum correlation nuclear magnetic resonance) provides a complete analysis of bio-oils, and the chemical shift assignments of different types of C–H bond presented in the pyrolysis oils produced from lignin and cellulose were readily identified. In this study, the detailed characterization of pyrolysis oils obtained from tannin and hemicellulose were accomplished using HSQC-NMR. The fingerprint analysis of these biomass components will open up a new way of understanding and utilizing pyrolysis products from biomass.

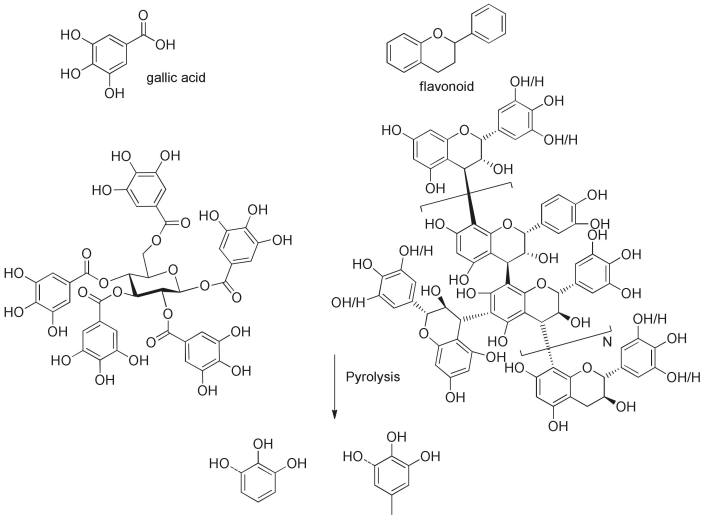

Figure 1. Model structures of tannin, and major pyrolysis products from tannin.

2. Experimental Section

2.1. Materials and Methods

All reagents used in this study were purchased from VWR International or Sigma-Aldrich (St. Louis, MO, USA) and used as received. Loblolly pine (*Pinus taeda*) bark and residue (mixture of stumps, limbs, tops, and dead trees) were collected from a University of Georgia research plot in Macon, GA [5]. The wood samples (Figure S1, Supplementary Materials) were refined with a Wiley mill through a 0.13-cm screen and dried under high vacuum at 50 °C for 48 h, and stored at ~0 °C prior to use. Cellulose was commercially purchased from Sigma-Aldrich. Xylan was also commercially purchased from Sigma-Aldrich, which is produced from oak wood, and was used to present hemicellulose in this study.

2.2. Tannin Extraction [30]

The tannin used in this study was obtained from *Pinus radiata* bark, which was collected in the MADECAM saw mill, located in the Concepción Province, Bio Region, Chile. The bark was obtained with a log debarker from 15-year-old and 20-year-old trees. The time since harvesting was less than one month and the debarking occurred during the last 24 h. The bark was treated in

a slow-speed shredder, with a 20-mm cutting gap, and was dried under atmospheric conditions up to a water content of 20–30%.

The extraction of pine bark tannin was done in two sequential extractions steps, with a 75% methanolic solution (*w*/*w*) at 120 °C for 2 h. The details of this procedure involved a 4-m^3 conical stainless-steel reactor being filled with the equivalent of 300 kg of dry bark. Concentrated methanol and water were added, to achieve a methanol concentration of 75% (*w*/*w*) and a solid/liquid relationship of 1/5 (*w*/*w*). The solution was continuously pumped through an external head exchanger, fed with 500 kPa. The temperature of the solution was heated up from ambient conditions to 120 °C in 4 h. This maximum temperature was maintained for 120 min. Thereafter, the solution was cooled, by opening a relief valve, to 80 °C in 40 min. The day after the solution was drained from the reactor, fresh methanol and water were added to achieve the same concentration and solid/liquid ratio as in the first extraction step. The same procedure was repeated in an analogous manner.

The methanolic solutions with the dissolved bark from the first and second extraction steps were combined and evaporated from 4–5% to 15–20% solid content. During the evaporation, the methanol was preferentially removed from the solution yielding an aqueous slurry. The insoluble material was separated by decantation, and the water-soluble phase was concentrated further and spray-dried. The water-soluble tannin was dried under high vacuum at 50 °C for 48 h and stored at ~0 °C prior to use. The tannin used in this study was characterized by quantitative ^{13}C NMR (Figure S2, Table S1, Supplementary Materials).

2.3. Kraft Pulping

The softwood kraft pulping liquor used was prepared using a conventional method [31]. Loblolly pine was employed as the wood source for the pulping process. Some relevant preparation conditions are presented in Table 1.

Table 1. Conventional pulping conditions [31].

Kraft Pulping	Conventional
Sulfidity, %	34.6
Effective Alkali, %	19.7
Impregnation	19.7
Temperature, °C	170
Time, min	95

2.4. Lignin Separation and Purification [23]

Lignin was isolated from a softwood (pine wood) kraft pulping liquor using the following methods: in brief, the cooking liquor was filtered through filter paper and the filtrate was treated with ethyenediaminetetraacetic acid (EDTA)–2Na^+ (0.50 g/100.00 mL liquor) and stirred for 1 h. The liquor was adjusted to a pH value of 6.0 with 2.00 M H_2SO_4 and stirred vigorously for 1 h. The liquors were then further acidified to a pH of 3.0 and frozen at −20 °C. After thawing, the precipitates were collected on a medium sintered glass funnel and washed three times with cold water by suspending the precipitates in the water and stirring vigorously at 0 °C for 1 h. The precipitates were collected, air-dried, and Soxhlet-extracted with pentane for 24 h. The solid product was air-dried and further dried under high vacuum at 45 °C for 48 h. The resulting purified kraft lignin sample was stored at −5 °C. The lignin used in this study was characterized by quantitative ^{13}C NMR (Figure S2, Table S1, Supplementary Materials).

2.5. Equipment and Process of Pyrolysis [23]

Pyrolysis experiments were conducted in a quartz pyrolysis tube heated with a split-tube furnace. Typically, the pyrolysis sample (4.00 g) was placed in a quartz sample boat that was then positioned in the center of a pyrolysis tube. A K-type thermal couple was immersed in the sample powder

during the pyrolysis to measure the heating rate (the heating rate was ~2.7 °C/s). The pyrolysis tube was flushed with nitrogen gas and the flow rate was adjusted to a value of 500 mL/min, and then the tube was inserted into the pre-heated furnace. The outflow from pyrolysis was passed through two condensers, which were immersed in liquid N_2. Upon completion of pyrolysis, the reaction tube was removed from the furnace and allowed to cool to room temperature under constant N_2 flow. The condensers were then removed from liquid nitrogen. The pyrolysis char and oil were collected for subsequent chemical analysis. In general, the liquid products contained two immiscible phases, referred to as heavy and light oil. The light oil was acquired by decantation, and the heavy oil was recovered by washing the reactor with acetone, followed by evaporation under reduced pressure. Char yields were determined gravimetrically, and gas formation was calculated by mass difference.

2.6. Characterization of Pyrolysis Oil by HSQC-NMR [24]

All NMR spectral data reported in this study were recorded with a Bruker Avance/DMX 400 MHz NMR spectrometer. HSQC-NMR spectra were acquired using 70.0 mg of pyrolysis oil (combined light oil and heavy oil by dissolving of two immiscible phases in acetone, followed by evaporation under reduced pressure) dissolved in 450 μL of dimethyl sulfoxide (DMSO-d_6), employing a standard Bruker pulse sequence "hsqcetgpsi.2" with a 90° pulse, 0.11-s acquisition time, a 1.5-s pulse delay, a $^1J_{C–H}$ of 145 Hz, 48 scans, and the acquisition of 1024 data points (for ^{1}H) and 256 increments (for ^{13}C). The ^{1}H and ^{13}C pulse widths were p1 = 11.30 μs and p3 = 10.00 μs, respectively. The ^{1}H and ^{13}C spectral widths were 13.02 ppm and 220.00 ppm, respectively. The central solvent peak was used for chemical shift calibration. HSQC-NMR data processing and plots were carried out using MestReNova v7.1.0 software's default processing template and automatic phase and baseline correction.

3. Results and Discussion

To further understand the pyrolytic behavior of whole biomass, the thermal decomposition process for several biomass components including cellulose, hemicellulose, lignin, and tannin was examined at 600 °C, which was found as the optimal temperature to yield the highest amount of pyrolysis oils (Tables 2 and 3). The yields of the light oil, heavy oil, char, and gas for the pyrolysis of these major components are summarized in Table 1. The results show that, compared to the two aromatic-based components (lignin and tannin), carbohydrates including cellulose and hemicellulose produced much less char but more gas, which indicates that carbohydrates are relatively readier to decompose than lignin and tannin. In addition, lignin produced mostly organic products (heavy oil) compared to the other biomass components, which represents a potential resource for a biofuel precursor. Surprisingly, tannin produced a significant amount of water-soluble products (light oil). Further analysis of the composition of tannin pyrolysis oil indicated that tannin could produce a large amount of catechols, which are water-soluble and could be used as a bio-chemical resource. Hemicellulose was reported [24] to be the very first biomass component to decompose during thermal treatment, which supports the results shown in Table 1 that hemicellulose produced most gas products compare to the other biomass components.

The pyrolysis process for the two sources of waste biomass (pine bark and pine residues) were examined at different temperatures, and the results are shown in Tables 3 and 4. The results indicate that the yield of char decreased, and the yield of gas increased at higher reactor temperatures for both biomasses. Compare to the pine bark, pine residue produced more (up to 15 wt.% of dry biomass) pyrolysis oils under the same conditions. The higher yields of pyrolysis oils are due to the higher carbohydrate (cellulose and hemicellulose) contents in pine residue (65.9%) than the pine bark (50.9%) [5], which could produce more pyrolysis oils than lignin and tannin.

Table 2. Yields of light oil, heavy oil, char, and gas for the pyrolysis of cellulose, hemicellulose, lignin, and tannin at 600 °C.

Biomass Components	Light Oil	Heavy Oil	Total Pyrolysis Oil	Char	Gas
Cellulose [a]	58.83	10.47	69.30	11.17	19.53
Hemicellulose	36.13	13.49	49.26	23.03	27.35
Lignin [a]	14.20	30.01	44.21	40.48	15.31
Tannin	37.85	9.11	46.96	40.33	12.71

[a] Based on a literature report [24]. The analytical methods (GC–MS, elemental analysis, and gel permeation chromatography (GPC)) used to characterize these pyrolysis oils can also be found in the literature [23,24].

Table 3. Yields of light oil, heavy oil, char, and gas for the pyrolysis of bark at 400, 500, and 600 °C.

Pyrolysis Temperature (°C)	Light Oil	Heavy Oil	Total Pyrolysis Oil	Char [a]	Gas
400	12.95	27.65	40.60	48.72	10.68
500	15.67	30.84	46.51	39.53	13.96
600 [b]	20.23	30.65	50.88	34.58	14.54

[a] The ash percentage (w/w) of bark is 0.9%. [b] Based on a literature report [4], a higher temperature above 600 °C will produce more gas products but fewer liquid products; therefore, the highest temperature used in this study was 600 °C.

Table 4. Yields of light oil, heavy oil, char, and gas for the pyrolysis of pine residue at 400, 500, and 600 °C.

Pyrolysis Temperature (°C)	Light Oil	Heavy Oil	Total Pyrolysis Oil	Char [a]	Gas
400	25.01	30.43	55.44	33.26	11.30
500	26.45	31.95	58.40	26.02	15.58
600	26.16	34.88	61.04	22.29	16.67

[a] The ash percentage (w/w) of pine residue is 0.8%.

Due to the limitation of GC–MS for the characterization of pyrolysis products, many researchers have pursued alternative characterization methods, which could analyze the whole portion of pyrolysis oil, such as NMR. HSQC-NMR exhibits a superior ability to deal with such complicated mixtures than other NMR methods. The strengths of this methodology include less spectral overlap problems and reduced NMR acquisition time. In this study, the first reports of NMR chemical shift databases for tannin and hemicellulose pyrolysis oils were created to facilitate this analysis. The detailed information of the databases can be found in the Supplementary Materials as Tables S11 and S12. Similar NMR databases for lignin and cellulose pyrolysis products were reported previously in the literature [24].

The aromatic C–H bonds, levoglucosan, methoxyl groups, and aliphatic C–H bonds in the HSQC-NMR spectra for the pyrolysis oils produced from cellulose, hemicellulose, lignin, and tannin at 600 °C are shown in Figure 2a–d. Figure 2a shows that there were substantially more aromatic products in lignin and tannin pyrolysis oils than in cellulose and hemicellulose pyrolysis oils, which is also consistent with the yield results (more heavy organic products in lignin and tannin pyrolysis oils) shown in Table 1. In addition, Figure 2a also indicates that hemicellulose produced relatively more aromatic products than cellulose, which is also consistent with yield results and a literature report [32]. Compared to lignin pyrolysis oil, tannin pyrolysis oil contains a large amount of catechols and a relatively lower content of mono-hydroxyl phenols, which is consistent with the GC–MS analysis and ^{13}C NMR results (Table S11, Supplementary Materials; Figure 3). Ohara et al. [7] also reported a similar result, where they used pyrolysis gas chromatography to analyze the pyrolysis products from the model compounds of tannin. Catechol and 4-methylcatechol were detected as the major components in the pyrolysis oil produced from procyanidin (PC, structure shown in Figure 3), which is the major type of tannin present in pine barks. The formation of catechol was attributed to the cleavage of C1′ and C2 in the PC structure, and 4-methylcatechol was formed via the fission of the pyran ring, followed by the cleavage of the ether bond. The possible pathways

of the formation of these two major components in the tannin pyrolysis oil are shown in Figure 3. Figure 2d shows that the major type of aliphatic C–H bonds belonged to methyl-aromatic carbon, which is also evidence that 4-methylcatechol was one of the major components in the tannin pyrolysis oil. The large amount of light oil produced from tannin indicated that there was a significant amount of water generated during the pyrolysis process, which could be attributed to the dehydration of hydroxyl groups in the pyran ring. As expected, levoglucosan (Figure 2b) was the major component in the cellulose pyrolysis oil. Lignin and tannin did not produce any similar structures during the thermal decomposition process. A very similar dehydrated five-carbon monosaccharide was found in the hemicellulose pyrolysis oil, which indicates that similar decomposition pathways to those seen with cellulose also occur during the decomposition of hemicellulose. Figure 2c indicates that methoxyl groups only appeared in the lignin pyrolysis oil. Two different types of methoxyl groups indicate the rearrangement process during the thermal treatment of lignin [24]. Figure 2d shows that, compared to the other biomass components, hemicellulose produced a significant amount of aliphatic C–H bonds, which could be assigned as methyl groups in the furan ring (could be produced from deep dehydration/decomposition of the five-carbon monosaccharide), α and β positions of a carbonyl group (could be produced from uncompleted dehydration/decomposition of the five-carbon monosaccharide), and an aliphatic chain (could be produced from the cleavage of side chains of hemicellulose). Similar results were reported by Patwardhan et al. [32]. In their study the pyrolytic behaviors of switchgrass hemicellulose were examined, and 2-methyl furan and several anhydro xyloses were found as major components in the pyrolysis oil. On the basis of Figure 2d, lignin and tannin pyrolysis oils had a very similar group of aliphatic C–H bonds, which represent the methyl groups in the aromatic rings. Compared to the other biomass components, cellulose produced a very limited amount of aliphatic C–H bonds, and most of them could be assigned as α and β positions of a carbonyl group.

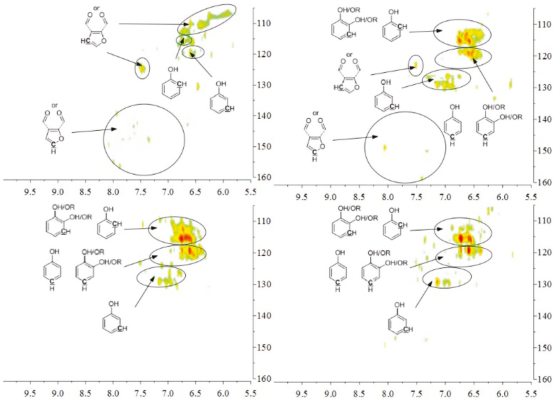

(a)

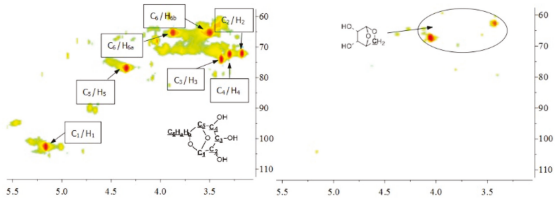

(b)

Figure 2. *Cont.*

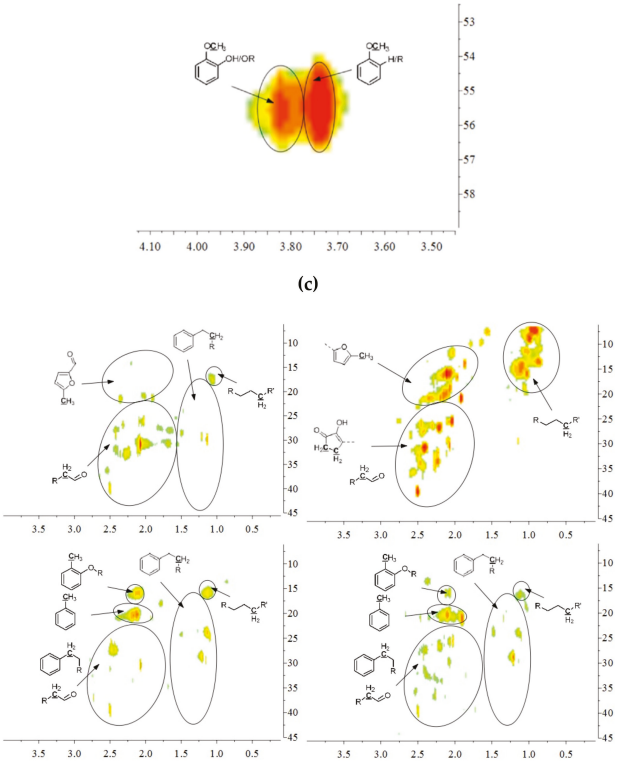

Figure 2. (**a**) Aromatic C–H bonds in HSQC-NMR spectra for the pyrolysis oils produced from cellulose, hemicellulose, lignin, and tannin (from top left to bottom right) at 600 °C. (**b**) Levoglucosan and a similar dehydrated monosaccharide in HSQC-NMR spectra for the pyrolysis oils produced from cellulose and hemicellulose (from left to right) at 600 °C. As expected, there would be no similar components in lignin and tannin pyrolysis oils, if samples were purified. (**c**) Methoxyl groups in HSQC-NMR spectra for the pyrolysis oils produced from lignin at 600 °C. As expected, methoxyl groups were only present in lignin pyrolysis oil, if samples were purified. (**d**) Aliphatic C–H bonds in HSQC-NMR spectra for the pyrolysis oils produced from cellulose, hemicellulose, lignin, and tannin (from top left to bottom right) at 600 °C.

A detailed understanding of the chemical structures in the pyrolysis oils produced from major biomass components is anticipated to facilitate the characterization of whole-biomass pyrolysis oils. Figure 4a,b show the HSQC-NMR spectral data and the assignments of each carbon in the levoglucosan, which was present in the pine bark and residue pyrolysis oils [33], as the intensity of those peaks indicated that levoglucosan was one of the major products. The content of levoglucosan slightly increased with elevated pyrolysis temperatures, which is consistent with a literature report [24]. Similarly, most of other peaks in this area also increased with a higher reactor temperature, which could represent similar dehydrated five-carbon monosaccharide produced from hemicellulose. Therefore, a higher thermal decomposition temperature will favor the production of a more dehydrated monosaccharides. Figure 4c,d show the aromatic C–H bonds in the HSQC-NMR spectra for the pine bark and residues pyrolysis oils. The results indicate that the major aromatic components in the pine bark and residue pyrolysis oils contained catechol, guaiacol, and phenol types of aromatic C–H bonds, which was comparable with the lignin and tannin pyrolysis oils. There was a relatively more furfural type of aromatic C–H bonds in the pine residue pyrolysis oil than in the pyrolysis oil produced from pine bark, which indicated that there were more carbohydrate decomposition products in the pine residue pyrolysis oil. Huang et al. [5]

indicated that there were more carbohydrates in pine residue (65.9%) than pine bark (50.9%), but less lignin (pine residue 26.7%, pine bark 33.7%) and tannin (pine residue 3.7%, pine bark 11.6%), which supports the results shown in Figure 4c,d. Very interestingly, the influences from different temperatures on the aromatic products appear to be very limited, which may be due to the relatively thermal stable structures for these aromatic products. The slight increase in the number of aromatic C–H bonds in the phenolic structure at a higher temperature may have been due to the decomposition of side chains. Figure 4e,f indicate that there were more rearranged methoxyl groups with no hydroxyl or ether bond in the *ortho* position of the methoxyl group than the native type (a hydroxyl or ether bond in the *ortho* position of the methoxyl group) in the pyrolysis oils produced from pine bark and residue, indicating that such a rearrangement of methoxyl groups also occurred during the pyrolysis of whole biomass. Figure 4g,h show that the contents of aliphatic C–H bonds slightly increased with the elevated reactor temperatures, and most of those aliphatic C–H bonds (α and β positions in aromatic ring) resulted from the pyrolysis of lignin and tannin components in the pine bark and pine residue, indicating that these aromatic biomass components require a relatively higher temperature to further decompose into small fragments. Figure 3 shows the formation pathways for one of the major pyrolysis products from tannin, 4-methylcatechol. The pyrolysis of lignin was also reported [23,24] to produce a significant amount of methyl-aromatic bonds via a rearrangement of methoxyl groups. Due to the relatively high lignin and tannin contents in the pine bark and residue, the aliphatic C–H bonds in the α and β positions in aromatic rings could be expected as one of the major types of aliphatic bonds in the pyrolysis oils produced from pine bark and residue. To further investigate the pyrolytic behaviors of biomass components, several comparisons between artificial spectra (a mixture of pyrolysis oils produced from lignin, tannin, cellulose, and hemicellulose) and whole biomasses were examined and the results are shown in Figures S3–S6 (Supplementary Materials). The results show that the artificial spectra could represent whole-biomass pyrolysis oil very well, whereby almost all the major peaks in the real pyrolysis oils could be found in the artificial spectra, indicating that the technique developed in this study could be employed as a new method to fully characterize the whole portion of pyrolysis oils produced from various biomass components and whole sources of biomass, and to facilitate the high-throughput screening of pyrolysis oils. Very interestingly, compared to the artificial spectra, only a very limited number of "new" peaks could be found in the aliphatic and dehydrated monosaccharide ranges of whole-biomass pyrolysis oils, indicating that there may only have been very limited cross-link reactions between biomass components. The products from these possible cross-link reactions could have become the "new" side chains in the major pyrolysis components.

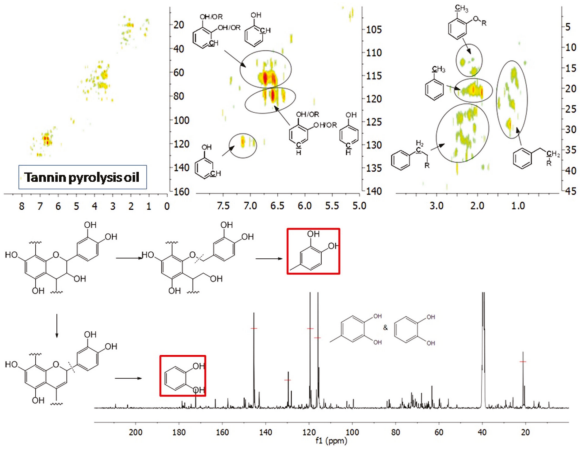

Figure 3. Major pyrolysis products produced from tannin and possible pathways.

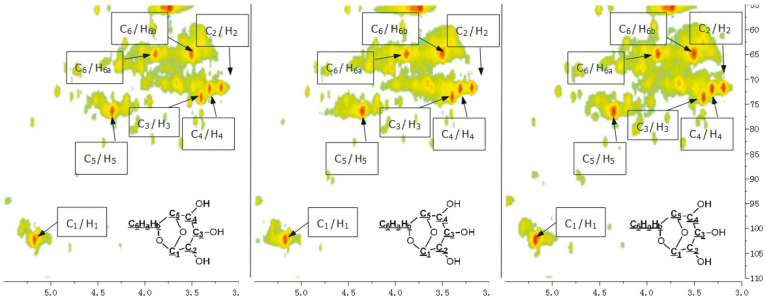

(a)

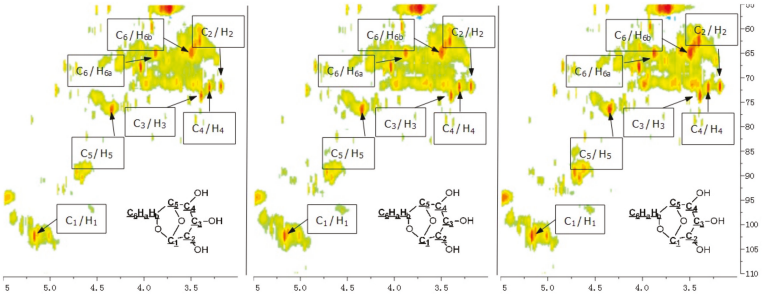

(b)

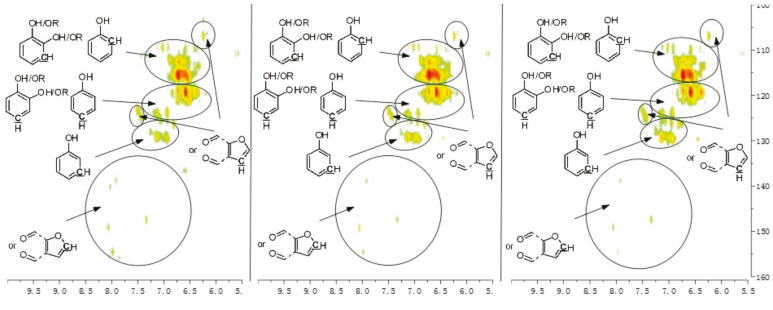

(c)

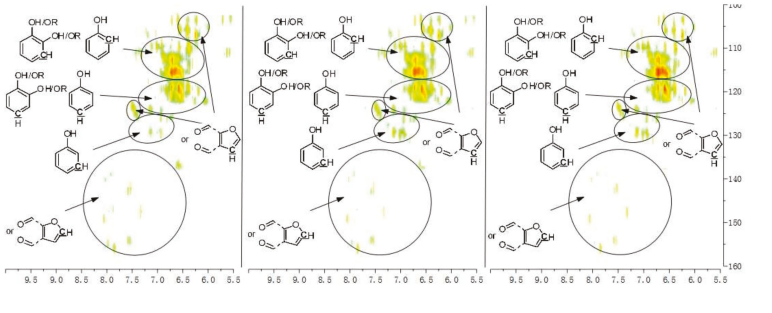

(d)

Figure 4. *Cont.*

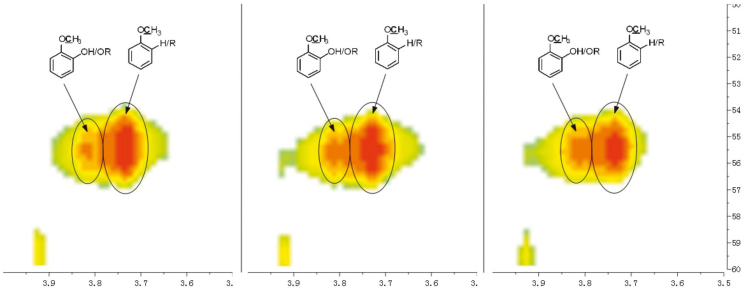

(e)

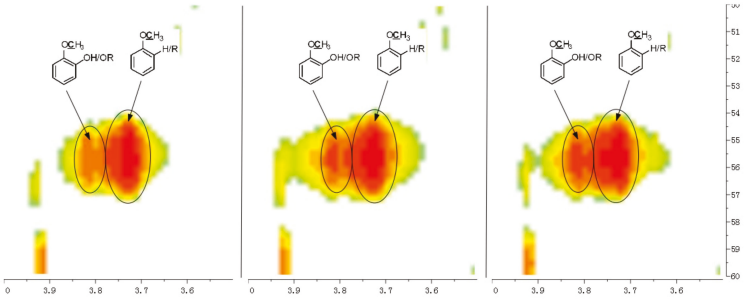

(f)

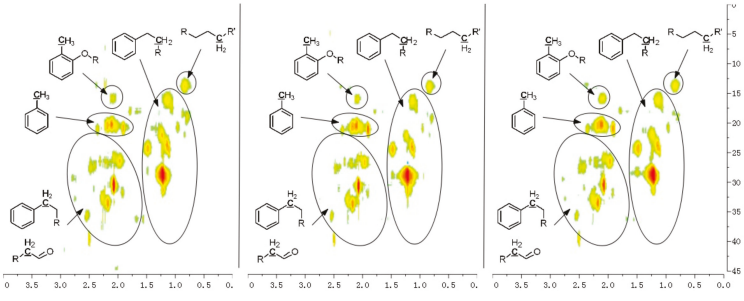

(g)

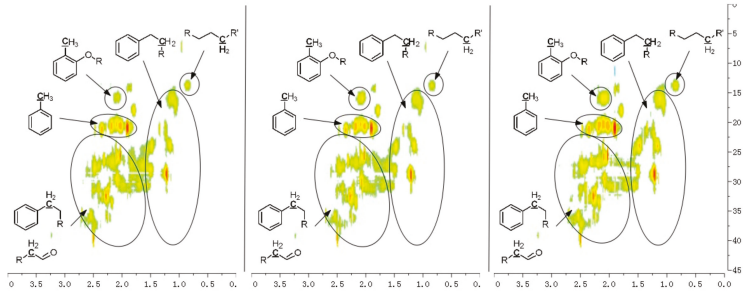

(h)

Figure 4. HSQC-NMR spectra and the assignments of each carbon in the levoglucosan present in the pyrolysis oils (**a**) produced from the pyrolysis of pine bark from 400 to 600 °C (from left to right),

(**b**) produced from the pyrolysis of pine residue from 400 to 600 °C (from left to right). (**c**) Aromatic C–H bonds in the HSQC-NMR spectra for the pyrolysis oils produced from the pyrolysis of pine bark from 400 to 600 °C (from left to right). (**d**) Aromatic C–H bonds for the pyrolysis oils produced from the pyrolysis of pine residue from 400 to 600 °C (from left to right). (**e**) Methoxyl groups in the HSQC-NMR spectra for the pyrolysis oils produced from the pyrolysis of pine bark from 400 to 600 °C (from left to right). (**f**) Methoxyl groups for the pyrolysis oils produced from the pyrolysis of pine residue from 400 to 600 °C (from left to right). (**g**) Aliphatic C–H bonds in the HSQC-NMR spectra for the pyrolysis oils produced from the pyrolysis of pine bark from 400 to 600 °C (from left to right). (**h**) Aliphatic C–H bonds for the pyrolysis oils produced from the pyrolysis of pine residue from 400 to 600 °C (from left to right).

Several experimental approaches [34–36] for quantitative HSQC-NMR characterization were reported; however, they all involved special pulse sequences and prolonged experimental time. In this study, a preliminary investigation for a quantitative application of normal HSQC-NMR on the characterization of pyrolysis oil, produced from a pilot plant reactor [37], was also accomplished. Several model compounds for the pyrolysis oil, including guaiacol, levoglucosan, toluene, anisole, and *n*-propylbenzene were used to create calibration curves. The HSQC-NMR results for the standard mixtures and the pyrolysis oil produced from a pilot plant reactor are shown in Figures S7 and S8 (Supplementary Materials). Aromatic C–H, levoglucosan C–H, methoxyl C–H, and aliphatic C–H bonds in the standard mixtures were analyzed and the integrations for these C–H bonds in different standards with different concentrations were plotted as shown in Figure S9a–d (Supplementary Materials) to create calibration curves. To evaluate the calibration curves, three artificial mixtures of pyrolysis oil with model compounds (guaiacol, levoglucosan, and *n*-propylbenzene) were examined by HSQC-NMR. The calculated concentrations for different C–H bonds agreed with the designed values in these artificial mixtures (Table S2, Supplementary Materials). To further evaluate the proposed method, quantitative ^{13}C NMR, and DEPT 135 and DEPT 90 were also employed to further characterize the pyrolysis oil (Figure S10, Supplementary Materials). The use of chemical shift assignment ranges (Table S3, Supplementary Materials) for pyrolysis oils in the ^{13}C NMR were previously reported in the literature [23,38]. The quantitative ^{13}C NMR used in this study was examined using two commercial petroleum standard mixtures (Table S4 and S5, Supplementary Materials), which can represent complicated mixtures, such as petroleum oils or pyrolysis oils. The results shown in Table S6 and S7 (Supplementary Materials) indicate that the employed quantitative ^{13}C NMR can provide precise analysis for different functional groups and different carbons for very complicated mixtures. To ensure the accuracy, the T1 values for different functional groups in the pyrolysis oil were measured (Table S8, Supplementary Materials). The further characterization of pyrolysis oil (produced from a pilot plant reactor) and artificial mixtures were analyzed using quantitative ^{13}C NMR (Tables S9 and S10, Supplementary Materials). The results indicate that the quantitative ^{13}C NMR procedure used in this study can provide precise data for different functional groups in the pyrolysis oil using the internal standards. Furthermore, the quantitative data for different aromatic C–H, levoglucosan C–H, methoxyl C–H, and aliphatic C–H bonds in the pyrolysis oil proposed using calibration curves and HSQC-NMR are shown in Table S10 (Supplementary Materials), and comparable results with quantitative ^{13}C NMR were found, indicating that the proposed method can provide quantitative data on different C–H bonds in the pyrolysis oils. Another interesting result is that, based on the HSQC NMR data, there were 6.46 μmol of aliphatic C–H bonds in 1 mg of pyrolysis oil, while the quantitative ^{13}C NMR indicated that there were 2.58 μmol of aliphatic carbons (in aliphatic C–C bonds) in 1 mg of pyrolysis oil, indicating that each aliphatic carbon in this pyrolysis oil should attach an average of 6.46/2.58 = 2.5 protons. Due to the limited overlaps between aliphatic C–C and C–O bonds in ^{13}C NMR, it is highly possible that a similar result can also be provided by employing quantitative ^{13}C NMR, and DEPT 135 and DEPT 90. The proposed CH_x number using such a method is 2.6, which is very close to the result (x = 2.5) correlating both

^{13}C NMR and HSQC-NMR investigations, which is also further evidence that the proposed HSQC-NMR method can provide a precise analysis of different C–H bonds in the pyrolysis oil.

4. Industrial Application of Pyrolysis Bio-Oils

Pyrolysis bio-oils are mixtures of about 200 organic compounds. It was reported that all determined compounds can be classified into nine groups: furans, aldehydes, ketones, phenols, acids, benzenes, alcohols, alkanes, and polycyclic aromatic hydrocarbons (PAHs) [39]. The characterized chemical compounds of bio-oils are used in different industrial fields due to their unique properties [40]. Catechol obtained from the pyrolysis of tannin has a very high added value and is widely used in the fields of rubber, electroplating, antiseptic, sterilization, etc. Moreover, furfural, a natural dehydrating product of five-carbon sugars (e.g., arabinose and xylose) from hemicellulose biomass [41], regained attention as a bio-based alternative for the production of everything from antacids and fertilizers to plastics and paints [42]. It was reported that levoglucosan can be used as a specific molecular indicator to trace biomass combustion in sediments [43]. The application of this novel molecular tracer may bring benefits to research areas such as paleoecology, archeology, and environmental science [43]. Furthermore, aromatic hydrocarbons have good rubber compatibility, high temperature resistance, and low volatility, and they significantly improve the processing properties of rubber. Therefore, they attracted wide attention in the field of reclaimed rubber and various rubber products.

5. Conclusions

In this study, HSQC-NMR was utilized to characterize the whole portion of pyrolysis oils produced from various biomass components including cellulose, hemicellulose, lignin, and tannin. The fingerprint analysis of HSQC-NMR spectral data could provide semi-quantitative chemical shift assignments of more than 30 different types of C–H bond present in the pyrolysis oils. Catechols were found as major components in the tannin pyrolysis oils. Levoglucosan was the major component in the cellulose pyrolysis oil. A very similar dehydrated five-carbon monosaccharide was found in the hemicellulose pyrolysis oil, indicating that hemicellulose has a similar decomposition pathway to that of cellulose. Compared to the other biomass components, hemicellulose produced a significant amount of aliphatic C–H bonds, which could be assigned as methyl groups in the furan ring, α and β positions of a carbonyl group, and aliphatic chains. The HSQC-NMR analysis results also indicated that most of the aromatic C–H and aliphatic C–H bonds in the pyrolysis oils produced from pine bark and pine residue resulted from the lignin and tannin components. A preliminary study of the quantitative application of HSQC-NMR on the characterization of pyrolysis oil was also accomplished in this study, and the results indicate that, by employing the proposed HSQC-NMR method, a precise analysis of different C–H bonds in the pyrolysis oil can be provided. Nevertheless, the concepts established in this work open up new methods to fully characterize the whole portion of pyrolysis oils produced from various biomass components and whole sources of biomass, which could facilitate the high-throughput screening of pyrolysis oils.

Supplementary Materials: The following are available online at http://www.mdpi.com/2073-4360/11/2/324/s1: Figure S1: Pine bark (left) and pine residues (right) used in this study; Figure S2: Quantitative 13C NMR for the tannin (top) and lignin (bottom) used in this study; Figure S3a: Aliphatic C–H bonds in the HSQC-NMR spectra for artificial mixture of pyrolysis oils produced from lignin, tannin, cellulose, and hemicellulose (left) and pine bark pyrolysis oil (right) produced at 600 °C; Figure S3b: Aliphatic C–H bonds in the HSQC-NMR spectra for artificial mixture of pyrolysis oils produced from lignin, tannin, cellulose, and hemicellulose (left) and pine residue pyrolysis oil (right) produced at 600 °C; Figure S4a: Aromatic C–H bonds in the HSQC-NMR spectra for artificial mixture of pyrolysis oils produced from lignin, tannin, cellulose, and hemicellulose (left) and pine bark pyrolysis oil (right) produced at 600 °C; Figure S4b: Aromatic C–H bonds in the HSQC-NMR spectra for artificial mixture of pyrolysis oils produced from lignin, tannin, cellulose, and hemicellulose (left) and pine residue pyrolysis oil (right) produced at 600 °C; Figure S5a: Levoglucosan in the HSQC-NMR spectra for artificial mixture of pyrolysis oils produced from lignin, tannin, cellulose, and hemicellulose (left) and pine bark pyrolysis oil (right) produced at 600 °C; Figure S5b: Levoglucosan in the HSQC-NMR spectra for artificial mixture of pyrolysis oils produced from lignin, tannin, cellulose, and hemicellulose (left)

and pine residue pyrolysis oil (right) produced at 600 °C; Figure S6a: Methoxyl groups in the HSQC-NMR spectra for artificial mixture of pyrolysis oils produced from lignin, tannin, cellulose, and hemicellulose (left) and pine bark pyrolysis oil (right) produced at 600 °C; Figure S6b: Methoxyl groups in the HSQC-NMR spectra for artificial mixture of pyrolysis oils produced from lignin, tannin, cellulose, and hemicellulose (left) and pine residue pyrolysis oil (right) produced at 600 °C; Figure S7: HSQC-NMR for standard mixtures of pyrolysis oil model compounds; Figure S8: HSQC-NMR for pyrolysis oil produced from a pilot plant reactor; Figure S9a: Integrations and linear fit for aromatic C–H bonds in the HSQC-NMR for standard mixtures (100%, 50%, 25%, 10%, and 5% concentrations) of pyrolysis oil model compounds; Figure S9b: Integrations and linear fit for aliphatic C–H bonds in the HSQC-NMR for standard mixtures (100%, 50%, 25%, 10%, and 5% concentrations) of pyrolysis oil model compounds; Figure S9c: Integrations and linear fit for levoglucosan C–H bonds in the HSQC-NMR for standard mixtures (100%, 50%, 25%, 10%, and 5% concentrations) of pyrolysis oil model compounds; Figure S9d: Integrations and linear fit for aliphatic C–H bonds in the HSQC-NMR for standard mixtures (100%, 50%, 25%, 10%, and 5% concentrations) of pyrolysis oil model compounds; Figure S10: Quantitative ^{13}C NMR and DEPT 135 and DEPT 90 (from top to bottom) for the pyrolysis oil produced from a pilot plant reactor; Table S1: Quantitative 13C NMR results for the tannin and lignin used in this study; Table S2: Functional group recovery ratios for artificial mixtures of pyrolysis oil (produced from a pilot plant reactor) and pyrolysis oil model compounds based on HSQC-NMR; Table S3: 13C NMR chemical shift assignment ranges for pyrolysis oil (on the basis of Reference [1]); Table S4: Certified values for standard #1; Table S5: Certified values for standard #2; Table S6: Evaluations for quantitative 13C NMR of standard #1; Table S7: Evaluations for quantitative ^{13}C NMR of standard #2; Table S8: T1 value for different functional groups in pyrolysis oil produced from a pilot plant reactor when employing 5 mg/ml Cr(acac)3 as a relaxing reagent; Table S9: Integrations for each 1 mmol carbon in the functional groups calculated from analysis for artificial mixtures of pyrolysis oil (produced from a pilot plant reactor) and pyrolysis oil model compounds based on quantitative ^{13}C NMR; Table S10: Comparisons of quantitative ^{13}C NMR and HSQC-NMR investigations on pyrolysis oil sample (a pilot plant product); Table S11: ^{1}H and ^{13}C NMR chemical shift assignments for the compounds reported present in tannin pyrolysis oils; Table S12: ^{13}C NMR chemical shift assignments for the compounds reported present in hemicellulose pyrolysis oils. The compounds in this database are based on References [2–4].

Author Contributions: H.B. conceived and designed the experiment; H.B. conducted all the major experiments and wrote the manuscript; Z.W. and W.J. did some NMR tests and helped with the manuscript preparation; G.H. provided the NMR facility in Qingdao University to finish some additional tests from China; A.R. provided very valuable input for the conceptualization of the study, and helped write the manuscript.

Acknowledgments: The authors would like to acknowledge the financial support from the National Science Foundation of China (51706044), the Natural Science Foundation of the Jiangsu of China (BK20170666), and the Recruitment Program for Young Professionals in China.

Conflicts of Interest: The authors declare no conflicts of interest.

References

1. Ragauskas, A.J.; Williams, C.K.; Davison, B.H.; Britovsek, G.; Cairney, J.; Eckert, C.A.; Frederick, W.J., Jr.; Hallett, J.P.; Leak, D.J.; Liotta, C.L.; et al. The path forward for biofuels and biomaterials. *Science* **2006**, *311*, 484–489. [CrossRef] [PubMed]
2. David, K.; Ragauskas, A.J. Switchgrass as an energy crop for biofuel production: A review of its ligno-cellulosic chemical properties. *Energ. Environ. Sci.* **2010**, *3*, 1182–1190. [CrossRef]
3. Sannigrahi, P.; Ragauskas, A.J.; Tuskan, G.A. Poplar as a feedstock for biofuels: A review of compositional characteristics. *Biofuels Bioprod. Biorefin.* **2010**, *4*, 209–226. [CrossRef]
4. Ragauskas, A.J.; Nagy, M.; Kim, D.H.; Eckert, C.A.; Hallett, J.P.; Liotta, C.L. From wood to fuels: Integrating biofuels and pulp production. *Indust. Biotechnol.* **2006**, *2*, 55–65. [CrossRef]
5. Huang, F.; Singh, P.M.; Ragauskas, A.J. Characterization of milled wood lignin (MWL) in Loblolly pine stem wood, residue, and bark. *J. Agric. Food Chem.* **2011**, *59*, 12910–12916. [CrossRef] [PubMed]
6. Hernes, P.J.; Hedges, J.I. Tannin signatures of barks, needles, leaves, cones, and wood at the molecular level. *Geochim. Cosmochim. Acta* **2004**, *68*, 1293–1307. [CrossRef]
7. Seiji, O.; Yasuta, Y.; Ohi, H. Structure elucidation of condensed tannins from barks by pyrolysis/gas chromatography. *Holzforschung* **2003**, *57*, 145–149.
8. Gaugler, M.; Grigsby, W.J. Thermal Degradation of Condensed Tannins from Radiata Pine Bark. *J. Wood Chem. Technol.* **2009**, *29*, 305–321. [CrossRef]
9. US Department of Energy. 2011 US Billion-Ton Update: Biomass Supply for a Bioenergy and Bioproducts Industry RD Perlack and BJ Stokes (Leads). ORNL/TM-2011/224; Oak Ridge National Laboratory: Oak Ridge, TN, USA; pp. 227.

10. Mohan, D.; Pittman, C.U.; Steele, P.H. Pyrolysis of wood/biomass for bio-oil: A critical review. *Energy Fuels* **2006**, *20*, 848–889. [CrossRef]
11. Pakdel, H.; Amen-Chen, C.; Roy, C. Phenolic compounds from vacuum pyrolysis of wood wastes. *Can. J. Chem. Eng.* **1997**, *75*, 121–126. [CrossRef]
12. Ingram, L.; Mohan, D.; Bricka, M.; Steele, P.; Strobel, D.; Crocker, D.; Mitchell, B.; Mohammad, J.; Cantrell, K.; Pittman, C.U., Jr. Pyrolysis of wood and bark in an auger reactor: Physical properties and chemical analysis of the produced bio-oils. *Energy Fuels* **2008**, *22*, 614–625. [CrossRef]
13. Arpiainen, V.; Lappi, M. Products from the flash pyrolysis of peat and pine bark. *J. Anal. Appl. Pyrolysis* **1989**, *16*, 355–376. [CrossRef]
14. Lomax, T.D.; Franich, R.A. Pyrolysis products of Pinus contorta bark. *N. Z. J. Forest. Sci.* **1990**, *20*, 349–352.
15. Lomax, T.D.; Franich, R.A.; Kroese, H. Pyrolysis products of Pinus radiata bark. *N. Z. J. Forest. Sci.* **1991**, *21*, 111–115.
16. Pan, S.; Pu, Y.; Foston, M.; Ragauskas, A. Compositional characterization and pyrolysis of Loblolly pine and douglas-fir bark. *BioEnergy Res.* **2013**, *6*, 24–34. [CrossRef]
17. Abdelnur, P.V.; Vaz, B.G.; Rocha, J.D.; de Almeida, M.B.B.; Teixeira, M.A.G.; Pereira, R.C.L. Characterization of bio-oils from different pyrolysis process steps and biomass using high-resolution mass spectrometry. *Energy Fuels* **2013**, *27*, 6646–6654. [CrossRef]
18. Kekäläinen, T.; Venäläinen, T.; Jänis, J. Characterization of birch wood pyrolysis oils by ultrahigh-resolution fourier transform ion cyclotron resonance mass spectrometry: Insights into thermochemical conversion. *Energy Fuels* **2014**, *28*, 4596–4602. [CrossRef]
19. Dhungana, B.; Becker, C.; Zekavat, B.; Solouki, T.; Hockaday, W.C.; Chambliss, C.K. Characterization of Slow-Pyrolysis Bio-Oils by High-Resolution Mass Spectrometry and Ion Mobility Spectrometry. *Energy Fuels* **2015**. [CrossRef]
20. Sudasinghe, N.; Dungan, B.; Lammers, P.; Albrecht, K.; Elliott, D.; Hallen, R.; Schaub, T. High resolution FT-ICR mass spectral analysis of bio-oil and residual water soluble organics produced by hydrothermal liquefaction of the marine microalga Nannochloropsis salina. *Fuel* **2014**, *119*, 47–56. [CrossRef]
21. Negandar, L.; Gonzalez-Quiroga, A.; Otyuskaya, D.; Toraman, H.E.; Liu, L.; Jastrzebski, J.T.B.H.; Van Geem, K.M.; Marin, G.B.; Thybaut, J.W.; Weckhuysen, B.M. Characterization and comparison of fast pyrolysis bio-oils from pinewood, rapeseed cake, and wheat straw using C-13 NMR and comprehensive GC x GC, *ACS Sustain. Chem. Eng.* **2016**, *4*, 4974–4985.
22. Cole, D.P.; Smith, E.A.; Dalluge, D.; Wilson, D.M.; Heaton, E.A.; Brown, R.C.; Lee, Y.J. Molecular characterization of nitrogen-containing species in switchgrass bio-oils at various harvest times. *Fuel* **2013**, *111*, 718–726. [CrossRef]
23. Ben, H.; Ragauskas, A.J. NMR Characterization of pyrolysis oils from kraft lignin. *Energy Fuels* **2011**, *25*, 2322–2332. [CrossRef]
24. Ben, H.; Ragauskas, A.J. Heteronuclear single-quantum correlation–nuclear magnetic resonance (HSQC–NMR) fingerprint analysis of pyrolysis oils. *Energy Fuels* **2011**, *25*, 5791–5801. [CrossRef]
25. Ben, H.; Ragauskas, A.J. Torrefaction of Loblolly pine. *Green Chem.* **2012**, *14*, 72–76. [CrossRef]
26. Ben, H.; Ragauskas, A.J. In situ NMR characterization of pyrolysis oil during accelerated aging. *ChemSusChem.* **2012**, *5*, 1687–1693. [CrossRef] [PubMed]
27. Huang, F.; Pan, S.; Pu, Y.; Ben, H.; Ragauskas, A.J. 19F NMR spectroscopy for the quantitative analysis of carbonyl groups in bio-oils. *RSC Adv.* **2014**, *4*, 17743–17747. [CrossRef]
28. David, K.; Ben, H.; Muzzy, J.; Feik, C.; Iisa, K.; Ragauskas, A. Chemical characterization and water content determination of bio-oils obtained from various biomass species using ^{31}P NMR spectroscopy. *Biofuels* **2012**, *3*, 123–128.
29. Mullen, C.A.; Strahan, G.D.; Boateng, A.A. Characterization of various fast-pyrolysis bio-oils by NMR spectroscopy. *Energy Fuels* **2009**, *23*, 2707–2718. [CrossRef]
30. Gebert, A.B.; Pozo, L.O.; Fuentes, P.N. Process for obtaining low and medium molecular weight Polyphenols and standardized solid fuel from tree wood or bark. U.S. Patent. US20090077871A1, 26 March 2009.
31. Froass, P.M.; Ragauskas, A.J.; Jiang, J. Chemical structure of residual lignin from kraft pulp. *J. Wood Chem. Technol.* **1996**, *16*, 347–365. [CrossRef]
32. Patwardhan, P.R.; Brown, R.C.; Shanks, B.H. Product distribution from the fast pyrolysis of hemicellulose. *ChemSusChem* **2001**, *4*, 636–643. [CrossRef]

33. Ren, X.; Meng, J.; Chang, J.; Kelley, S.S.; Jameel, H.; Park, S. Effect of blending ratio of Loblolly pine wood and bark on the properties of pyrolysis bio-oils. *Fuel Process. Technol.* **2017**, *167*, 43–49. [CrossRef]
34. Hu, K.; Westler, W.M.; Markley, J.L. Simultaneous quantification and identification of individual chemicals in metabolite mixtures by two-dimensional extrapolated time-zero (1)H-(13)C HSQC (HSQC(0)). *J. Am. Chem. Soc.* **2011**, *133*, 1662–1665. [CrossRef] [PubMed]
35. Sette, M.; Lange, H.; Crestini, C. Quantitative HSQC analyses of lignin: A practical comparison. *Comput. Struct. Biotechnol. J.* **2013**. [CrossRef] [PubMed]
36. Sassaki, G.L.; Guerrini, M.; Serrato, R.V.; Santana Filho, A.P.; Carlotto, J.; Simas-Tosin, F.; Cipriani, T.R.; Iacomini, M.; Torri, G.; Gorin, P.A. Monosaccharide composition of glycans based on Q-HSQC NMR. *Carbohydr. Polym.* **2014**, *104*, 34–41. [CrossRef] [PubMed]
37. Baldwin, R.M.; Feik, C.J. Bio-oil stabilization and upgrading by hot gas filtration. *Energy Fuels* **2013**, *27*, 3224–3238. [CrossRef]
38. Peng, Y.; Wu, S. The structural and thermal characteristics of wheat straw hemicellulose. *J. Anal. Appl. Pyrolysis* **2010**, *88*, 134–139. [CrossRef]
39. Özbay, G. Catalytic pyrolysis of pine wood sawdust to produce bio-oil: Effect of temperature and catalyst additives. *J. Wood Chem. Technol.* **2015**, *35*, 302–313. [CrossRef]
40. Aysu, T.; Sanna, A. Nannochloropsis algae pyrolysis with ceria-based catalysts for production of high-quality bio-oils. *Biores. Technol.* **2015**, *194*, 108–116. [CrossRef]
41. Birtill, J. Catalysis for renewables: From feedstock to energy production. *Platinum Metals Rev.* **2008**, *52*, 229–230. [CrossRef]
42. Lange, J.-P. Lignocellulose conversion: an introduction to chemistry, process and economics. *Biofuels Bioprod. Bioref.* **2007**, *1*, 39–48. [CrossRef]
43. Elias, V.O.; Simoneit, B.R.T.; Cordeiro, R.C.; Turcq, B. Evaluating levoglucosan as an indicator of biomass burning in Carajás, Amazônia: A comparison to the charcoal record. *Geochim. Cosmochim. Acta* **2001**, *65*, 267–272. [CrossRef]

polymers

MDPI

Review

A Review on the Partial and Complete Dissolution and Fractionation of Wood and Lignocelluloses Using Imidazolium Ionic Liquids

Hatem Abushammala [1,*] and Jia Mao [2]

[1] Fraunhofer Institute for Wood Research (WKI), Bienroder Weg 54E, 38108 Braunschweig, Germany
[2] Department of Mechanical Engineering, Al-Ghurair University, Dubai International Academic City, Dubai P.O. Box 37374, UAE; jia.mao@agu.ac.ae
* Correspondence: hatem.abushammala@wki.fraunhofer.de; Tel.: +49-531-215-5409

Received: 5 December 2019; Accepted: 8 January 2020; Published: 11 January 2020

Abstract: Ionic liquids have shown great potential in the last two decades as solvents, catalysts, reaction media, additives, lubricants, and in many applications such as electrochemical systems, hydrometallurgy, chromatography, CO_2 capture, etc. As solvents, the unlimited combinations of cations and anions have given ionic liquids a remarkably wide range of solvation power covering a variety of organic and inorganic materials. Ionic liquids are also considered "green" solvents due to their negligible vapor pressure, which means no emission of volatile organic compounds. Due to these interesting properties, ionic liquids have been explored as promising solvents for the dissolution and fractionation of wood and cellulose for biofuel production, pulping, extraction of nanocellulose, and for processing all-wood and all-cellulose composites. This review describes, at first, the potential of ionic liquids and the impact of the cation/anion combination on their physiochemical properties and on their solvation power and selectivity to wood polymers. It also elaborates on how the dissolution conditions influence these parameters. It then discusses the different approaches, which are followed for the homogeneous and heterogeneous dissolution and fractionation of wood and cellulose using ionic liquids and categorize them based on the target application. It finally highlights the challenges of using ionic liquids for wood and cellulose dissolution and processing, including side reactions, viscosity, recyclability, and price.

Keywords: cellulose; wood; lignocellulose; ionic liquid; imidazolium; fractionation; dissolution

1. Introduction

The dependency on fossil feedstock and the current consumption style are global challenges that triggered the search for sustainable processes for the efficient utilization of renewable resources such as biomass [1,2]. Lignocellulosic biomass is the Earth's most abundant renewable resource, which includes forest and food crops, their harvesting residues, and industrial and municipal lignocellulosic waste [3,4]. In Europe, hundreds of millions of tons of lignocellulosic residues are generated every year, most of which are underutilized, burnt, or end up in dumping sites releasing greenhouse gases into the atmosphere [5]. In more detail, around 80 million tons of forest residues, 350 million tons of crop residues, 90 million tons of industrial lignocellulosic residues, and 200 million tons of municipal lignocellulosic waste are generated every year in Europe, one-third of which is available for utilization [6]. In Germany, for instance, a fraction (ca. 2–3 million tons/year) of saw-rest wood as a residue is processed into pellets, which are burnt as a source of bioenergy [7].

Other than the urgent need for utilizing biomass and bio-residues, there is also the need to develop green technologies for processing these massive amounts to bio-based materials and products. Wood and its polymers are insoluble in most of the common industrial solvents due to the strong

intermolecular and intramolecular networks of hydrogen bonds and complex microstructure [8,9]. For cellulose processing, carbon disulfide (toxic), N-methylmorpholine-N-oxide (more environmentally acceptable), and dimethylsulfoxide (DMSO), dimethylformamide (DMF), and dimethylacetamide (DMAc) in combination with lithium chloride are used [10,11]. However, there is still a need to develop more environmentally friendly solvents for cellulose and wood processing.

In the 1990s, ionic liquids were proposed as "green solvents" for wood and cellulose dissolution. They are salts that are liquids at temperatures below 100 °C. They have unique properties such as low vapor pressure, high thermal and chemical stability, non-flammability, chemical tunability, and a broad electrochemical window [12–14]. The low vapor pressure of ionic liquids, which is a result of the strong interaction forces between their constituting ions, made them considered green solvents in general as they do not emit potentially hazardous organic compounds during use, handling, and transportation [15]. They also have a wide range of solvation power and selectivity by simply tuning the chemistry of the ions they are made of. They are, therefore, excellent substitutes for volatile organic solvents in chemical processes. Other than their potential as solvents, they have also shown great potential in a wide range of applications, including electrochemical systems, energy-harvesting devices, chromatography, lubrication, chemical catalysis, CO_2 capture, and hydrometallurgy [16–20].

The first report on ionic liquids goes back to 1914 by Paul Walden, who prepared the ionic liquid ethylammonium nitrate [21]. They did not, however, receive much attention until 1999, before which there was less than 35 publications on ionic liquids per year compared to more than 4500 in 2018 (Figure 1). Ionic liquids production has also been industrialized by many companies such as BASF (Germany), Acros Organics (Belgium), EMD (USA), Iolitec (Germany), Sigma-Aldrich (Germany), and TCI Chemicals (Japan). The market of ionic liquids is estimated to be 2.2 billion US dollars in 2022 and to continue to grow [22]. The first report on the use of ionic liquid for cellulose processing is thought to be in 2002 by Swatloski et al., who explored the solubility of pulp cellulose in different ionic liquids [23]. However, two patents in 1933 and 1934 by Graenacher claim the use of molten pyridinium and ammonium salts to dissolve cellulose [24,25]. On the other hand, the first report on wood dissolution using ionic liquids seems to go back to 2006 by Honglu and Tiejun, who dissolved the dawn redwood (softwood) using two imidazole-based ionic liquids and showed that ionic liquids could be better liquefaction agents than phenol/H_2SO_4, a common liquefaction agent at the time [26]. Few reports on wood and ionic liquids were published earlier to Honglu's, which, however, investigated the potential of ionic liquids for wood preservation and electrostatic control [27–29]. More reports followed Honglu's by Kilpelainen et al. and Fort et al. [30,31]. In the last five years (2014–2018), the literature was enriched by around 2000 publications on the use of ionic liquids for wood and cellulose dissolution and processing.

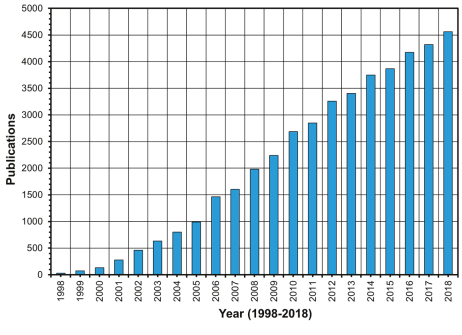

Figure 1. The number of publications in the last two decades showing the increasing interest in ionic liquids (Web of Science, November 2019, ionic liquids).

Ionic liquids can almost be made of unlimited combinations of cations and anions, which are relatively less regular in size than those constituting simple salts such as sodium chloride (Figure 2) [32]. This results in crystalline structures with significantly lower lattice energies and melting points. The cations of most common ionic liquids varied from tetra-alkyl ammonium and tetra-alkyl phosphonium to imidazolium, pyridinium, and pyrrolidinium. Cations that are even more complex have been reported in the literature [33]. The anions also varied from simple halides, acetate, nitrate, hydrogen sulfate to more complicated anions such as acesulfamate [34]. As a result, it is possible to synthesize ionic liquids with a specific melting point, density, viscosity, hydrophilicity, and electrical conductivity to be used for a certain application or chemical process [35,36]. For the processing of wood, lignocellulose, and cellulose, imidazolium ionic liquids have been the most commonly used, which are all based on 1-alkyl-3-alkylimidazolium as a cation (Table 1).

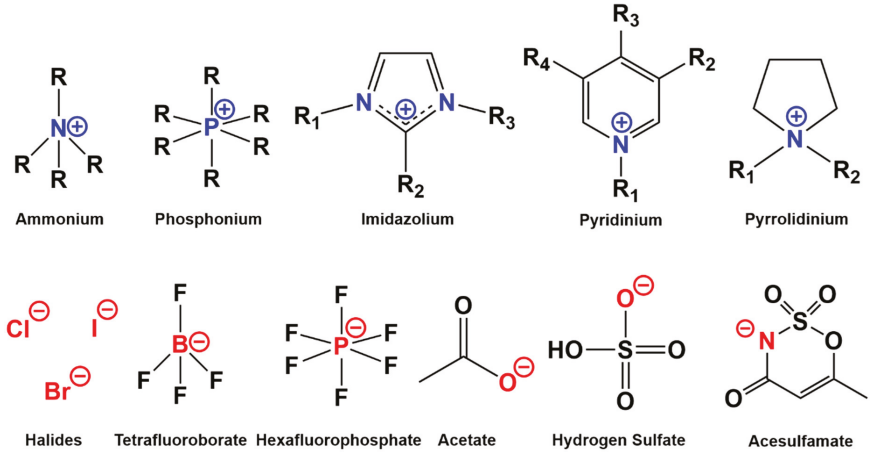

Figure 2. Some of the cations and anions that constitute most of the commonly used ionic liquids for wood and cellulose dissolution and fractionation.

The impact of the constituting ions on the physicochemical properties of ionic liquids is significant. For instance, [BMIM][Cl] and [EMIM][Cl] are solid at room temperature while [BMIM][OAc] and [EMIM][OAc] are liquid. [BMIM][BF_4] and [EMIM][BF_4] are liquid at room temperature while [BnMIM][BF_4] is solid. In terms of viscosity, [BMIM][HSO_4] has a viscosity of ca. 3100 cP compared to ca. 1500 cP for [EMIM][HSO_4] due to the higher van der Waal forces for longer alkyl chains [37,38]. Both are significantly more viscous than [BMIM][PF_6] and [EMIM][PF_6], [BMIM][BF_4], and [EMIM][BF_4], respectively. A study on [BMIM] ionic liquids with carboxylates of different chain lengths (formate, acetate, propionate, and butyrate) showed that increasing the chain length significantly increases the viscosity of the ionic liquid [39]. It is important to mention here that the values of melting temperature and viscosity are strongly affected by the presence of water and impurities. This is the reason behind the variation in the melting point and viscosity values in the literature. The density of imidazolium ionic liquids ranged between 1.0 to 1.4 g/cm^3, which is slightly higher than that for common organic solvents (0.7–1.0 g/cm^3) [40]. It is strongly dependent on the molecular mass of the cation and anion. For instance, the density of [BMIM][PF_6] is higher than [BMIM][BF_4] and they are both higher than [BMIM][Cl], [BMIM][Br], and [BMIM][OAc] [41]. The thermal stability of imidazolium ionic liquids is strongly dependent on the anion. The degradation temperature varies between 200 to 500 °C and increases in the following order [PF_6] > [BF_4] > [Cl] = [Br] = [I] [42]. Minor changes in the degradation temperature were reported between [EMIM] and [BMIM] [43].

Imidazolium ionic liquids may exhibit acid/base properties, which play an important role in their performance. [BMIM][HSO_4] is an acidic ionic liquid while [BMIM][OAc] is basic due to the acidity of

hydrogen sulfate and the basicity of acetate, respectively [44,45]. The acidity/basicity of imidazolium ionic liquids strongly depends on the acidity/basicity of the anion. For instance, [BMIM][OAc] is significantly more basic than [BMIM][Cl] because the acetate anion is more basic than chloride while [EMIM][OAc] showed slightly higher basicity than [BMIM][OAc] [46].

Table 1. Summary of the most commonly used imidazolium ionic liquids for wood and cellulose dissolution and fractionation and their physicochemical properties.

Ionic Liquid	Properties				Ref.
	Melting Temp. (°C)	Density (g/cm^3) at 25 °C	Viscosity (cP) at 20–30 °C	Electrical Conduct. (mS/cm) at 25 °C	
[BMIM][OAc]	−20	1.1	208	1.4	[47,48]
[BMIM][Cl]	41–70	1.1	Solid	-	[47,48]
[BMIM][Br]	60–81	1.1	Solid	-	[47–49]
[BMIM][I]	−72	1.4–1.5	1110–1183	0.5	[47,48]
[BMIM][HSO_4]	-	1.3	3088	-	[47,48]
[BMIM][BF_4]	−83–−74	1.1–1.3	72–233	3.2	[47,48]
[BMIM][PF_6]	11	1.3–1.4	207–450	1.5–4.8	[47,48]
[BMIM][Ace]	30	1.2	800	0.5	[50]
[EMIM][OAc]	−45–−14	1.0–1.1	91–162	2.5–2.8	[47,48]
[EMIM][Cl]	80–89	1.1–1.2	Solid	-	[47,48]
[EMIM][Br]	65–91	-	Solid	-	[47,48]
[EMIM][I]	79–85	-	Solid	-	[47,48]
[EMIM][HSO_4]	-	1.4	1510	0.5	[48]
[EMIM][BF_4]	6–15	1.2–1.4	34–66	13.0–14.1	[47,48]
[EMIM][PF_6]	58–64	1.4	450	5.2	[47–49]
[EMIM][Ace]	34	1.3	556	0.6	[50]
[AMIM][Cl]	47	-	-	-	[48]
[AMIM][I]	57	-	-	-	[48]
[BnMIM][Cl]	75	-	Solid	-	[48]
[BnMIM][BF_4]	78	-	Solid	-	[48]
[BnMIM][PF_6]	130–135	-	Solid	-	[47,48]

[BMIM]: 1-butyl-3-methylimidazolium, [EMIM]: 1-ethyl-3-methylimdiazolium, [AMIM] 1-allyl-3-methylimidazolium, [BnMIM]: 1-benzyl-3-methylimidazolium, [OAc]: acetate, [Ace]: acesulfamate, [BF_4]: tetrafluoroborate, [PF_6]: hexafluorophospohate.

This review discusses the potential of ionic liquids with a focus on 1-alkyl-3-methylimidazium as cation for the dissolution and fractionation of wood and cellulose. The literature reports will be categorized based on the following target applications: (1) dissolution of wood and cellulose to overcome their recalcitrance to enzymatic hydrolysis for biofuel production, (2) fractionation of wood to its individual components before each being utilized in a certain application, (3) processing wood and cellulose to all-wood and all-cellulose composites, and (4) extraction of cellulose nanoparticles from wood and cellulose. This review will not cover the use of ionic liquids as solvents for the chemical modification of cellulose as it has been thoroughly reviewed [51,52].

2. Dissolution Capability and Selectivity of Imidazolium Ionic Liquids to Wood Polymers

The selection of a cation and anion combination does not only influence the physicochemical properties of ionic liquids but also their performance in certain applications and processes. With the

focus on the dissolution and processing of wood and cellulose, it is of great importance to have an idea about the solvation power and selectivity of ionic liquids to wood polymers: cellulose, hemicelluloses, and lignin. Some studies relied on the solubility of the individual wood polymers in ionic liquids, while others compared the amount of each polymer that can be dissolved when the wood is treated with an ionic liquid [53]. Although it is believed that ionic liquids are able to dissolve wood and its polymers simply by disrupting the strong hydrogen bond networks between their molecular chains, the process is more complicated and may involve other processes such as hydrolysis and chemical derivatization. These side processes will be thoroughly discussed at a later stage in this review.

2.1. Impact of the Cation and Anion Combination

There are four imidazolium cations that are most commonly used for the dissolution of wood and cellulose: 1-ethyl-3-methylimidazolium ([EMIM]), 1-butyl-3-methylimidazolium ([BMIM]), 1-allyl-3-methylimidazolium ([AMIM]), and 1-benzyl-3-methylimidazolium ([BnMIM]). The main difference is the substituent at the N1 position at the imidazolium ring. Ionic liquids with no substituent at that position, i.e., [HMIM] where H stands for hydrogen, tend to be acidic [54]. Studies showed that [EMIM] and [BMIM] ionic liquids are better solvents for cellulose than [AMIM] and [BnMIM] ionic liquids due to the hydrophobicity introduced to the imidazolium ring by the allyl and the benzyl groups. On the other hand, [AMIM] and [BnMIM] are better lignin solvents due to the pi-pi interaction of the allyl group and benzyl group with the phenolic rings of lignin [55]. For the same reason, [BnMIM][Cl] can mainly dissolve lignin but not cellulose while [EMIM][Cl], [BMIM][Cl], and [AMIM][Cl] can dissolve all wood components [56]. [AMIM][Cl] is a better wood solvent than [EMIM][Cl] and [BMIM][Cl] because it better interacts with both lignin and cellulose, which supports it accessibility inside wood microstructure [30,57]. The same applies to [AMIM][OAc], [BMIM][OAc], and [EMIM][OAc] [58]. It has also been reported that [EMIM][OAc] can dissolve more cellulose but slightly less lignin than [BMIM][OAc] due to the higher hydrophobicity of butyl compared to ethyl, which is favored by lignin [59]. The same applies to [EMIM][Cl] and [BMIM][Cl] [60,61].

The chemistry of the anion has also a strong impact on the dissolution capability and selectivity of the ionic liquid [62]. Due to its high basicity, the acetate anion [OAc] can efficiently break hydrogen bonding and therefore allows better wood dissolution compared to chloride [Cl] [63]. It also showed a higher dissolution affinity to lignin than chloride [61,64]. The acetate ion is more capable of attacking the hydrogen of the β carbon of lignin inducing the cleaving of β-O-4 bonds in lignin [65]. The formate [OF] anion showed the same power of acetate to lignin dissolution but more power to the dissolution of hemicelluloses [58]. Due to its big size, the acesulfamate anion showed a complete selectivity to lignin dissolution because it hinders its diffusion into the crystalline regions of cellulose [50,66] while dicyanamide ionic liquids cannot dissolve wood or cellulose [62]. Unlike acetate and chloride ions, hydrogen sulfate is an acidic anion, which supports the hydrolysis of wood polysaccharides and lignin condensation in a behavior similar to sulfuric acid [44,67,68]. To better categorize the polarity and acidity/basicity of ionic liquids and foresee their interaction with wood polymers and other materials, their Kamlet–Taft parameters have been determined [69,70]. Finally, it is important to mention that part of the impact of the cation and anion on the interaction of ionic liquids with wood polymers is due to their influence on the viscosity of the ionic liquid. Ionic liquids with lower viscosities tend to have more solvation power to wood and cellulose.

2.2. Impact of the Addition of Water, Organic Solvents, and Salts

Ionic liquids are miscible with water and most organic solvents, and their mixtures have been explored for processing wood and cellulose. Some of these studied only aimed at reducing the viscosity of the ionic liquid while others investigated the impact of water or organic solvent addition on the properties of the ionic liquid and its dissolution power to wood polymers [71]. Fendt et al. have shown that the addition of 5% (w/w) of water or organic solvents (acetonitrile and ethylene glycol) to [EMIM][OAc] and [BMIM][OAc] decreased their viscosity by 50% [72]. Many reports showed that

the presence of water decreased the solubility of cellulose in ionic liquids because the water supports the reformation of hydrogen bonding of cellulose and affects the cation/anion interactions [23,73–75]. Similar behavior was reported for some organic solvents [76]. On the other hand, water addition to ionic liquids facilitated lignin dissolution and depolymerization [77], hemicelluloses dissolution [78–80], and hydrolysis of the lignin-carbohydrate complex [81], which assisted the disintegration of wood. These observations, however, do not apply to DMSO, DMF, and DMAc, which reduced the viscosity of the ionic liquids and supported the dissolution of wood polymers, including cellulose [82–85]. They also supported the dissociation of the ionic liquid and increasing the concentration of the ions as a result [86]. Some studies tailored the dissolution power and selectivity to wood polymers by adjusting the pH of the ionic liquid [87,88] or by the addition of salts such as LiCl and Na_2SiO_3 [89–91].

2.3. Impact of Dissolution Conditions

It is not only the chemistry of the ionic liquid that determines the efficiency of wood dissolution. Process parameters, such as temperature and time have a significant influence [92]. Temperature does not only push the kinetics of the process forward but also reduces the viscosity of the ionic liquid, supporting further dissolution. Temperature also affects the selectivity of ionic liquids to wood polymers. For instance, many studies have reported the strong capability of [EMIM][OAc] to wood dissolution, most of which have used high dissolution temperatures and time. However, It has been shown that reducing the reaction severity allows the dissolution of the majority of lignin and hemicelluloses of wood with a minimum cellulose dissolution in a similar scenario to wood pulping [93]. On the other hand, [BMIM][Ace], which was proven not to be able to dissolve cellulose [50], could disintegrate cellulose at high dissolution temperatures (130 °C) [94].

Other process parameters such as stirring speed, solid/liquid ratio, wood and cellulose particle and molecular size [60,95,96], the use of microwave heating [97,98], and ultrasonication [99] are also important and have been thoroughly explored in the literature. It has also been observed that wood dissolution is affected by environmental conditions. For instance, humidity and oxygen supported the depolymerization of wood polymers in [EMIM][Cl] [100].

3. Fractionation and Regeneration of Lignocellulosic Polymers upon Dissolution in Ionic Liquids

Upon a complete (homogeneous) or partial (heterogonous) dissolution of wood, different strategies have been used to separate the dissolved and undissolved fractions, which can be summarized into four (Figure 3). In the first strategy, the wood is partially or completely dissolved, and the reaction mixture is then fully regenerated using an anti-solvent without any fractionation. The regenerated wood is collected by centrifugation or filtration, and the ionic liquid is then recycled. This strategy is mostly used for processing wood into composites, as there is no need for wood fractionation. It is also used when the main aim of dissolution is breaking the recalcitrant of wood for biofuel production [101]. In the second strategy, the wood is dissolved, mainly completely, and the dissolved wood is fractioned to polysaccharide-rich fraction and lignin fraction by selective regeneration. The polysaccharide-rich fraction is usually explored for biofuel production, as the removal of lignin facilitates the enzymatic hydrolysis of the polysaccharides to simple sugars. It can also be fractioned further to hemicelluloses and cellulose using alkaline hydrolysis. The third and fourth strategies are mostly used for a thorough fractionation of wood upon partial dissolution. The third strategy separates the dissolved wood from the undissolved using centrifugation or filtration, which is then regenerated completely with no fractionation resulting in two fractions: dissolved wood and undissolved. While the fourth strategy fractions the dissolved wood further to lignin and polysaccharide fractions resulting in three fractions: undissolved wood, polysaccharide-rich fraction, and lignin. The undissolved wood in both strategies could be processed further to pulp fibers or cellulose nanoparticles. The procedure to separate the dissolved wood from the undissolved depends on the viscosity of the reaction mixture. If the reaction is viscous as in the case of using ionic liquids with no dilution, centrifugation is usually used as filtration

could be impossible to perform. Sometimes, a co-solvent such as DMSO, DMF, or DMAc is added to the reaction mixture upon dissolution to allow the separation of wood fractions by filtration [102,103].

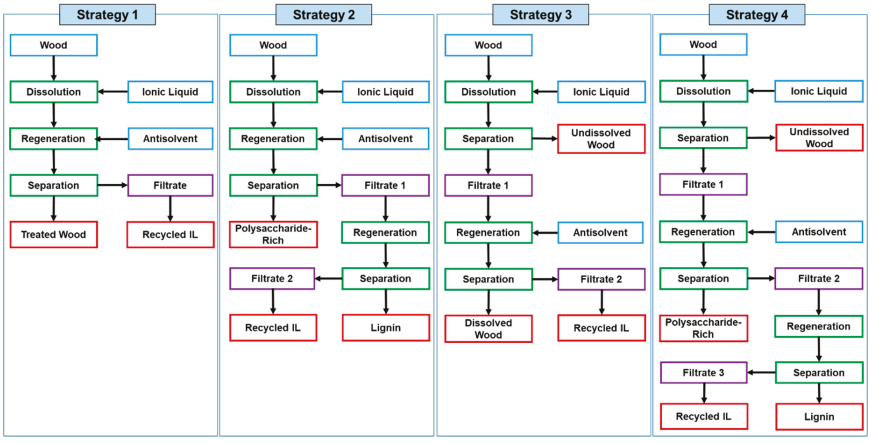

Figure 3. The different fractionation strategies followed in the literature upon partial or complete dissolution of wood or lignocelluloses.

The regeneration of the dissolved wood using antisolvents is a crucial process. The selection of anti-solvent affects the recovery of the dissolved wood and the efficiency of fractionation. When an anti-solvent is added to a reaction mixture, the ions of the ionic liquids are extracted into the liquid phase through hydrogen bonding and coulombic forces shielding them from direct interaction with wood polymers. This also disrupts the cation/anion solvation network triggering the hydrogen bonds to reform [104,105]. Water is the most used antisolvent for complete regeneration of wood with no fractionation. Methanol and ethanol have also been used [106,107]. To fraction the dissolved wood to a polysaccharide-rich fraction and lignin fraction, a variety of antisolvents has been used. Among these, acetone:water (Ac/W) mixtures are the most commonly used [108] due to the easiness of tailoring its polarity by controlling the Ac/W mixing ratio and by evaporating the acetone. When added to dissolved wood, the polysaccharides (with some lignin) are regenerated while keeping lignin soluble in the mixture. The acetone is then evaporated, increasing the polarity of the mixture and triggering lignin to precipitate, which can then be isolated. The efficiency of the fractioning process and the purity of the polysaccharide fraction are higher using high Ac/W ratios. Unfortunately, Ac/W mixtures with high Ac\W ratios (2:1 and more) could be immiscible with some ionic liquids such as [EMIM][OAc]. A ratio of 9:1 is recommended for [BMIM][Cl] and 1:1 for [EMIM][OAc] [108,109]. In some reports, Ac/W-based regeneration is differently performed. The acetone is added at first to precipitate the polysaccharides, then water is added to precipitate lignin [110]. The same approach was used using ethanol instead of acetone [96,111]. A solution of sodium hydroxide (usually 0.1M) was also used as an antisolvent for wood fractionation [112]. When added to a dissolved wood mixture, the polysaccharides (with some lignin) are regenerated and separated. The IL/antisolvent mixture is then acidified to a pH of 2 to regenerate lignin [97,113].

4. Applications of Ionic Liquids for Lignocellulose and Cellulose Dissolution and Processing

4.1. Wood and Cellulose Dissolution for Biofuel Production

Ionic liquids have received a significant attention because of their effectiveness in reducing the recalcitrance of biomass to enzymatic hydrolysis towards the production of bioethanol [114]. Ionic liquids also reduce the need for corrosive and toxic chemicals and the accompanying waste streams that are usually generated with alkaline and acidic reagents [115,116]. An ionic liquid-mediated

pretreatment of wood aims at effective (1) delignification, (2) breaking lignin-carbohydrate bonds, (3) destroying the crystalline regions of cellulose, and (4) hydrolysis of polysaccharides. To achieve some or all of these goals, different approaches have been followed, which mostly operated at high temperatures for long durations (Table 2). The most common approach is achieving maximum wood disintegration in general without delignification. In such approach, the wood is dissolved completely then fully regenerated using water as antisolvent following the first fractionation strategy as shown in Figure 3 [110,117–119]. The disintegrated wood is then subjected to enzymatic hydrolysis using cellulase enzymes to produce glucose and other simple sugars, which are ultimately fermented to bioethanol. In some systems, the cellulase enzyme and ionic liquids were simultaneously used for wood disintegration and hydrolysis but they have to be compatible with each other in such systems [120–122]. Another approach disintegrates and delignifies wood and the dissolved lignin is separated using an acetone:water mixture or sodium hydroxide solution as antisolvent following the second fractionation strategy [112,123].

The most commonly used ionic liquids for wood disintegration were [EMIM][OAc], [AMIM][Cl], and [BMIM][Cl]. In general [EMIM][OAc] was more powerful than [AMIM][Cl], which was more powerful than [BMIM][Cl] [124]. In a few cases, DMSO was added to support further wood disintegration [125–127]. In some studies, aqueous solutions of ionic liquids were used to disintegrate wood by targeting the hemicelluloses as they are crucial for wood disintegration [58,128,129]. Similar studies aimed at selectively extracting the polysaccharides (mainly hemicelluloses) from wood to be hydrolyzed and fermented to biofuels at a later stage. In these studies, the acidic ionic liquid [BMIM][HSO_4] was mainly used [96,130].

Table 2. Summary of the literature on wood and cellulose dissolution for biofuel production.

Wood/Lignocellulose	Dissolution Conditions			Regeneration		Ref.
	Ionic Liquid	Temp. (°C)	Time (h)	Strategy	Antisolvent	
Triticale, Wheat Straw	[EMIM][OAc]	150	1.5	2	0.1 M NaOH then Acidification	[112]
Cellulose	[EMIM][Cl], [AMIM][Cl], [BMIM][Cl]	100	2	1	Water	[131]
Radiata Pine, Eucalyptus	[EMIM][OAc]	50–150	0.8	1	Water	[132,133]
Scots Pine	[BHIM][HSO_4] /Water	120–170	1–4	2	Ethanol then Water	[96]
Corn Stalk	[BMIM][BF_4] /Water	150	5	1	Water	[117]
Yellow Pine	[EMIM][OAc]	140	0.25–0.75	1	Water	[134]
Guinea Grass	[EMIM][OAc]	157	0.5	1	Water	[118]
Japanese Cedar	[EMIM][OAc]	80	3	3	Acetone then Water	[110]
Japanese Cedar	[EMIM][OAc]	60–100	2–8	1	Water	[110]
Mixed Softwood	[BMIM][OAc]	100	15	1	Water	[119]
Hornbean, Spruce	[BMIM][Cl]	50–150	0.5–2	1	Water	[135]
Cedar, Eucalyptus, Bagasse Powder	[EMIM][OAc]	110	16	1	Water	[136]
Beech Wood Waste	[EMIM][OAc]	120	3	1	Water	[137]
Sugarcane	[BMIM][OAc]	110	0.5	3	Water	[138]
Poplar Wood Flour	[EMIM][OAc]	90	0.3–0.7	1	Water	[139]

Table 2. *Cont.*

Wood/Lignocellulose	Dissolution Conditions			Regeneration		Ref.
	Ionic Liquid	Temp. (°C)	Time (h)	Strategy	Antisolvent	
Sawdust of Norway Spruce, Scots Pine, and Silver Birch and Winter Wheat Straw	[BMIM][OAc], [EMIM][Cl], [BMIM][Cl]	100–110	Up to 100	1	Water	[140]
Polar Wood	[BMIM][OAc], [MMIM][MEP]	130	18	2	Acetone then Water	[141]
Oil Palm Biomass	[EMIM][DEP]	70–100	4	2	1:1 Ac/W	[123]
Eastern White Pine	[AMIM][Cl] /DMSO	110	1	2	1:1 Ac/W	[125]
Norway Spruce	[BMIM][OAc]	100	20	1	Methanol	[142]
Pine Wood	[EMIM][Cl] /[EMIM][OAc] mixture	80–120	3	1	Water	[143]
Beech Wood	[EMIM][OAc] /Water	115	1.5	1	1:1 Ac/W	[81]
White Poplar and Pine	[EMIM][OAc] /DMSO	110	3	1	Water	[126]
P. tomentosa	[EMIM][OAc], [BMIM][Cl], [AMIM][Cl]	130	2	1	5% NaOH	[113]
Hybrid Pennisetum	[AMIM][Cl]	100–190	0.5–5.5	1	Water	[144]
Sugarcane Bagasse	[EMIM][OAc], [BMIM][Cl], [AMIM][Cl]	100	1	1	Water	[124]
Mixed Pine	[BMIM][Cl]	70–150	5–24	1	Water	[145]
Spruce and Oak Sawdust	[EMIM][OAc]	110	0.65	1	Methanol, Ethanol, Water	[146]
Silver Wattle	[EMIM][OAc]	90–150	0.5–24	1	Water, Ethanol, Methanol, 1:1 Ac/W	[147]
Sugarcane Bagasse Cellulose	[EMIM][OAc]	90	6	1	Water	[148]
Cassava Residues	[BMIM][Cl]	130	2	1	Water	[149]
Norway Spruce, Sugarcane	[AMIM][OF]	45–120	2–48	1	Water	[150]
Laminaria japonica Seaweed	[AMIM][Cl]	60–90	2	1	Water	[151]
Cotton Stalks	[EMIM][OAc]	150	0.5	1	Water	[152]
Spruce and Beech	[EMIM][OAc]	115	1.5	4	Ethanol then Water	[111]
Polar Wood	[EMIM][OAc]	110	12	1	Water	[153]
Birch and Pine Wood	[EMIM][OAc], [BMIM][Cl]	25	1–3	1	Ethanol	[154]
Aspen Wood	[EMIM][OAc]	120	1–5	1	Water	[155]
Eucalyptus	[EMIM][OAc] /DMSO	80–140	2–4	1	Water	[127]
Eucalyptus Cellulose	[EMIM][OAc], [AMIM][Cl], [BMIM][Cl], [BMIM][Ace]	130	1	1	Water	[94]
Douglas-Fir Wood	[EMIM][OAc]	120–160	3	1	Water	[156]

Table 2. *Cont.*

Wood/Lignocellulose	Dissolution Conditions			Regeneration		Ref.
	Ionic Liquid	Temp. (°C)	Time (h)	Strategy	Antisolvent	
Yellow Pine	[HMIM][Cl]	110–150	Up to 5	2	1:1 Ac/W	[54]
Pine, Eucalyptus, Switchgrass	[EMIM][OAc]	160	3	1	Water	[157]
Norway Spruce	[EMIM][OAc], [BMIM][OAc]	120	1–15	1	Water	[158]
Sago Waste	[BMIM][Cl]	140–155	0.5–2.5	1	Water	[159]
Oil Palm Fronds	[BMIM][Cl]	80–120	0.5–3	1	Water	[160]
Kenaf Powder	[BMIM][Cl], [AMIM][Cl], [EMIM][Cl], [EMIM][DEP], [EMIM][OAc]	110	2	1	Water	[161]
Sugarcane Bagasse	[EMIM][OAc]	120	2	1	Water	[162]
Sugarcane Bagasse	[BMIM][Cl]	150	1.5	1	Water	[163]
Wheat Straw	[EMIM][OAc] /Water	130–170	0.5–5.5	1	Water	[128,129]
Miscanthus giganteus, Pine, Willow	[BMIM][HSO_4] /Water, [BMIM][MSO_4] /Water	120	2	3	Water	[130]
Eucalyptus, Southern Pine, Norway spruce	[AMIM][Cl]	120	5	1	Water, Methanol	[106]
Switch grass	[BMIM][Cl], [EMIM][OAc], [BMIM][OAc]	110	0.25	1	Water	[59]
Maple Wood Flour	[EMIM][OAc]	50–130	0.5–20	1	Water	[57]

Abbreviations: [OF]: formate, [DEP]: diethylphosphate, [MMIM]: 1-methyl-3-methylimidazolium, [MEP]: methylphosphite, [MSO_4]: methylsulfate, Ac/W: acetone/water mixture.

4.2. Ionic Liquid-Mediated Fractionation and Pulping of Wood and Lignocellulose

Traditional wood pulping, including Kraft and Sulfite pulping, are considered environmentally unfriendly due to the use of strong acidic and alkaline solutions, which require special treatments [164,165]. Furthermore, the separation of dissolved hemicelluloses and lignin from the pulping liquor is relatively difficult. When extracted, lignin and hemicelluloses can be strongly modified (sulfonation, oxidation) during pulping limiting their potential in certain applications [166]. Ionic liquids offer a solution for these challenges and provide many possibilities for wood fractionation and pulping, depending on the aim of the treatment. The fractionation procedure is also relatively simple, and the separated fractions are not/slightly modified [167].

Some fractionation procedures dissolve wood completely and fraction it to its individual components without paying attention to the crystalline structure of cellulose (Table 3) [168,169]. The individual polymers are then used separately or together for certain applications. For example, cellulose and hemicelluloses can be used for the production of bioethanol, furfural compounds [170], pyrolysis products [108], and synthetic wood composites [171] while lignin can be used for the production of adhesives and phenolic compounds [172,173]. Sometimes, wood components are selectively extracted. Acesulfamate and methylsulfate ionic liquids were suggested as selective solvents for lignin [50,174], while a mixture of ionic liquids with water and certain organic solvents were proved efficient for the extraction of hemicelluloses [175]. The aqueous and organic mixture of ionic liquids were used to upgrade Kraft pulp to high-quality dissolving pulp by reducing its hemicellulose content [176–178]. Ionic liquids acidified to a pH of 4–5 were found to be able to dissolve hemicelluloses selectively. If the pH is adjusted to 2–3, they become capable of dissolving cellulose.

In both scenarios, lignin stays undissolved [87]. During the selective extraction of hemicelluloses and lignin, the crystalline structure could be degraded, especially if high dissolution temperatures are used. At lower temperatures (60 °C and less) and short dissolution time (two hours and less), it was possible to extract Cellulose I pulp [179,180]. Different studies have shown that the dissolution of hemicelluloses and cellulose is mainly affected by the anion, while lignin dissolution is affected by both the cation and anion [181–183]. Significant pi-pi stacking of imidazolium with the benzene rings supports lignin dissolution and depolymerization [184,185].

Table 3. Summary of the literature on wood fractionation for the separation of its individual polymers.

Wood/Lignocellulose	Dissolution Conditions			Regeneration		Ref.
	Ionic Liquid	Temp. (°C)	Time (h)	Strategy	Antisolvent	
Cypress Wood	[EMIM][OAc]	80	1	2	1:1 Ac/W	[186]
Rubber Wood	[MMIM][MSO_4]	25–100	0.5–2.5	3	Methanol	[187]
Sugarcane Straw	[EMIM][OAc]	90	5	2	1:1 Ac/W	[108]
Eucalyptus urophylla	[EMIM][OAc]	140–170	0.5–6	4	Water then Acidic Water	[97]
Maritime Pine	[BMIM][HSO_4] /Water	170	0.5–2	2	Ethanol then Water	[170]
Norway spruce	[EMIM][OAc] /DMSO	80–150	2–6	4	Acetone	[188]
Steam-exploded Angelim Vermelho	[EMIM][OAc]	30	0.25	4	1:1 Ac/W	[179]
Angelim Vermelho	[EMIM][OAc]	60	2	4	1:1 Ac/W	[180]
Wheat Straw	[EMIM][OAc]	110–120	1–16	1	0.1M NaOH or 9:1 Ac/W	[109]
Radiata Pine, Eucalyptus globlus	[AMIM][Cl]	120–170	0.3–1	4	DMSO then Methanol	[102,103]
Birch Wood	[EMIM][OAc]	110	16	2	1:1 Ac/W	[189]
Wheat Straw	[EMIM][OAc]	80–140	2–18	2	Alkaline Water, Neutral, then Acidic	[168]
Poplar Wood	[EMIM][OAc]	110	16	2	1:1 Ac/W	[167]
Sugarcane Bagasse	[BMIM][Cl]	110	72	2	9:1 Ac/W	[169]
Bagasse	[EMIM] [Xylenesulfonate]	170–190	0.5–2	1	0.1M NaOH then Acidification	[190]
Southern Pine, Red Oak	[EMIM][OAc], [BMIM][OAc]	110	16	2	1:1 Ac/W	[61]
Radiata Pine	[BMIM][Ace]	80–140	1–16	3	Acetone	[50]

4.3. Ionic Liquids for Processing All-Wood and All-Cellulose Composites

Wood liquefaction is necessary for its processing and fractionation. In the past, it was not possible to liquefy wood without the use of high pressure and temperature. Various liquefaction and dissolution agents were then explored, such as phenol and ethylene carbonate, in the presence of strong acids as catalysts [191,192]. In 2006, Honglu and Teijun showed that ionic liquids, in addition to their green properties, can be better wood liquefaction agents than phenol/sulfuric acid [26]. Since then, ionic liquids were explored as solvents and liquefaction agents for wood modification [193], wood processing [194], and to facilitate wood grinding [195]. They were also used for processing synthetic wood composites of controlled amounts of cellulose/hemicelluloses/lignin [171].

Wood liquefaction with ionic liquids causes major changes in the anatomic and molecular levels, including swelling, fibrillation, disintegration, plasticization, and derivatization [66,196]. Wood swelling in ionic liquids is comparable, and sometimes better, to that in water and organic

solvents [66]. It is also reversible, which means that cellulose can keep its native crystalline structure upon the removal of the ionic liquid [197], although strong fibrillation and disintegration are observed. Thermomechanical studies showed that ionic liquids are capable of lowering the glass transition of lignin in wood to values similar to or lower than those obtained using water as a plasticizer [198]. [EMIM][OAc]-plasticized Norway spruce showed a glass transition around 60 °C, which is lower than those obtained using water and ethylene glycol (84 and 74 °C, respectively) [199,200]. Such kind of strong plasticization and swelling are advantageous for wood processing, as they determine its energy requirement [199,201,202].

All-wood and all-cellulose composites have been processed following one main procedure (Table 4). The wood or cellulose is partially or completely dissolved in an ionic liquid before hot-pressed [203]. The ionic liquid is taken out of the composite, and the wood is fully regenerated before or after pressing by washing or extraction using an antisolvent such as water or ethanol. Sometimes, the composite is made of a mixture of wood and cellulose [204–206]. Other times, the plasticized wood is processed with another polymer such as thermoplastic starch [207].

Table 4. Summary of the literature on processing all-wood and all-cellulose composites using ionic liquids.

Wood/Lignocellulose	Dissolution Conditions			Regeneration Mechanism		Ref.
	Ionic Liquid	Temp. (°C)	Time (h)	Strategy	Antisolvent	
Wheat Straw and Cellulose	[AMIM][Cl]	120	4	1	Casting then Water	[208]
Chinese Fir	[AMIM][Cl]	80	4	1	Water then Hot-pressing	[203]
Birch Wood	[EMIM][OAc]	95	0.5	1	Water and Hot-pressing	[209]
Paper Cellulose	[EMIM][OAc] /Water	80–95	1–16	1	Water then Wet-pressing and Drying	[210]
Oil Palm Frond	[EMIM][OAc], [BMIM][Cl]	90	3	1	1:1 Ac/W then Hot-pressing with Starch	[207]
Bleached and Unbleached Soda Pulps	[BMIM][Cl]	85–95	1	1	Casting then Water	[211]
Poplar Wood with Paper	[EMIM][OAc]	100	1	1	Hot-pressing then Water	[205]
Lyocell Fibers	[BMIM][Cl]	110	0.5–4	1	Hot-pressing then Water	[204]
Aspen Wood with Cotton	[EMIM][OAc]	60–80	0.5–20	1	Water then Hot-pressing	[212]
Cotton, Japanese Cypress Lumber	[BMIM][Cl]	100	0.5	1	Hot-pressing then Acetonitrile	[206]
Cedar Flour, Bark Flour	[BMIM][Cl]	100	0.15	1	Hot-pressing then Ethanol	[213]
Cedar, Bark Flour	[BMIM][Cl]	100	0.2	1	Extraction with Ethanol	[213]

4.4. Extraction of Cellulose Nanoparticles from Wood and Cellulose

Upon wood pulping, cellulose is extracted in the form of 20–40 μm-thick fibers, which can be processed to nanocellulose using a wide range of chemical and mechanical procedures [45]. Nanocellulose is an interesting material because of its high mechanical strength, high surface area, the ability to modify its surface and to form liquid crystalline structures, in addition to biodegradability and biocompatibility [214–217]. Thanks to these properties, nanocellulose has

shown great potential in a wide range of applications, including automotive industry [218], water filtration [219,220], tissue engineering [221], pharmaceutical formulation [222], electronics [223], etc. Cellulose nanocrystals (CNCs), one form of nanocellulose, are rod-like nanoparticles with a thickness of 3–10nm and a length of a few hundreds of nanometers [224]. They are extracted chemically by hydrolyzing the amorphous regions of cellulose using strong acids using a procedure that has already been industrialized [45]. Sulfuric acid is the most commonly used for the extraction of CNCs, although many such as hydrochloric acid, phosphoric acid, and acetic acid have been also explored [45]. The acid-based procedure suffers high severity, corrosion of reactors, the need to treat the effluents, and the low CNC yield, which is in the range of 20–40% (g-CNCs/g-cellulose) [225–227].

Ionic liquids have been explored to extract CNCs under milder, controllable, and greener conditions. Most of the reports in the literature focused on the use of the mildly acidic ionic liquid, 1-butyl-3-methylimidazolium hydrogen sulfate [BMIM][HSO_4] [228]. Man et al. have used this ionic liquid for the first time in 2011 to extract CNCs, but the extracted cellulose did not have the optimum morphological characteristics of CNCs [229]. Mao et al. were able to extract higher quality CNCs in almost theoretical yields using the same ionic liquid upon dilution with water [44,230,231]. Grzabka-Zasadzinska et al. studied the impact of the imidazolium substituents on the properties of the CNCs extracted using this ionic liquid [232]. Regenerated CNCs were also produced upon the dissolution of cellulose in [BMIM][Cl] [233].

Cellulose nanofibrils (CNFs), another form of nanocellulose, are spaghetti-like nanoparticles with a thickness of 5–30 nm and a length of few micrometers [224]. They are produced by mechanically fibrillating cellulose fibers using a wide range of techniques, including homogenization, microfluidization, microgrinding, and extrusion [234–237]. There are some reports that used ionic liquids to prepare regenerated CNFs [238]. In these reports, cellulose is dissolved in an ionic liquid then electrospun. The produced CNFs are significantly thicker than traditional CNFs (thickness of around 500 nm) [239]. Mao et al. have reported the use of imidazole to produce both CNCs and CNFs. Imidazole, alone, was found able to fibrillate cellulose to produce CNFs, and to hydrolyze the amorphous regions of cellulose to liberate the CNCs when mixed with water [240].

Most of the reports in the literature on the production of CNCs and CNFs used pure or almost pure cellulose as a starting material, including pulp fibers and microcrystalline cellulose [45]. In other words, there were no technologies for the extraction of nanocellulose directly from wood and lignocelluloses. This is not surprising, as there was no single reagent that is capable of pulping wood and extracting nanocellulose at the same time. Using [EMIM][OAc], Abushammala et al. developed a method to pulp wood and simultaneously hydrolyze the amorphous regions of the cellulose to liberate the crystallite in the form of CNCs [180,241]. The extracted CNCs were lignin-coated, which can be bleached to obtain lignin-free CNCs [179]. Such technology could foster the utilization of lignocellulosic residues and the use of naoncellulose [242]. Ionic liquids were also used for the preparation of lignin nano- and micro-spheres by dissolving alkali lignin in [MMIM][DEP] followed by a gradual regeneration in water [243].

5. Challenges of Using Ionic Liquids for Wood and Cellulose Dissolution and Processing

Around 20 years ago, ionic liquids were introduced as the "magic solvents" for processing wood and cellulose and received strong attention due to their advantageous properties. Years later, it became clear that ionic liquids are not that innocent, as they seemed to be. Many issues and challenges appeared that hindered industrializing some promising ionic liquid-mediated technologies developed in academia for processing wood and cellulose:

5.1. Side Reactions

For many years, it was assumed that ionic liquids are chemically inert solvents for cellulose and wood. However, recent studies have reported possible side reactions that could take place during processing cellulose and wood using ionic liquids. Acetylation has been reported to take

place at varying degrees using acetate ionic liquids, such as [EMIM][OAc]. Small degrees of cellulose acetylation (less than 0.1%) were reported when cellulose was treated with this ionic liquid [244,245]. Acetylation was proven to be caused by one of the impurities in the ionic liquid, 1-acetylimidazole [246]. This impurity is continuously generated because of the thermal degradation of the ionic liquid during the reaction and during the recycling of the ionic liquid. Acetylation was more significant (>10%) in the presence of certain molecules such as 2-furoyl chloride, which provided an electropositive carbon for the acetate ion to attach and be activated [247]. Cellulose acetylation was also more significant when wood was treated with [EMIM][Ace] (>10%) [180]. It was confirmed, in this scenario, that lignin acted as a catalyst [248].

Many studies have also reported the hydrolysis of cellulose when treated with ionic liquids [179,180,249,250]. Some attributed it to the formation of acetic acid, when acetate ionic liquids are used or because of hemicellulose deacetylation [248,251,252], while others linked it to the hydrolytic power of the imidazolium ring [253]. The hydrolytic power of imidazolium is a result of releasing the proton of the ring by the action of the anion [254,255]. This was more significant for acetate ionic liquids compared to chloride ionic liquids due to the high basicity of the acetate ion [256]. In the process, a carbene is formed, which is reactive with the reducing end and C2 of cellulose [254,257–259]. This explains the traces of nitrogen detected in cellulose after processing with [EMIM][OAc]. Other than the degradation of the cation, the anions can also degrade. For instance, the acesulfamate anion was proved to degrade significantly to ammonium sulfate salt, which was detected in significant amounts in lignin extracted from wood using acesulfamate ionic liquids [260].

Sulfonation and phosphorylation were also detected when wood and cellulose were processed with [BMIM][HSO_4] and [EMIM][MEP], respectively [141,230]. Acidic ionic liquids such as [EMIM][HSO_4] and [BMIM][HSO_4] were found to convert sugars to 5-hydroxymethylfufural [261,262]. Sometimes, these side reactions, in addition to acetylation and hydrolysis, were advantageous as they supported the dissolution of lignin and cellulose [141]. For instance, the acetylation of lignin and cellulose and hydrolysis of cellulose during wood treatment with [EMIM][OAc] supported the direct extraction of CNCs from wood through simultaneous wood delignification, cellulose fibrillation, and liberation of cellulose crystallites. Lignin acetylation prevented lignin from repolymerizing while cellulose acetylation reduced the cohesive forces between cellulose microfibrils during pulping, preventing them from aggregating [248].

5.2. Recyclability

Most of the reports in the literature recycled ionic liquids upon wood dissolution or processing by evaporating all added co-solvents and anti-solvents after the separation of all wood fractions relying on the fact that ionic liquids will not evaporate at the typical drying temperatures [114]. It was often claimed that ionic liquids are recyclable with almost no losses due to their low vapor pressure and high thermal stability. However, many studies have shown that ionic liquids degrade due to the high temperatures used for wood and cellulose dissolution [263]. Their degradation might also be catalyzed by the wood moieties generated during dissolution [260]. The side reactions mentioned previously are also a possible cause of losses [180,247].

Ionic liquid recyclability is not only assessed by mass loss but also by the performance of the ionic liquid after recycling. Under high dissolution temperatures, wood could degrade, and oligomers could form, which cannot be regenerated out of the ionic liquid. These oligomers accumulate in the ionic liquid reducing its efficiency [264,265]. The accumulation of wood oligomers, in addition to thermal degradants, can be visually detected as ionic liquids tend to darken [230]. It is worth to mention that it could be possible to evaporate ionic liquids to get rid of these oligomers. Such a process would need a high-energy input in the form of heat and vacuum [266,267]. Some approaches have been developed to overcome this issue, including the formation of distillable carbenes and the back-alkylation of the anion [268]. In conclusion, lowering wood dissolution temperature, if possible, is recommended to suppress both wood and ionic liquid degradation.

5.3. High Viscosity and Low Wood/Ionic Liquid Mixing Ratio

Some of the commonly used ionic liquids are solid at room temperature, while others have a viscosity of 100-2000 cP at room temperature (Table 1). Halide- and hydrogen sulfate-based ionic liquids tend to be solid or have a high viscosity of more than 1000 CP while acetate, tetrafluoroborate, and hexafluorophosphate ionic liquids are liquid and have a viscosity of few hundreds' cP or less. These viscosities are still significantly higher than the viscosities of commonly used organic solvents (less than 2 cP) [269]. The high viscosity of ionic liquids has a negative impact on four major process parameters: (1) energy input (2) solid/liquid ratio, (3) reaction homogeneity, and (4) filtration of the reaction mixture. High temperature is needed to melt and reduce the viscosity of ionic liquid, while vigorous mixing is needed to improve reaction homogeneity. To improve the solid/liquid ratio and allow the filtration of the reaction mixture, cosolvents such as DMSO are added to the ionic liquid to reduce their viscosity, which would result in an extra effort in ionic liquid recycling at the end [188].

5.4. Prices of Ionic Liquids

The prices of most imidazolium ionic liquids ranged in 2019 between 500 and 5000 euros per kilogram (Table 5) [270–273]. These prices are up to 100 times higher than commonly used organic solvents such as acetone, ethanol, toluene, and DMSO [270–273], which consequently hinder the inclusion of ionic liquids in many applications and processes. However, these prices are lower than those in the past and will continue to drop due to the growth of the ionic liquids market [22].

Table 5. The prices of the most commonly used ionic liquids for wood and cellulose processing. The prices are not enlisted for comparison as they are based on products of different purities (95–100%) and sizes (5–1000 g).

Ionic Liquid	Price (EUR/kg)			
	Sigma-Aldrich [270]	**TCI [271]**	**Alfa Aesar [272]**	**Acros [273]**
[BMIM][OAc]	821	-	-	-
[BMIM][Cl]	1264	1250	2300	882
[BMIM][Br]	517	5600	1836	-
[BMIM][I]	4880	5200	-	-
[BMIM][HSO_4]	421	3080	-	-
[BMIM][BF_4]	1776	1420	5940	2070
[BMIM][PF_6]	1992	2520	2440	2390
[EMIM][OAc]	746	7160	15,580	-
[EMIM][Cl]	363	1224	4680	1080
[EMIM][Br]	2080	3520	1800	1250
[EMIM][I]	3960	3400	3720	-
[EMIM][HSO_4]	511	2880	1572	-
[EMIM][BF_4]	5660	6000	-	-
[EMIM][PF_6]	9000	5040	6380	-
[AMIM][Cl]	5240	6000	4880	-
[AMIM][Br]	21,600	-	2940	-
[AMIM][I]	14,400	-	-	-
[BnMIM][Cl]	4600	7000	4880	-
[BnMIM][BF_4]	4840	4800	5580	-
[BnMIM][PF_6]	4740	6200	4960	-

5.5. Health and Environmental Concerns

The possibility to synthesize a huge number of ionic liquids with tuned properties fostered their use in a wide range of applications. However, this requires thorough studies of the health and environmental impact of all newly synthesized ionic liquids before commercialization. This is important due to the fact that ionic liquids are not innocent solvents as they seemed to be, and some traces may exist in final products even upon careful washing and as a result of side reactions. They may also leash to water and soil [274,275]. Some toxicity studies have shown that ionic liquids are/could be toxic to humans and animals [276–280], and microorganisms [281–283], which was mainly linked to the imidazolium cation and influenced by the anion [280,284,285]. Other studies have shown that using ionic liquid for cellulose dissolution might be less environmentally friendly than the traditional NMMO process [286]. Due to the toxicity of the imidazolium ring, other cations have been suggested, such as morpholinium and choline [287,288], which showed similar and sometimes better performance as solvents [289]. Amino acids as anions have been also explored [290,291]. In conclusion, there is a strong need to standardize a system to study the impact of ionic liquids on human health (including genotoxicity, cytotoxicity, and neurotoxicity) and to understand their fate and transport in the environment. A systematic approach to tackle this issue would further accelerate the inclusion of ionic liquids in chemical processes and commercial products.

6. Conclusions

Ionic liquids offer a variety of possibilities for the dissolution, fractionation, and processing of wood, lignocelluloses, and cellulose. They allow the utilization of these bioresources for biofuel production, processing wood-based composites, extraction of nanocellulose, and the production of a variety of chemicals and materials. This is a result of the possibility to synthesize unlimited number of ionic liquids with tailored chemical and physical properties and controlled dissolution power and selectivity to wood and its polymers. Ionic liquids have been able to destruct wood and significantly facilitate the enzymatic hydrolysis of its polysaccharides. They have also been proven potent agents for wood pulping and fractionation and for the extraction of cellulose nanoparticles from cellulose and wood. For processing all-wood composites, they have shown superior plasticization capabilities compared to water and traditional plasticization agents. Despite their fascinating performance, ionic liquids are not innocent and green solvents as they seemed to be two decades ago. Many side reactions have been reported, including acetylation, hydrolysis, and thermal and chemical degradation, which significantly affect their recyclability. They also suffer high viscosity and are still more expensive than commonly used organic solvents. However, their market continues to grow due to their inclusion in more applications and processes.

Funding: The authors would like to thank the Fraunhofer Institute for Wood Research (WKI) for funding this research work through the Wilhelm–Klauditz Fellowship.

Conflicts of Interest: The authors declare no conflict of interest.

References

1. Sivasubramanian, V. *Bioprocess Engineering for a Green Environment*; CRC Press: Boca Raton, FL, USA, 2018.
2. Tumuluru, J.S. *Biomass Preprocessing and Pretreatments for Production of Biofuels: Mechanical, Chemical and Thermal Methods*; CRC Press: Boca Raton, FL, USA, 2018.
3. Sun, R. *Cereal Straw as a Resource for Sustainable Biomaterials and Biofuels: Chemistry, Extractives, Lignins, Hemicelluloses and Cellulose*, 1st ed.; Elsevier: Amsterdam, The Netherlands, 2010.
4. Klemm, D.; Heublein, B.; Fink, H.P.; Bohn, A. Cellulose: Fascinating biopolymer and sustainable raw material. *Angew. Chem. Int. Ed.* **2005**, *44*, 3358–3393. [CrossRef] [PubMed]
5. Vishtal, A.G.; Kraslawski, A. Challenges in industrial applications of technical lignins. *BioResources* **2011**, *6*, 3547–3568.

6. Searle, S.; Malins, C. *Availability of Cellulosic Residues and Wastes in the EU*; The International Council on Clean Transportation: Washington, DC, USA, 2013.
7. Council, E.P. *Bioenergy Europe Pellet Report*; European Pellet Council: Ixelles, Belgium, 2018.
8. Parthasarathi, R.; Bellesia, G.; Chundawat, S.; Dale, B.; Langan, P.; Gnanakaran, S. Insights into hydrogen bonding and stacking interactions in cellulose. *J. Phys. Chem. A* **2011**, *115*, 14191–14202. [CrossRef] [PubMed]
9. Himmel, M.E.; Ding, S.-Y.; Johnson, D.K.; Adney, W.S.; Nimlos, M.R.; Brady, J.W.; Foust, T.D. Biomass recalcitrance: Engineering plants and enzymes for biofuels production. *Science* **2007**, *315*, 804–807. [CrossRef]
10. Williamson, S.L.; McCormick, C.L. Cellulose derivatives synthesized via isocyanate and activated ester pathways in homogeneous solutions of lithium chloride/N, N-dimethylacetamide. *J. Macromol. Sci. Pure Appl. Chem.* **1998**, *35*, 1915–1927. [CrossRef]
11. Rosenau, T.; Potthast, A.; Sixta, H.; Kosma, P. The chemistry of side reactions and byproduct formation in the system NMMO/cellulose (Lyocell process). *Prog. Polym. Sci.* **2001**, *26*, 1763–1837. [CrossRef]
12. Welton, T. Room-temperature ionic liquids. Solvents for synthesis and catalysis. *Chem. Rev.* **1999**, *99*, 2071–2084. [CrossRef]
13. Wang, H.; Gurau, G.; Rogers, R.D. Ionic liquid processing of cellulose. *Chem. Soc. Rev.* **2012**, *41*, 1519–1537. [CrossRef]
14. Huddleston, J.G.; Visser, A.E.; Reichert, W.M.; Willauer, H.D.; Broker, G.A.; Rogers, R.D. Characterization and comparison of hydrophilic and hydrophobic room temperature ionic liquids incorporating the imidazolium cation. *Green Chem.* **2001**, *3*, 156–164. [CrossRef]
15. Rogers, R.D.; Seddon, K.R. Ionic liquids–solvents of the future? *Science* **2003**, *302*, 792–793. [CrossRef]
16. Lewandowski, A.; Świderska-Mocek, A. Ionic liquids as electrolytes for Li-ion batteries—An overview of electrochemical studies. *J. Power Sources* **2009**, *194*, 601–609. [CrossRef]
17. De Souza, R.F.; Padilha, J.C.; Gonçalves, R.S.; Dupont, J. Room temperature dialkylimidazolium ionic liquid-based fuel cells. *Electrochem. Commun.* **2003**, *5*, 728–731. [CrossRef]
18. Dupont, J.; de Souza, R.F.; Suarez, P.A. Ionic liquid (molten salt) phase organometallic catalysis. *Chem. Rev.* **2002**, *102*, 3667–3692. [CrossRef] [PubMed]
19. Huang, K.; Chen, F.-F.; Tao, D.-J.; Dai, S. Ionic liquid–formulated hybrid solvents for CO_2 capture. *Curr. Opin. Green Sustain. Chem.* **2017**, *5*, 67–73. [CrossRef]
20. Meindersma, G.W.; De Haan, A.B. Cyano-containing ionic liquids for the extraction of aromatic hydrocarbons from an aromatic/aliphatic mixture. *Sci. China Chem.* **2012**, *55*, 1488–1499. [CrossRef]
21. Angell, C.A.; Ansari, Y.; Zhao, Z. Ionic liquids: Past, present and future. *Faraday Discuss.* **2012**, *154*, 9–27. [CrossRef]
22. Kunal Ahuja, S.D. *Ionic Liquids Market Size by Application (Catalysis/Synthesis, Food, Paper & Pulp, Electronics, Biotechnology, Automotive, Pharmaceuticals), Industry Analysis Report, Regional Outlook, Application Potential, Price Trends, Competitive Market Share & Forecast, 2015–2022*; Global Market Insights Inc.: Selbyville, DE, USA, 2016.
23. Swatloski, R.P.; Spear, S.K.; Holbrey, J.D.; Rogers, R.D. Dissolution of cellose with ionic liquids. *J. Am. Chem. Soc.* **2002**, *124*, 4974–4975. [CrossRef]
24. Charles, G. Cellulose Solution and Cellulose Derivative and Process of Making Same. U.S. Patents 1924238A, 29 August 1933.
25. Charles, G. Cellulose Solution. U.S. Patents 1943176A, 9 January 1934.
26. Honglu, X.; Tiejun, S. Wood liquefaction by ionic liquids. *Holzforschung* **2006**, *60*, 509–512. [CrossRef]
27. Li, X.; Geng, Y.; Simonsen, J.; Li, K. Application of ionic liquids for electrostatic control in wood. *Holzforschung* **2004**, *58*, 280–285. [CrossRef]
28. Pernak, J.; Zabielska-Matejuk, J.; Kropacz, A.; Foksowicz-Flaczyk, J. Ionic liquids in wood preservation. *Holzforschung* **2004**, *58*, 286–291. [CrossRef]
29. Pernak, J.; Goc, I.; Fojutowski, A. Protic ionic liquids with organic anion as wood preservative. *Holzforschung* **2005**, *59*, 473–475. [CrossRef]
30. Kilpeläinen, I.; Xie, H.; King, A.; Granstrom, M.; Heikkinen, S.; Argyropoulos, D.S. Dissolution of wood in ionic liquids. *J. Agric. Food Chem.* **2007**, *55*, 9142–9148. [CrossRef] [PubMed]
31. Fort, D.A.; Remsing, R.C.; Swatloski, R.P.; Moyna, P.; Moyna, G.; Rogers, R.D. Can ionic liquids dissolve wood? Processing and analysis of lignocellulosic materials with 1-n-butyl-3-methylimidazolium chloride. *Green Chem.* **2007**, *9*, 63–69. [CrossRef]

32. Seddon, K.R. Ionic liquids for clean technology. *J. Chem. Technol. Biotechnol. Int. Res. Process Environ. AND Clean Technol.* **1997**, *68*, 351–356. [CrossRef]
33. Pinkert, A.; Marsh, K.N.; Pang, S.; Staiger, M.P. Ionic liquids and their interaction with cellulose. *Chem. Rev.* **2009**, *109*, 6712–6728. [CrossRef] [PubMed]
34. Wasserscheid, P.; Welton, T. *Ionic liquids in synthesis*; John Wiley & Sons: Hoboken, NJ, USA, 2008.
35. MacFarlane, D.R.; Forsyth, S.A. *Acids and bases in ionic liquids*; ACS Publications: Washington, DC, USA, 2003.
36. Plechkova, N.V.; Seddon, K.R. Applications of ionic liquids in the chemical industry. *Chem. Soc. Rev.* **2008**, *37*, 123–150. [CrossRef]
37. Rooney, D.; Jacquemin, J.; Gardas, R. Thermophysical properties of ionic liquids. In *Ionic Liquids*; Springer: New York, NY, USA, 2009; pp. 185–212.
38. Handy, S.T. Room temperature ionic liquids: Different classes and physical properties. *Curr. Org. Chem.* **2005**, *9*, 959–988. [CrossRef]
39. Xu, A.; Zhang, Y.; Li, Z.; Wang, J. Viscosities and conductivities of 1-butyl-3-methylimidazolium carboxylates ionic liquids at different temperatures. *J. Chem. Eng. Data* **2012**, *57*, 3102–3108. [CrossRef]
40. Meindersma, G.W.; Maase, M.; De Haan, A.B. Ionic liquids. In *Ullmann's Encyclopedia of Industrial Chemistry*; Wiley: Hoboken, NJ, USA, 2000.
41. Othman, Z.S.; Hassan, N.H.; Zubairi, S.I. Imidazolium-Based Ionic Liquid Binary Solvent System as an Extraction Medium in Enhancing the Rotenone Yield Extracted from Derris elliptica Roots. In *Progress and Developments in Ionic Liquids*; IntechOpen: London, UK, 2017.
42. Chancelier, L.; Boyron, O.; Gutel, T.; Santini, C. Thermal stability of imidazolium-based ionic liquids. *Fr. Ukr. J. Chem.* **2016**, *4*, 51–64. [CrossRef]
43. Erdmenger, T.; Vitz, J.; Wiesbrock, F.; Schubert, U.S. Influence of different branched alkyl side chains on the properties of imidazolium-based ionic liquids. *J. Mater. Chem.* **2008**, *18*, 5267–5273. [CrossRef]
44. Mao, J.; Heck, B.; Reiter, G.; Laborie, M.-P. Cellulose nanocrystals' production in near theoretical yields by 1-butyl-3-methylimidazolium hydrogen sulfate ([Bmim] HSO4)–mediated hydrolysis. *Carbohydr. Polym.* **2015**, *117*, 443–451. [CrossRef] [PubMed]
45. Mao, J.; Abushammala, H.; Brown, N.; Laborie, M.-P. Comparative assessment of methods for producing cellulose I nanocrystals from cellulosic sources. In *Nanocelluloses: Their Preparation, Properties, and Applications, ACS Symposium Series*; ACS Publications: Washington, DC, USA, 2017; Volume 1251, pp. 19–53.
46. Liu, C.; Li, Y.; Hou, Y. Basicity characterization of imidazolyl ionic liquids and their application for biomass dissolution. *Int. J. Chem. Eng.* **2018**, *2018*. [CrossRef]
47. Zhang, S.; Lu, X.; Zhou, Q.; Li, X.; Zhang, X.; Li, S. *Ionic Liquids: Physicochemical Properties*; Elsevier: Amsterdam, The Netherlands, 2009.
48. Iolitec Website. Available online: www.iolitec.de (accessed on 20 November 2019).
49. Han, D.; Row, K.H. Recent applications of ionic liquids in separation technology. *Molecules* **2010**, *15*, 2405–2426. [CrossRef] [PubMed]
50. Pinkert, A.; Goeke, D.F.; Marsh, K.N.; Pang, S. Extracting wood lignin without dissolving or degrading cellulose: Investigations on the use of food additive-derived ionic liquids. *Green Chem.* **2011**, *13*, 3124–3136. [CrossRef]
51. Feng, L.; Chen, Z.-L. Research progress on dissolution and functional modification of cellulose in ionic liquids. *J. Mol. Liq.* **2008**, *142*, 1–5. [CrossRef]
52. Isik, M.; Sardon, H.; Mecerreyes, D. Ionic liquids and cellulose: Dissolution, chemical modification and preparation of new cellulosic materials. *Int. J. Mol. Sci.* **2014**, *15*, 11922–11940. [CrossRef]
53. Zavrel, M.; Bross, D.; Funke, M.; Büchs, J.; Spiess, A.C. High-throughput screening for ionic liquids dissolving (ligno-) cellulose. *Bioresour. Technol.* **2009**, *100*, 2580–2587. [CrossRef]
54. Cox, B.J.; Ekerdt, J.G. Pretreatment of yellow pine in an acidic ionic liquid: Extraction of hemicellulose and lignin to facilitate enzymatic digestion. *Bioresour. Technol.* **2013**, *134*, 59–65. [CrossRef]
55. Pang, J.; Liu, X.; Zhang, X.; Wu, Y.; Sun, R. Fabrication of cellulose film with enhanced mechanical properties in ionic liquid 1-allyl-3-methylimidaxolium chloride (AmimCl). *Materials* **2013**, *6*, 1270–1284. [CrossRef]
56. Jiang, M.; Zhao, M.; Zhou, Z.; Huang, T.; Chen, X.; Wang, Y. Isolation of cellulose with ionic liquid from steam exploded rice straw. *Ind. Crop. Prod.* **2011**, *33*, 734–738. [CrossRef]

57. Lee, S.H.; Doherty, T.V.; Linhardt, R.J.; Dordick, J.S. Ionic liquid-mediated selective extraction of lignin from wood leading to enhanced enzymatic cellulose hydrolysis. *Biotechnol. Bioeng.* **2009**, *102*, 1368–1376. [CrossRef] [PubMed]
58. Moyer, P.; Smith, M.D.; Abdoulmoumine, N.; Chmely, S.C.; Smith, J.C.; Petridis, L.; Labbé, N. Relationship between lignocellulosic biomass dissolution and physicochemical properties of ionic liquids composed of 3-methylimidazolium cations and carboxylate anions. *Phys. Chem. Chem. Phys.* **2018**, *20*, 2508–2516. [CrossRef] [PubMed]
59. Zhao, H.; Baker, G.A.; Cowins, J.V. Fast enzymatic saccharification of switchgrass after pretreatment with ionic liquids. *Biotechnol. Prog.* **2010**, *26*, 127–133. [CrossRef] [PubMed]
60. Barthel, S.; Heinze, T. Acylation and carbanilation of cellulose in ionic liquids. *Green Chem.* **2006**, *8*, 301–306. [CrossRef]
61. Sun, N.; Rahman, M.; Qin, Y.; Maxim, M.L.; Rodríguez, H.; Rogers, R.D. Complete dissolution and partial delignification of wood in the ionic liquid 1-ethyl-3-methylimidazolium acetate. *Green Chem.* **2009**, *11*, 646–655. [CrossRef]
62. Brandt, A.; Hallett, J.P.; Leak, D.J.; Murphy, R.J.; Welton, T. The effect of the ionic liquid anion in the pretreatment of pine wood chips. *Green Chem.* **2010**, *12*, 672–679. [CrossRef]
63. Vo, H.T.; Kim, C.S.; Ahn, B.S.; Kim, H.S.; Lee, H. Study on dissolution and regeneration of poplar wood in imidazolium-based ionic liquids. *J. Wood Chem. Technol.* **2011**, *31*, 89–102. [CrossRef]
64. Strehmel, V.; Strunk, D.; Wetzel, H.; Strehmel, N. Investigation of lignin obtained by processing of Betula pendula with ionic liquids. *Sustain. Chem. Pharm.* **2017**, *6*, 107–113. [CrossRef]
65. Yang, Y.; Fan, H.; Meng, Q.; Zhang, Z.; Yang, G.; Han, B. Ionic liquid [OMIm][OAc] directly inducing oxidation cleavage of the β-O-4 bond of lignin model compounds. *Chem. Commun.* **2017**, *53*, 8850–8853. [CrossRef]
66. Abushammala, H.; Pontes, J.F.; Gomes, G.H.; Osorio-Madrazo, A.; Thiré, R.M.; Pereira, F.V.; Laborie, M.-P.G. Swelling, viscoelastic, and anatomical studies on ionic liquid-swollen Norway spruce as a screening tool toward ionosolv pulping. *Holzforschung* **2015**, *69*, 1059–1067. [CrossRef]
67. Wang, Z.; Gräsvik, J.; Jönsson, L.J.; Winestrand, S. Comparison of $[HSO_4]^-$,$[Cl]^-$ and $[MeCO_2]^-$ as anions in pretreatment of aspen and spruce with imidazolium-based ionic liquids. *BMC Biotechnol.* **2017**, *17*, 82. [CrossRef] [PubMed]
68. De Gregorio, G.F.; Weber, C.C.; Gräsvik, J.; Welton, T.; Brandt, A.; Hallett, J.P. Mechanistic insights into lignin depolymerisation in acidic ionic liquids. *Green Chem.* **2016**, *18*, 5456–5465. [CrossRef]
69. Padró, J.M.; Reta, M. Solvatochromic parameters of imidazolium-, hydroxyammonium-, pyridinium- and phosphonium-based room temperature ionic liquids. *J. Mol. Liq.* **2016**, *213*, 107–114. [CrossRef]
70. Doherty, T.V.; Mora-Pale, M.; Foley, S.E.; Linhardt, R.J.; Dordick, J.S. Ionic liquid solvent properties as predictors of lignocellulose pretreatment efficacy. *Green Chem.* **2010**, *12*, 1967–1975. [CrossRef]
71. Liu, R.; Zhang, J.; Sun, S.; Bian, Y.; Hu, Y. Dissolution and recovery of cellulose from pine wood bits in ionic liquids and a co-solvent component mixed system. *J. Eng. Fibers Fabr.* **2019**, *14*, 1558925019838440. [CrossRef]
72. Fendt, S.; Padmanabhan, S.; Blanch, H.W.; Prausnitz, J.M. Viscosities of acetate or chloride-based ionic liquids and some of their mixtures with water or other common solvents. *J. Chem. Eng. Data* **2010**, *56*, 31–34. [CrossRef]
73. Lee, Y.J.; Kwon, M.K.; Lee, S.J.; Jeong, S.W.; Kim, H.C.; Oh, T.H.; Lee, S.G. Influence of water on phase transition and rheological behavior of cellulose/ionic liquid/water ternary systems. *J. Appl. Polym. Sci.* **2017**, *134*. [CrossRef]
74. Ding, Z.-D.; Chi, Z.; Gu, W.-X.; Gu, S.-M.; Liu, J.-H.; Wang, H.-J. Theoretical and experimental investigation on dissolution and regeneration of cellulose in ionic liquid. *Carbohydr. Polym.* **2012**, *89*, 7–16. [CrossRef]
75. Marks, C.; Mitsos, A.; Viell, J. Change of C (2)-Hydrogen–Deuterium Exchange in Mixtures of EMIMAc. *J. Solut. Chem.* **2019**, *48*, 1188–1205. [CrossRef]
76. Castro, M.C.; Arce, A.; Soto, A.; Rodríguez, H.c. Influence of methanol on the dissolution of lignocellulose biopolymers with the ionic liquid 1-ethyl-3-methylimidazolium acetate. *Ind. Eng. Chem. Res.* **2015**, *54*, 9605–9614. [CrossRef]
77. Sun, Y.; Xue, B. Understanding structural changes in the lignin of Eucalyptus urophylla during pretreatment with an ionic liquid-water mixture. *Ind. Crop. Prod.* **2018**, *123*, 600–609. [CrossRef]

78. Laine, C.; Asikainen, S.; Talja, R.; Stépán, A.; Sixta, H.; Harlin, A. Simultaneous bench scale production of dissolving grade pulp and valuable hemicelluloses from softwood kraft pulp by ionic liquid extraction. *Carbohydr. Polym.* **2016**, *136*, 402–408. [CrossRef] [PubMed]
79. Shi, J.; Balamurugan, K.; Parthasarathi, R.; Sathitsuksanoh, N.; Zhang, S.; Stavila, V.; Subramanian, V.; Simmons, B.A.; Singh, S. Understanding the role of water during ionic liquid pretreatment of lignocellulose: Co-solvent or anti-solvent? *Green Chem.* **2014**, *16*, 3830–3840. [CrossRef]
80. Roselli, A.; Hummel, M.; Vartiainen, J.; Nieminen, K.; Sixta, H. Understanding the role of water in the interaction of ionic liquids with wood polymers. *Carbohydr. Polym.* **2017**, *168*, 121–128. [CrossRef] [PubMed]
81. Viell, J.; Inouye, H.; Szekely, N.K.; Frielinghaus, H.; Marks, C.; Wang, Y.; Anders, N.; Spiess, A.C.; Makowski, L. Multi-scale processes of beech wood disintegration and pretreatment with 1-ethyl-3-methylimidazolium acetate/water mixtures. *Biotechnol. Biofuels* **2016**, *9*, 7. [CrossRef] [PubMed]
82. Rinaldi, R. Instantaneous dissolution of cellulose in organic electrolyte solutions. *Chem. Commun.* **2011**, *47*, 511–513. [CrossRef]
83. Xu, A.; Zhang, Y.; Zhao, Y.; Wang, J. Cellulose dissolution at ambient temperature: Role of preferential solvation of cations of ionic liquids by a cosolvent. *Carbohydr. Polym.* **2013**, *92*, 540–544. [CrossRef]
84. Xu, A.; Guo, X.; Xu, R. Understanding the dissolution of cellulose in 1-butyl-3-methylimidazolium acetate+ DMAc solvent. *Int. J. Biol. Macromol.* **2015**, *81*, 1000–1004. [CrossRef]
85. Xu, A.; Cao, L.; Wang, B. Facile cellulose dissolution without heating in [C4mim][CH3COO]/DMF solvent. *Carbohydr. Polym.* **2015**, *125*, 249–254. [CrossRef]
86. Xu, A.; Chen, L.; Wang, Y.; Liu, R.; Niu, W. Development of Diallylimidazolium Methoxyacetate/DMSO (DMF/DMA) Solvents for Improving Cellulose Dissolution and Fabricating Porous Material. *Polymers* **2019**, *11*, 845. [CrossRef]
87. Yin, W.P.; Li, X.; Ren, Y.L.; Zhao, S.; Wang, J.J. Selective hydrolysis of lignocelluloses from corn stalk in an ionic liquid. *J. Appl. Polym. Sci.* **2013**, *129*, 472–479. [CrossRef]
88. van Spronsen, J.; Cardoso, M.A.T.; Witkamp, G.-J.; de Jong, W.; Kroon, M.C. Separation and recovery of the constituents from lignocellulosic biomass by using ionic liquids and acetic acid as co-solvents for mild hydrolysis. *Chem. Eng. Process. Process Intensif.* **2011**, *50*, 196–199. [CrossRef]
89. Xu, A.; Wang, J.; Wang, H. Effects of anionic structure and lithium salts addition on the dissolution of cellulose in 1-butyl-3-methylimidazolium-based ionic liquid solvent systems. *Green Chem.* **2010**, *12*, 268–275. [CrossRef]
90. Pang, Z.; Dong, C.; Pan, X. Enhanced deconstruction and dissolution of lignocellulosic biomass in ionic liquid at high water content by lithium chloride. *Cellulose* **2016**, *23*, 323–338. [CrossRef]
91. Sun, X.; Sun, X.; Zhang, F. Combined pretreatment of lignocellulosic biomass by solid base (calcined Na_2SiO_3) and ionic liquid for enhanced enzymatic saccharification. *RSC Adv.* **2016**, *6*, 99455–99466. [CrossRef]
92. Wei, X.; Wang, Y.; Li, J.; Wang, F.; Chang, G.; Fu, T.; Zhou, W. Effects of temperature on cellulose hydrogen bonds during dissolution in ionic liquid. *Carbohydr. Polym.* **2018**, *201*, 387–391. [CrossRef]
93. Abushammala, H. Novel Ionic Liquid-Mediated Technologies for the Extraction of Nanocellulose Directly from Wood. Ph.D. Thesis, Albert-Ludwigs-Universitat, Freiburg im Breisgau, Germany, 2015.
94. Sun, Y.-C.; Xu, J.-K.; Xu, F.; Sun, R.-C. Structural comparison and enhanced enzymatic hydrolysis of eucalyptus cellulose via pretreatment with different ionic liquids and catalysts. *Process Biochem.* **2013**, *48*, 844–852. [CrossRef]
95. Bahcegul, E.; Apaydin, S.; Haykir, N.I.; Tatli, E.; Bakir, U. Different ionic liquids favor different lignocellulosic biomass particle sizes during pretreatment to function efficiently. *Green Chem.* **2012**, *14*, 1896–1903. [CrossRef]
96. Gschwend, F.J.; Chambon, C.L.; Biedka, M.; Brandt-Talbot, A.; Fennell, P.S.; Hallett, J.P. Quantitative glucose release from softwood after pretreatment with low-cost ionic liquids. *Green Chem.* **2019**, *21*, 692–703. [CrossRef]
97. Sun, Y.-C.; Liu, X.-N.; Wang, T.-T.; Xue, B.-L.; Sun, R.-C. Green Process for Extraction of Lignin by the Microwave-Assisted Ionic Liquid Approach: Toward Biomass Biorefinery and Lignin Characterization. *ACS Sustain. Chem. Eng.* **2019**, *7*, 13062–13072. [CrossRef]
98. Chen, T.; Li, Y.; Xu, J.; Hou, Y. Dissolution of eucalyptus powder with alkaline ionic liquid [Mmim] DMP under microwave conditions. *BioResources* **2016**, *11*, 9710–9722. [CrossRef]
99. Chen, J.; Jiang, Q.; Yang, G.; Wang, Q.; Fatehi, P. Ultrasonic-assisted ionic liquid treatment of chemithermomechanical pulp fibers. *Cellulose* **2017**, *24*, 1483–1491. [CrossRef]

100. Nakamura, A.; Miyafuji, H.; Saka, S. Influence of reaction atmosphere on the liquefaction and depolymerization of wood in an ionic liquid, 1-ethyl-3-methylimidazolium chloride. *J. Wood Sci.* **2010**, *56*, 256–261. [CrossRef]
101. Abushammala, H.; Hashaikeh, R. Enzymatic hydrolysis of cellulose and the use of TiO_2 nanoparticles to open up the cellulose structure. *Biomass Bioenergy* **2011**, *35*, 3970–3975. [CrossRef]
102. Casas, A.; Oliet, M.; Alonso, M.V.; Santos, T.M.; Rodriguez, F. Dissolution of Pinus radiata and Eucalyptus globulus woods in 1-allyl-3-methylimidazolium chloride for cellulose or lignin regeneration. *Ind. Eng. Chem. Res.* **2013**, *52*, 3628–3636. [CrossRef]
103. Casas, A.; Alonso, M.; Oliet, M.; Santos, T.; Rodriguez, F. Characterization of cellulose regenerated from solutions of pine and eucalyptus woods in 1-allyl-3-methilimidazolium chloride. *Carbohydr. Polym.* **2013**, *92*, 1946–1952. [CrossRef]
104. Crosthwaite, J.M.; Aki, S.N.; Maginn, E.J.; Brennecke, J.F. Liquid phase behavior of imidazolium-based ionic liquids with alcohols: Effect of hydrogen bonding and non-polar interactions. *Fluid Phase Equilibria* **2005**, *228*, 303–309. [CrossRef]
105. Liu, H.; Sale, K.L.; Simmons, B.A.; Singh, S. Molecular dynamics study of polysaccharides in binary solvent mixtures of an ionic liquid and water. *J. Phys. Chem. B* **2011**, *115*, 10251–10258. [CrossRef]
106. Li, B.; Asikkala, J.; Filpponen, I.; Argyropoulos, D.S. Factors Affecting Wood Dissolution and Regeneration of Ionic Liquids. *Ind. Eng. Chem. Res.* **2010**, *49*, 2477–2484. [CrossRef]
107. Hashaikeh, R.; Abushammala, H. Acid mediated networked cellulose: Preparation and characterization. *Carbohydr. Polym.* **2011**, *83*, 1088–1094. [CrossRef]
108. Halder, P.; Kundu, S.; Patel, S.; Parthasarathy, R.; Pramanik, B.; Paz-Ferreiro, J.; Shah, K. TGA-FTIR study on the slow pyrolysis of lignin and cellulose-rich fractions derived from imidazolium-based ionic liquid pre-treatment of sugarcane straw. *Energy Convers. Manag.* **2019**, *200*, 112067. [CrossRef]
109. da Costa Lopes, A.M.; João, K.G.; Rubik, D.F.; Bogel-Łukasik, E.; Duarte, L.C.; Andreaus, J.; Bogel-Łukasik, R. Pre-treatment of lignocellulosic biomass using ionic liquids: Wheat straw fractionation. *Bioresour. Technol.* **2013**, *142*, 198–208. [CrossRef] [PubMed]
110. Hamidah, U.; Arakawa, T.; H'ng, Y.Y.; Nakagawa-izumi, A.; Kishino, M. Recycled ionic liquid 1-ethyl-3-methylimidazolium acetate pretreatment for enhancing enzymatic saccharification of softwood without cellulose regeneration. *J. Wood Sci.* **2018**, *64*, 149–156. [CrossRef]
111. Viell, J.; Wulfhorst, H.; Schmidt, T.; Commandeur, U.; Fischer, R.; Spiess, A.; Marquardt, W. An efficient process for the saccharification of wood chips by combined ionic liquid pretreatment and enzymatic hydrolysis. *Bioresour. Technol.* **2013**, *146*, 144–151. [CrossRef] [PubMed]
112. Fu, D.; Mazza, G.; Tamaki, Y. Lignin extraction from straw by ionic liquids and enzymatic hydrolysis of the cellulosic residues. *J. Agric. Food Chem.* **2010**, *58*, 2915–2922. [CrossRef]
113. Yang, H.; Shi, Z.; Xiong, L.; Wang, K.; Sun, R.-C. Ionic Liquids Assisted Alkaline Fractionation Enhanced Triploid Poplar Bioconversion for Bioethanol Production. *Wood Res.* **2016**, *61*, 83–94.
114. Liu, C.-Z.; Wang, F.; Stiles, A.R.; Guo, C. Ionic liquids for biofuel production: Opportunities and challenges. *Appl. Energy* **2012**, *92*, 406–414. [CrossRef]
115. Kringstad, K.P.; Lindström, K. Spent liquors from pulp bleaching. *Environ. Sci. Technol.* **1984**, *18*, 236A–248A. [CrossRef]
116. Thompson, G.; Swain, J.; Kay, M.; Forster, C. The treatment of pulp and paper mill effluent: A review. *Bioresour. Technol.* **2001**, *77*, 275–286. [CrossRef]
117. Hu, X.; Cheng, L.; Gu, Z.; Hong, Y.; Li, Z.; Li, C. Effects of ionic liquid/water mixture pretreatment on the composition, the structure and the enzymatic hydrolysis of corn stalk. *Ind. Crop. Prod.* **2018**, *122*, 142–147. [CrossRef]
118. Odorico, F.H.; de Araújo Morandim-Giannetti, A.; Lucarini, A.C.; Torres, R.B. Pretreatment of Guinea grass (Panicum maximum) with the ionic liquid 1-ethyl-3-methyl imidazolium acetate for efficient hydrolysis and bioethanol production. *Cellulose* **2018**, *25*, 2997–3009. [CrossRef]
119. Trinh, L.T.P.; Lee, Y.-J.; Lee, J.-W.; Lee, W.-H. Optimization of ionic liquid pretreatment of mixed softwood by response surface methodology and reutilization of ionic liquid from hydrolysate. *Biotechnol. Bioprocess Eng.* **2018**, *23*, 228–237. [CrossRef]
120. Bose, S.; Barnes, C.A.; Petrich, J.W. Enhanced stability and activity of cellulase in an ionic liquid and the effect of pretreatment on cellulose hydrolysis. *Biotechnol. Bioeng.* **2012**, *109*, 434–443. [CrossRef] [PubMed]

121. Wahlström, R.; Rovio, S.; Suurnäkki, A. Partial enzymatic hydrolysis of microcrystalline cellulose in ionic liquids by Trichoderma reesei endoglucanases. *RSC Adv.* **2012**, *2*, 4472–4480. [CrossRef]
122. Xu, J.; Xiong, P.; He, B. Advances in improving the performance of cellulase in ionic liquids for lignocellulose biorefinery. *Bioresour. Technol.* **2016**, *200*, 961–970. [CrossRef]
123. Financie, R.; Moniruzzaman, M.; Uemura, Y. Enhanced enzymatic delignification of oil palm biomass with ionic liquid pretreatment. *Biochem. Eng. J.* **2016**, *110*, 1–7. [CrossRef]
124. Xie, W.-H.; Hu, B.-B.; Zhang, X.-B.; Yi, X.-M.; Tan, W.-X.; Zhu, M.-J. Enhanced Enzymatic Digestibility of Sugarcane Bagasse Pretreated by Ionic Liquids. *J. Biobased Mater. Bioenergy* **2015**, *9*, 493–501. [CrossRef]
125. Tian, X.; Rehmann, L.; Xu, C.C.; Fang, Z. Pretreatment of eastern white pine (Pinus strobes L.) for enzymatic hydrolysis and ethanol production by organic electrolyte solutions. *ACS Sustain. Chem. Eng.* **2016**, *4*, 2822–2829. [CrossRef]
126. Zhang, X.; Zhao, W.; Li, Y.; Li, C.; Yuan, Q.; Cheng, G. Synergistic effect of pretreatment with dimethyl sulfoxide and an ionic liquid on enzymatic digestibility of white poplar and pine. *RSC Adv.* **2016**, *6*, 62278–62285. [CrossRef]
127. Wu, L.; Lee, S.-H.; Endo, T. Effect of dimethyl sulfoxide on ionic liquid 1-ethyl-3-methylimidazolium acetate pretreatment of eucalyptus wood for enzymatic hydrolysis. *Bioresour. Technol.* **2013**, *140*, 90–96. [CrossRef]
128. Fu, D.; Mazza, G. Optimization of processing conditions for the pretreatment of wheat straw using aqueous ionic liquid. *Bioresour. Technol.* **2011**, *102*, 8003–8010. [CrossRef] [PubMed]
129. Fu, D.; Mazza, G. Aqueous ionic liquid pretreatment of straw. *Bioresour. Technol.* **2011**, *102*, 7008–7011. [CrossRef] [PubMed]
130. Brandt, A.; Ray, M.J.; To, T.Q.; Leak, D.J.; Murphy, R.J.; Welton, T. Ionic liquid pretreatment of lignocellulosic biomass with ionic liquid–water mixtures. *Green Chem.* **2011**, *13*, 2489–2499. [CrossRef]
131. Funazukuri, T.; Ozawa, S. Effects of Pretreatment with Ionic Liquids on Cellulose Hydrolysis under Hydrothermal Conditions. *Molecules* **2019**, *24*, 3572. [CrossRef]
132. Rigual, V.; Domínguez, J.C.; Santos, T.M.; Rivas, S.; Alonso, M.V.; Oliet, M.; Rodriguez, F. Autohydrolysis and microwave ionic liquid pretreatment of Pinus radiata: Imaging visualization and analysis to understand enzymatic digestibility. *Ind. Crop. Prod.* **2019**, *134*, 328–337. [CrossRef]
133. Rigual, V.; Santos, T.M.; Domínguez, J.C.; Alonso, M.V.; Oliet, M.; Rodriguez, F. Combining autohydrolysis and ionic liquid microwave treatment to enhance enzymatic hydrolysis of Eucalyptus globulus wood. *Bioresour. Technol.* **2018**, *251*, 197–203. [CrossRef]
134. Elmacı, S.B.; Özçelik, F. Ionic liquid pretreatment of yellow pine followed by enzymatic hydrolysis and fermentation. *Biotechnol. Prog.* **2018**, *34*, 1242–1250. [CrossRef]
135. Dotsenko, A.S.; Dotsenko, G.S.; Senko, O.V.; Stepanov, N.A.; Lyagin, I.V.; Efremenko, E.N.; Gusakov, A.V.; Zorov, I.N.; Rubtsova, E.A. Complex effect of lignocellulosic biomass pretreatment with 1-butyl-3-methylimidazolium chloride ionic liquid on various aspects of ethanol and fumaric acid production by immobilized cells within SSF. *Bioresour. Technol.* **2018**, *250*, 429–438. [CrossRef]
136. Ninomiya, K.; Ochiai, K.; Eguchi, M.; Kuroda, K.; Tsuge, Y.; Ogino, C.; Taima, T.; Takahashi, K. Oxidative depolymerization potential of biorefinery lignin obtained by ionic liquid pretreatment and subsequent enzymatic saccharification of eucalyptus. *Ind. Crop. Prod.* **2018**, *111*, 457–461. [CrossRef]
137. Goshadrou, A.; Lefsrud, M. Synergistic surfactant-assisted [EMIM] OAc pretreatment of lignocellulosic waste for enhanced cellulose accessibility to cellulase. *Carbohydr. Polym.* **2017**, *166*, 104–113. [CrossRef]
138. Hashmi, M.; Sun, Q.; Tao, J.; Wells Jr, T.; Shah, A.A.; Labbe, N.; Ragauskas, A.J. Comparison of autohydrolysis and ionic liquid 1-butyl-3-methylimidazolium acetate pretreatment to enhance enzymatic hydrolysis of sugarcane bagasse. *Bioresour. Technol.* **2017**, *224*, 714–720. [CrossRef] [PubMed]
139. Chen, S.; Zhang, X.; Ling, Z.; Xu, F. Characterization of the micromorphology and topochemistry of poplar wood during mild ionic liquid pretreatment for improving enzymatic saccharification. *Molecules* **2017**, *22*, 115. [CrossRef] [PubMed]
140. Aid, T.; Hyvärinen, S.; Vaher, M.; Koel, M.; Mikkola, J.-P. Saccharification of lignocellulosic biomasses via ionic liquid pretreatment. *Ind. Crop. Prod.* **2016**, *92*, 336–341. [CrossRef]
141. Vo, H.T.; Kim, C.S.; Lee, S.D.; Lee, H. Ionic Liquid-assisted Separation of Carbohydrates from Lignocellulosic Biomass. *Bull. Korean Chem. Soc.* **2016**, *37*, 1305–1312. [CrossRef]

142. Normark, M.; Pommer, L.; Gräsvik, J.; Hedenström, M.; Gorzsás, A.; Winestrand, S.; Jönsson, L.J. Biochemical conversion of torrefied Norway spruce after pretreatment with acid or ionic liquid. *Bioenergy Res.* **2016**, *9*, 355–368. [CrossRef]
143. Torr, K.M.; Love, K.T.; Simmons, B.A.; Hill, S.J. Structural features affecting the enzymatic digestibility of pine wood pretreated with ionic liquids. *Biotechnol. Bioeng.* **2016**, *113*, 540–549. [CrossRef]
144. Wang, S.; You, T.; Xu, F.; Chen, J.; Yang, G. Optimization of [Amim] Cl pretreatment conditions for maximum glucose recovery from hybrid Pennisetum by response surface methodology. *BioResources* **2015**, *10*, 7021–7037. [CrossRef]
145. Trinh, L.T.P.; Lee, Y.J.; Lee, J.-W.; Lee, H.-J. Characterization of ionic liquid pretreatment and the bioconversion of pretreated mixed softwood biomass. *Biomass Bioenergy* **2015**, *81*, 1–8. [CrossRef]
146. Auxenfans, T.; Buchoux, S.; Larcher, D.; Husson, G.; Husson, E.; Sarazin, C. Enzymatic saccharification and structural properties of industrial wood sawdust: Recycled ionic liquids pretreatments. *Energy Convers. Manag.* **2014**, *88*, 1094–1103. [CrossRef]
147. Yáñez, R.; Gómez, B.; Martínez, M.; Gullón, B.; Alonso, J.L. Valorization of an invasive woody species, Acacia dealbata, by means of Ionic liquid pretreatment and enzymatic hydrolysis. *J. Chem. Technol. Biotechnol.* **2014**, *89*, 1337–1343. [CrossRef]
148. Bian, J.; Peng, F.; Peng, X.-P.; Xiao, X.; Peng, P.; Xu, F.; Sun, R.-C. Effect of [Emim] Ac pretreatment on the structure and enzymatic hydrolysis of sugarcane bagasse cellulose. *Carbohydr. Polym.* **2014**, *100*, 211–217. [CrossRef] [PubMed]
149. Cui, L.H.; Wang, M.; Li, J.H.; Wang, Q.H. Effect of Ionic Liquid Pretreatment on the Structure and Enzymatic Saccharification of Cassava Stillage Residues. *Adv. Mater. Res.* **2014**, 59–63. [CrossRef]
150. Soudham, V.P.; Gräsvik, J.; Alriksson, B.; Mikkola, J.P.; Jönsson, L.J. Enzymatic hydrolysis of Norway spruce and sugarcane bagasse after treatment with 1-allyl-3-methylimidazolium formate. *J. Chem. Technol. Biotechnol.* **2013**, *88*, 2209–2215. [CrossRef]
151. Wang, J.; Wang, H.; Mou, H. 1-allyl-3-methylimidazolium chloride pretreatment of seaweed industrial waste for bioethanol conversion. *J. Renew. Sustain. Energy* **2013**, *5*, 063111. [CrossRef]
152. Haykir, N.I.; Bakir, U. Ionic liquid pretreatment allows utilization of high substrate loadings in enzymatic hydrolysis of biomass to produce ethanol from cotton stalks. *Ind. Crop. Prod.* **2013**, *51*, 408–414. [CrossRef]
153. Yuan, T.-Q.; Wang, W.; Xu, F.; Sun, R.-C. Synergistic benefits of ionic liquid and alkaline pretreatments of poplar wood. Part 1: Effect of integrated pretreatment on enzymatic hydrolysis. *Bioresour. Technol.* **2013**, *144*, 429–434. [CrossRef]
154. Mou, H.-Y.; Orblin, E.; Kruus, K.; Fardim, P. Topochemical pretreatment of wood biomass to enhance enzymatic hydrolysis of polysaccharides to sugars. *Bioresour. Technol.* **2013**, *142*, 540–545. [CrossRef]
155. Goshadrou, A.; Karimi, K.; Lefsrud, M. Characterization of ionic liquid pretreated aspen wood using semi-quantitative methods for ethanol production. *Carbohydr. Polym.* **2013**, *96*, 440–449. [CrossRef]
156. Socha, A.M.; Plummer, S.P.; Stavila, V.; Simmons, B.A.; Singh, S. Comparison of sugar content for ionic liquid pretreated Douglas-fir woodchips and forestry residues. *Biotechnol. Biofuels* **2013**, *6*, 61. [CrossRef]
157. Li, C.; Sun, L.; Simmons, B.A.; Singh, S. Comparing the recalcitrance of eucalyptus, pine, and switchgrass using ionic liquid and dilute acid pretreatments. *Bioenergy Res.* **2013**, *6*, 14–23. [CrossRef]
158. Shafiei, M.; Zilouei, H.; Zamani, A.; Taherzadeh, M.J.; Karimi, K. Enhancement of ethanol production from spruce wood chips by ionic liquid pretreatment. *Appl. Energy* **2013**, *102*, 163–169. [CrossRef]
159. Lee, K.M.; Ngoh, G.C.; Chua, A.S.M. Process optimization and performance evaluation on sequential ionic liquid dissolution–solid acid saccharification of sago waste. *Bioresour. Technol.* **2013**, *130*, 1–7. [CrossRef] [PubMed]
160. Tan, H.T.; Lee, K.T. Understanding the impact of ionic liquid pretreatment on biomass and enzymatic hydrolysis. *Chem. Eng. J.* **2012**, *183*, 448–458. [CrossRef]
161. Ninomiya, K.; Kamide, K.; Takahashi, K.; Shimizu, N. Enhanced enzymatic saccharification of kenaf powder after ultrasonic pretreatment in ionic liquids at room temperature. *Bioresour. Technol.* **2012**, *103*, 259–265. [CrossRef] [PubMed]
162. da Silva, A.S.A.; Lee, S.-H.; Endo, T.; Bon, E.P. Major improvement in the rate and yield of enzymatic saccharification of sugarcane bagasse via pretreatment with the ionic liquid 1-ethyl-3-methylimidazolium acetate ([Emim][Ac]). *Bioresour. Technol.* **2011**, *102*, 10505–10509. [CrossRef] [PubMed]

163. Kimon, K.S.; Alan, E.L.; Sinclair, D.W.O. Enhanced saccharification kinetics of sugarcane bagasse pretreated in 1-butyl-3-methylimidazolium chloride at high temperature and without complete dissolution. *Bioresour. Technol.* **2011**, *102*, 9325–9329. [CrossRef] [PubMed]
164. Holmbom, B. A procedure for analysis of toxic compounds in pulp and paper mill waste waters. *Pap. Puu (Pap. Pulp)* **1980**, *62*, 523–531.
165. Servos, M.R. *Environmental Fate and Effects of Pulp and Paper: Mill Effluents*; CRC Press: Boca Raton, FL, USA, 1996.
166. Zhu, J.; Chai, X.-S.; Pan, X.; Luo, Q.; Li, J. Quantification and reduction of organic sulfur compound formation in a commercial wood pulping process. *Environ. Sci. Technol.* **2002**, *36*, 2269–2272. [CrossRef]
167. Kim, J.-Y.; Shin, E.-J.; Eom, I.-Y.; Won, K.; Kim, Y.H.; Choi, D.; Choi, I.-G.; Choi, J.W. Structural features of lignin macromolecules extracted with ionic liquid from poplar wood. *Bioresour. Technol.* **2011**, *102*, 9020–9025. [CrossRef]
168. da Silva, S.P.M.; da Costa Lopes, A.M.; Roseiro, L.B.; Bogel-Łukasik, R. Novel pre-treatment and fractionation method for lignocellulosic biomass using ionic liquids. *RSC Adv.* **2013**, *3*, 16040–16050. [CrossRef]
169. Lan, W.; Liu, C.-F.; Sun, R.-C. Fractionation of Bagasse into Cellulose, Hemicelluloses, and Lignin with Ionic Liquid Treatment Followed by Alkaline Extraction. *J. Agric. Food Chem.* **2011**, *59*, 8691–8701. [CrossRef] [PubMed]
170. Penín, L.; Peleteiro, S.; Rivas, S.; Santos, V.; Parajo, J.C. Production of 5-Hydroxymethylfurfural from Pine Wood via Biorefinery Technologies Based on Fractionation and Reaction in Ionic Liquids. *BioResources* **2019**, *14*, 4733–4747.
171. Simmons, T.J.; Lee, S.H.; Miao, J.; Miyauchi, M.; Park, T.-J.; Bale, S.S.; Pangule, R.; Bult, J.; Martin, J.G.; Dordick, J.S. Preparation of synthetic wood composites using ionic liquids. *Wood Sci. Technol.* **2011**, *45*, 719–733. [CrossRef]
172. Barta, K.; Warner, G.R.; Beach, E.S.; Anastas, P.T. Depolymerization of organosolv lignin to aromatic compounds over Cu-doped porous metal oxides. *Green Chem.* **2014**, *16*, 191–196. [CrossRef]
173. Younesi-Kordkheili, H.; Pizzi, A. Properties of plywood panels bonded with ionic liquid-modified lignin–phenol–formaldehyde resin. *J. Adhes.* **2018**, *94*, 143–154. [CrossRef]
174. Prado, R.; Erdocia, X.; Labidi, J. Lignin extraction and purification with ionic liquids. *J. Chem. Technol. Biotechnol.* **2013**, *88*, 1248–1257. [CrossRef]
175. Xu, J.-K.; Sun, Y.-C.; Xu, F.; Sun, R.-C. Characterization of hemicelluloses obtained from partially delignified Eucalyptus using ionic liquid pretreatment. *BioResources* **2013**, *8*, 1946–1962. [CrossRef]
176. Sixta, H.; Iakovlev, M.; Testova, L.; Roselli, A.; Hummel, M.; Borrega, M.; van Heiningen, A.; Froschauer, C.; Schottenberger, H. Novel concepts of dissolving pulp production. *Cellulose* **2013**, *20*, 1547–1561. [CrossRef]
177. Roselli, A.; Hummel, M.; Monshizadeh, A.; Maloney, T.; Sixta, H. Ionic liquid extraction method for upgrading eucalyptus kraft pulp to high purity dissolving pulp. *Cellulose* **2014**, *21*, 3655–3666. [CrossRef]
178. Froschauer, C.; Hummel, M.; Iakovlev, M.; Roselli, A.; Schottenberger, H.; Sixta, H. Separation of hemicellulose and cellulose from wood pulp by means of ionic liquid/cosolvent systems. *Biomacromolecules* **2013**, *14*, 1741–1750. [CrossRef]
179. Abushammala, H.; Goldsztayn, R.; Leao, A.; Laborie, M.-P. Combining steam explosion with 1-ethyl-3-methylimidazlium acetate treatment of wood yields lignin-coated cellulose nanocrystals of high aspect ratio. *Cellulose* **2016**, *23*, 1813–1823. [CrossRef]
180. Abushammala, H.; Krossing, I.; Laborie, M.-P. Ionic liquid-mediated technology to produce cellulose nanocrystals directly from wood. *Carbohydr. Polym.* **2015**, *134*, 609–616. [CrossRef] [PubMed]
181. Janesko, B.G. Modeling interactions between lignocellulose and ionic liquids using DFT-D. *Phys. Chem. Chem. Phys.* **2011**, *13*, 11393–11401. [CrossRef] [PubMed]
182. Payal, R.S.; Bejagam, K.K.; Mondal, A.; Balasubramanian, S. Dissolution of Cellulose in Room Temperature Ionic Liquids: Anion Dependence. *J. Phys. Chem. B* **2015**, *119*, 1654–1659. [CrossRef]
183. Guo, J.; Zhang, D.; Duan, C.; Liu, C. Probing anion–cellulose interactions in imidazolium-based room temperature ionic liquids: A density functional study. *Carbohydr. Res.* **2010**, *345*, 2201–2205. [CrossRef]
184. George, A.; Tran, K.; Morgan, T.J.; Benke, P.I.; Berrueco, C.; Lorente, E.; Wu, B.C.; Keasling, J.D.; Simmons, B.A.; Holmes, B.M. The effect of ionic liquid cation and anion combinations on the macromolecular structure of lignins. *Green Chem.* **2011**, *13*, 3375–3385. [CrossRef]

185. Nakamura, A.; Miyafuji, H.; Saka, S. Liquefaction behavior of Western red cedar and Japanese beech in the ionic liquid 1-ethyl-3-methylimidazolium chloride. *Holzforschung* **2010**, *64*, 289–294. [CrossRef]
186. Moniruzzaman, M.; Ono, T. Separation and characterization of cellulose fibers from cypress wood treated with ionic liquid prior to laccase treatment. *Bioresour. Technol.* **2013**, *127*, 132–137. [CrossRef]
187. Shamsuri, A.A.; Abdullah, D.K. Isolation and characterization of lignin from rubber wood in ionic liquid medium. *Mod. Appl. Sci.* **2010**, *4*, 19. [CrossRef]
188. Ladesov, A.; Belesov, A.; Kuznetsova, M.; Pochtovalova, A.; Malkov, A.; Shestakov, S.; Kosyakov, D. Fractionation of Wood with Binary Solvent 1-Butyl-3-methylimidazolium Acetate+ Dimethyl Sulfoxide. *Russ. J. Appl. Chem.* **2018**, *91*, 663–670. [CrossRef]
189. Wen, J.-L.; Sun, S.-L.; Xue, B.-L.; Sun, R.-C. Quantitative structures and thermal properties of birch lignins after ionic liquid pretreatment. *J. Agric. Food Chem.* **2013**, *61*, 635–645. [CrossRef] [PubMed]
190. Tan, S.S.Y.; MacFarlane, D.R.; Upfal, J.; Edye, L.A.; Doherty, W.O.S.; Patti, A.F.; Pringle, J.M.; Scott, J.L. Extraction of lignin from lignocellulose at atmospheric pressure using alkylbenzenesulfonate ionic liquid. *Green Chem.* **2009**, *11*, 339–345. [CrossRef]
191. El-barbary, M.H.; Shukry, N. Polyhydric alcohol liquefaction of some lignocellulosic agricultural residues. *Ind. Crop. Prod.* **2008**, *27*, 33–38.
192. Alma, M.; Yoshioka, M.; Yao, Y.; Shiraishi, N. Preparation and characterization of the phenolated wood using hydrochloric acid (HCl) as a catalyst. *Wood Sci. Technol.* **1995**, *30*, 39–47. [CrossRef]
193. Xie, H.; King, A.; Kilpelainen, I.; Granstrom, M.; Argyropoulos, D.S. Thorough chemical modification of wood-based lignocellulosic materials in ionic liquids. *Biomacromolecules* **2007**, *8*, 3740–3748. [CrossRef]
194. Ou, R.; Xie, Y.; Wang, Q.; Sui, S.; Wolcott, M.P. Thermoplastic deformation of poplar wood plasticized by ionic liquids measured by a nonisothermal compression technique. *Holzforschung* **2014**, *68*, 555–566. [CrossRef]
195. Brandt, A.; Erickson, J.K.; Hallett, J.P.; Murphy, R.J.; Potthast, A.; Ray, M.J.; Rosenau, T.; Schrems, M.; Welton, T. Soaking of pine wood chips with ionic liquids for reduced energy input during grinding. *Green Chem.* **2012**, *14*, 1079–1085. [CrossRef]
196. Kanbayashi, T.; Miyafuji, H. Influence of ionic liquid treatment on wood cell walls: Anatomical changes in opposite wood. *Eur. J. Wood Wood Prod.* **2016**, *74*, 905–908. [CrossRef]
197. Lucas, M.; Wagner, G.L.; Nishiyama, Y.; Hanson, L.; Samayam, I.P.; Schall, C.A.; Langan, P.; Rector, K.D. Reversible swelling of the cell wall of poplar biomass by ionic liquid at room temperature. *Bioresour. Technol.* **2011**, *102*, 4518–4523. [CrossRef]
198. Ou, R.; Xie, Y.; Wang, Q.; Sui, S.; Wolcott, M.P. Material pocket dynamic mechanical analysis: A novel tool to study thermal transition in wood fibers plasticized by an ionic liquid (IL). *Holzforschung* **2015**, *69*, 223–232. [CrossRef]
199. Salmén, L. Viscoelastic properties ofin situ lignin under water-saturated conditions. *J. Mater. Sci.* **1984**, *19*, 3090–3096. [CrossRef]
200. Goring, D.A. Thermal softening of lignin, hemicelluolose and cellulose. *Pulp Pap* **1963**, *64*, T517–T527.
201. Blechschmidt, J.; Engert, P.; Stephan, M. The glass transition of wood from the viewpoint of mechanical pulping. *Wood Sci. Technol.* **1986**, *20*, 263–272.
202. Eriksson, I.; Haglind, I.; Lidbrandt, O.; Sahnén, L. Fiber swelling favoured by lignin softening. *Wood Sci. Technol.* **1991**, *25*, 135–144. [CrossRef]
203. Zhang, K.; Xiao, H.; Su, Y.; Wu, Y.; Cui, Y.; Li, M. Mechanical and Physical Properties of Regenerated Biomass Composite Films from Lignocellulosic Materials in Ionic Liquid. *BioResources* **2019**, *14*, 2584–2595.
204. Adak, B.; Mukhopadhyay, S. Effect of the dissolution time on the structure and properties of lyocell-fabric-based all-cellulose composite laminates. *J. Appl. Polym. Sci.* **2016**, *133*. [CrossRef]
205. Shu, Z.; Song, J.; Yuan, Y.; Chen, J.; Zhang, S.; Huang, L.; Liu, S. Preparation and Mechanical Properties of Lignocellulosic Composite Films Based on Poplar Wood Flour and Waste Filter Paper. *BioResources* **2018**, *13*, 7935–7943. [CrossRef]
206. Shibata, M.; Teramoto, N.; Nakamura, T.; Saitoh, Y. All-cellulose and all-wood composites by partial dissolution of cotton fabric and wood in ionic liquid. *Carbohydr. Polym.* **2013**, *98*, 1532–1539. [CrossRef]
207. Mahmood, H.; Moniruzzaman, M.; Yusup, S.; Akil, H.M. Ionic liquid pretreatment at high solids loading: A clean approach for fabrication of renewable resource based particulate composites. *Polym. Compos.* **2018**, *39*, 1994–2003. [CrossRef]

208. Li, J.; Zhang, X.; Zhang, J.; Mi, Q.; Jia, F.; Wu, J.; Yu, J.; Zhang, J. Direct and complete utilization of agricultural straw to fabricate all-biomass films with high-strength, high-haze and UV-shielding properties. *Carbohydr. Polym.* **2019**, *223*, 115057. [CrossRef]
209. Khakalo, A.; Tanaka, A.; Korpela, A.; Hauru, L.K.; Orelma, H. All-Wood Composite Material by Partial Fiber Surface Dissolution with an Ionic Liquid. *ACS Sustain. Chem. Eng.* **2019**, *7*, 3195–3202. [CrossRef]
210. Tanaka, A.; Khakalo, A.; Hauru, L.; Korpela, A.; Orelma, H. Conversion of paper to film by ionic liquids: Manufacturing process and properties. *Cellulose* **2018**, *25*, 6107–6119. [CrossRef]
211. Khosravani, A.; Pourjafar, M.; Behrooz, R. The effect of lignin on processing and the properties of lignocellulose material recovered by ionic liquid. In Proceedings of the IOP Conference Series: Materials Science and Engineering, Selangor, Malaysia, 21–23 November 2017; p. 012029.
212. Tisserat, B.; Larson, E.; Gray, D.; Dexter, N.; Meunier, C.; Moore, L.; Haverhals, L. Ionic liquid-facilitated preparation of lignocellulosic composites. *Int. J. Polym. Sci.* **2015**. [CrossRef]
213. Shibata, M.; Yamazoe, K.; Kuribayashi, M.; Okuyama, Y. All-wood biocomposites by partial dissolution of wood flour in 1-butyl-3-methylimidazolium chloride. *J. Appl. Polym. Sci.* **2013**, *127*, 4802–4808. [CrossRef]
214. Abushammala, H.; Mao, J. A Review of the Surface Modification of Cellulose and Nanocellulose Using Aliphatic and Aromatic Mono-and Di-Isocyanates. *Molecules* **2019**, *24*, 2782. [CrossRef]
215. Dufresne, A. Nanocellulose: A new ageless bionanomaterial. *Mater. Today* **2013**, *16*, 220–227. [CrossRef]
216. Klemm, D.; Cranston, E.D.; Fischer, D.; Gama, M.; Kedzior, S.A.; Kralisch, D.; Kramer, F.; Kondo, T.; Lindström, T.; Nietzsche, S.; et al. Nanocellulose as a natural source for groundbreaking applications in materials science: Today's state. *Mater. Today* **2018**, *21*, 720–748. [CrossRef]
217. Eyley, S.; Thielemans, W. Surface modification of cellulose nanocrystals. *Nanoscale* **2014**, *6*, 7764–7779. [CrossRef]
218. Kiziltas, A.; Kiziltas, E.E.; Boran, S.; Gardner, D.J. Micro-and nanocellulose composites for automotive applications. In Proceedings of the SPE Automotive Composites Conference and Exhibition (ACCE), Novi, MI, USA, 11–13 September 2013.
219. Voisin, H.; Bergström, L.; Liu, P.; Mathew, A.P. Nanocellulose-based materials for water purification. *Nanomaterials* **2017**, *7*, 57. [CrossRef]
220. Sharma, P.R.; Chattopadhyay, A.; Sharma, S.K.; Geng, L.; Amiralian, N.; Martin, D.; Hsiao, B.S. Nanocellulose from Spinifex as an Effective Adsorbent to Remove Cadmium(II) from Water. *ACS Sustain. Chem. Eng.* **2018**, *6*, 3279–3290. [CrossRef]
221. Pirani, S.; Abushammala, H.M.; Hashaikeh, R. Preparation and characterization of electrospun PLA/nanocrystalline cellulose-based composites. *J. Appl. Polym. Sci.* **2013**, *130*, 3345–3354. [CrossRef]
222. Abushammala, H.; Hashaikeh, R.; Cooney, C. Microcrystalline cellulose powder tableting via networked cellulose-based gel material. *Powder Technol.* **2012**, *217*, 16–20. [CrossRef]
223. Shi, Z.; Phillips, G.O.; Yang, G. Nanocellulose electroconductive composites. *Nanoscale* **2013**, *5*, 3194–3201. [CrossRef] [PubMed]
224. *Standard Terms and Their Definition for Cellulose Nanomaterial*; International Organization for Standardization (ISO): Geneva, Switzerland, 2017.
225. Li, C.; Zhao, Z.K. Efficient acid-catalyzed hydrolysis of cellulose in ionic liquid. *Adv. Synth. Catal.* **2007**, *349*, 1847–1850. [CrossRef]
226. Bondeson, D.; Mathew, A.; Oksman, K. Optimization of the isolation of nanocrystals from microcrystalline cellulose by acid hydrolysis. *Cellulose* **2006**, *13*, 171. [CrossRef]
227. Fan, J.-S.; Li, Y.-H. Maximizing the yield of nanocrystalline cellulose from cotton pulp fiber. *Carbohydr. Polym.* **2012**, *88*, 1184–1188. [CrossRef]
228. Reyes, G.; Aguayo, M.G.; Fernández Pérez, A.; Pääkkönen, T.; Gacitúa, W.; Rojas, O.J. Dissolution and Hydrolysis of Bleached Kraft Pulp Using Ionic Liquids. *Polymers* **2019**, *11*, 673. [CrossRef]
229. Man, Z.; Muhammad, N.; Sarwono, A.; Bustam, M.A.; Kumar, M.V.; Rafiq, S. Preparation of cellulose nanocrystals using an ionic liquid. *J. Polym. Environ.* **2011**, *19*, 726–731. [CrossRef]
230. Mao, J.; Osorio-Madrazo, A.; Laborie, M.-P. Preparation of cellulose I nanowhiskers with a mildly acidic aqueous ionic liquid: Reaction efficiency and whiskers attributes. *Cellulose* **2013**, *20*, 1829–1840. [CrossRef]
231. Mao, J.; Abushammala, H.; Pereira, L.B.; Laborie, M.-P. Swelling and hydrolysis kinetics of Kraft pulp fibers in aqueous 1-butyl-3-methylimidazolium hydrogen sulfate solutions. *Carbohydr. Polym.* **2016**, *153*, 284–291. [CrossRef]

232. Grząbka-Zasadzińska, A.; Skrzypczak, A.; Borysiak, S. The influence of the cation type of ionic liquid on the production of nanocrystalline cellulose and mechanical properties of chitosan-based biocomposites. *Cellulose* **2019**, *26*, 4827–4840. [CrossRef]
233. Han, J.; Zhou, C.; French, A.D.; Han, G.; Wu, Q. Characterization of cellulose II nanoparticles regenerated from 1-butyl-3-methylimidazolium chloride. *Carbohydr. Polym.* **2013**, *94*, 773–781. [CrossRef] [PubMed]
234. Mao, J.; Heck, B.; Abushammala, H.; Reiter, G.; Laborie, M.-P. A structural fibrillation parameter from small angle X-ray scattering to quantify pulp refining. *Cellulose* **2019**, *26*, 4265–4277. [CrossRef]
235. Turbak, A.F.; Snyder, F.W.; Sandberg, K.R. Microfibrillated cellulose, a new cellulose product: Properties, uses, and commercial potential. *J. Appl. Polym. Sci. Appl. Polym. Symp.* **1983**, *37*, 815–827.
236. Nair, S.S.; Zhu, J.; Deng, Y.; Ragauskas, A.J. Characterization of cellulose nanofibrillation by micro grinding. *J. Nanoparticle Res.* **2014**, *16*, 2349. [CrossRef]
237. Sharma, P.R.; Joshi, R.; Sharma, S.K.; Hsiao, B.S. A Simple Approach to Prepare Carboxycellulose Nanofibers from Untreated Biomass. *Biomacromolecules* **2017**, *18*, 2333–2342. [CrossRef]
238. Viswanathan, G.; Murugesan, S.; Pushparaj, V.; Nalamasu, O.; Ajayan, P.M.; Linhardt, R.J. Preparation of biopolymer fibers by electrospinning from room temperature ionic liquids. *Biomacromolecules* **2006**, *7*, 415–418. [CrossRef]
239. Ahn, Y.; Hu, D.-H.; Hong, J.H.; Lee, S.H.; Kim, H.J.; Kim, H. Effect of co-solvent on the spinnability and properties of electrospun cellulose nanofiber. *Carbohydr. Polym.* **2012**, *89*, 340–345. [CrossRef]
240. Mao, J.; Abushammala, H.; Hettegger, H.; Rosenau, T.; Laborie, M.-P. Imidazole, a New Tunable Reagent for Producing Nanocellulose, Part I: Xylan-Coated CNCs and CNFs. *Polymers* **2017**, *9*, 473. [CrossRef]
241. Laborie, M.P.; Abushammala, H. Ionic-Liquid Mediated Production of Cellulose Nanocrystals Directly from Wood, Grass or Bioresidues. U.S. Patent 20180037702A1, 8 February 2018.
242. Rajinipriya, M.; Nagalakshmaiah, M.; Robert, M.; Elkoun, S. Importance of Agricultural and Industrial Waste in the Field of Nanocellulose and Recent Industrial Developments of Wood Based Nanocellulose: A Review. *ACS Sustain. Chem. Eng.* **2018**, *6*, 2807–2828. [CrossRef]
243. Liu, C.; Li, Y.; Hou, Y. Preparation and structural characterization of lignin micro/nano-particles with ionic liquid treatment by self-assembly. *Express Polym. Lett.* **2018**, *12*, 946–956. [CrossRef]
244. Karatzos, S.K.; Edye, L.A.; Wellard, R.M. The undesirable acetylation of cellulose by the acetate ion of 1-ethyl-3-methylimidazolium acetate. *Cellulose* **2012**, *19*, 307–312. [CrossRef]
245. Çetinkol, Ö.P.; Dibble, D.C.; Cheng, G.; Kent, M.S.; Knierim, B.; Auer, M.; Wemmer, D.E.; Pelton, J.G.; Melnichenko, Y.B.; Ralph, J. Understanding the impact of ionic liquid pretreatment on eucalyptus. *Biofuels* **2010**, *1*, 33–46. [CrossRef]
246. Zweckmair, T.; Hettegger, H.; Abushammala, H.; Bacher, M.; Potthast, A.; Laborie, M.-P.; Rosenau, T. On the mechanism of the unwanted acetylation of polysaccharides by 1, 3-dialkylimidazolium acetate ionic liquids: Part 1—Analysis, acetylating agent, influence of water, and mechanistic considerations. *Cellulose* **2015**, *22*, 3583–3596. [CrossRef]
247. Köhler, S.; Liebert, T.; Schöbitz, M.; Schaller, J.; Meister, F.; Günther, W.; Heinze, T. Interactions of Ionic Liquids with Polysaccharides 1. Unexpected Acetylation of Cellulose with 1-Ethyl-3-methylimidazolium Acetate. *Macromol. Rapid Commun.* **2007**, *28*, 2311–2317.
248. Abushammala, H.; Hettegger, H.; Bacher, M.; Korntner, P.; Potthast, A.; Rosenau, T.; Laborie, M.-P. On the mechanism of the unwanted acetylation of polysaccharides by 1, 3-dialkylimidazolium acetate ionic liquids: Part 2—The impact of lignin on the kinetics of cellulose acetylation. *Cellulose* **2017**, *24*, 2767–2774. [CrossRef]
249. Hauru, L.K.; Ma, Y.; Hummel, M.; Alekhina, M.; King, A.W.; Kilpeläinen, I.; Penttilä, P.A.; Serimaa, R.; Sixta, H. Enhancement of ionic liquid-aided fractionation of birchwood. Part 1: Autohydrolysis pretreatment. *RSC Adv.* **2013**, *3*, 16365–16373. [CrossRef]
250. Ohno, E.; Miyafuji, H. Reaction behavior of cellulose in an ionic liquid, 1-ethyl-3-methylimidazolium chloride. *J. Wood Sci.* **2013**, *59*, 221–228. [CrossRef]
251. Leskinen, T.; King, A.W.; Argyropoulos, D.S. Fractionation of lignocellulosic materials with ionic liquids. In *Production of Biofuels and Chemicals with Ionic Liquids*; Springer: New York, NY, USA, 2014; pp. 145–168.
252. King, A.W.; Xie, H.; Fiskari, J.; Kilpelaeinen, I. Chapter 5: Reduction of Biomass Recalcitrance via Ionic Liquid Pretreatments. In *Materials for Biofuels*; World Scientific: Singapore, 2014; pp. 95–125.
253. Gazit, O.M.; Katz, A. Dialkylimidazolium ionic liquids hydrolyze cellulose under mild conditions. *ChemSusChem* **2012**, *5*, 1542–1548. [CrossRef]

254. Ebner, G.; Schiehser, S.; Potthast, A.; Rosenau, T. Side reaction of cellulose with common 1-alkyl-3-methylimidazolium-based ionic liquids. *Tetrahedron Lett.* **2008**, *49*, 7322–7324. [CrossRef]
255. Handy, S.T.; Okello, M. The 2-position of imidazolium ionic liquids: Substitution and exchange. *J. Org. Chem.* **2005**, *70*, 1915–1918. [CrossRef] [PubMed]
256. Clough, M.T.; Geyer, K.; Hunt, P.A.; Son, S.; Vagt, U.; Welton, T. Ionic liquids: Not always innocent solvents for cellulose. *Green Chem.* **2015**, *17*, 231–243. [CrossRef]
257. Du, H.; Qian, X. The effects of acetate anion on cellulose dissolution and reaction in imidazolium ionic liquids. *Carbohydr. Res.* **2011**, *346*, 1985–1990. [CrossRef]
258. Cremer, T.; Kolbeck, C.; Lovelock, K.R.; Paape, N.; Wölfel, R.; Schulz, P.S.; Wasserscheid, P.; Weber, H.; Thar, J.; Kirchner, B. Towards a Molecular Understanding of Cation–Anion Interactions—Probing the Electronic Structure of Imidazolium Ionic Liquids by NMR Spectroscopy, X-ray Photoelectron Spectroscopy and Theoretical Calculations. *Chem. A Eur. J.* **2010**, *16*, 9018–9033. [CrossRef] [PubMed]
259. Rodríguez, H.; Gurau, G.; Holbrey, J.D.; Rogers, R.D. Reaction of elemental chalcogens with imidazolium acetates to yield imidazole-2-chalcogenones: Direct evidence for ionic liquids as proto-carbenes. *Chem. Commun.* **2011**, *47*, 3222–3224. [CrossRef] [PubMed]
260. Abushammala, H.; Winter, H.; Krossing, I.; Laborie, M.-P. On the prevalence of side reactions during ionosolv pulping of Norway spruce with 1-butyl-3-methylimidazolium acesulfamate. *Cellulose* **2014**, *21*, 4607–4619. [CrossRef]
261. Peleteiro, S.; Santos, V.; Garrote, G.; Parajó, J.C. Furfural production from Eucalyptus wood using an acidic ionic liquid. *Carbohydr. Polym.* **2016**, *146*, 20–25. [CrossRef]
262. Ito, R.; Miyafuji, H.; Miyazaki, Y.; Kawai, T. Production of 5-hydroxymethylfurfural from wood by ionic liquid treatment. *J. Wood Sci.* **2016**, *62*, 349–355. [CrossRef]
263. Li, W.; Sun, N.; Stoner, B.; Jiang, X.; Lu, X.; Rogers, R.D. Rapid dissolution of lignocellulosic biomass in ionic liquids using temperatures above the glass transition of lignin. *Green Chem.* **2011**, *13*, 2038–2047. [CrossRef]
264. Rigual, V.; Santos, T.M.; Domínguez, J.C.; Alonso, M.V.; Oliet, M.; Rodriguez, F. Recovery and Reuse of 1-Allyl-3-methylimidazolium Chloride in the Fractionation of Pinus radiata Wood. *ACS Sustain. Chem. Eng.* **2017**, *5*, 2384–2392. [CrossRef]
265. Ohno, E.; Miyafuji, H. Decomposition of cellulose in an ionic liquid, 1-ethyl-3-methylimidazolium chloride. *J. Wood Sci.* **2014**, *60*, 428–437. [CrossRef]
266. Brennan, T.C.; Datta, S.; Blanch, H.W.; Simmons, B.A.; Holmes, B.M. Recovery of sugars from ionic liquid biomass liquor by solvent extraction. *Bioenergy Res.* **2010**, *3*, 123–133. [CrossRef]
267. Lipscomb, G.; Varanasi, S.; Paripati, P.; Dadi, A.P. Ionic Liquid Recovery and Purification in Biomass Treatment Processes. W.O. Patent 2012064868A2, 18 May 2012.
268. Abu-Eishah, S.I. Ionic liquids recycling for reuse. *Ion. Liq. Cl. Prop.* **2011**, 239–272.
269. Wohlfarth, C. *Viscosity of Pure Organic Liquids and Binary Liquid Mixtures*; Springer Science & Business Media: Berlin, Germany, 2009; Volume 25.
270. Sigma-Aldrich Website. Available online: www.sigmaaldrich.com (accessed on 20 November 2019).
271. TCI Chemicals Website. Available online: www.tcichemicals.com (accessed on 20 November 2019).
272. Alfa Aesar Website. Available online: www.alfa.com (accessed on 20 November 2019).
273. Acros Organics Website. Available online: www.acros.com (accessed on 20 November 2019).
274. Stepnowski, P.; Mrozik, W.; Nichthauser, J. Adsorption of alkylimidazolium and alkylpyridinium ionic liquids onto natural soils. *Environ. Sci. Technol.* **2007**, *41*, 511–516. [CrossRef] [PubMed]
275. Pham, T.P.T.; Cho, C.-W.; Yun, Y.-S. Environmental fate and toxicity of ionic liquids: A review. *Water Res.* **2010**, *44*, 352–372. [CrossRef] [PubMed]
276. Docherty, K.M.; Hebbeler, S.Z.; Kulpa, C.F., Jr. An assessment of ionic liquid mutagenicity using the Ames Test. *Green Chem.* **2006**, *8*, 560–567. [CrossRef]
277. Hassoun, E.; Abraham, M.; Kini, V.; Al-Ghafri, M.; Abushaban, A. Cytotoxicity of the ionic liquid, 1-N-butyl-3-methyl imidazolium chloride. *Res. Commun. Pharmacol. Toxicol.* **2002**, *7*, 23–32.
278. Pretti, C.; Chiappe, C.; Pieraccini, D.; Gregori, M.; Abramo, F.; Monni, G.; Intorre, L. Acute toxicity of ionic liquids to the zebrafish (Danio rerio). *Green Chem.* **2006**, *8*, 238–240. [CrossRef]
279. Wells, A.S.; Coombe, V.T. On the freshwater ecotoxicity and biodegradation properties of some common ionic liquids. *Org. Process Res. Dev.* **2006**, *10*, 794–798. [CrossRef]

280. Bernot, R.J.; Brueseke, M.A.; Evans-White, M.A.; Lamberti, G.A. Acute and chronic toxicity of imidazolium-based ionic liquids on Daphnia magna. *Environ. Toxicol. Chem. Int. J.* **2005**, *24*, 87–92. [CrossRef]
281. Docherty, K.M.; Kulpa, C.F., Jr. Toxicity and antimicrobial activity of imidazolium and pyridinium ionic liquids. *Green Chem.* **2005**, *7*, 185–189. [CrossRef]
282. Pernak, J.; Sobaszkiewicz, K.; Mirska, I. Anti-microbial activities of ionic liquids. *Green Chem.* **2003**, *5*, 52–56. [CrossRef]
283. Pernak, J.; Goc, I.; Mirska, I. Anti-microbial activities of protic ionic liquids with lactate anion. *Green Chem.* **2004**, *6*, 323–329. [CrossRef]
284. Stolte, S.; Arning, J.; Bottin-Weber, U.; Matzke, M.; Stock, F.; Thiele, K.; Uerdingen, M.; Welz-Biermann, U.; Jastorff, B.; Ranke, J. Anion effects on the cytotoxicity of ionic liquids. *Green Chem.* **2006**, *8*, 621–629. [CrossRef]
285. Latała, A.; Stepnowski, P.; Nędzi, M.; Mrozik, W. Marine toxicity assessment of imidazolium ionic liquids: Acute effects on the Baltic algae Oocystis submarina and Cyclotella meneghiniana. *Aquat. Toxicol.* **2005**, *73*, 91–98. [CrossRef]
286. Righi, S.; Morfino, A.; Galletti, P.; Samorì, C.; Tugnoli, A.; Stramigioli, C. Comparative cradle-to-gate life cycle assessments of cellulose dissolution with 1-butyl-3-methylimidazolium chloride and N-methyl-morpholine-N-oxide. *Green Chem.* **2011**, *13*, 367–375. [CrossRef]
287. Kahani, S.; Shafiei, M.; Abdolmaleki, A.; Karimi, K. Enhancement of ethanol production by novel morpholinium ionic liquids. *J. Clean. Prod.* **2017**, *168*, 952–962. [CrossRef]
288. Ninomiya, K.; Abe, M.; Tsukegi, T.; Kuroda, K.; Omichi, M.; Takada, K.; Noguchi, M.; Tsuge, Y.; Ogino, C.; Taki, K. Ionic liquid pretreatment of bagasse improves mechanical property of bagasse/polypropylene composites. *Ind. Crop. Prod.* **2017**, *109*, 158–162. [CrossRef]
289. Ninomiya, K.; Ohta, A.; Omote, S.; Ogino, C.; Takahashi, K.; Shimizu, N. Combined use of completely bio-derived cholinium ionic liquids and ultrasound irradiation for the pretreatment of lignocellulosic material to enhance enzymatic saccharification. *Chem. Eng. J.* **2013**, *215*, 811–818. [CrossRef]
290. Hamada, Y.; Yoshida, K.; Asai, R.-I.; Hayase, S.; Nokami, T.; Izumi, S.; Itoh, T. A possible means of realizing a sacrifice-free three component separation of lignocellulose from wood biomass using an amino acid ionic liquid. *Green Chem.* **2013**, *15*, 1863–1868. [CrossRef]
291. Muhammad, N.; Man, Z.; Mutalib, M.A.; Bustam, M.A.; Wilfred, C.D.; Khan, A.S.; Ullah, Z.; Gonfa, G.; Nasrullah, A. Dissolution and separation of wood biopolymers using ionic liquids. *Chembioeng Rev.* **2015**, *2*, 257–278. [CrossRef]

polymers

MDPI

Article

Valorization of Alkaline Peroxide Mechanical Pulp by Metal Chloride-Assisted Hydrotropic Pretreatment for Enzymatic Saccharification and Cellulose Nanofibrillation

Huiyang Bian [1], Xinxing Wu [1,2], Jing Luo [1,2], Yongzhen Qiao [1], Guigan Fang [3] and Hongqi Dai [1,*]

[1] Jiangsu Co-Innovation Center of Efficient Processing and Utilization of Forest Resources, Nanjing Forestry University, Nanjing 210037, China; hybian1992@njfu.edu.cn (H.B.); xinxingwu@njfu.edu.cn (X.W.); luojing@njfu.edu.cn (J.L.); qiaoyz0210@163.com (Y.Q.)

[2] College of Chemical Engineering, Nanjing Forestry University, Nanjing Forestry University, Nanjing 210037, China

[3] China Institute of Chemical Industry of Forestry Products, Chinese Academy of Forestry, Nanjing 210042, China; fangguigan@icifp.cn

* Correspondence: daihq@vip.sina.com; Tel.: +86-25-85428932

Received: 26 January 2019; Accepted: 12 February 2019; Published: 14 February 2019

Abstract: Developing economical and sustainable fractionation technology of lignocellulose cell walls is the key to reaping the full benefits of lignocellulosic biomass. This study evaluated the potential of metal chloride-assisted *p*-toluenesulfonic acid (*p*-TsOH) hydrolysis at low temperatures and under acid concentration for the co-production of sugars and lignocellulosic nanofibrils (LCNF). The results indicated that three metal chlorides obviously facilitated lignin solubilization, thereby enhancing the enzymatic hydrolysis efficiency and subsequent cellulose nanofibrillation. The $CuCl_2$-assisted hydrotropic pretreatment was most suitable for delignification, resulting in a relatively higher enzymatic hydrolysis efficiency of 53.2%. It was observed that the higher residual lignin absorbed on the fiber surface, which exerted inhibitory effects on the enzymatic hydrolysis, while the lower lignin content substrates resulted in less entangled LCNF with thinner diameters. The metal chloride-assisted rapid and low-temperature fractionation process has a significant potential in achieving the energy-efficient and cost-effective valorization of lignocellulosic biomass.

Keywords: hydrotropic treatment; metal chloride; delignification; enzymatic saccharification; lignocellulosic nanofibrils

1. Introduction

Lignocellulose biomass is an abundant and sustainable, carbon-neutral resource. It can be converted into different high-value-added products (e.g., biofuels and nanocellulose). Biofuels, as a promising renewable energy alternative to fossil fuels, are usually derived from relatively inexpensive, abundant, and renewable agricultural or industrial byproducts, such as wheat straw, corn stover, or forestry residues [1–3]. Nanocellulose, as a green alternative to artificial polymers, exhibits excellent properties, such as high elastic modulus, high specific surface area, optical transparency, low thermal expansion coefficient, and chemical reactivity [4–6]. However, lignocellulose consists of carbohydrate polymers (cellulose and hemicellulose) and an aromatic polymer (lignin), which are tightly bonded together by ester and ether linkages [7]. The complexity of these components and their arrangement makes the cell wall naturally resistant, therefore making pretreatment necessary for its deconstruction or fractionation, which is the key to achieving a green, biobased economy.

To date, various pretreatment approaches have been investigated on economical and sustainable deconstruction or fractionation of lignocellulose cell walls [8–12]. These strategies facilitate the exposure of more cellulose and hemicellulose for enzymatic saccharification or cellulose nanofibrillation. Delignification is critical for successful cell wall deconstruction because lignin is a major cell wall polymer, with the middle lamella lignin acting as a glue to hold cells together in plant biomass [13]. Conventional delignification methods include alkaline wood pulping (120 °C or higher for 2 h), kraft pulping (120–160 °C for 1–2 h), and aromatic salts pretreatment (170 °C for 2 h) [14–17]. However, the high demand of reaction temperature and pressure and long reaction periods constitute major challenges in the delignification process, which increase the cost of downstream production. It has been demonstrated that the hydrotropic *p*-toluenesulfonic acid (*p*-TsOH) can dissolve approximately 90% of poplar wood (NE222) lignin at 80 °C in 20 min [18]. Unlike the traditional approach of alkaline and acid sulfite cooking by the extraction of lignin at the expense of degrading a considerable amount of another components, this hydrotropic pretreatment can maintain cellulose and hemicellulose for a low energy input and sustainable production of valuable building blocks, such as sugars, fibers, and wood-based nanomaterials [19–22]. Limited attention, however, has been paid to discuss the lignin redistribution on the fiber surface after *p*-TsOH pretreatment and its effect on subsequent enzymatic saccharification or lignocellulose nanomaterials production.

Note that some metal chlorides can effectively hydrolyze carbohydrates into useful chemicals and exhibit higher catalytic activity than inorganic acids [23]. Some studies have reported on the production of ethanol or cellulose nanocrystals using metal chlorides to pretreat rice straw or enhance cellulose hydrolysis [24–28]. In order to reduce the acid and energy consumption, three inorganic chlorides ($FeCl_3$, $AlCl_3$, and $CuCl_2$) were introduced into hydrotropic pretreatment of alkaline peroxide mechanical pulp (APMP) fiber at a relatively low acid concentration and reaction temperature in this work. The enzymatic digestibility of cellulose after pretreatment was investigated. The enzyme-treated residual solids were further fibrillated to produce lignocellulosic nanofibrils (LCNF). The amount of lignin retained in hydrolyzed lignocellulose can be tuned by selecting various metal chlorides as the catalysts, thereby endowing LCNF with different morphologies and physicochemical properties. Our research includes delignification, enzymatic efficiency, and LCNF physicochemical properties to gain insight into the valorization of APMP. Compared to pure *p*-TsOH hydrolysis, the metal chloride-assisted hydrotropic pretreatment can achieve equivalent delignification using lower acid concentration and temperature, providing useful information in economic and environmental utilization of lignocellulosic biomass for biofuels and materials.

2. Materials and Methods

2.1. Materials

Alkaline peroxide mechanical pulp (APMP) fiber was provided from Huatai Paper Co., Ltd., Shandong, China. *p*-Toluenesulfonic acid (*p*-TsOH) was the analytical reagent and purchased from LiFeng Chemical Reagent Co. Ltd., Shanghai. Ferric chloride hexahydrate ($FeCl_3 \cdot 6H_2O$), aluminum chloride hexahydrate ($AlCl_3 \cdot 6H_2O$), and copper chloride dehydrate ($CuCl_2 \cdot 2H_2O$) were purchased from Aladdin Co. Ltd., Shanghai, China. Cellulase (Cellic® CTec2) was kindly provided by Novozymes North America (Franklinton, NC, USA), with filter paper activity of 250.0 FPU/mL and cellubiase activity of 2731 U/mL.

2.2. Metal Chloride-Assisted Hydrotropic Pretreatment

Briefly, 5 g of APMP fibers were hydrolyzed in 70% (w/w) concentration *p*-TsOH solution with 0.1 mM three different metal chlorides ($FeCl_3 \cdot 6H_2O$, $AlCl_3 \cdot 6H_2O$ and $CuCl_2 \cdot 2H_2O$) at 65 °C with a liquid to solid mass ratio of 10:1 (g/g). The fiber suspension was constantly agitated using a mixer at 500 rpm for 35 min. The reaction was immediately quenched by adding 100 mL of DI water, then the hydrolysate was separated by vacuum filtration through a filter paper and the residual solids were

dialyzed until the pH of the water no longer changed. For comparison, hydrotropic pretreatment without adding metal chloride was also performed under the same condition.

2.3. Enzymatic Saccharification

Enzymatic hydrolysis of pretreated samples was carried out in 0.05 M sodium citrate buffer (pH 4.8) with a substrate concentration of 1% (w/v) on a rotary shaker (50 °C, 150 rpm). The enzyme (Cellulase, Cellic® CTec2) loading was 20 FPU/g glucan during the hydrolysis experiment. Samples were taken at different time points (2, 4, 6, 12, 24, 48 and 72 h), incubated in boiling water to inactivate the enzymes, then centrifuged to remove residual solids. To quantify monosaccharides in hydrolysate, the supernatants were diluted for HPLC (high performance liquid chromatography) analysis. All experiments were carried out in duplicate and results were presented as the average value of two replicated tests.

2.4. Lignocellulosic Nanofibrils Production

All enzyme treated residual samples were mechanically fibrillated for producing LCNF using a high pressure homogenizer (FB-110Q, LiTu Mechanical Equipment Co., Ltd, Shanghai, China) with an operation pressure of 600 bar for 5 passes. A schematic flow diagram describing the routes for the valorization of APMP using metal chloride-assisted hydrotropic pretreatment is shown in Figure 1.

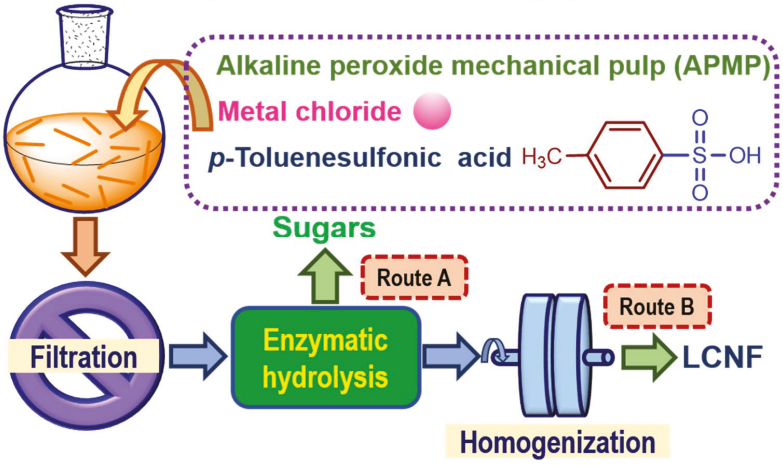

Figure 1. Routes for the valorization of alkaline peroxide mechanical pulp (APMP) using metal chloride-assisted hydrotropic pretreatment. Route A, enzymatic saccharification; Route B, lignocellulosic nanofibrils production.

2.5. Characterization

The chemical compositions (including structural polysaccharides and lignin) of all samples were measured using the National Renewable Energy Laboratory (NREL) standard method [29]. Monosaccharides and inhibitors in this study were analyzed by the HPLC system (Agilent 1260 series, Agilent Technologies, Santa Clara, CA, USA). Recovery yields of carbohydrates (glucan and xylan), degree of delignification, and enzymatic efficiency were calculated according to the following equations:

$$\text{Glucan recovery yield } (\%) = \frac{\text{glucan in pretreated APMP (g)}}{\text{glucan in raw APMP (g)}} \times 100\% \quad (1)$$

$$\text{Xylan recovery yield } (\%) = \frac{\text{xylan in pretreated APMP (g)}}{\text{xylan in raw APMP (g)}} \times 100\% \quad (2)$$

$$\text{Delignification } (\%) = 1 - \frac{\text{lignin in pretreated APMP (g)}}{\text{lingin in raw APMP (g)}} \times 100\% \quad (3)$$

$$\text{Enzymatic efficiency } (\%) = \frac{\text{glucose in enzymatic hydrolyzate (g)}}{\text{inital glucose in substrate (g)}} \times 100\% \quad (4)$$

The morphologies of the acid hydrolyzed samples were observed using scanning electron microscopy (SEM) and laser scanning confocal fluorescence microscopy (LSCM). For SEM analyses, samples were sputter-coated with gold to provide adequate conductivity. Images were observed and recorded using a SEM system (Quanta 200, FEI, Hillsboro, OR, USA). For LSCM analyses, samples were diluted in DI water and deposited onto clean glass substrates. A Zeiss LSM 710 laser scanning confocal microscopy was used with excitation lased at Ar 488 nm over an emission range of 490 to 560 nm and 40× C-Apochromat objective (1.1 W NA) zoom to acquire multichannel fluorescence image.

LCNF morphology was observed using atomic force microscopy (AFM, Dimension Edge, Bruker, Germany). Samples were diluted to a solids consistency of 0.01 wt %, deposited onto clean mica substrates and air-dried overnight at room temperature. AFM topographical images were obtained in tapping mode at 300 kHz using a standard silicon cantilever and a tip with a radius of curvature of 8 nm. Fibril height distribution was measured using Gwyddion software (Department of Nanometrology, Czech Metrology Institute, Jihlava, Crezh Republic, 64-bit). The surface charges of LCNF samples were measured using a zeta potential analyzer (Malvern Instruments Ltd., Zetasizer NanoZS, Malvern, UK). Five measurements were determined and the results were presented as average values. The XRD patterns were measured using an Ultima IV diffractometer at a voltage of 40 kV and a current of 30 mA (Rigaku Corp., Tokyo, Japan). Scattering radiation was detected in a 2θ range from 10° to 40° in steps of 0.02°. The crystallinity index (CrI) of LCNF samples was calculated in accordance with the Segal method (without baseline substrate) as described previously [30]. The FTIR spectra of LCNF samples were obtained by a Fourier-transform infrared spectrometer (Nicolet 380, Waltham, MA, USA). Samples were ground into powders and blended with KBr powder, then pressed into a disk at 30 MPa. The spectrum for each sample was recorded in the region of 4000–500 cm^{-1}. The thermal properties of the LCNF samples were analyzed using a thermogravimetric analyzer (Q5000IR, TA instruments, New Castle, DE, USA). Samples of approximately 5 mg were heated from 50 to 600 °C under a 20 mL/min high-purity nitrogen stream using a heating rate of 10 °C/min.

3. Results

3.1. Component Change of the Fibers after Pretreatments

Component change of lignocellulosic biomass is helpful to assess the influence of pretreatment. The chemical compositions and yields of the APMP from fractionation runs under different metal chloride-assisted hydrotropic pretreatments are summarized in Table 1, along with the glucose and xylose concentrations in the spent liquors. The results indicated that the solid yields obviously decreased from 80.18% to 65.94%, 63.32%, and 64.47%, respectively, after the addition of metal chlorides ($FeCl_3 \cdot 6H_2O$, $AlCl_3 \cdot 6H_2O$, and $CuCl_2 \cdot 2H_2O$) during hydrotropic pretreatment. Metal chlorides could have formed hydrated complexes in aqueous solution and coordinated with the glycosidic oxygen of cellulose. These metal cations acting as Lewis acids could have helped to break down the glycosidic linkages and then facilitate the cellulose hydrolysis process, resulting in the mass loss of biomass [31]. As shown in Figure 2, the low recovery yield of xylan and high lignin removal rate (expressed as delignification) also confirmed the low solid yield of pretreated APMP. However, glucan losses were only at approximately 10%, suggested that the *p*-TsOH had the great selectivity of solubilizing lignin. It is worth noting that $FeCl_3$-assisted acid hydrolysis showed strong catalytic activity to facilitate the hydrolysis process, however it also had the lowest degree of delignification compared with the other metal chlorides. This result may be due to the competition between ionic bonds and intermolecular forces during the delignification. To be specific, it has been known that the *p*-TsOH can readily provide protons in an aqueous solution to break glycosidic, ether, and ester bonds in carbohydrates and

lignin–carbohydrate complexes [18]. The lipophilic nonpolar part (toluene moiety) of the *p*-TsOH molecule can shield the separated lignin by π–π stacking or hydrophobic interaction to form micellar aggregates to prevent the aggregation of lignin, while the hydrophilic end (sulfonic acid moiety) is directed outward to the water for effective dissolution [32]. However, metal cations possess higher catalytic activity and ability to attract electron pairs, which can capture the hydrophilic end (sulfonic acid moiety) to form strong ionic bonds. The separated lignin undergoes intermolecular condensation, or recondensation in the absence of a hydrophobic solute, to be redeposited onto a solid substrate [18].

Table 1. Chemical composition of raw material and metal chloride-assisted hydrotropic pretreated materials along with byproduct concentration in pretreatment spent liquor.

Sample Abbreviation [1]	Solid					Spent Liquor	
	Glucan (%)	Xylan (%)	Acid Soluble Lignin (%)	Klason Lignin (%)	Solid Yield (%)	Glucose (g/L)	Xylose (g/L)
APMP	46.07	16.03	2.92	17.73	100	–	–
P	51.18	14.70	1.07	12.13	80.18	ND	1.1
P–$FeCl_3$	53.31	13.02	0.67	10.80	65.94	0.2	1.6
P–$AlCl_3$	58.59	13.22	0.83	9.17	63.32	0.1	1.6
P–$CuCl_2$	61.64	13.02	0.74	9.03	64.47	0.2	1.7

[1] APMP and P stand for alkaline peroxide mechanical pulp and *p*-TsOH hydrolysis, respectively.

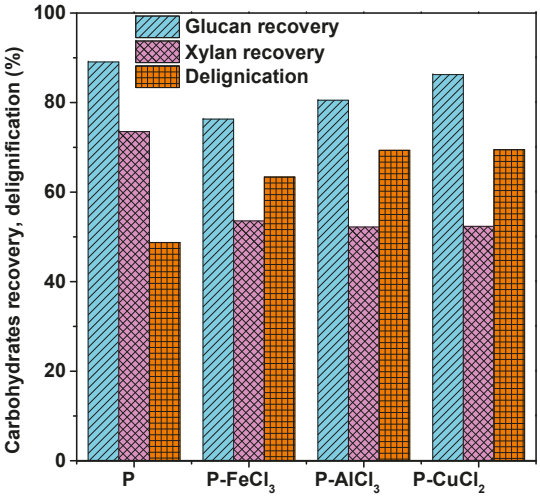

Figure 2. Carbohydrate (glucan and xylan) recovery and lignin removal rate of pretreated materials after different metal chloride-assisted hydrotropic pretreatments.

3.2. Effect of Treatments on Fiber Morphology and Microstructure

The morphological changes of APMP during the different metal chloride-assisted hydrotropic pretreatments were observed by scanning electron and confocal microscopy techniques (Figure 3). The left row of each figure shows the SEM images of original and hydrolyzed APMP fibers. After the *p*-TsOH treatment, the obtained solid residues were substantially shortened compared to the original APMP fibers. The fiber shortening was more pronounced for metal chloride-assisted hydrotropic pretreatment than pristine *p*-TsOH, due to the presence of metal cations that facilitated carbohydrate degradation. Since no severe pretreatment (temperature = 65 °C) was applied, it was likely that partial lignin distributed itself on the fiber surface. To track the residual lignin distribution, confocal imaging was performed on feedstock and hydrolyzed samples. The green autofluorescence in the right row of

each figure is from lignin [33]. The APMP fiber with highest lignin content had homogenous lignin distribution on the fiber surface. After hydrotropic pretreatments with or without metal chloride, partial lignin was removed from the fiber surface due to the presence of *p*-TsOH. Among three different metal cations, the APMP–P–$CuCl_2$ fiber exhibited the least green autofluorescence, i.e., the minimal residual lignin content, which was consistent with the data from chemical composition analysis (Table 1). The lignin content and redistribution may affect the downstream production (enzymatic hydrolysis and LCNF production), as discussed in the following text.

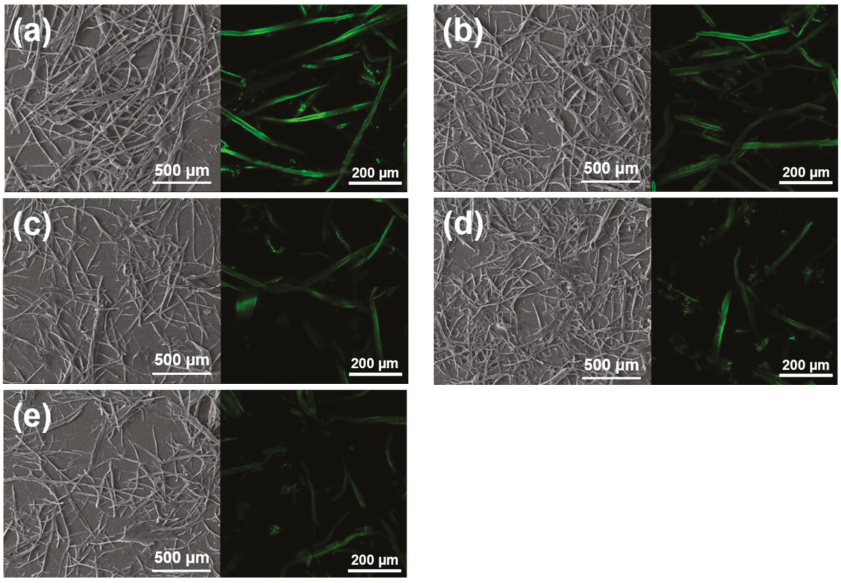

Figure 3. Scanning electron image and confocal microscopy image of alkaline peroxide mechanical pulp with different metal chloride-assisted hydrotropic pretreatments. (**a**) APMP; (**b**) APMP–P; (**c**) APMP–P–$FeCl_3$; (**d**) APMP–P–$AlCl_3$; (**e**) APMP–P–$CuCl_2$.

3.3. Enzymatic Digestibility of Acid-Hydrolyzed Fraction

To evaluate the effects of different metal cations on APMP sugar generation, all pretreated residues were used as the substrates for enzymatic hydrolysis. The enzymatic efficiency was only 16.1% for the raw material. After various metal chloride-assisted (Fe^{3+}, Al^{3+}, and Cu^{2+}) hydrotropic pretreatments, the enzymatic efficiency was found to be greater than that of the APMP without pretreatment (Figure 4). For example, the 72-h enzymatic hydrolysis efficiency of P–APMP and P–$CuCl_2$–APMP were 29.3% and 53.2%, respectively, which were 1.8 and 3.3-fold higher than that of the raw material without pretreatment. It has been reported that the "blocking effect" of xylan was one of the major obstacles which limited the enhancement of enzymatic efficiency [34]. The xylan recovery of P–APMP was higher than those with metal chloride-assisted hydrotropic pretreatments, therefore the enzymatic efficiency was relatively low. However, it should be noted that although the xylan recovery of the three metal chloride-assisted treated APMP fibers were almost the same (approximately 53%), their enzymatic efficiencies were significantly different. This phenomenon might be due to the presence of residual lignin, which had a negative effect on the yields of enzymatic hydrolysis. It has been reported that iron–lignin complexation exerted inhibitory effects on the enzymatic hydrolysis of autohydrolyzed biomass [35]. Therefore, although different *p*-TsOH pretreatments removed partial lignin, the residual lignin absorbed on the fiber surface still led to the formation of a lignin–enzyme complex, which was considered to be ineffective for the enzymatic hydrolysis process. In view of all enzymatic hydrolysis

data, a conclusion can be made that the removal of plenty of hemicelluloses and lignin during the pretreatment process was highly related to the substrate enzymatic efficiency.

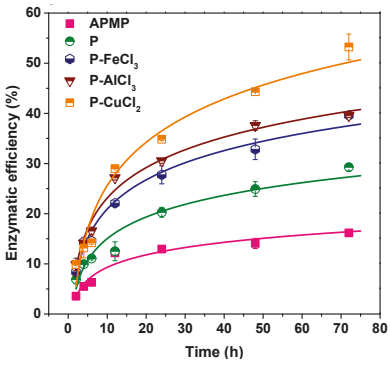

Figure 4. Time-dependent enzymatic efficiency of fractionated APMP fibers from various metal chloride-assisted (Fe^{3+}, Al^{3+}, and Cu^{2+}) hydrotropic pretreatment under constant cellulase (Cellic® CTec2) loading of 20 FPU/g glucan.

3.4. Properties of LCNF

Subsequent mechanical fibrillation of various partially enzyme-hydrolyzed samples using high pressure homogenizer produced LCNF with varied morphologies, as shown by AFM in Figure 5. Some small, globular-shaped lignin particles were visible, especially at P–LCNF without metal chloride-assisted fractionation [36]. Introducing metal ions during hydrotropic pretreatments resulted in less entangled LCNF with thinner diameters as observed from the AFM images and AFM measured height distributions (Figure 5e). Furthermore, the distribution of P–metal chloride–LCNF became narrower or more uniform as different metal chlorides were added. The number averaged fibril heights were 25.2, 15.1, 11.5, and 9.0 nm, respectively, for P–LCNF and the three different P–metal chloride ($FeCl_3$, $AlCl_3$, and $CuCl_2$)–LCNFs (Table 2). This was due to the fact that higher residual lignin content in P–APMP was considered to be the barrier to impede mechanical fibrillation, consistent with the results found in the literature using medium-density fiberboard and agricultural waste to produce LCNF [20,21].

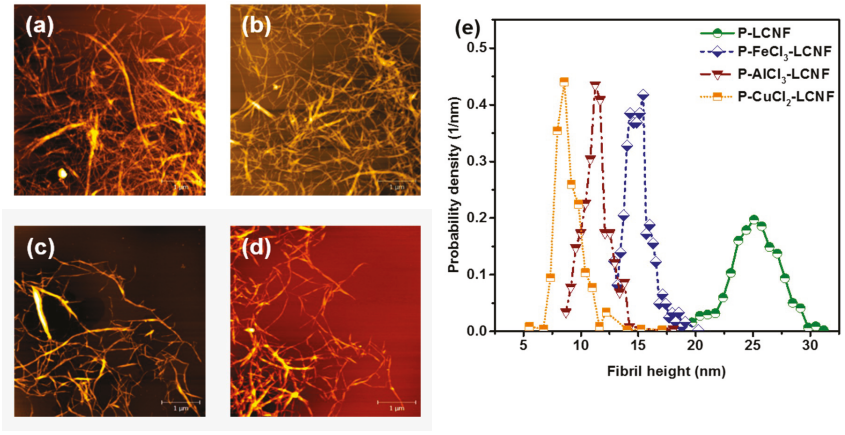

Figure 5. Effect of different metal chloride-assisted hydrotropic pretreatment on the morphologies of the resulting lignocellulosic nanofibrils (LCNF) measured by atomic force microscopy (AFM). All scale bar = 1 μm. (**a**) P–LCNF, mean height = 25.2 nm; (**b**) P–$FeCl_3$–LCNF, mean height = 15.1 nm; (**c**) P–$AlCl_3$–LCNF, mean height = 11.5 nm; (**d**) P–$CuCl_2$–LCNF, mean height = 9.0 nm; (**e**) AFM measured LCNF height probability density distributions.

The XRD patterns of both raw and resulting LCNFs are presented in Figure 6a. XRD analysis was conducted to investigate the crystalline features of the fibers and the relationship between structures and properties. Two main characteristic peaks at about 2θ = 16.4° and 22.6° corresponded to the (100) and (200) reflection planes, indicating that only cellulose I structure was present in all samples [37]. These results suggest various treatments did not destroy or alter the inherent crystal structure of cellulose. The crystallinity index (CrI) of all LCNF samples was higher than the APMP (Table 2), despite the fact that enzymatic hydrolysis and mechanical fibrillation could break up cellulose crystals. This is because hydrotropic pretreatment dissolved substantial amounts of amorphous lignin and hemicellulose (mainly xylan), as also revealed by the compositional analysis of the substrates (Table 1).

Table 2. List of morphological, crystallinity index, surface charge, and thermal properties of the resulting lignocellulosic nanofibrils.

Sample Abbreviation	Average Height (nm)	CrI (%)	Zeta Potential (mV)	T_{maxI} (°C)	T_{maxII} (°C)
APMP	–	53.8	–		368.7
P–LCNF	25.2	44.3	–31.4 ± 1.7	197.0	282.0
P–$FeCl_3$–LCNF	15.1	44.7	–30.7 ± 1.7	197.2	282.2
P–$AlCl_3$–LCNF	11.5	47.8	–33.7 ± 2.7	195.5	280.5
P–$CuCl_2$–LCNF	9.0	51.9	–35.4 ± 1.8	197.6	282.6

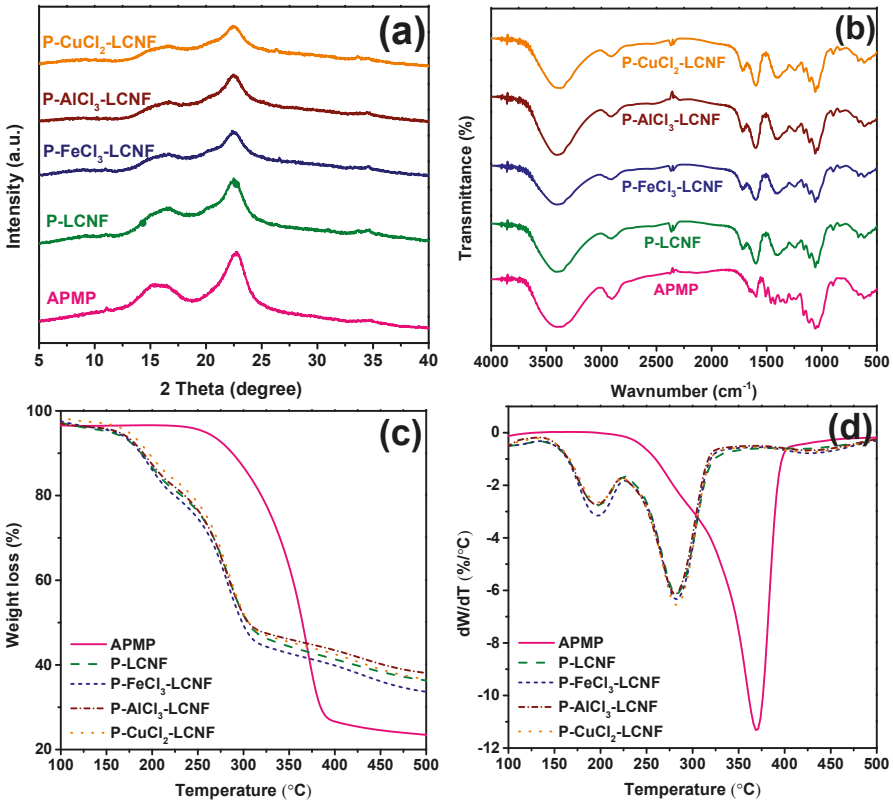

Figure 6. Comparisons of raw material and lignocellulosic nanofibrils produced from different metal chloride-assisted hydrotropic pretreatment. (**a**) XRD diffractogram; (**b**) FTIR spectra; (**c**) TGA weight loss; (**d**) TGA temperature derivative weight loss.

The zeta-potentials of all LCNF samples were not much different (Table 2), suggesting that metal ions (Fe^{3+}, Al^{3+}, and Cu^{2+}) only acted as catalysts to help to break down the glycosidic linkages and did not induce the formation of new charged functional groups in undissolved carbohydrates. This can be verified from the comparison of the FTIR spectra between the APMP and LCNF samples (Figure 6b). Only small variations in the lignin region were due to the removal of partial lignin during the hydrotropic pretreatment.

The thermal behaviors of raw APMP fiber and resulting LCNF samples are presented in Figure 6c,d. The maximum degradation temperature (T_{max}) was determined from the derivative thermogravimetric (DTG) peak at which the maximum decomposition rate was obtained. Lignin presents a wide range of decomposition temperatures, is known to be thermally more stable than cellulose and hemicellulose, and the increased surface area from enzymatic hydrolysis and nanofibrillation may have facilitated increased thermal degradation. Therefore, the APMP fiber with a lignin content of 20.65% showed excellent thermal stability with a T_{max} of 368.7 °C, higher than those LCNF samples with a lower lignin content. It should be noted that the degradation of LCNF showed two peaks evident from DTG curves (Figure 6d). The first peak can probably be attributed to the removal of enzyme that remained during the enzymatic hydrolysis. The second one in the dW/dT plot was associated with the degradation of residual lignin [38]. Although P–$CuCl_2$–LCNF had the lowest lignin content among three different P–metal chloride–LCNFs, it exhibited similar thermal

stability. The reason, perhaps, is due to the higher crystalline structure (CrI value in Table 2) for the P–$CuCl_2$–LCNF sample, which required higher degradation temperature.

4. Conclusions

A rapid and efficient approach was performed to remove lignin at a low temperature, in which three metal chlorides ($FeCl_3$, $AlCl_3$, and $CuCl_2$) were introduced into the hydrotropic pretreatment. Alkaline peroxide mechanical pulp can be fractionated into cellulose-rich solid fraction to produce sugar and LCNF. The metal ions exhibited excellent catalytic activity and obviously enhanced the degree of delignification, especially when using $CuCl_2$. The confocal images highlighted the lignin redistribution on the fiber walls, which affected the downstream production. The pretreated APMP fiber with the lower lignin content was enzymatically hydrolyzed to produce sugars with higher enzymatic efficiency and mechanically fibrillated to produce LCNF with lower height. This work demonstrated that the metal chloride-assisted hydrotropic process has potential applications for low-cost fractionation of lignocellulosic biomass.

Author Contributions: H.B., G.F., and H.D. conceived and designed the experiments; H.B., X.W., and J.L. performed the experiments; H.B. and Y.Q. analyzed the data; H.B. wrote the paper; G.F. and H.D. reviewed and edited the manuscript.

Funding: This work was funded by National Key R&D Program of China (Grant number: 2017YFD0601005) and the Doctorate Fellowship Foundation of Nanjing Forestry University.

Acknowledgments: The authors thank Buhong Gao and Jing Yang of Advanced Analysis & Testing Center, Nanjing Forestry University for providing valuable guidance on the use of SEM, AFM and LSCM.

Conflicts of Interest: The authors declare no conflict of interest.

References

1. Huang, C.; Lai, C.; Wu, X.; Huang, Y.; He, J.; Huang, C.; Li, X.; Yong, Q. An integrated process to produce bio-ethanol and xylooligosaccharides rich in xylobiose and xylotriose from high ash content waste wheat straw. *Bioresour. Technol.* **2017**, *241*, 228–235. [CrossRef] [PubMed]
2. Huang, C.; Ma, J.; Liang, C.; Li, X.; Yong, Q. Influence of sulfur dioxide-ethanol-water pretreatment on the physicochemical properties and enzymatic digestibility of bamboo residues. *Bioresour. Technol.* **2018**, *263*, 17–24. [CrossRef] [PubMed]
3. Kamireddy, S.R.; Li, J.; Tucker, M.; Degenstein, J.; Ji, Y. Effects and mechanism of metal chloride salts on pretreatment and enzymatic digestibility of corn stover. *Ind. Eng. Chem. Res.* **2013**, *52*, 1775–1782. [CrossRef]
4. Long, L.-Y.; Weng, Y.-X.; Wang, Y.-Z. Cellulose aerogels: Synthesis, applications, and prospects. *Polymers* **2018**, *10*, 623. [CrossRef]
5. Chen, W.; Yu, H.; Lee, S.Y.; Wei, T.; Li, J.; Fan, Z. Nanocellulose: A promising nanomaterial for advanced electrochemical energy storage. *Chem. Soc. Rev.* **2018**, *47*, 2837–2872. [CrossRef] [PubMed]
6. Lin, W.; Hu, X.; You, X.; Sun, Y.; Wen, Y.; Yang, W.; Zhang, X.; Li, Y.; Chen, H. Hydrophobic modification of nanocellulose via a two-step silanation method. *Polymers* **2018**, *10*, 1035. [CrossRef]
7. Ji, H.; Song, Y.; Zhang, X.; Tan, T. Using a combined hydrolysis factor to balance enzymatic saccharification and the structural characteristics of lignin during pretreatment of Hybrid poplar with a fully recyclable solid acid. *Bioresour. Technol.* **2017**, *238*, 575–581. [CrossRef] [PubMed]
8. Zhou, X.; Zhou, X.; Liu, G.; Xu, Y.; Balan, V. Integrated production of gluconic acid and xylonic acid using dilute acid pretreated corn stover by two-stage fermentation. *Biochem. Eng. J.* **2018**, *137*, 18–22. [CrossRef]
9. Wu, H.; Dai, X.; Zhou, S.L.; Gan, Y.Y.; Xiong, Z.Y.; Qin, Y.H.; Ma, J.; Yang, L.; Wu, Z.K.; Wang, T.L.; et al. Ultrasound-assisted alkaline pretreatment for enhancing the enzymatic hydrolysis of rice straw by using the heat energy dissipated from ultrasonication. *Bioresour. Technol.* **2017**, *241*, 70–74. [CrossRef]
10. Mohtar, S.S.; Tengku Malim Busu, T.N.Z.; Md Noor, A.M.; Shaari, N.; Mat, H. An ionic liquid treatment and fractionation of cellulose, hemicellulose and lignin from oil palm empty fruit bunch. *Carbohydr. Polym.* **2017**, *166*, 291–299. [CrossRef]
11. Romani, A.; Garrote, G.; Lopez, F.; Parajo, J.C. Eucalyptus globulus wood fractionation by autohydrolysis and organosolv delignification. *Bioresour. Technol.* **2011**, *102*, 5896–5904. [CrossRef]

12. Bian, H.; Chen, L.; Dai, H.; Zhu, J.Y. Integrated production of lignin containing cellulose nanocrystals (LCNC) and nanofibrils (LCNF) using an easily recyclable di-carboxylic acid. *Carbohydr. Polym.* **2017**, *167*, 167–176. [CrossRef]
13. Ferrer, A.; Quintana, E.; Filpponen, I.; Solala, I.; Vidal, T.; Rodríguez, A.; Laine, J.; Rojas, O.J. Effect of residual lignin and heteropolysaccharides in nanofibrillar cellulose and nanopaper from wood fibers. *Cellulose* **2012**, *19*, 2179–2193. [CrossRef]
14. Mou, H.; Li, B.; Fardim, P. Pretreatment of corn stover with the modified hydrotropic method to enhance enzymatic hydrolysis. *Energy Fuels* **2014**, *28*, 4288–4293. [CrossRef]
15. Luo, X.; Liu, J.; Wang, H.; Huang, L.; Chen, L. Comparison of hot-water extraction and steam treatment for production of high purity-grade dissolving pulp from green bamboo. *Cellulose* **2014**, *21*, 1445–1457. [CrossRef]
16. Huang, C.; Chu, Q.; Xie, Y.; Li, X.; Jin, Y.; Min, D.; Yong, Q. Effect of kraft pulping pretreatment on the chemical composition, enzymatic digestibility, and sugar release of moso bamboo residues. *Bioresources* **2014**, *10*, 240–255. [CrossRef]
17. Gabov, K.; Gosselink, R.J.; Smeds, A.I.; Fardim, P. Characterization of lignin extracted from birch wood by a modified hydrotropic process. *J. Agric. Food Chem.* **2014**, *62*, 10759–10767. [CrossRef]
18. Chen, L.; Dou, J.; Ma, Q.; Li, N.; Wu, R.; Bian, H.; Yelle, D.J.; Vuorinen, T.; Fu, S.; Pan, X.; et al. Rapid and near-complete dissolution of wood lignin at $\leq$80 °C by a recyclable acid hydrotrope. *Sci. Adv.* **2017**, *3*, e1701735. [CrossRef]
19. Dou, J.; Bian, H.; Yelle, D.J.; Ago, M.; Vajanto, K.; Vuorinen, T.; Zhu, J. Lignin containing cellulose nanofibril production from willow bark at 80 °C using a highly recyclable acid hydrotrope. *Ind. Crops Prod.* **2019**, *129*, 15–23. [CrossRef]
20. Bian, H.; Gao, Y.; Yang, Y.; Fang, G.; Dai, H. Improving cellulose nanofibrillation of waste wheat straw using the combined methods of prewashing, p-toluenesulfonic acid hydrolysis, disk grinding, and endoglucanase post-treatment. *Bioresour. Technol.* **2018**, *256*, 321–327. [CrossRef]
21. Bian, H.; Chen, L.; Gleisner, R.; Dai, H.; Zhu, J.Y. Producing wood-based nanomaterials by rapid fractionation of wood at 80 °C using a recyclable acid hydrotrope. *Green Chem.* **2017**, *19*, 3370–3379. [CrossRef]
22. Ji, H.; Chen, L.; Zhu, J.Y.; Gleisner, R.; Zhang, X. Reaction kinetics based optimization of furfural production from corncob using a fully recyclable solid acid. *Ind. Eng. Chem. Res.* **2016**, *55*, 11253–11259. [CrossRef]
23. Cheng, M.; Qin, Z.; Chen, Y.; Hu, S.; Ren, Z.; Zhu, M. Efficient extraction of cellulose nanocrystals through hydrochloric acid hydrolysis catalyzed by inorganic chlorides under hydrothermal conditions. *ACS Sustain. Chem. Eng.* **2017**, *5*, 4656–4664. [CrossRef]
24. Chen, L.; Chen, R.; Fu, S. $FeCl_3$ pretreatment of three lignocellulosic biomass for ethanol production. *ACS Sustain. Chem. Eng.* **2015**, *3*, 1794–1800. [CrossRef]
25. Du, H.; Liu, C.; Mu, X.; Gong, W.; Lv, D.; Hong, Y.; Si, C.; Li, B. Preparation and characterization of thermally stable cellulose nanocrystals via a sustainable approach of $FeCl_3$-catalyzed formic acid hydrolysis. *Cellulose* **2016**, *23*, 2389–2407. [CrossRef]
26. Wu, X.; Huang, C.; Tang, W.; Huang, C.; Lai, C.; Yong, Q. Use of metal chlorides during waste wheat straw autohydrolysis to overcome the self-buffering effect. *Bioresour. Technol.* **2018**, *268*, 259–265. [CrossRef]
27. Li, J.; Qiang, D.; Zhang, M.; Xiu, H.; Zhang, X. Joint action of ultrasonic and Fe^{3+} to improve selectivity of acid hydrolysis for microcrystalline cellulose. *Carbohydr. Polym.* **2015**, *129*, 44–49. [CrossRef]
28. Mao, L.; Zhang, L.; Gao, N.; Li, A. Seawater-based furfural production via corncob hydrolysis catalyzed by $FeCl_3$ in acetic acid steam. *Green Chem.* **2013**, *15*, 727–737. [CrossRef]
29. Sluiter, A.; Hames, B.; Ruiz, R.; Scarlata, C.; Sluiter, J.; Templeton, D. *Determination of Structural Carbohydrates and Lignin in Biomass*; NREL Chemical Analysis and Testing Laboratory Analytical Procedures; NREL/TP-510-42618; NREL: Golden, CO, USA, 2008.
30. Segal, L.; Creely, J.J.; Martin, A.E.; Conrad, C.M. An empirical method for estimating the degree of crystallinity of native cellulose using the X-ray diffractometer. *Text. Res. J.* **1959**, *29*, 786–794. [CrossRef]
31. Vom Stein, T.; Grande, P.; Sibilla, F.; Commandeur, U.; Fischer, R.; Leitner, W.; de María, P.D. Salt-assisted organic-acid-catalyzed depolymerization of cellulose. *Green Chem.* **2010**, *12*, 1844–1849. [CrossRef]

32. Chen, L.; Zhou, X.; Shi, Y.; Gao, B.; Wu, J.; Kirk, T.B.; Xu, J.; Xue, W. Green synthesis of lignin nanoparticle in aqueous hydrotropic solution toward broadening the window for its processing and application. *Chem. Eng. J.* **2018**, *346*, 217–225. [CrossRef]
33. Tripathi, A.; Ferrer, A.; Khan, S.A.; Rojas, O.J. Morphological and thermochemical changes upon autohydrolysis and microemulsion treatments of coir and empty fruit bunch residual biomass to isolate lignin-rich micro- and nanofibrillar cellulose. *ACS Sustain. Chem. Eng.* **2017**, *5*, 2483–2492. [CrossRef]
34. Hu, J.; Arantes, V.; Saddler, J.N. The enhancement of enzymatic hydrolysis of lignocellulosic substrates by the addition of accessory enzymes such as xylanase: Is it an additive or synergistic effect? *Biotechnol. Biofuels* **2011**, *4*, 36. [CrossRef] [PubMed]
35. Liu, H.; Zhu, J.Y.; Fu, S.Y. Effects of lignin-metal complexation on enzymatic hydrolysis of cellulose. *J. Agric. Food Chem.* **2010**, *58*, 7233–7238. [CrossRef] [PubMed]
36. Rojo, E.; Peresin, M.S.; Sampson, W.W.; Hoeger, I.C.; Vartiainen, J.; Laine, J.; Rojas, O.J. Comprehensive elucidation of the effect of residual lignin on the physical, barrier, mechanical and surface properties of nanocellulose films. *Green Chem.* **2015**, *17*, 1853–1866. [CrossRef]
37. Jia, C.; Chen, L.; Shao, Z.; Agarwal, U.P.; Hu, L.; Zhu, J.Y. Using a fully recyclable dicarboxylic acid for producing dispersible and thermally stable cellulose nanomaterials from different cellulosic sources. *Cellulose* **2017**, *24*, 2483–2498. [CrossRef]
38. Nair, S.S.; Yan, N. Effect of high residual lignin on the thermal stability of nanofibrils and its enhanced mechanical performance in aqueous environments. *Cellulose* **2015**, *22*, 3137–3150. [CrossRef]

polymers

MDPI

Review

Nanocelluloses: Natural-Based Materials for Fiber-Reinforced Cement Composites. A Critical Review

Ana Balea, Elena Fuente, Angeles Blanco and Carlos Negro *

Department of Chemical Engineering and Materials, University Complutense of Madrid, Av. Complutense s/n, 28040 Madrid, Spain; anabalea@ucm.es (A.B.); helenafg@ucm.es (E.F.); ablanco@ucm.es (A.B.)
* Correspondence: cnegro@ucm.es; Tel.: +34-91-394-4242

Received: 1 February 2019; Accepted: 15 March 2019; Published: 19 March 2019

Abstract: Nanocelluloses (NCs) are bio-based nano-structurated products that open up new solutions for natural material sciences. Although a high number of papers have described their production, properties, and potential applications in multiple industrial sectors, no review to date has focused on their possible use in cementitious composites, which is the aim of this review. It describes how they could be applied in the manufacturing process as a raw material or an additive. NCs improve mechanical properties (internal bonding strength, modulus of elasticity (MOE), and modulus of rupture (MOR)), alter the rheology of the cement paste, and affect the physical properties of cements/cementitious composites. Additionally, the interactions between NCs and the other components of the fiber cement matrix are analyzed. The final result depends on many factors, such as the NC type, the dosage addition mode, the dispersion, the matrix type, and the curing process. However, all of these factors have not been studied in full so far. This review has also identified a number of unexplored areas of great potential for future research in relation to NC applications for fiber-reinforced cement composites, which will include their use as a surface treatment agent, an anionic flocculant, or an additive for wastewater treatment. Although NCs remain expensive, the market perspective is very promising.

Keywords: nanocelluloses; cellulose nanofibers; cellulose nanocrystals; bacterial cellulose; cement; fiber-cement; Hatscheck process

1. Introduction

The improvement of cement properties through the addition of fibers of different natures (steel, glass, synthetic, and natural) and sizes (macro and microfiber) has been in practice for decades [1–5]. Most researchers have reported that cellulosic fibers are not only non-toxic, renewable, cost-effective, and abundant compared to other fibers (e.g., asbestos, polyvinyl alcohol (PVOH), and polypropylene (PP)), but also provide adequate bonding capacity to cement-based matrices for substantial improvements of toughness, ductility, flexural capacity, and impact resistance [6–8]. The drawbacks are long-term durability [9–11], mineralization of the fibers [6], and poor dispersion [12]. Therefore, a better scenario would be that in which nano-structurated cellulose materials, also called nanocelluloses (NCs), are used to overcome these problems. Cellulose is the most abundant bio-based polymer on earth with endless applications for engineered materials [13]. NCs have gained substantial consideration due to their exceptional properties that combine both cellulose properties and the unique features of nanomaterials [14]. NCs present several advantages versus cellulose, which include a high surface area, excellent stiffness, unique barrier and optical properties, a light weight, high strength, and the powerful interaction of these products with surrounding species, such as water and inorganic and polymeric compounds [15–22]. Moreover, their inherent cellulose properties, such as biodegradability,

renewability, and sustainability, have attracted great interest in many scientific and technical areas as potential sustainable natural-based materials with hundreds of possibilities in multiple industrial sectors [15].

In general terms, NCs can be produced in two different ways: the first is the top-down process, which includes cellulose nanofibers (CNFs) and cellulose nanocrystals (CNCs) production; the second is the bottom-up process, which considers the synthetization of bacterial cellulose (BC). The top-down process to reduce mechanically the size of the fibers down to the nano-scale [23–26] or to hydrolytically extract and isolate CNCs [27–30] has been widely described in the past. On the other hand, BC is produced by the fermentation of low-molecular-weight sugar using cellulose-producing bacteria, such as *Komagataeibacter xylinus* species [31].

This diversity of treatments, together with the huge variety of cellulose sources used as a raw material [24,32,33] (e.g., hardwood, softwood, lignocellulosic wastes, cellulose from a biorefinery, seed fibers, bast fibers, grasses, marine animals, such as a tunicate, algae, fungi, and invertebrates) and taking into account the possibility of chemical modification of an NC during or after its production [19,34], lead to a vast array of NCs with different morphologies as well as different physical and chemical properties.

NCs have wide potential in both high- and low-volume industrial applications [35–38]. The industrial sectors that have the largest potential volume of NCs are paper, paperboard, packaging products, plastics, building and construction materials, textiles, automobile parts, and environmental treatments [22,39–46]. Low-volume applications include medical implants, tissue engineering, drug carriers, wound dressings, aerospace materials, cosmetics, hygiene products, pharmaceuticals, food additives/stabilizers, and paint additives [47–49]. In recent years, many research groups and industries have been extensively working on groundbreaking innovations to expand the market for NC products and to open up new potential applications in different areas, such as three-dimensional (3D) printing [50], energy devices [51], printed electronics [52], or energy smart materials [53].

Cementitious composites, such as fiber cement composites (FCCs), have a complex structure that ranges from macro to nanoscale. The incorporation of nanoparticles to increase the contact surface area and its reactivity enables the application of the concepts of high-performance and functionally graded materials. In this scenario, NCs make possible the production of more resistant cement composites or composites with special properties, replacing synthetic polymeric or inorganic fibers. The use of NCs can contribute to achieving the goal of minimizing the carbon footprint of an infrastructure's materials, driving interest in biodegradable, non-petroleum-based, and low-environmental-impact materials [29,54–60]. The need for further research is recognized in most research programs worldwide, such as in the E.U.'s Horizon Europe, and many organizations have pointed out the importance of meeting future societal needs by promoting the development of new and better products with a negligible environmental footprint [61].

Most of the NC applications as a reinforcement agent are related to paper or polymer matrices [39,45,59,62–67], although, during the last 10 years, studies have also focused on the use of NC to improve cementitious composites materials, such as fiber cement.

Nowadays, the significant number of published papers on this topic calls for a critical review. Only two book chapters provide a general overview of the use of NCs [68,69], summarizing the main improvements and findings from a few research papers. The highly scattered and controversial results of the published studies give this critical review great importance at this time and in this moment so as to explain the differences amongst the behaviors observed in the literature for the efficient future application of NCs in FCCs. Additionally, this review opens up unexplored uses of NCs in the cement industry, giving some ideas for future research.

Therefore, this paper reviews the different ways of using NCs in the Hatscheck process as raw materials or additives. It presents the strong and weak points regarding the conventional raw materials, additives, or procedures. A detailed summary is given on both the mechanism explaining the effects of NCs on the composites' properties (mechanical properties and rheology) and the variables affecting

the reinforcing efficiency of NCs in order to shed light on the controversial aspects related to what seem to be contradictory results. Finally, some new potential applications are reviewed, including their use as a surface treatment agent, an anionic flocculant, or an additive for wastewater treatment.

2. Nanocelluloses in the Cement and Fiber-Cement Industry

Two main drawbacks restrict the performance of cellulose fiber cement composites (C-FCCs): (1) the maximum weight content of cellulosic fibers that can be incorporated into the composites; and (2) the long-term durability of the composite [70].

In a Hatschek process, with a good dispersion of the fibers in the fiber cement slurry, the maximum fiber dosage is 10 wt.% due to the effect of fibers on workability, porosity, and density. Additionally, although there is an increase in the toughness using higher dosages, the strength and Young modulus are not further improved. A likely feasible alternative for increasing the reinforcement capacity of the fibers without increasing their percentage is to use cellulose at the nanoscale level.

In general, NCs exhibit enhanced flexural properties compared to cellulose fibers, but they show a brittle behavior since the nanofibrils' capacity for incipient macrocracks bridging is low as a result of their nano size. In addition, the high specific surface area of NCs leads to an excessive fiber–matrix bonding, which involves a better stress transfer from the matrix to the nanofibers, but, on the contrary, it could contribute to the embrittlement of the composite [71]. Therefore, a combination of NC and cellulose fibers is needed to match the good flexural properties provided by the nanofibers (Young modulus and flexural strength) with the high toughness rendered by the cellulose fibers [71]. Despite this, many of the studies do not combine fibers and NCs. Peter et al. [72] combined micro and nanocelluloses and observed a synergic effect.

Table 1 summarizes the published data on the use of different types of NC to reinforce cement and C-FCCs. It is divided into three parts as a function of the kind of NC used: CNF, nano/micro-crystalline cellulose, and BC. A total of 54% of the publications used CNF, and only three of the papers consider the use of BC in cementitious composites. A total of 32% of the papers studied the effects of CNC or microcrystalline cellulose (MCC) on cement and C-FCCs. The use of CNF to improve the mechanical properties of cement mortar has been studied more than the use of CNF on C-FCCs, and there is nothing on the use of CNC on C-FCCs. However, BC has been preferentially used to improve C-FCCs rather than cement mortar. Table 1 also includes an analysis of the improvements in mechanical properties and other relevant effects on rheological or physical properties. When several doses were used, improvements at the optimal dose or, if possible, the interval of improvements were given. It is observed that the results are very heterogeneous even when the same kind of NC is used. This indicates that there are different factors affecting the efficiency of NCs and this table can help to study them, which is one of the aims of this review.

NCs can be used in different parts of the Hatschek process: (a) as a raw material, combined with cellulose fibers as an alternative to refining; (b) as an additive in coating formulations for surface treatment of the fiberboard; and (c) as a flocculant, since NCs can interact with fibers and mineral particles in a similar way to an anionic flocculant in the wet-end of the machine.

It is important to consider that the high reactive surface of NCs allows for interactions with other components of C-FCCs, such as PVOH fibers, SiO_2, or alkaline ions, modifying the final properties of the product; however, this has yet to be studied.

Table 1. Effect of nanocelluloses (NCs) in cement and fiber-cement composites.

NC Type	Source NC	NC Dose (wt.%)	Cementitious Material	Effect on Mechanical Properties	Other Effects	Ref.
Cellulose nanofibers (CNFs)						
High intensity refining process in a Valley Beater Refining time: 6 h d = 25–250 nm	Sisal (*Agave sisalana*)	3.3	**Cement mortar** - Type I cement - Sand - Ratio (C:S:W) = 1:1:0.67	ΔMOE (%) = 70.83 * ΔMOR (%) = 35.92 * ΔFracture Energy (%) = −52.96 *		[71]
		4	**Cement mortar** - Type I cement - Silica Fume - Sand - Ratio (C:Si:S) = 0.9:0.1:1 - Ratio (W:C) = 0.6	ΔMOE (%) = 30.77 * ΔMOR (%) ≈ 5 * ΔFracture Energy (J) ≈ −83.33 *		[73]
		2	**Fiber cement** - Type I cement - Silica Fume - Cellulose fibers (2 wt.%) - Sand - Ratio (C:Si:S) = 0.9:0.1:1 - Ratio (W:C) = 0.7	ΔMOE (%) = 50 * ΔMOR (%) ≈ −5 * ΔFracture Energy (%) ≈ −46.67 *		[73]
		8	**Cement mortar** - Type I cement - Silica Fume - Sand - Ratio (C:Si:S) = 0.9:0.1:1 - Ratio (W:C) = 0.56	ΔMOE (%) = 55.55 * ΔMOR (%) = 37.07 * ΔFracture Energy (%) = −90.55 *		[70]
		2–6	**Fiber cement** - Type I cement - Silica Fume - Cellulose fibers (2–6 wt.%) - Sand - Ratio (C:Si:S) = 0.9:0.1:1 - Ratio (W:C) = 0.56–0.69	ΔMOE (%) = 27.78–113.89 * ΔMOR (%) = 3.45–23.27 * ΔFracture Energy (%) = −51.32–(−83.88) *		[70]
		3.4	**Cement mortar** - Type I cement - Silica fume - Sand coarse - Ratio (C:Si:S) = 0.7:0.3:1 - Ratio (W:C) = 0.84	ΔMOE (%) = 10.17 * ΔMOR (%) = 1.55 * ΔFracture Energy (%) = −81.90 *		[74]

Table 1. *Cont.*

NC Type	Source NC	NC Dose (wt.%)	Cementitious Material	Effect on Mechanical Properties	Other Effects	Ref.
		3.3	**Cement mortar** - Type I cement - Silica fume - Sand fine - Ratio (C:Si:S) = 0.7:0.3:1 - Ratio (W:C) = 0.89	ΔMOE (%) = 60.71 * ΔMOR (%) = 6.06 * ΔFracture Energy (%) = 6.45 *		[74]
Bleaching ($NaClO$) Deproteinization ($NaOH$) and removing of oil and pigments ($CHCl_3$) Demineralization (HCl) d = 37–55 nm	Waste algae (*Cladophora* sp.)	0.1–1.0	**Cement mortar** - Portland cement - Sand - Ratio (C:S:W) = 1:4:1	ΔMOE (%) = 3.62–169.68 (adding 0.1 and 1.00 wt.% CNF, respectively)		[75]
Commercial supplied by Sigma-Aldrich, CAS: 9004-34-6 d < 35 nm	Cotton	0.1–1.0	**Cement mortar** - Portland cement - Sand - Ratio (C:S:W) = 1:4:1	ΔMOE (%) = −37.10–(−36.20) (adding 0.1 and 1.00 wt.% CNF, respectively)		[75]
TEMPO oxidation and fibrillation L = 0.6–1.7 μm d = 20–100 nm COOH = 1850 μmol/g	Bleached hardwood pulp	0–0.4	**Cement mortar** - Type I cement - Ratio (W:C) = 0.5	ΔCompression strength (%) = 20 ΔFlexural strength (%) = 15 Both with the optimal dose of CNF (0.15 wt.%)	The porosity notably decreased with the increasing dose of CNF	[74]
TEMPO oxidation and fibrillation at 600 bar at 1.5% to obtain a gel (5–6 cycles) L = 1–2 μm d = 5–10 nm COOH = 500 μmol/g,	Bleached Eucalyptus Kraft	0–0.5	**Cement mortar** - Type I cement 32.5 N EN197-1:2000 - Ratio (W:C) = 0.26	ΔCompression strength (%) = 43	ΔHardening (%) = 66 ΔConductivity (%) = 36 ΔPorosity (%) = −36	[76]
- TEMPO oxidation and grinding at 1 wt.% - COOH = 1130 μmol/g,	Bleached Eucalyptus chemithermomechanical pulp	0–1.2	**Cement mortar** - Portland Type II cement C3A < 8% - Ratio (W:C) = 0.485		ΔYield stress (%) = 94 (0.2 wt.% CNF) ΔPlastic viscosity (%) = 25 (0.2 wt.% CNF) Reduced bleeding and leaching ΔCrack area (%) = 27 (0.8 wt.% of CNF)	[77]

Table 1. *Cont.*

NC Type	Source NC	NC Dose (wt.%)	Cementitious Material	Effect on Mechanical Properties	Other Effects	Ref.
- Cellulose filaments (CFs): Commercial supplied by Kruger Biomaterials Mechanical fibrillation L = 100–2000 µm d = 20–200 nm	Wood	0–0.2	**Cement mortar** - General used cement (GU) - Fly ash (FA) - Ratio (GU:FA:W) = 1:0.33:0.5	ΔCompression strength (%) = −20 ΔFlexural strength (%) = 38 (with 0.2 wt.% CF)	ΔSlump (%) = −61 (with 0.2 wt.% CF) ΔPlastic viscosity (%) = 41 ΔAutogeneous shrinkage (%) = −43	[78]
		0–0.2	**Self-consolidating concrete** - General used cement (GU) - Sand (S) - Coarse aggregate (CA) - Superplasticizer (SP) - Ratio (GU:S:CA:SP:W) = 1:0.33:0.5:2:2.15	ΔCompression strength = 16% ΔFlexural strength = 28% ΔEnergy absorption = 96% with 0.2 wt.% CF	ΔSlump (%) = −50 (with 0.2 wt.% CF) ΔPlastic viscosity (%) = 113 ΔYield stress (%) = 794	[78]
Disc grinding method Grinding cycles: 15 L = 1–2.5 µm d = 20–200 nm	Bleached softwood pulp	0–0.4	**Limestone based cement** - Ratio (W:C) = 0.5 - Superplasticizer (1.6 wt.% on cement)	ΔFlexural strength = 106% ΔEnergy absorption = 186% with 0.1 wt.% of CNF	ΔHardening (%) = 10	[79]
Super Masscolloider method Grinding cycles: 35 d (55%) = 40 nm, Mean d = 50 nm	Bleached Eucalyptus Kraft	0, 0.5, 1	**Extruded cement** Cement plus limestone	ΔMOE and ΔMOR insignificant changes Δabsorbed Energy (%) = −72 (with 1wt.% CNF)	ΔPorosity (%) = 95 (with 1 wt.% CNF) ΔWater absorption ability (%) = 80 (with 1 wt.% CNF)	[80]
Grinding method Grinding cycles: 10 L > 1 µm mean d = 16.2 nm	Unbleached bamboo organosolv	1	**Fiber cement** - Type I cement - Limestone filler - Unbleached bamboo organosolv pulp (9 wt.%) - Ratio (C:Li) = 3:1 - Ratio (W:C) = 0.57	ΔMOE (%) = 5.20 * ΔMOR (%) = 34.46 * ΔFracture Energy (%) = 6.86 * ΔFracture toughness (%) = 12.74 *	Significant effects were not observed on density and porosity	[81]
Chemical and mechanical pretreatment Homogenization	Pine Kraft	0.14, 0.27, 0.41	**Cement mortar** - Portland-limestone cement (CEM II/A-LL 42.5R) - Sand - Superplasticizer - Anti-washout admixture - Ratio (W:C) = 0.6 - Ratio (C:S:W) = 1:1.07:0.6	ΔMOR (%) = 4.93–18.64 ΔCompressive Strength (%) = 3.96–4.56	ΔMini-slump flow (%) = −14.54–(−24.73) ΔYield stress (%) = 100–142.10 ΔPlastic viscosity (%) = −40–200	[82]

Table 1. *Cont.*

NC Type	Source NC	NC Dose (wt.%)	Cementitious Material	Effect on Mechanical Properties	Other Effects	Ref.
Only chemical treatment L = 1.1. mm Mean d = 45 µm L/d = 24.4 Density = 30 kg/m^3	Recycled cartonboard	0.045	**Cement mortar** - CEM I CALCIA cement 52.5 N - Sand (0.125–4 mm) - Filler (F): calcium carbonate - Superplasticizer: modified polycarboxylate -Ratio (W:C) = 0.48 -Ratio (C:S:F) = 1:2.6:0.37	ΔMOR (%) = 4.35 ΔCompressive Strength (%) = 10	ΔWater porosity (%) = 12.5	[83]
		5.7	**Cement concrete** - CEM I CALCIA cement 52.5 N 2 - Sand (0.125–4 mm) plus Gravel (G) (4–16 mm) - Filler (F): calcium carbonate - Superplasticizer: modified polycarboxylate -Ratio (W:C) = 0.48 -Ratio (C:S+G:F) = 1:4.65:0.37	ΔCompressive Strength (%) = 25	ΔMercury intrusion porosimetry (%) = −7.25 ΔPermeability (%) = −25	[83]
Microcellulose Sigmacell 101 Nanocellulose in gel at 3%	unknown	1, 3, 5	**Reactive powder concrete** - Sand - Silica flour - Silica fume - Superplasticizer 1.6% on cement -Ratio (C:S:Sflour:Sfume:) = 1:0.98:0.28:0.39 -Ratio (W:C) = 0.22–0.35	ΔMOE and ΔMOR insignificant changes with 1% of micro or nanocellulose ΔFracture Energy (%) = 24 * with 2 wt.% of mixture micro-nanocellulose ΔFracture Energy (%) = 50 * with 3 wt.% of microcellulose		[72]
Cellulose micro and nanocrystals (MCCs and CNCs)						
- CNC Produced via sulfuric acid hydrolysis 0.814 wt.% surface sulfate content Freeze-dried powder	Eucalyptus	0–0.77	**Cement paste** - Type V cement - Ratio (W:C) = 0.35	ΔMOR (%) = 20 with 0.10 wt.% of CNC (max improvement)	ΔYield stress (%) = from −67.2 (with 0.02% of CNC) to 1137 (with 1.5 wt.% of CNC) ΔCumulative heat (%) = 16 with 0.77 wt.% of CNC (at an age of 200 h) ΔPorosity (%) = −16% ΔDegree of hydration (%) = 20 with 0.77 wt.% of CNC	[84]

Table 1. *Cont.*

NC Type	Source NC	NC Dose (wt.%)	Cementitious Material	Effect on Mechanical Properties	Other Effects	Ref.
CNC Produced via sulfuric acid hydrolysis 0.814 wt.% surface sulfate content Dispersed in water by sonication	Eucalyptus	0–0.77	**Cement paste** - Type V cement - Ratio (W:C) = 0.35	ΔMOR (%) = 23 with 0.10 wt.% of CNC, but 30 with 0.5 wt.% of CNC	ΔPorosity (%) = −16%	[85,86]
Commercial MCC, Sigma Aldrich	Cotton	0, 3	**Cement mortar** - Portland cement - Ratio (W:C) = 0.45	ΔCompressive strength (%) = −12 ΔFlexural strength (%) = −25	ΔCritical yield stress (%) = 155	[87]
MCC (Avicel® PH101) plus Carbon nanotubes (CNTs) L = 2–260 µm mean d = 49.1 µm (MCC) L = 10–30 µm d (inner) = 2–5 nm; d (outer) < 8 nm (CNTs)	Cotton linters	0.2 (+ 0.1 wt.% CNTs)	**Cement mortar** -Portland cement (CEM I 42.5R) -Sand (NP-EN 196-1) - 1.5 wt.% Plutonic F-127 surfactant to dispersed MCC plus CNTs in water - 0.75 wt.% defoamer (tri-butyl phosphate (TBP)) to suppress the foam formation -Ratio (W:C) = 0.5 -Ratio (C:S:W) = 1:3:0.5	ΔMOR (%) = 2.9 ΔMOE (%) = 24.1 ΔFracture Energy (%) = 16.1 ΔCompressive Strength (%) = 16.98	ΔDry bulk density (%) = 8.24 ΔPore diameter = −40.51 ΔPorosity = 32.38	[88]
		0.5 (+ 0.3 wt.% CNTs)	**Cement mortar** -Portland cement (CEM I 42.5R) -Sand (NP-EN 196-1) - 1.0 wt.% CTAB surfactant to dispersed MCC plus CNTs in water - 1.0 wt.% defoamer (TBP) to suppress the foam formation -Ratio (W:C) = 0.5 -Ratio (C:S:W) = 1:3:0.5	ΔMOR (%) = 12.3 ΔMOE (%) = 12.7 ΔFracture Energy (%) = 85.2 ΔCompressive Strength (%) = 16.26	ΔDry bulk density (%) = 4.49 ΔPore diameter = −36.08 ΔPorosity = 22.86	[88]

Table 1. *Cont.*

NC Type	Source NC	NC Dose (wt.%)	Cementitious Material	Effect on Mechanical Properties	Other Effects	Ref.
MCC Sulphuric acid solution L = 75–400 µm L > 150 µm, for about 40% of MCC; d = 10–30 µm Maximum weight loss temperature (°C) = 300	Cotton linters	2.5	**Cement mortar** - Portland cement - Sand - Ratio (W:C) = 0.45 - Ratio (C:S) = 1:3	ΔMOR (%) = 50 ΔCompressive Strength (%) = −21.45		[89]
		2.5	**Cement mortar** - Portland cement - Sand -Superplasticizer: polycarboxylate ether (1 wt.% of cement) - Ratio (W:C) = 0.4 - Ratio (C:S:W) = 1:2.5:0.4	ΔMOR (%) = 16 ΔCompressive Strength (%) = −9.47		[89]
Tetraethyl orthosilicate (TEOS) surface-modified MCC Sulphuric acid solution TEOS as silane agent L = 75–400 µm L > 150 µm, for about 40% of MCC; d = 10–30 µm Maximum weight loss temperature (°C) = 360	Cotton linters	2.5	**Cement mortar** - Portland cement - Sand - Ratio (W:C) = 0.45 - Ratio (C:S) = 1:3	ΔMOR (%) = 94 ΔCompressive Strength (%) = 45		[89]
			Cement mortar - Portland cement - Sand -Superplasticizer: polycarboxylate ether (1 wt.% of cement) -Ratio (W:C) = 0.4 -Ratio (C:S) = 1:3	ΔMOR (%) = 59 ΔCompressive Strength (%) = 57		[89]
Commercial MCC (Sigma Aldrich) Bulk density = 0.459 g/mL	-	3	**Cement mortar** - Portland Low Alkali CP40 cement - Sand -Ratio (W:C) = 0.45 -Ratio (C:S) = 1:2.7	ΔMOR (%) = −26.31 ΔCompressive Strength (%) = −13.46	ΔDensity (%) = −2.16 ΔDiameter (mini-slump test)(%) = −17.65 ΔYield stress (mini-slump test) (%) = 160 ΔGlobal heat transference coefficient (%) = −24 ΔTemperature adiabatic max (%) = −5.28	[90]

Table 1. *Cont.*

NC Type	Source NC	NC Dose (wt.%)	Cementitious Material	Effect on Mechanical Properties	Other Effects	Ref.
			Bacterial cellulose (BC)			
		0.02	**Cement mortar**	ΔMOR (%) = 20 ** ΔCompressive strength (%) = 8 **	Accelerated production of calcium silicate hydrate (CSH)	[91]
Zetasizer (75 nm) crystallinity (DXR) = 65% BC was used for coating bagasse fibers before mixing	*Gluconacetobacter xylinus* cultured in Hestrin–Schramm medium	0, 3	**Fiber cement** - Portland Type II - 5% $CaCl_2$ - Unbleached bagasse fibers (6 wt.%) -Polycarboxilated superplasticizer	ΔMOE (%) = 38 ** ΔMOR (%) = 68 ** ΔInternal Bonding strength (%) = 50 ** ΔFracture toughness (%) = 70 **	Decreased fiber mineralization Increased durability Decreased porosity Great increase in the surface basicity	[92,93]
Zetasizer (75 nm) crystallinity (DXR) = 65% Freeze-dried powder	*Gluconacetobacter xylinus* cultured in Hestrin–Schramm medium	0, 3	**Fiber cement** - Portland Type II - 5% $CaCl_2$ - Unbleached bagasse fibers (6 wt.%) -Polycarboxilated superplasticizer	ΔMOE (%) = 11 ** ΔMOR (%) = 47 ** ΔInternal Bonding strength (%) = 10 ** ΔFracture toughness (%) = 60 **	Decreased fiber mineralization, surface porosity, and surface roughness	[92,93]
Zetasizer (75 nm) crystallinity (DXR) = 65% BC dispersed in water forming a gel	*Gluconacetobacter xylinus* cultured in Hestrin–Schramm medium	0, 3	**Fiber cement** - Portland Type II - 5% $CaCl_2$ - Unbleached bagasse fibers (6 wt.%) -Polycarboxilated superplasticizer	ΔMOE (%) = 33 ** ΔMOR (%) = 58 ** ΔInternal Bonding strength (%) = 30 ** ΔFracture toughness (%) = 40 **	Decreased fiber mineralization Increased durability Decreased porosity, surface basicity, and roughness Increased the organic compounds on the surface	[92,93]

(*) with respect to the properties reached with the same dosage of cellulose fibers; (**) with respect to the properties reached without NC. MOE, modulus of elasticity; MOR, modulus of rupture.

2.1. Use of NC as a Reinforcing Raw Material to Reduce Pulp Refining Requirements

The refining of pulp is required to improve its ability for processing and to enhance the mechanical properties of C-FCCs. Furthermore, pulp beating increases the durability of composites, as proven by Tonoli et al. [94], due to the improved surface contact area after refining, which enhances the adhesion of the sort fibers to the matrix. Refining is carried out through a disc refiner with a relatively narrow gap between rotor and stator. The main effect is the fibrillation of the fiber surface due to the partial breakage of the bonds between the fibrils. A higher specific surface area increases the capacity of the fibers to bond with the cement matrix and among themselves, which improves the mechanical properties. However, disc refining also causes fibers to be cut-off, decreasing their ability to bridge macrocracks.

In this scenario, the use of micro/nano celluloses could be an alternative to the refining process (Figure 1).

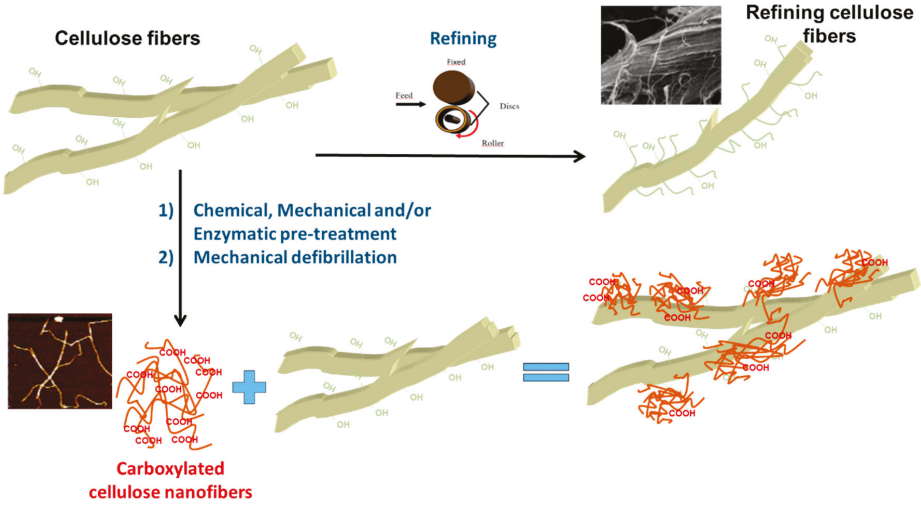

Figure 1. An approach to the potential use of NCs as an alternative to the refining process.

NC and cellulose fibers have a high tendency to form hydrogen bridges. In the presence of fibers and in the absence of other particles, NCs adsorb on the fiber surface by hydrogen bonding, causing the fibers to be coated with nanofibrils that can have extended tails in the suspension. Coating fibers with NCs increases the specific surface area and the available reactive groups, which can be performed by selecting the appropriate NC [93]. They can be, for example, carboxylic groups if 2,2,6,6-tetramethylpiperidine-1-oxyl (TEMPO)-mediated oxidation is used to prepare NCs. Therefore, interaction between fibers and cement can be improved compared to using refined fibers. The most interesting benefits of using NCs are better fiber–matrix interface adhesion and higher mechanical properties. Table 2 shows the expected effects of using NCs and refining on the fibers and on the C-FCC production process and products.

On the other hand, the refining energy requirement is high and it depends on the desired fibrillation degree, which is usually expressed by the Shopper Riegler scale (°SR) (ISO 5267-1) or Canadian Standard Freeness (mL) (ISO 5267-2). As the fiber length decreases with refining, a compromise between energy consumption and fiber quality has to be achieved for each pulp [95]. Reducing or removing the refining requirements will result in energy savings. However, producing NC is still not cheap enough since it requires high energy and/or chemicals consumption for the low profit margin of the fiber cement product. Moreover, it can be difficult to disperse the NC in the cementitious

matrix [86]. These are the main limitations to the use of NC as a raw material in fiber cement. The keys for solving these challenges are: to optimize the dose of NC and to select the right NC.

Table 2. Comparison of refining versus using NC in fiber-cement composites.

	Refining	**NC**
Production requirements	High energy demands	High energy demand and/or chemical reactives
Type and properties of cellulose fibers produced	Cellulose fibers with internal and external fibrillation Production of fines	Nano- or microcellulose fibers No fines production
	Medium specific surface area	Very high specific surface area
	Macroscale dimensions	Nanoscale dimensions
	Length reduction (cutting)	Length and diameter reduction
	Formation of hydrogen bridges	High tendency to form hydrogen bridges
	Increases swelling ability	Very high swelling ability, gel formation
Chemical modification	Easy (after refining)	Even during production, many different possibilities for chemical modification
Cracks prevention	Macrocracks	Microcracks
Interactions	Increasing the capacity of the cellulose fibers to bond with cement matrix	Highly reactive with the cellulose fibers and the cement matrix, coating the cellulose fibers
Mechanical properties	Improves mechanical properties and network strength	Highly improved mechanical properties in combination with the cellulose fibers
Durability	Increases durability, reducing strength losses by increasing interaction with the matrix	Increases durability: preventing lumen mineralization, increasing interaction with the matrix, decreasing porosity
Drainage	Decrease in the drainage rate	It likely decreases the drainage rate; however, there are no studies on that in C-FCCs

Improvements in compressive and flexural strength can be achieved by combining the soft refining of fibers with a low dose of NC, leading to a superior-quality product with a higher added value. In this way, refined fibers bridge macrocracks and nanofibers bridge microcracks [71].

The combination of NCs with fibers to replace the refining of fibers has been explored by Mohammadkazemi et al. [93]. They coated bagasse fibers with BC, previously dispersed in water, before using them as reinforcing fibers in the manufacture of C-FCCs. They observed that coating fibers was more efficient in improving mechanical properties than using BC in a powder or gel form directly in the fiber cement slurry. A dose of 3 wt.% of BC, coating half of the bagasse fibers, was enough to increase by more than 50% the modulus of rupture (MOR), absorb energy, favor internal bonding, and increase by almost 40% the modulus of elasticity (MOE). The values of MOR, fracture energy, internal bonding strength and MOE of the C-FCC without BC (28 days curing) were: 4.71 MPa, 0.1 kJ/m^2, 2.00 MPa, and 5.77 GPa, respectively. When using BC-coated fibers, these values were: 6.51 MPa, 0.17 kJ/m^2, 2.99 MPa, and 9.71 GPa, respectively. They observed that the BC increases the interaction of fibers with the matrix and encourages hydration reactions at the fiber surface, which increased fiber–matrix bonding. Furthermore, BCs prevent the entrance of alkaline hydration products into the fiber lumen, protecting them from embrittlement and improving the long-term durability. This protection has been demonstrated by SEM micrographs and EDX analysis of elemental compositions on the surface and inside the lumen of fibers. The Ca/Si ratio on the fiber surface was 5.5, half of that in the lumen (10.6), while in the case of C-FCC with BC it was 5.8, four times higher than inside the lumen (1.4). This demonstrates that the hydration products accumulate on the surface of the fibers coated with BC without entering the lumen [92].

Other authors have studied the effect of combining fibers with nanofibers just by replacing some of the fibers by an NC. Claramunt et al. [70] studied the effect of replacing some of the sisal fibers by

sisal mechanical micro-nanofibers obtained by high intensity refining, maintaining an 8 wt.% total cellulose dose. The effect of CNF increased with the percentage of replacement of fibrous raw material, reaching a maximal value of MOE (7.7 GPa) when 75% of fibers were replaced by CNF. In this case, the value of MOE increased up to 114% (from 3.6 to 7.7 GPa) and the value of MOR up to 23% (from 11.6 to 14.3 MPa). However, the fracture energy decreased notably (from 1.51 to 0.244 kJ/m^2), which indicates the effect of embrittlement. The elasticity modulus and fracture energy decayed notably when all of the fibers were replaced by CNF, which was attributed to the low macrocrack bridging capacity of CNF and the lower friction of fracture, both due to their small length. Similar effects were observed by Ardanuy et al. [71] when fiber cement was prepared only with 3.3 wt.% of CNF, instead of fibers, since the MOE and MOR were improved (from 2.4 GPa and 10.3 MPa, for C-FCC, to 4.1 GPa and 14 MPa, respectively, when all of the fibers were replaced by CNF), but the fracture energy decreased by more than 50% (from 759 to 357 kJ/m^2). The effects on MOE and MOR were lower when the percentage of CNF was 4 wt.% (they reached 3.4 GPa and 10.5 MPa, respectively) and the fracture energy decreased by more than 80% (from 0.3 to 0.05 kJ/m^2) [73]. However, the replacement of only half of the fibers by CNF resulted in better mechanical properties; the MOE increased by up to 50% (3.9 GPa) and the fracture energy decreased by less than 50% (0.17 kJ/m^2).

It is well-known that one of the main drawbacks associated with C-FCCs is their limited durability, which is associated with the sensitivity of cellulose fibers to water, carbonation, and strong alkalis, and the generation of incompatible stresses. Loss of adhesion at the fiber–cement interface and increasing micro and macrocracks contribute to strength and durability losses in C-FCCs. However, few studies have highlighted the effect of NCs on cement and concrete durability. In fact, Onuaguluchi and Banthia [96] have stated that future studies should investigate the effects of CNF and CNC on cement durability properties, among other issues. Claramunt et al. [70] compared the durability of cement reinforced with conventional pulps, CNF, or a combination of both by measuring the flexural modulus after 28 days of humidity chamber curing and 20 wet–dry accelerating aging cycles. The results showed that the flexural strength and fracture energy of C-FCC without CNF or with an amount of CNF lower than 4 wt.% decreased due to the fiber debonding and mineralization. However, the use of high content of CNF (4 wt.% or more) increased the flexural strength and maintained the fracture energy after aging. They explained this effect as a consequence of a densification of the interfacial zones combined with strong interactions between CNF and the matrix [70]. CNF do not have a lumen to suffer mineralization, and they have a higher surface area than fibers. Therefore, the replacement of fibers by CNF decreases the contribution of fiber lumen mineralization, which is responsible for embrittlement, and increases the interaction of both phases, which increases the flexural strength and fracture energy. Porosity has been proven to contribute to the lack of durability in wet/dry cycle aging because it allows water to enter into the matrix to dissolve hydration products, mainly calcium hydroxide, which precipitates again by water evaporation during the dry stage of the cycle, causing fiber mineralization. This effect is reduced when using CNFs, since they decrease porosity [74,76,80,81,84–86]. SEM images of the C-FCC with 1 wt.% of CNF and 8 wt.% of bamboo pulp show that the nanofiber bridges between the fibers and the matrix remained after 200 aging cycles, which explains the higher fracture toughness after aging (1.3 MPa/m$^{1/2}$) compared with the C-FCC without CNF (1.0 MPa/m$^{1/2}$) [81]. Aging reduced the fracture energy, MOR, and dynamic MOE of both composites, but the values were still higher for the C-FCC with CNF compared to that without (0.382 kJ/m^2, 19.9 MPa, and 13.4 GPa versus 0.379 kJ/m^2, 17.8 MPa, and 12.0 GPa, respectively). Banthia et al. [97] observed that the use of a 0.3% of MCC (vol. fraction) on concrete slabs formulation increased their durability, which was evaluated by measuring the curling of the slabs after aging. The presence of MCC led to crack control and curl reduction. Despite the high increase in MOE and MOR that can be reached, the use of CNF is limited by the fracture energy and the cost of CNFs.

2.2. Use of NC as an Additive

The use of NC as an additive in fiber cement production has four main aims: (1) to improve mechanical properties, such as bonding strength, MOE, and MOR; (2) to modify the slurry rheology; (3) to reduce the porosity; and (4) to drive interactions with other components of the slurry.

Most of the studies on cementitious materials showed high improvements with NC doses lower than 1 wt.%, and some of them have proved that the effects of NCs can be reverted if they are overdosed. Despite that, the doses of NC used for the studies carried out on C-FCCs are from 1 to 3 wt.% on solids and some improvements have been observed.

2.2.1. Mechanical Improvement

The use of NC as an additive in fiber cement production has four main effects: (1) it improves the bonding strength, MOE, and MOR; (2) it enhances hardening, mainly after 7 days; (3) it reduces the pull out of the fibers and the shrinkage, especially autogenous shrinkage during hardening, reducing the risk of product losses; and (4) it reduces the porosity and thermal expansion.

The reinforcing mechanism is mainly studied for the use of NCs in cement, but it can be extrapolated to fiber cement products. There are five different interconnected mechanisms:

1. The bridging of microcracks;
2. The increase of fiber–matrix interaction;
3. The increase of hardening kinetics near the NC surface;
4. The protection of the fiber lumen from mineralization; and
5. The decrease of autogeneous shrinkage.

Some authors have obtained different effects when using NC or microcellulose in C-FCCs, which indicates the complexity of the reinforcing mechanism. Doses of CNF lower than 1 wt.% associated with 8 wt.% of fibers have been proved to be sufficient to form stress transfer bridges in nano- and microcracks, which result in a higher MOR of the hybrid composites (19.9 MPa) with respect to the C-FCCs (14.8 MPa) and a higher fracture energy (0.422 versus 0.395 kJ/m^2) [81]. The bridging of microcracks by NC has been observed by means of SEM in cement mortars too, being one of the mechanisms that was initially proposed to explain the notable improvements in compressive and flexural strength [98,99]. The use of 3 wt.% of dispersed BC in gel form increased by up to 58%, 33%, and 30% the MOR, MOE, and internal bonding strength values of C-FCCs with 6 wt.% of bagasse fibers, reaching an MOR value of 9.16 MPa, and an MOE of 6.26 GPa. Lower, but still notable, improvements in mechanical properties were reached when BC was used as a powder, prepared by freeze-drying and milling (an MOR of 8.48 MPa and an MOE of 5.23 GPa) [93]. This indicates that the addition method has a significant influence on the reinforcing mechanism of NCs.

The specific surface area increases significantly (from 50 to 500 m^2/g) when cellulose fibers are nanofibrilated [64]. The high hydrogen bonding ability of the CNF, due to its high number of hydroxyl groups and specific and reactive surface compared to the fibers, favors both matrix–fiber and fiber–CNF interactions, as demonstrated by da Correia et al. 2018 [81]. Thus, stress transfer bridges are formed at the fiber–matrix interface, which improves the bonding strength, MOE, and MOR and reduces the pull out of the fibers, as proved by Mohammadkazemi et al. [92,93].

Physical bonding occurs during the hydration of cement when crystals interlock with each other and the fiber surfaces and grow into any other openings and permeable parts of the fiber. Several studies have proved that the hydrophilic and hygroscopic features of CNF can provide a sort of internal water reservoir in the nanofibril network (Figure 2), with a higher concentration of Ca^{2+} ions electrostatically attracted by the anionic nanofibril surface [76–79,100]. Furthermore, the diffusion of water molecules in the nanofibril network is easier and faster than that in the matrix [84]. These two facts accelerate the production of calcium silicate hydrate (CSH) gel during hydration at the fiber–matrix interface. This causes the accumulation of hydration products at the interface and increases physical bonding between fibers and the matrix, thus improving the mechanical properties

and preventing pull out, as proved by means of EDX analysis of elemental compositions in the fiber surface [93] and by X-ray diffraction and FTIR of the composites [76]. The accelerated carbonation curing contributes to the densification of the matrix and increases the dynamic modulus of elasticity [81] and the compressive strength [76].

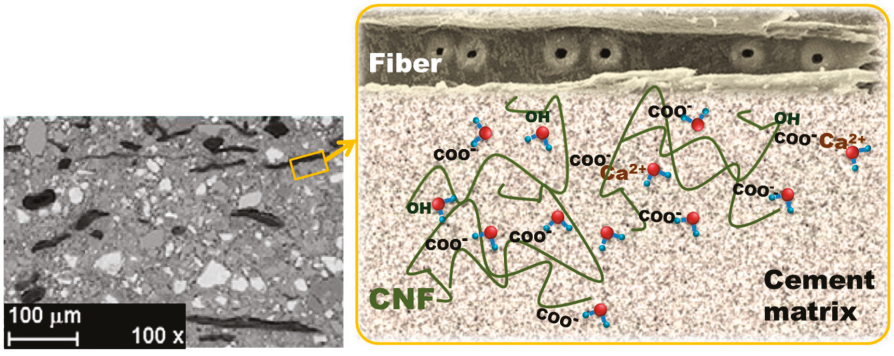

Figure 2. A schematic example of the CNF–water interactions in a cement matrix.

The effect of nano and microcelluloses on cement hydration has been proved by different researchers. Shuzhen et al. [91] were one of the first to report that the presence of BC accelerated the production of CSH during the hardening of cement. Hoyos el al. [90] studied the cement hydration reaction by thermogravimetric analysis and proved that the use of a 3 wt.% MCC increased the hydration rate during the accelerated curing of the cement paste, as shown by the increase in the intensity of the peaks corresponding to water evaporation and calcium hydroxide (CH) dehydration in a cement paste with 3 wt.% of MCC. Onuaguluchi et al. [79] explained this effect in terms of internal curing. The alkaline matrix hydrolyzes the part of the cellulose that produces organic acids and nonacidic products, and this reaction provides energy to increase the kinetics of the hydration reaction. This was proved by the increase in the hydration heat, proportional to the NC dose, as it had been already observed for fibers by Knill and Kenedy [101] and thoroughly studied by Mezencevova et al. [102]. Mohammadkazemi et al. [93] monitored the temperature during hydration of Portland cement, which was carried out by natural curing of the corresponding C-FCCs and fiber-cement with BNC. They observed that, while the presence of fibers in the C-FCCs decreased the hydration rate and hydration maximum temperature (47 °C) with respect to that for Portland cement (52 °C), the addition of a BC coating on the fibers increased the kinetics of the process with respect to that in the C-FCC and the hydration temperature, which reached 58 °C. Mejdoub et al. [76] proved this by determining the hydration degree for Portland cement with different CNFs based on the amount of the non-evaporable water in the cement paste. The degree of cement hydration at 1, 7, and 28 days increased proportionally to the CNF dose. It was 20%, 40%, and 45%, respectively, for the cement paste and it reached 40%, 49%, and 58%, respectively, for cement containing 0.5 wt.% of CNF. They proposed two additional mechanisms to justify this effect. First, CNF and CNC supply a uniform distribution of cement particles during the hydration process due to the steric stabilization effect. Similar to the mechanism of action of superplasticizers, this steric stabilization increases the hydration process, as was also observed by Cao et al. 2015 [84]. Second, the higher surface area provided by CNF and CNC acts as nuclei to promote the nucleation of hydration product crystals at the early stages of the cement hardening [64]. This favors the accumulation and precipitation of hydrated products in the open pores that were originally filled with water, leading to the formation of a more homogeneous, dense, and compact microstructure than the mixture without CNF addition, as proved by the effect of adding only 0.3 wt.% of CNF to the cement, which reduced the porosity more than the 30% [76]. This contributes to improving the fiber cement's performance, but it also allows us to control the porosity.

Cao et al. [84] observed that the concentration of CNC around the unhydrated cement cores that formed a ring or shell, which ultimately lead to the steric stabilization effect, was higher than that in the hydration product (Figure 3). Therefore, the majority of CNCs are adsorbed on the cement surface (>94%) instead of being free in the water phase [85].

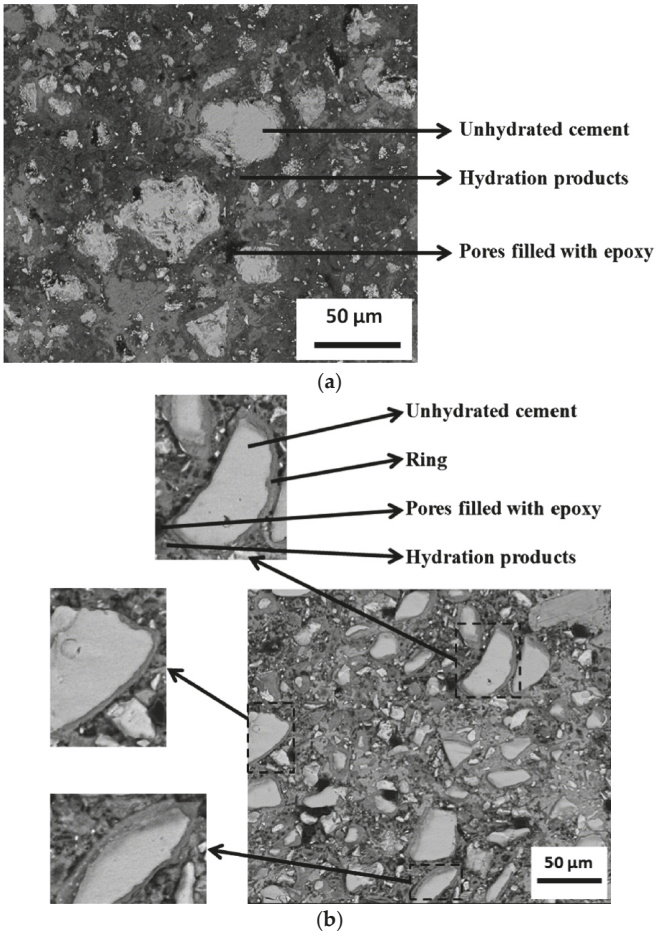

Figure 3. Backscattered scanning electron (BSE-SEM) microscope images of hardened pastes with (**a**) 0% CNC and (**b**) CNC/cement (vol.%) = 1.5 (≈0.77 wt.% CNC) at the age of 7 days. Reprinted from [84] with permission. Copyright Elsevier, 2014.

The observed reduction in autogenous shrinkage deformations in pastes with CNF has been associated with the effect of CNF on the hydration of cement [68,100]. The accumulation of water in the NC surface, due to swelling, regulates the matrix's internal moisture and decreases the initial cement hydration rate, but not the global rate. This avoids the destabilization of the matrix by fast water loss as cement hydration proceeds and decreases thermally induced cracking due to the lower heat generation rate. The CNFs retain water and dispatch it to the matrix to partially replenish the emptying cement pores. This has been proved by different studies to be the mechanism that reduces self-desiccation and attenuates early-age deformations [77,78,98]. This is key for composites with a low water/cement ratio, such as the ultra-high-performance concretes. Since internal curing is an effective

means to reduce the autogenous shrinkage of high-performance concrete [103], cellulosic fibers are efficient internal curing aids to prevent autogenous shrinkage in concrete [12]. Some researchers have proved that CNFs perform even better [76–79,100].

2.2.2. Rheology Modifier

The rheology of cement pastes is key for their workability (pumping, spreading, moulding, and compaction). The required rheology depends on the cementitious product; e.g., a C-FCC slurry or an oil well cement must be pumpable, while self-consolidating cement needs to have a very high yield stress.

In freshly prepared cement paste, the small particles interact via colloidal forces, such as Van der Waals, electrostatic repulsion, steric hindrance, and hydrogen bonding forces, and some larger particles interact via direct contact, such as friction or collisions. The presence of NC notably affects these interactions since their large active surface interacts with water, fibers, and particles.

Mohamed et al. [83] studied the effect of CMF on the workability of self-compacting concrete, and proved that the percentage, by mass, of superplasticizer required to obtain a slump of 70 cm and a V-funnel of 10 s was 0.85% of binder for a self-compacting cement with 41% (in volume over volume of cement) CMF, while it was 1.35% in the absence of CMF. However, most studies have shown that the addition of CNF reduces the cement's workability [72,78,79]. Hisseine et al. [78] proved that the use, in self-compacting concrete, of 0.1 wt.% of CMF was enough to reduce the slump-flow diameter from 785 mm to 538 mm and that a dose of 0.15 wt.% reduced it to 320 mm. In this case, the V-funnel passing time increased from 2.13 to 14.75 s. They also measured the slump-flow diameter of cement with and without CMF and observed that the presence of CMF significantly altered the mixture's workability, since the slump-flow diameter was reduced from 160 mm to 100, 90, and 85 mm by the use of 0.1, 0.15, and 0.2 wt.% of CMF, respectively. An effect on workability was also confirmed by V-funnel (the passing time increased from 3.5 to 42 s by adding 0.2 wt.% of CMF), and it was consistent with the rheological measurements [78].

Peters et al. [72] showed how the workability of concrete varies nearly linearly in the presence of increasing dosages of CMF and CNF in terms of the water-to-cement ratio and superplasticizer requirements.

The workability of cement depends on its rheological properties. The rheological behavior of fresh cement paste follows a Bingham plastic model. The use of CNF increases the yield stress of the fresh cement, as proved by Mejdoub et al. [76], Hisseine et al. [78], El Bakkari et al. [77], and Nilson and Sargenius [82]. El Bakkari et al. [77] observed that the use of 0.2 wt.% of CNF in a fresh cement paste formulation increased the yield stress from 11.36 to 22 Pa, but the plastic viscosity only increased from 0.5 to 0.68 Pa·s. This effect was due to the high swelling ability of the CNF. Water molecules adhere peripherally to NC, thereby fixing some of the mixing water and thickening the fresh cement paste. The enhancement of the interactions among fibers contributes to an increase in the yield stress of the fiber cement. This contributes to a reduction in the rate of sedimentation of solids particles and the slump, while the limited effect on plastic viscosity still allows us to mix and pump. Furthermore, for certain construction applications, where the fresh paste should retain its shape, a high yield stress is an advantage (e.g., in rigid pavements, stucco, or plastering tiles). Furthermore, pumping is more affected by the plastic viscosity of the cement paste, which increases with the CNF dose too, but with a lower sensitivity to the CNF dose, as proved by the results of El Bakkari et al. [77] and other different studies, which are shown in Table 1 [77,78].

The effect of CNC on rheology depends on the dose [84]. Therefore, CNC can be used to increase the pumping ability of cement or to decrease the slump. This is related to the smallest length of the CNC (100–250 nm) compared to CNF (0.2–3 μm) [14,64]. At low dosages, CNC would tend to adhere to the surface of cement particles rather than agglomerate, carrying water molecules as proved by SEM images [84]. Under shearing, CNC liberates entrapped water molecules and disperses cement particles through electrostatic and steric stabilization while lowering the yield stress [84,87,90]. The yield stress

of fresh cement paste decreased from 48.5 Pa to the minimum of 15.9 Pa by using 0.04 wt.% of CNC. As a result, the cement paste flows easily, thus decreasing the energy consumption when pumping. This is desirable for, e.g., reducing superplasticizer demand. At higher CNC loadings, the yield stress increased with the dose, reaching values of 600 Pa for 1.5 wt.% of CNC. For doses higher than 0.2 wt.%, the yield stress increased linearly with the dose due to CNC agglomeration, which requires higher forces to break CNC networks and also the higher reduction of the free water in the matrix [84]. This is interesting for applications where the cement must not have slump, e.g., in 3D printing.

2.3. Interaction with Other Components

Different studies on the use of NC in cement mortars and in fiber cement prove that the interaction of NC with the different components of the composite is key for the reinforcing efficiency of NC. For example, the size of the sand used has a great effect on the improvements made by the NC [104]. The use of 3.4 wt.% of CNF on mortar with a cement:silica fume:sand ratio of 0.7:0.3:1 increased the MOE from 5.9 to 6.5 GPa, but decreased the fracture energy from 431 to 78 J/m^2 when the sand was coarser than the cement particles (the d_{50} of sand was 250 μm and the d_{50} of cement was 15 μm). However, the use of sand with a similar size distribution to cement particles increased the value of MOE and fracture energy in the presence of 3.3% of CNF to 9 GPa and 348 J/m^2, respectively (the values of MOR and fracture energy of mortar with fine sand and without CNF were 5.6 GPa and 372 J/m^2, respectively).

NC can be used to modify raw materials before adding them to the mixture because of the high reactive surface that makes possible the interaction with other components of the C-FCC matrix (Figure 4).

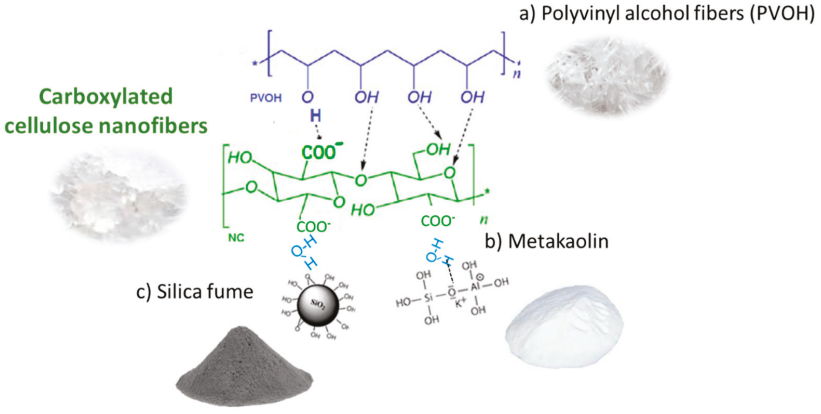

Figure 4. Potential interactions between carboxylated CNF and the different components of the C-FCC matrix, such as (**a**) polyvynil alcohol fibers (PVOH); (**b**) metakaolin; and (**c**) silica fume.

NC can also stablish hydrogen bonding with PVOH fibers to form a composite PVOH/NC with better mechanical properties [105]. There are strong interactions between hydroxyl groups of PVOH and carboxylic groups at the NC surface, which lead to the formation of a rigid network, resulting in improved mechanical properties of the PVOH fibers [106,107]. PVOH fibers could be covered with NC before being added to the mixture and this could increase their interaction with the matrix.

NC can also interact with SiO_2, i.e., silica fume, which has spherical particles less than 1 μm in diameter (the average is about 0.15 μm) that are very difficult to retain in the matrix [68]. SiO_2 interacts with NC through the adsorbed water molecules, NC-water-SiO_2. The amount of silica fume used in fiber cement is small. The dispersion of silica fume in the NC hydrogel could form a suspension of silica fume particles preflocculated with NC or coated with NC depending on the relative doses of silica fume and NC. The high interaction of NC with the cellulosic fibers and matrix would improve

the retention of silica fume in fiber cement. The same can be said for metakaolin, although the particle size of metakaolin is smaller than that of cement particles, and it is not as fine as silica fume; thus, it is easier to retain [68,106].

On the other hand, NCs interact with Ca and alkaline ions through electrostatic attractive forces and with anionic flocculants through the attached Ca ions, with some contribution of Van der Waals forces due to the high molecular weight of the polymeric flocculant. Furthermore, NCs can be modified by carboximethylation, cationization, sylilation, grafting with polymers, etc. [14,64]. This allows us to control the interactions with the other components of the composite.

2.4. Understanding the Effect of Nanocelluloses

Table 1 shows that the use of NC in cementitious composites has many different effects on mechanical properties, even if the same dose of NC is used. Some researchers showed reductions in the fracture energy or in the compressive strength, while others obtained significant improvements in these properties [74,78].

The mechanical properties of cementitious composites are controlled by at least six main factors: (1) the intrinsic mechanical properties of the reinforcing fibers and/or nanofibers (bending strength, stiffness, tensile strength); (2) the dimensions; (3) the dispersion and orientation of the fibers and/or NCs in the matrix; (4) interactions between reinforcing fibers and the matrix; (5) the effects of NC on cement hydration; and (6) the mechanical properties of the matrix, which are related to the matrix's composition and microstructure.

These factors depend on several variables that can be optimized: (1) the type of cellulose reinforcement; (2) the cellulose's or NC's surface chemistry and morphology, which depend on the mechanical or chemical treatment used for their production; (3) the dose of NC; (4) the way the NCs are incorporated into the composite; (5) the curing process; and (6) the morphology and nature of the components of the matrix, such as sand or silica.

The intrinsic mechanical properties of NCs are similar to those of steel fibers and several others of higher magnitude than those for cellulose fibers. Therefore, this factor is always improved when nanofibers are used in reinforced cement. However, the surface chemistry plays a relevant role in controlling interactions among nanofibrils and the matrix. These interactions increase with the hydrophilic character of the NC's surface as shown by the 20% shrinkage reduction in a cement reinforced with 0.8 wt.% of TEMPO-oxidized CNF when the amount of carboxylic acid groups was 1.13 mmol COOH/g [77]. Mejdoub et al. [76] observed an increase in cement hardening (up to 66%) when TEMPO-oxidized CNFs were used. The amount of water adsorbed by the nanofibers increases with the carboxylation grade [108], and this improves the water reservoir function of the NC during the cement's hydration, reducing autogenous shrinkage. Furthermore, the increase in water retention reduces the leaching and bleeding in the cement, as observed by El Bakkari et al. [77].

The kind of NC is a key factor, as proven by studies carried out by Vazquez et al. [87], Hoyos et al. [90], Cengiz et al. [75], and Alshaghel et al. [88]. They used commercial MCC, which has a lower aspect ratio (from 0.04 to 5) and a higher tendency to aggregate in clusters than those of CNF (the aspect ratio can reach values over 100), as showed by SEM images obtained by Alshaghel et al. [88], Cengiz et al. [75], and Tanpichai [109]. The low aspect ratio of MCC and its aggregate-forming clusters decrease its ability to bond cracks, reducing its reinforcing effect. In fact, Cengiz et al. [75] compared the reinforcing effect of commercial NC from Sigma Aldrich, SEM images of which indicate that it could be actually an MCC, with that of CNF produced from waste algae. While the commercial product notably decreased the flexural strength of the cement mortar, the CNF increased it by up to 170%. Most of the researchers working with MCC have observed similar effects on different cement mortars. Anju et al. [89] prepared MCC by limited acid hydrolysis, instead of using commercial MCC, resulting in a product with a larger aspect ratio (from 10 to 80) than the commercial MCC. They observed an increase of 50% of MOR by using 2.5 wt.% of MCC in the cement mortar, but the compressive strength decreased by 21%. The reinforcing effect of MCC was notably improved by means of tetraethyl

orthosilicate (TEOS) modification, because of the lower hydrophilic character and the higher siliceous character of the surface of modified MCC. These results prove the effect of morphology and surface nature on NC behavior.

The dispersion of NCs is a key aspect for their efficiency [110]. This has been studied for CNC by Cao et al. [85,86]. They proved that the use of CNCs dispersed in water and sonicated for 2 h increases their effect on cement reinforcement and reduces the large size porosity. They studied the maximum CNC dose that can be used because CNC aggregates retain larger amounts of water and CNC powder can entrap air too.

The curing process must also be taken into account. Hoyos et al. [90] studied the effect of MCC on the standard process of Portland cement hydration (by keeping the specimens for 28 days in a limestone-saturated solution at room temperature) and on accelerated hydration (by keeping the specimens for 7 days in a limestone-saturated solution at 50 °C followed by a dry oven at 60 °C for 48 h). They observed that, while the presence of MCC increased the hydration rate during the accelerated hardening, it decreased the hydration rate when hydration took place at room temperature, as proved by TGA, SEM, and EDX analysis of cured composites with 3 wt.% MCC [90]. The presence of solved polysaccharides in the water resulting from the cellulose hydrolysis could be the responsible for that. Polysaccharides can adsorb on the surface of cement and calcium hydroxide crystals, consuming water molecules in their own hydrolysis reaction, and reducing the availability of water to react with the cement particles, as demonstrated by Pourchez et al. [111,112]. Furthermore, they can complex with calcium ions to reduce the crystallization of CH and calcium silicate hydrate (CSH), as demonstrated by Peschard et al. [113,114]. These phenomena compete with the slow cement hydration process at room temperature. However, when the cement hydration is accelerated by increasing the temperature, the internal curing action of the NC is the predominant effect, resulting in a higher cement hydration grade at the end of the process. This explains the results obtained by Anju et al. [89], since they used natural curing at room temperature. The compressive strength of a cement mortar at 28 days decayed from 42 to 33 MPa and the flexural strength increase was low, from 5 to 5.8 MPa, by using a dose of 2.5 wt.% MCC. The TEOS modification of MCCs protects them from alkaline hydrolysis, which reduces the presence of solved polysaccharides and contributes to an improvement in its reinforcing effect. In this case, the use of TEOS-modified MCCs increased the compressive strength to 65 MPa and the flexural strength to 8 MPa [89].

Amorphous parts of the CNF could suffer hydrolysis too, forming soluble polysaccharides that could affect the hardening depending on cement composition and CNF characteristics. However, the improvements in the hardening rate observed with CNF for natural curing (the degree of hydration after 1 day of curing) increased from 20% to 40% when a dose of 0.5 wt.% CNF was used in the formulation of the cement paste. This proved that the effect of solved polysaccharides is lower than the internal curing effect of the CNF [76].

Not many studies have been carried out with a scan of NC doses in reinforcing cementitious materials. Several studies have been carried out with CNF, and most of them used doses lower than 1 wt.% [75,78,80]. The reinforcing effect of CNF usually increased with a dose up to a maximal value and decreased at high doses because the aggregation of CNF leads to dispersion difficulties and contributes to the formation of weak points, as reported by Mejdoub et al. [76] for CNF prepared by TEMPO-mediated oxidation and by Onuaguluchi et al. [79] for CNF obtained by mechanical fibrillation without pretreatment. In the case of CNC, similar observations were published by Cao et al. [84].

On the other hand, even at the same dose, kind, and morphology of NC, the addition method for NC has a notable influence on its reinforcing effect. This was proved by Mohammadkazemi et al. [93], who prepared a fiber cement composite reinforced with BC. They added lyophilized BC in powder form and water-dispersed BC in gel form. In this case, they tried the direct addition of BC gel to a mixture of cement and fibers and a previous coating of 50% of the fibers with BC by mixing them with a gel containing 0.1 wt.% of dispersed BC overnight before mixing them with the cement. The highest reinforcing effect was obtained in this way because of the additional fiber protective action of

the BC adsorbed onto the fibers, which helped to avoid lumen mineralization, and the increase in the hydration rate in the fiber surface. The BC was distributed in the whole matrix when it was added directly to the fiber cement slurry, which reduced the presence of the protective mechanic as a lower amount of BC was adsorbed onto the fibers. The lowest reinforcing effect was obtained by adding the BC in powder form because of the fewer accessible OH groups in the BC powder, resulting in a reduction of the hydrogen bonding ability. The MOE values for C-FCC without BC, with BC-coated fibers, with BC as a powder, and with BC in gel form (the dose of BC was 0.3 wt.% in the three cases) were 5.77, 9.71, 8.48, and 9.16 GPa respectively, which illustrates the relevance of the addition method. The MOR values were 4.71, 6.5, 5.23, and 6.26, respectively.

Claramunt et al. [74] observed that the effect of CNF on fiber cement reinforcement could be magnified by decreasing the particle size of sand. They multiplied by almost six times the reinforcing effect of the CNF and avoided its negative effect on fracture energy by using fine sand instead of coarse sand (the values are given in Section 2.3). Although interactions between the CNF, fibers, and cement were observed, the three components formed a homogeneous paste surrounding coarse sand particles with a low number of interactions with them. However, the use of fine sand particles increased the homogeneity of the matrix and the interaction among sand particles and fibers.

3. Further Applications to the C-FCC Production Process

According to studies carried out in other sectors, there are other possible ways to improve the product or the C-FCC production process that have yet to be studied. Here are three possible uses that are worth studying in the future.

3.1. Surface Treatment of Fiber Cement Boards

Fiber cement products receive different surface treatments to improve their resistance to water staining, dirt, algae, mold, and extreme climatic conditions and to improve the adhesion of fiber cement corrugated sheets. Most of these treatments consist of coating the surface with a synthetic product, such as acrylic paint or epoxy resins. NC could be used as a coating agent in a promising surface treatment of the composite layers. In this scenario, NCs attach to the surface to improve the adhesion between C-FCC corrugated sheets because NCs have the same nature as the cellulose fibers that are used as a reinforcement agent and enhance the network formation between fibers of different layers via hydrogen bonding.

Additionally, NC can be modified to provide special surface properties in the cement composite, such as hydrophobicity. Modified NC can form a waterproof film when the NC gel is applied, for example by spraying, onto the C-FCC surface. Hydrophobization of TEMPO cellulose nanofibrils has been targeted through coupling amine-functionalized molecules onto the surfaces of NC [115]. This type of NC product may be of interest for fiber cement production.

3.2. Use of NC as a Flocculant

The production of C-FCCs by the Hatscheck process requires the use of flocculants to attach the minerals to the cellulosic fibers that form the composite material. This is because of the great difference in nature and density between cellulose and the minerals, leading to poor affinity among them and poor retention [116]. Inorganic particles tend to segregate from the slurry and pass through the wire, without being retained in the sheet, if flocculants are not used. The flocculants induce the aggregation of particles, improving the retention at the primary sheet's formation and the drainage of water. This makes the formation of the composite sheets feasible and reduces the recirculating load of fine particles in the water system [117].

The most common flocculants used in C-FCC production by the Hatscheck process are anionic polyacrylamides (APAMs). This is because the flocculation process is enhanced by the interaction of the Ca^{2+} ions, produced by the cement hydration, with the carboxylic groups of the polymer chains [118] (Figure 5a).

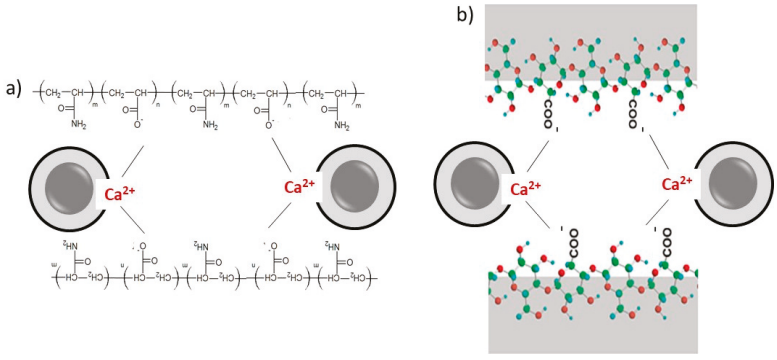

Figure 5. The flocculation interactions between cement grains or hydrates and anionic polyacrylamide (APAM) (**a**) or carboxylated NC as a promising flocculation agent (**b**).

However, the use of APAMs can reduce the flexural strength of the composite. Several studies have been carried out to mitigate the strength deterioration due to the use of APAMs. Negro et al. [119] have shown that this effect is lower when the charge density of APAM increases and the molecular weight decreases. They have also proposed the use of alternative flocculants as dual systems formed by polyethylene oxide and phenolic resins [120,121].

Another approach to improve the mechanical properties of C-FCCs is surface chemical treatment of the fibers to reduce their hydrophility, such as etherification, esterification, silanization, and urethane formation, improving the bonding between cellulose fibers and the cement matrix [122].

Although some advances have been achieved, it is of interest for the industry to find alternative flocculation aids that improve the process's efficiency without affecting the product quality. In this context, NC could replace APAMs as an alternative flocculant agent with a synergic effect. In this case, the carboxylic groups of NC, produced by TEMPO-mediated oxidation, would attach Ca^{2+} ions, interacting with the cement and other anionic particles by electrostatic forces, as shown in Figure 5b.

Moreover, NCs enhance cement hardening in contrast to the use of APAMs. Although no studies have been published on the use of NCs as flocculant aids in the C-FCCs industry, some researchers have evaluated the flocculation efficiency of NC and cationic NC in other industrial processes [123–130].

Sun et al. [126] reported that anionic CNCs are very effective for the depletion flocculation of colloidal size bacteria, in which the phase separation of bacteria occurs at very low concentrations of CNC (less than 0.1 wt.%). Suopajärvi et al. [127] studied five anionic dicarboxyl acid CNFs with variable charge densities and demonstrated that CNFs with a high charge density (1.7 mmol carboxylic groups/g) and a high nanofibrillation degree produced the best flocculation performance in the coagulation–flocculation treatment of municipal wastewater. One year later, Suopajärvi et al. [128] reported that sulfonated CNF had better flocculation performance than that reported earlier for the dicarboxyl acid CNF due to the sulfonic groups probably having a higher affinity towards iron patches of coagulant than the carboxyl acid groups. Yu et al. [129] demonstrated that CNCs with high carboxylic group content (1.39 mmol carboxylic groups/g) have a remarkable coagulation–flocculation performance in a kaolin suspension with a turbidity removal of 99.5%. Yu et al. [130] reported that CNFs flocculated microalgae via mechanical entrapment and hydrogen bonding.

In the manufacture of C-FCCs, NC may constitute a promising flocculant agent that forms a tridimensional network inside the cement composite in which the anionic charge density of the NC can be easily controlled by different chemical oxidation pretreatments (e.g., by the NaClO concentration used during TEMPO-mediated oxidation pretreatment). Moreover, NC can be grafted with flocculants or chemically modified to obtain the required flocculant efficiency and flocculant properties [131].

3.3. Wastewater Treatment

Most modern factories require a closed water circuit for manufacture in order to promote an environmentally friendly process. The accumulation of cations (e.g., K^+, Na^+, Ca^{2+}) and sulphates (e.g., K_2SO_4, Na_2SO_4, and $2CaSO_4 \cdot K_2O_4$) decreases the durability of the fiber cement and affects the process. Therefore, they must be removed from the water before its reuse. Precipitation of alkaline ions is not affordable due to the high solubility of K^+ and Na^+. Such methods as osmosis are too expensive and require extensive pretreatment, and ionic exchange resins are also expensive and generate non-biodegradable wastes. Therefore, other methods must be developed. Recent advances in nanoscale science suggest that many of the current water treatment problems might be solved or greatly ameliorated by using NC [42,132]. NCs supported on a biodegradable matrix can be a feasible ionic catcher as they have a very highly reactive surface [133,134]. Additionally, they can be modified to increase their affinity for different compounds (e.g., NC could be useful to remove the excess of flocculant from the wastewater).

Carboxylation of NC is the most-used process, in which the high density of carboxylic acids (COO^-) could react with cations, such as K^+, Na^+ and Ca^{2+}, present in the wastewaters and remove them [133]. For removing sulphates, NC should be modified. Cationic NCs are efficient adsorbents to remove negatively charged water ions [135], such as nitrates, phosphates, fluorides, and sulphates (Figure 6). Additionally, cationic CNF displayed a higher selectivity toward multivalent ions (PO_4^{3-} and SO_4^{2-}) than monovalent ions (F^- and NO_3^-) [136].

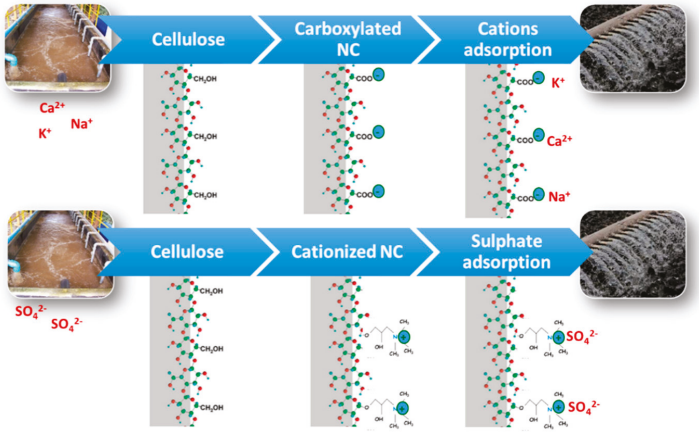

Figure 6. A representation of cation and sulphate adsorption using NC.

4. Market and Sustainability

We have analyzed different promising applications when using NC for functionally graded cement and fiber cement production based on the improvement of the properties of these materials. The major driver for utilizing CNF as a reinforcement for fiber cement products is the possibility of exploiting the high tensile moduli (a single cellulose nanofiber possess a tensile moduli between 100 and 160 GPa). However, the general consensus for the next stage of development is to continue exploring a broader marketplace beyond the conventional "stronger and stiffer" structural reinforcement application, as well as to address sustainable development issues.

4.1. Sustainability

An important issue for future market development is to consider the sustainability aspects of using NC. As mentioned above, CNFs are natural, abundant, renewable, bio-degradable, high in

strength, and low in weight, making them attractive for developing bio-based, more sustainable building solutions. However, in this aspect, one major question still remains: Are cellulose nanofibrils truly environmentally friendly compared to commercially available engineering materials?

NCs, which are obtained from renewable resources, are an example of a material under development for which a reduced environmental impact is expected compared with existing materials. However, this question is difficult to answer as these products are in their earlier stages and data for functionally graded cement and fiber cement production applications are limited to the research stage only, meaning that just lab-scale data are available.

Life cycle assessment (LCA) has been widely used for eco-design purposes to highlight the bottlenecks and hotspots in the production process and the new material compared with competing products. A few LCA studies have been published that take into account the environmental impacts of NC [137–140]. These LCAs used a combination of lab- and pilot-scale measurements to look at different processing routes and provide important insights into future large-scale industrial production in the absence of industry data.

These studies show that the main environmental impacts are related to the high energy consumption of fibrillation for all analyzed fabrication route scenarios [140,141]. During the last few years, different pretreatments, prior to fibrillation, have been developed with the aim of reducing the energy consumption of such processes as enzymatic hydrolysis, carboxymetlylation, mechanical refining, and TEMPO-mediated oxidation, and have led to a reduction in the energy requirements for fibrillation from values higher than 100 to only 2–4 Kwh/Kg [14,64].

4.2. Market

The commercialization of CNF is still at an early stage. Cellulose has only gained prominence as a nanostructured material over the past few years. This market is still under development and has a number of shortcomings, especially for high-volume applications, such as those in the building sector. For this reason, no industrial commercial applications have been implemented to date. However, this situation is expected to change in a few years; for instance, the CNF market is growing in Japan with paper manufacturers, such as Nippon Paper and Oji Holdings, and Japanese chemical manufacturers establishing large nanofiber production facilities. Facilities have also been recently established in Europe, Canada, and the United States; however, Japan is by far the largest current market for cellulose nanofiber producers, product developers, and products.

An impediment to commercial progress with CNF is cost-competitiveness with traditional technology and the availability of volumes relevant for large-scale industrial use, such as in building products. The high energy consumption needed to produce CNF has so far prevented it from competing with other mass products, such as cellulose or synthetic polymers. However, these challenges are being overcome and CNF is expected to have a substantial impact in high-volume applications. The main applications that are currently targeted by most producers include reinforcing agents in paper, cement, natural rubber, biocomposites, and plastic films for packaging. The recent developments in energy-efficient and up-scalable production methods developed by a number of companies have significantly reduced the cost of production. Currently, most CNF producers sell cellulose nanofibers for less than \$100/kg, being \$9/kg the minimum market price so far. This does not make CNF competitive against current competitive materials in many industries; however, the effort to develop low-cost production methods or target higher-value applications could change this situation in a few years, especially if the price is reduced below \$1.5/Kg [142].

In this respect, most of the major paper producers view the commoditization of NC as achievable. Production to date is, in the majority of companies, on a pilot scale and pre-commercial. Many paper producers are planning to construct large commercial production facilities in the near future. This could lead to a significant market change both in terms of availability and price. The end goal of most major producers is bulk supply rather than niche or low-volume applications; as a consequence, the

price will continue to drop over the next few years and open up possibilities in other sectors, such as those that deal with cement and fiber-reinforced materials.

5. Future Research Requirements

Dispersion is a requirement for success in using NC, since most nanocrystals and nanofibrils tend to self-agglomerate via hydrogen bonding and van der Waals forces. NC must be dispersed in the water phase before mixing it with the cement, but this will affect the rheology of the water phase and can cause difficulties when mixing it with the solid phase. If NC is not properly dispersed, the aggregates can induce the formation of large pores in the composite, and they act as stress concentration points under loading conditions [76,84,85]. Dispersion is even more difficult in the case of BC, with a high energy requirement to disperse the gel, and CNCs, which have a high tendency to agglomerate themselves [143]. Decreasing the NC concentration could be an effective way to improve the NC dispersion while decreasing the energy requirements; however, it is not feasible when the ratio water/cement is low. This limits the amount of NC that can be used. Moreover, the analyzed studies show that the reinforcing effect of NCs is related to their aspect ratio, which provides a complete dispersion of the NC. However, mechanical entanglement and NC network formation increase with the aspect ratio, which increases the difficulty of its dispersion.

The use of ultrasonication, high shearing forces, and dispersing agents are the most common ways to improve NC dispersion in the slurry [84–86]. However, there are few studies on the effect of dispersion of CNF on cementitious composites and the question of how to optimize their dispersion in the highly viscous water–cement slurry. Another strategy to improve dispersion is the functionalization of the NC surface to create disruption electrostatic forces and to increase the interaction between the NC and the matrix. This has been proven by Anju, Ramamurthy, and Dhamodharan [89] to be efficient when MCCs were used to reinforce cement mortar.

Despite the requirement of fast drainage in a Hatscheck machine, there is a lack of knowledge about the effect of the use of NC on the drainage of the C-FCCs slurry. It is known that the use of NCs in papermaking can notably decrease the drainage rate and this is one of the drawbacks for their application in papermaking [64]. As has been recently proven in papermaking, NC retention and drainage can be decoupled by changing the retention aids [144,145]. This is an important issue that could be controlled online by means of Focus Beam Reflectance Measurements [146,147]. Furthermore, the type of flocculant is also relevant to flocculant resistance and reflocculation capacity [148,149]. However, no studies exist on how the use of NC affects the retention and drainage in the Hatscheck process. In contrast to papermaking, the C-FCC suspension consists mainly of small inorganic particles and a few fibers. This could reduce the effect of adding NC to the drainage process and quite likely increase its effect on retention due to the high increase in the surface area available to interact with the mineral particles. However, this is only a prediction based on previous studies on the effect of fiber morphology on drainage carried out by Tonoli et al. [150], who observed that pulp refining decreases the drainage rate of the fiber cement suspensions; however, it notably improved the solids retention.

Finally, one of the most common worries related to the use of NC in low-value-added products is the high cost. Although the price of NC is controversial and the given values are very different from one author to another depending on the kind of NC production, the NC properties, and the sources taken into account for the economic analysis, there is the common perception that it is too expensive for the manufacture of low-value-added products. There is increasing interest in three strategies to reduce the costs of using NC in these kind of processes: (1) reducing the cost by simplifying the pretreatment in the production of CNF by using new methods for hydrolysis, separation in the production of CNC, or plant wastes and novel bioreactor designs in the production of BC [14]; (2) in situ production by means of simple treatments that allow us to use the facilities and equipment already existing in the mill when possible or at least to avoid the costs of transporting/removing the water contained in the NC suspension, which can be over 99 wt.%; and (3) fitting the properties of NC for the specific

requirements, which includes their functionalization to enhance certain properties or reduce dispersion or fibrillation costs.

6. Conclusions

Although the performance of C-FCCs has been improved in the last few decades, new strategies are required to further improve the durability and the mechanical properties of these composites, while developing ecofriendly technologies. In this context, bio-based nano-structurated cellulose materials, such as NC, can open up new solutions to overcome these limits. The addition of NC as an additive in fiber cement production has been demonstrated to be efficient in improving mechanical properties, such as internal bonding strength, MOE, and MOR, modifying the slurry's rheology, reducing the porosity, and driving interactions with other components of the slurry. However, many variables must be considered when NCs are used to reinforce fiber–cement composites. The type of cellulose fiber, the surface chemistry and morphology of NC, the dosage of NC, the way that NCs are incorporated into the composite, the curing process, and the morphology and nature of the components of the matrix, such as sand, aggregates, or silica, all have an important impact on the results. Only a small part of the huge variety of possible combinations of these factors has been studied, and it has been demonstrated that NCs have great potential to improve the mechanical properties of C-FCCs, mortars, and other cementitious composites. A greater research effort on underexplored combinations could reveal a great diversity of possibilities for sustainable natural-based fiber-reinforced cementitious composites.

Future studies are required in order to evaluate the effects of NC as a surface treatment agent, an anionic flocculant, or an additive for wastewater treatment in the fiber cement industry.

Finally, the main drawbacks of NCs are their cost, when compared to other traditional strategies, and their availability in large quantities, when they are to be used in high-volume applications. However, in the short term, these perspectives allow us to consider as likely the production of NC in large quantities and thus a drop in its cost, which would open up possibilities in the building sector.

Author Contributions: Conceptualization, C.N. and A.B. (Angeles Blanco); formal analysis, A.B. (Ana Balea) and E.F.; investigation, A.B. (Ana Balea), E.F., and C.N.; data curation, A.B. (Ana Balea) and E.F.; writing—original draft preparation, A.B. (Ana Balea), E.F., and C.N.; writing—review and editing, A.B. (Ana Balea), E.F., and A.B. (Angeles Blanco); supervision, A.B. (Angeles Blanco) and C.N.; project administration, C.N.; funding acquisition, A.B. (Angeles Blanco) and C.N.

Funding: The authors wish to thank the Community of Madrid and the Economy and Competitiveness Ministry of Spain for the support of the projects S2013/MAE-2907 (RETO-PROSOST-CM) and CTQ2017-85654-C2-2-R, respectively.

Conflicts of Interest: The authors declare no conflict of interest.

References

1. Chen, Z.-S.; Zhou, X.; Wang, X.; Guo, P. Mechanical behavior of multilayer GO carbon-fiber cement composites. *Constr. Build. Mater.* **2018**, *159*, 205–212. [CrossRef]
2. Qiu, J.; Lim, X.N.; Yang, E.-H. Fatigue-induced in-situ strength deterioration of micro-polyvinyl alcohol (PVA) fiber in cement matrix. *Cem. Concr. Compos.* **2017**, *82*, 128–136. [CrossRef]
3. Beglarigale, A.; Yazıcı, H. Electrochemical corrosion monitoring of steel fiber embedded in cement based composites. *Cem. Concr. Compos.* **2017**, *83*, 427–446. [CrossRef]
4. Bentur, A.; Mindess, S. *Fibre Reinforced Cementitious Composites*; CRC Press: London, UK, 1990.
5. Balaguru, P.N.; Shah, S.P. *Fiber-Reinforced Cement Composites*, 1st ed.; Mc Graw Hill International Editions: New York, NY, USA, 1992.
6. Ardanuy, M.; Claramunt, J.; Toledo Filho, R.D. Cellulosic fiber reinforced cement-based composites: A review of recent research. *Constr. Build. Mater.* **2015**, *79*, 115–128. [CrossRef]
7. Morton, J.H.; Cooke, T.; Akers, S. Performance of slash pine fibers in fiber cement products. *Constr. Build. Mater.* **2010**, *24*, 165–170. [CrossRef]
8. Savastano, H., Jr.; Warden, P.G.; Coutts, R. Mechanically pulped sisal as reinforcement in cementitious matrices. *Cem. Concr. Compos.* **2003**, *25*, 311–319. [CrossRef]

9. Mohr, B.; Nanko, H.; Kurtis, K. Durability of kraft pulp fiber–cement composites to wet/dry cycling. *Cem. Concr. Compos.* **2005**, *27*, 435–448. [CrossRef]
10. Toledo Filho, R.D.; Scrivener, K.; England, G.L.; Ghavami, K. Durability of alkali-sensitive sisal and coconut fibres in cement mortar composites. *Cem. Concr. Compos.* **2000**, *22*, 127–143. [CrossRef]
11. Ardanuy, M.; Claramunt, J.; García-Hortal, J.A.; Barra, M. Fiber-matrix interactions in cement mortar composites reinforced with cellulosic fibers. *Cellulose* **2011**, *18*, 281–289. [CrossRef]
12. Kawashima, S.; Shah, S.P. Early-age autogenous and drying shrinkage behavior of cellulose fiber-reinforced cementitious materials. *Cem. Concr. Compos.* **2011**, *33*, 201–208. [CrossRef]
13. Klemm, D.; Heublein, B.; Fink, H.P.; Bohn, A. Cellulose: Fascinating biopolymer and sustainable raw material. *Angew. Chem. Int. Ed.* **2005**, *44*, 3358–3393. [CrossRef]
14. Klemm, D.; Cranston, E.D.; Fischer, D.; Gama, M.; Kedzior, S.A.; Kralisch, D.; Kramer, F.; Kondo, T.; Lindström, T.; Nietzsche, S. Nanocellulose as a natural source for groundbreaking applications in materials science: Today's state. *Mater. Today* **2018**, *21*, 720–748. [CrossRef]
15. Blanco, A.; Monte, M.C.; Campano, C.; Balea, A.; Merayo, N.; Negro, C. Nanocellulose for industrial use: Cellulose nanofibers (CNF), cellulose nanocrystals (CNC), and bacterial cellulose (BC). In *Handbook of Nanomaterials for Industrial Applications*; Elsevier: Newark, NJ, USA, 2018; pp. 74–126.
16. Abitbol, T.; Rivkin, A.; Cao, Y.; Nevo, Y.; Abraham, E.; Ben-Shalom, T.; Lapidot, S.; Shoseyov, O. Nanocellulose, a tiny fiber with huge applications. *Curr. Opin. Biotechnol.* **2016**, *39*, 76–88. [CrossRef]
17. Klemm, D.; Kramer, F.; Moritz, S.; Lindstrom, T.; Ankerfors, M.; Gray, D.; Dorris, A. Nanocelluloses: A new family of nature-based materials. *Angew. Chem. Int. Ed.* **2011**, *50*, 5438–5466. [CrossRef] [PubMed]
18. Moon, R.J.; Martini, A.; Nairn, J.; Simonsen, J.; Youngblood, J. Cellulose nanomaterials review: Structure, properties and nanocomposites. *Chem. Soc. Rev.* **2011**, *40*, 3941–3994. [CrossRef] [PubMed]
19. Mondal, S. Preparation, properties and applications of nanocellulosic materials. *Carbohyd. Polym.* **2017**, *163*, 301–316. [CrossRef] [PubMed]
20. Lindström, T. Aspects on nanofibrillated cellulose (NFC) processing, rheology and NFC-film properties. *Curr. Opin. Colloid Interface Sci.* **2017**, *29*, 68–75. [CrossRef]
21. kumar Mishra, R.; Sabu, A.; Tiwari, S.K. Materials chemistry and the futurist eco-friendly applications of nanocellulose: Status and prospect. *J. Saudi Chem. Soc.* **2018**, *22*, 949–978. [CrossRef]
22. Lavoine, N.; Desloges, I.; Dufresne, A.; Bras, J. Microfibrillated cellulose—Its barrier properties and applications in cellulosic materials: A review. *Carbohyd. Polym.* **2012**, *90*, 735–764. [CrossRef]
23. Khalil, H.A.; Davoudpour, Y.; Islam, M.N.; Mustapha, A.; Sudesh, K.; Dungani, R.; Jawaid, M. Production and modification of nanofibrillated cellulose using various mechanical processes: A review. *Carbohyd. Polym.* **2014**, *99*, 649–665. [CrossRef]
24. Chirayil, C.J.; Mathew, L.; Thomas, S. Review of recent research in nano cellulose preparation from different lignocellulosic fibers. *Rev. Adv. Mater. Sci.* **2014**, *37*, 20–28.
25. Phanthong, P.; Reubroycharoen, P.; Hao, X.; Xu, G.; Abudula, A.; Guan, G. Nanocellulose: Extraction and application. *Carbon Resour. Convers.* **2018**, *1*, 32–43. [CrossRef]
26. Nechyporchuk, O.; Naceur Belgacem, M.; Bras, J. Production of cellulose nanofibrils: A review of recent advances. *Ind. Crop. Prod.* **2016**, *93*, 2–25. [CrossRef]
27. Trache, D.; Hussin, M.H.; Haafiz, M.M.; Thakur, V.K. Recent progress in cellulose nanocrystals: Sources and production. *Nanoscale* **2017**, *9*, 1763–1786. [CrossRef] [PubMed]
28. George, J.; Sabapathi, S. Cellulose nanocrystals: Synthesis, functional properties, and applications. *Nanotechnol. Sci. Appl.* **2015**, *8*, 45. [CrossRef]
29. Azizi Samir, M.A.S.; Alloin, F.; Dufresne, A. Review of recent research into cellulosic whiskers, their properties and their application in nanocomposite field. *Biomacromolecules* **2005**, *6*, 612–626. [CrossRef]
30. Mariano, M.; El Kissi, N.; Dufresne, A. Cellulose nanocrystals and related nanocomposites: Review of some properties and challenges. *J. Polym. Sci. Pol. Phys.* **2014**, *52*, 791–806. [CrossRef]
31. Campano, C.; Balea, A.; Blanco, A.; Negro, C. Enhancement of the fermentation process and properties of bacterial cellulose: A review. *Cellulose* **2016**, *23*, 57–91. [CrossRef]
32. Jonoobi, M.; Mathew, A.P.; Oksman, K. Producing low-cost cellulose nanofiber from sludge as new source of raw materials. *Ind. Crop. Prod.* **2012**, *40*, 232–238. [CrossRef]

33. Jonoobi, M.; Oladi, R.; Davoudpour, Y.; Oksman, K.; Dufresne, A.; Hamzeh, Y.; Davoodi, R. Different preparation methods and properties of nanostructured cellulose from various natural resources and residues: A review. *Cellulose* **2015**, *22*, 935–969. [CrossRef]
34. Chin, K.M.; Sung Ting, S.; Ong, H.L.; Omar, M. Surface functionalized nanocellulose as a veritable inclusionary material in contemporary bioinspired applications: A review. *J. Appl. Polym. Sci.* **2018**, *135*, 46065. [CrossRef]
35. Shatkin, J.A.; Wegner, T.H.; Bilek, E.M.; Cowie, J. Market projections of cellulose nanomaterial-enabled products—Part 1: Applications. *Tappi J.* **2014**, *13*, 9–16.
36. Cowie, J.; Bilek, E.M.; Wegner, T.H.; Shatkin, J.A. Market projections of cellulose nanomaterial-enabled products—Part 2: Volume estimates. *Tappi J.* **2014**, *13*, 57–69.
37. Charreau, H.; L Foresti, M.; Vázquez, A. Nanocellulose patents trends: A comprehensive review on patents on cellulose nanocrystals, microfibrillated and bacterial cellulose. *Recent Pat. Nanotechnol.* **2013**, *7*, 56–80. [CrossRef]
38. Kim, J.H.; Shim, B.S.; Kim, H.S.; Lee, Y.J.; Min, S.K.; Jang, D.; Abas, Z.; Kim, J. Review of nanocellulose for sustainable future materials. *Int. J. Precis. Eng. Manuf. Green Technol.* **2015**, *2*, 197–213. [CrossRef]
39. Boufi, S.; González, I.; Delgado-Aguilar, M.; Tarrès, Q.; Pèlach, M.À.; Mutje, P. Nanofibrillated cellulose as an additive in papermaking process: A review. *Carbohyd. Polym.* **2016**, *154*, 151–166. [CrossRef]
40. Li, F.; Mascheroni, E.; Piergiovanni, L. The potential of nanocellulose in the packaging field: A review. *Packag. Technol. Sci.* **2015**, *28*, 475–508. [CrossRef]
41. Mahfoudhi, N.; Boufi, S. Nanocellulose as a novel nanostructured adsorbent for environmental remediation: A review. *Cellulose* **2017**, *24*, 1171–1197. [CrossRef]
42. Carpenter, A.W.; de Lannoy, C.F.; Wiesner, M.R. Cellulose nanomaterials in water treatment technologies. *Environ. Sci. Technol.* **2015**, *49*, 5277–5287. [CrossRef]
43. Brodin, F.W.; Gregersen, O.W.; Syverud, K. Cellulose nanofibrils: Challenges and possibilities as a paper additive or coating material—A review. *Nord. Pulp Pap. Res. J.* **2014**, *29*, 156–166. [CrossRef]
44. Vilarinho, F.; Sanches Silva, A.; Vaz, M.F.; Farinha, J.P. Nanocellulose in green food packaging. *Crit. Rev. Food Sci. Nutr.* **2018**, *58*, 1526–1537. [CrossRef]
45. Balea, A.; Blanco, A.; Monte, M.C.; Merayo, N.; Negro, C. Effect of bleached eucalyptus and pine cellulose nanofibers on the physico-mechanical properties of cartonboard. *Bioresources* **2016**, *11*, 8123–8138. [CrossRef]
46. Balea, A.; Blanco, A.; Merayo, N.; Negro, C. Effect of nanofibrillated cellulose to reduce linting on high filler-loaded recycled papers. *Appita J.* **2016**, *69*, 148–156.
47. Gomez, C.; Serpa, A.; Velasquez-Cock, J.; Ganan, P.; Castro, C.; Velez, L.; Zuluaga, R. Vegetable nanocellulose in food science: A review. *Food Hydrocoll.* **2016**, *57*, 178–186. [CrossRef]
48. Lin, N.; Dufresne, A. Nanocellulose in biomedicine: Current status and future prospect. *Eur. Polym. J.* **2014**, *59*, 302–325. [CrossRef]
49. Sanchez-Salvador, J.L.; Balea, A.; Monte, M.C.; Blanco, A.; Negro, C. Pickering emulsions containing cellulose microfibers produced by mechanical treatments as stabilizer in the food industry. *Appl. Sci.* **2019**, *9*, 359. [CrossRef]
50. Dai, L.; Cheng, T.; Duan, C.; Zhao, W.; Zhang, W.; Zou, X.; Aspler, J.; Ni, Y. 3D printing using plant-derived cellulose and its derivatives: A review. *Carbohyd. Polym.* **2018**, *203*, 71–86. [CrossRef]
51. Du, X.; Zhang, Z.; Liu, W.; Deng, Y.L. Nanocellulose-based conductive materials and their emerging applications in energy devices—A review. *Nano Energy* **2017**, *35*, 299–320. [CrossRef]
52. Hoeng, F.; Denneulin, A.; Bras, J. Use of nanocellulose in printed electronics: A review. *Nanoscale* **2016**, *8*, 13131–13154. [CrossRef]
53. Li, Y.; Yu, S.; Chen, P.; Rojas, R.; Hajian, A.; Berglund, L. Cellulose nanofibers enable paraffin encapsulation and the formation of stable thermal regulation nanocomposites. *Nano Energy* **2017**, *34*, 541–548. [CrossRef]
54. Hubbe, M.A.; Rojas, O.J.; Lucia, L.A.; Sain, M. Cellulosic nanocomposites: A review. *Bioresources* **2008**, *3*, 929–980.
55. Ching, Y.C.; Ali, M.E.; Abdullah, L.C.; Choo, K.W.; Kuan, Y.C.; Julaihi, S.J.; Chuah, C.H.; Liou, N.-S. Rheological properties of cellulose nanocrystal-embedded polymer composites: A review. *Cellulose* **2016**, *23*, 1011–1030. [CrossRef]

56. Eichhorn, S.J.; Dufresne, A.; Aranguren, M.; Marcovich, N.E.; Capadona, J.R.; Rowan, S.J.; Weder, C.; Thielemans, W.; Roman, M.; Renneckar, S.; et al. Review: Current international research into cellulose nanofibres and nanocomposites. *J. Mater. Sci.* **2010**, *45*, 1–33. [CrossRef]
57. Siró, I.; Plackett, D. Microfibrillated cellulose and new nanocomposite materials: A review. *Cellulose* **2010**, *17*, 459–494. [CrossRef]
58. Kargarzadeh, H.; Mariano, M.; Huang, J.; Lin, N.; Ahmad, I.; Dufresne, A.; Thomas, S. Recent developments on nanocellulose reinforced polymer nanocomposites: A review. *Polymer* **2017**, *132*, 368–393. [CrossRef]
59. Lee, K.Y.; Aitomaki, Y.; Berglund, L.A.; Oksman, K.; Bismarck, A. On the use of nanocellulose as reinforcement in polymer matrix composites. *Compos. Sci. Technol.* **2014**, *105*, 15–27. [CrossRef]
60. Oksman, K.; Aitomaki, Y.; Mathew, A.P.; Siqueira, G.; Zhou, Q.; Butylina, S.; Tanpichai, S.; Zhou, X.J.; Hooshmand, S. Review of the recent developments in cellulose nanocomposite processing. *Compos. Part A Appl. Sci. Manuf.* **2016**, *83*, 2–18. [CrossRef]
61. Negro, C.; Garcia-Ochoa, F.; Tanguy, P.; Ferreira, G.; Thibault, J.; Yamamoto, S.; Gani, R. Barcelona declaration–10th world congress of chemical engineering, 1–5 october 2017. *Chem. Eng. Res. Des.* **2018**, *129*, A1–A2. [CrossRef]
62. Chinga-Carrasco, G.; Averianova, N.; Gibadullin, M.; Petrov, V.; Leirset, I.; Syverud, K. Micro-structural characterisation of homogeneous and layered MFC nano-composites. *Micron* **2013**, *44*, 331–338. [CrossRef]
63. Jonoobi, M.; Harun, J.; Mathew, A.P.; Oksman, K. Mechanical properties of cellulose nanofiber (CNF) reinforced polylactic acid (PLA) prepared by twin screw extrusion. *Compos. Sci. Technol.* **2010**, *70*, 1742–1747. [CrossRef]
64. Osong, S.H.; Norgren, S.; Engstrand, P. Processing of wood-based microfibrillated cellulose, and applications relating to papermaking: A review. *Cellulose* **2016**, *23*, 93–123. [CrossRef]
65. Dufresne, A. Cellulose nanomaterials as green nanoreinforcements for polymer nanocomposites. *Philos. Trans. R. Soc. A Math. Phys. Eng. Sci.* **2017**, *376*, 20170040. [CrossRef]
66. Siqueira, G.; Bras, J.; Dufresne, A. Cellulosic bionanocomposites: A review of preparation, properties and applications. *Polymers* **2010**, *2*, 728–765. [CrossRef]
67. Balea, A.; Merayo, N.; Fuente, E.; Delgado-Aguilar, M.; Mutje, P.; Blanco, A.; Negro, C. Valorization of corn stalk by the production of cellulose nanofibers to improve recycled paper properties. *Bioresources* **2016**, *11*, 3416–3431. [CrossRef]
68. Fu, T.; Moon, R.J.; Zavattieri, P.; Youngblood, J.; Weiss, W.J. Cellulose nanomaterials. In *Cellulose-Reinforced Nanofibre Composites*, 1st ed.; Jawaid, M., Boufi, S., Khalil, A.H.P.S., Eds.; Elsevier: Duxford, UK, 2017; pp. 455–482.
69. Parveen, S.; Rana, S.; Fangueiro, R. Macro-and nanodimensional plant fiber reinforcements for cementitious composites. In *Sustainable and Nonconventional Construction Materials Using Inorganic Bonded Fiber Composites*, 1st ed.; Savastano, H., Jr., Fiorelli, F., Dos Santos, S.F., Eds.; Elsevier: Duxford, UK, 2017; pp. 343–382.
70. Claramunt, J.; Ardanuy, M.; Fernandez-Carrasco, L.J. Wet/dry cycling durability of cement mortar composites reinforced with micro-and nanoscale cellulose pulps. *BioResources* **2015**, *10*, 3045–3055. [CrossRef]
71. Ardanuy Raso, M.; Claramunt Blanes, J.; Arévalo Peces, R.; Parés Sabatés, F.; Aracri, E.; Vidal Lluciá, T. Nanofibrillated cellulose (NFC) as a potential reinforcement for high performance cement mortar composites. *BioResources* **2012**, *7*, 3883–3894.
72. Peters, S.; Rushing, T.; Landis, E.; Cummins, T. Nanocellulose and microcellulose fibers for concrete. *Transp. Res. Rec.* **2010**, 25–28. [CrossRef]
73. Ardanuy, M.; Clarmunt, J.; Toledo Filho, R.D. Evaluation of durability to wet/dry cycling of cement mortar composites reinforced with nanofibrillated cellulose. In *Brittle Matrix Composites 10*; Brandt Glinicki, M.A., Olek, J., Leung, C.K.Y., Eds.; Elsevier: Duxford, UK, 2013; pp. 33–41.
74. Claramunt Blanes, J.; Ardanuy Raso, M.; Arévalo Peces, R.; Parés Sabatés, F.; Tolêdo Filho, R.D. Mechanical performance of ductile cement mortar composites reinforced with nanofibrilated cellulose. In *Strain Hardening Cementitious Composites (SHCC2-Rio)*; Proceedings of the 2nd International RILEM Conference, Río de Janeiro, Brazil, 12–14 December; Toledo Filho, R.D., Silva, F.A., Koenders, E.A.B., Fairbairn, E.M.R., Eds.; RILEM Publications: Paris, France, 2011; pp. 131–138.
75. Cengiz, A.; Kaya, M.; Bayramgil, N.P. Flexural stress enhancement of concrete by incorporation of algal cellulose nanofibers. *Constr. Build. Mater.* **2017**, *149*, 289–295. [CrossRef]

76. Mejdoub, R.; Hammi, H.; Sunol, J.J.; Khitouni, M.; M'Nif, A.; Boufi, S. Nanofibrillated cellulose as nanoreinforcement in portland cement: Thermal, mechanical and microstructural properties. *J. Compos. Mater.* **2017**, *51*, 2491–2503. [CrossRef]
77. El Bakkari, M.; Bindiganavile, V.; Goncalves, J.; Boluk, Y. Preparation of cellulose nanofibers by tempo-oxidation of bleached chemi-thermomechanical pulp for cement applications. *Carbohyd. Polym.* **2019**, *203*, 238–245. [CrossRef]
78. Hisseine, O.A.; Omran, A.F.; Tagnit-Hamou, A. Influence of cellulose filaments on cement paste and concrete. *J. Mater. Civ. Eng.* **2018**, *30*, 04018109. [CrossRef]
79. Onuaguluchi, O.; Panesar, D.K.; Sain, M. Properties of nanofibre reinforced cement composites. *Constr. Build. Mater.* **2014**, *63*, 119–124. [CrossRef]
80. Soares Fonseca, C.; Ferreira da Silva, T.; Silva, M.F.; Rodrigues de Campos Oliveira, I.; Farinassi Mendes, R.; Gherardi Hein, P.R.; Marin Mendes, L.; Denzin Tonoli, G.H. Micro/nanofibrilas celulósicas de eucalyptus em fibrocimentos extrudados. *CERNE* **2016**, *22*, 59–68. [CrossRef]
81. da Costa Correia, V.; Santos, S.F.; Teixeira, R.S.; Junior, H.S. Nanofibrillated cellulose and cellulosic pulp for reinforcement of the extruded cement based materials. *Constr. Build. Mater.* **2018**, *160*, 376–384. [CrossRef]
82. Nilsson, J.; Sargenius, P. *Effect of Microfibrillar Cellulose on Concrete Equivalent Mortar Fresh and Hardened Properties*; KTH: Stockholm, Sweden, 2011.
83. Mohamed, M.; Ghorbel, E.; Wardeh, G. Valorization of micro-cellulose fibers in self-compacting concrete. *Constr. Build. Mater.* **2010**, *24*, 2473–2480. [CrossRef]
84. Cao, Y.; Zavaterri, P.; Youngblood, J.; Moon, R.; Weiss, J. The influence of cellulose nanocrystal additions on the performance of cement paste. *Cem. Concr. Compos.* **2015**, *56*, 73–83. [CrossRef]
85. Cao, Y.; Tian, N.; Bahr, D.; Zavattieri, P.D.; Youngblood, J.; Moon, R.J.; Weiss, J. The influence of cellulose nanocrystals on the microstructure of cement paste. *Cem. Concr. Compos.* **2016**, *74*, 164–173. [CrossRef]
86. Cao, Y.; Zavattieri, P.; Youngblood, J.; Moon, R.; Weiss, J. The relationship between cellulose nanocrystal dispersion and strength. *Constr. Build. Mater.* **2016**, *119*, 71–79. [CrossRef]
87. Vazquez, A.; Piqué, T.M.; Hoyos, C.G.; Escobar, M.M. Study of kinetic, structure and properties evaluation of organically modified montmorillonites and micro nanocellulose added to cement paste. In Proceedings of the ASME 2012 31st International Conference on Ocean, Offshore and Arctic Engineering, Rio de Janeiro, Brazil, 1–6 July 2012; American Society of Mechanical Engineers: New York, NY, USA; pp. 829–833.
88. Alshaghel, A.; Parveen, S.; Rana, S.; Fangueiro, R. Effect of multiscale reinforcement on the mechanical properties and microstructure of microcrystalline cellulose-carbon nanotube reinforced cementitious composites. *Compos. Part B Eng.* **2018**, *149*, 122–134. [CrossRef]
89. Anju, T.; Ramamurthy, K.; Dhamodharan, R. Surface modified microcrystalline cellulose from cotton as a potential mineral admixture in cement mortar composite. *Cem. Concr. Compos.* **2016**, *74*, 147–153. [CrossRef]
90. Hoyos, C.G.; Cristia, E.; Vázquez, A. Effect of cellulose microcrystalline particles on properties of cement based composites. *Mater. Des.* **2013**, *51*, 810–818. [CrossRef]
91. Shuzhen, L.; Ning, C.; Zhonghua, P.; Yanhua, P.; Huang, T. Preparation and properties of bacterial cellulose reinforced cement composites. *China Powder Sci. Technol.* **2011**, *17*, 57–60.
92. Mohammadkazemi, F.; Aguiar, R.; Cordeiro, N. Improvement of bagasse fiber–cement composites by addition of bacterial nanocellulose: An inverse gas chromatography study. *Cellulose* **2017**, *24*, 1803–1814. [CrossRef]
93. Mohammadkazemi, F.; Doosthoseini, K.; Ganjian, E.; Azin, M. Manufacturing of bacterial nano-cellulose reinforced fiber—Cement composites. *Constr. Build. Mater.* **2015**, *101*, 958–964. [CrossRef]
94. Tonoli, G.H.D.; dos Santos, S.F.; Joaquim, A.P.; Savastano, H., Jr. Effect of accelerated carbonation on cementitious roofing tiles reinforced with lignocellulosic fibre. *Constr. Build. Mater.* **2010**, *24*, 193–201. [CrossRef]
95. De Lhoneux, B.; Alderweireldt, L.; Boersma, A.; Bordin, R.; Saenen, W.; Heyden, L.; Verleene, D. Selected issues of fibre-cement sustainability: Wood pulp refining energy and accelerated ageing of fibres and composites. In Proceedings of the IIBCC 11th International Inorganic-Bonded Fiber Composites Conference, Madrid, Spain, 5–8 November 2011.
96. Onuaguluchi, O.; Banthia, N. Plant-based natural fibre reinforced cement composites: A review. *Cem. Concr. Compos.* **2016**, *68*, 96–108. [CrossRef]

97. Banthia, N.; Bindiganavile, V.; Azhari, F.; Zanotti, C. Curling control in concrete slabs using fiber reinforcement. *J. Test. Eval.* **2014**, *42*, 390–397. [CrossRef]
98. Stephenson, K.M. *Characterizing the Behavior and Properties of Nano Cellulose Reinforced Ultra High Performance Concrete*; University of Maine: Orono, ME, USA, 2011.
99. Dai, H.; Jiao, L.; Zhu, Y.; Pi, C. Nanometer Cellulose Fibre Reinforced Cement-Based Material. Patent Publication No. CN105174768A, 23 December 2015.
100. Ferrara, L.; Ferreira, S.R.; della Torre, M.; Krelani, V.; de Silva, F.A.; Toledo Filho, R.D. Effect of cellulose nanopulp on autogenous and drying shrinkage of cement based composites. In *Nanotechnology in Construction*; Konstantin Sobolev, K., Shah, S.P., Eds.; Springer: Basel, Switzerland, 2015; pp. 325–330.
101. Knill, C.J.; Kennedy, J.F. Degradation of cellulose under alkaline conditions. *Carbohyd. Polym.* **2003**, *51*, 281–300. [CrossRef]
102. Mezencevova, A.; Garas, V.; Nanko, H.; Kurtis, K.E. Influence of thermomechanical pulp fiber compositions on internal curing of cementitious materials. *J. Mater. Civ. Eng.* **2011**, *24*, 970–975. [CrossRef]
103. Wu, L.; Farzadnia, N.; Shi, C.; Zhang, Z.; Wang, H. Autogenous shrinkage of high performance concrete: A review. *Constr. Build. Mater.* **2017**, *149*, 62–75. [CrossRef]
104. Claramunt, J.; Ardanuy, M.; García-Hortal, J.A.; Tolêdo Filho, R.D. The hornification of vegetable fibers to improve the durability of cement mortar composites. *Cem. Concr. Compos.* **2011**, *33*, 586–595. [CrossRef]
105. Hakalahti, M.; Salminen, A.; Seppälä, J.; Tammelin, T.; Hänninen, T. Effect of interfibrillar PVA bridging on water stability and mechanical properties of TEMPO/$NaClO_2$ oxidized cellulosic nanofibril films. *Carbohyd. Polym.* **2015**, *126*, 78–82. [CrossRef] [PubMed]
106. Reid, M.S.; Villalobos, M.; Cranston, E.D. The role of hydrogen bonding in non-ionic polymer adsorption to cellulose nanocrystals and silica colloids. *Curr. Opin. Colloid Interface Sci.* **2017**, *29*, 76–82. [CrossRef]
107. Changsarn, S.; Mendez, J.D.; Shanmuganathan, K.; Foster, E.J.; Weder, C.; Supaphol, P. Biologically inspired hierarchical design of nanocomposites based on poly (ethylene oxide) and cellulose nanofibers. *Macromol. Rapid Commun.* **2011**, *32*, 1367–1372. [CrossRef] [PubMed]
108. Isogai, A.; Saito, T.; Fukuzumi, H. TEMPO-oxidized cellulose nanofibers. *Nanoscale* **2011**, *3*, 71–85. [CrossRef] [PubMed]
109. Tanpichai, S. A comparative study of nanofibrillated cellulose and microcrystalline cellulose as reinforcements in all-cellulose composites. *J. Met. Mater. Miner.* **2018**, *28*.
110. Campano, C.; Merayo, N.; Balea, A.; Tarrés, Q.; Delgado-Aguilar, M.; Mutjé, P.; Negro, C.; Blanco, Á. Mechanical and chemical dispersion of nanocelluloses to improve their reinforcing effect on recycled paper. *Cellulose* **2018**, *25*, 269–280. [CrossRef]
111. Pourchez, J.; Grosseau, P.; Ruot, B. Changes in c3s hydration in the presence of cellulose ethers. *Cem. Concr. Res.* **2010**, *40*, 179–188. [CrossRef]
112. Pourchez, J.; Govin, A.; Grosseau, P.; Guyonnet, R.; Guilhot, B.; Ruot, B. Alkaline stability of cellulose ethers and impact of their degradation products on cement hydration. *Cem. Concr. Res.* **2006**, *36*, 1252–1256. [CrossRef]
113. Peschard, A.; Govin, A.; Grosseau, P.; Guilhot, B.; Guyonnet, R. Effect of polysaccharides on the hydration of cement paste at early ages. *Cem. Concr. Res.* **2004**, *34*, 2153–2158. [CrossRef]
114. Peschard, A.; Govin, A.; Pourchez, J.A.E.; Fredon, E.; Bertrand, L.; Maximilien, S.; Guilhot, B. Effect of polysaccharides on the hydration of cement suspension. *J. Eur. Ceram. Soc.* **2006**, *26*, 1439–1445. [CrossRef]
115. Johnson, R.K.; Zink-Sharp, A.; Glasser, W.G. Preparation and characterization of hydrophobic derivatives of TEMPO-oxidized nanocelluloses. *Cellulose* **2011**, *18*, 1599–1609. [CrossRef]
116. Agopyan, V.; Savastano, H., Jr.; John, V.; Cincotto, M. Developments on vegetable fibre–cement based materials in São Paulo, Brazil: An overview. *Cem. Concr. Compos.* **2005**, *27*, 527–536. [CrossRef]
117. Negro, C.; Blanco, A.; San Pío, I.; Tijero, J. Methodology for flocculant selection in fibre–cement manufacture. *Cem. Concr. Compos.* **2006**, *28*, 90–96. [CrossRef]
118. Negro, C.; Sánchez, L.M.; Fuente, E.; Blanco, Á.; Tijero, J. Polyacrylamide induced flocculation of a cement suspension. *Chem. Eng. Sci.* **2006**, *61*, 2522–2532. [CrossRef]
119. Negro, C.; Blanco, A.; Fuente, E.; Sánchez, L.M.; Tijero, J. Influence of flocculant molecular weight and anionic charge on flocculation behaviour and on the manufacture of fibre cement composites by the Hatschek process. *Cem. Concr. Res.* **2005**, *35*, 2095–2103. [CrossRef]

120. Negro, C.; Fuente, E.; Sánchez, L.M.; Blanco, Á.; Tijero, J. Evaluation of an alternative flocculation system for manufacture of fiber–cement composites. *Ind. Eng. Chem. Res.* **2006**, *45*, 6672–6678. [CrossRef]
121. Negro, C.; Blanco, A.; Fuente, E.; Sánchez, L.; Tijero, J. Evaluation of a flocculation dual system as a novel alternative for fiber-cement manufacture: Effect on product strength. *Chem. Eng. Process.* **2008**, *47*, 755–760. [CrossRef]
122. Tonoli, G.; Rodrigues Filho, U.; Savastano, H., Jr.; Bras, J.; Belgacem, M.; Lahr, F.R. Cellulose modified fibres in cement based composites. *Compos. Part A Appl. Sci. Manuf.* **2009**, *40*, 2046–2053. [CrossRef]
123. Korhonen, M.H.J.; Laine, J. Flocculation and retention of fillers with nanocelluloses. *Nord. Pulp Pap. Res. J.* **2014**, *29*, 119–128. [CrossRef]
124. Diab, M.; Curtil, D.; El-shinnawy, N.; Hassan, M.L.; Zeid, I.F.; Mauret, E. Biobased polymers and cationic microfibrillated cellulose as retention and drainage aids in papermaking: Comparison between softwood and bagasse pulps. *Ind. Crop. Prod.* **2015**, *72*, 34–45. [CrossRef]
125. Brockman, A.C.; Hubbe, M.A. Charge reversal system with cationized cellulose nanocrystals to promote dewatering of a cellulosic fiber suspension. *Cellulose* **2017**, *24*, 4821–4830. [CrossRef]
126. Sun, X.; Danumah, C.; Liu, Y.; Boluk, Y. Flocculation of bacteria by depletion interactions due to rod-shaped cellulose nanocrystals. *Chem. Eng. J.* **2012**, *198*, 476–481. [CrossRef]
127. Suopajärvi, T.; Liimatainen, H.; Hormi, O.; Niinimäki, J. Coagulation–flocculation treatment of municipal wastewater based on anionized nanocelluloses. *Chem. Eng. J.* **2013**, *231*, 59–67. [CrossRef]
128. Suopajärvi, T.; Koivuranta, E.; Liimatainen, H.; Niinimäki, J. Flocculation of municipal wastewaters with anionic nanocelluloses: Influence of nanocellulose characteristics on floc morphology and strength. *J. Environ. Chem. Eng.* **2014**, *2*, 2005–2012. [CrossRef]
129. Yu, H.-Y.; Zhang, D.-Z.; Lu, F.-F.; Yao, J. New approach for single-step extraction of carboxylated cellulose nanocrystals for their use as adsorbents and flocculants. *ACS Sustain. Chem. Eng.* **2016**, *4*, 2632–2643. [CrossRef]
130. Yu, S.I.; Min, S.K.; Shin, H.S. Nanocellulose size regulates microalgal flocculation and lipid metabolism. *Sci. Rep. UK* **2016**, *6*, 35684. [CrossRef]
131. Sanchez-Salvador, J.; Balea, A.; Monte, M.; Blanco, A.; Negro, C. Study of the reaction mechanism to produce nanocellulose-graft-chitosan polymer. *Nanomaterials* **2018**, *8*, 883. [CrossRef]
132. Balea, A.; Monte, M.C.; Negro, C.; Blanco, A. Application of cellulose nanofibers to remove water-based flexographic inks from wastewaters. *Environ. Sci. Pollut. Res.* **2017**, *24*, 5049–5059. [CrossRef]
133. Voisin, H.; Bergström, L.; Liu, P.; Mathew, A. Nanocellulose-based materials for water purification. *Nanomaterials* **2017**, *7*, 57. [CrossRef]
134. Liang, H.; Hu, X. A quick review of the applications of nano crystalline cellulose in wastewater treatment. *J. Bioresour. Bioprod.* **2016**, *1*, 199–204.
135. Shak, K.P.Y.; Pang, Y.L.; Mah, S.K. Nanocellulose: Recent advances and its prospects in environmental remediation. *Beilstein J. Nanotechnol.* **2018**, *9*, 2479–2498. [CrossRef]
136. Sehaqui, H.; Mautner, A.; de Larraya, U.P.; Pfenninger, N.; Tingaut, P.; Zimmermann, T. Cationic cellulose nanofibers from waste pulp residues and their nitrate, fluoride, sulphate and phosphate adsorption properties. *Carbohyd. Polym.* **2016**, *135*, 334–340. [CrossRef] [PubMed]
137. Hohenthal, C.; Ovaskainen, M.; Bussini, D.; Sadocco, P.; Pajula, T.; Lehtinen, H.; Kautto, J.; Salmenkivi, K. Final assessment of nano enhanced new products. In *SUNPAP (Scale-up Nanoparticles in Modern Papermaking), Oct.31, 2012. CTT Technical Research Center of Finland, InnovHub-SSCCP, Poyry Management Consulting Oy. Funded by European Community's 7th Frame Work Programme under Grant Agreement n° 228802*; VTT Technical Research Centre of Finland: Espoo, Findland, 2012.
138. De Figueirêdo, M.C.B.; de Freitas Rosa, M.; Ugaya, C.M.L.; de Souza, M.d.S.M.; da Silva Braid, A.C.C.; de Melo, L.F.L. Life cycle assessment of cellulose nanowhiskers. *J. Clean. Prod.* **2012**, *35*, 130–139. [CrossRef]
139. Hervy, M.; Evangelisti, S.; Lettieri, P.; Lee, K.-Y. Life cycle assessment of nanocellulose-reinforced advanced fibre composites. *Compos. Sci. Technol.* **2015**, *118*, 154–162. [CrossRef]
140. Piccinno, F.; Hischier, R.; Seeger, S.; Som, C. Predicting the environmental impact of a future nanocellulose production at industrial scale: Application of the life cycle assessment scale-up framework. *J. Clean. Prod.* **2018**, *174*, 283–295. [CrossRef]
141. Li, Q.Q.; McGinnis, S.; Sydnor, C.; Wong, A.; Renneckar, S. Nanocellulose life cycle assessment. *ACS Sustain. Chem. Eng.* **2013**, *1*, 919–928. [CrossRef]

142. *Nanocellulose Investment and Pricing Guide 2019*; Future Markets, Inc.: Dublin, Ireland, 2019.
143. Habibi, Y.; Lucia, L.A.; Rojas, O.J. Cellulose nanocrystals: Chemistry, self-assembly, and applications. *Chem. Rev.* **2010**, *110*, 3479–3500. [CrossRef]
144. Merayo, N.; Balea, A.; de la Fuente, E.; Blanco, Á.; Negro, C. Interactions between cellulose nanofibers and retention systems in flocculation of recycled fibers. *Cellulose* **2017**, *24*, 677–692. [CrossRef]
145. Merayo, N.; Balea, A.; de la Fuente, E.; Blanco, Á.; Negro, C. Synergies between cellulose nanofibers and retention additives to improve recycled paper properties and the drainage process. *Cellulose* **2017**, *24*, 2987–3000. [CrossRef]
146. Alonso, A.; Negro, C.; Blanco, A.; San Pío, I. Application of advanced data treatment to predict paper properties. *Math. Comput. Model. Dyn. Syst.* **2009**, *15*, 453–462. [CrossRef]
147. Blanco, A.; Negro, C.; Hooimeijer, A.; Tijero, J. Polymer optimization in paper mills by means of a particle size analyser: An alternative to zeta potential measurements. *Appita J.* **1996**, *49*, 113–116.
148. Rasteiro, M.; Garcia, F.; Ferreira, P.; Blanco, A.; Negro, C.; Antunes, E. Evaluation of flocs resistance and reflocculation capacity using the lds technique. *Powder Technol.* **2008**, *183*, 231–238. [CrossRef]
149. Lopez-Exposito, P.; Negro, C.; Blanco, A. Direct estimation of microalgal flocs fractal dimension through laser reflectance and machine learning. *Algal Res.* **2019**, *37*, 240–247. [CrossRef]
150. Tonoli, G.; Savastano, H., Jr.; Fuente, E.; Negro, C.; Blanco, A.; Lahr, F.R. Eucalyptus pulp fibres as alternative reinforcement to engineered cement-based composites. *Ind. Crop. Prod.* **2010**, *31*, 225–232. [CrossRef]

polymers

MDPI

Article

Preparation and Characterization of Microcellulose and Nanocellulose Fibers from *Artemisia Vulgaris* Bast

Kai Nie [1,2], Yan Song [1,2], Shaoyang Liu [3], Guangting Han [1], Haoxi Ben [1], Arthur J. Ragauskas [1,4,5] and Wei Jiang [1,2,*]

1 State Key Laboratory of Bio-Fibers and Eco-Textiles, Qingdao University, Qingdao 266071, China; 15021329163@163.com (K.N.); 18765915091@163.com (Y.S.); kychgt@qdu.edu.cn (G.H.); benhaoxi@163.com (H.B.); aragausk@utk.edu (A.J.R.)
2 College of Textile & Clothing, Qingdao University, Qingdao 266071, China
3 Department of Chemistry and Physics, Troy University, Troy, AL 36082, USA; lius@troy.edu
4 Department of Forestry, Wildlife, and Fisheries, Department of Chemical and Biomolecular Engineering, University of Tennessee, Knoxville, TN 37996, USA
5 Oak Ridge National Lab, Oak Ridge, TN 37831, USA
* Correspondence: weijiangqd@qdu.edu.cn

Received: 25 April 2019; Accepted: 16 May 2019; Published: 19 May 2019

Abstract: *Artemisia vulgaris* is an economic plant that is spreading widely in central China. Its unused bast generates a large amount of biomass waste annually. Utilizing the fibers in *Artemisia vulgaris* bast may provide a new solution to this problem. This research attempts to strengthen the understanding of *Artemisia vulgaris* by analyzing its fiber compositions and preparing micro- and nano-cellulose fibers, which can be used as raw materials for composites. In this work, *Artemisia vulgaris* bast powder (AP) and microcellulose and nanocellulose fibers (AMFs and ANFs) were produced and characterized by optical microscopy, transmission electron microscopy (TEM), X-ray diffraction (XRD), thermogravimetric analysis (TG), and bacteriostatic test. The results indicated that cellulose, hemicellulose, and lignin were the main components in the *Artemisia vulgaris* bast. The cellulose content reached 40.9%. The *Artemisia vulgaris* single fibers were microcellulose fibers with an average length of 850.6 μm and a diameter of 14.4 μm. Moreover, the AMF had considerable antibacterial ability with an antibacterial ratio of 36.6%. The ANF showed a length range of 250–300 nm and a diameter of 10–20 nm, and it had a higher crystallinity (76%) and a lower thermal stability (initial degradation temperature of 183 °C) compared with raw ANF (233 °C). This study provides fundamental information on *Artemisia vulgaris* bast cellulose for its subsequent utilization.

Keywords: *Artemisia vulgaris*; microcellulose fiber; nanocellulose fibers; natural fibers

1. Introduction

Natural fibers are composed of cellulose, which is the most abundant renewable biomaterial on earth and is completely biodegradable [1,2]. *Artemisia vulgaris* likely originated from eastern Asia [3] and is a very common weed with a strong aroma. Most *Artemisia* species are found growing abundantly throughout temperate climate areas and are cold-resistant [4]. They are widely distributed in most provinces and autonomous regions in China. Their extracts have been used throughout history to control insect pests [5]. At present, *Artemisia vulgaris* is mainly used in health care products and function foods because of the benefits of its volatile oils and flavonoids. There have been many reports on *Artemisia vulgaris*' medicinal properties, chemical compositions, pharmacological effects, clinical applications, functional food applications, as well as processes and quality control methods [6].

However, all of the above applications only used its leaves, and the other parts were abandoned as wastes.

It should be noticed that *Artemisia vulgaris* bast contains a considerable amount of cellulose, which could be a good source of microcellulose and nanocellulose fibers. Microcellulose fibers from agricultural residues can be used as a reinforcing material in polymer composites, which have attracted increasing interest in recent years [7–10]. Microcellulose fibers can also be used in biomedicine, paper packaging, food additives, electronic devices, and many other fields [11]. Nanocellulose fiber is a renewable nanomaterial with superior properties, such as unique optical, rheological, and mechanical properties. It is light, biodegradable, biocompatible, and recyclable, which provide it with a bright future for a wide range of applications [12–14].

However, there is little research on the utilization of *Artemisia vulgaris* residues, especially the abundant cellulose in its bast. The production and characterization of mirco- and nanocellulose fibers from *Artemisia vulgaris* may help utilize its waste bast and improve its economic feasibility. In addition, the cellulose fibers separated from *Artemisia vulgaris* may still retain some functions of its leaves, which might add extra value to the fibers.

In the current work, micro- and nanocellulose fibers were produced from *Artemisia vulgaris* bast. The fiber properties, including their antibacterial function, were characterized. This study provides a deeper understanding of *Artemisia vulgaris* cellulose fibers and their potential applications.

2. Materials and Methods

2.1. Materials

Artemisia vulgaris bast were purchased from Linyi City, Shandong Province, China. The samples were cut into 1–2 cm lengths and dried at 105 °C before the experiment. Laboratory degrade reagents (including benzene, ethanol, ammonium oxalate, sodium hydroxide, concentrated sulfuric acid, sodium chlorite, and glacial acetic acid) were used in this work.

2.2. Methods

Figure 1. briefly introduces the experimental route of this research. The fresh *Artemisia vulgaris* plant straw is dried and the bast is taken out. The micron-sized fiber (AMF) is prepared by degumming with alkali, and the nano-sized fiber (ANF) is prepared by oxidation of TEMPO. In order to understand the size information of products, TEM and OM characterization tests were performed on AMF and ANF.

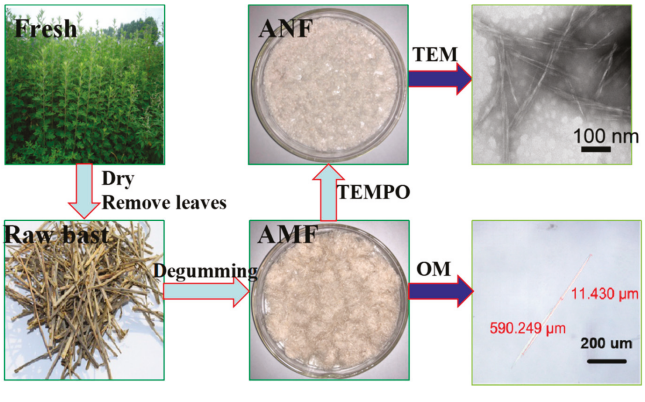

Figure 1. Flowchart of the *Artemisia vulgaris* bast microcellulose fiber (AMF) and *Artemisia vulgaris* bast nanocellulose fiber (ANF) extraction. (TEM, transmission electron microscopy. OM, optical microscopy. TEMPO, 2,2, 6,6-tetramethylpiperidine-1-oxyl).

2.2.1. Determination of Chemical Composition of the Bast

According to China's National Food Safety Standard (GB5009.3—85), a gravimetric method was used to determine the moisture content of the *Artemisia vulgaris* bast samples. The samples were processed by following China's National Textile Standard (GB5889—86) to determine major chemical compositions, including lipid, water-soluble substances, pectin, lignin, hemicellulose, and cellulose, of the *Artemisia vulgaris* bast. All experiments were performed independently in triplicate and the results given are the means of the results.

2.2.2. Preparation of *Artemisia Vulgaris* Bast Cellulose Fiber (Microcellulose Fiber)

In order to obtain *Artemisia vulgaris* bast cellulose powder (AMF), the dried bast was cut, crushed, and passed through a 60 mesh screen. In the experiment, 2.0 g of *Artemisia vulgaris* bast powder was extracted for 3 h with a mixture of 40 mL benzene and 20 mL ethanol at 90 °C in a Soxhlet extractor. The products were washed with methanol and deionized water. A bleaching process was conducted with 0.24 g of sodium chlorite and 0.2 mL of glacial acetic acid in 30 mL aqueous solution under aeration for 3 h at 75 °C (adding the same amounts of chemicals per hour). The bleached bast powder was boiled in an NaOH aqueous solution (20 g/L) for 3 h, then washed until neutral to obtain *Artemisia vulgaris* bast cellulose powder (AMF) [15].

2.2.3. Preparation of *Artemisia Vulgaris* Bast Nanocellulose Fiber

First, 1.0 g of the *Artemisia vulgaris* bast cellulose powder (AMF) was soaked in 30 mL dimethyl sulfoxide (DMSO, which has a certain swelling effect on cellulose) for 5 h while stirring at 600 r/min at 60 °C, filtered, and washed 3 times with distilled water, and then dried to a constant weight. After, the treated powder was added to a mixture of TEMPO (2,2, 6,6-tetramethylpiperidine-1-oxyl) (0.03%) and KBr (0.6%) at a bath ratio of 1:100 and placed at 4 °C for 12 h. Next, sodium hypochlorite (0.4%) was added into the bath while stirring for 2 h. The pH was adjusted to 10.5 with 0.1 mol/L hydrochloric acid during the whole 2 h reaction. Methanol was added to terminate the reaction when the pH stabilized. Finally, the suspension of *Artemisia vulgaris* bast cellulose powder was obtained by adjusting pH to neutral with 0.1 mol/L hydrochloric acid. The suspension was then centrifuged at 12,000 r/min for 10 min in a high-speed centrifuge. The upper supernatant was removed, fresh distilled water was added, and the centrifuging was repeated 6 times to obtain a gelatinous precipitate. The precipitate was treated in distilled water at 4 °C at a bath ratio of 1:100 and dispersed at a speed of 15,000 r/min for 5 min using a high-speed disperser to obtain an *Artemisia vulgaris* nanocellulose fiber suspension. The suspension was frozen at −20 °C for 12 h, then freeze-dried for 24 h [16].

2.2.4. Bacteriostatic Test and Analysis

According to Chinese National Standard (Evaluation of antibacterial properties of textiles) (GB/T 20944), an oscillating method was used to determine the antibacterial properties of raw bast, AMF and ANF. Cotton fiber without antibacterial activity was selected as the control. The selected strain was *Escherichia coli*, and all samples and equipment were subjected to high-temperature and high-pressure sterilization before use. Two parallel samples were tested of each type of material. The formula for calculating the bacteriostatic rate is

$$Br\% = \left(\frac{Qc - Qx}{Qc}\right) \quad (1)$$

where $Br\%$ is bacteriostatic rate; Qc is the colony quantities of cotton fibers; and Qx is the colony quantities of samples (raw bast, AMF, ANF).

2.2.5. Optical Microscopy (OM) Analysis

The appearance and fiber dimensional size of the AP (*Artemisia vulgaris* bast powder), AMF, and ANF samples were observed by optical microscopy (OM, LeicaDM2700M, Wetzlar, Germany).

2.2.6. SEM Analysis

The microstructure, surface morphology, and cross-section of the nanocrystal cellulose were observed by scanning electron microscopy. After being coated with gold, samples were observed and photographed with the microscope operating at 10 kV (SEM, JEM-1200EX, Tokyo, Japan).

2.2.7. TEM Analysis

Artemisia vulgaris bast nanocellulose fiber samples were monitored by transmission electron microscopy (TEM, JEM-1200EX microscope, Tokyo, Japan) to measure its size. One percent of the ANF liquid was dispersed with ultrasonic equipment. One drop of the suspension was placed on carbon film-covered copper grids (400 mesh). The grid was dried in an oven at 70 °C before being observed and photographed.

2.2.8. FTIR Analysis

In order to obtain the chemical composition changes of *Artemisia vulgaris* bast fibers, samples of *Artemisia vulgaris* bast, *Artemisia vulgaris* bast cellulose, and *Artemisia vulgaris* bast cellulose nanocrystal were investigated with Fourier transform infrared spectroscopy (FTIR, Thermo Fisher Scientific NICOLET 5700, Waltham, MA, USA) in a wavenumber range of 500–4000 cm^{-1}. A KBr disc mixed with 1% milled samples was pressed before the FTIR analysis.

2.2.9. XRD Analysis

An X-ray diffraction (XRD) test was carried out to obtain the change in crystallinity index (CrI) of cellulose samples during the preparation process. The crystallinity index of samples was calculated using the height ratios between the intensities of the crystalline peak (I002-Iamorph) and total intensity (I002) [17,18]. The samples were scanned by a Bruker D8 Advance X-ray diffractometer (under a voltage of 40 kV and a current of 50 mA) (Bruker, Karlsruhe, Germany) in the range of 5° to 50°. The maximum intensity of the natural cellulose crystallinity lattice (002) diffraction was taken at $2\theta = 22°$, and the maximum intensity of the amorphous phase was taken at $2\theta = 18°$ [19].

2.2.10. TG Analysis

In order to understand the change in thermodynamic properties during the preparation process of ANF, thermogravimetric analysis was carried out from room temperature to 700 °C under nitrogen atmosphere with a constant heating rate of 10 °C/min on a TGA (Pyris, PerkinElmer, Waltham, MA, USA).

3. Results and Discussion

3.1. Chemical Compositions Analysis

The major chemical composition of *Artemisia vulgaris* bast included cellulose, lignin, and hemicellulose, which composed 40.92%, 28.25%, and 29.10% of the bast (*w/w*), respectively, as shown in Table 1. Collectively, they accounted for 98.2% of the bast. In Chinese medicine producing processes, producers often discard the cellulose in *Artemisia vulgaris* after extracting pharmaceutical ingredients. This is a waste of the most abundant natural resource in the bast; the residue from the process may extract valuable cellulose with functions such as antibacterial abilities. The cellulose content of *Artemisia vulgaris* was equivalent with hardwood (43.71%), and a little lower than kenaf (56.81%), as listed in Table 1. It is known that kenaf and wood are two common materials to produce cellulose fibers to

make composite [20–23]. Therefore, *Artemisia vulgaris* bast would also be a promising resource to make micro- and nanocellulose fibers.

Table 1. Chemical compositions of *Artemisia vulgaris* bast, kenaf bast, and hardwood.

Species	Hemicellulose	Lignin	Cellulose	Lipid	Water Soluble Matter	Pectin	Gum Content
Artemisia vulgaris bast	29.10% ± 0.97%	28.25% ± 0.45%	40.92% ± 0.70%	1.05% ± 0.04%	13.6% ± 2.41%	3.2% ± 0.34%	35.90% ± 1.16%
Kenaf bast [20–22]	15.75% ± 1.07%	15.65% ± 1.53%	56.81% ± 2.95%	8.42% ± 0.08%	6.28% ± 0.23%	4.43% ± 0.39%	28.46% ± 0.95%
Wood [23]	35.97% ± 3.88%	26.24% ± 2.41%	43.71% ± 2.10%	2.11% ± 1.42%	-	-	-

3.2. Morphology of the Samples and Powder/Fiber Size Analysis

Figure 2 shows the appearance of freeze-dried samples of AP, AMF, and ANF. The raw *Artemisia vulgaris* bast powder was light yellow, which contained more plant phloem substances. After the bleaching and degumming processes, the color of the AMF became whiter, and rod-like substances increased; the ANF looked even finer and the size of the fiber was further reduced.

(**a**) (**b**) (**c**)

Figure 2. Photographs of (**a**) raw *Artemisia vulgaris* bast powder; (**b**) *Artemisia vulgaris* bast microcellulose fibers; (**c**) freeze-dried powders of nanocellulose fibers.

As illustrated in Figure 3, the surface of the raw AP was very rough, and large number of gum materials were attached to it. During the production of AMF, a large number of colloids, e.g., pectin, lignin, and hemicellulose, were removed through the treatment, and many finer fibers were obtained (Figure 3b). The NaOH boiling separated the raw fibers and shortened them. To determine the length and fineness of AMF, 100 single fibers were randomly selected and measured under an optical microscope. The dates of length, diameter, and aspect ratio of micro- and nano-fibers are shown in Table 2. Most fibers had lengths between 600–1000 μm. The averages of the length and diameter of the fibers were 850.6 ± 119.1 μm and 14.3 ± 1.9 μm, respectively. The aspect ratio was about 60. Although it is too short for the traditional textile industry, the fiber is very suitable for making nanocellulose. The cost and difficulty of micron size to nanometer size is greatly reduced with this fiber length. The larger aspect ratio could provide a large specific surface area, which could improve the reinforcing effect for polymer composite application [24].

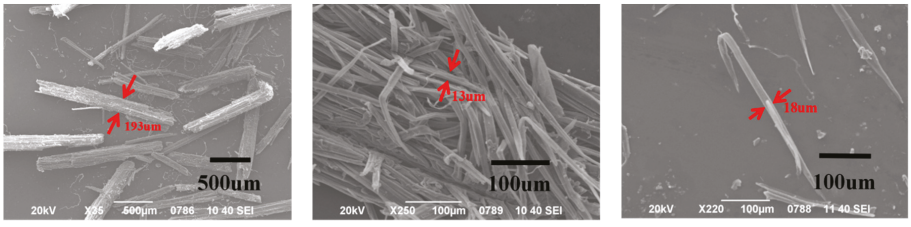

(**a**) (**b**) (**c**)

Figure 3. SEM images of (**a**) *Artemisia vulgaris* bast; (**b**,**c**) *Artemisia vulgaris* bast microcellulose fibers.

Table 2. The length and diameter of micro- and nano-fibers.

Species	Length				Diameter				Aspect Ratio
	Avg.	Max.	Min.	SD	Avg.	Max.	Min.	SD	
AMF	850.6 µm	1212 µm	400.2 µm	119.1	14.3 µm	15.8 µm	12.3 µm	1.9	59.5
ANF	260.5 nm	307.7 nm	207.7 nm	33.6	11.4 nm	15.7 nm	7.7 nm	1.9	22.8

The morphology analysis of the ANFs was carried out with a TEM (Figure 4). It can be observed that the ANFs obtained through TEMPO (2,2, 6,6-tetramethylpiperidine-1-oxyl) oxidative hydrolysis were rod-shaped and evenly dispersed. To analyze the size of ANFs, 100 single fibers were randomly selected and observed. The typical size of an individual ANF was about 250–300 nm long and 10–20 nm wide with an aspect ratio of 15–25.

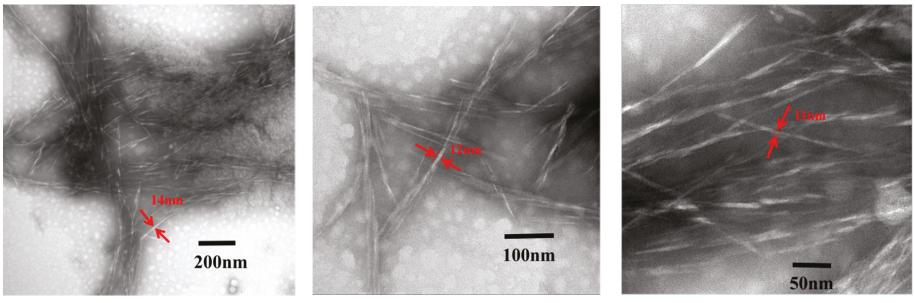

(**a**) (**b**) (**c**)

Figure 4. TEM images under different ruler conditions ((**a**), 200 nm; (**b**), 100 nm; (**c**), 50 nm) of *Artemisia vulgaris* bast nanocellulose fibers.

3.3. Antibacterial Properties

Artemisia vulgaris is well known by its high antibacterial property, but the data were mostly obtained from the extracts of its leaves [25]. The study of the antibacterial ability [26,27] of raw bast powder, AMF and ANF, would offer additional information for their potential functional applications. Figure 5 shows the bacteriostatic rates of the three samples. The original *Artemisia vulgaris* bast powder had good antibacterial activity against *Escherichia coli*, and the antibacterial rate reached 76%. After the degumming and TEMPO oxidation processes, the antibacterial rates of AMF and ANF decreased to 36.6% and 18.3%, respectively. It suggests that the effective ingredients against bacteria were partially removed by the treatments. However, some active ingredients did remain on the fibers and they still maintained an extent of antibacterial ability. So, the AMF and ANF from *Artemisia vulgaris* would be especially useful for applications preferring antibacterial function, which may add extra value to the fibers.

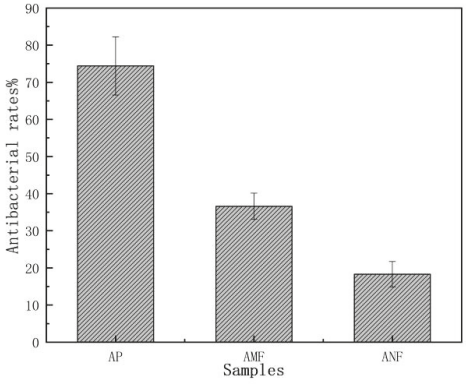

Figure 5. The antibacterial rates of *Artemisia vulgaris* bast powder, microcellulose fibers, and *Artemisia vulgaris* bast nanocellulose fibers.

3.4. FTIR Spectroscopy Analysis

To understand the chemical composition change during the process, FTIR spectra of the AP, AMF, and ANF were obtained (Figure 6). The composition change was manifested by the change of certain absorption peaks which can be linked to certain components in the samples [28,29]. The absorption peak at 1062 cm^{-1} represents the C–O single bond in cellulose [30]. Their relative intensities did not change after the treatments, suggesting the cellulose in the *Artemisia vulgaris* did not change or degrade during the process. On the other side, the absorption peak at 1739 cm^{-1}, which corresponds to the C=O bond in pectin or hemicellulose, disappeared on the AMF and ANF spectra. This indicates that the pectin and hemicellulose contents were effectively removed by the treatments [31]. The peaks at 1244 cm^{-1}, 1522 cm^{-1}, and 1638 cm^{-1} represent the C–O stretching vibration, benzene ring vibration, and C=C stretching vibration, respectively, in lignin. They significantly were reduced during the process, suggesting a large portion of lignin was removed. The β-(1, 4) glycosidic linkage between the monosaccharides of the cellulose characteristically peaked at 896 cm^{-1}. In summary, cellulose was retained during the process while other components in the bast, e.g., hemicellulose and lignin, were effectively removed by the treatments.

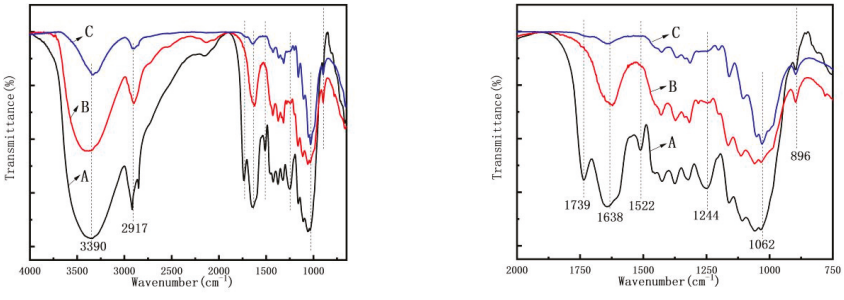

Figure 6. The FTIR spectra (**a**) of (A) *Artemisia vulgaris* bast powder; (B) *Artemisia vulgaris* bast microcellulose fiber, and (C) *Artemisia vulgaris* bast nanocellulose fiber. (**b**) A clearer view of peak changes in the 750–2000 cm^{-1} range.

3.5. Crystallinity Index of Samples

The XRD spectra of AP, AMF, and ANF are shown in Figure 7. All the samples had diffraction peaks of 2θ at 15.1° and 22.5°, which were assigned to the (110) and (200) planes of cellulose crystal, respectively [32–34]. It confirmed that the cellulose *I* crystal structure of cellulose did not degrade during the process. The crystallinity index related to mechanical properties were calculated to be 36.72%, 66.71%, and 76.33% for AP, AMF and ANF, respectively. The higher crystallinity of the nanocellulose was because of the removal of amorphous components, such as hemicellulose, lignin, and less-perfect regions of cellulose.

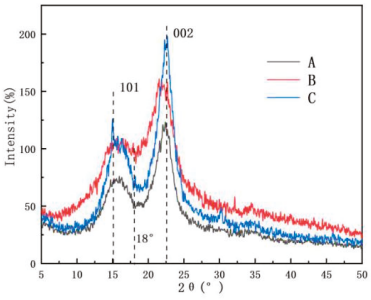

Figure 7. XRD spectra of (A) *Artemisia vulgaris* bast powder; (B) *Artemisia vulgaris* bast microcellulose fiber, and (C) *Artemisia vulgaris* bast nanocellulose fiber.

3.6. TG Analysis

The thermal stability of AP, AMF, and ANF under a nitrogen environment was investigated by thermogravimetric (TG) analysis, as illustrated in Figure 8. The analysis of the thermal stability of the fibers was essential to characterize the limit of their processing temperature for various applications [35]. The initial degradation temperature, the maximum degradation rate temperature, and the termination degradation temperature of the ANF were 183 °C, 298 °C, and 485 °C, respectively, which were far lower than those of the AMF (233 °C, 341 °C, and 655 °C, respectively). Regarding the mass change rate (Figure 8b), the degradation rate of ANF was much lower than those of AP and AMF. Figure 8a also shows that ANF had about 21% mass residue after the thermal degradation, which was much higher than the other two samples. The slower degradation rate (between about 200–500 °C) and higher residue were probably due to the removal of amorphous regions in the ANF cellulose, which only left well organized crystal areas in the fibers.

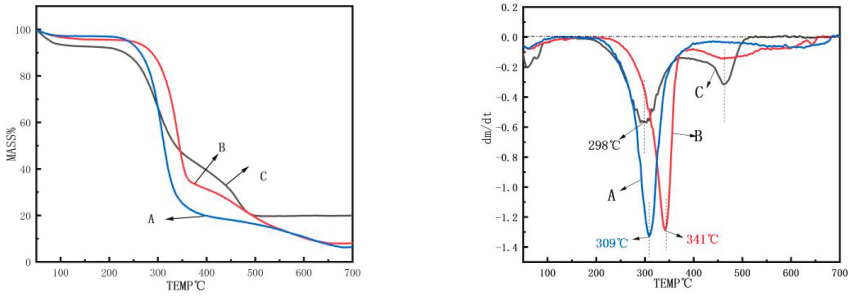

(**a**) (**b**)

Figure 8. (**a**) TG spectra and (**b**) the first derivative TG thermograms of (A) *Artemisia vulgaris* bast powder; (B) *Artemisia vulgaris* bast microcellulose fiber, and (C) *Artemisia vulgaris* bast nanocellulose fiber.

The thermal stability change was probably due to the presence of three main reasons: First, compared to AMF, the particle size of ANF was reduced, the specific surface area was increased, and the exposed carbon and reactive group activity were increased. Second, the fiber segment was broken by the treatments, which caused low molecular weight segments and breakpoint defects in ANF [36,37]. They were more susceptible to thermal degradation. Last, the lower stability of TEMPO-oxidized cellulose nanofibers might also be attributed to the introduction of the carboxylate group on the cellulose surface [38]. As a result, the thermal stability of ANF was lowered.

4. Conclusions

In this work, the micro- and nanocellulose fibers of *Artemisia vulgaris* bast were successfully obtained through an alkali degumming process and TEMPO chemical treatments, respectively. The FTIR and XRD analyses showed that non-cellulosic components were effectively removed during the process and the crystallinities of the samples were gradually increased. It was found that the obtained microcellulose fiber had an average length and diameter of 850 μm and 14.3 μm, respectively, while the nanocellulose fibers showed a length range of 250–300 nm and a diameter of 10–20 nm with good thermal property and high crystallinity. Both micro- and nano-fibers retained certain antibacterial properties. The results suggest that *Artemisia vulgaris* bast waste is a good natural resource for efficient production of micro- and nanocellulose fiber with good performance, which could provide additional value to the economic plant.

Author Contributions: Funding acquisition, G.H.; Investigation, K.N., Y.S. and H.B.; Methodology, A.J.R.; Project administration, W.J.; Supervision, W.J.; Writing—original draft, K.N. and Y.S.; Writing—review and editing, S.L. and W.J.

Acknowledgments: This research was financially supported by the State Key Laboratory of Bio-Fibers and Eco-Textiles (Qingdao University) and the Natural Science Foundation of Shandong Province (ZR2017BEM045, ZR201807061133).

Conflicts of Interest: The authors declare no conflict of interest.

References

1. Thomas, M.G.; Abraham, E.; Jyotishkumar, P.; Maria, H.J.; Pothen, L.A.; Thomas, S. Nanocelluloses from jute fibres and their nanocomposites with natural rubber: Preparation and characterisation. *Int. J. Biol. Macromol.* **2015**, *81*, 768–777. [CrossRef]
2. Jiang, W.; Song, Y.; Liu, S.; Ben, H.; Zhang, Y.; Zhou, C.; Han, G.; Ragauskas, A.J. A green degumming process of ramie. *Ind. Crops Prod.* **2018**, *120*, 131–134. [CrossRef]
3. Hwang, Y.S. Isolation and identification of mosquito repellents in *Artemisia vulgaris*. *J. Chem. Ecol.* **1985**, *11*, 1297–1306. [CrossRef] [PubMed]
4. Wang, J. Repellent and fumigant activity of essential oil from *Artemisia vulgaris* to *Tribolium castaneum* (Herbst) (Coleoptera: Tenebrionidae). *J. Stored Prod. Res.* **2006**, *42*, 339–347. [CrossRef]
5. Ding, W.; Liu, H.; Li, L.S. The main dtratagems and technology for stored product pest control in ancient China. *J. Southwest Agric. Univ.* **2000**, *22*, 335–338.
6. Barney, J.N.; Hay, A.G.; Weston, L.A. Isolation and characterization of allelopathic volatiles from mug wort (*Artemisia vulgaris*). *J. Chem. Ecol.* **2005**, *31*, 247–265. [CrossRef]
7. Hassan, M.L.; Hassan, E.A.; Oksman, K.N. Effect of pretreatment of bagasse fibers on the properties of chitosan/microfibrillated cellulose nanocomposites. *J. Mater. Sci.* **2011**, *46*, 1732–1740. [CrossRef]
8. Logaranjan, K. Shape- and size-controlled synthesis of silver nanoparticles using aloe vera plant extract and their antimicrobial activity. *Nanoscale Res. Lett.* **2016**, *11*, 520. [CrossRef] [PubMed]
9. Theivasanthi, T. Synthesis and characterization of cotton fiber-based nanocellulose. *Int. J. Biol. Macromol.* **2018**, *109*, 832–836. [CrossRef]
10. Oliver-Borrachero, B.; Sánchez-Caballero, S.; Fenollar, O. Natural-fiber-reinforced polymer composites for automotive parts manufacturing. *Key Eng. Mater.* **2019**, *793*, 9–16. [CrossRef]
11. Siró, I.; Plackett, D. Microfibrillated cellulose and new nanocomposite materials: A review. *Cellulose* **2010**, *17*, 459–494. [CrossRef]

12. Prasad, V.; Suresh Kumar, P. A review of recent developments in natural fiber composites and their mechanical, thermal & machinabilty properties. *Adv. Mater. Res.* **2018**, *1148*, 61–71.
13. Ghasemi, S. Reinforcement of natural fiber yarns by cellulose nanomaterials: A multi-scale study. *Ind. Crops Prod.* **2018**, *111*, 471–481. [CrossRef]
14. Song, Y.; Jiang, W.; Zhang, Y.; Wang, H.; Zou, F.; Yu, K.; Han, G. A novel process of nanocellulose extraction from kenaf bast. *Mater. Res. Express* **2018**, *5*, 085032. [CrossRef]
15. Jiang, W.; Han, G.; Zhang, Y.; Wang, M. Fast compositional analysis of ramie using near-infrared spectroscopy. *Carbohydr. Polym.* **2010**, *81*, 937–941. [CrossRef]
16. Koga, H.; Saito, T.; Kitaoka, T.; Nogi, M.; Suganuma, K.; Isogai, A. Transparent, Conductive, and Printable Composites Consisting of TEMPO-Oxidized Nanocellulose and Carbon Nanotube. *Biomacromolecules* **2013**, *14*, 1160–1165. [CrossRef]
17. Wang, L.; Han, G.; Zhang, Y. Comparative study of composition, structure and properties of *Apocynum venetum* fibers under different pretreatments. *Carbohydr. Polym.* **2007**, *69*, 391–397. [CrossRef]
18. Maache, M. Characterization of a novel natural cellulosic fiber from *Juncus effusus* L. *Carbohydr. Polym.* **2017**, *171*, 163–172. [CrossRef]
19. El Miri, N.; Abdelouahdi, K.; Zahouily, M.; Fihri, A.; Barakat, A.; Solhy, A.; El Achaby, M. Bio-nanocomposite films based on cellulose nanocrystals filled polyvinyl alcohol/chitosan polymer blend. *J. Appl. Polym. Sci.* **2015**, *132*. [CrossRef]
20. Akil, H.M. Kenaf fiber reinforced composites: A review. *Mater. Des.* **2011**, *32*, 4107–4121. [CrossRef]
21. Serizawa, S.; Inoue, K.; Iji, M. Kenaf-fiber-reinforced poly(lactic acid) used for electronic products. *J. Appl. Polym. Sci.* **2010**, *100*, 618–624. [CrossRef]
22. Nishino, T.; Hirao, K.; Kotera, M.; Nakamae, K.; Inagaki, H. Kenaf reinforced biodegradable composite. *Compos. Sci. Technol.* **2003**, *63*, 1281–1286. [CrossRef]
23. Zhou, C. Prediction of mixed hardwood lignin and carbohydrate content using ATR-FTIR and FT-NIR. *Carbohydr. Polym.* **2015**, *121*, 336–341. [CrossRef]
24. Silvério, H.A.; Neto, W.P.F.; Dantas, N.O.; Pasquini, D. Extraction and characterization of cellulose nanocrystals from corncob for application as reinforcing agent in nanocomposites. *Ind. Crops Prod.* **2013**, *44*, 427–436. [CrossRef]
25. Pandey, B.P.; Thapa, R.; Upreti, A. Chemical composition, antioxidant and antibacterial activities of essential oil and methanol extract of, artemisia vulgaris, and, gaultheria fragrantissima, collected from nepal. *Asian Pac. J. Trop. Med.* **2017**, *10*, 952–959. [CrossRef]
26. Bajalan, I.; Rouzbahani, R.; Pirbalouti, A.G.; Maggi, F. Chemical composition and antibacterial activity of Iranian lavandula×hybrida. *Chem. Biodivers.* **2017**, *14*, e1700064. [CrossRef]
27. Frydrysiak, E.; Śmigielski, K.; Zabielska, J.; Kunicka-Styczyńska, A.; Frydrysiak, M. Antibacterial activity of essential oils potentially used for natural fiber pantiliner textronic system development. *Procedia Eng.* **2017**, *200*, 416–421. [CrossRef]
28. Abraham, E. Extraction of nanocellulose fibrils from lignocellulosic fibres: A novel approach. *Carbohydr. Polym.* **2011**, *86*, 1468–1475. [CrossRef]
29. Rwawiire, S.; Tomkova, B. Morphological, thermal, and mechanical characterization of *Sansevieria trifasciata* fibers. *J. Nat. Fibers* **2015**, *12*, 201–210. [CrossRef]
30. Sun, B.L. Application of NIR spectroscopy to estimate of MFA and fiber length of *Neosinocalamus affinis*. *Spectrosc. Spectr. Anal.* **2011**, *31*, 3251–3255.
31. Kavkler, K. FTIR spectroscopy of biodegraded historical textiles. *Polym. Degrad. Stab.* **2011**, *96*, 574–580. [CrossRef]
32. Song, Y.; Han, G.; Li, M.; Jiang, W. Performance analysis of kudzu fiber prepared by using combined steam explosion and chemical degumming. *J. Nat. Fibers* **2017**, *14*, 759–768. [CrossRef]
33. Yadav, M.; Chiu, F.C. Cellulose nanocrystals reinforced k-carrageenan based UV resistant transparent bionanocomposite films for sustainable packaging applications. *Carbohydr. Polym.* **2019**, *211*, 181–194. [CrossRef]
34. Liu, Z.; Sun, X.; Hao, M.; Huang, C.; Xue, Z.; Mu, T. Preparation and characterization of regenerated cellulose from ionic liquid using different methods. *Carbohydr. Polym.* **2015**, *117*, 99–105. [CrossRef]
35. Magniez, K. Overcoming interfacial affinity issues in natural fiber reinforced polylactide biocomposites by surface adsorption of amphiphilic block copolymers. *ACS Appl. Mater. Interfaces* **2013**, *5*, 276–283. [CrossRef]

36. Dai, H.; Ou, S.; Huang, Y.; Huang, H. Utilization of pineapple peel for production of nanocellulose and film application. *Cellulose* **2018**, *25*, 1743–1756. [CrossRef]
37. Shahabi-Ghahafarrokhi, I.; Khodaiyan, F.; Mousavi, M. Preparation and characterization of nanocellulose from beer industrial residues using acid hydrolysis/ultrasound. *Fibers Polym.* **2015**, *16*, 529–536. [CrossRef]
38. Fukuzumi, H.; Saito, T.; Okita, Y.; Isogai, A. Thermal stabilization of tempo-oxidized cellulose. *Polym. Degrad. Stab.* **2010**, *95*, 1502–1508. [CrossRef]

polymers

MDPI

Article

One-Pot Method of Synthesizing TEMPO-Oxidized Bacterial Cellulose Nanofibers Using Immobilized TEMPO for Skincare Applications

Seung-Hyun Jun, Sun-Gyoo Park and Nae-Gyu Kang *

LG Household and Health Care R&D Center, Seoul 100-859, Korea; junsh@lghnh.com (S.-H.J.); skparke@lghnh.com (S.-G.P.)

* Correspondence: ngkang@lghnh.com; Tel.: +82-2-6980-1533

Received: 23 May 2019; Accepted: 12 June 2019; Published: 14 June 2019

Abstract: In the skincare field, water-dispersed bacterial cellulose nanofibers synthesized via an oxidation reaction using 2,2,6,6–tetramethyl–1–piperidine–N–oxy radical (TEMPO) as a catalyst are promising bio-based polymers for engineered green materials because of their unique properties when applied to the surface of the skin, such as a high tensile strength, high water-holding capacity, and ability to block harmful substances. However, the conventional method of synthesizing TEMPO-oxidized bacterial cellulose nanofibers (TOCNs) is difficult to scale due to limitations in the centrifuge equipment when treating large amounts of reactant. To address this, we propose a one-pot TOCN synthesis method involving TEMPO immobilized on silica beads that employs simple filtration instead of centrifugation after the oxidation reaction. A comparison of the structural and physical properties of the TOCNs obtained via the proposed and conventional methods found similar properties in each. Therefore, it is anticipated that due to its simplicity, efficiency, and ease of use, the proposed one-pot synthesis method will be employed in production scenarios to prepare production quantities of bio-based polymer nanofibers in various potential industrial applications in the fields of skincare and biomedical research.

Keywords: bacterial cellulose; surface modification; TEMPO oxidation; one-pot synthesis; immobilized TEMPO; physical property; skincare

1. Introduction

Human skin plays an essential role in preventing water loss in the body as it provides the outermost layer of protection from the external environment. In skincare applications, bio-polymers, synthetic polymers, and organic polymers are used to control formulation viscosities, transfer moisture to the skin, increase the stability of the formulation and active ingredient, and protect the skin by forming a coating on its surface [1]. In particular, bio-polymers, such as cellulose, chitosan, and polysaccharide, are known to be skin-friendly substances as they are biocompatible and biodegradable. Among these, cellulose is the most abundant bio-polymer in plants and microorganisms and possesses a number of unique properties that, depending on its origin and the extraction process, allow it to be used in various applications.

Recently, cellulose nanofibers (CNFs) have attracted wide interest due to their nanoscopic size, ease of preparation, low cost, tunable surface properties, and enhanced mechanical properties, which makes them well suited for use as drug carriers, tissue regenerating scaffolds, water purifying membranes, electrodes, supercapacitors, fluorescent probes, and flexible electronics [2]. In the field of skincare, CNFs have attracted attention as a new potential bio-material with thixotropic properties that allow it to be used for emulsion stabilization, water retention, and rheology modification applications [3].

Bacterial cellulose (BC), which is referred to as bio-cellulose in the skincare field, is a bio-based polymer that is synthesized directly from microorganisms, such as Acetobacter xylinum (*A. xylinum*). BC nanofibers (BCNFs) have a number of advantages over plant-derived cellulose, including a high physical strength, water absorption and retention properties, and a uniform fiber network structure [4–7]. They are also available in a variety of structural forms, including spheres, gels, sheets, membranes, mats, etc., all of which can be produced by introducing simple modifications into the production strategy. However, a limitation is that it is challenging to use conventional CNF preparation methods to create BCNFs that can be dispersed in water.

CNFs obtained from plant sources can be prepared using chemical, physical, or oxidation methods [8]. Chemical methods typically involve preparing cellulosic nanofibers via the acid digestion of an amorphous area of fibers that, when destroyed, yield nanocrystalline nanofibers. Some physical methods produce CNFs by the mechanical nanofibrillation of chemically purified cellulose pulps using a grinder, high-pressure homogenizer, blender, and high intensity ultrasonicator [8]. Alternatively, aqueous cellulose dispersions of nano-sized structures have been prepared by aqueous counter collision (ACC) using paired water jets without any chemical modification and were then used to convert naturally occurring cellulose fibers into nanofibers [9].

In contrast, a higher yield of CNFs can be obtained through the oxidation of cellulose mediated via 2,2,6,6–tetramethyl–1–piperidine–N–oxy radical (TEMPO), which is an oxidation catalyst capable of replacing alcoholic groups of cellulose with aldehyde, ketone, and carboxy groups under mild conditions at room temperature and normal pressure. TEMPO-oxidized cellulose can be dispersed in the aqueous phase by the repulsion force caused by the anionic charge on the surface of the carboxyl groups in the modified cellulose [10,11]. As the resulting material has the advantage of maintaining its physical fiber structure when dispersed in water, its use has been studied in a variety of fields, such as papermaking, membrane filters, heavy metal removal, and cell transfer.

A number of researchers have studied TEMPO immobilized on solid supports, such as polystyrene-bound TEMPO (PS-TEMPO) [12], FibreCat TEMPO [13], TurboBeads-TEMPO (TEMPO immobilized on the outer surface of Fe_3O_4 magnetic nanoparticles) [14], and organosilica xerogel (SiliaCat TEMPO) [15,16]. While these types of heterogeneous TEMPO catalyst clouds have been applied to the conversion of molecular chemicals, their use in the form of structured polymers, such as cellulose nanofibers, has been limited due to the steric hindrance between the solid supports and the nanofibers. Recently, Patanker et al. studied nanofibrillated cellulose that had been synthesized via the magnetically separable TEMPO-mediated oxidation and mechanical disintegration of wood pulp [17]. However, to the best of our knowledge, no researchers have yet studied the TEMPO oxidation of bacterial cellulose using immobilized TEMPO as a catalyst.

Previously, we reported the synthesis of TEMPO-oxidized bacterial cellulose nanofibers suitable for use as bio-based polymers for engineered green materials without sodium bromide, which were confirmed to exhibit unique properties on the skin surface [7]. In this case, the TEMPO-oxidized cellulose nanofibers were obtained conventionally using a centrifugation method for washing or drying. However, while these results are promising, it is difficult to implement centrifugation at an industrial scale. In addition, the chemicals used in the drying process, which contain N–oxyl compounds, bromide or iodide, and an oxidizing agent, all remain after drying; thus, this drying method is unsuitable for use in skincare applications.

In contrast, the one-pot synthesis method proposed in this study for producing TOCNs, using TEMPO immobilized on silica beads, is simple, efficient, and easy to use, and the synthesis process can use a simple filtration instead of washing after the cellulose nanofiber dispersion has been prepared. When the TOCNs produced via the one-pot synthesis were applied to the skin surface, they were found to exhibit unique properties similar to those of conventional TOCNs. Thus, they are not only a viable alternative for industrial production for use in the real field, they are also potentially suitable for use in skincare and biomedical research applications.

2. Materials and Methods

2.1. Materials

A key material in the proposed one-pot process is SiliaCat TEMPO, which is a heterogeneous catalyst/reagent fabricated from a proprietary class of organosilica-entrapped radicals, and which is suitable for the selective oxidation of delicate substrates into higher valued carbonyl derivatives [15]. The SiliaCat TEMPO material used in this study was purchased from SiliCycle Inc. (Quebec, QC, Canada). With regard to the other materials used in the study, sheets of BC were purchased from EZ Costec Co. Ltd. (Gyeonggi, Korea); TEMPO, sodium bromide, and sodium hypochlorite were purchased from Sigma-Aldrich (St Louis, MO, USA), and ethanol was purchased from Daejung Chemical & Metal Co. Ltd. (Gyeonggi, Korea). All other reagents were purchased from Sigma-Aldrich in the highest available commercial grade.

2.2. TEMPO Oxidation of BC

The synthesis of TOCNs via the conventional process (C-TOCNs): 20 g of a bacterial cellulose sheet that had been cut into small pieces was suspended in 500 mL of distilled (DI) water containing dissolved sodium hypochlorite and 20 mg of TEMPO catalyst. The oxidation reaction was maintained at a pH of 10 with 0.5 M NaOH. The mixture was vigorously agitated overnight using a magnetic stirrer at 25 °C. The oxidation reaction was then quenched by adding ethanol to the suspension. The products were washed with DI by centrifugation at 10,000× *g* several times, until all of the reactants were completely removed. The final product was stored at room temperature for later use.

The synthesis of TOCNs via the proposed one-pot process (O-TOCNs): the same amounts of bacterial cellulose and sodium hypochlorite were used for the chemical treatment of the process-cellulose. Before SiliaCat-TEMPO was used in the oxidation reaction, it was pretreated to activate the catalyst (Figure 1) by stirring a mixture containing SiliaCat-TEMPO (1 eq.), 4 M HCl (6 eq.) in dioxane, and a 0.5 M solution of N-chlorosuccinimide (5 eq.) in dichloromethane (DCM) was stirred for 15 min. The activated SiliaCat TEMPO was then washed with ethanol and dried completely under vacuum to ensure that all of the reactant had evaporated [15]. An oxidation reaction consisting of bacterial cellulose, sodium hypochlorite, and the activated SiliaCat-TEMPO was facilitated by stirring while the pH was maintained at 10.

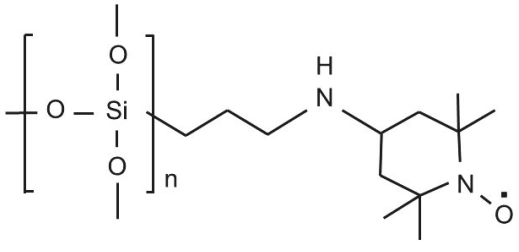

Figure 1. Schematic showing the structure of the immobilized 2,2,6,6–tetramethyl–1–piperidine–N–oxy radical (TEMPO) on silica beads.

A pure bacterial cellulose aqueous solution was obtained by preparing the aqueous dispersion of cellulose as follows. Ascorbic acid was added to the reacted cellulose solution to neutralize the hypochlorite acid. Then, the SiliaCat-TEMPO was removed by filtering the solution through a vacuum decompression device using a nylon mesh through which only the cellulose nanofiber solution could pass. As a result, the SiliaCat-TEMPO beads remained on the nylon mesh, while the cellulose nanofiber solution passed through to produce a pure nanofiber solution.

2.3. Detection of the Sodium Hypochlorite Content

To neutralize the hypochlorous acid remaining in the reacted cellulose solution, ascorbic acid with a different concentration was added, and the mixture was stirred. Then, a quantitative analysis was conducted using a phosphate buffer solution and N,N–diethyl–p–phenylenediamine (DPD) reagent to determine the amount of free chlorine content. In this test, if residual hypochlorous acid is present, then the color of the reactant will turn red, and its value can be obtained at a wavelength of 510 nm on a spectrophotometer.

2.4. Characterization by Scanning Electron Microscopy

Oil in water (o/w) emulsions containing TOCNs were prepared, consisting of TOCNs, 1% dimethicone, 3% pentaerythrityl tetraethylhexanoate, 1% hydrogenated polydecene, 7% dipropylene glycol, 7% glycerin, 0.4% methyl glucose sesquistearate, 3% cyclopentasiloxane, 4% xanthan gum, 12% carbomer, 1.5% sorbitol, 0.4% chelating agent, 2% trisodium ethylenediaminetetraacetic acid (EDTA), 2% pH adjusting agent, and water up to 100%. When investigating the surface characteristics, 0.05% of O-TOCNs and C-TOCNs were prepared by casting the solution on porcine skin (1 × 1 cm) and drying at room temperature overnight. These samples were then observed using a field-emission-type scanning electron microscope (FE-SEM; Hitachi S-4000, Tokyo, Japan) after platinum sputtering at 20 mA for 120 s.

2.5. Fourier Transform Infrared Spectroscopy (FT-IR) Analysis

The chemical structures of three types of BC samples (pure BC, C-TOCN, and O-TOCN) were analyzed via Fourier transform infrared spectroscopy (PerkinElmer, FT-IR microscope spotlight 200i, Courtaboeuf, France) over a frequency range of 4000 to 450 cm^{-1} and a resolution of 8 cm^{-1}.

2.6. X-ray Diffractometer (XRD) Analysis

The XRD patterns of the BC samples were obtained with an X-ray diffractometer (Rigaku, MiniFlex 300/600, Tokyo, Japan) using copper Cu Kα radiation (λ = 1.5406 Å) at 40 kV and 15 mA. The samples were examined with a scanning angle of 2θ from 10° to 80° at a rate of 5°/min, the crystallinity index (CrI) was calculated as a function of the maximum intensity of the diffraction peak from the crystalline region (I_{200}) at a 2θ of about 22.5°, and the minimum intensity from the amorphous region (I_{am}) at a 2θ angle of about 18° [18].

2.7. Contact Angle Measurements

The surface wettability of the TOCNs and o/w emulsions containing various concentrations of TOCNs were evaluated by contact angle measurements using a Contact Angle System (OCA, Dataphysics, Filderstadt, Germany) and a high-speed camera. During the measurements, wate droplets were deposited directly on the surface of the dried cellulose solution on the porcine skin, and the water contact angles were measured. Three measurements were performed per sample, and the results were averaged. The volume of each water droplet was 10 μL, and each drop was placed using a precision stainless steel tip (Gauge 32, EFD).

3. Results and Discussion

3.1. One-Pot Synthesis of TOCNs

When synthesizing TOCNs, it is necessary to substitute a certain number of carboxyl groups for those dispersed in the aqueous solution, and the reactants used in the oxidation reaction in the final synthesized TOCNs should be removed. The complete removal of the reactants is especially important in the skincare field. In our previous work, we found that TOCNs synthesized without

sodium bromide as a co-oxidant during the conventional TEMPO oxidation reaction did not exhibit significant differences in their physical properties (Figure S1) [7].

As a neutralizing agent for sodium hypochlorite, ascorbic acid can completely remove hypochlorite anions and return the solution to its original state without by-products; thus, it is also appropriate for use in skincare applications. To confirm the effect of ascorbic acid for neutralizing hypochlorite anions, the amount of free residual chlorine, dependent on the concentration of ascorbic acid, was measured via the free chlorine DPD method. Note that the available chlorine is present in the form of aqueous molecular chlorine, hypochlorous acid, and hypochlorite ions. The results of the measurements confirmed that the free residual chlorine via the DPD method was completely removed when more than 0.3% of ascorbic acid was added (Figure 2), and it was also confirmed that the sodium hypochlorite could be removed without washing.

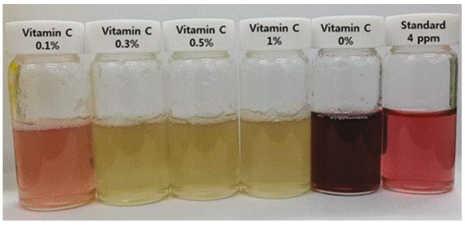

Figure 2. Neutralization of the sodium hypochlorite using ascorbic acid.

Although it was possible to remove the oxidant chemicals, it was difficult to remove the TEMPO catalysts, which is a large problem facing the one-pot synthesis process. During the oxidation reaction of BC using conventional water-soluble TEMPO, repetitive centrifugal separation was found to be the most effective process for removing the TEMPO catalyst. However, when scaling up production for industrial applications, centrifuge equipment does not typically support continuous processing at high levels of relative centrifugal force (RCF) while handing a large amount of reactant. While vacuum filtration can be used to continuously separate TOCN products from a reactant, if the size of the filter pores is too large, they cannot be used to separate the nanofibers. On the other hand, when the size of the filter pores is too small, the reactant does not pass through the filter when the nanofibers are stacked. The large size of the organosilica beads (63–250 μm), which is much larger than the diameter of the TOCNs (30–60 nm), can be selectively separated during the filtration process. Here, the filtration process was conducted using a vacuum decompression device and a nylon mesh (pore size: 50 μm), through which only the cellulose nanofiber solution could pass. In other words, the SiliaCat-TEMPO beads remained on the nylon mesh while the cellulose nanofiber solution passed through, leaving a pure nanofiber solution. Images of the TOCNs taken after filtration showed that the final TOCN solution did not contain silica beads (Figure S2).

The reaction rate and production yield of the O-TOCNs after the initial oxidation reaction were 72 h and about 80%, while those of the C-TOCNs were 18 h and about 99%, respectively. However, it should be noted that there are several problems with the purification of TOCNs via centrifugation in the conventional process used for industrial applications. For example, low density TOCNs require a high speed centrifugator operating at 13,000 rpm or higher, and the production yield is reduced to less than 70% when the process is repeated more than five times, as is the case when a tubular type centrifuge is used for treating the bulk scale product. Second, the treatment of large amounts of TOBCNs via centrifugation is challenging due to the lack of automated equipment that is capable of continuous centrifugation. In contrast, the proposed one-pot synthesis method is a viable alternative that does not suffer from these limitations. Moreover, other reactants such as sodium bromide and sodium hypochlorite were used for the conventional synthesis of TOCNs. The complete removal of the reactants is especially important in the skincare field. Our proposed process is a very efficient way to remove all reactants without any additional process.

3.2. Characterization of the TOCNs Obtained via One-Pot Synthesis

It was confirmed that the properties of the TOCNs obtained after the one-pot synthesis (O-TOCNs) were different from those of the TOCNs obtained via the conventional synthesis method (C-TOCNs). The carboxyl and aldehyde contents were measured using the conductivity titration method and found to be 1.02 ± 0.08 mmol g^{-1} and 0.12 ± 0.03 mmol g^{-1}, respectively, for the O-TOCNs, and 1.12 ± 0.10 mmol g^{-1} and 0.08 ± 0.04 mmol g^{-1}, respectively, for the C-TOCNs. The carboxyl and aldehyde contents of pure BC were 0.02 ± 0.01 mmol g^{-1} and 0.00 mmol g^{-1}, respectively. The carboxyl and aldehyde groups of both of the TOCNs were increased compared to those of the original BC, but those of the two samples were found to follow a similar trend. From the SEM images in Figure 3, it can be seen that the average diameter of the BC nanofibers was approximately 100 nm, decreasing to 30–50 nm after oxidation in the conventional process. However, the average diameter of the TOCNs was about 80 nm, which is closer to the diameter of the original BC nanofibers than that of the C-TOCNs (Figure 3). This implies that when soluble TEMPO is used, the ionic charge between the fibrils that bundles them into fibers is weakened. In contrast, the immobilized TEMPO catalyst does not penetrate the fiber bundle but only acts on the surface of the BC fiber. To confirm whether the O-TOCNs were structurally different from other water-soluble biopolymers, the nanometer-resolution structures of the bio-polymers were observed via high-resolution imaging provided by an FE-SEM (Figure S3). Carbopol (polyacrylic acid), xanthan gum (polysaccharide), and carboxymethyl cellulose (CMC) were selected for comparison purposes as water-soluble bio-polymers that are commonly used in the skincare field. When compared, the results showed that while the other bio-polymers did not exhibit any particular structure, the TOCNs had fiber structures in which bundles of nanofibers were entangled. This suggests that, as water-dispersed biopolymers with a unique fiber structure, the synthesized TOCNs will likely maintain their characteristics on the surface of the skin.

Figure 3. SEM images of (**a**) pure BC, (**b**) C-TOCNs and (**c**) O-TOCNs. Scale bar = 500 nm.

The FT-IR spectra of the three types of BC samples are shown in Figure 4. As can be seen in the figure, the pure BC had no obvious absorption band from 1500 to 2000 cm^{-1} (Figure 4a); in Figure 4b,c, the signal at 1603 cm^{-1} attributed to the carboxyl groups was consistent with that of the carboxyl-functionalized BC, which indicates that the hydroxyl groups at the C6 position in the BC had been successfully converted into carboxyl groups [19].

The XRD patterns of the pure BC and two types of TOCNs exhibited 2θ diffraction peaks at 14.5°, 16.4°, and 22.5°, usually attributed to the 101 (amorphous region), 10 (amorphous region), and 200 (crystalline region) crystallographic planes, respectively (Figure 5) [20]. These represent the primary diffraction of the (1–10), (110), and (200) crystal planes, respectively, which elucidates the structure of the cellulose I crystal. After oxidation via different methods, the diffraction peaks showed a slightly higher intensity compared to those of the BC, which indicates that the TOCNs retained the crystal structure of cellulose I with an unexpected small improvement in the crystallinity [18]. In other words, the oxidation process was shown to have little impact on the crystal structure of the BC. The crystallinity of the pure BC, C-TOCNs, and O-TOCNs were 75.7%, 79.5%, and 75.3%, respectively, which indicates that the crystallinity of the two TOCNs was similar.

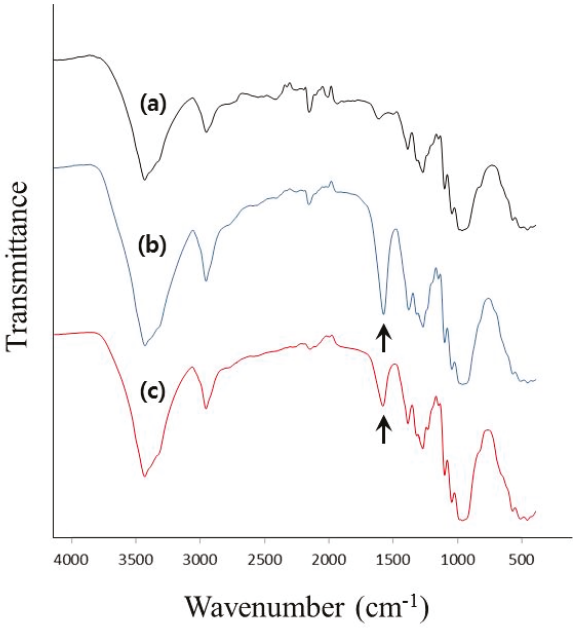

Figure 4. The FT-IR spectra of (**a**) pure BC, (**b**) C-TOCNs and (**c**) O-TOCNs.

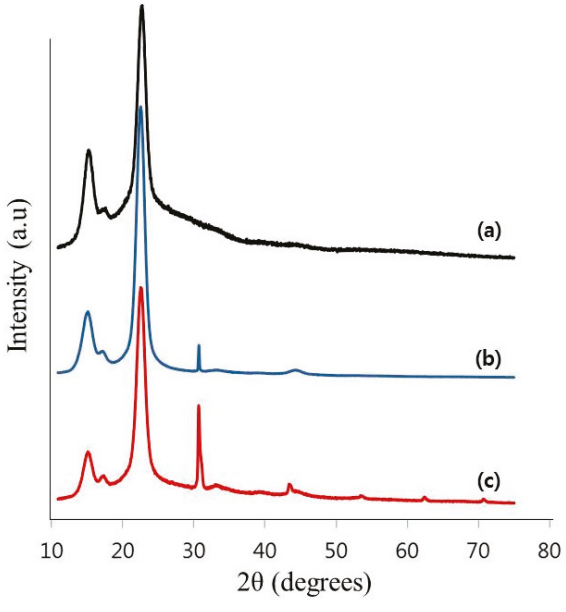

Figure 5. The XRD patterns of (**a**) pure BC, (**b**) C-TOCNs and (**c**) O-TOCNs.

3.3. Properties of O-TOCNs on the Surface of Skin

In a previous study, it was found that the nanofibrous structure of TOCNs give them unique physical properties, such as a water-absorbing capacity, elasticity, and the ability to block particulate

matter (PM) on the skin surface [7]. Here, it was confirmed that the one-pot synthesized TOCNs exhibited similar properties on the skin surface with respect to their water-absorbing capacity and blockage of PM on the skin. A water droplet was placed on porcine skin covered with O-TOCNs in an o/w emulsion containing different concentrations of O-TOCNs, and the changes in the water contact angle over time were measured. As shown in Figure 6a, the contact angle of the water over time was greatly reduced as the TOCNs' content in the o/w emulsion increased. These results suggest that the high carboxylate content of the TOCNs contributes to their excellent water-absorbing ability, resulting in a low resistance to water along with their other unique properties. It also indicates that the TOCNs have a water-absorption capacity, even when mixed with other materials. In the experiment conducted to evaluate the removal of PM on the skin, the samples (a combination of water and o/w emulsions with and without TOCNs) were applied on a 2 × 2 cm area on the upper arm, along with 8 μL of a carbon black solution (1.25 wt %), and they were then dried. The area was rubbed ten times with a small amount of water before being washed with tap water. The images before and after the application of carbon black were taken with a magnifier and analyzed with the Image Pro Plus software package (Media Cybernetics). We previously reported that TOCNs, which form a network of nanofibers on the skin surface, play a role in blocking particular matter. In this test, the o/w emulsion containing TOCNs was found to prevent the carbon black from entering into the microgrooves on the surface of the skin, and thereby allowed it to be easily removed (Figure 6b).

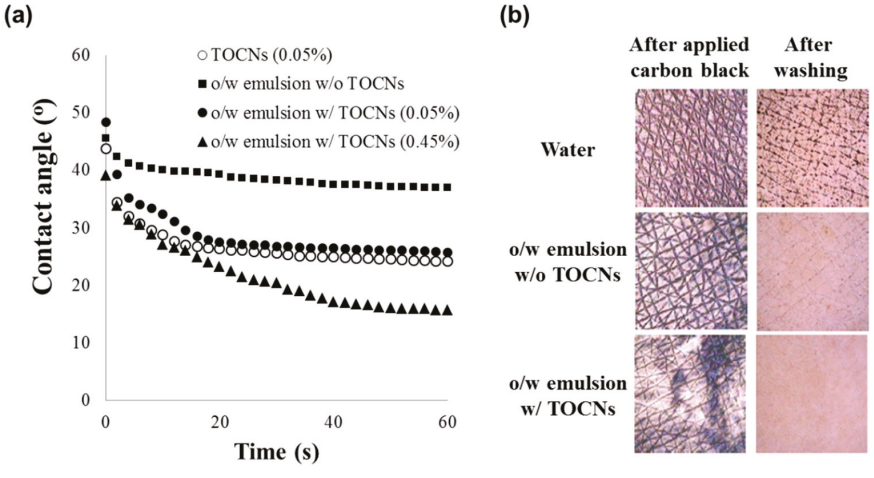

Figure 6. (**a**) Changes in the contact angle of various concentrations of TOCNs in o/w emulsion over time and (**b**) the washing experiment conducted to remove the carbon black from the skin.

4. Conclusions

A one-pot synthesis of water-dispersed bacterial cellulose nanofibers was prepared using a process that combined the neutralization of sodium hypochlorite via the addition of ascorbic acid and a filtration process using TEMPO that was immobilized on silica beads. The TOCNs obtained after the one-pot synthesis were found to have nanofibrous structures with the unique properties of bacterial cellulose, a water-absorbing capacity, and the ability to remove PM from the surface of skin. Based on our results, our proposed one-pot synthesis method for TOCNs is simple, efficient, and easy to use, and is therefore ideally suited to the preparation of bio-based polymer nanofibers in production quantities. It is therefore anticipated to have potential industrial applications in the skincare and biomedical research fields.

Supplementary Materials: The following are available online at http://www.mdpi.com/2073-4360/11/6/1044/s1.

Author Contributions: Conceptualization, S.-H.J. and N.-G.K.; methodology, S.-H.J.; validation, S.-H.J.; investigation, S.-H.J. and N.-G.K.; writing—original draft preparation, S.-H.J.; writing—review and editing, S.-G.P. and N.-G.K.; supervision, S.-G.P. and N.-G.K.; project administration, N.-G.K.

Acknowledgments: We would like to thank J. Song for assistance with XRD analysis of celluloses and Editage for editing and reviewing this manuscript for English language.

Conflicts of Interest: The authors declare no conflict of interest.

References

1. Gross, R.A.; Kalra, B. Biodegradable Polymers for the Environment. *Science* **2002**, *297*, 803–807. [CrossRef] [PubMed]
2. Menon, M.P.; Selvakumar, R.; Kumar, P.S.; Ramakrishna, S. Extraction and modification of cellulose nanofibers derived from biomass for environmental application. *RSC Adv.* **2017**, *7*, 42750–42773. [CrossRef]
3. Halib, N.; Perrone, F.; Cemazar, M.; Dapas, B.; Farra, R.; Abrami, M.; Chiarappa, G.; Forte, G.; Zanconati, F.; Pozzato, G.; et al. Potential Applications of Nanocellulose-Containing Materials in the Biomedical Field. *Materials* **2017**, *10*, 977. [CrossRef] [PubMed]
4. Tahara, N.; Tabuchi, M.; Watanabe, K.; Yano, H.; Morinaga, Y.; Yoshinaga, F. Degree of Polymerization of Cellulose from Acetobacter xylinum BPR2001 Decreased by Cellulase Produced by the Strain. *Biosci. Biotechnol. Biochem.* **1997**, *61*, 1862–1865. [CrossRef] [PubMed]
5. Naritomi, T.; Kouda, T.; Yano, H.; Yoshinaga, F. Effect of lactate on bacterial cellulose production from fructose in continuous culture. *J. Ferment. Bioeng.* **1998**, *85*, 89–95. [CrossRef]
6. Lee, J.W.; Deng, F.; Yeomans, W.G.; Allen, A.L.; Gross, R.A.; Kaplan, D.L. Direct Incorporation of Glucosamine and *N*-Acetylglucosamine into Exopolymers by Gluconacetobacter xylinus (5Acetobacter xylinum) ATCC 10245: Production of Chitosan-Cellulose and Chitin-Cellulose Exopolymers. *Appl. Environ. Microbiol.* **2001**, *67*, 3970–3975. [CrossRef] [PubMed]
7. Svensson, A.; Nicklasson, E.; Harrah, T.; Panilaitis, B.; Kaplan, D.L.; Brittberg, M.; Gatenholm, P. Bacterial cellulose as a potential scaffold for tissue engineering of cartilage. *Biomaterials* **2005**, *26*, 419–431. [CrossRef] [PubMed]
8. Chen, W.; Li, Q.; Cao, J.; Liu, Y.; Li, J.; Zhang, J.; Luo, S.; Yu, H. Revealing the structures of cellulose nanofiber bundles obtained by mechanical nanofibrillation via TEM observation. *Carbohydr. Polym.* **2015**, *117*, 950–956. [CrossRef]
9. Kondo, T.; Kose, R.; Naito, H.; Kasai, W. Aqueous counter collision using paired water jets as a novel means of preparing bio-nanofibers. *Carbohydr. Polymer.* **2014**, *112*, 284–290. [CrossRef]
10. Spaic, M.; Small, D.P.; Cook, J.R.; Wan, W. Characterization of Anionic and Cationic Functionalized Bacterial Cellulose Nanofibres for Controlled Release Applications. *Cellulose* **2014**, *21*, 1529–1540. [CrossRef]
11. Jun, S.-H.; Lee, S.-H.; Kim, S.; Park, S.-G.; Lee, C.-K.; Kang, N.-K. Physical properties of TEMPO-oxidized bacterial cellulose nanofibers on the skin surface. *Cellulose* **2017**, *24*, 5267–5274. [CrossRef]
12. Biotage® PS-TEMPO. Available online: https://www.biotage.com/product-page/biotage-ps-tempo (accessed on 13 June 2019).
13. Gilhespy, M.; Loka, M.; Baucherel, X. Polymer-supported nitroxyl radical catalyst for selective aerobic oxidation of primary alcohols to aldehydes. *Chem. Commun.* **2005**, *8*, 1085–1086. [CrossRef] [PubMed]
14. Tucker-Schwartz, A.K.; Garrell, R.L. Simple Preparation and Application of TEMPO-Coated Fe_3O_4 Superparamagnetic Nanoparticles for Selective Oxidation of Alcohols. *Chem. Eur. J.* **2010**, *16*, 12718–12726. [CrossRef] [PubMed]
15. Michaud, A.; Gingras, G.; Morin, M.; Béland, F.; Ciriminna, R.; Avnir, D.; Pagliaro, M. SiliaCat TEMPO: An Effective and Useful Oxidizing Catalyst. *Org. Process Res. Dev.* **2007**, *11*, 766–768. [CrossRef]
16. Ciriminna, R.; Pandarus, V.; Béland, F.; Pagliaro, M. Sol–gel Entrapped Nitroxyl Radicals: Catalysts of Broad Scope. *ChemCatChem* **2018**, *10*, 1731–1738. [CrossRef]
17. Patankar, S.C.; Renneckar, S. Greener synthesis of nanofibrillated cellulose using magnetically separable TEMPO nanocatalyst. *Green Chem.* **2017**, *19*, 4792–4797. [CrossRef]

18. Vasconcelos, N.F.; Feitosa, J.P.; Da, G.F.; Morais, J.P.; Andrade, F.K.; de Souza Filho, M.S.M.; Rosa, M.F. Bacterial cellulose nanocrystals produced under different hydrolysis conditions: Properties and morphological features. *Carbohydr. Polym.* **2017**, *155*, 425–431. [CrossRef] [PubMed]
19. Ifuku, S.; Tsuji, M.; Morimoto, M.; Saimoto, H.; Yano, H. Synthesis of silver nanoparticles templated by TEMPO-mediated oxidized bacterial cellulose nanofibers. *Biomacromolecules* **2009**, *10*, 2714–2717. [CrossRef] [PubMed]
20. Cui, Q.; Zheng, Y.; Lin, Q.; Song, W.; Qiao, K.; Liu, S. Selective oxidation of bacterial cellulose by NO2–HNO3. *RSC Adv.* **2014**, *4*, 1630–1639. [CrossRef]

polymers

MDPI

Article

Structure–Property Relationships of Pure Cellulose and GO/CEL Membranes Regenerated from Ionic Liquid Solutions

Czesław Ślusarczyk * and Beata Fryczkowska

Institute of Textile Engineering and Polymer Materials, University of Bielsko-Biala, Willowa 2, 43-309 Bielsko-Biala, Poland

* Correspondence: cslusarczyk@ath.bielsko.pl

Received: 10 May 2019; Accepted: 9 July 2019; Published: 12 July 2019

Abstract: Two types of cellulose membranes were produced by a classical wet phase inversion method from a solution of the polymer in 1-ethyl-3-methylimidazolium acetate (EMIMAc) by coagulation in water and selected primary alcohols. The first type were membranes made from pure cellulose (CEL). The second type were membranes obtained by adding nanosized graphene oxide (GO) to the cellulose solution. The process of precipitation and selection of the coagulant affected the structure of the membranes, which in turn affected their usability and applicability. The results of the presented studies show that the physicochemical properties of the coagulant used (e.g., molecular mass and dipole moment) play important roles in this process. It was found that both the content and dimensions of the pores depended on the molecular mass of the coagulant used. It was also found that the dipole moment of coagulant molecules had a large influence on the volume content of the pores (e.g., the 1-octanol (Oc) membrane had a dipole moment of 1.71 D; Φ = 1.82%). We investigated the effect of the type of coagulant on the porous structure of CEL membranes and how this affected the transport properties of the membranes (e.g., for the distilled water (W) membrane, J_v = 5.24 ± 0.39 L/m^2 h; for the Oc membrane, J_v = 92.19 ± 1.51 L/m^2 h). The paper presents the results of adding GO nanoparticles in terms of the structure, morphology, and transport properties of GO/CEL membranes (e.g., for composite membrane F (containing 20% GO), J_v = 40.20 ± 2.33 L/m^2 h). In particular, it describes their extremely high ability to remove heavy metal ions.

Keywords: cellulose; graphene oxide; ionic liquid; membrane; transport properties; heavy metals; porous structure; SAXS; WAXS

1. Introduction

Cellulose is one of the oldest natural polymers. It is renewable, biodegradable, and can be derivatized to yield various useful products, such as paper, films, fibers, membranes, hydrogels, aerosols, microspheres, and beads [1,2]. Hence, cellulose is already the basis of a large industry, and although it cannot compete with petrochemistry in terms of costs, it seems very likely that it will be the main chemical resource of the future, as it will still be available when other substances become increasingly scarce due to exhausted reserves or environmental difficulties.

Cellulose is a linear polymer linked with stable glycosidic bonds accompanied by intra- and intermolecular hydrogen bonds. The presence of these bonds as well as the presence of crystalline areas in cellulose makes this polymer insoluble in water and in most organic solvents [3]. Many systems capable of dissolving the polymer have been developed, including NaOH/CS_2, dimethyl sulfoxide and tetrabutylammonium fluoride mixture (DMSO/TBAF), LiCl/dimethylacetamide (DMAc), and N_2O_4/*N*,*N*-dimethylformamide (DMF) [4,5], whose disadvantages are volatility, toxicity- or flammability.-. Another system used to dissolve cellulose is a mixture of *N*-methylmorpholine-*N*-oxide

and water (NMMO/H_2O), which—unlike the previously mentioned systems—is environmentally friendly and cost-effective [6].

Recent cellulose research has paid a great deal of attention to ionic liquids, often referred to as "green" solvents. Due to their biodegradability [7] and low toxicity [8], they are considered to be environmentally friendly solvents, and may eventually replace traditional systems that are capable of dissolving cellulose [9,10]. Ionic liquids are a type of organic salt with a liquid phase below boiling temperature. Their cationic component determines their chemical stability, while their anionic part plays an important role in chemical reactions [11–13]. The use of ionic liquids for making cellulose solutions renders several advantages such as a lower dissolving temperature, lower or even zero toxicity, better thermal stability, and easy solvent recovery [14,15].

Swatloski et al. [16] were the first to describe the dissolution of cellulose in 1-butyl-3-methyl imidazolium chloride, and they found that the chemical structure of the imidazole cation in the ionic liquid has a strong influence on the viscosity of the obtained polymer solutions. Kosan et al. [11] investigated the properties of various ionic liquids, but the most interesting turned out to be 1-butyl-3-methyl imidazolium acetate, which enabled the preparation of a 13.5% cellulose solution. This liquid has even more advantages, such as a low melting point, high boiling point, and good thermal stability [17]. In their studies on the dissolution of cellulose in ionic liquids, Ding et al. used a 5% solution of microcrystalline cellulose which they dissolved in 1-ethyl-3-methylimidazolium acetate (EMIMAc). Mahadeva et al. [18] used a 2% solution of cellulose for membrane molding, and coagulation was carried out in water, methanol, a mixture of methanol with water (30:70), and isopropyl alcohol. Sun et al. [19] reported that the 5% solution of cellulose in EMIMAc was coagulated in the acetone–water mixture (1:1 *v/v*). Hermanutz et al. [15] used 10%, 12%, and 16% cellulose solutions in EMIMAc to produce cellulose fibers by coagulation in water. Livazovic et al. [20] described the preparation of cellulose solutions at concentrations of 2.0%, 5.0%, and 10% cellulose in 1-ethyl-3-methylimidazolium acetate by heating at 80 °C for 24 h. The solutions obtained were molded with a casting knife with an adjustable thickness fixed at 0.15 mm, and the resulting films were coagulated in distilled water.

Cellulose dissolved in ionic liquid can easily be precipitated using polar solvents such as water, acetone, ethanol, dichloromethane, acetonitrile, or by using a mixture of these solvents [14,21], to obtain useful products. The process of precipitation and the selection of the coagulant affects the coagulated polymer structure.

Membranes are among the products made from regenerated cellulose which deserve special attention. These materials are widely used in a variety of membrane separation techniques, such as the dialysis, ultrafiltration-, and purification of mixtures, and are used in sewage treatment plants in the process of water treatment, in the chemical and food industries, as well as in environmental protection, biochemistry, and medicine [22,23]. According to literature reports, the factors affecting the properties of membranes include the type of coagulating bath, its concentration, and the time of film formation, among others [22].

However, most often the membranes described by the literature are composites. The authors describe the process of obtaining a cellulose/iron oxide bionanocomposite by the mixing blends technique [24,25]. Rac-Rumijowska et al. described a method for the preparation of cellulose-based fibrous composites with the addition of silver nanoparticles [26]. Yue's group constructed anti-bacterial composites based on paper pulp with the addition of silver ions [27]. Other researchers made composite membranes based on cellulose with the addition of chitosan and carbon nanotubes [28]. Graphene oxide (GO) has also been used for the preparation of composites with cellulose [29–31]. Yadav et al. used cellulose derivatives [32,33] to obtain GO-containing composites.

This paper presents a study on the production of cellulose membranes by the classical wet phase inversion method. EMIMAc was selected as the solvent, since—according to Sun et al. [19] and also confirmed by studies of Gupta et al. [34]—this ionic liquid breaks the hydrogen bonds in cellulose most easily. The cellulose dissolved in ionic liquids can be coagulated in polar solvents [35]. In our experiment, water and primary alcohols differing in polarity such as methanol, ethanol, 1-propanol,

1-butanol, 1-hexanol, and 1-octanol were used for the coagulation of cellulose membranes. In this paper, we describe the study of two types of membranes. The first type were membranes made from pure cellulose (CEL). The second type were membranes obtained by adding nanosized graphene oxide (GO) to the cellulose solution. A method of combining the cellulose solution with the dispersion of GO additive was developed to obtain a homogeneous solution from which the composite membranes (GO/CEL) were then formed using the phase inversion method by coagulation in distilled water.

The process of precipitation and selection of the coagulant affects the structure of the membranes, which in turn affects their usability and applicability. The effect of the type of coagulant on the porous structures of CEL membranes was investigated, in addition to how this affects the transport properties of the membranes. For GO/CEL membranes, this paper presents the results of investigations of the effect of adding GO nanoparticles on the structure, morphology, and transport properties of these membranes. In particular, it describes their extremely high ability to remove heavy metal ions.

2. Materials and Methods

2.1. Materials

Cellulose (long fibers), ionic liquid (EMIMAc), and graphite powder (<20 μm) were purchased from Sigma-Aldrich (Poznań, Poland). $NaNO_3$, 98% H_2SO_4, $KMnO_4$, 30% H_2O_2, *N*,*N*-dimethylformamide (DMF), $Co(NO_3)_2$, $Ni(NO_3)_2$, $Pb(NO_3)_2$, and $ZnCl_2$ were purchased from Avantor Performance Materials Poland S.A. (Gliwice, Poland). All chemicals were used without further purification.

2.2. Preparation of the Cellulose Solution

Initially, a 5% solution of cellulose in the ionic liquid (EMIMAc) was prepared. For this purpose, adequate amounts of cellulose and ionic liquid were combined to obtain solutions with concentrations of 2.5%, 5.0%, 7.5%, and 10% by weight. The solutions were then mixed thoroughly and heated in a laboratory microwave oven at three intervals of 5 s, keeping the temperature of the mixture below approximately 40 °C. Previously, it was observed that very accurate mixing at intervals between heating prevents the local overheating of cellulose and its degradation [36]. The obtained cellulose solutions were allowed to de-aerate for 24 h. The viscosity of the prepared cellulose solutions was measured at room temperature by means of a Myr V2-L rotary viscosity gauge, equipped with an L3 spindle and temperature sensor (Especialidades Medicas Myr, SL, Tarragona, Spain) (Figure 1).

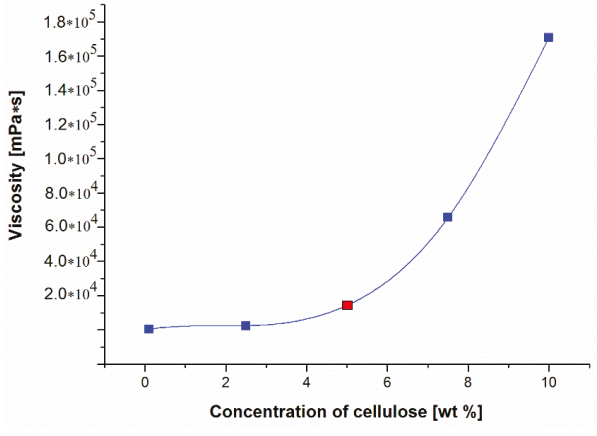

Figure 1. The results of viscosity tests of cellulose solutions in 1-ethyl-3-methylimidazolium acetate (EMIMAc) (measurement temperature 25 °C).

Looking at Figure 1, we can see that the viscosities of the obtained cellulose solutions in EMIMAc increased drastically with their concentration. Above 10% wt. concentration, the cellulose solutions formed a gel that prevented further dissolution of cellulose. As a result, 5% cellulose solution was selected for further investigation. A solution of this concentration was also used by Ding et al. for their research [37].

2.3. GO Synthesis and Preparation of GO/DMF Dispersion

GO synthesis was carried out in our laboratory using the modified Hummers' method [38], as described in our earlier work [39]. Wet GO was dried in a laboratory drier at 60 °C to obtain a brown precipitate which was then dispersed in DMF in an ultrasonic bath to obtain a 5.2% GO/DMF dispersion (Figure 2).

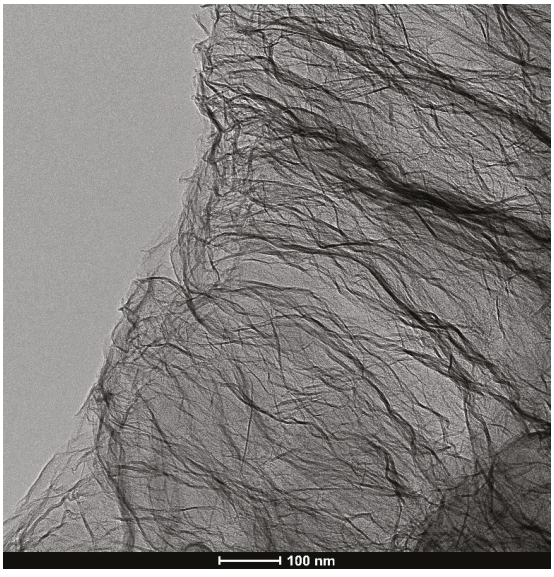

Figure 2. TEM (transmission electron microscopy) image of graphene oxide (GO) flakes.

2.4. Pure Cellulose Membrane and GO/CEL Membrane Formation

Cellulose membranes were prepared using the phase inversion method. For this purpose, a 5% cellulose solution in EMIMAc was poured onto a level, clean glass plate. Then, a polymeric film was formed using a casting knife with an adjustable thickness fixed at 0.2 mm. After that, the plate and the cellulose solution distributed over it were transferred to a coagulant bath at room temperature and kept in it until the membrane peeled off the glass. The following solvents were used in coagulation solutions: distilled water (W), methanol (Me), ethanol (Et), 1-propanol (Pr), 1-butanol (Bu), 1-pentanol (Pe), 1-hexanol (He), and 1-octanol (Oc). In the presence of water, cellulose membranes coagulated rapidly (10–30 min). Then the membranes were immersed in alcohols containing one to four carbon atoms in their molecules. The coagulation of cellulose solutions in higher alcohols was very slow, and it took 1 day (1-pentanol), 4 days (1-hexanol), and 5 days (1-octanol) for the membranes to separate from the glass plate, indicating the finalization of the process. After the completion of this process, the membranes - Pe, He, and Oc were repeatedly rinsed, alternately with distilled water and methanol, until the characteristic odor of the alcohol disappeared. Then, they were air-dried at room temperature. In our laboratory, a thin layer of polyester fabric followed by layers of tissue paper were used to separate the cellulose membranes. This prevented the cellulose from sticking to the filter paper and

facilitated drying. Finally, the dried membranes were loaded onto a glass plate to prevent membrane ripple (Figure 3).

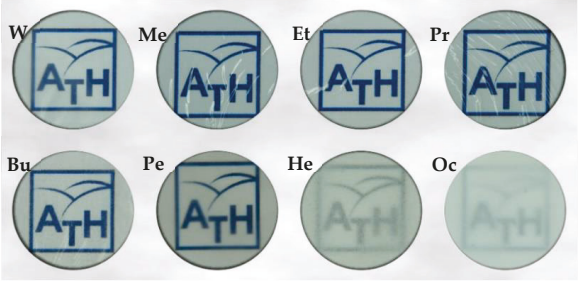

Figure 3. Images of a pure cellulose membrane coagulated in distilled water (W), methanol (Me), ethanol (Et), 1-propanol (Pr), 1-butanol (Bu), 1-pentanol (Pe), 1-hexanol (He) and 1-octanol (Oc) (our university's logo was placed under the membranes for a better display of their transparency).

In order to prepare solutions for forming the GO/CEL composite membranes, adequate amounts of cellulose and ionic liquid were first weighed (Table 1), and cellulose solutions were prepared as described above. Appropriate amounts of 5.2% GO/DMF solution (Table 1) were then added to the cellulose solutions, thoroughly mixed, and sonicated for 15 min. The obtained GO/CEL solutions were allowed to de-aerate for 24 h. GO/CEL composite membranes were prepared using the phase inversion method, as was done for the membranes made from pure cellulose.

Table 1. The composition of the solutions for the preparation of membranes. CEL: pure cellulose; DMF: *N*,*N*-dimethylformamide.

Membrane Designation	"0"	A	B	C	D	E	F
Amount of 5.2% GO/DMF Solution (g)	0	0.05	0.1	0.5	0.97	4.8	9.7
Amount of CEL (g)	2.5	2.5	2.5	2.5	2.5	2.5	2.5
Amount of EMIMAc (g)	47.5	47.45	47.4	47.0	46.53	42.7	37.8
Concentration of GO (% *w*/*w*)	0	0.1	0.2	1	2	10	20
Concentration of CEL (% *w*/*w*)	100	99.9	99.8	99	98	90	80

2.5. Measurements of Water Flux

The transport properties of the formed membranes were tested using a Millipore Amicon 8400 ultrafiltration (UF) cell with a 350 mL capacity and a 7.6 cm membrane diameter that was equipped with an equalizing tank with an 800 mL capacity (Merck Millipore, Burlington, MA, USA). First, dry membranes were immersed in distilled water for 1 h. Then, they were treated with room-temperature distilled water) for an additional 2 h under a pressure of 0.2 MPa to improve the membrane stability. UF tests were performed at operational pressures of 0.1, 0.15, or 0.2 MPa. Permeate flux (J_v) was calculated using the following Equation (1) [40]:

$$J_v = \frac{Q}{A\,t} \tag{1}$$

where J_v is the water flux (L/m^2 h), Q is the permeate volume (L), A is the effective membrane area (m^2), and t is the permeation time (h).

2.6. Measurements of Rejection

Standard solutions of $Pb(NO_3)_2$ with a concentration of 60 mg/L and NaCl, $Co(NO_3)_2$, $Ni(NO_3)_2$, and $ZnCl_2$ with concentrations of 6 mg/L were prepared to study the separation properties of the

produced GO/CEL membranes. In addition, a mixture of synthetic wastewater containing 6 mg/L $Co(NO_3)_2$, $Ni(NO_3)_2$, $ZnCl_2$, and 60 mg/L $Pb(NO_3)_2$ was prepared.

Then, 200 mL of successive standard solutions were added to the UF cell with the test membrane and the stirrer (stirring of the feed solution avoids fouling). The permeation process was carried out at a working pressure of 0.2 MPa, and 20 mL doses of permeate were tapped, simultaneously measuring the time taken for the permeate discharge to from the test tank. The permeate flux (J_v) was calculated using Equation (1), assuming that Q was the permeate volume (specific test solution).

The ion concentrations of the subsequent metals were determined using atomic absorption spectrometry (AAnalist 100 AAS, Perkin-Elmer International Rotkreutz Branch P.O., Rotkreutz, Switzerland), and the rejection coefficient (R) was calculated using Equation (2) [40]:

$$R = \left(1 - \frac{C_p}{C_f}\right)100\%, \quad (2)$$

where R is the rejection performance of the membrane (%), and C_p and C_f are the concentrations of metal ions in the permeate and feed solution (mg/L), respectively.

2.7. Analytical Methods

Small-angle X-ray scattering (SAXS) measurements were carried out with the compact Kratky camera equipped with the SWAXS optical system of HECUS-MBRAUN (Graz, Austria). The Cu target X-ray tube operating at U = 30 kV and I = 10 mA was used as a radiation source (λ = 0.154 nm). The SAXS data were collected as a function of the scattering vector, $q = (4\pi/\lambda) \sin \theta$, where 2θ is the scattering angle. The moving slit method [41] was applied for determination of the transmittance factor of the sample. The sample holder background was subtracted from the SAXS curves, and the next curves were corrected, taking both the sample thickness and transmittance into consideration. The data were converted to absolute intensities with a calibrated Lupolen® (polyethylene) standard [42].

Wide-angle X-ray scattering (WAXS) investigations were carried out with a URD-65 Seifert (Germany) diffractometer. Cu Kα radiation was used at 40 kV and 30 mA. Monochromatization of the beam was obtained by means of a nickel filter and a graphite crystal monochromator placed in the diffracted beam path. A scintillation counter was used as a detector. Investigations were performed in the angle range of 3° to 40° in steps of 0.1°.

Observations of the – morfology of membranes surface and cross-section were carried out using a JSM-5500 LV JEOL (Tokyo, Japan) scanning electron microscope (SEM). All samples were coated with a layer of gold in a JEOL JFC 1200 vacuum coater at 3×10^{-5} Tr.

3. Results and Discussion

3.1. Pure Cellulose (CEL) Membranes

3.1.1. Porous Structure of CEL Membranes

The porous structure of membranes is one of their most important features, as it determines their usability and applications. This structure is mainly formed at the coagulation stage; therefore, the type of coagulant used has an influence on it [18,19]. In this paper, an analysis of the porous structure of the CEL membrane was carried out by the SAXS method. Using this method, the pore dimensions and the pore volume fraction were determined. The studies characterized pore sizes on length scales from 1 to 60 nm, according to the resolution of the SAXS equipment used.

The SAXS curves of the investigated cellulose membranes are shown in Figure 4 in double-logarithmic plots. It is clear that the scattering intensities of the membranes coagulated in 1-hexanol and 1-octanol were much stronger than those for other membranes. Because small-angle X-ray scattering is conditioned by the existence of the electron density inhomogeneities in the sample,

which in the case of cellulose membranes is due to the existence of pores in them, the higher intensity was caused by the higher content of pores in these membranes.

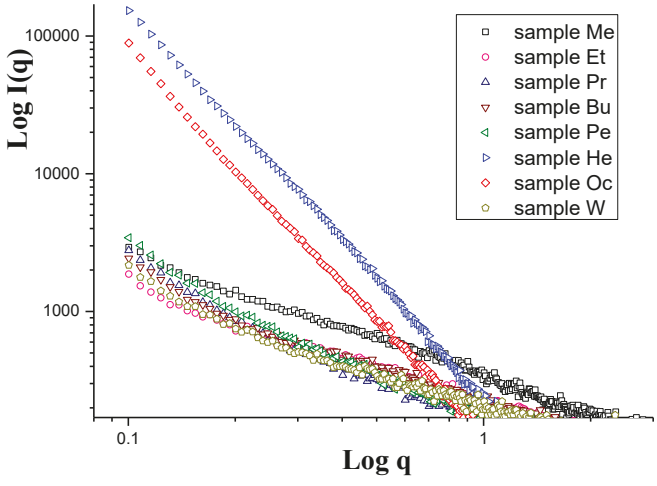

Figure 4. Double-logarithmic small-angle X-ray scattering (SAXS) curves of cellulose membranes.

The content of pores can be determined by calculating the so-called scattering power, or invariant Q, using the equation

$$Q = \int_0^\infty q^2 I(q) dq = \phi(1-\phi)(\Delta\rho)^2 \quad (3)$$

where $I(q)$ is the corrected SAXS intensity, Φ is the volume fraction of pores, and $\Delta\rho$ is the electron density difference between the pores and cellulose. The pores can be assumed to be entirely air-filled in dry membranes. The electron density difference between cellulose and pores was calculated to be $\Delta\rho$ = 511 electrons/nm^3 [43]. The values of Φ calculated by Equation (3) are presented in Table 2.

Table 2. Characteristics of the pure cellulose (CEL) membranes used for the study and values of structural parameters obtained by means of the SAXS method. R_G: radius of gyration, Φ: volume fraction of pores.

Sample	Coagulant			SAXS Results	
	Type	Molar Mass (g/mol)	Dipole Moment (D)	R_G (nm)	Φ (%)
Me	methanol	32.04	1.70	11.0 ± 0.3	0.71
Et	ethanol	46.07	1.69	12.2 ± 0.2	0.39
Pr	1-propanol	60.1	1.58	12.9 ± 0.3	0.30
Bu	1-butanol	74.12	1.66	13.9 ± 0.4	0.39
Pe	1-pentanol	88.15	1.64	15.0 ± 0.4	0.32
He	1-hexanol	102.17	1.42	16.7 ± 0.3	0.69
Oc	1-octanol	130.23	1.71	19.3 ± 0.5	1.82
W	water	18.02	1.85	13.9 ± 0.3	0.30

The Guinier approximation can be used for the determination of pore sizes, which describes the scattering intensity for small values of the scattering vector q:

$$I(q) = I_0 e^{-\frac{q^2 R_G^2}{3}} \quad (4)$$

This equation describes the mean intensity of the radiation scattered by a particle of any shape, averaged through all its possible orientations in space. The parameter R_G is the electron radius of gyration, also called Guinier's radius. R_G can be determined from the slope of the plot of ln $I(q)$-versus q^2 using the intensity data in the low q region. An example of a Guinier plot for a membrane (B) is shown in Figure 5, and the R_G values for all investigated membranes are given in Table 1.

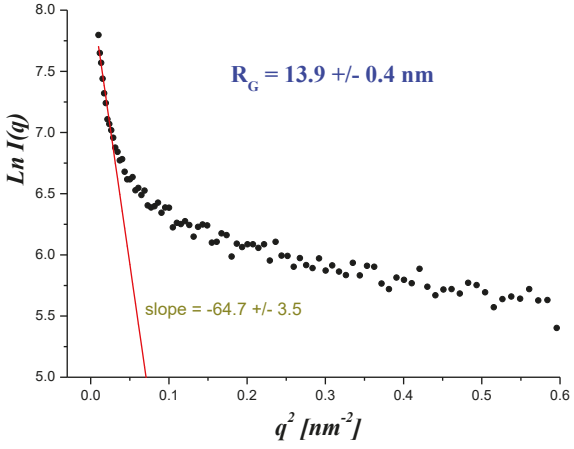

Figure 5. The Guinier plot for the Bu sample.

The analysis of the results (Table 1) indicated a strong dependence of the Guinier's radius of the pores on the molar mass of the coagulant used. Figure 6 shows that the R_G increased almost linearly as the molar mass of the organic coagulant increased. Water is an inorganic compound, so it is not surprising that in this case the value of R_G did not correspond to this relationship (sample W). Water is the simplest and cheapest polar solvent, and therefore it has been used as a coagulant to obtain cellulose membranes. This coagulant has the lowest molar mass and largest dipole moment of all the coagulants used in this work. The role of these two factors is discussed later in this article. The volume fraction of pores in the studied membranes also depended on the coagulant molar mass. In Figure 6, it can be seen that the pore content was almost the same in the molar mass range from 18.02 to 88.15 g/mol. The only exception was for the Me sample, for which the Φ considerably exceeded the average value in that range. For membranes prepared using coagulants of the highest molecular mass, the content of the pores increased rapidly, and for the membrane coagulated in 1-octanol, it was almost five times higher than in membranes obtained using coagulants of lower molar mass.

To better understand the obtained results, the mechanism of solvation of cellulose at the microscopic level should be considered. The ionic liquid used to dissolve the cellulose was a chemical compound consisting of ion-bonded anions and cations. In the liquid state, at room temperature, these solvent molecules dissociate. After mixing the cellulose and the ionic liquid, these cations and anions attack the hydrogen bonds of cellulose, tearing them apart. The disruption of hydrogen bonds results in the separation of individual cellulose chains and allows them entry into the solution. The regeneration of cellulose is based on the precipitation of the cellulose solution by the polar solvent (coagulant), which washes the ionic liquid but does not dissolve the cellulose. Washing the ionic liquid results in the formation of hydrogen bonds between cellulose chains, resulting in the recovery of the structure of the

regenerated cellulose. The process of removing the solvent molecules by the coagulant molecules leads to the formation of the porous structure of the resulting cellulose. It appears that the molecular weight of the coagulant molecules had a significant impact on the size of the pores formed in this process.

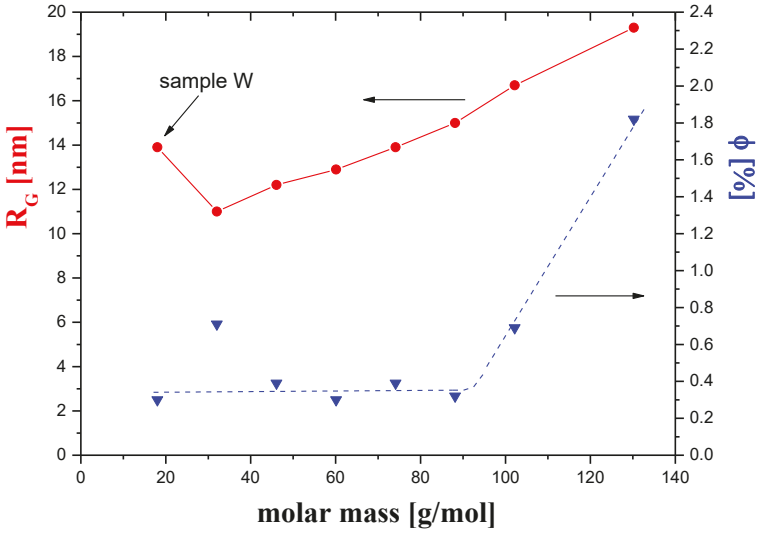

Figure 6. The radius of gyration (R_G) and the volume fraction of pores (Φ) as a function of the coagulant molar mass.

The coagulation process described above is mainly based on Coulomb interactions between the molecules of the solvent and the coagulant. It therefore seems reasonable that this process will also depend on the value of the dipole moments of interacting molecules. Our research shows that the dipole moment of the coagulant was the second factor involved in determining the pore content of membranes, in addition to the molar mass. However, the effects of both these factors are complex, as illustrated by the dependence of the content of pores as a function of the dipole moment shown in Figure 7.

Undoubtedly, the content of the pores in the membrane was greatest when the values of the two factors were large, as in the case of sample Oc. If the dipole moment was large and the molar mass was small, as in the case of water, the pore content was small. The same was true in the opposite case, when the molecular weight was relatively large but the dipole moment was small, as in the case of the membrane H.

Summing up, studies have shown the influences of both the molar mass and the dipole moment of the coagulant on the content and size of the pores in cellulose membranes. However, it is difficult to definitely determine which of these factors has a crucial impact on the number of pores in the membranes. It should be emphasized that, to our knowledge, the presented studies represent the first attempts to establish the physical factors affecting these structural parameters of membranes at the molecular level, which is important from the perspective of their application.

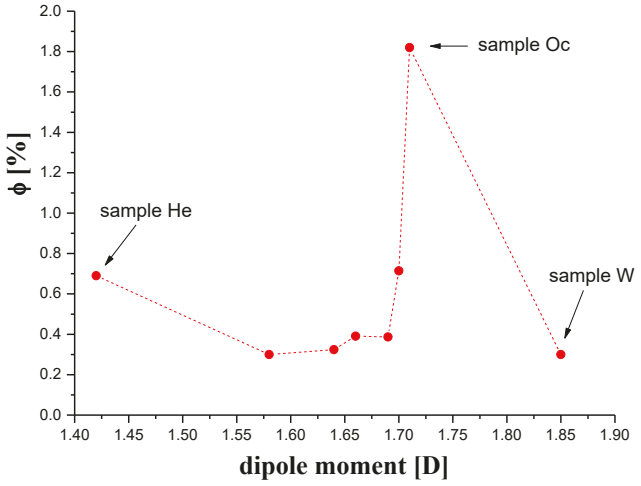

Figure 7. The volume fraction of pores (Φ) as a function of the coagulant dipole moment.

3.1.2. Morphology and Crystallinity of CEL Membranes

Cellulose is a partially crystalline polymer characterized by a polymorphism of crystallites, which can be studied by wide-angle X-ray (WAXS). WAXS investigations of CEL membranes gave an additional interesting result that completes the above-discussed SAXS findings. The native cellulose used in the membrane preparation of exhibited the cellulose I crystal structure (WAXS pattern not shown here). After dissolution and subsequent coagulation with primary alcohols, the transformation from cellulose I to the cellulose II crystalline form occurred. This phenomenon is consistent with that reported in most other known solvent systems for cellulose. The WAXS diffraction patterns (Figure 8) of the CEL membranes exhibited the characteristic cellulose II peak at $2\theta = 12.6°$ and two peaks close to each other at $2\theta = 20.3°$ and 21.2°, which were assigned to the (-110), (110), and (-121) crystalline planes, respectively [21].

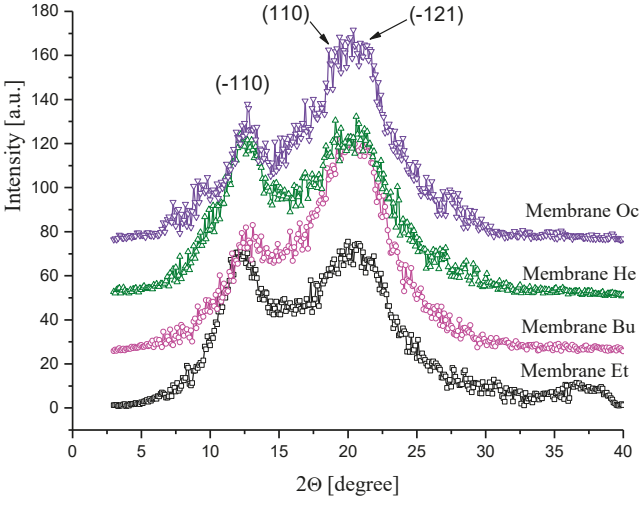

Figure 8. Examples of wide-angle X-ray (WAXS) patterns of CEL membranes.

To quantitatively examine the crystallinity of the membranes, their crystallinity indexes were evaluated from the WAXS measurements. For this purpose, each WAXS curve was deconvoluted into crystalline and amorphous scattering components using the profile fitting program WaxsFit [44]. Each peak was modeled using a Gaussian–Cauchy peak shape. The crystallinity index was calculated as the ratio of the area under the crystalline peaks to the total area of the scattering curve. The crystallinity index of native cellulose was found to be 0.756, whereas for membranes the value of this parameter ranged from 0.31 to 0.45, and this was significantly affected by the type of coagulant.

Figure 9 shows the dependence of the membrane crystallinity on the membrane pore content, and it shows that the crystallinity index decreased almost linearly as the volume fraction of the pores increased. This reflects the complexity of the process of membrane formation at the molecular level. The ionic liquid used to dissolve the cellulose broke the intermolecular and intramolecular hydrogen bonds and destroyed the primary crystalline structure. The process of removing the solvent molecules by the coagulant molecules, resulting in the recovery of the crystalline structure of cellulose, also led to the formation of its porous structure. The obtained results indicate that the formation of pores hinders the crystallization process of regenerated cellulose to some extent.

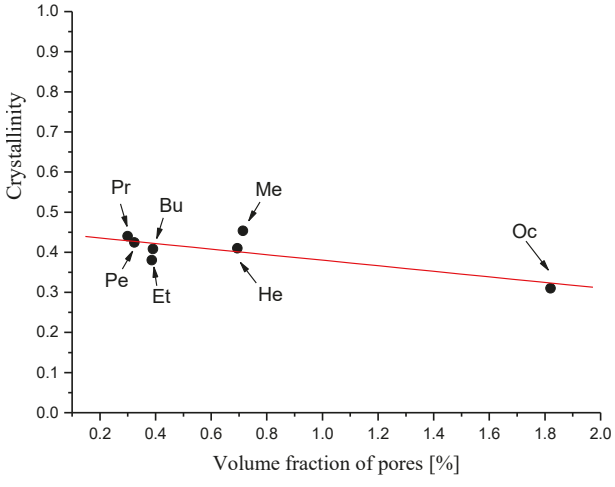

Figure 9. Effect of the pore volume fraction on the membrane crystallinity.

Scanning electron microscopy enabled the observation of the surface morphology of the skin layer, the support layer, and cross sections of the obtained cellulose membranes (Figure 10). The SEM images of membranes W, Et, and Pr (Figure 10-1) show cellulose layers arranged in parallel, similar to the results shown in [18]. For Me, Bu, and Pe membranes, on the other hand, a compact structure with minor inclusions was seen. The cross section of membrane He, with large, symmetrically arranged, closed chambers, was diametrically different from the other ones, whereas the SEM image of the cross section of membrane Oc was distinguished by a thin skin layer, based on the large, open, asymmetrical chambers of the support layer. In the photographs of membranes W, Me, and Et, the surface of the skin layer (Figure 10-2) was smooth, while that of membrane Pr was rough and covered with inclusions. The pictures of membranes Bu, Pe, He, and Oc reveal a very rich skin layer surface, which changed from large and flat to finer with deeper hollows. The surface of the support layers of all membranes (Figure 10-3) was richer in various morphological elements as compared to the skin layer. In the case of membrane Oc, large multilayer chambers with walls covered with micropores were observed.

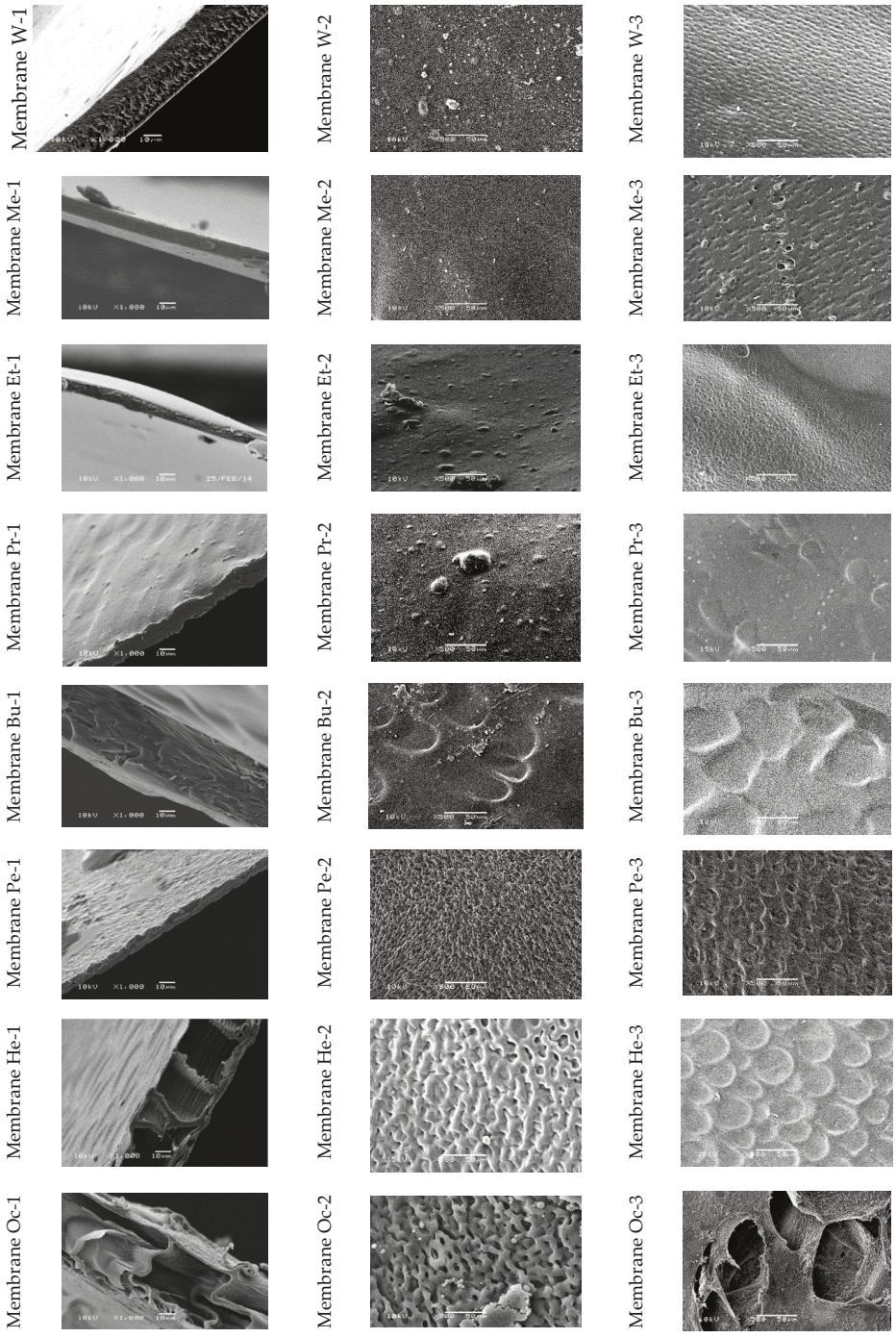

Figure 10. SEM images for cellulose membranes: (**1**) cross-section; (**2**) skin layer; (**3**) bottom layer.

3.1.3. Transport Properties of CEL Membranes

An important parameter determining membrane properties is the volumetric permeate flux. Figure 10 shows that for CEL membranes, this parameter depended on the coagulant used. The lowest values of volumetric permeate flux, recorded for the membrane W for pressures of 0.1, 0.15, and 0.2 MPa, were respectively 3.33 ± 0.12; 3.87 ± 0.13, and 5.24 ± 0.39 L/m^2 h. A slow but slight increase in the permeate flux, which was observed with the increase of working pressure, may indicate the compact structure of membrane W. It can therefore be assumed that membrane W was composed of closed pores.

The transport properties of cellulose membranes Et, Pr, and Pe were found to be similar. The permeate flux for these membranes increased slowly with the increase in working pressure, and at 0.2 MPa, their values were 9.27 ± 0.55 (membrane Et), 9.27 ± 0.37 (membrane Pr), and 7.95 ± 0.25 (membrane Pe) L/m^2 h, respectively.

A much greater increase in the volumetric permeate flux was observed for membranes Bu and Me. Thus, as the working pressure rose, the permeate flux increased by 2–3 times for membrane Bu and 5–8 times for membrane Me. The exact values of this parameter were 4.89 ± 0.49, 10.19 ± 0.52, and 14.17 ± 0.63 L/m^2 h (membrane Bu) and 1.25 ± 0.08, 6.22 ± 0.25, and 10.19 ± 0.46 L/m^2 h (membrane Me).

Membranes He and Oc were characterized by very high volumetric permeate flux values. For the cellulose membrane coagulated in 1-hexanol, the following values were recorded: 15.36 ± 0.59 L/m^2 h (for a pressure of 0.1 MPa), 42.85 ± 0.99 L/m^2 h (for a pressure of 0.15 MPa), and 56.09 ± 1.07 L/m^2 h (for a pressure of 0.2 MPa). The obtained results were confirmed by the high porosity of membrane He (Figure 10) observed in the SEM images, which facilitated the transport of water through the membrane. For membrane Oc, the following results were obtained: 12.72 ± 0.45 L/m^2 h (for a pressure of 0.1 MPa), 65.70 ± 2.15 L/m^2 h (for a pressure of 0.15 MPa), and 92.19 ± 1.51 L/m^2 h (for a pressure of 0.2 MPa). These results show that during the operation of cellulose membrane Oc, the permeate flux increased by 5 to 7 times with the increase in working pressure. The obtained results and the SEM images (Figure 10) confirm that the cellulose membrane coagulated in 1-octanol has very good transport properties (Figure 11) because of became of large pores.

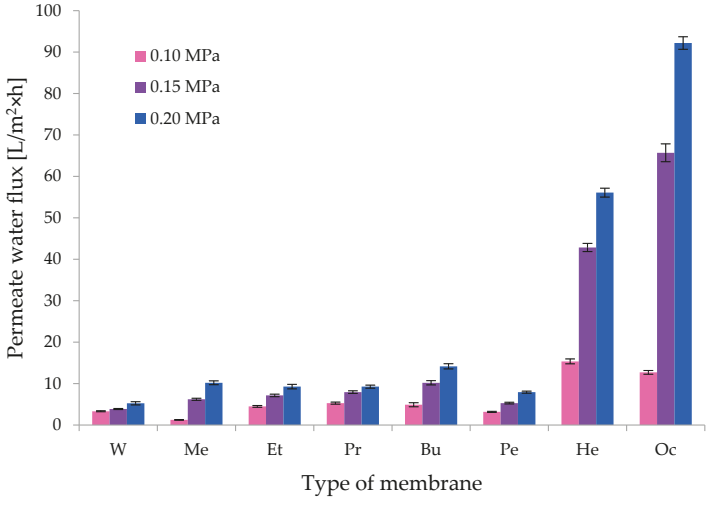

Figure 11. Water flux for the obtained cellulose membranes.

It should be noted that, as shown in Figure 11, the course of changes in the volumetric permeate flux correlated very well with the course of changes in the pore content versus the molecular mass of the coagulant, as shown above in Figure 6. The transport properties of the cellulose membranes

undoubtedly depend on their porous structures, and this in turn depends on the physico-chemical properties of the coagulant used to obtain them [18,19].

3.1.4. Separation Properties of CEL Membranes

It is known that cellulose-based composite membranes have been used to remove metal ions such as Fe(III) and Cu(II) [45]. A 0.1 g/dm^3 aqueous solution of iron salt ($FeCl_3$) was selected to study the separation properties of the investigated CEL membranes. A volumetric permeate flux and rejection coefficient were observed during the study (Figures 11 and 12). Studies have shown that the introduction of iron ion solution into CEL membranes causes a rapid decrease in the permeate flux by approximately 67–96% at the beginning of the process. Flow through the membrane constantly decreased during membrane operation, and after about 60 min, it was about 95–98%. The obtained result may indicate that the introduction of iron ions to CEL membranes resulted in fouling on all membranes in the experiment. Kongdee et al. [46] proved that ferrous ions can be complexed on cellulose fibers, which was confirmed in our experiment.

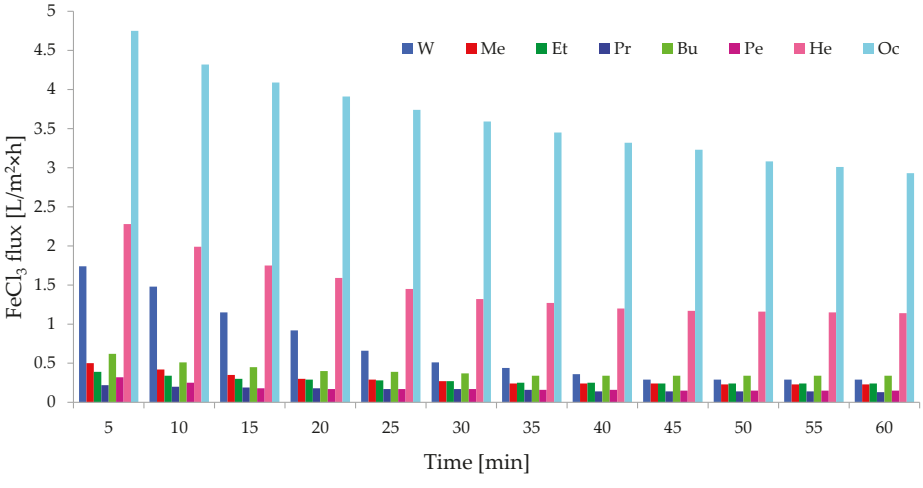

Figure 12. Volumetric permeate flux for the solution of $FeCl_3$.

The detailed analysis of our results showed that the highest volumetric permeate flux values during the permeation of iron ions occurred with membrane Oc. Initially, the permeate flux was 4.75 L/m^2 h, and after 60 min, it decreased to 2.93 L/m^2 h. For membrane Oc, the decrease in flux was 94.85–96.82% at the beginning and end of the process, respectively. At the same time, it was observed (Figure 13) that the $FeCl_3$ rejection coefficient was ~61%, so membrane Oc was not clogged completely. This result confirms that it was very porous with large pores. Similar results were obtained for the study of transport properties of membrane He for which the volumetric permeate flux values were in the range of 2.28–1.14 L/m^2 h (Figure 12). The decrease in the permeate flux was 95.94–97.97% relative to that obtained for distilled water. The $FeCl_3$ rejection coefficient on membrane He was 62.32%, confirming the high porosity of this membrane. A similar rejection coefficient result of 61.31% was obtained for membrane W (Figure 13). At the same time, it was observed that the decrease of the volumetric rejection coefficient at the beginning of the process was the lowest (66.78%) during the flow of iron(III) ions through membrane W, and this increased to 94.46% after 60 min. The obtained results suggest that membranes Oc, He, and W, characterized by low density and high porosity, had similar separation properties relative to the aqueous solution of $FeCl_3$.

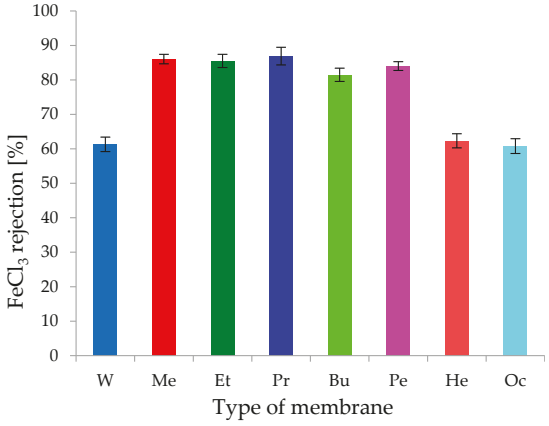

Figure 13. Rejection coefficient (R) for $FeCl_3$ solution.

For the remaining cellulose membranes (Me, Et, Pr, Bu, and Pe), the decrease in the specific permeate flux for iron ions was similar and ranged between 95% and 98%, with a rejection coefficient of ~81.5% (for membrane Bu), ~84% (for membrane Pe), ~85.5% (for membrane Et), ~86% (for membrane Me), and 86.9% (for membrane Pr). These membranes almost completely blocked iron(III) ions, while the permeate flux decreased to very low values of 0.15–0.34 L/m^2 h. Membranes Me, Et, Pr, Bu, and Pe could be used to remove metals from solutions, as suggested in the work of Cifci et al. [45]. The phenomenon of removal of Fe(III) ions on cellulose membranes may be a result of the formation of chemical bonds between metal ions and the functional groups of cellulose. Yadav [33] used the phenomenon of Fe ion complexation on cellulose, obtaining new, previously unmentioned bionanocomposites.

3.2. Graphene Oxide/Cellulose (GO/CEL) Membranes

Graphene oxide (GO) is a modern material used for the production of polymer composites. GO has many different oxygen-containing functional groups, such as epoxy, hydroxyl, carbonyl, and carboxyl [47,48]. Oxygen groups give hydrophilic properties to graphene oxide, making it easy to form stable aqueous dispersions [49,50] at concentrations above 3 mg/mL [51]. GO is also used in membranes, along with carbon nanotubes [52–55] and graphene [56–58]. It allows thin monolayer films to be obtained [54–57], which can be used for desalination and purification [56,57,59,60] as well as membrane distillation [61].

The GO/CEL membranes are composites in which cellulose chains containing hydroxyl groups form hydrogen bonds with oxygen functional groups on the surfaces and edges of GO flakes (Figure 14) [38,62].

For the preparation of GO/CEL membranes, a method of combining the cellulose solution with a GO dispersion was developed to obtain a homogeneous solution from which the composite membranes were then formed using the phase inversion method by coagulation in distilled water. As a result, cellulose composite membranes (labeled A–F) which differed in color depending on the amount of GO added were obtained (Figure 15). A pure cellulose membrane (labelled "0") was also obtained to compare its properties with the properties of membranes containing GO. As shown in Figure 14, membrane "0" was colorless, while the other diaphragms were shades of grey. The -bigger amount of GO was added the darker the GO/CEL composite membranes became.

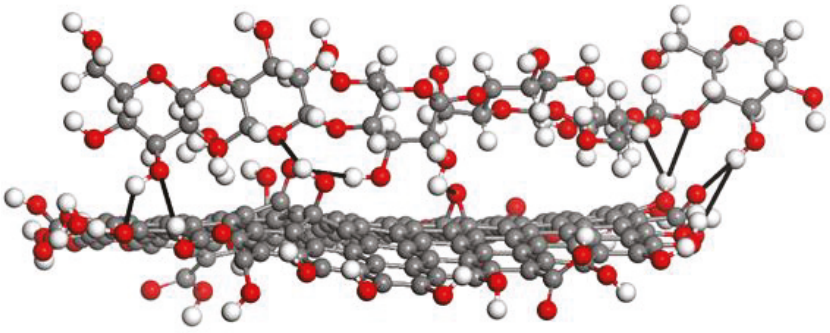

Figure 14. Schematic diagram of hydrogen bonds (black bold line) between the GO (bottom) and CEL macromolecular chains (top). Grey balls—carbon, white balls—hydrogen, red balls—oxygen.

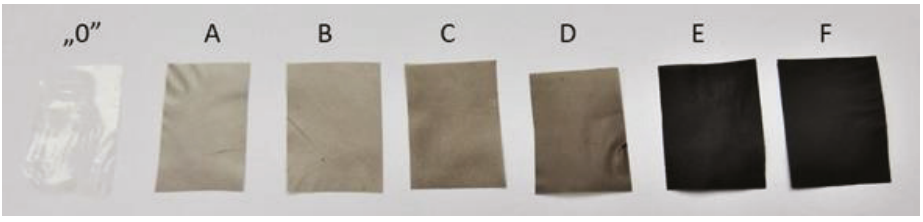

Figure 15. Images of a pure cellulose membrane ("0") and GO/CEL composite membranes (A—0.1% GO, B—0.2% GO, C—1% GO, D—2% GO, E—10% GO, F—20% GO).

3.2.1. Morphology and Structure of GO/CEL Membranes

In the SEM images of membrane cross sections (Figure 1601–F1), the pure cellulose membrane ("0") was observed to be compact but slightly rough, which made it clearly distinguishable from the GO/CEL composite membranes. The cross sections of membranes A and B were similar to each other. In the case of composite membranes A and B, apart from the roughness, horizontal cracks appeared. Further, the addition of 0.1% and 0.2% GO increased the thickness of the membranes (Figure 16A1,B1). The cross-sectional structures of membranes C and D were different from all others. Membranes containing 1% and 2% GO had compact structures but with visible horizontal cracks (Figure 16C1,D1). By comparing the thickness of the membranes, it was seen that a 1% addition of GO to composite membrane C reduced its thickness, which was comparable with the thickness of the "0" membrane. Many horizontal cracks were observed in the SEM images of membrane E. The structure of can be observed as being entirely composed of transversely arranged flakes. The effect of GO addition on the cellulose matrix was easily observed using the microscopic observations of membrane cross sections. The effect of increasing the amount of GO in the composite membrane was the appearance of an increasing number of cracks, which may have resulted from the arrangement of components in the composite. Phiri et al. also observed the formation of layers in the cross sections of composite membranes based on microfibrillated cellulose with the addition of GO [63].

The morphology of the skin layers of the membranes can be observed in Figure 1602–F2. Membrane "0" was characterized by an even, smooth surface, while the surfaces of composite membranes with small amounts of added GO (membranes A, B, C) were very rich in corrugations, spherical beads, and recesses. In contrast, the skin layers of membranes D, E, and F were different from the others. On the relatively flat surface of these membranes, cracks and recesses were observed, the number and size of which increased with the amount of GO added in the direction of membranes D to F.

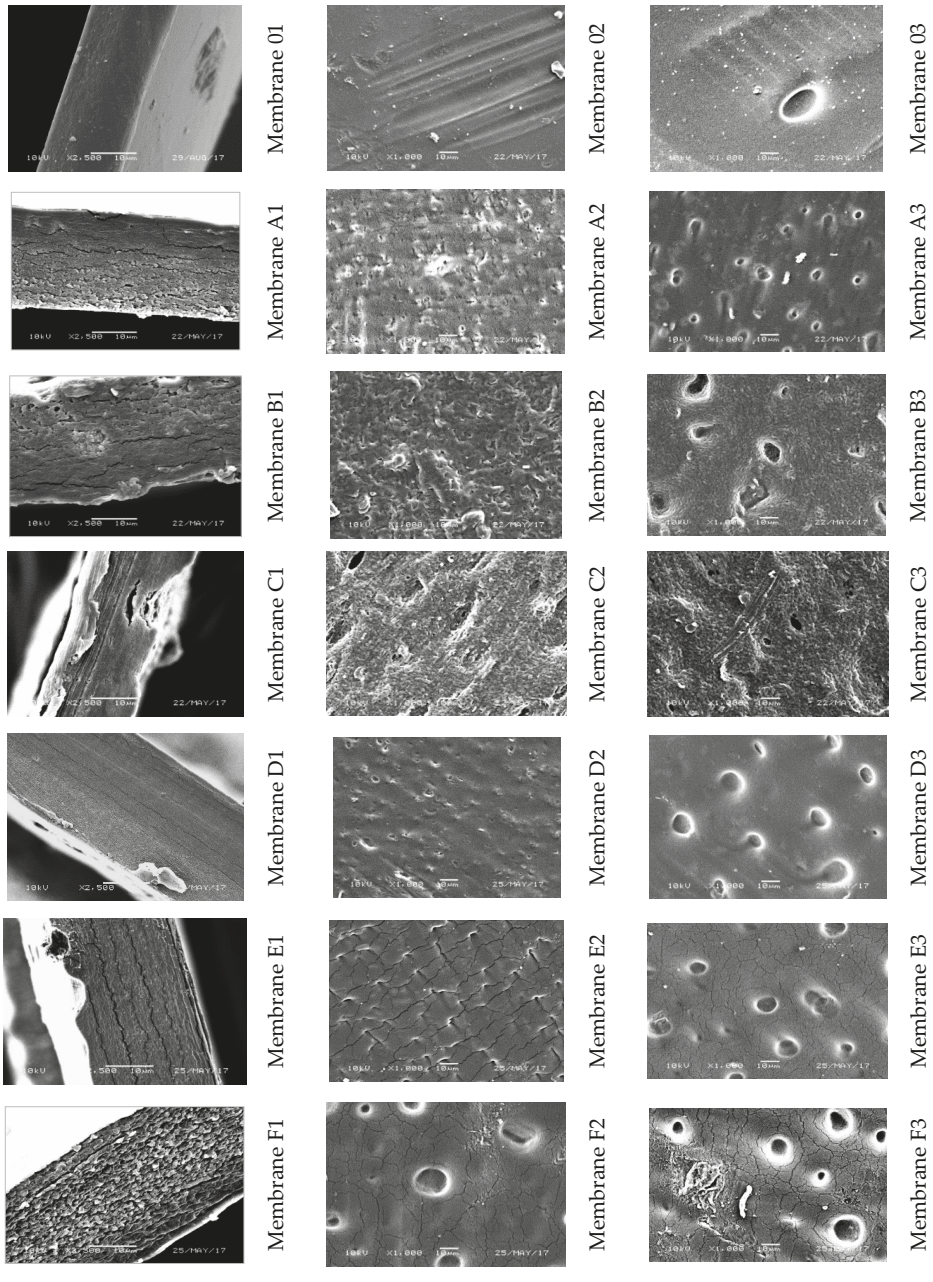

Figure 16. SEM images for the pure cellulose membrane and GO/CEL composite membranes: (**1**) cross section; (**2**) skin layer; (**3**) bottom layer.

The surface of the support layers of all membranes (Figure 1603–F3) was richer in various morphological structure elements compared with the skin layer. Hollows and spherical beads were observed, the number and size of which increased with the amount of added GO. In the case of membranes E and F, apart from hollows, numerous cracks appeared on the surface of the support layer.

Figure 17 shows the WAXS diffraction curves of membrane "0" (the pure cellulose) and the pure GO. As described in Section 3.1.2 (Figure 8), the cellulose curve contains all peaks characteristic for cellulose II. The WAXS curve of the GO shows a sharp diffraction peak at 2θ = 9.0° (d-spacing = 0.98 nm), which reflects the gallery gap of the layered structure of the GO.

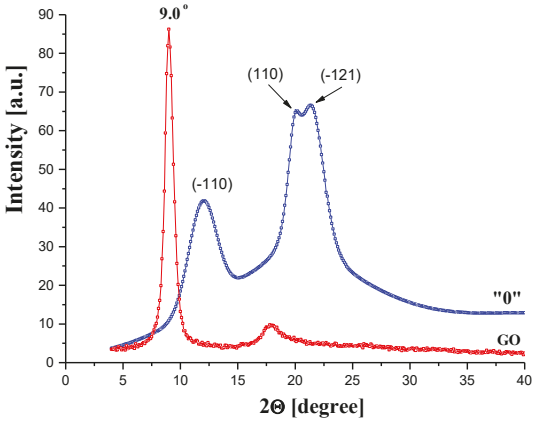

Figure 17. WAXS patterns of membrane "0" (pure cellulose) and pure GO.

Figure 18 presents the WAXS diffraction patterns of the GO/CEL membranes. The angular position of the GO peak was shifted towards the lower diffraction angles with a decreasing GO content. This peak shift indicates an increase in the distance between the carbon layers in the GO. Compared to pure GO, this distance increased from 0.98 to 1.6 nm for membranes B and D, respectively. The stepwise increase in d-spacing might be due to the interactions between GO and cellulose by hydrogen bonds (Figure 14), which might have already been saturated at a low loading of the GO. Therefore, the increase in the distance between carbon galleries in GO was more pronounced when the ratio of cellulose content to GO content increased.

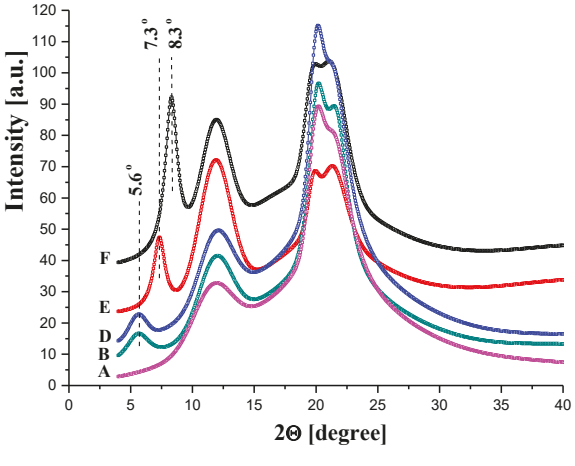

Figure 18. Examples of WAXS patterns of cellulose membranes (the letters on the left indicate the membrane codes).

3.2.2. Transport Properties of GO/CEL Membranes

In order to investigate the effect of adding GO on the transport properties of cellulose membranes, we determined the permeate water flux for the obtained membranes. The course of changes in the value of this parameter for individual membranes is illustrated in Figure 19. The lowest values of volumetric permeate flux were recorded for membrane "0", and for the subsequent pressures of 0.1, 0.15, and 0.2 MPa, they were respectively 2.93 ± 0.02, 3.76 ± 0.07, and 4.36 ± 0.03 L/m^2 h. A slow but slight increase in the permeate flux which was observed with the increase of working pressure suggests that membrane "0" had a compact structure. It can therefore be assumed that membrane "0" was composed of closed pores, as confirmed by SEM images (Figure 1601).

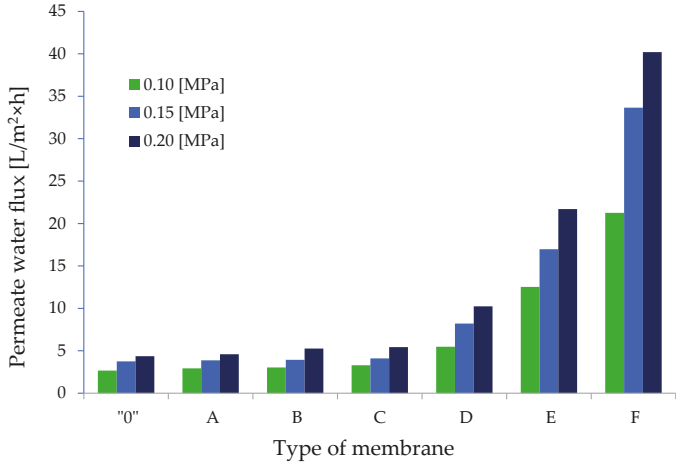

Figure 19. Pure water permeability for the pure cellulose membrane and GO/CEL composite membranes.

The transport properties of the composite membranes A, B, and C were similar. The permeate flux for these membranes increased slowly with the increase in working pressure, and at 0.2 MPa, it was 4.58 ± 0.32 (membrane A), 5.26 ± 0.10 (membrane B), and 5.43 ± 0.07 (membrane C) L/m^2 h. The results show that the addition of 0.1%, 0.2%, and 1.0% *w/w* of GO to the cellulose only slightly improved the transport properties of the obtained GO/CEL membranes. In the case of membranes A and B, it can be assumed that the structures observed in SEM images contained mainly closed pores. However, in the case of membrane C, low values of the permeate water flux may have been a result of the formation of hydrogen bonds between GO molecules and cellulose chains (Figure 14), which results in hydrophobic membranes, as described in our earlier publication [64]. This could be confirmed by the low thickness of membrane C observed in SEM images (Figure 16C1).

An increase in the distilled water flow through cellulose composite membranes was observed for GO added at concentrations of 2%, 10%, and 20% *w/w*. The permeate volumetric flux values for the working pressure of 0.2 MPa were 10.24 ± 0.22 (membrane D), 21.71 ± 0.68 (membrane E), and 40.20 ± 2.33 (membrane F) L/m^2 h, respectively. The results show that the addition of graphene oxide to cellulose in amounts of 2%, 10%, and 20% *w/w* improved the transport properties of the obtained GO/CEL membranes by 2, 5, and 10 times in comparison to membrane "0". Thus, it can be assumed that due to the large amount of GO, membranes D, E, and F had layered structures (Figure 16D1,E1,F1) facilitating the transport of water despite the high thickness of these composite membranes.

3.2.3. Separation Properties of GO/CEL Membranes

The present study also examined whether the obtained membranes could be used to remove bivalent heavy metal ions from aqueous solutions. All obtained membranes—both pure cellulose

and cellulose with added components—were characterized by high rejection coefficient (R) values. Membrane "0" (Figure 20a) was characterized by rejection coefficients of 100% (Co), 93% (Zn), ~69% (Pb), 40% (Ni), and 1% (Na). On the other hand, the studies carried out on the synthetic wastewater mixture (Figure 20b) showed that the R coefficients for the pure cellulose membrane were 100% (Co), ~ 87% (Zn), ~71% (Pb), ~79% (Ni), and ~2% (Na). It was observed that in the mixture of synthetic wastewater, preferential rejection of nickel ions on membrane "0" and an increase in the degree of lead ion rejection with respect to zinc ions, for which the R coefficient decreased, occurred.

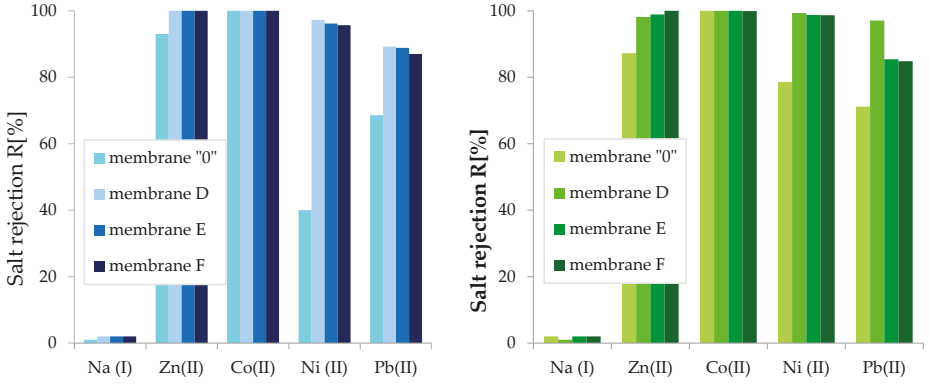

Figure 20. Rejection coefficients on pure cellulose membrane and GO/CEL composite membranes of (**a**) single metals; (**b**) subsequent metals in synthetic wastewater.

All cellulose GO/CEL composite membranes studied in the experiment were characterized by higher rejection coefficient values than membrane "0" (Figure 20). Thus, the nanoaddition of GO in the cellulose matrix increased the amount of heavy metal ions deposited on the membranes. By analyzing the results obtained for membrane D, it was observed that the addition of 2% *w/w* of graphene oxide resulted in the highest R coefficient values of 100% (Co); 98–100% (Zn); 97–99% (Ni); and 69–71% (Pb). An increase in the amount of GO addition to 10% or 20% did not improve the degree of ion rejection on membranes; rather, it slightly decreased it by 1%.

The explanation of the observed phenomenon may be that the concentration of GO in the composite was too high, resulting in the formation of layers and cracks, which were observed in cross sections (Figure 16D1,E1,F1). We do not know exactly how the cellulose and GO layers were arranged in our composite. However, Chen et al. [65] showed that the arrangement of the electronegative and electropositive components of the composite is responsible for the separation properties of the membranes, as well as the order in which heavy metals are removed from solution.

The results of this study show that the membranes obtained in the experiment were characterized by very high rejection coefficients in relation to the divalent metal ions cobalt, zinc, nickel, and lead. For Co (II) ions, total rejection was observed on each studied membrane, both for the solution containing single ions and for the synthetic wastewater mixture. In the case of other ions, on the other hand, the degree of rejection (R) of divalent ions was in the range of 85–99%. The low rejection coefficient for sodium ions (1–2%) indicates that we obtained an ultrafiltration membrane.

The observed changes may be the result of interactions between functional groups of cellulose chains and metal ions. The cellulose membrane is negatively charged, and the charge is derived from hydroxyl groups (primary and secondary), which, according to Lewis theory, are hard bases. Co^{2+}, Ni^{2+}, Zn^{2+}, and Pb^{2+} ions, on the other hand, are indirect acids. Thus, the formation of chemical (ionic and hydrogen) bonds between metal ions and cellulose chains is possible. The resulting combination rejects heavy metal ions on the membrane but does not cause fouling. The increase in the permeate

flow, on the other hand, may result from the formation of channels through which small particles of water flow freely.

4. Conclusions

This paper presents the results of research on the production of cellulose membranes from cellulose solution in EMIMAc ionic liquid. The membranes were formed by phase inversion using water and primary alcohols as coagulants. The results of structural investigations performed by X-ray methods (WAXS and SAXS) reflected the complexity of the membrane formation process at the molecular level. Our research shows that the physicochemical properties of the coagulant used, such as molecular mass and dipole moment, play important roles in this process. It was found that both the content and dimensions of the pores depended on the molecular mass of the coagulant used. It was also found that the dipole moment of coagulant molecules had a large influence on the volume content of the pores. The highest content of pores was obtained when these two factors represented a substantial value. In cases where any of these factors was of little value, the pore content decreased significantly. The discussed studies also revealed the effect of the pore content on the crystallinity of cellulose membranes; namely, the degree of crystallinity decreased almost linearly as the volume fraction of pores increased. This indicates that the formation of pores hinders the crystallization process of regenerated cellulose to some extent.

The porous structure of CEL membranes has a significant impact on their transport properties. The lowest values of the volumetric permeate flux occurred for membrane (W), which was formed using the coagulant of the lowest molecular mass, while the highest value of this parameter occurred for the membranes (He and Oc) coagulated using coagulants with large molecular masses.

Studies of the separation properties of CEL membranes carried out using iron(III) solution showed a very high decrease in flow of 67–96% and a high rejection coefficient (82–87%), indicating a lack of resistance to the unfavorable phenomenon of fouling.

The introduction of GO into the cellulose matrix influenced the process of membrane formation and, consequently, the physicochemical, transport, and separation properties of the GO/CEL composite membranes. Structural studies have shown that the incorporation of a small GO additive into the cellulose membranes results in a homogeneous composite in which the individual components are connected by hydrogen bonds. The use of SEM and WAXS showed that in the case of a relatively high GO content, the excess admixture separated and an isolated GO phase occurred in the GO/CEL membrane structure, and this was responsible for very good transport and separation membrane properties. The addition of graphene oxide improved the flow of water through membranes by up to 10 times. For these reasons, it is advisable to add GO to the CEL matrix. Composite membranes containing 2%, 10%, and 20% GO also had very good rejection of heavy metal ions. Due to the bactericidal GO admixture, GO/CEL membranes could also find a potential application in water disinfection [66].

Author Contributions: Conceptualization, C.S. and B.F.; SAXS and WAXS investigation, C.S.; membrane preparation, transport and separation properties, B.F.; writing—original draft preparation, C.S.; writing—review and editing, C.S. and B.F; supervision B.F.

Funding: This research received no external funding.

Conflicts of Interest: The authors declare no conflict of interest.

References

1. Ramamoorthy, S.K.; Skrifvars, M.; Persson, A. A review of natural fibers used in biocomposites: Plant, animal and regenerated cellulose fibers. *Polym. Rev.* **2015**, *55*, 107–162. [CrossRef]
2. Klemm, D.; Heublein, B.; Fink, H.P.; Bohn, A. Cellulose: Fascinating biopolymer and sustainable raw material. *Angew. Chem. Int. Ed.* **2005**, *44*, 3358–3393. [CrossRef] [PubMed]

3. Singh, P.; Duarte, H.; Alves, L.; Antures, F.; Le Moigne, N.; Dormanns, J.; Duchemi, B.; Staiger, M.P. From cellulose dissolution and regeneration to added value applications—Synergism between molecular understanding and material development. In *Cellulose—Fundamental Aspects and Current Trends. Cellulose—Fundamental Aspects and Current Trends*; SE1 9SG; Poletto, M., Ed.; IntechOpen Limited: London, UK, 2015; pp. 237–261.
4. Edgar, K.J.; Buchanan, C.M.; Debenham, J.S.; Rundquist, P.A.; Seiler, B.D.; Shelton, M.C.; Tindall, D. Advances in cellulose ester performance and application. *Prog. Polym. Sci.* **2001**, *26*, 1605–1688. [CrossRef]
5. Jin, H.; Zha, C.; Gu, L. Direct dissolution of cellulose in NaOH/thiourea/urea aqueous solution. *Carbohydr. Res.* **2007**, *342*, 851–858. [CrossRef] [PubMed]
6. Fink, H.P.; Weigel, P.; Purz, H.J.; Ganster, J. Structure formation of regenerated cellulose materials from NMMO-solutions. *Prog. Polym. Sci.* **2001**, *26*, 1473–1524. [CrossRef]
7. Gathergood, N.; Garcia, M.T.; Scammells, P.J. Biodegradable ionic liquids: Part I. Concept, preliminary targets and evaluation. *Green Chem.* **2004**, *6*, 166. [CrossRef]
8. Jastorff, B.; Störmann, R.; Ranke, J.; Mölter, K.; Stock, F.; Oberheitmann, B.; Hoffmann, W.; Hoffmann, J.; Nüchter, M.; Ondruschka, B.; et al. How hazardous are ionic liquids? Structure-activity relationships and biological testing as important elements for sustainability evaluation. *Green Chem.* **2003**, *5*, 136–142. [CrossRef]
9. Earle, M.J.; Seddon, K.R. Ionic liquids. Green solvents for the future. *Pure Appl. Chem.* **2000**, *72*, 1391–1398. [CrossRef]
10. Novoselov, N.P.; Sashina, E.S.; Kuz'mina, O.G.; Troshenkova, S.V. Ionic liquids and their use for the dissolution of natural polymers. *Russ. J. Gen. Chem.* **2007**, *77*, 1395–1405. [CrossRef]
11. Kosan, B.; Michels, C.; Meister, F. Dissolution and forming of cellulose with ionic liquids. *Cellulose* **2008**, *15*, 59–66. [CrossRef]
12. Greaves, T.L.; Drummond, C.J. Solvent nanostructure, the solvophobic effect and amphiphile self-assembly in ionic liquids. *Chem. Soc. Rev.* **2013**, *42*, 1096–1120. [CrossRef] [PubMed]
13. Hu, X.M.; Xiao, Y.B.; Niu, K.; Zhao, Y.; Zhang, B.X.; Hu, B.Z. Functional ionic liquids for hydrolysis of lignocellulose. *Carbohydr. Polym.* **2013**, *97*, 172–176. [CrossRef] [PubMed]
14. Zhu, S.D.; Wu, Y.X.; Chen, Q.M.; Yu, Z.N.; Wang, C.W.; Jin, S.W. Dissolution of cellulose with ionic liquids and its application: A mini-review. *Green Chem.* **2006**, *8*, 325–327. [CrossRef]
15. Hermanutz, F.; Gähr, F.; Uerdingen, E.; Meister, F.; Kosan, B. New developments in dissolving and processing of cellulose in ionic liquids. *Macromol. Symp.* **2008**, *262*, 23–27. [CrossRef]
16. Swatloski, R.P.; Spear, S.K.; Holbrey, J.D.; Rogers, R.D. Dissolution of cellulose with ionic liquids. *J. Am. Chem. Soc.* **2002**, *124*, 4974–4975. [CrossRef]
17. Wendler, F.; Todi, L.N.; Meister, F. Thermostability of imidazolium ionic liquids as direct solvents for cellulose. *Thermochim. Acta* **2012**, *528*, 76–84. [CrossRef]
18. Mahadeva, S.K.; Kim, J. Influence of residual ionic liquid on the thermal stability and electromechanical behavior of cellulose regenerated from 1-ethyl-3-methylimidazolium acetate. *Fibers Polym.* **2012**, *13*, 289–294. [CrossRef]
19. Sun, N.; Rahman, M.; Qin, Y.; Maxim, M.L.; Rodríguez, H.; Rogers, R.D. Complete dissolution and partial delignification of wood in the ionic liquid 1-ethyl-3-methylimidazolium acetate. *Green Chem.* **2009**, *11*, 646. [CrossRef]
20. Livazovic, S.; Li, Z.; Behzad, A.R.; Peinemann, K.V.; Nunes, S.P. Cellulose multilayer membranes manufacture with ionic liquid. *J. Membr. Sci.* **2015**, *490*, 282–293. [CrossRef]
21. Pinkert, A.; Marsh, K.N.; Pang, S.; Staiger, M.P. Ionic liquids and their interaction with cellulose. *Chem. Rev.* **2009**, *109*, 6712–6728. [CrossRef]
22. Ruan, D.; Zhang, L.; Mao, Y.; Zeng, M.; Li, X. Microporous membranes prepared from cellulose in NaOH/thiourea aqueous solution. *J. Membr. Sci.* **2004**, *241*, 265–274. [CrossRef]
23. Rambo, C.R.; Recouvreux, D.O.S.; Carminatti, C.A.; Pitlovanciv, A.K.; Antônio, R.V.; Porto, L.M. Template assisted synthesis of porous nanofibrous cellulose membranes for tissue engineering. *Mater. Sci. Eng. C* **2008**, *28*, 549–554. [CrossRef]
24. Yadav, M. Study on thermal and mechanical properties of cellulose/iron oxide bionanocomposites film. *Compos. Commun.* **2018**, *10*, 1–5. [CrossRef]

25. Rotaru, R.; Savin, M.; Tudorachi, N.; Peptu, C.; Samoila, P.; Sacarescu, L.; Harabagiu, V. Ferromagnetic iron oxide–cellulose nanocomposites prepared by ultrasonication. *Polym. Chem.* **2018**, *9*, 860–868. [CrossRef]
26. Rac-Rumijowska, O.; Fiedot, M.; Karbownik, I.; Suchorska-Woźniak, P.; Teterycz, H. Synthesis of silver nanoparticles in NMMO and their in situ doping into cellulose fiber. *Cellulose* **2017**, *24*, 1355–1370. [CrossRef]
27. Yue, X.; Zhang, T.; Yang, D.; Qiu, F.; Li, Z.; Wei, G.; Qiao, Y. Ag nanoparticles coated cellulose membrane with high infrared reflection, breathability and antibacterial property for human thermal insulation. *J. Colloid Interface Sci.* **2019**, *535*, 363–370. [CrossRef] [PubMed]
28. Suna, Z.; Yanga, L.; Zhangc, D.; Songa, W. High performance, flexible and renewable nano-biocomposite artificial muscle based on mesoporous cellulose/ionic liquid electrolyte membrane. *Sens. Actuators B Chem.* **2019**, *283*, 579–589. [CrossRef]
29. Liu, P.; Zhu, C.; Mathew, A.P. Mechanically robust high flux graphene oxide—Nanocellulose membranes for dye removal from water. *J. Hazard. Mater.* **2019**, *371*, 484–493. [CrossRef]
30. Lv, J.; Zhang, G.; Zhang, H.; Yang, F. Graphene oxide-cellulose nanocrystal (GO-CNC) composite functionalized PVDF membrane with improved antifouling performance in MBR: Behavior and mechanism. *Chem. Eng. J.* **2018**, *352*, 765–773. [CrossRef]
31. Lyu, Y.; Zhang, Q.; Wang, Z.; Pu, J. A graphene oxide nanofiltration membrane intercalated with cellulose nano-crystals. *BioResources* **2018**, *13*, 9116–9131. [CrossRef]
32. Yadav, M.; Rhee, K.Y.; Jung, I.H.; Park, S.J. Eco-friendly synthesis, characterization and properties of a sodium carboxymethyl cellulose/graphene oxide nanocomposite film. *Cellulose* **2013**, *20*, 687–698. [CrossRef]
33. Yadav, M.; Rhee, K.Y.; Park, S.J. Synthesis and characterization of grapheneoxidecarboxymethylcellulose/alginate composite blend films. *Carbohydr. Polym.* **2014**, *110*, 18–25. [CrossRef] [PubMed]
34. Gupta, K.M.; Hu, Z.; Jiang, J. Mechanistic understanding of interactions between cellulose and ionic liquids: A molecular simulation study. *Polymer* **2011**, *52*, 5904–5911. [CrossRef]
35. Tan, H.T.; Lee, K.T.; Mohamed, A.R. Pretreatment of lignocellulosic palm biomass using a solvent-ionic liquid [BMIM]Cl for glucose recovery: An optimisation study using response surface methodology. *Carbohydr. Polym.* **2011**, *83*, 1862–1868. [CrossRef]
36. Feng, L.; Ian Chen, Z. Research progress on dissolution and functional modification of cellulose in ionic liquids. *J. Mol. Liq.* **2008**, *142*, 1–5. [CrossRef]
37. Ding, Z.D.; Chi, Z.; Gu, W.X.; Gu, S.M.; Liu, J.H.; Wang, H.J. Theoretical and experimental investigation on dissolution and regeneration of cellulose in ionic liquid. *Carbohydr. Polym.* **2012**, *89*, 7–16. [CrossRef]
38. Hummers, W.S.; Offeman, R.E. Preparation of graphitic oxide. *J. Am. Chem. Soc.* **1958**, *80*, 1339. [CrossRef]
39. Fryczkowska, B.; Sieradzka, M.; Sarna, E.; Fryczkowski, R.; Janicki, J. Influence of a graphene oxide additive and the conditions of membrane formation on the morphology and separative properties of poly(vinylidene fluoride) membranes. *J. Appl. Polym. Sci.* **2015**, *132*, 42789. [CrossRef]
40. Moulik, S.; Vaishnavi, B.A.; Nagar, H.; Sridhar, S. Water competitive diffusion. In *Encyclopedia of Membranes*; Drioli, E., Giorno, L., Eds.; Springer: Berlin/Heidelberg, Germany, 2016; pp. 1973–1983.
41. Stabinger, H.; Kratky, O. A new technique for the measurement of absolute intensity of X-ray small-angle scattering. The moving slit method. *Makromol. Chem.* **1978**, *179*, 1655–1659. [CrossRef]
42. Kratky, O.; Pilz, I.; Schmitz, P.J. Absolute intensity measurement of small angle X-ray scattering by means of standard sample. *J. Colloid Interface Sci.* **1966**, *21*, 24–34. [CrossRef]
43. Crawshaw, J.; Cameron, R.E. A small angle X-ray scattering study of pore structure in Tencel cellulose fibres and the effects of physical treatments. *Polymer* **2000**, *41*, 4691–4698. [CrossRef]
44. Rabiej, M. Application of the particle swarm optimization method for the analysis of wide-angle X-ray diffraction curves of semicrystalline polymers. *J. Appl. Crystallogr.* **2017**, *50*, 221–230. [CrossRef]
45. Çifci, C.; Kaya, A. Preparation of poly(vinyl alcohol)/cellulose composite membranes for metal removal from aqueous solutions. *Desalination* **2010**, *253*, 175–179. [CrossRef]
46. Kongdee, A.; Bechtold, T. The complexation of Fe(III)-ions in cellulose fibres: A fundamental property. *Carbohydr. Polym.* **2004**, *56*, 47–53. [CrossRef]
47. Guerrero-Contreras, J.; Caballero-Briones, F. Graphene oxide powders with different oxidation degree, prepared by synthesis variations of the Hummers method. *Mater. Chem. Phys.* **2015**, *153*, 209–220. [CrossRef]
48. Ghosh, T.; Biswas, C.; Oh, J.; Arabale, G.; Hwang, T.; Luong, N.D.; Jin, M.; Lee, Y.H.; Do Nam, J. Solution-processed graphite membrane from reassembled graphene oxide. *Chem. Mater.* **2012**, *24*, 594–599. [CrossRef]

49. Yoon, K.Y.; An, S.J.; Chen, Y.; Lee, J.H.; Bryant, S.L.; Ruoff, R.S.; Huh, C.; Johnston, K.P. Graphene oxide nanoplatelet dispersions in concentrated NaCl and stabilization of oil/water emulsions. *J. Colloid Interface Sci.* **2013**, *403*, 1–6. [CrossRef] [PubMed]
50. Texter, J. Graphene dispersions. *Curr. Opin. Colloid Interface Sci.* **2014**, *19*, 163–174. [CrossRef]
51. Konkena, B.; Vasudevan, S. Understanding aqueous dispersibility of graphene oxide and reduced graphene oxide through p K a measurements. *J. Phys. Chem. Lett.* **2012**, *3*, 867–872. [CrossRef]
52. Goh, K.; Setiawan, L.; Wei, L.; Jiang, W.; Wang, R.; Chen, Y. Fabrication of novel functionalized multi-walled carbon nanotube immobilized hollow fiber membranes for enhanced performance in forward osmosis process. *J. Membr. Sci.* **2013**, *446*, 244–254. [CrossRef]
53. Das, R.; Ali, M.E.; Hamid, S.B.A.; Ramakrishna, S.; Chowdhury, Z.Z. Carbon nanotube membranes for water purification: A bright future in water desalination. *Desalination* **2014**, *336*, 97–109. [CrossRef]
54. Hinds, B.J.; Chopra, N.; Rantell, T.; Andrews, R.; Gavalas, V.; Bachas, L.G. Aligned multiwalled carbon nanotube membranes. *Science* **2004**, *303*, 62–65. [CrossRef] [PubMed]
55. Celik, E.; Park, H.; Choi, H.; Choi, H. Carbon nanotube blended polyethersulfone membranes for fouling control in water treatment. *Water Res.* **2011**, *45*, 274–282. [CrossRef] [PubMed]
56. Mahmoud, K.A.; Mansoor, B.; Mansour, A.; Khraisheh, M. Functional graphene nanosheets: The next generation membranes for water desalination. *Desalination* **2015**, *356*, 208–225. [CrossRef]
57. Han, Y.; Xu, Z.; Gao, C. Ultrathin graphene nanofiltration membrane for water purification. *Adv. Funct. Mater.* **2013**, *23*, 3693–3700. [CrossRef]
58. Joshi, R.K.; Alwarappan, S.; Yoshimura, M.; Sahajwalla, V.; Nishina, Y. Graphene oxide: The new membrane material. *Appl. Mater. Today* **2015**, *1*, 1–12. [CrossRef]
59. Goh, P.S.; Ismail, A.F. Graphene-based nanomaterial: The state-of-the-art material for cutting edge desalination technology. *Desalination* **2015**, *356*, 115–128. [CrossRef]
60. Nair, R.R.; Wu, H.A.; Jayaram, P.N.; Grigorieva, I.V.; Geim, A.K. Unimpeded permeation of water through helium-leak-tight graphene-based membranes. *Science* **2012**, *335*, 442–444. [CrossRef] [PubMed]
61. Bhadra, M.; Roy, S.; Mitra, S. Desalination across a graphene oxide membrane via direct contact membrane distillation. *Desalination* **2016**, *378*, 37–43. [CrossRef]
62. Zhang, X.; Yu, H.; Yang, H.; Wan, Y.; Hu, H.; Zhai, Z.; Qin, J. Graphene oxide caged in cellulose microbeads for removal of malachite green dye from aqueous solution. *J. Colloid Interface Sci.* **2015**, *437*, 277–282. [CrossRef] [PubMed]
63. Phiria, J.; Johanssona, L.S.; Ganea, P.; Maloney, T. A comparative study of mechanical, thermal and electrical properties ofgraphene-, graphene oxide- and reduced graphene oxide-dopedmicrofibrillated cellulose nanocomposites. *Compos. Part B* **2018**, *147*, 104–113. [CrossRef]
64. Fryczkowska, B.; Wiechniak, K. Preparation and properties of cellulose membranes with graphene oxide addition. *Pol. J. Chem. Technol.* **2017**, *19*, 41–49. [CrossRef]
65. Chen, Y.; Liu, F.; Wang, Y.; Lin, H.; Han, L. A tight nanofiltration membrane with multi-charged nanofilms for high rejection to concentrated salts. *J. Membr. Sci.* **2017**, *537*, 407–415. [CrossRef]
66. Song, B.; Zhang, C.; Zeng, G.; Gong, J.; Chang, Y.; Jiang, Y. Antibacterial properties and mechanism of graphene oxide-silver nanocomposites as bactericidal agents for water disinfection. *Arch. Biochem. Biophys.* **2016**, *604*, 167–176. [CrossRef]

polymers

MDPI

Article

Efficient Adsorption on Benzoyl and Stearoyl Cellulose to Remove Phenanthrene and Pyrene from Aqueous Solution

Yohan Kim [1,†], Daham Jeong [1,†], Kyeong Hui Park [1], Jae-Hyuk Yu [2] and Seunho Jung [1,*]

[1] Department of Systems Biotechnology, Microbial Carbohydrate Resource Bank (MCRB), Center for Biotechnology Research in UBITA (CBRU), Konkuk University, Seoul 05029, Korea; shsks1@hanmail.net (Y.K.); amir@konkuk.ac.kr (D.J.); kyeonghee17@naver.com (K.H.P.)

[2] Departments of Bacteriology and Genetics, University of Wisconsin-Madison, Madison, WI 53706, USA; jyu1@wisc.edu

* Correspondence: shjung@konkuk.ac.kr; Tel.: +82-2450-3520

† These authors contributed equally to this work.

Received: 31 July 2018; Accepted: 17 September 2018; Published: 19 September 2018

Abstract: Benzoyl and stearoyl acid grafted cellulose were synthesized by a simple chemical grafting method. Using these as chemical adsorbents, polycyclic aromatic hydrocarbons (PAHs), like pyrene and phenanthrene, were effectively removed from aqueous solution. The structural and morphological properties of the synthesized adsorbents were determined through X-ray diffraction analysis (XRD), thermal gravimetric analysis (TGA), Fourier transform infrared (FT-IR), FE-SEM, and NMR analyses. Through this method, it was confirmed that benzoyl and stearoyl acid were successfully grafted onto the surface of cellulose. The 5 mg of stearoyl grafted cellulose (St–Cell) remove 96.94% pyrene and 97.61% phenanthrene as compared to unmodified cellulose, which adsorbed 1.46% pyrene and 2.99% phenanthrene from 0.08 ppm pyrene and 0.8 ppm phenanthrene aqueous solution, suggesting that those results show a very efficient adsorption performance as compared to the unmodified cellulose.

Keywords: adsorption; phenanthrene; pyrene; benzoyl cellulose; stearoyl cellulose

1. Introduction

Industrial and agricultural contaminants, the number of which has dramatically increased due to worldwide development, are the most serious pollutants globally. Water resources can be contaminated with organic compounds, which are highly hazardous in every aspect. It has been reported that organic molecules in water from manufacturing activities, such as dyes, agrichemicals, and combustion byproducts, are not only a global concern owing to their long-term potential risk to ecosystems, but also have an effect on human health due to their high toxicity and low biodegradability [1]. Therefore, numerous countries regard water resource policy as a government priority project for decades. Activated carbon is a common adsorption material for the harmful substance, but it is expensive and the regeneration is difficult [2]. Recently, research on environmentally friendly materials for the removal of these pollutants have been intensified. Candidate materials have been reported in various forms such as hydrogel, nanocomposite, and membrane. These various platform materials were prepared by chemical modification with bio-based materials such as alginate [3], chitosan, cellulose [4], lignin [5], gelatin [6], and soy [7], thereby controlling harmful substances.

Among the organic products of incomplete combustion found in coal and in tar deposits, Polycyclic Aromatic Hydrocarbons (PAHs) are some of the most harmful carcinogenic substances [8,9]. PAHs are composed of multiple aromatic rings, which renders them stable and bioavailable from

months up to several years. Therefore, many researchers have attempted, through various treatments, to efficiently remove PAHs from water. However, it is difficult to completely convert PAHs to nontoxic molecules, such as CO_2 and H_2O, by chemical treatments [10]. The highly effective treatments, such as ozonation, high energy electron beam irradiation, and catalytic combustion, are high-cost methods, and so they are not extensively employed [11,12]. Among the diverse treatment techniques that have been applied by many researchers, sorption technology is the most common method to remove organic pollutants in waste water. This method is advantageous due to its simple and efficient methodology, which can be applied at any scale. Therefore, adsorption techniques can be used to remove both hazardous and less soluble organic molecules, such as PAHs, from water. However, the effectiveness of this method can be restricted because the sorption capacity can be affected by the chemical structure of the material and by its characteristics, such as porosity, specific surface area, swelling, and diffusivity. Many studies have been conducted to prove the sorption efficiency of various candidate materials as an adsorbent to remove PAHs. Amongst these candidate materials, cellulose has some advantages as an adequate adsorbent [13].

Cellulose is inexpensive and environmentally friendly because it is the most abundant naturally made polymer on the earth. Cellulose derivatives have been applied to the filtration process as these materials can trap organic and inorganic pollutants [14–16]. However, the adsorption ability of these naturally made products varies due to its dependence on the chemical environment. In order to complement the insufficient adsorption capacity, modification of cellulose has been carried out in numerous studies for decades [17–19]. Because the chemical modification on the hydroxyl group of the cellulose backbone changes the performance, as well as its properties, this method has been used to alter certain features of cellulose, such as hydrophobic or hydrophilic properties and elasticity [20]. Among many chemical cellulose modification methods, such as esterification, halogenation, oxidation, and etherification, determining adequate chemical reaction conditions is essential. Acylation of cellulose is a rapid esterification reaction with a high yield [21–23]. Particularly, the desired modified cellulose can be obtained by treating cellulose with other organic polymers containing long chains or specific functional groups. These hydrocarbon moieties or functional groups on the cellulose are then able to interact with organic molecules in aqueous solutions.

In this study, the modified cellulose that was successfully prepared by esterification reaction with stearoyl chloride and benzoyl chloride is presented. The properties and surface morphology of the synthesized material were determined and characterized by various modern characterization techniques. Also, the sorption efficiency of stearoyl and benzoyl cellulose, as measured by spectroscopic analysis, was shown as the removal percentages of phenanthrene and pyrene from aqueous solution. From the results of this study, the direction and efficiency of the experiment were determined and discussed in comparison with previous studies.

2. Materials and Methods

2.1. Materials

A cellulose microcrystalline powder (20 μm) was purchased from Sigma-Aldrich (St. Louis, MO, USA). The cellulose was dried in a vacuum oven at 60 °C for 12 h to remove moisture before further reaction. Benzoyl chloride (99.0%), stearoyl chloride (97.0%), 4-dimethylamino pyridine (DMAP) (99.0%), lithium chloride (LiCl) (99.0%), anhydrous 4-*N*,*N*-dimethylacetamide (DMAc) (99.8%), phenanthrene (98.0%), and pyrene (98.0%) were purchased from Sigma-Aldrich.

2.2. Synthesis of Benzoyl Cellulose (Bz–Cell) and Stearoyl Cellulose (St–Cell)

Bz–Cell and St–cell were prepared based on previously described methods with some modification [24]. The whole reaction performed under nitrogen atmosphere. A cellulose microcrystalline powder (1 g) was dissolved in 40 mL of DMAc containing 8 wt % LiCl at 100 °C for 4 h. Then, benzoyl chloride (4.336 g) or stearoyl chloride (9.345 g) was added and DMAP (0.376 g) was used for catalyst. The reaction was

constantly stirred at 100 °C for more than 12 h. The reaction mixture was precipitated with deionized water, and the resulting solid was filtered out and washed repeatedly using chloroform/methanol. The obtained Bz–Cell or St–Cell was kept in a vacuum oven at 80 °C for 24 h and then utilized for further study. The yields of Bz–Cell and St–Cell were 93% and 99%, respectively. The synthesized compounds (Bz–Cell and St–Cell) were deposited in the Microbial Carbohydrate Resource Bank (MCRB) at Konkuk University, Korea.

2.3. NMR Spectroscopy

NMR spectra was recorded on a Bruker Avance 600 MHz spectrometer (A Bruker Avance spectrometer, Bruker, Karlsruhe, Germany) for ^{1}H NMR and ^{13}C NMR experiments. The chloroform-d was used for dissolution of the samples at 25 °C for measurement.

2.4. Fourier Transform Infrared (FT-IR) Spectroscopy

Fourier transform infrared (FT-IR) spectra were conducted with a Bruker IFS-66/S spectrometer (Bruker, Karlsruhe, Germany) while using KBr pellets as support in the scanning range of 650–4000 cm^{-1}.

2.5. Field Emission Scanning Electron Microscopy (FE-SEM)

Hitachi S-4700, which is manufactured by Hitachi High-Technologies Corporation (Tokyo, Japan) was used for field emission scanning electron microscopy (FE-SEM). Double-sided adhesive carbon tape was used to fix the samples on a brass stub. The powder samples were coated on the surface in a thin layer of gold. The images were photographed at an excitation voltage of 10 kV.

2.6. X-ray Diffraction Analysis (XRD)

X-ray diffraction analysis (XRD) was performed on a Bruker D8 DISCOVER diffractometer (Bruker, Karlsruhe, Germany) while using Cu-Kα radiation. It recorded XRD patterns by analyzing diffractions at a 2θ angle values between 3° and 43° in 1° min^{-1} increments and a recording time.

2.7. Thermal Gravimetric Analysis (TGA)

Thermogravimetric analysis (TGA) curves were obtained with TA Instruments (Q20, New Castle, DE, USA). For TGA measurements, it recorded the percentage weight loss of the dried sample under a flowing nitrogen atmosphere from 25 to 600 °C and a heating rate of 10 °C min^{-1}.

2.8. Adsorption of Phenanthrene and Pyrene

We chose phenanthrene and pyrene as PAHs representative. Due to the low water solubility of phenanthrene and pyrene (1.1 and 0.13 mg/L), the both PAHs were dissolved in methanol high concentrations. To avoid co-solvent effects, the solutions were diluted with deionized water to make 0.1% of final methanol concentrations [25]. Each of Bz–Cell and St–Cell were placed into screw cap vials with 0.8 ppm of phenanthrene or 0.08 ppm of pyrene solution, respectively, and the mixture solutions were stirred and equilibrated at 25 °C for 24 h. The solutions containing phenanthrene and pyrene were filtered and then measured by a spectrofluorophotometer with ex/em wavelengths of phenanthrene (ex/em = 248 nm/364 nm) and pyrene (ex/em = 335 nm/392 nm). The obtained emission spectra were shown in the each range of phenanthrene (300–450 nm) and pyrene (300–450 nm). The excitation and emission slits was 3.0 and 1.5 nm widths, respectively. The removal efficiency of PAHs could be calculated, as follows:

$$\text{Removal efficiency} = \frac{C_0 - C_e}{C_0} \times 100\% \quad (1)$$

where C_0 is the initial concentration of PAHs, and C_e is the concentration of PAHs after adsorption process.

2.9. Recyclability of Bz–Cell and St–Cell

After completion of the adsorption experiment, the Bz–Cell and St–Cell were collected by centrifugation, washed with methanol, and then lyophilized. The recovered Bz–Cell and St–Cell were then reused for the next run. We also measured fluorescence of methanol, which was used in washing step for each adsorbent to check the desorption of both phenanthrene and pyrene (Figure S1, Supplementary Materials).

3. Results

3.1. Characterization of Bz–Cell and St–Cell

The Bz–Cell and St–Cell were synthesized via the reaction of benzoyl chloride and stearoyl chloride with dimethylacetamide (DMAP), respectively (Scheme 1). Cellulose was dissolved by DMAc and LiCl. Strong hydrogen bonds are formed between the hydroxyl protons of cellulose and the Cl^- ion with solvation of the Li^+ ions by free DMAc molecules. Once nucleophile (DMAP) donated an electron pair to acyl carbons of the substituents, such as benzoyl chloride and stearoyl chloride, it would be able to react with hydroxyl groups on 2, 3, and 6 position of cellulose. In the ^{1}H NMR spectrum of the Bz–Cell, cellulose backbone protons appear in the range of 3.00–5.00 ppm, and the benzoyl ring protons are visible at 7.49 ppm (10–12) and 7.9 ppm (9, 13). The peaks of remained solvent appeared at around 1.5–2.0 ppm. In fact, some solvents were difficult to remove by washing because the Bz–Cell was aggregated and kept hydroxyl groups of cellulose making strong binding with DMAc molecules [26]. It has been reported that when synthesizing benzoyl cellulose in the DMAc/LiCl system with DMAP, remained solvent peak can be appeared in the ^{1}H NMR spectrum despite a sufficient washing process (Figure 1a) [27]. In the ^{13}C NMR downstream spectrum, the peaks of the benzoyl ring carbons were distributed over 125 ppm (Figure 1b). In the same way, cellulose backbone protons of the Bz–Cell were in the same ^{1}H NMR spectrum range (Figure 1a). The ^{1}H NMR and ^{13}C NMR spectra of the St–Cell are shown in Figure 2. The characteristic peaks due to stearoyl carbon chain protons are observed, ranging from 0.86 to 2.18 ppm (9–24) (Figure 2a). In the ^{13}C NMR upstream spectrum, the peaks of stearoyl carbons were distributed in the region under 35 ppm (Figure 2b).

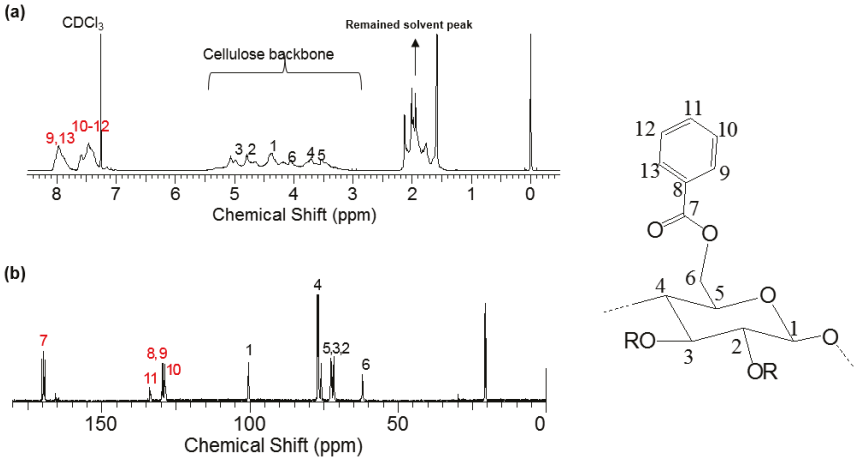

Figure 1. ^{1}H NMR spectrum (**a**) and ^{13}C NMR spectrum (**b**) of the Bz–Cell.

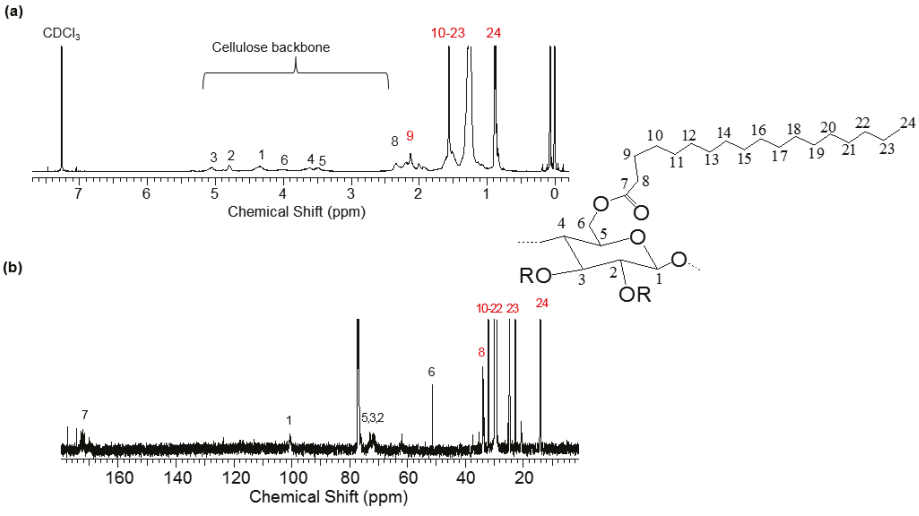

Figure 2. ^{1}H NMR spectrum (**a**) and ^{13}C NMR spectrum (**b**) of the St–Cell.

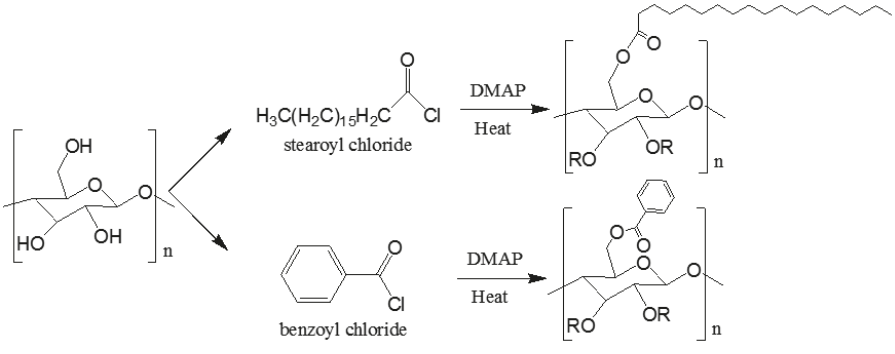

Scheme 1. Stearoyl cellulose (St–Cell) and benzoyl cellulose (Bz–Cell) synthesis method.

3.2. FT-IR Spectroscopic Analysis

A broad absorption band at 3331.4 cm^{-1}, which corresponds to hydroxyl group valence vibrations in cellulose, was observed in the pure cellulose. In the case of the Bz–Cell and St–Cell, this band was not observed because of the esterification reaction of pure cellulose, which modified with benzoyl and stearoyl chloride on an OH-group of the pure cellulose (Figure 3). The other characteristic band, representing the ester C=O bond (1723.1, 1743.3 cm^{-1}) was also observed due to the esterification of the Bz–Cell and St–Cell (Table 1). The appearance of a C=C band at 1642.0 cm^{-1} in the Bz–Cell suggests the presence of benzoyl groups in the Bz–Cell. The vibrations of C–H bonds in stearoyl moiety in the St–Cell corresponded to the appearance of strong bands around 2917.8 cm^{-1} supporting that the esterification reaction successfully occurred in the synthesis of St–Cell.

From the FT-IR spectra of the modified cellulose Bz–Cell and St–Cell, the number of hydrogen bonds decreased due to the low solubility from the substitution of hydroxyl groups with hydrophobic substituent benzoyl chloride and stearoyl chloride, respectively, on the cellulose backbone. Therefore, a substantial reduction was observed in the –OH detecting area and the characteristic ester C=O absorption band at 1723.1 and 1743.3 cm^{-1} was observed. Even though the hydroxyl groups on the cellulose backbone were not fully substituted, all the peaks belonging to the benzoyl and stearoyl

groups were absent in pure cellulose, and, therefore, the cellulose was modified by the esterification reaction and thus, Bz–Cell and St–Cell were successfully synthesized.

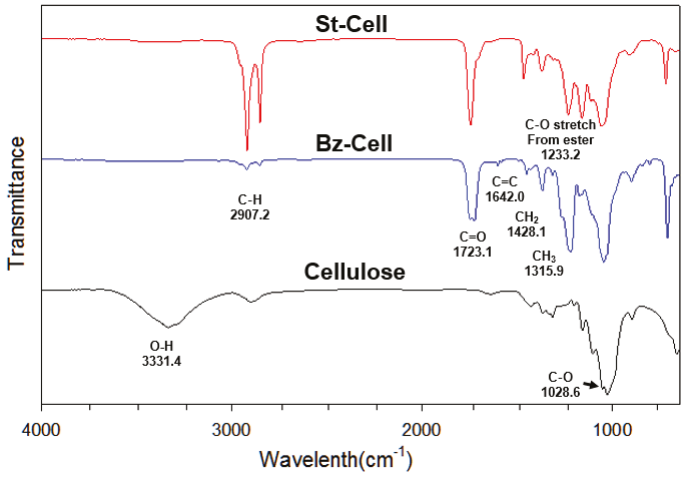

Figure 3. Fourier transform infrared (FT-IR) spectra of cellulose (black); Bz–Cell (blue); and St–Cell (red).

Table 1. FT-IR absorption bands for cellulose, Bz–Cell, and St–Cell.

Assignment	Cellulose (cm^{-1})	Bz–Cell (cm^{-1})	St–Cell (cm^{-1})
ν (O–H)	3331.4	-	-
ν (C–H)	2897.6	2907.6	2917.8
ν (C=O)	-	1723.1	1743.3
ν (C–O–C)	1028.6	1062.6	1052.9
ν (C–C(=O)–O–C)	-	1220.0	1233.2
C=C aromatic ring	-	1642.0	-

3.3. Thermal Gravimetric Analysis (TGA)

Thermogravimetric analysis of pure cellulose, Bz–Cell, and St–Cell was carried out to monitor the effect of the benzoyl and stearoyl groups on the thermogravimetric properties of the prepared materials. The decomposition temperature (°C) of pure cellulose, and the benzoyl and stearoyl cellulose materials, against weight loss (%), are plotted in Figure 4. The increase in T_g value reflects the modification of benzoyl and stearoyl on cellulose and the stearoyl chain interactions between them, which enhances the chain packing of the material. In particular, pure cellulose showed a T_g at 328 °C, whereas benzoyl cellulose and stearoyl cellulose had a T_g of 379 and 341 °C, respectively (Table 2). These results suggest that pure cellulose was modified with benzoyl and stearoyl groups along its backbone, as evidenced by the higher T_g of the Bz–Cell and St–Cell.

Table 2. TGA data of cellulose, Bz–Cell, and St–Cell.

Sample	Initial Decomposition Temperature, T_i (°C)	Glass Transition Temperature, T_g (°C)	50% Weight Loss Temperature (°C)
Cellulose	200	328	364
Bz–Cell	278	379	385
St–Cell	268	341	350

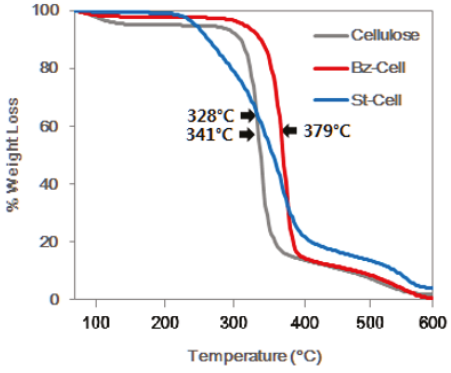

Figure 4. Thermal Gravimetric Analysis (TGA) analysis of cellulose (gray); Bz-Cell (red); and St-Cell (blue).

3.4. XRD Analysis

The influence of the crystalline behavior of pure cellulose and the modified celluloses of the esterification reaction on the crystallinity of cellulose were studied by wide angle XRD. Figure 5 shows the XRD diagrams of pure cellulose, the Bz–Cell, and the St–Cell. The conventional characteristic diffraction peaks of pure cellulose micro-crystalline were appeared at 2θ around 15°, 22°, and 35°. These characteristic peaks were changed after modification. Especially, the diffraction peaks of the Bz–Cell were showed a broader and lower intensity peak than those of pure cellulose because the benzoyl group could increase the amorphous character in the Bz–Cell. In the case of St–Cell, diffraction peaks, which were found at 4° and 21°, were different from the peaks of existing pure cellulose. However, a peak similar to pure cellulose was observed at 21°, rather than Bz–Cell, confirming that the stearoyl group had a relatively less effect on crystallinity change of pure cellulose [12,15,18]. From the above results, it was confirmed that crystallinity of the cellulose was changed by the application of benzoyl group and stearoyl group.

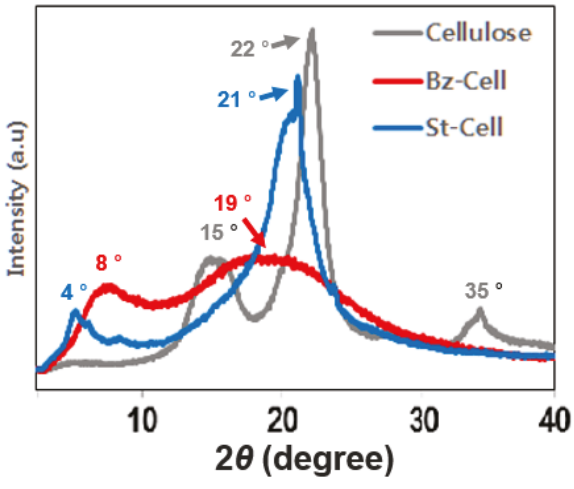

Figure 5. X-ray diffraction analysis (XRD) analysis of Cellulose (gray); Bz-Cell (red); and St-Cell (blue).

3.5. FE-SEM Analysis

FE-SEM was used to study the morphological characteristics of the inclusion complex. The SEM images of cellulose, Bz–Cell, and St–Cell are shown in Figure 6a,b,e. Cellulose appeared as an

irregular fold-like structure (Figure 6a), Bz–Cell as aggregated particles (Figure 6b) and St–Cell showed relatively cellulose-like surface morphology, but it is more rough, which is favorable for the adsorption of chemicals (Figure 6e) [28]. These surface phenomena correspond to the XRD results. We also analyzed the surface morphology of the modified cellulose after PAHs adsorption. After phenanthrene adsorption onto the Bz–Cell (Figure 6c), the materials appeared as more aggregated small particles because the benzoyl groups on Bz–Cell could interact with the poly aromatic rings of phenanthrene by π–π interactions. This tendency was also confirmed to the other Bz–cell after the adsorption with the pyrene with a larger poly aromatic rings than phenanthrene (Figure 6d). Figure 6f,g show the morphological surface characteristics of the St–Cell after adsorption with phenanthrene and pyrene, respectively. Differences in the flatness of the material were clearly observed before and after the adsorption of the phenanthrene and pyrene on the St–Cell. The difference of surface roughness was also shown in the FE-SEM data. However, St–Cell did not show any aggregations even in the presence of PAHs. We expect that the aggregation appeared in the Bz–cell might be a disadvantage in adsorbing PAHs because of the reduced surface area. In the case of the St–Cell shown in Figure 6f,g, both phenanthrene and pyrene were well attached on its surface, since the aliphatic groups on St–Cell could interact with the aromatic rings on PAHs.

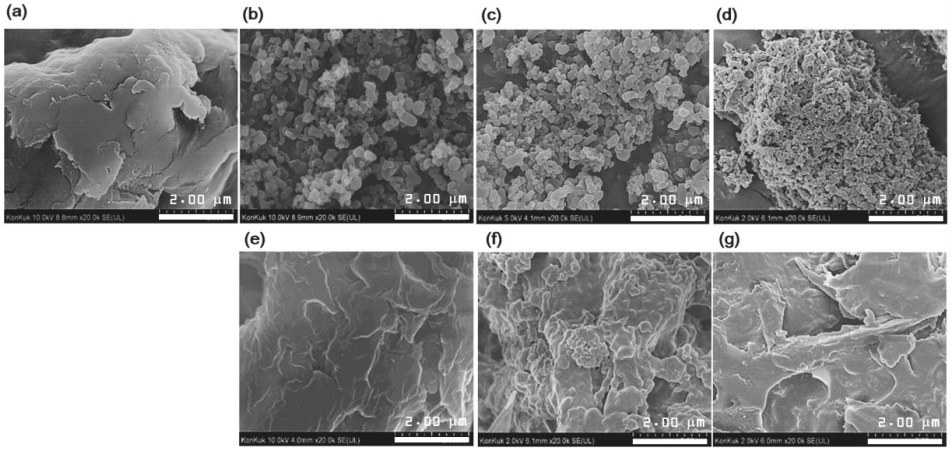

Figure 6. SEM images of cellulose (**a**); Bz–Cell (**b**); Bz–Cell after adsorption with phenanthrene (**c**); Bz–Cell after adsorption with pyrene (**d**); St–Cell (**e**); St–Cell after adsorption with phenanthrene (**f**); and St-Cell after adsorption with pyrene (**g**).

3.6. Emission Spectra and Removal Test

To clarify the sorption effects of PAHs onto the Bz–Cell and St–Cell, the fluorescence emission spectra of the PAHs were measured in the phenanthrene and pyrene solution of 0.8 and 0.08 ppm. After 24 h of stirring to equilibrate between the adsorbents and PAHs in aqueous solution, the emission spectra of the remained PAHs in solution were measured for the analysis. Each experiment was triplicated to obtain mean results (percentage removal of PAHs) [29]. The intensity of phenanthrene was not significantly affected by the addition of cellulose, while the addition of the Bz–Cell and St–Cell decreased the concentration by 95% and 97%, respectively (Figure 7a,c). In the case of pyrene, cellulose also had no effect, while the Bz–Cell and St–Cell displayed 78% and 96% removal efficiency (Figure 7b,d). Meanwhile, activated carbon and polystyrene are well known adsorbents for pollutants. Especially, the phenanathrene adsorption capacities of absorbent-grade activated carbon and polystyrene were around 8 to 50 and 3.91 mg/g, respectively [30,31]. In the case of polystyrene, the adsorption capacity was relatively small when compared to our material. Therefore, we tested the adsorption capacity of adsorption-grade activated carbon against PAHs. We used the Carbon black

XC-72, which is commercially available adsorbent-grade activated carbon [32]. In the case of activated carbon, it showed the higher removal efficiency of 98% in phenanthrene and 99% in pyrene than those of Bz–Cell and St–Cell (Figure S3, Supplementary Materials). However, it showed very lower recovery efficiency of 8% in phenanthrene and 5% in pyrene. It also meant that the activated carbon could not be reusable practically due to its very low recovery. We actually measured the fluorescence of methanol from washing step of the activated carbon (Figure S1, Supplementary Materials). Those results indicate that reactivation of activated carbon is very difficult. It was also reported that activated carbons are expensive and their recovery are very difficult [2,33]. Efficient both recovery and recyclability with relatively high removal efficiency could be the strong advantages of our modified cellulose comparing with the activated carbon. The contact time significantly affected the adsorption of phenanthrene and pyrene. The effect of time on adsorption was determined by collecting the sample at pre-determined time intervals, up to the 180 min stirring time. The adsorption capacity of the prepared Bz–Cell and St–Cell showed rapid adsorption up to almost 10 min; as the adsorbent was mixed up to 10 min stirring time, the adsorption capacity gradually increased, and at 10 min, the adsorbent reached the saturation point. After this, no major adsorption changes were found. The time-dependence curve (0–180 min) of phenanthrene and pyrene adsorption is shown in Figure 8. The expected equilibrium point is at 10 min for both materials in a phenanthrene or pyrene solution of 0.8 and 0.08 ppm, respectively. This result can be explained by the materials' hydrophobicity. By contrast, pure cellulose is a hydrophilic material. Cellulose is easy to disperse in water to bring the solid surface close to phenanthrene and pyrene in water. However, modified cellulose has organic chains grafted onto the surface, which enhance the interaction with phenanthrene and pyrene molecules, resulting in a higher adsorption capacity than pure cellulose.

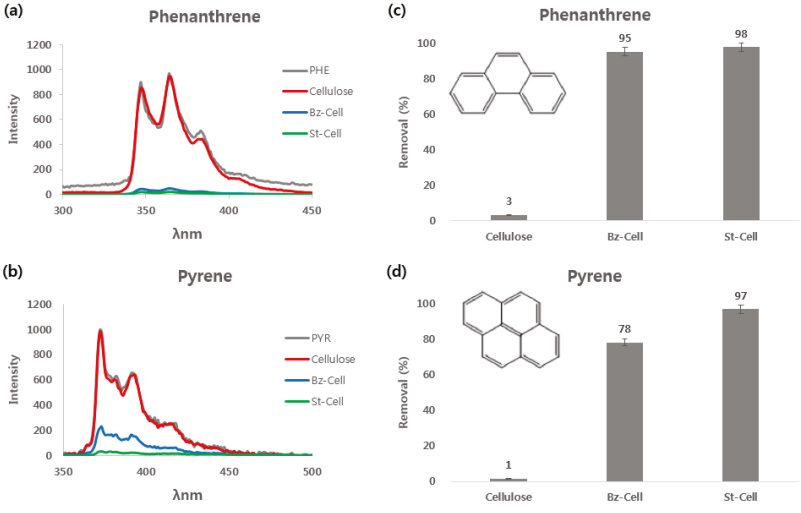

Figure 7. Emission spectra of phenanthrene (**a**) and pyrene (**b**). Removal efficiency (%) of phenanthrene (**c**) and pyrene (**d**), as compared with cellulose. The insets in (**c**) and (**d**) show the chemical structure of phenanthrene and pyrene, respectively.

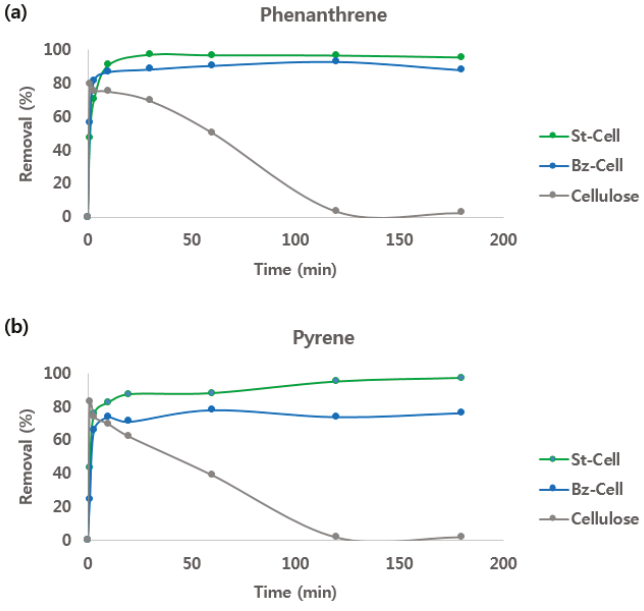

Figure 8. The time-dependent removal (%) of phenanthrene (**a**) and pyrene (**b**) by the Bz–Cell and St–Cell, compared with cellulose.

3.7. Reusability of Bz–Cell and St–Cell

Finally, the regeneration and reusability of the Bz–Cell and St–Cell for the sorption of the model PAHs were examined. Figure 9 shows the adsorption percentage of the model PAHs after consecutive recycling of the Bz–Cell and St–Cell. The removal efficiencies of phenanthrene in the Bz–Cell and St–Cell remained above 83.9% for up to five sequential cycles. Both adsorbents still have enough efficiency to be reused even after five cycles. However, some reduction of recyclability were observed at the 10th cycle. We expect to use it up to 15 cycles with more than 50% efficiency (Figure S2, Supplementary Materials). Thus, these modified celluloses could be used repeatedly as efficient adsorbents to remove phenanthrene and pyrene from aqueous solutions.

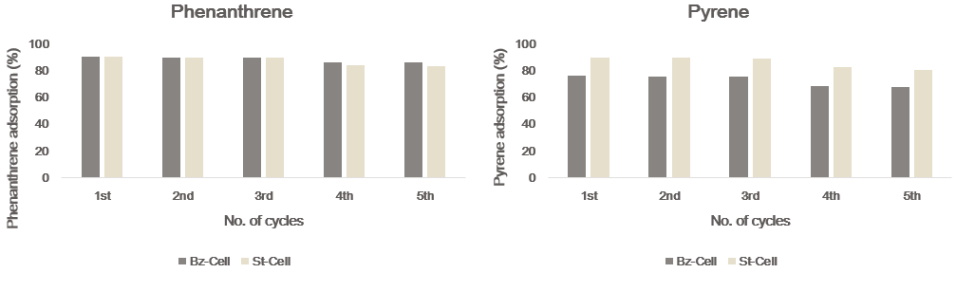

Figure 9. Recycling of Bz–Cell and St–Cell for the removal of phenanthrene and pyrene.

4. Conclusions

Cellulose materials, modified by benzoyl and stearoyl groups, were prepared by a simple chemical grafting method. Using these reactions, functionalized cellulose, the Bz–Cell and St–Cell respectively, was successfully synthesized. The characterization results that were obtained by NMR, FT-IR, TGA, XRD, and SEM indicated that the benzoyl and stearoyl groups were grafted on the cellulose backbone.

The Bz–Cell and St–Cell were estimated to have ability of potential adsorbents to remove two model of PAHs (phenanthrene and pyrene) in adsorption study. Especially, both the removal and reusability efficiency of St–Cell are higher than those of Bz–Cell, as shown in Figures 7 and 9. This might be due to the aggregated surface properties of Bz–Cell with benzoyl moieties as shown in Figure 6b. In addition to the comparison between the two modification groups, both modified cellulose adsorbents showed higher adsorption efficiencies than previous studies [24]. Although the activated carbon showed the high PAHs absorptions, it has a clear disadvantage of very low recovery. However, the Bz–Cell and St–Cell can show the excellent both recovery and reusability with relatively high adsorption percentages of phenanthrene above 83.9%, up to the fifth cycle. Furthermore, the cellulose polymer is cheap comparing with activated carbon. Cellulose microcrystalline (powder, 20 μm Sigma-Aldrich) costs $150 per kilogram, as compared to $1000 for activated carbon Carbon black XC-72 (Fuel Cell Earth). This study could suggest that further research into the use of cellulose with various functional substituents can be applied to the molecular adsorbent of various organic pollutants in industrial scales, as well as for the removal of PAH. We also expect that the Bz–Cell and St–Cell would have the potential as basic biomaterials for various formulation studies, such as hydrogels, membranes, and filters.

Supplementary Materials: The following are available online at http://www.mdpi.com/2073-4360/10/9/1042/s1, Figure S1: Recovery percentage (%) of PAHs from Bz-Cell, St-Cell, and activated carbon by MeOH, Figure S2: Recycling of Bz-Cell and St-Cell for the removal of phenanthrene and pyrene up to 10th cycles, Figure S3: Removal efficiency (%) of phenanthrene and pyrene by activated carbon.

Author Contributions: S.J. conceived and designed the experiments; Y.K. and K.H.P. performed the experiments; J.-H.Y. advised PAH analysis; D.J., Y.K. and S.J. analyzed the data; Y.K. and D.J. wrote the paper.

Funding: This research was supported by Basic Science Research Program through the National Research Foundation of Korea (NRF) funded by the Ministry of Education (NRF-2015R1D1A1A01058686) and the Bio & Medical Technology Development Program of the NRF funded by the Korean Government, MSIP (NRF-2015M3A9B8031831) SDG.

Conflicts of Interest: The authors declare no conflict of interest.

References

1. Zhu, X.; Shi, S.; Wei, J.; Lv, F.; Zhao, H.; Kong, J.; He, Q.; Ni, J. Electrochemical oxidation characteristics of p-substituted phenols using a boron-doped diamond electrode. *Environ. Sci. Technol.* **2007**, *41*, 6541–6546. [CrossRef] [PubMed]
2. San Miguel, G.; Lambert, S.; Graham, N. The regeneration of field-spent granular-activated carbons. *Water Res.* **2001**, *35*, 2740–2748. [CrossRef]
3. Thakur, S.; Sharma, B.; Verma, A.; Chaudhary, J.; Tamulevicius, S.; Thakur, V.K. Recent progress in sodium alginate based sustainable hydrogels for environmental applications. *J. Clean. Prod.* **2018**, *198*, 143–159. [CrossRef]
4. Thakur, V.K.; Voicu, S.I. Recent advances in cellulose and chitosan based membranes for water purification: A concise review. *Carbohydr. Polym.* **2016**, *146*, 148–165. [CrossRef] [PubMed]
5. Thakur, S.; Govender, P.P.; Mamo, M.A.; Tamulevicius, S.; Mishra, Y.K.; Thakur, V.K. Progress in lignin hydrogels and nanocomposites for water purification: Future perspectives. *Vacuum* **2017**, *146*, 342–355. [CrossRef]
6. Thakur, S.; Govender, P.P.; Mamo, M.A.; Tamulevicius, S.; Thakur, V.K. Recent progress in gelatin hydrogel nanocomposites for water purification and beyond. *Vacuum* **2017**, *146*, 396–408. [CrossRef]
7. Thakur, M.K.; Thakur, V.K.; Gupta, R.K.; Pappu, A. Synthesis and applications of biodegradable soy based graft copolymers: A review. *Sustain. Chem. Eng.* **2015**, *4*, 1–17. [CrossRef]
8. White, P.A.; Claxton, L.D. Mutagens in contaminated soil: A review. *Rev. Mutat. Res.* **2004**, *567*, 227–345. [CrossRef] [PubMed]

9. Wang, X.-T.; Miao, Y.; Zhang, Y.; Li, Y.-C.; Wu, M.-H.; Yu, G. Polycyclic aromatic hydrocarbons (pahs) in urban soils of the megacity shanghai: Occurrence, source apportionment and potential human health risk. *Sci. Total Environ.* **2013**, *447*, 80–89. [CrossRef] [PubMed]
10. May, W.E.; Wasik, S.P.; Freeman, D.H. Determination of the solubility behavior of some polycyclic aromatic hydrocarbons in water. *Anal. Chem.* **1978**, *50*, 997–1000. [CrossRef]
11. Holman, H.-Y.N.; Nieman, K.; Sorensen, D.L.; Miller, C.D.; Martin, M.C.; Borch, T.; McKinney, W.R.; Sims, R.C. Catalysis of pah biodegradation by humic acid shown in synchrotron infrared studies. *Environ. Sci. Technol.* **2002**, *36*, 1276–1280. [CrossRef] [PubMed]
12. Mastral, A.; García, T.; Callén, M.; Navarro, M.; Galbán, J. Removal of naphthalene, phenanthrene, and pyrene by sorbents from hot gas. *Environ. Sci. Technol.* **2001**, *35*, 2395–2400. [CrossRef] [PubMed]
13. Wang, X.; Yang, K.; Tao, S.; Xing, B. Sorption of aromatic organic contaminants by biopolymers: Effects of ph, copper (ii) complexation, and cellulose coating. *Environ. Sci. Technol.* **2007**, *41*, 185–191. [CrossRef] [PubMed]
14. Rafatullah, M.; Sulaiman, O.; Hashim, R.; Ahmad, A. Adsorption of methylene blue on low-cost adsorbents: A review. *J. Hazard. Mater.* **2010**, *177*, 70–80. [CrossRef] [PubMed]
15. O'Connell, D.W.; Birkinshaw, C.; O'Dwyer, T.F. Heavy metal adsorbents prepared from the modification of cellulose: A review. *Bioresour. Technol.* **2008**, *99*, 6709–6724. [CrossRef] [PubMed]
16. Huang, L.; Boving, T.B.; Xing, B. Sorption of pahs by aspen wood fibers as affected by chemical alterations. *Environ. Sci. Technol.* **2006**, *40*, 3279–3284. [CrossRef] [PubMed]
17. Tashiro, T.; Shimura, Y. Removal of mercuric ions by systems based on cellulose derivatives. *J. Appl. Polym. Sci.* **1982**, *27*, 747–756. [CrossRef]
18. Maekawa, E.; Koshijima, T. Properties of 2,3-dicarboxy cellulose combined with various metallic ions. *J. Appl. Polym. Sci.* **1984**, *29*, 2289–2297. [CrossRef]
19. Jonker, M.T. Absorption of polycyclic aromatic hydrocarbons to cellulose. *Chemosphere* **2008**, *70*, 778–782. [CrossRef] [PubMed]
20. Saliba, R.; Gauthier, H.; Gauthier, R. Adsorption of heavy metal ions on virgin and chemically-modified lignocellulosic materials. *Adsorpt. Sci. Technol.* **2005**, *23*, 313–322. [CrossRef]
21. Gurdag, G.; Yasar, M.; Gurkaynak, M. Graft copolymerization of acrylic acid on cellulose: Reaction kinetics of copolymerization. *J. Appl. Polym. Sci.* **1997**, *66*, 929–934. [CrossRef]
22. Rao, S.R.; Kapur, S. Grafting of acrylonitrile onto cellulose initiated by ceric ion. *J. Appl. Polym. Sci.* **1969**, *13*, 2649–2656. [CrossRef]
23. Gourson, C.; Benhaddou, R.; Granet, R.; Krausz, P.; Saulnier, L.; Thibault, J.-F. Preparation of biodegradable plastic in microwave oven and solvent-free conditions. *C. R. Acad. Sci. Ser. Chem.* **1999**, *2*, 75–78. [CrossRef]
24. Jadhav, A.H.; Mai, X.T.; Appiah-Ntiamoah, R.; Lee, H.; Momade, F.W.; Seo, J.G.; Kim, H. Preparation and characterization of palmitoyl grafted cellulose nano absorbent for the efficient adsorption of pyrene from aqueous solution. *J. Nanosci. Nanotechnol.* **2015**, *15*, 7980–7987. [CrossRef] [PubMed]
25. Rao, P.; Hornsby, A.; Kilcrease, D.; Nkedi-Kizza, P. Sorption and transport of hydrophobic organic chemicals in aqueous and mixed solvent systems: Model development and preliminary evaluation 1. *J. Environ. Qual.* **1985**, *14*, 376–383. [CrossRef]
26. Dawsey, T.; McCormick, C.L. The lithium chloride/dimethylacetamide solvent for cellulose: A literature review. *J. Macromol. Sci. Rev. Macromol. Chem. Phys.* **1990**, *30*, 405–440. [CrossRef]
27. Williamson, S.L.; McCormick, C.L. Cellulose derivatives synthesized via isocyanate and activated ester pathways in homogeneous solutions of lithium chloride/N,N-dimethylacetamide. *J. Macromol. Sci.* **1998**, *35*, 1915–1927. [CrossRef]
28. Hameed, B. Equilibrium and kinetic studies of methyl violet sorption by agricultural waste. *J. Hazard. Mater.* **2008**, *154*, 204–212. [CrossRef] [PubMed]
29. Cho, E.; Tahir, M.N.; Choi, J.M.; Kim, H.; Yu, J.-H.; Jung, S. Novel magnetic nanoparticles coated by benzene-and β-cyclodextrin-bearing dextran, and the sorption of polycyclic aromatic hydrocarbon. *Carbohydr. Polym.* **2015**, *133*, 221–228. [CrossRef] [PubMed]
30. Ahn, C.K.; Kim, Y.M.; Woo, S.H.; Park, J.M. Selective adsorption of phenanthrene dissolved in surfactant solution using activated carbon. *Chemosphere* **2007**, *69*, 1681–1688. [CrossRef] [PubMed]
31. Wang, L.-C.; Cao, Y.-H. Adsorption behavior of phenanthrene on ctab-modified polystyrene microspheres. *Colloids Surf. A* **2018**, *553*, 689–694. [CrossRef]

32. Ren, X.; Shao, D.; Yang, S.; Hu, J.; Sheng, G.; Tan, X.; Wang, X. Comparative study of pb (ii) sorption on xc-72 carbon and multi-walled carbon nanotubes from aqueous solutions. *Chem. Eng. J.* **2011**, *170*, 170–177. [CrossRef]
33. Hameed, B.; Krishni, R.; Sata, S. A novel agricultural waste adsorbent for the removal of cationic dye from aqueous solutions. *J. Hazard. Mater.* **2009**, *162*, 305–311. [CrossRef] [PubMed]

polymers

MDPI

Article

Efficient Hydrophobic Modification of Old Newspaper and Its Application in Paper Fiber Reinforced Composites

Weiwei Zhang, Jin Gu, Dengyun Tu, Litao Guan and Chuanshuang Hu *

College of Materials and Energy, South China Agricultural University, Guangzhou 510642, China; zhangww@scau.edu.cn (W.Z.); gujin@scau.edu.cn (J.G.); tudengyun@scau.edu.cn (D.T.); ltguan@scau.edu.cn (L.G.)

* Correspondence: cshu@scau.edu.cn; Tel.: +86-020-85280319

Received: 21 March 2019; Accepted: 6 May 2019; Published: 10 May 2019

Abstract: Paper fibers have gained broad attention in natural fiber reinforced composites in recent years. The specific problem in preparing paper fiber reinforced composites is that paper fibers easily become flocculent after pulverization, which increases difficulties during melt-compounding with polymer matrix and results in non-uniform dispersion of paper fibers in the matrix. In this study, old newspaper (ONP) was treated with a low dosage of gaseous methyltrichlorosilane (MTCS) to solve the flocculation. The modified ONP fibers were characterized by Scanning Electron Microscope (SEM), Fourier Transform Infrared Spectroscopy (FTIR), and Thermogravimetric Analysis (TG). Then the modified ONP fibers and high-density polyethylene (HDPE) were extruded and pelletized to prepare ONP/HDPE composites via injection molding. Maleic anhydride-grafted polyethylene (MAPE) was added to enhance the interfacial bonding performance with the ultimate purpose of improving the mechanical strength of the composites. The mechanical properties such as tensile, flexural, and impact strength and the water absorption properties of the composite were tested. The results showed that the formation of hydrogen bonding between ONP fibers was effectively prevented after MTCS treatment due to the reduction of exposed –OH groups at the fiber surface. Excessive dosage of MTCS led to severe fiber degradation and dramatically reduced the aspect ratio of ONP fibers. Composites prepared with ONP fibers modified with 4% (*v*/*w*) MTCS showed the best mechanical properties due to reduced polarity between the fibers and the matrix, and the relatively long aspect ratio of treated ONP fibers. The composite with or without MAPE showed satisfactory water resistance properties. MTCS was proven to be a cheap and efficient way to pretreat old newspaper for preparing paper fiber reinforced composites.

Keywords: ONP fibers; silanization; composites; mechanical properties

1. Introduction

Natural fibers, as an alternative to conventional reinforcement in polymer composites, have received significant interest during the past decades [1,2]. Compared with synthetic fibers, natural fibers possess many advantages such as low cost, low density, CO_2 neutral, sustainability, biodegradability, high specific strength/modulus, and being non-abrasive to processing machinery. In natural fiber reinforced composites, the compatibility between hydrophilic natural fibers and hydrophobic thermoplastics is the main problem to be solved since the interfacial properties play an important role in the physical and mechanical performances of the composites. Results showed that interfacial adhesion could be improved through physical treatments [3,4], chemical modification [5,6], or a combination of both [7,8] to natural fibers. Recently, researchers have focused on preparing composites with paper fibers [9–17]. Usually paper fibers have a length in the range of 500–5000 μm and a diameter of

10–50 μm. Their absolute length is shorter than that of hemp fiber but their aspect ratio is larger than that of wood powder fiber. Such properties make them suitable for fabricating reinforced composites with applications in construction, automobiles, and outdoor furniture.

In the injection molding process, waste paper needs mechanical milling to produce individual fibers, followed by melt-compounding with thermoplastic polymers to disperse paper fibers uniformly within the composites. However, paper fibers are always flocculent after direct pulverization. Such flocs makes paper fibers difficult to melt-compound with the polymer matrix, which results in non-uniform dispersion of paper fibers in the matrix. Valente et al. [18] reported that paper turned prevalently wad-like after micronization and a turbo-mixing had been developed to introduce higher fiber percentages and better dispersion in the high-density polyethylene (HDPE) matrix. The agglomeration of paper fibers is mainly attributed to their relatively high aspect ratio and hydrogen bonding with each other. Therefore, methods that could reduce the formation of hydrogen bonds between fibers would facilitate their melt-compounding with polymer matrix. Serrano and Espinach et al. [19,20] used a water–diglyme (1:3) mixture to disperse old newspaper fibers before an oven drying process to limit the hydrogen bonding between the cellulosic fibers. Yang and Wang et al. [21] investigated several methods for dispersing pulp fibers in the HDPE matrix, and found that combining twice twin-screw melt-blending with pre-pressing and oven drying would obtain composites with the most uniform fiber dispersion and the best mechanical properties. The hydrophobic modification at fiber surface by acetylation [22,23], silane treatment [24,25], maleic anhydride treatment [6], etc., could also improve compatibility between the paper fibers and the polymer matrix through the reduction of fiber polarity. However, the concentration of paper fibers in the reaction system is usually kept as low as 2% or less to ensure that the chemical modification is uniform and sufficient, which meant the amount of organic solvents used was at least 50 times more than the paper fibers. Even for potassium methyl siliconate-treated pulp fibers, which were treated in water instead of organic solvents [26,27], 300 g fibers required 990 g potassium methyl siliconate for the modification process. It seemed that the solvent reaction system was not an efficient method for mass paper fiber modification.

Methyltrichlorosilane (MTCS) is an active silane coupling agent and has been successfully used to prepare superhydrophobic surfaces. Gao and McCarthy [28] prepared a perfectly hydrophobic surface with advancing and receding angles of 180° using an MTCS/toluene system. Water traces in this liquid reaction system were used to adjust the three dimensional nanostructured geometry and the hydrophobicity of the modified surface [29,30]. The silicone nanofilaments could also be formed in closed gaseous environments with controlled water vapor [31]. Superhydrophobic textiles and cellulosic products were fabricated by a one-step gas phase coating procedure using gaseous MTCS [32,33]. If the hydrophobic modification of paper fibers was carried out in a liquid solvent, 300 g fibers required 15 L toluene (with a fiber concentration of 2%) and 224 g MTCS (with a MTCS concentration of 0.1 mol/L). However, it only takes 15 g MTCS (nearly 15 times less) if the reaction happens in the gas phase and no organic solvents are required. Thus the gas phase reaction has the potential to be suitable for paper fiber hydrophobization.

In this study, old newspaper (ONP) was recycled as a typical waste paper to prepare natural fiber composites. High-density polyethylene (HDPE) was chosen as the matrix in consideration of the relatively low processing temperature so that the degradation on ONP fibers from high temperature and high pressure in a twin-screw extruder could be minimized. The flocculation problem of paper fibers was solved by hydrophobic modification using MTCS. The effect of MTCS treatment on the fiber properties and mechanical properties of ONP–HDPE composites was investigated. FTIR results showed that some exposed –OH groups still existed at the fiber surface after MTCS modification, indicating that the interface compatibility between hydrophobic ONP fibers and HDPE matrix was still flawed. Therefore, maleic anhydride-grafted polyethylene (MAPE), a common coupling agent used in natural fiber–plastic composites [34–36], was further added into the composite to improve its physical and mechanical properties.

2. Materials and Methods

2.1. Materials

Old newspaper (ONP) with an apparent density of 0.89 g/cm^3 was provided by Nanfang Metropolis Daily, Guangzhou, China. The main components contained 46.9% cellulose, 24.0% hemicellulose, 16.5% lignin, and 10.9% ash. Its moisture content was measured to be 6.7% at room temperature and 60% relative humidity. Methyltrichlorosilane (MTCS, 98%) was supplied by J&K Chemical, Beijing, China. High-density polyethylene (HDPE, 5000S) pellets with a density of 0.954 g/cm^3 and a melt flow index of 0.92 g/10 min (190 °C, 2.16 kg according to ASTM D1238) were purchased from Yangzi Petrochemical in Guangzhou, China. The tensile and flexural strength of pure HDPE was measured to be 19.6 and 12.2 MPa, respectively. Maleic anhydride-grafted polyethylene (MAPE) with an MA grafting ratio of 0.9 wt.% was supplied by Bochen Polymer New Materials, Foshan, China. The free radical grafting reaction happened between MA and HDPE at around 170 °C.

2.2. ONP Pretreatment

In a typical pretreatment, one batch of ONP (100 g) was cut into 4 mm × 25 mm strips using a paper shredder and dried at 105 °C for 2 h. The dried ONP strips were sealed in a plastic bag containing a dish with a certain volume of MTCS. The MTCS dosages of 2, 4, 6, and 8 mL were marked as 2%, 4%, 6%, and 8% (*v*/*w*), respectively. The bag was sealed and placed in an oven at 60 °C for 3 h. The liquid silane completely volatilized during this period. The bag was then opened and 20 mL of water was added into the dish. The bag was sealed and placed in an oven at 60 °C for another 3 h to hydrolyze the residual MTCS. The treated ONP fibers were washed with deionized water until they were pH neutral. Then they were oven-dried at 120 °C for 2 h. Three batches of the powdery fibers (300 g) were mixed with HDPE pellets (300 g, including MAPE pellets) in a high-speed mixer (SHR-10A, Grand Instrument Co. Ltd., Zhangjiagang, China) at 100 °C for 10 min. The well-mixed mixture was stored in sealed bags for further extrusion–pelletization processes.

2.3. Preparation of Composites

ONP/HDPE composites were prepared through extrusion–pelletization and injection molding. The melt-compounding and pelleting was carried out in a twin-screw extruder (SHJ-20B, Jieente, Nanjing, China) with an *L*/*D* ratio of 40. The temperatures of five zones in the extruder were set to be 130, 135, 155, 150, and 145 °C, respectively and the rotation speed was 16 rpm. The extruded cylindrical sample with a diameter of 3.5 mm, was cut by a granular QL-20 (SHJ-20B, Jieente, Nanjing, China) to produce pellets with a length of 5 mm. The pelletized composites were dried at 105 °C for 4 h before feeding into an injection molding machine (Y-35V, Yingbao Instrument Co. Ltd., Dongguan, China) for preparing the specimens for the testing of mechanical properties. The injection temperature was set to be 170 °C, injection pressure 95 bar, injection time 2 s and cooling time 4 s.

2.4. Characterization

2.4.1. Mechanical Properties

All test specimens were kept at 25 °C and 65% relative humidity for seven days before testing. Tensile and flexural properties were measured using an electromechanical universal testing machine (Model CMT5504, Shenzhen Rethink Cooperation, Shenzhen, China) according to GB/T 1040-2006 and GB/T 9341-2008, respectively. A dumbbell specimen was used for measuring the tensile strength and the loading speed was 5 mm/min. A flexural specimen, with the dimensions of 80 mm × 10 mm × 4 mm, was used for measuring the flexural strength and flexural modulus. The loading speed was 2 mm/min. The notched impact strength was measured by a load impact testing machine (XJU-5.5, Chengde Xinma Testing Instrument Co. Ltd., Chengde, China) according to GB/T 1843-2008. Notch

depth of the impact specimen was 0.25 mm. Five replicates were tested to obtain the average values of the above mechanical properties and their standard deviations.

2.4.2. Water Absorption Tests

The water resistance test was conducted according to GB/T 1934.1-2009. All the specimens were oven dried at 50 ± 3 °C for 24 h prior to water soaking and then immersed in water for 24 h at room temperature. Each specimen was weighed and measured for thickness at three marked locations. Five replicates were tested for each specimen.

2.4.3. Scanning Electron Microscope (SEM)

The morphologies of the modified ONP fibers and the fracture surfaces of the composites were observed with an SEM (Hitachi S-4800, Hillsboro, OR, USA) at an accelerating voltage of 20 kV. All samples were sputter-coated with gold before SEM observation.

2.4.4. Wettability Test

The wettability of original and MTCS-modified ONP fibers was characterized by water contact angle (CA) using Contact Angle System OCA20 (DataPhysics, Filderstadt, Germany). Flocculent and powdery ONP fibers were adhered to a glass sheet using double-sided tape to form a relative flat film. Then graphs of 5 μL water droplets on the film were recorded and their CAs were calculated by Young–Laplace fitting.

2.4.5. Fourier Transform Infrared Spectroscopy (FTIR)

Fourier transform infrared analysis of untreated and treated ONP fibers was carried out in a Fourier transform infrared spectrometer (Tensor-27, Bruker, Ettlingen, Germany). Each sample was scanned 64 times in transmittance mode, at 4 cm^{-1} resolution in the wave range from 400 to 4000 cm^{-1}.

2.4.6. Thermogravimetric Analysis

Thermogravimetric analysis was used to characterize the thermal stability of the modified ONP fibers with a TG 209 Instrument (Bruker Netzsch, Selb, Germany) at a heat rate of 10 °C/min from room temperature to 700 °C under nitrogen gas.

3. Results and Discussion

3.1. Characterization of Untreated and MTCS-Treated ONP Fibers

Direct mechanical pulverization of ONP without any treatment produced flocculent fibers as seen in Figure 1. These ONP fibers could not be fed into the twin-screw extruder for melt-compounding and pelleting with HDPE pellets. The modified ONP fibers pre-treated with MTCS were powdery and did not need further mechanical pulverization, which indicated that hydrogen bonding between fibers was effectively prevented. Thus ONP powder could be smoothly melt-compounded with HDPE via a twin-screw extruder, followed by injection molding.

Figure 1. Schematic diagram of old newspaper (ONP)/high-density polyethylene (HDPE) composite preparation.

The surface morphology of untreated and MTCS-treated ONP fibers was characterized using SEM. It can be observed from the SEM images shown in Figure 2 that there were no obvious changes at the fiber surface treated with 2% and 4% (*v*/*w*) MTCS compared with the untreated ONP fibers shown in Figure 2a. A monolayer of polymethylsilsesquioxane (PMS) was formed at the modified fiber surface because MTCS reacted with the cellulose –OH groups in the sealed dry environment [37]. A few fibrous fragments were observed when 2% and 4% (*v*/*w*) MTCS was used. However, no intact fibers were found when the MTCS dosage increased to 6% and 8% (*v*/*w*), and the aspect ratio of fiber debris decreased significantly to two or even smaller. The dimension of the powdery fiber decreased with the increase of the MTCS dosage. The degradation of ONP fibers was attributed to the presence of the by-product hydrogen halide from the MTCS hydrolysis. More severe degradation of the ONP fibers was observed when hydrogen halide concentration increased with the increased usage of MTCS during silanization modification.

The wettability of MTCS-modified ONP fibers was investigated through measuring their water contact angles. Before modification, a water droplet penetrated into ONP fibrous film within 5 s. Due to the introduction of Si–CH_3 groups at the ONP fiber surface, the water contact angle of the ONP fibers after treatment with 2% and 4% (*v*/*w*) dosage of MTCS increased to 129.1° ± 6.0° and 129.9° ± 3.8°, respectively. With the increase of the dosage of MTCS, the hydrophobicity of modified ONP fibers was further enhanced and the contact angles went up to 138.6° ± 3.2° for 6% (*v*/*w*) and 139.8° ± 0.3° for 8% (*v*/*w*). MTCS modification turned ONP fibers from hydrophilic to hydrophobic, which demonstrated that their interface compatibility would be improved with HDPE matrix.

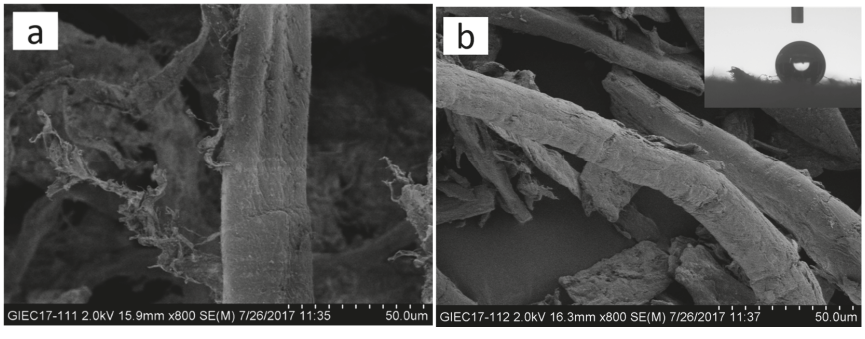

Figure 2. *Cont.*

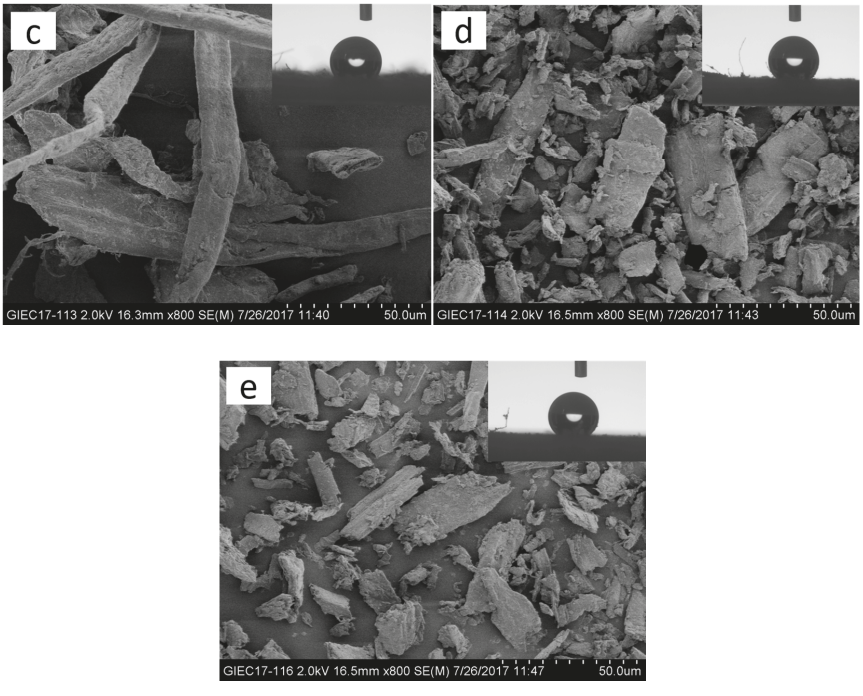

Figure 2. SEM images of ONP fibers treated with different methyltrichlorosilane (MTCS) dosages and their corresponding water contact angle photos: (**a**) 0 (*v*/*w*); (**b**) 2% (*v*/*w*); (**c**) 4% (*v*/*w*); (**d**) 6% (*v*/*w*); and (**e**) 8% (*v*/*w*).

FTIR spectra shown in Figure 3 were used to characterize the changes of the chemical groups that occurred at the treated ONP fibers. There existed the overlapping effects of C–O in cellulose and Si–O–Si, Si–O–C, which were derived from the reaction between the hydroxyl groups of fibers and MTCS at 1000–1130 cm^{-1} [38]. Characteristic absorption peaks at the 781 and 1276 cm^{-1} were assigned to the Si–C stretching vibration bond, and the deformation vibrations of $–CH_3$. However, these two peaks were only found in the 6% and 8% (*v*/*w*) MTCS-treated samples, which indicated the presence of PMS. Meanwhile the two characteristic absorption bands at 781 and 1276 cm^{-1} were not obvious in samples treated with 4% (*v*/*w*) MTCS, which supports that the modified fiber surface was covered with only a small amount of PMS. The broad peaks at 3200–3680 cm^{-1} and 2900 cm^{-1} were assigned to the stretching vibration of –OH and CH_2 groups from cellulose and they decreased with the increase of MTCS dosage to 4% (*v*/*w*). However, these bands became pronounced again in samples treated with the 6% (*v*/*w*) and 8% (*v*/*w*) MTCS. It was thought that more fiber fragmentation under these two conditions possibly exposed new hydrophilic hydroxyl groups within the ONP fibers.

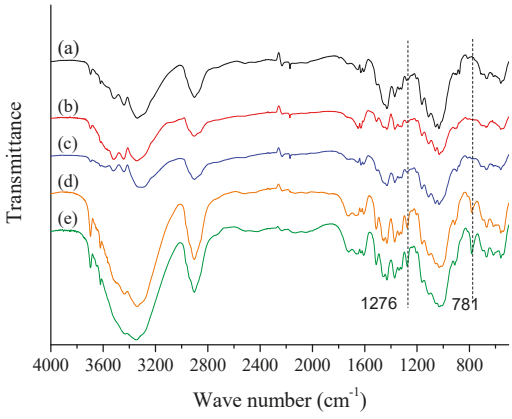

Figure 3. FTIR spectra of ONP fibers treated with different MTCS dosages: (a) 0 (*v*/*w*); (b) 2% (*v*/*w*); (c) 4% (*v*/*w*); (d) 6% (*v*/*w*); and (e) 8% (*v*/*w*).

The thermal stability of untreated and MTCS-modified ONP fibers was studied by TGA as shown in Figure 4. Usually, natural fibers exhibited three stages of mass loss under nitrogen atmosphere with increasing temperature. The initial stage took place before 120 °C due to the evaporation of adsorbed moisture. The second stage corresponded to swift decomposition between 275 and 370 °C, which was thought to be hemicellulose and partly cellulose degradation. An unsymmetrical peak at 362 °C in untreated ONP fibers was observed while the peak symmetry of MTCS-modified fibers was improved, indicating that partial hemicellulose was removed after the MTCS treatment and washing process. However, the degradation temperature at maximum rate shifted to 355 and 344 °C, corresponding to 2%, 4% (*v*/*w*) and 6%, 8% (*v*/*w*) MTCS treatment, respectively. The lower cellulose-breakdown temperature showed a degradation of thermal stability of the modified ONP fibers. The thermal stability degradation probably resulted from the HCl degradation of ONP fibers, which was consistent with information shown in the SEM images.

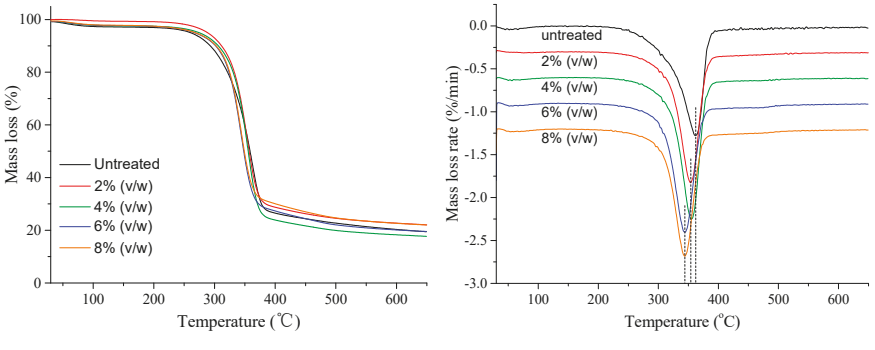

Figure 4. TG spectra of untreated and modified fibers with 2%, 4%, 6%, and 8% (*v*/*w*) MTCS dosages.

Based on the above characterization of MTCS-modified ONP fiber, the possible reaction mechanism is proposed in Figure 5. Gaseous MTCS could readily be impregnated into ONP strips through the interspaces. Since no free water existed on the ONP fibers, these reactive –Cl groups of MTCS assembled on the fiber surfaces and reacted with –OH group of cellulose to form Si–O–cellulose bonds. Such bonds per silane molecule reached at maximum two instead of three due to the steric hindrance [39]. However, no condensation took place among free- or anchored-MTCS molecules due to the absence of water molecules. Hydrolysis reaction of residue Si–Cl groups happened in the next

step where water was introduced. Therefore, a monolayer of PMS was finally formed at the ONP fiber surface, producing hydrophobic properties. Note that the PMS layer was not complete as some –OH groups were preserved at the fiber surface after MTCS modification.

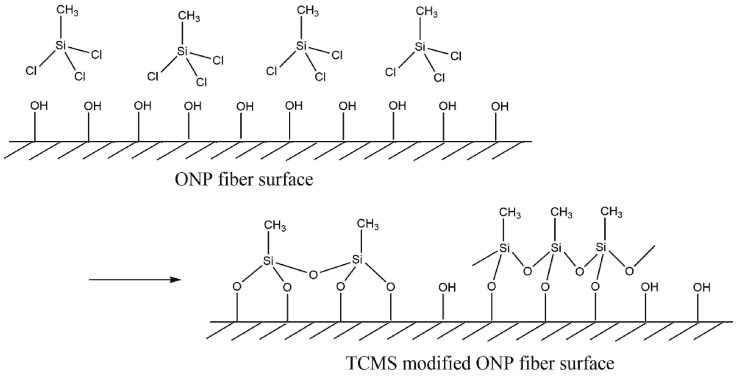

Figure 5. Formation of polymethylsilsesquioxane (PMS) on ONP fiber surface.

3.2. Effect of MTCS Dosage on Mechanical Properties and Water Resistance of ONP/HDPE Composites

Powdery ONP fibers were obtained after MTCS treatment due to the reduced polarity and decreased hydrogen bonding among ONP fibers. Macro-morphology transition of ONP fibers was essential because flocculent fibers could not be fed into the twin-screw extruder for melt-compounding and pelleting with HDPE pellets.

The relationship between the MTCS dosages and the mechanical properties of ONP/HDPE composites was investigated and the results are shown in Figure 6. The impacts of MTCS dosage on tensile and flexural strength were similar. The increase of tensile and flexural strengths with the increase of MTCS dosage from 2% to 4% (*v*/*w*) could be attributed to the improved compatibility between the modified fibers and HDPE. The fiber orientation and the degree of dispersion might be also enhanced due to weakened forces between the modifier fibers [40]. However, tensile and flexural strengths fluctuated when the MTCS dosage was larger than 4% (*v*/*w*), which might be caused by the compromise between decreased aspect ratio and improved compatibility. Although the notched impact strength also increased at first with the increase of MTCS dosage and then decreased, the highest notched impact strength was obtained when the MTCS dosage was 6% (*v*/*w*). The SEM images showed that the modified ONP fibers were dramatically damaged with a relatively high dosage of MTCS. Fibers treated with 8% (*v*/*w*) MTCS even appeared irregularly shaped. The reduced aspect ratio led to more fibers pulled out of the matrix rather than fracture when the ONP/HDPE composite failed to reduce its mechanical strength [9]. It seemed that impact strength was less sensitive to the aspect ratio of paper fiber reinforcement than tensile and flexural strength.

Water absorption of ONP/HDPE composites was low and decreased with the increased dosage of MTCS up to 6% (*v*/*w*). The prepared composites showed worse water resistance when large amounts of MTCS were used to modify the ONP fibers. As mentioned above, ONP fibers treated with 8% (*v*/*w*) MTCS were intensively fragmented, which exposed more hydrophilic hydroxyl groups within the ONP fibers and would result in more interfacial bonding and more moisture uptake.

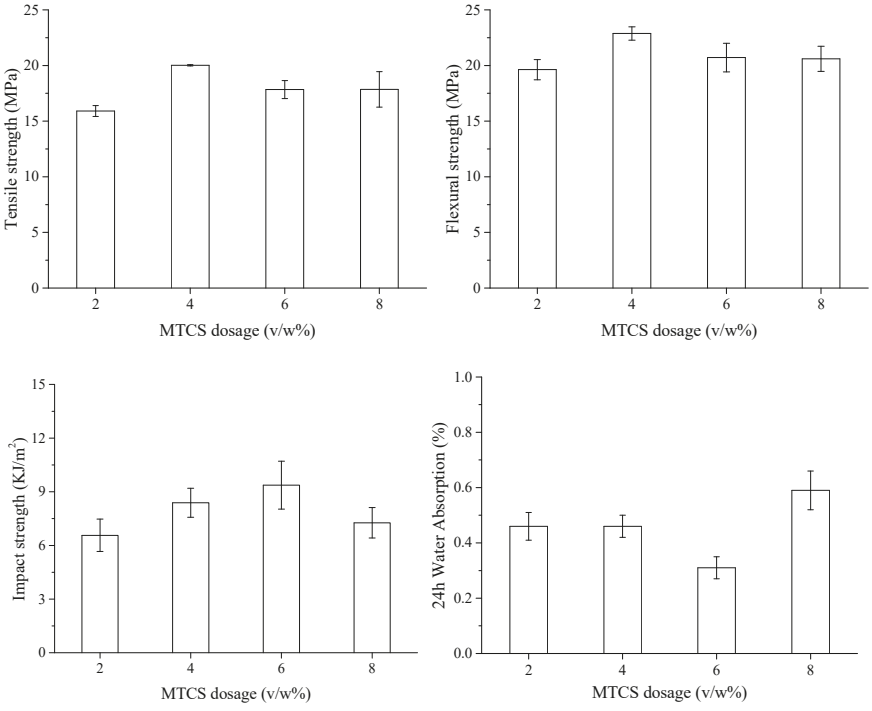

Figure 6. Impacts of MTCS dosages on mechanical properties and water resistance of ONP/HDPE composites.

3.3. Effect of MAPE Content on Mechanical Properties and Water Resistance of ONP/HDPE Composites

The hydrophobic modification at the ONP fibers improved interfacial compatibility with HDPE matrix. However, the promoted mechanical properties of the composites were limited. There were still large amounts of free hydroxyl groups at the MTCS-treated fibers according to the information obtained from the FTIR results. Therefore, the coupling agent MAPE was added during the extrusion–pelletization process to improve the interface bonding and to enhance the mechanical properties. The presence of MAPE in the composites created a significant increase in tensile strength, flexural strength, and notched impact strength as shown in Figure 7. The tensile strength of the composite quickly increased with 3 wt.% of MAPE and after that slowly reached the highest value of 32.57 ± 0.07 MPa, which was up to a 63.2% enhancement compared to the one without MAPE. The flexural strength quickly increased when the MAPE content was 3 wt.% and then decreased linearly from 35.08 ± 0.88 to 33.89 ± 0.54 MPa when the MAPE content increased from 3 to 9 wt.%. The notched impact strength of the ONP/HDPE composite was less affected by the addition of MAPE. The strengthening effect of MAPE on the ONP/HDPE composites can be attributed to the ester linkages of the unreacted hydroxyl groups on the fibers and the acid anhydride groups of MAPE while the nonpolar long chain from MAPE was entangled with the molecular chain of the matrix. The improved interface adhesion between the ONP fibers and HDPE matrix also reduced the water absorption of composites. Since the ONP fibers turned hydrophobic after MTCS modification, the 24 h water absorption of the ONP/HDPE was as low as 0.56% ± 0.02%. Thus, the increase of MAPE content only slightly reduced the water absorption behavior of the ONP/HDPE composites.

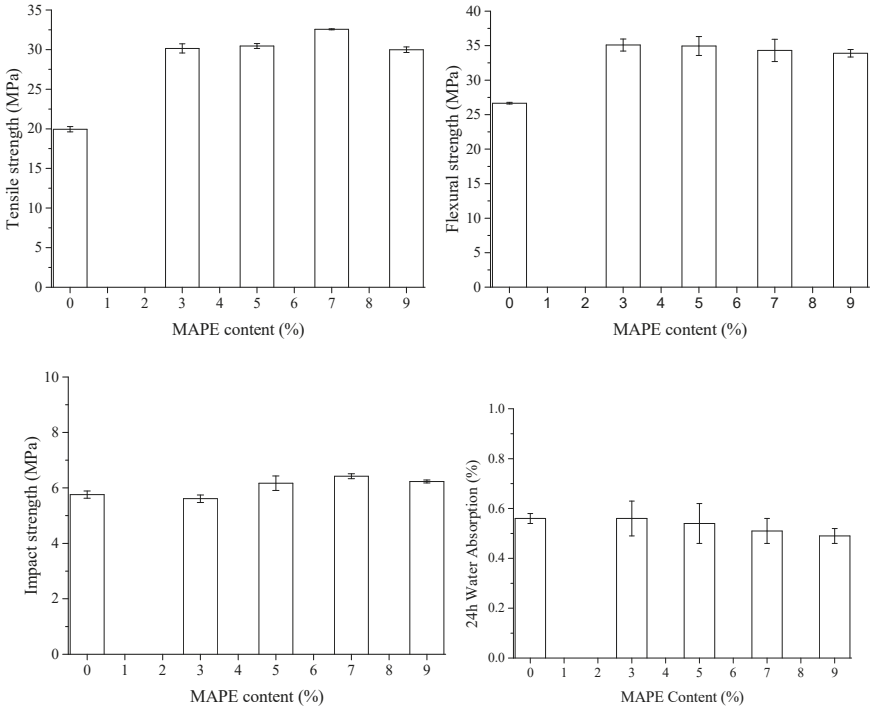

Figure 7. Impacts of maleic anhydride-grafted polyethylene (MAPE) content on mechanical properties and water resistance of ONP–HDPE composites.

3.4. Interfacial Characterization of ONP/HDPE Composites

The interfacial adhesion of ONP and HDPE could be inferred from the fracture surface microstructure of ONP/HDPE composite. SEM images of fracture surfaces of the composites reinforced with 50% fibers which were treated with 4% (*v*/*w*) MTCS are shown in Figure 8. A composite prepared without MAPE showed identifiable ONP fibers as well as gaps around them, which indicated that the interfacial adhesion between modified fibers and the matrix was weak. The reason was thought to be that the polarity difference between the modified ONP fibers and HDPE had decreased but not disappeared, since cellulose –OH groups still existed at the modified fiber surface with 4% (*v*/*w*) MTCS according to the FTIR results. The interface of ONP and HDPE became more and more ambiguous and no debonding of fibers was observed with increased MAPE loading shown in Figure 8b–e. The interfacial adhesion was enhanced since carboxyl groups of MAPE connected with hydroxyl groups of ONP fibers through ester and/or hydrogen bonding.

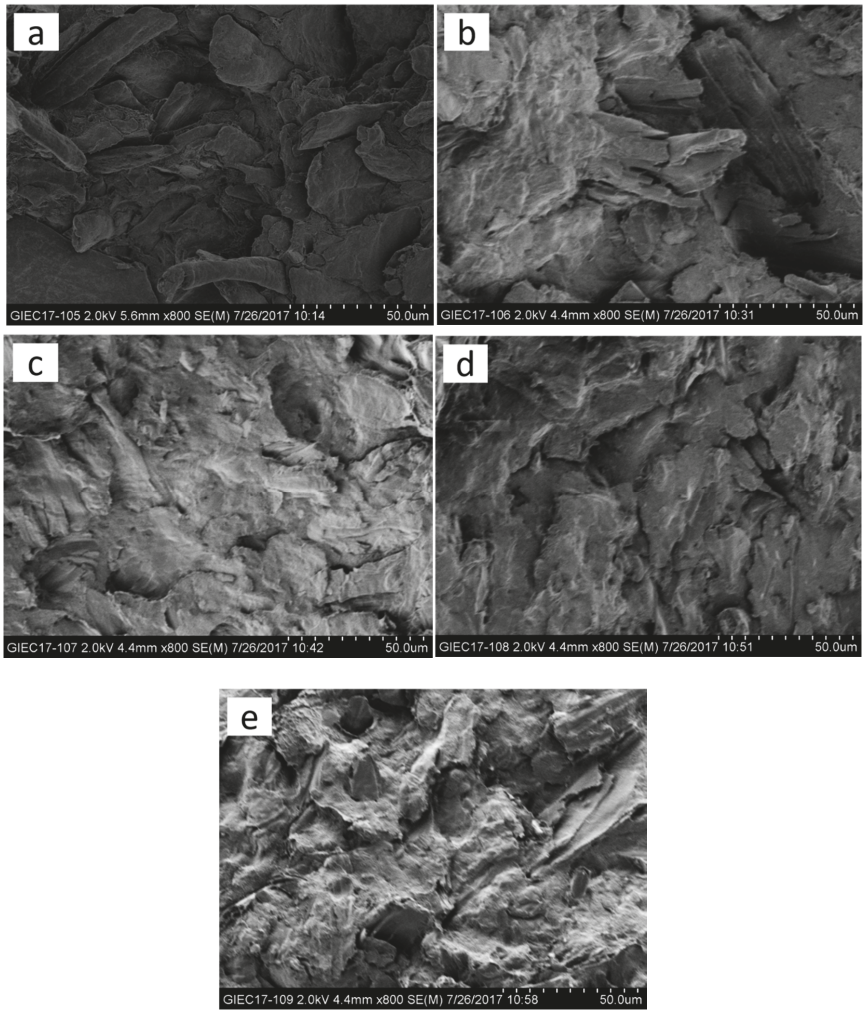

Figure 8. SEM images of interfacial adhesion with different MAPE contents: (**a**) 0%; (**b**) 3%; (**c**) 5%; (**d**) 7%; and (**e**) 9%.

4. Conclusions

In this study, hydrophobic modification using gaseous MTCS was proved to be an efficient method for ONP to solve the flocculation problem after pulverization. The formation of hydrogen bonding between ONP fibers was effectively prevented after MTCS treatment due to the reduction of exposed –OH groups at the fiber surface. However, excessive dosage of MTCS (larger than 6% (*v*/*w*)) led to severe fiber degradation and dramatically reduced the aspect ratio of ONP fibers. ONP/HDPE composites prepared with ONP fibers modified with 4% (*v*/*w*) MTCS showed the best mechanical properties due to reduced polarity between fibers and matrix, and the relatively long aspect ratio of treated ONP fibers. The composite with or without MAPE showed satisfactory water resistance properties. The interfacial bonding performance between ONP fibers and HDPE matrix as well as the physical and mechanical properties of the composites was further enhanced with the assistance of the coupling agent MAPE.

Author Contributions: Writing—original draft preparation, W.Z.; writing—review and editing, J.G., D.T., L.G.; funding acquisition, C.H.

Funding: This project is financially supported by the Guangdong Provincial Department of Science and Technology (Project No. 2017B020238003) and the Natural Science Foundation of Guangdong Province (2018A030313233) and the Guangdong-Hongkong Joint Innovation Program (2014B050505019).

Conflicts of Interest: The authors declare no conflict of interest.

References

1. Sanjay, M.R.; Madhu, P.; Jawaid, M.; Senthamaraikannan, P.; Senthil, S.; Pradeep, S. Characterization and properties of natural fiber polymer composites: A comprehensive review. *J. Clean. Prod.* **2018**, *172*, 566–581. [CrossRef]
2. Lau, K.T.; Hung, P.Y.; Zhu, M.H.; Hui, D. Properties of natural fibre composites for structural engineering applications. *Compos. Part B* **2018**, *136*, 222–233. [CrossRef]
3. Benyahia, A.; Merrouche, A.; Rahmouni, Z.E.A.; Rokbi, M.; Serge, W.; Kouadri, Z. Study of the alkali treatment effect on the mechanical behavior of the composite unsaturated polyester-Alfa fibers. *Mech. Ind.* **2014**, *15*, 69–73. [CrossRef]
4. Goriparthi, B.K.; Suman, K.N.S.; Rao, N.M. Effect of fiber surface treatments on mechanical and abrasive wear performance of polylactide/jute composites. *Compos. Part. A* **2012**, *43*, 1800–1808. [CrossRef]
5. Demir, H.; Atikler, U.; Balköse, D.; Tıhmınlıoğlu, F. The effect of fiber surface treatments on the tensile and water sorption properties of polypropylene–luffa fiber composites. *Compos. Part. A* **2006**, *37*, 447–456. [CrossRef]
6. Ibrahim, M.M.; Dufresne, A.; El-Zawawy, W.K.; Agblevor, F.A. Banana fibers and microfibrils as lignocellulosic reinforcements in polymer composites. *Carbohydr. Polym.* **2010**, *81*, 811–819. [CrossRef]
7. Lu, T.; Jiang, M.; Jiang, Z.; Hui, D.; Wang, Z.; Zhou, Z. Effect of surface modification of bamboo cellulose fibers on mechanical properties of cellulose/epoxy composites. *Compos. Part B* **2013**, *51*, 28–34. [CrossRef]
8. Lu, T.; Liu, S.; Jiang, M.; Xu, X.; Wang, Y.; Wang, Z.; Gou, J.; Hui, D.; Zhou, Z. Effects of modifications of bamboo cellulose fibers on the improved mechanical properties of cellulose reinforced poly(lactic acid) composites. *Compos. Part B* **2014**, *62*, 191–197. [CrossRef]
9. López, J.P.; Boufi, S.; El Mansouri, N.E.; Mutjé, P.; Vilaseca, F. PP composites based on mechanical pulp, deinked newspaper and jute strands: A comparative study. *Compos. Part B* **2012**, *43*, 3453–3461. [CrossRef]
10. Granda, L.A.; Espinach, F.X.; Tarrés, Q.; Méndez, J.A.; Delgado-Aguilar, M.; Mutjé, P. Towards a good interphase between bleached kraft softwood fibers and poly(lactic) acid. *Compos. Part B* **2016**, *99*, 514–520. [CrossRef]
11. Delgado-Aguilar, M.; Julián, F.; Tarrés, Q.; Méndez, J.A.; Mutjé, P.; Espinach, F.X. Bio composite from bleached pine fibers reinforced polylactic acid as a replacement of glass fiber reinforced polypropylene, macro and micro-mechanics of the Young's modulus. *Compos. Part B* **2017**, *125*, 203–210. [CrossRef]
12. Espinach, F.X.; Boufi, S.; Delgado-Aguilar, M.; Julián, F.; Mutjé, P.; Méndez, J.A. Composites from poly(lactic acid) and bleached chemical fibres: Thermal properties. *Compos. Part B* **2018**, *134*, 169–176. [CrossRef]
13. Huda, M.S.; Drzal, L.T.; Mohanty, A.K.; Misra, M. Chopped glass and recycled newspaper as reinforcement fibers in injection molded poly(lactic acid) (PLA) composites: a comparative study. *Compos. Sci. Technol.* **2006**, *66*, 1813–1824. [CrossRef]
14. Huda, M.S.; Drzal, L.T.; Mohanty, A.K.; Misra, M. The effect of silane treated-and untreated-talc on the mechanical and physico-mechanical properties of poly(lactic acid)/newspaper fibers/talc hybrid composites. *Compos. Part B* **2007**, *38*, 367–379. [CrossRef]
15. Iyer, K.A.; Lechanski, J.; Torkelson, J.M. Green polypropylene/waste paper composites with superior modulus and crystallization behavior: Optimizing specific energy in solid-state shear pulverization for filler size reduction and dispersion. *Compos. Part A* **2016**, *83*, 47–55. [CrossRef]
16. Zhang, X.; Bo, X.; Cong, L.; Wei, L.; Mcdonald, A.G. Characteristics of undeinked, alkaline deinked, and neutral deinked old newspaper fibers reinforced recycled polypropylene composites. *Polym. Compos.* **2017**, *39*, 3537–3544. [CrossRef]
17. Mitchell, J.; Vandeperre, L.; Dvorak, R.; Kosior, E.; Tarverdi, K.; Cheeseman, C. Recycling disposable cups into paper plastic composites. *Waste Manag.* **2014**, *34*, 2113–2119. [CrossRef]

18. Valente, M.; Tirillò, J.; Quitadamo, A.; Santulli, C. Paper fiber filled polymer. Mechanical evaluation and interfaces modification. *Compos. Part B* **2017**, *110*, 520–529. [CrossRef]
19. Serrano, A.; Espinach, F.X.; Tresserras, J.; Pellicer, N.; Alcala, M.; Mutje, P. Study on the technical feasibility of replacing glass fibers by old newspaper recycled fibers as polypropylene reinforcement. *J. Clean. Prod.* **2014**, *65*, 489–496. [CrossRef]
20. Serrano, A.; Espinach, F.X.; Julian, F.; del Rey, R.; Mendez, J.A.; Mutje, P. Estimation of the interfacial shears strength, orientation factor and mean equivalent intrinsic tensile strength in old newspaper fiber/polypropylene composites. *Compos. Part B* **2013**, *50*, 232–238. [CrossRef]
21. Yang, X.; Wang, G.; Miao, M.; Yue, J.; Hao, J.; Wang, W. The dispersion of pulp-fiber in high-density polyethylene via different fabrication processes. *Polymers* **2018**, *10*, 122. [CrossRef] [PubMed]
22. Tserki, V.; Zafeiropoulos, N.E.; Simon, F.; Panayiotou, C. A study of the effect of acetylation and propionylation surface treatments on natural fibres. *Compos. Part A* **2005**, *36*, 1110–1118. [CrossRef]
23. Nedjma, S.; Djidjelli, H.; Boukerrou, A.; Benachour, D.; Chibani, N. Deinked and acetylated fiber of newspapers. *J. Appl. Polym. Sci.* **2013**, *127*, 4795–4801. [CrossRef]
24. Asim, M.; Jawaid, M.; Abdan, K.; Ishak, M.R. Effect of alkali and silane treatments on mechanical and fibre-matrix bond strength of kenaf and pineapple leaf fibres. *J. Bionic Eng.* **2016**, *13*, 426–435. [CrossRef]
25. Seki, Y.; Sarikanat, M.; Sever, K.; Erden, S.; Gulec, H.A. Effect of the low and radio frequency oxygen plasma treatment of jute fiber on mechanical properties of jute fiber/polyester composite. *Fibers Polym.* **2010**, *11*, 1159–1164. [CrossRef]
26. Piao, C.; Cai, Z.; Stark, N.M.; Monlezun, C.J. Dimensional stability of wood–plastic composites reinforced with potassium methyl siliconate modified fiber and sawdust made from beetle-killed trees. *Eur. J. Wood Wood Prod.* **2014**, *72*, 165–176. [CrossRef]
27. Piao, C.; Cai, Z.; Stark, N.M.; Monlezun, C.J. Potassium methyl siliconate-treated pulp fibers and their effects on wood plastic composites: Water sorption and dimensional stability. *J. Appl. Polym. Sci.* **2013**, *129*, 193–201. [CrossRef]
28. Gao, L.; McCarthy, T.J. A perfectly hydrophobic surface (θ_A/θ_R = 180°/180°). *J. Am. Chem. Soc.* **2006**, *128*, 9052–9053. [CrossRef]
29. Khoo, H.S.; Tseng, F.G. Engineering the 3D architecture and hydrophobicity of methyltrichlorosilane nanostructures. *Nanotechnology* **2008**, *19*, 345603. [CrossRef]
30. Jin, M.; Wang, J.; Hao, Y.; Liao, M.; Zhao, Y. Tunable geometry and wettability of organosilane nanostructured surfaces by water content. *Polym. Chem.* **2011**, *2*, 1658–1660. [CrossRef]
31. Artus, G.R.; Jung, S.; Zimmermann, J.; Gautschi, H.P.; Marquardt, K.; Seeger, S. Silicone nanofilaments and their application as superhydrophobic coatings. *Adv. Mater.* **2006**, *18*, 2758–2762. [CrossRef]
32. Li, S.; Xie, H.; Zhang, S.; Wang, X. Facile transformation of hydrophilic cellulose into superhydrophobic cellulose. *Chem. Commun.* **2007**, *46*, 4857–4859. [CrossRef]
33. Zimmermann, J.; Reifler, F.A.; Fortunato, G.; Gerhardt, L.C.; Seeger, S. A simple, one-step approach to durable and robust superhydrophobic textiles. *Adv. Funct. Mater.* **2008**, *18*, 3662–3669. [CrossRef]
34. Saini, A.; Yadav, C.; Bera, M.; Gupta, P.; Maji, P.K. Maleic anhydride grafted linear low-density polyethylene/waste paper powder composites with superior mechanical behavior. *J. Appl. Polym. Sci.* **2017**, *134*, 45167. [CrossRef]
35. Avella, M.; Avolio, R.; Bonadies, I.; Carfagna, C.; Errico, M.E.; Gentile, G. Recycled multilayer cartons as cellulose source in HDPE-based composites: Compatibilization and structure-properties relationships. *J. Appl. Polym. Sci.* **2010**, *114*, 2978–2985. [CrossRef]
36. Araujo, J.R.; Waldman, W.R.; De Paoli, M.A. Thermal properties of high density polyethylene composites with natural fibres: Coupling agent effect. *Polym. Degrad. Stab.* **2008**, *93*, 1770–1775. [CrossRef]
37. Fadeev, A.Y.; McCarthy, T.J. Self-assembly is not the only reaction possible between alkyltrichlorosilanes and surfaces: monomolecular and oligomeric covalently attached layers of dichloro-and trichloroalkylsilanes on silicon. *Langmuir* **2000**, *16*, 7268–7274. [CrossRef]
38. Li, S.; Zhang, S.; Wang, X. Fabrication of superhydrophobic cellulose-based materials through a solution-immersion process. *Langmuir* **2008**, *24*, 5585–5590. [CrossRef] [PubMed]

39. Roumeliotis, P.; Unger, K.K. Structure and properties of *n*-alkyldimethylsilyl bonded silica reversed-phase packings. *J. Chromatogr. A* **1978**, *149*, 211–224. [CrossRef]
40. Ansari, F.; Granda, L.A.; Joffe, R.; Berglund, L.A.; Vilaseca, F. Experimental evaluation of anisotropy in injection molded polypropylene/wood fiber biocomposites. *Compos. Part A* **2017**, *96*, 147–154. [CrossRef]

polymers

MDPI

Article

The Effect of Glycerol, Sugar, and Maleic Anhydride on Pectin-Cellulose Thin Films Prepared from Orange Waste

Veronika Bátori *, Magnus Lundin, Dan Åkesson, Patrik R. Lennartsson, Mohammad J. Taherzadeh and Akram Zamani

Swedish Centre for Resource Recovery, University of Borås, 50190 Borås, Sweden; magnus.lundin@hb.se (M.L.); dan.akesson@hb.se (D.Å.); patrik.lennartsson@hb.se (P.R.L.); mohammad.taherzadeh@hb.se (M.J.T.); akram.zamani@hb.se (A.Z.)

* Correspondence: veronika.batori@hb.se; Tel.: +46-33-4355903

Received: 14 January 2019; Accepted: 20 February 2019; Published: 27 February 2019

Abstract: This study was conducted to improve the properties of thin films prepared from orange waste by the solution casting method. The main focus was the elimination of holes in the film structure by establishing better cohesion between the major cellulosic and pectin fractions. For this, a previously developed method was improved first by the addition of sugar to promote pectin gelling, then by the addition of maleic anhydride. Principally, maleic anhydride was introduced to the films to induce cross-linking within the film structure. The effects of concentrations of sugar and glycerol as plasticizers and maleic anhydride as a cross-linking agent on the film characteristics were studied. Maleic anhydride improved the structure, resulting in a uniform film, and morphology studies showed better adhesion between components. However, it did not act as a cross-linking agent, but rather as a compatibilizer. The middle level (0.78%) of maleic anhydride content resulted in the highest tensile strength (26.65 $\pm$ 3.20 MPa) at low (7%) glycerol and high (14%) sugar levels and the highest elongation (28.48% $\pm$ 4.34%) at high sugar and glycerol levels. To achieve a uniform film surface with no holes present, only the lowest (0.39%) level of maleic anhydride was necessary.

Keywords: bio-based; film; mechanical properties; polysaccharides; resource recovery; solution casting; orange waste

1. Introduction

The post-plastic era induces several industries, such as the biomedical, building, and packaging industries, to move towards the use of bio-based films. Thin films prepared from lignocellulosic by-products of food and agricultural industries not only have a great potential to replace petroleum-based films, but the recovery of biopolymers also forms an essential part of the bioeconomy [1]. Cellulose, in particular, is abundant and is a favorable reinforcement material because of its features, such as its crystalline structure and good mechanical properties [2].

An attractive research area is the production of bio-based films from fruit and vegetable residues, often with the film-casting method [3–8]. During film-casting, the suspension of a colloidal dispersion of polymers is poured onto a non-sticky surface and dried to a film. Various fruit and vegetable residuals are rich sources of different biopolymers, such as pectin, starch, cellulose, hemicellulose, lignin, and proteins, which can be used to form firm films with properties rivaling those of commodity plastics. By choosing the right additives, biopolymers can be dissolved, plasticized, or kept undissolved in order to perform the required function in the bio-based film, i.e. turned into a matrix, blended, or used as reinforcement. One study [6], for example, reported that in bio-based films made from carrot

powders, the insoluble, mostly crystalline cellulose fractions were responsible for the film structure, while the soluble, mostly pectin and sugar phase had a plasticizing effect.

When fabricating bioplastics from polysaccharides, one has to bear in mind that these are hydrophobic substances that have low water vapor barrier properties [9] and that the mechanical and barrier properties are affected by moisture content. Several methods exist to enhance the barrier and mechanical properties of hydrocolloid films; one promising alternative is the modification of physical properties by inducing intra-, and intermolecular bonding by chemical, enzymatic, or physical cross-linking [10]. Formaldehyde, glutaraldehyde, and glyoxal are potent cross-linking agents that enhance water barrier properties and increase the strength of edible protein-based films [11]. Due to their toxicity, however, their use is limited for environmentally friendly applications. A low hazard profile compound and cross-linking agent is maleic anhydride [12,13]. Maleic anhydride has also been used as a compatibilizer between natural fibers and poly(lactic acid) matrices [14,15] to improve adhesion.

Bio-based films from the by-product of industrial orange juice processing, mostly containing peels, seeds, pulp, and membrane residues, have previously been developed with suitable mechanical properties, such as a tensile strength ranging between 27.3 and 36.7 MPa [8]. Briefly, a citric acid solution containing orange waste (composed mainly of pectin and cellulosic fibers) powder and glycerol was casted for bio-based film production. Due to the mechanism of drying of colloidal films, a number of holes were present in the structure, however. In the same study, the use of a rotary movement during drying showed positive effects, but film thicknesses were uneven, and the continuous rotary movement had a higher energy consumption. To deal with this unfavorable aspect, further improvement in the preparation conditions and structure of the films was necessary.

Thus, this study was dedicated first to investigating the enhancement of pectin gelling, establishing a three-dimensional network in which other components are trapped [16]. To achieve this goal, conditions for solubilizing pectin first had to be provided, followed by conditions that allow pectin gelling. The reason for this was the fact that within conditions for gelling, solubilization would not happen, and vice versa. This meant that the addition of citric acid (acid being one of the triggers for pectin gelling), together with sugar, took place in a later stage to promote pectin gelling [16]. This step aimed to reduce the holes by establishing an improved structure of pectin. This study also investigated the use of maleic anhydride to improve the properties of orange waste pectin–cellulose thin films. Maleic anhydride has been used previously to develop maleic anhydride-grafted orange waste [17]; therefore, it was expected that it would have a cross-linking effect on the films. Mechanical tests and morphological studies were performed to investigate the effect of each component and optimize the preparation conditions.

2. Materials and Methods

2.1. Materials

Orange waste, obtained in the juice production process and consisting of mostly pectin, hemicelluloses, and cellulose [8], was kindly provided by Brämhults AB (Borås, Sweden) before the headquarters changed location, and was kept at −20 °C until further use. Maleic anhydride (≥99%, Sigma Aldrich, St. Louise, MO, USA), citric acid (monohydrate, >99.5%, Duchefa Biochemie, Haarlem, the Netherlands), D-(+)-glucose (≥99.5%, Sigma Aldrich, St. Louise, MO, USA), herein referred to as sugar, and glycerol (>99 % ARCOS Organics, Antwerp, Belgium) were other materials used in the experiments.

2.2. Pretreatment of Orange Waste

Pretreatment of orange waste was performed according to a previous study [17] in which soluble sugars were removed prior to size reduction, drying, and milling of the material to a fine powder. In the first step of milling, a variable speed rotor mill (Pulverisette 14, Fritsch, Idar-Oberstein, Germany)

was used with a sequence of sieve sizes of 1 and 0.2 mm at 10,000 rpm for a maximum of 1 min each. The powder was further milled with a ball-mill (MM 400, Retsch, Haan, Germany) at a frequency of 30 Hz for 10 min. The second step of milling was necessary in order to obtain the same range of particles (mostly between 125 and 75 μm) as in a previous study [8].

2.3. Film Formation

Film formation of orange waste was further developed from the method applied in our previous study [8]. The first step of the modification was done by applying a "sol-gel method". In the sol-gel method, first, conditions for solubilizing the pectin are provided, followed by conditions for gelling the pectin [16]. By this method, 2% (*w*/*v*) orange waste was introduced to 100 mL of vigorously stirred distilled water that already contained 7% glycerol (*w*/*w* of orange waste powder) and 1 drop of organic antifoam (Antifoam 204, Sigma Aldrich, St. Louise, MO, USA) at 40–50 °C. The mixture was then heated up to 70 °C and cooled to about 60 °C. At that point, citric acid (to obtain a 1% (*w*/*v*) solution) and 7% sugar (*w*/*w* of orange waste powder) were added to the mixture to initiate the gelling, and rotation was reduced to 200 rpm to support pectin gelling. Then, 30 g of the suspension was poured through a metal sieve, to capture occasionally formed air bubbles, onto non-sticky polytetrafluoroethylene plates and dried in a laboratory oven (Termaks, TS9026, Bergen, Norway) at 40 °C.

The "sol-gel-ma method" was a further step in which maleic anhydride, as a potential crosslinking agent, was also incorporated into the recipe of the sol-gel method, while antifoam was removed to reduce the number of chemicals. In the sol-gel-ma method, different concentrations of maleic anhydride (100, 50, 25, 12.5, 6.25, 3.13, and 1.56 (*w*/*w*) %) were used in the preliminary experiments, and maleic anhydride was added to distilled water as one of the initial ingredients, together with glycerol. All other steps and concentrations were the same as in the sol-gel method. A schematic image of the different methods is presented in Figure 1.

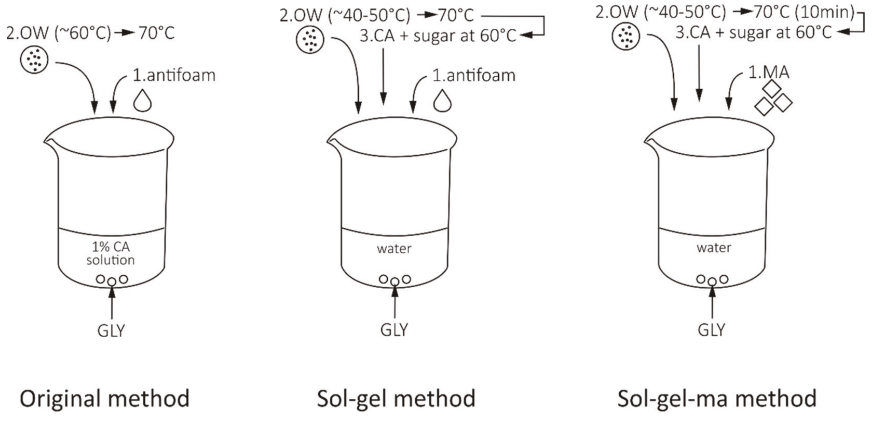

Figure 1. Schematic image of the different film-forming methods discussed in this study. Glycerol (GLY), orange waste (OW), citric acid (CA), and maleic anhydride (MA) were ingredients used in the methods.

A 3-2-2 factorial experiment for the sol-gel-ma method with factors maleic anhydride, sugar, and glycerol was performed to optimize preparation conditions and to determine the minimum amount of maleic anhydride needed. All of the concentrations are shown in Table 1, demonstrating the randomized treatments used. This experiment is further referred to as "optimization", and concentrations of 7% (as used in former studies) are referred to as low, while concentrations of 14% (doubled amount) are referred to as high concentrations. Preliminary experiments showed that only

films prepared with citric acid had a good appearance, therefore it was concluded that citric acid is necessary for film formation in order to induce pectin gelation.

Table 1. Different concentrations (*w*/*w* %) of maleic anhydride, sugar, and glycerol in the optimization experiment. Citric acid concentration was constant at 1% (*w*/*v*).

Maleic Anhydride	Sugar	Glycerol
1.56	7	7
0.39	7	14
0.78	14	7
1.56	7	14
1.56	14	14
0.78	7	7
0.78	14	14
0.39	7	7
0.39	14	14
0.78	7	14
0.39	14	7
1.56	14	7

2.4. Characterization of Films

2.4.1. Thickness

The thickness of films was measured by a constant-load micrometer. Two measurements were taken of each specimen and the average was reported (mm).

2.4.2. Mechanical Testing

Mechanical testing was performed according to ISO 527 using a Tinius Olsen H10KT tensile tester and data was analyzed with the QMat software package. A moving cross-head was used to pull the specimens with a load cell of 100 N and a velocity of 10 mm/sec. Tensile strength (MPa) and elongation at maximum tensile strength (%) were measured for 5 specimens and the average was reported.

2.4.3. Water Vapor Permeability

The water vapor transmission permeability (WVP) was determined according to ASTM E96 [18] with modifications and calculated according to Dayarian et al. [19]. A pre-dried (at 70 °C) glass container was filled with 20 ml distilled water, covered with the bio-based films, and sealed with paraffin film. The distance between the film and water was 16 mm. The weight of the whole system was recorded at 0 h and was placed into a desiccator for 5 days. Every 24 h, the weight of the system was recorded to observe the reduction of weight from day 1 to day 5. The mass loss was plotted against time and the slope obtained was used for calculation. The WVP of the films was calculated according to the following equation:

$$WVP = \frac{S * t}{A * \Delta P} \quad (1)$$

where S is the slope of the plot (kg/s), t is the thickness of the film (m), A is the cross-sectional area of the film (m^2), and ΔP is the difference between the vapor pressure of water in the desiccator (assumed to be zero) and inside the container (assumed to be the saturation value at room temperature) (Pa) [19]. The test was performed in duplicates, and averages are reported as the water vapor transmission rate (kg/m Pa s).

2.4.4. Interaction with Water

An interaction-with-water test for selected specimens was performed according to Perotto et al. [6], with slight modifications. A specified size (30 mm × 15 mm) of pre-dried film

(for 1 h at 70 °C) was immersed in 20 ml distilled water for 30 min and then dried for 1 h at 70 °C, and the weight loss was calculated by the gravimetric method. The measurements were performed in duplicates and the results are reported as weight loss (%).

2.4.5. Morphology

Surface and transversal morphology was studied by field emission scanning electron microscopy (FE-SEM) (Zeiss, Sigma, Jena, Germany) imaging. For surface visualization, films were attached to a carbon tape and covered with gold. For transversal visualization, cross-sectional images of films were taken as follows: films were immersed in liquid nitrogen for one minute before they were broken and immediately attached to a carbon tape and covered with gold. Photomicrographs were taken at 500, 1.00, 5.00, and 10.00 K × magnifications using an accelerating voltage of 10.00 and 20.00 kV.

2.4.6. Biodegradation Test

Biodegradation of the films was measured by anaerobic digestion. The test was performed according to a previous study [20]. In brief, the films were incubated in 120 mL glass bottles in thermophilic conditions (55 °C) for 30 days. The working volume of the reactors was 50 mL (containing 35.5 mL inoculum with distilled water) and each bottle contained 0.15 g of film volatile solids (VS). The inoculum was obtained from Borås Energi & Miljö AB (Borås, Sweden), a large-scale thermophilic biogas plant. Samples were taken at specified times and analyzed for gas composition with a gas chromatograph (Clarus 500, Perkin-Elmer, Waltham, MA, USA).

2.5. Statistical Analysis

Statistical analyses were performed using MINITAB® software (version 17.1.0, Minitab Inc., State College, PA, USA). Analysis of variance, ANOVA, using the general linear model, was performed to determine the main effects and interactions of different components in the optimization experiment using a 5% significance level. Model assumptions of homogeneity of residuals were checked by inspection of residual plots during model fitting for tensile strength and elongation.

3. Results and Discussion

Lignocellulosic by-products and waste materials are important participants of the bio-economy: their valuable biopolymer content makes them attractive for the bioplastics industry, which at the same time helps address waste handling issues. An example of such a case is bio-based film prepared from orange waste, demonstrated in a previous study [8], which had some holes in its structure. The goal of this study was to modify the film formation method in order to develop a uniform film structure with no holes and in which the adhesion of polymeric components is promoted.

3.1. Effect of Pectin Gelling and Incorporation of Maleic Anhydride on Properties of Films from Orange Waste

The hypothesis that a more coherent film structure would result in the reduction or even elimination of holes in the orange waste film was tested first by the improvement of pectin gelling, followed by the addition of maleic anhydride into the film.

3.1.1. Appearance

Films prepared by the original method had some holes present in the structure, which could be eliminated by a rotary movement during drying; however, that method resulted in uneven thicknesses [8] and required more energy. Inducing pectin gelling prior to casting improved pectin binding and resulted in a reduced number of holes of a smaller size. By applying this method, the use of rotary movement was not necessary and films had even thicknesses. Because some smaller holes were still present, however, further improvements were necessary and maleic anhydride was used.

When maleic anhydride was used for film preparation, the holes completely disappeared and films with uniform structure were obtained.

3.1.2. Morphology

On a microstructural level, according to FE-SEM images, a more compact film construction was achieved using maleic anhydride compared to the sol-gel method (Figure 2). The micrographs also seem to show smoother surface morphology with increasing maleic anhydride concentration (Figure 2a,c,e).

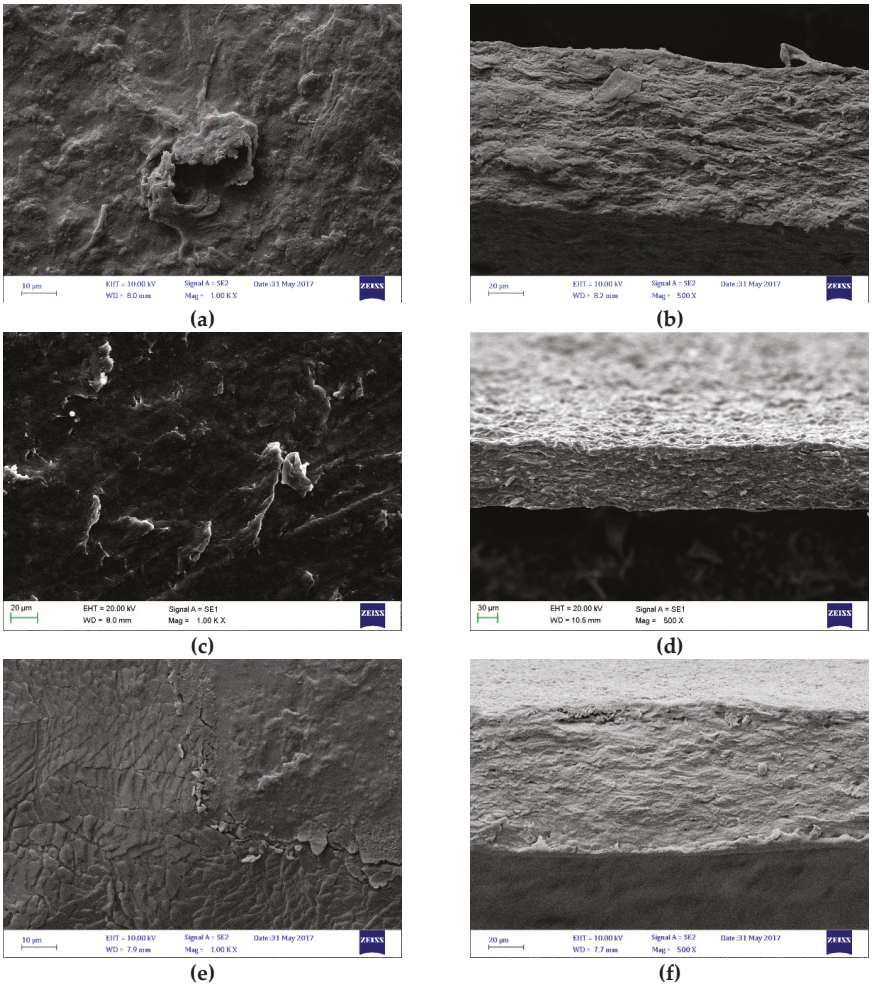

Figure 2. Field emission scanning electron microscopy (FE-SEM) micrographs of the film surface and cross-sectional images prepared with the sol-gel method (**a**,**b**); sol-gel-ma (1.56% maleic anhydride) (**c**,**d**); and sol-gel-ma (25% maleic anhydride) (**e**,**f**). The magnification of surface images was 1.00 K × and that of cross-sectional images was 500×.

The smoother and more compact structure is probably the direct effect of the additional ester bonds between grafted maleic anhydride intermediates and cellulose [21] and/or pectin [22] and/or

glycerol [23]. Since the bio-based films prepared in this study represent a complex mixture of biopolymers (e.g. pectin, cellulose, hemicellulose) and other hygroscopic substances such as glycerol and sugar, which contain OH groups and can function as plasticizers [24], it is difficult to determine which component reacted most with maleic anhydride.

As the introduction of maleic anhydride improved the appearance and structure of the films in general, the next step was to find the optimal concentration of maleic anhydride and other components in the films. Aiming to reduce the amount of chemicals used, the goal was to find the minimum concentration of maleic anhydride in which a film with improved characteristics is obtained.

3.1.3. Thickness and Mechanical Properties

The thicknesses of the films prepared by the original and sol-gel methods ranged between 0.098 and 0.135 mm, with an average value of 0.115 $\pm$ 0.010 mm (standard deviation). The mechanical properties of the films made by the original and sol-gel methods were not significantly different, resulting in a tensile strength of 21.08 $\pm$ 7.78 and 21.69 $\pm$ 8.72 MPa and elongation of 3.67 $\pm$ 1.80 and 4.83% $\pm$ 1.79%, respectively. In general, the addition of maleic anhydride into the films resulted in lower tensile strength and higher elongation compared to those of the sol-gel method (Table 2). At higher concentrations of maleic anhydride ($\geq$ 1.56%), the elongation of the films increased as maleic anhydride content was reduced. This fact contradicts the hypothesis that maleic anhydride would act as a cross-linker in the pectin-cellulose system because cross-linking generally increases the strength and stiffness and reduces elongation. Therefore, instead of a cross-linking agent, maleic anhydride could rather be considered as a compatibilizer that improved film formation and also provided a significant plasticizing effect. The plasticizing effect of maleic anhydride on cellulose diacetate has also been confirmed before [23].

Table 2. Mean values of tensile strength (TS) and elongation at max (E) of films prepared in the preliminary experiment using different concentrations of maleic anhydride (MA) and sugar (S).

method	MA (%)	S (%)	TS (MPa)	st. dev.	E (%)	st. dev.
original [1]	0	0	31.67	4.21	3.02	0.62
original [2]	0	0	34.76	2.64	4.23	1.71
original	0	0	21.08	7.78	3.67	1.80
sol-gel	0	7	21.69	8.72	4.83	1.79
sol-gel-ma	100	7	13.28	1.71	11.03	0.55
sol-gel-ma	50	7	12.51	1.97	14.43	3.00
sol-gel-ma	25	7	10.58	3.18	18.60	3.55
sol-gel-ma	12.5	7	5.79	0.76	14.53	3.83
sol-gel-ma	6.25	7	9.80	1.63	20.70	1.85
sol-gel-ma	3.13	7	10.00	2.14	20.23	2.30
sol-gel-ma	1.56	7	9.75	2.13	21.98	3.25

[1] Films dried in an oven according to Bátori *et al.* [8]. [2] Films dried in a rotary incubator according to Bátori *et al.* [8].

3.2. Optimization of Maleic Anhydride, Sugar, and Glycerol Concentrations to Enhance the Film Properties

In order to reduce the amount of maleic anhydride needed for the production of the films, and in continuation of the preliminary experiment (Section 3.1), the effect of maleic anhydride was also studied at levels of 0.78% and 0.39%. At the same time, the effect of sugar and glycerol at elevated levels (14%) and the interaction between the components affecting the mechanical properties was also studied.

3.2.1. Morphology

The morphology of films containing the most glycerol, sugar, or maleic anhydride with the lowest concentrations of the other two components were studied and are shown in Figures 3–5.

The surface images of the films containing the highest amount of glycerol (Figure 3a,b) show softer, more curvy edges of particles, and a fluffier cross-section image can also been seen (Figure 3c,d). The fluffiness of the structure can be explained by the plasticizing effect of the glycerol, in which the small molecular weight compound is pushing the molecules slightly farther apart to enhance the mobility and the softness of the structure.

The surface images of films containing the highest concentrations of sugar show elegantly arranged flower-like patterns (Figure 4a,b). These patterns may be from the formation of sugar crystals when sugar is present at a high concentration in the solution. A possible explanation could be that as water evaporates during the drying of films, the solution becomes more saturated with sugar and the molecules continuously come out to the surface to re-arrange themselves into crystals [25]. This phenomenon was only observed when sugar was added to the mixture at a high concentration, which may be due to excess sugar in the system not taking part in the film-forming reactions. However, this needs to be confirmed in future studies. There is no evidence that this phenomenon is the re-crystallization [26] of sugar and of how it could have a positive impact on elongation. However, different sugars are known to act as plasticizers in biopolymer films [24].

Films that contain the highest concentration of maleic anhydride have a leather-like and denser appearance on the surface (Figure 5a,b), and they represent a more compact structure when the cross-sectional images are observed (Figure 5c,d). The denseness of the films could be the result of the additional bonds formed between maleic anhydride and other molecules.

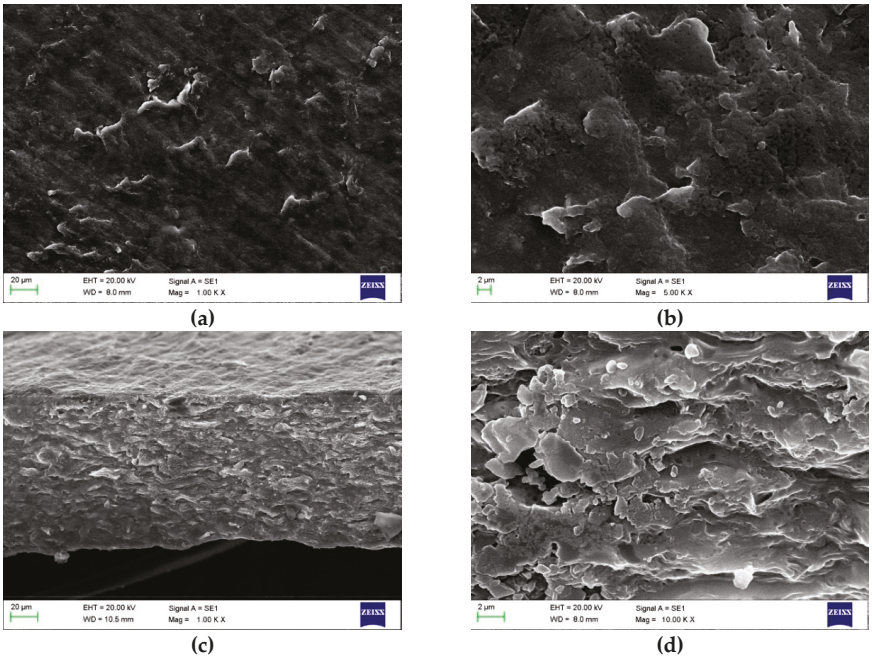

Figure 3. E-SEM micrographs of film surfaces with a magnification of 1.00 K × (**a**) and 5.00 K × (**b**) and cross-sectional images with a magnification of 1.00 K × (**c**) and 10.00 K × (**d**) containing the highest concentration of glycerol (14%) prepared according to the sol-gel-ma method (maleic anhydride and sugar concentrations were 0.39% and 7%, respectively).

Attention was also paid to films that contain high concentrations of both, sugar and glycerol at various maleic anhydride levels. Specifically, the possible morphological differences between specimens containing various maleic anhydride levels have been investigated. The same morphology

that was observed for high sugar and high glycerol content can also be observed on all of these images: floral patterns are formed on a fluffy background, representing the excess sugar and the loosening effect of glycerol. The effect of maleic anhydride, however, is difficult to observe when glycerol and sugar are used in high concentrations. Because of the high number of FE-SEM images, these images are available as supplementary material (Figure S1).

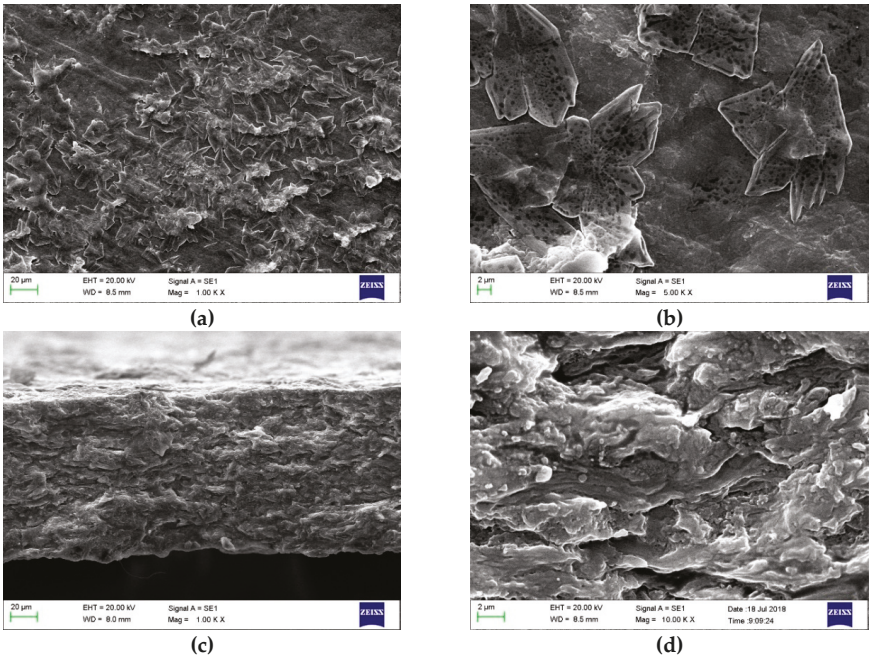

Figure 4. FE-SEM micrographs of film surfaces with a magnification of 1.00 K × (**a**) and 5.00 K × (**b**) and cross-sectional images with a magnification of 1.00 K × (**c**) and 10.00 K × (**d**) containing the highest concentration of sugar (14%) prepared according to the sol-gel-ma method (maleic anhydride and glycerol concentrations were 0.39% and 7%, respectively).

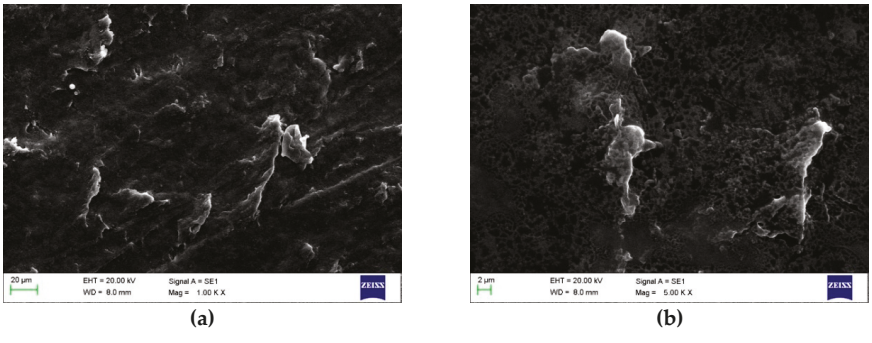

Figure 5. *Cont*.

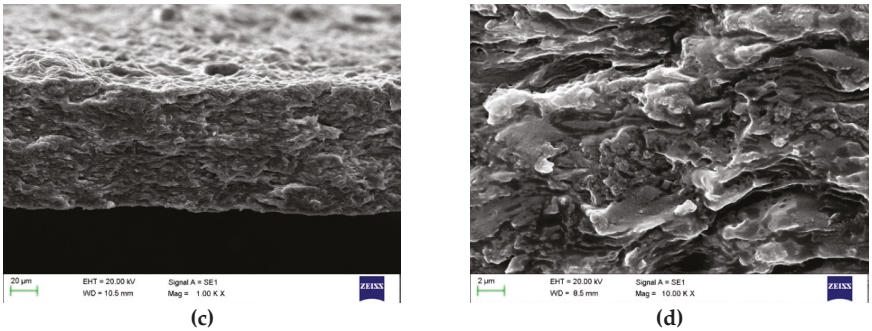

(c) **(d)**

Figure 5. FE-SEM micrographs of film surfaces with a magnification of 1.00 K × (**a**) and 5.00 K × (**b**) and cross-sectional images with a magnification of 1.00 K × (**c**) and 10.00 K × (**d**) containing the highest concentration of maleic anhydride (1.56%) prepared according to the sol-gel-ma method (both glycerol and sugar concentrations were 7%).

3.2.2. Thickness of Films

The thickness of the films prepared in the optimization experiment ranged between 0.095 and 0.139 mm, with an average value of 0.120 ± 0.010 mm (standard deviation), which was similar to preliminary experiments (Section 3.1.3). The use of different concentrations of glycerol had a significant positive effect on film thickness ($p = 0.000$), while sugar had small but non-significant effect ($p = 0.067$), and maleic anhydride had no effect ($p = 0.620$). A clear trend could not be observed, however.

3.2.3. Mechanical Properties

Glycerol appears to have a significant negative effect (coefficient −3.64, $p = 0.000$) on the tensile strength (Figure 6a) when increased from low (7%) to high (14%) concentration, as was expected. Sugar and maleic anhydride ($p = 0.213$ and $p = 0.231$, respectively) did not have any significant effect on tensile strength.

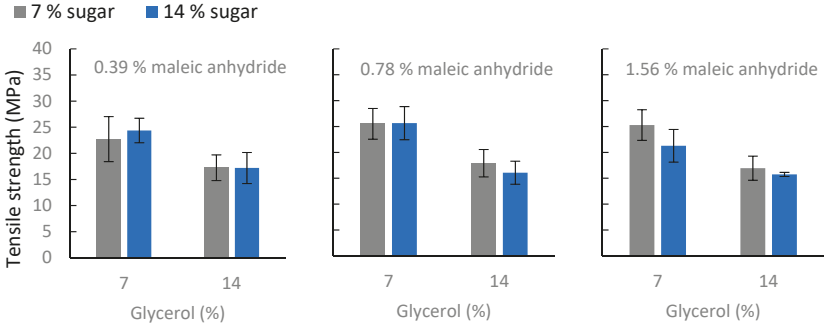

(**a**)

Figure 6. *Cont.*

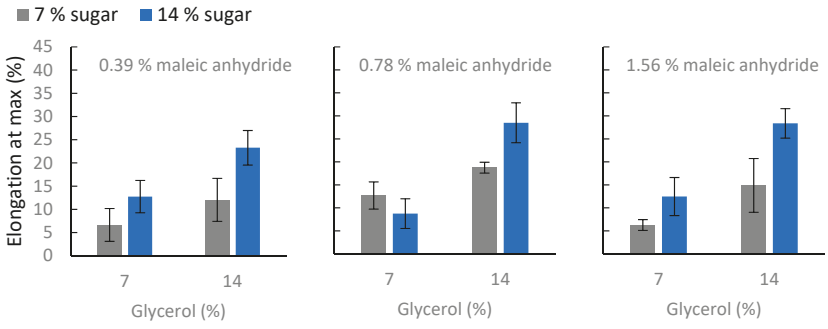

(**b**)

Figure 6. Mean values of tensile strength (**a**) and elongation at max (**b**) of films from the optimization experiment for different maleic anhydride levels. The X-axis represents the concentrations (%) of glycerol (7 and 14); and the grey and blue colors represent 7 and 14 % sugar levels, respectively, used in the films. Individual standard deviations were used to calculate the intervals.

The elongation values are clearly more complicated, as a number of mechanisms may be involved in the plasticization of bioplastics with low molecular weight compounds [27]. Elongation was significantly affected by glycerol (the reverse effect of that for tensile strength, as expected) and sugar (coefficient 5.52, p = 0.000 and coefficient 3.57, p = 0.000, respectively). Their interaction also had a significant positive effect on elongation (coefficient 2.18, p = 0.000). This result, in the observed pattern of high glycerol and high sugar levels, gives the highest elongation for all maleic anhydride levels (Figure 6b). The effect of maleic anhydride concentration on elongation is made up of a main effect and varying interaction effects. The maleic anhydride main effect on elongation and the maleic anhydride*sugar interaction are both significant. When maleic anhydride was used at a low (0.39%) concentration, the effect on elongation was negative (coefficient −1.76, p = 0.013). When maleic anhydride was used at a concentration of 0.78%, the effect was positive (coefficient 1.72, p = 0.015), and when it was used at a concentration of 1.56%, the effect was also positive but smaller than at the middle level (0.78%) (coefficient 0.046, p = 0.946). The maleic anhydride*sugar interaction was most noticeable when 0.78% maleic anhydride was used (coefficient 2.18, p = 0.03). From the general linear model, significant positive effects were found for high (14%) sugar and glycerol levels, and a positive sugar*glycerol interaction for this combination was also found. Furthermore, the modelled values and 95% confidence intervals calculated for the different maleic anhydride concentrations at the highest levels of glycerol and sugar (14%) were 24.16 (21.2, 27.23), 27.24 (24.18, 30.30), and 28.71 (25.65, 31.77) for 0.39%, 0.78% and 1.56% maleic anhydride, respectively.

3.2.4. Water Vapor Permeability and Interaction with Water

In general, all films were flexible and uniform, and among them, four were selected randomly in regards to the experimental design (containing 1.56%, 0.78%, 0.38%, and 1.56% maleic anhydride, 14%, 7%, 14%, and 14% sugar, and 14%, 14, 7%, and 7% glycerol, respectively) for water vapor permeability and water interaction testing. The selected specimens also had the most uniform structure, based on observation.

Low water vapor permeability is often a requirement, e.g., for food packaging materials. The lower the value, the higher is the resistance to water vapor. The water vapor permeability of bio-based films prepared in the optimization experiment, regardless of preparation method, had a mean value of 1.19 ($\pm$ 0.08) $\times$ 10^{-13} kg/m Pa s, which can be compared with the WVP of fungal biomass-reinforced pectin films of 2.35 $\times$ 10^{-13} kg/m Pa s [28] and edible films from alginate-acerola reinforced with

cellulose whiskers of 1.67 ($\pm$ 0.42) $\times$ 10^{-13} kg/m Pa s [29]. Both of these studies reported lower WVP values when the reinforcement load increased. The lowest value was obtained when fungal biomass load was 35 wt % [28] and when cotton cellulose whiskers were used at 15 wt % [29].

These results are, however, higher than those of polysaccharides-based locust bean gum films prepared by solution casting with different plasticizers (polyethylene glycol 200, glycerol, propylene glycol, and sorbitol), which range between 1.2 and 2.6 $\times$ 10^{-14} kg/m Pa s [30], meaning a lower resistance to the passage of water vapor.

All of the specimens used for the test lost more than half of their dry weight, 56.15% $\pm$ 3.37%. In a study performed by Perotto et al. [6], bioplastic films fabricated from vegetable wastes showed approximately 35% solubility after 108 h of immersion in water, however. These results indicate the unfortunate feature of polysaccharides-based bioplastics: their hydrophilic nature.

3.3. Biodegradation

A concentration of 1.56% maleic anhydride was the highest used in the optimization experiment; therefore, it was used for the study of biodegradation. The maximal biodegradation rate of orange waste films made with the sol-gel and sol-gel-ma methods was 63% and 52%, respectively (Table 3). According to a previous study [8], orange waste films produced with the original method showed 90% biodegradability within approximately 15 days. The reason for a lower degradation rate in this study could be that (1) the effect of maleic anhydride present in the structure may make the film more difficult for the microorganisms to degrade (however, sol-gel films did not contain maleic anhydride); (2) the inoculum was not the same as in the previous study [8]. The available microbial community in a digester, used as inoculum, depends on the actual composition of the food waste available, which cannot be guaranteed to be the same. Therefore, in this case, although the same experiment was performed with the same parameters and with the same source of inoculum, it resulted in lower biodegradation rates.

Table 3. Biodegradation rate (%) of bio-based films produced by the sol-gel and sol-gel-ma methods, containing 1.56 *w*/*w* % maleic anhydride.

Days	0	3	6	9	12	15	20	25	30
Sol-gel	0	22	40	59	60	63	59	58	59
Sol-gel-ma	0	22	39	53	51	52	49	49	49

4. Conclusions

The present study recognized the complexity of the different components used in the pectin–cellulose system and that the interpretation of the contrasting behavior can be rather difficult. The enhancement of pectin gelling prior to film casting had a positive effect on the film structure, reducing the number of holes present. The positive effect of maleic anhydride was further shown to eliminate holes in orange waste films via an improved structure with a smooth and uniform surface. For this effect, maleic anhydride was only necessary at very low concentration (0.39%). On the other hand, statistical analyses proved that the tensile strength of the films depended on glycerol content, and elongation was mainly dependent on both glycerol and sugar. The interaction between these was also significant. The highest elongation was reached at the highest levels of sugar and glycerol for both 0.78% and 1.56% maleic anhydride concentrations; therefore, to reach the highest elongation values, the use of maleic anhydride at a concentration of 0.78% was satisfactory. This observation led to the rejection of the hypothesis that maleic anhydride would act as a cross-linking agent; therefore, it was concluded that maleic anhydride in the orange waste films acts as a compatibilizer.

Because orange waste film is biodegradable in anaerobic conditions, it could be suitable as a future material for collecting bag of the organic fraction of municipal solid waste; however, the hydrophilicity of the material needs to be improved. The degradation test performed here contained 1.56% maleic

anhydride, but results of other analyses showed that as little as 0.39% is sufficient for a uniform material. The degradation of orange waste film containing 0.39% maleic anhydride would probably be acceptable in a biogas plant, but to state this, exact measurements would be needed.

Supplementary Materials: The following are available online at http://www.mdpi.com/2073-4360/11/3/392/s1, Figure S1: FE-SEM micrographs of film surfaces with a magnification of 1.00 K × (a) and 5.00 K × (b) and cross-sectional images with a magnification of 1.00 K × (c) and 10.00 K × (d) containing the highest concentrations of glycerol and sugar and the lowest concentration of MA (0.39%); film surfaces with a magnification of 1.00 K × (e) and 5.00 K × (f) and cross-sectional images with a magnification of 1.00 K × (g) and 10.00 K × (h) containing the highest concentrations of glycerol and sugar and the middle level of MA concentration (0.78%); film surfaces with a magnification of 1.00 K × (i) and 5.00 K × (i) and cross-sectional images with a magnification of 1.00 K × (k) and 10.00 K × (l) containing the highest concentrations of glycerol and sugar and the highest concentration of MA (1.56%).

Author Contributions: Conceptualization, B.V. and M.L., methodology and investigation, B.V.; formal analysis, B.V., software, M.L.; writing—original draft preparation, B.V.; writing—review and editing, A.Z., P.R.L., D.Å., M.L., M.J.T.; supervision, A.Z.; funding acquisition, M.J.T.

Funding: This research was funded by the University of Borås.

Acknowledgments: The authors are grateful to Brämhults AB for providing the raw materials and to Ilona Sárvári Horváth for the discussions about biodegradation studies.

Conflicts of Interest: The authors declare no conflict of interest.

References

1. European Bioplastics. *FAQ on Bioplastics—How Can the Environmental Impact of Bioplastics Be Assessed?* European Bioplastics: Berlin, Germany, 2018.
2. Ansari, F.; Skrifvars, M.; Berglund, L. Nanostructured biocomposites based on unsaturated polyester resin and a cellulose nanofiber network. *Compos. Sci. Technol.* **2015**, *117*, 298–306. [CrossRef]
3. Bayer, I.S.; Guzman-Puyol, S.; Heredia-Guerrero, J.A.; Ceseracciu, L.; Pignatelli, F.; Ruffilli, R.; Cingolani, R.; Athanassiou, A. Direct Transformation of Edible Vegetable Waste into Bioplastics. *Macromolecules* **2014**, *47*, 5135–5143. [CrossRef]
4. Choi, I.; Chang, Y.; Shin, S.-H.; Joo, E.; Song, H.; Eom, H.; Han, J. Development of Biopolymer Composite Films Using a Microfluidization Technique for Carboxymethylcellulose and Apple Skin Particles. *Int. J. Mol. Sci.* **2017**, *18*, 1278. [CrossRef] [PubMed]
5. Moro, T.M.A.; Ascheri, J.L.R.; Ortiz, J.A.R.; Carvalho, C.W.P.; Meléndez-Arévalo, A. Bioplastics of Native Starches Reinforced with Passion Fruit Peel. *Food Bioprocess Technol.* **2017**, *10*, 1798–1808. [CrossRef]
6. Perotto, G.; Ceseracciu, L.; Paul, U.C.; Guzam-Puyol, S.; Tran, T.-N.; Bayer, I.S.; Athanassiou, A. Bioplastics from vegetable waste via an eco-friendly water-based process. *Green Chem.* **2018**. [CrossRef]
7. Sultan, N.F.K.; Johari, W.L.W. The Development of Banana Peel/Corn Starch Bioplastic Film: A Preliminary Study. *Bioremediat. Sci. Technol. Res.* **2017**, *5*, 12–17.
8. Bátori, V.; Jabbari, M.; Åkesson, D.; Lennartsson, P.R.; Taherzadeh, M.J.; Zamani, A. Production of Pectin-Cellulose Biofilms: A New Approach for Citrus Waste Recycling. *Int. J. Polym. Sci.* **2017**, *2017*, 9. [CrossRef]
9. Guilbert, S.; Gontard, N.; Cuq, B. Technology and applications of edible protective films. *Packag. Technol. Sci.* **1995**, *8*, 339–346. [CrossRef]
10. Benbettaïeb, N.; Gay, J.-P.; Karbowiak, T.; Debeaufort, F. Tuning the Functional Properties of Polysaccharide–Protein Bio-Based Edible Films by Chemical, Enzymatic, and Physical Cross-Linking. *Compr. Rev. Food Sci. Food Saf.* **2016**, *15*, 739–752. [CrossRef]
11. Hernández-Muñoz, P.; Villalobos, R.; Chiralt, A. Effect of cross-linking using aldehydes on properties of glutenin-rich films. *Food Hydrocolloid.* **2004**, *18*, 403–411. [CrossRef]
12. Yoon, K.J.; Woo, J.H.; Seo, Y.S. Formaldehyde free cross-linking agents based on maleic anhydride copolymers. *Fibers Polym.* **2003**, *4*, 182–187. [CrossRef]
13. Lu, Z.J.; Wu, Q.; McNabb, H.S.J. Chemical coupling in wood fiber and polymer composites: A review of coupling agents and treatments. *Wood Fiber Sci.* **2000**, *32*, 88–104.

14. Yu, T.; Jiang, N.; Li, Y. Study on short ramie fiber/poly(lactic acid) composites compatibilized by maleic anhydride. *Compos. Part A* **2014**, *64*, 139–146. [CrossRef]
15. Zhang, J.F.; Sun, X. Mechanical Properties of Poly(lactic acid)/Starch Composites Compatibilized by Maleic Anhydride. *Biomacromolecules* **2004**, *5*, 1446–1451. [CrossRef] [PubMed]
16. Thakur, B.R.; Singh, R.K.; Handa, A.K.; Rao, M.A. Chemistry and uses of pectin—A review. *Crc. Cr. Rev. Food Sci.* **1997**, *37*, 47–73. [CrossRef] [PubMed]
17. Bátori, V.; Jabbari, M.; Srivastava, R.K.; Åkesson, D.; Lennartsson, P.R.; Zamani, A.; Taherzadeh, M.J. Synthesis and Characterization of Maleic Anhydride-grafted Orange Waste for Potential Use in Biocomposites. *Bioresources* **2018**, *13*. [CrossRef]
18. ASTM. *Standard Test Methods for Water Vapor Transmission of Materials*; American Society for Testing and Materials: Philadelphia, PA, USA, 1996.
19. Dayarian, S.; Zamani, A.; Moheb, A.; Masoomi, M. Physico-Mechanical Properties of Films of Chitosan, Carboxymethyl Chitosan, and Their Blends. *J. Polym. Environ.* **2014**, *22*, 409–416. [CrossRef]
20. Hansen, T.L.; Schmidt, J.E.; Angelidaki, I.; Marca, E.; Jansen, J.L.C.; Mosbæk, H.; Christensen, T.H. Method for determination of methane potentials of solid organic waste. *Waste Manag.* **2004**, *24*, 393–400. [CrossRef] [PubMed]
21. Freudenberg, U.; Zschoche, S.; Simon, F.; Janke, A.; Schmidt, K.; Behrens, S.H.; Auweter, H.; Werner, C. Covalent Immobilization of Cellulose Layers onto Maleic Anhydride Copolymer Thin Films. *Biomacromolecules* **2005**, *6*, 1628–1634. [CrossRef] [PubMed]
22. Almeida, E.A.M.S.; Facchi, S.P.; Martins, A.F.; Nocchi, S.; Schuquel, I.T.A.; Nakamura, C.V.; Rubira, A.F.; Muniz, E.C. Synthesis and characterization of pectin derivative with antitumor property against Caco-2 colon cancer cells. *Carbohyd. Polym.* **2015**, *115*, 139–145. [CrossRef] [PubMed]
23. Lee, S.H.; Shiraishi, N. Plasticization of cellulose diacetate by reaction with maleic anhydride, glycerol, and citrate esters during melt processing. *J. Appl. Polym. Sci.* **2001**, *81*, 243–250. [CrossRef]
24. Vieira, M.G.A.; da Silva, M.A.; dos Santos, L.O.; Beppu, M.M. Natural-based plasticizers and biopolymer films: A review. *Eur. Polym. J.* **2011**, *47*, 254–263. [CrossRef]
25. Hartel, R.W.; Shastry, A.V. Sugar crystallization in food products. *Crc. Cr. Rev. Food Sci.* **1991**, *30*, 49–112. [CrossRef] [PubMed]
26. Mullin, J.W. *Crystallization*; Reed Educational and Professional Publishing Ltd.: London, UK, 2001.
27. Chang, Y.P.; Abd Karim, A.; Seow, C.C. Interactive plasticizing–antiplasticizing effects of water and glycerol on the tensile properties of tapioca starch films. *Food Hydrocolloid.* **2006**. [CrossRef]
28. Gurram, R.; Souza Filho, P.F.; Taherzadeh, M.J.; Zamani, A. A Solvent-Free Approach for Production of Films from Pectin and Fungal Biomass. *J. Polym. Environ.* **2018**. [CrossRef]
29. Azeredo, H.M.C.; Miranda, K.W.E.; Rosa, M.F.; Nascimento, D.M.; de Moura, M.R. Edible films from alginate-acerola puree reinforced with cellulose whiskers. *LWT Food Sci. Technol.* **2012**, *46*, 294–297. [CrossRef]
30. Bozdemir, O.A.; Tutas, M. Plasticizer effect on water vapour permeability properties of locust bean gum-based edible films. *Turk. J. Chem.* **2003**, *27*, 773–782.

polymers

MDPI

Article

Influence of the Lignin Content on the Properties of Poly(Lactic Acid)/lignin-Containing Cellulose Nanofibrils Composite Films

Xuan Wang [1,*], Yuan Jia [1], Zhen Liu [1] and Jiaojiao Miao [2]

[1] College of Chemical Engineering, Xi'an University, Xi'an 710065, China; jiayu_an_happy@126.com (Y.J.); liuzhen_lz@163.com (Z.L.)
[2] School of Life Sciences, Northwestern Polytechnical University, Xi'an 710072, China; mjj.smile@163.com
* Correspondence: wangxuan201441@163.com; Tel.: +86-177-9169-6569

Received: 15 July 2018; Accepted: 10 September 2018; Published: 11 September 2018

Abstract: Poly(lactic acid) (PLA)/lignin-containing cellulose nanofibrils (L-CNFs) composite films with different lignin contents were produced bythe solution casting method. The effect of the lignin content on the mechanical, thermal, and crystallinity properties, and PLA/LCNFs interfacial adhesion wereinvestigated by tensile tests, thermogravimetric analysis, differential scanning calorimetry (DSC), dynamic mechanical analysis, Fourier transform infrared spectroscopy (FTIR), and scanning electron microscopy (SEM). The tensile strength and modulus of the PLA/9-LCNFs (9 wt % lignin LCNFs) composites are 37% and 61% higher than those of pure PLA, respectively. The glass transition temperature (T_g) decreases from 61.2 for pure PLA to 52.6 °C for the PLA/14-LCNFs (14 wt % lignin LCNFs) composite, and the composites have higher thermal stability below 380 °C than pure PLA. The DSC results indicate that the LCNFs, containing different lignin contents, act as a nucleating agent to increase the degree of crystallinity of PLA. The effect of the LCNFs lignin content on the PLA/LCNFs compatibility/adhesion was confirmed by the FTIR, SEM, and T_g results. Increasing the LCNFs lignin content increases the storage modulus of the PLA/LCNFs composites to a maximum for the PLA/9-LCNFs composite. This study shows that the lignin content has a considerable effect on the strength and flexibility of PLA/LCNFs composites.

Keywords: lignin-containing cellulose nanofibrils; poly(lactic acid) and composite films; lignin content; compatibility

1. Introduction

As a renewable bio-based polymer, poly(lactic acid) (PLA) is considered to be a promising alternative to petroleum-based plastics because of its excellent physical properties and thermal process ability [1,2]. However, its disadvantages are inherent brittleness, low degree of crystallization, and relatively poor thermal stability, which limits its wide application in packing, automotive, and biomedical fields [3,4]. Incorporating nanoparticle fillers as a reinforcing agent has been shown to improve the physical, thermal, and crystallization properties of PLA [5]. Cellulose nanocrystals (CNCs) have attracted academic and industrial interest as a reinforcing agent for PLA composites owing to their excellent strength, biodegradability, high specific surface area, and crystallization [6,7]. CNCs are mainly derived from the cellulose of lignin-free wood by acid hydrolysis. The high hydrophilicity of natural CNCs is because of the large amount of hydroxyl groups on their surface, which leads to poor interfacial interactions and compatibility between CNCs and hydrophobic PLA [8,9]. The tendency to form agglomerates upon incorporation into the PLA matrix prevents realization of the full potential of CNCs as a reinforcing phase [10].

Adding compatible materials is an effective approach to improve the dispersion of CNCs in the polymer matrix. Lignin improves the interfacial interaction in CNC/hydrophobic polymer composites because of its higher hydrophobicity than cellulose [11–14]. Furthermore, hydrogen bonds can be hindered by embedding lignin molecules between the cellulose chains, which results in less agglomeration compared with lignin-free CNCs [15]. Lignin is the second most abundant bio-based polymer on earth. It is composed of repeating phenyl propane units with aliphatic and aromatic hydroxyl groups and carboxylic acid groups, which plays a key role in improving the compatibility between CNCs and hydrophobic polymers through hydrogen bonding and van der Waals interactions [16–19]. The presence of lignin makes the dispersion and compatibility of CNCs better, and lignin-containing CNCs are expected to be an excellent reinforcing agent for PLA composites.

Actually, the lignin-containing CNFs have been studied in a lot of papers [20,21]. While, there are few papers recently published on lignin-containing CNFs based PLA biocomposites. Nair et al. [22] learned the improved mechanical, thermal, and barrier properties of polylactic acid bio-composites reinforced with nanocellulose fibrils with high lignin content; the different amount of high lignin nanocellulose fibrils (NCFHL) have made differences to the properties of PLA and the presence of lignin imparted a strong compatibility between the NCFHL and PLA matrix. Winter et al. [23] showed the reduced surface polarity, improved dispersion, and improved reinforcement efficiency of micro-fibrillated cellulose in poly(lactic acid), provided by residual lignin and hemicellulose content, compared to conventional microfibrillated cellulose (MFC) produced from bleached pulp.

In a recent study, we reported that lignin-containing cellulose nano-fibrils (LCNFs) can be dispersed in PLA by the solvent casting technique, and the thermal, mechanical, and crystallization properties of PLA are enhanced [24]. A lignin coating on the CNFs aids in initial dispersion and also prevents re-aggregation of cellulose nano-fibrils (CNFs) in the PLA matrix. The lignin on the CNF surface might make the PLA chains fold onto the LCNFs surface through improved interactions and compatibility, which also may allow for the efficient load transfer between the CNFs and the PLA matrix. The lignin content in the LCNFs is an important factor in studying the dispersion and compatibility improvement efficiency of LCNFs in PLA. In the present study, LCNFs with different lignin contents were dispersed in the PLA matrix by the solvent casting method, and their properties were investigated by Fourier transform infrared (FTIR) spectroscopy, thermogravimetric (TG) analysis, differential scanning calorimetry (DSC), dynamic mechanical analysis (DSC), and scanning electron microscopy (SEM). Compared with the researches of Nair and Winter, which focused on the performance of different amount of high lignin nano-cellulose fibrils and microfibrillated cellulose with residue lignin and hemicellulose in PLA matrix, respectively [22,23], our work aimed at the performance of PLA bio-composites with lignin-containing cellulose nano-fibrils from low lignin to high lignin content. Additionally, the effect of lignin content on the properties of PLA/LCNFs bio-composites has not been studied, so far. The current work demonstrates that the lignin content in the LCNFs plays an important role in improving the mechanical performance and process behavior of PLA composites.

2. Materials and Methods

2.1. Materials

L-PLA was provided by Shanghai Yisheng Industry, Ltd., Shanghai, China. The lignin-containing cellulose pulp boards (lignin contents of ~0, 6, 12, and 18 wt %) were purchased from a pulp and paper mill in Inner Mongolia, Orient Paper Plant Co., Ltd., Ulanchab, China. *N*,*N*-Dimethylacetamide (DMAc) and sulfuric acid (98 wt %) were obtained from Sinopharm Chemical Reagent Co., Ltd., Shanghai, China.

2.2. Preparation of the LCNFs Suspension

The LCNFs were prepared by sulfuric acid hydrolysis and high-pressure homogenization of lignin-containing cellulose pulp boards, according to a previously reported method [24]. In a typical procedure, 5 g of pulp board was mixed with 100 mL of 15 wt % sulfuric acid at a constant speed for 4 h at 85 °C. The suspension was diluted with deionized water and then centrifuged at 4000 rpm for 10 min to concentrate the residue and to remove H^+ and SO_4^{2-} ions. The resultant precipitate was dispersed in DMAc by the solvent exchange method. The suspension was then further dispersed by homogeneous treatment (GEA Niro Soavi homogenizer, Parma, Italy, diameter of 10 mm, and process volume of 100 mL) at a pressure of 100 MPa for 10 cycles. A well-dispersed LCNFs suspension was then obtained. The LCNFs with different lignin contents were prepared by the same procedure, the lignin in the resulting LNCFs were tested and they are referred to as CNFs (0-LCNFs), 5-LCNFs, 9-LCNFs, and 14-LCNFs for lignin contents of ~0, 5, 9, and 14 wt %, respectively. The yield of the LCNFs from the pulp boards with acid hydrolysis and homogenization was about 60%.

2.3. Preparation of PLA/LCNFs Composite Films

The desired amount of 16 wt % DMAc solution of PLA was mixed with the LCNFs suspension by vigorous stirring with a magnetic stirrer (Shanghai, China). The mixture was sonicated and further stirred at 70 °C for 2 h. The suspension was then cast on glass with a scraper and dried at 80 °C for 30 min on an electric heating board. The obtained composite films were heated at 40 °C under a vacuum for 24 h to ensure that the solvent completely evaporated. By varying the added type of LCNFs, composite films with different lignin contents were prepared. The weight percentage of the LCNFs solid, in the PLA composite films, was 3 wt %.

2.4. Characterization

The lignin content was measured by the half-scale kappa test method, which is based on the AS/NZS 1301.201.2002 method, Papro 1.106 kappa number, and TAPPI T236 standard [25]. The morphologies of the LCNFs samples were observed by TEM. A drop of a 0.01 wt % water suspension of LCNFs was deposited on a carbon-coated grid and negatively strained with 2% phosphotungstic acid. The images of the specimens were obtained with a Hitachi H-600 transmission electron microscope (Hitachi Limited, Tokyo, Japan) operated at an acceleration voltage of 80 kV. The initial contact angle (CA) measurements of the LCNFs were performed with three pure liquids with different polarities, namely, water, formamide, and ethylene glycol. The LCNFs–water suspensions were diluted to a 1 wt % solid content in DMAc and sonicated for 1 h at room temperature. Each suspension was poured into an over-pressurized filtration device equipped with a qualitative filter paper with particle retention of 12–15 μm to remove water and retain the fibrils. The CA was determined by a Harke-Space CA instrument (Beijing, China). The surface free energy of the LCNFs was determined by the calculation method provided in the Supporting Information. The FTIR spectra of the PLA/LCNFs composite films were obtained with a FTIR spectrometer (VERTES TOV, Bruker, Germany) over the wavenumber range 400–4000 cm^{-1}. All of the samples were directly detected. The tensile properties of the composites were measured by a mechanical tester (ZB-WL300, Beijing, China) with a cross-head speed of 20 mm/min, a gauge length of 50 mm, and a 300 N load cell. Rectangular specimen strips 100 mm long, 15 mm wide, and 100 μm thick were tested. At least five measurements were performed for each sample and the data were averaged to obtain a mean value. TGA of the LCNFs and PLA/LCNFs composites was performed with a TG analyzer (TGA Q5000 IR, TA instrument, New Castle, DE, USA) under 100 mL/min nitrogen gas flow. Samples of about 6.0 mg were heated from room temperature (25 °C) to 500 °C at a heating rate of 10 °C/min. The cross-sections of the PLA/LCNFs composite films were observed with a Hitachi S-3400 scanning electron microscope (Tokyo, Japan) under an accelerating voltage of 15 kV. All of the samples were tensile broken in order to expose the internal structure (tensile specimens) before the examination, and the entire surface was

sputtered with gold. The thermo mechanical properties of PLA and the PLA/LCNFs composites were determined with a DMA instrument (Q800, TA Instruments, New Castle, DE, USA). The tensile storage modulus and tan delta were determined at a frequency of 1 Hz, a strain rate of 0.05%, and a heating rate of 5 °C over the temperature range 0–100 °C. The test samples were prepared by cutting strips with a width of 10 mm and a length of 40 mm from the films. A TA Instruments Q2000 differential scanning calorimeter (New Castle, DE, USA) was used to record the DSC scans under N_2. The sample (about 6–8 mg) was first heated from 20 to 200 °C at a heating rate of 10 °C/min and then kept at 200 °C for 5 min to remove the thermal history of the material. The sample was then cooled to 20 °C at 5 °C/min and kept at 20 °C for 5 min before heating to 200 °C again at the same heat rate. The degree of crystallinity X_c was calculated with the following equation:

$$X_c[\%] = [(\Delta H_m/\Phi_{PLA})/\Delta H_m^0] \times 100 \quad (1)$$

where ΔH_m (J/g) is the enthalpy of fusion of the polymer composite, ΔH_m^0 is the enthalpy of fusion of a PLA crystal of infinite size (assumed to be 93.6 J/g), and Φ_{PLA} is the fraction of PLA in the composite.

3. Results and Discussion

3.1. Properties of LCNFs with Different Lignin Content

To investigate the stability of the LCNFs suspension, DMAc suspensions with 0.01 g/mL CNFs, 5-LCNFs, 9-LCNFs, and 14-LCNFs were kept in plastic centrifuge tubes for one week at room temperature (Figure 1A). The LCNFs containing lignin were well-dispersed in DMAc and the color of the suspensions was darker with increasing lignin content. The CNFs without lignin showed stratification through the flocculation process. This is because the high hydrophilicity of the CNFs without lignin means that they easily form agglomerates in DMAc. Furthermore, increasing the hydrophobicity enhances the dispersion stability of the LCNFs. The morphologies of the dispersed LCNFs suspensions with different lignin contents were evaluated by TEM analysis (Figure 1B). CNFs and LCNFs with widths of 50 nm and lengths of several hundred nanometers are clearly observed in the images. The research of Rojo showed the AFM images of the lignin containing fibrils appeared to be quite similar than CNF. However, some small, globular shaped particles could be identified in addition to the fibrils in the lignin containing fibrils sample. These particles are predominantly located between the cellulosic nano-fibers, forming complex composite structures with the 30 fibrils [26]. These observations are consistent with the role of lignin in native wood cell wall, where it exists as a stiff phase between cellulosic fibers. Thus, in our work, the LNCFs with different lignin contents show the same morphology by TEM, while the globular shaped particles (lignin) could not be obviously observed. The high lignin could form complex composite structures in LCNFs. Thus, the LCNFs are more likely to form a cross-linked network structure with increasing lignin content. In addition, The thermal stability of the LCNFs was characterized by TGA, and the thermal degradation curves of the CNFs, 5-LCNFs, 9-LCNFs, and 14-LCNFs are shown in Figure 1C. The results reveal that the thermal stability is highly affected by the lignin content. The thermal degradation onset temperature (T_{onset}) of the LCNFs decreases with increasing lignin content (14-LCNFs < 9-LCNFs < 5-LCNFs < CNFs) and the residue weight of the LCNFs also increases. This can be attributed to the high thermal stability of lignin [27,28]. However, the weight loss of lignin is greater than that of cellulose under low temperature (T < 300°C) [29]. When the temperature is above 400 °C, cellulose is almost completely degraded, whereas lignin shows low weight loss. The presence of aromatic char, originating from the lignin, is responsible for the beneficial effect on the thermal stability of the CNFs. The average CAs for three probing liquids were measured on LCNFs with different lignin contents, and these were used in surface energy evaluation, as shown in Figure 1D, and summarized in Table 1. The highest CAs were obtained with water, whereas ethylene glycol gave the lowest CA in most of the cases. For a given liquid, the CA increases with increasing lignin content. Acid–base theory can be used to evaluate the surface energy components using the CA value. Using the acid–base framework to describe the

surface energy has been found to be suitable to explain the properties of the wood surface, and it gives detailed information about the surface chemistry [26,30]. As a characteristic parameter, the surface free energy has a large effect on many interfacial processes, such as absorption, wetting, and adhesion. The literature surface free energy parameters for the test liquids and the surface energy components of the LCNFs, calculated by the acid–base approach, are listed in Table 1. The total surface free energy of the LCNFs with different lignin contents ranges from 47.6 to 53.6 mJ/m^2, which is consistent with the range of 43.1–53.7 mJ/m^2 previously reported by Peng et al. [31]. The total surface energy decreases with increasing lignin content, from 51.7 mJ/m^2 for the 5-LCNFs sample, to 46.7 mJ/m^2 for the 14-LCNFs sample. Therefore, lignin decreases the surface energy of the nano-fibrils, which is expected because of the large percentage of C–C and C–H bonds, and the lower ratio compared with cellulose [32]. The increasing hydrophobicity of the LCNFs, with increasing lignin content, contributes to the compatibility with the hydrophobic polymer matrix [33,34].

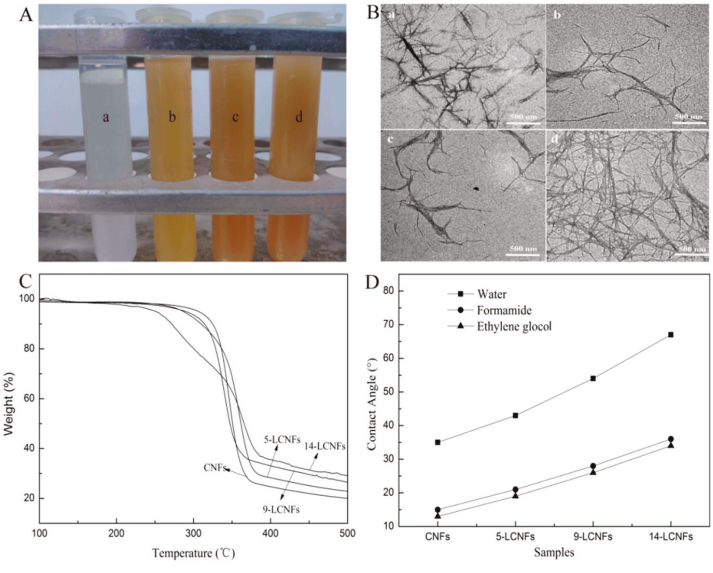

Figure 1. Properties of LCNFs with different lignin contents. (**A**) Dispersion in DMAc solution: (a) CNFs, (b) 5-LCNFs, (c) 9-LCNFs, and (d) 14-LCNFs; (**B**) TEM morphology: (a) CNFs, (b) 5-LCNFs, (c) 9-LCNFs, and (d) 14-LCNFs; (**C**) Thermal stability; (**D**) Contact angles for three different probing liquids.

Table 1. Surface free energies of LCNFs with different lignin contents.

Test Liquids	γ_L	γ_L^p	γ_L^d
Water	72.8	51.0	21.8
Formamide	58.2	18.7	39.5
Ethylene glycol	48.3	19	29.3
Solid Samples	γ_S	γ_S^p	γ_S^d
CNFs	53.6	4	49.6
5-LCNFs	51.7	8.5	43.2
9-LCNFs	50.5	7.8	42.7
14-LCNFs	47.6	3.5	44.1

3.2. PLA/LCNFs Composite Films

3.2.1. FTIR Spectroscopy

The FTIR spectra of PLA and the PLA/CNFs and PLA/LCNFs composites are shown in Figure 2. The PLA/CNFs composite has the same peaks as pure PLA except for a stronger and wider peak around 3343–3432 cm^{-1}, which can be attributed to the –OH groups of the pyranose rings of the CNFs [35]. This is because of the physical blending mode of PLA and CNFs. Furthermore, the C=O stretching vibration peak at 1749 cm^{-1} for PLA shifts in the low wave number direction by two cm^{-1} for the PLA/CNFs composite. This can be ascribed to the weak interaction between PLA and CNFs, which is not sufficient to form strong interface interactions. Comparing the spectra of the PLA/5-LCNFs, PLA/9-LCNFs, and PLA/14-LCNFs composites, the intensity of the –OH stretching vibration peak shows decreases with increasing lignin content. The C=O stretching vibration peak at 1749 cm^{-1} for PLA shifts in the low wave number direction by 10 cm^{-1} for the PLA/5-LCNFs composite (1739 cm^{-1}), 16 cm^{-1} for the PLA/9-LCNFs composite (1733 cm^{-1}), and 17 cm^{-1} for the PLA/14-LCNFs composite (1732 cm^{-1}). The intensity of the C=O peak also increases with increasing lignin content. This suggests that there is a strong interaction between the LCNFs and PLA, which indicates that lignin improves the compatibility between the CNFs and PLA. Furthermore, the interaction increases with increasing lignin content.

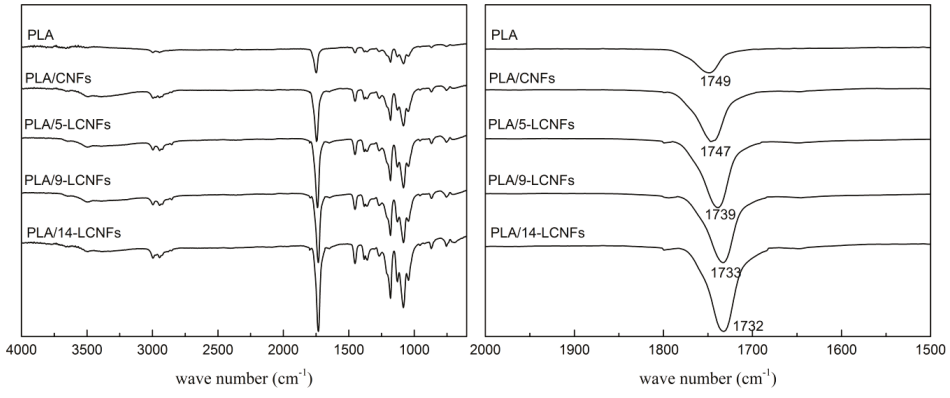

Figure 2. FTIR spectra of PLA, the PLA/CNFs composite, and PLA/LCNFs composites with different lignin contents.

3.2.2. Mechanical Properties

Tensile strength evaluation is important to investigate the fracture flexibility of polymer composites. As shown in Figure 3a, the tensile strength and modulus of the PLA/LCNFs composite tend to increase with increasing lignin content for low lignin content (0 to 9 wt %), but they slightly decrease for high lignin content (14 wt %). The tensile strength and modulus decrease from 35.7 MPa and 1.8 GPa, for PLA, to 31.6 MPa and 1.5 GPa for the PLA/CNFs composite, respectively. For the PLA/LCNFs composites, there are statistically significant changes in the tensile strength and modulus for lignin contents of five and nine wt %, compared with the PLA/CNFs composite. Compared with pure PLA, the PLA/5-LCNFs and PLA/9-LCNFs composites show statistically significant improvements in the tensile strength of 28% (45.7 MPa) and 37% (48.9 MPa), and tensile modulus of 44.4% (2.6 GPa) and 61.1% (2.9 GPa). These observations can be attributed to the better compatibility of the LCNFs than the CNFs with PLA. Moreover, the strong hydrogen-bonding interaction between lignin and cellulose, as well as the van der Waals forces and polar interaction of lignin with PLA, makes it possible for good adhesion between the LCNFs and PLA. However, the tensile strength and modulus of the PLA/14-LCNFs composite (5.5% and 17.2%, respectively)

is slightly lower than those of the PLA/9-LCNFs composite. This is probably because, even though the interface interaction between the LCNFs and PLA improves with increasing lignin content in the LCNFs, the mechanical properties of the LCNFs are also affected by the lignin content.

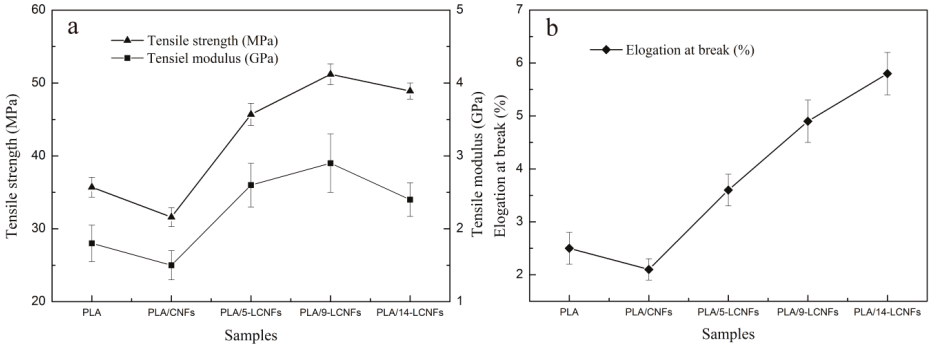

Figure 3. Mechanical properties of PLA and the PLA/LCNFs composites determined by tensile testing. (**a**) Tensile strength and modulus and (**b**) elongation at break.

The elongation at break values of the PLA/LCNFs composites are shown in Figure 3b. The results suggest that the flexibility of PLA increases by blending with LCNFs. The increasing flexibility of the PLA/LCNFs composites with increasing lignin content results in an increase in the elongation at break percentage.

3.2.3. Morphological Analysis of Fracture Surface

The effect of the lignin content on the miscibility between the LCNFs and PLA can be investigated by morphology analysis. The solubility parameter can be used to estimate the miscibility of polymer blends. The solubility's of PLA and lignin are 20.2 and 19.02 $MPa^{1/2}$, respectively [36], which indicates that there should be good miscibility between PLA and lignin. When LCNFs are blended with PLA, lignin can act as a compatibilizer to form a uniform blend system.

To better understand the results obtained by the tensile tests, the fractured samples were observed by SEM. Figure 4a–e show the representative SEM images of the cross-sectional regions of PLA and the PLA/CNF, PLA/5-LCNFs, PLA/9-LCNFs, and PLA/14-LCNFs composites, respectively. PLA has relatively smooth fractures, which indicates that PLA is prone to brittle fracture [37]. After CNFs are added to PLA, the fracture surface of the PLA/CNF composite becomes irregular because of plastic deformation. The brittle rupture of PLA changes to ductile rupture with addition of CNFs, whereas the poor dispersion state of CNFs in the PLA matrix results in interfacial compatibility and decreases the mechanical properties of the PLA/CNF composite, compared with pure PLA. When LCNFs with different lignin contents are added to the PLA matrix, the fracture surfaces of the PLA/LCNFs composites (Figure 4c–e) show a different microstructure: At lower lignin content (5 wt%), samples showed roughness and litter wire drawing phenomenon in Figure 4c, while increasing the lignin content (14 wt%), the samples showed obvious tough character and the wire drawing phenomenon [38]. The results indicate that increasing the lignin content of the LCNFs promotes ductile rupture of PLA. From the SEM results, we can conclude that lignin and the lignin content plays important roles in improving the performance of PLA.

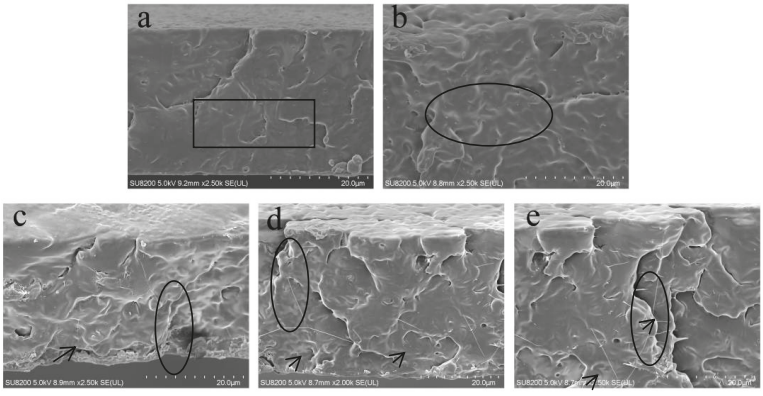

Figure 4. SEM images of the fractured surfaces after tensile testing: (**a**) PLA and the (**b**) PLA/CNFs, (**c**) PLA/5-LCNFs, (**d**) PLA/9-LCNFs, and (**e**) PLA/14-LCNFs composites.

3.2.4. Thermal Properties

In general, the thermal stability of polymers can be improved by blending with nano-fillers. The dispersion state of the nano-filler in the polymer matrix and the interaction between them significantly affect the thermal stability. The TG and derivative TG (DTG) curves of PLA and the PLA/LCNFs composites are shown in Figure 5, and the degradation parameters are summarized in Table 2. The onset temperature (10% weight loss, $T_{10\%}$) of thermal degradation decreases after blending with CNFs, while it increases by blending with LCNFs. This can be attributed to formation of a cross-linked structure, which reduces the chain mobility and inhibits chain unzipping during propagation of the degradation process [39]. As shown in Figure 5, the lignin content has a clear effect on the T_{max} (The temperature of the maximum weight loss) value of the PLA/LCNFs composites. The T_{max} value of the PLA/9-LCNFs composite is 5 °C higher than that of PLA. The lignin content affects the T_{max} value, and the thermal stability of the PLA/LCNFs composite improves with increasing lignin content in the considered temperature region. The thermal stability of the LCNFs decreases with increasing lignin content, so the PLA/14-LCNFs composite has lower thermal stability than the PLA/9-LCNFs composite. It can be concluded that lignin has a positive effect on the miscibility between PLA and the LCNFs, and increasing the lignin content also affects the thermal resistance of the LCNFs. In addition, the residue mass of the PLA/LCNFs composite in the thermal degradation process increases with increasing lignin content.

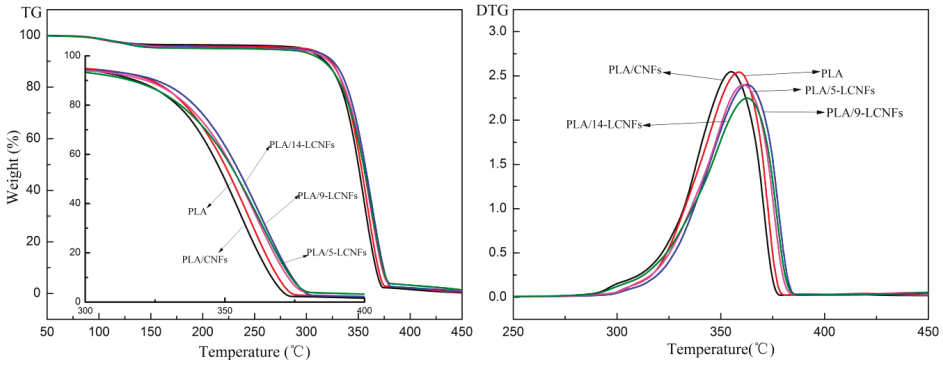

Figure 5. TG and DTG curves of PLA and the PLA/LCNFs composites.

Table 2. Thermal degradation data of PLA/LCNFs composites with different lignin contents.

Sample	$T_{10\%}$ (°C)	$T_{50\%}$ (°C)	T_{max} (°C)
PLA	318.1	352.4	358.7
PLA/CNFs	316.3	349.9	354.9
PLA/5-LCNFs	321.8	354.8	360.8
PLA/9-LCNFs	325.4	356.4	363.1
PLA/14-LCNFs	323.7	354.8	362.6

The glass transition is a complex phenomenon that depends on a number of factors, such as the chain flexibility, the molecular weight, branching, cross-linking, intermolecular interactions, and steric effects [40]. The thermal behavior of PLA and the PLA/CNFs, PLA/5-LCNFs, PLA/9-LCNFs, and PLA/14-LCNFs composites were determined by DSC measurements (Figure 6). The thermal properties of these materials are given in Table 3. The glass transition temperature (T_g) of pure PLA is 61.2 °C, and the PLA/CNFs composite has a slightly lower T_g of 60.8 °C. This can be ascribed to the fact that the CNFs and PLA do not form strong interfacial interactions. However, the PLA/LCNFs composites have considerably lower T_g values than PLA. The T_g value of the PLA/14-LCNFs composite is 52.6 °C. This probably indicates that a relatively small amount of LCNFs is sufficient to change the PLA chain mobility within the glass transition region. This observation shows that there are strong interfacial forces between the LCNFs and PLA, and the lignin content has a positive effect on compatibility.

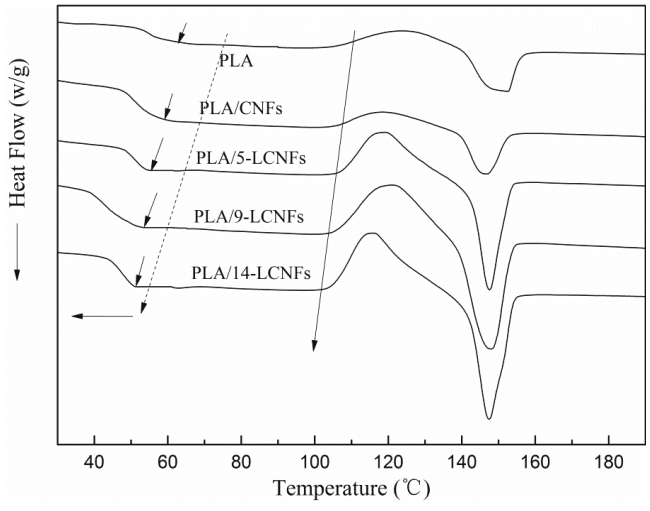

Figure 6. DSC curves of PLA and the PLA/LCNFs composites.

Table 3. DSC data of PLA and PLA/LCNFs composites with different lignin contents.

Samples	T_g (°C)	T_c (°C)	T_m (°C)	ΔH_m (J/g)	X_c (%)
PLA	61.2	124	150.1	11.7	12.1
PLA/CNFs	60.8	119	147.6	13.8	14.7
PLA/5-LCNFs	55.3	118	148.2	16.8	17.9
PLA/9-LCNFs	54.2	120	148.5	17.5	18.7
PLA/14-LCNFs	52.6	115	148.9	16.4	17.5

Blending with CNFs and LCNFs decreases the crystallization temperature (T_c) of PLA, and T_c decreases with increasing lignin content, as shown in Table 3. The lower T_c in heat flow indicates that

the crystallization rate of PLA markedly increases. The results show that the CNFs in the LCNFs can be used as a nucleating agent in PLA composites.

The melting temperature (T_m) of all of the PLA composites is about 148 °C (Table 3). This indicates that the lignin content plays an important role in increasing the melting enthalpy (ΔH_m) of the LCNFs-reinforced PLA matrix (Table 3). The degree of crystallinity increase from 12.1% for pure PLA to 14.7% for the PLA/CNFs composite, 17.9% for the PLA/5-LCNFs composite, 18.7% for the PLA/9-LCNFs composite, and 17.5% for the PLA/14-LCNFs composite. There is a significant increase in the degree of crystallinity of PLA when high lignin content LCNFs are used, which is because the nucleating agent concentration in the LCNFs is low for high lignin content (14-LCNFs).

3.2.5. Dynamic Mechanical Properties

DMA is a useful technique to investigate the relationship between the structure and viscoelastic behavior of polymers and polymer-nano-filler composites. The storage modulus (E') indicates the tendency and ability of energy storage in materials, and it is also directly related to the Young's modulus. Figure 7a shows the plots of E' versus temperature for pure PLA and the PLA/LCNFs composites with various lignin contents. When LCNFs are added, E' is significantly higher in the whole temperature range studied. For example, E' at 20 °C increases from 1800 MPa for pure PLA to 3650 MPa for the PLA/9-LCNFs composite. The increase in E' can be explained by the reinforcing effect provided by lignin of the LCNFs on the PLA matrix. The thickness of the interface is affected by the lignin content and it affects the transition of stress, so the PLA/14-LCNFs composite has a lower E' than the PLA/9-LCNFs composite, which is consistent with the mechanical strength results.

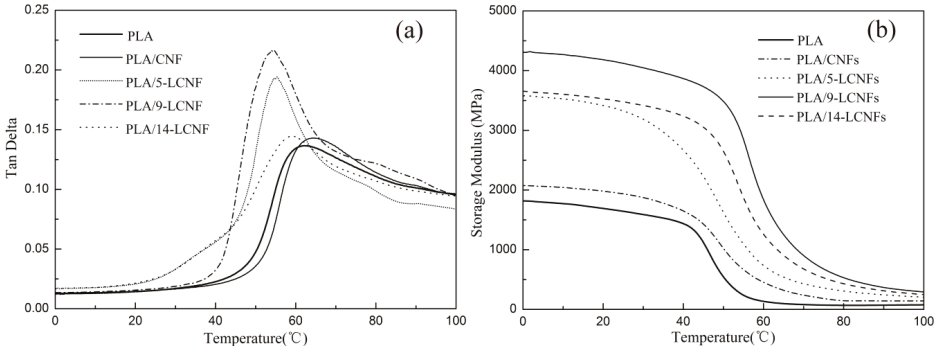

Figure 7. (**a**) Storage modulus and (**b**) tan Δ versus temperature for PLA and the PLA/LCNFs composites.

The effect of LCNFs with different lignin contents on the damping behavior of PLA was investigated by plotting tan Δ against temperature (Figure 7b). The tan Δ peak shifts to lower temperature with increasing lignin content in the LCNFs. The tan Δ peaks for the PLA/CNFs composite, PLA, and the PLA/5-LCNFs, PLA/9-LCNFs, and PLA/14-LCNFs composites are at 61, 60, 57, 55, and 54 °C, respectively. Moreover, the intensities of the tan Δ peaks for the PLA/LCNFs composites are considerably higher than the peak for pure PLA. This can be attributed to the liberation effect of the LCNFs enhancing the chain mobility of the amorphous region for the PLA/LCNFs composites with higher lignin content.

3.2.6. Mechanism Analysis of the Interfacial Interaction

The mechanism of the interfacial interaction between the LCNFs and PLA is shown in Figure 8. Lignin can be used as an additive to improve the compatibility between CNFs and PLA. Considering the LCNFs as an ensemble, lignin combines well with cellulose through hydrogen bonds and

dipole–dipole interactions, and van der Waals interactions occur among the non-polar groups of lignin and PLA. Moreover, the polar and polarizable groups of lignin, such as hydroxyl and phenyl groups, form hydrogen bonds or dispersion interactions with the ester groups of the PLA matrix, which makes it possible for lignin to be in a well-dispersed state in the PLA matrix. As a result, the interfacial compatibility between LCNFs and PLA is enhanced.

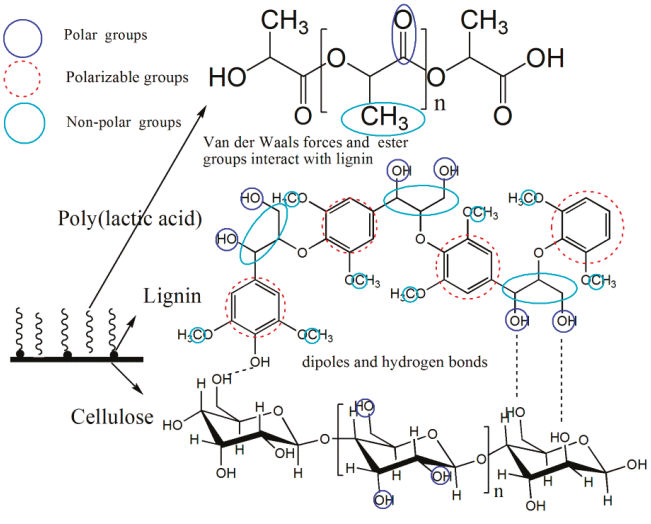

Figure 8. Reaction mechanism of PLA and LCNFs.

Figure 9 shows the mechanism of the effect of the lignin content on the compatibility between PLA and the LCNFs. It can be concluded that increasing the lignin content has a positive effect on the compatibility, and the interfacial layer thickness increases with increasing lignin content, which results in increased flexibility of the PLA/LCNFs composite.

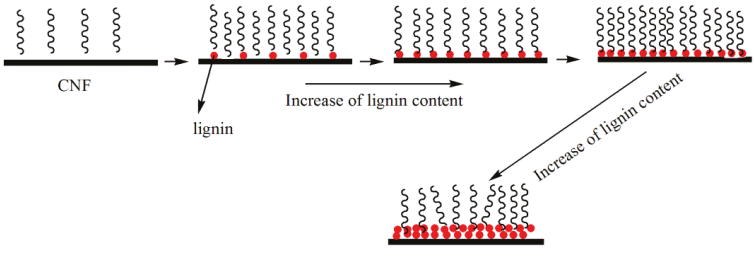

Figure 9. Effect of the lignin content on the compatibility between PLA and the LCNFs.

4. Conclusions

Addition of LCNFs with different lignin contents to PLA changes the mechanical properties, thermo-mechanical properties, thermal behavior, and morphology. The tensile strength and modulus are the highest (48.9 MPa and 2.9 GPa) when the lignin content is 9 wt %. The elongation at break increases with increasing lignin content, and the thermo-mechanical properties show the same trend as the tensile strength. FTIR spectroscopy shows that there is a clear interaction between the LCNFs and the carbonyl groups of PLA. The T_g decreases from 61.2 °C for pure PLA, to 52.6 °C for the PLA/14-LCNFs composite, indicating increased flexibility with LCNFs addition with increasing lignin content. The crystallization temperature of the PLA/LCNFs composite decreases with increasing lignin

content in the LCNFs, indicating that the crystallization efficiency and degree of crystallinity improve. The thermal stabilities of the PLA/LCNFs composites are higher than that of PLA, which was below 380 °C, and the thermal stability increases with increasing lignin content in the LCNFs. The PLA/9-LCNFs composite has the highest T_{max} value (4.4 °C higher than that of pure PLA). The cross-sectional morphologies of PLA and the PLA/LFCNFs composites show the strengthening and toughening effect of LCNFs, and the lignin content has a considerable effect on the flexibility of the PLA/LCNFs composite.

Supplementary Materials: The supplementary materials are available online at http://www.mdpi.com/2073-4360/10/9/1013/s1.

Author Contributions: X.W., Y.J., Z.L. and J.M. conceived and designed the experiments; X.W., Y.J. performed the experiments and initially analyzed the data; X.W. drafted the manuscript; all the authors contributed in the writing process and approved the final version of the paper.

Funding: This research was funded by the Project of Science and Technology of Xi'an for financial support (2016CXWL01 and 2017CGWL26).

Acknowledgments: We thank Liwen Bianji, Edanz Group China (www.liwenbianji.cn/ac), for editing the English text of a draft of this manuscript.

Conflicts of Interest: The authors declare no conflict of interest.

References

1. Pang, X.; Zhuang, X.; Tang, Z.; Chen, X. Polylactic acid (PLA): Research, development and industrialization. *Biotechnol. J.* **2010**, *5*, 1125–1136. [CrossRef] [PubMed]
2. Hamad, K.; Kaseem, M.; Yang, H.; Deri, F.; Ko, Y. Properties and medical applications of polylactic acid: A review. *Express Polym. Lett.* **2015**, *9*, 435–455. [CrossRef]
3. Drumright, R.E.; Gruber, P.R.; Henton, D.E. Polylactic acid technology. *Adv. Mater.* **2000**, *12*, 1841–1846. [CrossRef]
4. Jonoobi, M.; Harun, J.; Mathew, A.P.; Oksman, K. Mechanical properties of cellulose nanofiber (CNF) reinforced polylactic acid (PLA) prepared by twin screw extrusion. *Compos. Sci. Technol.* **2010**, *70*, 1742–1747. [CrossRef]
5. Mohanty, A.K.; Misra, M.; Drzal, L. Sustainable bio-composites from renewable resources: Opportunities and challenges in the green materials world. *J. Polym. Environ.* **2002**, *10*, 19–26. [CrossRef]
6. Moon, R.J.; Martini, A.; Nairn, J.; Simonsen, J.; Youngblood, J. Cellulose nanomaterials review: Structure, properties and nanocomposites. *Chem. Soc. Rev.* **2011**, *40*, 3941–3994. [CrossRef] [PubMed]
7. Khalil, H.A.; Bhat, A.; Yusra, A.I. Green composites from sustainable cellulose nanofibrils: A review. *Carbohyd. Polym.* **2012**, *87*, 963–979. [CrossRef]
8. Wei, L.; McDonald, A.G. A review on grafting of biofibers for biocomposites. *Materials* **2016**, *9*, 303. [CrossRef] [PubMed]
9. Pracella, M.; Haque, M.M.-U.; Puglia, D. Morphology and properties tuning of PLA/cellulose nanocrystals bio-nanocomposites by means of reactive functionalization and blending with PVAc. *Polymer* **2014**, *55*, 3720–3728. [CrossRef]
10. Gupta, A.; Simmons, W.; Schueneman, G.T.; Hylton, D.; Mintz, E.A. Rheological and thermo-mechanical properties of poly(lactic acid)/lignin-coated cellulose nanocrystal composites. *ACS Sustain. Chem. Eng.* **2017**, *5*, 1711–1720. [CrossRef]
11. Thakur, V.K.; Thakur, M.K.; Raghavan, P.; Kessler, M.R. Progress in green polymer composites from lignin for multifunctional applications: A review. *ACS Sustain. Chem. Eng.* **2014**, *2*, 1072–1092. [CrossRef]
12. Ago, M.; Jakes, J.E.; Rojas, O.J. Thermomechanical properties of lignin-based electrospun nanofibers and films reinforced with cellulose nanocrystals: A dynamic mechanical and nanoindentation study. *ACS Appl. Mater. Interfaces* **2013**, *5*, 11768–11776. [CrossRef] [PubMed]
13. Chung, Y.-L.; Olsson, J.V.; Li, R.J.; Frank, C.W.; Waymouth, R.M.; Billington, S.L.; Sattely, E.S. A renewable lignin–lactide copolymer and application in biobased composites. *ACS Sustain. Chem. Eng.* **2013**, *1*, 1231–1238. [CrossRef]

14. Hambardzumyan, A.; Foulon, L.; Chabbert, B.; Aguié-Béghin, V.R. Natural organic UV-absorbent coatings based on cellulose and lignin: Designed effects on spectroscopic properties. *Biomacromolecules* **2012**, *13*, 4081–4088. [CrossRef] [PubMed]
15. Wei, L.; Agarwal, U.P.; Matuana, L.; Sabo, R.C.; Stark, N.M. Performance of high lignin content cellulose nanocrystals in poly(lactic acid). *Polymer* **2018**, *135*, 305–313. [CrossRef]
16. Gupta, A.; Simmons, W.; Schueneman, G.T.; Mintz, E.A. Lignin-coated cellulose nanocrystals as promising nucleating agent for poly(lactic acid). *J. Therm. Anal. Calorim.* **2016**, *126*, 1243–1251. [CrossRef]
17. Graupner, N. Application of lignin as natural adhesion promoter in cotton fibre-reinforced poly(lactic acid)(PLA) composites. *J. Mater. Sci.* **2008**, *43*, 5222–5229. [CrossRef]
18. Dai, L.; Liu, R.; Hu, L.-Q.; Zou, Z.-F.; Si, C.-L. Lignin nanoparticle as a novel green carrier for the efficient delivery of resveratrol. *ACS Sustain. Chem. Eng.* **2017**, *5*, 8241–8249. [CrossRef]
19. Nair, S.S.; Kuo, P.Y.; Chen, H.; Yan, N. Investigating the effect of lignin on the mechanical, thermal, and barrier properties of cellulose nanofibril reinforced epoxy composite. *Ind. Crop Prod.* **2017**, *100*, 208–217. [CrossRef]
20. Bian, H.; Chen, L.; Dai, H.; Zhu, J.-Y. Integrated production of lignin containing cellulose nanocrystals (LCNC) and nanofibrils (LCNF) using an easily recyclable di-carboxylic acid. *Carbohyd. Polym.* **2017**, *167*, 167–176. [CrossRef] [PubMed]
21. Bian, H.; Chen, L.; Dai, H.; Zhu, J.-Y. Effect of fiber drying on properties of lignin containing cellulose nanocrystals and nanofibrils produced through maleic acid hydrolysis. *Cellulose* **2017**, *24*, 4205–4216. [CrossRef]
22. Sudhakaran Nair, S.; Chen, H.; Peng, Y.; Huang, Y.; Yan, N. Polylactic acid biocomposites reinforced with nanocellulose fibrils with high lignin content for improved mechanical, thermal and barrier properties. *ACS Sustain. Chem. Eng.* **2018**, *6*, 10058–10068. [CrossRef]
23. Winter, A.; Andorfer, L.; Herzele, S.; Zimmermann, T.; Saake, B.; Edler, M.; Gindl-Altmutter, W. Reduced polarity and improved dispersion of microfibrillated cellulose in poly(lactic-acid) provided by residual lignin and hemicellulose. *J. Mater. Sci.* **2017**, *52*, 60–72. [CrossRef]
24. Wang, X.; Sun, H.; Bai, H.; Zhang, L.-P. Thermal, mechanical, and degradation properties of nanocomposites prepared using lignin-cellulose nanofibers and poly(lactic acid). *Bioresources* **2014**, *9*, 3211–3224. [CrossRef]
25. Beg, M.D.H.; Pickering, K.L. Accelerated weathering of unbleached and bleached kraft wood fibre reinforced polypropylene composites. *Polym. Degrad. Stab.* **2008**, *93*, 1939–1946. [CrossRef]
26. Rojo, E.; Peresin, M.S.; Sampson, W.W.; Hoeger, I.C.; Vartiainen, J.; Laine, J.; Rojas, O.J. Comprehensive elucidation of the effect of residual lignin on the physical, barrier, mechanical and surface properties of nanocellulose films. *Green Chem.* **2015**, *17*, 1853–1866. [CrossRef]
27. Nair, S.S.; Yan, N. Effect of high residual lignin on the thermal stability of nanofibrils and its enhanced mechanical performance in aqueous environments. *Cellulose* **2015**, *22*, 3137–3150. [CrossRef]
28. Bian, H.; Gao, Y.; Wang, R.; Liu, Z.; Wu, W.; Dai, H. Contribution of lignin to the surface structure and physical performance of cellulose nanofibrils film. *Cellulose* **2018**, *25*, 1309–1318. [CrossRef]
29. Liu, Q.; Wang, S.; Zheng, Y.; Luo, Z.; Cen, K. Mechanism study of wood lignin pyrolysis by using TG–FTIR analysis. *J. Anal. Appl. Pyrolysis* **2008**, *82*, 170–177. [CrossRef]
30. Gindl, M.; Sinn, G.; Gindl, W.; Reiterer, A.; Tschegg, S. A comparison of different methods to calculate the surface free energy of wood using contact angle measurements. *Colloids Surf. A* **2001**, *181*, 279–287. [CrossRef]
31. Peng, Y.; Gardner, D.J.; Han, Y.; Cai, Z.; Tshabalala, M.A. Influence of drying method on the surface energy of cellulose nanofibrils determined by inverse gas chromatography. *J. Colloid Interface Sci.* **2013**, *405*, 85–95. [CrossRef] [PubMed]
32. Lin, N.; Dufresne, A. Supramolecular hydrogels from in situ host–guest inclusion between chemically modified cellulose nanocrystals and cyclodextrin. *Biomacromolecules* **2013**, *14*, 871–880. [CrossRef] [PubMed]
33. Shen, W.; Parker, I.H.; Sheng, Y.J. The effects of surface extractives and lignin on the surface energy of eucalypt kraft pulp fibres. *J. Adhes. Sci. Technol.* **1998**, *12*, 161–174. [CrossRef]
34. Laine, J.; Stenius, P.; Carlsson, G.; Ström, G. Surface characterization of unbleached kraft pulps by means of ESCA. *Cellulose* **1994**, *1*, 145–160. [CrossRef]

35. Meng, X.; Bocharova, V.; Tekinalp, H.; Cheng, S.; Kisliuk, A.; Sokolov, A.P.; Kunc, V.; Peter, W.H.; Ozcan, S. Toughening of nanocelluose/PLA composites via bio-epoxy interaction: Mechanistic study. *Mater. Des.* **2018**, *139*, 188–197. [CrossRef]
36. Karst, D.; Yang, Y. Using the solubility parameter to explain disperse dye sorption on polylactide. *J. Appl. Polym. Sci.* **2005**, *96*, 416–422. [CrossRef]
37. Yang, W.; Dominici, F.; Fortunati, E.; Kenny, J.M.; Puglia, D. Melt free radical grafting of glycidyl methacrylate (GMA) onto fully biodegradable poly(lactic) acid films: Effect of cellulose nanocrystals and a masterbatch process. *RSC Adv.* **2015**, *5*, 32350–32357. [CrossRef]
38. Lizundia, E.; Fortunati, E.; Dominici, F.; Vilas, J.L.; León, L.M.; Armentano, I.; Kenny, J.M. PLLA-grafted cellulose nanocrystals: Role of the CNC content and grafting on the PLA bionanocomposite film properties. *Carbohyd. Polym.* **2016**, *142*, 105–113. [CrossRef] [PubMed]
39. Ahmad, E.; Luyt, A. Morphology, thermal, and dynamic mechanical properties of poly(lactic acid)/sisal whisker nanocomposites. *Polym. Compos.* **2012**, *33*, 1025–1032. [CrossRef]
40. Krishnamachari, P.; Zhang, J.; Lou, J.; Yan, J.; Uitenham, L. Biodegradable poly(lactic acid)/clay nanocomposites by melt intercalation: A study of morphological, thermal, and mechanical properties. *Int. J. Polym. Anal. Charact.* **2009**, *14*, 336–350. [CrossRef]

polymers

MDPI

Article

Poly(lactic acid)/Cellulose Films Produced from Composite Spheres Prepared by Emulsion-Solvent Evaporation Method

Sónia Sousa [1,*], Ana Costa [1], Abílio Silva [2] and Rogério Simões [1]

[1] FibEnTech—Fiber Materials and Environmental Technologies Research Unit, Universidade da Beira Interior, Rua Marquês d'Ávila e Bolama, 6201-001 Covilhã, Portugal; anacosta@ubi.pt (A.C.); rmss@ubi.pt (R.S.)

[2] C-MAST—Centre for Mechanical and Aerospace Science and Technology, Universidade da Beira Interior, Rua Marquês d'Ávila e Bolama, 6201-001 Covilhã, Portugal; abilio@ubi.pt

* Correspondence: scls@ubi.pt; Tel.: +351-275-241-346

Received: 28 November 2018; Accepted: 3 January 2019; Published: 4 January 2019

Abstract: The compound of poly(lactic acid) (PLA) and cellulose was made by the emulsion-solvent evaporation technique in order to obtain spheres which are then compression molded to produce a biocomposite film. The effect of the dispersant (poly(vinyl alcohol)—PVA)/PLA ratio on the spheres yield was studied. Moreover, to evaluate the effect of cellulose particle size and surface chemistry on the process yield, unbleached eucalypt kraft pulp and microcrystalline cellulose (MCC), both unmodified and physically or chemically modified were used. PLA/cellulose spheres were characterized regarding its physical properties. It was found that the spheres yield is essentially determined by the PVA/PLA ratio and the percentage of cellulose incorporation is greatly affected by the surface chemistry of cellulose. Regarding the films, DSC runs showed a significant effect of the cellulose type incorporated into PLA matrix on the cold crystallization temperature and on the degree of crystallinity of the biocomposite films. The measurement of tensile properties of the biocomposite films revealed that the strength, elongation at break and toughness (tensile energy absorption at break) of the films incorporating unmodified and chemically modified MCC were substantially improved.

Keywords: poly(lactic acid); pulp fibers; biocomposite; emulsion-solvent evaporation method; films; mechanical properties

1. Introduction

In the packaging industry, plastic materials are customizable, easy to process and cheap. The great majority of plastics materials are made up from non-renewable petroleum-based fossil fuels. Due to limited nature of fossil fuels and the growing environmental concern on their use, there is a need for finding more environmentally friendly materials. Currently, the development of biodegradable polymer composites combining biodegradable matrices and natural fibers as reinforcement is of great importance [1]. Starch, poly(caprolactone) (PCL), poly(lactic acid), poly(butylene succinate) (PBS) and poly(hydroxyalkanoates) (PHAs) are most commonly used as matrix phase biopolymers [1–6]. Among the polymer matrices, PLA is one of the most used and at present PLA-based materials find applications in the biomedical, textile and packaging areas [5,7]. PLA is a high molecular weight polyester usually produced by ring-opening polymerization of lactide. The monomer, lactic acid, can be derived from corn, potato, cane, beet sugar or cheese residues by fermentation [1,3,7]. The commercial PLA, however, is a brittle material and various reinforcing materials such as natural fibers can be used to improve its toughness [8,9]. In addition, natural fibers as reinforcement materials present other advantages as their low density, high specific strength and modulus, nonabrasive

character and low cost [3]. Various forms of cellulose have been explored as reinforcements into PLA composites. These include fibers from jute, kenaf, henequen, flax, cotton, bamboo [10–16], wood pulp [3,4,17], microcrystalline cellulose (MCC) [9,18,19] and, micro and nanocellulose in different forms and from different origins [8,20–28]. Due to its hydrophilic nature, cellulose is not easily uniformly dispersed into hydrophobic PLA matrix which leads to poor interfacial adhesion, thus reducing the mechanical properties of the composites [16,18,22,23]. To overcome this limitation, many physical or chemical treatments have been applied for cellulose modification. The effect of plasma treatment on interfacial interaction of lyocell fibers in a poly(lactic acid) matrix was investigated [29]. According to Cho et al. [10], natural fibers treated with tap water by static soaking and dynamic ultrasonication, followed by drying leads to PLA composites with improved interfacial shear strength, flexural and dynamic mechanical properties. Treatment of cellulosic fibers with alkali or enzymes were also tested [12,13]. Incorporation of casein protein or bioadimide in cellulose/PLA composites was found to improve the dispersion and fiber/matrix adhesion [15,30]. In addition, Magniez et al. [16] demonstrated that the adsorption of amphiphilic poly(ethylene glycol)-b-poly(L-lactide) block copolymers increases the interfacial affinity in a jute and polylactide biocomposite. Methods such as acetylation, silylation or grafting with other hydrophobic monomers have been used for cellulose surface modification [6,11,20,31]. The preparation of microcrystalline cellulose-graft-poly(lactic acid) via melt copolycondensation was carried out by Hua et al. [18]. These authors observed that the microcrystalline cellulose grafting increases the compatibility with PLA matrix thus improving the dispersion of the cellulose. Graupner [12] and Graupner et al. [32] found that the use of lignin in PLA/cellulose fiber composites improved the adhesion between fiber and matrix. Recently, nanofibrillated cellulose with high lignin content was used to enhance the PLA/cellulose compatibility in the composites [33,34].

In addition to cellulose chemical properties and its dispersion in the PLA matrix, the biocomposite properties are also affected by the processing conditions. Melt-compounding is traditionally used for many types of biocomposites as it is fast and easier to scale-up to industrial scale [35]. However, as PLA is sensitive to temperature, shearing and hydrolysis, some precautions are required during the processing step to avoid its degradation [7]. Solvent casting is a simple and widely used technique to prepare cellulose nanocomposites using different matrices, but it is mostly applied at laboratory scale [7,25,30,35]. This technique can lead to differences in the properties of the composites compared to another processing methods [7,36]. In another approach, a papermaking based process was used, which enables the production of sheets made from aqueous suspension containing a mixture of cellulose fibers or microfibrillated cellulose (MFC) and PLA fibers [8,37]. This process gives good dispersions even at high MFC contents (up to 90 wt %) and the composites obtained by compression molding of the stacked sheets presented an increase of tensile properties with the MFC content [8]. The use of PLA microparticles is an alternative to PLA fibers resulting in nanocomposites with good cellulose nanofibers dispersions [20,22]. The production of PLA microparticles was carried out by solvent evaporation technique which is widely used in pharmaceutical industry for drug microencapsulation [22,38,39]. In a typical procedure, a volatile organic phase containing the dissolved polymers is emulsified in an aqueous phase at continuous constant stirring rate. Then, the volatile solvent is gradually evaporated to form the spherical polymer particles [39]. This technique was also used by Lee and Ji [40] to encapsulate hydrophilic entities such as cellulose nanowhiskers and microfibrils within polymeric nano/microspheres. However, to the best of our knowledge, until now the solvent evaporation technique was never used to produce PLA spheres incorporating pulp fibers, which have a much higher size. In another study, Lee et al. [26] developed a method based on thermally induced phase separation to produce composite microspheres of bacterial cellulose with PLA that can be processed in conventional extrusion.

The aim of this work is to produce biocomposite spheres of PLA and both pulp fibers and MCC, using emulsion-solvent evaporation method. In order to evaluate the effect of size and surface properties of the pulp fibers, unbleached pulp fibers and the corresponding grinded fibers, either

unmodified or surface modified by lignin deposition were used and the effectiveness of cellulose incorporation into PLA spheres was analyzed. MCC and MCC surface modified were also studied. Spheres of the PLA/cellulose biocomposite were characterized for its physical and chemical properties. The produced spheres are processed by compression molding to obtain composite films, which are characterized regarding its thermal, structural and mechanical properties.

2. Materials and Methods

2.1. Materials

PLA used in this study was Ingeo 2500HP from NatureWorks LLC (Minnetonka, MN, USA) having a density of 1.24 g/cm^3 and relative viscosity of 4.0 (tested at 1.0 g/dL in chloroform). Microcrystalline cellulose (MCC) was Avicell® purchased from Merck (Darmstadt, Germany). Hexadecyltrimethylammonium bromide (CTAB) and poly(vinyl alcohol) (PVA, 98–99% hydrolysis, M_w = 85,000–124,000) were purchase from Sigma-Aldrich (St. Louis, MO, USA). Dichloromethane (DCM) (Scharlau, Sentmenat, Spain), hydrochloric acid (Merck, Darmstadt, Germany), sulfuric acid (Sigma-Aldrich, USA), potassium permanganate (Merck, Darmstadt, Germany), potassium iodide (VWR, Leuven, Belgium) and sodium thiosulfate pentahydrate (Merck, Darmstadt, Germany) were analytical grade and used as received. The carbohydrate standards D-glucose and D(+)-xylose were acquired from Pronalab (Sintra, Portugal) and Merck (Darmstadt, Germany), respectively. Cellulosic fibers from *Eucalyptus globulus* unbleached kraft pulp and kraft black liquor were supplied by Celtejo—Empresa de Celulose do Tejo, S.A (Vila Velha de Ródão, Portugal). Kraft black liquor was used as a source of lignin for fiber surface modification. Their organic and inorganic content were 12.7% and 14.4%, respectively, determined using the standard methods TAPPI 650 om-09 and TAPPI T211 om-02.

2.2. Cellulose Modification

The average size of the pulp fibers was modified using the mixer mill CryoMill (Retsch, Haan, Germany). For that, 2.5 g of unbleached pulp fibers (UP) were grinded at room temperature using one grinding cycle of 2.5 min at 30 s^{-1} frequency. This sample will be designated by GUP. The fiber morphology of UP and GUP samples were characterized using the fiber analyzer Morfi (Techpap, Grenoble, France). The arithmetic average fiber length (mm), width (μm) and fines content (% in length) of UP were 0.641, 18.7 and 28.7, whereas the corresponding values for GUP were 0.447, 20.9 and 62.9. Particles with less than 0.2 mm in length are considered as fines [41]. The mean particle size of MCC was 13 μm, determined by laser diffraction particle size analyzer (Beckman Coulter, Inc., Brea, CA, USA).

In order to modify the surface chemistry of the cellulose, kraft lignin was precipitated over the MCC and the grinded pulp fibers as follows: 2.5 g of cellulose in aqueous suspension (50 mL deionized water) was mixed with 50 mL of black liquor. Then the pH of the cellulose-lignin was lowered by addition of 5 M HCl solution, until pH around 3. The suspension was centrifuged at 3000× *g* for 10 min, the supernatant removed and the cellulose modified with lignin was washed three times with deionized water. In order to obtain cellulose samples with different lignin content, an additional assay was carried out using 2.5 g of GUP suspended in 90 mL deionized water and 10 mL of black liquor. These samples were designated as MCC-L61, GUP-L61 and GUP-L25, respectively, where L61 and L25 means the lignin content in the modified cellulosic materials. The lignin content was determined according to TAPPI T236 om-99 standard and was found to be 4.1%, 25.4%, 60.9% and 61.4% for GUP, GUP-L25, GUP-L61 and MCC-L61 samples, respectively.

2.3. Preparation and Characterization of PLA/Cellulose Biocomposite Spheres

In a typical laboratorial procedure, a suitable amount of PVA was dissolved in 110 mL deionized water containing 0.1 g CTAB and stirred at 300 rpm using a mechanical stirrer (Heidolph RZR 2021,

Schwabach, Germany). Separately, 0.5 g cellulose fibers was suspended in 50 mL of deionized water using an IKA® T25 UltraTurrax® homogenizer at 10,000 rpm for 1 min, and after this suspension was added to the PVA solution. After homogenization of the PVA and the cellulose fibers, the solution of 2 g PLA in 40 mL dichloromethane (previously prepared) was poured into the aqueous suspension producing an oil-in-water emulsion (Figure 1). PVA is commonly used in emulsification solvent evaporation formulations as dispersant to prevent the coalescence of the oil droplets, having been observed that the used amount affects the preparation of microspheres [38,39,42]. Since the cellulose pulp has carboxylic groups, a cationic surfactant (CTAB) was used together with PVA to stabilize the emulsion and to promote cellulose incorporation in the PLA. The amount of CTAB was kept constant and PVA concentration was changed in order to evaluate its effect on the process yield. The system was mechanically stirred at constant rate (300 rpm) for 24 h at room temperature (20 °C) to evaporate the organic solvent. The spheres were recovered from the liquid phase by sedimentation, thoroughly washed with deionized water in order to remove the dispersants (PVA and CTAB) and dried at 40 °C for 2 days. An assay without cellulose addition was also carried out using the same procedure, and the PLA spheres were recovered.

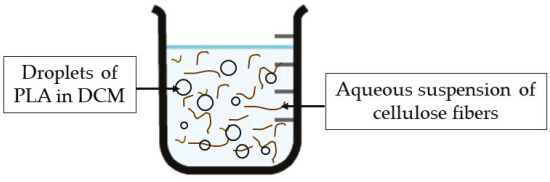

Figure 1. Illustration to show the oil-in-water emulsion in the process to obtain the PLA/cellulose biocomposite spheres.

2.3.1. Process Yield

The spheres yield was determined by the ratio of the weight of spheres and the sum of the weight of PLA and cellulose charged in the assay, assuming that the entire amount of dispersants (PVA and CTAB) remains in the liquid phase (supernatant). The amount of cellulose and lignin incorporated in the biocomposite spheres was estimated by mass balance, after measuring their corresponding amounts remaining in the liquid phase after solid separation. Therefore, the percentage of cellulose and lignin incorporation into PLA spheres was calculated by the difference between the initial amount of cellulose and lignin used in each assay and the amount of cellulose and lignin in the liquid phase, regarding the initial charge. The cellulose and lignin in the liquid phase were determined following the standard procedure usual in the wood and pulp filed. For cellulose determination, the NREL procedure (NREL/TP-510-42618) was followed. It should be noted that cellulose term used throughout the work also includes the residual hemicellulose in the pulp fibers. The dissolved lignin in the liquid phase was determined following the TAPPI T236 om-99 standard procedure; a blank test was carried out using the same proportions of PVA and CTAB as those used in the corresponding assay.

2.3.2. Physical Characterization of PLA/Cellulose Spheres

The particle size distributions and external specific surface area of the most representative samples of PLA/cellulose spheres was obtained by the laser diffraction method using the Coulter LS200 particle size analyzer (Beckman Coulter Inc., Brea, CA, USA). The density of the spheres was measured by the pycnometer method. Global specific surface area was measured according to the Brunauer-Emmett-Teller (BET) method using ASAP 2000 V2.04 (Micromeritics Instruments Corp., Norcross, GA, USA) apparatus. To further evaluate the morphology of the biocomposite spheres, scanning electron micrographs were taken on a Hitachi S-2700 scanning electron microscope (Tokyo, Japan) at 20 kV accelerating voltage. A cross-section of the spheres was obtained by imbedding the spheres into melted paraffin. After complete solidification, the hardened paraffin was cut into

pieces using a Microm HM 315 rotary microtome and the sphere slices were washed with xylene. The samples were coated with a gold layer allowing for surface and cross-section visualization.

2.3.3. Attenuated Total Reflectance-Fourier Transform Infrared Spectroscopy

The efficiency of chemical surface modification was analyzed by ATR-FTIR spectroscopy. The ATR-FTIR spectra have been recorded on a Thermo Scientific Nicolet iS10 spectrometer (Thermo Fisher Scientific, Waltham, MA, USA) equipped with an ATR unit. The cellulose samples and the PLA/cellulose biocomposite spheres were analyzed in the form of pellets. A total of 64 scans were performed over each sample with a resolution of 4 cm^{-1}. The spectrum was obtained from a range of 600–4000 cm^{-1}.

2.3.4. Contact Angle Measurements

In order to determine the changes in the hydrophilic character of the cellulose after surface modification, as well as the hydrophilicity of the PLA/cellulose composite spheres, contact angle measurements were carried out with deionized water using a DataPhysics OCAH 200 system (DataPhysics Instruments GmbH, Filderstadt, Germany) by means of sessile drop method. Uniform and practically porosity-free pellets (obtained by high compression at room temperature) of cellulose and lignin samples and PLA/cellulose spheres were used for this purpose. The initial contact angle was measured after ca. 50 ms of the water drop fall on the pellet surface. This time may be considered short enough to avoid absorption and thus an equilibrium drop shape could be assumed. All measurements were performed at 22 °C and each sample was measured with a minimum of four drops.

2.4. Production and Characterization of Biocomposite Films from PLA/Cellulose Spheres

The produced biocomposite PLA/cellulose spheres were compression molded into films using a hot press at 180 °C, progressively increasing the compression pressure to 3 MPa for 1 min. This temperature and pressure were kept constant for 1 min. Then, the heating was turned off and the hot press was cooled down to 110 °C at a rate of 6 °C/min using a circulating bath. The pressure was relieved and the film taken out.

2.4.1. Differential Scanning Calorimetry Analysis

Thermal properties of the PLA and biocomposite films were analyzed by Differential Scanning Calorimetry (DSC). The analyses were conducted with a Netzsch instrument DSC200 Cell and TASC 414/3 controller (Netzsch-Gerätebau GmbH, Selb, Germany). Samples of about 10 mg were placed in aluminum pans and heated from 30 to 500 °C at 10 °C/min using nitrogen as a purge gas. The degree of crystallinity (X_c) of the film samples was calculated by [43]:

$$X_c(\%) = \frac{(\Delta H_m - \Delta H_{cc})}{\Delta H_m^0 \cdot w} \cdot 100 \quad (1)$$

where ΔH_m and ΔH_m^0 is the melting enthalpy of the sample and of the pure crystalline PLA (93.6 J/g) [25], respectively; ΔH_{cc} is the cold crystallization enthalpy and w is the weight fraction of PLA in the biocomposite.

2.4.2. Structural Properties of the Biocomposite Films

Basis weight was determined by the ratio between the weight and the area of the films according to ISO 536:2012. The films were weighed in an analytical balance (±0.0001 g). The thickness of the films was measured according to ISO 534:2011 using the micrometer Adamel Lhomargy model MI 20 (Ivry-sur-Seine, France). Apparent density of the biocomposite films corresponds to the ratio between the basis weight and the thickness, according to ISO 534:2011. Structural properties were evaluated at 23 °C and 50% RH.

2.4.3. Mechanical Testing of Biocomposite Films

Tensile tests were performed on a tensile tester Thwing-Albert Instrument Co. (West Berlin, NJ, USA), EJA series based on ISO 1924/2:2008 standard. The biocomposite films were cut into rectangular pieces with 10 mm wide and 40 mm length, and then subjected to tensile test at a strain rate of 10 mm/min, using the initial grip distance of 10 mm. Tensile strength, elongation at break, Young's modulus and toughness (tensile energy absorption at break) were calculated. Bending tests were accomplished on a Lorentzen and Wettre stiffness tester (Stockholm, Sweden) at bending angle of 15°, based on ISO 2493/1:2010 standard and the bending elastic modulus was calculated according to Niskanen [44]. All tests were performed at 23 °C and 50% RH.

3. Results and Discussion

3.1. Spheres Yield and Effectiveness of Cellulose Incorporation

PLA/cellulose biocomposite spheres were successfully obtained (as seen in Figure 2) by solvent evaporation technique with yields ranging from close to 0 to 87.2% (Table 1); this yield represents the percentage of the PLA and cellulose (jointly accounted) recovered as spheres regarding to the initial amounts used.

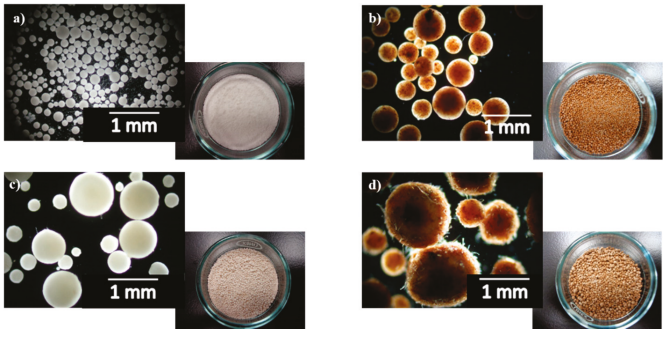

Figure 2. Pictures of some PLA/cellulose biocomposite spheres: (**a**) PLA/MCC; (**b**) PLA/MCC-L61; (**c**) PLA/GUP; (**d**) PLA/GUP-L61 (see Table 1 for sample identification).

Table 1. Effect of PVA/PLA ratio on PLA/cellulose spheres yield, for different samples (cellulose can be UP: unbleached pulp, GUP—grinded UP, GUP-L25—GUP with 25 wt % lignin, GUP-L61—GUP with 61 wt % lignin, MCC—microcrystalline cellulose, MCC-L61—MCC with 61 wt % lignin).

Sample	PVA/PLA Ratio	Spheres Yield (%)
PLA	0.13	36.4 ± 4.1
PLA	0.28	85.9 ± 2.2
PLA *	0.35	93.2 ± 0.9
PLA/UP *	0.13	79.9 ± 1.2
PLA/UP	0.20	75.8 ± 1.2
PLA/GUP *	0.13	82.8 ± 3.1
PLA/GUP	0.20	76.3 ± 2.1
PLA/GUP-L25	0.28	79.6 ± 0.4
PLA/GUP-L61	0.13	7.5 ± 7.3
PLA/GUP-L61	0.20	0 ± 0
PLA/GUP-L61 *	0.28	87.2 ± 1.8
PLA/MCC	0.13	4.0 ± 1.5
PLA/MCC	0.20	4.5 ± 6.4
PLA/MCC *	0.28	74.0 ± 0.3
PLA/MCC-L61 *	0.13	84.3 ± 4.3

* Samples characterized more deeply throughout the work.

As observed in Table 1, the PVA/PLA ratio determines the spheres yield, as can be seen for the PLA samples with PVA/PLA ratios of 0.13, 0.28 and 0.35, the PLA/GUP-L61 samples obtained with

0.13, 0.20 and 0.28 PVA/PLA ratios, and the PLA/MCC samples with 0.13, 0.20 and 0.28 PVA/PLA ratios. When only PLA was used, the increase of PVA/PLA ratio from 0.13 to 0.35 leads to the increase of spheres yield from 36.4% to 93.2%. For the low PVA/PLA ratio, a significant spheres agglomeration occurs. Increasing the amount of PVA stabilize the emulsion, prevents the droplets coalescence during the dichloromethane evaporation by providing a protective layer around the droplets. Thus, the droplets aggregation into large particles does not occur and the spheres yield increase with higher PVA/PLA ratio. Jiang et al. [42] also observed an increase of PLA nanoparticles yield with the increase of PVA concentration. When the emulsion contains cellulose fibers (original or grinded) besides PLA, the PVA/PLA ratio required to form individualized spheres is lower than those required by PLA only (0.13 versus 0.35); however the average spheres size is much higher and the external specific surface area much lower (Table 2). Reducing cellulose fiber length from 0.641 mm (UP) to 0.447 mm (GUP) with the concomitant increase of the cellulose fine material content (from 28.7% to 62.9%), the spheres yield increased only slightly from 79.9% to 82.8% (PLA/UP vs. PLA/GUP), which suggest that the particle dimensions are not a key parameter in spheres yield. In addition, the increase of PVA/PLA ratio from 0.13 to 0.20 (PLA/GUP) does not improve the spheres yield. In the case of MCC, the amount of dispersant required is higher than for the cellulose fibers. For PVA/PLA ratios of 0.13 or 0.20, the formation of agglomerates of irregular size occurred, providing a very low spheres yield (around 4%), whereas with the 0.28 PVA/PLA ratio a spheres yield of 74.0% was obtained. This high amount of PVA required for spheres formation is in accordance with the very high external specific surface area of these particles (Table 2). In addition, as we will see later on, the MCC incorporation is very low and therefore the droplets are almost only PLA; as a consequence, the PVA/PLA ratios were also of the same magnitude.

Table 2. Physical properties of selected samples of PLA/cellulose spheres (see Table 1 for sample identification).

Sample	Density (g/cm^3)	Laser Diffraction			BET
		Average Spheres Size (μm)		External Surface Area (cm^2/g)	Global Surface Area (cm^2/g)
		Weighted by Volume	Weighted by Number		
PLA	0.78 ± 0.03	126.2 ± 1.5	46.0 ± 1.9	525.0 ± 21.2	not measured
PLA/UP	0.91 ± 0.03	796.5 ± 1.3	633.4 ± 1.3	78.3 ± 0.4	10,600
PLA/GUP	0.69 ± 0.01	611.1 ± 1.4	447.2 ± 1.3	104.5 ± 0.7	11,400
PLA/GUP-L61	0.77 ± 0.01	888.0 ± 1.4	648.4 ± 1.4	71.1 ± 0.2	9300
PLA/MCC	0.78 ± 0.00	130.9 ± 1.6	10.9 ± 1.6	579. 7 ± 11.3	5700
PLA/MCC-L61	0.83 ± 0.02	641.7 ± 1.4	305.5 ± 1.9	101.0 ± 4.5	7400

In addition to spheres yield, it is important to investigate the cellulose material incorporation into the spheres composite. The PLA:cellulose ratio initially charged into the medium was fixed at 80:20. The cellulose incorporation was calculated by mass balance (charged cellulose—cellulose recovered in the liquid phase after solid/spheres recover), regarding the cellulose charged, and the corresponding values are in Figure 3.

Grinding the cellulose fibers led to a small increase in incorporation (from 31.4% to 36.0%, Figure 3), which suggests that the particle dimension is not the main parameter determining the cellulose fibers incorporation. According to Maa and Hsu [45] and Al-Azzam et al. [46], the incorporation of solid protein particles (0.4–79 μm particle sizes) in poly(metyl methacrylate) and poly(lactic-co-glycolic acid) polymers was improved with decreasing protein particle size. It was also found that the protein particle with irregular shape resulted in microspheres with lower amount of protein than if protein particles are spherical, for protein particle size higher than 5 μm. For finer particle, the effect was less significant [45]. In the present work, the UP and GUP fibers have irregular shape and their sizes (641 and 447 μm) are much higher than the protein particle sizes used in the abovementioned

work (0.4–79 μm). Considering their size, the behavior of microcrystalline cellulose (MCC) is at first glance unexpected, because the lowest incorporation was observed despite its lowest average particle size (13 μm). This result demonstrates the low affinity of pure cellulose to the PLA (dissolved in dichloromethane). On the contrary, the unbleached pulp fibers (UP and GUP) even with a very small amount of lignin (4.1%), exhibit higher affinity to PLA. These results observed in the emulsion are in agreement with those reported for the solid phase. In fact, several authors [10,32,33], stated that lignin can be used as coupling agent in cellulose fiber reinforced composites as it improves chemical interactions between the cellulose fiber and PLA matrix through non-polar groups.

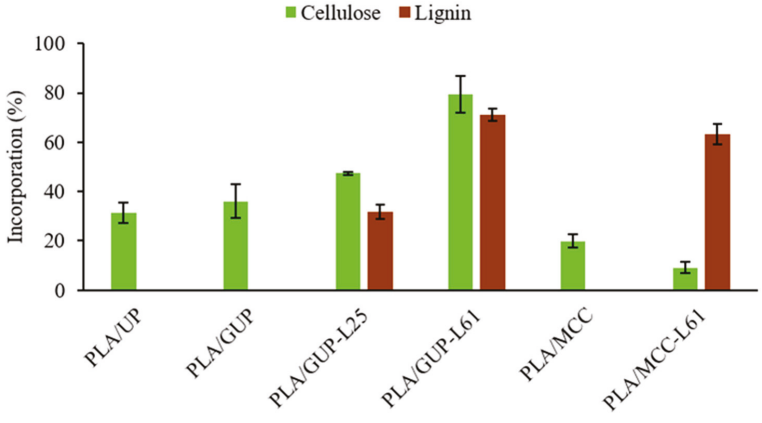

Figure 3. Cellulose and lignin incorporation (based on the corresponding amounts initially charged) into the PLA spheres (see Table 1 for abbreviations).

Therefore, the other approach exploited in this work was the cellulose fibers surface modification, using a natural product, kraft lignin. Kraft lignin is a sub-product of the kraft pulp production process, easily removed from the black liquor (a side stream of the process) by acidification. In wood, lignin has an important hydrophobic character; in the kraft process it is partially depolymerized and chemically modified in order to make it soluble in strong alkaline medium. By acidification it turns again water insoluble and can be adsorbed on the fibers. This lignin, however, is not hydrophobic according to the standard definition (surface having a water contact angle greater than 90°), as the water contact angle measured in the lignin pellets was around 57°. Nevertheless, this value is higher than those measured on MCC (41.2°) and unbleached pulp pellets (48.3°).

In order to investigate the effect of this surface modification on both the spheres yield and cellulose incorporation into PLA spheres, MCC and grinded pulp fibers (GUP) with precipitated lignin were prepared. Comparing GUP (without precipitated lignin) and GUP-L61 (with precipitated lignin) samples in Table 1, it was observed that for the pulp fibers with 61% lignin (GUP-L61), the PVA/PLA ratio should be increased from 0.13 to 0.28 in order to obtain individualized spheres with a yield of 87.2%. For a PVA/PLA ratio of 0.13 or 0.20, practically only formation of agglomerates occurred. A possible explanation for the higher PVA/PLA ratio required may be the more hydrophobic nature of lignin; PLA alone also requires high PVA/PLA ratio. During the dichloromethane evaporation, the coalescence of the droplets may occur by hydrophobic affinity, leading to a higher amount of PVA required to prevent the aggregation of the GUP with adsorbed lignin. Concerning to the MCC, unmodified and modified with 61% lignin (MCC vs. MCC-L61), it was found that the presence of lignin decreases the PVA/PLA ratio required for the formation of individualized spheres from 0.28 to 0.13, with a spheres yield of 84.3%, but the average spheres size (weighted in volume) increased from 131 to 642 μm (Table 2) and the corresponding external specific surface area decreased from 580 to 101 cm^2/g. Considering that the GUP-L61 sample had required a PVA/PLA of 0.28, it was not expected

that the PVA/PLA ratio of 0.13 would be enough for MCC-L61 sample, even because the external specific surface areas of the two samples are of the same magnitude. As it is well known in paper technology that the cohesion energy of fiber flocks increases with fiber length, we can speculate that higher PVA/PLA ratio is required to counterbalance the cohesion energy of the long fibers, regarding the MCC particles (447 μm vs. 13 μm).

Regarding cellulose fibers incorporation (Figure 3), for the GUP fibers it was observed an increase of cellulose incorporation from 36.0% to 79.4% with the increase of lignin content from 4% to 61%. Moreover, the lignin retention exhibits a similar trend. In other words, the pulp fiber incorporation in the PLA spheres increases from 36% to over 70%, with the increase of the fiber lignin content. For the MCC, the behavior is the opposite; there is a decrease when the cellulose is modified with lignin (Figure 3). This result may be due to desorption of the previously precipitated lignin on the MCC, by preferential dissolution in dichloromethane. On the other hand, the high lignin incorporation (63.1%) in the PLA spheres is a clear indication of the high affinity of the lignin to the PLA (see, also Table 3).

Based on the amount of cellulose and lignin charged and the corresponding incorporation, the content of each component in the composite spheres was calculated and the values are presented in Table 3. It was observed that the cellulose content in the spheres ranged from 1.0 to 8.8%, with pulp fibers in clear advantage.

Table 3. Composition of the PLA/cellulose biocomposite spheres (see Table 1 for sample identification).

Sample	PLA (%)	Cellulose (%)	Lignin (%)
PLA/UP	92.8	7.2	≈ 0
PLA/GUP	92.2	7.8	≈ 0
PLA/GUP-L25	89.1	8.8	2.0
PLA/GUP-L61	82.7	7.2	10.1
PLA/MCC	95.0	5.0	0
PLA/MCC-L61	88.1	1.0	10.9

3.2. Physical Characterization of PLA/Cellulose Spheres

Some of the most representative samples of PLA/cellulose biocomposite spheres (indicated in Table 1 by asterisks) were characterized concern to physical properties, namely density, particle size distributions and external specific surface area (Table 2). All samples presented multimodal particle size distributions (Figure 4). PLA spheres size range between 20 and 325 μm with low average size (126.2 μm and 46.0 μm, respectively weighted in volume and number) with a high external specific surface area of 525 cm^2/g (Table 2). The incorporation of unbleached pulp (PLA/UP) provides particles size ranging from 390 to 1400 μm with an average size of 796.5 μm (volume weighted) and 633.4 μm (number weighted), close to the magnitude of the fiber length. The external specific surface area of these spheres, determined by laser diffraction technique, was 78.3 cm^2/g. The grinding of the pulp fibers (PLA/GUP sample) results in spheres with smaller size (average size volume weighted of 611.1 μm and number weighted of 447.2 μm) than PLA/UP spheres. The lower average size provides a higher external specific surface area for the PLA/GUP spheres compared with original unbleached pulp (PLA/UP) (104.5 cm^2/g versus 78.3 cm^2/g). Thus, it can be concluded that fibers with lower length (0.447 mm) yields smaller spheres than the corresponding original fibers (average fiber length of 0.641 mm). As reported in Table 2, the incorporation of grinded pulp fibers modified by lignin precipitation produces spheres with the largest average size (888.0 μm and 648.4 μm, respectively weighted in volume and number) with a size distribution ranging from 370 to 1900 μm. Notice that these spheres have average size higher than those obtained by incorporation of original pulp fibers. Moreover, they also present the lowest external specific surface area (71.1 cm^2/g). Thus, the spheres size is not only affected by the size of the incorporated fibers but also by their surface chemistry. PLA/MCC spheres differ from the others biocomposite spheres by having the smallest size weighted in volume and in number (130.9 μm and 10.9 μm, respectively). The modification of MCC with lignin

leads to spheres with much higher size than MCC (average size increases from 130.9 to 641.7 μm, weighted in volume, and from 10.9 to 305.5 μm weighted in number) and lower external specific surface area (101.0 cm^2/g).

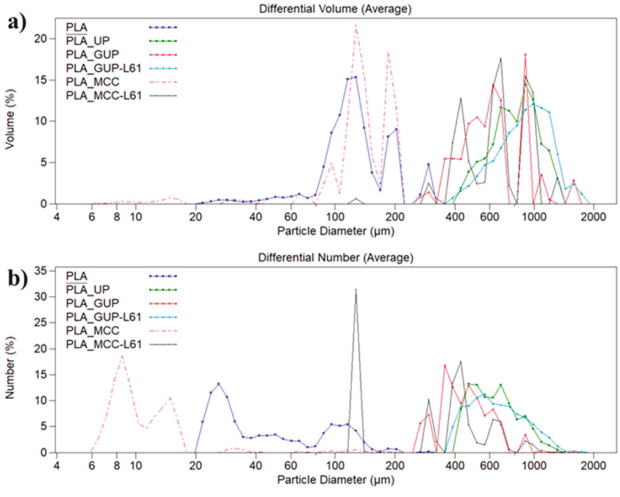

Figure 4. Particle size distributions in volume (**a**) and in number (**b**) for some PLA/cellulose biocomposite spheres (see Table 1 for abbreviations).

The global (external and internal) specific surface area provided by BET analysis is one or two orders of magnitude higher than those obtained by laser diffraction. This is an expected result due to the surface roughness and the internal porosity, accounted by BET analysis, and also revealed by the SEM images (Figures 5 and 6). The PLA/UP sample exhibits a high roughness due to the presence of the larger fibers, whereas others such as PLA and PLA/MCC-L61 are much smoother. All the biocomposite spheres are spherical except in the case of PLA/UP sample. The cross-sections of the spheres (Figure 6) show that the inner structure has some pores, presenting the PLA/UP sample a more compact structure. The internal porosity observed in Figure 6 is in good agreement with the spheres density (0.69–0.91 g/cm^3, Table 2), which is significantly lower than the 1.24 g/cm^3 reported for the PLA used in the present study.

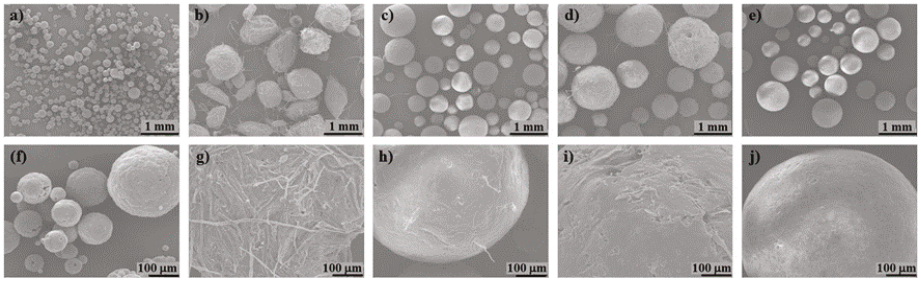

Figure 5. SEM images of the surface morphology of biocomposite spheres: (**a**,**f**) PLA; (**b**,**g**) PLA/UP); (**c**,**h**) PLA/GUP; (**d**,**i**) PLA/GUP-L61; (**e**,**j**) PLA/MCC-L61; (**a**) 200× and (**f**) 1000× magnification; (**b**–**e**) 25× and (**g**–**j**) 200× magnification (see Table 1 for sample identification).

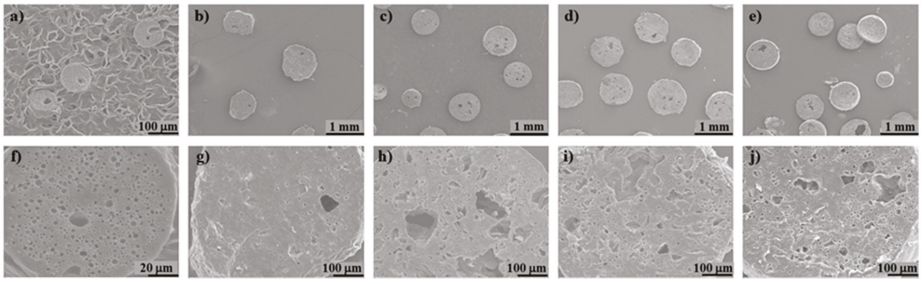

Figure 6. SEM images of the inner structure of biocomposite spheres: (**a**,**f**) PLA; (**b**,**g**) PLA/UP; (**c**,**h**) PLA/GUP; (**d**,**i**) PLA/GUP-L61; (**e**,**j**) PLA/MCC-L61; (**a**) 200× and (**f**) 1000× magnification; (**b**–**e**) 25× and (**g**–**j**) 200× magnification (see Table 1 for sample identification).

3.3. Chemical Characterization of PLA/Cellulose Spheres

Surface chemistry induced by the chemical modifications of the cellulose samples as well as of the PLA/cellulose biocomposite spheres were investigated by ATR-FTIR (spectra in Figure 7). When compared with MCC, ATR-FTIR spectrum of unbleached pulp fibers showed an additional band at 1590 cm^{-1} characteristic of lignin which is associated to aromatic ring vibration [32,47]. Both spectra exhibit the typical bands of cellulose, namely the broad band at 3331–3333 cm^{-1} attributed to the OH stretching vibration of intramolecular hydrogen bonds [32,48]. The spectra of GUP and MCC modified with precipitated lignin (GUP-L61 and MCC-L61) showed new peaks (at 1605 and 1608 cm^{-1}, respectively) comparatively to GUP and MCC spectra, assigned to lignin [47,48], confirming the lignin adsorption. PLA spectrum showed distinctive absorption bands assigned to their different functional groups, corresponding the major peak at 1748 cm^{-1} to the C=O stretching vibration [49]. The biocomposite spheres spectra confirm the presence of lignin (peak around 1598–1605 cm^{-1}), cellulose (for example, the peak around 3331–3347 cm^{-1}) and PLA (for example the peak around 1707–1708 cm^{-1}). The PLA/MCC spectrum is very similar to that of PLA due to the very low incorporation of MCC into the spheres (these are constituted by 95% PLA). Comparing the spectra of the cellulose samples and PLA/cellulose biocomposites, it was observed a decrease in the intensity of the peak assigned to OH stretching vibration (around 3331–3347 cm^{-1}) for the biocomposites, as expected. Compared to the PLA, the wavenumber of C=O peak in the biocomposites remains practically unchanged (1748 vs. 1747 cm^{-1} for PLA/MCC-L61 sample) suggesting a relatively weak interaction between cellulose (UP, GUP-L61 and MCC-L61) and PLA.

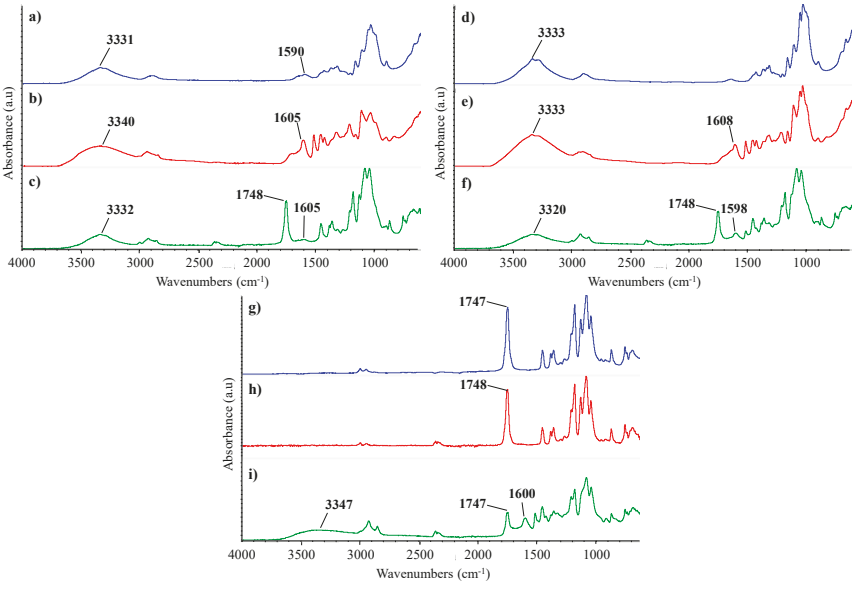

Figure 7. ATR-FTIR spectra of cellulose samples, PLA and biocomposite spheres: (**a**) UP or GUP; (**b**) GUP-L61; (**c**) PLA/UP; (**d**) MCC; (**e**) MCC-L61; (**f**) PLA/GUP-L61; (**g**) PLA; (**h**) PLA/MCC; (**i**) PLA/MCC-L61 (see Table 1 for abbreviations).

Figure 8 shows the water contact angle for the starting materials and the composites spheres as well, measured in pellets produced under high pressure (0.9 GPa) at room temperature in order to preserve the chemistry and minimize the porosity and roughness of the pellet which both affect contact angle measurement. By this way, the contact angle reflects mainly the chemistry of the material. MCC presents the lowest water contact angle (41.2°), which is the most hydrophilic sample. In turn, unbleached pulp presents a higher contact angle (48.3°) due to the presence of residual lignin. As expected, the lignin precipitation on the cellulose fibers and MCC increases very significantly the water contact angle. For the unbleached pulp, the contact angle increases from 48.3° to 75.4° (GUP-L25; around 25% lignin) and then decreases to 59.6° (GUP-L61; around 61% lignin). This decrease from 75.4° to 59.6° is probably due to the co-precipitation of sugar-lignin complex for the more concentrated black liquor solution. In fact, the lignin precipitated from the more diluted solution exhibited a darker tone than that precipitated from the more concentrated solution, despite the same final pH value used (pH = 3). Comparing the unbleached fibers and MCC, before and after lignin precipitation, we can observe a very significant increase of the water contact angle, although none samples have reached hydrophobic character (water contact angle higher than 90°), they have a contact angle value much closer to that of PLA which is 83.3°, consistent with those found in literature [50,51]. Thus, it would be expected that chemically modified cellulose samples were more compatible with PLA than those unmodified, resulting in higher percentage of cellulose incorporation (Figure 3). This behavior was in fact confirmed for GUP-L25 and GUP-L61, pulp fibers. For the microcrystalline cellulose reversible lignin desorption in aqueous medium was reported by Maximova et al. [52], which render the MCC-L61 sample hydrophilic and with low affinity to PLA; on the contrary, the desorbed lignin was strongly retained in the PLA (see Figure 3 and Table 3). Regarding the contact angles for the PLA/cellulose biocomposite spheres, the values are always inferior to that of PLA, ranging from 59.0° to 75.0° for PLA/MCC and PLA/MCC-L61 samples, respectively. Overall, the cellulose samples with higher contact angle leads to the corresponding PLA/cellulose spheres with slightly higher contact angle.

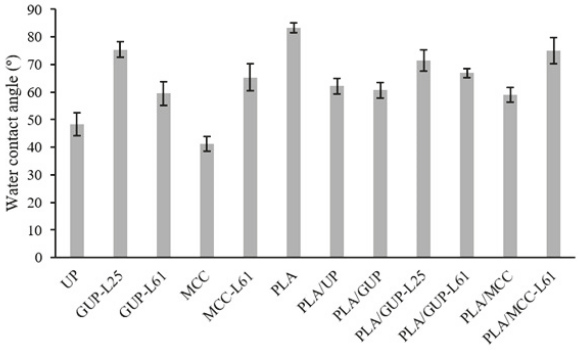

Figure 8. Water contact angle of cellulose samples, PLA and PLA/cellulose biocomposite spheres (see Table 1 for abbreviations).

3.4. Characterization of the Biocomposite Films

Composite spheres were compression molded into films and these were characterized concerning their thermal, structural and mechanical properties. Thermal properties were investigated via DSC. The DSC curves are depicted in Figure 9 and were used to determine the glass transition temperature (T_g), cold crystallization temperature (T_{cc}), cold crystallization enthalpy (ΔH_{cc}), melting temperature (T_m), melting enthalpy (ΔH_m) and degradation temperature (T_d) of the different samples. At the end of the DSC test, the aluminum pans were weighed in order to determine the solid residue at 500 °C. These results are shown in Table 4 along with the degree of crystallinity (X_c). It can be seen that the PLA exhibited a T_g at 62.1 °C and the composite films have a slightly lower T_g, except the PLA/MCC-L61 film (1% cellulose) that presented similar T_g to the PLA. The decrease of the T_g signifies that cellulose incorporation increases the chain mobility of the PLA polymer. It was also observed that the PLA fraction undertaken cold crystallization in the DSC test is composite dependent. For example, the original cellulose fiber (UP) led to the smallest cold crystallization peak (Figure 9), but the film exhibits the highest PLA crystallinity degree (Table 4). This indicates that this composite had favorable conditions to crystallize in the film making process. The contrary occurred for the composite incorporating grinded UP (GUP). Compared with PLA, the cold peaks shifts to lower temperatures for PLA/UP, PLA/GUP and PLA/MCC composites, indicating that cold crystallization occurs earlier induced by UP, GUP and MCC which act as nucleating agents for PLA crystallization, in good agreement with results reported by other authors [26,43,53,54]. On the contrary, the presence of lignin in the cellulose materials (PLA/GUP-L61 and PLA/MCC-L61) led to higher T_{cc}. This result is in agreement with reported by Gordobil et al. [50] which found that the introduction of lignin in the PLA matrix affects the crystallization behavior causing that the PLA chains have a lower mobility and crystallize with greater difficult and higher temperatures. According to the reported by Graupner [12] and Graupner et al. [32], lignin improves the fiber/matrix adhesion, which may explain the decrease of the mobility of the PLA chains, and consequently hindering the crystallization process leading to composites with lower crystallinity and higher values of T_{cc} as well. Frone et al. [54] observed a similar behavior in PLA nanocomposites reinforced with silane treated nanofibers.

The incorporation of lignin in the composites has also a very favorable impact on the composite thermal stability, as we can see in Figure 9 (325–385 °C). The extent of degradation is substantially reduced taking into account the value of the endothermic transition. The solid residue at 500 °C is also higher due to the formation of highly condensed aromatic structures which have the ability to form char [55]. The rise of the residue at 500 °C with the addition of lignin into PLA composites was reported in other studies [56].

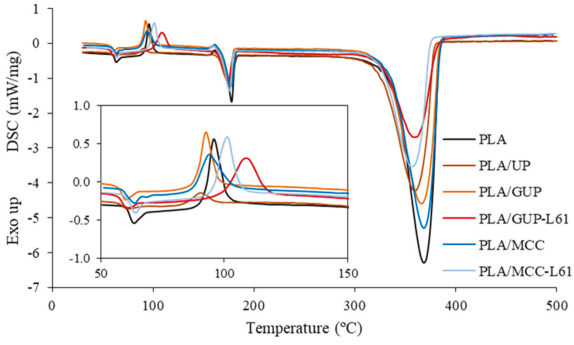

Figure 9. DSC curves of PLA and biocomposite films with the crystallization region in the insert (see Table 1 for abbreviations and Table 3 for composite composition).

Table 4. DSC parameters for PLA and its biocomposite films (see Table 1 for sample identification).

Sample	T_g (°C)	T_{cc} (°C)	ΔH_{cc} (J/g)	T_m (°C)	ΔH_m (J/g)	X_c (%)	T_d (°C)	Solid Residue (%)
PLA	62.1	96.1	32.72	177.7	60.04	29.2	368.2	1.2
PLA/UP	60.0	90.7	7.09	175.2	54.49	54.6	359.4	2.0
PLA/GUP	58.6	92.7	26.58	174.8	51.54	28.9	365.7	1.2
PLA/GUP-L61	58.7	108.9	37.04	174.3	45.13	10.5	358.9	10.0
PLA/MCC	61.3	93.8	29.00	176.7	55.09	29.3	368.3	1.0
PLA/MCC-L61	62.1	100.8	34.07	175.9	53.88	24.0	357.1	5.4

Table 4 shows a substantial increase of the degree of crystallinity of the PLA films with the inclusion of cellulose fibers in its original dimension (from 29.2% to 54.6%). The same fibers, after being ground (GUP), which have much higher fines content, provokes a substantial decrease of the crystallinity of the PLA in the film. The additional inclusion of lignin on the fibers surface causes a huge decrease of the PLA crystallinity from 28.9% to 10.5%, in accordance with the lower mobility of the lignin adsorbed PLA molecules previously commented. The same trend occurs for the MCC, but with lower extent. Figure 10 shows that more and larger spherulites are formed in the PLA/UP biocomposite film than in the PLA/MCC. The higher specific surface area of the MCC (and grinded fibers) provides much higher nucleation points for crystallization, which hypothetically did not provide conditions for appropriate spherulites growing. On the contrary, the reduced number of nucleation points in UP fibers provides conditions for good spherulites growing, which led to very high crystallinity degree.

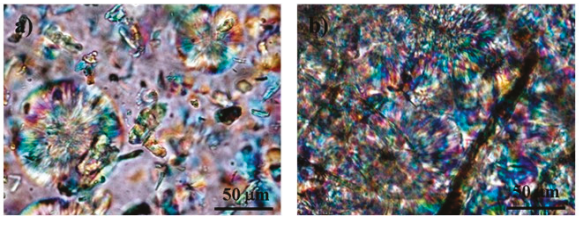

Figure 10. Polarized optical microscopy images of: (**a**) PLA/MCC and (**b**) PLA/UP biocomposite films (see Table 1 for sample identification).

Structural and mechanical properties of the PLA and composite films are presented in Tables 5 and 6, and the images of the dispersion of the cellulose into PLA matrix examined by optical microscopy are shown in Figure 11. As can be seen in Table 5, the apparent density of the films, calculated by the basis

weight and thickness ratio is close to the theoretical PLA density (1.24 g/cm^3) indicating the production of a practically porosity-free film.

Table 5. Structural properties of PLA/cellulose biocomposite films (see Table 1 for sample identification).

Sample	Basis Weight (g/m^2)	Thickness (μm)	Apparent Density (g/cm^3)
PLA	153.4 ± 8.2	127.8 ± 10.2	1.205 ± 0.087
PLA/UP	163.3 ± 13.3	134.0 ± 12.4	1.220 ± 0.039
PLA/GUP	152.8 ± 10.5	125.7 ± 11.0	1.218 ± 0.037
PLA/GUP-L61	153.5 ± 7.9	126.3 ± 11.1	1.223 ± 0.122
PLA/MCC	161.9 ± 8.0	132.7 ± 11.6	1.224 ± 0.054
PLA/MCC-L61	154.4 ± 2.8	127.0 ± 4.4	1.217 ± 0.020

Tensile strength of the composite films incorporating UP, GUP and GUP-L61 does not improve when compared with the PLA film (Table 6). In the case of PLA/UP film, the loss of tensile strength is particularly relevant and is probably due to more brittle nature of the film due to the much higher crystallinity of the PLA (Table 4). The brittle nature of the film is clearly revealed in the extremely low value of toughness determined by the integration of the stress-strain curve. In turn, the incorporation of MCC and MCC-L61 improves tensile strength and, particularly, the toughness (Table 6), due to the high increase in elongation. The relatively good dispersion of the MCC in PLA matrix (Figure 11) and the high number of interface between the crystals can tentatively explain these elongations.

The toughness performance of PLA/GUP is much higher than the PLA/UP due to the lower crystallinity of the PLA. However, it is much lower than PLA/MCC probably because of the lower elongation of the PLA/GUP composite due to the restrain imposed by cellulose fiber network.

Table 6. Mechanical properties of PLA/cellulose biocomposite films (see Table 1 for sample identification).

Sample	Tensile Strength (MPa)	Elongation at Break (%)	Young's Modulus (GPa)	Toughness (kJ/m^3)	Bending Elastic Modulus (MPa)
PLA	35.1 ± 5.0	2.7 ± 0.4	1.82 ± 0.27	520 ± 78	4.45 ± 0.46
PLA/UP	23.4 ± 3.6	1.5 ± 0.2	1.65 ± 0.26	211 ± 49	4.15 ± 1.01
PLA/GUP	30.6 ± 6.8	2.2 ± 0.3	1.66 ± 0.16	383 ± 149	3.83 ± 0.63
PLA/GUP-L61	35.6 ± 6.1	2.3 ± 0.4	1.66 ± 0.09	408 ± 125	4.34 ± 1.13
PLA/MCC	43.0 ± 3.4	3.6 ± 0.7	1.53 ± 0.18	937 ± 267	4.07 ± 0.79
PLA/MCC-L61	44.9 ± 2.4	3.8 ± 0.3	1.55 ± 0.09	970 ± 129	4.36 ± 0.42

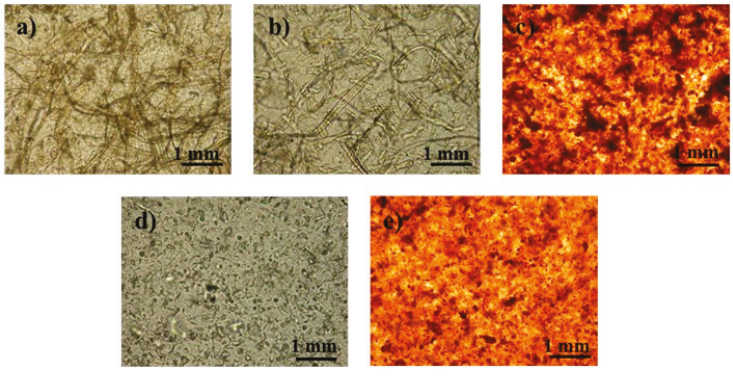

Figure 11. Optical microscopy images of the PLA/cellulose composite films: (**a**) PLA/UP; (**b**) PLA/GUP; (**c**) PLA/GUP-L61; (**d**) PLA/MCC; (**e**) PLA/MCC-L61 (see Table 1 for sample identification).

Contrarily to observed in the present work, Mathew et al. [9] found that PLA composites with pulp fibers have better tensile properties than those with MCC. However, pulp fibers loads are higher

(10–25 wt %) than that used herein. Regarding the reinforcement ability of MCC in PLA composites, the literature shows contradictory results [9,19,57,58]. Our results are in agreement with those obtained by Xian et al. [19], who observed that PLA composites with low MCC loads (2–6 wt %) improved tensile strength. According to these authors, MCC can be uniformly dispersed in PLA matrix and had good interfacial bonding with PLA, as MCC has high specific surface area, surface activity and can form hydrogen bonds with PLA [19].

Concerning to Young's modulus, it was observed a decrease for the composite films when compared with PLA film, being this decrease more pronounced in the case of PLA/MCC and PLA/MCC-L61 films, in accordance with their higher elongation at break (Table 6). However, these outcomes are apparently contradictory to those reported in other studies, which found an increase of Young's modulus and the decrease of elongation at break for PLA composites reinforced with MCC [9,19,57,58].

All composites show a decrease in the bending elastic modulus when compared with PLA film meaning that the composites are less stiff than PLA film.

In summary, results show that PLA/MCC composite films present better mechanical properties than that of PLA/pulp fibers composite films.

4. Conclusions

The solvent evaporation technique was used to produce PLA/cellulose biocomposite spheres, which were processed by compression molding. It was shown that spheres yield is primarily determined by the PVA/PLA ratio, as a suitable amount of PVA must be present in the emulsion to stabilize them, preventing the droplets coalescence. As expected, the PVA/PLA ratio required increases with the decrease of spheres size. Moreover, the increase of the hydrophobic character of the cellulose fibers led to the increase of the required PVA/PLA ratio. For the optimized PVA/PLA ratio, the spheres yield ranged from 74.0% to 87.2%. The results showed the importance of cellulose surface chemistry on the spheres yield and on the percentage of cellulose incorporated. The effectiveness of cellulose fibers incorporation was improved more than 50% when the GUP pulp fibers were surface modified with 61% lignin (GUP-L61), in accordance with the increase of pulp fibers hydrophobicity. It was also shown that the reduction of the fiber size by grinding only increased cellulose incorporation from 31.4% to 36.0% confirming that the particle dimension is not the main parameter affecting cellulose incorporation. The average spheres size (weighted in volume) ranged from 130.9 to 888.0 μm for the PLA/MCC and PLA/GUP-L61 samples, respectively. The corresponding external specific surface area, determined by laser diffraction, decreased from 579.7 to 71.1 cm^2/g. The BET specific surface area is, in general, two orders of magnitude higher, in accordance with the observed internal porosity of spheres by SEM. Despite this, practically porosity-free films were produced; the apparent density of the films is close to the density of the PLA used to produce the spheres. The incorporation of cellulose in its different forms led to a slightly decrease of the glass and melting temperature of the biocomposite films. The decrease is particularly noted in the cold crystallization temperature. On the other hand, the incorporation of UP fibers greatly increases the degree of crystallinity of the PLA. On the contrary, cellulose modified with lignin (GUP-L61 and MCC-L61) hinder the crystallization process (also noted in the significant increase in T_{cc}) and yields biocomposite films with lower crystallinity. The mechanical properties of the biocomposite films are affected by the cellulose type. MCC improves these properties, doubling the toughness value compared with PLA film. In contrast, the incorporation of UP fibers results in substantial loss of tensile strength and toughness due to higher PLA crystallinity in the PLA/UP film. The grinded pulp fibers originate composite films with lower crystallinity and higher tensile strength and toughness compared with UP fibers.

Author Contributions: Funding acquisition, A.C. and R.S.; Investigation, S.S.; Resources: A.S.; Supervision, R.S.; Writing—original draft, S.S.; Writing—review & editing, A.C. and R.S.

Funding: This research was funded by [Thermocel—Desenvolvimentos de compósitos de base cellulose—POCI-01-0247-FEDER-003306] co-financed by FEDER funds through COMPETE 2020.

Conflicts of Interest: The authors declare no conflict of interest.

References

1. Mitra, B.C. Environment friendly composite materials: Biocomposites and green composites. *Def. Sci. J.* **2014**, *64*, 244–261. [CrossRef]
2. Sahari, J.; Sapuan, S.M. Natural fibre reinforced biodegradable polymer composites. *Rev. Adv. Mater. Sci.* **2011**, *30*, 166–174.
3. Loureiro, N.C.; Esteves, J.L.; Viana, J.C.; Ghosh, S. Development of polyhydroxyalkanoates/poly(lactic acid) composites reinforced with cellulosic fibers. *Compos. Part B Eng.* **2014**, *60*, 603–611. [CrossRef]
4. Ren, H.; Zhang, Y.; Zhai, H.; Chen, J. Production and evaluation of biodegradable composites based on polyhydroxybutyrate and polylactic acid reinforced with short and long pulp fibers. *Cellul. Chem. Technol.* **2015**, *49*, 641–652.
5. Avérous, L. Polylactic Acid: Synthesis, Properties and Applications. In *Monomers, Polymers and Composites from Renewable Resources*; Belgacem, M.N., Gandini, A., Eds.; Elsevier Ltd.: New York, NY, USA, 2008; pp. 433–451. ISBN 978-0-08-045316-3.
6. Khalil, H.A.; Bath, A.; Yusra, A. Green composites from sustainable cellulose nanofibrils: A review. *Carbohydr. Polym.* **2012**, *87*, 963–979. [CrossRef]
7. Murariu, M.; Dubois, P. PLA composites: From production to properties. *Adv. Drug Deliv. Rev.* **2016**, *107*, 17–46. [CrossRef] [PubMed]
8. Nakagaito, A.N.; Fujimura, A.; Sakai, T.; Hama, Y.; Yano, H. Production of microfibrillated cellulose (MFC)-reinforced polylactic acid (PLA) nanocomposites from sheets obtained by a papermaking-like process. *Compos. Sci. Technol.* **2009**, *69*, 1293–1297. [CrossRef]
9. Mathew, A.P.; Oksman, K.; Sain, M. Mechanical properties of biodegradable composites from poly lactic acid (PLA) and microcrystalline cellulose (MCC). *J. Appl. Polym. Sci.* **2005**, *97*, 2014–2025. [CrossRef]
10. Cho, D.; Seo, J.M.; Lee, H.S.; Cho, C.W.; Han, S.O.; Park, W.H. Property improvement of natural fiber-reinforced green composites by water treatment. *Adv. Compos. Mater.* **2007**, *16*, 299–314. [CrossRef]
11. Le Duigou, A.; Bourmaud, A.; Balnois, E.; Davies, P.; Baley, C. Improving the interfacial properties between flax fibres and PLLA by a water fibre treatment and drying cycle. *Ind. Crops Prod.* **2012**, *39*, 31–39. [CrossRef]
12. Graupner, N. Application of lignin as natural adhesion promoter in cotton fibre-reinforced poly(lactic acid) (PLA) composites. *J. Mater. Sci.* **2008**, *43*, 5222–5229. [CrossRef]
13. Le Moigne, N.; Longerey, M.; Taulemesse, J.M.; Bénézet, J.C.; Bergeret, A. Study of the interface in natural fibres reinforced poly(lactic acid) biocomposites modified by optimized organosilane treatments. *Ind. Crops Prod.* **2014**, *52*, 481–494. [CrossRef]
14. Raj, G.; Balnois, E.; Baley, C.; Grohens, Y. Role of polysaccharides on mechanical and adhesion properties of flax fibres in flax/PLA biocomposite. *Int. J. Polym. Sci.* **2011**, *2011*, 1–11. [CrossRef]
15. Tokoro, R.; Vu, D.M.; Okubo, K.; Tanaka, T.; Fujii, T.; Fujiura, T. How to improve mechanical properties of polylactic acid with bamboo fibers. *J. Mater. Sci.* **2008**, *43*, 775–787. [CrossRef]
16. Magniez, K.; Voda, A.S.; Kafi, A.A.; Fichini, A.; Guo, Q.; Fox, B.L. Overcoming interfacial affinity issues in natural fiber reinforced polylactide biocomposites by surface adsorption of amphiphilic block copolymers. *ACS Appl. Mater. Interfaces* **2013**, *5*, 276–283. [CrossRef] [PubMed]
17. Awal, A.; Rana, M.; Sain, M. Thermorheological and mechanical properties of cellulose reinforced PLA bio-composites. *Mech. Mater.* **2015**, *80*, 87–95. [CrossRef]
18. Hua, S.; Chen, F.; Liu, Z.; Yang, W.; Yang, M. Preparation of cellulose-graft-polylactic acid via melt copolycondensation for use in polylactic acid based composites: Synthesis, characterization and properties. *RSC Adv.* **2016**, *6*, 1973–1983. [CrossRef]
19. Xian, X.; Wang, X.; Zhu, Y.; Guo, Y.; Tian, Y. Effects of MCC content on the structure and performance of PLA/MCC biocomposites. *J. Polym. Environ.* **2018**, *26*, 1–9. [CrossRef]
20. Larsson, K.; Berglund, L.A.; Ankerfors, M.; Lindström, T. Polylactide latex/nanofibrillated cellulose bionanocomposites of high nanofibrillated cellulose content and nanopaper network structure prepared by a papermaking route. *J. Appl. Polym. Sci.* **2012**, *125*, 2460–2466. [CrossRef]
21. Song, Z.; Xiao, H.; Zhao, Y. Hydrophobic-modified nano-cellulose fiber/PLA biodegradable composites for lowering water vapor transmission rate (WVTR) of paper. *Carbohydr. Polym.* **2014**, *111*, 442–448. [CrossRef]
22. Wang, T.; Drzal, L.T. Cellulose-nano fiber-reinforced poly(lactic acid) composites prepared by a water-based approach. *ACS Appl. Mater. Interfaces* **2012**, *4*, 5079–5085. [CrossRef] [PubMed]

23. Iwatake, A.; Nogi, M.; Yano, H. Cellulose nanofiber-reinforced polylactic acid. *Compos. Sci. Technol.* **2008**, *68*, 2103–2106. [CrossRef]
24. Yu, H.Y.; Zhang, H.; Song, M.L.; Zhou, Y.; Yao, J.; Ni, Q.Q. From cellulose nanospheres, nanorods to nanofibers: Various aspect ratio induced nucleation/reinforcing effects on polylactic acid for robust-barrier food packaging. *ACS Appl. Mater. Interfaces* **2017**, *9*, 43920–43938. [CrossRef] [PubMed]
25. Hossain, K.M.Z.; Ahmed, I.; Parsons, A.J.; Scotchford, C.A.; Walker, G.S.; Thielemans, W.; Rudd, C.D. Physico-chemical and mechanical properties of nanocomposites prepared using cellulose nanowhiskers and poly(lactic acid). *J. Mater. Sci.* **2012**, *47*, 2675–2686. [CrossRef]
26. Lee, K.Y.; Blaker, J.J.; Bismarck, A. Surface functionalisation of bacterial cellulose as the route to produce green polylactide nanocomposites with improved properties. *Compos. Sci. Technol.* **2009**, *69*, 2724–2733. [CrossRef]
27. Immonen, K.; Lahtinen, P.; Pere, J. Effects of Surfactants on the Preparation of Nanocellulose-PLA Composites. *Bioengineering* **2017**, *4*, 91. [CrossRef]
28. Ghasemi, S.; Behrooz, R.; Ghasemi, I.; Yassar, R.S.; Long, F. Development of nanocellulose-reinforced PLA nanocomposite by using maleated PLA (PLA-g-MA). *J. Thermoplast. Compos. Mater.* **2018**, *31*, 1090–1101. [CrossRef]
29. Graupner, N.; Albrecht, K.; Hegemann, D.; Müssig, J. Plasma modification of man-made cellulose fibers (Lyocell) for improved fiber/matrix adhesion in poly(lactic acid) composites. *J. Appl. Polym. Sci.* **2013**, *128*, 4378–4386. [CrossRef]
30. Gu, J.; Catchmark, J.M. Polylactic acid composites incorporating casein functionalized cellulose nanowhiskers. *J. Biol. Eng.* **2013**, *7*, 31. [CrossRef]
31. Frone, A.N.; Berlioz, S.; Chailan, J.-F.; Panaitescu, D.M.; Donescu, D. Cellulose fiber-reinforced polylactic acid. *Polym. Compos.* **2011**, *32*, 976–985. [CrossRef]
32. Graupner, N.; Fischer, H.; Ziegmann, G.; Müssig, J. Improvement and analysis of fibre/matrix adhesion of regenerated cellulose fibre reinforced PP-, MAPP- and PLA-composites by the use of Eucalyptus globulus lignin. *Compos. Part B Eng.* **2014**, *66*, 117–125. [CrossRef]
33. Wang, X.; Jia, Y.; Liu, Z.; Miao, J. Influence of the lignin content on the properties of poly(lactic acid)/lignin-containing cellulose nanofibrils composite films. *Polymers (Basel)* **2018**, *10*, 1013. [CrossRef]
34. Nair, S.S.; Chen, H.; Peng, Y.; Huang, Y.; Yan, N. Polylactic acid biocomposites reinforced with nanocellulose fibrils with high lignin content for improved mechanical, thermal, and barrier properties. *ACS Sustain. Chem. Eng.* **2018**, *6*, 10058–10068. [CrossRef]
35. Oksman, K.; Aitomäki, Y.; Mathew, A.P.; Siqueira, G.; Zhou, Q.; Butylina, S.; Tanpichai, S.; Zhou, X.; Hooshmand, S. Review of the recent developments in cellulose nanocomposite processing. *Compos. Part A Appl. Sci. Manuf.* **2016**, *83*, 2–18. [CrossRef]
36. Samir, M.A.S.A.; Alloin, F.; Dufresne, A. Review of recent research into cellulosic whiskers, their properties and their application in nanocomposite field. *Biomacromolecules* **2005**, *6*, 612–626. [CrossRef]
37. Mesic, N.; Friman, A. Process for Manufacturing a Composition Comprising Cellulose Pulp Fibers and Thermoplastic Fibers. U.S. Patent 9,297,112, 29 March 2013.
38. Freitas, S.; Merkle, H.P.; Gander, B. Microencapsulation by solvent extraction/evaporation: Reviewing the state of the art of microsphere preparation process technology. *J. Controll. Release* **2005**, *102*, 313–332. [CrossRef]
39. Hong, Y.; Gao, C.; Shi, Y.; Shen, J. Preparation of porous polylactide microspheres by emulsion-solvent evaporation based on solution induced phase separation. *Polym. Adv. Technol.* **2005**, *16*, 622–627. [CrossRef]
40. Lee, I.; Ji, S. Device and Method for Encapsulation of Hydrophilic Materials. U.S. Patent 9308172, 12 April 2016.
41. Guay, D.; Sutherland, N.; Rantanen, W.; Malandri, N.; Stephens, A.; Mattingly, K.; Schneider, M. Comparison of fiber length analyzers. In Proceedings of the 2005 TAPPI Practical Papermaking Conference, Milwaukee, WI, USA, 22–26 May 2005; Tappi Press: Atlanta, GA, USA, 2005.
42. Jiang, X.; Zhou, C.; Tang, K. Preparation of PLA and PLGA nanoparticles by binary organic solvent diffusion method. *J. Cent. South. Univ. Technol.* **2003**, *10*, 202–206. [CrossRef]
43. Sullivan, E.M.; Moon, R.J.; Kalaitzidou, K. Processing and characterization of cellulose nanocrystals/polylactic acid nanocomposite films. *Materials* **2015**, *8*, 8106–8116. [CrossRef]

44. Kajanto, I. Structural mechanisms of paper and board. In *Papermaking Science and Technology—Paper Physics*; Niskanen, K., Ed.; Fapet Oy in cooperation with the Paper Engineers' Association and TAPPI: Helsinki, Finland, 1998; pp. 192–221, ISBN 10: 9525216160, ISBN 13: 9789525216165.
45. Maa, Y.F.; Hsu, C.C. Effect of primary emulsions on microsphere size and protein-loading in the double emulsion process. *J. Microencapsul.* **1997**, *14*, 225–241. [CrossRef]
46. Al-Azzam, W.; Pastrana, E.A.; Griebenow, K. Co-lyophilization of bovine serum albumin (BSA) with poly(ethylene glycol) improves efficiency of BSA encapsulation and stability in polyester microspheres by a solid-in-oil-in-oil technique. *Biotechnol. Lett.* **2002**, *24*, 1367–1374. [CrossRef]
47. Ludueña, L.N.; Vecchio, A.; Stefani, P.M.; Alvarez, V.A. Extraction of cellulose nanowhiskers from natural fibers and agricultural byproducts. *Fibers Polym.* **2013**, *14*, 1118–1127. [CrossRef]
48. Pandey, K.K. A study of chemical structure of soft and harwood and wood polymers by FTIR spectrscopy. *J. Appl. Polym. Sci.* **1999**, *71*, 1969–1975. [CrossRef]
49. Kister, G.; Cassanas, G.; Vert, M. Effects of morphology, conformation and configuration on the IR and Raman spectra of various poly(lactic acid)s. *Polymer* **1998**, *39*, 267–273. [CrossRef]
50. Gordobil, O.; Delucis, R.; Egüés, I.; Labidi, J. Kraft lignin as filler in PLA to improve ductility and thermal properties. *Ind. Crops Prod.* **2015**, *72*, 46–53. [CrossRef]
51. Darie-Niţə, R.N.; Vasile, C.; Irimia, A.; Lipşa, R.; Râpa, M. Evaluation of some eco-friendly plasticizers for PLA films processing. *J. Appl. Polym. Sci.* **2016**, *133*, 1–11. [CrossRef]
52. Maximova, N.; Österberg, M.; Koljonen, K.; Stenius, P. Lignin adsorption on cellulose fibre surfaces: Effect on surface chemistry, surface morphology and paper strength. *Cellulose* **2001**, *8*, 113–125. [CrossRef]
53. Mathew, A.P.; Oksman, K.; Sain, M. The Effect of morphology and chemical characteristics of cellulose reinforcements on the crystallinity of polylactic acid. *J. Appl. Polym. Sci.* **2006**, *101*, 300–310. [CrossRef]
54. Frone, A.N.; Berlioz, S.; Chailan, J.F.; Panaitescu, D.M. Morphology and thermal properties of PLA-cellulose nanofibers composites. *Carbohydr. Polym.* **2013**, *91*, 377–384. [CrossRef]
55. Watkins, D.; Nuruddin, M.; Hosur, M.; Tcherbi-Narteh, A.; Jeelani, S. Extraction and characterization of lignin from different biomass resources. *J. Mater. Res. Technol.* **2015**, *4*, 26–32. [CrossRef]
56. Li, J.; He, Y.; Inoue, Y. Thermal and mechanical properties of bodegradable blends of poly(L-lactic acid) and lignin. *Polym. Int.* **2003**, *52*, 949–955. [CrossRef]
57. Haafiz, M.K.M.; Hassan, A.; Zakaria, Z.; Inuwa, I.M.; Islam, M.S.; Jawaid, M. Properties of polylactic acid composites reinforced with oil palm biomass microcrystalline cellulose. *Carbohydr. Polym.* **2013**, *98*, 139–145. [CrossRef] [PubMed]
58. Abdulkhani, A.; Hosseinzadeh, J.; Dadashi, S.; Mousavi, M. A study of morphological, thermal, mechanical and barrier properties of PLA based biocomposites prepared with micro and nano sized cellulosic fibers. *Cellul. Chem. Technol.* **2015**, *49*, 7–8.

polymers

MDPI

Article

Mechanical Strength Enhancement of Polylactic Acid Hybrid Composites

Ji-Won Park [1,2], Jae-Ho Shin [1], Gyu-Seong Shim [1], Kyeng-Bo Sim [1], Seong-Wook Jang [1,2] and Hyun-Joong Kim [1,2,*]

[1] Lab of Adhesion and Bio-Composite, Program in Environmental Materials Science, Department of Forest Science, Seoul National University, Seoul 08826, Korea; roorouny@gmail.com (J.-W.P.); pass2462@snu.ac.kr (J.-H.S.); sks6567@snu.ac.kr (G.-S.S.); skb181@snu.ac.kr (K.-B.S.); jangsw0202@snu.ac.kr (S.-W.J.)

[2] Research Institute of Agriculture and Life Sciences, Seoul National University, Seoul 08826, Korea

* Correspondence: hjokim@snu.ac.kr

Received: 10 January 2019; Accepted: 14 February 2019; Published: 17 February 2019

Abstract: In recent years, there has been an increasing need for materials that are environmentally friendly and have functional properties. Polylactic acid (PLA) is a biomass-based polymer, which has attracted research attention as an eco-friendly material. Various studies have been conducted on functionality imparting and performance improvement to extend the field of application of PLA. Particularly, research on natural fiber-reinforced composites have been conducted to simultaneously improve their environmental friendliness and mechanical strength. Research interest in hybrid composites using two or more fillers to realize multiple functions are also increasing. Phase change materials (PCMs) absorb and emit energy through phase transition and can be used as a micro encapsulated structure. In this study, we fabricated hybrid composites using microcapsulated PCM (MPCM) and the natural fibrous filler, kenaf. We aimed to fabricate a composite material with improved endothermic characteristics, mechanical performance, and environmental friendliness. We analyzed the endothermic properties of MPCM and the structural characteristics of two fillers and finally produced an eco-friendly composite material. The PCM and kenaf contents were varied to observe changes in the performance of the hybrid composites. The endothermic properties were determined through differential scanning calorimetry, whereas changes in the physical properties of the hybrid composite were determined by measuring the mechanical properties.

Keywords: microencapsulated phase change material (MPCM); polylactic acid (PLA); toughening; endothermic effect; kenaf fiber; hybrid composites

1. Introduction

Polymer-based packaging materials are increasingly utilized because they are easy to process, can be molded into a variety of designs, and are lightweight [1–3]. The demand for materials with special functionality is increasing owing to their use in diverse applications such as ultraviolet (UV) absorption, special heating, and thermal shielding [4]. Among them, the heating function is one of the core functions required in biomedical and cosmetic industries, as the contents can be safely preserved from thermal deformation [5,6]. In addition, polymer-based packaging materials are developed as eco-friendly materials to mitigate environmental problems caused by waste generated during use [7,8].

Polylactic acid (PLA) is a thermoplastic polymer with a linear aliphatic polyester structure, which can be obtained by polymerizing monomers from renewable resources such as corn and potato starch [9,10]. PLA is biodegradable, environmentally friendly, and can be used in various applications, such as bio-plastic. Therefore, the use of these biodegradable materials can reduce the burden on container waste and the cost of environmental preservation. Various studies have been conducted

on imparting functionality and performance improvement to extend the field of application of PLA. Particularly, research on natural fiber-reinforced composites have been carried out to simultaneously improve the environmental friendliness and mechanical strength [11,12].

Phase change material (PCM) refers to thermal storage material used for controlling temperature changes [13]. PCMs are substances that accumulate or store heat through a type of physical change process from solid to liquid state, from liquid to solid state, from liquid to gaseous state, and from gaseous to liquid state. As the external temperature increases, the PCM reaches its own melting point. The material then changes phase from solid to liquid state and absorbs a certain amount of heat, known as melting enthalpy. The temperature of the material remains constant despite the application of heat. These properties are suitable for energy conservation and are increasingly utilized in the energy sector [14,15].

A fibrous, reinforced material with natural fibers has a low aspect ratio compared to conventional fibrous materials. Although its mechanical reinforcement performance is poor, its lightweight structure and low cost of the material makes it an economical option [16,17]. It also has the strength needed to maximize the utilization of biomass as well as to improve the durability of materials. PCM, on the other hand, is typically composed of a micro-shell type in which a shell protects the core material. Therefore, if the two materials are used simultaneously as fillers, other structural reinforcement effects can be achieved in one material. A composite material that utilizes such a heterostructure system is known as a hybrid composite material [18].

Result predictions in hybrid composites are difficult, as they are expected to have different effects for different fillers. The direction of the analysis changes according to the degree of interaction between the filler and the matrix. In hybrid composites research based on natural fibers, synergistic effects are expressed using the interaction of the two fillers with the matrix [18]. In the study of ceramic and natural-fiber hybrid composite, only the change in strength of one filler has been confirmed [19].

In this study, we investigated changes in the mechanical properties when fillers with different structures are dispersed in a PLA matrix. The study aimed to verify the feasibility of developing eco-friendly composites with improved endothermic characteristic and mechanical performance. In particular, we investigated the effect of toughening when using core-shell particles and the possibility of improving the performance. We analyzed the characteristics of PCM and kenaf fiber and investigated the feasibility of producing a new type of biocomposite material with multiple functions.

2. Experimental

2.1. Materials

In this study, the polymer matrix used in green composites was PLA, which was obtained from NatureWorks LLC (Minnetonka, MN, USA). The PLA was provided in granular form with an average diameter of 81 μm and density of 1.24 g/cm^3. Its melt flow index (MFI), glass transition temperature (T_g), and melting temperature (T_m) were 7 g/10 min (210 °C/2160 g), 57.3 ± 0.6 °C, and 146 ± 6 °C. Microencapsulated PCMs (MPCMs) were obtained from J&C Microchem, Inc. (Anseong-si, Korea) and the core consisted of paraffin wax, whereas the shell was composed of melamine formaldehyde resin. The kenaf fibers were donated by Sutongsang Company (Gyeongju-si, Korea) which was manufactured as 200 meshes using a pulverizing machine. The fibers were laid out in plastic bags after drying at 80 °C for 24 h to remove excess moisture.

2.2. Preparation of MPCMs/Kenaf Fiber/PLA Hybrid Composites

The PLA was dried at 80 °C for 12 h and stored in polyethylene bags. The dried PLA pellets were compounded with 10 and 20 phr (parts per hundred resin) of MPCMs and 10, 30, and 50 phr of kenaf fiber using a laboratory sized twin-screw extruder (BA-19 in Bautek, Pocheon, Korea) The barrel of the extruder was divided into eight zones and the barrel temperature zones of the extruder when extruding the materials were 185/195/200/200/200/195/165/140. The speed of the screws

was maintained at 200 rpm. After extruding the materials, the extruded strand was cooled in a water bath and pelletized using a pelletizer (Bautek, Korea). The zone temperature control played a key role since the dispersion of the PCM and the kenaf fiber had to be induced. Table 1 presents the mixing conditions of the hybrid composite. In general, the higher the temperature, the better the flowability of PLA and the better the dispersion. However, when cellulose is the main component of natural fiber, it is carbonized when exposed for a long time at a temperature higher than 180 °C. Byproducts from carbonization should be minimized as they affect the color and physical properties of the composite. Therefore, the composite material should be made by varying the temperature and time conditions that minimize the carbonization of kenaf [19].

Table 1. PLA (polylactic acid) hybrid composite mixing conditions (weight ratio).

Materials	Matrix	Filler	
	PLA	MPCM	Kenaf Fiber
HC.PLA 1-0	100	10	0
HC.PLA 1-1			10
HC.PLA 1-3			30
HC.PLA 1-5			50
HC.PLA 2-0		20	0
HC.PLA 2-1			10
HC.PLA 2-3			30
HC.PLA 2-5			50

2.3. Characterization

2.3.1. Scanning Electron Microscopy (SEM)

Field emission scanning electron microscopy (FE-SEM, SUPRA 55VP, Carl Zeiss, Oberkochen, Germany) was performed at acceleration voltage of 10 kV to observe the morphology of the MPCMs. Before the measurement was carried out, the sample was pre-coated with a homogeneous platinum layer (purity, 99.99 %) by ion sputtering to eliminate electron charging.

2.3.2. Differential Scanning Calorimetry (DSC)

Differential scanning calorimetry (DSC) was performed using a DSC Q200 system (TA Instruments, Chicago, IL, USA) with an RCS 90 refrigerator cooler to determine the glass transition temperature (T_g), crystallization temperature (T_c), and melting temperature (T_m) of the MPCMs and composites. Approximately 5 mg of the sample was loaded in a T_{zero} aluminum pan and high-purity nitrogen gas was used as purge gas at a flow rate of 50.0 mL/min. The samples were scanned from 0 to 150 °C at a heating rate of 5 °C/min.

2.3.3. Tensile and Flexural Strengths

The tensile and flexural strengths of the specimens were measured using a universal testing machine (AllroundLine Z010, 2000N load cell, Zwick, Ulm, Germany) according to the ASTM D 638–10 and ASTM D 790–10 standard test methods. A cross speed of 5 mm/min was used during the measurement and the mechanical properties were analyzed at room temperature. Six specimens were measured to calculate the margin of error.

2.3.4. Izod Impact Test

The Unnotched Izod Impact Strength tests were conducted at room temperature. Each value obtained represents the average for five samples.

3. Results and Discussion

The basic characteristics of the MPCM used in this study were analyzed. The SEM image and thermal properties of the PCM microcell used in this study is shown in Figure 1. The material was partially composed of small particles, mostly in the range of 10–20 μm. DSC was used to identify the endothermic part of MPCM. Furthermore, a cycle test was conducted to determine the stability of MPCM, as it exhibits different thermal characteristics during the heating and cooling process. In this study, we focused on the characteristics of temperature rise.

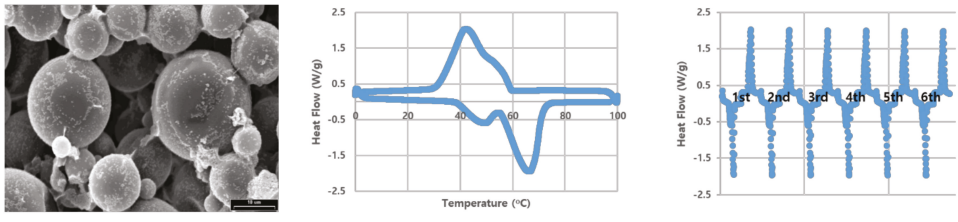

Figure 1. Basic characteristics of microencapsulated phase change material (MPCM): (**a**) SEM image (×2000); (**b**) endothermic/exothermic reaction (bottom—elevated temperature, above—decreased temperature) with DSC; (**c**) cycle test with DSC.

Figure 2 shows the results of the DSC analysis of hybrid composites with a PCM content of 10 phr. When a composite material is formed, the thermal properties of the material are changed by the interaction of the matrix and filler. In this study, the inherent endothermic characteristics of PCM should be fully reflected. Three specific temperature changes can be confirmed by DSC measurement. Zone (A) is the crystallization zone of PLA. The crystallization temperature of PLA is 89.7 °C; in this study, the crystallization temperature was determined as 87.1 °C when only PCM was used and 79.4, 87.8, and 88.4 °C when 10, 30, and 50 phr of kenaf were used, respectively. Thus, the use of PCM resulted in some reduction in the crystallization temperature. This is because the fine particles of PCM serve as a nucleus of PLA crystallization. In this case, when 10 phr of kenaf was added, the crystallization temperature decreased sharply. Small amounts of fibers and PCM particles can improve the mobility of PLA and accelerate crystallization in this process. The particles may also serve as a starting point for some crystallization. However, as the content of kenaf increases, the crystallization temperature increases. As the ratio of fibers increases, the formation of the crystal structure inside the polymer is limited, which affects the increase in the crystallization temperature. Zone (B) is the primary endothermic section formed by PCM; the primary endothermic interval is determined by the change in paraffin wax, which constitutes the PCM. The primary endothermic section of the PCM is 49.1 °C. Such an endothermic section cannot be confirmed at neat PLA. In this study, the primary endothermic section was formed in the range of 47–49 °C when PCM was utilized; this endothermic section also occurred when kenaf was used. Zone (C) is the core endothermic phase by PCM. PCM exhibited the largest endothermic characteristic at 66 °C. The core endothermic phase showed a characteristic that appears at the T_g of PLA, which was formed at 61 °C. However, in the hybrid system, the maximum endothermic characteristic occurred at 62 °C. This was determined to be influenced by the phase change of PLA. Figure 2c shows that the change in the endotherm is not affected by kenaf fiber. The PCM/PLA composites have a higher first endothermic section and a lower second endothermic section compared to neat PCM. The reason the temperature of the first endothermic section is higher is that heat conduction is delayed inside the composite material. On the other hand, it can be interpreted that the second endothermic section changes together with the T_g of the PLA.

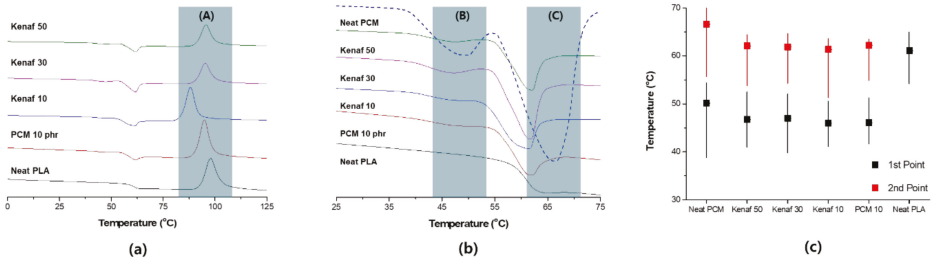

Figure 2. Analysis of heat absorption characteristics of PLA hybrid composites with phase change material (PCM) 10 phr: (**a**) Entire temperature range showing the crystallization section (A); (**b**) expansion of the heat absorption section showing the primary endothermic section (B) and the secondary endothermic section (C); (**c**) endothermic temperature of each sample.

The results of the DSC analysis of hybrid composites with a PCM content of 20 phr are shown in Figure 3. As the content of PCM increased, the main peak became more pronounced. The crystallization temperatures were 84.8 °C for only PCM 20 phr, and 77.6 °C, 82.2 °C, and 86.5 °C for 10 phr, 30 phr, and 50 phr, respectively. When kenaf was used, the endothermic temperature was partially reduced, however, it tended to increase minimally as the content increased. Zones (B) and (C) are similar to those obtained in PCM 10 phr test group. It was observed that the endothermic curve was more pronounced owing to the increase in the content of PCM.

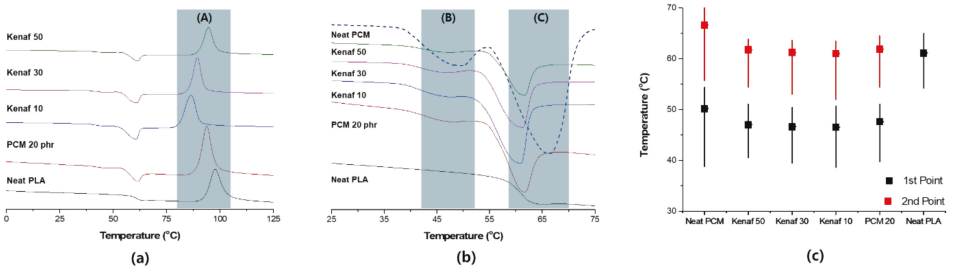

Figure 3. Analysis of heat absorption characteristics of PLA hybrid composites with PCM 20 phr: (**a**) Entire temperature showing the crystallization section (A); (**b**) expansion of the heat absorption section showing the primary endothermic section (B) and the secondary endothermic section (C); (**c**) endothermic temperature of each sample.

Figure 4 shows the change in the tensile strength according to the content of kenaf with PCM 10 phr. When PCM was used, the tensile strength was slightly reduced, however, the reduction in strength was restored by adding kenaf. The notable result was that the tensile elongation increased as the strength was maintained. In general, the use of fibers such as kenaf increases the stiffness of the composite and thus tends to decrease tensile elongation. This tendency is considered to be due to the structural characteristics of PCM. Unlike kenaf, PCM is free of strain. These deformation characteristics complement the section where the fracture is formed during the tensile process. As a result, resistance to fracture tends to improve, which is known as the toughening effect. In general, PLA is a brittle polymer, and such properties must be improved when the material is used. This trend has the same effect even when the content of PCM increases. As shown in Figure 5, the tensile strength decreased significantly when the content of PCM was increased to 20 phr. However, tensile strength recovery by kenaf fiber occurred in a similar process. The tensile elongation was larger at small contents of PCM. PCM was distributed throughout and served to compensate for the increase in stiffness due to kenaf. It can be concluded that PCM, which is a spherical particle, and kenaf, which is a linear particle, complement each other. The use of linear fillers increases the modulus of elasticity, but leads to

brittleness. When a spherical filler is used, the impact absorption properties are strengthened, whereas the tensile strength is weakened. However, the two materials used in this study tend to overcome the disadvantages of using each material individually through a synergistic effect [20].

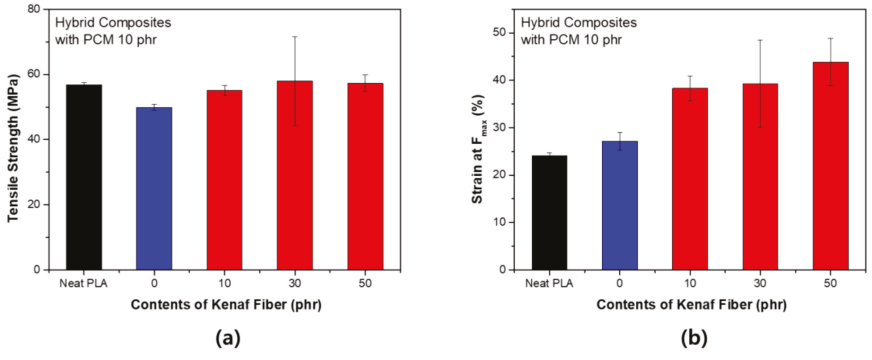

Figure 4. Tensile strength of PLA hybrid composites with PCM 10 phr: (**a**) Maximum stress (F_{max}); (**b**) strain at F_{max}.

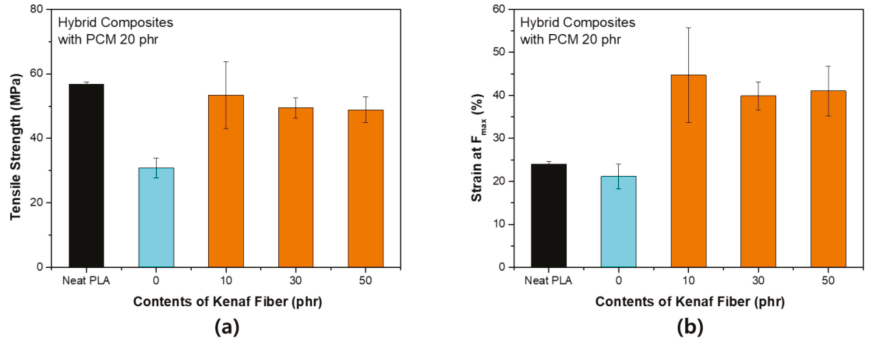

Figure 5. Tensile strength of PLA hybrid composites with PCM 20 phr: (**a**) Maximum stress (F_{max}); (**b**) strain at F_{max}.

Figure 6 shows a graphical representation of the changing tensile failure phenomena when MPCM was used. The improved tensile properties of MPCM were due to the increased degree of freedom, which changed internally through the use of MPCM. A neat PLA is a material with Poisson's ratio of 0.36 [21] and is vulnerable to deformation. However, if the MPCM is dispersed internally, it compresses, making it relatively advantageous to vary the tensile strength. The tensile strength characteristics change depending on the structural characteristics [22]. When hybrid filler is used, the spherical filler is placed between the fibrous filler and matrix and the fluidity of the polymer is enhanced. Therefore, the hybrid filler exhibits a completely different characteristic compared to when it is used individually. The use of two fillers tends to increase brittleness, however, when used together, a synergistic toughening effect can be expected [23,24].

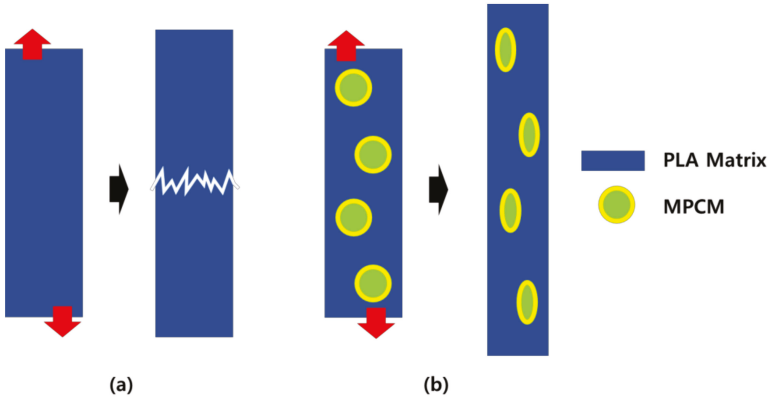

Figure 6. Estimation of the toughening effect according to use of MPCM: (**a**) Neat PLA; (**b**) PLA with MPCM.

Figure 7 shows the S–S curve from the tensile strength test of each sample. In Figure 7a,b, the strength decreased when PCM was used, whereas the graph tended to move upward when kenaf was used. At a PCM content of 10 phr, the graph shifted to the right as the kenaf content increased, whereas at a PCM content of 20 phr, the graph shifted to the left as the kenaf content increased. The shift in the graph indicates that the characteristics of the material were changing. At a small content of PCM, a hybrid effect occurred between PCM and kenaf fibers, whereas when the PCM content increased, it can be considered that a negative effect occurred in the spatial arrangement. PCM, which spatially occupies a large area, inhibits the dispersion of kenaf fibers so that a negative result can occur. At a PCM content of 10 phr, the tensile strength increased slightly when kenaf was added, whereas the strength tended to decrease slightly at a PCM content of 20 phr. The two trends can be interpreted to be due to the increase in the spatial ratio of the PCM and kenaf fibers in the composite material. The distribution of the matrix is important for the composite material to exhibit sufficient mechanical strength. As the filler content increased, the dispersion and bonding of the filler were adversely affected.

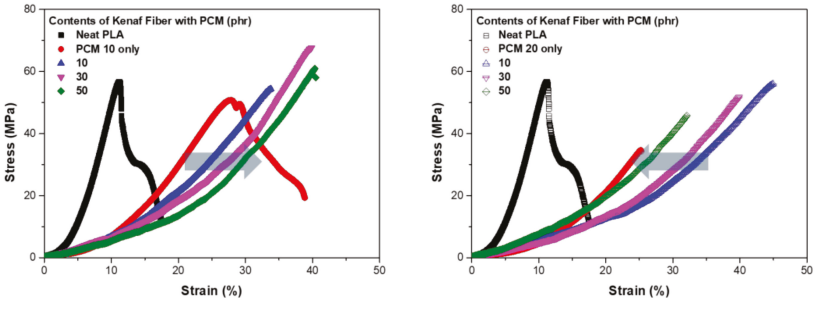

Figure 7. S–S curve from tensile strength test: (**a**) PCM 10 phr; (**b**) PCM 20 phr.

Figure 8 shows the change in the flexural strength according to the content of kenaf for PCM 10 phr. The flexural strength tended to be quite different from the tensile strength. As the content of kenaf increased, both the flexural strength and the maximum load deflection tended to decrease. The fibers did not play a major role in reinforcing the mechanical strength during the bending process, since the surface of the kenaf fiber was not subjected to any surface treatment. In addition, PCM has a relatively flexible shell. The shell compensates for fracture during deformation in the tensile process, however, in the bending process, it reduces the flexural strength according to the fracture due

to compression and weak interfacial bonding characteristics. When the content of PCM increased to 20 phr, a larger decrease occurred. However, as shown in Figure 9, the flexural strength seemed to be partially restored by the partial reinforcement effect of the fibers. There was no overall tendency for PCM 20 phr. This is because the bending strength decreased significantly when only the PCM was used. It is considered that even if kenaf fibers were used, the strength could not be supplemented.

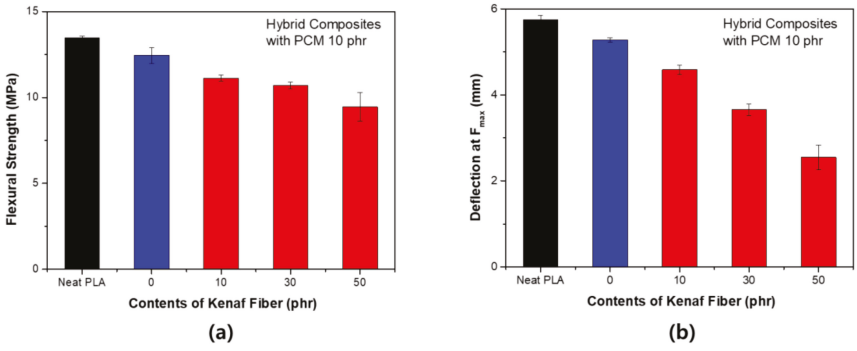

Figure 8. Flexural strength of PLA hybrid composites with PCM 10 phr: (**a**) Maximum stress (F_{max}); (**b**) deflection at F_{max}.

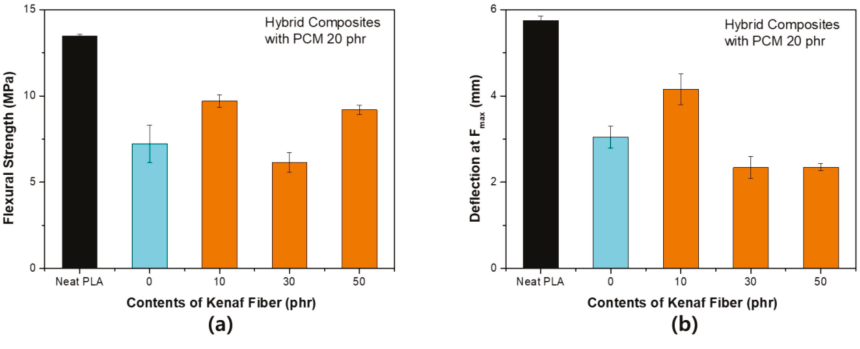

Figure 9. Flexural strength of PLA hybrid composites with PCM 20 phr: (**a**) Maximum stress (F_{max}); (**b**) deflection at F_{max}.

Figure 10 shows the S–S curve obtained from the flexural strength test of each specimen. As the filler was used differently compared to the tensile strength, the slope of the graph increased, and the maximum strength tended to decrease. The S–S curves between samples were not significantly different under PCM 20 phr conditions. These results highlighted the irregularity of the results in Figure 9. The fracture shape at the flexural strength showed a completely different tendency compared to that of the tensile strength. In the process of using the composite filler, the destruction tended to proceed straight after the yield point. The elastic modulus at the flexural strength can be expressed by the following equation [25]:

$$\text{Flexural modulus} = \frac{FL^3}{4wdh^3} \quad (1)$$

where L is the support span, w and h are the width and height of the beam, respectively, and d is the deflection due to the load F applied in the middle of the beam. In this case, $L/(wh)$ is constant. Therefore, the elastic modulus is proportional to the strength and inversely proportional to the deflection.

$$\text{Flexural modulus} \propto \frac{F}{d} \quad (2)$$

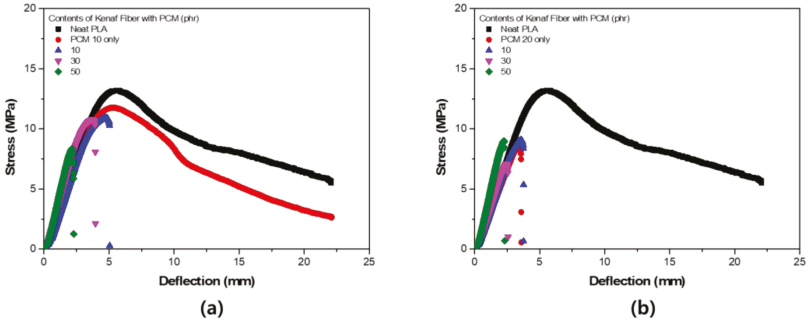

Figure 10. S–S curve of flexural strength test: (**a**) PCM 10 phr; (**b**) PCM 20 phr.

Figure 11 shows the scale factor of the flexural modulus. The utilization of PCM served to reduce the scale factor. This means that PCM did not play a strong binding role in compression and tensioning of the material. On the other hand, when kenaf was used, the scale factor tended to increase as the content increased. The increase in the elasticity factor was considered to be due to the fiber-reinforcing effect. The strong elastic force of the fiber was reflected in the interaction with the fiber, but the bond with the fiber deteriorated, leading to the destruction. These characteristics were considered to be the result of the short fiber-reinforced structure.

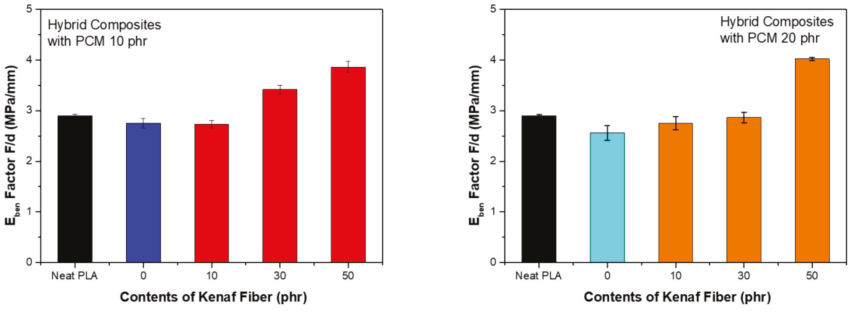

Figure 11. Scale factor of flexural modulus: (**a**) PCM 10 phr; (**b**) PCM 20 phr.

Figure 12 shows the impact strength evaluation results of each specimen. When PCM was utilized, the impact strength tended to increase, whereas when kenaf was used, the impact strength tended to decrease. When PCM alone was used, the impact strength greatly increased when 10 phr is used, but when the PCM was used at 20 phr, the strength tended to decrease again. The impact strength was improved when the spherical filler is used, but the strength tended to reduce when the specific amount was exceeded. As the amount of filler increases, the bond between the fillers also strengthens. The optimum content depends on the size and shape of the filler [26]. In the previous tensile strength test, the tensile elongation increased, but the tensile strength did not change significantly. Overall, the modulus of elasticity tended to decrease, which indicates that the material itself was becoming soft. It can be deduced that the impact strength tended to decrease as the physical properties of the material weakened. In general, the fiber reinforced composite material tended to exhibit increased impact strength depending on the fiber content. However, in this case, it can be expected that the fiber acted as a crack initiation point for reducing the impact strength owing to the weak bonding force between the fiber and the matrix. Thus, the increase in the fiber content had a negative effect.

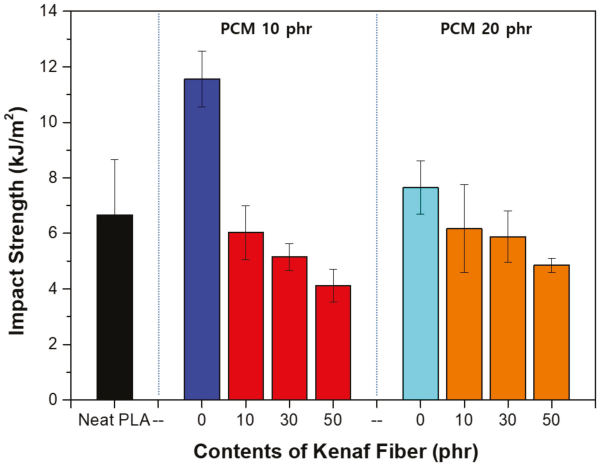

Figure 12. Impact strength of PLA hybrid composites.

Figure 13 shows the toughening effect process of MPCM. The toughening effect of MPCM was confirmed again by the impact strength evaluation. When an external impact is applied, it is possible to change the fracture pathway and at the same time absorb the impact so that excellent toughening effect can be achieved. The impact absorption characteristics tended to decrease with the content because the porosity increased inside the composite due to an increase in the bonds between the particles present in Figure 13.

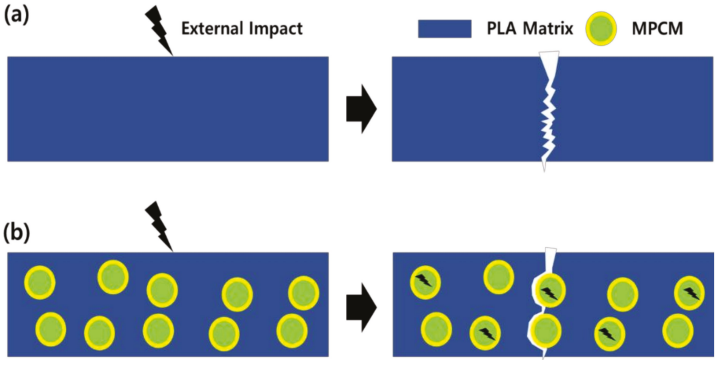

Figure 13. Toughening effect according to use of MPCM under external effect: (**a**) Neat PLA; (**b**) PLA with MPCM.

4. Conclusions

Hybrid composites fabricated using MPCM and kenaf fibers reflect the characteristics of the fillers. The endothermic characteristics tended to increase as the content of PCM increased. The use of kenaf fibers reinforced both the tensile strength and elongation. However, both fillers had a negative influence on the flexural strength. The toughening effect of the micro-shell was verified by evaluating the impact strength. The results showed that the weaker interfacial bonding force had a negative effect on the impact strength. By combining the fillers with two different structures and functions, we identified areas where complementary effects were realized and where they were not. Therefore, the findings of this study will be useful in developing eco-friendly composites with improved functions in the future.

Author Contributions: J.-W.P. and H.-J.K. conceived and designed the experiments; J.-H.S. and G.-S.S. performed the experiments; J.-W.P. and S.-W.J. analyzed the data; G.-S.S. and K.-B.S. contributed reagents/materials/analysis tools; J.-W.P. wrote the manuscript.

Acknowledgments: This work was supported by 'SEOUL R&BD Program CI160061'.

Conflicts of Interest: The authors declare no conflict of interest.

References

1. Peyroux, J.; Dubois, M.; Tomasella, E.; Petit, E.; Flahaut, D. Enhancement of surface properties on commercial polymer packaging films using various surface treatment processes (fluorination and plasma). *Appl. Surf. Sci.* **2014**, *315*, 426–431. [CrossRef]
2. Ghaani, M.; Cozzolino, C.A.; Castelli, G.; Farris, S. An overview of the intelligent packaging technologies in the food sector. *Trends Food Sci. Technol.* **2016**, *51*, 1–11. [CrossRef]
3. Kissi, E.; Ahmed, I.; Mohamed, S. PLA/PBAT bionanocomposites with antimicrobial natural rosin for green packaging. *ACS Appl. Mater.* **2017**, *9*, 20132–20141.
4. Blanco, I.; Siracusa, V. Kinetic study of the thermal and thermo-oxidative degradations of polylactide-modified films for food packaging. *J. Therm. Anal. Calorim.* **2013**, *112*, 1171–1177. [CrossRef]
5. Youssef, A.M.; El-Sayed, S.M. Bionanocomposites materials for food packaging applications: Concepts and future outlook. *Carbohydr. Polym.* **2018**, *193*, 19–27. [CrossRef] [PubMed]
6. Râpă, M.; Miteluţ, A.C.; Tănase, E.E.; Grosu, E.; Popescu, P.; Popa, M.E.; Rosnes, J.T.; Sivertsvik, M.; Darie-Niţă, R.N.; Vasile, C. Influence of chitosan on mechanical, thermal, barrier and antimicrobial properties of PLA-biocomposites for food packaging. *Compos. Part B Eng.* **2016**, *102*, 112–121. [CrossRef]
7. Bharimalla, A.; Deshmukh, S.; Vigneshwaran, N.; Patil, P.; Prasad, V. Nanocellulose-polymer composites for applications in food packaging: Current status, future prospects and challenges. *Polym. Plast. Technol. Eng.* **2017**, *56*, 805–823. [CrossRef]
8. Rabnawaz, M.; Wyman, I.; Auras, R.; Cheng, S. A roadmap towards green packaging: The current status and future outlook for polyesters in the packaging industry. *Green Chem.* **2017**, *19*, 4737–4753. [CrossRef]
9. Carlson, D.; Nie, L.; Narayan, R.; Dubois, P. Maleation of polylactide (PLA) by reactive extrusion. *J. Appl. Polym. Sci.* **1999**, *72*, 477–485. [CrossRef]
10. Nyambo, C.; Mohanty, A.K.; Misra, M. Effect of maleated compatibilizer on performance of PLA/wheat straw-based green composites. *Macromol. Mater. Eng.* **2011**, *296*, 710–718. [CrossRef]
11. Attaran, S.A.; Hassan, A.; Wahit, M.U. Materials for food packaging applications based on bio-based polymer nanocomposites: A review. *J. Thermoplast. Compos. Mater.* **2017**, *30*, 143–173. [CrossRef]
12. Bher, A.; Uysal Unalan, I.; Auras, R.; Rubino, M.; Schvezov, C.E. Toughening of poly (lactic acid) and thermoplastic cassava starch reactive blends using graphene nanoplatelets. *Polymers* **2018**, *10*, 95. [CrossRef]
13. Akeiber, H.; Nejat, P.; Majid, M.Z.A.; Wahid, M.A.; Jomehzadeh, F.; Famileh, I.Z.; Calautit, J.K.; Hughes, B.R.; Zaki, S.A. A review on phase change material (PCM) for sustainable passive cooling in building envelopes. *Renew. Sustain. Energy Rev.* **2016**, *60*, 1470–1497. [CrossRef]
14. Pielichowska, K.; Pielichowski, K. Phase change materials for thermal energy storage. *Prog. Mater. Sci.* **2014**, *65*, 67–123. [CrossRef]
15. Yang, J.; Qi, G.-Q.; Liu, Y.; Bao, R.-Y.; Liu, Z.-Y.; Yang, W.; Xie, B.-H.; Yang, M.-B. Hybrid graphene aerogels/phase change material composites: Thermal conductivity, shape-stabilization and light-to-thermal energy storage. *Carbon* **2016**, *100*, 693–702. [CrossRef]
16. Ahmad, F.; Choi, H.S.; Park, M.K. A review: Natural fiber composites selection in view of mechanical, light weight, and economic properties. *Macromol. Mater. Eng.* **2015**, *300*, 10–24. [CrossRef]
17. Campilho, R.D. *Natural Fiber Composites*; CRC Press: Boca Raton, FL, USA, 2015.
18. Kwon, H.-J.; Sunthornvarabhas, J.; Park, J.-W.; Lee, J.-H.; Kim, H.-J.; Piyachomkwan, K.; Sriroth, K.; Cho, D. Tensile properties of kenaf fiber and corn husk flour reinforced poly (lactic acid) hybrid bio-composites: Role of aspect ratio of natural fibers. *Compos. Part B Eng.* **2014**, *56*, 232–237. [CrossRef]
19. Park, J.W.; Kim, H.; Lee, J.H.; Jang, S.W.; Kim, H.J. Evaluation of mechanical performance and flame retardant characteristics of biomass-based eva composites using intumescent flame retardant technology. *J. Korean Wood Sci. Technol.* **2018**, *46*, 189–201.

20. Chung, T.J.; Park, J.W.; Lee, H.J.; Kwon, H.J.; Kim, H.J.; Lee, Y.K.; Yin Tze, W.T. The improvement of mechanical properties, thermal stability, and water absorption resistance of an eco-friendly PLA/kenaf biocomposite using acetylation. *Appl. Sci.* **2018**, *8*, 376. [CrossRef]
21. Torres, J.; Cotelo, J.; Karl, J.; Gordon, A.P. Mechanical property optimization of FDM PLA in shear with multiple objectives. *JOM* **2015**, *67*, 1183–1193. [CrossRef]
22. Yu, Z.Z.; Ou, Y.C.; Qi, Z.N.; Hu, G.H. Toughening of nylon 6 with a maleated core-shell impact modifier. *J. Polym. Sci. Part B Polym. Phys.* **1998**, *36*, 1987–1994. [CrossRef]
23. Mittal, V. *Spherical and Fibrous Filler Composites*; John Wiley & Sons: Hoboken, NJ, USA, 2016; Volume 8.
24. Rasana, N.; Jayanarayanan, K. Polypropylene/short glass fiber/nanosilica hybrid composites: Evaluation of morphology, mechanical, thermal, and transport properties. *Polym. Bull.* **2018**, *75*, 2587–2605. [CrossRef]
25. Zweben, C.; Smith, W.S.; Wardle, M.W. Test methods for fiber tensile strength, composite flexural modulus, and properties of fabric-reinforced laminates. In *Composite Materials: Testing and Design (Fifth Conference)*; ASTM International: West Conshohocken, PA, USA, 1979.
26. Fu, S.-Y.; Feng, X.-Q.; Lauke, B.; Mai, Y.-W. Effects of particle size, particle/matrix interface adhesion and particle loading on mechanical properties of particulate–polymer composites. *Compos. Part B Eng.* **2008**, *39*, 933–961. [CrossRef]

polymers

MDPI

Article

Polymeric Composites with Embedded Nanocrystalline Cellulose for the Removal of Iron(II) from Contaminated Water

Anayet Kabir [1], Matthew J. Dunlop [1,2], Bishnu Acharya [2], Rabin Bissessur [1] and Marya Ahmed [1,2,*]

[1] Department of Chemistry, University of Prince Edward Island, Charlottetown, PE C1A 4P3, Canada; akabir@upei.ca (A.K.); mdunlop@upei.ca (M.J.D.); rabissessur@upei.ca (R.B.)

[2] Faculty of Sustainable Design & Engineering, University of Prince Edward Island, Charlottetown, PE C1A 4P3, Canada; bacharya@upei.ca

* Correspondence: marahmed@upei.ca

Received: 16 November 2018; Accepted: 9 December 2018; Published: 12 December 2018

Abstract: The exponential increase in heavy metal usage for industrial applications has led to the limited supply of clean water for human needs. Iron is one of the examples of heavy metals, which is responsible for an unpleasant taste of water and its discoloration, and is also associated with elevated health risks if it persists in drinking water for a prolonged period of time. The adsorption of a soluble form of iron (Fe^{2+}) from water resources is generally accomplished in the presence of natural or synthetic polymers or nanoparticles, followed by their filtration from treated water. The self-assembly of these colloidal carriers into macroarchitectures can help in achieving the facile removal of metal-chelated materials from treated water and hence can reduce the cost and improve the efficiency of the water purification process. In this study, we aim to develop a facile one-pot strategy for the synthesis of polymeric composites with embedded nanocrystalline cellulose (NCC) for the chelation of iron(II) from contaminated water. The synthesis of the polymeric composites with embedded nanoparticles was achieved by the facile coating of ionic monomers on the surface of NCC, followed by their polymerization, crosslinking, and self-assembly in the form of three-dimensional architectures at room temperature. The composites prepared were analyzed for their physiochemical properties, antifouling properties, and for their iron(II)-chelation efficacies in vitro. The results indicate that the embedded-NCC polymeric composites have antifouling properties and exhibit superior iron(II)-chelation properties at both acidic and basic conditions.

Keywords: polymeric composites; antifouling; metal binding; iron chelation; polydopamine coating; free-radical polymerization

1. Introduction

The exponential increase in heavy metal usage due to rapid urbanization and industrialization has caused detrimental effects on human health and the environment [1–4]. According to a recent estimate, the toxicity of heavy metal ions and their contamination in water resources leads to an estimated two million casualties per year. The presence of heavy metal ions such as cadmium, mercury, chromium, lead, and iron in drinking water is associated with organ damage, birth defects, and carcinogenesis [1]. Iron is one of the most common heavy metals in the Earth's crust, which is required for normal physiological functions of the human body, in trace amounts. However, the presence of high concentrations of iron in ground water due to natural resources or human activity and the continuous exposure of high iron content to humans is associated with elevated health risks, including organ damage, heart diseases, and ophthalmic disorders [1–7]. The soluble form of iron (Fe^{2+}) is associated

with an unpleasant taste, discoloration, turbidity, and microbial growth in water resources, and its removal from drinking water is the most cumbersome task [1–7]. Recently, tremendous efforts have been focused on the removal of iron(II) from water resources and some of the most studied techniques for this purpose are oxidation, electrolysis, ion exchange, adsorption, and electrocoagulation [1–9].

In comparison to the other methods, adsorption is the most economical, facile, and commonly used method for the removal of heavy metal ions from drinking water, and polymeric materials, specifically polyelectrolytes, comprise the major group of chemical adsorbents, being capable of excellent metal-chelating efficacies, due to the presence of diverse functional groups on their surface and their facile regeneration in acidic or basic conditions [2–4,7,9–11]. The incorporation of polyelectrolytes on nanoparticles further improves the metal-chelation efficacies, as the embellishment of functional group-laden polymers on the three-dimensional surface of nanomaterials enhances the metal ion-binding capacities of the resultant nanocomposites [12,13]. Owing to their biocompatibility, low toxicity, and low density, carbon-based nanoadsorbents such as carbon nanotubes, nanocrystalline cellulose (NCC), carbon aerogels, and their polymeric nanocomposites have received significant interest for water purification applications [12–14]. For example, the synthesis of polydopamine-coated NCC was recently reported, and these polymer-doped nanomaterials were found to exhibit superior iron(II) and iron(III)-binding efficacies [13]. However, the usage of polyelectrolytes or their nanocomposites for the chelation of heavy metal ions requires extra steps of separation, such as centrifugation, filtration, or sedimentation, to remove the metal-adsorbed colloidal carriers from purified water, which further increases the complexity and cost of the water purification system. To simplify the process of water purification, the self-assembly of nanomaterials into three-dimensional macroscopic architectures may produce diverse composites with superior properties compared to those of individual nanomaterials [12,15].

The self-assembly of polyelectrolytes into three-dimensional architectures has recently been reported by Kulig et al. [15], but the incorporation of nanoparticles such as NCC into these macroscopic architectures can be a complex task. The covalent attachment of polyelectrolytes on the surface of NCC, followed by their self-assembly into discrete materials, may require complex chemical reactions, which will reduce the number of active sites available on the polymer backbone, hence reducing the metal-chelation properties and self-assembly capabilities of the resultant composites. Zhi and coworkers reported the synthesis of graphene foams with lead ion-binding efficacies; these composites were prepared by electrostatic interactions between cationic moieties, tetraethylenepentamine (TEPA), and anionic carboxyl groups of graphene oxide, but the reaction was performed at high pressure and temperature [14].

The recent interest in the strongly adhesive properties of polydopamine coatings, along with their capability to polymerize ionic and nonionic monomers on a variety of surfaces under slightly basic conditions, may provide an alternative and facile method to coat ionic species on the surface of NCC, hence eliminating the need for complex chemical methods to achieve the surface functionalization of NCC [16,17]. Moreover, in comparison to natural polyelectrolyte-based complexes, which offer limited control regarding tuning the physiochemical properties (cation-to-anion ratio and molecular weights) of self-assembled materials, the coating of ionic monomers on the surface of NCC, followed by their facile polymerization, crosslinking, and self-assembly may provide greater control of the physiochemical properties of resultant composites, and this may translate into their superior iron(II)-chelation properties. In this study, we aim to develop polymeric composites with embedded NCC by a one-pot method, by coating NCC with polydopamine under slightly basic conditions. Polydopamine-coated NCC was then decorated with ionic monomers, namely methacrylic acid and tetraethylenepentamine methacrylamide (TEPMA), followed by their self-assembly, polymerization, and crosslinking in the presence of *N*,*N*′-methylenebisacrylamide by a free-radical polymerization method to yield polymeric composites with embedded NCC which have optimal strength. The composites produced were characterized by Fourier transform infrared spectroscopy (FTIR), thermogravimetric analysis (TGA), scanning electron microscopy (SEM), and X-ray diffraction analysis (XRD) and were studied for

iron(II)-chelation efficacies and antifouling properties in vitro. To the best of our knowledge, this is the first report describing the preparation of polyelectrolytes with embedded nanoparticles by the physical and chemical crosslinking of ionic monomers on the surface of nanoparticles, in which the materials are studied for their iron(II)-chelation efficacies in situ.

2. Experimental Procedure

2.1. Materials

Nanocrystalline cellulose was extracted from tunicates according to a previously established procedure [18]. Briefly, club tunicates were collected from Malpeque Bay, Prince Edward Island (PEI). The tunicate samples were taken from several mussel socks, immediately placed into freezer bags, and frozen. Frozen samples were thawed in a fume hood. The tunic was then liberated from the internal organs of the tunicate using a scalpel. The tunic samples were extensively washed with deionized water. Crystalline cellulose was then isolated from club and vase tunicates isolated from Malpeque Bay, PEI, via the prehydrolysis–kraft cooking–bleaching method. The prehydrolysis, kraft cooking, and bleaching steps were done in a PARR 4748 Large Capacity Acid Digestion Bomb equipped with polytetrafluoroethylene (PTFE) liner. Prehydrolysis and kraft cooking reactions were each carried out at 180 °C for 2 h. The bleaching step was carried out at 75 °C for a 1-h duration. A 20:1 ratio of solid to solution was used. The reactor was heated to temperature in a Paragon Sentry Xpress 4.0 oven, and agitation was accomplished by physical shaking of the reactor at 10-minute intervals. Products were isolated via vacuum filtration using medium-pore-size fritted filters. The product was then dried in a vacuum oven at 60 °C for 24 h. The isolation and drying method was kept consistent for each step. The crystalline cellulose obtained following the bleaching step was centrifuged at 10,000 rpm and dialyzed against deionized water for 5 days to purify the product. Ultrasonication of the purified crystalline cellulose resulted in the formation of NCC [18]. The length of the NCC used was 1567 ± 638 nm and the diameter was 18.3 ± 10.1 nm.

Tetraethylenepentamine (TEPA), methacrylic anhydride, hydroquinone (HQ), methacrylic acid (MA), potassium persulfate (KPS), *N*,*N*,*N*′,*N*′-tetramethylethylenediamine (TEMEDA), and *N*,*N*′-methylenebisacrylamide were purchased from Sigma-Aldrich (Canada). Dopamine hydrochloride (DOPA) was purchased from Alfa Aesar, (Canada). Methanol, acetone, 2-propanol, and ammonium hydroxide (NH_4OH) were purchased from Fisher Scientific (Canada).

2.2. Synthesis of Tetraethylenepentamine Methacrylamide (TEPMA·2HCl)

In brief, 5 mmol of TEPA was dissolved in 2 mL of methanol in the presence of small amount (~1 mg) of hydroquinone, followed by the addition of 6.5 mmol of methacrylic anhydride dropwise into the solution. The solution was stirred overnight. Next day, the solution was protonated with 2.5 mL of 12.1 M hydrochloric acid (HCl) and methanol was removed under reduced pressure. The creamy substance was crystallized with acetone and the dried solid obtained was stirred in the presence of 10 mL of 2-propanol in a 70 °C preheated oil bath for 20 min to remove multi-methacrylamide amines. The crude TEPMA obtained was dissolved in 10 mL of methanol at room temperature for 20 min and the mixture was filtered to obtain pure TEPMA·2HCl at 70% yield. The purified TEPMA salt was analyzed by ^{1}H-NMR and ^{13}C NMR using a Bruker 300 MHz NMR instrument. The molar mass of the monomer was obtained by electron spray ionization mass spectrophotometry (ESI-MS) (University of Toronto mass spectrophotometer facility).

The ESI-MS result reveals that the molecular weight of the pure TEPMA salt is 326.6 g/mol, which corresponds to TEPMA·2HCl formation.

^{1}H NMR (D_2O, ppm): δ 1.8 (s, 3H, CH_3), 3.2–3.8 (m, 16H, CH_2), 5.6 (s, 1H, C=CH_2), 5.8 (s, 1H, C=CH_2).

DEPT-45 spectrum of ^{13}C-NMR (D_2O, ppm): δ 17.8, 35.6, 36.4, 43.4, 43.6, 43.7, 43.9, 44.9, 48.5, 122.4.

2.3. Synthesis of Composites

NCC stock solution was prepared at 10% *w*/*v* in deionized water. The commercially available methacrylic acid was passed through a silica column to remove any inhibitor. Then, 1 mL of NCC stock solution was coated with 68 μmol of DOPA in the presence of 1.14 mM NH_4OH and the solution was stirred for 20 min. The reaction was cooled to 0 °C and varying concentrations of TEPMA·2HCl and methacrylic acid were added in the presence of 10–20 mol % *N*,*N*′-methylenebisacrylamide (cross-linker), 10 μM potassium persulfate, and 20 μL TEMEDA. The formation of composites was confirmed by vial inversion test and the gelation time was recorded. The stoichiometric details of the synthesis of NCC-embedded polymeric composites are summarized in Table 1. The composites prepared were washed three times with deionized water and were vacuum-dried at room temperature to obtain pure materials. Sample 5 (polymeric composite 5 (PC5) in Table 1) resulted in the successful formation of the desired composites and was further subjected to thermal, mechanical, and physical characterization and was evaluated for its iron-chelation efficacies in situ.

Table 1. The stoichiometric ratios of monomers and crosslinker studied for the synthesis of polymeric composites.

Sample ID	NCC (mg/mL)	TEPMA:MA (μM)	Crosslinker (mol %)	Gelation Time (min)	Gel Morphology
PC1	10	90:90	10	N/A	N/A
PC2	10	90:180	10	45	Thixotropic gel
PC3	10	90:180	20	30	Thixotropic gel
PC4	10	90:360	10	45	Thixotropic gel
PC5	10	90:360	20	15	Hard gel

Polydopamine-coated NCC was prepared as a control, by reacting 10 mg/mL of NCC with 68 μmol of DOPA in the presence of 1.14 mM NH_4OH and stirring the solution for 20 min. Polydopamine (PDA)-coated NCC was purified by centrifugation and was washed with deionized water three times to remove any unreacted material. PDA-coated NCC was dried and used for further characterization and analysis.

2.4. Protein Absorption Capacity of Composites

The protein absorption capacity of the NCC-embedded polymeric composites was measured as follows: Bovine serum albumin (BSA) (500 μg/mL) was incubated with 4 mg/mL of composites in phosphate buffer saline (PBS) buffer (pH 7.4) for 24 h. The composites were then washed 3 times, the supernatant was discarded, and the composites were immersed in PBS for 24 h to release any imbibed protein. The supernatant was then analyzed for the presence of BSA using the bicinchoninic acid (BCA) assay, according to the manufacturer's protocol.

2.5. Evaluation of Iron Ion-Binding Capacity

Ferrous sulfate was used as the iron source for the metal-binding experiments, and the amount of the Fe^{2+} ion adsorbed by the composites was measured by UV spectrophotometry, according to a recently reported protocol [19]. The general procedure for the iron-binding (Fe^{2+}) analysis is given below.

Ferrous sulfate solutions of various concentrations (1.37–30 μg/mL) were prepared in a 0.23 mM sodium chloride and 0.31 μM citric acid stock solution of pH 3.8 and 10, respectively. The mixture was incubated for three hours and the pH of the resultant suspension was adjusted to 3.8. Then, 0.3% (*w*/*w*) aqueous phenanthroline and 10.0% (*w*/*w*) aqueous hydroxylamine hydrochloride was added into the solution. The solution was stirred for 5 minutes and was allowed to stand for another 3 h. The absorption spectrum of the solution was recorded at 508 nm, and a calibration curve of the absorbance versus concentration of iron(II) was prepared (see Supporting Information, Figure S6).

To evaluate the efficacies of polymeric composites for iron(II)-chelation, 4 mg/mL concentration of dried NCC composites were added into the ferrous sulfate stock solutions with different pH (3.8 and 10) and the mixtures were incubated for various time periods (1 min–72 h). The pH of the filtrate was adjusted to 3.8 and the amount of iron in the supernatant was evaluated as described above. The equilibrium adsorption of the composites (Qe, mg/g) was calculated by taking into consideration the initial amount of iron in the solution and the amount of iron present in supernatant after the adsorption, according to Equation (1); the metal removal efficiency % (R%) was calculated by Equation (2); and the adsorption capacity (Q_t) at time 't' was calculated by Equation (3):

$$Q_e = [(C_0 - C_e) \times V]/m \quad (1)$$

$$R\ (\%) = [C_0 - C/m] \times 100 \quad (2)$$

$$Q_t = [(C_0 - C_t) \times V]/m \quad (3)$$

where C_0 is the initial concentration, C_t is the concentration at given time t, and C_e is the equilibrium concentration of metal ions (mg/L) in solution; V is the total volume of solution (L); and m is the mass of composites [14,20,21].

2.6. Sorption Kinetics

To describe the sorption kinetics, pseudo-first-order kinetic and pseudo-second-order kinetic models were tested. The linear form of pseudo-first-order kinetics was used for fitting the sorption kinetics and is formulated below:

$$\ln (q_e - q_t) = \ln q_e - k_1 t \quad (4)$$

where q_e and q_t are the amount of metal ions absorbed in mg/g at equilibrium and at time 't', respectively. k_1 is the rate constant of the sorption per hour. The graph of $\ln (q_e - q_t)$ versus t was plotted, and k_1 and $\ln q_e$ were calculated from the slope and intercept of the line, respectively.

The pseudo-second-order kinetic model is expressed as:

$$t/q_t = 1/k_2\ (q_e)^2 + (1/q_e)\ t \quad (5)$$

The graph of t/q_t versus t was plotted, and q_e (theoretical value) and k_2 (rate constant in g/mg/hr) was calculated from the slope and intercept of the line, respectively.

Sorption isotherms were fitted by linear form of the Langmuir isotherm:

$$C_e/Q_e = C_e/q_m + 1/K_L\ q_m \quad (6)$$

where q_m is the maximum absorption capacity of polymeric composites embedded with NCCs (mg/g), C_e is the equilibrium concentration of the adsorbate in solution (mg/L), and K_L is the Langmuir affinity constant (L/mg).

The data were also fitted by the linear form of the Freundlich model:

$$\ln q_e = \ln K_F + 1/n \ln C_e \quad (7)$$

where K_F is the Freundlich constant of the relative adsorption capacity of the adsorbent and $1/n$ indicates the heterogeneity factor or adsorption intensity [20,21].

2.7. Characterization Techniques

2.7.1. Powder X-ray Diffraction (XRD)

XRD diffractograms of the NCC composite samples were recorded using a Bruker AXS D8 Advance instrument, which was equipped with a graphite monochromator, variable divergence slit,

variable antiscatter slit, and a scintillation detector. Cu (Kα) radiation (λ = 1.524 Å) was used, and the measurements were performed in air at room temperature from 2°–60° (2θ). Dried samples were milled to powder and deposited on double-sided scotch tape, which was mounted on glass slides.

2.7.2. Thermogravimetric Analysis (TGA)

The thermal properties of composites were studied using TGA (TA Instruments TGA Q500). The samples were heated from 25 to 650 °C at a heating rate of 10 °C/min under an atmosphere of 40 mL/min nitrogen and 60 mL/min air.

2.7.3. Scanning Electron Microscopy (SEM)

To assess the surface morphology via scanning electron microscopy (SEM), micrographs were obtained on a Delong America LVEM5 Benchtop SEM instrument. Powdered samples were deposited onto stubs and held in place with carbon tape. All samples were sputter-coated with 60:40 Au/Pd prior to imaging using a SPI-Module Sputter Coater (SPI Supplies).

2.7.4. Attenuated Total Reflection Fourier Transform Infrared Spectroscopy (ATR-FTIR)

ATR-FTIR was performed on a Bruker Alpha-T single-reflection attenuated ATR module equipped with a platinum–diamond crystal. Samples were dried, milled to powder, and immediately analyzed. Spectra were collected from 16 scans per sample and subtracted from a background spectra between 375–4000 cm^{-1} at a resolution of 0.9 cm^{-1}.

3. Results and Discussion

3.1. Synthesis of NCC-Embedded Composites

Polymer composites with embedded nanoparticles been the subject of much interest for the development of novel materials with improved mechanical and physiochemical properties [22–26]. The synthesis of polymeric composites with embedded NCC generally involves the mixing of nanoparticles in preformed polymeric solution, followed by their chemical crosslinking to yield the desired composites. However, the packing of NCC into polymeric materials often provides limited advantages, due to the problems in achieving high concentrations of NCC in polymeric solutions and issues associated with the compatibility of functional groups on the surface of NCC with those of the polymeric materials [22–25]. In an effort to develop NCC–polyelectrolyte-complexed composites, we utilized the strongly adhesive properties of polydopamine to anchor ionic monomers on the surface of NCC, followed by their polymerization, crosslinking, and self-assembly at room temperature (Scheme 1). The first step in the synthesis of polyelectrolyte composites with embedded nanoparticles for the study of iron(II)-chelation efficacies is the choice of ionic monomers. The research on water-purifying materials indicates that amine-containing moieties, namely tetraethylenepentamine (TEPA) and carboxylic acid-based monomers, such as methacrylic acid, are among the most studied ionic materials for water purification applications [14,26–29]. The incorporation of TEPA into nanocomposites is generally obtained by electrostatic interactions between amine groups of TEPA and anionic groups of composites (carboxyl, sulfate), followed by their crosslinking at high temperature and pressure to obtain macroarchitectures [14]. We argue that the conversion of TEPA into a methacrylamide-based monomer, namely tetraethylenepentamine methacrylamide (TEPMA), may present a simple and convenient method to develop amine-functionalized polymeric composites by the free-radical polymerization method. The synthesis of TEPMA was achieved by the modification of TEPA in the presence of methacrylic anhydride, followed by the precipitation of the TEPMA salt (TEPMA·2HCl) in methanol. The synthesis of the TEPMA salt is depicted in Scheme 1. The chemical structure of pure TEPMA·2HCl was confirmed by FTIR, ^{1}H NMR, and ^{13}C NMR. ESI-MS provides the molar mass of the TEPMA salt and indicates the degree of protonation of TEPMA as TEPMA·2HCl (Supporting Information, Figures S1–S4).

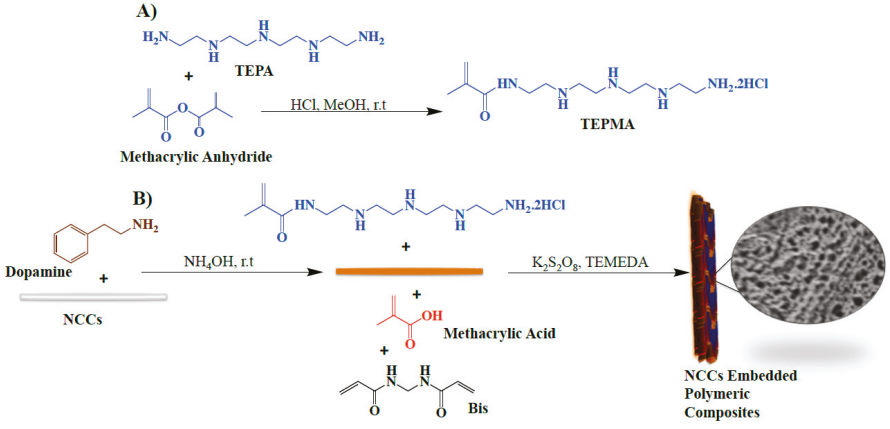

Scheme 1. Schematics depicting (**A**) the synthesis of TEPMA·2HCl and (**B**) the synthesis of polymeric composites with embedded nanocrystalline cellulose (NCC) via the polydopamine coating of NCC, followed by the incorporation of ionic monomers, their polymerization, crosslinking, and self-assembly at room temperature (r.t): Tetraethylenepentamine (TEPA), Tetraethylenepentamine Methacrylamide (TEPMA·2HCl), *N*,*N*,*N*′,*N*′-tetramethylethylenediamine (TEMEDA).

The synthesized ionic monomers are then functionalized on the surface of NCC by utilizing the strongly adhesive properties of dopamine. NCC are coated with polydopamine, followed by their attachment with ionic monomers (TEPMA·2HCl and methacrylic acid), polymerization, and crosslinking in a one-pot reaction in the presence of *N*,*N*′-methylenebisacrylamide (Scheme 1 and Supporting Information, Figure S5). Polymeric composites with embedded NCC were allowed to self-assemble in the form of macrocomposites, and the gelation of composites was confirmed by vial inversion test and gelation time was recorded (Table 1). The colloidal nature of the polydopamine-coated NCC composites and the well-defined three-dimensional architecture of the NCC–polymer composites are compared in photographs (Supporting Information, Figure S6).

The molar ratios of the monomers (TEPMA, methacrylic acid) and crosslinker were optimized to obtain polymeric composites of optimal strength (Table 1). As shown in Table 1, a critical molar ratio of 1:1 of amine/carboxyl groups (that is, a 2:1 molar ratio of methacrylic acid/TEPMA·2HCl) is required to achieve the polymeric composites in the form of thixotropic gels, highlighting the role of electrostatic interactions in the structure of composites (Table 1). Further increases in both the crosslinking density (20 mol %) and the molar ratio of methacrylic acid in the composites led to significant reduction in the gelling time and exhibited improved strength of the resultant materials, suggesting that both chemical crosslinking and ionic interactions are critically important to obtain embedded-nanoparticle polymeric composites of high strength. It should be noted that the coating of NCC with one type of ionic monomer, namely methacrylic acid or TEPMA, did not produce polymeric composites of optimal strength at any of the studied concentrations, possibly due to the electrostatic repulsion of polymer chains formed, which impaired the self-assembly or setting behavior of composites. This further highlights the role of electrostatic interactions in the assembly of composites achieved (Supporting Information, Figure S7). The composite with reduced gelling time and of optimum strength (the sample indicated as PC5 (polymeric composite 5) in Table 1) was chosen for physiochemical characterization and for the study of iron(II)-binding efficacies in vitro. The polymeric composites prepared in the absence of NCC showed poor gelation properties and significantly low yield (~20%), indicating that the concentration of ionic monomers used for composite formation was too low to form an ionic gel and that NCC provides the major scaffold for the coating of ionic monomers and for facilitating their polymerization into polymeric composites.

3.2. Characterization of Composites

The polymeric composite (sample PC5 in Table 1) was characterized regarding its surface morphology by FTIR spectroscopy and XRD analysis (Figure 1A,C). The FTIR spectra of NCC reveal two sharp peaks at 1100 and 3250 cm^{-1}, indicating the stretching of the C–O and O–H groups in the NCC structure [26,27]. The subsequent polymerization and crosslinking of TEPMA·2HCl and methacrylic acid on the surface of NCC in the presence of polydopamine results in polymeric composites with the appearance of functional groups associated with ionic monomers. The broadening of the 3250 cm^{-1} peak indicates the presence of bound O–H groups of methacrylic acid. The presence of peaks at 1388 and 1420 cm^{-1} are due to the symmetric and asymmetric bending vibrations of NH_2, and the strong band at 1658 cm^{-1} is due to the bending vibrations of N(R)H in the TEPMA structure [14,26]. The peak at 1130 cm^{-1} indicates the C–O stretching of methacrylic acid, and the asymmetric stretching of C=O is indicated by the vibrational peak at 1725 cm^{-1} [26,27] (Figure 1A). The crystalline structure of the materials was then analyzed by XRD.

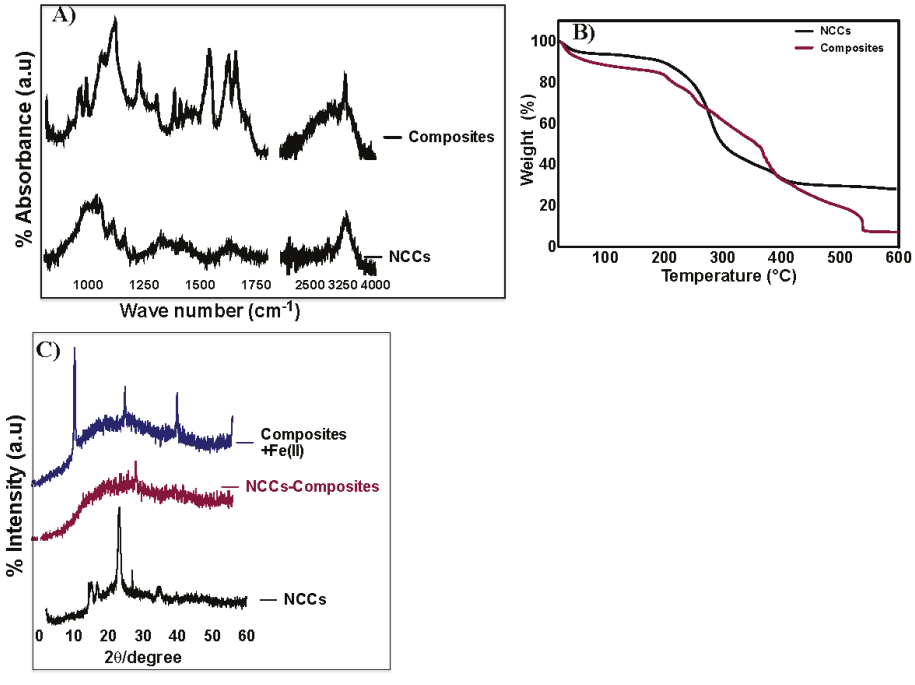

Figure 1. (**A**) FTIR spectra of NCC and embedded-NCC polymeric composite. (**B**) TGA analysis of NCC and embedded-NCC composite. (**C**) XRD patterns of NCC, embedded-NCC polymeric composite, and iron-loaded composite.

XRD patterns of NCC revealed a typical cellulose-I structure, as indicated by 2θ = 16.5°, 22.4°, and 34.6° [27] (Figure 1C). In comparison to the longitudinal fiber-like, crystalline morphology of NCC, the embedded-NCC polymeric composite prepared at the NCC concentration of 10 mg/mL exhibited a completely amorphous structure, which may indicate that concentration of NCC in the composite was significantly low and the diffraction of cellulose nanocrystals was not observed. (Figure 1C and Supporting Information, Figure S8). The modification of NCC with polymeric structures is well known to amorphize or mask the crystalline structure of NCC [24]. We also report that the embedded-NCC composite yielded a clay-like amorphous structure. The surface morphology of the embedded-NCC composite as studied by SEM further confirms the amorphous clay-like nature of the

composite (Figure 2). SEM images of the composite obtained at higher magnification unveiled a highly porous structure, which is considered ideal for the heavy metal adsorption behavior of polymeric composites (Figure 2A,B). The presence of metal-chelating groups (hydroxyl, amine, and carboxyl groups) and the highly porous structure of embedded-NCC polymeric composites warrant the study of their metal ion-binding efficacies [1,14,25–27,30]. The composite prepared was incubated with 60 mg/L of iron(II) for the period of three hours, and iron-loaded composite was evaluated for its physiochemical properties by XRD and SEM. Figure 1C reveals characteristic differences in the XRD patterns of the iron-loaded and iron-free composite. The appearance of crystalline peaks in the XRD patterns of iron(II)-loaded composite may be associated with the presence of iron(II) on the surface of the composite (Supporting Information, Figure S9). Furthermore, the smooth, nonporous surface of the iron-loaded composite as observed by SEM may suggest the packing of iron(II) into the multifunctional porous surface of the polymeric composite (Figure 2C).

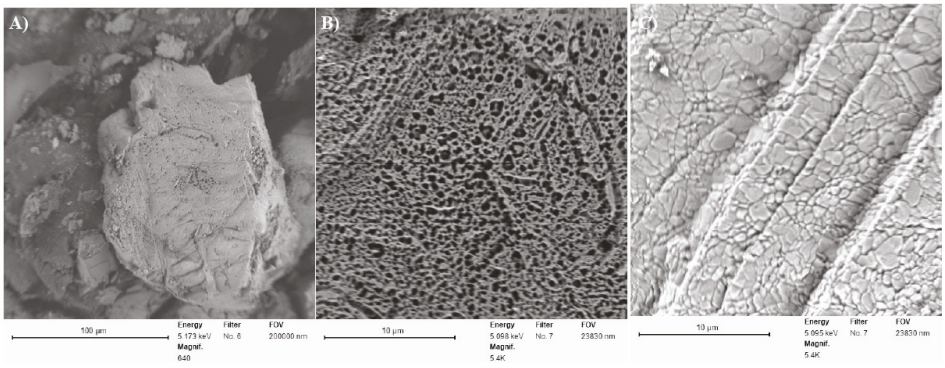

Figure 2. SEM images of polymeric composite (**A**) at low magnification (100 µm) and (**B**) high magnification (10 µm), and (**C**) high-magnification (10 µm) SEM images of iron-loaded polymeric composite.

The thermal properties of the composite were then studied by TGA. As expected, the embedded-NCC composite showed higher thermal stability in comparison to NCC alone (Figure 1B). TGA analysis revealed the higher stability of NCC at lower temperatures (less than 200 °C); however, at temperatures above 200 °C, rapid weight loss (more than 60%) was observed due to the thermal degradation of NCC in the oxidizing atmosphere. The embedded-NCC composite, in contrast, exhibited a slower and characteristic three-step degradation profile. At low temperatures (less than 200 °C), the slight changes in the weight of the composite (~20%) were due to the loss of moisture entrapped in the composite's architecture. The slow and continuous weight loss from 200 to 400 °C (~40%) indicates the disruption of ionic interactions within the composite. The complete thermal degradation of the composite occurred from 400–520 °C, and can be attributed to the breakage of covalent bonds in the composites at high temperatures [22].

3.3. pH-Dependent Iron-Binding Capabilities of the Composite

The binding of the soluble form of iron (Fe^{2+}) on the surface of the composite was investigated in detail as a function of the initial concentration of iron in solution, at both acidic and basic pH (Figure 3A and Supporting Information, Figure S10). The pH of the solution is one of the most important factors, affecting the biosorption of iron(II) ions onto the surface of composites [7,20]. Zhang and coworkers indicated that an increase in the pH of the solution increased the amount of iron adsorbed onto rice husk materials, possibly due to the electrostatic interactions of the materials with cationic metal ions [20]. Moreover, at high pH values, the conversion of iron(II) into its hydroxide forms may lead to the precipitation and adsorption of iron(II) on the surface of composites, hence facilitating its removal [20]. In contrast, Yan et al. reported that decreased iron(II) adsorption on the surface of magnetic graphene

oxide at highly acidic pH is due to the electrostatic repulsion between protonated anionic groups and metal ions. Similarly, strongly basic pH resulted in the competitive binding of hydroxyl and metal ions in solution, hence reducing the metal-chelation properties of materials [7]. We evaluated the role of solution pH in the removal of iron(II) in the presence of a constant amount of composite (4 g/L). As expected, the increase in the pH of the solution increased the iron(II)-binding efficacies of the composite. At acidic pH, the embedded-NCC composite showed low iron-chelating efficacies (R% = 30%–32%). However, at high pH, the iron-binding efficacy of the composite was increased by ~3-fold and the equilibrium iron-binding capacity of the composite increased from 30% to 89% (Figure 3A). This increase in the iron(II)-removal efficacies of the composite at basic pH was attributed to the activation (deprotonation) of carboxyl and amine groups of the composite, hence exhibiting superior iron(II)-binding capabilities by electrostatic interactions [7,31]. At acidic pH, in contrast, metal-chelating groups of the composite are in protonated form and electrostatic repulsion between the cationic metal ions and functional groups reduces their metal ion-binding efficacies.

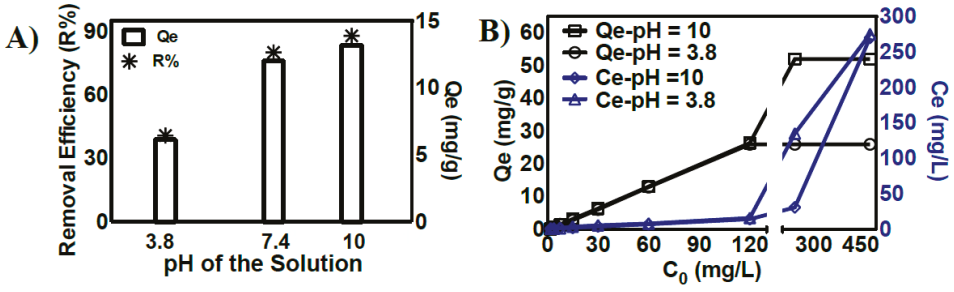

Figure 3. (**A**) Effect of pH on the amount of iron adsorbed at equilibrium (Qe, mg/g) and its removal efficiency (R%) in the presence of a constant amount (4 g/L) of polymeric composite. (**B**) Analysis of iron adsorbed at equilibrium (Qe, mg/g) on the surface of the composite and the concentration of free iron (Ce), as a function of iron concentration in solution, at pH 3.8 and pH 10.

3.4. Sorption Isotherms of the Embedded-NCC Composite

The adsorption isotherms were then evaluated from the relationship between the amount of metal ions adsorbed on the surface of materials and that of the solution at equilibrium. These isotherms play a fundamental role in describing the nature of interactions between the sorbent and metal ions [7,14,20,21]. The adsorption isotherms of the composite for the removal of iron at acidic and basic pH were evaluated at a wide range of initial metal ion concentrations (Figure 3B). The increase in the concentration of iron(II) from 1.75–120 mg/L at pH 3.8 linearly increases the amount of iron adsorbed on the surface of the composite from 1–32.6 mg/g, and low concentrations of soluble iron (less than 10 mg/L) were observed in the solution form. However, further increase in the initial iron concentration of the solution (240–720 mg/L) led to the complete saturation of active metal-binding sites on the surface of the composite, and the adsorption of iron(II) achieved equilibrium. The iron-binding capacities of magnetic graphene oxide showed similar adsorption behavior, and complete saturation of metal-binding sites was observed at the saturation capacity of 43 mg/g of nanocomposite [7]. The iron(II)-binding efficacies of the embedded-NCC polymeric composite at basic pH yielded a similar trend; however, an increase in iron-binding capacity (Qe of 52.5 mg/g and 90% removal efficiency) was observed due to the stronger electrostatic interactions between the iron ions and deprotonated functional groups of the polymeric composites [21]. The iron-binding capacity of the composite at equilibrium was found to be 32.3 mg/g and 52.5 mg/g at pH = 3.8 and pH = 10, respectively (Figure 3B). The iron-binding analysis at equilibrium was subjected to the Langmuir and Freundlich sorption isotherms to investigate the adsorption mechanism of the composite (Table 2 and Supporting Information, Figure S11).

Table 2. Sorption isotherms of iron(II) on the surface of the composite at pH = 3.8 and 10.

Langmuir Isotherm		Freundlich Isotherm		
pH	R^2	R^2	n	K_F
3.8	0.347	0.96	1.1	0.044
10	0.145	0.99	1.18	0.068

Where, n represents the heterogeneity factor and K_F is Freundlich Isotherm.

The fitting results for the adsorption of iron (II) on the surface of the composite are summarized in Table 2. The correlation coefficients of linear form of Langmuir isotherm showed poor agreement with the experimental data. However, the Freundlich isotherm was found to be suitable (R^2 = 0.96 at pH = 3.8 and R^2 = 0.99 at pH = 10) to explain the mechanism of iron(II) adsorption on the surface of the composite. The Freundlich isotherm is one of the most widely used mathematical descriptions, which gives an expression of surface heterogeneity and indicates the presence of active sites and their energies on the surface of materials [7]. The conformity of the data with the Freundlich isotherm suggests the multisite sorption capacity of the embedded-NCC polymeric composite, possibly due to the presence of various functional groups (hydroxyl, amine, carboxyl) on the surface of the composite with undoubtedly different metal ion adsorption capacities. This may present a heterogenous surface of the composite that follows the Freundlich isotherm [7]. Moreover, the stronger interactions between the polymeric composite and metal ions calculated from the Freundlich isotherm (n = 1.1; n >1 indicates stronger affinity) suggests that the sorption of iron(II) is facilitated on the surface of the composite [21] (Table 2). PEG-blended chitosan surfaces prepared for the chelation of iron(II) from contaminated water resources also showed strong correlation with the Freundlich isotherm and revealed that the adsorption of iron on the chitosan membranes was a heterogeneous process [28,29,31,32].

In summary, sorption isotherms analysis suggests that the Freundlich mechanism is the predominant method of iron(II) adsorption on the surface of the polymeric composite, and although pH has no significant affect on the mechanism of adsorption, the adsorption of iron on the surface of the composite is indeed facilitated at high pH. This effect is possibly attributed to the adsorption of iron(II) on the surface of the composite by electrostatic interactions between carboxyl groups of methacrylic acid [23]. The maximum iron-binding capacity of the composite was 26.5 mg/g at pH 3.8 and was 52.5 mg/g at pH 10. The maximum iron adsorption capacity of the polymeric composite was found to be similar to or even higher than some of the recently reported materials evaluated for their iron adsorption capabilities (Table 3).

Table 3. Summary of iron-chelating adsorbents evaluated in research.

Material	pH Studied	Maximum Fe-Removal Capacity (mg/g)	Reference
Embedded-NCC polymeric composites	3.8, 10	26.5, 52.5	This work
Magnetic graphene oxide	5.5	43.3	[7]
Rice husk ash	5	6.2	[20]
Chitosan–PEG blends	5–10	90.9	[31]
Natural zeolite	7	1.1	[32]
Activated charcoal	4–7	0.8	[33]
Granular activated carbon	Not provided	3.6	[34]
Apatite	4–6.6	57.1–124.2	[35]
Bentonite clay		7.09	[36]

3.5. Adsorption Kinetics of the Composite

The change in the initial concentration of iron salt in the presence of the polymeric composite and the adsorption of iron(II) on the surface of the composite was studied as a function of time at both acidic and basic pH (3.8 and 10) (Figure 4A,B). The results indicate that the adsorption of iron on the surface of the composite was significantly faster at basic pH and that ~80% of iron was adsorbed on the

composite's surface within 15 min of incubation. The adsorption of iron at acidic pH (3.8), however, was relatively slow, and maximum adsorption was achieved in a 24-h time period. The kinetics of iron adsorption was then evaluated using pseudo-first-order and pseudo-second-order kinetic models using a constant amount of composite (4 g/L) and 60 mg/L of iron solution at 25 °C. For the applicability of the pseudo-first-order kinetic model, $\ln(q_e - q_t)$ versus t should give a straight line; however, the fitting of iron adsorption data for the polymeric composite showed poor agreement with pseudo-first-order kinetics (R^2 = 0.18 at pH = 3.8 and R^2 = 0.46 at pH = 10), hence the pseudo-first-order kinetic model was deemed unsuitable to describe the study (Table 4). For the analysis with pseudo-second-order kinetics, the plot of t/q_t versus t should provide a straight line [32]. As shown in Table 3 (and Supporting Information, Figure S12), the iron adsorption data fits well with pseudo-second-order kinetics and the calculated $q_{ecalc.}$ = 11.68 mg/g is in close agreement with the experimentally obtained q_e (13.6 mg/g) at any studied pH.

Table 4. Kinetics of iron(II) adsorption on the surface of composites.

	Pseudo-First-Order Kinetics	Pseudo-Second-Order Kinetics		
	R^2	R^2	K_2 (g/mg/hr)	$Q_{ecalc.}$ (mg/g)
pH = 3.8	0.178	0.98	0.034	11.68
pH = 10	0.498	0.98	0.043	11.54

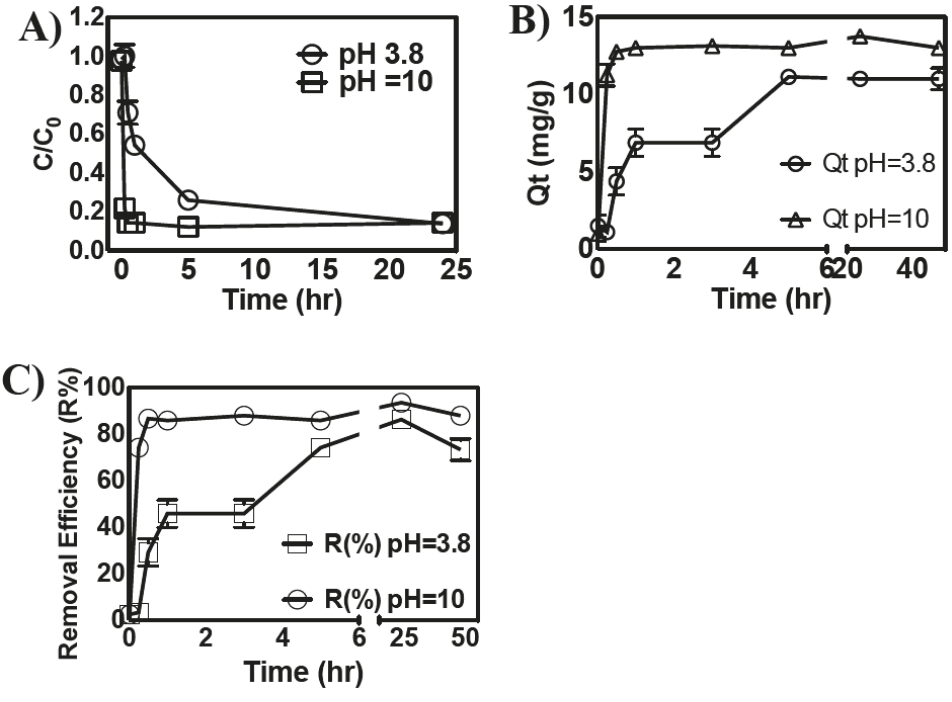

Figure 4. (**A**) Change in the initial concentration of iron(II) as a function of time in the presence of composite at pH 3.8 and 10; (**B**) effect of contact time on the iron adsorption capacity of the composite at pH 3.8 and 10; and (**C**) iron removal efficiency of the composite as a function of time at pH 3.8 and 10.

3.6. Reusability and Antifouling Properties of the Composite

The reusability of metal-chelating composites is of utmost importance for their economical and practical applications [20,21]. Since the iron(II) uptake of composites is strongly pH-dependent, we evaluated the role of acidic and basic pH on the reusability of the material. The composite was first saturated with iron(II), then treated with dilute acid or base, followed by a subsequent assessment of its iron-binding capacities. The iron-binding capacities of the recycled composite showed a significant difference in the iron adsorption capabilities of the composite, depending upon the method of treatment used to remove the adsorbed iron from the composite. As shown in Figure 5, acid-treated composite showed poor iron-binding efficacies at acidic pH, while in contrast, iron(II)-binding efficacies of base-treated composite were unchanged or even higher at basic pH (Figure 5A). We suggest that improved iron(II)-binding efficacies at basic pH are due to the facile removal of adsorbed iron, along with the deprotonation of multiple functional groups present on the surface of composites, which maintained superior iron-chelation properties of the materials upon repeated exposure to iron-containing solutions (Figure 5B).

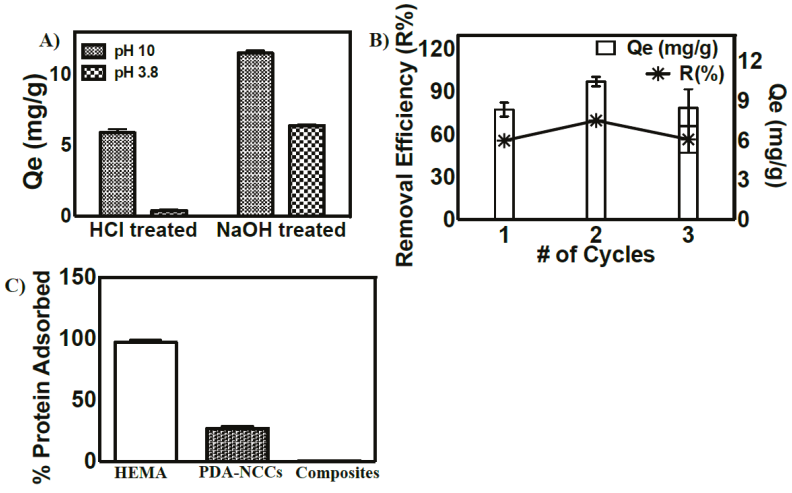

Figure 5. (**A**) The evaluation of the reusability of the composite at acidic and basic pH; (**B**) Iron absorption (shown by Qe) and desorption (shown by R%) on the surface of the polymeric composite after multiple cycles of NaOH treatment; (**C**) Evaluation of % protein adsorption efficacies on the surface of hydrogels (HEMA gels), polydopamine-coated NCC, and on the polymeric composite.

The antifouling behavior of metal-chelating materials is another important parameter to consider to evaluate their potential for water purification applications. The adsorption of organic matter on the surface of composites indeed reduces their metal ion-binding capacities and hence their applicability in water resources for prolonged periods of time [1–7]. We evaluated the adsorption of bovine serum albumin (BSA) (one of the most abundant proteins, which is well known for its high absorption behavior) on the surface of the polymeric composite. The adsorption behavior of BSA on the surface of the composite was compared with the adsorption of BSA on the surface of polydopamine-coated NCC and with a 2-hydroxyethyl methacrylate (HEMA)-based hydrogel. HEMA gels were used as a positive control and are well known for their protein-absorbing capabilities [37]. As expected, HEMA gels exhibited superior protein adsorption behavior. Although slight adsorption of BSA (~17%) on the surface of polydopamine-coated NCC was observed, the embedded-NCC polymeric composite showed negligible adsorption of protein on its surface (>1%) (Figure 5C). The slight adsorption of BSA on the surface of polydopamine-coated NCC may be attributed to the strong adhesion capacity of

polydopamine [16,17]. The poor interactions of BSA on the surface of the polymeric composite further highlights its applicability for the chelation of iron(II) from water resources.

4. Conclusions

The study provides a simple and efficient method for the synthesis of polymeric composites embedded with nanoparticles with good metal ion-binding efficacies. The amorphous polymeric composite prepared at optimized amine-to-carboxyl group molar ratios exhibited a highly porous structure and superior capability for iron(II) chelation. The mechanism of iron adsorption on the surface of the polymeric composite was explained by the Freundlich isotherm. The analysis of the kinetics of iron adsorption on the surface of the composite revealed that the iron adsorption followed pseudo-second-order kinetics, and calculated q_e values were in strong agreement with experimental data. The results also revealed that the pH of the solution did not alter the mechanism of adsorption and its kinetics; however, the adsorption of iron on the anionic surface of the composite was facilitated at basic pH. The superior iron-binding capacities of the polymeric composite and its excellent antifouling properties suggest that this material is suitable for water purification applications.

Supplementary Materials: The following are available online at http://www.mdpi.com/2073-4360/10/12/1377/s1.

Author Contributions: Conceptualization, M.A. and A.K.; Methodology, A.K., M.J.D.; Software, M.A., M.J.D.; Validation, A.K., M.J.D.; Formal Analysis, A.K., M.J.D. and M.A.; Investigation, A.K., M.J.D.; Resources, R.B., B.A., M.A.; Writing-Original Draft Preparation, M.A.; Writing-Review & Editing, M.A., R.B.; X.X.; Supervision, M.A., R.B., B.A.; Project Administration, M.A.; Funding Acquisition, M.A.

Funding: This research was funded by Natural Science and Engineering Research Council of Canada (NSERC) and by the Seed Grant of UPEI.

Conflicts of Interest: The authors declare no conflict of interest.

References

1. Sun, D.T.; Peng, L.; Reeder, W.S.; Moosavi, S.M.; Tiana, D.; Britt, D.K.; Oveisi, E.; Queen, W.L. Rapid, Selective Heavy Metal Removal from Water by a Metal-Organic Framework/Polydopamine Composite. *ACS Cent. Sci.* **2018**, *4*, 349–356. [CrossRef] [PubMed]
2. Hashim, K.S.; Shaw, A.; Al Khaddar, R.; Pedrola, M.O.; Phipps, D. Iron Removal, Energy Consumption and Operating Cost of Electrocoagulation of Drinking Water using a New Flow Column Reactor. *J. Environ. Manag.* **2017**, *189*, 98–108. [CrossRef] [PubMed]
3. Doggaz, A.; Attour, A.; Mostefa, M.L.P.; Tlili, M.; Lapicque, F. Iron Removal from Waters by Electrocoagulation: Investigations of the Various Physicochemical Phenomena Involved. *Sep. Purif. Technol.* **2018**, *203*, 217–225. [CrossRef]
4. Chaturvedi, S.; Dave, P.N. Removal of Iron for Safe Drinking Water. *Desalination* **2012**, *303*, 1–11. [CrossRef]
5. Mai, N.T.; Tran, C.T.; Lai, T.Q.; Nguyen, L.T.K.; Nguyen, H.X.; Luong, V.T.T.; Nguyen, K.M.; Nguyen, M.N. Removal of Iron from Aqueous Solution using Phytolith-aided Aggregation. *J. Water Process Eng.* **2018**, *25*, 39–44. [CrossRef]
6. Khatri, N.; Tyagi, S.; Rawtani, D. Recent Strategies for the Removal of Iron from Water: A Review. *J. Water Process Eng.* **2017**, *19*, 291–304. [CrossRef]
7. Yan, H.; Li, H.; Tao, X.; Li, K.; Yang, H.; Li, A.; Xiao, S.; Cheng, R. Rapid Removal and Separation of Iron(II) and Manganese(II) from Micropolluted Water using Magnetic Graphene Oxide. *ACS Appl. Mater. Interface* **2014**, *6*, 9871–9880. [CrossRef] [PubMed]
8. Tekerlekopoulou, A.G.; Vasiliadou, I.A.; Vayenas, D.V. Physico-chemical and Biological Iron Removal from Potable Water. *Biochem. Eng. J.* **2006**, *31*, 74–83. [CrossRef]
9. Zhao, G.; Huang, X.; Tang, Z.; Huang, Q.; Niu, F.; Wang, X. Polymer-based Nanocomposites for Heavy Metal Ions Removal from Aqueous Solution: A Review. *Polym. Chem.* **2018**, *9*, 3562–3582. [CrossRef]
10. Gao, H.; Sun, Y.; Zhou, J.; Xu, R.; Duan, H. Mussel-Inspired Synthesis of Polydopamine-Functionalized Graphene Hydrogel as Reusable Adsorbents for Water Purification. *ACS Appl. Mater. Interface* **2013**, *5*, 425–432. [CrossRef]

11. Mo, J.; Yang, Q.; Zhang, N.; Zhang, W.; Zheng, Y.; Zhang, Z. A Review on Agro-Industrial Waste (AIW) Derived Adsorbent for Water and Wastewater Treatment. *J. Environ. Manag.* **2018**, *227*, 395–405. [CrossRef]
12. Han, Y.; Wu, X.; Zhang, X.; Zhou, Z.; Lu, C. Dual Functional Biocomposites Based on Polydopamine Modified Cellulose Nanocrystal for Fe3+ Pollutant Detecting and Autoblocking. *ACS Sustain. Chem. Eng.* **2016**, *4*, 5667–5673. [CrossRef]
13. Lin, N.; Dufresne, A. Nanocellulose in Biomedicine: Current Status and Future Prospect. *Eur. Polym. J.* **2014**, *59*, 302–325. [CrossRef]
14. Han, Z.; Tang, Z.; Sun, Y.; Yang, J.; Zhi, L. Controllable Synthesis of Tetraethylenepentamine Modified Graphene Foam (TEPA-GF) for the Removal of Lead Ions. *Sci. Rep.* **2015**, *5*, 16730. [CrossRef] [PubMed]
15. Kulig, D.; Zimoch-Korzycka, A.; Jarmoluk, A.; Marycz, K. Study on Alginate-Chitosan Complex Formed with Different Polymers Ratio. *Polymers* **2016**, *8*, 167. [CrossRef]
16. Zhang, C.; Ma, M.; Chen, T.; Zhang, H.; Hu, D.; Wu, B.; Ji, J.; Xu, Z. Dopamine-Triggered One-Step Polymerization and Codeposition of Acrylate Monomers for Functional Coatings. *ACS Appl. Mater. Interfaces* **2017**, *9*, 34356–34366. [CrossRef] [PubMed]
17. Kolewe, K.W.; Dobosz, M.K.; Emrick, T.; Nonnenmann, S.S.; Schiffman, J.D. Fouling-Resistant Hydrogels Prepared by the Swelling- assisted Infusion and Polymerization of Dopamine. *ACS Appl. Bio Mater.* **2018**, *1*, 33–41. [CrossRef]
18. Dunlop, M.J.; Acharya, B.; Bissessur, R. Isolation of Nanocrystalline Cellulose from Tunicates. *J. Environ. Chem. Eng.* **2018**, *6*, 4408–4412. [CrossRef]
19. Polomoscanik, S.C.; Cannon, C.P.; Neenan, T.X.; Holmes-Farley, S.R.; Mandeville, W.H.; Dhal, P.K. Hydroxamic acid-Containing Hydrogels for Nonabsorbed Iron Chelation Therapy: Synthesis, Characterization, and Biological Evaluation. *Biomacromolecules* **2005**, *6*, 2946–2953. [CrossRef] [PubMed]
20. Zhang, Y.; Zhao, J.; Jiang, Z.; Shan, D.; Lu, Y. Biosorption of Fe(II) and Mn(II) Ions from Aqueous Solution by Rice Husk Ash. *BioMed Res. Int.* **2014**, *2014*, 973095–9730100. [CrossRef]
21. Ko, D.; Mines, P.D.; Jakobsen, M.H.; Yavuz, C.T.; Hansen, H.C.B.; Andersen, H.R. Disulfide Polymer Grafted Porous Carbon Composites for Heavy Metal Removal from Stormwater Runoff. *Chem. Eng. J.* **2018**, *348*, 685–692. [CrossRef]
22. Tanpichai, S.; Oksman, K. Cross-linked Nanocomposite Hydrogels based on Cellulose Nanocrystals and PVA: Mechanical Properties and Creep Recovery. *Compos. Part A* **2016**, *88*, 226–233. [CrossRef]
23. Julkapli, N.M.; Bagheri, S. Progress on Nanocrystalline Cellulose Biocomposites. *React. Funct. Polym.* **2017**, *112*, 9–21. [CrossRef]
24. Chakrabarty, A.; Teramoto, Y. Recent Advances in Nanocellulose Composites with Polymers: A Guide for Choosing Partners and How to Incorporate Them. *Polymers* **2018**, *10*, 517. [CrossRef]
25. Zhu, Q.; Wang, Y.; Wang, D.; Li, M.; Liu, K.; Hu, C.; Yan, K.; Sun, G. Activable Carboxylic Acid Functionalized Crystalline Nanocellulose/PVA-co-PE Composite Nanofibrous Membrane with Enhanced Adsorption for Heavy Metal Ions. *Sep. Purif. Technol.* **2017**, *186*, 70–77. [CrossRef]
26. Wang, N.; Yang, L.; Wang, Y.; Ouyang, X. Fabrication of Composite Beads Based on Calcium Alginate and Tetraethylenepentamine-Functionalized MIL-101 for Adsorption of Pb(II) from Aqueous Solutions. *Polymers* **2018**, *10*, 750. [CrossRef]
27. Winston, A.; Kirchner, D. Hydroxamic Acid Polymers. Effect of Structure on the Selective Chelation of Iron in Water. *Macromolecules* **1978**, *11*, 597–603. [CrossRef]
28. Kumar, A.; Negi, Y.-S.; Choudhary, V.; Bhardwaj, N.K. Characterization of Cellulose Nanocrystals Produced by Acid-Hydrolysis from Sugar Cane Bagasse as Agro-Waste. *J. Mater. Chem. Phys.* **2014**, *2*, 1–8.
29. Bhatia, M.; Rajulapati, S.B.; Sonawane, S.; Girdhar, A. Synthesis and Implication of Novel Poly(acrylic acid)/Nanosorbent Embedded Hydrogel Composite for Lead Ion Removal. *Sci. Rep.* **2017**, *7*, 16413–16416. [CrossRef]
30. Yu, J.; Xiong, W.; Zhu, J.; Chi, R. Separation of Cu2+ and Pb2+ by Tetraethylenepentamine-Modified Sugarcane Bagasse Fixed-Bed Column: Selective Adsorption and Kinetics. *Int. J. Environ. Sci. Technol.* **2016**, *13*, 1933–1940. [CrossRef]
31. Reiad, N.A.; Abdel Salam, O.E.; Abadir, E.F.; Harraz, F.A. Adsorptive Removal of Iron and Manganese Ions from Aqueous Solutions with Microporous Chitosan Polyethylene glycol Blend Membrane. *J. Environ. Sci.* **2012**, *24*, 1425–1432. [CrossRef]

32. Shavandi, M.A.; Haddadian, Z.; Ismail, M.H.S.; Abdullah, N.; Abidin, Z.Z. Removal of Fe(III), Mn(II) and Zn(II) from Palm Oil Mill Effluent (POME) by Natural Zeolite. *J. Taiwan Inst. Chem. Eng.* **2012**, *43*, 750–759. [CrossRef]
33. Akl, M.A.; Yousef, M.A.; AbdElnasser, S. Removal of Iron and Manganese in Water Samples Using Activated Carbon Derived from Local Agro-Residues. *J. Chem. Eng. Process Technol.* **2013**, *4*. [CrossRef]
34. bin Jusoh, A.; Cheng, W.H.; Low, W.M.; Nora'aini, A.; Megat Mohd Noor, M.J. Study on the Removal of Iron and Manganese in Groundwater by Granular Activated Carbon. *Desalination* **2005**, *182*, 347–353. [CrossRef]
35. Oliva, J.; De Pablo, J.; Cortina, J.; Cama, J.; Ayora, C. The use of Apatite to Remove Divalent Metal Ions Zinc (II), Lead (II), Manganese (II), Iron (II) from Water in Passive Treatment Systems: Column Experiments. *J. Hazard. Mater.* **2010**, *184*, 364–367. [CrossRef] [PubMed]
36. Al-Shahrani, S.S. Treatment of wastewater contaminated with Fe(II) by Adsorption onto Saudi Activated Bentonite. *Int. J. Eng. Technol.* **2013**, *6*, 58–66.
37. Kabir, A.; Dunlop, M.J.; Acharya, B.; Bissessur, R.; Ahmed, M. Water Recycling Efficacies of Extremely Hygroscopic, Antifouling Hydrogels. *RSC Adv.* **2018**. Accepted. [CrossRef]

polymers

MDPI

Article

Flexible Textile Strain Sensor Based on Copper-Coated Lyocell Type Cellulose Fabric

Waleri Root *, Tom Wright, Barnaby Caven, Thomas Bechtold and Tung Pham

Research Institute for Textile Chemistry/Physics, University of Innsbruck, Hoechsterstrasse 73, 6850 Dornbirn, Austria; tom.wright@uibk.ac.at (T.W.); barnaby.caven@uibk.ac.at (B.C.); thomas.bechtold@uibk.ac.at (T.B.); tung.pham@uibk.ac.at (T.P.)

* Correspondence: waleri.root@uibk.ac.at

Received: 11 April 2019; Accepted: 29 April 2019; Published: 2 May 2019

Abstract: Integration of sensors in textile garments requires the development of flexible conductive structures. In this work, cellulose-based woven lyocell fabrics were coated with copper during an electroless step, produced at 0.0284 M copper sulfate pentahydrate, 0.079 M potassium hydrogen L-tartrate, and 0.94 M formaldehyde concentrations. High concentrations led to high homogeneous copper reaction rates and the heterogeneous copper deposition process was diffusion controlled. Thus, the rate of copper deposition did not increase on the cellulose surface. Conductivity of copper coatings was investigated by the resistance with a four probe technique during fabric deformation. In cyclic tensile tests, the resistance of coated fabric (19×1.5 cm^2) decreased from 13.2–3.7 Ω at 2.2% elongation. In flex tests, the resistance increased from 5.2–6.6 Ω after 5000 bending cycles. After repeated wetting and drying cycles, the resistance increased by 2.6×10^5. The resistance raised from 11–23 Ω/square with increasing relative humidity from 20–80%, which is likely due to hygroscopic expansion of fibers. This work improves the understanding of conductive copper coating on textiles and shows their applicability in flexible strain sensors.

Keywords: cellulose; electrical resistance; copper coating; electroless deposition; humidity sensor; strain sensor; lyocell fiber

1. Introduction

Flexible conductive materials have been extensively investigated according to their promising potential applications in energy storage devices, photodetectors, pressure sensors, and light emitting displays [1–3]. The current research shows the feasibility of fiber/fabric coating to induce electrical conductivity. Coating of metallic copper layers on woven cellulose lyocell (CLY) fabrics through electroless deposition is important to achieve a large area sensor network for wearable smart textiles.

Cellulose is an important textile substrate due to its biodegradable, biocompatible, eco-friendly, non-toxic, and renewable properties [4]. It is chosen according to its high mechanical modulus property, a high strength and an inflexible crystallinity [5]. Several approaches are reported in the literature about how conductive substrates are implemented in large area fabrics. Flexible large area sensors are used for pressure and temperature sensing consisting of an organic coating on plastic and rubber substrates [6,7]. Huang et al. used a 150 cm^2 cloth on a woolen band consisting of steel yarns for energy storage [8]. Shur performed the deposition of CdS/CuS films on 8×10 inches foils, which were suitable for application in e-textiles [9]. Yang et al. manufactured a carbon cloth of 160 cm^2, which is embedded with Nickel nanoparticles through a metal-mediated pitting method [10]. Matsuhisa et al. printed elastic textile conductors of 30×20 cm^2 size with silver nanoparticles which showed high conductivity after treatment [11].

Understanding the relationship between electrical conductivity and mechanical deformations of metal coated/electrical textiles remains under reported. Permanent stress and deformation of conductive

textiles on textiles could lead to damages. It is essential to investigate the electrical resistance of conductive textiles during tensile strength and bending. Abry et al. investigated the damage in Carbon Fiber Reinforce Polymer (CFRP) by means of the electrical resistance [12]. Zhang et al. showed that knitted carbon fiber fabrics displayed greater changes in resistance under loading compared to stainless steel fabrics [13]. Lin et al. measured the electrical resistance during tensile loading on blended yarns consisting of polypropylene (PP) and polyethylene terephthalate (PET) coated with multi-walled carbon nanotubes (MWCNT) [14]. Perumalraj investigated the effect of the resistance on polyaniline (PANI) impregnated polyester/viscose, Bamboo, Bamboo/cotton and cotton fabrics [15]. Hansen et al. showed that Poly(3,4-ethylenedioxythiophene) and aliphatic polyurethane substrate retained conductive property during stretching and relaxation [16]. Kageyama et al. investigated a $BaTiO_3$ impregnated carbon fabric, which indicated an electrical resistance during tensile tests [17]. The resistance of carbon nanotubes coated textile capacitor was studied by Yun et al. which investigated the behavior of resistance during mechanical strain in textile-based capacitors consisting of Carbon nanotubes coated fabrics [18]. Qu et al. reported the manufacture of extruded carbon fiber/polymethylmethacrylate composites, which increased their conductive property as the carbon fiber volume fraction for filaments of 1mm and 3mm diameter increased [19]. Won et al. explored copper nanowires with a high stretchable property for the application as stretchable electrodes [20]. Ali et al. detected the conductive property of cotton textiles impregnated with copper particles during an applied load as a function of elongation [21]. Nishio et al. used the four probe technique to measure the change of the electrical resistance of a woven fabric during cyclic elongation [22]. De Baere et al. measured the voltage in a carbon fabric composite by evaluating its electrical resistance [23]. Cui et al. investigated the electrical conductivity of cupro fabrics impregnated with silver nanowires during bending, shrinking and stretching [24]. Application in medicine, sports, energy storage [25] security and personal protection, military and fire departments are all suggested [26,27]. Conductive coatings on cotton textiles were used for sweat detection in a garment by measuring resistance [28] and for monitoring electrical signals of a plant during stimulation [29]. Zieba and Frydrysiak reported the response of resistance to elongation, strain or bending in a textile sensor for monitoring breathing [30]. Ehrmann et al. tested textile sensors in knitted fabrics for human breathing application by detecting the electrical resistance during elongation [31]. Li et al. investigated the increase of the length resistance of knitted conductive fabrics during extensile force [32]. In the review of Kongahage and Foroughi, conjugated double bond conductive polymers (CP) were described as promising materials for actuators consisting of polypyrrole (PPy), polyaniline (PANI) and PEDOT:PSS substrates. Those CP actuators can be used to monitor bending and linear motion [33]. Atalay et al. constructed a knitted textile strain sensor made of conductive yarns for human body motion detection [34]. In a different work, Atalay et al. used silver (Ag) plated nylon yarns for measuring the tensile strength [35]. Body motion was monitored by a strain sensors during resistance change based on a stretchable and conductive plain woven polyester fabric [36].

In summary, the above-mentioned works showed a successful implementation of conductive materials as metals (e.g., Cu, Ag), carbon substrates, conductive polymers (e.g., PET, PANI) to introduce an electric property in non-conductive substrates (e.g., PP, polyester, Bamboo, cotton). Using silver as conducive material in non-conductive substrates can be explained due to its high electrical conductivity of 6.3×10^7 Sm^{-1} compared to 5.9×10^7 Sm^{-1} of copper and 2×10^5 Sm^{-1} carbon (graphite) substrates. Despite the lower cost of copper ($ 6.7/kg) compared to silver ($ 510 /kg), immediate oxide layer formation on the copper surface makes its application difficult [25]. The implementation of conductive materials in knitted fabrics and woven fabrics can be used in electronic components in textiles. An advantage of knitted fabrics is their good stretch ability, softness and durability, which makes their applications in strain/pressure sensors important. Woven fabrics were reported to be effective for the monitoring of the bending motion [26]. In the work of Ding et al., polyurethane (PU) nonwoven substrates were manufactured by electrospinning and were subsequently dip coated with conductive poly(3,4-ethylenedioxythiophene):poly(styrenesulfonate) (PEDOT:PSS) polymers. The PEDOT:PSS/PU substrates indicated a sheet resistance of 35–240 Ω/sq, withstand a strain of 200% and showed a

constant resistance after 10 stretch release cycles [37]. Mahmood et al., showed the manufacture of conductive graphene oxide glass fiber substrates, which impart an electrical resistivity of $10^1 \Omega$m after electrophoretical deposition [38]. In the review, Ding et al. reported on the conductive sponges as pressure sensors like neat conductive sponges (e.g., impregnated with Cu nanowires, CNT), composite conductive sponges (e.g., composed of polyimide (PU), polyacrylonitrile (PAN)), conductive sponges impregnated with elastomers (e.g., silicone, polydimethylsiloxane (PDMS)) and like conductive material coated sponges (e.g., coated with carbon, Ag). The conductive sponges can be used for the human motion detection [39]. Baima et al. investigated fluoropolymer wrapped conductive threads in an electrical touch sensor assembly by using the triboelectric method known as the change of the surface potential resulted from the skin contact [40]. Ebrahimi and Gashti used PPy materials as electrical substrates in clay Ag-polypyrrole nanocomposites, which showed an enhanced electromagnetic shielding and conductive properties compared to untreated PPy materials after the photo reduction technique [41]. The use as wearable electronics to monitor different parameters from the environment such as temperature, pressure, moisture is clear.

Monitoring conductivity of electrical textiles through the resistance in a wet environment mimics the exposure of fabrics to rain and different humidity's. Wet and dry treatments of textiles might lead to stiffness or reactivity changes [42,43]. Kramar et al. measured the electrical resistance of cotton and viscose fabrics impregnated with Ag^+, Zn^{2+}, and Cu^{2+} ions at different relative humidity conditions [44], apart from the change in resistance due to the ion treatment the resistance also decreased with increasing humidity. Shim et al. used carbon nanotubes coated cotton threads for humidity sensing and for mechanical/chemical durability tests [45]. The advantage of using copper as conductive substrate is its high conductivity/cost ratio in comparison to silver or nickel [25]. In previous work, copper layers were formed by electroless deposition on small woven CLY fabrics inducing conductivity [46]. To the authors best knowledge, there are few treatise reporting on electroless copper deposition (ECD) on a large (or easily scalable) area, i.e., 21×29 cm^2 woven CLY fabric. Specifically, none dealing with the investigation of the influence of cyclic tensile tests, flex tests, extended water treatment for 18 h and different relative humidity on resistance. The aim of this work was to coat a 21×29 cm^2 CLY textile surface with a copper layer during electroless deposition from aqueous solution and investigate its resistance as a function of fabric deformation. It included an optimization of chemical concentrations of $CuSO_4$, formaldehyde and potassium hydrogen tartrate to achieve a strong adhesive and continuous copper layer.

2. Experimental

Samples cut from 21×29 cm^2 copper-coated CLY fabrics were used for investigation of resistance change during extended water treatment times, different relative humidity, flex and cyclic tensile tests. The four probe technique was used to monitor the resistance during different relative humidity (RH), during tensile testing and after flex tests. For humidity tests, a climate chamber was used at 25 °C for 6 h.

2.1. Materials

The chemicals were used as received. Potassium hydrogen L-tartrate ($C_4H_5KO_6$ 99 wt %) was purchased form Fulka (Buchs, Switzerland). Tin(II) chloride × 2 hydrate ($SnCl_2 \times 2H_2O$) and formaldehyde (H_2CO 36.5 wt %) were received from Riedel-de-Haen (Seelze, Germany). copper sulphate pentahydrate ($CuSO_4 \times 5\ H_2O$ 99.5 wt %), ethanol (C_2H_6O > 99.8% with ca. 1% Methyl Ethyl Ketone) and ammonia (NH_3 25 wt %) were purchased from Carl ROTH GmbH + Co. KG (Karlsruhe, Germany). Sodium carbonate (Na_2CO_3 99 wt %) was obtained form MERCK (Darmstadt, Germany). Silver nitrate ($AgNO_3$ 99.9 wt %) was obtained from VWR PROLABO (Leuven, Belgium). Sodium hydroxide (NaOH 50 wt % solution) was obtained form Deuring GmbH & Co KG (Hörbranz, Austria). The woven cellulose lyocell fabrics were kindly provided by Lenzing AG (Lenzing, Austria), which is a plain woven cellulose lyocell fabric (143 g/m^2 weight, fibers of 1.3 dtex linear density and 39 mm length, 40 warp and 31 fill threads per cm). Filter papers (MN 615 1/4, 70 g/m^2, thickness

0.16 mm, surface smooth, ash content 0.1%, α-Cellulose content 95%, average retention capacity 4–12 μm) of 110 mm diameter were obtained form MACHEREY-NAGEL GmbH/Düren/Germany.

2.2. Electroless Copper Deposition on A4 Sized Fabrics

The CLY fabrics (A = 21 cm × 29.7 cm = 623.7 cm^2 m = 5 g) were cleaned with 1.35 M NaOH, 20 mL H_2O de-ionized (DI) solution for 10 min. The surface of the CLY fabric was rinsed with 50 ml H_2O (DI) and dried at ambient conditions for 24 h. The CLY fabric was dipped into 19.8 M EtOH (MEK) 100 mL and 0.029 M $SnCl_2 \times 2H_2O$ solution for 1 min. Afterwards, it was dried at ambient conditions for 1h. The CLY fabric was immersed into a 0.042 M $AgNO_3$, 100 mL H_2O (DI) and 2.64 mL (1.43 M) NH_3 solution for 1 min at pH 11.58. The CLY fabric was dried at ambient conditions for 24 h. Different concentration of $C_4H_5KO_6$, $CuSO_4 \times 5\ H_2O$, NaOH, H_2O (DI) and CH_2O were used. Constant contents of 0.019 M Na_2CO_3 and H_2O (DI) were used in all experiments. As shown in Table 1, all experiments were performed for 3h at pH 12.5 and room temperature.

Table 1. Concentrations of chemicals used for electroless copper deposition.

Sample Name	$C_4H_5KO_6$ (M)	NaOH (50 wt %) (M)	$CuSO_4 \times 5\ H_2O$ (M)	CH_2O (M)
CU 1	0.079	0.5	0.0284	0.94
CU 2	0.158	1	0.0568	1.88
CU 3	0.236	1.5	0.0852	2.82

2.3. Flex Test

The characteristics of fatigue due to cyclic bending of copper-coated CLY fabric strip were determined with an adapted method according to DIN 53 543:1979-02, DIN EN ISO 17707:2005-10 and EN ISO 20344:2004-10 standards. A Cu-coated strip with a size of 1.5 cm × 20 cm was attached to the permanent bending machine and was exposed to a total number of 6000 bending cycle. All bending tests were performed at a bending rate of 180 cycle/min. The top and bottom part of the copper-coated CLY fabric strip was fixed with two jaws. 10 cm length of the copper-coated fabric strip were suspended to permanent bending at bending apparat (Biegeprüfmaschine (BPM), Pirmasens, Germany). The angle of friction change from 111° to 179° during flex tests.

2.4. Resistance During Cyclic Elongation

The sheet resistance of copper-coated CLY fabrics was investigated during repetitive elongation in relation to the ASTM D 257-07 standard. The copper-coated CLY fabric strips had the size of 1.5 × 19 cm^2 and were placed between jaws with a rubber isolation layer at a grip to grip separation of 100 mm. Metallic copper strips monitored the resistance of the copper-coated CLY fabrics. The fabric was elongated and relaxed during permanent elongation cycles (Zwick/Roell/Ulm/Germany (Z010 test Control II)). The preload was set to 5 N with 50 mm/min speed and 60 sec time. The standard force increased from 2.24 N, 10 N, 20 N, until a maximum of 30 N and decreased back to 20 N, 10 N, 2.24 N at a speed of 100 mm/min. Measurements were taken at a constant current of 20 mA applied by the power supply and voltage was monitored with a multimeter during fabric deformation tests. The two inner strips recorded the voltage during each load for 30 s and the resistance (R) was evaluated according to the equation below:

$$R = (U \times w)/(I \times l) \quad (1)$$

where U is the measured voltage, I the applied current, w the width of the Cu fabric strip and l the investigated distance between the electrodes. During extended water treatments, the resistance of copper layer on CLY fabrics was measured with a multimeter (FLUKE) in a 100 mL H_2O (DI) solution stirring at 750 rpm for 18 h.

2.5. Electrical Resistivity Tests in Fabrics

The electrical resistivity of dry fabric was measured with METRISO/3000 resister tester (Wolfgang Warmbler/Eppingen/Germany) for silver seeded CLY fabrics relating to the DIN 54345 standard. The values were recorded after one minute at 505 V and the measurements were repeated for three times.

2.6. Four Probe Technique Measurements

The sheet resistance (R_{sh}) was measured in a coaxial arrangement with a four point probe technique at a spacing of 1cm between the electrodes. The resistance was evaluated according to the equation below:

$$R_{sh} = 4.532 \times (U/I) \quad (2)$$

where U is the measured voltage and I the applied current. All measurements were related to the ASTM standard F1529-94.

2.7. Copper and Silver Determined with AAS (Atomic Absorption Spectroscopy)

50 mg of the copper-coated fabric was cut from a 5 g CLY fabric and was immersed into a (15 wt %) nitric acid (HNO_3) solution (30 mL) at 80 °C for 2 h. The extraction solution was filtered with a filter paper (d = 110 mm) for 5 min. A 10 mg/L stock solution of Ag^+ (0.46×10^{-3} M $AgNO_3$) and 10 mg/L of Cu^{2+} (0.16×10^{-3} M $CuSO_4 \times 5H_2O$) were used to prepare calibration solutions in the range of 0–2 mg/L for Cu^{2+}, 0–1.5 mg/L for Ag^+. The flasks (100 mL) and tubes (50 mL) were rinsed with (6 wt %) HNO_3 before AAS measurement. Silver (Ag) and copper (Cu) contents in CLY fabrics were determined with AAS (contrAA 300, Analytic, Jena Germany) in an air-acetylene flame with a 100 mm burner at a wavelength of 328.1 nm for Ag and of 324.8 nm for Cu. Linear regression of the calibration standards and the sample absorbance were used for the metal content detection in CLY fabrics. The metallic content was obtained due to Equation (3) in CLY fabrics. The analysis was related to DIN 38404 Teil 18, EN ISO 17294-2 and DIN 38406 Teil 7.

$$Cu_f = (Cu_s \times V)/W \quad (3)$$

where Cu_f is a copper content in fabric (mg/g), Cu_s is a Cu content in dilute solution (mg/L), W is the mass of the investigated fabric piece (g) and V is a volume of extraction solution (mL).

2.8. Topology Investigations

The environmental scanning electron microscopy (ESEM) and energy-dispersive X-ray spectroscopy (EDX) were conducted with the JEOL JSM-7100F microscope, which was operated in the range of 10–20 keV. The copper-coated CLY samples were placed on an aluminium specimen with a conductive carbon layer on top without any coating. All machine operating are given specific parameters in the figures. The topology was investigated with a laser scanning microscope (VK-X100 series LSM 3D Profile Measurement from KEYENCE). The images were recorded with a 100× lens at a working distance of 4.7 mm. The samples were not under tension and were placed on a paper sheet during measurements. The topology of copper-coated CLY samples was characterized with Laser Scanning Microscopy (VK-X100 series LSM 3D Profile Measurement, KEYENCE, Tokyo, Japan). All FTIR measurements were conducted with the ATR-FTIR device (Vector 22, Bruker, Karlsruhe, Germany).

3. Results and Discussion

3.1. Electroless Copper Deposition on 21 × 29 cm^2 Cellulose Fabrics

Table 2 shows a summary of results of CLY fabrics produces at different molar concentrations of $CuSO_4$, H_2CO and $C_4H_5KO_6$ during the ECD. The silver content [Ag] on the cellulose substrate indicates a high resistance (R) due to silver seeds, which are not connected to one another. The copper-coated fabrics

(CU 1, CU 2, CU 3) indicated different copper contents [Cu], roughness along the line values (S_h), sheet resistances (R_{sh}) and sheet conductance values (G_{sh}). The Cu1 sample showed the lowest sheet resistance, lowest copper content and the highest sheet conductance comparing to Cu2 and Cu3 samples.

Table 2. Summary of metallic content, moisture and conductivity in copper-coated cellulose lyocell (CLY) fabrics. Values defined as mean ± standard deviation.

Sample Name	[Ag] mg/g	*R* Ag Seed Fabric (Ω)	Cu Content mg/g	S_h μm	R_{sh} Ωsq^{-1}	G_{sh} Ω^{-1}	η Efficiency of the Process
CU 1	6.5 ± 0.5	1.3×10^{11}	147 ± 0.3	2.75 ± 0.7	1.89 ± 0.9	0.66 ± 1.1	0.81
CU 2	14 ± 0.4	1.3×10^{11}	234 ± 1.7	1.94 ± 0.3	5.24 ± 1.9	0.21 ± 0.1	0.65
CU 3	42 ± 1.0	1.3×10^{11}	198 ± 0.2	1.54 ± 0.3	2.46 ± 2.0	0.62 ± 0.4	0.37

In Table 2, sample CU 3 showed a coated and uncoated copper surface, although the amount of copper was high due to the high Cu concentrations in solution. The overall deposition rate (dCu^0/dt) of the electroless copper deposition can be explained by Equation (4). The first term describes a heterogeneous copper deposition rate ($dCu^0/dt)_{het}$ on the textile surface (A) and the second term shows a homogenous copper reaction rate ($dCu^0/dt)_{hom}$ in solution.

$$\frac{dCu^0}{dt} = \left(\frac{dCu^0}{dt}\right)_{het} + \left(\frac{dCu^0}{dt}\right)_{hom} \quad (4)$$

The heterogeneous copper deposition rate depends on the $[OH^-]$ hydroxyl, $\left[Cu^{2+}\right]$ ion, $[Tartrate]$ complexing agent, $[CH_2O]$ formaldehyde concentrations and the textile surface (A) as is shown in Equation (5).

$$\left(\frac{dCu^0}{dt}\right)_{het} = k_{het} \times [OH^-] \times \left[Cu^{2+}\right] \times [CH_2O] \times A \times 1/[Tartrate] \quad (5)$$

The homogeneous copper reaction rate in solution does not depend on the textile surface (A), which is shown in Equation (6).

$$\left(\frac{dCu^0}{dt}\right)_{hom} = k_{hom} \times [OH^-] \times \left[Cu^{2+}\right] \times [CH_2O] \times 1/[Tartrate] \quad (6)$$

where k_{het} and k_{hom} are kinetic constants for heterogeneous and homogenous reactions.

At low OH^-, Tartrate, Cu^{2+} and CH_2O concentrations in solution, the overall copper deposition reaction rate is slow and occurs mainly on the textile surface as highlighted by the green arrow (Figure 1a). The heterogeneous copper deposition rate is large comparing to the homogenous copper reaction rate, which leads to a slow reaction in solution (red arrow).

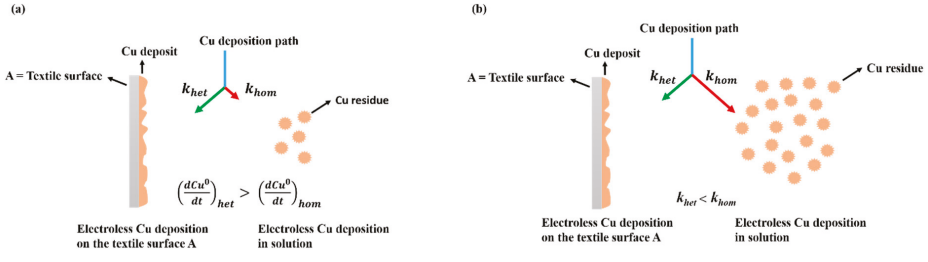

Figure 1. A schematic drawing of the electroless copper deposition during low (**a**) and high (**b**) Cu^{2+} concentrations in solution.

At high OH^-, Cu^{2+}, Tartrate and CH_2O concentrations in solution, the heterogeneous copper deposition rate on CLY surface (*A*) competes with the homogeneous copper reaction rate in solution (Figure 1b). The diffusion of Cu^{2+} ions to the textile surface (a) limits the copper deposition rate. Thus, the formation of copper residue occurs in solution simultaneously to the copper deposition on the textile surface (*A*) and the overall copper deposition rate is large.

An adaptation of the overall Cu^0 deposition rate will be necessary if the Cu^{2+} concentration changes. Figure 2a,b depicts a theoretical and experimental work of the electroless Cu deposition.

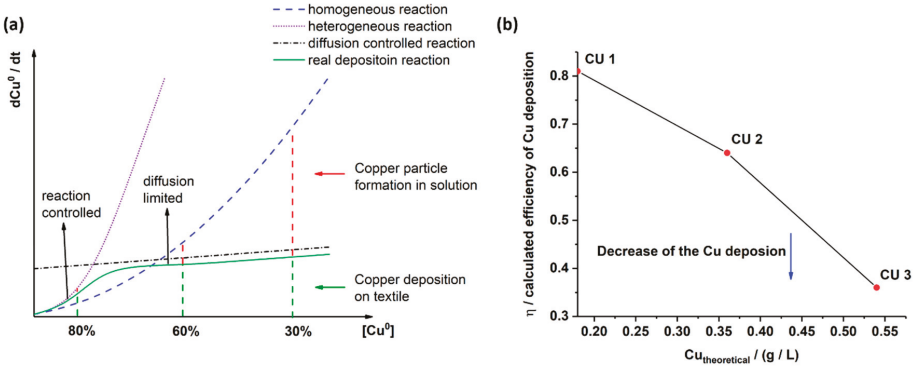

Figure 2. Theoretical (**a**) and experimental work (**b**) of the copper deposition on the textile surface.

At low chemical concentrations (Figure 2a, the reduction and deposition of metallic copper on the silver seeded textile surface depends on Cu^{2+} ion diffusion in solution (diffusion controlled reaction). The reduction of Cu^{2+} to Cu^0 near the surface (*A*) is fast (heterogeneous reaction) and for the copper layer formation Cu^{2+} ions diffuse from solution to the silver seed textile surface where reduction to Cu^0 occurs. Thus, a copper layer grows continuously by contributing more Cu^{2+} ions from solution (real reaction), which explains the large amount of copper (80%) detected on the silver seed textile surface. Side reaction as copper deposition on the beaker walls and the not reduced Cu^{2+} ions in solution are not pronounced. Increasing chemical concentrations (Cu^{2+}, $C_4H_5KO_6$, CH_2O, OH^-) lead to pronounced reduction rate and copper particle formation in solution (homogeneous reaction). As a result, the amount of copper on the textile surface decreases (60%). The formation of copper particles refers to the nucleation in solution, which compete with silver seeds on the textile for the Cu^{2+} ion consumption. At high chemical concentrations (Cu^{2+}), nucleation and growth of copper particles in solution dominate over the copper deposition on the textile surface. The heterogeneous deposition of copper at the textile surface enters into a diffusion controlled reaction, thus further increase in Cu^0 formation does not occur (30%). The Cu^0 formation in the bulk solution however gain importance. The plots were made with regard to various simplifying assumptions such as a constant volume of H_2O (DI), beaker shape and textile surface during the experiments. In Figure 2b the calculated efficiency η of the copper deposition is high at low Cu^{2+} concentrations (CU 1). It drops for CU 2 and CU 3 samples at high Cu^{2+} concentrations. Based on the conditions in CU 1 an enhancement of copper deposition on textiles can be worked out by adding small OH^-, Cu^{2+} and CH_2O concentrations to the solution over time. The theoretical work corresponds well to the experimental work of CU 1, CU 2 and CU 3 samples manufacture.

Apart from the copper coating deposition at the silver seeded CLY fabric, high Cu^{2+} concentrations (0.0568 M, 0.0852 M) enhanced the kinetic reaction for the copper residue formation in solution (Figure 3). At high Cu^{2+}, formaldehyde and $C_4H_5KO_6$ concentrations, copper residue of 1 µm formed in solution, which is shown in Figure 3b for the CU 2 sample. According to EDX (Figure 3c), the copper residue shows peaks of higher relative intensity for copper with respect to the oxygen peak, which may indicate the formation of copper particles in solution.

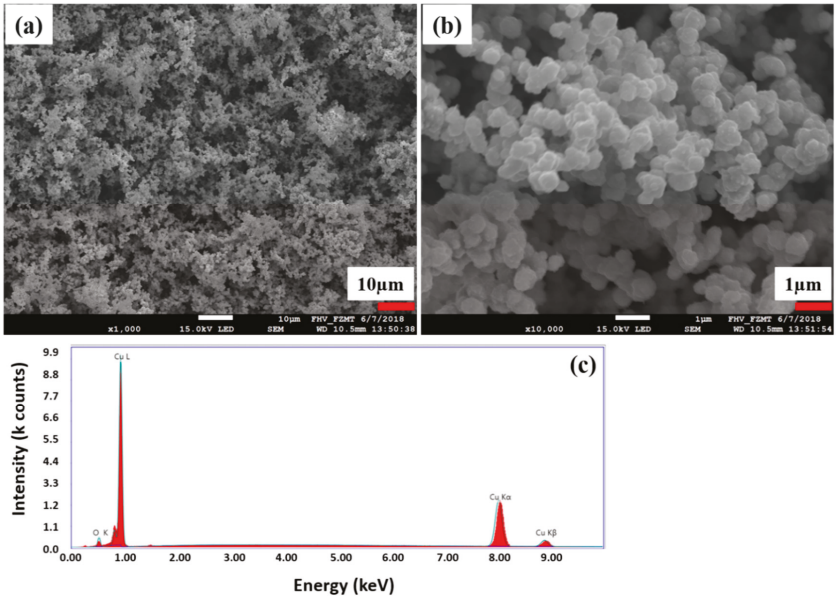

Figure 3. Fragile copper residue (**a**,**b**) formed during the electroless copper coating of fabric (CU 2) is investigated with EDX (**c**).

Due to the lowest sheet resistance and continuous copper layer, the Cu1 sample was chosen for further investigation in mechanical tests.

Figure 4a,b shows a random distribution of the silver seeds on CLY fabric, which build a catalytic surface for the electroless copper deposition. Relative intensity peaks of Ag and Sn are high when the EDX investigation is focused on a single silver seed (Figure 4c,d) comparing to the yarn surface. High relative intensity peaks of C (carbon), O (oxygen) species resulting from the cellulose substrate. Sn^{2+} reduced Ag^{+} to Ag^{0} (metallic) from aqueous solution and formed a silver seed as catalytic surface on the CLY fabric. No continuous Ag layer was observed on the CLY surface.

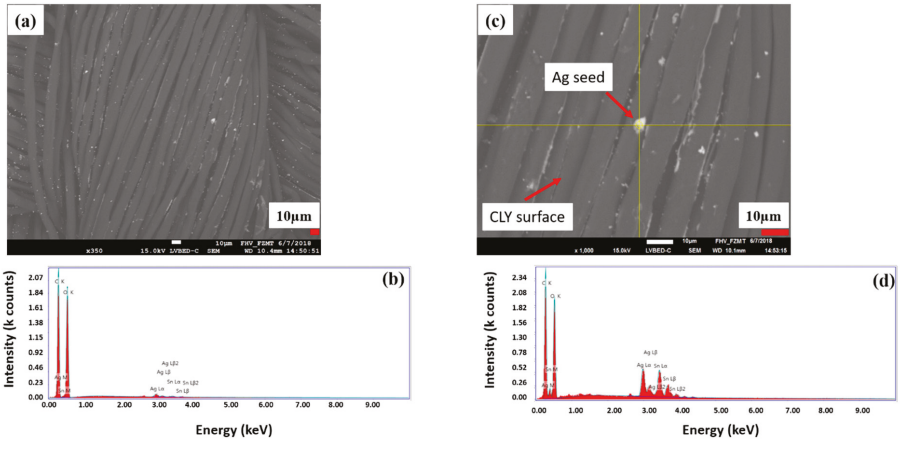

Figure 4. The surface of a silver seeded CLY (CU 1) sample is investigated with SEM (**a**) and EDX investigation (**b**). The magnification a silver seed (**c**) is shown, which is investigated with EDX (**d**).

The silver content in Table 2 is too high to be related only to silver seed of 8 µm size (Figure 3c) and Figure 4c shows silver seeds smaller than 8 µm. The silver seeds had different sizes and were randomly distributed on the CLY surface. In Table 2, the content of silver [Ag] is lower in comparison to the copper content. Thus, silver seeded CLY fabrics indicated a high resistance in GΩ (Giga Ohm) range, which drops to 1.89 Ωsq^{-1} and 5.24 Ωsq^{-1} after the ECD. The copper-coated CLY fabrics reveal a conductive property due to the copper coating.

3.2. Topological Investigation of the Copper Coating

Figure 5 indicates topological investigations of untreated (a), a silver seeded (b) and copper-coated CU 1 (c) samples.

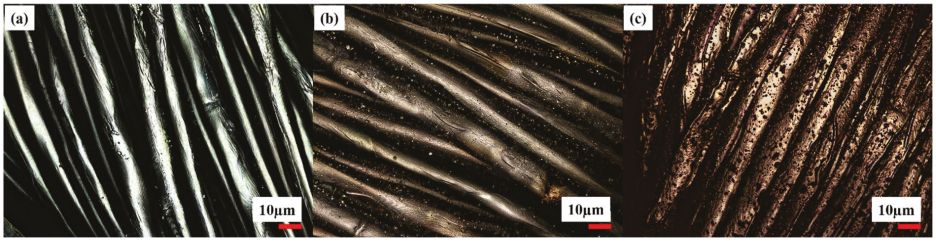

Figure 5. Topology investigation of uncoated (**a**), silver seeded (treated at 0.042M $AgNO_3$) (**b**), and copper layer coated (**c**) CLY CU 1 sample.

The topology investigations showed a gray image of untreated (Figure 5a), a bright yellow image after silver seeding (Figure 5b) and dark red copper-coated image of the CLY fabric (Figure 5c). For additional topological investigation, the copper-coated CLY CU 1 sample is investigated with SEM/EDX (Figure 6). Bright areas consists of a higher copper density in comparison to dark areas. Copper islands (bright areas) grow on a continuous copper layer (dark areas) as highlighted in Figure 6a,b. The surface might contain impurities like copper oxides, or organics due to EDX spectra (Figure 6d). Besides Cu, O and C elements were detected, which were related to the CLY.

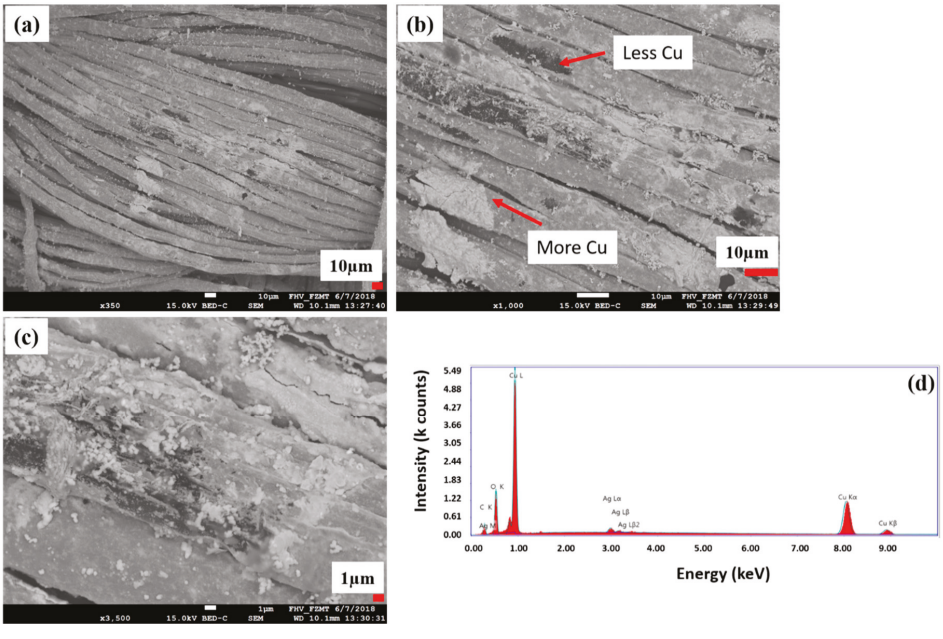

Figure 6. Topology of the copper-coated CLY (CU 1) fabric investigated with SEM (**a**–**c**) and EDX (**d**). High copper amount appears in bright color and low copper amount in dark color.

Figure 6c depicts copper islands smaller than 1 µm, which could be explained by a staggered layer growth during the ECD. Copper might grow in two directions as a copper island (bright color) by increasing its thickness and as a layer (dark color) covering the cellulose surface.

Table 3 is related to the EDX spectra in Figure 6a,d, which shows the elemental distribution of Cu, O, C and Ag from the copper-coated cellulose surface (CU 1). It indicates that the Cu element has the highest weight proportion of 81.36% compared to the O element of 9.46%, C element of 7.4% and Ag element of 1.77% on the copper-coated cellulose sample.

Table 3. Summary of the elemental distribution from the copper-coated cellulose (CU 1) fabric.

Element	Weight (%)	Atom (%)	Net. Int.	Error (%)
C (K)	7.40	24.60	66.92	11.67
O (K)	9.46	23.62	303.38	8.55
Ag (L)	1.77	0.66	51.29	13.88
Cu (K)	81.36	51.12	632.75	3.85

3.3. Cross-Section and Copper-Coated Lyocell Yarn

In Figure 7, a cross-section of the copper-coated CU 1 sample is investigated. According to the topological LSM and SEM investigations, the CU 1 sample shows less copper amount (bright color) in the interior side comparing to its outer surface (Figure 7a,c).

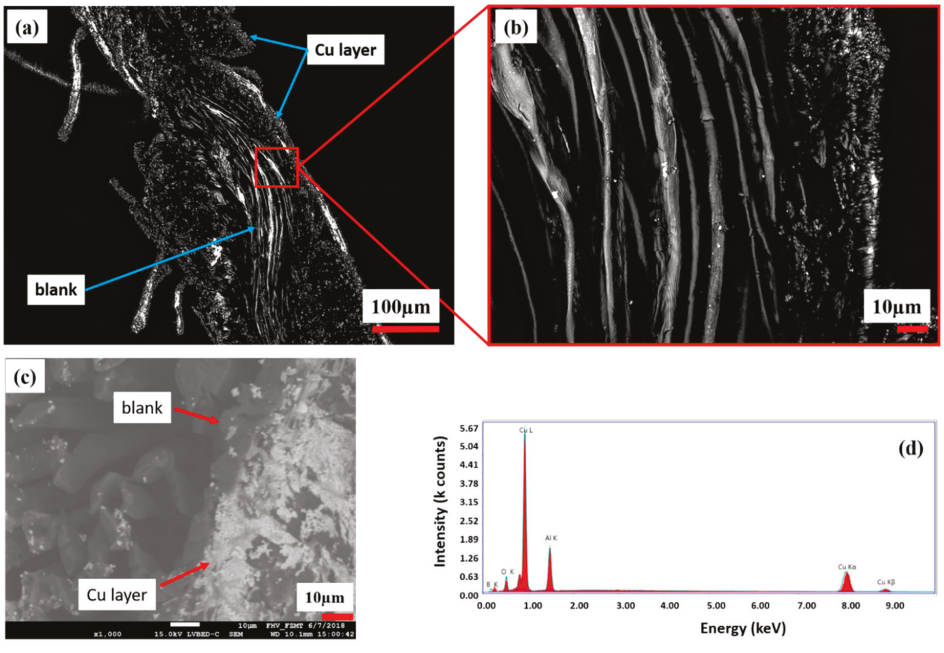

Figure 7. Cross section of the copper-coated CLY fabric (CU 1) and its magnification (**a**,**b**) captured with LSM. SEM/EDX investigation of the same cross section are shown in (**c**,**d**).

In Figure 7c, bright areas are related to the copper layer, which is formed on the outer surface of the CU 1 cross section. Figure 7d indicates high relative intensity Cu peaks comparing to O peaks, which are recorded from the cross section. The appearance of Al and B peaks resulted from the Al table as unwanted side effects and could not be excluded during measurement. There was no continuous copper layer observed in the interior side of the CLY cross section. The Cu deposition occurred on the silver seeded CLY fabric surface and stagnated in the interior side due the low accessibility of solution.

One single yarn was separated from the copper-coated CU 1 CLY fabric and its topology was characterized with SEM/EDX (Figure 8a). Figure 8b shows three copper areas on the CLY yarn appearing in bright color for the copper coating (area 1), in grey for an intermediate coating (area 2) and in dark for non-coated area 3. Each area was investigated separately with EDX, which revealed different copper amounts. Different copper coatings are related to the yarn directions in warp and weft on the CLY sample.

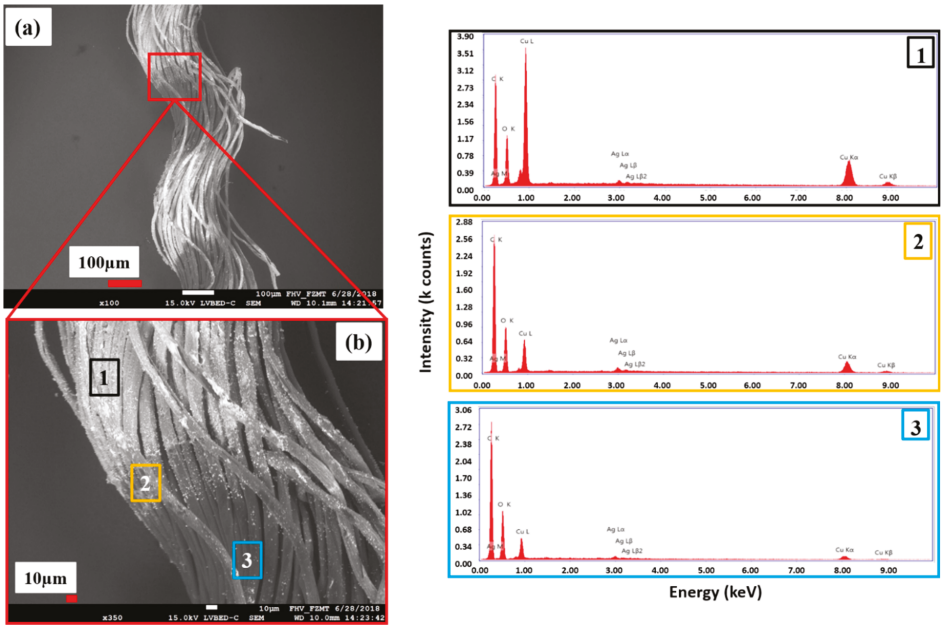

Figure 8. SEM/EDX investigations of the copper-coated CLY (CU1) yarn (**a**) show three different coating areas (**b**) (1, 2, 3).

During the ECD, the copper species was differently distributed on the CLY fabric in an unstirred solution. Consequently, three different areas of copper species (areas 1, 2, 3) appeared on the CLY yarn (Figure 8b). This can be explained by different copper diffusion rates from the bulk to the surface and in the inner part of the CLY fabric. The Cu^{2+} ions diffused from solution and were reduced to Cu^{0} on the silver seed surface of the CLY leading to a copper coating. The diffusion of Cu^{2+} ions to the interior part of the CLY fabric was less efficient, which lead to no copper coating. According to the EDX spectra, copper peaks of low relative intensity were detected in area three (Figure 8) in comparison to area one and two. The relative intensity of copper peaks decreased from area one to area two and reached its lowest value in area three. Ag peaks from the Ag seeds were recorded at a low relative intensity comparing to the copper peaks while the C and O relative intensity peaks were similar in all EDX spectra.

3.4. Mechanical Testing of the Copper-Coated Lyocell

To design spatial copper conductor lines across the garment, one must take into account the critical places like knees and elbows. Such places are highly vulnerable with regard to bending and load during movement. Continuous flex cycles might cause permanent deformation of the garment, which could lead to a damaged copper layer and a loss of an electrical signal. The copper-coated CLY strip was subjected to continuous flex cycles around a cylinder of 15 mm radius in a flex test. During the flex cycles, the fabric did not come under tension. Therefore it is essential to investigate the sheet resistance of the copper layer after flex tests. Figure 9a depicts the results after different flex cycles of the copper-coated strip.

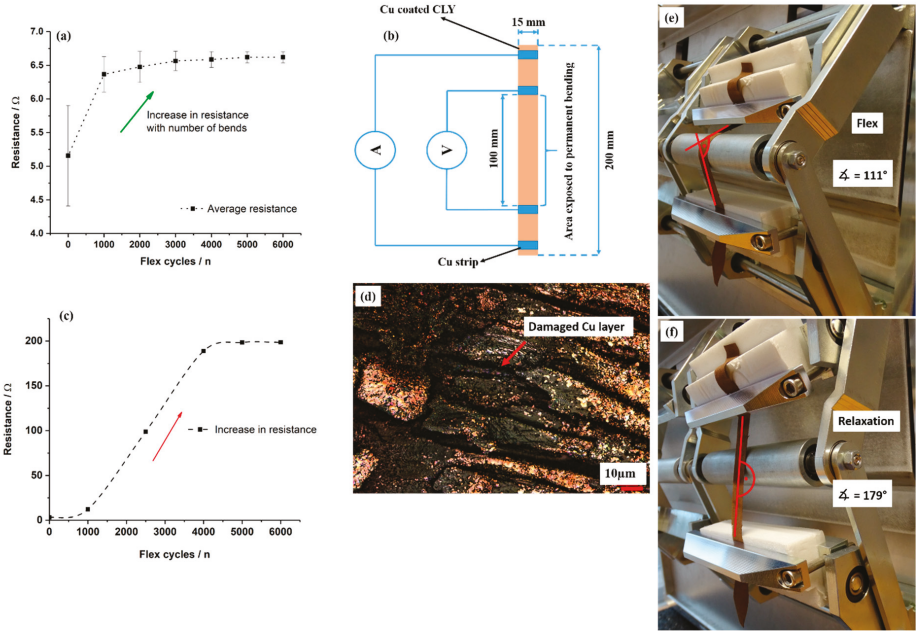

Figure 9. The change of resistance after flex tests (**a**) is measured with the four probe method (**b**). and with the two probe method (**c**). A damaged Cu layer of the CLY strip (CU 1) (**d**) is recorded with LSM after flex tests at different bending angles (**e**,**f**).

The resistance of the copper-coated CLY strip went up from 5.1 Ω before flex cycles to 6.5 Ω after 2000 flex cycles. It approached a plateau of 6.6 Ω/1500 mm^2 from 4000 to 6000 flex cycles. The large error bars at zero flex cycles can be explained with the different local resistances of each copper-coated strip. After 1000 flex cycles, the topology indicated a damage of the copper coating, which increased the resistance (Figure 9d). The copper deposit broke apart after 1000 flex cycles by creating cracks in the coating. Due to the low change of resistance with extended flex cycles no further damage of the copper layer was observed. During flex cycles the angle of bending changed from 111° to 179° (Figure 9e,f) when the copper-coated strip was bended by a metallic cylinder. The resistance was measured after each 1000 flex cycle when the copper-coated CLY strip was placed on an isolating paper background without applying pressure during measurement (Figure 9b). In Figure 9c, the resistance was measured with a two probe method during flex tests and approached a constant value of 200 Ω after 6000 bending cycles. Abry et al. investigated a carbon fiber epoxy substrate, and obtained different electrical resistance [12]. In their post-buckling tests, the applied compressive load to carbon fiber differs to this work, in which a copper coating is investigated on non-conductive cellulose material.

3.5. Cyclic Elongation of the Copper-Coated Lyocell

In Figure 10, the resistance (R) of the copper-coated CLY fabric changed as a function of cyclic elongation. The copper-coated CLY fabric was elongated and relaxed in a cycle, which was fixed between two jaws with an isolating rubber layer. The resistance change during elongation of Cu-coated CLY strip of 28.5 cm^2 was investigated with the four point method. During cyclic elongation, current was applied by the two outer Cu strips while measuring the voltage with two inner Cu strips (Figure 10c,d).

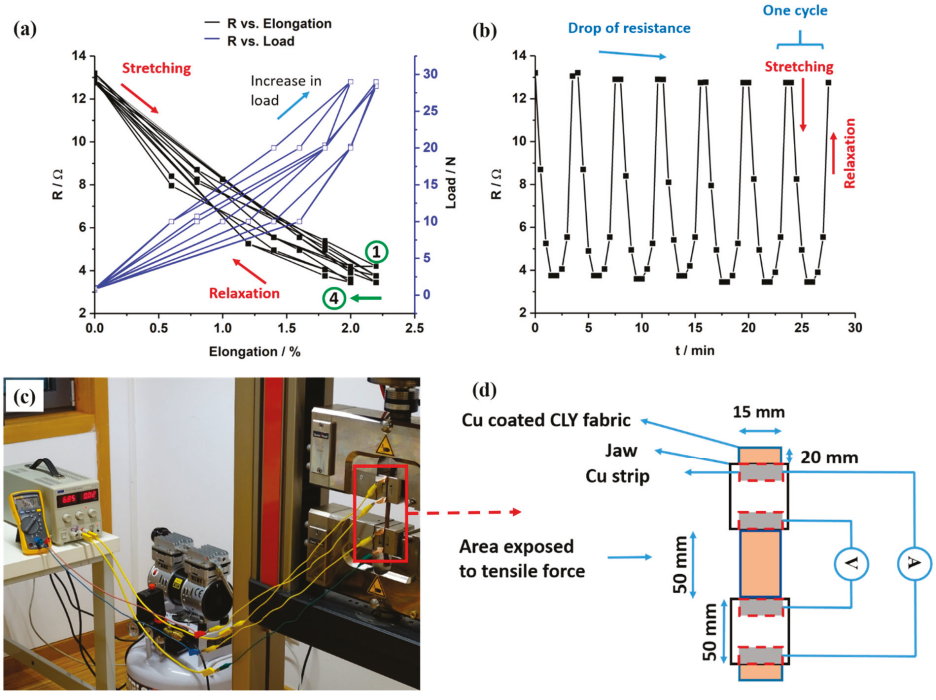

Figure 10. The change of resistance *R* (Ohm) of the Cu-coated CLY fabric (CU 1) (d = 15 mm, l = 50 mm) and applied load are recorded as a function of elongation (**a**) and time (**b**). The detection of the resistance change was conducted with the four point technique (**c**,**d**).

The decrease and increase in resistance of the copper-coated CLY strip are investigated during cyclic elongation marked by black curves in Figure 10a. Blue curves show the elongation and relaxation of the copper-coated strip caused by an applied load. The resistance of the copper-coated CLY strip decreased during elongation and reached a stable value of 2% after 4 cycles as marked by a green arrow. Numbers one and four label those cycles. The contact between Cu-coated yarns influenced the resistance of the CLY strip during elongation. During elongation, the Cu-coated CLY fibers are smashed by an applied load leading to an enlargement of the contact area and to a decrease in resistance. At relaxation, the resistance increased due to separation of the Cu-coated CLY yarns caused by a lower tensile force. Figure 10b depicts a steady decrease of the fabric's resistance with applied tensile force and an increase with relaxation. It is assumed that the applied tensile force squeezed the copper-coated yarns closer together by decreasing their distance. Thus, the copper-coated yarns were oriented in the direction of the applied tensile force, which caused a decrease in resistance during elongation. During relaxation, the resistance of the copper-coated cellulose increased upto 13.2 Ω, which can be explained through the small fabric's elongation of 2%. The purpose for conducting the elongation test up to 2% was to investigate the suitability of the copper-coated cellulose fabric to be used in a respiration sensor. Since the movement of the human body during breathing does not have high strains, the respiratory sensor can be implemented in a garment to monitor breathing. The elongation of 2% is investigated on the inelastic cellulose material and is related its small thickness. After four cycles, the resistance went up and reached a constant value of 13 Ω during further cycles. It is assumed that some copper fibers did not relax after four cycles. Long-time cyclic tests are predicated to show a constant resistance over time due to the smashed state of the copper-coated cellulose fibers during elongation. The resistance of the copper-coated cellulose fibers is expected to increase due to abrasion

and damage of the copper coating during extended durability test, resulting in the sensitivity loss of the strain sensor. We expect the behavior of the Cu-coated cellulose similar to the PEDOT:PSS/PU sample as reported in the work of Ding et al. [37]. The results emphasize the potential of copper-coated CLY fabrics for strain sensors by monitoring textile deformation on a large scale (e.g., during breathing). Zhang et al. used stainless steel and carbon knitted fabrics during cyclic strain tests, whose work showed higher values of resistance during cyclic elongation [13]. In their experimental set-up, high strain and high resistances were related to a loosen sample structure comparing to a woven copper-coated cellulose in this work. Abu-Khalaf et al. produced stretchable circuits composed of PDMS (polydimethylsiloxane) and silver nanoparticle inks, which showed a resistance of 800 Ω during stretching of 25% at 45° [47]. In this work, a copper coating covered the surface of non-conductive cellulose.

3.6. Copper-Coated Cellulose as Moisture Sensor

In Figure 11, the resistance and the weight of a copper-coated CLY were investigated as a function of RH. The change of the RH was measured between 20% and 80% in a climate chamber in air at 25 °C. The copper-coated fabric was preconditioned for 2 h in a climate chamber at 20% RH and 25 °C. Subsequently, the change in RH was recorded stepwise at 30%, 50%, 70% and 80% RH. A period of acclimatization was needed between the steps for monitoring the fabric's weight. Using the mass balance for weight monitoring, allowed the time to be determined when the fabric´s weight did not change leading to an equilibrium. After equilibrium, the resistance of the copper-coated fabric was measured with a four point technique and the RH was set to the next step. Its resistance and mass raised with the increase in RH, which could be explained due to hygroscopic swelling of the cellulose yarns. An increase in the fabric's resistance might be explained due to the disruption of the current along the copper layer caused by hygroscopic expansion of the CLY fabric. During hygroscopic expansion of the CLY fabric, the copper coating was damaged between fibers and current can flow through a smaller copper coating area, which increased the resistance.

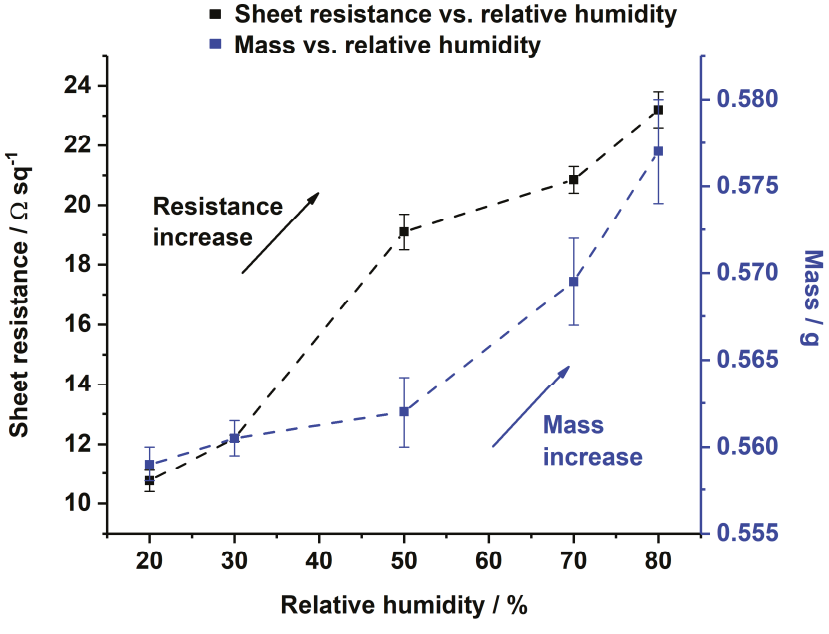

Figure 11. Change of sheet resistance (from 10.8 Ωsq^{-1} to 23 Ωsq^{-1}) and mass change (from 0.55 g to 0.58 g) of the Cu-coated CLY (CU 1) fabric as a function of relative humidity.

Kramar et al. investigated the decrease in electrical resistance of cotton and viscose impregnated metal ion fabrics from Giga Ohm to the Mega Ohm magnitude [44]. Their material was not conductive due to the impregnation of metal ions, which differs to the conductive copper coating in this work.

3.7. Durability in Water

The resistance (R) change of the copper-coated CLY strip was recorded as a function of time (t) in air and in stirred H_2O (DI) solution for 18 h. It was measured with a two probe technique by using a Handheld LCR Meter. In air, it indicates a value of 35 Ω in comparison to the resistance in water of 53 Ω/375 mm^2 (Figure 12a). The aim of this work was to investigate the stability of copper-coated layer on CLY fabrics during repeated wetting/drying cycles. After first wetting (blue line) in H_2O (DI), the electrical resistance was recorded over a time period of 18 h and raised from 53 Ω to 85 Ω comparing to the measurement in air. The copper-coated CLY fabric was dried for 14 h and immersed in to the second H_2O (DI) solution for further 18 h. Its resistance went up from 6 kΩ to 9.5 kΩ, which might result from swelling and loosening of CLY fibers during wetting and drying. During the second measurement in air, the resistance of the copper-coated layer increased from 4 MΩ to 8 MΩ. The repeated wetting and drying steps destroyed the copper layer on the CLY fabric due to the high resistance. Movement of non-coated fibers due to the inside swelling might damage the Cu layer on the surface. Oxidative corrosion might destroy the copper layer, which was not observed after the experiment due to the Figure 12b. Thus, the copper layer could be damaged by the mechanical deformation of the fabric, which led an increase in resistance. The Cu-coated CLY has a wavy structure, which makes monitoring of the resistance (R) in water challenging due to the plain structure of the Cu strip electrodes (Figure 12b).

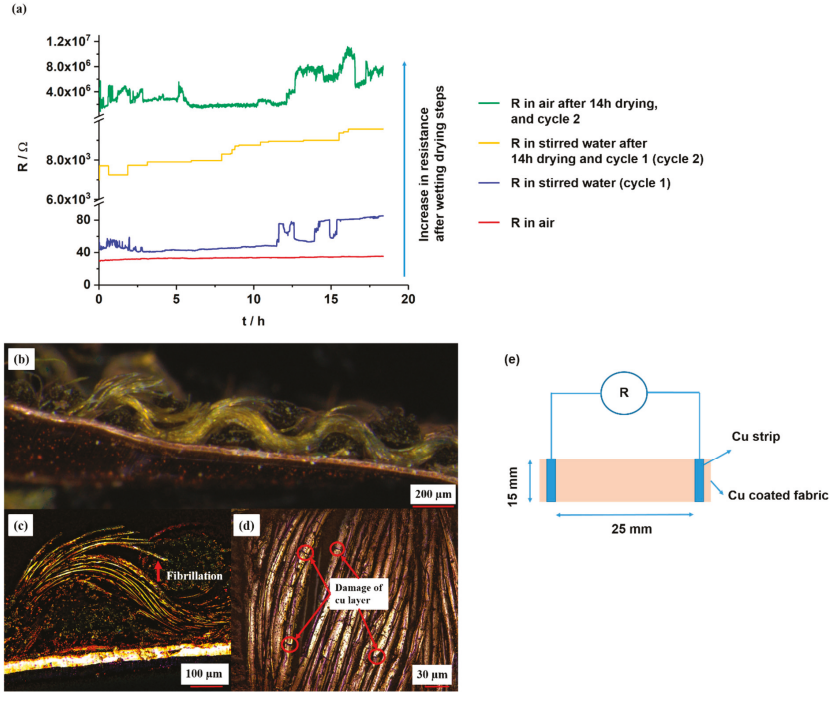

Figure 12. Resistance change of Cu-coated CLY (CU 1) fabrics (d = 15 mm, l = 25 mm) measured in air (red and green curves) and during stirring in water at 25 °C at a stirring speed of 750 rpm (blue and orange curves) (**a**). The figure shows a connection between Cu-coated CLY and Cu foil (**b**), the fibrillation of Cu-coated CLY fibers (**c**), the damaged copper coating (**d**) and the measuring procedure (**e**).

Fibrillation of copper-coated CLY fibers from the yarn might lead to a decrease of the conductive contact area (Figure 12c). The decrease of the contact area between copper-coated fibers raised the electrical resistance during swelling. Swelling of cellulose fabric separated the copper-coated fibers in aqueous environment during which the CLY fabric was soaked with water. During drying in air, the water content evaporated from the copper-coated fabric, and the copper-coated fibers remain in a loosen state. Long term water treatment caused damage in the copper coating and increased its resistance from 38 Ω to 16 MΩ, which was observed after second drying step (Figure 12d). The copper-coated fabrics remained conductive after first wetting in water (DI) which can be explained through a good adhesion between the copper layer and the CLY substrate. Thus the cellulose material could be incorporated in smart textiles for an extended operation time during wet weather (e.g., raining). No peeling of the copper layer was observed during resistance measurement in water. As an alternative, a PES substrate can be used instead of cellulose to avoid swelling. The copper-coated CLY fabric was not a plane substrate, which was connected to the Cu strip through its wavy structure.

3.8. FTIR Investigation

In Figure 13, ATR-FTIR spectrum of uncoated and Cu-coated cellulose is shown, which confirms the chemical changes of the Cu coating at the textile surface. The Cu-coated sample does not indicated characteristic cellulose peaks at 3442 cm^{-1} (O(2)H O(6) intramolecular hydrogen bond), 3340 cm^{-1} (O(3)H O(5) intramolecular hydrogen bond), 2887 cm^{-1} (C–H stretch), 1018 cm^{-1} (C–O vibration at C(3) O(3)H), 991 cm^{-1} (C–O valence vibration at C(6)) and 892 cm^{-1} (C–O–C valence vibration) [48].

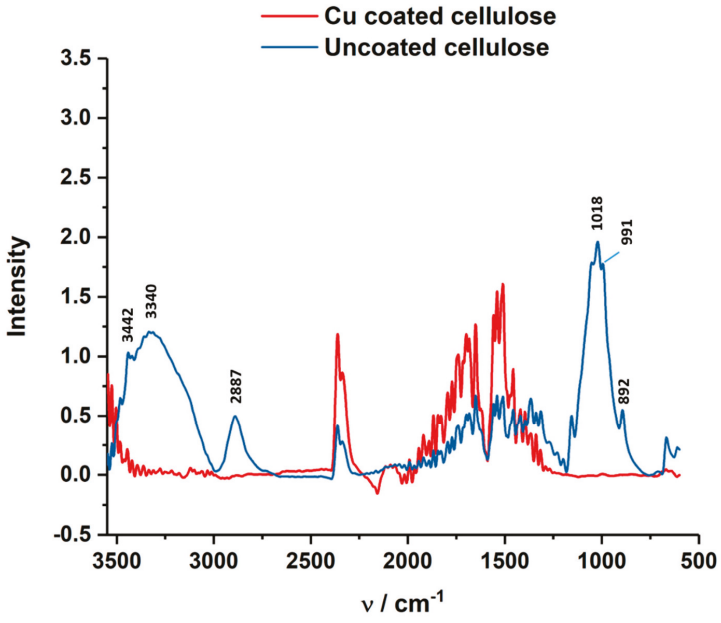

Figure 13. ATR-FTIR spectrum of Cu-coated cellulose (red) of the CU1 sample, which are compared to uncoated cellulose fabric (blue).

It is believed that the coating do not affect the crystallinity of the cellulose structure because of the 0.5M NaOH concentration used during the electroless coating. In the work of Široký et al. molecular reorganization in the amorphous and quasi-crystalline areas is reported at 3.3 and 4.5 mol dm^{-3} of NaOH [48].

4. Conclusions

This work showed that it was possible to slow down the chemical reaction of the electroless copper deposition at the silver seeded CLY surface by using different concentration of Cu^{2+}, CH_2O, $C_4H_5KO_6$, and NaOH. High Cu^{2+}, $C_4H_5KO_6$, NaOH, Tartrate, and CH_2O concentrations led to a diffusion-controlled heterogeneous copper deposition and high homogeneous copper reaction in solution. The heterogeneous rate constant k_{het} was large comparing to the homogeneous rate constant k_{hom}. Thus, the copper deposition on the cellulose surface did not increase further. The copper-coated CLY fabric was sensitive to mechanical deformations and humidity changes. Thus, it was able to transfer an electrical signal through the large surface area even at stretched and deformed condition by maintaining highly conductive due to the low resistance. The copper-coated CLY fabrics maintained conductivity after flex tests, cyclic tensile tests, during different RH, and duringwetting for 18 h (cycle 1) (Figure 12) in water (DI). After 6000 bending cycles, the copper layer was partially damaged but the fabric kept its conductivity by indicating a resistance of 6.6 Ω/1500 mm^2. During cyclic elongation, the resistance of the copper-coated CLY textile decreased. At elongated state, the distance between copper-coated yarns decreased with an increase in contact area. The resistance of the copper-coated textile reached a similar value of 13 Ω/750 mm^2 due to small elongation of 2% after cyclic elongation tests. After cyclic elongation and flex tests, the copper layer was still attached to the CLY substrate, which reveals its strong adhesion to the textile. Continuous swelling and loosening of copper-coated CLY textile during wetting and drying increased the fabrics resistance. The increase in resistance to 16 MΩ/375 mm^2 can be related to damages in the Cu coating due to swelling and expansion of the CLY fabric. Fibrillation of the copper-coated CLY fabric was not observed according to LSM investigations.

Author Contributions: T.B. and T.P. defined the general concept of the study and revised the manuscript. T.W. designed experiments, revised and interpreted the data for cyclic elongation tests. B.C. designed experiments, revised and interpret the data for humidity tests. W.R. conducted the experiments, analyzed the Cu content with AAS and characterized the topology with LSM.

Funding: This research was funded by the CORNET framework in the project Ambitex – "Textile integrated sensors for monitoring of ambient parameters" (FFG 855282) and NanoStretch (FFG 865927).

Acknowledgments: The authors express thanks for providing woven CLY fabrics to Lenzing AG (Austria). Authors voice their gratitude to the Höhere Technische Bundeslehr- und Versuchsanstalt Dornbirn for the AAS accessibility. Additionally, authors thank Prof. Heinz Duelli from the Research Centre for Microtechnology of the FH Vorarlberg for the SEM images and EDX spectrum.

Conflicts of Interest: The authors declare no conflict of interest.

References

1. Hu, L.; Pasta, M.; La Mantia, F.; Cui, L.; Jeong, S.; Deshazer, H.D.; Choi, J.W.; Han, S.M.; Cui, Y. Stretchable, porous, and conductive energy textiles. *Nano Lett.* **2010**, *10*, 708–714. [CrossRef]
2. Ramuz, M.; Tee, B.C.K.; Tok, J.B.H.; Bao, Z. Transparent, optical, pressure-sensitive artificial skin for large-area stretchable electronics. *Adv. Mater.* **2012**, *24*, 3223–3227. [CrossRef]
3. Rogers, J.A.; Someya, T.; Huang, Y. (review)Materials and Mechanics for Stretchable Electronics. *Science* **2010**, *327*, 1603–1607. [CrossRef] [PubMed]
4. Wang, S.; Lu, A.; Zhang, L. Recent advances in regenerated cellulose materials. *Prog. Polym. Sci.* **2016**, *53*, 169–206. [CrossRef]
5. Singha, K. Importance of the Phase Diagram in Lyocell Fiber Spinning. *Int. J. Mater. Eng.* **2012**, *2*, 10–16. [CrossRef]
6. Someya, T.; Kato, Y.; Sekitani, T.; Iba, S.; Noguchi, Y.; Murase, Y.; Kawaguchi, H.; Sakurai, T. Conformable, flexible, large-area networks of pressure and thermal sensors with organic transistor active matrixes. *Proc. Natl. Acad. Sci. USA* **2005**, *102*, 12321–12325. [CrossRef] [PubMed]
7. Someya, T.; Sekitani, T.; Iba, S.; Kato, Y.; Kawaguchi, H.; Sakurai, T. A large-area, flexible pressure sensor matrix with organic field-effect transistors for artificial skin applications. *Proc. Natl. Acad. Sci. USA* **2004**, *101*, 9966–9970. [CrossRef]

8. Huang, Y.; Hu, H.; Huang, Y.; Zhu, M.; Meng, W.; Liu, C.; Pei, Z.; Hao, C.; Wang, Z.; Zhi, C. From industrially weavable and knittable highly conductive yarns to large wearable energy storage textiles. *ACS Nano* **2015**, *9*, 4766–4775. [CrossRef] [PubMed]
9. Shur, M. Semiconductor Thin Films and Thin Film Devices for Electrotextiles. *Int. J. High Speed Electron. Syst.* **2002**, *12*, 317–390. [CrossRef]
10. Yang, L.; Zhou, W.; Jia, J.; Xiong, T.; Zhou, K.; Feng, C.; Zhou, J.; Tang, Z.; Chen, S. Nickel nanoparticles partially embedded into carbon fiber cloth via metal-mediated pitting process as flexible and efficient electrodes for hydrogen evolution reactions. *Carbon N. Y.* **2017**, *122*, 710–717. [CrossRef]
11. Matsuhisa, N.; Inoue, D.; Zalar, P.; Jin, H.; Matsuba, Y.; Itoh, A.; Yokota, T.; Hashizume, D.; Someya, T. Printable elastic conductors by in situ formation of silver nanoparticles from silver flakes. *Nat. Mater.* **2017**, *16*, 834–840. [CrossRef]
12. Abry, J.C.; Bochard, S.; Chateauminois, A.; Salvia, M.; Giraud, G. In situ detection of damage in CFRP laminates by electrical resistance measurements. *Compos. Sci. Tech.* **1999**, *59*, 925–935. [CrossRef]
13. Zhang, H.; Tao, X.; Yu, T.; Wang, S. Conductive knitted fabric as large-strain gauge under high temperature. *Sensors Actuators, A Phys.* **2006**, *126*, 129–140. [CrossRef]
14. Lin, Z.I.; Lou, C.W.; Pan, Y.J.; Hsieh, C.T.; Huang, C.H.; Huang, C.L.; Chen, Y.S.; Lin, J.H. Conductive fabrics made of polypropylene/multi-walled carbon nanotube coated polyester yarns: Mechanical properties and electromagnetic interference shielding effectiveness. *Compos. Sci. Technol.* **2017**, *141*, 74–82. [CrossRef]
15. Perumalraj, R. Electrical Surface Resistivity of Polyaniline Coated Woven Fabrics. *J. Text. Sci. Eng.* **2015**, *5*, 1–5. [CrossRef]
16. Hansen, T.S.; West, K.; Hassager, O.; Larsen, N.B. Highly stretchable and conductive polymer material made from poly(3,4-ethylenedioxythiophene) and polyurethane elastomers. *Adv. Funct. Mater.* **2007**, *17*, 3069–3073. [CrossRef]
17. Kageyama, K.; Yoshikawa, T.; Kato, H. Variation in Electrical Properties of Laminates with Woven Carbon Fabric and Ferroelectric or Piezoelectric Particulate Epoxy due to Tensile Loading. *Mater. Trans.* **2005**, *46*, 697–703. [CrossRef]
18. Yun, T.G.; Oh, M.; Hu, L.; Hyun, S.; Han, S.M. Enhancement of electrochemical performance of textile based supercapacitor using mechanical pre-straining. *J. Power Sources* **2013**, *244*, 783–791. [CrossRef]
19. Qu, M.; Nilsson, F.; Schubert, D. Effect of Filler Orientation on the Electrical Conductivity of Carbon Fiber/PMMA Composites. *Fibers* **2018**, *6*, 3. [CrossRef]
20. Won, Y.; Kim, A.; Yang, W.; Jeong, S.; Moon, J. A highly stretchable, helical copper nanowire conductor exhibiting a stretchability of 700. *NPG Asia Mater.* **2014**, *6*, e132. [CrossRef]
21. Ali, A.; Baheti, V.; Militky, J.; Khan, Z.; Tunakova, V.; Naeem, S. Copper coated multifunctional cotton fabrics. *J. Ind. Text.* **2017**, *48*, 448–464. [CrossRef]
22. Nishio, Y.; Todoroki, A.; Mizutani, Y.; Suzuki, Y. Piezoresistive effect of plain-weave CFRP fabric subjected to cyclic loading. *Adv. Compos. Mater.* **2017**, *26*, 229–243. [CrossRef]
23. De Baere, I.; Van Paepegem, W.; Degrieck, J. Electrical resistance measurement for in situ monitoring of fatigue of carbon fabric composites. *Int. J. Fatigue* **2010**, *32*, 197–207. [CrossRef]
24. Cui, H.; Suganuma, K.; Uchida, H. Highly stretchable, electrically conductive textiles fabricated from silver nanowires and cupro fabrics using a simple dipping – drying method. *Nano Res.* **2015**, *8*, 1604–1614. [CrossRef]
25. Wang, D.; Zhang, Y.; Lu, X.; Ma, Z.; Xie, C.; Zheng, Z. Chemical formation of soft metal electrodes for flexible and wearable electronics. *Chem. Soc. Rev.* **2018**, *47*, 4611–4641. [CrossRef] [PubMed]
26. Tao, X. *Handbook of Smart Textiles*, 1st ed.; Springer: Hong Kong, 2015; ISBN 9789814451451.
27. Dias, T. *Electronic Textiles: Smart Fabrics and Wearable Technology*, 1st ed.; Dias, T., Ed.; Woodhead: Oxford, UK, 2015; ISBN 9780081002018.
28. Jia, J.; Xu, C.; Pan, S.; Xia, S.; Wei, P.; Noh, H.Y.; Zhang, P.; Jiang, X. Conductive Thread-Based Textile Sensor for Continuous Perspiration Level Monitoring. *Sensors* **2018**, *18*, 3775. [CrossRef] [PubMed]
29. Bajgar, V.; Penhaker, M.; Martinková, L.; Pavlovic, A.; Bober, P.; Trchová, M.; Stejskal, J. Cotton Fabric Coated with Conducting Polymers and its Application in Monitoring of Carnivorous Plant Response. *Sensors* **2016**, *16*, 498. [CrossRef] [PubMed]
30. Zieba, J.; Frydrysiak, M. Textronics - Electrical and electronic textiles. Sensors for breathing frequency measurement. *Fibres Text. East. Eur.* **2006**, *14*, 43–48.

31. Ehrmann, A.; Heimlich, F.; Brücken, A.; Weber, M.; Haug, R. Suitability of knitted fabrics as elongation sensors subject to structure, stitch dimension and elongation direction. *Text. Res. J.* **2014**, *84*, 2006–2012. [CrossRef]
32. Li, L.; Liu, S.; Ding, F.; Hua, T.; au, W.M.; Wong, K.S. Electromechanical analysis of length-related resistance and contact resistance of conductive knitted fabrics. *Text. Res. J.* **2012**, *82*, 2062–2070. [CrossRef]
33. Kongahage, D.; Foroughi, J. Actuator Materials: Review on Recent Advances and Future Outlook for Smart Textiles. *Fibers* **2019**, *7*, 21. [CrossRef]
34. Atalay, O.; Richard Kennon, W.; Dawood Husain, M. Textile-based weft knitted strain sensors: Effect of fabric parameters on sensor properties. *Sensors (Switzerland)* **2013**, *13*, 11114–11127. [CrossRef]
35. Atalay, O.; Kennon, W. Knitted Strain Sensors: Impact of Design Parameters on Sensing Properties. *Sensors* **2014**, *14*, 4712–4730. [CrossRef]
36. Hu, J.; Zhou, S.; Shi, J.; Zhang, H.; Zhu, F.; Yang, X. Determinants of electrical resistance change of in situ PPy-polymerized stretch plain woven fabric under uniaxial tensile strain. *J. Text. Inst.* **2017**, *108*, 1545–1551. [CrossRef]
37. Ding, Y.; Xu, W.; Wang, W.; Fong, H.; Zhu, Z. Scalable and Facile Preparation of Highly Stretchable Electrospun PEDOT:PSS@PU Fibrous Nonwovens toward Wearable Conductive Textile Applications. *ACS Appl. Mater. Interfaces* **2017**, *9*, 30014–30023. [CrossRef] [PubMed]
38. Mahmood, H.; Dorigato, A.; Pegoretti, A. Temperature Dependent Strain/Damage Monitoring of Glass/Epoxy Composites with Graphene as a Piezoresistive Interphase. *Fibers* **2019**, *7*, 17. [CrossRef]
39. Ding, Y.; Xu, T.; Onyilagha, O.; Fong, H.; Zhu, Z. Recent advances in flexible and wearable pressure sensors based on piezoresistive 3D monolithic conductive sponges. *ACS Appl. Mater. Interfaces* **2019**, *11*, 6685–6704. [CrossRef]
40. Baima, M.; Andrew, T. Fluoropolymer-Wrapped Conductive Threads for Textile Touch Sensors Operating via the Triboelectric Effect. *Fibers* **2018**, *6*, 41. [CrossRef]
41. Ebrahimi, I.; Gashti, M.P. Chemically reduced versus photo-reduced clay-Ag-polypyrrole ternary nanocomposites: Comparing thermal, optical, electrical and electromagnetic shielding properties. *Mater. Res. Bull.* **2016**, *83*, 96–107. [CrossRef]
42. Široká, B.; Manian, A.P.; Noisternig, M.F.; Henniges, U.; Kostic, M.; Potthast, A.; Griesser, U.J.; Bechtold, T. Wash-dry cycle induced changes in low-ordered parts of regenerated cellulosic fibers. *J. Appl. Polym. Sci.* **2012**, *126*, E396–E407. [CrossRef]
43. Jaturapiree, A.; Ehrhardt, A.; Groner, S.; Öztürk, H.B.; Siroka, B.; Bechtold, T. Treatment in swelling solutions modifying cellulose fiber reactivity - Part 1: Accessibility and sorption. *Macromol. Symp.* **2008**, *262*, 39–49. [CrossRef]
44. Kramar, A.D.; Asanović, K.A.; Obradović, B.M.; Kuraica, M.M.; Kostić, M.M. Electrical Resistivity of Plasma Treated Viscose and Cotton Fabrics with Incorporated Metal Ions. *Fibers Polym.* **2018**, *19*, 571–579. [CrossRef]
45. Shim, B.S.; Chen, W.; Doty, C.; Xu, C.; Kotov, N.A. Smart electronic yarns and wearable fabrics for human biomonitoring made by carbon nanotube coating with polyelectrolytes. *Nano Lett.* **2008**, *8*, 4151–4157. [CrossRef] [PubMed]
46. Root, W.; Aguiló-Aguayo, N.; Pham, T.; Bechtold, T. Conductive layers through electroless deposition of copper on woven cellulose lyocell fabrics. *Surf. Coatings Technol.* **2018**, *348*, 13–21. [CrossRef]
47. Abu-khalaf, J.; Saraireh, R.; Eisa, S.; Al-Halhouli, A. Experimental Characterization of Inkjet-Printed Stretchable Circuits forWearable Sensor Applications. *Sensors* **2018**, *18*, 3476. [CrossRef]
48. Široký, J.; Blackburn, R.S.; Bechtold, T.; Taylor, J.; White, P. Attenuated total reflectance Fourier-transform Infrared spectroscopy analysis of crystallinity changes in lyocell following continuous treatment with sodium hydroxide. *Cellulose* **2010**, *17*, 103–115. [CrossRef]

polymers

MDPI

Article

Electrospin-Coating of Paper: A Natural Extracellular Matrix Inspired Design of Scaffold

Kelvin Ng [1], Pedram Azari [1,2], Hui Yin Nam [3], Feng Xu [4,5] and Belinda Pingguan-Murphy [1,2,*]

1 Department of Biomedical Engineering, Faculty of Engineering, University of Malaya, Kuala Lumpur 50603, Malaysia; ngkelvin88@hotmail.com (K.N.); pedram.azari@gmail.com (P.A.)
2 Centre for Applied Biomechanics, Department of Biomedical Engineering, Faculty of Engineering, University of Malaya, Kuala Lumpur 50603, Malaysia
3 Tissue Engineering Group, Department of Orthopaedic Surgery (NOCERAL), Faculty of Medicine, University of Malaya, Kuala Lumpur 50603, Malaysia; huiyin26@yahoo.com
4 The Key Laboratory of Biomedical Information Engineering of Ministry of Education, School of Life Science and Technology, Xi'an Jiaotong University, Xi'an 710049, China; fengxu@xjtu.edu.cn
5 Bioinspired Engineering and Biomechanics Center (BEBC), Xi'an Jiaotong University, Xi'an 710049, China
* Correspondence: bpingguan@um.edu.my; Tel.: +603-7967-4491

Received: 12 March 2019; Accepted: 2 April 2019; Published: 9 April 2019

Abstract: Paper has recently found widespread applications in biomedical fields, especially as an alternative scaffolding material for cell cultures, owing to properties such as its fibrous nature, porosity and flexibility. However, paper on its own is not an optimal material for cell cultures as it lacks adhesion moieties specific to mammalian cells, and modifications such as hydrogel integration and chemical vapor deposition are necessary to make it a favorable scaffolding material. The present study focuses on modification of filter paper through electrospin-coating and dip-coating with polycaprolactone (PCL), a promising biomaterial in tissue engineering. Morphological analysis, evaluation of cell viability, alkaline phosphatase (ALP) activity and live/dead assays were conducted to study the potential of the modified paper-based scaffold. The results were compared to filter paper (FP) and electrospun PCL (ES-PCL) as reference samples. The results indicate that electrospin-coating paper is a simple and efficient way of modifying FP. It not only improves the morphology of the deposited electrospun layer through reduction of the fiber diameter by nearly 75%, but also greatly reduces the scaffold fabrication time compared to ES-PCL. The biochemical assays (Resazurin and ALP) indicate that electrospin-coated filter paper (ES-PCL/FP) provides significantly higher readings compared to all other groups. The live/dead results also show improved cell-distribution and cell-scaffold attachment all over the ES-PCL/FP.

Keywords: electrospinning; tissue engineering; paper-based scaffolds; osteoblast proliferation; polycaprolactone

1. Introduction

Paper, with history dating back thousands of years to when it was initially invented as a tool to record and preserve information, has recently found widespread applications in biomedical fields, such as paper-based electronics [1], low-cost and disposable analytical platforms [2–4], microfluidic devices for drug screening [5], and disease modeling [6–9]. As a biomaterial, paper offers several advantages such as low cost of production, biocompatibility, ease of chemical alteration, and physical modifiability [10]. For example, paper has shown great potential as an alternative scaffolding material for cell cultures owing to properties such as its fibrous nature, porosity and flexibility. Its porous structure produces a wicking capability which allows the flow of medium across the paper, thus facilitating the transportation of nutrients and release of waste products [11]. The cellulose fibers in

the paper provide a platform for physical and biological support of the cultured cells, enabling them to grow into functioning tissue in an in vitro environment [10,12–14]. These advantages exhibited by versatile paper materials have enticed researchers into further exploring the potential of the paper as a cell culture scaffold.

Although paper has several favorable properties for biomedical applications, on its own, it is not an optimal material for cell cultures. Some properties, such as lack of cell adhesion moiety [15] and relatively large pore size, have been found to create difficulty for cell migration along the paper scaffold, in which the cell will need to take a longer path in situation where the void gap is too wide for the filopodia to bridge [10]. Several studies have shown that modification of paper is necessary to manipulate its chemical and physical properties and create a more feasible environment for cell proliferation, migration, and differentiation [16,17]. Various modification methods for paper have been reported, including binding of ceramics to the paper surface with latex binder to modify the topography [18], chemical vapor deposition of polymers onto paper to increase the cell adhesion moiety for better cell growth [9], wax printing on paper to manipulate the proliferation direction of cells, and the addition of hydrogels to permit better cell migration within a stacked-up paper scaffold [7,8]. Most of these modification methods use polymers to modify the properties of paper scaffolds to be more biochemically favorable for cell culture. While for scaffolding applications it is critically important to maintain the porous structure of paper upon the addition of polymer [19], some of the modification methods involve use of heat or chemicals that might damage paper's natural fibrous microstructure. Furthermore, the pore size and fiber diameter of paper are far bigger than natural extracellular matrices (ECM), which is an interwoven random fibrous structure primarily made of proteins (mainly collagen and elastin), proteoglycans, and glycosaminoglycans [20,21]. ECM plays a crucial role in providing support for cell attachment and growth as well as serving as a reservoir of water, nutrients, cytokines, and growth factors for maintenance of tissue homeostasis [20]. An ideal scaffold must mimic the structure and geometry of ECM to significantly enhance tissue formation [13] and provide explicit biophysical and biochemical cues to distinctly modulate cellular response for promoting tissue restoration.

The electrospinning technique has gained popularity in recent years as a feasible method to fabricate biomimetic polymeric scaffolds that resemble native ECM [22–25]. Among a wide range of polymers that have been electrospun [26], polycaprolactone (PCL) has found extensive applications in tissue engineering. PCL is soluble in organic solvents, such as chloroform, and toluene at room temperature with low cost of synthesis [27]. When PCL is electrospun, apart from its favorable intrinsic properties, it also gains advantages such as high surface-area-to-volume ratio, high porosity and an interconnected porous network, all of which are crucial in a biomimetic material [28]. However, the hydrophobic nature of PCL is not favorable for cell adhesion as it prevents cells from proliferating into the pores of the scaffold, leading to low cell affinity and uncontrolled biological interactions with the scaffold [27,29]. Additional surface modification methods are often required to alter the surface hydrophobicity for the improvement of cell affinity [30,31]. Blending or using PCL in combination with other hydrophilic biopolymers has been a very popular strategy to address some of the shortcomings of PCL [29]. In a recent study, Yew et al. reported modification of nitrocellulose membranes with electrospun PCL, where electrospun PCL was able to alter the wicking properties of the membrane and enhance the protein binding, as well as improving detection sensitivity of nucleic acid-based lateral flow assay [28]. Protein binding is an important aspect of scaffolds for cell anchoring and a combination of paper and PCL has the potential to produce a scaffold with a controllable degree of hydrophilicity and wicking properties. Further, electrospinning PCL on paper could resolve the morphological issue of paper for cell work and produce an ECM-like scaffold, with paper performing as a reservoir basement layer to enhance the nutrient delivery. However, the potential for modification of paper-based scaffolds with electrospun PCL has not yet been explored.

Bone tissue lesions—one of the most widely occurring injuries to human body—are results of trauma, increased life expectancy, ageing population and obesity. It is estimated that bone injuries

requiring treatment will double between 2012 and 2020 [32]. Tissue engineering-inspired therapies are the only feasible solution to the current clinical challenge of providing bone replacements [33]. Bone cells (osteoblasts, osteocytes and osteoclasts), as the building blocks of bone tissue, have increasingly been the subject of studies in vivo and in vitro due to their significant role in acceleration of bone tissue regeneration. The need for improved scaffolding materials to function as an artificial ECM, to facilitate the localization and delivery cells to the desired sites in the body, is never ending [34]. Paper-based platforms have shown great potential in osteogenic differentiation of stem cells [9,35]. The promising results obtained in previous studies motivated us to use human fetal osteoblast (hFOB) to evaluate the in vitro performance of our scaffold designs. Although translation of in vivo results into practice is easier, in vitro studies provide a more cost-effective initial insight in terms of cell viability and scaffolds capability in maintaining phenotype and functionality [36]. Besides, progress in understanding the causes of in vivo transplantation failure has led to improvements in design of scaffolding materials to provide more accurate results in relevance to future transplantation trials [36,37].

This article focuses on the modification of paper with PCL and studies scaffolds in terms of physical and morphological properties, as well as hFOB cell viability. To evaluate the effect of a combination of the filter paper (FP) and PCL, two groups of samples were prepared through electrospin-coating and dip-coating. FP and electrospun PCL (ES-PCL) were used as reference samples. The results suggest that electrospin-coating of paper has great potential to improve cell viability and tissue formation as a scaffolding material.

2. Materials and Methods

2.1. Dip-Coating of Filter Paper (DFP)

The filter papers (Whatman®grade 114) were cut into 1 × 1 cm pieces using a paper guillotine cutter. The cut filter paper was submerged in a 10 wt.% solution of PCL (Sigma Aldrich, St. Louis, MO, USA, Mn = 80,000 g/mol) in chloroform (Frinedemann Schmidt, Perth, Australia) for approximately 3 s and then left to dry at room temperature (Figure 1a).

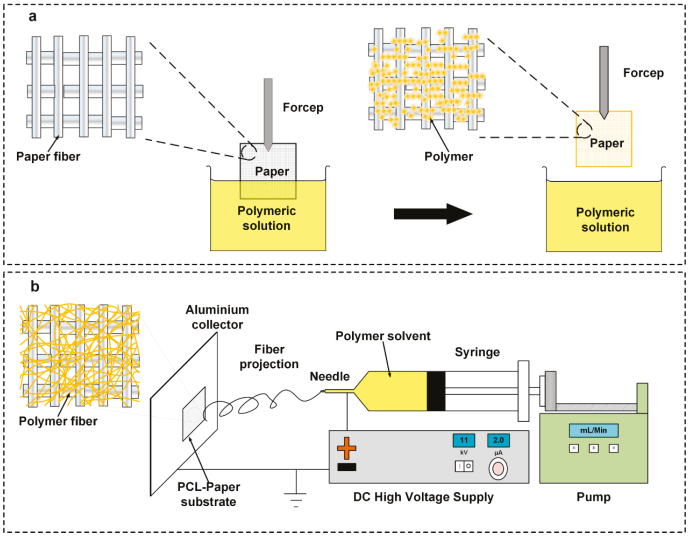

Figure 1. Schematics of filter paper modification. (**a**) Dip-coating of filter paper with polycaprolactone (PCL) solution (DFP), (**b**) Electrospinning of PCL on Filter paper (ES-PCL/FP).

2.2. Electrospin-Coating of Paper (ES-PCL/FP)

The spinning dope was prepared by dissolving PCL pellets (10% w/v) in a co-solvent mixture, comprising 9 volumetric parts of chloroform and 1 volumetric part of N, N-dimethylformamide (DMF) (Sigma Aldrich, St. Louis, MO, USA). The solution was prepared at room temperature under magnetic stirring in a condensed conical flask to obtain a clear homogenous solution. The solution was loaded into a 10 mL syringe (Terumo) with a 20 G blunt needle horizontally placed 18 cm from the aluminum collector. The feeding rate of the syringe pump (KD-100, KD Scientific Inc, Holliston, MA, USA) was adjusted at 3 mL/h. The electrospin-coating was carried out using a DC voltage of 12 kV (Gamma High Voltage Research, Ormond Beach, FL, USA) while a piece of filter paper (5 cm × 5 cm) was stuck on the aluminum collector (Figure 1b). The duration of the electrospin-coating was 30 min.

2.3. Electrospun PCL (ES-PCL)

Electrospinning of PCL was carried using the same parameters reported in Section 2.2 directly on aluminum foil. 20 mL PCL solution was electrospun to obtain a scaffold with sufficient thickness for cell culturing.

2.4. Porosity Measurement

The porosity of the scaffolds was measured using a Pycnometer (Marienfeld, Lauda-Königshofen, Germany) based on the Archimedes Principle. Absolute ethanol (John Kollin Corporation, Midlothian, UK) was used as the medium and gravimetric displacement of liquid was measured at room temperature [38]. The porosity of the scaffolds was calculated based on Equation (1).

$$\text{Porosity } (\%) = \frac{W_2 - W_3 - W_m}{\rho_e} / \frac{W_1 - W_3}{\rho_e} \times 100 \quad (1)$$

where W_1 represents the weight of the pycnometer filled with absolute ethanol, W_2 is the weight of pycnometer filled with absolute ethanol and scaffold, W_3 is the weight of pycnometer and absolute ethanol when the ethanol-soaked scaffold had been taken out from W_2, W_m is the dry weight of the scaffold, and ρ_e is the density of the absolute ethanol.

2.5. Characterization of Scaffold Mechanical Properties

Tensile tests were carried out using an INSTRON 3345 device with a load of 100 N based on ASTM D 638. The specimens were punched in dumbbell-shaped geometries with dimensions of 50 mm × 9 mm (length × width). The support span length was set at 50 mm. The testing speed was set at 1 mm/min. The strain (ε) was evaluated as the ratio between the elongation of the specimen Δl and the original length l_0 as shown in Equation (2).

$$\varepsilon = \Delta l / l_0 \quad (2)$$

2.6. Field Emission Scanning Electron Microscopy (FESEM)

The morphology of the scaffolds was studied using FESEM (Carl Zeiss Auriga, Oberkochen, Germany). Samples were sputter coated with gold and analyzed under FESEM. For samples seeded with cells, cell fixation was conducted prior to coating as described in Section 2.8.4. The fiber diameter and pore size were measured based on the obtained FESEM images using ImageJ software (version 1.48).

2.7. Cell Culture

The osteoblast cell lines, hFOB 1.19, (ATCC, Manassas, VA, USA), were used in this research. hFOB cells were cultured in T-75 flasks (Thermo Fisher Scientific, Waltham, MA, USA) by using Dulbecco's Modified Eagle's Medium (DMEM F12, Gibco™, Waltham, MA, USA) with 10% fetal bovine serum (FBS, Gibco™, Waltham, MA, USA), and 1% Geneticin® (G418, Thermo Fisher, Waltham, MA, USA).

The cells were cultured at 34 °C in a humidified (5% CO_2, 95% air) atmosphere. When cells reached confluence, cells were detached with Accutase®(Innovative Cell Technologies, USA). Cell suspension at a density of 5×10^6 cells/ml was prepared for further use. 10 μL of the cell suspension was seed onto each presoaked scaffold (1 × 1 cm). The scaffolds were incubated for 2 hours. 1 mL of medium was micropipette into each well to submerge the scaffolds. Only passage 5 cells were used in this study.

2.8. Characterization of Cell Viability and Morphology

2.8.1. Resazurin Reduction Assay

The Resazurin Reduction assay was performed at three time points, namely, days 1, 4, and 7. Resazurin Stock solution was prepared by dissolving 140 mg of Resazurin powder (Sigma-Aldrich, St. Louis, MO, USA) into 1000 mL of phosphate buffer saline (PBS) (Sigma-Aldrich, St. Louis, MO, USA). Resazurin working solution was prepared by mixing stock solution with PBS at a volumetric ratio of 1:9. The samples were incubated for 4 h at 34 °C with a 5% CO_2 atmosphere for the conversion of resazurin to resorufin. Triplicates of 100 mL of the Resazurin working solution incubated with cells grown on each scaffold were taken for absorbance measurements. The optical densities were then measured using a microplate reader (FLUOstar OPTIMA, BMG labtech, GmbH, Ortenberg, Germany) at an absorbance wavelength of 570 nm, with 595 nm set as the reference wavelength. Unseeded sterilized scaffolds were incubated under the same conditions in resazurin working solution as blanks and absorbance values were calculated accordingly.

2.8.2. Live/Dead Confocal

The Live/Dead Viability/Cytotoxicity Kit (Life Technologies, Carlsbad, CA, USA) measures the cell viability based on the integrity of cell membranes. Specimens were supplemented with 10 μL of PBS mixture containing calcein-AM and ethidium homodimer-1 in a 1:4 ratio and incubated for 20 min at room temperature.

2.8.3. Alkaline Phosphatase (ALP) Assay

RIPA Lysis, extraction buffer and p-nitrophenyl phosphate (p-NPP) (Thermo Fisher, Waltham, MA, USA) were used to perform the ALP assay. pNPP solution used to lyse the substrate was incubated with cell lysate. ALP in cell lysate converted pNPP substrate to p-nitrophenol. A standard curve of Optical Density (OD) plotted against 4-nitrophenol concentration was generated and used in estimation of ALP activity. By comparing the OD obtained from reaction mixture to standard curve of 4-nitrophenol, the quantity of pNPP substrate converted to p-nitrophenol over time was estimated.

2.8.4. Cell Fixation for FESEM

The samples seeded with cells were washed 3 times in PBS and fixed with 2.4% glutaraldehyde solution (Sigma Aldrich Co., St. Louis, MO, USA) for 24 h. After fixing, the specimens were washed 3 times again with PBS, placed through a series of graded ethanol solutions for dehydration, and allowed to dry overnight in a freeze dryer (FreeZone, Labconco, Hampton, NH, USA) prior to FESEM.

2.9. Statistical Analysis

For statistical analysis of biochemical assay results, a minimum of six technical replications (N = 6) were used for each group of samples. Data were tested by one-way analysis of variance (ANOVA) with Turkey post hoc test using IBM SPSS version 23 software (SPSS Inc., Chicago, IL, USA). P-values less than 0.05 ($p < 0.05$) were reported as statistically significant.

3. Results and Discussion

3.1. Scaffold Morphological Analysis

Figure 2 shows the morphologies of 4 different types of scaffold, namely electrospun PCL (ES-PCL) (Figure 2a), electrospun PCL on filter paper (ES-PCL-FP) (Figure 2b), filter paper (FP) (Figure 2c) and dip-coated filter paper (DFP) (Figure 2d). With FP serving as the collecting platform during electrospinning, the diameters of the PCL fibers produced have been reduced by approximately 75% (Figure 1b). Separately, when FP was just dipped into the PCL solution, there was only a small change in FP fiber diameter, a reduction of 12%. Using filter paper as the collecting platform helps the removal of solvent from the electrospinning jet, through adsorption of excess solvent and facilitation of evaporation. Other studies reported that a higher rate of solvent removal leads to formation of fibers with smaller diameters. For example, Liu et al. reported that the porosity of the collector can affect the morphology of the deposited fibers [39]. Porous surfaces such as paper can affect the packing density of the deposited nanofibers as well as faster evaporation of residual solvents due to their higher surface area. Paper has the capability of absorbing liquid through capillary action, owing to its porous structure, which is able to absorb the residual solvent from the deposited fiber spun on the paper [10]. Wannatong et al. also reported that high boiling point solvents such as DMF, when used in electrospinning, could result in the formation of wet fibers on the collector [40], and that an increase in the evaporation rate of the solvent improved the morphology. Whatman 114# filter paper used in this research was capable of rapid absorption and enhancing the solvent evaporation.

Table 1. shows the average porosity, pore size, thickness and tensile strength of the 4 types of scaffold. ES-PCL had the highest porosity (66.71%), followed by ES-PCL/FP (25.26%), then FP (7.55%) and the lowest was DFP (3.23%). The comparison of ES-PCL/FP and FP showed that coating a thin layer of PCL could increase the overall porosity of the scaffold more than twofold. However, the formation of thinner and straighter fibers on the surface of ES-PCL/FP, as indicated in Figure 1b, has resulted in a reduction in pore size. This was due to multiple layers of thin and straight nanofibers overlapping each other and leading to a reduction in the pore size. DFP had lower porosity compared to FP as PCL solution had further reduced its porosity to 50%. Besides, the more densely packed and overlapped nanofibers also increase the degree of fiber to fiber fusion, which could lead to a significant increase in tensile strength [41,42]. ES-PCL has the lowest tensile strength, while ES-PCL/FP with the smallest fiber diameters has the highest tensile strength (Table 1). However, a similar event was not observed in DFP, as non-homogenous distribution of PCL within FP does not contribute significantly to the tensile strength. In fact, electrospinning caused more PCL to be deposited on the FP (49.69 ± 9.3 μm thickness n = 7, (ES-PCL/FP-FP)) in comparison with the dipping method (37.78 ± 22 μm thickness n = 7, (DFP-FP)). This shows that electrospinning forms an integrated layer of PCL onto FP and the elastic nature of ES-PCL contributes to tensile properties. The microscopic interfacial view of the ES-PCL/FP is presented in supplementary material Figure S1.

Table 1. Porosity percentage and thickness of scaffold.

Scaffold Properties	ES-PCL	ES-PCl/FP	FP	DFP
Tensile Strength (MPa)	1.68 ± 0.23	5.80 ± 0.32	3.52 ± 0.38	3.54 ± 0.17
Porosity (%)	66.71 ± 2.65	25.26 ± 1.60	7.55 ± 2.76	3.23 ± 0.59
Pore size (μm)	13.11 ± 1.07	5.42 ± 0.22	92.13 ± 11.98	73.67 ± 17.00
Thickness (μm)	232.07 ± 11.59	258.78 ± 9.03	209.09 ± 0.50	246.87 ± 21.81

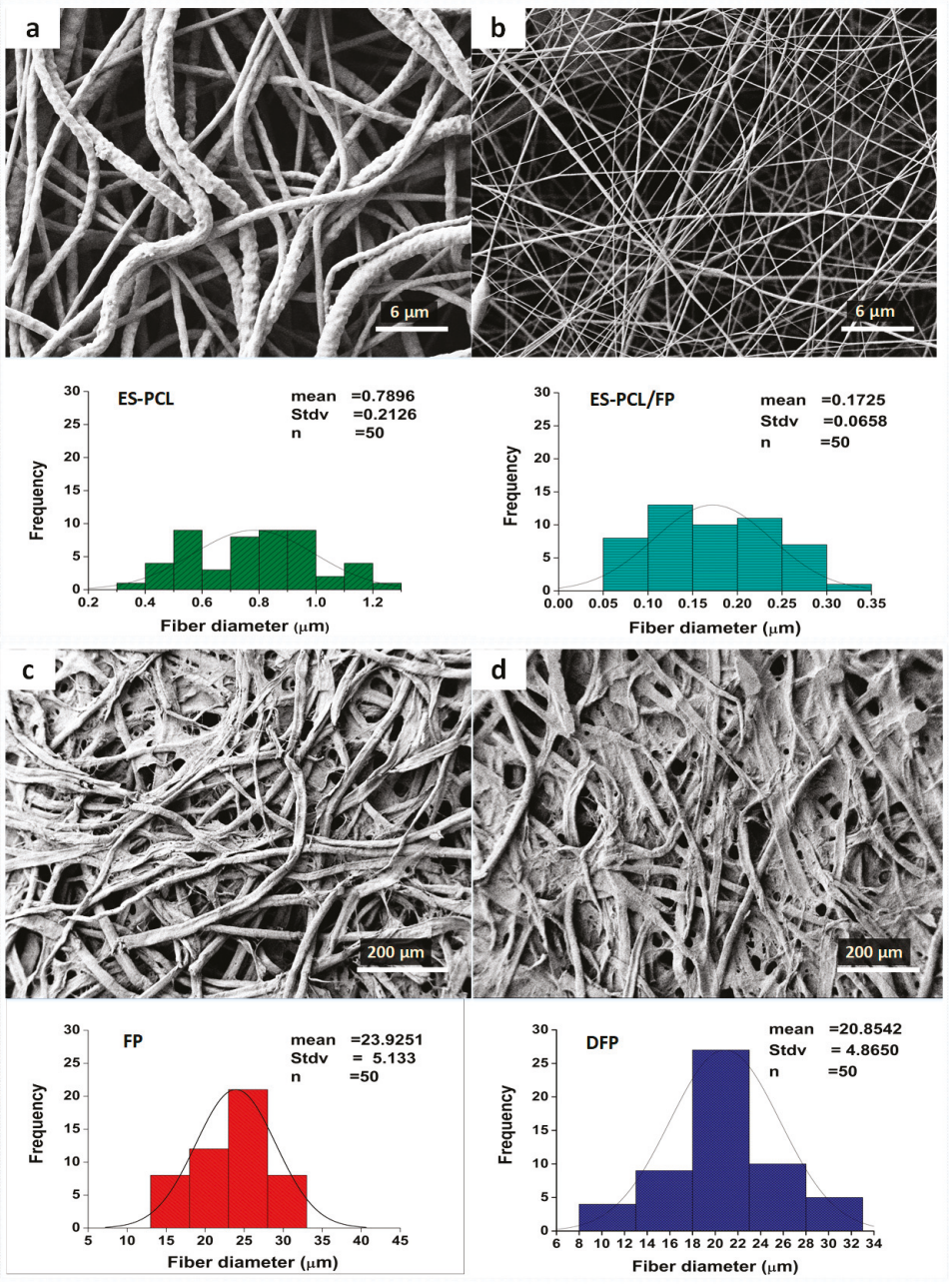

Figure 2. Scaffold morphological analysis. Field emission scanning electron microscopy (FESEM) microscopy of (**a**) ES-PCL, (**b**) ES-PCL/FP, (**c**) filter paper (FP) and (**d**) dip-coated filter paper (DFP) of their relevant fiber diameter distribution pattern.

3.2. Cell-Scaffold Interactions

FESEM was used to evaluate morphology, adhesion, and the interaction of hFOB cells within the scaffold. Figure 2 shows the microscopic images of the hFOB cells on the scaffold on day 1, day 4 and day 7. For the ES-PCL scaffold (Figure 3a–c), the cells spread on the surface of the fiber and were more flattened, thicker and showed less distinct filopodia. As for the ES-PCL/FP scaffolds (Figure 3d–f), cells were observed to be more elongated, well-anchored to the fiber through distinct filopodia and microvilli and proliferating well along the direction of fiber alignment. In the FP scaffold (Figure 3g–i), the cells were observed to attach to the struts of cellulose fibers. Figure 3g shows that the cells bridged between two struts, whereas Figure 3h–i shows that the cells grew and covered up pores of the cellulose. As for the DFP scaffold (Figure 3j–l), the cells were seen mainly at areas where there are pores. The smooth surface and low porosity of the DFP scaffold (Figure 3j–l) does not provide a good surface for cells to attach and spread. Cells attached very poorly on the flat surface and with short filopodia. Furthermore, the reduced porosity of DFP may have prohibited cell penetration and infiltration within the scaffold. The micrograph clearly shows that the cell morphology and proliferation depend on the topography of the scaffold, such as fiber diameter, orientation and pore size [23,43].

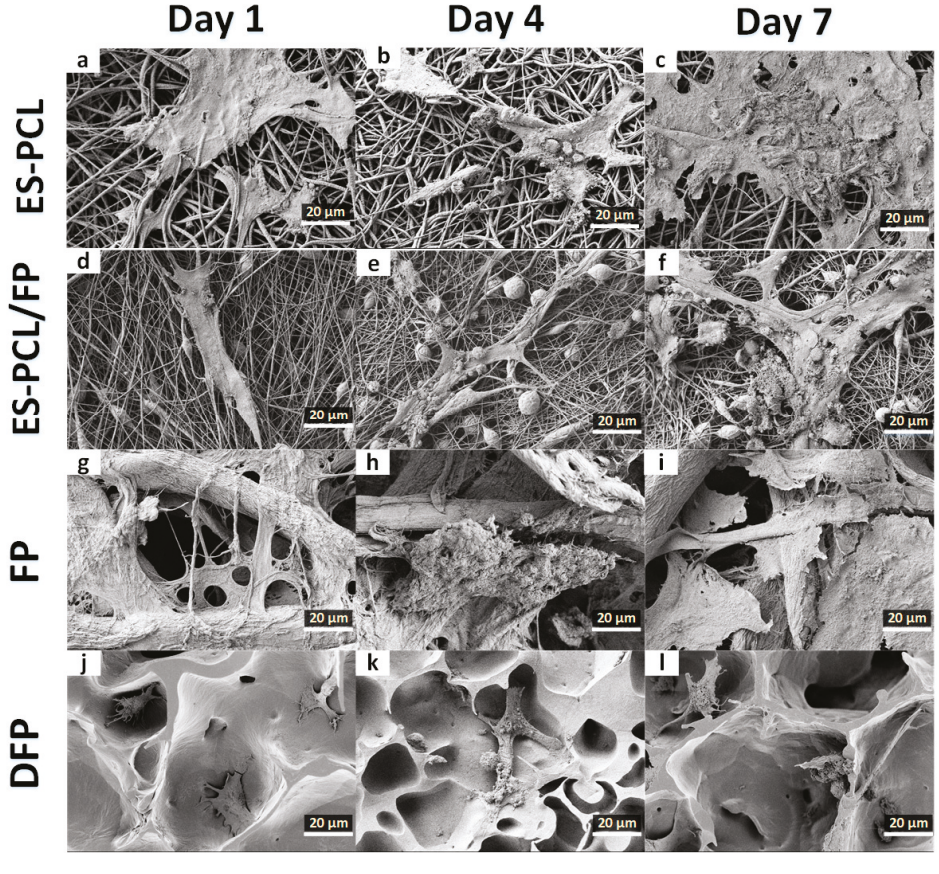

Figure 3. Cell morphological analysis. FESEM images showing the morphology of human fetal osteoblast (hFOB) plotted separately for each individual scaffold of ES-PCL (**a**–**c**), ES-PCL/FP (**d**–**f**), FP (**g**–**i**), and DFP (**j**–**l**) on different days. The magnification and resolution of all images are the same.

3.3. Cell Proliferation Assay

Figure 4 shows the metabolic activity of hFOB measured at the different time points (i.e., day 1, day 4 and day 7) for all groups of scaffolds. Comparison between the groups showed that ES-PCL/FP provided the highest proliferation readings on all days and the difference compared to other groups on the same day was significant. ES-PCL showed significantly lower metabolic activity on days 1 and 4 compared to other groups on the same day but reached the same level as FP and DFP on day 7. FP and DFP only indicated significant metabolic activity difference on day 1. While the two groups' metabolic activity continued to rise on days 4 and 7, the difference was insignificant.

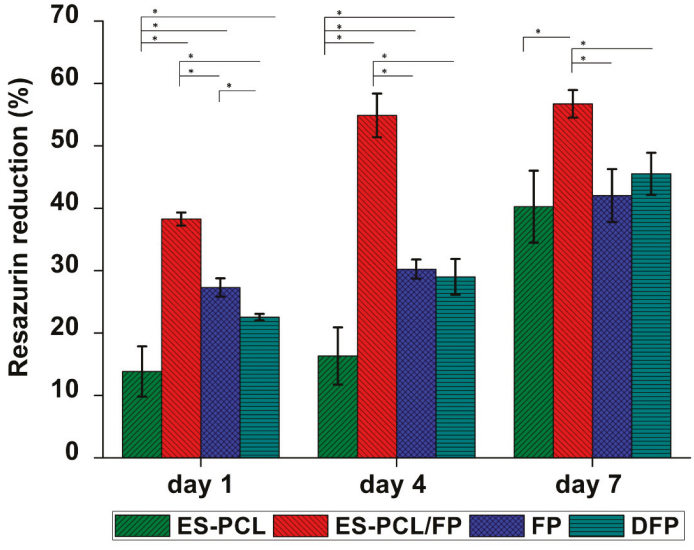

Figure 4. Cell proliferation analysis. Resazurin proliferation assay results for (ES-PCL, ES-PCL/FP, FP, and DFP). The resazurin reduction of hFOB increased on ES-PCL, ES-PCL/FP, FP, and DFP as a function of time. * indicates statistical significance ($P < 0.05$).

As shown in Figure 4, the metabolic activity of different scaffolds ascended steadily from day 1 to day 7. The increase in metabolic activity for FP and DFP was significant throughout the time period. However, metabolic activity measured on ES-PCL/FP scaffolds showed significant increase only until day 4, and there was no significant difference between day 4 and day 7. This suggests that the cells on ES-PCL/FP may have reached confluency between the two time points. For ES-PCL scaffold, the metabolic activity on day 1 and day 4 was not significantly different, however there was a sharp increase in metabolic activity after day 4 and there was a difference in metabolic activity between day 4 and 7. This data is in line with the live/dead images, in which the cell density was almost the same on day 1 as on day 4.

3.4. Live/Dead Assay

Figure 5 shows the microscopic images of the scaffolds under fluorescent excitation using live/dead staining. Abundance of green spots indicates the high viability of hFOB cells on the scaffolds in a period of 7-day incubation. The confocal fluorescent excitation of blank scaffolds is presented in supplementary material Figure S2. As expected, the results suggest that paper and PCL are biocompatible substrates for cell culture. The abundance of green cells could suggest attachment of hFOB cells on the scaffolds as the images exhibited cells anchored on the surface with extended filopodia, a typical characteristic of osteoblast morphology [44]. There were clearly more live cells on the ES-PCL/FP scaffold in all

three-time points (Figure 5d–f), cells were more well spread, and cell density was higher compared to other scaffolds on day 7 (Figure 5f). This result is in line with resazurin metabolic activity. The image (Figure 5f) also showed that the ES-PCL/FP surface was confluent with live cells without visible dead cells. DFP and FP scaffolds showed more individual cells. By day 4 cells on both DFP and FP scaffolds have spread out and occupied more space. The live-dead assay revealed that cell distribution was better on scaffolds with smaller fiber diameter than larger fiber diameters, as reflected by day 7 images (Figure 5c,f,i,l). Topography factors such as fiber diameter of a scaffold affect the cell growth, as the scaffold with a smaller fiber size provides a higher surface area for cell anchoring which leads to both higher cell growth and more even distribution [23,43].

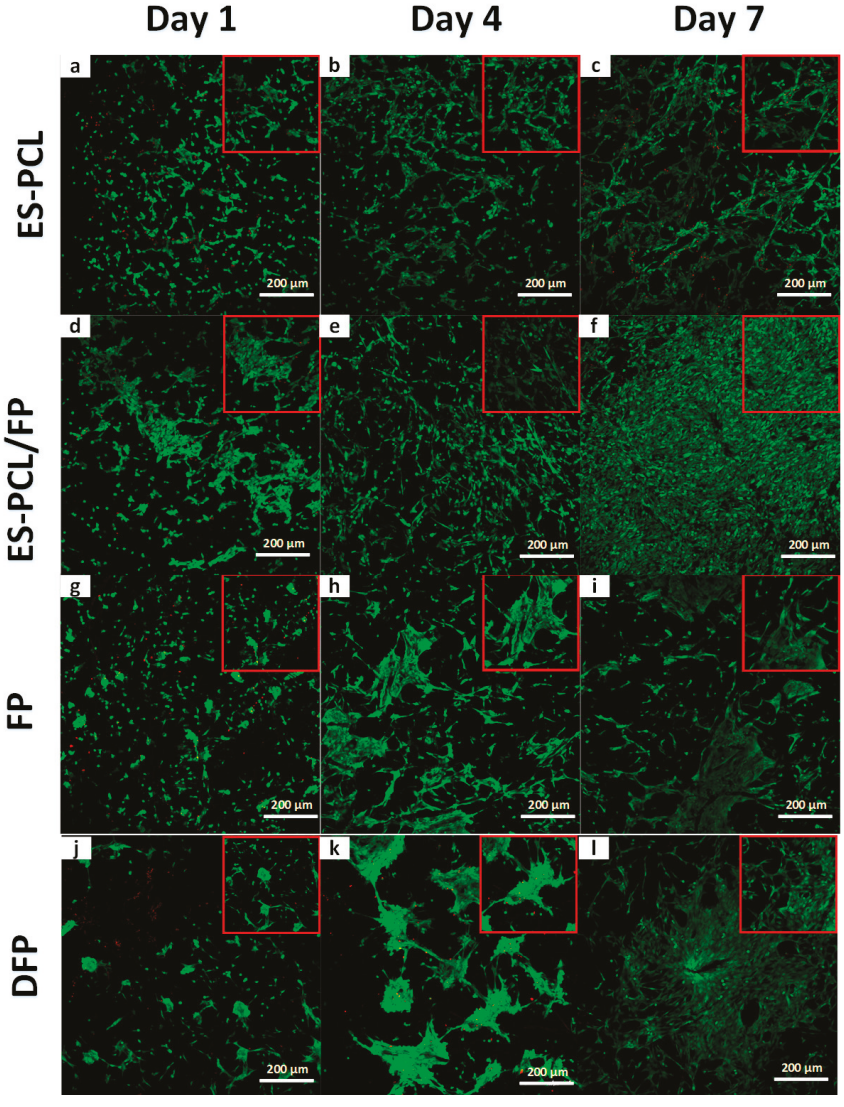

Figure 5. Cell viability analysis. Live/dead confocal of hFOB plotted separately for each individual substrate ES-PCL (**a**–**c**), ES-PCL/FP (**d**–**f**), FP (**g**–**i**), and DFP (**j**–**l**) on different days. The magnification and resolution of all images are the same.

3.5. Alkaline Phosphatase (ALP) Activity

Figure 6 shows the ALP activity of hFOB measured over a period of 14 days. As shown in Figure 6, the ALP activity on ES-PCL, FP and DFP scaffolds showed an ascending trend from day 1 till day 7. On day 14, DFP and -FP scaffolds showed a slight decrease in ALP activity. The ALP activity of ES-PCL/FP is significantly higher than other groups on all days. The ALP activity of ES-PCL/FP between day 7 and day 14 did not changed significantly, which indicates that the cells reached confluency, resulting in the ALP activity staying the same. The ALP activity results are in line with the resazurin assay, in which the ES-PCL/FP scaffold showed the highest readings in both. The ALP activity results also support the live/dead results. It has been reported that better distribution of cells can improve osteospecific differentiation [45]; based on live/dead assay (Figure 5f), ES-PCL/FP indicates the highest number of cells and cell spreading all over the surface of the scaffold.

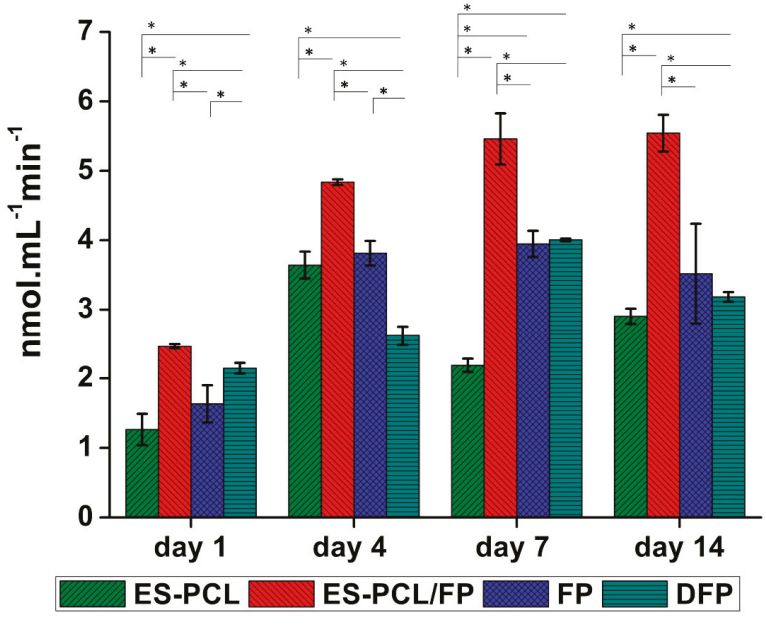

Figure 6. Bone metabolic activity analysis. Alkaline phosphatase (ALP) assay results for hFOB seeded-in (ES-PCL, ES-PCL/FP, FP, and DFP) at different time point. The ALP activity of hFOB increased on ES-PCL, ES-PCL/FP, FP, and DFP as a function of time. The results are statistically significant ($P < 0.05$).

4. Conclusions

The present study evaluated the modification of FP through combination with PCL using electrospinning and dip coating methods, and their characteristics were compared to each other. The potential of the fabricated scaffolds in terms of cell viability (e.g., proliferation, adhesion and osteoblast cell activity (ALP)) was measured and compared. Dip coating of FP provided the least favorable cellular response within the groups. This was a result of reduced porosity of DFP, which decreased the number of anchoring spots for the cells and limiting the overall penetration and distribution of the cells within the scaffold. Dip coating of FP is similar to modification of paper using hydrogels, where in both methods polymer is applied to bridge the gap between paper pores to attain better cell attachment and distribution over the scaffold [6,7]. However, the hydrogels should have an edge over the dip coating with high molecular weight polymers as they do not obstruct cell penetration and distribution within the scaffold. While DFP and ES-PCL/FP used the same material combination, the comparison between

the two groups showed that ES-PCL/FP is superior in cell viability and mechanical properties. This was due to better surface morphology and higher porosity of ES-PCL/FP. The biochemical assay results suggested that electrospin-coating of FP was a simple and effective way in which PCL and paper could complement each other. The fiber diameter of the electrospun PCL reduced greatly when it was collected on paper (ES-PCL/FP). The tensile strength of the ES-PCL/FP increased due to deposition of a layer of relatively elastic ES-PCL on top of FP and the rise in degree of fusion point. ES-PCL/FP also showed the highest metabolic and ALP activity as the most cell-viable among the scaffolds tested. The morphology of the cell attachment and distribution over the scaffolds indicated attachment to scaffold and anchoring of cells on ES-PCL/FP was more favorable. In conclusion, the electrospinning of PCL fibers on paper gives a synergistic outcome, in which the wicking capability of paper can retain cell suspension within the scaffold, improving the efficiency of cell seeding. Furthermore, electrospin-coating of paper reduces the scaffold fabrication time more than 10-fold compared to scaffolds fabricated purely based on electrospinning.

Supplementary Materials: The following are available online at http://www.mdpi.com/2073-4360/11/4/650/s1. Figure S1. Optical Microscopy of ES-PCL/FP after 14 days of immersion in culturing medium. Figure S2. Live/dead confocal microscopy of blank scaffolds.

Author Contributions: K.N. and P.A. conceived, designed and executed the experiments. K.N. and P.A. analyzed the data and wrote the manuscript. N.H.Y. assisted part of the experiments and data interpretation. F.X. and B.P.-M. contributed to the revision of the manuscript. Funding is acquired by B.P.-M.

Funding: This research was financially supported by RU Grant—Fakulti Program Project No. GPF054A-2018.

Acknowledgments: The authors wish to thank Liyana Abu for providing technical support in the tissue engineering lab during the conduction of the experiments. The authors also would express their gratitude to Poon Chi Tat and Yong Kar Wey for the valuable advices that they generously offered during cell culturing experiments.

Conflicts of Interest: The authors declare no conflict of interest. The funders had no role in the design of the study; in the collection, analyses, or interpretation of data; in the writing of the manuscript, or in the decision to publish the results.

References

1. Liu, H.; Qing, H.B.; Li, Z.D.; Han, Y.L.; Lin, M.; Yang, H.; Li, A.; Lu, T.J.; Li, F.; Xu, F. Paper: A promising material for human-friendly functional wearable electronics. *Mater. Sci. Eng. R-Rep.* **2017**, *112*, 1–22. [CrossRef]
2. Cheng, M.L.; Lin, C.C.; Su, H.L.; Chen, P.Y.; Sun, Y.M. Processing and characterization of electrospun poly(3-hydroxybutyrate-co-3-hydroxyhexanoate) nanofibrous membranes. *Polymer* **2008**, *49*, 546–553. [CrossRef]
3. Hu, J.; Wang, S.; Wang, L.; Li, F.; Pingguan-Murphy, B.; Lu, T.J.; Xu, F. Advances in paper-based point-of-care diagnostics. *Biosens. Bioelectron.* **2014**, *54*, 585–597. [CrossRef] [PubMed]
4. Martinez, A.W.; Phillips, S.T.; Butte, M.J.; Whitesides, G.M. Patterned paper as a platform for inexpensive, low-volume, portable bioassays. *Angew. Chem. Int. Ed. Engl.* **2007**, *46*, 1318–1320. [CrossRef]
5. Hong, B.; Xue, P.; Wu, Y.; Bao, J.; Chuah, Y.J.; Kang, Y. A concentration gradient generator on a paper-based microfluidic chip coupled with cell culture microarray for high-throughput drug screening. *Biomed. Microdevices* **2016**, *18*, 21. [CrossRef]
6. Derda, R.; Laromaine, A.; Mammoto, A.; Tang, S.K.; Mammoto, T.; Ingber, D.E.; Whitesides, G.M. Paper-supported 3D cell culture for tissue-based bioassays. *Proc. Natl. Acad. Sci. USA* **2009**, *106*, 18457–18462. [CrossRef]
7. Derda, R.; Tang, S.K.; Laromaine, A.; Mosadegh, B.; Hong, E.; Mwangi, M.; Mammoto, A.; Ingber, D.E.; Whitesides, G.M. Multizone paper platform for 3D cell cultures. *PLoS ONE* **2011**, *6*, e18940. [CrossRef]
8. Mosadegh, B.; Dabiri, B.E.; Lockett, M.R.; Derda, R.; Campbell, P.; Parker, K.K.; Whitesides, G.M. Three-dimensional paper-based model for cardiac ischemia. *Adv. Healthc. Mater.* **2014**, *3*, 1036–1043. [CrossRef] [PubMed]

9. Park, H.J.; Yu, S.J.; Yang, K.; Jin, Y.; Cho, A.N.; Kim, J.; Lee, B.; Yang, H.S.; Im, S.G.; Cho, S.W. Paper-based bioactive scaffolds for stem cell-mediated bone tissue engineering. *Biomaterials* **2014**, *35*, 9811–9823. [CrossRef] [PubMed]
10. Ng, K.; Gao, B.; Yong, K.W.; Li, Y.H.; Shi, M.; Zhao, X.; Li, Z.D.; Zhang, X.H.; Pingguan-Murphy, B.; Yang, H.; et al. Paper-based cell culture platform and its emerging biomedical applications. *Mater. Today* **2017**, *20*, 32–44. [CrossRef]
11. Cai, H.; Sharma, S.; Liu, W.; Mu, W.; Liu, W.; Zhang, X.; Deng, Y. Aerogel microspheres from natural cellulose nanofibrils and their application as cell culture scaffold. *Biomacromolecules* **2014**, *15*, 2540–2547. [CrossRef] [PubMed]
12. Diban, N.; Stamatialis, D.F. Functional Polymer Scaffolds for Blood Vessel Tissue Engineering. *Adv. Polym. Med.* **2011**, *309–310*, 93–99. [CrossRef]
13. O'Brien, F.J. Biomaterials & scaffolds for tissue engineering. *Mater. Today* **2011**, *14*, 88–95. [CrossRef]
14. Suwantong, O. Biomedical applications of electrospun polycaprolactone fiber mats. *Polym. Adv. Technol.* **2016**, *27*, 1264–1273. [CrossRef]
15. Qi, A.; Hoo, S.P.; Friend, J.; Yeo, L.; Yue, Z.; Chan, P.P. Hydroxypropyl cellulose methacrylate as a photo-patternable and biodegradable hybrid paper substrate for cell culture and other bioapplications. *Adv. Healthc. Mater.* **2014**, *3*, 543–554. [CrossRef] [PubMed]
16. Oliveira, C.; Sepulveda, G.; Aguiar, T.Q.; Gama, F.M.; Domingues, L. Modification of paper properties using carbohydrate-binding module 3 from the Clostridium thermocellum CipA scaffolding protein produced in Pichia pastoris: Elucidation of the glycosylation effect. *Cellulose* **2015**, *22*, 2755–2765. [CrossRef]
17. Levy, I.; Nussinovitch, A.; Shpigel, E.; Shoseyov, O. Recombinant cellulose crosslinking protein: A novel paper-modification biomaterial. *Cellulose* **2002**, *9*, 91–98. [CrossRef]
18. Juvonen, H.; Maattanen, A.; Lauren, P.; Ihalainen, P.; Urtti, A.; Yliperttula, M.; Peltonen, J. Biocompatibility of printed paper-based arrays for 2-D cell cultures. *Acta Biomater.* **2013**, *9*, 6704–6710. [CrossRef]
19. Agrawal, C.M.; Ray, R.B. Biodegradable polymeric scaffolds for musculoskeletal tissue engineering. *J. Biomed. Mater. Res.* **2001**, *55*, 141–150. [CrossRef]
20. Ong, J.L.; Guda, T. *Translating Biomaterials for Bone Graft: Bench-top to Clinical Applications*; CRC Press: Boca Raton, FL, USA, 2017.
21. Azari, P.; Hosseini, S.; Murphy, B.P.; Martinez-Chapa, S.O. Electrospun Biopolyesters: Hydrophobic Scaffolds With Favorable Biological Response. *J. Public Health Int.* **2018**, *1*, 5–9. [CrossRef]
22. Aghdam, R.M.; Shakhesi, S.; Najarian, S.; Mohammadi, M.M.; Tafti, S.H.A.; Mirzadeh, H. Fabrication of a Nanofibrous Scaffold for the In Vitro Culture of Cardiac Progenitor Cells for Myocardial Regeneration. *Int. J. Polym. Mater. Polym. Biomater.* **2014**, *63*, 229–239. [CrossRef]
23. Christopherson, G.T.; Song, H.; Mao, H.Q. The influence of fiber diameter of electrospun substrates on neural stem cell differentiation and proliferation. *Biomaterials* **2009**, *30*, 556–564. [CrossRef]
24. Dettin, M.; Zamuner, A.; Roso, M.; Gloria, A.; Iucci, G.; Messina, G.M.; D'Amora, U.; Marletta, G.; Modesti, M.; Castagliuolo, I.; et al. Electrospun Scaffolds for Osteoblast Cells: Peptide-Induced Concentration-Dependent Improvements of Polycaprolactone. *PLoS ONE* **2015**, *10*, e0137505. [CrossRef] [PubMed]
25. Nune, M.; Kumaraswamy, P.; Krishnan, U.M.; Sethuraman, S. Self-assembling peptide nanofibrous scaffolds for tissue engineering: Novel approaches and strategies for effective functional regeneration. *Curr. Protein Pept. Sci.* **2013**, *14*, 70–84. [CrossRef] [PubMed]
26. Azari, P.; Luan, N.S.; Gan, S.N.; Yahya, R.; Wong, C.S.; Chua, K.H.; Pingguan-Murphy, B. Electrospun Biopolyesters as Drug Screening Platforms for Corneal Keratocytes. *Int. J. Polym. Mater. Polym. Biomater.* **2015**, *64*, 785–791. [CrossRef]
27. Malikmammadov, E.; Tanir, T.E.; Kiziltay, A.; Hasirci, V.; Hasirci, N. PCL and PCL-based materials in biomedical applications. *J. Biomater. Sci. Polym. Ed.* **2018**, *29*, 863–893. [CrossRef]
28. Yew, C.T.; Azari, P.; Choi, J.R.; Li, F.; Pingguan-Murphy, B. Electrospin-coating of nitrocellulose membrane enhances sensitivity in nucleic acid-based lateral flow assay. *Anal. Chim. Acta* **2018**, *1009*, 81–88. [CrossRef]
29. Cipitria, A.; Skelton, A.; Dargaville, T.; Dalton, P.; Hutmacher, D. Design, fabrication and characterization of PCL electrospun scaffolds—A review. *J. Mater. Chem.* **2011**, *21*, 9419–9453. [CrossRef]
30. Amini, A.R.; Laurencin, C.T.; Nukavarapu, S.P. Bone tissue engineering: Recent advances and challenges. *Crit. Rev. Biomed. Eng.* **2012**, *40*, 363–408. [CrossRef]

31. Webb, A.; Clark, P.; Skepper, J.; Compston, A.; Wood, A. Guidance of Oligodendrocytes and Their Progenitors by Substratum Topography. *J. Cell Sci.* **1995**, *108*, 2747–2760.
32. Kargozar, S.; Mozafari, M.; Hamzehlou, S.; Brouki Milan, P.; Kim, H.-W.; Baino, F. Bone Tissue Engineering Using Human Cells: A Comprehensive Review on Recent Trends, Current Prospects, and Recommendations. *Appl. Sci.* **2019**, *9*, 174. [CrossRef]
33. Hoffman, T.; Khademhosseini, A.; Langer, R.S. Chasing the Paradigm: Clinical Translation of 25 Years of Tissue Engineering. *Tissue Eng.* **2019**. [CrossRef] [PubMed]
34. Iqbal, N.; Khan, A.S.; Asif, A.; Yar, M.; Haycock, J.W.; Rehman, I.U. Recent concepts in biodegradable polymers for tissue engineering paradigms: A critical review. *Int. Mater. Rev.* **2019**, *64*, 91–126. [CrossRef]
35. Li, J.; Liu, X.; Tomaskovic-Crook, E.; Crook, J.M.; Wallace, G.G. Smart graphene-cellulose paper for 2D or 3D "origami-inspired" human stem cell support and differentiation. *Colloids Surf. B Biointerfaces* **2019**, *176*, 87–95. [CrossRef]
36. Groeber, F.; Holeiter, M.; Hampel, M.; Hinderer, S.; Schenke-Layland, K. Skin tissue engineering—in vivo and in vitro applications. *Adv. Drug Deliv. Rev.* **2011**, *63*, 352–366. [CrossRef]
37. Polak, S. In vitro to human in vivo translation–pharmacokinetics and pharmacodynamics of quinidine. *ALTEX-Altern. Anim. Exp.* **2013**, *30*, 309–318.
38. Yew, C.H.T.; Azari, P.; Choi, J.R.; Muhamad, F.; Pingguan-Murphy, B. Electrospun Polycaprolactone Nanofibers as a Reaction Membrane for Lateral Flow Assay. *Polymers* **2018**, *10*, 1387. [CrossRef] [PubMed]
39. Liu, H.Q.; Hsieh, Y.L. Ultrafine fibrous cellulose membranes from electrospinning of cellulose acetate. *J. Polym. Sci. Part B-Polym. Phys.* **2002**, *40*, 2119–2129. [CrossRef]
40. Wannatong, L.; Sirivat, A.; Supaphol, P. Effects of solvents on electrospun polymeric fibers: Preliminary study on polystyrene. *Polym. Int.* **2004**, *53*, 1851–1859. [CrossRef]
41. You, Y.; Won Lee, S.; Jin Lee, S.; Park, W.H. Thermal interfiber bonding of electrospun poly(l-lactic acid) nanofibers. *Mater. Lett.* **2006**, *60*, 1331–1333. [CrossRef]
42. Wei, X.; Xia, Z.; Wong, S.-C.; Baji, A.; Biomechanics, C. Modelling of mechanical properties of electrospun nanofibre network. *Int. J. Exp. Comput. Biomech.* **2009**, *1*, 45–57. [CrossRef]
43. Badami, A.S.; Kreke, M.R.; Thompson, M.S.; Riffle, J.S.; Goldstein, A.S. Effect of fiber diameter on spreading, proliferation, and differentiation of osteoblastic cells on electrospun poly(lactic acid) substrates. *Biomaterials* **2006**, *27*, 596–606. [CrossRef] [PubMed]
44. Nakamura, H. Morphology, function, and differentiation of bone cells. *J. Hard Tissue Biol.* **2007**, *16*, 15–22. [CrossRef]
45. Sjostrom, T.; Lalev, G.; Mansell, J.P.; Su, B. Initial attachment and spreading of MG63 cells on nanopatterned titanium surfaces via through-mask anodization. *Appl. Surf. Sci.* **2011**, *257*, 4552–4558. [CrossRef]

polymers

MDPI

Article

Impact of Lignin Content on the Properties of Hemicellulose Hydrogels

Basel Al-Rudainy [1], Mats Galbe [1], Monica Arcos Hernandez [2], Patric Jannasch [2] and Ola Wallberg [1,*]

[1] Department of Chemical Engineering, Lund University, P.O. Box 124, SE-221 00 Lund, Sweden; basel.al-rudainy@chemeng.lth.se (B.A.-R.); mats.galbe@chemeng.lth.se (M.G.)

[2] Department of Chemistry, Polymer, and Materials Chemistry, Lund University, P.O. Box 124, SE-221 00 Lund, Sweden; monica.arcos_hernandez@chem.lu.se (M.A.H.); patric.jannasch@chem.lu.se (P.J.)

* Correspondence: ola.wallberg@chemeng.lth.se; Tel.: +46-46-222-46-41

Received: 4 December 2018; Accepted: 23 December 2018; Published: 27 December 2018

Abstract: Hemicellulose is a promising renewable raw material for the production of hydrogels. This polysaccharide exists in large amounts in various waste streams, in which they are usually impure and heavily diluted. Several downstream processing methods can be combined to concentrate and purify the hemicellulose. However, such an approach can be costly; hence, the effect of impurities on the formation and properties of hydrogels must be determined. Lignin usually exists in these waste streams as a major impurity that is also difficult to separate. This compound can darken hydrogels and decrease their swellability and reactivity, as shown in many studies. Other properties and effects of lignin impurities are equally important for the end application of hydrogels and the overall process economy. In this work, we examined the feasibility of producing hydrogels from hemicelluloses that originated from sodium-based spent sulfite liquor. A combination of membrane filtration and anti-solvent precipitation was used to extract and purify various components. The influence of the purity of hemicellulose and the addition of lignosulfonates (emulated impurities in the downstream processing) to the crosslinking reaction mixture on the mechanical, thermal, and chemical properties of hydrogels was determined.

Keywords: galactoglucomannan; lignin; lignin-carbohydrate complex; ultrafiltration; precipitation; hydrogel

1. Introduction

Hydrogels are hydrophilic networks of polymers that are commonly produced by crosslinking various types of synthetic polymers or polysaccharides [1]. The properties of the hydrogels that are produced today are shaped by the type of crosslinker, the inherent nature of the main polymer, and the process with which these hydrogels are produced. Synthetic polymers yield hydrogels with excellent water absorption, strength, and durability. However, the precursors to these synthetic polymers are petroleum-based which makes the products lacking in terms of sustainability.

Polysaccharides and natural polymers are alternatives to synthetic polymers, especially in the development of hydrogels for medical applications, for which biocompatibility and biodegradability are paramount [2]. Many hydrogel products have been synthesized using polysaccharides as raw materials, such as starch, dextran, alginate, cellulose, and chitosan [2–6].

Hemicellulose is a promising polysaccharide for the production of hydrogels. Its high abundance (constituting over 20% of wood cell walls) and current losses in pulp and paper waste streams (incinerated in recovery boilers) make this work important industrially and economically [7]. Hydrogels from hemicellulose with similar properties as synthetic polymer-based hydrogels have been produced by Söderqvist Lindblad, et al. [8], who showed that it is possible to replace fossil-based

polymers with renewable waste material. However, the hemicellulose that was used was derived from steam explosion of spruce chips and did not represent the readily available hemicelluloses that are found in other process water streams.

Maleki, et al. [9] produced hydrogels from hemicellulose (galactoglucomannan) that was derived from thermomechanical pulping process water of spruce chips. The resulting single-network hydrogels were weak, as evidenced by their low shear modulus, which improved after a secondary crosslinking reaction. Consequently, the swelling ratio declined, but the swelling rate increased. Hemicellulose that has been derived from sodium-based spent sulfite liquor is another promising raw material for hydrogel production [10]—the product has swelling equilibria of between 50 and 270 g/g, a desirable property for use as absorbents and in agriculture.

All of the hemicelluloses [in this work, galactoglucomannan (GGM)] in the process waters above have at least one common problem: they exist in impure and highly diluted solutions (total dry substance of 5–6 g/L) and thus can not be used directly without being subjected to a proper concentration and purification method. These challenges have been addressed by other researchers using various types of downstream processing methods, such as membrane filtration, precipitation, and preparative chromatography [11–15].

Membrane filtration is effective in concentrating and, in certain cases, even purifying dilute streams. Al Manasrah, et al. [14] recovered 70% of the GGM in pressurized hot water extracts of spruce sawdust by ultrafiltration and reached a purity of 63%. Thuvander and Jönsson [16] reported that it was possible to separate lignin and GGM from thermomechanical process water using a combination of microfiltration and ultrafiltration. However, in other cases, this separation was difficult, due to membrane fouling [13,16,17]. Thus, membrane filtration was sufficient for concentrating and removing pulping chemicals, but another method was needed to separate lignin and GGM.

In cases in which the separation of GGM and lignin is difficult, anti-solvent precipitation has proven to be an efficient method for separation after membrane filtration [11,15,18]. Zasadowski, et al. [11] precipitated GGM from TMP process water using acetone, obtaining a yield of 77% at an acetone concentration of 54.5%. Song, et al. [15] used ethanol as an anti-solvent to recover GGM from hot water extractives from spruce, achieving a yield of 78% at 90% ethanol and discovering that the precipitate contained solely polysaccharides with molecular weights that exceeded 4 kDa.

Al-Rudainy, et al. [18] combined membrane filtration and anti-solvent precipitation for softwood spent sulfite liquor. Their GGM yield was on the same order of magnitude as those of other groups but with less anti-solvent, as a result of the membrane filtration step. Economically, it is preferable that the separation occurs in one step without the addition of any chemicals, such as anti-solvents. This tactic, however, will decrease the purity of the GGM due to the higher amounts of lignin in the concentrated process water.

The effect of additional lignin on the formation and properties of various products has been studied in other fields, such as in enzymatic treatment, wherein lignin has inhibitory effects on the reactions [19]. With regard to hydrogel production, Maleki, et al. [10] compared 2 hydrogels that were produced using the same methods and the same hemicellulose and but from 2 sources: spent sulfite liquor using ethanol precipitation and centrifugation as the separation and purification step versus a side stream of the steam explosion of spruce wood chips. The solution was concentrated by ultrafiltration and purified through diafiltration. As a result, the second specimen contained more lignin. This led to darker hydrogels with lower reactivity and swellability, which were theorized to have been caused by hydrophobic groups on the lignin, reducing the overall hydrophilicity of the hydrogel. However, the other differences between the 2 hemicelluloses have not been examined since.

In this work, a one-pot reaction was chosen to study the effects of lignin impurities on the properties of GGM hydrogel. Epichlorohydrin (ECH) was used as the crosslinker, and the GGM and lignin were acquired by membrane filtration and anti-solvent precipitation of softwood spent sulfite liquor.

2. Materials and Methods

2.1. Raw Material and Reactants

For the raw material, sodium-based spent sulfite liquor was used, which was extracted from the first step in a 2-step softwood (60% *Picea abies* and 40% *Pinus sylvestris*) pulping process by Domsjö Fabriker (Örnsköldsvik, Sweden). The SSL contained 6.6% galactoglucomannan, 1.8% xylan, 0.8% arabinan, and 36.4% lignin, with a total dry substance of 84.6 g/L [17]. The remaining components were pulping chemicals, monosaccharides, acid-insoluble solids, and extractives.

The reactants that were used for the crosslinking reaction were 99% pure synthesis-grade epichlorohydrin and 50 wt % analytical-grade sodium hydroxide solution (Merck KGaA, Darmstadt, Germany).

2.2. Ultrafiltration and Anti-solvent Precipitation

The product was concentrated and low-molecular-weight components (such as pulping chemicals and monosaccharides) were removed by diafiltration per the membrane filtration methods in a previous study [17]. A 400-mL stirred filtration vessel that was equipped with a 50-kDa membrane (GR51PP, Alfa Laval Corp. AB, Lund, Sweden) and a 10-L feed tank were used for the membrane filtration setup. The pressure was monitored with a digital pressure gauge (DCS40.0AR, Trafag AG, Bubikon, Switzerland) and adjusted using a valve that was connected to a 6-bar nitrogen gas line. The crossflow velocity and temperature were controlled using a magnetic stirrer with a heating plate (MR2002, Heidolph Instruments GmbH & Co. KG, Schwabach, Germany), on top of which the 400-mL vessel was placed. The raw material was concentrated at 50 °C, a cross-flow velocity of 0.5 m/s, and 5.5 bar transmembrane pressure, decreasing in volume by 90% in fed batch mode. Diafiltration was then performed on the retentate to a diafiltration factor of 5 using deionized water in the feed tank. The membrane was washed with 0.04 wt % acid detergent solution (Ultrasil 73, Ecolab AB, Älvsjö, Sweden) at 50 °C for 1 h before and after each experiment. This procedure was repeated until the total weight of diafiltrated retentate exceeded 1 kg.

Precipitation was performed on 1 kg of diafiltrated retentate in a glass beaker with magnetic stirring (500 RPM) at room temperature, with acetone (SupraSolv MS, Merck Schuchardt OHG, Hohenbrunn, Germany) added gradually to a final concentration of 45 wt % [18]. The mixture was agitated for 15 min before being transferred to 750-mL centrifuge bottles (Beckman Coulter, Brea, California, USA) and was then centrifuged at 4000 RPM for 20 min (Jouan S.A., Model C412, Saint-herblain, Nantes, France). The liquid phase was carefully decanted, and the bottles that contained the precipitate (most of the galactoglucomannan) were dried in an oven at 50 °C for 48 h. The liquid phase (most of the lignin) was dried in a vacuum evaporator (BÜCHI Rotavapor R-153, BÜCHI Labortechnik AG, Flawil, Switzerland) at 50 °C and an average absolute pressure of 200 mbar for 60 h. Both powders were re-dissolved in deionized water (2 g powder to 18 g water) to make the stock solutions that were to be used in the hydrogel synthesis steps.

2.3. Preparing Hydrogels

Hydrogels were synthesized per reference [20]. A total of 2 mL stock solution (galactoglucomannan, lignin, or a mixture of both) was pipetted into a 3-mL vial, and 250 µL 50% sodium hydroxide solution was added and mixed for 5 min on a vortex mixer (MS2 Minishaker, IKA®-Werke GmbH & Co. KG, Staufen, Germany). The crosslinking reaction was then started by adding 100–300 µL epichlorohydrin and mixing it until the solution appeared to be homogeneous. Approximately 1 mL of the mixture was then transferred to a mold (flexible plastic bottle caps), covered, and left at room temperature for 48 h. The hydrogel was peeled off carefully from the mold and placed in 50 mL deionized water at room temperature for 24 h; the wash solution was then transferred to a container, and the same procedure was repeated to properly wash away any unbound

reactants. The wash solution that was collected (approximately 100 mL) was later analyzed for lignin, hemicellulose, acetic acid, and glycerol content and epichlorohydrin conversion.

2.4. Analysis

2.4.1. Swelling Capacity

Swelling capacity was measured by carefully patting the newly prepared and washed hydrogel (Section 2.3) dry with tissue paper and weighing it. After the hydrogel was dried at 50 °C for 24 h, it was reweighed, and the swelling capacity (SC) was calculated per the following equation:

$$SC = \frac{m_{wet} - m_{dry}}{m_{dry}} \quad (1)$$

where m_{wet} and m_{dry} are the mass of the hydrogel in the wet and dry states, respectively.

2.4.2. Lignin Content and Epichlorohydrin Conversion

The concentration of lignin in solution was determined on a UV spectrophotometer (Shimadzu UV-visible spectrophotometer UV-1800, Kyoto, Japan). The wavelength was set to 234 nm, and the extinction coefficient was 31.6 L/g·cm [17].

Epichlorohydrin conversion was measured using chloride titrator strips (Quantab Chloride Low Range titrators, HACH company, Loveland, CO, USA). Chloride concentration was determined for the hydrogel wash solution, which, after the conversion, was calculated as the amount of chloride ions in the wash solution divided by the amount of chloride in the epichlorohydrin that was added.

2.4.3. Hemicellulose, Acetic Acid, and Glycerol Content

The hemicellulose concentration and glycerol content were determined per previous studies [18]. Ten milliliters of a sample were acid-hydrolyzed using 0.75 mL 72% sulfuric acid solution and autoclaved (Systec DX 150, Wettenberg, Germany) at 121 °C for 1 h. The hydrolysate was then vacuum-filtered to remove acid-insoluble solids and analyzed for monosaccharide content on a HPAEC-PAD system (ICS-3000, Dionex Corp., Sunnyvale, CA, USA) with a CarboPac PA1 carbohydrate analytical column. Deionized water was used as the eluent at a flow rate of 1 mL/min and 0.5 mL/min 200 mM sodium hydroxide postcolumn addition. The injection volume was 10 µL, and the hemicellulose concentration was calculated by summing the monosaccharide content and anhydro corrections of 0.88 for pentoses and 0.90 for hexoses.

The acetic acid and glycerol content was determined on an HPLC system (LC-20AT, SIL-20AC, SCL-10A vp, RID-10A, CTO-20AC, Schimadzu Corp., Kyoto, Japan) with an Aminex HPX-87H column (Bio-Rad, Hercules, CA, USA), 5 mM sulfuric acid solution as eluent at a flow rate of 0.5 mL/min, a column temperature of 50 °C, and sample injection volume of 10 µL.

2.4.4. Size-exclusion Chromatography

The molecular weight distribution was examined in liquid samples on a Waters size-exclusion chromatography system (Waters, Milford, MA, USA), with a Waters 600E system controller, coupled with a refractive index detector (Waters 2414 Differential Refractometer), a UV detector (Waters 486 Tunable Absorbance Detector) that was set to 234 nm, and a pump (Waters 600 gradient pump). Samples were injected using an autosampler (Waters 717 plus autosampler) with an injection volume of 20 µL. Fractionation was performed on a TSKgel column (G4000PWXL, TOSOH Bioscience GmbH, Griescheim, Germany), with deionized water as the eluent at a flow rate of 0.5 mL/min. Polyethylene glycol standards (Merck Schuchardt OHG, Germany) were used for the column calibration (100 kDa, 35 kDa, 10 kDa, 4 kDa, 400 Da).

2.4.5. Fourier Transform Infrared Spectroscopy

The samples that were to be measured were dried at 50 °C in a furnace (Heraeus, Heraeus Holding GmbH, Hanau, Germany) and ground to a fine powder using a mortar and pestle. The pulverized samples were then measured with an FTIR (Bruker ALPHA-p FTIR spectrometer, Billerica, MA, USA) in attenuated total reflectance mode, in the wavenumber range of 4000 to 500 cm^{-1} with 2 cm^{-1} resolution and 72 scans per sample.

2.4.6. Compression Stress and Strain

Compression tests were performed on newly prepared and washed cylindrical hydrogels. The hydrogels were prepared per Section 2.3, except that the mold was a 3-mL vial. Compression stress and strain were measured using a scale (PL6001-l, Mettler Toledo Inc., Columbus, OH, USA) and motor-controlled piston, for which the rate of axial displacement was 1.0 mm/min. Given that the axial displacement was constant, the strain was calculated by multiplying the elapsed time with the axial displacement rate. Stress was calculated as the mass that was displayed on the scale divided by the cross-sectional area of the hydrogel.

2.4.7. Thermogravimetric Analysis

Thermogravimetric analysis was conducted on a Q500 TGA (TA Instruments Inc., New Castle, DE, USA). Powdered samples were predried in a furnace at 50 °C for 24 h and cooled to room temperature using a desiccator prior to analysis. The samples were placed in open aluminum trays (2 to 5 mg) and heated from 15 to 600 °C at 10 °C/min under a nitrogen atmosphere (60 mL/min).

2.4.8. Release of BTB from Hydrogels

Hydrogels were prepared as in Section 2.3, except that 4 mg of bromothymol blue powder (Merck Schuchardt OHG, Hohenbrunn, Germany) was added to the reaction mixture and dissolved by mixing prior to the addition of ECH. After 48 h, 2 hydrogel disks were carefully peeled off and placed into a mesh basket, which was then submerged into a beaker with 400 mL 4 g/L NaOH solution. The solution was then stirred magnetically (rod length of 2.5 cm) at 100 RPM, and 2-mL samples were taken at timed intervals to determine BTB concentrations.

The BTB concentration was measured on a UV spectrophotometer (Shimadzu UV-visible spectrophotometer UV-1800, Kyoto, Japan) at the isosbestic point (wavelength 498 nm). The extinction coefficient was 9.31 L/g·cm, which was calibrated using various concentrations of BTB in 4 g/L sodium hydroxide solution.

2.4.9. Liquid Chromatography-mass Spectrometry (LC-MS)

The LC instrument was part of the 1260 Infinity II line (Agilent Technologies, Waldbronn, Germany) and comprised a range of modules: a Quaternary Pump VL (G7111A), a Vialsampler (G7129A), and a temperature-controlled column compartment (G7130A). The column, a 4.6 mm × 100 mm Poroshell 120 EC-ECS, was operated at 50 °C. The eluent flow rate was 0.5 mL/min, with a gradient switch between eluents A (0.1% formic acid solution) and B (95% acetonitrile in 0.1% formic acid solution) according to the program in Table 1. The injection volume was 1 µL, and the total run time per sample was 12 min. LC detection was performed using a UV diode array detector (G7115A) with a peak width of 0.1 min and a 4-nm slit.

The LC system was connected to a mass spectrometer (G6545B Q-TOF) that was equipped with a dual AJS ESI ion source that was operated in ESI positive mode. The nitrogen gas temperature was set to 350 °C at a flow rate of 12 L/min. The nebulizer pressure was 35 psig, with a sheath gas temperature and flow rate of 400 °C and 12 L/min, respectively. The nozzle voltage was 1000 V, the collision energy was set to 0 eV, and the data were acquired in the range of 50 to 3200 m/z.

Table 1. Gradient program for LC of the LC/MS system. Eluent A was 0.1% formic acid solution, and eluent B was 95% acetonitrile in 0.1% formic acid solution. The flow rate was kept constant at 0.5 mL/min.

Time (min)	Eluent A (%)	Eluent B (%)
1	100.0	0.0
8	0.0	100.0
10	0.0	100.0
12	100.0	0.0

3. Results and discussion

3.1. Ultrafiltration and Anti-solvent Precipitation

Table 2 summarizes the results from the re-dissolved fractions after ultrafiltration and anti-solvent precipitation. The separation method clearly fractionated the spent sulfite liquor components into 2 major fractions: a polysaccharide-rich stream and another that contained primarily lignin.

Table 2. Compositions of the re-dissolved products from the ultrafiltered and anti-solvent precipitated fractions. The samples were dried at 50 °C.

Fraction	TS of Prepared Solutions (g/L)	Lignin Content (g/L)	Acetic Acid (g/L)	Arabinan (g/L)	Galactan (g/L)	Glucan (g/L)	Xylan (g/L)	Mannan (g/L)
GGM	100	8.40	3.60	0.60	15.9	13.0	4.60	23.5
Lignin	99.9	94.6	0.75	0.21	1.09	1.64	0.94	4.11

The difference in properties of these fractions was also observed using FTIR spectroscopy (Figure 1). In the region between 3000–3500 cm^{-1}, a broad signal appeared in both fractions and was assigned to the stretching of O–H bonds. The peaks at 2930 and 2852 cm^{-1} were caused by the stretching of C–H bonds in the lignin and polysaccharides [21,22]. The peak at 1736 cm^{-1} was assigned to the acetyl groups on the GGM and was visible in both fractions, albeit at greater intensity in the polysaccharide-rich fraction. Various peaks from aromatic skeletal vibrations appeared in the lignin-rich fraction (1602, 1509, 1451, and 1420 cm^{-1}). These peaks were missing or lower in intensity in the polysaccharide fraction, indicating proper separation between these entities. Other indicators of good separation were the peaks for various guaiacyl moieties (1262–1142 cm^{-1}), which also implicated the lignin as being guaiacyl-type, as shown in our previous study [18].

The signals at 1082 and 1026 cm^{-1} were ascribed to vibrations of asymmetrical C–O–C bonds. The signal at 1082 cm^{-1} was less intense in the lignin-rich fraction, indicating that it originated from internal vibrations of the pyranose structure in the polysaccharides [21]. Two signals were detected in the low wavenumber region and were assigned to the sulfonate groups in the lignin (650 and 517 cm^{-1}).

The properties of various components can also be characterized using TGA, as applied to our 2 fractions; the results are presented in Figure 2. The degradation of lignin occurred in 3 major stages, as indicated by the derivative of the TGA curve (DTG). In the first stage, the DTG peak temperature was approximately 33 °C, due to the release of absorbed water and other solvents, such as acetone, that were used during the precipitation [23,24].

In the second stage, which had a DTG peak temperature of 263 °C, residual hemicelluloses were degraded, perhaps as were lignin-carbohydrate complexes. Certain lignosulfonates begin to degrade at temperatures above 250 °C [24,25]. Because the observed mass of the second-stage peak (~20 wt %) was higher than the total amount of hemicelluloses (Table 2), this result was expected as a possibility, even in our case.

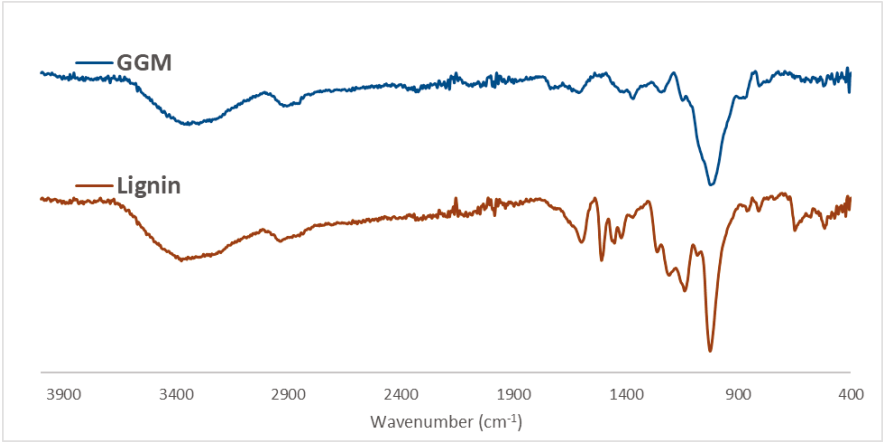

Figure 1. FTIR spectrum comparison of the GGM and lignin fraction.

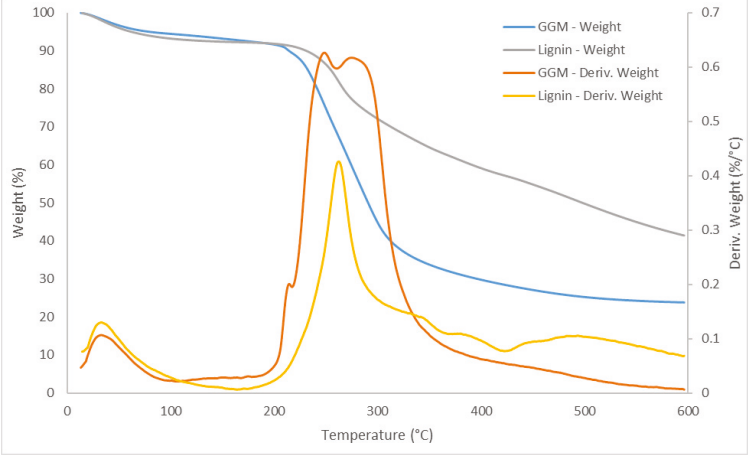

Figure 2. TGA and DTG curves for the GGM and lignin fraction.

In the third stage (temperatures above 300 °C), several DTG peaks were observed. The visible peaks appeared at 344, 390, 441 and 493 °C, corresponding to the pyrolytic degradation of lignin; the release of phenolic derivatives, mercaptans, SO_2, CO, and CO_2; and the decomposition of aromatic rings at temperatures exceeding 500 °C [23]. The residual mass of the lignin-rich fraction at 600 °C was roughly 41 wt %. This high char residue content was anticipated, given that the lignin was sulfonated. According to previous reports [25,26], the remaining chemically bonded sulfonate groups and sodium salts were responsible for the residue and require temperatures above 600 °C for further decomposition.

GGM decomposed in 2 major stages, the first of which was identical to the first stage of lignin decomposition. In the second stage, at least 3 DTG peaks could be observed at 215, 248, and 274 °C, with a residue of 24 wt % at the end of the run. The first DTG peak of the second stage had a mass that corresponded to 3.2 wt % of the total sample, similar to the amount of acetic acid (acetyl groups) in the sample per Table 2, indicating that the acetyl groups were the first components to leave the matrix, as shown by others [27]. The next DTG peak arose at 248 °C, near the reported temperature of the maximum rate of weight loss for softwood xylan [27]. However, the mass of the peak exceeded the amount of xylan that was available in the sample, suggesting that other compounds were decomposing

at approximately the same temperature—likely the highly branched GGM, which has been reported to have a low decomposition temperature compared with low-branched linear GGM.

The last DTG peak (274 °C) most likely contained the remaining GGM but also other galactan-based polysaccharides, as reported by Beall [27]. Overall, these results show that the lignin fraction is thermally more stable than the polysaccharide-rich fraction in terms of the temperature at the maximum rate of weight loss and the slower decomposition rate of the lignin fraction, as seen from the slope of the TGA curve.

3.2. Parameter Study

To determine the amounts of crosslinker and lignin that were required to form a stable gel, we performed a parameter study, based on the results that were presented in another report [20]. The various gels are shown in Figure 3. Vials 1B, 2B, and 3B are the results for the polysaccharide-rich stock solution after crosslinking 2 mL of the solution with 100, 200, and 300 µL epichlorohydrin (ECH), respectively, and a fixed amount of sodium hydroxide. A stable gel was formed with 200 µL ECH and higher. Decreasing the amount of ECH to 100 µL failed to form a coherent gel, due to the low degree of crosslinking, leaving the polysaccharide matrix stable in solution [28].

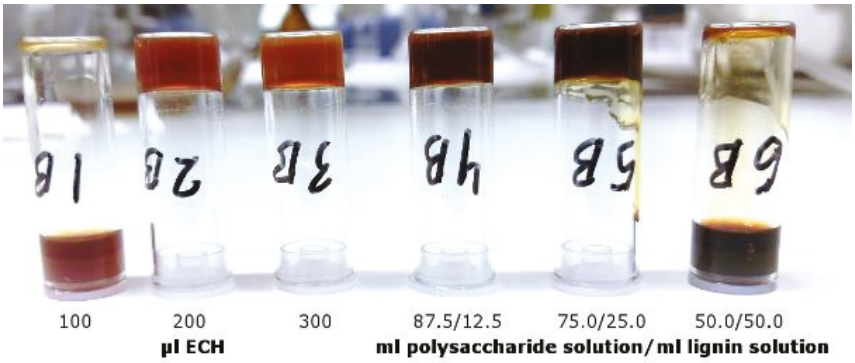

Figure 3. Visual representation of the resulting hydrogels after crosslinking of the polysaccharide solution (1B, 2B and 3B) at different ECH additions. The vials 4B to 6B show the effect of different lignin additions at a constant ECH dosage of 200 µL.

The color of the hydrogels differed, depending on the degree of crosslinking. The color forms from the dissociation of phenolic groups in the residual lignin in the stock polysaccharide solution [29,30] and is an indirect indication of the amount of sodium hydroxide that is consumed in the reaction; thus, the crosslinking reaction progressed further with the higher versus lowest amount of ECH.

Vials 4B to 6B show the effect of increasing amounts of lignin in the reaction mixture. The total dry substance, ECH, and sodium hydroxide levels were kept constant. To emulate the effect of greater lignin impurity in the stock solution, the amount of lignin was changed by decreasing the ratio of polysaccharide to lignin stock solution. Vials 4B to 6B had volumetric ratios of 87.5/12.5, 75.0/25.0, and 50.0/50.0 mL polysaccharide solution/mL lignin solution, respectively. In the latter sample, no coherent hydrogel formed; thus, the lignin concentration below this threshold was chosen for further study.

3.3. Effect of Crosslinking on Hydrogel Content

The parameters that were determined in Section 3.2 were applied to crosslink the polysaccharide-rich fraction with ECH volumes of 200, 250, and 300 µL. The results for the hydrogel content (percentage of component/total amount of component in the reaction mixture) are presented in Figure 4.

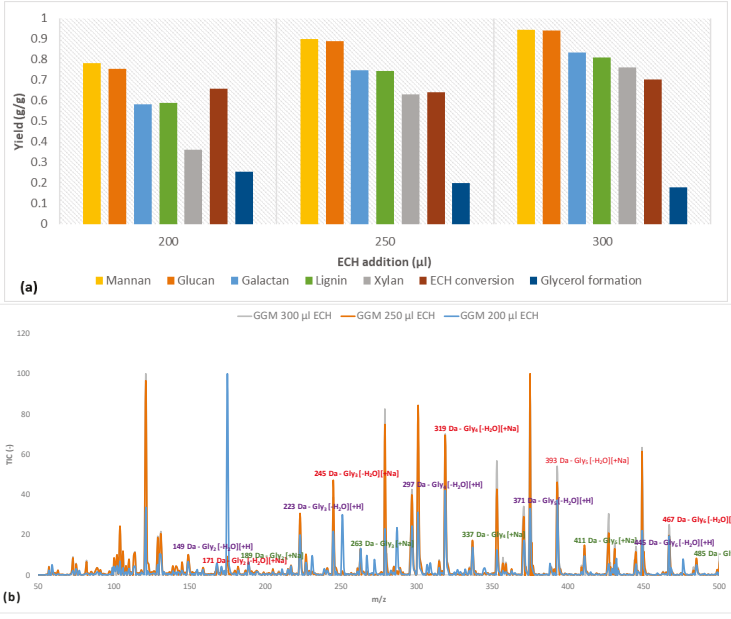

Figure 4. (**a**) The yields at different crosslinker additions for the various hydrogel bound solutes, ECH consumption and glycerol formation after the crosslinking reaction. (**b**) LC-MS of the wash solution (containing non-bound compounds) with highlighted m/z for the formed polyglycerols after the crosslinking reaction. Glyx is a polyglycerol with x number of subunits.

Initially, the mannan and glucan yields were approximately on the same order of magnitude for the 3 amounts of crosslinker. This result was not surprising, because the main polysaccharide in the solution was galactoglucomannan [18]. However, the small difference that existed might have been due to some of the glucans being bound to other components. The yields of galactan followed the increases in mannan and glucan throughout the series but were lower overall, because there were other galactan-based polysaccharides in the solution that were not associated with GGM. The 2 most common such polysaccharides in the raw material are arabinogalactan and B-galactan [18]. Also, certain polysaccharides were bound to lignin and formed lignin-carbohydrate complexes (LCCs). A clear indication of the existence of these complexes is found in the figure, in which the galactan yield approximated that of lignin for all samples (Figure 4). Furthermore, the galactans in the solution have a higher molecular weight than GGM [18,31], demonstrating that the crosslinking reaction did not depend on MW in this case. Overall, the yield was high in terms of the utilization of solutes, reducing the potential waste after the reaction.

The ECH conversion rate was between 64% and 70%; there was no discernable pattern versus the addition of ECH. However, the amount of ECH that was consumed increased as the proportion of ECH became larger, indicating that more glycerol bridges were formed between the polysaccharides (as evidenced by the rising yields in polysaccharides in Figure 4), but the formation of monoglycerol ether units could not be ruled out [32]. A common side reaction of crosslinking is the hydrolysis of ECH to glycerol, which in turn can react with ECH to form polyglycerols, as described by Kartha and Srivastava [32]. As shown in Figure 4, the formation of glycerol after the reaction decreased with higher ECH content.

Earlier studies provide explanations for the phenomenon [32]. One reason is that a higher level of ECH shifted the reaction from homogeneous to heterogeneous due to the low solubility of ECH in water (roughly 7%), wherein the heterogeneous reaction of ECH has been found to result in low

glycerol yields. Also, at an excess of ECH, the reaction may begin to polymerize ECH into dimers and trimers. Therefore, it is also possible that these polyglycerols form and bind to the hydrogels at higher amounts of ECH, thus lowering the observed glycerol yield. This phenomenon was also indicated by the LC-MS measurements, as seen in Figure 4b, in which glycerol polymers were found to contain up to 6 glycerol units. The large number of peaks that were detected was the result of various existing adducts (sodium and proton) and the dehydration of polyglycerols to varying extents [33]. However, the trend was the same, regardless of which adduct or dehydrated peak was compared.

By comparing the signals with the strongest intensity (mono-dehydrated polyglycerols with sodium adduct), we found that the intensity for polyglycerols with over 4 glycerol units rose with increasing ECH levels. Notably, this finding was consistent with decreasing intensity in the region with fewer than 4 glycerol units for the sample with the highest amount of ECH, highlighting the transition from crosslinking monoglycerol units to oligomers. The overall trend in Figure 4b was a shift in the distribution of polyglycerol toward a higher degree of polymerization with increasing ECH levels, strengthening the observations made regarding the decrease in the formation of glycerol.

3.4. Effect of Addition of Lignin on Hydrogel Content

Based on the results of the parameter study (Section 3.2), various amounts of the lignin fraction were added to the reaction mixture. The data on the content of the synthesized hydrogels are presented in Figure 5. Adding lignin to the mixture decreased the yield for most solutes. Mannan and glucan continued to follow the same trend regarding yields, as shown in Section 3.3. The yields at high lignin content (29.9 g/L) were nearly identical to those for GGM hydrogels with low crosslinking (Figure 4), indicating that the crosslinking reaction favored the reaction with GGM, followed by galactans and xylans, independent of the lignin that was added.

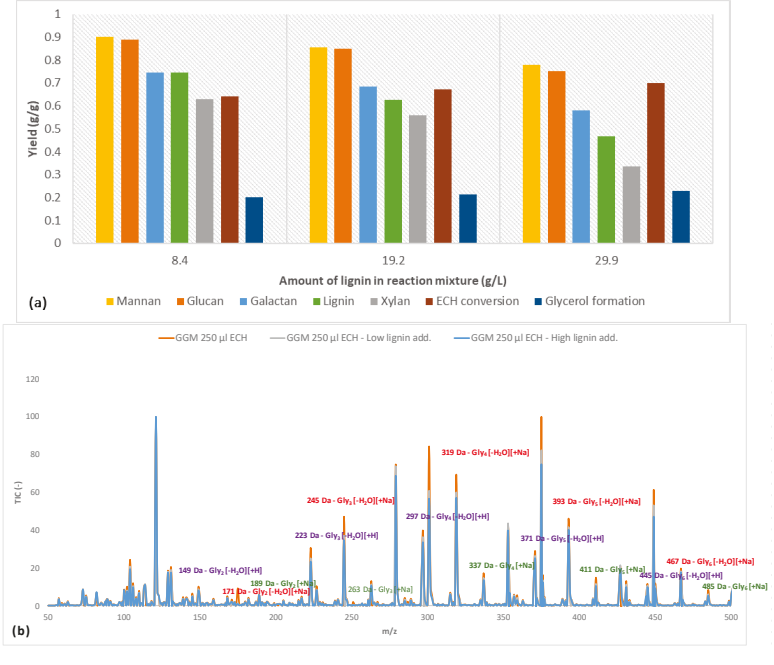

Figure 5. (**a**) The yields at different lignin additions for the various hydrogel bound solutes, ECH consumption and glycerol formation after the crosslinking reaction. (**b**) LC-MS of the wash solution (containing non-bound compounds) with highlighted m/z for the formed polyglycerols after the crosslinking reaction. Glyx is a polyglycerol with x number of subunits.

However, the yields for lignin differed from those in Figure 4. The trend was for more of the lignin to bind to the hydrogel, even with decreasing yield. These results implicate fewer crosslinks between the polysaccharides after the addition of lignin. Nevertheless, the consumption of ECH clearly rose, attributed to the formation of more glycerol (Figure 5a) but also perhaps to the crosslinking of low-MW non-gel-bound lignin. The polymerization of glycerol declined with increases in lignin addition by LC-MS (Figure 5b), supporting the possibility of the polymerization of low-MW non-gel-bound lignin.

3.5. FTIR on Hydrogels

FTIR measurements were performed on the hydrogels (see Figure 6a). The spectra for the hydrogels were nearly identical to that of the polysaccharide fraction, differing only by the disappearance of the peak at 1736 cm^{-1} (acetyl groups) for the hydrogels. Deacetylation usually occurs when the pH is higher than 3 and at high temperatures [34,35]. Further, at high sodium hydroxide concentrations, it could ensue at lower temperatures [20]. Given that the pH after the addition of sodium hydroxide to the reaction mixture was over 13, this latter mechanism was what likely occurred.

No other differences were expected, because the major modification to the hydrogels was the addition of the glycerol bridge and the removal of hydroxyl groups, both of which had signals that coincided with those in the polysaccharide fraction. However, the intensities of these signals will vary, depending on the type of modification that occurred. These changes in intensities were seen by comparing the ratios of the absorbance peak height on various signals (Figure 6b). The gels had a higher ether bond (C-O-C) intensity than the polysaccharide fraction, which was expected, because crosslinking increases the formation of ether bonds and the removal of hydroxyl (OH) groups. However, the ratio decreased with rising ECH, which does not necessarily mean that the proportion of ECH that reacted declined overall. Yet, the proportion of crosslinks was smaller than that of hydroxyl groups, perhaps due to the formation of mono-glycerol ether units instead of a glycerol bridge, instead increasing the hydroxyl groups overall, in turn supporting the previous claim (Figure 4).

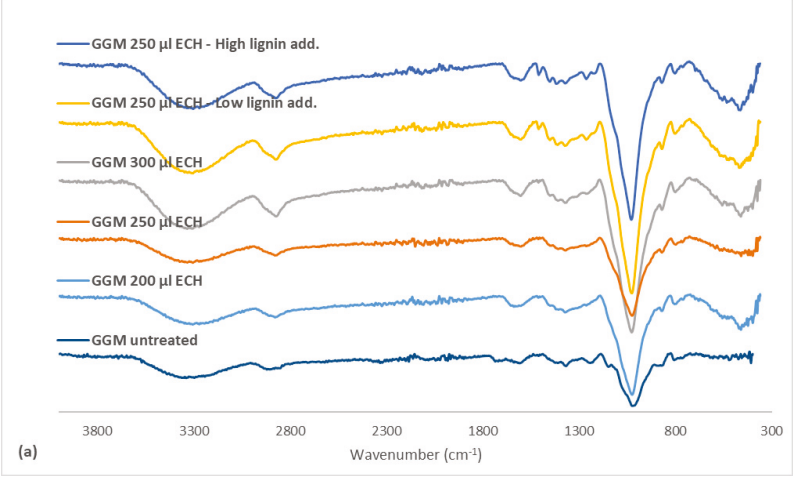

Figure 6. *Cont.*

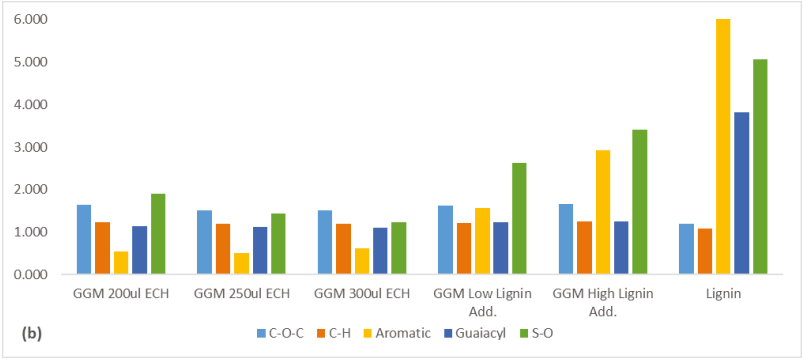

Figure 6. (**a**) FTIR spectrum comparing the produced hydrogels. (**b**) The ratio between the FTIR absorbance of a hydrogel and the non-treated GGM at different wavenumbers. C–O–C is the ratio for the ether bonds (1026 cm^{-1}), the C–H ratio was based on the wavenumber 2930cm^{-1}, aromatic was measured at 1509 cm^{-1}, guaiacyl was calculated as the sum of the three wavenumbers between 1262–1142 cm^{-1} and S–O absorbance was measured at 650 cm^{-1}. The legend includes the ECH and lignin additions for the crosslinking reaction. Low lignin addition represented the 87.5/12.5 mL polysaccharide solution/mL lignin solution and the high lignin addition 75.0/25.0 mL polysaccharide solution/mL lignin solution.

The addition of lignin to the samples increased the C–O–C/OH ratio, likely due to the higher C–O–C/OH ratio in the added lignin. The strong indicators for bound lignin was the peak at 1509 (aromatic skeletal vibrations), the sum of the peaks for guaiacyl structures (1262–1142 cm^{-1}), and the sulfonate groups (650 cm^{-1}). The rise in crosslinking did not have a major impact on the ratios of the aromatic skeletal vibrations or the sum for the guaiacyl signals, indicating that the base structure of the lignin was consistent. However, the ratio for the sulfonate groups decreased. These results thus show that the highly charged (sulfonated) lignin was bound first, followed by the less sulfonated lignin. The increase in lignin before the crosslinking reaction enhanced the intensity of these peaks, wherein the sample that contained the highest amount of lignin had the strongest signals in this region. These results, coupled with the trend in Figure 5, thus show that some of the added lignin bonded to the hydrogel.

3.6. Size-Exclusion Chromatography

The SEC results (Figure 7a) demonstrated that the GGM fraction contained 3 major MW regions. The high-MW region (between 5 and 10 min of retention time) contains the lignin and lignin-carbohydrate complexes [17,18], as evidenced by the UV absorption of that fraction (Figure 7b). The mid-MW region (approximately 20 min, Figure 7a) contained GGM and has little to no UV absorption; thus, it harbored low to negligible amounts of lignin. The third peak (>25 min) contained most of the remaining low-MW compounds, such as monosaccharides and pulping chemicals.

The results in Figure 7a also show the MW of components that were not bound during the hydrogel synthesis (wash solution) at various degrees of crosslinking. The results implicated the mid-MW compounds being consumed first at low ECH concentrations, followed by the high-MW compounds, the consumption of which rose with the addition of ECH. The remaining peak in the mid-MW region was possibly lignin that was released from the high-MW lignin-carbohydrate complexes by hydrolysis, based on the increase in UV absorption in that region, as seen in Figure 7b and confirmed in our previous work [17], in which enzymatic hydrolysis of the carbohydrate segment of the LCCs released lignin in the same MW range. The same trend was seen for the case in which the lignin concentration increased in the reaction mixture (Figure 7c,d).

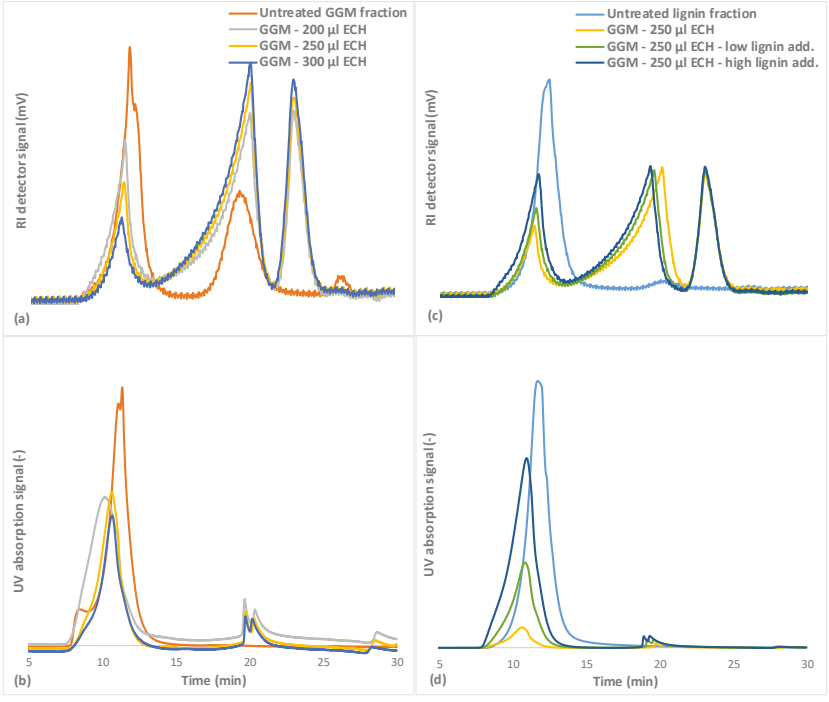

Figure 7. SEC for the untreated GGM and lignin solutions and the wash solutions after the crosslinking reaction. (**a**,**c**) is showing the response from the RI detector, and (**b**,**d**) the UV detector. The legend includes the ECH and lignin additions for the crosslinking reaction. Low lignin addition represented the 87.5/12.5 mL polysaccharide solution/mL lignin solution and the high lignin addition 75.0/25.0 mL polysaccharide solution/mL lignin solution.

Previous observations (Sections 3.4 and 3.5) showed that not all of the lignin was bound to the hydrogel but that more ECH was consumed with increases in lignin, because the crosslinking of the lignin yielded larger water-soluble macromolecules that did not bind to the hydrogel.

The rise in MW can be observed in Figure 7d, in which the MW of the lignin shifted toward the heavier end of the spectrum after the crosslinking reaction. The reason for the lignin failing to bind to the hydrogel could be the difference in solubility between these components. The solubility of GGM likely decreased after the addition of sodium hydroxide to the reaction mixture, due to the deacetylation of the polysaccharide, leading to heterogeneous (slow) crosslinking [36]. The solubilities of lignin and lignosulfonates during alkali conditions do not change (at room temperature), and thus, the crosslinking reaction is more homogeneous (fast). A third peak was observed after the crosslinking reaction in the region at approximately 23 min (Figure 7), likely comprising crosslinked monosaccharides and oligosaccharides or possibly polyglycerols, as identified by LC-MS in Figures 4b and 5b.

3.7. Swelling Degree and Drug Release

The swelling behavior of the hydrogels was determined in deionized water. Swelling degree can be altered by changes in the amount of crosslinker or by the concentration of functional materials [10]. The swelling behavior was therefore expected to change, depending on the amount of ECH that was added but also possibly the lignin levels.

The results on the swelling degree of the hydrogels are presented in Figure 8a. The hydrogel with the lowest degree of crosslinking had an initial swelling degree of 137 g water/g dry hydrogel, which was in the same range as reported by Maleki, et al. [10] using the same raw material. As expected, the swelling degree of the hydrogels decreased with greater amounts of crosslinker, because the higher amount of crosslinks that are formed in turn compacts the hydrogel structure and decreases the number of available sites for water to penetrate [37,38]. At the highest level of ECH, the hydrogel had a swelling degree of approximately 38 g/g—much lower than the low-crosslinked hydrogel but still in the range of usable hydrogels for many applications.

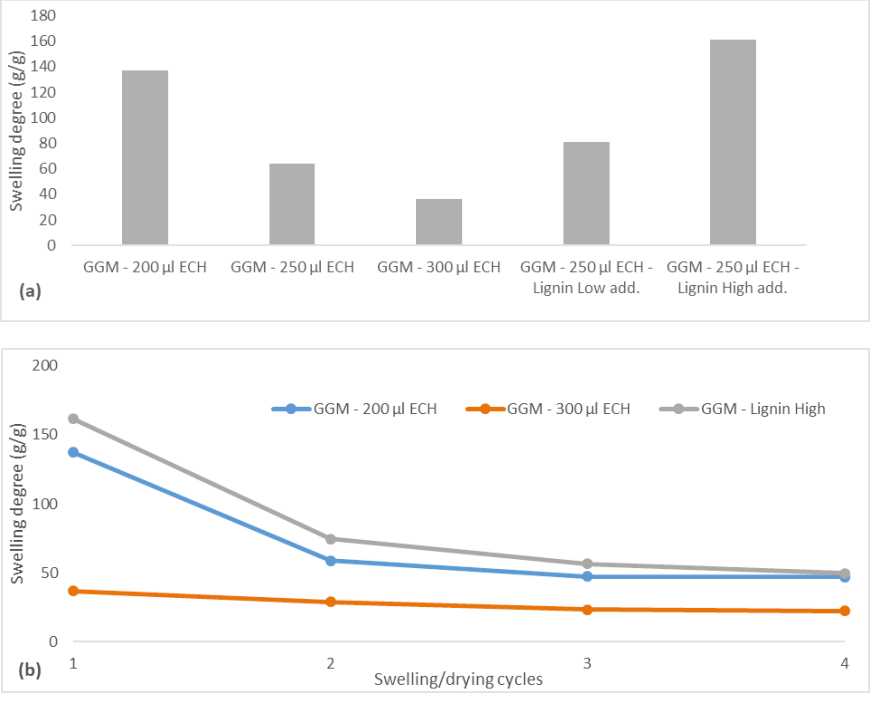

Figure 8. (**a**) The swelling degree for the different hydrogels after synthesis. (**b**) The swelling degree for three selected hydrogels after consecutive swelling and drying cycles. The legend includes the ECH and lignin additions for the crosslinking reaction. Low lignin addition represented the 87.5/12.5 mL polysaccharide solution/mL lignin solution and the high lignin addition 75.0/25.0 mL polysaccharide solution/mL lignin solution.

Increasing the amount of lignin in the hydrogels had the opposite effect, with the swelling degree instead rising, perhaps because the lignin consumed the ECH and remained soluble, yielding a hydrogel that was less crosslinked and had higher swellability, as indicated. Another explanation is that the addition of ionizable components (lignosulfonates) increased the initial osmotic pressure during swelling, thus resulting in a higher driving force for water uptake [39]. This phenomenon was observed when the BTB release was measured (Figure 9). By comparing the hydrogel with low and high ECH content, it was clear that the release of BTB was slower in the latter case, as expected, because the reduced mobility of the polymer impeded the penetration of the solvent [39]. The opposite effect was anticipated for the sample to which a higher amount of lignin was added, given that the swellability was greater (Figure 8a). However, the release was slower, as shown in Figure 9, likely due to the higher osmotic pressure and thus greater water influx at the beginning of the release of BTB.

This effect diminished after approximately 30 min, at which point the high-lignin hydrogel was nearly completely swollen, and thus, the release of BTB increased.

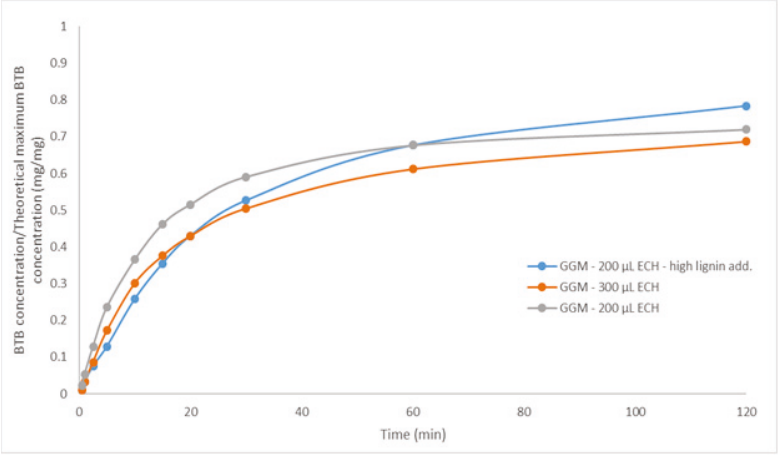

Figure 9. The release of BTB from three different hydrogels as a function of time. The legend includes the ECH and lignin additions for the crosslinking reaction. High lignin addition corresponds to 75.0/25.0 mL polysaccharide solution/mL lignin solution.

The repeated swelling and drying of hydrogels is an important property for certain applications in which the reusability of hydrogels is a key element, such as in agriculture [10]. This step was performed for 3 of the hydrogels, as seen in Figure 8b. All hydrogels experienced the largest change at the beginning of the swelling-drying cycles and reached a constant swelling degree after 2 consecutive cycles. The high-lignin hydrogel and that with the low ECH reached a stable swelling degree of approximately 50 g/g, which was greater than for the highly crosslinked hydrogel (22 g/g). That these hydrogels reached the same equilibrium strengthens the observations in Figure 8a.

3.8. Mechanical Strength

The cylindrical hydrogels were tested mechanically to obtain compression stress-versus-strain curves. All of the hydrogels demonstrated strain tolerances of over 44%, as seen in Figure 10. The curves were not linear but followed an exponential increase, demonstrating the softness of the gels [40]. The maximum ultimate tensile strength (UTS) for these hydrogels was 21 kPa, which is in the same range as for other pure hemicellulose hydrogels [41]. The graphs also show that a yield strength existed wherein further compression of the hydrogels resulted in irreversible deformation, due to internal fractures or breaks, which were visible throughout the transparent hydrogel during compression.

Greater crosslinking enhanced the UTS of the hydrogels, decreasing the strain (Figure 10a), thus yielding hydrogels with greater mechanical strength and less flexibility (higher brittleness). This finding was not apparent from the results because the strain also increased with the addition of ECH. However, the compression modulus—the ratio between compression stress and strain—rose with the addition of ECH; thus, the stiffness of the hydrogels increased [40]. The opposite effect was observed with higher lignin content (Figure 10b). The UTS of the hydrogels decreased with greater amounts of lignin, likely attributed to the fewer crosslinks that formed when lignin was added. The compression modulus also declined, indicating that the hydrogels had greater flexibility, likely caused by the higher swelling degree.

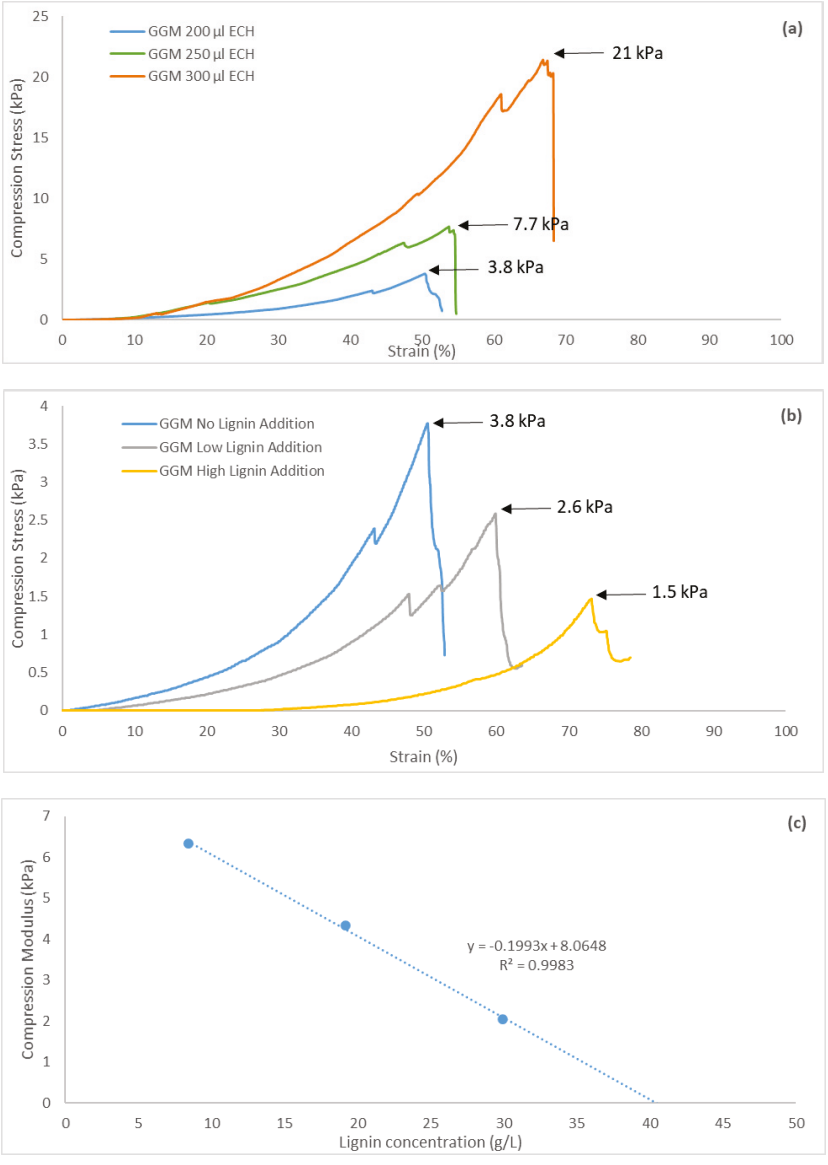

Figure 10. Compression stress and strain for (**a**) three hydrogels at different ECH additions and (**b**) three hydrogels with different lignin additions and a constant (200 µL) ECH addition. Low lignin addition represented the 87.5/12.5 mL polysaccharide solution/mL lignin solution and the high lignin addition 75.0/25.0 mL polysaccharide solution/mL lignin solution. (**c**) A curve of the compression modulus as a function of lignin concentration in the base reaction mixture. The compression modulus was determined at the point of maximum UTS.

During the parameter study, a limit for hydrogel formation was reached when 50/50 mL polysaccharide solution/mL lignin solution was added, corresponding to a near-zero compression modulus, based on the lack of a network structure that resisted the compressible forces [42]. A linear

relationship was observed between compression modulus and lignin concentration in the bulk solution (Figure 10c). Extrapolation of the curve to a compression modulus of 0 gave the lignin a concentration of 40.5 g/L, which was well in the range of the limit that was observed during the parameter study.

3.9. Thermo-gravimetric Analysis

TGA was performed on the synthesized hydrogels (Figure 11). All of the hydrogels had a DTG peak at approximately 33 °C, which corresponded to residual solvents, as seen with the purified GGM and lignin in Section 3.1. In the second degradation stage, 1 DTG peak was observed for the hydrogels with varying amounts of ECH (Figure 11a). For the lowest amount of ECH that was added, the DTG peak occurred at 265 °C, higher than the degradation temperatures of GGM and xylan, as seen in Figure 2. Further, a significant amount of GGM was consumed at the lowest ECH level, as evidenced by SEC and the yields (Figures 4 and 7); thus, the rise in temperature was possibly the result of additional bonds (crosslinks), which was also a factor when the ECH was increased from 200 to 250 µL and the DTG peak temperature climbed to 293 °C. However, the LCCs in the solution were bound at higher ECH levels, which also contributed to the increase in DTG peak temperature (Figure 2). The enhancement in yield between 250 and 300 µL ECH was minimal (Figure 4), which explains the small increase in DTG peak temperature from 293 to 298 °C.

Greater amounts of lignin in the bulk mixture before the reaction had the opposite effect, as apparent from the decrease in DTG peak temperature from 293 to 282 °C in the low-lignin sample and to 271 °C in the high-lignin sample (Figure 11b). This finding is explained by the lower crosslinking, which decreased the amount of bound LCCs, as observed by the change in yields in Figure 5. For the same reason, the results in the previous sections show that the properties of the hydrogel to which the highest amount of lignin was added were similar to that with the lowest ECH content.

In contrast, the thermal properties of the hydrogels developed a disparate pattern. In addition to the higher DTG peak temperature of 271 °C, an increase in the region of 400 to 600 °C could be observed. The peaks in this region were clearly visible on TGA of the lignin but absent in the GGM sample, as seen in Figure 2, confirming previous indications that the added lignin bound to the hydrogel. This bond was also likely the reason for the increase in temperature for the peak in the region of 200 to 300 °C, wherein lignin had a higher degradation temperature compared with GGM (Figure 2). Although the degradation temperature declined with the addition of lignin, the rate of decomposition decreased as well; thus, the thermal properties of the hydrogels approached those of lignin (Figure 2).

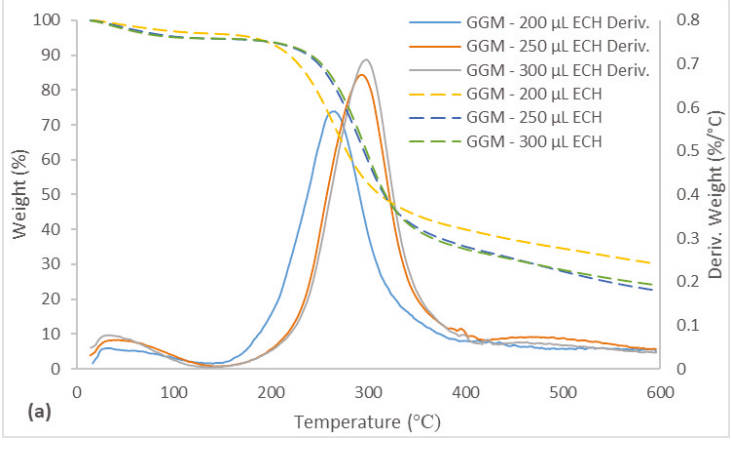

Figure 11. *Cont.*

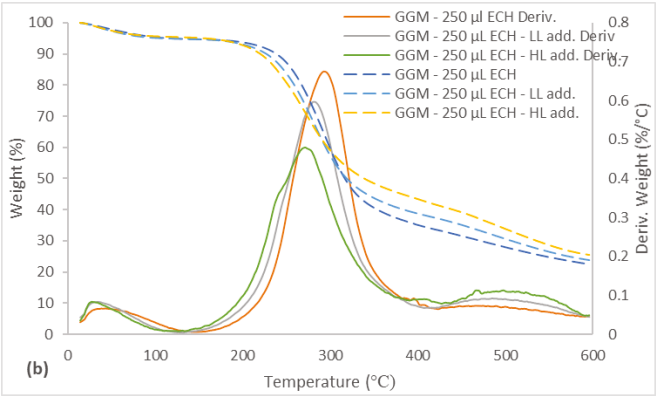

Figure 11. TGA and DTG curves for the synthesized hydrogels between the temperatures of 15 and 600 °C. (**a**) The legend includes the ECH and lignin additions for the crosslinking reaction. (**b**) (LL) Low lignin addition represented the 87.5/12.5 mL polysaccharide solution/mL lignin solution and (HL) the high lignin addition 75.0/25.0 mL polysaccharide solution/mL lignin solution. Deriv. is the acronym for the DTG curve.

4. Conclusions

The combination of ultrafiltration and anti-solvent precipitation was successful in fractionating SSL into 2 streams: polysaccharide-rich and lignin-rich. FTIR measurements of these fractions confirmed the separation of these entities. TGA revealed distinct profiles for GGM and lignin, the latter of which had higher thermal stability. The parameter study showed that the least amount of ECH that was needed for the formation of a hydrogel was 200 µL when 2 mL of stock solution was used. The lignin concentration should also be kept under ~50 g/L to synthesize a coherent gel.

Based on the variation in the degree of crosslinking, the mannan and glucan were linked, given that their yields during the reactions had the same trend and magnitude. Galactans also followed the same pattern, but their overall yield was low compared with the mannans and glucans, because other galactans existed in the mixture. By LC-MS, the increase in crosslinker concentration accelerated the hydrolysis of ECH to glycerol but also the polymerization of glycerol to di-, tri-, tetra-, penta-, and hexamers. The addition of lignin to the reaction mixture decreased the yields for the polysaccharides and the polymerization of glycerol. However, the consumption of ECH rose, due to the lignin consuming the crosslinker and forming larger water-soluble macromolecules, as seen by LC-MS and SEC. Some of the lignin bound to the hydrogel, as confirmed by the FTIR measurements, wherein the peak intensities for aromatic skeletal vibrations (1509 cm^{-1}), guaiacyl structures (1142–1262 cm^{-1}), and sulfonate groups (650 cm^{-1}) increased.

With regard to swelling degree, hydrogels with low crosslinking reached an equilibrium of approximately 137 g water/g dry hydrogel, and for hydrogels that contained lignin, higher water absorption was observed. The hydrogel with the greatest amount of lignin had the slowest initial release of BTB due to the higher osmotic pressure and water uptake. Repeated swelling and drying of the hydrogels yielded an equilibrium after 2 consecutive cycles, peaking at roughly 50 g/g for hydrogels with the lowest amounts of ECH.

The hydrogels were tested mechanically, based on compression (stress vs strain). A maximum UTS of 21 kPa was reached for the pure GGM hydrogels, whereas the UTS fell with increasing amounts of lignin. A linear relationship between lignin concentration and compression modulus was observed, which also yielded a peak lignin concentration of 40.5 g/L for the formation of a coherent hydrogel.

The TGA results showed that the degree of crosslinking had a minor effect on the maximum DTG peak temperature; instead, the DTG temperature depended on the yield of the bound LCCs.

The addition of lignin to the reaction mixture negatively impacted the DTG peak temperature (decreasing). However, the decomposition rate also declined, increasing the thermal stability of the hydrogel.

Author Contributions: Funding acquisition, O.W.; Investigation, B.A.-R. and M.A.H.; Methodology, B.A.-R. and M.G.; Supervision, P.J. and O.W.; Validation, B.A.-R., M.A.H., P.J. and O.W.; Visualization, B.A.-R.; Writing—original draft, B.A.-R.; Writing—review & editing, M.G., P.J. and O.W.

Funding: This research was partially funded by the Swedish Foundation for Strategic Research (SSF) (RBP 14-0046), which is gratefully acknowledged.

Acknowledgments: Thanks to Domsjö Fabriker for providing us with the raw material that was used in this study. Many thanks to Dr. Herje Schagerlöf for the help with the LC-MS analysis.

Conflicts of Interest: The authors declare no conflict of interest. The funders had no role in the design of the study; in the collection, analyses, or interpretation of data; in the writing of the manuscript, or in the decision to publish the results.

References

1. Ahmed, E.M. Hydrogel: Preparation, characterization, and applications: A review. *J. Adv. Res.* **2015**, *6*, 105–121. [CrossRef] [PubMed]
2. Ahmadi, F.; Oveisi, Z.; Samani, S.M.; Amoozgar, Z. Chitosan based hydrogels: Characteristics and pharmaceutical applications. *Res. Pharm. Sci.* **2015**, *10*, 1–16. [PubMed]
3. Lee, K.Y.; Mooney, D.J. Alginate: Properties and biomedical applications. *Prog. Polym. Sci.* **2012**, *37*, 106–126. [CrossRef] [PubMed]
4. Chang, C.; Zhang, L. Cellulose-based hydrogels: Present status and application prospects. *Carbohydr. Polym.* **2011**, *84*, 40–53. [CrossRef]
5. Wang, J.; Sun, H.; Li, J.; Dong, D.; Zhang, Y.; Yao, F. Ionic starch-based hydrogels for the prevention of nonspecific protein adsorption. *Carbohydr. Polym.* **2015**, *117*, 384–391. [CrossRef] [PubMed]
6. Lin, C.; Zhao, P.; Li, F.; Guo, F.; Li, Z.; Wen, X. Thermosensitive in situ-forming dextran–pluronic hydrogels through Michael addition. *Mater. Sci. Eng. C* **2010**, *30*, 1236–1244. [CrossRef]
7. Wenzl, H. *The Chemical Technology of Wood*; Elsevier: Amsterdam, The Netherlands, 2012.
8. Söderqvist Lindblad, M.; Albertsson, A.-C.; Ranucci, E.; Laus, M.; Giani, E. Biodegradable polymers from renewable sources: Rheological characterization of hemicellulose-based hydrogels. *Biomacromolecules* **2005**, *6*, 684–690. [CrossRef]
9. Maleki, L.; Edlund, U.; Albertsson, A.-C. Synthesis of full interpenetrating hemicellulose hydrogel networks. *Carbohydr. Polym.* **2017**, *170*, 254–263. [CrossRef] [PubMed]
10. Maleki, L.; Edlund, U.; Albertsson, A.-C. Unrefined wood hydrolysates are viable reactants for the reproducible synthesis of highly swellable hydrogels. *Carbohydr. Polym.* **2014**, *108*, 281–290. [CrossRef] [PubMed]
11. Zasadowski, D.; Yang, J.; Edlund, H.; Norgren, M. Antisolvent precipitation of water-soluble hemicelluloses from TMP process water. *Carbohydr. Polym.* **2014**, *113*, 411–419. [CrossRef]
12. Jacobs, A.; Lundqvist, J.; Stålbrand, H.; Tjerneld, F.; Dahlman, O. Characterization of water-soluble hemicelluloses from spruce and aspen employing SEC/MALDI mass spectroscopy. *Carbohydr. Res.* **2002**, *337*, 711–717. [CrossRef]
13. Krawczyk, H.; Arkell, A.; Jönsson, A.-S. Impact of prefiltration on membrane performance during isolation of hemicelluloses extracted from wheat bran. *Sep. Purif. Technol.* **2013**, *116*, 192–198. [CrossRef]
14. Al Manasrah, M.; Kallioinen, M.; Ilvesniemi, H.; Mänttäri, M. Recovery of galactoglucomannan from wood hydrolysate using regenerated cellulose ultrafiltration membranes. *Bioresour. Technol.* **2012**, *114*, 375–381. [CrossRef] [PubMed]
15. Song, T.; Pranovich, A.; Holmbom, B. Separation of polymeric galactoglucomannans from hot-water extract of spruce wood. *Bioresour. Technol.* **2013**, *130*, 198–203. [CrossRef] [PubMed]
16. Thuvander, J.; Jönsson, A.-S. Extraction of galactoglucomannan from thermomechanical pulp mill process water by microfiltration and ultrafiltration—Influence of microfiltration membrane pore size on ultrafiltration performance. *Chem. Eng. Res. Des.* **2016**, *105*, 171–176. [CrossRef]

17. Al-Rudainy, B.; Galbe, M.; Wallberg, O. Influence of prefiltration on membrane performance during isolation of lignin-carbohydrate complexes from spent sulfite liquor. *Sep. Purif. Technol.* **2017**, *187*, 380–388. [CrossRef]
18. Al-Rudainy, B.; Galbe, M.; Schagerlöf, H.; Wallberg, O. Antisolvent precipitation of hemicelluloses, lignosulfonates and their complexes from ultrafiltrated spent sulfite liquor (SSL). *Holzforschung* **2018**, *72*, 839–850. [CrossRef]
19. Vermaas, J.V.; Petridis, L.; Qi, X.; Schulz, R.; Lindner, B.; Smith, J.C. Mechanism of lignin inhibition of enzymatic biomass deconstruction. *Biotechnol. Biofuels* **2015**, *8*, 217. [CrossRef]
20. Zhao, W.; Odelius, K.; Edlund, U.; Zhao, C.; Albertsson, A.-C. In situ synthesis of magnetic field-responsive hemicellulose hydrogels for drug delivery. *Biomacromolecules* **2015**, *16*, 2522–2528. [CrossRef] [PubMed]
21. Palamarchuk, I.; Brovko, O.; Bogolitsyn, K.; Boitsova, T.; Ladesov, A.; Ivakhnov, A. Relationship of the structure and ion-exchange properties of polyelectrolyte complexes based on biopolymers. *Russ. J. Appl. Chem.* **2015**, *88*, 103–109. [CrossRef]
22. Rönnols, J.; Schweinebarth, H.; Jacobs, A.; Stevanic, J.S.; Olsson, A.-M.; Reimann, A.; Aldaeus, F. Structural changes in softwood kraft lignin during thermal treatment. *Nord. Pulp Pap. Res. J.* **2015**, *30*, 550–561.
23. Watkins, D.; Nuruddin, M.; Hosur, M.; Tcherbi-Narteh, A.; Jeelani, S. Extraction and characterization of lignin from different biomass resources. *J. Mater. Res. Technol.* **2015**, *4*, 26–32. [CrossRef]
24. Ye, H.; Zhang, Y.; Yu, Z. Effect of desulfonation of lignosulfonate on the properties of poly (lactic acid)/lignin composites. *BioResources* **2017**, *12*, 4810–4829. [CrossRef]
25. Lemes, A.P.; Soto-Oviedo, M.A.; Waldman, W.R.; Innocentini-Mei, L.H.; Durán, N. Effect of Lignosulfonate on the Thermal and Morphological Behavior of Poly(3-hydroxybutyrate-*co*-3-hydroxyvalerate). *J. Polym. Environ.* **2010**, *18*, 250–259. [CrossRef]
26. Leger, C.A.; Chan, F.D.; Schneider, M.H. Fractionation and characterisation of technical ammonium lignosulphonate. *BioResources* **2010**, *5*, 2239–2247.
27. Beall, F. Thermogravimetric analysis of wood lignin and hemicelluloses. *Wood Fiber Sci.* **2007**, *1*, 215–226.
28. Gebelein, C.; Koblitz, F. *Biomedical and Dental Applications of Polymers*; Springer Science & Business Media: Berlin, Germany, 2013; Volume 14.
29. Mussatto, S.I.; Fernandes, M.; Roberto, I.C. Lignin recovery from brewer's spent grain black liquor. *Carbohydr. Polym.* **2007**, *70*, 218–223. [CrossRef]
30. Swamy, N.K.; Singh, P.; Sarethy, I.P. Precipitation of phenols from paper industry wastewater using ferric chloride. *Rasayan J. Chem.* **2011**, *4*, 452–456.
31. Laine, C. *Structures of Hemicelluloses and Pectins in Wood and Pulp*; Helsinki University of Technology: Espoo, Finland, 2005.
32. Kartha, K.; Srivastava, H. Reaction of epichlorhydrin with carbohydrate polymers. Part II. Starch reaction mechanism and physicochemical properties of modified starch. *Starch-Stärke* **1985**, *37*, 297–306. [CrossRef]
33. Medeiros, M.A.; Araujo, M.H.; Augusti, R.; de Oliveira, L.C.; Lago, R.M. Acid-catalyzed oligomerization of glycerol investigated by electrospray ionization mass spectrometry. *J. Braz. Chem. Soc.* **2009**, *20*, 1667–1673. [CrossRef]
34. Xu, C.; Pranovich, A.; Vähäsalo, L.; Hemming, J.; Holmbom, B.; Schols, H.A.; Willför, S. Kinetics of acid hydrolysis of water-soluble spruce O-acetyl galactoglucomannans. *J. Agric. Food Chem.* **2008**, *56*, 2429–2435. [CrossRef] [PubMed]
35. Nebreda, A.P.; Grénman, H.; Mäki-Arvela, P.; Eränen, K.; Hemming, J.; Willför, S.; Murzin, D.Y.; Salmi, T. Acid hydrolysis of *O*-acetyl-galactoglucomannan in a continuous tube reactor: A new approach to sugar monomer production. *Holzforschung* **2016**, *70*, 187–194. [CrossRef]
36. Lundqvist, J.; Teleman, A.; Junel, L.; Zacchi, G.; Dahlman, O.; Tjerneld, F.; Stålbrand, H. Isolation and characterization of galactoglucomannan from spruce (*Picea abies*). *Carbohydr. Polym.* **2002**, *48*, 29–39. [CrossRef]
37. Jyothi, A.N.; Moorthy, S.N.; Rajasekharan, K.N. Effect of cross-linking with epichlorohydrin on the properties of cassava (*Manihot esculenta* crantz) starch. *Starch-Stärke* **2006**, *58*, 292–299. [CrossRef]
38. Hasanah, A.N.; Muhtadi, A.; Elyani, I.; Musfiroh, I. Epichlorohydrin as Crosslinking Agent for Synthesis of Carboxymethyl Cellulose Sodium (Na-CMC) as Pharmaceutical Excipient from Water Hyacinth (*Eichorrnia Crassipes* L.). *Int. J. Chem. Sci.* **2015**, *13*, 1227–1237.
39. Körner, A. *Dissolution of Polydisperse Polymers in Water*; Physical Chemistry 1, Lund University: Lund, Sweden, 2006.

40. Qi, X.-M.; Chen, G.-G.; Gong, X.-D.; Fu, G.-Q.; Niu, Y.-S.; Bian, J.; Peng, F.; Sun, R.-C. Enhanced mechanical performance of biocompatible hemicelluloses-based hydrogel via chain extension. *Sci. Rep.* **2016**, *6*, 33603. [CrossRef]
41. Peng, X.-W.; Ren, J.-L.; Zhong, L.-X.; Peng, F.; Sun, R.-C. Xylan-rich hemicelluloses-graft-acrylic acid ionic hydrogels with rapid responses to pH, salt, and organic solvents. *J. Agric. Food Chem.* **2011**, *59*, 8208–8215. [CrossRef]
42. Sakai, T.; Matsunaga, T.; Yamamoto, Y.; Ito, C.; Yoshida, R.; Suzuki, S.; Sasaki, N.; Shibayama, M.; Chung, U.-I. Design and fabrication of a high-strength hydrogel with ideally homogeneous network structure from tetrahedron-like macromonomers. *Macromolecules* **2008**, *41*, 5379–5384. [CrossRef]

polymers

MDPI

Article

Reinforcement of Thermoplastic Corn Starch with Crosslinked Starch/Chitosan Microparticles

Diana Paiva [1], André M. Pereira [2], Ana L. Pires [2], Jorge Martins [1,3], Luísa H. Carvalho [1,3] and Fernão D. Magalhães [1,*]

[1] LEPABE, Faculdade de Engenharia da Universidade do Porto, Rua Dr. Roberto Frias, 4200-465 Porto, Portugal; diana.paiva@fe.up.pt (D.P.); jmmartins@estv.ipv.pt (J.M.); lhcarvalho@estv.ipv.pt (L.H.C.)

[2] IFIMUP and IN—Institute of Nanoscience and Nanotechnology, Departamento de Física e Astronomia, Faculdade de Ciências, Universidade do Porto, 4169-007 Porto, Portugal; ampereira@fc.up.pt (A.M.P.); ana.pires@fc.up.pt (A.L.P.)

[3] DEMad—Instituto Politécnico de Viseu, Campus Politécnico de Repeses 3504-510 Viseu, Portugal

* Correspondence: fdmagalh@fe.up.pt; Tel.: +351-22-508-1601

Received: 25 July 2018; Accepted: 31 August 2018; Published: 4 September 2018

Abstract: Microparticles of corn starch and chitosan crosslinked with glutaraldehyde, produced by the solvent exchange technique, are studied as reinforcement fillers for thermoplastic corn starch plasticized with glycerol. The presence of 10% *w*/*w* chitosan in the microparticles is shown to be essential to guaranteeing effective crosslinking, as demonstrated by water solubility assays. Crosslinked chitosan forms an interpenetrating polymer network with starch chains, producing microparticles with a very low solubility. The thermal stability of the microparticles is in agreement with their polysaccharide composition. An XRD analysis showed that they have crystalline fraction of 32% with V_a-type structure, and have no tendency to undergo retrogradation. The tensile strength, Young's modulus, and toughness of thermoplastic starch increased by the incorporation of the crosslinked starch/chitosan microparticles by melt-mixing. Toughness increased 360% in relation to unfilled thermoplastic starch.

Keywords: thermoplastic starch; corn starch; chitosan; crosslinked microparticles

1. Introduction

Environmental concerns have increased public awareness over the use and disposal of common petroleum-based plastics, especially those used in manufacturing short-lifetime products, like disposable eating utensils, food packaging, bags, and so on. [1–3]. Bioplastics, sourced from natural materials, have been the growing focus of attention, as they are based on renewable raw materials and are biodegradable. Currently, the most widely used bioplastic is thermoplastic starch (TPS), either alone or blended with natural or synthetic polymers. TPS has some limitations, mainly related to high hydrophilicity, low processability, and a tendency to increase brittleness with time due to recrystallization (retrogradation) [4,5].

Native starch is composed of amylose, a linear polymer of D-glucose units linked by (1→4) bonds, and amylopectin, a highly branched polymer of D-glucose units linked by (1→4) bonds, branched with (1→6) linkages at intervals of approximately 20 units [6–8]. Starch granules have amorphous and crystalline fractions composed mostly of amylose and amylopectin, respectively [9,10].

The production of thermoplastic starch (TPS) requires the disruption of starch granules, in a process called gelatinization. Water or another solvent able to form hydrogen bonds with the starch chains is used, in conjunction with heat. As the amylose molecules dissolve and the amylopectin crystallites melt, a gelatinous paste is obtained [11–13]. After drying, the previously gelatinized starch is not processable, because of strong intermolecular hydrogen bonding in amylose and amylopectin

chains. Plasticizers must therefore be used to allow for processing by extrusion or injection molding. Common starch plasticizers are water, glycerol, sorbitol, and urea [14–17]. As the plasticizer content increases in TPS, so does the elongation at break, but the stiffness and tensile resistance decrease [18]. Depending on the desired application, the amount of plasticizer must be adjusted in order to achieve the intended performance. The source of the starch will also be determinant for the mechanical properties of TPS, as it affects the amylose/amylopectin ratio and thus the crystallinity of the material [19]. Starches with high amylose content typically crystallize to a higher extent after processing, and thus have a higher tensile strength and lower elongation at break [20–22].

Lignocellulosic fibers are known to provide good mechanical reinforcement in TPS [23]. Examples include sisal, hemp and green coconut fibers [24,25], cotton cellulose nanofibers [26], and cellulose fibers from recycled paper [27]. Particulate fillers, like graphene [28], calcium carbonate nanoparticles [29], and clays [30,31] have also been reported to improve the mechanical properties of TPS.

In this work, a new approach for reinforcing thermoplastic corn starch is studied, which is based on the incorporation of starch/chitosan microparticles crosslinked with glutaraldehyde. The fact that the filler particles are of the same nature as the matrix should ensure a good compatibility between the two, and provide strong interfacial interactions. The filler microparticles are intended to be mechanically tough, thus taking advantage of the known affinity between starch and chitosan, and the ability of dialdehydes to chemically crosslink these blends [32].

2. Materials and Methods

2.1. Materials

The corn starch was purchased from Frutalcarmo (Alcoentre, Portugal), chitosan ([CS] degree of acetylation 90%) from Golden-Shell Pharmaceutical Co., Ltd. (Yuhuan County, Zhejiang, China), glutaraldehyde solution (25% in H_2O) and propionic acid from Sigma-Aldrich (Lisbon, Portugal), glycerol from JMGS (Odivelas, Portugal), ethanol from PanReac AppliChem (Madrid, Spain), and hydrochloric acid from Fisher (Porto Salvo, Portugal). All of the materials were used as purchased, unless otherwise noted.

2.2. Preparation of Crosslinked Starch/Chitosan Microparticles

The starch/chitosan microparticles (SCM) were prepared using the solvent exchange technique, adapting procedures previously described in the literature for microparticles composed solely of starch [6,33]. The first step consists of the gelatinization of corn starch in order to disrupt the granules. 8 g (0.049 mol) of polysaccharide (either starch alone, or a mixture of 90% w/w starch and 10% w/w chitosan) was added to 25 mL of distilled water under mechanical agitation (Heidolph RZR2041, 300 rpm, Schwabach, Germany). To ensure complete dissolution, chitosan was added in the form of an acidic aqueous solution with 5% chitosan and 6% propionic acid. The aqueous mixture of the starch and chitosan was heated to 80 °C, the vessel's external jacket was connected to a recirculating thermostatic bath for a period of 20 min, and was kept at that temperature for an additional 20 min, under mild agitation. The obtained gel was then cooled to 50 °C over a period of 1 h. Then, 100 mL of ethanol was added and the mechanical stirring increased to 700 rpm and was maintained for 15 min. A visibly agglomerated precipitate was formed. In order to promote deagglomeration, the dispersion was kept for 15 min under high shear, using an IKA T-18 Ultra-turrax (Staufen, Germany) at 10,000 rpm. The precipitate was then filtered using qualitative filter paper (5–13 μm, VWR international, Radnor, PA, USA, Grade 413) in a Buchner funnel under a vacuum, in order to remove the excess water. To promote crosslinking, the particles were re-suspended in 100 mL of 90% (v/v) ethanol and the dispersion was heated to 50 °C under mechanical stirring (500 rpm). Glutaraldehyde was added in different amounts, from 0 to 10 g per 100 g of polysaccharide, mixed with 0.5 mL of HCl 1 M, after which the dispersion was kept at 50 °C for 1 h. The resulting particles were filtered as described

above and re-suspended in 100 mL of ethanol under mechanical stirring at 300 rpm for a period of 15 min, to remove any unreacted glutaraldehyde. The particles were finally filtered and dried to constant weight at 105 °C.

2.3. Preparation of Thermoplastic Starch

The thermoplastic materials were prepared by melt mixing, using 30% glycerol as a plasticizer, as described by Carvalho et al. [34]. The SCM content was varied from 0 to 50%. Dried native corn starch granules and glycerol were pre-mixed the day before use, to promote the absorption of glycerol by the granules. This pre-mixture and the intended amount of SCM were fed to a DSM Xplore 5 twin screw microcompounder (Sittard, The Netherlands), having a 5.5 mL conical barrel and recirculation channel. The mixing chamber temperature was 140 °C. The twin screws were operated at 200 rpm and the mixture time after loading was 5 min. The resulting mixture was then injected into a mold, using a DSM 10 cc micro injection molder (Sittard, The Netherlands), in order to produce dog-bone shaped specimens with a 2 mm thickness and 80 mm length. The injection pressure was 10 bar, the temperature in the injection nozzle was set to 150 °C, and the mold temperature to 60 °C.

2.4. Characterization

The water solubility and boiling water solubility of the SCM were evaluated in terms of the total soluble matter (TSM). Both tests were performed in an aqueous solution with two pH values (4 and 7). The water solubility was evaluated for a period of 24 h under constant magnetic stirring. The boiling water solubility was evaluated for a period of 1 h. Previously dried and weighted particles were used. After the conclusion of the tests, the liquid was filtered and the residue was dried to a constant weight. The TSM value, in a percentage, is given by Equation (1), where m_{final} is the final mass after drying and $m_{initial}$ is the initial mass of the particles, as follows:

$$\text{TSM } (\%) = 1 - \frac{m_{final}}{m_{initial}} \times 100 \quad (1)$$

An FTIR analysis of the native starch and microparticles was performed on a VERTEX 70 FTIR spectrometer (BRUKER, Billerica, MA, USA) in absorbance mode, with a high sensitivity DLaTGS detector at room temperature. The samples were measured in ATR mode, with a A225/Q PLATINUM ATR Diamond crystal (Billerica, MA, USA) with single reflection accessory. The spectra were recorded from 4000 to 500 cm^{-1} with a resolution of 4 cm^{-1}.

X-ray diffraction (XRD) measurements were performed on native cornstarch granules and on SCM crosslinked with 7.5% glutaraldehyde, after one day and 30 days after production. The experiments were performed at the IFIMUP-IN facilities, in a Rigaku SmartLab diffractometer (Tokyo, Japan) that operates with 9 kW power (45 kV and 200 mA) and a Cu source with a wavelength λ = 1.540593 Å in Bragg-Brentano geometry. All of the samples were measured at room temperature over the range 2θ = 5–30° in rotation mode.

The mean diameter of crystallite was calculated with the Debye-Scherrer equation, as follows:

$$D_{hkl} = \frac{K\lambda}{B_{hkl}cos\theta} \quad (2)$$

where D_{hkl} is considered on the direction perpendicular to the lattice planes, hkl is the Miller indices of the planes being analysed, λ is the wavelength of the source Cu Kα (λ = 1.5406 Å), B_{hkl} is the full-width at half-maximum (FWHM) of the principal peak, and (002) θ is the Bragg angle [35].

The volumetric crystallinity fraction was determined accordingly to the following equation [36]:

$$\text{Crystallinity}(\%) = \frac{I_T - I_A}{I_T} \times 100 \quad (3)$$

where I_T is the total area under the intensity curve and I_A is the area under the amorphous halo.

The FWHM/area determinations were performed using the free license Fityk software (version 0.9.8) [37].

The morphological characterization of SCM was performed using a scanning electron microscope (SEM, Hillsboro, OR, USA), FEI QUANTA 400 FEG ESEM/EDAX Pegasus X4M, property of CEMUP-Centro de Materiais da Universidade do Porto. The sample was placed on carbon tape and coated with a gold–palladium (Au-Pd) layer to ensure conductivity, and then analyzed at a voltage of 15 kV.

The thermogravimetry analysis (TGA) of SCM was performed in a STA 449 F3 Jupiter (Netzsch, Selb, Germany). The samples weights were about 10 mg. The runs were carried out from 30 to 550 °C, at a rate of 10 K·min^{-1}, in aluminum pans under a nitrogen flow.

The tensile tests of the composite thermoplastic starch specimens were performed in a Tinius Olsen H50KT universal tensile testing machine equipped with a load cell of 10 kN at crosshead speed of 2 mm/min, according to the standard of ISO 527-1. The tension tests were conducted at ambient conditions (20 °C, 65% relative humidity) on dog-bone shaped samples (80 mm × 11 mm × 2 mm), according to ISO 527-2. The ultimate tensile strength, percentage elongation at break, and tensile modulus values were recorded using the software Tinius Olsen Horizon, according to ISO 527-1.

Water absorption of thermoplastic starch was evaluated as described by Prachayawarakorn et al. [38]. The specimens were stabilized at room temperature for over a month. After stabilization, the samples from five different specimens of each composition were dried for 12 h in a vacuum oven at 50 °C and 125 mbar. The samples were then placed in a desiccator to cool to room temperature for 1 h, and then placed in a closed container at 100% relative humidity (RH). The samples were weighed after 8 h, 24 h, 3 days, 7 days, and 14 days, and the water absorption was computed according to the following equation:

$$\% \, abs = \left(\frac{m_{wet} - m_{dry}}{m_{dry}} \right) \times 100 \quad (4)$$

3. Results and Discussion

3.1. Starch/Chitosan Microparticles

Figure 1 shows a representative SEM image of the crosslinked starch/chitosan microparticles (SCM). These microparticles have roughly spherical shapes with diameters between about 10 and 20 μm, independent on the amount of glutaraldehyde crosslinker used.

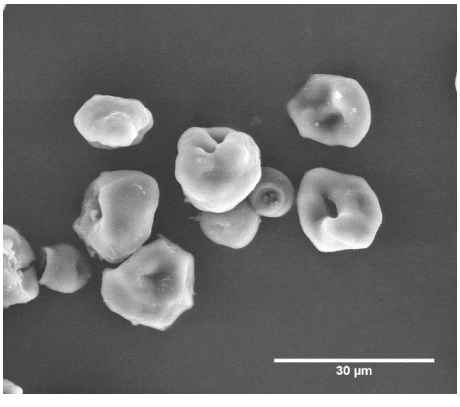

Figure 1. SEM image of starch/chitosan microparticles crosslinked with 7.5% of glutaraldehyde.

The use of dialdehydes, such as glutaraldehyde or glyoxal, as crosslinking agents for polysaccharides is commonly mentioned in the literature [39–41]. A straightforward form of evaluating the effectiveness of the crosslinking reaction is by determining the product solubility. As new intermolecular covalent bonds have been formed, the water solubility is expected to decrease significantly. SCM with different amounts of glutaraldehyde were prepared, and the particles' solubility was measured using two different assays, after 24 h immersion at room temperature, and after 1 h immersion in boiling water. As chitosan is insoluble at a neutral pH and completely soluble under acidic conditions (pH < 5), because of the hydrophilic character of the protonated amine groups, the particles' solubility was evaluated for two pH values (7 and 4). Figure 2 presents the results obtained in terms of the total soluble matter (TSM).

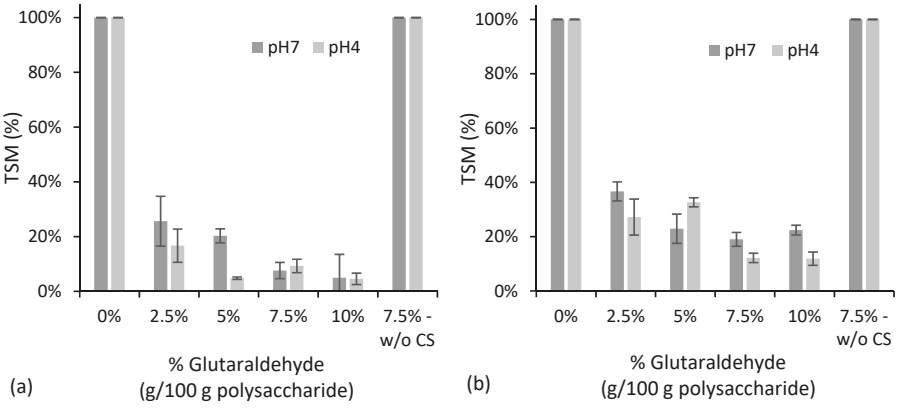

Figure 2. Water solubility at room temperature (**a**) and at boiling conditions (**b**), expressed in terms of total soluble matter (TSM), for starch/chitosan microparticles with different glutaraldehyde contents. All of the microparticles contain chitosan except the one labeled "w/o CS".

The SCMs prepared without the glutaraldehyde addition are completely soluble at both pH values. The physical interaction between the starch and chitosan did not prevent solubility, even at a neutral pH. However, the addition of crosslinker greatly decreased the solubility. For both room temperature and boiling water immersion tests, increasing the glutaraldehyde concentration up to 7.5% tends to increase the water resistance. A further increase to 10% does not improve the results. Therefore, 7.5% seems to be an appropriate value for attaining effective crosslinking. TSM is higher when SCM is in contact with boiling water, as expected for such extreme conditions. Somewhat unexpectedly, however, TSM tends to be higher for pH 7 than for pH 4. The opposite could have been predicted, considering that chitosan is soluble only under an acidic pH. However, reaction of aldehydes with amines is known to be catalyzed by acids. Therefore, the lower TSM observed at pH 4 is probably a consequence of further crosslinking taking place between residual unreacted glutaraldehyde and amino groups in chitosan. When chitosan is not used, the microparticles become completely soluble, despite of the presence of glutaraldehyde. This suggests that only chitosan's amino groups, and not starch's hydroxyl groups, intervene in the crosslinking process with the aldehyde.

A FTIR analysis was performed on native starch and on starch microparticles containing 7.5% glutaraldehyde, both with and without the chitosan addition. The results are show in Figure 3. The microparticles without chitosan did not present significant changes on the spectra when compared to the native starch, which may be an indication that the reaction between the starch and glutaraldehyde is unlikely. Because of its low concentration, the addition of chitosan to the microparticles was not detectable by FTIR, as the typical bands of NH_2 group (1650–1580 cm^{-1}) are not present in the

corresponding spectrum. As a consequence, the bands that would result from the reaction of chitosan with glutaraldehyde are also not detectable. Nonetheless, in order to demonstrate the feasibility of this chemical reaction under the conditions used for production of the microparticles, the same synthesis procedure was followed using chitosan alone, with and without the glutaraldehyde addition. The resulting spectra are also shown in Figure 3. When glutaraldehyde is added to chitosan, a new band appears at 1658 cm^{-1}, confirming the formation of the N=C linkage, originated by the reaction between an amine group from chitosan and an aldehyde group from glutaraldehyde. In addition, a small band around 1720 cm^{-1} is visible, which may be attributed to the unreacted aldehyde groups from glutaraldehyde. It must be noted that glutaraldehyde was already known to be an efficient crosslinker for chitosan [42,43]. It can therefore be suggested that the crosslinked SCM particles consist of an interpenetrating polymer network of starch and crosslinked chitosan chains.

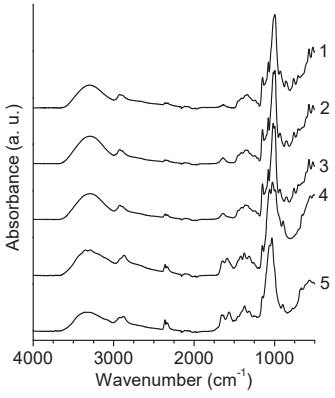

Figure 3. FTIR spectra of: (1) native starch, (2) starch + 7.5% glutaraldehyde, (3) starch + 10% chitosan + 7.5% glutaraldehyde, (4) chitosan, and (5) chitosan + 7.5% glutaraldehyde.

Thermogravimetric curves were obtained for the native corn starch, chitosan, and SCM crosslinked with 7.5% glutaraldehyde. These are shown in Figure 4.

All of the materials show an initial mass loss consistent with the desorption of water molecules, corresponding to roughly 6% of the original mass. The onset of thermal degradation for corn starch is 311 °C, which is consistent with the literature [44,45]. On the other hand, for chitosan, the onset occurs earlier, at 280 °C, and the mass fraction remaining at 500 °C is much higher than for starch (41% compared to 16%). The onset of degradation for crosslinked SCM occurs at the same temperature as for chitosan, and the residual mass fraction is 27%. Considering the starch/chitosan ratio (9:1) present in the microparticles, and the residual mass fraction measured for each single compound, a residual mass of 19% would be expected for the microparticles. The higher value obtained is a consequence of crosslinking with glutaraldehyde, improving thermal stability of the material.

X-ray diffraction measurements were performed on native cornstarch granules and on SCM crosslinked with 7.5% glutaraldehyde. For the SCM, the XRD spectra were obtained one day and 30 days after production, in order to evaluate the possible changes in the crystallinity over time. A 30-day period is considered sufficient for retrogradation to occur in starch molecules after gelatinization [46–48]. Figure 5 presents the XRD diffractograms in the range 2θ = 10–30°.

Native corn starch exhibits diffraction peaks at 2θ = 15.1°, 17.6°, and 23.0°, consistent with a crystalline structure with A-type polymorphism that is usually found in cereal starches [49,50]. The A-type crystallites are, normally, denser and less hydrated because of the double-helical arrangement of amylopectin chains. One day after production, the starch/chitosan particles show peaks at 2θ = 13.2° and 20.2°, resembling the V_a-type microstructure [18,51]. This polymorphism

usually appears after gelatinization, and, with time, may undergo a transformation into V_h-type crystals as a result of exposure to humidity. This process is called retrogradation and is associated with an increase in the brittleness of the starch material [52,53]. The XRD pattern obtained for the same particles after 30 days does not exhibit the peak characteristic of the V_h-type structure (2θ = 18.3°), indicating that the V_a-type crystalline structure is maintained. Therefore, one may conclude that crosslinking with glutaraldehyde after gelatinization/precipitation induces the stability of the crystalline structure, hindering the retrogradation of starch chains. The mean diameter of the crystals was determined by the Debye-Scherrer equation (Equation (2)), and the fraction of crystallinity by peak area integration (Equation (3)). In native starch, the crystals presented diameters around 6.7 nm and a 55% crystallinity. The crosslinked particles presented a smaller crystal mean diameter and lower crystallinity of 4.1 nm and 32%, respectively, on day 1. On day 30, the crystal size and fraction of crystallinity were similar, as expected in the absence of retrogradation.

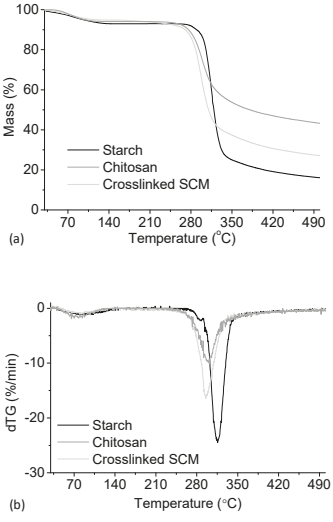

Figure 4. Mass loss (**a**) and first derivative (**b**) for native corn starch, chitosan, and starch/chitosan microparticles (SCM) crosslinked with 7.5% of glutaraldehyde. The thermogravimetric runs were performed under nitrogen atmosphere.

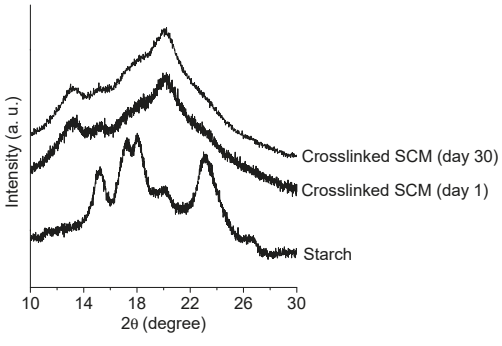

Figure 5. X-ray diffraction patterns for native corn starch and starch/chitosan microparticles with 7.5% of glutaraldehyde (crosslinked SCM), at day 1 and day 30 after production.

3.2. Reinforced Thermoplastic Starch

Thermoplastic starch samples containing different amounts of SCM crosslinked with 7.5% glutaraldehyde were produced by melt mixing followed by injection molding. Their mechanical performance was evaluated in stress-strain tests. Figure 6 shows representative examples of the curves obtained.

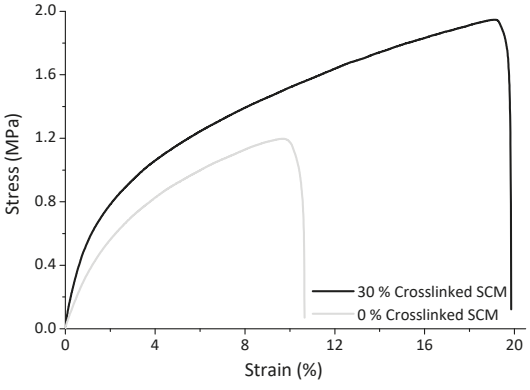

Figure 6. Representative stress-strain curve obtained for thermoplastic starch containing 30% SCM crosslinked with 7.5% glutaraldehyde and without SCM.

The shape of the stress-strain curves indicates that linear elastic behavior is present only at low strains, and is followed by extensive ductile deformation, without a defined stress yield point. This behavior is typical of thermoplastic starches [19]. Strain hardening occurs during the plastic deformation regime, as a consequence of the reorientation of molecular chains and/or crystalline regions in the direction of the applied stress. This contributes to increase the toughness of the material under tensile strain [54].

The ultimate tensile strength (UTS) obtained for the thermoplastic starch samples is plotted in Figure 7a. Figure 7b represents the corrected ultimate tensile strength (UTS_{corr}), that is, the UTS divided by the fraction of thermoplastic starch present in the sample. If the SCM acted as an inert filler, having no effect on mechanical reinforcement, UTS would decrease with the increasing SCM content, but the UTS_{corr} should remain constant.

Figure 7a shows that the UTS reaches a value 58% higher than the neat TPS for the 30% SCM content, and decreases afterwards. This reinforcement is a consequence of an efficient stress transfer through a strong interfacial bond between the thermoplastic matrix and the microparticles. As expected, concomitantly with the UTS decrease above the 30% SCM content, the UTS_{corr} stabilizes, showing that no additional reinforcement is obtained by incrementing the amount of SCM. This is probably due to microparticle agglomeration within the thermoplastic starch matrix, which does not contribute to an increase in the interfacial stress transfer.

Figure 8 presents the elongation at break, Young's modulus, and toughness for all of the materials. All of the properties exhibit a maximum for the 30% SCM content. The initial increase in elongation at break with filler content, seen in Figure 8a, is not the most common behavior. Reinforcement with a filler usually translates into a continuous decrease in elongation at break, concomitantly with an increase in rigidity (Young's modulus), as the chain mobility is restrained by matrix-filler interactions [24]. The observed 84% increase may be due to the microparticles being able to undergo elastic deformation while maintaining strong physical bonding with the thermoplastic matrix. The work of Kvien and co-workers with potato starch plasticized with sorbitol and filled with cellulose nanowhiskers also evidenced an increase in elongation at break with the filler content. The authors proposed that the

interaction of the nanofibers with the plasticizer could maximize the plasticizer effect as well as reinforce the Young's modulus of the material [55]. Teixeira and co-workers reported a 66% increase in elongation at break with the incorporation of 5% cotton cellulose nanofibers in thermoplastic corn starch [26].

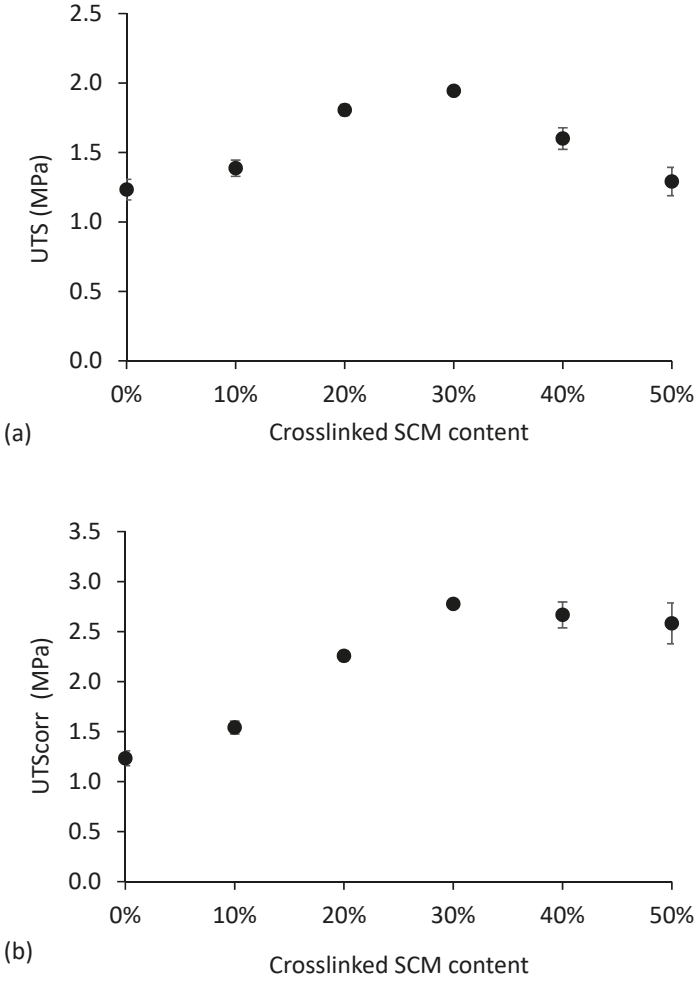

Figure 7. Ultimate tensile strength (UTS) (**a**) and corrected ultimate tensile strength (UTS_{corr}) (**b**) as a function of crosslinked SCM content in thermoplastic starch.

The combined increase in rigidity, strength, and elongation at break for the SCM contents up to 30% leads to a significant improvement in toughness, computed as the area under the stress-strain curves. Toughness is about 360% higher for the 30% SCM content than for the neat thermoplastic starch, which translates into a much higher capacity to absorb energy without fracture. Above this filler content, all of the properties decrease, due to an inefficient dispersion of the microparticles, as mentioned before. Agglomerates behave as defects with lower cohesion than the rest of the material.

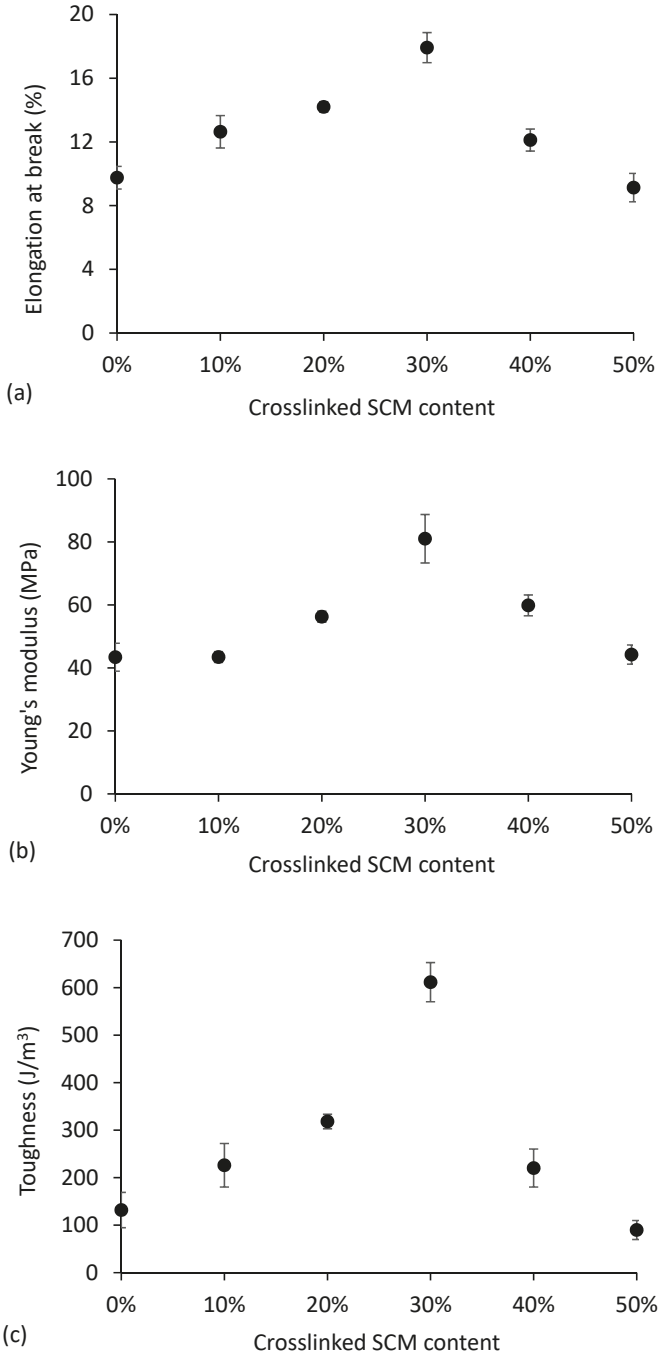

Figure 8. Elongation at break (**a**), Young's modulus (**b**), and toughness (**c**) as a function of crosslinked SCM content in thermoplastic starch.

The water absorption was measured along the time under 100% relative humidity for all of the materials (Figure 9). In all cases, the maximum absorption is attained after three days. The kinetics of the water uptake is similar to that previously reported for thermoplastic corn starch reinforced with wood fiber [56]. The equilibrium absorption values, shown in Figure 9b, show that there is not a clear relation with the SCM content. The variations observed are probably due to an inaccuracy of the measurement method. The microparticles, despite being insoluble, are able to absorb water and therefore do not seem to affect the hydrophilicity of the material. Other researchers have reported some reduction in the water uptake for some types of fillers. As an example, glycerol-plasticized potato starch reinforced with 30% cellulose microfibrils had water uptake 14% lower than unfilled starch [57].

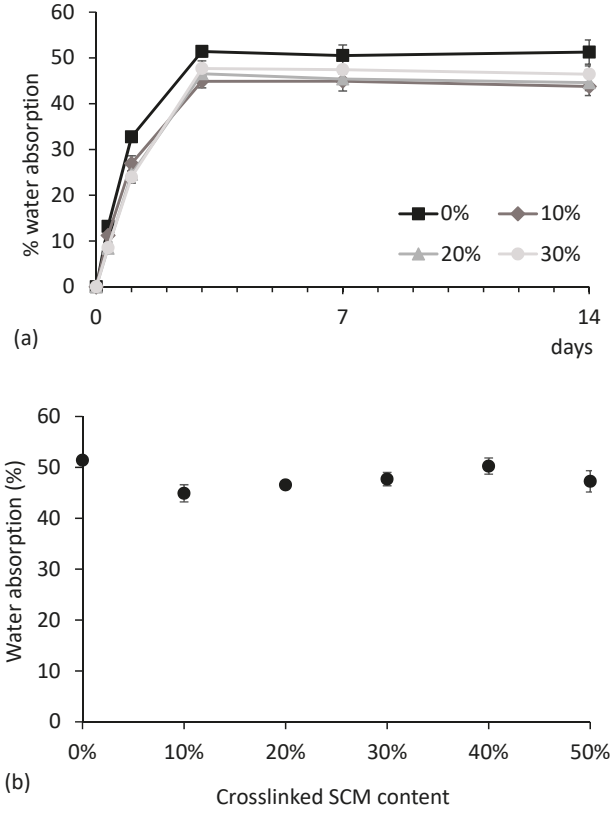

Figure 9. Examples of water uptake at 100% relative humidity for some crosslinked SCM contents in thermoplastic starch (**a**), and equilibrium water absorption after 3 days as a function of crosslinked SCM content (**b**).

4. Conclusions

Microparticles composed of corn starch and chitosan were produced by solvent exchange and crosslinked with glutaraldehyde. The effectiveness of crosslinking was evaluated by measuring the fraction of soluble matter. The results showed that the microparticles are completely soluble when composed of only starch. When 10% w/w chitosan is used, the soluble fraction becomes relatively low, tending to decrease as the crosslinker content is increased. For 7.5 g glutaraldehyde per 100 g of polysaccharide, the total soluble matter is lower than 10% after one day of immersion in

water at room temperature, and lower than 20% after one hour in boiling water, even under acidic conditions that facilitate the chitosan dissolution. The presence of chitosan's amino groups is therefore essential for a reaction with glutaraldehyde, forming an interpenetrating polymer network with starch chains. Thermogravimetry indicated that the microparticles' thermal degradation behavior is coherent with their polysaccharide composition. An XRD analysis showed that the microparticles have 32% crystalline fraction with V_a-type structure, and do not exhibit a tendency to undergo retrogradation.

The crosslinked starch/chitosan microparticles were melt-mixed with corn starch plasticized with glycerol and were able to reinforce its mechanical properties in terms of tensile strength, rigidity, and toughness. Contrary to what is usual, elongation at break also increases with the filler content, probably due to the microparticles being able to deform while providing an interfacial stress transfer. An optimum weight fraction of 30% was identified, leading to 58%, 87%, and 84% increases in ultimate tensile strength, Young's modulus, and elongation at break, respectively. The materials toughness increased 360% in relation to unfilled thermoplastic starch.

Author Contributions: Conceptualization, D.P.; data curation, D.P., A.M.P., A.L.P., J.M. and L.H.C.; formal analysis, D.P., A.M.P., A.L.P., J.M. and L.H.C.; investigation, D.P.; methodology, D.P.; supervision, F.D.M.; writing (original draft), D.P.; writing (review and editing), F.D.M.

Funding: This work was financially supported as follows: project POCI-01-0145-FEDER-006939 (Laboratory for Process Engineering, Environment, Biotechnology, and Energy—UID/EQU/00511/2013), funded by the European Regional Development Fund (ERDF) through COMPETE2020—Programa Operacional Competitividade e Internacionalização (POCI), and by national funds through FCT—Fundação para a Ciência e a Tecnologia; project "LEPABE-2-ECO-INNOVATION"—NORTE-01-0145-FEDER-000005, funded by Norte Portugal Regional Operational Programme (NORTE 2020), under PORTUGAL 2020 Partnership Agreement, through the European Regional Development Fund (ERDF). The authors also acknowledge FCT through project NORTE-01-0145-FEDER-022096 from NECL, which enabled the XRD measurements.

Acknowledgments: The authors acknowledge the lab IMICROS-CEMUP for the SEM analysis.

Conflicts of Interest: The authors declare no conflict of interest.

References

1. Shogren, R.L.; Swanson, C.L.; Thompson, A.R. Extrudates of cornstarch with urea and glycols: Structure/mechanical property relations. *Starch-Stärke* **1992**, *44*, 335–338. [CrossRef]
2. Stevens, E.S.; Klamczynski, A.; Glenn, G.M. Starch-lignin foams. *Express Polym. Lett.* **2010**, *4*, 311–320. [CrossRef]
3. Patel, S.V.; Venditti, R.A.; Pawlak, J.J. Dimensional changes of starch microcellular foam during the exchange of water with ethanol and subsequent drying. *BioResources* **2009**, *5*, 121–134.
4. Jiankang, W.; Ruilin, M.; Liang, H. Recent research and patents on preparation and application of starch-based plastics. *Recent Patents Mech. Eng.* **2017**, *10*, 111–117.
5. Carvalho, A.J.F. Chapter 6: Chemical Modification of Thermoplastic Starch. In *RSC Green Chemistry*; RSC: Cambridge, UK, 2016; pp. 217–235.
6. Patel, S.; Venditti, R.A.; Pawlak, J.J.; Ayoub, A.; Rizvi, S.S.H. Development of cross-linked starch microcellular foam by solvent exchange and reactive supercritical fluid extrusion. *J. Appl. Polym. Sci.* **2009**, *111*, 2917–2929. [CrossRef]
7. El-Tahlawy, K.; Venditti, R.; Pawlak, J. Effect of alkyl ketene dimer reacted starch on the properties of starch microcellular foam using a solvent exchange technique. *Carbohydr. Polym.* **2008**, *73*, 133–142. [CrossRef]
8. Bastioli, C.; Magistrali, P.; Garcia, S.G. Starch. In *Bio-Based Plastics: Materials and Applications*; Kabasci, S., Ed.; Wiley: Chichester, UK, 2013; p. 392.
9. Soykeabkaew, N.; Thanomsilp, C.; Suwantong, O. A review: Starch-based composite foams. *Compos. Part A Appl. Sci. Manuf.* **2015**, *78*, 246–263. [CrossRef]
10. Blazek, J.; Gilbert, E.P. Application of small-angle X-ray and neutron scattering techniques to the characterisation of starch structure: A review. *Carbohydr. Polym.* **2011**, *85*, 281–293. [CrossRef]
11. Carvalho, A.J.F. Starch: Major Sources, Properties and Applications as Thermoplastic Materials a2—Belgacem, Mohamed Naceur. In *Monomers, Polymers and Composites from Renewable Resources*; Gandini, A., Ed.; Elsevier: Amsterdam, The Netherlands, 2008; pp. 321–342.

12. Wang, S.; Li, C.; Copeland, L.; Niu, Q.; Wang, S. Starch retrogradation: A comprehensive review. *Compr. Rev. Food Sci. Food Saf.* **2015**, *14*, 568–585. [CrossRef]
13. Mihai, M.; Huneault, M.A.; Favis, B.D.; Li, H. Extrusion foaming of semi-crystalline PLA and PLA/thermoplastic starch blends. *Macromol. Biosci.* **2007**, *7*, 907–920. [CrossRef] [PubMed]
14. Mihai, M.; Huneault, M.A.; Favis, B.D. Foaming of polystyrene/thermoplastic starch blends. *J. Cell. Plast.* **2007**, *43*, 215–236. [CrossRef]
15. Chen, M.; Chen, B.; Evans, J.R.G. Novel thermoplastic starch-clay nanocomposite foams. *Nanotechnology* **2005**, *16*, 2334–2337. [CrossRef] [PubMed]
16. Karger-Kocsis, J.; Kmetty, Á.; Lendvai, L.; Drakopoulos, S.; Bárány, T. Water-assisted production of thermoplastic nanocomposites: A review. *Materials* **2015**, *8*, 72–95. [CrossRef] [PubMed]
17. Bahram, K.; Muhammad, B.K.N.; Ghufrana, S.; Zaib, J. Thermoplastic starch: A possible biodegradable food packaging material—A review. *J. Food Process Eng.* **2017**, *40*, e12447.
18. Esmaeili, M.; Pircheraghi, G.; Bagheri, R. Optimizing mechanical and physical properties of thermoplastic starch via tuning the molecular microstructure through co-plasticization by sorbitol and glycerol. *Polym. Int.* **2017**, *66*, 809–819. [CrossRef]
19. Graaf, R.A.; Karman, A.P.; Janssen, L.P.B.M. Material properties and glass transition temperatures of different thermoplastic starches after extrusion processing. *Starch-Stärke* **2003**, *55*, 80–86. [CrossRef]
20. Mali, S.; Grossmann, M.V.E.; García, M.A.; Martino, M.N.; Zaritzky, N.E. Effects of controlled storage on thermal, mechanical and barrier properties of plasticized films from different starch sources. *J. Food Eng.* **2006**, *75*, 453–460. [CrossRef]
21. Xie, F.; Luckman, P.; Milne, J.; McDonald, L.; Young, C.; Tu, C.Y.; Pasquale, T.D.; Faveere, R.; Halley, P.J. Thermoplastic starch: Current development and future trends. *J. Renew. Mater.* **2014**, *2*, 95–106. [CrossRef]
22. Salam, A.; Pawlak, J.J.; Venditti, R.A.; El-tahlawy, K. Synthesis and characterization of starch citrate−chitosan foam with superior water and saline absorbance properties. *Biomacromolecules* **2010**, *11*, 1453–1459. [CrossRef] [PubMed]
23. Gutiérrez, T.J.; Alvarez, V.A. Cellulosic materials as natural fillers in starch-containing matrix-based films: A review. *Polym. Bull.* **2017**, *74*, 2401–2430. [CrossRef]
24. Gironès, J.; López, J.P.; Mutjé, P.; Carvalho, A.J.F.; Curvelo, A.A.S.; Vilaseca, F. Natural fiber-reinforced thermoplastic starch composites obtained by melt processing. *Compos. Sci. Technol.* **2012**, *72*, 858–863. [CrossRef]
25. Lomelí-Ramírez, M.G.; Kestur, S.G.; Manríquez-González, R.; Iwakiri, S.; de Muniz, G.B.; Flores-Sahagun, T.S. Bio-composites of cassava starch-green coconut fiber: Part ii—Structure and properties. *Carbohydr. Polym.* **2014**, *102*, 576–583. [CrossRef] [PubMed]
26. Teixeira, E.; Lotti, C.; Corrêa, A.C.; Teodoro, K.B.R.; Marconcini, J.M.; Mattoso, L.H.C. Thermoplastic corn starch reinforced with cotton cellulose nanofibers. *J. Appl. Polym. Sci.* **2011**, *120*, 2428–2433. [CrossRef]
27. Wattanakornsiri, A.; Pachana, K.; Kaewpirom, S.; Traina, M.; Migliaresi, C. Preparation and properties of green composites based on tapioca starch and differently recycled paper cellulose fibers. *J. Polym. Environ.* **2012**, *20*, 801–809. [CrossRef]
28. Jose, J.; Al-Harthi, M.A.; AlMa'adeed, M.A.A.; Dakua, J.B.; De, S.K. Effect of graphene loading on thermomechanical properties of poly(vinyl alcohol)/starch blend. *J. Appl. Polym. Sci.* **2015**, *132*, 1–8. [CrossRef]
29. Kellermayer, M.S.; Sun, Q.; Xi, T.; Li, Y.; Xiong, L. Characterization of corn starch films reinforced with caco3 nanoparticles. *PLoS ONE* **2014**, *9*, e106727.
30. Chen, B.; Evans, J.R.G. Thermoplastic starch–clay nanocomposites and their characteristics. *Carbohydr. Polym.* **2005**, *61*, 455–463. [CrossRef]
31. López, O.V.; Castillo, L.A.; García, M.A.; Villar, M.A.; Barbosa, S.E. Food packaging bags based on thermoplastic corn starch reinforced with talc nanoparticles. *Food Hydrocoll.* **2015**, *43*, 18–24. [CrossRef]
32. Kumari, K.; Rani, U. Controlled release of metformin hydrochloride through crosslinked blends of chitosan-starch. *Adv. Appl. Sci. Res.* **2011**, *2*, 48–54.
33. El-Tahlawy, K.; Venditti, R.A.; Pawlak, J.J. Aspects of the preparation of starch microcellular foam particles crosslinked with glutaraldehyde using a solvent exchange technique. *Carbohydr. Polym.* **2007**, *67*, 319–331. [CrossRef]
34. Carvalho, A.J.F.; Curvelo, A.A.S.; Agnelli, J.A.M. A first insight on composites of thermoplastic starch and kaolin. *Carbohydr. Polym.* **2001**, *45*, 189–194. [CrossRef]

35. Holzwarth, U.; Gibson, N. The scherrer equation versus the 'debye-scherrer equation'. *Nat. Nanotechnol.* **2011**, *6*, 534–534. [CrossRef] [PubMed]
36. Jollet, V.; Chambon, F.; Rataboul, F.; Cabiac, A.; Pinel, C.; Guillon, E.; Essayem, N. Non-catalyzed and pt/γ-Al_2O_3-catalyzed hydrothermal cellulose dissolution–conversion: Influence of the reaction parameters and analysis of the unreacted cellulose. *Green Chem.* **2009**, *11*, 2052–2060. [CrossRef]
37. Wojdyr, M. Fityk: A general-purpose peak fitting program. *J. Appl. Crystallogr.* **2010**, *43*, 1126–1128. [CrossRef]
38. Prachayawarakorn, J.; Hanchana, A. Effect of neem wood sawdust content on properties of biodegradable thermoplastic acetylated cassava starch/neem wood sawdust composites. *Starch-Stärke* **2017**, *69*, 1600113. [CrossRef]
39. Mikkonen, K.S.; Heikkilä, M.I.; Willför, S.M.; Tenkanen, M. Films from glyoxal-crosslinked spruce galactoglucomannans plasticized with sorbitol. *Int. J. Polym. Sci.* **2012**, *2012*, 482810. [CrossRef]
40. Patel, A.K.; Michaud, P.; de Baynast, H.; Grédiac, M.; Mathias, J.-D. Preparation of chitosan-based adhesives and assessment of their mechanical properties. *J. Appl. Polym. Sci.* **2013**, *127*, 3869–3876. [CrossRef]
41. Yang, Q.; Dou, F.; Liang, B.; Shen, Q. Investigations of the effects of glyoxal cross-linking on the structure and properties of chitosan fiber. *Carbohydr. Polym.* **2005**, *61*, 393–398. [CrossRef]
42. Monteiro, O.A.C.; Airoldi, C. Some studies of crosslinking chitosan–glutaraldehyde interaction in a homogeneous system. *Int. J. Biol. Macromol.* **1999**, *26*, 119–128. [CrossRef]
43. Beppu, M.M.; Vieira, R.S.; Aimoli, C.G.; Santana, C.C. Crosslinking of chitosan membranes using glutaraldehyde: Effect on ion permeability and water absorption. *J. Membr. Sci.* **2007**, *301*, 126–130. [CrossRef]
44. Liu, X.; Wang, Y.; Yu, L.; Tong, Z.; Chen, L.; Liu, H.; Li, X. Thermal degradation and stability of starch under different processing conditions. *Starch-Stärke* **2013**, *65*, 48–60. [CrossRef]
45. Liu, X.; Yu, L.; Liu, H.; Chen, L.; Li, L. Thermal decomposition of corn starch with different amylose/amylopectin ratios in open and sealed systems. *Cereal Chem.* **2009**, *86*, 383–385. [CrossRef]
46. Ma, X.F.; Yu, J.G.; Wan, J.J. Urea and ethanolamine as a mixed plasticizer for thermoplastic starch. *Carbohydr. Polym.* **2006**, *64*, 267–273. [CrossRef]
47. Zobel, H.F. Chapter IX—Gelatinization of Starch and Mechanical Properties of Starch Pastes. In *Starch: Chemistry and Technology*, 3rd ed.; BeMiller, J., Whistler, R., Eds.; Academic Press: London, UK, 2009.
48. Arık Kibar, E.A.; Gönenç, İ.; Us, F. Modeling of retrogradation of waxy and normal corn starches. *Int. J. Food Prop.* **2011**, *14*, 954–967. [CrossRef]
49. Cheetham, N.W.H.; Tao, L.P. Variation in crystalline type with amylose content in maize starch granules: An X-ray powder diffraction study. *Carbohydr. Polym.* **1998**, *36*, 277–284. [CrossRef]
50. Zhang, C.-W.; Li, F.-Y.; Li, J.-F.; Wang, L.-M.; Xie, Q.; Xu, J.; Chen, S. A new biodegradable composite with open cell by combining modified starch and plant fibers. *Mater. Des.* **2017**, *120*, 222–229. [CrossRef]
51. Van Soest, J.J.G.; Hulleman, S.H.D.; de Wit, D.; Vliegenthart, J.F.G. Crystallinity in starch bioplastics. *Ind. Crop Prod.* **1996**, *5*, 11–22. [CrossRef]
52. Shanks, R.; Kong, I. Thermoplastic starch. In *Thermoplastic Elastomers*; El-Sonbati, P.A., Ed.; InTech: Rijeka, Croatia, 2012.
53. Nafchi, A.M.; Moradpour, M.; Saeidi, M.; Alias, A.K. Thermoplastic starches: Properties, challenges, and prospects. *Starch-Staerke* **2013**, *65*, 61–72. [CrossRef]
54. Roylance, D. *Mechanics of Materials*; Wiley: Hoboken, NJ, USA, 1996.
55. Kvien, I.; Sugiyama, J.; Votrubec, M.; Oksman, K. Characterization of starch based nanocomposites. *J. Mater. Sci.* **2007**, *42*, 8163–8171. [CrossRef]
56. Carvalho, A.J.F.; Curvelo, A.A.S.; Agnelli, J.A.M. Wood pulp reinforced thermoplastic starch composites. *Int. J. Polym. Mater. Polym. Biomater.* **2002**, *51*, 647–660. [CrossRef]
57. Dufresne, A.; Vignon, M.R. Improvement of starch film performances using cellulose microfibrils. *Macromolecules* **1998**, *31*, 2693–2696. [CrossRef]

polymers

MDPI

Article

Compressive Alginate Sponge Derived from Seaweed Biomass Resources for Methylene Blue Removal from Wastewater

Xiaojun Shen [1,2], Panli Huang [1], Fengfeng Li [1], Xiluan Wang [1,*], Tongqi Yuan [1,*] and Runcang Sun [1,3]

[1] Beijing Key Laboratory of Lignocellulosic Chemistry, Beijing Forestry University, Beijing 100083, China; shenxiaojun@iccas.ac.cn (X.S.); huangpanli@bjfu.edu.cn (P.H.); qhxylifeng@163.com (F.L.); rcsun3@bjfu.edu.cn (R.S.)

[2] Beijing National Laboratory for Molecular Sciences, Key Laboratory of Colloid and Interface and Thermodynamics, Institute of Chemistry, Chinese Academy of Sciences, Beijing 100190, China

[3] Center for Lignocellulose Science and Engineering, and Liaoning Key Laboratory Pulp and Paper Engineering, Dalian Polytechnic University, Dalian 116034, China

* Correspondence: wangxiluan@bjfu.edu.cn (X.W.); ytq581234@bjfu.edu.cn (T.Y.); Tel.: +86-10-6233-6903 (X.W. & T.Y.)

Received: 12 April 2019; Accepted: 20 May 2019; Published: 2 June 2019

Abstract: Low cost fabrication of water treatment polymer materials directly from biomass resources is urgently needed in recent days. Herein, a compressive alginate sponge (AS) is prepared from seaweed biomass resources through a green two-step lyophilization method. This material is much different from conventional oven-, air-, vacuum-dried alginate-based adsorbents, which show limitations of shrinkage, rigidness, tight nonporous structure and restricted ions diffusion, hindering its practical applications, and was used to efficiently remove methylene blue (MB), a main colorful contaminant in dye manufacturing, from wastewater. The batch adsorption studies are carried out to determine the impact of pH, contact time and concentration of dye on the adsorption process. The maximum adsorption capacity can be obtained at 1279 mg g^{-1}, and the shape-moldable AS can be facilely utilized as a fixed-bed absorption column, providing an efficient approach for continuous removal of MB within a short time. It is also important that such a compressive AS can be regenerated by a simple squeezing method while retaining about 70% capacity for more than ten cycles, which is convenient to be reused in practical water treatment. Compressive AS demonstrates its merits of high capability, large efficiency and easy to recycle as well as low cost resources, indicating widespread potentials for application in dye contaminant control regarding environmental protection.

Keywords: alginate sponge; two-step lyophilization; methylene blue; adsorption capacity; biomass resources

1. Introduction

Recently, industrial developments led to the undesirable environmental problems in the world, especially water pollution [1–3]. Many industries like the textile industry produce much wastewater, which contains a number of contaminants, including acidic or caustic dissolved solids, toxic compounds, and any different dyes, many of these dyes are carcinogenic, mutagenic, and teratogenic and also toxic to human beings, fish species, and microorganisms [1,4–8]. Among these contaminants, dyes are common contaminants in water discharged from various industries, such as plastics, textiles, printing, paper and leather industry. Due to its complex aromatic molecular structures, dyes in contaminated water are stable and resistant to biodegradation, which has become a serious environmental problem [9–11]. Therefore, the development of industrially applicable and efficient treatments for dye

containing effluents is urgently needed [12–14]. Technologies such as coagulation/flocculation [15], biological treatment [16], oxidation or ozonation [17], membrane separation [18], electrochemical methodology [19] and adsorption [20] have been extensively applied to remove dye pollutants from wastewater. Among them, adsorption method is quite popular due to its convenience, ease of operation, low energy consumption and availability of various adsorbents [21–24]. Currently, a number of adsorbent materials, such as activated carbon [25], mesoporous silica [26], hybrid xerogel [27], nanoporous alumina [28], zeolites [29] and carbon-based nanomaterials [13], have demonstrated their capability as an effective adsorbent for dye contaminants. However, their widespread use in water treatment is sometimes restricted due to its high cost and complexity of material preparation.

Recently, the three-dimensional (3D) porous structures ensure a large surface area for efficient dye adsorption, and exhibits the desirable merits of biocompatibility, biodegradability and economic efficiency [30]. Hence, much attention has been paid to developing sponge and porous materials as absorbers and they can achieve oil−water separation via a simple, fast, and effective absorption process [31–35]. Generally, an ideal absorbent material should have high oil absorption capacity, high selectivity, low density, and excellent recyclability, and it should be environmentally friendly. A large variety of low-cost adsorbents including natural species (plant fiber [36], silk cotton [37], leaves [38], etc.), industrial/agricultural wastes or by-product (citrus waste peels [39], bagasse [40], rice husk [41], etc.) and extractive biopolymers (chitosan [42], guar gum [43], alginate [44–47], etc.) have been explored as they are inexpensive, non-toxic and environmentally friendly. In the past few years, numerous efforts have been focused on the development of more effective and cheaper adsorbents derived from natural biomass resources rather than commercial adsorbents. Alginate, isolated from natural brown seaweeds, is a linear, unbranched and anionic polysaccharide biopolymer composed of β-D-mannuronic acid (M) and α-L-guluronic acid (G) units in the form of homopolymeric (MM- or GG-blocks) and heteropolymeric sequences (MG or GM-blocks) [48–50]. Alginate can be facilely converted into a porous sponge monolith forming the so-called "egg-box" conjunct structure [51]. In addition, the presence of negative carboxylate functional groups along polymer chains provides sufficient active sites, which guarantees its high affinity and binding ability for dye species [52,53]. Previous studies have demonstrated that conventional oven-, air-, vacuum-dried alginate-based adsorbents show limitations of shrinkage, rigidness, tight nonporous structure and restricted ions diffusion, hindering its practical applications [54].

In the paper, our aim is the fabrication of sponge-like adsorbing polymers directly from biomass resources, which is consistent with the object of low cost and renewable material design. Herein, we describe a green two-step lyophilization strategy to prepare a compressive alginate sponge (AS) derived from natural seaweed biomass resources with a large surface area, high porosity and controllable morphology. This method has advantages of low cost, simple and eco-friendly approach that does not include toxic or expensive resources, complicated or multistep chemical reactions. In this work, the as-prepared sponge was used to efficiently remove methylene blue (MB), a main colorful contaminant in dye manufacturing, from aqueous solution through the batch and continuous fixed-bed column adsorption. Their kinetics, thermodynamic analysis and adsorption mechanism are investigated. More importantly, the regeneration of the compressive sponge just by squeezing demonstrates its large potential to be used in practical applications for water treatment.

2. Materials and Methods

2.1. Materials

Waste brown seaweeds were collected from Shandong province, China. It was exhaustively washed with tap water, air-dried, and cut into pieces before use. Sodium carbonate (≥99.8%), calcium chloride (≥96.0%), hydrochloric acid (36.0~38.0%), sodium hydroxide (≥96.0%), methylene blue (≥90%) were purchased from Sinoparm Chemical Reagent Beijing Co., Ltd (Beijing, China).

2.2. Extraction of Seaweed

Sodium alginate was extracted from seaweed resources according to our previous work in our lab [43]. Firstly, the pigments of seaweed samples (5 g) on the surface were fixed by soaking in 1 wt % formaldehyde solution (300 mL). Then, the seaweeds were treated with 4 wt % Na_2CO_3 (300 mL) at 46 °C for 3 h. After that, the mixture was filtered, neutralized and precipitated by dropping the 10 wt % $CaCl_2$ to obtain the calcium alginate. The crude calcium alginate was washed thoroughly with distilled water and then acidified with 5 wt % HCl for 1 h. After that, gel materials of alginic acid were gained by filtering and washed several times with distilled water. The alginic acid was then dispersed in distilled water and converted into sodium alginate by neutralization (pH 6–7) with 1 wt % NaOH. Finally, the sodium alginate was precipitated and purified by ethanol, and collected for further use after freeze-drying. Its weight-average molecular weight (Mw) and M/G (M is β-D-mannuronic acid and G is α-L-guluronic acid) value were 1.51×10^6 g mol^{-1} and 0.86, respectively.

2.3. Preparation of AS

The AS was prepared by a green two-step lyophilization method from seaweed biomass resources, which was presented in Scheme 1. 0.2 g sodium alginate powder extracted from seaweed biomass resources was dissolved in 9.8 g distilled water (2 wt %) under vigorous stirring until homogeneous dispersion was formed. Then, the alginate solution was carefully cast into Petri dish plates and freeze-dried at −50 °C for 48 h. After that, the lyophilized sodium alginate sample was rinsed with 5 wt % $CaCl_2$ aqueous solution under quiescent conditions. The ionic crosslinking process was maintained for 12 h allowing the Ca^{2+} ions to be fully crosslinked with sodium alginate. Hereafter, the crosslinked alginate sample was soaked with distilled water and washed for several times to remove the excessive salts. After that, the ionic crosslinked sample was freeze-dried at −50 °C for 48 h. The as-obtained AS could be cut and shaped into different geometrical shapes easily by scissors and cutters. For clearly understanding, the involved chemical equations of different steps in Scheme 1 were supported by Scheme S1.

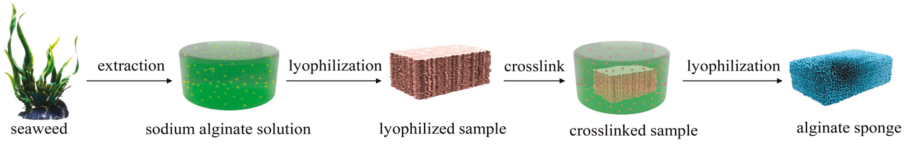

Scheme 1. The scheme of the two-step lyophilization method for the preparation of compressive alginate sponge (AS) from seaweed biomass resources.

2.4. Characterizations

The morphology of the AS was examined by the field-emission scanning electron microscope (SEM) (HitachiS-5500, Tokyo, Japan) operating at 10 kV acceleration voltage. All samples were coated with gold prior to acquiring the images. The pore size distributions were calculated by the Mercury Intrusion Porosimetry (Demo AutoPore IV 9500, Micromeritics, Atlanta, GA, USA). The Fourier transform infrared spectroscopy (FT-IR) spectra of the AS was collected by a Thermo Scientific Nicolet iN10 FT-IR Microscope (Thermo Nicolet Corporation, Waltham, MA, USA) equipped with an MCT detector cooled by liquid nitrogen in the reflection mode. The spectra were recorded in the range from 4000 to 670 cm^{-1} with 64 scans at a 4 cm^{-1} resolution. The crystalline structure measurement was performed on an XRD-7000 X-ray diffractometer (Shimadzu, Kyoto, Japan) with a Cu Kα radiation source (λ = 0.154 nm) at 40 kV and 30 mA. The X-ray photoelectron spectra (XPS) were determined on the photoelectron spectrometer (ESCALAB 250Xi, Thermo Fisher, Waltham, MA, USA) using an Al Kα (1486.6 eV) radiation. Mechanical properties were carried out on a UTM6503 universal tensile Machine (Shenzhen Suns Technology stock CO. LTD. Shenzhen, China) equipped with a 100 N load cell at the

rate of 10 mm min^{-1}. The thermal behaviour was studied by thermogravimetric analyses (TGA) using a DTG-60 simultaneous thermal analyzer (Shimadzu, Tokyo, Japan) under nitrogen atmosphere. 3–6 mg samples were loaded in an alumina crucible and heated from 40 °C to 900 °C at the rate of 10 °C min^{-1}.

2.5. Adsorption Measurement

The dye adsorption capability for AS was investigated at room temperature with methylene blue (MB). The MB solution was prepared by dissolving the MB powder in deionized water. Then, it was diluted with deionized water into a desired concentration varied between 50–1800 mg L^{-1}. Typical batch adsorption tests were accomplished by suspending 20 mg AS in 50 mL MB aqueous solution with different concentrations at an initial natural pH value in a flask. Afterwards, the flask was continuously shaken in a rotary shaker with 100 rpm for a period time to reach the adsorption equilibrium. In the study of the pH effect, the required pH value of the solution was adjusted with 0.1 mol L^{-1} HCl or NaOH aqueous solutions. After the adsorption equilibrium, the residual concentrations of the MB supernatants were evaluated by an UV-vis spectrometer at the absorbance of 664 nm. The amount of MB adsorbed by AS was calculated as following equation:

$$Q_e = \frac{(C_0 - C_e)V}{m} \quad (1)$$

where Q_e (mg g^{-1}) represents the adsorption capacity at equilibrium, C_0 (mg L^{-1}) and C_e (mg L^{-1}) are the MB concentrations at the initial and equilibrium, respectively. V is the volume of the solution (mL), and m is the mass of dry adsorbent (mg).

The continuous fixed-bed column adsorption experiments were conducted in a U-tube glass column with an inner diameter of 0.8 cm and volume capacity of 15 mL. The AS was cut with the desired column (diameter: 0.8 cm, height: 0.45 cm, weight: 7.8 mg) and then packed into the glass column tightly. Two layers of adsorbent cotton and bugles (diameter 400–800 μm) were embedded on the top and bottom of the packed column. 50 mL MB solution with an initial concentration of 1000 mg L^{-1} was pumped through the column in a down-flow mode using a peristaltic pump with the rate of 10 mL min^{-1} at room temperature.

3. Results and Discussions

3.1. Material Properties

The as-obtained sponge was elastic enough to be easily handled and cut into desired shapes, such as rods, cylinders, papers or cubes to satisfy various absorption requirements (Figure 1a). Moreover, the AS has an ideal density (34.6 mg cm^{-3}) compared with conventional compacted alginate-based materials [54], which could effortlessly stand on a grass leaf (Figure 1b). The strength and lightweight of AS were closely related to its three-dimensional (3D) porous framework with abundant pores as shown in Figure 1c,d. As a result, the interior sponge possessed a wide range of pore sizes from nanometers to hundreds of micrometers (mostly less than 100 μm) calculated by the mercury intrusion porosimetry method (Figure S1). The FT-IR analysis and XRD pattern revealed that the carboxyl groups penetrated in the AS network and the AS has none of the distinct crystalline formation (Figure 1e,f). Through the photoelectron lines of the wide-scan XPS spectrum (Figure S2), the presence of carbon (57.72% area), oxygen (39.03% area) and calcium (3.25% area) atoms in the AS were confirmed. Further investigation of atomic binding states on the surface of the AS was conducted by XPS analysis (Figure 1g,h).

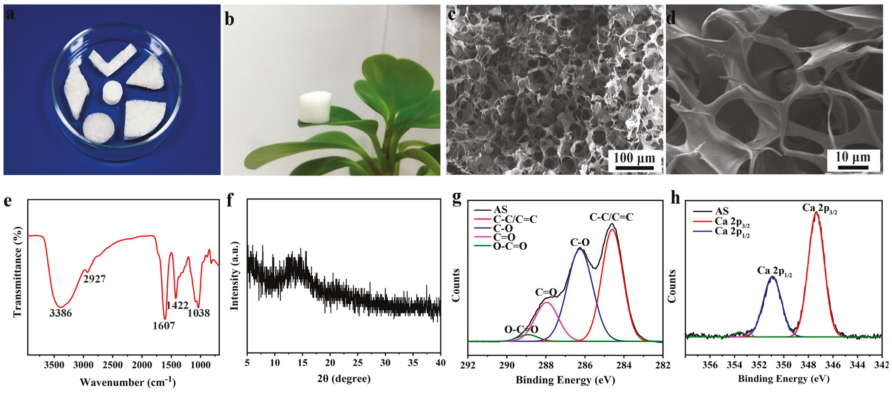

Figure 1. (**a**) Photographs of AS with desired shapes which is easy to be handled and cut by scissors; (**b**) a photograph of a column of AS free-standing on a grass leaf to support its weight; (**c**,**d**) SEM images of AS samples with different magnifications; (**e**) the FT-IR spectra and (**f**) the XRD pattern of AS; (**g**,**h**) high-resolution XPS of C 1s peaks and Ca 2p peaks for AS.

3.2. Absorption Properties

The 3D multiporosity and large active surfaces of AS make it an ideal candidate for the removal of methylene blue (MB) dye from wastewater. It should be noted that the initial pH value plays a significant role in the adsorption performances. It determines the adsorption reactions between MB and the adsorbent surface, attributing to the ionization in the solution and charge distribution on the adsorbent surface. In order to optimize the pH value to obtain the maximum adsorption capacity, batch adsorption experiments were conducted at pH values ranging from 2.0 to 10.0 with an initial MB concentration of 1000 mg L^{-1} for a contact time of 12 h. As shown in Figure 2a, the adsorption capacity was strongly related to the initial pH value. The lowest valve of Q_e (188 mg g^{-1}) was found at the pH value of 2.0. It can be speculated that surfaces of AS were highly protonated due to the high concentration of H^+. Thus, the $–COO^-$ active sites for adsorption of MB were occupied and those surface negative charges that were reduced, weaken the electrostatic attraction forcers between surfaces of AS and MB. Resultantly, the adsorption capacity is decreased with the decrease of pH from 4 to 2. However, when the pH value was higher than 4.0 (above the pKa value of MB), the surface charges of AS became more negative which was confirmed by Zeta potential data, promoting the electrostatic interaction between surface active sites and adsorbate, improving the adsorption capacity for MB. Additionally, the presence of excess of H^+ ions at low pH will compete with the MB cations for adsorption sites, resulting in a decrease of adsorption capacity, while more negatively charged surfaces of adsorbents become available with increased pH value [55,56]. This efficient adsorption behavior of the AS at pH = 4–10 demonstrates that it is potentially applicable in a relatively wide pH range. Nonetheless, considering the instability of calcium alginate in the strong alkaline condition, all the following experiments were conducted at pH = 4.

To evaluate the adsorption capacity of AS for MB, adsorption isotherms with different initial MB concentrations (5–1800 mg L^{-1}) were measured at room temperature of 25 °C with a contact time of 12 h. As shown in Figure 2b, it could be distinctly observed that the value of adsorption capacity increased with the increase of initial MB concentrations, until trended toward the equilibrium state. This can explain that the higher initial concentration generated a stronger driving force resulting from the concentration gradient, in favor of a mass transfer for MB from aqueous solution to adsorbent. With the initial concentration up to 1000 mg L^{-1}, the active adsorption sites of the adsorbent were almost occupied by MB molecules, thus the adsorption capacity attained at the maximum value and kept constant even at higher initial concentration of MB [57]. The equilibrium adsorption capacity could finally reach at 1279 mg g^{-1} with the initial MB concentration of 1800 mg L^{-1}. In addition, we also

calculated the removal ratio of the sponge at different initial concentrations of MB. A higher removal ratio about 90% was obtained at the relatively low initial concentration. Even at low concentrations of 5 and 10 mg L^{-1}, the AS also has high sensitivity for efficient MB removal, which is important for adsorbents used in the water treatment. A clear comparison of the removal effect could be presented by the images before and after batch adsorption (Figure S3). In additional, the AS before and after adsorbing methylene blue was characterized by the FT-IR spectra. As shown in Figure S4, the infrared characteristic peaks (1607 and 1422 cm^{-1}) of the C=O group shifted to low infrared absorption peak, which suggested that the internal porous structure of AS was favorable to the electrostatic interaction between the polymer carboxylic functional groups and cationic groups of the MB.

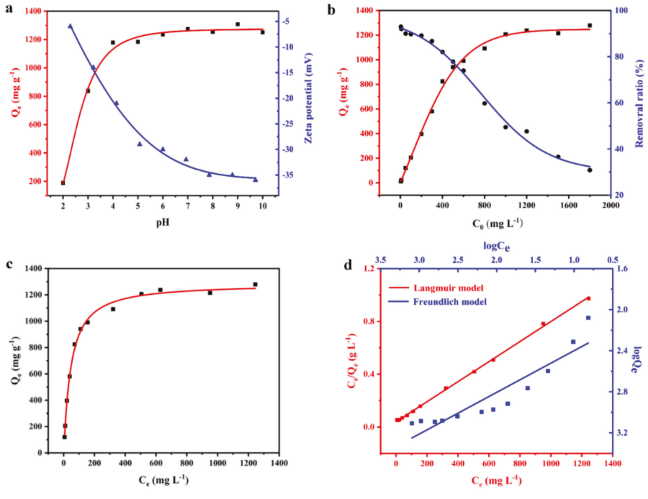

Figure 2. (**a**) The effect of the initial pH value on adsorption capacities of AS for methylene blue (MB) removal and the pH dependence of Zeta potential variation of MB adsorbed onto AS; (**b**) the removal ratio of AS for MB at different initial MB concentrations; (**c**) the adsorption isotherm of AS for MB removal; (**d**) the fitting adsorption data for the Langmuir and the Freundlich isotherm models.

The adsorption isotherm is essential for the adsorption to further explore its adsorption mechanism. In this study, the Langmuir and Freundlich isotherm models were used to fit the adsorption data, respectively, based on the adsorption isotherm of MB (Figure 2c). The Langmuir isotherm model assumes its monolayer adsorption over a homogeneous adsorbent surface with adsorption sites that are identical and energetically equivalent. Therefore, it can achieve at a saturate state without further adsorption activities. On the other hand, the Freundlich isotherm model is an empirical equation, which is employed to describe a multilayer adsorption onto heterogeneous surfaces with undefined sites. The two isotherm models can be described by two equations as follows:

$$\frac{C_e}{Q_e} = \frac{C_e}{Q_m} + \frac{1}{K_L Q_m} \tag{2}$$

$$logQ_e = logK_F + \frac{1}{n} logC_e \tag{3}$$

where C_e is the final equilibrium concentration (mg L^{-1}), Q_e is the adsorption capacity at equilibrium (mg g^{-1}), Q_m is the maximum adsorption capacity (mg g^{-1}), K_L is the Langmuir constant (L mg^{-1}), K_F is a constant related to the adsorption capacity (mg g^{-1}) (L mg^{-1}) $^{1/n}$ and n is an empirical parameter related to the adsorption intensity.

The linearized Langmuir and Freundlich adsorption isotherm plots were drawn as Figure 2d and their parameters were calculated from the adsorption isotherms listed in Table 1. The higher correlation coefficient (R^2 = 0.9991) of the Langmuir isotherm model indicated that it was better than the Freundlich isotherm model (R^2 = 0.8515) in simulating our experiment data. The fitting result presented that the adsorption behavior occurred on homogeneous surfaces of AS through a monolayer manner. Moreover, according to the Langmuir fitting result, the maximum adsorption capacity for MB of AS was 1310 mg g^{-1} in high concordance with the experimental equilibrium value (1279 mg g^{-1}), which is comparable with alginate based or other reported adsorbents for the MB adsorption listed in Table S1 and Table S2. Importantly, the synthesis of the AS adsorbent is quite green, economic and might be applied for large-scale production.

Table 1. Langmuir and Freundlich model fitting parameters for MB adsorption on AS.

Isotherm Model	Parameter	Value
Langmuir model	Q_m (mg g^{-1})	1317
	$K_L \times 10^{-2}$ (L mg^{-1})	1.90
	R^2	0.9991
Freundlich model	K_F (mg g^{-1}) (L $mg^{-1})^{1/n}$	98.5845
	n	2.4643
	R^2	0.8515

The adsorption kinetics was examined by measuring the adsorption capacity at initial MB concentrations of 500 and 1000 mg L^{-1}, respectively. The samples were collected at different time intervals up to 12 h. Figure 3a shows the effect of contact time on the adsorption capacity of AS for MB with different initial concentrations at an ambient temperature. It demonstrated that the adsorption capacity increased rapidly at the initial adsorption stage, then increased with the contact time at a relatively slow rate, and reached up to the equilibrium within 390 min. The adsorption capacity increased with higher initial concentrations, since the surface coverage was relatively low in the early stage, thus dye molecules could occupy the vacant adsorption sites rapidly. Once the adsorption process approached at the equilibrium, there would be less vacant active sites. Furthermore, the adsorbed MB molecules on the surface of AS could repel free MB molecules via the electrostatic repulsion.

To investigate the kinetic mechanism, the pseudo-second-order equation was used to describe the adsorption process. The time-dependent adsorption process was analysed using the pseudo-first-order and pseudo-second-order kinetic models (Figure 3b) according to the following equations:

$$\log(Q_{1e} - Q_t) = logQ_{1e} - \frac{k_1 t}{2.303} \quad (4)$$

$$\frac{t}{Q_t} = \frac{1}{k_2 Q_2{}^2} + \frac{t}{Q_{2e}} \quad (5)$$

where k_1 (min^{-1}) is the pseudo-first-order rate constant; k_2 [g (mg·min)$^{-1}$] is the pseudo-second-order kinetic rate constant; Q_e and Q_t are the amounts (mg g^{-1}) of adsorption at the equilibrium and at contact time referred as t (min). The pseudo-first-order assumes that the adsorption rate linear declines with the increase of the removal efficiency. The pseudo-second-order holds the opinion that the rate-controlling step of adsorption is the interaction between the adsorbent and adsorbate, such as ion sharing and transferring [19].

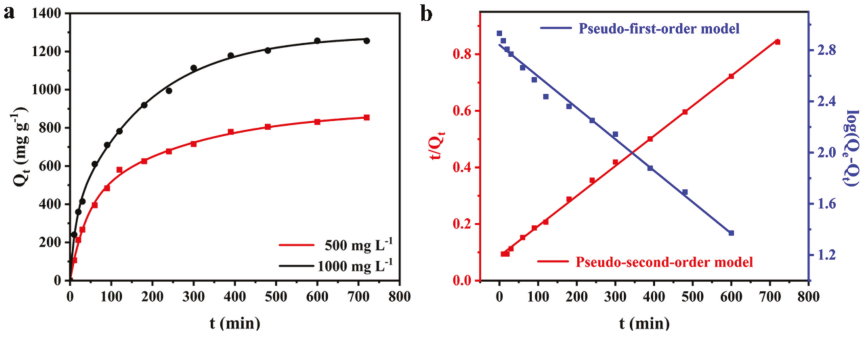

Figure 3. (**a**) The adsorption kinetic of AS for MB removal at initial MB concentrations of 500 and 1000 mg L^{-1}; (**b**) the fitting adsorption data for the pseudo-first-order and the pseudo-second-order kinetic models, C_0 = 500 mg L^{-1}.

The kinetic model parameters were obtained by the regression analysis of the experimental data (Table 2). It can be observed that the R^2 values for the pseudo-first order kinetic model was lower than that for the pseudo-second-order kinetic model. The pseudo-second-order kinetic model (R^2 = 0.9988) provided a better correlation in contrast to the pseudo-first-order kinetic model (R^2 = 0.9890) for MB adsorption. Additionally, the values of Q_{1e} (694 mg g^{-1}) failed to predicate the values of Q_{exp}, while the values of Q_{2e} (943 mg g^{-1}) is pretty close to Q_{exp} (845 mg g^{-1}), confirming that the kinetics of MB adsorption was identical when described by the pseudo-second-order kinetic model rather than the pseudo-first-order model. It means that the overall adsorption rate seems to be controlled by the chemical interaction through covalent forces during the process of exchanging electrons between adsorbent and adsorbate.

Table 2. Adsorption kinetics fitting results for MB on alginate sponge by pseudo-first-order and pseudo-second-order models.

Isotherm Model	Parameter	Value
Pseudo-First-Order Model	Q_e (mg g^{-1})	694
	$k_1 \times 10^{-2}$ (min^{-1})	0.567
	R^2	0.9890
Pseudo-Second-Order Model	Q_e (mg g^{-1})	943
	$k_2 \times 10^{-4}$ [g (mg·min)$^{-1}$]	0.130
	R^2	0.9988

Based on previous reported literature, the porous structure of AS favors the electrostatic interaction between the polymer carboxylic functional groups and cationic groups of the MB. A possible adsorption mechanism for MB adsorption was shown in Scheme 2. According to the "egg-box" model of gelation mechanism, the carboxyl functional groups of the α-L-guluronic acid in sodium alginate could form ionic bonds with divalent Ca^{2+} ions, leading to the transformation of the alginate solution into a stable sponge and forming abundant holes, which could trap MB molecules by the carboxyl functional groups in the network of AS. In addition, the hydroxyl groups of AS could also stabilize the MB–alginate complex.

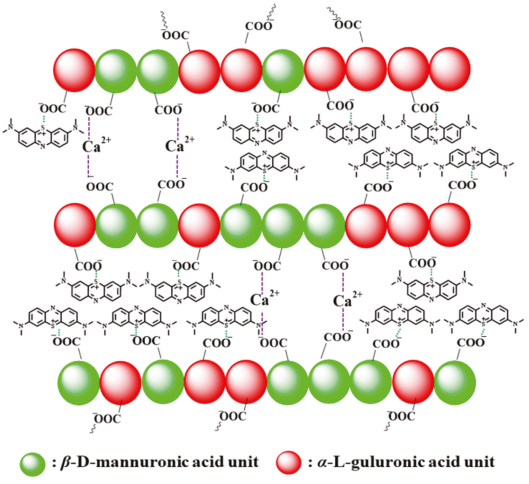

Scheme 2. The possible adsorption mechanism of AS for MB removal.

3.3. Compressive Properties and Recyclability

The performance of adsorbents in the continuous dyes adsorption process is an important factor in assessing the feasibility of adsorbents in real-time practical applications. Fortunately, the free-standing and elastic AS can be easily handled, superior to the other suspended adsorbents. The compressive properties of AS were examined by mechanical tests which were repeated within compress-release cycles. The AS sample exhibited excellent elastic resilience under compression, it could recover to its original morphology after removal of the external load (Figure 4a). The cyclic compression stress-strain (σ-ε) curves at a maximum strain of 30%, 50%, and 70% were shown in Figure 4b. In the first circle, the loading curve exhibited three distinct stages: (i) A linear-elastic regime during which the stress increases linearly at $\varepsilon < 20\%$, the sponge started to bend and the structure of the interior pore began to change; (ii) a plateau region at $20\% < \varepsilon < 60\%$, the sponge was compressed to a certain extent and the increase of stress was slow; (iii) a steep slope region at $\varepsilon > 60\%$ with rapidly rising stress because of the densification of the sponge, where the stress increases linearly again. Even under a maximum strain of 70%, AS can still recover its original elasticity after removal of the external load. Moreover, the maximum value of compression stress increased from 17.7 to 96.7 KPa with compression strain increased from 30% to 70%. Cyclic compression tests were also conducted as shown in Figure 4c. With the increase of the compression cycles, the hysteresis loop for the multicycle curve shrinks compared to the first circle, while after the 5th cycle almost coincided, indicating that the plastic deformation increased but gradually become stabilized. However, the maximum stress remains unchanged, suggesting that AS can retain its compressive strength for 10 cycles with the maximum strain of 50%. These phenomena can be explained by the mechanical elasticity of the pore walls constructed during the two-step lyophilization process.

Thus, we fabricated a mechanically strong and free-standing AS sample (height 1.2 cm, volume capacity 15 mL, internal diameter 0.8 cm) into a flexible column device for fast removing MB from water (Figure 5a). Different from the traditional shaking adsorption in the vessel, the fixed-bed column adsorption contains dynamic behaviors allowing continuous operation. The dynamic adsorption process under constant flow provided a more efficient pathway to utilize the internal multipores in the network of AS, thus improving the adsorption efficiency in quite a short time. The continuous adsorption experiments were undertaken with different contact times treating 50 mL MB aqueous solution. The initial concentration of MB was set as 1000 mg L^{-1}. The adsorption capacities along with the different contact time were presented in Figure 5b. It can be concluded that the adsorption

capacity increased with the increasing of the contact time, and reached up to a maximum capacity of 1100 mg g^{-1} within 50 min. Further prolonging the contact time could not enhance the adsorption capacity. This is mainly due to the fact that the interaction surface of AS can be utilized sufficiently in the first 50 min, and the further increase of the contact time cannot improve the efficient interaction surface area. The fixed-bed column adsorption demonstrates a large potential for practical application owing to their higher efficiency as compared with traditional shaking adsorption conditions (1279 mg g^{-1} in 720 min). The column-packed adsorbent could treat quantities of MB contained waste one time, which was considered to be an economic waste treatment.

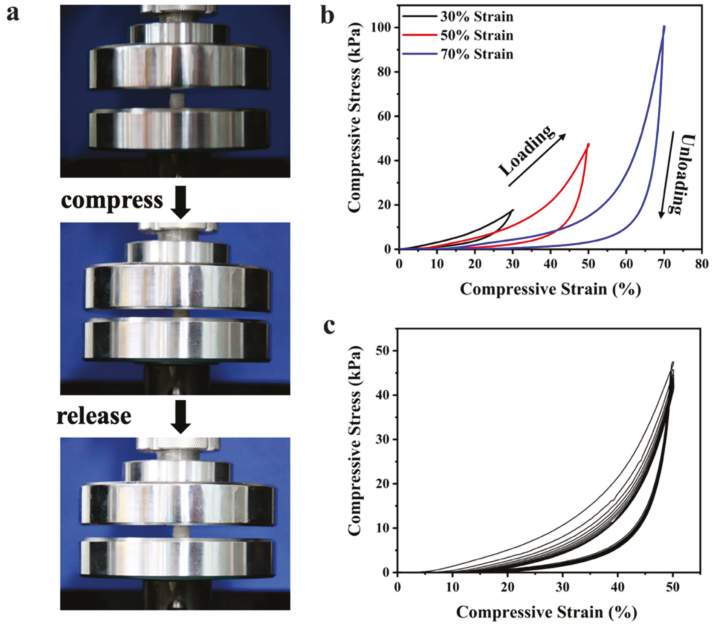

Figure 4. Mechanical compressive properties of AS. (**a**) A set of real-time images of a compressed sample showing the recovering process; (**b**) the cyclic compression stress-strain (σ-ε) curves at maximum strain of 30%, 50%, and 70%; (**c**) the cyclic compression stress-strain (σ-ε) curves for first 10 cycles at maximum strain of 50%.

The recyclability is also important in pollution control applications. A simple squeezing method was applied facilely to recycle the adsorbed AS and harvest the pollutants due to its compressive properties. The recyclability test was investigated through fixed-bed column adsorption. As shown in Figure 5c, the adsorption capacity for MB was maintained for about 70% after 10 cycles with 861 mg g^{-1}, exhibiting good recyclability upon the easy squeezing method. The main reason for the residual MB during the recycled use may be attributed to the stability of partial trapped MB molecules complexed within the network of AS chains. For further thoroughly removal of MB during the cyclic tests, chemical cleaning or heat treatment might be efficient.

Thermal stability is a key criterion to characterize the temperature limit for the environment of the absorbent during the procedure of adsorption. As shown in Figure S5, the first weight loss (about 10%) of AS in the temperature range from 40 to 190 °C was corresponded to the evaporation of free water and water-linked hydrogen bonds [52,53]. The second mass loss of almost 40% at 190–400 °C was mainly due to the thermal destroy of glycosidic bonds for alginate polar interactions with the carboxylate groups. The final step of mass loss (400–900 °C) might be attributed to the carbonate

formation under high temperature [54]. The final thermal degradation of alginate could be the result of forming $CaCO_3$.

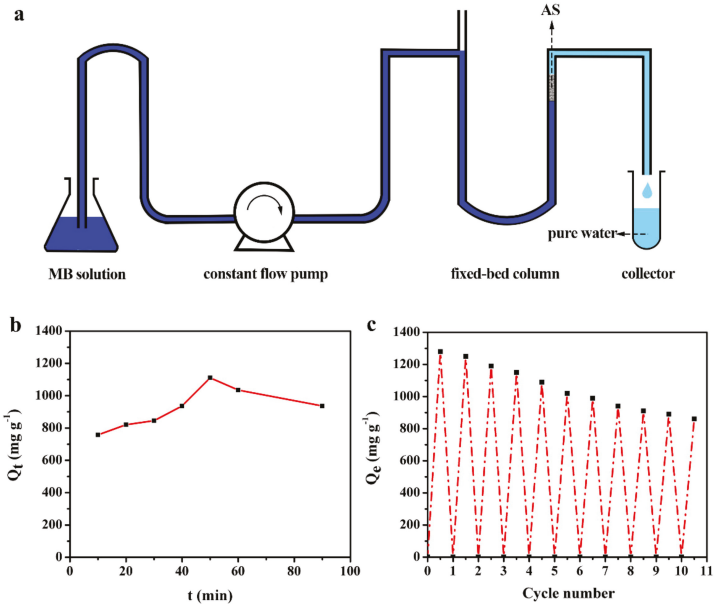

Figure 5. (**a**) The scheme of the adsorption process and equipment in the fixed-bed absorption column; (**b**) the adsorption capacities of AS with different contact time for MB removal; (**c**) the cyclic absorption capacities of AS for MB removal within 10 cycles through squeezing method.

4. Conclusions

A compressive AS was prepared from seaweed biomass resources via a green two-step lyophilization method, which was used to remove MB from wastewater for pollutant control. Due to the 3D multiporous structure, large specific surface area and sufficient active sites, the as-prepared AS exhibited high adsorption capacity (1279 mg g^{-1}) for MB removal, which is much different from the conventional oven-, air-, vacuum-dried alginate-based adsorbents, which show limitations of shrinkage, rigidness, tight nonporous structure and restricted ions diffusion, hindering its practical applications. Their kinetics, thermodynamic analysis and adsorption mechanism are investigated. Importantly, the freestanding and elastic AS was facilitated to assemble into a column-packed device for fixed-bed continuous wastewater treatment, indicative of excellent adsorption efficiency with 1100 mg g^{-1} just in 50 min. Furthermore, it can be regenerated for more than ten cycles by the simple squeezing method due to its unique compressive property. Considering the priority of low-cost, simple process and eco-friendship, the AS adsorbent derived from biomass resources show a bright future of low cost and renewable material resign of MB adsorbents, it suggests that the biomass resource could become a promising candidate for industrially applicable and efficient treatments of dye containing effluents.

Supplementary Materials: The following are available online at http://www.mdpi.com/2073-4360/11/6/961/s1, Scheme S1: The involved chemical equations of Scheme 1. Figure S1: The pore size distributions of AS calculated by the mercury intrusion porosimetry method. Figure S2: The XPS survey spectrum of the sample of AS. Figure S3: The images of MB solution before and after batch adsorption. Figure S4: FT-IR spectra of sodium alginate, AS and MB adsorbed onto AS. Figure S5: The TGA analysis result of the sample of AS. Table S1: The MB adsorption capacity of alginate-based adsorbents in literatures. Table S2: The MB adsorption capacity of other reported adsorbents in literatures.

Author Contributions: X.W. and T.Y. conceived and designed the experiments; X.S. and P.H. performed the experiments; X.S. and F.L. guided the experiments; T.Y., X.W. and R.S. analyzed the data; X.S. wrote the paper; X.W. proposed amendments and addenda to the first draft of the document. All these authors had contributed substantially to this work reported.

Funding: This research was funded by the National Natural Science Foundation of China [51603012] and the Fundamental Research Funds for the Central Universities [2018ZY07].

Conflicts of Interest: No conflict of interest exits in the submission of this manuscript, and the manuscript is approved by all authors for publication. The founding sponsors had no role in the design of the study; in the collection, analyses, or interpretation of data; in the writing of the manuscript, and in the decision to publish the results.

References

1. Adegoke, K.A.; Bello, O.S. Dye sequestration using agricultural wastes as adsorbents. *Water Resour. Ind.* **2015**, *12*, 8–24. [CrossRef]
2. Ahmed, S.M.; El-Dib, F.I.; El-Gendy, N.S.; Sayed, W.M.; El-Khodary, M. A kinetic study for the removal of anionic sulphonated dye from aqueous solution using nano-polyaniline and Baker's yeast. *Arab. J. Chem.* **2016**, *9*, S1721–S1728. [CrossRef]
3. Aljeboree, A.M.; Alshirifi, A.N.; Alkaim, A.F. Kinetics and equilibrium study for the adsorption of textile dyes on coconut shell activated carbon. *Arab. J. Chem.* **2017**, *10*, S3381–S3393. [CrossRef]
4. Aboelmagd, A.; El-Safty, S.A.; Shenashen, M.A.; Elshehy, E.A.; Khairy, M.; Sakaic, M.; Yamaguchi, H. Nanomembrane canister architectures for the visualization and filtration of oxyanion toxins with one-step processing. *Chem. Asian J.* **2015**, *10*, 2467–2478. [CrossRef] [PubMed]
5. Shenashen, M.A.; El-Safty, S.A.; Elshehy, E.A. Monolithic scaffolds for highly selective ion sensing/removal of Co(II), Cu(II), and Cd(II) ions in water. *Analyst* **2014**, *139*, 6393–6405. [CrossRef] [PubMed]
6. Gomaa, H.; Shenashen, M.A.; Yamaguchi, H.; Alamoudi, A.S.; El-Safty, S.A. Extraction and recovery of Co^{2+} ions from spent lithium-ion batteries using hierarchical mesosponge γ-Al_2O_3 monolith extractors. *Green Chem.* **2018**, *20*, 1841–1857. [CrossRef]
7. El-Sewify, I.M.; Shenashen, M.A.; Shahat, A.; Yamaguchi, H.; Selim, M.M.; Khalil, M.M.H.; El-Safty, S.A. Ratiometric fluorescent chemosensor for Zn^{2+} ions in environmental samples using supermicroporous organic-inorganic structures as potential platforms. *Chem. Sel.* **2017**, *2*, 11083–11090. [CrossRef]
8. Derbalah, A.; El-Safty, S.A.; Shenashen, M.A.; Abdel Ghany, N.A. Mesoporous alumina nanoparticles as host tunnel-like pores for removal and recovery of insecticides from environmental samples. *ChemPlusChem* **2015**, *80*, 1119–1126. [CrossRef]
9. El Qada, E.N.; Allen, S.J.; Walker, G.M. Adsorption of basic dyes from aqueous solution onto activated carbons. *Chem. Eng. J.* **2008**, *135*, 174–184. [CrossRef]
10. Han, R.; Ding, D.; Xu, Y.; Zou, W.; Wang, Y.; Li, Y.; Zou, L. Use of rice husk for the adsorption of congo red from aqueous solution in column mode. *Bioresour. Technol.* **2008**, *99*, 2938–2946. [CrossRef]
11. Pearce, C.I.; Lloyd, J.R.; Guthrie, J.T. The removal of colour from textile wastewater using whole bacterial cells: A review. *Dyes Pigments* **2003**, *58*, 179–196. [CrossRef]
12. Gómez, J.M.; Galán, J.; Rodríguez, A.; Walker, G.M. Dye adsorption onto mesoporous materials: PH influence, kinetics and equilibrium in buffered and saline media. *J. Environ. Manag.* **2014**, *146*, 355–361. [CrossRef] [PubMed]
13. Wan, X.; Zhan, Y.; Long, Z.; Zeng, G.; He, Y. Core@double-shell structured magnetic halloysite nanotube nano-hybrid as efficient recyclable adsorbent for methylene blue removal. *Chem. Eng. J.* **2017**, *330*, 491–504. [CrossRef]
14. He, X.; Male, K.B.; Nesterenko, P.N.; Brabazon, D.; Paull, B.; Luong, J.H.T. Adsorption and desorption of methylene blue on porous carbon monoliths and nanocrystalline cellulose. *ACS Appl. Mater. Interfaces* **2013**, *5*, 8796–8804. [CrossRef]
15. Lau, Y.-Y.; Wong, Y.-S.; Teng, T.-T.; Morad, N.; Rafatullah, M.; Ong, S.-A. Coagulation-flocculation of azo dye Acid Orange 7 with green refined laterite soil. *Chem. Eng. J.* **2014**, *246*, 383–390. [CrossRef]
16. Kokabian, B.; Bonakdarpour, B.; Fazel, S. The effect of salt on the performance and characteristics of a combined anaerobic–aerobic biological process for the treatment of synthetic wastewaters containing Reactive Black 5. *Chem. Eng. J.* **2013**, *221*, 363–372. [CrossRef]

17. Sakkas, V.A.; Islam, M.A.; Stalikas, C.; Albanis, T.A. Photocatalytic degradation using design of experiments: A review and example of the Congo red degradation. *J. Hazard. Mater.* **2010**, *175*, 33–44. [CrossRef]
18. Qiu, W.-Z.; Yang, H.-C.; Wan, L.-S.; Xu, Z.-K. Co-deposition of catechol/polyethyleneimine on porous membranes for efficient decolorization of dye water. *J. Mater. Chem. A* **2015**, *3*, 14438–14444. [CrossRef]
19. Martínez-Huitle, C.A.; Brillas, E. Decontamination of wastewaters containing synthetic organic dyes by electrochemical methods: A general review. *Appl. Catal. B* **2009**, *87*, 105–145. [CrossRef]
20. Fernandez, M.E.; Nunell, G.V.; Bonelli, P.R.; Cukierman, A.L. Activated carbon developed from orange peels: Batch and dynamic competitive adsorption of basic dyes. *Ind. Crops Prod.* **2014**, *62*, 437–445. [CrossRef]
21. Sun, L.; Chen, D.; Wan, S.; Yu, Z. Performance, kinetics, and equilibrium of methylene blue adsorption on biochar derived from eucalyptus saw dust modified with citric, tartaric, and acetic acids. *Bioresour. Technol.* **2015**, *198*, 300–308. [CrossRef] [PubMed]
22. Li, G.; Zhu, W.; Zhang, C.; Zhang, S.; Liu, L.; Zhu, L.; Zhao, W. Effect of a magnetic field on the adsorptive removal of methylene blue onto wheat straw biochar. *Bioresour. Technol.* **2016**, *206*, 16–22. [CrossRef] [PubMed]
23. Chen, C.; Li, F.; Zhang, Y.; Wang, B.; Fan, Y.; Wang, X.; Sun, R. Compressive, ultralight and fire-resistant lignin-modified graphene aerogels as recyclable absorbents for oil and organic solvents. *Chem. Eng. J.* **2018**, *350*, 173–180. [CrossRef]
24. Li, F.; Wang, X.; Yuan, T.; Sun, R. A lignosulfonate-modified graphene hydrogel with ultrahigh adsorption capacity for Pb(II) removal. *J. Mater. Chem. A* **2016**, *4*, 11888–11896. [CrossRef]
25. Albadarin, A.B.; Collins, M.N.; Naushad, M.; Shirazian, S.; Walker, G.; Mangwandi, C. Activated lignin-chitosan extruded blends for efficient adsorption of methylene blue. *Chem. Eng. J.* **2017**, *307*, 264–272. [CrossRef]
26. Fan, J.; Li, D.; Teng, W.; Yang, J.; Liu, Y.; Liu, L.; Elzatahry, A.A.; Alghamdi, A.; Deng, Y.; Li, G.; et al. Ordered mesoporous silica/polyvinylidene fluoride composite membranes for effective removal of water contaminants. *J. Mater. Chem. A* **2016**, *4*, 3850–3857. [CrossRef]
27. Ge, H.; Wang, C.; Liu, S.; Huang, Z. Synthesis of citric acid functionalized magnetic graphene oxide coated corn straw for methylene blue adsorption. *Bioresour. Technol.* **2016**, *221*, 419–429. [CrossRef] [PubMed]
28. Shu, Z.; Chen, Y.; Zhou, J.; Li, T.; Yu, D.; Wang, Y. Nanoporous-walled silica and alumina nanotubes derived from halloysite: Controllable preparation and their dye adsorption applications. *Appl. Clay Sci.* **2015**, *112–113*, 17–24. [CrossRef]
29. Han, R.; Zhang, J.; Han, P.; Wang, Y.; Zhao, Z.; Tang, M. Study of equilibrium, kinetic and thermodynamic parameters about methylene blue adsorption onto natural zeolite. *Chem. Eng. J.* **2009**, *145*, 496–504. [CrossRef]
30. Wang, L.; Cheng, C.; Tapas, S.; Lei, J.; Matsuoka, M.; Zhang, J.; Zhang, F. Carbon dots modified mesoporous organosilica as an adsorbent for the removal of 2,4-dichlorophenol and heavy metal ions. *J. Mater. Chem. A* **2015**, *3*, 13357–13364. [CrossRef]
31. Zhang, X.; Li, Z.; Liu, K.; Jiang, L. Bioinspired multifunctional foam with self-cleaning and oil/water separation. *Adv. Funct. Mater.* **2013**, *23*, 2881–2886. [CrossRef]
32. Bi, H.; Yin, Z.; Cao, X.; Xie, X.; Tan, C.; Huang, X.; Chen, B.; Chen, F.; Yang, Q.; Bu, X.; et al. Carbon fiber aerogel made from raw cotton: a novel, efficient and recyclable sorbent for oils and organic solvents. *Adv. Mater.* **2013**, *25*, 5916–5921. [CrossRef] [PubMed]
33. Gui, X.; Zeng, Z.; Lin, Z.; Gan, Q.; Xiang, R.; Zhu, Y.; Cao, A.; Tang, Z. Magnetic and highly recyclable macroporous carbon nanotubes for spilled oil sorption and separation. *ACS Appl. Mater. Interfaces* **2013**, *5*, 5845–5850. [CrossRef] [PubMed]
34. Gui, X.; Wei, J.; Wang, K.; Cao, A.; Zhu, H.; Jia, Y.; Shu, Q.; Wu, D. Carbon nanotube sponges. *Adv. Mater.* **2010**, *22*, 617–621. [CrossRef] [PubMed]
35. Radetic, M.; Ilic, V.; Radojevic, D.; Miladinovic, R.; Jocic, D.; Jovancic, P. Efficiency of recycled wool-based nonwoven material for the removal of oils from water. *Chemosphere* **2008**, *70*, 525–530. [CrossRef]
36. Sajab, M.S.; Chia, C.H.; Zakaria, S.; Jani, S.M.; Ayob, M.K.; Chee, K.L.; Khiew, P.S.; Chiu, W.S. Citric acid modified kenaf core fibres for removal of methylene blue from aqueous solution. *Bioresour. Technol.* **2011**, *102*, 7237–7243. [CrossRef] [PubMed]
37. Deng, H.; Lu, J.; Li, G.; Zhang, G.; Wang, X. Adsorption of methylene blue on adsorbent materials produced from cotton stalk. *Chem. Eng. J.* **2011**, *172*, 326–334. [CrossRef]

38. Dural, M.U.; Cavas, L.; Papageorgiou, S.K.; Katsaros, F.K. Methylene blue adsorption on activated carbon prepared from *Posidonia oceanica* (L.) dead leaves: Kinetics and equilibrium studies. *Chem. Eng. J.* **2011**, *168*, 77–85. [CrossRef]
39. Bhatnagar, A.; Sillanpää, M.; Witek-Krowiak, A. Agricultural waste peels as versatile biomass for water purification—A review. *Chem. Eng. J.* **2015**, *270*, 244–271. [CrossRef]
40. Yu, J.-X.; Chi, R.-A.; Guo, J.; Zhang, Y.-F.; Xu, Z.-G.; Xiao, C.-Q. Desorption and photodegradation of methylene blue from modified sugarcane bagasse surface by acid TiO_2 hydrosol. *Appl. Surf. Sci.* **2012**, *258*, 4085–4090. [CrossRef]
41. Adam, F.; Appaturi, J.N.; Khanam, Z.; Thankappan, R.; Nawi, M.A.M. Utilization of tin and titanium incorporated rice husk silica nanocomposite as photocatalyst and adsorbent for the removal of methylene blue in aqueous medium. *Appl. Surf. Sci.* **2013**, *264*, 718–726. [CrossRef]
42. Auta, M.; Hameed, B.H. Chitosan–clay composite as highly effective and low-cost adsorbent for batch and fixed-bed adsorption of methylene blue. *Chem. Eng. J.* **2014**, *237*, 352–361. [CrossRef]
43. Yan, L.; Chang, P.R.; Zheng, P.; Ma, X. Characterization of magnetic guar gum-grafted carbon nanotubes and the adsorption of the dyes. *Carbohydr. Polym.* **2012**, *87*, 1919–1924. [CrossRef]
44. Hassan, A.F.; Abdel-Mohsen, A.M.; Fouda, M.M.G. Comparative study of calcium alginate, activated carbon, and their composite beads on methylene blue adsorption. *Carbohydr. Polym.* **2014**, *102*, 192–198. [CrossRef]
45. Wang, Y.; Wang, W.; Wang, A. Efficient adsorption of methylene blue on an alginate-based nanocomposite hydrogel enhanced by organo-illite/smectite clay. *Chem. Eng. J.* **2013**, *228*, 132–139. [CrossRef]
46. Ma, T.; Chang, P.R.; Zheng, P.; Zhao, F.; Ma, X. Fabrication of ultra-light graphene-based gels and their adsorption of methylene blue. *Chem. Eng. J.* **2014**, *240*, 595–600. [CrossRef]
47. Liu, L.; Wan, Y.; Xie, Y.; Zhai, R.; Zhang, B.; Liu, J. The removal of dye from aqueous solution using alginate-halloysite nanotube beads. *Chem. Eng. J.* **2012**, *187*, 210–216. [CrossRef]
48. Draget, K.I.; Taylor, C. Chemical, physical and biological properties of alginates and their biomedical implications. *Food Hydrocoll.* **2011**, *25*, 251–256. [CrossRef]
49. Fuks, L.; Filipiuk, D.; Majdan, M. Transition metal complexes with alginate biosorbent. *J. Mol. Struct.* **2006**, *792–793*, 104–109. [CrossRef]
50. Robitzer, M.; David, L.; Rochas, C.; Di Renzo, F.; Quignard, F. Nanostructure of calcium alginate aerogels obtained from multistep solvent exchange route. *Langmuir* **2008**, *24*, 12547–12552. [CrossRef]
51. Grant, G.T.; Morris, E.R.; Rees, D.A.; Smith, P.J.C.; Thom, D. Biological interactions between polysaccharides and divalent cations: The egg-box model. *FEBS Lett.* **1973**, *32*, 195–198. [CrossRef]
52. Obeid, L.; El Kolli, N.; Dali, N.; Talbot, D.; Abramson, S.; Welschbillig, M.; Cabuil, V.; Bée, A. Adsorption of a cationic surfactant by a magsorbent based on magnetic alginate beads. *J. Colloid Interfaces Sci.* **2014**, *432*, 182–189. [CrossRef] [PubMed]
53. Peretz, S.; Cinteza, O. Removal of some nitrophenol contaminants using alginate gel beads. *Colloids Surf. A* **2008**, *319*, 165–172. [CrossRef]
54. Deze, E.G.; Papageorgiou, S.K.; Favvas, E.P.; Katsaros, F.K. Porous alginate aerogel beads for effective and rapid heavy metal sorption from aqueous solutions: Effect of porosity in Cu^{2+} and Cd^{2+} ion sorption. *Chem. Eng. J.* **2012**, *209*, 537–546. [CrossRef]
55. Shi, H.; Li, W.; Zhong, L.; Xu, C. Methylene blue adsorption from aqueous solution by magnetic cellulose/graphene oxide composite: Equilibrium, kinetics, and thermodynamics. *Ind. Eng. Chem. Res.* **2014**, *53*, 1108–1118. [CrossRef]
56. Liu, G.; Hu, Z.; Guan, R.; Zhao, Y.; Zhang, H.; Zhang, B. Efficient removal of methylene blue in aqueous solution by freeze-dried calcium alginate beads. *Korean J. Chem. Eng.* **2016**, *33*, 3141–3148. [CrossRef]
57. Gupta, V.K.; Nayak, A.; Agarwal, S. Bioadsorbents for remediation of heavy metals: Current status and their future prospects. *Environ. Eng. Res.* **2015**, *20*, 1–18. [CrossRef]

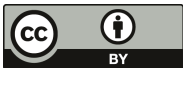

polymers

MDPI

Article

Deterioration in the Physico-Mechanical and Thermal Properties of Biopolymers Due to Reprocessing

Jamileh Shojaeiarani [1,*], Dilpreet S. Bajwa [1], Chad Rehovsky [1], Sreekala G. Bajwa [2] and Ghazal Vahidi [1]

[1] Department of Mechanical Engineering, North Dakota State University, Fargo, ND 58108, USA; dilpreet.bajwa@ndsu.edu (D.S.B.); Chad.rehovsky@ndsu.edu (C.R.); ghazal.vahidi@ndsu.edu (G.V.)

[2] Department of Agriculture and Biosystem Engineering, North Dakota State University, Fargo, ND 58108, USA; sreekala.bajwa@ndsu.edu

* Correspondence: jamileh.shojaeiarani@ndsu.edu; Tel.: +1-701-799-7759

Received: 30 November 2018; Accepted: 18 December 2018; Published: 2 January 2019

Abstract: Biopolymers are an emerging class of materials being widely pursued due to their ability to degrade in short periods of time. Understanding and evaluating the recyclability of biopolymers is paramount for their sustainable and efficient use in a cost-effective manner. Recycling has proven to be an important solution, to control environmental and waste management issues. This paper presents the first recycling assessment of Solanyl, Bioflex, polylactic acid (PLA) and PHBV using a melt extrusion process. All biopolymers were subjected to five reprocessing cycles. The thermal and mechanical properties of the biopolymers were investigated by GPC, TGA, DSC, mechanical test, and DMA. The molecular weights of Bioflex and Solanyl showed no susceptible effect of the recycling process, however, a significant reduction was observed in the molecular weight of PLA and PHBV. The inherent thermo-mechanical degradation in PHBV and PLA resulted in 20% and 7% reduction in storage modulus, respectively while minimal reduction was observed in the storage modulus of Bioflex and Solanyl. As expected from the Florry-Fox equation, recycled PLA with a high reduction in molecular weight (78%) experienced 9% reduction in glass transition temperature. Bioflex and Solanyl showed 5% and 2% reduction in molecular weight and experienced only 2% reduction in glass transition temperature. These findings highlight the recyclability potential of Bioflex and Solanyl over PLA and PHBV.

Keywords: recycling; thermal degradation; mechanical degradation; polylactic acid; Bioflex; Solanyl; PHBV

1. Introduction

There is a huge interest in the development of bio-based materials to lessen the dependency on petroleum-based polymers owing to the growth in environmental concerns, fluctuating crude oil price, and the depletion of fossil fuels [1]. Biopolymers derived from renewable resources have a wide range of applications in different industries due to their specific characteristics. The packaging industry represents the largest demand for plastic and nearly 70% of the biopolymer global market is attributed to the packaging industry [2]. The short-term or single-use application of packaging materials is of great concern as it leads to the pollution of water. The recycling process is one of the most important alternatives to control environmental and waste management issues.

The recycling process is a waste management treatment available to lessen the environmental impact related to the disposal of plastics. Recycling not only extends the life of polymeric materials but helps the biopolymer market financially by providing circular materials of thermoplastics [3]. The recycling process involves mechanical and thermal processing [4]. In the mechanical recycling process, grinding, sorting, and drying are utilized to resize the used polymeric materials. In the thermal

processing step of recycling, the used materials are subjected to high temperature. In general, the most common recycling process is melt extrusion and injection molding to reshape the used material into a new product through the application of high pressure and shear force [5].

Despite the positive aspects of the recycling process, some recycling methods result in a significant deterioration in the material properties. Loss of mechanical and thermal properties, as well as discolorations, are some common degradation issues in biopolymers as a result of the recycling process [6]. The recycled polymers should possess a set of minimum performance characters to meet the specific requirements after the recycling process. Therefore, comprehensive knowledge on the impact of successive reprocessing conditions on the physical, mechanical, and thermal properties of polymers is of paramount interest.

This paper discusses the degradation behavior of four bio-based and bio-degradable thermoplastic polymers of major commercial importance including of poly(lactic acid) (PLA), Bioflex (PLA and co-polyester blend), Solanyl (starch-based polymer), and poly (3-hydroxybutyrate-*co*-3-hydroxyvalerate) (PHBV). Among all thermoplastic biopolymers capable of recycling, PLA is one of the most commercially available biodegradable polymers owing to its superior mechanical properties and high heat resistance [7]. Bioflex is a blend of PLA and thermoplastic copolyester (TPC). Bioflex is a biodegradable and easy processing polymer with potential applications in the food packaging and medical devices [8]. In spite of the competitive mechanical properties, to the best of our knowledge, only a small number of studies have focused on the characterization of Bioflex. Solanyl, a starch-based bio-polymer, is made out of potato starch reclaimed from potato processing [9]. Solanyl consists of oxygen-based polymers with different processing and products features. There is a low energy input to produce products from Solanyl as compared to petroleum-based polymers. PHBV with an inherent biodegradability characteristic is made by bacterial and archaea fermentation. PHBV as a member of the broad PHA (polyhydroxyalkanoates) family [1] exhibits similar mechanical properties to polyolefins. It has gained a lot of attention as an environmentally friendly substitute for petroleum-based polymers [10].

The goal of this work is focused on understanding the impact of processing on the properties of bio-based and biodegradable polymers. It is hypothesized that biopolymers exhibit different degradation mechanisms, as some of these polymers can be recycled without significant loss of various properties. Therefore, a comprehensive study was conducted on the influence of recycling processes on molecular weight, mechanical properties, flow characteristics, thermal properties and thermomechanical properties of PLA, Bioflex, Solanyl, and PHBV polymers after five reprocessing cycles.

2. Materials and Methods

2.1. Materials

A list of the polymers used in this study is shown in Table 1.

Table 1. List of Polymers used in this study.

Polymer	Grade	M_w (g/mol) *	Supplier
PLA	2003D	200,000	NatureWorks LLC (Minnetonka, MN, USA)
Bioflex	F-2110	53,000	FKuR Kunststoff GmbH (Willich, Germany)
Solanyl	C2201	NA	Rodenburg Biopolymers (Oosterhout, Netherlands)
PHBV	Y1000P	300,000	TianAn Biopolymer (Ningbo, China)

* The specifications are derived from the supplier technical bulletin.

2.2. Polymer Processing

Prior to extrusion, each polymer was dried for 24 h at 80 °C in a convection oven to remove any absorbed moisture. The polymers were extruded using a micro 18 lab-scale twin screw co-rotating extruder with a length to diameter ratio of 40/1 (Leistritz Ltd., Somerville, NJ, USA). The polymer strands were cooled in a water bath and then pelletized. The extruded pellets were then compression molded and considered as the virgin polymer (E1). The extrusion process was then repeated for four more times for each polymer to manufacture recycled polymer (E5). The temperature profile used for each polymer in the extrusion process is shown in Table 2.

Table 2. Extrusion temperature profiles for each polymer.

	Extruder Temperature at Different Zones (°C)									
Polymer	**Zone 1**	**Zone 2**	**Zone 3**	**Zone 4**	**Zone 5**	**Zone 6**	**Zone 7**	**Gate Adaptor**	**Die**	**Screw RPM**
PLA	152	154	157	160	160	163	166	168	160	180
Bioflex	154	160	166	171	177	179	182	185	170	200
Solanyl	93	121	132	135	138	141	143	146	140	120
PHBV	177	166	160	154	149	143	138	132	125	200

2.3. Compression Molding

After the extrusion process, the extruded pellets were dried at 60 °C in an oven for 24 h. A compression-molding machine (Model 3856, Carver, Wabash, IN, USA) was used to manufacture test specimens. The samples were compression molded under 50 atm pressure with a platen temperature of 160 °C for 5 min. The sheets were air-dried for 5 min at room temperature of approximately 25 °C. The molded 150 mm^2 sheets with a thickness of 4.5 mm then were cut into test specimens for various tests, following corresponding standard methods.

2.4. Gel Permeation Chromatography (GPC)

Weight average molecular weight (M_w), weight average molecular number (M_n), and molecular weight distribution (M_w/M_n) of polymers were measured using gel permeation chromatography (EcoSEC HLC-8320GPC, Tosoh Bioscience, Tokyo, Japan) equipped with a refractive index detector. GPC calibration was conducted using PS standards (Agilent EasiVial PS-H 4mL, Santa Clara, CA, USA).

Virgin and recycled polymers were dissolved in tetrahydrofuran solvent (THF) with a final concentration of 1 mg/mL. Polymer solutions were pre-filtered using a 0.22 µm syringe filter. The column temperature was 40 °C, and the solvent flow rate was set at 0.35 mL/min. Moreover, the average number of random chain scissions per unit mass of each polymer (n_t) was calculated according to the following Equation (1).

$$n_t = \left(\frac{1}{M_{nt}}\right) - \left(\frac{1}{M_{n0}}\right) \quad (1)$$

where, n_t is the number of chain scission at a given reprocessing cycle, M_{n0} and M_{nt} represent the number average molecular weight of samples after the initial and a given processing cycle, respectively.

2.5. Melt Flow Index (MFI)

Melt flow index testing was conducted in accordance with the ASTM D1238 standard. A Tinius Olsen Model MP 600 Extrusion Plastometer (Tinius Oslen Co., Horsham, PA, USA) was used to perform the testing. The applied temperatures for PLA, Bioflex, Solanyl, and PHBV were 210, 190, 170, 180 °C respectively. The applied load was 2.16 kg.

2.6. Differential Scanning Calorimetry (DSC)

A TA Instruments DSC Q200 (New Castle, DE, USA) was used to perform differential scanning calorimetry testing. Each sample was heated from 25 °C to 200 °C with a ramp rate of 3 °C/min. A nitrogen flow rate of 10 mL/min was used. Each sample weighed between 6 and 10 mg. The level of crystallinity of virgin (E1) and recycled polymer after five times extrusion (E5) was calculated using the following equation (Equation (2)):

$$Crystallinity\ \% = \left(\frac{\Delta H_m - \Delta H_{cc}}{\Delta H_m^0}\right) \times 100 \quad (2)$$

where ΔH_m is the specific melting enthalpy of the sample, ΔH_{cc} is the specific cold crystallization enthalpy of the sample, ΔH_m^0 is the melting enthalpy of the 100% crystalline polymer. The melting enthalpy of 100% crystalline PLA was 93.7 J/g. Since Bioflex is a PLA-based polymer, 93.7 J/g was also used as its melting enthalpy. The melting enthalpy of 100% crystalline PHBV was 146 J/g [2].

2.7. Dynamic Mechanical Analyzer (DMA)

A TA Instruments DMA Q800 (New Castle, DE, USA) was used to evaluate the dynamic mechanical behavior of each polymer. Measurements were conducted in a dual cantilever mode and the temperature swept from 25 to 90 °C at a heating rate of 1 °C/min, with a fixed frequency of 1 Hz. A preload force of 0.015 N was applied, and the oscillation amplitude was 15 µm for PLA, Bioflex, and PHBV. An amplitude of 5 µm was used for Solanyl to prevent yielding during the test. The sample dimensions were 60 mm × 4.5 mm × 1.5 mm, and the initial length of the specimen was measured using the dynamic mechanical analyzer once it was secured in the clamp. The storage modulus and damping coefficient (tanδ) were recorded as a function of temperature.

2.8. Thermogravimetric Analysis (TGA)

Thermogravimetric analysis of polymers was performed using a Perkin Elmer model (Shelton, CT, USA) analyzer in a nitrogen atmosphere (10 mg/min). The heating rate was 10 °C/min, and the determination range was 25–600 °C. The weight lost and the first derivative data (DTG) of TGA were obtained to calculate the thermal degradation behavior in polymers. T_{onset} (the temperature at which the polymer starts to degrade), T_{peak} (the temperature corresponding to the maximum degradation rate), and T_{endset} (final temperature at which the degradation process ends) were reported for virgin and recycled biopolymers.

2.9. Flexural Testing

The Three-Point bending test was carried out to determine the flexural strength on standard beam specimens of size 150 mm × 13 mm × 4.5 mm and support span of 75 mm. The test was conducted using a universal testing machine, Instron Model 5567 (Norwood, MA, USA) following ASTM D790 standard. The Instron machine was equipped with a load cell of 2 kN and the crosshead speed was set at 2 mm/min.

2.10. Izod Impact Testing

Izod impact testing was conducted in accordance with the ASTM D256 standard using Tinius Olsen impact tester (IT504, Tinius Olsen, Horsham, PA, USA). The pendulum weight and radius were 4.497 kg and 334.949 mm, respectively. No additional load was added to the pendulum for PLA, Solanyl, and PHBV. Weights of 0.453 kg were assigned to each side of the pendulum for Bioflex to achieve complete breaks. Test sample dimensions were 63.5 mm × 13 mm × 4.5 mm with a 2 mm notch in the middle of the sample.

2.11. Statistical Analysis

Minitab software version 17 (Minitab Inc., State College, PA, USA) was used to statistically analyze the mean values and standard deviations of the mechanical properties (Flexural testing, Izod impact testing, and DMA). The analysis of variance (ANOVA) and Tukey's test with a significance level of 5% ($\alpha = 0.05$) was used to analyze the data. Eight replicates of each formulation were tested in Flexural testing and Izod impact testing. In the case of DMA, for each formulation, three replicates were used, and the mean values are reported.

3. Results

3.1. Gel Permeation Chromatography (GPC)

In order to investigate the influence of the successive recycling process on the molecular structure of the polymers, GPC analysis was performed and the weight average molecular weight (M_w), the number average of molecular weight (M_n), and the molecular weight distribution (M_w/M_n) are all reported in Table 3. It can be seen that for all polymers with a thermo-mechanical history of the successive recycling process, M_w and M_n values decreased. These observations indicate that chain scission occurs especially in long chains, as a result of high shear and high temperature during the extrusion process. Scaffaro et al. reported similar observations in PLA with increasing number of recycling processes [3]. The higher decline in M_w was observed in PHBV by 82% reduction, followed by PLA by 78%, suggesting the structure of PHBV and PLA are more susceptible to high shear and temperature in comparison with Bioflex and Solanyl. Indeed, chain scission mainly occurs in polymers with higher M_w (PHBV and PLA) to form polymer chains of medium size. However, Bioflex and Solanyl with relatively lower M_w as compared to PLA and PHBV exhibited a negligible reduction in M_w (5% and 2%) after five reprocessing cycles. PLA and PHBV experienced a noticeable reduction in the molecular weight distribution (M_w/M_n) by about 15% and 31%, respectively (see Table 3), indicating that recycled PLA and PHBV have a more homogenous composition than virgin polymers. An increase in molecular weight distribution indicates that recycled Bioflex and Solanyl are more polydisperse than the corresponding virgin polymers. Martin et al. reported that polymeric materials consisting of a blend of two or more polymers possess a wider range of molecular weight after the recycling process [4].

Table 3. The number averaged (M_n), weight averaged molecular weight (M_w), disparity, and average number of random chain scissions (n_t) of biopolymers.

Polymer	Extrusion Cycles	Molecular Weight (g/mol)	Molecular Number (g/mol)	(M_w/M_n)	n_t
PLA	1	203,500	152,245	1.3	1.9×10^{-5}
	5	44,149	39,663	1.1	
Bioflex	1	52,132	39,759	1.3	7.2×10^{-6}
	5	49,276	30,891	1.5	
Solanyl	1	61,109	31,047	1.9	2.4×10^{-6}
	5	59,695	28,885	2.0	
PHBV	1	298,500	176,383	1.6	1.5×10^{-5}
	5	52,262	48,525	1.1	

As expected, one can observe that PLA and PHBV exhibited higher values for the average number of random chain scission per unit mass (n_t) after five times of reprocessing cycles (Table 3). In fact, higher values for n_t indicates that the polymer chains are more sensitive to thermomechanical degradation. On the contrary, the lower values for n_t in Bioflex and Solanyl can be probably attributed to the lower rate of polymer chain scissoring due to the cross-linking phenomenon which occurs in polymers above the melting temperature [5]. Moreover, the most probable reaction involved in the thermal degradation of polymers with a considerable reduction in molecular weight is random scission occurring as a result of high temperature and high shear force.

In PHBV polymer, the significant reduction in molecular weight of the polymer can be attributed to the unzipping reaction in PHBV through cis-elimination mechanism (Mclafferty arrangement) just above its melting temperature [6]. The formation of a variety of oligomers after degradation is illustrated in Figure 1 [7].

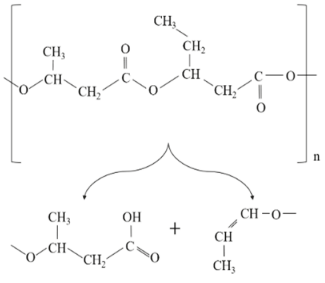

Figure 1. Schematic diagram of poly (3-hydroxybutyrate-*co*-3-hydroxyvalerate) (PHBV) random chain scission during thermal degradation.

Similarly, the degradation of PLA is because the generation of acidic molecules act as catalyst to accelerate the degradation. The considerable reduction in the molecular weight of PLA was more likely associated with the thermal degradation caused by polymer chain scissions into linear and cyclic oligomers [8] (Figure 2).

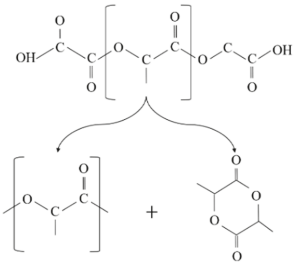

Figure 2. Schematic diagram of poly(lactic acid) (PLA) random chain scission during thermal degradation.

In addition, changes in the molecular weight of PLA can be linked to the cleavage of the long chains to shorter ones due to hydrolysis and intermolecular transesterification. The small value of the activation energy for the thermal degradation of PLA (21–23 kJ/mol) in comparison to other polymers indicates that PLA is highly sensitive to thermal treatment [9].

The molecular weight of the recycled Solanyl exhibited a limited reduction by 2% after five times of the recycling process. This observation can probably be attributed to either a less sensitive structure to the recycling process or the crosslinking phenomenon which occurs in recycled polymers as a result of subsequent recombination in the molecular chain cleavage as evidenced by Kale et al. They claimed the formation of new crosslinking in the structure of polymers under high temperature [10]. Solanyl is a starch-based polymer, having a similar chemical structure to starch; the probable thermal decomposition for Solanyl could be as illustrated in Figure 3. The starch-based polymers have a complex thermal degradation [11] and the chemical structure of the polymer ruptures to release the constituent molecules.

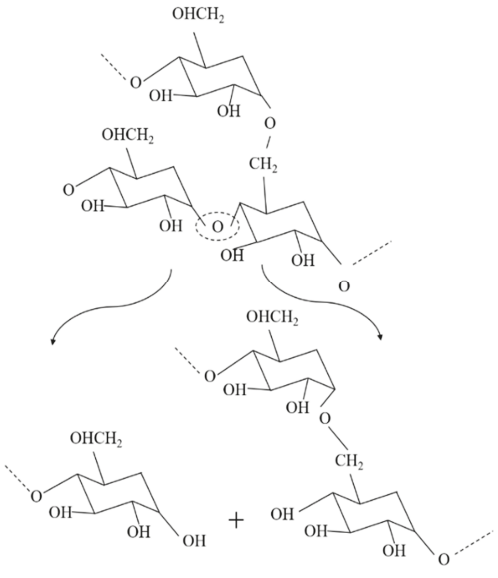

Figure 3. Schematic diagram of Solanyl thermal degradation and molecular cleavage.

The complex nature of starch contains amylose and amylopectin homopolymer blends. Starch is reported to undergo thermal reactions around 300 °C [11] anda lower processing temperature was used in this study (Table 2). It has been reported that degradation of these components leads to the formation of interpenetrating structures or helical structures which crystallize. Generally, starch thermal degradation leads to the formation of hydroxyl, ether links, as well as de-hydration of hydroxyl groups present on the glucose ring which we did not observe in FTIR results (not included in this study).

In Bioflex, which is a PLA-starch blend, 5% reduction in the M_w was observed. To improve the compatibility, interfacial adhesion, and enhance the dispersion between the two polymers, glycerol, formamide, and water are used as plasticizers. In the presence of heat and moisture, the strong intermolecular and intramolecular hydrogen bonding between polymers and plasticizers weakens which results in degradation of polymer. In Bioflex, degradation primarily occurs through the chain scission reaction of PLA. Bioflex is a USDA certified bio-based product. It is a polymer blend with PLA as the main component and it is certified as compostable material according to European standard (EN 13432). There is no information regarding its chemical structure, however, the molecular weight, flow rate, mechanical properties, and thermal properties of this polymer are reported in this work.

3.2. Effect of Recycling on Flow Characteristics

The flow characteristics of polymer melts were studied, and Table 4 displays the melt flow index of virgin and recycled polymers. The melt flow index increased by 71% for PLA, 44% for Bioflex, 13% for Solanyl, and 108% for PHBV as the number of the extrusion process increased from one to five. Collins and Metzger reported a relationship between flow activation energy and molecular weight of polymers. They found that flow activation energy in polymers is inversely proportional to the molecular weight [12]. Therefore, the observed increment in the melt flow index was a result of the reduction in the molecular weights (Table 3). The inverse relationship between melt flow index and molecular weight in polymers can explain the significantly higher increase in the melt flow index in recycled PLA and PHBV as compared with their corresponding virgin polymers.

Table 4. Melt flow index of virgin and recycled biopolymers.

Polymer	Extrusion Cycles	Melt Flow Index (g/10 min)
PLA	1	10.60
	5	18.20
Bioflex	1	6.37
	5	9.18
Solanyl	1	12.73
	5	14.51
PHBV	1	18.18
	5	37.90

3.3. Differential Scanning Calorimetry (DSC)

The influence of the recycling process on the thermal properties and degree of crystallinity of the polymers is shown in the DSC heating thermograms in Figure 4 and the data are summarized in Table 5.

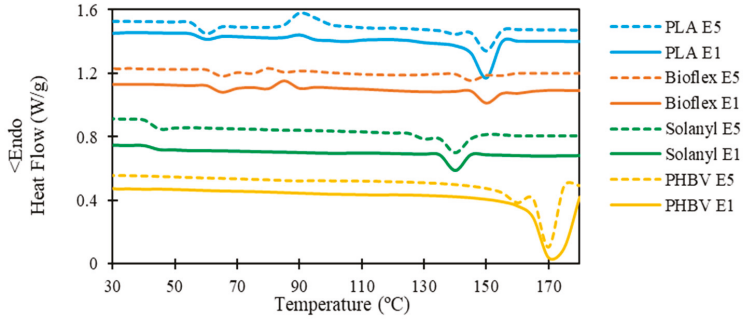

Figure 4. Representative DSC analysis curve of virgin and recycled polymers.

Table 5. Evaluation of the thermal properties of polymers as a function of the recycling process.

Polymer	Extrusion Cycles	T_g (°C)	T_c (°C)	T_m (°C)	X%
PLA	1	60.36	90.87	150.86	33.17
	5	55.04	91.23	151.87	7.01
Bioflex	1	65.73	85.34	151.36	2.72
	5	64.23	80.24	148.12	2.67
Solanyl	1	45.23	-	141.22	-
	5	44.40	-	140.53	-
PHBV	1	-	-	168.57	55.91%
	5	-	-	175.62	54.46%

T_g: Glass transition temperature; T_c: Crystallization temperature; T_m: Melting temperature; X%: Degree of crystallinity.

3.3.1. PLA

From the thermographs, virgin PLA showed a slightly higher glass transition temperature (T_g) in comparison with its recycled one. The Flory-Fox equation (Equation (3)) can be employed to explain the observation in T_g of the polymers regarding the molecular number:

$$T_g = T_{g\infty} - \frac{K}{M_n} \quad (3)$$

In which, T_g is the glass transition and $T_{g\infty}$ reveals the maximum glass transition temperature which occurs theoretically for the polymer with an infinite molecular weight. K is an empirical constant associated with the free volume in the polymer chains. In fact, polymer samples with lower molecular number possess more free volume associated with the end group in the polymer chains, inducing chain mobility. This, in turn, can facilitate the transition from a glassy to a rubbery state and thereby reducing the glass transition temperature [13].

No significant change was observed in the crystallization temperature, and the recycling process hardly changed the crystallization temperature of PLA. However, PLA E5 possessed a higher exothermic peak at the crystallization point (i.e., $(\Delta H_c)E1 < (\Delta H_c)E5$). This observation confirmed that less energy is required for the crystallization process in PLA E1, and these results let us propose that the degree of crystallinity of PLA E1 could be higher than PLA E5. This hypothesis was confirmed by calculating the degree of crystallinity using Equation 1 (Table 5). The substantial decrease in the degree of crystallinity in PLA E5 as compared with PLA E1 was probably attributed to the radical reaction as a result of the thermal degradation of PLA during the recycling process [14].

In general, the thermal degradation of polymers includes three steps as initiation, propagation, and termination [15]. In the initiation step, the loss of a hydrogen atom from the polymer chain occurs when heat is imposed on the polymer chain as the energy input. This process leads to the formation of highly reactive and unstable free radical (R*) and a hydrogen ion with an unpaired electron (H*). In the propagation step, the free radical reacts with an oxygen molecule (O_2), forming a proxy radical (ROO*) with a high level of activity and capable of removing a hydrogen atom from another polymer chain to form a hydroperoxide (ROOH). Therefore, the free radical regeneration occurs in the propagation step. Moreover, the hydroperoxide splits into two new free radicals, (RO*) and (*OH), which will propagate the chain degradation to form other polymer molecules. The final step of polymer chain degradation (termination) is attained through 'mopping up' the free radicals to form inert products. This step takes place naturally by combining free radicals or it can be aided by using stabilizers in the plastic (Figure 5).

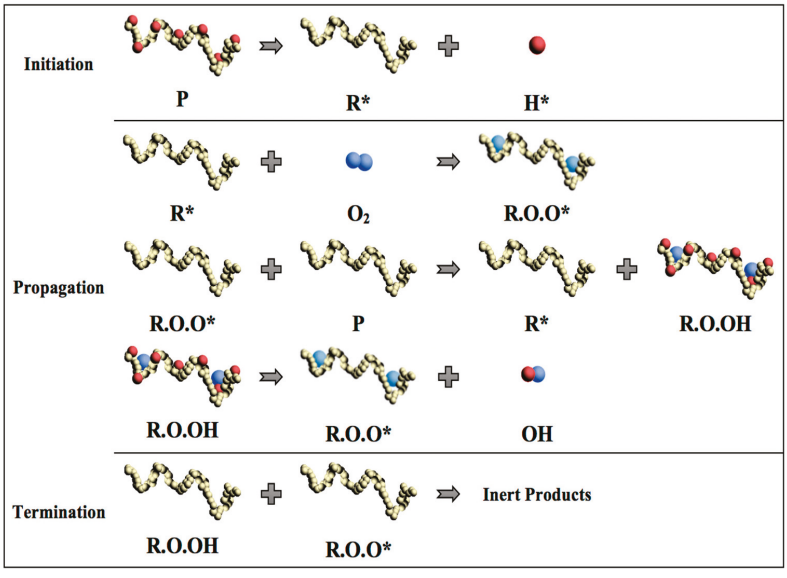

Figure 5. Schematic diagram of polymer chain thermal degradation and formation of free radicals. (P: polymer chain; R*: Free radical; H*: Hydrogen ion; O_2: Oxygen molecule; R.O.O*: proxy radical; R.O.OH: Hydroproxide; RO* and *OH: Free radical).

A single melting peak in the range of 150–152 °C was observed in PLA E1, however, PLA E5 exhibited a bimodal endothermic peak owing to the formation of different crystalline structures with different sizes and degree of perfection during successive recycling processes [16].

3.3.2. Bioflex

For Bioflex, the glass transition temperature experienced a non-significant decrease as the number of recycling process increased. This observation indicates a moderate shortening of the polymer chains after recycling, which means a slightly higher segmental chain mobility in Bioflex E5 as compared to E1. Morreale et al. reported a similar observation for Bioflex-based composites as a result of reprocessing [17]. Chain scission and crosslinking occurs simultaneously, and chain scission in polymer chains lowers the crosslink density, and results in the formation of more or longer dangling chain ends [18].

Similarly, the crystallization temperature exhibited a non-significant decrease after five reprocessing cycles, suggesting that crystallization took place at a lower temperature for Bioflex E5. This observation proves that polymer chains scissor after recycling processing which facilitates the crystallization kinetics [19]. No significant change was observed in the melting points of Bioflex. A slightly lower degree of crystallinity was observed in Bioflex E5 as compared to Bioflex E1 (1.8%). The reduction in the level of crystallinity can be attributed to the crosslinking phenomenon, which occurred in the polymer during exposure to either heat or shear above its melting point. In general, the degree of crystallinity in the polymer decreases with an increase in the crosslinking [20]. This observation can provide further proof of the cross-linking phenomenon in Bioflex, which limited the decline in M_w of Bioflex after the recycling process (see Table 3). After polymer chain branching, some of the polymer chains become linked together which results in cross-linking and embrittlement of the polymer.

3.3.3. Solanyl

As expected from the Florry-Fox equation, no significant decrease was observed in the glass transition temperature of Solanyl as the number of recycling processes increased. Moreover, cross-linking formation between the polymer chains above their melting point which was confined to the polymer chains and hindered the transition from glassy rigid to a rubbery state, was compensated by the scissoring process in Solanyl E5. Therefore only a non-significant decrease was observed in the glass transition temperature of Solanyl E5 in comparison with Solanyl E1. Crystallization was not likely to have occurred since no crystallization peak was observed in virgin and recycled Solanyl. This could be attributed to the slow crystallization in Solanyl. In addition, the shortness of the side-chain length in Solanyl might be another reason for the poor crystallization ability in Solanyl. A bimodal melting peak was observed in Solanyl E5 with a big peak at 140.53 °C and a smaller peak at 130.34 °C, while Solanyl E1 exhibited one endothermic peak at a slightly higher temperature (141.22 °C). The bimodal endothermic peaks in Solanyl E5 might be attributed to the presence of a species with a lower molecular weight (M_w) than the original material formed as a result of chain scission caused by different resistance to heat [21].

3.3.4. PHBV

Neither the glass transition nor the crystallization temperature was observed in PHBV polymer, which was attributed to either the slow crystallization rate in PHBV [22] or the occurrence of crystallization out of the range of the temperature studied in this work [23]. PHBV E5 exhibits two melting peaks; a large peak at low temperature (165.25 °C) and a small peak centered at high temperature (175.11 °C). This bimodal melting peak occurred because the imperfect crystals had adequate time to melt and reorganize into crystals with higher structural perfection. However, PHBV E1 melting possessed only one peak. No significant change was observed in the degree of crystallinity.

3.4. Dynamic Mechanical Analyzer (DMA)

The DMA investigation was performed to study the influence of reprocessing cycles on the dynamic-mechanical performance of the polymers. Figure 6 illustrates the storage modulus (E') and the mechanical loss factor (tanδ) for virgin (E1) and recycled (E5) polymers as a function of temperature. All the polymers experienced a declining trend in storage modulus throughout the whole temperature range used in this study. In the case of PLA, a drastic drop was observed in the vicinity of the glass transition temperature. This behavior can be attributed to an increase in the molecular mobility of the polymer chains above the T_g. However, Solanyl, Bioflex, and PHBV experienced a gentle decrease throughout the whole temperature range.

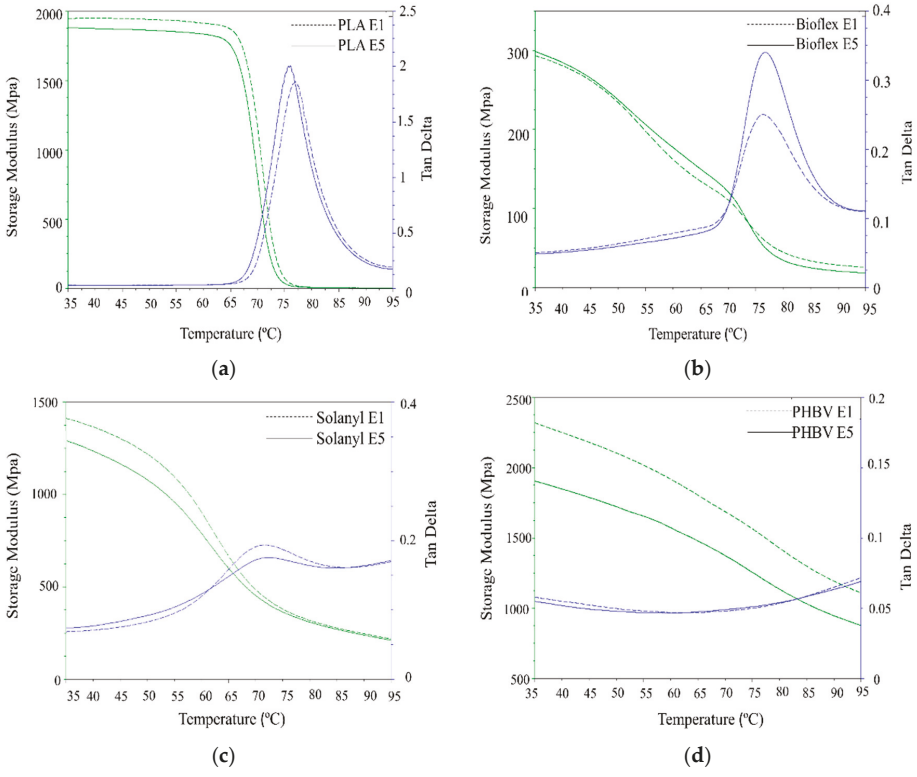

Figure 6. DMA analysis curve of virgin (E1) and recycled (E5) polymers: (**a**) PLA; (**b**) Bioflex; (**c**) Solanyl; and (**d**) PHBV.

3.4.1. PLA

PLA exhibited a non-significant decline in storage modulus in the glassy (7.25%) and leathery regions with an increase in the number of reprocessing times. The lower storage modulus in recycled PLA can be attributed to the lower molecular weight in the recycled polymers caused by thermomechanical degradation occurring during the reprocessing polymer degradation [24]. tanδ, as the mechanical loss factor, indicates the energy dissipation of materials under cyclic load at elevated temperatures. A higher tanδ intensity indicates more viscous (dashpot-like) behavior than elastic (spring-like) nature in materials [25]. It is seen from Figure 6a that, the recycled PLA exhibited significantly higher tanδ peak intensity (6.6%) as compared to virgin PLA, suggesting more viscoelastic behavior in recycled PLA than virgin PLA. This observation can be explained by the fact that the

decrease in M_w of the polymer can increase segmental motion, hence, leading to more viscous behavior in the polymer. A similar observation was reported for different polymers as a result of the recycling process [26].

3.4.2. Bioflex

Storage modulus curves were almost identical for both virgin and recycled Bioflex, and no significant change was observed in the glassy state. However, Bioflex E5 exhibited a slightly higher storage modulus in the leathery region (Figure 6b) and in the rubbery state Bioflex E1 was somewhat stiffer than virgin Bioflex. This was mainly ascribed to the efficient mechanical interlocked cross-linking of the polymer chain, which partially strengthen the polymer at a temperature above the glass transition temperature in the rubbery state. Similar behavior was reported for Bioflex reinforced with wood fibers [17]. In the tanδ curve, the peak intensity becomes significantly higher (45%) upon recycling, indicating a significant change in the molecular structure of recycled Bioflex as supported by the molecular weight values. The lower molecular weight makes the segmental motion easier and this, in turn, can increase the viscoelastic properties (damping behavior) in polymers [27].

3.4.3. Solanyl

Solanyl E5 exhibited a non-significantly lower storage modulus in the glassy (4.2%) and rubbery regions as compared with Solanyl E1, however, this discrepancy decreased as the temperature increased (Figure 6c). This result can be an indicator of the limited segmental mobility in the polymer chain due to the presence of the cross-links in the recycled Solanyl network. The formation of cross-linking in the polymer matrix hinders the untangling of the polymer chains and the sliding over each other after the glass transition temperature in the rubbery state [28]. In the DMA test, the mobility of the polymer chains is a response against the dynamic deformations of a particular frequency, and the viscoelastic properties of the polymers can be evaluated through the peak values of the tanδ curves [29]. Surprisingly, the recycled Solanyl displayed a lower tanδ peak intensity as compared with virgin Solanyl, suggesting, fewer polymer chains participate in the transition from a glassy to a rubbery state.

3.4.4. PHBV

A significant decrease occurred in the storage modulus of recycled PHBV throughout the temperature range studied in this work, because of thermomechanical degradation during the reprocessing cycles (see Table 3). In fact, an 80% decline in M_w led to a decrease of 20% in storage modulus of PHBV E5 in comparison with PHBV E1. In the case of tanδ, a completely different behavior was observed for PHBV, and the tanδ was almost temperature-independent, indicating that extrusion temperature had little or no effect on the viscosity of the polymer in the temperature range studied in this work.

3.5. Thermogravimetric Analysis (TGA)

Thermogravimetric analysis (TGA) and the derivative thermogravimetry (DTG) curve were used for assessment of the thermal stability of virgin and recycled polymers. The area of the DTG peak is directly proportional to the mass loss of the polymer over the same temperature range and the DTG peak height indicates the rate of mass loss at the corresponding temperature.

3.5.1. PLA

Figure 7a exhibits that the weight-loss trend for virgin and recycled PLA is almost identical. A single step decomposition in a narrow temperature interval was observed for PLA E1 and PLA E5. The mass started decreasing at temperatures of 287 °C and 294 °C in recycled and virgin PLA, respectively. Increase in the number of reprocessing cycles led to a slight decrease in the T_{onset}. Typically, an increase in the T_{onset} illustrates a more thermally stable polymer [30]. The observation

that virgin PLA was more thermally stable as compared with recycled PLA was probably attributed to the molecular weight reduction that took place during the recycling process. It is reported that there is a linear relationship between thermal stability (referred as T_{onset}) and the average molecular weight, in which, the higher molecular weight can result in more thermally stable polymer materials [31,32]. As expected from the single step weight loss in TGA curve, only one peak was noticed in the DTG curve. The T_{peak} shifted to a lower temperature for recycled PLA. Moreover, the DTG peak value was higher for the recycled polymer, suggesting a higher thermal degradation rate in PLA E5 as compared to PLA E1. These observations occurred because less energy is needed to degrade polymers with lower molecular weight.

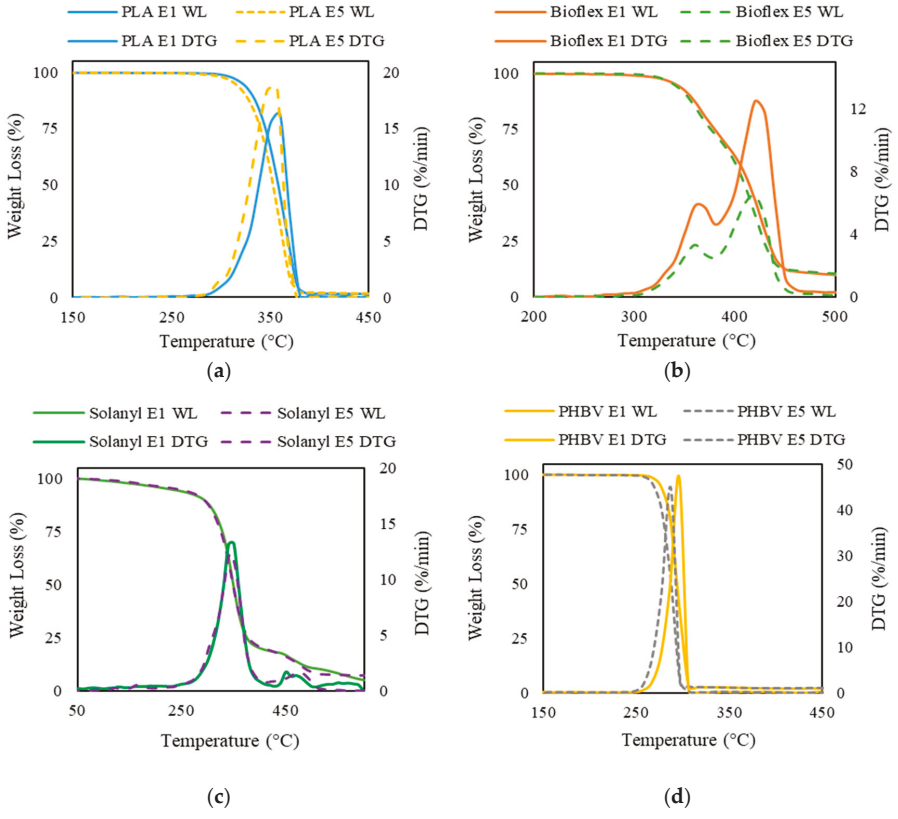

Figure 7. Thermogravimetric traces of virgin polymers (solid line) and recycled polymers (dashed line): (**a**) PLA; (**b**) Bioflex; (**c**) Solanyl; and (**d**) PHBV.

3.5.2. Bioflex

The thermogram of Bioflex E1 exhibits two degradation steps and the second step dominates the overall weight loss (Figure 7b). In the first stage, a weight loss of about 18 wt % occurred between ~300–380 °C; whereas a further 81 wt % loss was verified between ~380–470 °C during the second degradation step. The maximum rate of weight loss was centered at ~420 °C. A similar degradation profile but lower loss rate was observed in the thermal decomposition of Bioflex E5. The first degradation step in the temperature range of ~300–370 °C contributed towards the 32 wt % of the weight loss and the main weight loss (by 66 wt %) occurred in the temperature range of 385–450 °C. T_{onset} in recycled Bioflex shifted slightly to lower temperature as compared to virgin Bioflex by about

2 °C. This result implies that a higher activation energy is needed to decompose Bioflex E1, which can be explained by the higher molecular weight of Bioflex E1. The solid residue of the Bioflex E1 and E5 was 8.7 wt %, and 7.8 wt %, respectively. This indicates an incomplete thermal decomposition of both Bioflex E1 and E5.

3.5.3. Solanyl

No notable differences were observed in TGA results for Solanyl E1 and E5 up to 372 °C (Figure 7c). Both virgin and recycled Solanyl decomposed within a relatively wide temperature interval through a multi-step decomposition. The initial weight loss occurred as the temperature increased from room temperature to ~230–240 °C. During this stage, a weight loss of 6 wt % and 10 wt % were observed for virgin and recycled Solanyl, indicating moisture evaporation and dehydration. The main weight loss took place in the range of 250–425 °C. This step was accompanied by 80% of weight loss recorded on the TGA curve. The higher loss rate in Solanyl E1, indicates faster decomposition in Solanyl E1 than Solanyl E5. The solid residue left from Solanyl E1 at 600 °C was slightly higher than Solanyl E5 and resembles a foam structure, indicating the formation of oxidation products during heating. It was reported that thermal decomposition at a relatively high rate could make a close pack, forming a solid shell layer which inhibits the degradation of the inner layers and increases the char residue in carbohydrate polymers [33].

3.5.4. PHBV

The TGA curves of virgin and recycled PHBV are illustrated in Figure 7d. A single step weight loss in a narrow temperature range of 251–297 °C and 256–306 °C was inspected for virgin and recycled PHBV, respectively. The T_{onset}, T_{peak}, and T_{endset} shifted to a lower temperature for recycled PHBV. Hence, it can be concluded that virgin PHBV needs more activation energy for decomposition and degradation.

3.6. Effect of Recycling on Mechanical Properties

The mechanical properties of virgin and recycled polymers were studied through flexural and impact tests and the results are summarized in Table 6. PLA, Bioflex, and PHBV exhibited a slight reduction of 3.5%, 8.7%, and 1.7% in flexural strength on increasing the number of reprocessing cycles. These observations can probably be attributed to the lower molecular weight in the recycled polymers because of the deterioration of the polymer chains during successive extrusion cycles. In general, the mechanical properties of biopolymers are strongly dependent on M_w. Therefore, any changes in the polymer chain as a result of degradation due to high temperature and shear in the extrusion process are likely to influence the mechanical properties.

Table 6. Changes in mechanical properties of the polymers after the recycling process.

Polymer	Extrusion Cycles	Flexural Strength (MPa)	Flexural Modulus (GPa)	Impact Strength (kJ/m^2)
PLA	1	77.7 ± 7.4^{a}	2.5 ± 0.7^{a}	7.7 ± 0.2^{a}
	5	75.0 ± 3.4^{b}	2.2 ± 0.1^{b}	7.0 ± 0.1^{b}
Bioflex	1	9.0 ± 0.8^{a}	0.3 ± 0.0^{a}	9.1 ± 0.5^{a}
	5	8.2 ± 0.2^{b}	0.2 ± 0.0^{b}	8.7 ± 0.2^{b}
Solanyl	1	15.1 ± 0.4^{a}	1.4 ± 0.0^{a}	2.1 ± 0.4^{a}
	5	15.2 ± 0.1^{a}	1.3 ± 0.1^{b}	2.1 ± 0.3^{a}
PHBV	1	47.4 ± 3.6^{a}	3.2 ± 0.3^{a}	3.7 ± 0.1^{a}
	5	46.5 ± 4.9^{b}	2.7 ± 0.2^{b}	2.6 ± 0.1^{b}

Different letter superscripts for each of the polymers' properties indicate a statistically significant difference ($p < 0.005$).

Flexural strength was significantly lower for recycled PLA and PHBV as compared to their corresponding virgin counterparts, however, no significant change was observed in Bioflex and

Solanyl after the reprocessing cycle, which is more likely due to the reduction trend in the molecular weight in the recycled polymers (see Table 3).

The flexural modulus for all polymers shows a decreasing trend as the number of recycling processes was increased. A higher decline in flexural modulus was observed in PHBV E5 as compared to PHBV E1 by 11% followed by PLA by 9% decrease. These observations can be attributed to the fact that the recycling procedure includes polymer crushing and melting, which leads to polymer chain degradation. In addition, thermal degradation in the melting process contributes to the failing of intermolecular bonding between the polymer chains and the flexural strength in polymers tends to decrease as the number of recycling processes increased [34,35].

The impact strength of the polymers is shown in Table 6. It can be seen that all recycled polymers exhibit lower impact strength as compared with their corresponding virgin polymer. These results are consistent with another work which reported lower impact strength for PBT/PC/ABS after five times of the reprocessing cycle [36]. This may be explained by the lower molecular weight of recycled polymers due to the degradation phenomenon caused by heating and shear stress through the recycling process. PHBV with the higher reduction in molecular weight (Table 3) showed more reduction in impact strength after five times of reprocessing cycles (30%). Although Solanyl exhibited lower impact strength as compared with other polymers, the results showed that the effect of the recycling process on the impact strength was not significant and the impact strength remained constant after the recycling process.

4. Conclusions

In this study, detailed experimental analyses of molecular structure, the mechanical and thermal properties of recycled PLA, Bioflex, Solanyl, and PHBV after five extrusion and molding cycles were carried out. The molecular weight of the aforementioned polymers was studied using GPC. The mechanical properties were tested through flexural and impact tests. DSC was used to investigate the thermal properties of the virgin and recycled polymers and the overall conclusions can be summarized as follows:

1. PHBV and PLA exhibited a considerable reduction in molecular weight after five times of undergoing extrusion cycles.
2. DMA results showed a higher storage modulus for virgin polymers and a more viscoelastic behavior in the recycled polymers.
3. Solanyl exhibited better thermal processability compared to the other biopolymers studied in this work. The molecular structure of Solanyl possessed lower recycling sensitivity.
4. The maximum flexural strength in all polymers except Solanyl declined as the number of extrusion cycles increased.

Author Contributions: J.S., C.R., and G.V. carried out the experiments. J.S. analyzed the results and wrote the manuscript. S.G.B. provided critical feedback, and D.S.B. designed the experiments and supervised findings of this work.

Funding: This research received no external funding.

Conflicts of Interest: The authors declare no conflict of interest.

References

1. Koller, M.; Maršálek, L.; de Sousa Dias, M.M.; Braunegg, G. Producing microbial polyhydroxyalkanoate (PHA) biopolyesters in a sustainable manner. *New Biotechnol.* **2017**, *37*, 24–38. [CrossRef] [PubMed]
2. Li, J.; Lai, M.; Liu, J. Control and development of crystallinity and morphology in poly (β-hydroxybutyrate-co-β-hydroxyvalerate)/poly (propylene carbonate) blends. *J. Appl. Polym. Sci.* **2005**, *98*, 1427–1436. [CrossRef]
3. Scaffaro, R.; Morreale, M.; Mirabella, F.; La Mantia, F.P. Preparation and recycling of plasticized PLA. *Macromol. Mater. Eng.* **2011**, *296*, 141–150. [CrossRef]

4. Martín-Alfonso, J.; Valencia, C.; Sánchez, M.; Franco, J.; Gallegos, C. Rheological modification of lubricating greases with recycled polymers from different plastics waste. *Ind. Eng. Chem. Res.* **2009**, *48*, 4136–4144. [CrossRef]
5. Beyler, C.L.; Hirschler, M.M. Thermal decomposition of polymers. In *SFPE Handbook of Fire Protection Engineering*; National Fire Protection Association: Quincy, MA, USA, 2002; Volume 2, pp. 111–131.
6. Abe, H. Thermal degradation of environmentally degradable poly (hydroxyalkanoic acid)s. *Macromol. Biosci.* **2006**, *6*, 469–486. [CrossRef]
7. Xiang, H.; Wen, X.; Miu, X.; Li, Y.; Zhou, Z.; Zhu, M. Thermal depolymerization mechanisms of poly (3-hydroxybutyrate-co-3-hydroxyvalerate). *Prog. Nat. Sci. Mater. Int.* **2016**, *26*, 58–64. [CrossRef]
8. Dai, X.; Cao, Y.; Shi, X.; Wang, X. Non-isothermal crystallization kinetics, thermal degradation behavior and mechanical properties of poly (lactic acid)/MOF composites prepared by melt-blending methods. *RSC Adv.* **2016**, *6*, 71461–71471. [CrossRef]
9. Nicolae, C.-A.; Grigorescu, M.A.; Gabor, R.A. An Investigation of Thermal Degradation of Poly (Lactic Acid). *Eng. Lett.* **2008**, *16*, 568–571.
10. Kale, G.; Auras, R.; Singh, S.P. Degradation of commercial biodegradable packages under real composting and ambient exposure conditions. *J. Polym. Environ.* **2006**, *14*, 317–334. [CrossRef]
11. Mano, J.; Koniarova, D.; Reis, R. Thermal properties of thermoplastic starch/synthetic polymer blends with potential biomedical applicability. *J. Mater. Sci. Mater. Med.* **2003**, *14*, 127–135. [CrossRef]
12. Collins, E.; Metzger, A. Polyvinylchloride melt rheology II—the influence of molecular weight on flow activation energy. *Polym. Eng. Sci.* **1970**, *10*, 57–65. [CrossRef]
13. Zhu, L.; Wang, X.; Gu, Q.; Chen, W.; Sun, P.; Xue, G. Confinement-induced deviation of chain mobility and glass transition temperature for polystyrene/Au nanoparticles. *Macromolecules* **2013**, *46*, 2292–2297. [CrossRef]
14. Pedroso, A.G.; Rosa, D.S. Mechanical, thermal and morphological characterization of recycled LDPE/corn starch blends. *Carbohydr. Polym.* **2005**, *59*, 1–9. [CrossRef]
15. Thermal Degradation of Plastics. *Technical Whitepaper*; Zeus, Ed.; Zeus Industrial Products, Inc.: Orangeburg, SC, USA, 2005; pp. 3–5.
16. Suksut, B.; Deeprasertkul, C. Effect of nucleating agents on physical properties of poly (lactic acid) and its blend with natural rubber. *J. Polym. Environ.* **2011**, *19*, 288–296. [CrossRef]
17. Morreale, M.; Liga, A.; Mistretta, M.C.; Ascione, L.; Mantia, F.P.L. Mechanical, thermomechanical and reprocessing behavior of green composites from biodegradable polymer and wood flour. *Materials* **2015**, *8*, 7536–7548. [CrossRef] [PubMed]
18. Kömmling, A.; Jaunich, M.; Wolff, D. Revealing effects of chain scission during ageing of EPDM rubber using relaxation and recovery experiment. *Polym. Test.* **2016**, *56*, 261–268. [CrossRef]
19. Sherwood, C.H. The Effect of Shear on Polymer Crystallization Kinetics. Ph.D. Thesis, University of Massachusetts Amherst, Amherst, MA, USA, 1977.
20. Najafi, S.K. Use of recycled plastics in wood plastic composites—A review. *Waste Manag.* **2013**, *33*, 1898–1905. [CrossRef]
21. Gunaseelan, S.; Rao, R.; Manimaran, A.; Ramu, E.; Sivakumar, B. Determination of traces of amorphous cefuroxime axetil content in cefuroxime axetil crystalline drug substance using modulated differential scanning calorimetry (MDSC). *J. Chem. Pharm. Res.* **2012**, *4*, 4743–4751.
22. Li, H.; Huneault, M.A. Effect of nucleation and plasticization on the crystallization of poly (lactic acid). *Polymer* **2007**, *48*, 6855–6866. [CrossRef]
23. Thiré, R.M.d.S.M.; Arruda, L.C.; Barreto, L.S. Morphology and thermal properties of poly (3-hydroxybutyrate-co-3-hydroxyvalerate)/attapulgite nanocomposites. *Mater. Res.* **2011**, *14*, 340–344. [CrossRef]
24. Wang, K.; Bahlouli, N.; Addiego, F.; Ahzi, S.; Rémond, Y.; Ruch, D.; Muller, R. Effect of talc content on the degradation of re-extruded polypropylene/talc composites. *Polym. Degrad. Stab.* **2013**, *98*, 1275–1286. [CrossRef]
25. Cheng, S.; Lau, K.-T.; Liu, T.; Zhao, Y.; Lam, P.-M.; Yin, Y. Mechanical and thermal properties of chicken feather fiber/PLA green composites. *Compos. Part B Eng.* **2009**, *40*, 650–654. [CrossRef]
26. Bourmaud, A.; Le Duigou, A.; Baley, C. What is the technical and environmental interest in reusing a recycled polypropylene–hemp fibre composite? *Polym. Degrad. Stab.* **2011**, *96*, 1732–1739. [CrossRef]

27. Prasad, D.S.; Shoba, C.; Varma, K.R. Damping behavior of commonly used reinforcement powders–an experimental approach. *Eng. Sci. Technol. Int. J.* **2015**, *18*, 674–679. [CrossRef]
28. Bandzierz, K.; Reuvekamp, L.; Dryzek, J.; Dierkes, W.; Blume, A.; Bielinski, D. Influence of network structure on glass transition temperature of elastomers. *Materials* **2016**, *9*, 607. [CrossRef] [PubMed]
29. Shojaeiarani, J.; Bajwa, D.; Stark, N. Green esterification: A new approach to improve thermal and mechanical properties of poly (lactic acid) composites reinforced by cellulose nanocrystals. *J. App. Polym. Sci.* **2018**, *135*, 46468. [CrossRef]
30. Huda, M.S.; Drzal, L.T.; Mohanty, A.K.; Misra, M. Chopped glass and recycled newspaper as reinforcement fibers in injection molded poly (lactic acid)(PLA) composites: a comparative study. *Compos. Sci. Technol.* **2006**, *66*, 1813–1824. [CrossRef]
31. Carrasco, F.; Pagès, P.; Gámez-Pérez, J.; Santana, O.; Maspoch, M.L. Processing of poly (lactic acid): Characterization of chemical structure, thermal stability and mechanical properties. *Polym. Degrad. Stab.* **2010**, *95*, 116–125. [CrossRef]
32. Crompton, T.R. *Thermal Stability of Polymers*; Smithers Rapra: Akron, OH, USA, 2012.
33. Peng, Y.; Gardner, D.J.; Han, Y.; Kiziltas, A.; Cai, Z.; Tshabalala, M.A. Influence of drying method on the material properties of nanocellulose I: thermostability and crystallinity. *Cellulose* **2013**, *20*, 2379–2392. [CrossRef]
34. Jiun, Y.L.; Tze, C.T.; Moosa, U.; Tawawneh, M. Effects of Recycling Cycle on Used Thermoplastic Polymer and Thermoplastic Elastomer Polymer. *Polym. Polym. Compos.* **2016**, *24*, 735. [CrossRef]
35. Jahani, B.; Brooks, A.; Azarmi, F. Development of antibacterial surfaces via thermal spray coating techniques. *Biomed. Sci. Instrum.* **2018**, *54*, 1.
36. Kuram, E.; Ozcelik, B.; Yilmaz, F.; Timur, G.; Sahin, Z.M. The effect of recycling number on the mechanical, chemical, thermal, and rheological properties of PBT/PC/ABS ternary blends: With and without glass-fiber. *Polym. Compos.* **2014**, *35*, 2074–2084. [CrossRef]

polymers

MDPI

Article

Natural Silkworm Cocoon Composites with High Strength and Stiffness Constructed in Confined Cocooning Space

Lan Cheng [1,2], Xiaoling Tong [1], Zhi Li [2], Zulan Liu [2], Huiming Huang [3], Hongping Zhao [3,*] and Fangyin Dai [1,*]

[1] State Key Laboratory of Silkworm Genome Biology, Key Laboratory of Sericultural Biology and Genetic Breeding, Ministry of Agriculture, College of Biotechnology, Southwest University, Chongqing 400715, China; chenglan2018@swu.edu.cn (L.C.); xltong@swu.edu.cn (X.T.)

[2] Chongqing Engineering Research Center of Biomaterial Fiber and Modern Textile, College of Textile and Garment, Southwest University, Chongqing 400715, China; tclizhi@swu.edu.cn (Z.L.); 13658349461@163.com (Z.L.)

[3] Institute of Biomechanics and Medical Engineering, Tsinghua University, Beijing 100084, China; hhm207@163.com

* Correspondence: zhaohp@mail.tsinghua.edu.cn (H.Z.); fydai@swu.edu.cn (F.D.); Tel.: +86-13372679083 (F.D.)

Received: 10 October 2018; Accepted: 29 October 2018; Published: 31 October 2018

Abstract: In this study, using round paper tubes (PTs) and rectangular cardboard boxes (CBs) as external constraints to control the size of the cocooning space, we fabricated a series of modified silkworm cocoons (PT cocoons and CB cocoons). Their microstructures, morphologies, compositions, and mechanical properties were characterized and compared with normal silkworm cocoons. These two kinds of modified silkworm cocoons exhibit dense and homogeneous layer structures. Tensile test results indicate that above a size limit of cocooning space, their tensile strengths, Young's moduli, and strain energy densities increase with the decrease in cocooning space. Especially in comparison with the normal cocoons, the tensile strength and Young's modulus of the PT-14 cocoon increase by 44% and 100%, respectively. Meanwhile, PT cocoons and CB cocoons, except PT-12, also possess better peeling resistance than normal cocoons. Owing to the dense structure and low porosity, the modified cocoons form robust fiber networks that result in high strength and toughness. This study provides a green and efficient method to fabricate mechanically enhanced silkworm cocoons with special shapes and dense layer structures. The method can be easily subjected to further modification processes and has potential applications in the production of high-performance green cocoon composites and biomimetic materials.

Keywords: silkworm cocoons; dense structure; porosity; robust fiber network; mechanical properties

1. Introduction

Silkworm cocoons are biological structural materials constructed by silkworm larvae and provide protection from the natural environment, parasitism, or predators of silkworm pupae [1–5]. The silkworm cocoon could be used as protective materials, sorbent materials, gas filters, and biosensors considering its porous hierarchical structure, good impact resistance [6], sorption capacity [7], temperature- and humidity-dependent electrical properties [8], and photoelectrical properties [9–12]. Increasing attention has been paid to modifying the microstructure and improving the properties of silkworm cocoons without damaging their biological structures for further applications to the field of composites and biomimetic materials [13–19].

Cocooning behavior is an important factor that affects the properties of silkworm cocoons. When cocooning begins, a silkworm larva starts to construct a widely spaced supporting network

by stretching and turning its segmented body to search for potential attachment substrates and constructs a framework. Then, the larva turns its body around by swinging its head in figure-of-eight motions to overlap the silk fibers, ultimately producing a cocoon to protect the pupa from predators' attacks. The construction strategy of silkworm larvae depends on the silkworm species and the natural environment, resulting in diverse cocoon sizes, microstructures, morphologies, and mechanical properties [20–24]. On one hand, the relationship between the cocooning behaviors of a silkworm larva and the silkworm cocoon's characteristics has been systematically revealed and visually examined by 3D computer graphics software [25–30]. On the other hand, the cocooning environment, such as the size of the cocooning space, can also affect the cocoon's characteristics, including the shape [23] and the mechanical properties. Silkworms have evolved by the process of natural selection over millions of years to construct its corresponding shield housing for survival under a complex confined cocooning space. However, to date, little research has been conducted on the relationship between the confined cocooning space and the mechanical properties of silkworm cocoons.

Owing to its special biological structure, the silkworm cocoon can be regarded as a nonwoven fiber composite and has inspired people to design and fabricate advanced engineering materials [31–33]. However, silkworm cocoons are difficult to be directly used for manufacturing artificial composites due to their irregular shape, as well as the inhomogeneous cocoon layers [1,5]. Meanwhile, the *Bombyx mori* cocoon has been categorized as a "weak" cocoon with high porosity and relatively lower mechanical properties compared to some wild silkworm cocoons [3]. The study by Guan et al. [18] on the structure and properties of different kinds of cocoons revealed that the mechanical properties of cocoons are determined by fiber networks and fiber properties. A prerequisite of the cocoon structure is a robust fiber network, in which fibers with good mechanical properties play a part [18]. Tremendous efforts have been made to investigate the mechanical properties of the silk fibers [34,35] and to fabricate enhanced silk fibers using various methods [36–41]. However, there is a lack of studies on the preparation of enhanced silkworm cocoons, especially in a practical and green way, without damaging their special biological structures. Taking advantage of the ability of silkworm larvae to construct their shield housing under complex external constraints, silkworm cocoons with controllable shapes and strengthened fiber networks could be obtained.

In this study, we chose round paper tubes (PTs) and rectangular cardboard boxes (CBs) as the spinning regions for silkworm larvae in the lab when cocooning begins. The sizes of the constructed spaces were controlled by the spatial alternation of tube diameter for the PTs and the box width for the CBs to obtain a series of modified silkworm cocoons, named PT cocoons and CB cocoons, respectively. Normal silkworm cocoons (NCs) were constructed with common paper cocooning frames for silkworm larvae. The morphologies, microstructures, sericin contents, and mechanical properties of these modified silkworm cocoons were experimentally characterized and subsequently compared with those of normal silkworm cocoons. Finally, the relationship between the mechanical properties and the microstructures of the silkworm cocoons was further investigated. The results revealed that enhanced mechanical properties of silkworm cocoons constructed in a confined space were obtained, especially due to the dense cocoon microstructure. This study could help to develop strengthened cocoon materials using highly efficient strategies for potential applications in the field of composite engineering and biomimetic science.

2. Materials and Methods

2.1. Fabrication of Normal and Modified Cocoons

Bombyx mori silkworms (Chinese strain *Xiafang* × *Qiubai*) were obtained from the State Key Laboratory of Silkworm Genome Biology (Chongqing, China). They were reared under standard conditions and fed with fresh mulberry leaves until they started spinning. Then, each silkworm larva was put into specific PTs with different diameters (25, 20, 14, and 12 mm) or CBs with different widths (20, 17.5, 15, and 12.5 mm) until the cocooning completed. Corresponding modified silkworm cocoons

in special shapes were obtained, and the detailed procedure can be seen in Figure 1. The silkworm cocoons produced in the paper tubes with a diameter of 25 mm was labeled as the PT-25 cocoon. Similar labels were applied to the other groups. NCs obtained from normal spinning tools were set as the control group. Twenty cocoons from each group were collected, and their sizes were measured by vernier caliper. Then, the cocoon shell specimens for subsequent measurements were prepared by carefully cutting the cocoons into strips along their longitudinal directions and removing the pupae inside.

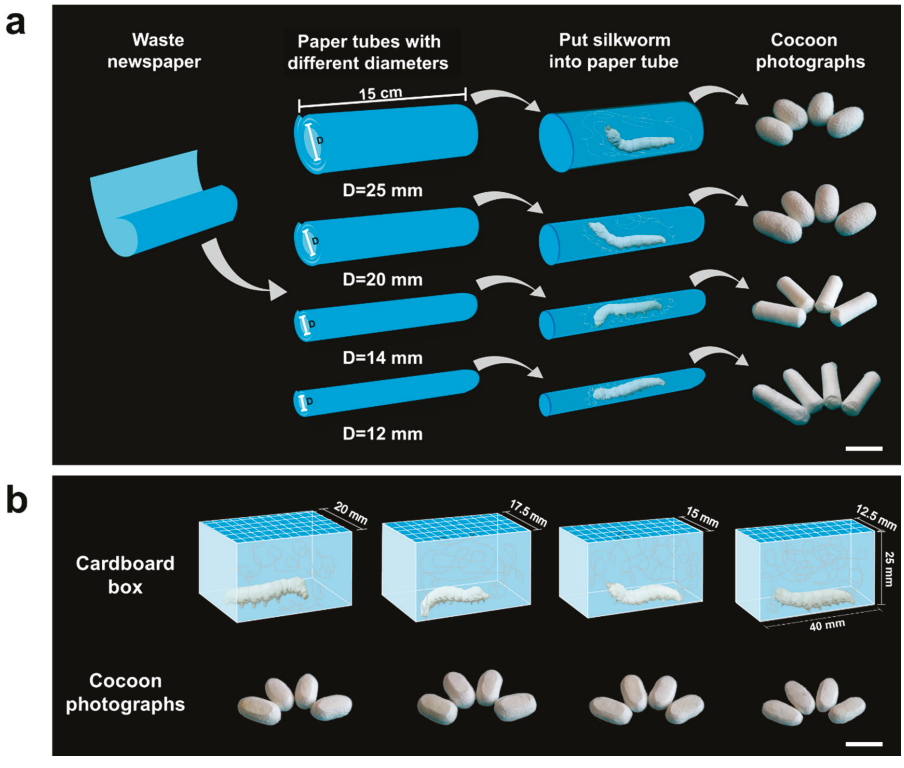

Figure 1. Schematic illustrations for the fabrication processes, and photographs of each type of modified silkworm cocoon: (**a**) paper tube (PT) cocoons and (**b**) cardboard box (CB) cocoons. Scale bar for silkworm cocoons is 2 cm.

2.2. Scanning Electron Microscopy (SEM) Observation

Samples were mounted on a platform with a conductive tape backing and then sputter-coated with gold for 2 min. The morphologies of silkworm cocoon layers and cross-sections were examined by SEM (Phenom Pro, Holland, The Netherlands) at an acceleration voltage of 5 kV.

2.3. Sericin Concentration

Dried cocoon shell specimens were immersed in 0.5% Na_2CO_3 solution at 100 °C for 30 min and then washed with distilled water, followed by drying for 24 h at 40 °C. The concentrations of sericin were calculated by $(w_0 - w_1)/w_0$, where w_0 and w_1 are the mass of the samples before and after the degumming, respectively [41].

2.4. Porosity of Cocoon Shell Specimens

The density (ρ_c) of each cocoon shell specimen was calculated from the weight, area, and thickness of the rectangular specimens. The density (ρ_f) of the silk fibers was set at 1300 kg/m^3 according to previous studies [18,42]. The porosity (P) of the cocoon shell specimens was calculated by the formula $P = 1 - \rho_c/\rho_f$. Three samples from each group were used, and all results are given as mean ± standard deviation.

2.5. Tensile Tests of Cocoons

Cocoons were cut into strips with a width of 3 mm along the longitudinal direction to prepare the tensile test samples. Quasi-static uniaxial tension tests were performed using an MTS E44-1 kN universal test machine (Shakopee, MN, USA) with a loading rate of 2 mm/min and a gauge length of 10 mm. The thickness of each cocoon shell was measured by vernier caliper. Six samples from each group were examined, and all results are reported as mean ± standard deviation.

2.6. Peel Tests of Cocoons

Cocoons were cut into strips with 20 mm lengths and 3 mm widths and peeled artificially from the middle layer to create an interlayer crack of 5 mm. The separated parts of each sample were clamped and peeled at an angle of 90° using the universal test machine with a tensile speed of 2 mm/min and a gauge length of 5 mm. Force-displacement curves for each sample were recorded. Six samples from each group were examined, and all results are reported as mean ± standard deviation.

2.7. Theoretical Characterization Models for Porosity

Porosity is an important factor influencing the mechanical performance of silkworm cocoons. Thus, it is necessary to characterize the relationship between porosity and the mechanical properties of silkworm cocoons. Young's modulus and tensile strength of silkworm cocoons have a similar dependence on the porosity. Based on the studies in [43,44], the Young's modulus–porosity relationship for silkworm cocoon composites can be defined as:

$$E = E_0(1 - P/P_c)^n \quad (1)$$

where E is the effective Young's modulus of porous material with porosity P, E_0 is Young's modulus of the silkworm cocoon, P_c is a percolation threshold, i.e., the porosity at which the effective Young's modulus becomes zero, and n is the characteristic exponent. Equation (1) can be directly used to fit the experimentally measured Young' modulus. In this study, the value of the percolation threshold P_c was set as 1 in the fitting process. This equation should follow the conditions: $E = E_0$, at $P = 0$; $E = 0$, at $P = 1$.

The strength–porosity relationship for silkworm cocoons can be characterized by the following widely known inverse proportional mathematic expression [45]:

$$\sigma = A\exp(-kP) \quad (2)$$

where σ is the strength, A is the strength at zero porosity, P is the porosity, and k is a characteristic exponent. The strengths of the silkworm cocoons at other porosities can be estimated by Equation (2) based on the strength data measured at given porosities.

2.8. Statistical Data Analysis

All statistical data are expressed as the mean ± standard deviation. Statistical analyses were conducted using one-way ANOVA as implemented by SPSS statistical software (New York, NY, USA). A p-value of <0.05, compared with the control group, was considered to be statistically significant.

3. Results and Discussion

3.1. Morphology and Microstructure

Photographs (Figure 1) and SEM images (Figures 2 and 3) of PT and CB cocoons clearly show the comparison between their morphologies and microstructures. These images reveal that different cocooning shapes or spaces lead to different cocoon morphologies and microstructures. By controlling the cocooning shape or space, the silkworm cocoons are shaped according to the given spinning tool (Figure 1). PT cocoons were spun by silkworms in paper tubes with different diameters, while CB cocoons were obtained from cardboard boxes with different widths. Figure 4a,b show the size (including length, width, and height) of each cocoon. For PT cocoons, their width decreases and the length increases as the diameter of the paper tube decreases. Meanwhile, the length of CB cocoons increases, and the height of the cocoon decreases with the decrease in the box's width.

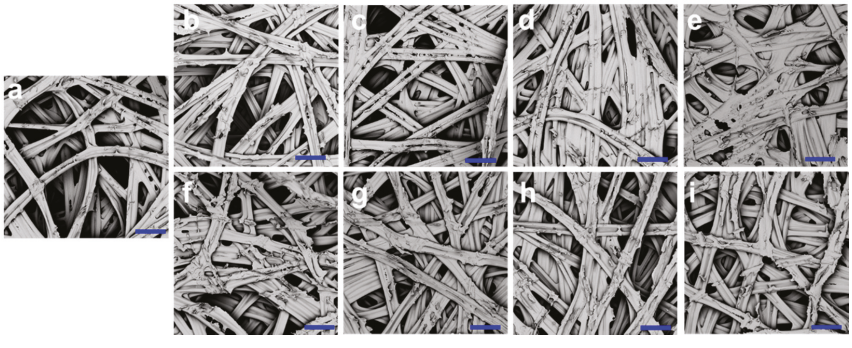

Figure 2. SEM images of cocoon layer structure. (**a**) Normal cocoon; (**b**) PT-25 cocoon; (**c**) PT-20 cocoon; (**d**) PT-14 cocoon; (**e**) PT-12 cocoon; (**f**) CB-20 cocoon; (**g**) CB-17.5 cocoon; (**h**) CB-15 cocoon; (**i**) CB-12.5 cocoon. Scale bar: 100 μm.

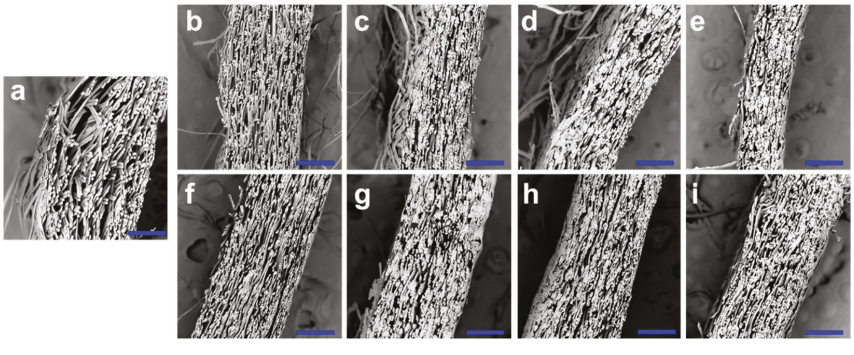

Figure 3. SEM images of cocoon cross-section structures. (**a**) Normal cocoon; (**b**) PT-25 cocoon; (**c**) PT-20 cocoon; (**d**) PT-14 cocoon; (**e**) PT-12 cocoon; (**f**) CB-20 cocoon; (**g**) CB-17.5 cocoon; (**h**) CB-15 cocoon; (**i**) CB-12.5 cocoon. Scale bar: 300 μm.

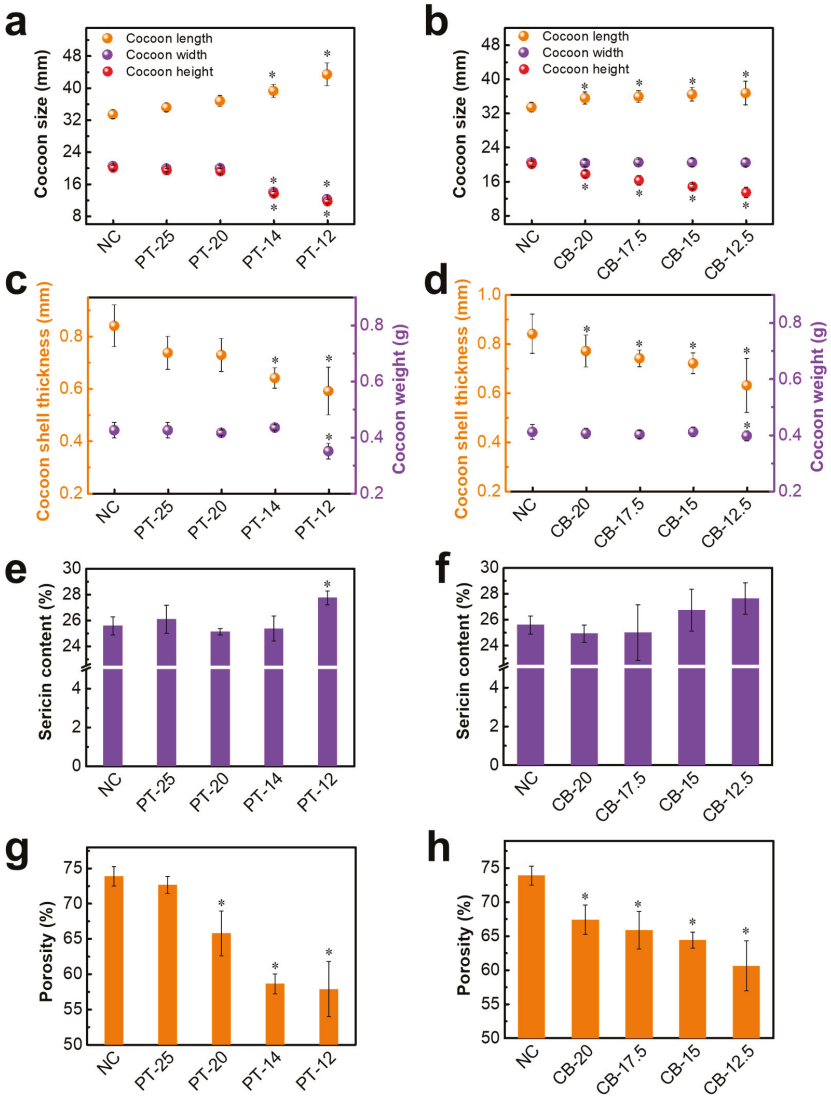

Figure 4. Parameters of silkworm cocoons. (**a**,**b**) Cocoon size; (**c**,**d**) cocoon thickness and weight; (**e**,**f**) cocoon sericin content; (**g**,**h**) cocoon porosity. Data are mean ± sd. Statistical analyses were performed using unpaired two-tailed Student's *t* test (* $p < 0.05$).

Both PT and CB cocoons have similar nonwoven composite structures with multiple layers parallel to the surface direction (see SEM images in Figures 2 and 3). Compared to the NCs, the PT and CB cocoons are more compact and have denser fiber networks. Figure 4c shows that the shell thickness of PT cocoons decreases from 0.74 to 0.59 mm with the decrease in paper tube diameter. The cocoon shell thickness of CB cocoons changes in a similar way. Figure 4d indicates that there is no significant difference between the weight of normal cocoons and the PT and CB cocoons, except for PT-12. This means that decreasing the cocooning space to a certain limit does not change the number of silk fibers produced by silkworm larvae. When the cocooning space is smaller than the size limit,

silkworm larvae are in a state of subhealth and cannot finish the cocooning process, resulting in a reduction in the number of silk fibers.

In addition, solidification contraction of silk fibers occurs when they are spun from the spinneret to the air during the construction of the cocoon frame, resulting in a rough cocoon surface. The sericin coating in the outer layer of the cocoon does not interconnect the fibers, so it does not form additional bonding between fibers. In contrast, for cocoons prepared from a confined cocooning space, there is not enough room for silkworm larvae to build a capacious cocoon frame. The fibers are confined and bonded together in a relatively narrow space. This method avoids the contraction of the surface layer and can form a smooth cocoon surface and a highly bonded network. Overall, the modified cocoons whose shapes are in accordance with the given cocooning space are constructed without any negative influence on cocoon weight. Both PT and CB cocoons show a denser structure and better homogeneity compared to the normal ones (shown in Figures 2 and 3). The homogeneity of the layer structure of most of the modified cocoons is superior to that of the normal cocoons and may contribute to the enhanced mechanical performance of these modified cocoons.

3.2. Sericin Content

Comparison between the sericin content of PT cocoons and CB cocoons was carried out and is shown in Figure 4e,f. It can be observed that the average sericin content of NCs is about 26%, which matches well with the results in previous studies [10]. Most of the modified cocoons, except PT-12, do not exhibit a significant increase or decrease in the sericin content compared to NCs, indicating that the decrease in cocooning space, to some extent, has little effect on the sericin content of silk fibers. However, there is a significant increase in the sericin content of PT-12. Combining the results of cocoon weight in Figure 4c with the sericin content of PT-12, the significant increase in the sericin content of PT-12 can be explained. Silkworm larvae in an excessively confined cocooning space cannot freely move their bodies and finish the cocooning process, which causes the lower weight of PT-12. The cocoon shell of PT-12 is speculated to be mainly made up of the silk fibers produced by silkworm larvae during the beginning of the cocooning process, and these initial fibers correspond to the outer layer of the normal silkworm cocoons. Furthermore, the test results by Kaur et al. [10] indicate that the outer layer of the normal cocoons has a higher sericin content compared to the other layers. Therefore, the higher sericin content of PT-12 can be well explained by this information.

3.3. Porosity of Cocoon Shells

To better understand the inner structure of these cocoons, cocoon shell porosity was calculated and averaged from six cocoon samples for each group, as shown in Figure 4g,h. The NC has a high porosity because there is a great deal of inter-fiber and interlayer free space [1–3,18]. However, the porosities of the PT-20, PT-14, and PT-12 cocoons were only 66%, 59%, and 58%, respectively, which are much lower than that of the NC (73%). The porosity of CB cocoons also decreases sharply with decreasing cocoon width, changing from 74% to 61%. The lower porosity of PT cocoons and CB cocoons is consistent with the microstructural observations shown in Figures 2 and 3. The decrease in porosity of the two cocoons was achieved by the restriction of the cocooning space, which causes a decrease in interlayer distance. Silkworm cocoons have been proved to be structural property-dependent biocomposites from both experimental and theoretical results [1]. A tough and strong cocoon can be obtained through the design of the microstructure and with the effective introduction of stronger inter-fiber bonding [18]. The study by Guan et al. [18] indicates that the silk fiber network plays an important role in cocoon properties. Thus, the relatively lower porosity of the modified silkworm cocoons in this study could be beneficial to the formation of robust fiber networks and lead to enhanced tensile and peeling properties.

3.4. Mechanical Properties of Cocoon Specimens

The tensile stress–strain curves and the tensile strength, elongation, Young's modulus, and strain energy density (calculated from the accumulated stress–strain area prior to maximum stress) from

different cocoon shell specimens are given in Figure 5. The stress–strain curves of PT cocoons and CB cocoons exhibit a similar trend with the decrease in cocooning space. The tensile strength, Young's modulus, and strain energy density of both types of cocoons gradually increase. Particularly, PT-25 has similar mechanical properties to the NC. The PT-14 cocoon shows considerably improved Young's modulus, tensile strength, and toughness with values of 1.2 GPa, 30.5 MPa, and 3.8 MJ/m^3, which are much higher than those of the NC: 0.6 GPa, 21.2 MPa, and 2.9 MJ/m^3. CB-12.5 is the most compact and solid in structure, resulting in the highest tensile strength, Young's modulus, and strain energy density, which are increased by 66.7%, 48.6%, and 82.8%, respectively, compared to those of the NC. Nevertheless, when the cocooning space was smaller than the size limit (such as PT-12), silkworm larvae can no longer build a robust cocoon. This can be explained by the fact that too small a cocooning space limits the movement of the silkworm body and hinders silkworm cocoon formation, which finally leads to the degradation of the mechanical properties of the cocoon.

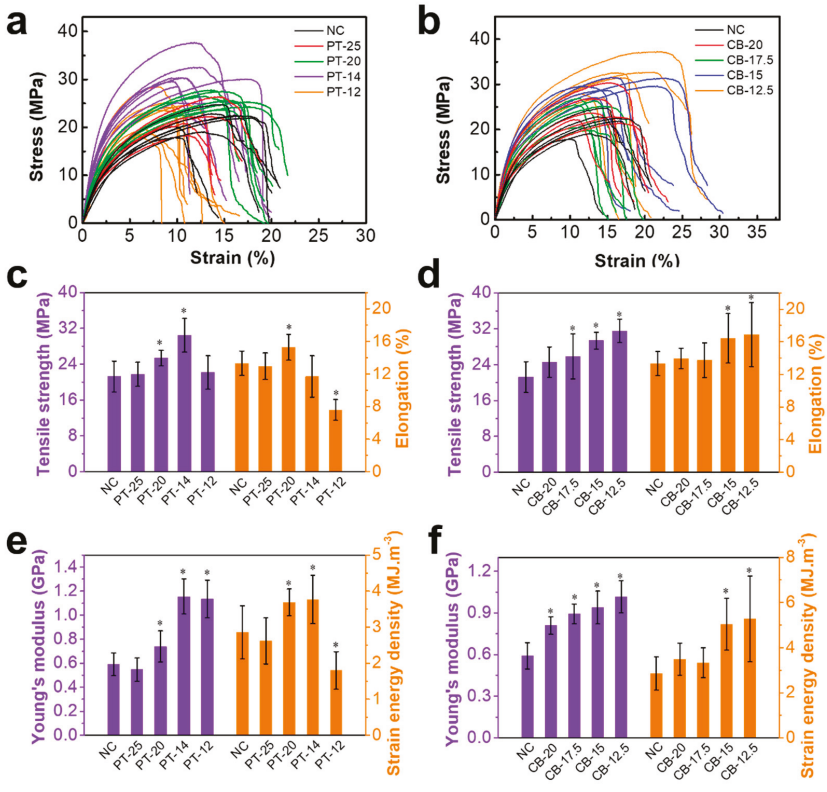

Figure 5. Mechanical properties of each type of silkworm cocoon. (**a**,**b**) Stress–strain curves; (**c**,**d**) tensile strength and elongation; (**e**,**f**) Young's modulus and strain energy density. Data are mean ± sd. Statistical analyses were performed using unpaired two-tailed Student's *t* test (* $p < 0.05$).

The enhanced mechanical properties are mainly due to the denser layer structure of the modified silkworm cocoons. The porosity should especially be integrated into the evaluation of composite mechanical performance [46–48]. The porosity dependence of Young's modulus or tensile strength for silkworm cocoons is shown in Figure 6. Young's modulus of silkworm cocoons increases from 0.5 GPa to 1.2 GPa with a decrease in porosity from 74% to 58%, while the tensile strength increases from 21 MPa to 32 MPa. Then, the porosity-dependent Young's modulus (Figure 6a) and tensile strength (Figure 6b) of silkworm cocoons were fitted by Equations (1) and (2), respectively. A high

goodness of fit of Young's modulus (R^2 = 0.93) was obtained, which indicates that Young's modulus of the cocoons follows an exponential increase with decreasing porosity. However, the goodness of fit of tensile strength (R^2 = 0.26) is quite low. Notably, the tensile strength of PT-12 is far from having a good fitting result. According to the low weight and higher sericin content of PT-12, we can find that silkworm larvae in an excessively confined cocooning space cannot freely move their bodies and finish the cocooning process, and therefore, PT-12 is not a complete cocoon. It may no longer follow the variation tendency of the tensile strength of other PT cocoons. To verify this, we present the fitting results without the PT-12 values of Young's modulus and tensile strength in Figure 6c,d. A high goodness of fit for Young's modulus (R^2 = 0.93) and tensile strength (R^2 = 0.91) is obtained. This result indicates that the mechanical properties of these silkworm cocoons, except for those of PT-12, follow an exponential relation. PT-12, which is not a complete cocoon and was constructed in very limited cocooning space, exhibits an anomalous low tensile strength, meaning that an excessively confined cocooning space has a negative effect on the tensile strengths of silkworm cocoons. For the other cocoon groups, the lower porosity is related to denser fiber networks and the larger bonding area between fibers. Then, as the fibers bonding increases, fibers are more prone to fracture, rather than unraveling from each other, which leads to the increase in Young's modulus and tensile strength.

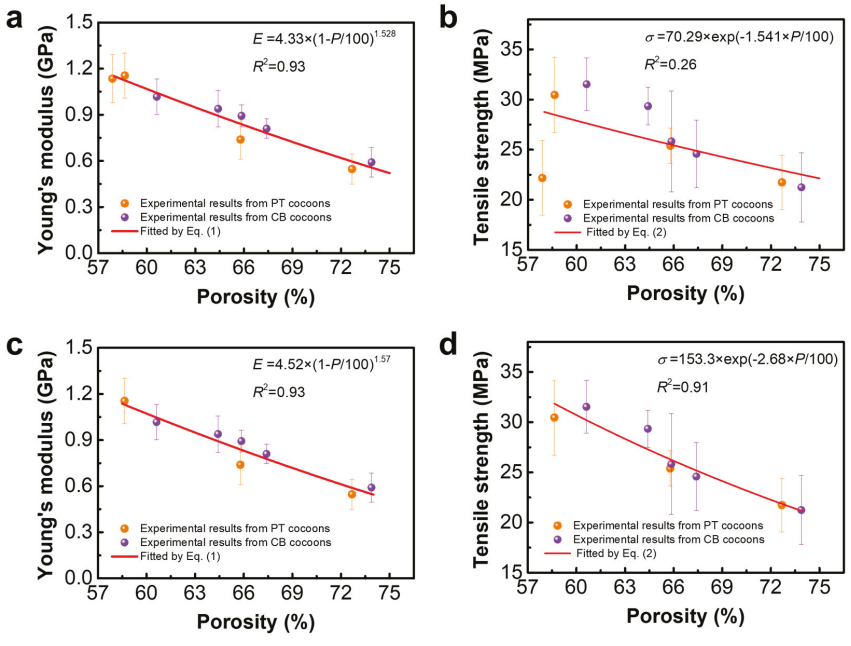

Figure 6. Porosity dependence of (**a**) Young's modulus and (**b**) tensile strength for all the silkworm cocoons; porosity dependence of (**c**) Young's modulus and (**d**) tensile strength for the silkworm cocoons without PT-12.

3.5. Interlaminar Peel Properties

The peeling force-displacement relation, maximum peeling force, and average peeling force of PT cocoons and CB cocoons are shown in Figure 7. The interlayer connectivity in these cocoons has a similar nonlinear load-displacement relation (Figure 7a). The average and maximum peeling force of normal cocoons are 0.29 N and 0.54 N, respectively. The layer of the NC is easy to peel apart due to the uneven spatial distribution of sericin bonds and low interlaminar bonding [42]. PT cocoons exhibit relatively higher peel forces, with an average and maximum force of 0.34 N and 0.58 N for

PT-25, 0.36 N and 0.69 N for PT-20, 0.50 N and 1.10 N for PT-14, and 0.39 N and 0.65 N for PT-12. The highest average and maximum force (PT-14 cocoon) are 1.72 times and 2.04 times higher than those of the control group. As for CB cocoons, their average peel forces increase from 0.29 N to 0.69 N while the maximum forces increase from 0.54 N to 1.14 N. The significant increase in the peel forces for PT and CB cocoons (except PT-12) indicates that high interlaminar bonding can be obtained using methods to control the cocooning space. The relatively weak interlaminar bonding in PT-12 indicates that too narrow a cocooning space has a negative effect on the peel resistance of silkworm cocoons. As discussed in the above sections, this could be explained by (1) the spinning motions of silkworm larvae are limited by too narrow a cocooning space; (2) the limited spinning motions increase the inhomogeneity and induce more flaws in the silk fiber networks. If the cocooning space is set just as the body size of the silkworm larvae, their cocooning process can hardly be completed. This case should be avoided. In summary, in a relatively narrow space, the silk fibers from silkworm larvae more easily bond together and the process can be regarded as a natural pressing process. It is reported that the peel load of silkworm cocoons obtained by hot pressing at room temperature is lower than that of normal silkworms, which indicates that the high-pressure compression process can destroy the interlayer bonding structure of the cocoon and lead to cracks in the silkworm cocoon [42]. However, the natural pressing process in this study does not damage their quality or interlayer bonding structure and provides silkworm cocoons with robust fiber networks and compact layer structures. More fiber bonds and a larger bonding area located in the compact layers are key contributors to the higher peel resistance of these modified cocoons.

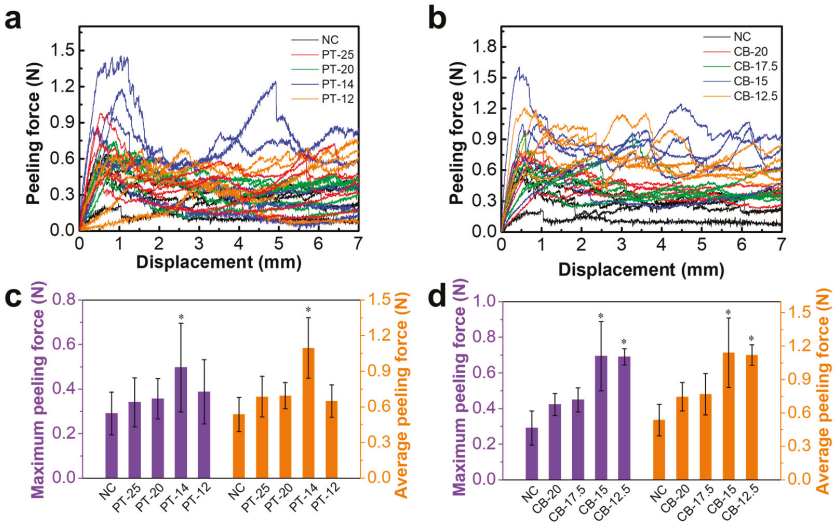

Figure 7. Comparison of peeling properties among different types of cocoons. (**a**–**b**) Peeling force curves of the cocoon specimens; (**c**–**d**) maximum peeling force and average peeling force. Data are mean ± sd. Statistical analyses were performed using unpaired two-tailed Student's *t* test (* $p < 0.05$).

4. Conclusions

In this study, we first fabricated a series of modified silkworm cocoons (PT cocoons and CB cocoons) with special shapes, dense structures, and excellent mechanical properties through a kind of natural pressing process. The microstructures, morphologies, compositions, and mechanical properties of these novel cocoons were characterized and compared with the normal silkworm cocoons. Most of these modified silkworm cocoons have denser fiber networks and lower porosities. Above a size limit of the cocooning space, the tensile strengths, Young's moduli, and strain energy densities of

these modified silkworm cocoons increase with the decrease in cocooning space. Notably, the tensile strength and Young's modulus of the PT-14 cocoon are found to be 1.44 and 2 times higher than those of the normal cocoons, respectively. As expected, most of these modified silkworm cocoons also exhibit excellent peeling resistance. The strengthening mechanisms underlying the method for controlling the cocooning space are attributed to the densification of silkworm cocoons by a natural pressing process, which leads to a robust fiber network and improves the load capacity of these cocoons. These special cocoons with excellent mechanical properties could have potential applications in the production of high-performance artificial cocoon composites and biomimetic materials.

Author Contributions: L.C. and Z.L. (Zhi Li) conceived and designed the experiments; L.C. performed the experiments; L.C., Z.L. (Zulan Liu) and H.H. analyzed the data; X.T., H.Z. and F.D. contributed reagents/materials/analysis tools; L.C. wrote the paper.

Funding: This research was funded by [the National Natural Science Foundation of China] grant number [31830094, 11872232 and 11432008], [863 program] grant number [2013AA102507] and [Funds of China Agriculture Research System] grant number [No. CARS-18].

Conflicts of Interest: The authors declare no conflict of interest.

References

1. Zhao, H.P.; Feng, X.Q.; Yu, S.W.; Cui, W.Z.; Zou, F.Z. Mechanical properties of silkworm cocoons. *Polymer* **2005**, *46*, 9192–9201. [CrossRef]
2. Zhao, H.P.; Feng, X.Q.; Cui, W.Z.; Zou, F.Z. Mechanical properties of silkworm cocoon pelades. *Eng. Fract. Mech.* **2007**, *74*, 1953–1962. [CrossRef]
3. Chen, F.; Porter, D.; Vollrath, F. Silk cocoon (*Bombyx mori*): Multi-layer structure and mechanical properties. *Acta Biomater.* **2012**, *8*, 2620–2627. [CrossRef] [PubMed]
4. Chen, F.; Porter, D.; Vollrath, F. Morphology and structure of silkworm cocoons. *Mater. Sci. Eng. C* **2012**, *32*, 772–778. [CrossRef]
5. Chen, F.; Porter, D.; Vollrath, F. Structure and physical properties of silkworm cocoons. *J. R. Soc. Interface* **2012**, *9*, 2299–2308. [CrossRef] [PubMed]
6. Chen, F.; Hesselberg, T.; Porter, D.; Vollrath, F. The impact behaviour of silk cocoons. *J. Exp. Biol.* **2013**, *216*, 2648–2657. [CrossRef] [PubMed]
7. Moriwaki, H.; Kitajima, S.; Kurashima, M.; Hagiwara, A.; Haraguchi, K.; Shirai, K.; Kanekatsu, R.; Kiguchi, K. Utilization of silkworm cocoon waste as a sorbent for the removal of oil from water. *J. Hazard. Mater.* **2009**, *165*, 266–270. [CrossRef] [PubMed]
8. Tulachan, B.; Meena, S.K.; Rai, R.K.; Mallick, C.; Kusurkar, T.S.; Teotia, A.K.; Sethy, N.K.; Bhargava, K.; Bhattacharya, S.; Kumar, A.; et al. Electricity from the silk cocoon membrane. *Sci. Rep.* **2014**, *4*, 5434. [CrossRef] [PubMed]
9. Roy, M.; Meena, S.K.; Kusurkar, T.S.; Singh, S.K.; Sethy, N.K.; Bhargava, K.; Sarkar, S.; Das, M. Carbondioxide gating in silk cocoon. *Biointerphases* **2012**, *7*, 1–11. [CrossRef] [PubMed]
10. Kaur, J.; Rajkhowa, R.; Tsuzuki, T.; Millington, K.; Zhang, J.; Wang, X. Photoprotection by silk cocoons. *Biomacromolecules* **2013**, *14*, 3660–3667. [CrossRef] [PubMed]
11. Kusurkar, T.S.; Gangwar, A.; Bawankar, M.; Mandal, A.; Dethe, D.; Thakur, A.K.; Singh, S.K.; Bhargava, K.; Khurana, S.; Sethy, N.K.; et al. A glowing antioxidant from Tasar silk cocoon. *RSC Adv.* **2015**, *5*, 104563–104573. [CrossRef]
12. Tulachan, B.; Srivastava, S.; Kusurkar, T.S.; Sethy, N.K.; Bhargava, K.; Singh, S.K.; Philip, D.; Bajpai, A.; Das, M. The role of photo-electric properties of silk cocoon membrane in pupal metamorphosis: A natural solar cell. *Sci. Rep.* **2016**, *6*, 21915. [CrossRef] [PubMed]
13. Horrocks, N.P.; Vollrath, F.; Dicko, C. The silkmoth cocoon as humidity trap and waterproof barrier. *Comp. Biochem. Physiol. Part A Mol. Integr. Physiol.* **2013**, *164*, 645–652. [CrossRef] [PubMed]
14. Zhang, J.; Rajkhowa, R.; Li, J.; Liu, X.Y.; Wang, X.G. Silkworm cocoon as natural material and structure for thermal insulation. *Mater. Des.* **2013**, *49*, 842–849. [CrossRef]

15. Kusurkar, T.S.; Tandon, I.; Sethy, N.K.; Bhargava, K.; Sarkar, S.; Singh, S.K.; Das, M. Fluorescent silk cocoon creating fluorescent diatom using a "Water glass-fluorophore ferry". *Sci. Rep.* **2013**, *3*, 3290. [CrossRef] [PubMed]
16. Blossman-Myer, B.; Burggren, W.W. The silk cocoon of the silkworm, *Bombyx mori*: Macro structure and its influence on transmural diffusion of oxygen and water vapor. *Comp. Biochem. Physiol. Part A Mol. Integr. Physiol.* **2010**, *155*, 259–263. [CrossRef] [PubMed]
17. Xu, J.; Zhang, W.; Gao, X.; Meng, W.; Guan, J. Strain rate and anisotropic microstructure dependent mechanical behaviors of silkworm cocoon shells. *PLoS ONE* **2016**, *11*, e0149931. [CrossRef] [PubMed]
18. Guan, J.; Zhu, W.; Liu, B.; Yang, K.; Vollrath, F.; Xu, J. Comparing the microstructure and mechanical properties of *Bombyx mori* and Antheraea pernyi cocoon composites. *Acta Biomater.* **2017**, *47*, 60–70. [CrossRef] [PubMed]
19. Shah, D.U.; Vollrath, F. 6—Silk for sustainable composites. *Nat. Fiber-Reinf. Biodegrad. Bioresorbable Polym. Compos.* **2017**, 91–109.
20. Van Der Kloot, W.G.; Williams, C.M. Cocoon construction by the Cecropia silkworm, I. the role of the external environment. *Behaviour* **1953**, *5*, 141–156. [CrossRef]
21. Van Der Kloot, W.G.; Williams, C.M. Cocoon construction by the Cecropia silkworm II. the role of the internal environment. *Behaviour* **1953**, *5*, 157–174. [CrossRef]
22. Van Der Kloot, W.G.; Williams, C.M. Cocoon construction by the Cecropia silkworm III. the alteration of spinning behavior by chemical and surgical techniques. *Behaviour* **1954**, *6*, 233–255. [CrossRef]
23. Miura, M.; Morikawa, H.; Kato, H.; Iwasa, M. Analysis of the construction process of cocoon shape by *Bombyx Mori*. *J. Seric. Sci. Jpn.* **1997**, *66*, 23–30.
24. Kiyosawa, M.; Ito, E.; Shirai, K.; Kanekatsu, R.; Miura, M.; Kiguchi, K. Cocoon spinning behavior in the silkworm, *Bombyx mori*: Comparison of three strains constructing different cocoons in shape. *Zool. Sci.* **1999**, *16*, 215–223. [CrossRef]
25. Lounibos, L. The cocoon spinning behaviour of the Chinese oak silkworm, *Antheraea Pernyi*. *Anim. Behav.* **1975**, *23*, 843–853. [CrossRef]
26. Miura, M.; Hoshi, H.; Nishioka, T. Analysis of the spinning behaviour of silkworms. *J. Seric. Sci. Jpn.* **1990**, *59*, 118–126.
27. Miura, M.; Morikawa, H.; Sugiura, A. Statistical analysis of body movement and shape of *Bombyx mori* in spinning behaviour. *J. Seric. Sci. Jpn.* **1995**, *64*, 237–245.
28. Miura, M.; Morikawa, H.; Shimizu, T.; Mochizuki, S.; Kojima, T.; Iwasa, M.; Nakazawa, M. Analysis of the fixed direction of a silkworm body during cocoon construction. *J. Seric. Sci. Jpn.* **2000**, *69*, 207–214.
29. Khan, M.M.R.; Miura, M.; Banno, Y.; Morikawa, H.; Chen, Y. 3D analysis of the spinning behavior of flossy cocoon mutants in the silkworm, *Bombyx Mori*. *J. Insect Biotechnol. Seric.* **2009**, *78*, 3139–3147.
30. Miura, M.; Kuwako, N.; Nakamura, T.; Khan, M.M.R. Cocoon repair behavior of *Bombyx mori* silkworm. *J. Insect Biotechnol. Seric.* **2011**, *79*, 3085–3093.
31. Chen, F.; Porter, D.; Vollrath, F. Silkworm cocoons inspire models for random fiber and particulate composites. *Phys. Rev. E* **2010**, *82*, 041911. [CrossRef] [PubMed]
32. Chen, F.; Porter, D.; Vollrath, F. A nonwoven composite model based on silkworm cocoon (*Bombyx mori*). *J. Mater. Sci. Eng.* **2010**, *4*, 28–33.
33. Zhang, J.; Kaur, J.; Rajkhowa, R.; Li, J.L.; Liu, X.Y.; Wang, X.G. Mechanical properties and structure of silkworm cocoons: A comparative study of *Bombyx mori*, *Antheraea assamensis*, *Antheraea pernyi* and *Antheraea mylitta* silkworm cocoons. *Mater. Sci. Eng. C* **2013**, *33*, 3206–3213. [CrossRef] [PubMed]
34. Pérez-Rigueiro, J.; Viney, C.; Llorca, J.; Elices, M. Silkworm silk as an engineering material. *J. Appl. Polym. Sci.* **1998**, *70*, 2439–2447. [CrossRef]
35. Pérez-Rigueiro, J.; Viney, C.; Llorca, J.; Elices, M. Mechanical properties of single-brin silkworm silk. *J. Appl. Polym. Sci.* **2000**, *75*, 1270–1277. [CrossRef]
36. Shao, Z.; Vollrath, F. Surprising strength of silkworm silk. *Nature* **2002**, *418*, 741. [CrossRef] [PubMed]
37. Berardo, A.; Pantano, M.F.; Pugno, N.M. Slip knots and unfastening topologies enhance toughness without reducing strength of silk fibroin fibres. *Interface Focus* **2016**, *6*, 20150060. [CrossRef] [PubMed]
38. Pantano, M.F.; Berardo, A.; Pugno, N.M. Tightening slip knots in raw and degummed silk to increase toughness without losing strength. *Sci. Rep.* **2016**, *6*, 18222. [CrossRef] [PubMed]

39. Wang, Q.; Wang, C.; Zhang, M.; Jian, M.; Zhang, Y. Feeding Single-Walled Carbon Nanotubes or Graphene to Silkworms for Reinforced Silk Fibers. *Nano Lett.* **2016**, *16*, 6695. [CrossRef] [PubMed]
40. Cheng, L.; Huang, H.; Chen, S.; Wang, W.; Dai, F.; Zhao, H. Characterization of silkworm larvae growth and properties of silk fibres after direct feeding of copper or silver nanoparticles. *Mater. Des.* **2017**, *129*, 125–134. [CrossRef]
41. Cai, L.; Shao, H.; Hu, X.; Zhang, Y. Reinforced and ultraviolet resistant silks from silkworms fed with titanium dioxide nanoparticles. *ACS Sustain. Chem. Eng.* **2015**, *3*, 2551–2557. [CrossRef]
42. Wang, T.; Chen, L.; Du, L.; Shen, T.; Li, F.; Huang, L.; Li, Z.; Wu, D. Structure and properties of silkworm cocoon (*Bombyx mori*) treated by hot pressing. *Mater. Des.* **2017**, *134*, 132–138. [CrossRef]
43. Kováčik, J. Correlation between shear modulus and porosity in porous materials. *J. Mater. Sci. Lett.* **2001**, *20*, 1953–1955. [CrossRef]
44. Phani, K.K.; Niyogi, S. Young's modulus of porous brittle solids. *J. Mater. Sci.* **1987**, *22*, 257–263. [CrossRef]
45. Papayianni, I.; Stefanidou, M. Strength–porosity relationships in lime–pozzolan mortars. *Constr. Build. Mater.* **2006**, *20*, 700–705. [CrossRef]
46. Madsen, B.; Thygesen, A.; Lilholt, H. Plant fibre composites–porosity and stiffness. *Compos. Sci. Technol.* **2009**, *69*, 1057–1069. [CrossRef]
47. Kováčik, J. Correlation between Young's modulus and porosity in porous materials. *J. Mater. Sci. Lett.* **1999**, *18*, 1007–1010. [CrossRef]
48. Madsen, B.; Lilholt, H. Physical and mechanical properties of unidirectional plant fibre composites—An evaluation of the influence of porosity. *Compos. Sci. Technol.* **2003**, *63*, 1265–1272. [CrossRef]

polymers

MDPI

Article

Green-Synthesis of Anisotropic Peptone-Silver Nanoparticles and Its Potential Application as Anti-Bacterial Agent

Min Kim [1], Seung-Cheol Jee [1], Surendra K. Shinde [2], Bhupendra M. Mistry [3], Rijuta Ganesh Saratale [4], Ganesh Dattatraya Saratale [3], Gajanan S. Ghodake [2], Dae-Young Kim [2], Jung-Suk Sung [1] and Avinash A. Kadam [4,*]

1 Department of Life Sciences, Dongguk University-Seoul, Biomedi Campus, 32 Dongguk-ro, Ilsandong-gu, Goyang-si 10326, Gyeonggi-do, Korea; pipikimmin@naver.com (M.K.); markjee@naver.com (S.-C.J.); sungjs@dongguk.edu (J.-S.S.)

2 Department of Biological and Environmental Science, Dongguk University-Seoul, Biomedical Campus, Ilsandong-gu, Goyang-si 10326, Gyeonggi-do, Korea; surendrashinde.phy@gmail.com (S.K.S.); ghodakegs@gmail.com (G.S.G.); sbpkim@dongguk.edu (D.-Y.K.)

3 Department of Food Science and Biotechnology, Dongguk University-Seoul, Ilsandong-gu, Goyang-si 10326, Gyeonggi-do, Korea; b.mistry84@dongguk.edu (B.M.M.); gdsaratale@gmail.com (G.D.S.)

4 Research Institute of Biotechnology and Medical Converged Science, Dongguk University-Seoul, Biomedi Campus, Ilsandong-gu, Goyang-si 10326, Gyeonggi-do, Korea; rijutaganesh@gmail.com

* Correspondence: avikadam2010@gmail.com or kadamavinash@dongguk.edu; Tel.: +82319615616

Received: 20 January 2019; Accepted: 31 January 2019; Published: 5 February 2019

Abstract: This study demonstrates a green-route-based synthesis of high-concentration suspensions of anisotropic silver nanoparticles (AgNPs) by peptone (Pep), a soluble protein hydrolysate and an abundantly used nutrient source in microbial-media. The transformation of Ag ions from solution into a high-concentration suspension of anisotropic Pep-AgNPs, at an extremely low concentration of peptone (0.02%), indicates that the present green-route synthesis method follows "low volume high concentration nano-synthesis", and, hence, enhances the economic significance of the process. Process optimization with different concentrations of AgNPs (1–5 mM), NaOH solution (5–40 mM), and peptone (0.004%–0.12%) gave the optimized Pep-AgNPs synthesis at 3 mM of $AgNO_3$, 20 mM of NaOH, and 0.02% of the peptone concentrations. The green-route synthesized Pep-AgNPs were structurally characterized by the TEM, XPS, FT-IR, and XRD analyses. The Pep-AgNPs against the clinically relevant bacteria *Escherichia coli* and *Staphylococcus aureus* gave significant anti-bacterial properties, with a MIC (minimum inhibitory concentration) of 100 ppm. The colony counting and morphological observation of the bacterial cell under SEM corroborated an anti-bacterial potential of the Pep-AgNPs. Therefore, Pep-AgNPs are green-route synthesized, anisotropic, and have a significant anti-bacterial potential that can be used in many relevant applications.

Keywords: Peptone; Microbial nutrient; Anti-bacterial silver nanoparticle; *Escherichia coli*; *Staphylococcus aureus*

1. Introduction

As the development of nanotechnology progresses, the silver nanoparticles (AgNPs) have become one of the most demanding nanoparticles, owing to their increasing number of applications in different sectors [1–9]. The shape, surface chemistry, and size of the AgNPs gives them typical physical, optical, chemical, and electronic properties. Therefore, the specific design of AgNPs has been a central research topic for several years [7,10–15]. However, chemically synthesized AgNPs, using chemical agents such as hydrazine, sodium borohydride ($NaBH_4$), and dimethylformamide, exert

significant environmental cytotoxicity [16,17]. An alternative method, such as the whole cell-based AgNPs synthesis, also encompasses several limitations, such as adsorption of nanoparticles to the cell surface, downstream processing, and significantly less control over the shape and size [16]. Greener-route molecular manufacturing of AgNPs would be more economical, reproducible, and a more sustainable process [13,17–19]. The green-route synthesis of nanomaterials has significantly increased in the past few decades [20]. The greener nanoscience approach mainly aims to create and apply design rules proactively, and to develop efficient synthetic strategies to produce nano-materials with defined composition, structure, and purity [20]. Therefore, to fulfill the enormous demand in the growing nanotechnology market, rapid, high concentration, and greener-route synthesis hold significant importance.

Over time, there has been a continuous increase in the number of multidrug-resistant bacterial strains, due to pollution, mutation, and the changing environmental conditions [21]. To sidestep this difficulty, scientists are developing drugs for the treatment of these harder-to-treat microbial infections [21]. Numerous metal salts and metal oxide nanoparticles were applied to the task of inhibiting the growth of many infectious bacteria. Among these materials, AgNPs occupy a prominent place [5,14,16,17,20,22]. However, in the last decade, there has been a rapid upsurge in the greener-route synthesized AgNPs. Still, the fabrication of specifically targetable AgNPs is extremely needed in the present day to combat the upcoming challenges in microbial infections.

Peptone (Pep), a component of microbiological media, is mainly defined as protein hydrolysates prepared from proteinaceous materials [23]. They are mainly utilized as an assimilable nitrogen source in microbial media [23]. The basic peptone composition contains mainly amino acids, short chain peptides, and proteins. Due to the presence of different components, such as amino acids, short chain peptides, and proteins, it might be possible to produce a mixture of different-shaped AgNPs possessing the antimicrobial potential. While investigating the detailed mechanism of AgNPs synthesis by microorganisms, role microbial media component peptone I in AgNPs synthesis was mentioned [24]. However, the peptone capping for AgNPs for detailed anti-microbial assessment was not reported elsewhere in the literature. Therefore, in this study, facile and rapid synthesis of peptone-capped AgNPs with optimization of process parameters, detailed characterizations, and antimicrobial assessment was investigated. The synthesis of AgNPs with the peptones might give several advanced antimicrobial applications.

Therefore, this study aims at the rapid green-route synthesis of microbial nutrient peptone-coated silver nanoparticles (Pep-AgNPs) as an economically and environmentally feasible nano-formulation for accessing its potential in anti-bacterial applications. Pep-AgNPs were green-route facile synthesized, optimized for the process parameters, structurally characterized with TEM, FT-IR, XPS and XRD analyze, and finally applied for accessing the anti-bacterial potential against the clinically relevant *Escherichia coli* and *Staphylococcus aureus*.

2. Materials and Methods

2.1. Green-Route Synthesis of Pep-AgNPs

The chemicals, such as BD Bacto™ peptone and silver nitrate, were obtained from BD Biosciences, San Jose, CA, USA, and Sigma Aldrich, St. Louis, MI, USA, respectively. A stock solution of peptone (0.4% wt/v) was prepared using DI (deionized) water and used freshly in the synthesis of Pep-AgNPs. Synthesis of Pep-AgNPs was examined by varying concentrations of precursor reagents and alkaline additive (NaOH). A solution of NaOH was obtained from Dae Jung Chemicals, Shiheung, Korea. The effect of the peptone amount was tested at increasing concentrations (0.0, 0.004, 0.012, 0.024, 0.040, 0.08, and 0.12% wt/v) with 0.2 mL of NaOH (1 M) and 0.2 mL of $AgNO_3$ (20 mM) in 10 mL reaction mixture. The effect of NaOH concentration at 5, 10, 20, 30, and 40 mM was studied with a fixed amount of peptone (0.04% wt/v) and $AgNO_3$ (0.4 mM) in 10 mL aqueous reaction mixture. The initial $AgNO_3$ concentration varied from 1.0 to 5 mM, with a fixed amount of aqueous peptone

(0.04% wt/v) and 0.2 mL of NaOH (1 M) in 10 mL aqueous reaction mixture. The AgNP reactions were run at 65 °C for 48 h incubation and used to record the UV-vis absorption spectrum on a UV-vis spectrophotometer (Optizen 2120, Mecasys Co., Ltd. Banseok-dong, Yuseong-gu, Daejeon, Korea). The centrifugation process was used to remove any unbound silver ions and peptone components, followed by the thorough washing of Pep-AgNPs with DI water. Typically, well-washed Pep-AgNPs solution was diluted accordingly and placed in a cell for spectral analysis in the range of 300–800 nm. The synthesized nanoparticles were stored at room temperature (22–24 °C).

2.2. Characterization of Pep-AgNPs

A Pep-AgNPs sample was drop-cast onto a piece of the Formvar-coated 200-mesh copper grid and was visualized using a transmission electron microscope (TEM) (Technai G2, Ames Laboratory, Ames, Iowa). The size of ~164 nanoparticles were measured to determine the size-distribution pattern. X-ray diffraction (XRD) spectrum in the 2θ range of 20°–80° was obtained on a diffractometer system (X'Pert PRO, PANalytical, Malvern, UK) operated at 40 kV, and 30 mA spectrum was recorded by Cu-Kα radiation with a wavelength of 1.5406 Å. The chemical characterization of the Pep-AgNPs thin film was performed by X-ray photoemission spectroscopy (XPS), and was operated with Theta Probe AR-XPS System, Thermo Fisher Scientific, Waltham, MA, USA, in the constant-pass energy mode with a monochromatic Al-Kα X-ray source. The binding energy scale of the XPS spectrum was calibrated by measuring the C1s peak at 285.0 eV. Fourier transform infrared (FTIR) spectrum of the centrifuged Pep-AgNPs was recorded over a spectral range of 500–3500 cm^{-1} to identify the functional groups (Thermo Fisher Scientific, Nicolet iS10, UK).

2.3. Microbial Strains

Escherichia coli (KCCM 11234; *E. coli*) and *Staphylococcus aureus* (KCCM 11335; *S. aureus*) were obtained from the Korean Culture Center of Microorganisms (KCCM, Seoul, Korea). Each bacterium was cultivated on a Tryptic Soy Agar plate (TSA; BD, San Jose, CA, USA) at 37 °C for overnight. A single colony of each bacterium was inoculated in Tryptic Soy Broth (TSB; BD, San Jose, CA, USA) and incubated at 37 °C 150 rpm for 18 h. To analyze the anti-bacterial effect of nanoparticles, bacterial cells which had the exponential phase OD600 = 0.4−0.6 were used.

2.4. Antibacterial Test

Antibacterial effects of nanoparticles were evaluated against gram-negative *E. coli* and gram-positive *S. aureus*. The bacterial suspension was diluted to 10^5 CFU/mL with TSB and 100 μL was dispensed into each well of the 96-well microplate. Then, various concentrations of Pep-AgNPs were added into each well, which had inoculated bacteria. The inoculated 96-well microplates were incubated at 37 °C for 4 h. After incubation, Pep-AgNPs containing TSB were removed and replaced with Pep-AgNPs free media, prior to turbidity measurement. Its turbidity was measured under 600 nm of wavelength using an ELISA reader (Tecan, Männedorf, Switzerland). All data were analyzed statistically using one-way analysis of variance (one-way ANOVA). Minimal inhibitory concentration (MIC) was determined as the lowest concentration without bacterial growth. After measurement of turbidity, to observed colony formation assessment, 100 μL volumes from each well of the microplates were aspirated and diluted to 10^{-5}. Dilutions were cultured on TSA for 16–18 h. Colony-forming units were manually counted.

2.5. SEM Analysis of Bacterial Surface Morphology Observation

To attach the bacterium cells on cover-slips, a cover-slip was coated with poly-L-lysine (Sigma, St. Louis, MI, USA) according to the manufacturers protocols. A bacterial suspension of 107 CFU/mL was added on a coverslip for 1 h. To evaluate the destruction of the bacterial cell wall, the cover-slip was washed with phosphate-buffered saline (PBS, Bio-sensing, Seoul, Korea), and nanoparticle suspension was treated on it for 2 h. After incubation, the bacterium was fixed with 2.5% glutaraldehyde for

24 h at 4 °C. For dehydration, 30, 50, 60, 70, 80, 90, and 100% of ethanol were gradually treated for 10 min each.

3. Results and Discussions

3.1. Pep-AgNPs Synthesis

This study was designed to produce AgNPs under a direct molecular reduction mechanism, using diluted peptone water as a strong reducing and stabilizing agent. Hence, the present process was totally based on green chemistry principles. The formation of Pep-AgNPs was elicited by the addition of the aqueous NaOH solution, mainly due to the catalytic properties of OH- and/or hydration of peptone functional groups. The environmentally benign solvent water was used as a solvent for all the studies, including the preparation and storage of Pep-AgNPs. In the present work, peptone-capped AgNPs (Pep-AgNPs) were synthesized at a very low concentration of peptone and a temperature of 65 °C. Uv-vis spectrum of Pep-AgNPs synthesized at various initial concentrations (1–5 mM) of $AgNO_3$ with a dilution of (1:10) of synthesized nanoparticles were shown in Figure 1a. The obtained results clearly revealed significant enhancement in surface plasmon resonance of Pep-AgNPs, with a subsequent increase in the $AgNO_3$ concentration. The obtained absorbance unit of 2.1 for (1:10 diluted) at 5 mM $AgNO_3$ concentration corroborated a very high concentration synthesis of Pep-AgNPs. Figure 1b showed a subsequent increase in the concentrations of $AgNO_3$, which increased the concentration of Pep-AgNPs synthesis. The highest concentration of Pep-AgNPs was observed at the concentration of 3 mM, and remained stable through further increases in the concentrations. The optical properties of silver nanoparticles are highly reliant on the diameter of nanoparticles [24]. It is typically recognized that blue-shift of the plasmon band position occurs for a decrease in the particle size [24]. Hence, at the concentration of 4 and 5 mM of $AgNO_3$, the blue shift was observed in surface plasmon resonance of the Pep-AgNPs, therefore, increased absorbance with blue shift corroborated a high concentration synthesis with the reduced particle size of Pep-AgNPs. In the next step, the effect of NaOH concentrations on Pep-AgNPs synthesis was investigated (Figure 1c). An increase in the concentration of NaOH showed an increase in the Pep-AgNPs synthesis. The optimum NaOH concentration was obtained to be 20 mM, and beyond this concentration, the *Pep-AgNPs* nanoparticles remained stable with no further increase (Figure 1d). To make a specific coating of proteinaceous materials from peptone on AgNPs, and to make the process more economical, it was highly important to access the effect of various concentrations of peptone for Pep-AgNPs synthesis. The effect of increasing peptone concentrations is displayed in Figure 1e. The obtained results corroborate the significant increase in the Pep-AgNPs synthesis with an increase in peptone concentration until the 0.024%, however, further increases in the peptone concentration Pep-AgNPs synthesis decreased with specific blue/red shift effect. At the concentration of 0.004%, surface plasmon resonance showed absorption maxima at 400 nm. However, from the peptone concentrations of 0.004% to 0.12%, it gave the absorption maxima at 420 nm, respectively. These results corroborated that increases in the peptone concentration above 0.004% changed the surface plasmon resonance properties of Pep-AgNPs. The highest synthesis was observed at the concentration of 0.02% of peptone. The almost complete transformation of Ag ions into an identical Pep-AgNPs, at an extremely low concentration of peptone (0.02%), indicates that the present green-route synthesis method is highly suitable for the "low volume high concentration nano-synthesis", and enhances the economic significance. The overall optimizations of $AgNO_3$, NaOH, and peptone solution concentrations for Pep-AgNPs synthesis corroborated a well-optimized synthesis process. The synthesized Pep-AgNPs were further used for characterizations and anti-bacterial studies. In comparison to other AgNPs reported, the synthesized Pep-AgNPs are coated with microbial nutrients, hence, the micro-organism might attract towards the Pep-AgNPs and get killed. Therefore, the Pep-AgNPs were applied for anti-bacterial studies.

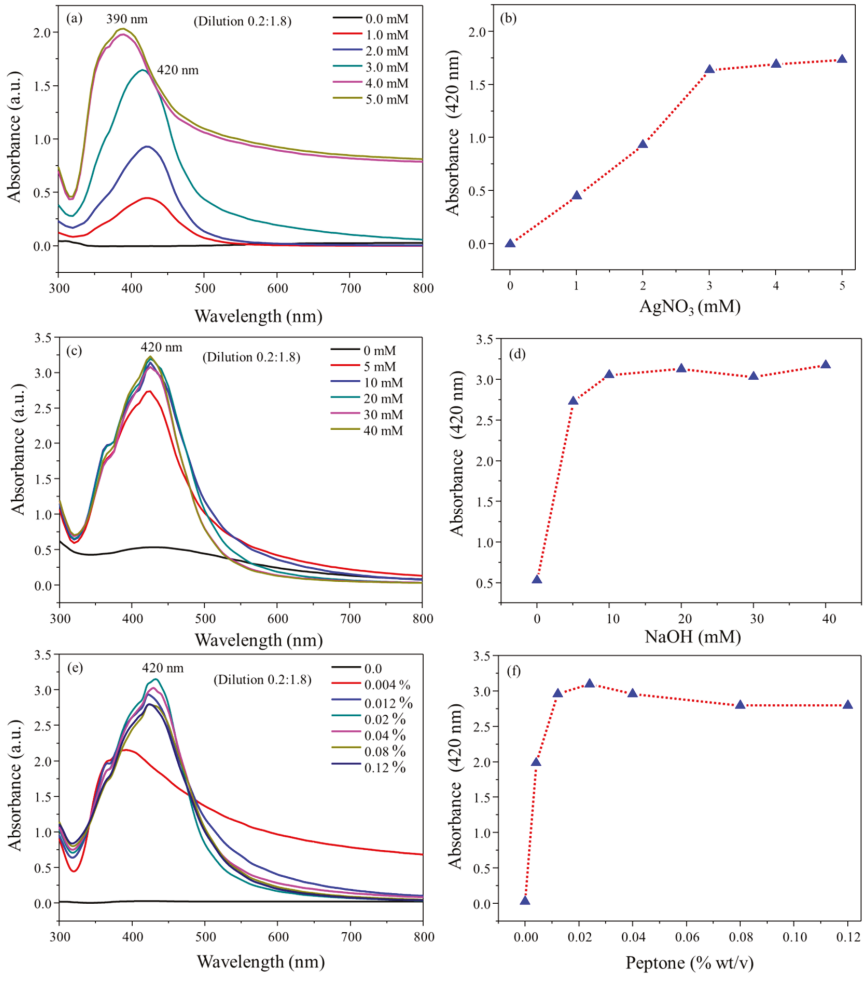

Figure 1. (**a**) Uv-vis wavelength scan of Pep-AgNPs synthesis at various $AgNO_3$ concentrations, (**b**) Absorbance at 420 nm for Pep-AgNPs synthesis at various $AgNO_3$ concentrations, (**c**) Uv-vis wavelength scan of Pep-AgNPs synthesis at various NaOH concentrations, (**d**) Absorbance at 420 nm for Pep-AgNPs synthesis at various NaOH concentrations, (**e**) Uv-vis wavelength scan of Pep-AgNPs synthesis at various peptone (Pep) concentrations and (**f**) Absorbance at 420 nm for Pep-AgNPs synthesis at various peptone concentrations.

3.2. Pep-AgNPs Characterizations

3.2.1. FT-IR Analysis

Surface functionalization of AgNPs with the peptone was analyzed by the FT-IR analysis. Figure 2a represents the FT-IR spectrum of peptone and Pep-AgNPs. The obtained FT-IR spectrum of peptone gave absorption peaks of 3400, 1654, 1594, and 1402 cm^{-1}, which corresponds to the stretching vibration of the attached water molecule, amide I of the proteins, amide II of the proteins, and amide III of the proteins, respectively (Figure 1) [25,26]. Similar characteristic proteins peaks (amide I, amide II and amide III) also appeared in the Pep-AgNPs sample (Figure 2a).

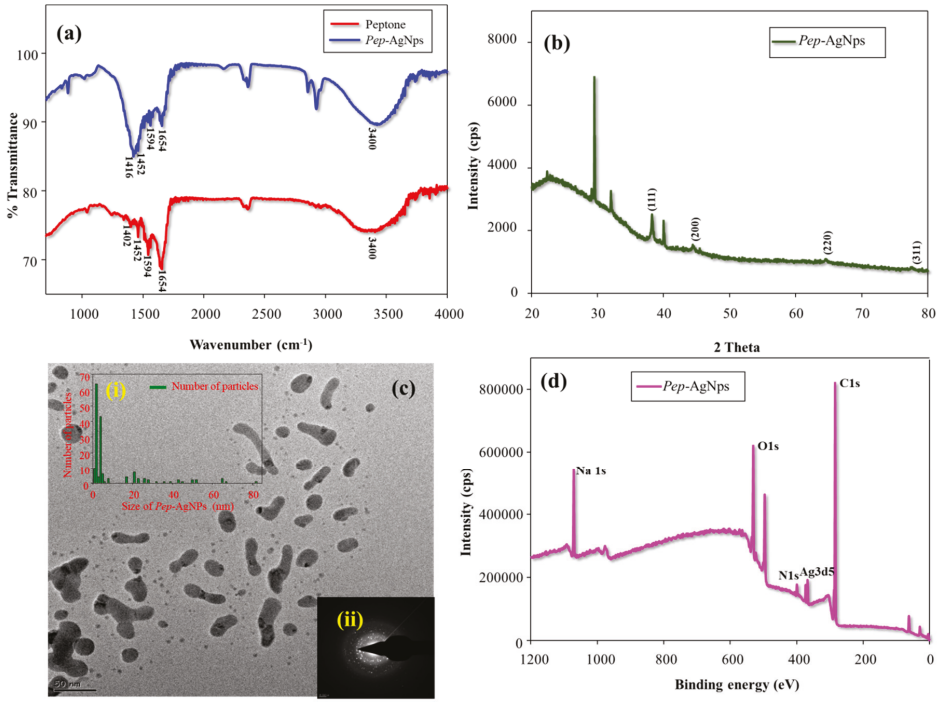

Figure 2. (**a**) FT-IR analysis of the peptone and Pep-AgNPs, (**b**) XRD analysis of Pep-AgNPs, (**c**) TEM images of Pep-AgNPs (i) Size histogram of Pep-AgNPs from TEM image (**c**) and (ii) SAED pattern of the Pep-AgNPs, and (**d**) XPS analysis spectrum of the Pep-AgNPs.

The obtained FT-IR results strongly corroborated a peptone functionalization of the silver nanoparticles. The proteins present over the silver nanoparticle surface may bind through the carbonyl and free amino groups, and act as a capping agent for stabilization of AgNPs [27].

3.2.2. XRD Analysis

Crystalline purity of Pep-AgNPs was investigated by XRD analysis (Figure 2b). The obtained pattern clearly displays the characteristic silver peaks at (2θ) angle of 38.30, 44.39, 64.49, and 77.45 corresponding to the (111), (200), (220), and (311) crystalline planes, respectively. Through comparing JCPDS (file no: 89-3722), the characteristic pattern of green-synthesized AgNPs were found to possess an fcc (face-centred cubic) structure of typical AgNPs. However, the other 5 unassigned peaks obtained at (2θ) angle of 22.32, 29.08, 29.46, 32.98, and 40.05 corroborated the peptone (amino acids, peptides and protein structures) modification of AgNPs. Similarly, additional peaks appeared in the XRD profile of green-route synthesized AgNPs by *Pedalium murex* leaf extract [28].

3.2.3. TEM Analysis

Structural morphology of the Pep-AgNPs was observed by TEM analysis. The TEM image showed a combination of long sheets and very small round-shaped Pep-AgNPs nano-particles. The anisotropic morphology shows different sizes and various shapes of the nanoparticle [27–29]. Therefore, the obtained TEM image corroborated that Pep-AgNPs has anisotropic particle morphologies. The method for obtaining the size of the distributed silver nanoparticles was used from the earlier report [17]. The size histogram of Pep-AgNPs nanoparticles was given in Figure 2c(i). The results displayed the different sizes of Pep-AgNPs. However, smaller and round-shaped nanoparticles

(1–4 nm) were found to be in higher densities than the long sheets of Pep-AgNPs (40–80). A similar distribution was observed by the flavonoid-derived anisotropic silver nanoparticles [29]. The different shape and size of the Pep-AgNPs are mainly due to the peptone chemical composition. The peptone contains different amino acids, peptides, and proteins. Therefore, the obtained results confirmed the differential reduction pattern of silver by various peptone components. A similar reduction of silver by various components yielded to the anisotropic silver nano-particles were obtained by the previous reports [30,31]. Though the monodisperse nature of silver nanoparticles is the main issue associated with synthesis, the green-route synthesized anisotropic silver nanoparticles are known to have a great advantage in biological platforms, as the silver nanoparticles interact with microorganisms in a shape-dependent manner [30,32]. Therefore, the presence of different-sized particles in Pep-AgNPs might act as highly versatile anti-microbial components [32]. Figure 2c(ii) gave the SAED pattern of the Pep-AgNPs. The obtained SAED pattern confirms the crystalline purity of the Pep-AgNPs. The obtained SAED patterns are in high accordance with the obtained XRD pattern.

3.2.4. XPS Analysis

The detailed surface elemental evaluation was made by XPS spectrum analysis. Figure 2d represents the Pep-AgNPs XPS spectrum. The obtained binding energies; 367.35, 284.6, 399.48, 1071.01, and 530.98 eV, corroborate the Ag3d5, C1s, N1s, Na1s, and O1s elemental peaks, respectively. Therefore, the obtained XPS spectrum of Pep-AgNPs confirmed successful synthesis. However, the more detailed individual high-resolution XPS spectrum was represented in Figure 3. The existence of two binding energies for Ag 3d in the Pep-AgNPs sample, 367.36, and 373.39 eV, with a difference of 6.0 eV, proved the formation of metallic silver (Figure 3a). However, the standard binding energies for pure silver are 368.1 and 374.1 eV [33]. The shift of both Ag 3d5/2 and Ag 3d3/2 to the lower binding energy in Pep-AgNPs compared to standard binding energies of the silver may be due to the occurrence of electron transfer between AgNP and peptone components. The high-resolution XPS spectrum of C1s and N1s have corroborated a typical protein structure (Figure 3b–c). Additionally, the presence of Na1s confirmed the binding of sodium salt from peptone to Pep-AgNPs. Therefore, the overall XPS investigations confirmed the successful Pep-AgNPs synthesis.

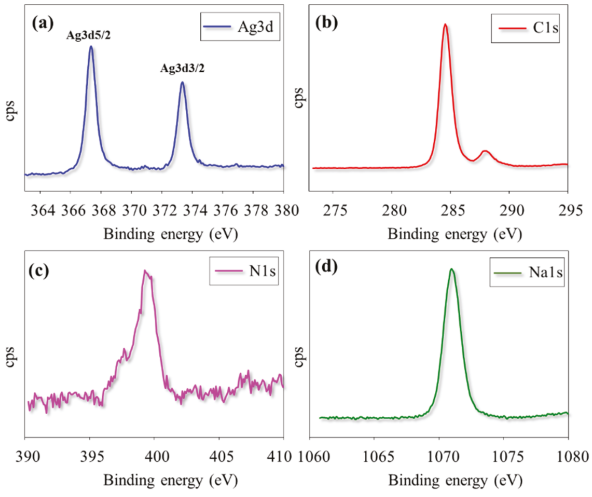

Figure 3. High resolution XPS spectra of (**a**) Ag3d, (**b**) C1s, (**c**) N1s and (**d**) Na1s from *Pep-AgNPs* sample.

3.3. Anti-Bacterial Assessments of Pep-AgNPs

After the successful synthesis and detailed characterizations, Pep-AgNPs was applied for anti-bacterial assessment against pathogenic bacteria, such as *E. coli* and *S. aureus*. The bactericidal activity of Pep-AgNPs against the *E. coli* and *S. aureus* was investigated using MIC, CFU formation, and SEM morphology of the bacterial cells. Figure 4 shows the anti-bacterial performance of the *Pep-AgNPs* towards *E. coli* and *S. aureus* after the 4 h incubation from treatment. With the subsequent increase in the Pep-AgNPs concentration, the bacterial growth inhibition was found to be dose-dependent. Gallic acid-coated silver nanoparticles also gave the dose dependent anti-bacterial activities to both the *E. coli* and *S. aureus*, respectively [17]. Figure 4 suggests that the MIC of Pep-AgNPs was observed to be 100 ppm for *E. coli* and *S. aureus*. At the concentration of 100 ppm, the almost-complete killing of the bacteria was observed. Therefore, the MIC of 100 ppm was determined as the lowest concentration of Pep-AgNPs without further observed bacterial growth. However, the obtained results suggest that the Pep-AgNPs are potent anti-bacterial materials for the gram-positive, as well as the gram-negative, bacteria. Anisotropic silver nanoparticles of silk fibroin gave anti-bacterial activity only towards the gram-negative bacteria, and gram-positive bacteria was found to be resistant [31]. However, the anisotropic Pep-AgNPs exhibited anti-bacterial activity towards both gram-positive and gram-negative bacteria, which might be due to the bacteria getting attracted towards the nutrient peptone and increased interactions with the Pep-AgNPs. Furthermore, the CFU analysis was performed for the anti-bacterial assessment. Figure 5 shows the photos of petri dishes that have the colonies of *E. coli* and *S. aureus* against the increasing concentrations of Pep-AgNPs.

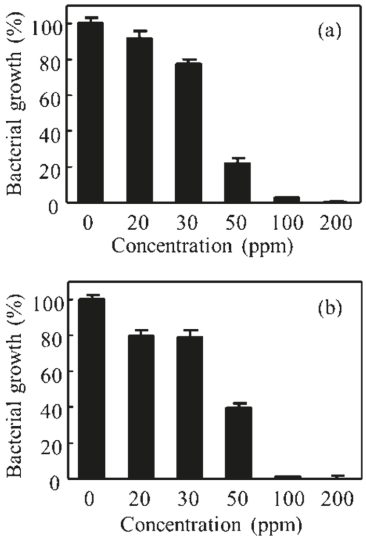

Figure 4. Bacterial viability of (**a**) *E. coli* and (**b**) *S. aureus*, with the various concentrations of *Pep-AgNPs*.

At the concentration of 100 ppm of Pep-AgNPs, no bacterial colonies were obtained in the *E-coli* culture, and very few colonies were observed in the *S. aureus* culture. The obtained results are in accordance with the earlier MIC experiment, and additionally corroborated a potent anti-bacterial capacity of the Pep-AgNPs. It is very important to observe the morphology of the bacterial cell after the silver nanoparticles treatment [14,16]. Therefore, the *E. coli* and *S. aureus* cells were observed under the SEM for analyzing the changes in morphology and membrane integrity after treatment with the Pep-AgNPs. The SEM image of the untreated *E. coli* gave an elongated rod shape (Figure 6b). The SEM image of the *E. coli* treated with Pep-AgNPs at 100 ppm revealed the shrinkage of the cell, with the formation of a porous structure and a distorted shape, from the adverse effect of Pep-AgNPs

(Figure 6b). Gram-negative bacterial cell wall was made up of a thin layer of peptidoglycan, and a lipopolysaccharide layer [16]. Therefore, the Pep-AgNPs easily disrupted the membrane structure of *E. coli* and shrunk it to a distorted shape (Figure 6b). However, the gram-positive bacteria possesses thick peptidoglycan layer of linear polysaccharide chains which cross-linked with short peptides to form a unique three-dimensional structure [16]. Hence, the *S. aureus* with a rigid gram-positive cell wall did not show significant cell wall damage (Figure 6d). The leakage of the cell wall occurred at particular sites (Figure 6d) and the rest of the cell wall structure remained intact. The leakage of the intracellular material occurred at specific sites by Pep-AgNPs, which leads to the ant-bacterial effect of the *S. aureus.* Similar morphological observations after treatment with AgNPs were obtained for *E. coli* and *S. aureus* [14]. The AgNPs antibacterial activity mechanism recently stated that lipopolysaccharides (LPS) typically interact with the positively charged AgNPs, and thus cause permeability of water [17]. Specifically, AgNPs are well-known to cause more damage to the *E. coli* cell membrane and significantly lower the activity of membranous enzymes, as reported earlier [17].

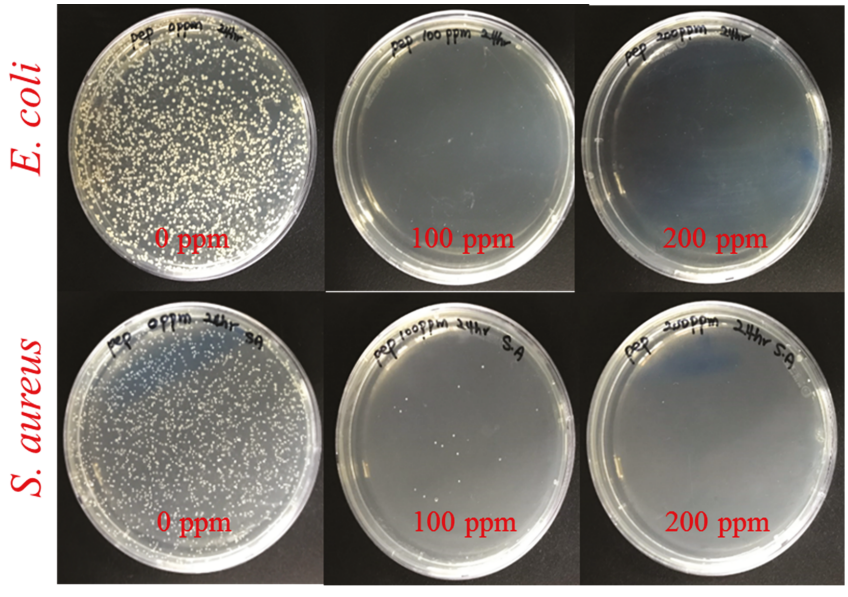

Figure 5. Photos showing the colonies of *E. coli* and *S. aureus* in agar petri dishes after treatment with 100 and 200 ppm of the Pep-AgNPs.

The antibacterial mechanism of the *S. aureus* cells in the presence of AgNPs was explained by the leakage of proteins and reducing sugars from the cell [34]. Nevertheless, looking at the well-established role of peptone in bacterial growth, it can be hypothesized that micro-organisms might get attracted towards the peptone, and be easily killed by well-known anti-bacterial anisotropic silver nanoparticles. However, to elaborate on this hypothesis, further highly selective research is needed to fill the data gaps. This study aimed to reports the synthesis, process optimizations, structural characterizations, and the anti-bacterial assessment of Pep-AgNPs. Therefore, anti-bacterial silver containing microbial nutrient peptone Pep-AgNPs can be a highly efficient anti-bacterial agent for several applications.

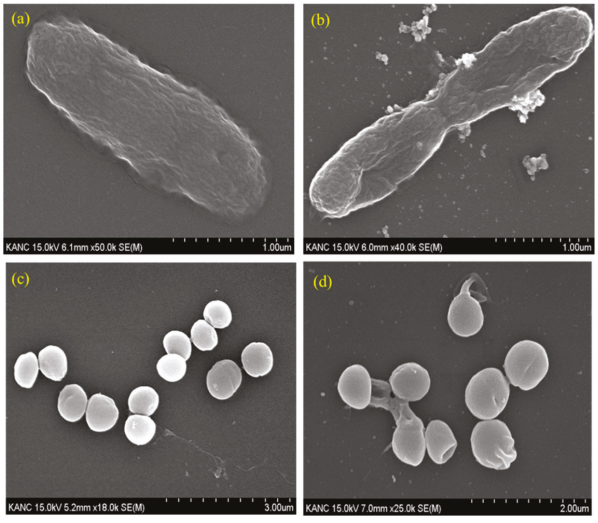

Figure 6. SEM image of (**a**) *E. coli* (untreated), (**b**) *E. coli* (treated with 100 ppm Pep-AgNPs), (**c**) *S. aureus* (untreated) and (**d**) *S. aureus* (treated with 100 ppm of Pep-AgNPs).

4. Conclusions

In summary, we applied a well-known microbiological media component, peptone, for the synthesis of anti-bacterial AgNPs. A greener-route based high-concentration synthesis of Pep-AgNPs was successfully achieved using a substantially low concentration of peptone (0.02%). Facile-synthesized Pep-AgNPs were structurally and functionally characterized by FT-IR, XPS, XRD, and TEM analyze. TEM analyses confirmed the anisotropic nature of Pep-AgNPs. The synthetic process parameters of Pep-AgNPs were optimized for higher production of Pep-AgNPs. Furthermore, Pep-AgNPs was assessed for the subsequent anti-bacterial properties against *Escherichia coli* and *Staphylococcus aureus*. Finally, the morphological observations were made after and before the *Pep-AgNPs* treatment to study microorganisms by FE-SEM analyses. Hence, Pep-AgNPs are anisotropic, economical, can be produced without any environmentally harmful by-products, and their potent anti-bacterial agents can be applied in several anti-bacterial applications.

Author Contributions: Formal analysis, M.K. and G.S.G.; Investigation, M.K. and G.S.G.; Methodology, S.-C.J. and G.S.G.; Resources, S.K.S. and B.M.M.; Supervision, A.A.K.; Validation, M.K. and A.A.K.; Writing—review and editing, M.K., R.G.S., G.D.S., D.-Y.K., J.-S.S. and A.A.K.

Funding: "This research was funded by Ministry of Environment of Korea, grant number 2017001970003" and "The APC was funded by Ministry of Environment of Korea, grant number 2017001970003".

Acknowledgments: This research was supported by National Research Foundation South Korea under the project number 2017R1C1B-5017360. This research was also supported by a grant (2017001970003) from the Ministry of Environment.

Conflicts of Interest: There are no conflicts of interest to declare.

References

1. Mao, X.; Cheng, R.; Zhang, H.; Bae, J.; Cheng, L.; Zhang, L.; Deng, L.; Cui, W.; Zhang, Y.; Santos, H.A.; et al. Self-Healing and Injectable Hydrogel for Matching Skin Flap Regeneration. *Adv. Sci.* **2018**, *1801555*.
2. Abu-Saied, M.A.; Taha, T.H.; El-Deeb, N.M.; Hafez, E.E. Polyvinyl alcohol/Sodium alginate integrated silver nanoparticles as probable solution for decontamination of microbes contaminated water. *Int. J. Biol. Macromol.* **2018**, *107*, 1773–1781. [CrossRef] [PubMed]

3. Shankar, S.; Rhim, J.W.; Won, K. Preparation of poly(lactide)/lignin/silver nanoparticles composite films with UV light barrier and antibacterial properties. *Int. J. Biol. Macromol.* **2018**, *107*, 1724–1731. [CrossRef] [PubMed]
4. Jung, J.; Raghavendra, G.M.; Kim, D.; Seo, J. One-step synthesis of starch-silver nanoparticle solution and its application to antibacterial paper coating. *Int. J. Biol. Macromol.* **2018**, *107*, 2285–2290. [CrossRef] [PubMed]
5. Ahmed, S.; Ahmad, M.; Swami, B.L.; Ikram, S. A review on plants extract mediated synthesis of silver nanoparticles for antimicrobial applications: A green expertise. *J. Adv. Res.* **2016**, *7*, 17–28. [CrossRef] [PubMed]
6. He, Y.; Li, X.; Zheng, Y.; Wang, Z.; Ma, Z.; Yang, Q.; Yao, B.; Zhao, Y.; Zhang, H. A green approach for synthesizing silver nanoparticles, and their antibacterial and cytotoxic activities. *New J. Chem.* **2018**, *42*, 2882–2888. [CrossRef]
7. Michalska, M.; Iwan, A.; Andrzejczuk, M.; Roguska, A.; Sikora, A.; Boharewicz, B.; Tazbir, I.; Hreniak, A.; Popłoński, S.; Korona, K.P.; et al. Analysis of the surface decoration of TiO_2 grains using silver nanoparticles obtained by ultrasonochemical synthesis towards organic photovoltaics. *New J. Chem.* **2018**, *42*, 7340–7354. [CrossRef]
8. Yan, L.; Xiang, Y.; Yu, J.; Wang, Y.; Cui, W. Fabrication of Antibacterial and Antiwear Hydroxyapatite Coatings via in Situ Chitosan-Mediated Pulse Electrochemical Deposition. *ACS Appl. Mater. Interfaces* **2017**, *9*, 5023–5030. [CrossRef]
9. Sokołowski, K.; Szynkowska, M.I.; Pawlaczyk, A.; Łukomska-Szymańska, M.; Sokołowski, J. The impact of nanosilver addition on element ions release form light-cured dental composite and compomer into 0.9% NaCl. *Acta Biochim. Pol.* **2014**, *61*, 317–323.
10. Nanda Kumar, D.; Chandrasekaran, N.; Mukherjee, A. Horseradish peroxidase-mediated *in situ* synthesis of silver nanoparticles: Application for sensing of mercury. *New J. Chem.* **2018**, *42*, 13763–13769. [CrossRef]
11. Li, X.; Yang, Z.; Peng, Y. The interaction of silver nanoparticles with papain and bromelain. *New J. Chem.* **2018**, *42*, 4940–4950. [CrossRef]
12. Raghavendra, G.M.; Jung, J.; kim, D.; Seo, J. Step-reduced synthesis of starch-silver nanoparticles. *Int. J. Biol. Macromol.* **2016**, *86*, 126–128. [CrossRef] [PubMed]
13. Shao, Y.; Wu, C.; Wu, T.; Yuan, C.; Chen, S.; Ding, T.; Ye, X.; Hu, Y. Green synthesis of sodium alginate-silver nanoparticles and their antibacterial activity. *Int. J. Biol. Macromol.* **2018**, *111*, 1281–1292. [CrossRef] [PubMed]
14. Ghodake, G.; Lim, S.R.; Lee, D.S. Casein hydrolytic peptides mediated green synthesis of antibacterial silver nanoparticles. *Colloids Surf. B Biointerfaces* **2013**, *108*, 147–151. [CrossRef] [PubMed]
15. Song, Z.; Ma, Y.; Xia, G.; Wang, Y.; Kapadia, W.; Sun, Z.; Wu, W.; Gu, H.; Cui, W.; Huang, X. In vitro and in vivo combined antibacterial effect of levofloxacin/silver co-loaded electrospun fibrous membranes. *J. Mater. Chem. B* **2017**, *5*, 7632–7643. [CrossRef]
16. Tamboli, D.P.; Lee, D.S. Mechanistic antimicrobial approach of extracellularly synthesized silver nanoparticles against gram positive and gram negative bacteria. *J. Hazard. Mater.* **2013**, *260*, 878–884. [CrossRef] [PubMed]
17. Kim, D.Y.; Suk Sung, J.; Kim, M.; Ghodake, G. Rapid production of silver nanoparticles at large-scale using gallic acid and their antibacterial assessment. *Mater. Lett.* **2015**, *155*, 62–64. [CrossRef]
18. Castro-Mayorga, J.L.; Freitas, F.; Reis, M.A.M.; Prieto, M.A.; Lagaron, J.M. Biosynthesis of silver nanoparticles and polyhydroxybutyrate nanocomposites of interest in antimicrobial applications. *Int. J. Biol. Macromol.* **2018**, *108*, 426–435. [CrossRef]
19. Calderón-Jiménez, B.; Johnson, M.E.; Montoro Bustos, A.R.; Murphy, K.E.; Winchester, M.R.; Vega Baudrit, J.R. Silver Nanoparticles: Technological Advances, Societal Impacts, and Metrological Challenges. *Front. Chem.* **2017**, *5*, 1–26. [CrossRef]
20. Hutchison, J.E. Greener nanoscience: A proactive approach to advancing applications and reducing implications of nanotechnology. *ACS Nano* **2008**, *2*, 395–402. [CrossRef]
21. Siddiqi, K.S.; Husen, A.; Rao, R.A.K. A review on biosynthesis of silver nanoparticles and their biocidal properties. *J. Nanobiotechnology* **2018**, *16*, 14. [CrossRef] [PubMed]
22. Kim, D.Y.; Kim, M.; Shinde, S.; Sung, J.S.; Ghodake, G. Cytotoxicity and antibacterial assessment of gallic acid capped gold nanoparticles. *Colloids Surf. B Biointerfaces* **2017**, *149*, 162–167. [CrossRef] [PubMed]
23. Orak, T.; Caglar, O.; Ortucu, S.; Ozkan, H.; Taskin, M. Chicken feather peptone: A new alternative nitrogen source for pigment production by Monascus purpureus. *J. Biotechnol.* **2018**, *271*, 56–62. [CrossRef] [PubMed]

24. Luo, K.; Jung, S.; Park, K.-H.; Kim, Y.-R. Microbial Biosynthesis of Silver Nanoparticles in Different Culture Media. *J. Agric. Food Chem.* **2018**, *66*, 957–962. [CrossRef] [PubMed]
25. Gallagher, W. FTIR Analysis of Protein Structure. *Biochemistry* **1997**, *392*, 662–666.
26. Barth, A. Infrared spectroscopy of proteins. *Biochim. Biophys. Acta-Bioenerg.* **2007**, *1767*, 1073–1101. [CrossRef] [PubMed]
27. Balaji, D.S.; Basavaraja, S.; Deshpande, R.; Mahesh, D.B.; Prabhakar, B.K.; Venkataraman, A. Extracellular biosynthesis of functionalized silver nanoparticles by strains of Cladosporium cladosporioides fungus. *Colloids Surfaces B Biointerfaces* **2009**, *68*, 88–92. [CrossRef]
28. Anandalakshmi, K.; Venugobal, J.; Ramasamy, V. Characterization of silver nanoparticles by green synthesis method using Pedalium murex leaf extract and their antibacterial activity. *Appl. Nanosci.* **2016**, *6*, 399–408. [CrossRef]
29. Osonga, F.J.; Akgul, A.; Yazgan, I.; Akgul, A.; Ontman, R.; Kariuki, V.M.; Eshun, G.B.; Sadik, O.A. Flavonoid-derived anisotropic silver nanoparticles inhibit growth and change the expression of virulence genes in Escherichia coli SM10†. *RSC Adv.* **2018**, *8*, 4649–4661. [CrossRef]
30. Singh, P.; Kim, Y.J.; Singh, H.; Mathiyalagan, R.; Wang, C.; Yang, D.C. Biosynthesis of anisotropic silver nanoparticles by bhargavaea indica and their synergistic effect with antibiotics against pathogenic microorganisms. *J. Nanomater.* **2015**, *2015*, 4. [CrossRef]
31. Sangappa, Y.; Latha, S.; Asha, S.; Sindhu, P.; Parushuram, N.; Shilpa, M.; Byrappa, K.; Narayana, B. Synthesis of anisotropic silver nanoparticles using silk fibroin: Characterization and antimicrobial properties. *Mater. Res. Innov.* **2017**, *23*, 79–85. [CrossRef]
32. Pal, S.; Tak, Y.K.; Song, J.M. Does the antibacterial activity of silver nanoparticles depend on the shape of the nanoparticle? A study of the gram-negative bacterium Escherichia coli. *J. Biol. Chem.* **2015**, *290*, 1712–1720. [CrossRef] [PubMed]
33. Chook, S.W.; Chia, C.H.; Zakaria, S.; Ayob, M.K.; Chee, K.L.; Huang, N.M.; Neoh, H.M.; Lim, H.N.; Jamal, R.; Rahman, R.M.F.R.A. Antibacterial performance of Ag nanoparticles and AgGO nanocomposites prepared via rapid microwave-assisted synthesis method. *Nanoscale Res. Lett.* **2012**, *7*, 541. [CrossRef] [PubMed]
34. Gomaa, E.Z. Silver nanoparticles as an antimicrobial agent: A case study on *Staphylococcus aureus* and *Escherichia coli* as models for Gram-positive and Gram-negative bacteria. *J. Gen. Appl. Microbiol.* **2017**, *63*, 36–43. [CrossRef] [PubMed]

polymers

MDPI

Article

Effect of Operational Conditions on the Behaviour and Associated Costs of Mixed Microbial Cultures for PHA Production

Francisco Cabrera [1], Álvaro Torres [1], José Luis Campos [2] and David Jeison [3,*]

[1] Department of Chemical Engineering, Universidad de La Frontera, Av. Francisco Salazar 01145, Temuco 4780000, Chile; f.cabrera01@ufromail.cl (F.C.); alvaro.torres@ufrontera.cl (Á.T.)
[2] Facultad de Ingeniería y Ciencias, Universidad Adolfo Ibáñez, Avda. Padre Hurtado 750, Viña del Mar 2520000, Chile; jluis.campos@uai.cl
[3] Escuela de Ingeniería Bioquímica, Pontificia Universidad Católica de Valparaíso, Av. Brasil 2085, Valparaíso 2362803, Chile
* Correspondence: david.jeison@pucv.cl; Tel.: +56-32-237-2017

Received: 28 December 2018; Accepted: 17 January 2019; Published: 22 January 2019

Abstract: Massive production and disposal of petrochemical derived plastics represent relevant environmental problems. Polyhydroxyalkanoates (PHA) are a renewable alternative that can even be produced from wastes. The production of PHA from acetate using mixed microbial cultures was studied. The effect of two key operational conditions was evaluated, i.e., substrate concentration and cycle length. The effects of these factors on several responses were studied using a surface response methodology. Several reactors were operated under selected conditions for at least 10 solids retention times to ensure stable operation. Results show that conditions providing higher PHA content involve lower biomass productivities. This has a great impact on biomass production costs. Results suggest then that PHA content alone may not be a reasonable criterion for determining optimal conditions for PHB production. If production costs need to be reduced, conditions that provide a lower PHA content in the selection reactor, but a higher biomass productivity may be of interest.

Keywords: PHA; mixed microbial cultures; bioplastics; feast-famine; cost

1. Introduction

Plastics represent a serious environmental problem. They are usually non-biodegradable, are produced from non-renewable resources, and have low densities, meaning that they occupy a large volume in municipal landfills. Moreover, marine plastics pollution is a growing source of concern. It is mainly caused by single use plastics, which is rapidly changing policies and legislation in many countries around the world [1]. Polyhydroxyalkanoates (PHA) have been proposed as a potential replacement for traditional petrochemical based plastics, since they can be used in a wide range of industrial applications [2]. PHA are polyoxoesters of hydroxyalkanoic acids, which are synthesized by some bacteria as intracellular storage compounds [3]. They are biodegradable and can be produced from renewable resources [4].

The production of PHAs has been shown to be technically feasible when using known high-PHA accumulating bacterial cultures, like *Cupravidus necator* [5,6], or modified bacteria, like *Escherichia coli*. These microorganisms have reached internal PHA contents up to 90% dry weight when working with batch reactors [7]. The costs associated with inoculum preservation, raw materials, and downstream processing in PHA production make these polymers nowadays five to 10-fold more expensive than their fuel-based counterparts [8]. Moreover, when well defined substrates are used, this item can contribute one third of the operational costs [9]. In order to decrease the costs of inoculum preservation

in axenic conditions, reduce the costs of raw materials, and increase the production efficiencies of PHAs, much research has been conducted during the last 20 years in the use of mixed microbial cultures (MMCs). The application of MMCs enables the use of volatile fatty acids (VFA) as substrates, which in turn can be derived from organic wastes by dark fermentation, further reducing potential costs and revalorizing waste organic compounds [10].

PHAs production using MMCs requires a first stage of culture enrichment of PHA accumulating microorganisms [11]. Transient conditions of carbon supply are normally used for this purpose: Consecutive phases of carbon source availability (feast) and scarcity (famine), which induces a selective pressure favouring the development of PHA accumulating microorganisms. This feast-famine operation strategy has also been regarded as aerobic dynamic feeding (ADF) [12]. Starvation for a certain period can cause a decrease in the amount of intracellular components needed for growth. After starvation, when the substrate is available again, storage occurs instead of growth since the amount of enzymes required for storage are lower than RNA and enzymes required for growth [13].

Several parameters have been identified as being relevant for the selection of MMC with an improved PHA accumulation capacity. Some of them are the organic load rate (OLR), influent substrate concentration, type of substrate, sludge retention time, temperature, pH, oxygen supply, carbon to nitrogen ratio, and cycle length [12,14,15]. In general, it has been observed that a very high OLR in selective reactors is related to a decrease in the polyhydroxybutyrate (PHB) storage capacity due to the prevalence of cellular growth [16]. Furthermore, differences on the feeding pattern and substrate concentration have been shown considerable differences in the PHA content and yields [17]. On the other hand, the length of the cycle (total cycle time) has been shown to influence the performance of PHA production as well, increasing the substrate uptake rate when decreasing the cycle length [18].

When considering PHA production using VFA from waste, significant variations in the substrate concentration, composition, and availability may be expected. Changes in conditions will most likely require adjusting operational parameters to ensure efficient selection of an active PHA producing population. This problem could be addressed by adjusting the feast and famine intervals of each operation cycle, according to the influent availability and characteristics. To do so, information is needed about the influence of conditions, such as the feed concentration (which determines OLR) and cycle length of the PHB accumulation. At the same time, different conditions also affect the costs associated with the production of PHA-enriched biomass. Then, conditions favouring maximal PHA accumulation may not coincide with those providing lower costs. The aim of this work is to evaluate the influence of the cycle length and carbon concentration on the dynamics of the feast-famine process. The influence of both parameters was determined using surface response methodology. By means of the kinetics of acetate and oxygen consumption, feast and famine phases were identified and studied. Moreover, costs estimations were performed to evaluate the effect of the same parameters on the first stages of PHA production: Selection, enrichment, and biomass separation. Studying the costs associated with PHA production is relevant, since the price of PHA would be mainly influenced by process costs [19].

2. Materials and Methods

2.1. Reactor Operation

Several sequential batch bioreactor (SBR) runs were performed. Four SBRs with a working volume of 2 L were implemented for that purpose. All SBRs were operated under ADF conditions, which consisted of a feed period, a variable period of aerobic reaction, and a final withdrawal of the mixed liquor from the mixed vessel. SBRs were operated using acetate as the sole carbon source. The feed and withdrawal periods were 6 and 10 min. The feed flow was 2.5 L/h. Withdraw was set to remove the same volume added during feeding (0.25 L). No settling phase was performed. Then, the sludge retention time (SRT) was equal to the hydraulic retention time (HRT).

Conditions imposed during SBR runs were organized using surface response methology, applying a face-centred central composite design [20]. Studied factors were the feed concentration and total cycle length (feast + famine). Each factor was studied at 3 levels: 30, 75, and 120 mM and 4, 8, and 12 h for the acetate concentration and total cycle length, respectively. The central point was replicated 3 times. Conditions applied are shown in Table 1 (11 reactor runs). Different responses were studied, such as the feast/famine (F/F) length ratio, biomass productivity, maximum PHB content, and PHB productivity. ANOVA analyses were made for each response. In all cases, the model significance and lack of fit tests were performed to check that models were relevant and fitted the experimental data. All statistical analyses were made considering $\alpha = 0.05$.

Table 1. Operational conditions in all enrichment SBRs from the experimental design.

Run	Cycle Length (h)	Acetate Concentration in the Feed (mM)	Organic Loading Rate (g/L·d)	SRT * (d)
SBR #1	4	30	1.4	1.3
SBR #2	4	75	3.4	1.3
SBR #3	4	120	5.4	1.3
SBR #4	8	30	0.7	2.7
SBR #5	8	75	1.7	2.7
SBR #6	8	75	1.7	2.7
SBR #7	8	75	1.7	2.7
SBR #8	8	120	2.7	2.7
SBR #9	12	30	0.5	4.0
SBR #10	12	75	1.1	4.0
SBR #11	12	120	1.8	4.0

* Since no biomass retention was applied, SRT is equal to HRT.

A complementary SBR was run to provide a fairly stable inoculum for each of the reactor runs described in Table 1. This SBR was in turn inoculated with activated sludge from the sewage treatment plant of the city of Temuco (Chile). The feed concentration was 120 mM, and the cycle length was 6 h. During the operation of all SBRs, aeration was provided at an airflow rate of 3–5 L/min. All reactors were also mechanically stirred at 60 rpm.

The influent was composed of sodium acetate and a mineral medium. The mineral medium composition was 600 mg/L $MgSO_4 \cdot 7H_2O$, 160 mg/L NH_4Cl, 100 mg/L mg EDTA, 92 mg/L mg K_2HPO_4, 45 mg/L KH_2PO_4, 70 mg/L $CaCl_2 \cdot 2H_2O$, thiourea (10 mg/L), and 2 mL/L of trace elements solution. The trace solution composition was 1500 mg/L $FeCl_3 \cdot 6H_2O$, 150 mg/L H_3BO_3, 150 mg/L $CoCl_2 \cdot 6H_2O$, 120 mg/L $MnCl_2 \cdot 4H_2O$, 120 mg/L $ZnSO_4 \cdot 7H_2O$, 60 mg/L $Na_2MoO_4 \cdot 2H_2O$, 30 mg/L $CuSO_4 \cdot 5H_2O$, and 30 mg/L of KI.

Dissolved oxygen (DO) and pH were acquired online by means of electrodes. DO was measured using an optic industrial probe (WQ401, Global Water, College Station, TX, USA). Signals from sensors and pumps control were handled using a CompactDAQ system (cDAQ-9178 chasis, National Instruments, Austin, TX, USA) and a routine specially programmed for this purpose using LabView software (National Instruments).

2.2. Analytical Methods

Acetate was determined by gas-chromatography using a Flame Ionization Detector (Clarus 400, Perkin Elmer), using a Nukol™ capillary column (Sigma-Aldrich, Darmstadt, Germany). The cell dry weight was quantified using the volatile suspended solids (VSS) technique according to Standard Methods (APHA 2011).

PHB determination was performed according to Serafim et al. [21]. 5 mL of homogenized culture were collected, and five drops of formaldehyde were added to stop biological activity: Samples were then frozen and lyophilized for storage. The biomass samples were later resuspended in 1 mL acidic methanol (20% H_2SO_4) with 0.65 mg/mL of benzoic acid as the internal standard (Sigma Aldrich™).

The chloroform phase was collected and molecular sieves (0.3 nm) were added for water adsorption. One mL of the chloroform phase obtained was injected on-column in the same gas chromatograph used for acetate determination. A calibration curve was prepared by injecting standard concentrations of hydroxybutyric acid sodium salt (Sigma Aldrich) previously submitted to the procedure described for reactor samples.

2.3. Estimation of Costs for PHA-enriched Biomass Production

An estimation of the costs associated with the production of PHA-enriched biomass was performed, for each of the conditions described in Table 1. Capital and operating costs were considered for the process described in Figure 1. It consisted of three stages: Biomass selection, PHA accumulation, and biomass harvest (by centrifugation). This study included only biomass production (and not PHA extraction or purification) since that stage is the one that will be most affected by any changes of the operational parameters studied in this research.

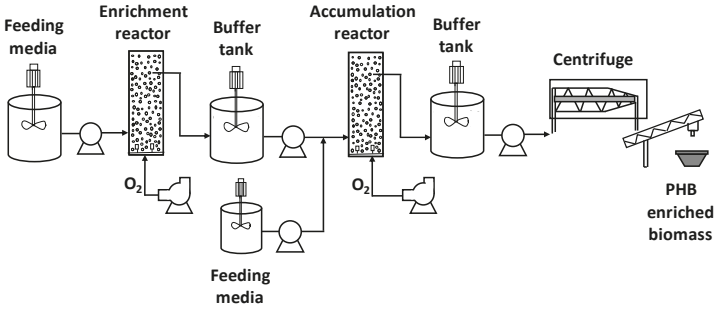

Figure 1. Process considered for costs estimation of biomass-enriched PHB.

Analysis was made considering the following conditions or assumptions:

- An annual production of 500 ton of PHA was considered as the calculation basis.
- The total volume needed for enrichment and accumulation stages were calculated according to the production rate of PHB of each stage. To calculate the number of reactors required, reactors with a useful volume of 8 m^3 were considered.
- The enrichment reactor produced biomass with a PHA content equal to that observed by the end of each operation cycle tested experimentally. The accumulation reactor produces biomass with a PHA content equal to that observed by the end of each feast cycle tested experimentally.
- The pumping capacity needed for each reactor was calculated taking into account the inlet flowrate supplied during the feeding time. Pumping energy consumption was calculated based on the inlet flowrate supplied and considering a reactor height of 4.6 m and an energy efficiency of the pump of 0.7.
- The oxygen requirements for the enrichment and accumulation reactors were determined by means of chemical oxygen demand (COD) mass balances. The air flowrate supplied was calculated using a mass transfer efficiency factor of 20%. Fans with a capacity of 3 m^3 air/s were considered.
- The total volume required for the feeding and buffer tanks was determined based on the flowrates of each stream and considering a storage period of 12 h. Tanks with a volume of 60 m^3 were chosen. Each tank was provided with one agitator whose specific power and energy efficiency were 0.01 kW·h/m^3 and 0.7, respectively.
- To separate the biomass generated during the accumulation stage, centrifuges with a capacity of 30 m^3/h were considered. A solid separation efficiency of 100% was assumed.

- Energy costs were calculated taking into account the energy consumed by agitators, pumps, and fans, considering a price of 15.8 cents USD/kW·h.
- Capital costs were calculated according to [22]. Prices were updated taking into account an annual increase of costs of 3%. A lifetime of 20 years was considered.

All equations used for costs estimations are reproduced in the Appendix A.

3. Results and Discussion

3.1. SBRs Operation

Figure 2A shows a typical operation cycle (data from SBR #2, see Table 1). After feeding, oxygen uptake increases, producing a sudden drop in DO. Oxygen concentration remains almost null, while acetate is present in the reactor, as a result of a high oxygen uptake rate. During this period, biomass PHB content increases. After acetate is depleted, oxygen rapidly increases as the oxygen consumption rate is reduced. As described by previous authors [23], these changes in the patterns of DO correlate well with the limits of the feast and famine phases. Then, the oxygen profile can then easily be used to determine the feast/famine boundary. Figure 2A also shows how PHB is produced during the feast and consumed during the famine. As a result, similar PHB concentrations were observed at the beginning and end of the cycle.

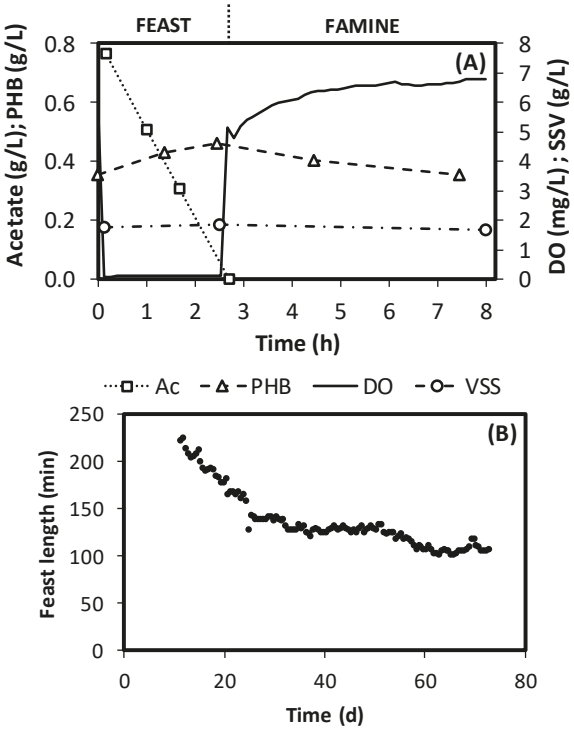

Figure 2. (**A**) Typical behaviour of an operation cycle (SBR #2). (**B**) Evolution of the feast length during operation of SBR #10.

Obviously, the application of the conditions described in Table 1 induced changes in the biomass developed in the reactors. Figure 2B presents the evolution of the feast phase length of SBR #10. It can be observed that the feast length decreases rapidly during the first 30 days of operation. No changes

are observed after day 60, indicating that SBR is in a stable state of operation. The time required to reach the steady state depended on the applied operational conditions. To ensure that the responses measured in the design of experiments were representative of the applied conditions, the operation was kept until steady state conditions were achieved, which was identified by a constant feast length. Only then analyses were performed, and responses were evaluated. As a result, all SBRs were operated for a period exceeding 10 SRT. As expected, SBR stabilization took longer in those cases when applied conditions were far from those applied in the SBR operated to provide the inoculum.

Table 2 presents feast and famine phases lengths for each SBR. Values from the end of the operation are presented, when the stable operation was identified, based on the criteria described above.

Table 2. Feast and famine phases length (by the end of operation) for the SBR runs described in Table 1.

Run	Feast Length (h)	Famine Length (h)
SBR #1	0.88	3.12
SBR #2	1.90	2.10
SBR #3	2.97	1.03
SBR #4	0.81	7.19
SBR #5	2.92	5.08
SBR #6	3.40	4.60
SBR #7	2.86	5.14
SBR #8	4.79	3.21
SBR #9	1.15	10.85
SBR #10	2.85	9.15
SBR #11	4.38	7.63

3.2. Effect of Substrate Concentration and Cycle Length on SBR Operation

Figure 3 presents the effect of the studied factors (cycle length and acetate concentration in the feed) over the studied responses. Figure 3A presents the OLR. Since the feed volume per cycle remained constant, changes in the influent concentration resulted in different applied OLRs. On the other hand, increases in the cycle time reduced the applied loading. As a result, OLRs were in the range of 0.5–5.5 g acetic acid/L·d. Figure 3B presents the F/F ratios, which is the relation between times presented in Table 2. Figure shows a direct relation between the F/F ratio and acetate concentration, and an inverse relation with the cycle length. Such a result is expected, since a higher feed concentration results in a higher loading rate, requiring more time for the culture to consume substrate, increasing the feast time. On the other hand, a higher total cycle will result in a higher famine time. In general, the F/F ratios observed in this study are high when compared with the ones reported by other authors [24–26], who normally applied values below 0.5. Famine lengths observed in this study were in the range of 1–11 h (see Table 2).

Figure 3C presents the maximum biomass PHB content, which is attained by the end of the feast period (beginning of famine), as can be seen in Figure 2A. The maximum PHB content ranged between 10% and 90%, revealing how determinant the studied parameters are in terms of selecting microorganisms with a high PHB storage capacity. An increase in the cycle time induced an increment on the maximum PHB content. This is most likely the result of the consequent increment of the famine length. Under tested conditions, the feast is mainly a function of the applied acetate concentration, so increases of the cycle time at a constant acetate concentration will increase the famine length. Decreasing F/F enhances growth limitation, favouring PHA storage [24]. On the other hand, a clear increase in the maximum PHB content was observed when increasing the acetate concentration (and, therefore, the organic loading rate), behaviour that has already been already observed in previous studies [16,27].

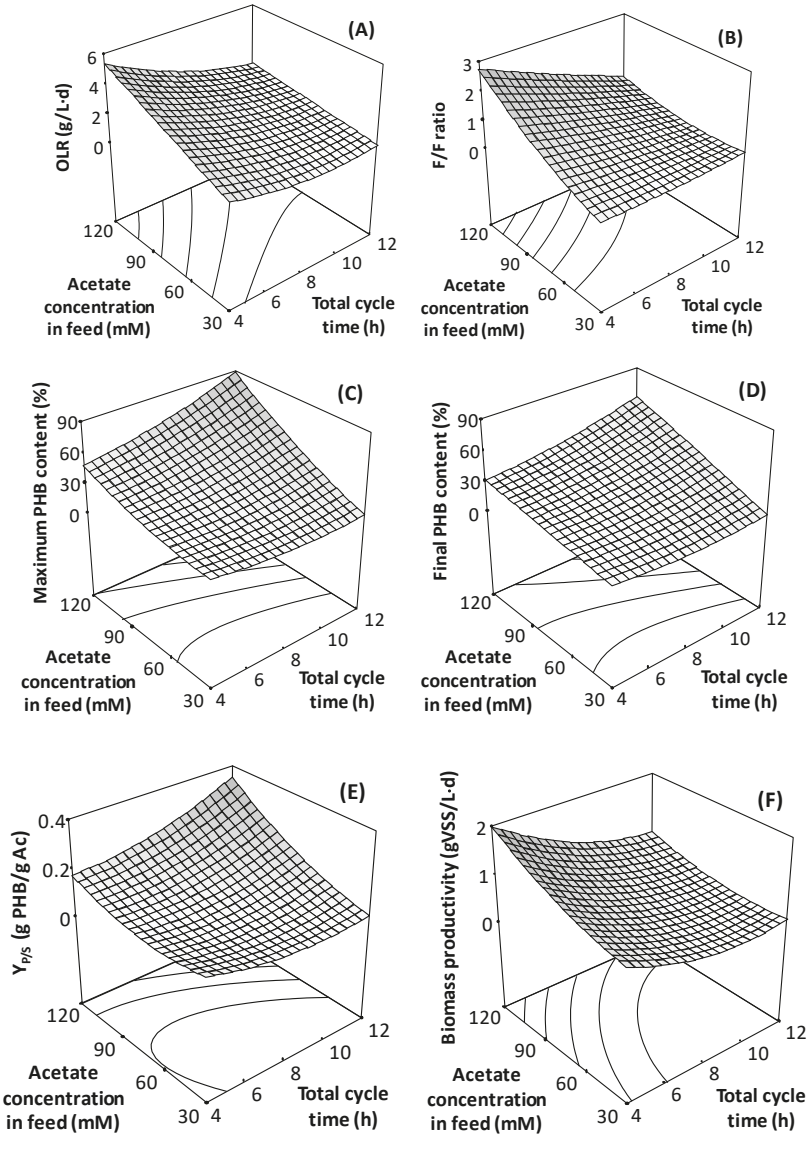

Figure 3. Selected responses observed during surface response methodology. Factors tested: Acetate concentration in the feed and total cycle time. Responses: (**A**) OLR, (**B**) F/F ratio, (**C**) maximum PHB content of biomass, (**D**) PHB content of biomass by the end of the cycle, (**E**) yield PHA/acetic acid, (**F**) biomass productivity.

Considering that the draw of biomass takes place by the end of each cycle, the final PHB content, i.e., the one by the end of famine, is probably a more relevant information for reactor operation, than maximum content (see Figure 3D). As expected, values are lower than those shown in Figure 3C, because of PHB consumption during the famine. Nevertheless, a constant relation between the maximum and final PHB contents was observed, irrespective of the conditions tested, as can be seen in Figure 4. It is clear that during famine, about 30% of the PHB was consumed. Proportionality between

the maximum and final PHB content indicates that the second value can be a good indicator of the first one. Then, decisions may be taken based on the PHB content at the end of the cycle, which may be easier to determine under full-scale operational conditions, or when detailed control or follow up of the reactor may not be feasible.

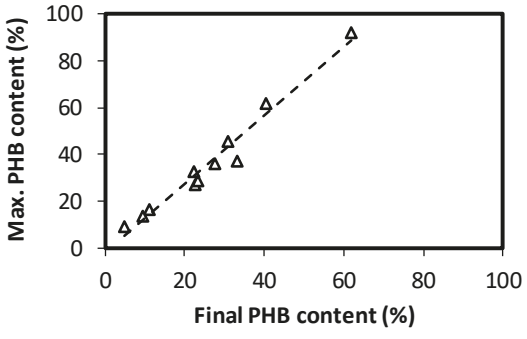

Figure 4. Relation between the maximum and final PHB contents for the operation of SBR reactors.

A similar trend as that described for the biomass PHB content can be observed for $Y_{P/S}$, the product/substrate yield (Figure 3E). This value has been computed considering the maximum PHB biomass content. As expected, conditions providing a higher $Y_{P/S}$ are those generating a higher PHB biomass content, since more substrate is oriented towards polymers' accumulation, as already described.

Results correspond to the selection reactors, which will produce biomass for an accumulation step, where further conditions may be imposed to enhance PHB accumulation (such as nitrogen limitation). Then, biomass productivity is also relevant for full-scale application, since a higher productivity will produce more biomass to potentially feed such an accumulating reactor. Biomass productivity, in terms of VSS, is presented in Figure 3F. The average productivity is presented, i.e., the mass of biomass exiting the reactor after each cycle per volume of reactor divided by the cycle length. Values presented correspond to the total biomass, including the intracellular accumulated PHB. As expected, biomass productivity follows the same pattern as the applied OLR (Figure 3A), since complete substrate consumption is obtained under all conditions. Comparison of Figure 3D,F shows a compromise between the biomass production and observed PHA accumulation, a phenomenon that has been previously descried [16,23]. Depending on the eventual performance of an accumulation step, a lower content of PHB may be accepted if a higher amount of biomass can be produced in the selection step. A parameter that may provide useful criteria for the determination of operational conditions could be PHB productivity during selection reactors operation. Unfortunately, PHB productivity cannot be presented in the form of a surface response, since ANOVA analysis showed a significant lack of fit ($\alpha = 5\%$), meaning that the second order model used does not correctly represent the observed response variation. Then, the observed PHB productivity is presented in Table 3. Two productivities can be evaluated, one in terms of the maximum PHB content (observed by the end of the feast) and one based on the amount of PHB at the end of the cycle. The first productivity would be the one observed if biomass is harvested by the end of the feast. Both productivities are proportional, as is the case of both biomass PHB contents (Figure 4).

Table 3. PHB average productivity for the operation of SBR.

Run	PHB Productivity Based on Maximum PHB (g/L·d)	PHB Productivity Based on Final PHB (g/L·d)
SBR #1	0.16	0.10
SBR #2	0.32	0.22
SBR #3	1.01	0.68
SBR #4	0.03	0.02
SBR #5	0.18	0.15
SBR #6	0.19	0.16
SBR #7	0.16	0.12
SBR #8	0.51	0.33
SBR #9	0.03	0.02
SBR #10	0.15	0.13
SBR #11	0.68	0.46

3.3. Estimation of Costs for PHA-Enriched Biomass Production

Figure 5 shows the costs estimation for PHA-enriched biomass, as a function of the biomass productivity and PHA content by the end of each cycle. To construct these charts, the data coming from the experiments described in Table 1 were used. Few reports are available dealing with costs of PHA production in literature, such as [28,29]. These studies are very useful to determine the industrial applicability of mixed culture based PHB production. However, the results are greatly dependent on the particular conditions and process selected for the analyses. In the case of this study, a sole reactor volume was considered, so the replication of reactors was considered when higher fermentation volumes were required. Then, the economy of scale is not taken into consideration. However, it provides an opportunity to visualise the potential impact of operational conditions on potential associated costs. Observation of Figure 5A,B clearly shows the already identified compromise between biomass productivity and PHA content. Conditions providing a high level of PHB accumulation in the selection process involve low biomass productivity, which in turn affect overall costs. Conditions tested in this research provided a wide range of PHB contents and biomass productivities, producing great differences in the associated costs for biomass production. Results provided by this research confirms the great relevance that selection appropriate conditions for biomass selection can produce on PHB-enriched biomass quality and production costs. Results also suggests that PHB content alone may not be a reasonable criterion for determining optimal conditions for PHB production. If costs need to be reduced, conditions providing a lower PHB content in the selection reactor, but a higher biomass productivity may be of interest, as long as the reduction of PHB content does not involve significant increases in PHB extraction and purification costs.

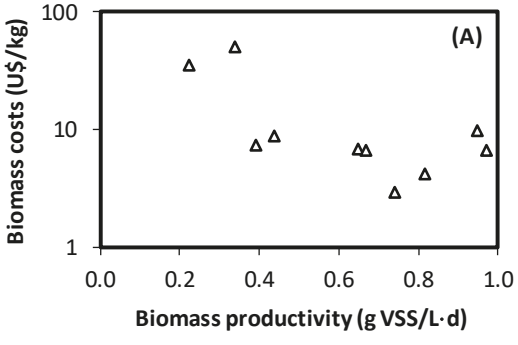

Figure 5. *Cont.*

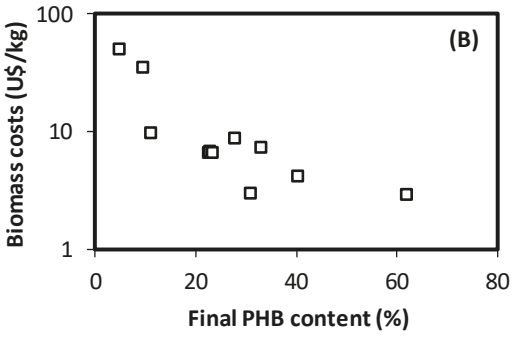

Figure 5. Cost estimation for production of PHA-enriched biomass as a function of (**A**) the total biomass productivity and (**B**) PHB content by the end of the cycle.

4. Conclusions

Substrate concentration and cycle length proved to have a deep impact on SBR operation for the selection of PHB-accumulating biomass. Both factors were shown to have statistically significant effects over biomass productivity, PHB content, and product/substrate yield. The PHB content by the end of the feast and famine stages was shown to have a constant relation, irrespective of the conditions tested. In all cases, 30% of the existing PHB was consumed during famine. Biomass productivity was expected to have a relevant effect on the costs associated with the production of PHA-enriched biomass. Since the results showed a negative relation between biomass productivity and PHA content, costs for biomass production are higher for those conditions providing higher PHA contents in the biomass. Thus, maximising PHB content in the selection reactor may provide excessive costs for biomass production.

Author Contributions: F.C. designed and performed the experiments, Á.T. analysed the data, J.L.C. performed the cost estimation, D.J. conceived and designed the experiments and analysed the data. All authors contributed with the writing and proofreading of the paper.

Funding: This research was funded by CRHIAM Centre grant number CONICYT/FONDAP/15130015. The APC was funded by Dirección de Investigación from Pontificia Universidad Católica de Valparaíso, grant number 203.735.

Conflicts of Interest: The authors declare no conflicts of interest.

Appendix A. Appendix: Equations for Costs Estimation of PHA-Enriched Biomass

Capital and operating costs were calculated for an annual production of PHB of 500 Tons.

Number of SBRs for PHB accumulation:

$$N_{SBR\ Accum} = round.up\left(\frac{PHB\ production\left(\frac{Ton\ PHB}{year}\right)\cdot 1000\left(\frac{kg\ PHB}{ton\ PHB}\right)\cdot\frac{1}{365}\left(\frac{year}{d}\right)}{\left[\left(r_{PHB}\right)_{feast}\cdot\left(\frac{kg\ PHB}{m^3\cdot d}\right)\cdot\frac{t_{feast}}{t_{fed}+t_{feast}+t_{withdrawal}}+[VSS]_{end\ of\ enrichment\ cycle}\left(\frac{kg\ VSS}{m^3}\right)\cdot PHH_{fraction\ end\ of\ enrichment\ cycle}\left(\frac{kg\ PHB}{kg\ VSS}\right)\cdot\left(1-VF_{fed}\cdot\frac{24\ \left(\frac{h}{d}\right)}{\left(t_{fed}+t_{feast}+t_{withdrawal}\right)\ (h)}\right)\right]\cdot V_r\left(\frac{m^3}{reactor}\right)}\right)+1$$

VF_{fed}= Volumetric fraction of feeding media supplied per cycle (1/8); V_r= Useful volume of the reactor (8.0 m^3; Total volume: 10.5 m^3; H/D: 4)

Number of SBRs needed to carry out biomass enrichment:

$$N_{SBR\ Enrichment} = round.up\left(\frac{PHB\ production\left(\frac{Ton\ PHB}{year}\right)\cdot 1000\left(\frac{kg\ PHB}{ton\ PHB}\right)\cdot\frac{1}{365}\left(\frac{year}{d}\right)-\left(r_{PHB}\right)_{feast}\cdot\left(\frac{kg\ PHB}{m^3\cdot d}\right)\cdot\frac{t_{feast}}{t_{fed}+t_{feast}+t_{withdrawal}}\cdot\left(N_{SBR\ Accum}-1\right)\ (reactor)\cdot V_r\ \left(\frac{m^3}{reactor}\right)}{\left[[VSS]_{end\ of\ enrichment\ cycle}\left(\frac{kg\ VSS}{m^3}\right)\cdot PHH_{fraction\ end\ of\ enrichment\ cycle}\left(\frac{kg\ PHB}{kg\ VSS}\right)\cdot\frac{24\ \left(\frac{h}{d}\right)}{icycle\ Enrichment\ (h)}\right]\cdot V_r\left(\frac{m^3}{reactor}\right)}\right)+1$$

$VER_{Enrichment}$= Volumetric exchange ratio of the enrichment reactor (1/8); V_r= Useful volume of the reactor (8.0 m^3; Total volume: 10.5 m^3; H/D: 4)

Flow rate fed of SBRs for PHB accumulation:

$$Flowrate_{Fed\ Acum}\left(\frac{m^3}{d}\right) = VF_{fed}\cdot V_r\left(\frac{m^3}{reactor}\right)\cdot(N_{SBR_{Accum}}-1)\ (reactor)\cdot\frac{24\left(\frac{h}{d}\right)}{(t_{fed}+t_{feast}+t_{withdrawal})\ (h)}$$

Flow rate from enrichment SBRs to SBRs for PHB accumulation:

$$Flowrate_{Enrich\ Accum}\left(\frac{m^3}{d}\right) = (1-VF_{fed})\cdot V_r\left(\frac{m^3}{reactor}\right)\cdot(N_{SBR_{Accum}}-1)\ (reactor)\cdot\frac{24\left(\frac{h}{d}\right)}{(t_{fed}+t_{feast}+t_{withdrawal})\ (h)}$$

Flow rate fed of SBRs for PHB accumulation:

$$Flowrate_{Fed\ Enrich}\left(\frac{m^3}{d}\right) = VER_{Enrichment}\cdot V_r\left(\frac{m^3}{reactor}\right)\cdot(N_{SBR_{Enrich}}-1)\ (reactor)\cdot\frac{24\left(\frac{h}{d}\right)}{t_{cycle\ Enrichment}\ (h)}$$

Pumping capacity:

$$Flowrate\ Pump_{Fed\ Accum}\left(\frac{m^3}{s}\right) = \frac{VF_{fed}\cdot V_{r\ Accum}(m^3)}{t_{fed}(\min)\cdot\frac{1}{60}\left(\frac{min}{s}\right)}$$

$$Flowrate\ Pump_{Enrich-Accum}\left(\frac{m^3}{s}\right) = \frac{\left(1-VF_{fed}\right)\cdot V_{r\ Accum}(m^3)}{t_{fed}(\min)\cdot\frac{1}{60}\left(\frac{min}{s}\right)}$$

$$Flowrate\ Pump_{Fed\ Enrichment}\left(\frac{m^3}{s}\right) = \frac{VER_{Enrichment}\cdot V_{r\ Enrichment}(m^3)}{t_{fed}(\min)\cdot\frac{1}{60}\left(\frac{min}{s}\right)}$$

Number of pumps:

$$N_{Pump\ fed\ Accum} = round.up\left(\frac{Flowrate_{Fed\ Accum}\left(\frac{m^3}{d}\right)}{Flowrate\ Pump_{Fed\ Accum}\left(\frac{m^3}{s}\right)\cdot 86400\left(\frac{s}{d}\right)}\right)+1$$

$$N_{Pump\ Enrich-Accum} = round.up\left(\frac{Flowrate_{Enrich-Accum}\left(\frac{m^3}{d}\right)}{Flowrate\ Pump_{Enrich-Accum}\left(\frac{m^3}{s}\right)\cdot 86400\left(\frac{s}{d}\right)}\right)+1$$

$$N_{Pump\ fed\ Enrichment} = round.up\left(\frac{Flowrate_{Fed\ Enrich}\left(\frac{m^3}{d}\right)}{Flowrate\ Pump_{Fed\ Enrichment}\left(\frac{m^3}{s}\right)\cdot 86400\left(\frac{s}{d}\right)}\right)+1$$

Pumping energy consumption:

$$Pump\ Power\ (W) = \frac{\rho_{H_2O}\left(\frac{kg}{m^3}\right)\cdot Flowrate\ Pump\left(\frac{m^3}{s}\right)\cdot H_r(m)}{\eta_{pump}}$$

η_{pump}= Energy efficiency of the pump (0.7); H_r= height of reactor (4.6 m)

$$Pumping\ energy\ consumption_{\ Fed\ Accum}\left(\frac{kW\cdot h}{d}\right) = \frac{Pump\ Power_{Fed\ Accum}\ (W)\cdot Flowrate_{Fed\ Accum}\left(\frac{m^3}{d}\right)}{Flowrate\ Pump_{Fed\ Accum}\left(\frac{m^3}{s}\right)\cdot 3.6\cdot 10^6\ \left(W/\left(\frac{kW\cdot h}{d}\right)\right)}$$

Sodium acetate consumption:

$$Inlet\ AcNa_{Enrichment}\left(\frac{kg\ AcNa}{d}\right) = [AcNa]_{fed}\left(\frac{kg\ AcNa}{m^3}\right)\cdot Flowrate_{Fed\ Enrichment}\left(\frac{m^3}{d}\right)$$

$$Inlet\ AcNa_{Accum}\left(\frac{kg\ AcNa}{d}\right) = [AcNa]_{fed}\left(\frac{kg\ AcNa}{m^3}\right)\cdot Flowrate_{Fed\ Acum}\left(\frac{m^3}{d}\right).$$

Oxygen consumption: Oxygen consumed during the operation of both the enrichment and accumulation systems was calculated based on a COD balance:

$$m_{O_2}\left(\frac{kg\ O_2}{d}\right) = m_{AcNa_i}\left(\frac{kg\ AcNa}{d}\right)\cdot \left[0.78\left(\frac{kg\ COD}{kg\ AcNa}\right) - Y_{\frac{PHB}{AcNa}}\left(\frac{kg\ PHB}{kg\ AcNa}\right)\cdot 1,67\left(\frac{kg\ COD}{kg\ PHB}\right) - Y_{\frac{X}{AcNa}}\left(\frac{kg\ Biomass}{kg\ AcNa}\right)\cdot 1,42\left(\frac{kg\ COD}{kg\ Biomass}\right)\right]$$

Fan flow rate calculation:

$$Q_{O_2}\left(\frac{m^3{}_{air}}{s}\right) = \frac{m_{O_2}\left(\frac{kg\ O_2}{d}\right)\cdot 22.4\left(\frac{m^3{}_{O_2}}{kmol\ O_2}\right)}{32\left(\frac{kg\ O_2}{kmol\ O_2}\right)\cdot 0.21\left(\frac{m^3{}_{O_2}}{m^3{}_{air}}\right)\cdot 86400\left(\frac{s}{d}\right)\cdot 0.2\left(\frac{kg\ O_2 transfered}{kg\ O_2 supplied}\right)}$$

Number of fan:

$$Number\ of\ fan_{Accum} = round.up\left(\frac{Q_{O_2}\left(\frac{m^3{}_{air}}{s}\right)}{Fan\ Flowrate\left(\frac{m^3{}_{air}}{s\cdot fan}\right)\cdot\frac{t_{feast}}{t_{fed}+t_{feast}+t_{withdrawal}}}\right)+1$$

$$Number\ of\ fan_{Enrichment} = round.up\left(\frac{Q_{O_2}\left(\frac{m^3{}_{air}}{s}\right)}{Fan\ Flowrate\left(\frac{m^3{}_{air}}{s\cdot fan}\right)\cdot\frac{t_{feast}+t_{famine}}{t_{fed}+t_{feast}+t_{famine}+t_{withdrawal}}}\right)+1$$

Fan flowrate: 3 m^3 air/s

$$Fan\ energy\ consumption\left(\frac{kW\cdot h}{d}\right) = 1\ \frac{kW\cdot h}{kg\ O_2}\cdot\left(m_{O_2 Enrich} + m_{O_2\ Acum}\right)\left(\frac{kg\ O_2}{d}\right)$$

Storage and buffer tanks:

To determine the total volume of tanks required in each stage, a storage period of 12 h was considered.

$$Number\ of\ storage\ tanks = round.up\left(\frac{Flowrate\left(\frac{m^3}{d}\right)\cdot 0.5\ d}{Volume\ of\ tank\ (m^3)}\right)+1$$

Volume of tank: 60 m^3

Agitators:

One agitator per tank was selected and the required power was calculated considering 0.01 kW·h/m^3 and an energy efficiency of 0.7.

Solids generated:

$$VSSgenerated\left(\frac{kg\ VSS}{d}\right) = \frac{PHB\ production\left(\frac{Ton\ PHB}{year}\right)\cdot 1000\left(\frac{kg\ PHB}{Ton\ PHB}\right)\cdot\frac{1}{365}\left(\frac{year}{d}\right)}{PHB_{fraction\ feast}\left(\frac{kg\ PHB}{kg\ VSS}\right)}$$

Centrifuge energy consumption:

$$Centrifuge\ energy\ consumption\left(\frac{kW{\cdot}h}{d}\right) = 0.3\ \frac{kW{\cdot}h}{kg\ VSS}{\cdot}VSSgenerated\left(\frac{kg\ VSS}{d}\right)$$

Number of centrifuges (centrifuge capacity: 30 m^3/h):

$$N_{centrifuge} = round.up\left(\frac{(Flowrate_{Enrichment-Accum} + Flowrate_{Fed-Accum})\left(\frac{m^3}{d}\right){\cdot}\frac{1}{24}\left(\frac{h}{d}\right)}{Centrifuge\ capacity\left(\frac{m^3}{h}\right)}\right) + 1$$

References

1. Xanthos, D.; Walker, T.R. International policies to reduce plastic marine pollution from single-use plastics (plastic bags and microbeads): A review. *Mar. Pollut. Bull.* **2017**, *118*, 17–26. [CrossRef] [PubMed]
2. Hong, C.; Hao, H.; Haiyun, W. Process optimization for PHA production by activated sludge using response surface methodology. *Biomass Bioenergy* **2009**, *33*, 721–727. [CrossRef]
3. Koller, M.; Gasser, I.; Schmid, F.; Berg, G. Linking ecology with economy: Insights into polyhydroxyalkanoate-producing microorganisms. *Eng. Life Sci.* **2011**, *11*, 222–237. [CrossRef]
4. Alvarez-Chavez, C.R.; Edwards, S.; Moure-Eraso, R.; Geiser, K. Sustainability of bio-based plastics: General comparative analysis and recommendations for improvement. *J. Clean. Prod.* **2012**, *23*, 47–56. [CrossRef]
5. Lee, W.-H.; Loo, C.-Y.; Nomura, C.T.; Sudesh, K. Biosynthesis of polyhydroxyalkanoate copolymers from mixtures of plant oils and 3-hydroxyvalerate precursors. *Bioresour. Technol.* **2008**, *99*, 6844–6851. [CrossRef] [PubMed]
6. Zhang, Y.-Z.; Liu, G.-M.; Weng, W.-Q.; Ding, J.-Y.; Liu, S.-J. Engineering of *Ralstonia eutropha* for the production of poly(3-hydroxybutyrate-co-3-hydroxyvalerate) from glucose. *J. Biotechnol.* **2015**, *195*, 82–88. [CrossRef] [PubMed]
7. Tan, G.Y.A.; Chen, C.L.; Li, L.; Ge, L.; Wang, L.; Razaad, I.M.N.; Li, Y.; Zhao, L.; Mo, Y.; Wang, J.Y. Start a research on biopolymer polyhydroxyalkanoate (PHA): A review. *Polymers* **2014**, *6*, 706–754. [CrossRef]
8. Raza, Z.A.; Abid, S.; Banat, I.M. Polyhydroxyalkanoates: Characteristics, production, recent developments and applications. *Int. Biodeterior. Biodegrad.* **2018**, *126*, 45–56. [CrossRef]
9. Choi, J.I.; Lee, S.Y. Process analysis and economic evaluation for poly(3-hydroxybutyrate) production by fermentation. *Bioprocess Eng.* **1997**, *17*, 335–342. [CrossRef]
10. Kleerebezem, R.; van Loosdrecht, M.C.M.M. Mixed culture biotechnology for bioenergy production. *Curr. Opin. Biotechnol.* **2007**, *18*, 207–212. [CrossRef]
11. Albuquerque, M.G.E.; Concas, S.; Bengtsson, S.; Reis, M.A.M. Mixed culture polyhydroxyalkanoates production from sugar molasses: The use of a 2-stage CSTR system for culture selection. *Bioresour. Technol.* **2010**, *101*, 7123–7133. [CrossRef]
12. Dias, J.M.L.; Lemos, P.C.; Serafim, L.S.; Oliveira, C.; Eiroa, M.; Albuquerque, M.G.E.; Ramos, A.M.; Oliveira, R.; Reis, M.A.M. Recent advances in polyhydroxyalkanoate production by mixed aerobic cultures: From the substrate to the final product. *Macromol. Biosci.* **2006**, *6*, 885–906. [CrossRef] [PubMed]
13. Daigger, G.T.; Grady, C.P.L. The dynamics of microbial growth on soluble substrates. A unifying theory. *Water Res.* **1982**, *16*, 365–382. [CrossRef]
14. Serafim, L.S.; Lemos, P.C.; Albuquerque, M.G.E.; Reis, M.A.M. Strategies for PHA production by mixed cultures and renewable waste materials. *Appl. Microbiol. Biotechnol.* **2008**, *81*, 615–628. [CrossRef] [PubMed]
15. Wen, Q.; Chen, Z.; Tian, T.; Chen, W. Effects of phosphorus and nitrogen limitation on PHA production in activated sludge. *J. Environ. Sci.* **2010**, *22*, 1602–1607. [CrossRef]
16. Dionisi, D.; Majone, M.; Vallini, G.A. Effect of the applied organic load rate on biodegradable polymer production by mixed microbial cultures in a sequencing batch reactor. *Biotechnol. Bioeng.* **2006**, *93*, 76–88. [CrossRef] [PubMed]
17. Valentino, F.; Beccari, M.; Fraraccio, S.; Zanaroli, G.; Majone, M. Feed frequency in a Sequencing Batch Reactor strongly affects the production of polyhydroxyalkanoates (PHAs) from volatile fatty acids. *New Biotechnol.* **2014**, *31*, 264–275. [CrossRef]

18. Beun, J.J.; Dircks, K.A. Poly-β-hydroxybutyrate metabolism in dynamically fed mixed microbial cultures. *Water Res.* **2002**, *36*, 1167–1180. [CrossRef]
19. Lettner, M.; Schoggl, J.P.; Stern, T. Factors influencing the market diffusion of bio-based plastics: Results of four comparative scenario analyses. *J. Clean. Prod.* **2017**, *157*, 289–298. [CrossRef]
20. Montgomery, D.C. *Design and Analysis of Experiments*, 7th ed.; Wiley: Hoboken, NJ, USA, 2009; p. 18.
21. Serafim, L.S.; Lemos, P.C.; Oliveira, R.; Reis, M.A.M. Optimization of polyhydroxybutyrate production by mixed cultures submitted to aerobic dynamic feeding conditions. *Biotechnol. Bioeng.* **2004**, *87*, 145–160. [CrossRef]
22. Couper, J.R.; Penney, W.R.; Fair, J.R.; Walas, S.M. *Chemical Process Equipment Selection and Design*; Elsevier Butterworth-Heinemann: Burlington, MA, USA; London, UK, 2009; 831p.
23. Villano, M.; Valentino, F.; Barbetta, A.; Martino, L.; Scandola, M.; Majone, M. Polyhydroxyalkanoates production with mixed microbial cultures: From culture selection to polymer recovery in a high-rate continuous process. *New Biotechnol.* **2014**, *31*, 289–296. [CrossRef] [PubMed]
24. Albuquerque, M.G.E.; Torres, C.A.V.; Reis, M.A.M. Polyhydroxyalkanoate (PHA) production by a mixed microbial culture using sugar molasses: Effect of the influent substrate concentration on culture selection. *Water Res.* **2010**, *44*, 3419–3433. [CrossRef] [PubMed]
25. Freches, A.; Lemos, P.C. Microbial selection strategies for polyhydroxyalkanoates production from crude glycerol: Effect of OLR and cycle length. *New Biotechnol.* **2017**, *39*, 22–28. [CrossRef]
26. Jiang, Y.; Marang, L.; Kleerebezem, R.; Muyzer, G.; van Loosdrecht, M.C.M. Effect of temperature and cycle length on microbial competition in PHB-producing sequencing batch reactor. *ISME J.* **2011**, *5*, 896–907. [CrossRef] [PubMed]
27. Jiang, J.G.; Zhang, Y.J.; Li, K.M.; Wang, Q.; Gong, C.X.; Li, M.L. Volatile fatty acids production from food waste: Effects of pH, temperature, and organic loading rate. *Bioresour. Technol.* **2013**, *143*, 525–530. [CrossRef]
28. Gurieff, N.; Lant, P. Comparative life cycle assessment and financial analysis of mixed culture polyhydroxyalkanoate production. *Bioresour. Technol.* **2007**, *98*, 3393–3403. [CrossRef] [PubMed]
29. Fernandez-Dacosta, C.; Posada, J.A.; Kleerebezem, R.; Cuellar, M.C.; Ramirez, A. Microbial community-based polyhydroxyalkanoates (PHAs) production from wastewater: Techno-economic analysis and ex-ante environmental assessment. *Bioresour. Technol.* **2015**, *185*, 368–377. [CrossRef] [PubMed]

polymers

MDPI

Article

Reducing off-Flavour in Commercially Available Polyhydroxyalkanoate Materials by Autooxidation through Compounding with Organoclays

Lidia García-Quiles [1,*], Arantzazu Valdés [2], Ángel Fernández Cuello [3], Alfonso Jiménez [4], María del Carmen Garrigós [4] and Pere Castell [5,*]

1 Tecnopackaging, Polígono Industrial Empresarium C/Romero N° 12, 50720 Zaragoza, Spain
2 Analytical Chemistry, Nutrition & Food Sciences Department, University of Alicante, P.O. Box 99, 03080 Alicante, Spain; arancha.valdes@ua.es
3 Escuela de Ingeniería y Arquitectura, University of Zaragoza, Av. María de Luna, 3, 50018 Zaragoza, Spain; afernan@unizar.es
4 NANOBIOPOL Research Group, University of Alicante, San Vicente del Raspeig, 03690 Alicante, Spain; alfjimenez@ua.es (A.J.); mc.garrigos@ua.es (M.d.C.G.)
5 Fundación Aitiip, Polígono Industrial Empresarium C/Romero N° 12, 50720 Zaragoza, Spain
* Correspondence: lgarcia@tecnopackaging.com (L.G.-Q.); pere.castell@aitiip.com (P.C.); Tel.: +34-607-018-803 (L.G.-Q.); +34-976-46-45-44 (P.C.)

Received: 30 April 2019; Accepted: 29 May 2019; Published: 31 May 2019

Abstract: Polyhydroxyalkanoates (PHAs) are nowadays considered competent candidates to replace traditional plastics in several market sectors. However, commercial PHA materials exhibit unsatisfactory smells that can negatively affect the quality of the final product. The cause of this typical rancid odour is attributed to oxidized cell membrane glycolipids, coming from Gram-negative production strains, which remain frequently attached to PHAs granules after the extraction stage. The aim of this research is the development of customised PHA bio-nano-composites for industrial applications containing organomodified nanoclays with high adsorbance properties able to capture volatile compounds responsible for the displeasing fragrance. To this end, a methodology for the detection and identification of the key volatiles released due to oxidative degradation of PHAs has been established using a headspace solid-phase microextraction technique. We report the development of nine bio-nano-composite materials based on three types of commercial PHA matrices loaded with three species of nanoclays which represent a different polar behaviour. It has been demonstrated that although the reached outcoming effect depends on the volatile nature, natural sepiolite might result in the most versatile candidate for any the PHA matrices selected.

Keywords: biopolymers; nanoclays; bio-nanocomposites; extrusion-compounding; polyhydroxyalkanoates; thermal properties; microstructure; volatiles; autoxidation; thermal gravimetric analysis; scanning electron microscope; headspace solid phase microextraction

1. Introduction

The poly(hydroxyalkanoates) (PHAs) market is poised to grow during the next decade at a compounded annual growth rate of 6.3% gaining more and more attention in the biopolymers market [1]. PHA biopolyesters are increasingly used owing to its biodegradable nature and processing versatility representing a potential sustainable replacement for fossil oil-based commodities [2]. PHA biopolymers are formed mainly from saturated and unsaturated hydroxyalkanoic acids in which the monomer unit harbours a side chain R group which is usually a saturated alkyl group. These polymers are generally classified in two categories depending on the number of carbon atoms in their monomer units: small chain length (*scl*)-PHA when the monomer units contain from three to five carbon

atoms and medium chain length (mcl)-PHA with monomer units possessing from six to 14 carbon atoms [3,4]. These features give rise to diverse PHA monomers and polymers with tailored molecular weights and melting points providing broad properties, such as isotactic poly(3-hydroxybutyrate) P3HB; poly(3-hydroxybutyrate-*co*-hydroxyvalerate) PHBV copolymer; 3-hydroxypropionate (3HP); 3-hydroxyoctanoate (3HO); or 4-hydroxybutyrate (4HB) among others [2,5].

Accumulation of PHA seems to be a common metabolic strategy adopted by many bacteria to cope with a series of various stress factors in the environment [6]. PHA biopolyesters are used as carbon and energy storage and are accumulated by various prokaryotes as intracellular "carbonosomes" [7] in the form of granules of 0.2–0.5 microns inside these bacterial cells in an amorphous state (chain disordered) are covered by an outer monolayer of phospholipids and proteins [8]. To recover the PHA granules is necessary to break bacterial cells, remove the monolayer and isolate the PHA with high molecular chains (unbroken chains). To this end, a combination of solvents is used, usually based in organic solvents and/or chlorinated. These solvents modify the cell membrane permeability and dissolve the PHA, which is able to escape through the monolayer and cell wall [9,10]. Recent works have studied the effect that carbon sources may have on the final odours released by PHA monomers [11].

The proposal of efficient methods to purify microbial PHAs to meet the legislative requirements in the pharmaceutical, medical or food sectors has been investigated [12,13]. Simple chemical methods, such as combinations of organic PHA solvents and anti-solvent or high-pressure extraction, can be applied to remove the remaining lipids and endotoxins that are frequently attached to PHAs from Gram-negative production strains [14]. In the case of PHAs, lipid residues often remain attached to the biopolymer after extraction, causing a typical rancid odour and smell that can negatively affect the quality of the final product. The flavour threshold of a particular chemical can vary greatly and is defined as the minimum quantity of a substance, which can be detected by 50% of the taste panel [15]. Regardless of the oxidation mechanism, it is recognised that lipids are oxidised to odourless and flavourless intermediates that could break into molecules giving off-flavours. These conditions are associated with the production of free radicals by autoxidation which have been recognized as a potential source of food quality shortcomings of PHA for many applications such as packaging [16,17]. Nowadays, plastic product converters purchase commercial PHA materials with unsatisfactory smelling because current PHA production methods are not solving this particular disadvantage. Our proposed solution approaches the compounding stage of customised blends for industrial applications by using nanoclays with high adsorbance properties able to capture volatile compounds responsible for the displeasing fragrance.

Up to now, microextraction methods have been used for the separation of specific analytes from complex matrices with high reproducibility, selectivity and sensitivity [18]. This is a very important process commonly used in the food sector in order to analyse the aroma properties. Among several extraction methods widely used for the extraction and determination of flavour compounds, the most frequently applied are those based on headspace (HS) analysis. Solid phase microextraction (SPME) is a sample preparation technique based on sorption that constitutes a reliable tool for the analysis of organic volatile and semi-volatile compounds [19]. In the plastic sector, the analysis of volatile organic compounds emissions from plastic and rubber materials through HS-SPME and other techniques such as (MAE)-GC-MS, (SPM)-GC-MS, (TGA)-GC-MS etc have been performed as a useful method for understanding polymer degradation and object damage made of conventional oil-based polymers such as high-density polyethylene (HDPE), low density polyethylene (LDPE), polyacrylonitrile (PAN), polyvinyl chloride (PVC), polypropylene (PP), polystyrene (PS), polymethyl methacrylate (PMMA), polyurethane (PU), and nylon 6,6 (PA) [20–22] Specific volatile emissions can be related to deterioration, including loss of additives and polymer degradation [23].

However, headspace solid-phase microextraction (HS-SPME) has not been used for the analysis of those volatile compounds released from PHAs. This technique used by the authors is combined with gas chromatography ion-trap/mass spectrometry (GC-IT/MS) in order to quantify a large number of

volatile compounds in PHA samples. To the best of our knowledge, this is the first time that a method for analysis of volatiles is used in PHA final/commercial materials for such purpose.

In the present work, three PHA materials were reinforced with organically modified and unmodified Sepiolite and Montmorillonite as described in the materials section. Clays and zeolite exchanged with various cationic surfactants have been shown to be effective adsorbents for a variety of organic compounds [24]. Sepiolite has outstanding sorption capacity and may adsorb a large variety of molecules as vapours as well as liquids due to its natural structure that forms inner zeolitic channels that provides a high microporosity and large specific surface area [25]. Sepiolite fibre leads to the presence of numerous silanol groups (Si–OH) all along the edges of the fibre [26] which are useful as fillers providing reinforcing characteristics with polar polymers [27]. Sodium montmorillonite (Na-MMT) is a smectite nanoclay that has two tetrahedral sheets of silica sandwiching a central octahedral sheet of alumina and largely used in industry too due to its swelling and adsorption properties [28,29].

The aim of this research was the development and characterization of novel composite materials based on different PHA matrices to diminish the release of undesirable oxidised lipid molecules through the introduction of organoclays. The objective is to establish a methodology for the identification of the key volatiles released by commercial PHAs which are responsible for unpleasant odours, and demonstrate that the introduction of commercial organoclays can be an efficient approach to capture those volatiles and reduce the displeasing aroma. The studied techniques used in this paper can be useful for processors in order to monitor the oxidative degradation of PHAs with storage time and to evaluate their acceptance on the market.

2. Materials and Methods

2.1. Materials

Three commercial PHA materials were used as a matrix. These were Mirel PHA1005 and Mirel PHA3002 (food contact P3HB-*co*-P4HB, purchased from Metabolix, Cambridge, MA, USA), and Biomer PHB P226 (homopolymer P3HB grade purchased from Biomer, Krailling, Germany).

Three different modified and unmodified organoclays were kindly provided by TOLSA (Madrid, Spain). A natural sepiolite (T2), a modified Sepiolite with aminosilane groups on its surface (T1) and a sodium montmorillonite modified with a quaternary ammonium salt (T3). The three candidates selected present different behaviours from polar (T1) and neutral (T2) to non-polar (T3) feature which directly affects their affinity for the PHAs polyesters (Table 1).

Table 1. Summary of material formulations. Table reproduced with permission of García-Quiles et al. [30].

Material Formulation	Commercial Matrix Used	Nature of the PHA	Type of Reinforcement (3 wt %)
PHA1005	PHA1005 (Metabolix)	P3HB-*co*-P4HB	(3HB-*co*-17 mol % 4HB) & Talc
PHA1005_T1	PHA1005 (Metabolix)	P3HB-*co*-P4HB	T1: Aminosilane Sepiolite
PHA1005_T2	PHA1005 (Metabolix)	P3HB-*co*-P4HB	T2: Natural Sepiolite
PHA1005_T3	PHA1005 (Metabolix)	P3HB-*co*-P4HB	T3: Sodium Montmorillonite-quaternary ammonium salt
PHA3002	PHA3002 (Metabolix)	P3HB-*co*-P4HB	(3HB-*co*-23.5 mol % 4HB) & Talc
PHA3002_T1	PHA3002 (Metabolix)	P3HB-*co*-P4HB	T1: Aminosilane Sepiolite
PHA3002_T2	PHA3002 (Metabolix)	P3HB-*co*-P4HB	T2: Natural Sepiolite
PHA3002_T3	PHA3002 (Metabolix)	P3HB-*co*-P4HB	T3: Sodium Montmorillonite-quaternary ammonium salt
PHB226	PHB226 (Biomer)	P3HB	Traces of PBA and plasticizer found, & Talc
PHB226_T1	PHB226 (Biomer)	P3HB	T1: Aminosilane Sepiolite
PHB226_T2	PHB226 (Biomer)	P3HB	T2: Natural Sepiolite
PHB226_T3	PHB226 (Biomer)	P3HB	T3: Sodium Montmorillonite-quaternary ammonium salt

Chemical patterns for volatile quantification (considered as main responsible for the odour), were purchased from Sigma-Aldrich. These are 1-hexanol, heptanal, octanal, decanal, α-Methylstyrene, 4-methylstyrene and Benzaldehyde.

2.2. Nano-Bio-Composites Preparation

A 26-mm twin-screw Coperion ZSK 26 compounder machine (Stuttgart, Germany) was used to prepare PHA/nanoclay formulations by extrusion-compounding. Twelve different formulations were studied in total accounting for the three control matrixes plus nine composite materials loading them with the three nanoclays at 3 wt % in all cases. The melted polymers and nanoclay powder were mixed at a screw speed of 125 rpm; temperature was increased from 150 °C in the feeding zone up to 165 °C at the nozzle for PHA1005 and PHA3002 (P3HB-*co*-P4HB formulations) and slightly decreased from 140 °C in the feeding zone up to 160 °C at the nozzle when blending PHB226 (P3HB). The compound was extruded through a 2 mm diameter die for a constant output of 10 kg/h. The extrudate was quenched in a water bath at room temperature, dried and cut into pellets. A total amount of 3 to 5 kg per material was produced.

Specimens for mechanical testing were obtained by injection moulding with a JSW 85 EL II electric injection machine (Tokyo, Japan) by following ISO 178 and ISO 527 standards. These were tested and broken samples were used to study the structural properties (results on mechanical properties are out of the scope of this paper). A complete characterization covering the structural, thermal and mechanical behaviour of the formulations developed, understanding the compatibility mechanisms between the different organoclays and the matrices can be found in a previous work carried out by the authors and published at García-Quiles et al.) [30].

2.3. General Characterisation Methods

2.3.1. Scanning Electron Microscopy

Structural properties were evaluated by scanning electron microscopy (SEM) with Hitachi S3400N equipment (Tokyo, Japan) in order to determine the morphology and dispersion of the nanoclay through the biopolymer-based materials. Samples for SEM observation were obtained from fractured mechanical specimens.

Energy-dispersive X-ray spectroscopy (EDX) was also used for samples for chemical characterization.

2.3.2. Thermogravimetric Analysis

Thermal characterisation was carried out by using thermogravimetric analysis (Mettler-Toledo TGA/SDTA 851e, Greifensee, Switzerland). Samples (5.0 ± 0.1 mg) were heated from 25 to 800 °C at 5 °C/min under N_2 atmosphere (50 mL/min).

2.3.3. Analysis of Volatile Compounds by HS-SPME-GC-MS

HS-SPME Extraction Procedure

The sample (1.00 ± 0.01 g) was mixed with 1 mL of distilled water and 2 µL of internal standard 4-methylstyrene (8 mg/kg, Sigma-Aldrich Inc., St. Louis, MO) and a small magnetic stirrer were placed in a 20 mL amber vial sealed with an aluminium pressure cap provided with a pierceable silicone septum. The extraction was carried out using the SPME fibre made of divinylbenzene/carboxen/polydimethylsiloxane (DVB/CAR/PDMS) 50/30 mm, StableFlex, 1 cm long, mounted on a manual support set SPME (Supelco, Bellefonte, PA, USA) [31,32]. The vial with the sample was placed in a water bath under a specific temperature. After 10 min of equilibrium of the sample, the SPME needle was inserted into the vial and exposed to the headspace of the vial for a specific time. After extraction, the fibre desorption was performed in the GC-MS injection port at

250 °C for 12 min (splitless mode). Blank tests were performed prior to the analysis of the samples to ensure that there was no contamination that could cause memory effects.

GC-MS Parameters

The analysis of the volatiles was carried out using an Agilent 6890N GC model gas chromatograph coupled to an Agilent 5973N MS mass spectrometer (Agilent Technologies, Palo Alto, CA, USA) with impact ionization source of electrons (EI 70 eV) and quadrupole analyzer. The temperatures of the transfer line "ion source" and GC-MS were 230 and 250 °C, respectively. A TRB-624 column (30 m × 0.25 mm × 1.4 µm) of Teknokroma was used, which was programmed from 50 °C (maintaining 2 min) to 250 °C (isotherm for 7 min) at 10 °C/min. Helium was used as the carrier gas (1.5 mL/min). The volatile compounds were identified in "scan" mode (m/z 30–550) by comparing their mass spectra with those of the standard compounds and the Wiley compound library. When standards were not available, volatile compounds having ≥80% similarity with Wiley library were tentatively identified using GC-MS spectra only. All patterns obtained from the commercial house Sigma-Aldrich, St. Louis, were quantified by HS-SPME-GC-MS using standard calibration curves. For this, mother solution (5 mg/kg) and working solutions were prepared using distilled water as a solvent. The HS-SPME and GC-MS sampling procedures were carried out as described for the samples. The analytical method used for the quantification was validated in terms of linearity, repeatability and limits of detection (LOD) and quantification (LOQ). The calibration curves were performed at five concentration levels, in triplicate, using adequately diluted standards and adjusted by linear regression.

Optimization of HS-SPME Extraction Parameters Box-Benhken Experimental Design (BBD)

The extraction of volatile compounds from PHAs was performed under different extraction conditions according to the experimental design shown in Table 2. The parameters considered during HS-SPME optimization were extraction temperature (50, 70 and 90 °C), and extraction time (15, 37.5 and 60 min) and sodium chloride addition (0, 0.5 and 1 M) in a final vial volume of 1 mL. The P3HB sample was selected for the optimization of HS-SPME conditions. The range of studied variables was selected on the basis of results obtained in previous studies reported in the literature [31–33]. A Box–Behnken design (BBD), comprising 12 experimental runs and four central points, was used, and experiments were carried out in randomized order from the experimental design were evaluated in terms of the sum of the peak areas of volatile compounds identified with a library similarity higher than 80%

Table 2. Box-Benkhen experimental design proposed for the headspace solid-phase microextraction (HS-SPME) optimization procedure.

Run	Temperature (°C)	Time (min)	NaCl (1 M)
1	70	37.5	0.5
2	50	60	0.5
3	90	60	0.5
4	70	60	0
5	90	15	0.5
6	70	15	1
7	70	37.5	0.5
8	90	37.5	0
9	90	37.5	1
10	70	15	0
11	50	37.5	1
12	70	37.5	0.5
13	50	37.5	0
14	70	60	1
15	50	15	0.5
16	70	37.5	0.5

2.3.4. Statistical Analysis

Statgraphics-Plus software 5.1 (Statistical Graphics, Rockville, MD, USA) was employed to generate and analyse the results of the BBD. Statistical significance of model parameters was determined at the 5% probability level ($\alpha = 0.05$).

All analytical tests were performed in triplicate. ANalysis Of VAriance (ANOVA) was applied to the results by using SPSS software (Version 15.0, Chicago, IL, USA). Tukey's test was used to assess differences between means and the significance of differences was considered at the level of $p < 0.05$.

3. Results & Discussion

3.1. SEM—Scanning Electron Microscopy

SEM micrographs (Figure 1) showed the dispersion and affinity between the nanoclays and each of the biopolymer matrices used. The good dispersion, debundling (T1 and T2) and exfoliation (T3) of the nanoclays may highly increase the capture of volatiles. The natural chemical behaviour (higher or lower polarity) of each organoclay surface show a clear effect in the interaction mode with each biopolymer matrix. The organophilic clays are not compatible with hydrophobic organic matrices as the spacing between the nanoclay sheets (T3) and inner channels (T1 and T2) is extremely narrow, and hence diffusion of polymer chains in the nanoclay galleries is not possible. This often leads to aggregation of clay particles, acting as stress-concentration sites in the polymer matrix [34]. The organic modification aims at broadening these channels and helps the polymer to penetrate and get fixed onto the surfaces.

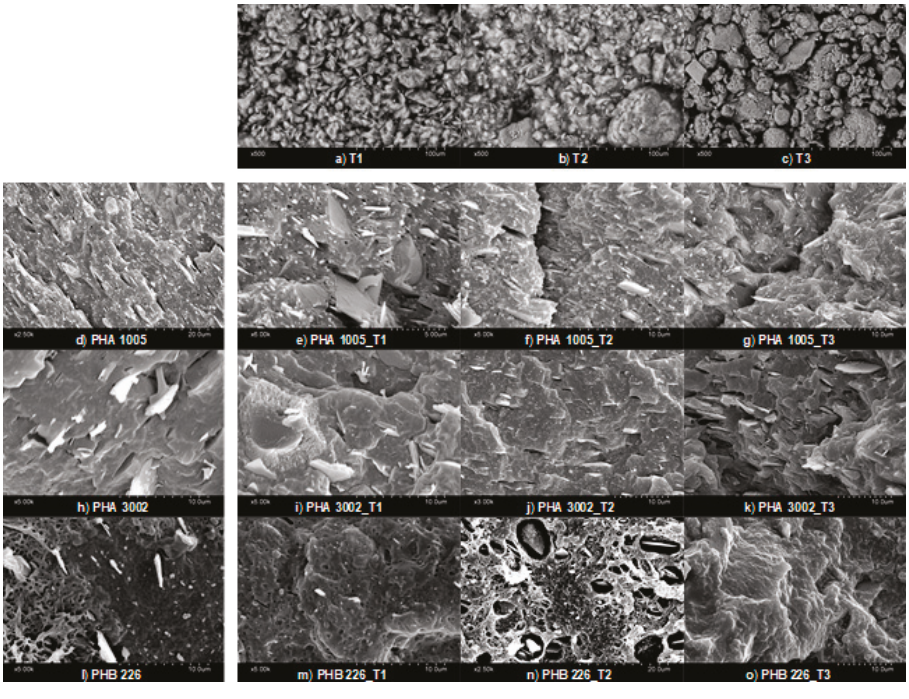

Figure 1. SEM micrographs of nanoclays (**a**–**c**); neat matrices (**d**,**k**,**l**) and composites: PHA1005 composites (**e**–**g**), PHA3002 composites (**i**–**k**); PHB226 composites (**m**–**o**).

On the one hand, analysing PHA3002 micrographs, T2 seems to appear better dispersed than T1 or at least better oriented in one direction. In addition, sepiolites (T1 and T2) appear to show a better

affinity with this P3HB-co-P4HB matrix as T3 micrographs show a lack of wetting contact layer or interphase between the nanoclay and the polymer. On the other hand, for PHA1005 matrix, T1 presents some agglomerates, which in principle should be avoided due to the aminosilane modification. At times, the greater the amount of organic modifier in nanoclays, the greater the impediment to debundle [35] and this might be the behaviour observed between T1 (modified) and T2 (natural) for this matrix.

Finally, when analysing PHB226 compounds, a clear lack of affinity for T2 PHB226 was observed. Similar behaviour was found for T1 in which a similar bubble-like reaction during the blend compounding might have started. However, the polar affinity between T1 and PHB226 probably cuts the kinetics of the reaction while for T2 (non-modified) the process is more pronounced. Therefore, a better interphase interaction between T1 and PHB226 can be observed when comparing to T2. This enhanced interaction was sought with the organoclay modification. However, a completely different affinity behaviour can be found for T3 and PHB226, for which the surface structure complies with a more ductile fracture. Montmorillonite layers are found well integrated and interphases are not discernible as in the other two cases. These results are in agreement with Mechanical and XRD results already published by authors, in which Montmorillonite seemed to be highly intercalated and even exfoliated, while sepiolite debundling was not so effective [30]. This favourable interaction between T3 and PHB226 may be attributed to the lack of P4HB and the appearance of PBA, which modifies the polar behaviour or the matrix, and indirectly affects the overall viscosity of the molten polymer when the blend is developed favouring or hindering miscibility [36].

Finally, for neat matrices, the difference in the amount of talc used by the manufacturer for PHA1005 and PHA3002 formulations respect to PHB226 can be observed, which seems in coherence with TGA findings.

3.2. TGA—Thermogravimetric Analysis

The thermal stability of the nanocomposite materials was evaluated through TGA. The temperature corresponding to the onset of decomposition (T onset) for the samples studied is essential for evaluating their thermal stability and is shown in Table 3.

Table 3. Thermal results obtained by TGA. T_{onset} %, T_{max} %, and T_{50} % represent the temperature of the initial degradation, the maximum degradation rate of decomposition, and 50 wt % loss of the samples, respectively. FR represents the final residue and DTG first derivative.

Materials	T_{onset} [°C]		T_{max} [°C]		T_{50} wt % [°C]	FR [%]
PHA1005	268.13		278.33		279.62	9.45
PHA1005_T1	267.94		275.51		278.89	12.93
PHA1005_T2	265.75		278.33		278.52	13.56
PHA1005_T3	263.20		278.33		277.25	13.27
PHA3002	290.01		307.67		305.34	8.39
PHA3002_T1	287.46		307.67		305.61	11.71
PHA3002_T2	283.63		302.33		300.23	10.93
PHA3002_T3	284.73		299.67		298.95	11.26
PHB226	275.97	386.87	297.00	403.70	293.84	2.73
PHB226_T1	283.63	384.31	299.82	411.67	301.50	5.61
PHB226_T2	278.52	383.03	297.00	407.30	296.40	5.83
PHB226_T3	272.14	347.29	291.49	382.86	287.46	6.37

In addition, the appearance of volatile traces in the first section of the DTG was evaluated. Theoretically, high amounts of some identified volatiles that might be found in the neat matrices, may have been released during the extrusion-compounding of the bio-nanocomposites due to the temperature profile reached during the material development (over 150 °C) [21,32]. However, the release rate is unknown and there is not a clear perception of volatile release. Nevertheless, the DTG range

between 100 and 220 °C was studied trying to observe substantial peaks. The signal noise of the apparatus seems too high compared to the amount of volatiles released in order to be able to obtain reliable results. Therefore the correct volatile analysis is left for the accurate technique HS-SPME and authors will focus the TGA results to study the thermal stability and the non-organic residue.

The degradation of PHA 3002 occurred in one step while PHA 1005F shows a smooth second step at higher temperatures which may correspond to a greater amount of inorganic fillers. Several steps occurred for the PHB226 sample too, distinctly exhibiting two decomposition platforms. This behaviour has been previously reported in the literature for some pure P3HB polymers and for different P3HB-*co*-P4HB co-blends. According to literature, pure P3HB thermally decomposes at around 270 °C, above its melting point (around 180 °C). However, a short exposure of PHB to temperatures near its melting point induce a severe degradation producing degraded products such as olefinic and carboxylic acid compounds due to the random chain scission reaction that takes place [37]. Wang et al. studied the thermal degradation of P3HB-*co*-P4HB composites [38]. The results showed that thermal degradation of P3HB occurs almost exclusively by random chain-scission involving a six-member ring formation while P4HB decomposes through intermolecular ester exchange reaction and generates a decomposition product ϒ-butyrolactone. Therefore, P4HB crystals are thermally more stable than P3HB. In addition, in a previous analysis carried out by the authors for these composites, the presence of PBA was corroborated in the NMR and DSC analyses for PHB226 [30]. Maximum degradation temperature of PBA is defined at T_{dmax} = 385.1 °C [39] which is aligned with the TGA results shown in Table 3. The presence of multi-component nature for PHB226 commercial formulation containing organic additives and polyesters has been also corroborated by further authors such as Y.M. Corre et al. [40].

Different residual weights remaining at 800 °C can be found for the three matrices being higher for P3HB-co-P4HB blends than for P3HB. Usually, two inorganic fillers are commonly used in polymers as nucleating agents to reduce crystallization rates: $Mg_3Si_4O_{10}(OH)_2$ and $CaCO_3$ [41,42]. Complementary EDS was used for the elemental analysis of the final residues revealing their correspondence to talc. In addition, the final amount of inorganic residue found for the bio-nano-composites developed, reveals an effective dosage of the nanoclays load introduced.

The thermal degradation of Sepiolite and montmorillonite nanoclay additives was characterised in order to better understand the effect these have over the final bio-nano-composites.

The T2 thermograph (Figure 2a) shows a typical curve for non-modified sepiolite. T1 thermograph shows a few deviations from respect to T2 due to the modification through organosilanes containing amine groups [25,27]. Our TGA results are in concordance with the aminosilane grafted Sepiolite (T1) characterisation made by G. Tartaglione et al., in previous publication [43]. In particular, four degradation steps are appreciated for T1. The clay presents degradations around 74, 232 and 305 °C. In addition, a less defined degradation phase is observed at 349–495 °C. To try to better define this area and separate the overlap of peaks, the heating rate was lowered from 10 to 5 °C/min. The first loss corresponds to mainly methanol, probably used as a solvent for the modification of the clay, followed by dehydration of water: moisture and zeolitic water (below 180 °C).

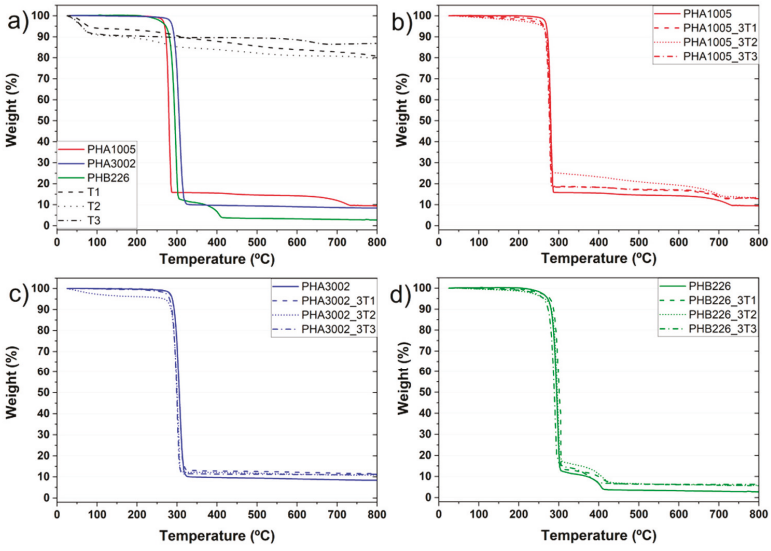

Figure 2. TGA curves: (**a**) neat matrices and nanoclays; (**b**) PHA1005 composites; (**c**) PHA3002 composites; (**d**) PHB226 composites.

The volatilization of the modifier takes place in two steps, the first one related to adsorbed molecules (non-grafted) at 215–250 °C. The grafted modifier is likely to volatilize over 400 °C. The grafted groups are very stable, being eliminated by heating at temperatures above 400 °C. In this way, the characteristic hydrophilic surface of Sepiolite becomes organophilic and the fibrous clays can then be easily dispersed in low-polar polymers [44]. The last loss observed approximately at 750 °C has been described in the literature to be related to a complete oxidation of the carbonaceous residue formed during previous thermal oxidation of the grafted molecules [45].

T3 (Na-MMT) presents a chemical structure modified with a quaternary alkyl ammonium surfactant which has a noticeable effect on the thermal stability of the organoclay itself. Analysing its thermal degradation behaviour, it can be observed that T3 DTG shows a water/solvent release at 68 °C and at 116 °C. In addition, two small mass loss peaks are found for 295 °C and for 526 °C, and finally an accentuated peak corresponding to 674 °C. According to the literature (Botana et al. [46] and Cervantes et al. [47]) free water loss in MMT nanoclays containing hydroxyl groups in the alkylammonium anion, shows free water loss at around 80 °C. Peaks in at 200–600 °C are attributed not only to structural water but also to the decomposition of the alkylammonium ions. In particular, peaks found at 297 and 528 °C are associated to the following chemical species for this organoclay sample: H_2O, CO_2, alkanes, alkenes, CHO's, COOH's, amines [47]. Finally, peaks attributed between 610 and 674 °C are attributed to some further structural water release.

In all the developed bio-nano-composites a decrease in T_{onset} and T_{max} can be appreciated except for PHB226-T1. Han et al. reported that P3HB-*co*-P4HB samples containing a 10 wt % silica presented a higher T_{onset} and T_{max} than that of pure P3HB-*co*-P4HB, in particular being 2.08 and 6.28 °C higher, respectively [48]. Our samples containing a 3 wt % of nanoclay content seems not to induce a high thermal stability increase. Nevertheless, results show that sepiolites (T1 and T2) seem more suitable for these polyhydroxyalkanoates materials than montmorillonite for thermal stability purposes, as sepiolites maintain the thermal stability of the original matrix. For P3HB-*co*-P4HB composites, it can be observed that T1 presents the same T_{onset}, T_{max} and T_{50} while a slight decrease is found for T2. For T3, the overall decrease for T_{onset}, T_{max} and T_{50} is noticeable. A similar tendency is found for P3HB composites. T1 is the nanoclay inducing a higher thermal stability for both degradation

steps (including PBA), while T2 tends to maintain the original matrix behaviour and T3 induces a remarkable decrease. Results are detailed in Table 3.

3.3. HS-SPME-GC-MS—Headspace Solid-Phase Microextraction Coupled to Gas Chromatography-Mass Spectrometry

3.3.1. Optimization of the HS-SPME Extraction Process

Seventeen different volatile compounds were identified with a library similarity higher than 80% in all runs of the BBD carried out in this study (Figure 3): 1, 1-butanol; 2, p-xylan; 3, heptanal; 4, α-methylstyrene; 5, benzaldehyde; 6, octanal; 7, limonene; 8, 1-hexanol; 9, undecane; 10, 1-octanol; 11, nonanal; 12, decanal; 13, 1-chloro-decane; 14, 1-decanol; 15, tetradecane; 16, biphenyl; 17, 2,6-bis (1-methylethyl)-benzeneamide.

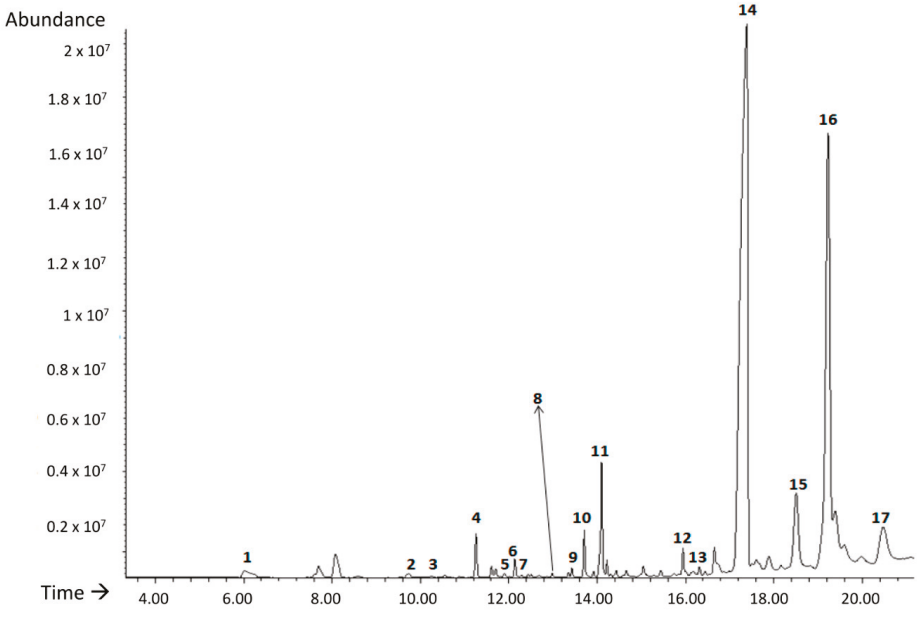

Figure 3. TIC chromatogram obtained for PHB 226 sample under run 3 of the BBD. * *Time refers to s*.

Benzaldehyde, heptanal, octanal, nonanal and decanal belong to the family of aldehydes. The presence of benzaldehyde in other matrices such as polystyrene has been related to oxidation processes together with p-xylan and α-methylstyrene [21]. Furthermore, heptanal, octanal, nonanal, decanal, are secondary oxidation compounds, which are characterized by strong and unpleasant odours characteristic of lipid degradation [49]. In addition, four alcohols were identified (butanol, 1-hexanol, octanol and decanol). In particular, 1-hexanol is one of the most important alcohols used for several processes of synthesis and degradation product of one of the most used plasticizers since 1950, the phthalate DEHP [50]. This compound has been detected in emissions of different plastics with undesirable odour [51]. As expected, some organic volatile compounds identified are linear or branched chain alkanes such as undecane and tetradecane due to the high affinity for SPME fibre coating [32]. Regarding limonene, it is a terpene which has acquired great importance in recent years due to its demand as a biodegradable solvent. Apart from industrial solvent it also has applications as an aromatic component and is widely used to synthesize new compounds [52].

The influence of extraction temperature (A), extraction time (B) and NaCl addition (C) in the sum of the peak areas of these seventeen compounds was evaluated by using standardized Pareto diagrams

(Figure 4). This kind of diagram allows for the determination of the magnitude and the importance of each independent variable or factors in a response. Figure 4 shows that only the extraction time was significant and it has a positive effect. That means that extraction by HS-SPME improves when the time increases from 15 min to 60 min. Nonetheless, the extraction temperature and the addition of NaCl and all possible interactions (AB, AC, BC, AA, BB, CC) do not have a significant effect with a confidence level of 95% ($\alpha = 0.05$). Based on the obtained results, the optimum HS-SPME extraction conditions were 60 min at 90 °C without the addition of NaCl.

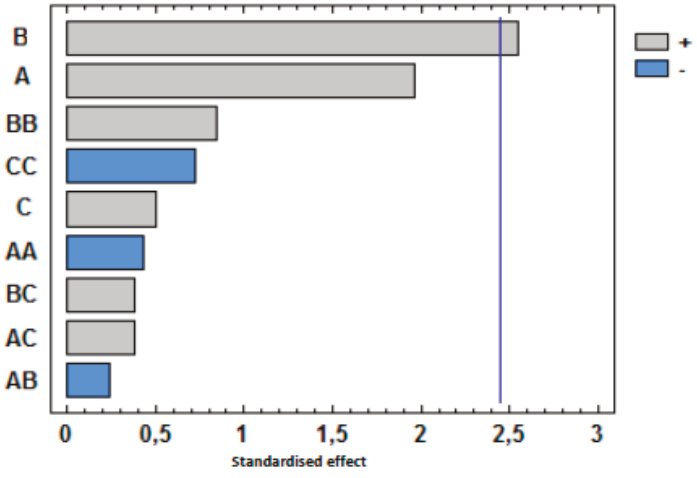

Figure 4. Pareto charts of factors and interactions obtained from the BBD for the sum of the volatile compounds. The vertical line indicates the statistical significance at 5% of the effects.

Finally, it was decided to quantified six main volatile compounds in the present work as a result of this negative effect on the final odour of samples: heptanal, α-methylstyrene, benzaldehyde, octanal, 1-hexanol and decanal. The adequacy of the fitted models was determined by evaluating the lack of fit, the coefficient of determination (R^2) and F test obtained from the analysis of variance (ANOVA). The computing program showed that the fitted models were considered satisfactory as the lack of fit was not significant with values of 0.852 for heptanal, 0.659 for α-methylstyrene, 0.457 for benzaldehyde, 0.940 for octanal, 0.816 for 1-hexanol and 0.983 for decanal. ($p > 0.05$). On the other hand, R^2 is defined as the ratio of the explained variation to the total variation and is a measurement of the degree of fitness. The model can fit well with the actual data when R^2 approaches unity with values of 0.733 for heptanal, 0.767 for α-methylstyrene, 0.775 for benzaldehyde, 0.861 for octanal, 0.853 for 1-hexanol and 0.681 for decanal. These values indicated a relatively high degree of correlation between the actual data and predicted values, indicating that models could be used to predict the studied responses.

3.3.2. Validation method

The analytical method used for the quantification of volatile compounds by HS-SPME-GC-MS was validated in terms of linearity, repeatability and detection (LOD) and quantitation (LOQ) limits. An acceptable level of linearity was obtained for all analytes (R^2 between 0.9076 and 0.9929), showing relative standard deviation (RSD) values lower than 5%. LOD and LOQ values were determined using the regression parameters of the calibration curves (3 Sy/x/a and 10 Sy/x/a, respectively, where Sy/x is the standard deviation of the residues and "a" is the curve slope). LOD and LOQ values obtained for heptanal ranged between 0.001 and 0.004 μg/kg, α-methylstyrene ranged between 2.76 and 9.19 μg/kg, benzaldehyde ranged between 0.003 and 0.011 μg/kg, octanal ranged between 0.071 and 0.236 μg/kg, 1-hexanol and decanal ranged between 0.001 and 0.002 μg/kg.

Volatile Compounds Quantification

Lipid oxidation is a complex process where unsaturated fatty acids react with molecular oxygen via a free radical mechanism or in a photosensitised oxidation process. The principal source of off-flavours developed by lipid oxidation is hydroperoxides, which are unstable and readily decompose to form aliphatic aldehydes, ketones and alcohols. Many of these secondary oxidation products have undesirable odours with particularly low odour thresholds [53,54]. As it is shown in Tables 3 and 4, the effect of studied nanoclays (T1, T2 and T3) were different depending on the polymer matrix (PHB226, PHA1005 or PHA3002).

In general, the volatile compound quantified in greater quantity for all the samples has been the decanal as it is the volatile with the highest M_w. Table 4 results suggest that there is a clear tendency which indicates that the content of the volatiles is related to the molecular weight, as the higher the M_w is, the more difficult the volatiles are to extract from the polymer and to clean during purification stages. Therefore, we can observe them in higher amounts. For the case of α-methylstyrene and benzaldehyde, these are more complex volatiles containing aromatic groups which may be also less accessible to solvents to be extracted and cleaned. Hence, they can be found also in higher quantities than simpler alcohols.

According to García-Quiles et al. [30], the addition of nanoclays may modify the structure of the polymers studied affecting the release of the studied undesirable volatile compounds. Regarding the control matrix polymers, PHB 226 initially shows lower contents of heptanal, α-methylstyrene, octanal and 1-hexanol while its content in decanal was the highest respect to the other two PHA matrices. However, benzaldehyde was initially quantified in similar amounts in all control matrices.

Concerning the effect of the addition of T1, T2 and T3, each studied volatile showed a different behaviour depending on the matrix and organoclay used (Figure 5 and Table 5).

Regarding 1-hexanol, PHB 3002 showed the lowest content in contrast to PHA1005 and PHB226. In this sample, no significant enhancement was found between the three nanoclays, although T1 at least maintained the level of release, while T3 and T2 showed non-desirable and remarkable increasing peaks of 200% and 515% respectively. For PHA 1005 all the nanoclays reduced the release of this compound, but it seems that T3 clay was much more effective reducing it in a 72%.

Heptanal, together with Decanal, seemed to be the most difficult volatile to be adsorbed by any of the organoclays. In this sense, T1 seemed to be more efficient maintaining heptanal release for PHA1005 and PHA3002 and reducing a 20% the release PHB226. In contrast, it seems that the addition of T3 could modify the structure of PHA1005 and PHA3002 polymers increasing the heptanal release in more than 400% while reducing 13% for PHB226.

Concerning octanal behaviour, the initial concentration was lower in PHB 226 but for this matrix, it seems that all organoclays provoke increases in the release of this volatile instead of retaining them. On the contrary, T3 prevents the release of octanal in PHA 1005 decreasing its release in a remarkable 92%. However, for PHA 3002, it seems that T2 suits better as it hinders the release of this volatile compound more efficiently than T3, 66%.

PHB 226 showed the highest decanal initial content. T2 was the most effective clay reducing the release of this compound in a 43%. T2 nanoclay was also the most efficient for the PHA 1005 matrix although there was no decrease for any of the three organoclays. The same tendency was found for PHA 3002, being in this case T3 the nanoclay increasing the release to a lesser extent.

Regarding α-methylstyrene, the lowest content was determined in PHB 226 and PHA1005 at equal rates by decreasing its release in 75%. For this compound and in particular for PHA 3002_T3 the developed formulation seems to be especially effective since it was not possible to detect the presence of this volatile compound therein.

Finally, Benzaldehyde was initially present in a similar quantity in all formulations. In this case, T2 could be more effective in PHB 226 and PHA 1005 matrices whereas for PHA 3002 no significant effect was observed.

Table 4. Volatile compounds content for the PHB 226 PHA 1005 and PHA 3002 controls and the T1, T2 and T3 formulations, expressed as the mean ± SD (n = 3).

Sample Material	Volatile Compound											
	1-Hexanol		Heptanal		Octanal		Decanal		α-Methylstyrene		Benzaldehyde	
	Average (μg/g sample)	SD	Average (μg/g sample)	SD	Average (μg/g sample)	SD	Average (μg/g sample)	SD	Average (μg/g sample)	SD	Average (μg/g sample)	SD
PHA 1005	18.8	3.8	14.8	6.8	68.6	14.9	900	500	102.8	35.4	6.4	0.3
PHA 1005_T1	13.2	1.1	15.8	1.5	68.1	7.1	2100	500	283.6	12.2	5.7	1.2
PHA 1005_T2	8.2	1.3	15.3	3.2	78.1	13.9	1300	200	25.7	10.0	4.3	0.3
PHA 1005_T3	5.3	0.7	81.2	29.3	5.3	0.7	5300	700	89.6	33.5	5.3	0.7
PHA 3002	2.7	1.0	18.8	10.0	75.4	18.8	1000	300	135.4	28.4	4.5	1.5
PHA 3002_T1	2.8	1.0	27.9	1.7	41.2	6.5	3300	500	279.5	17.6	7.1	0.3
PHA 3002_T2	16.6	2.9	41.4	16.3	25.3	7.4	2400	400	59.3	11.6	4.6	0.7
PHA 3002_T3	8.1	2.7	98.8	11.1	53.6	16.8	1800	400	nd	nd	6.7	1.1
PHB 226	3.7	0.9	4.0	0.6	26.7	0.5	2300	100	40.4	4.6	7.7	0.7
PHB 226_T1	1.2	0.9	3.2	1.1	32.6	6.0	1900	200	43.4	7.1	7.2	2.6
PHB 226_T2	2.3	0.6	10.3	0.9	39.3	7.7	1300	300	10.3	2.3	4.9	0.5
PHB 226_T3	1.6	0.6	3.5	7.6	71.3	17.9	2800	700	39.6	17.3	6.5	2.7

nd = no data.

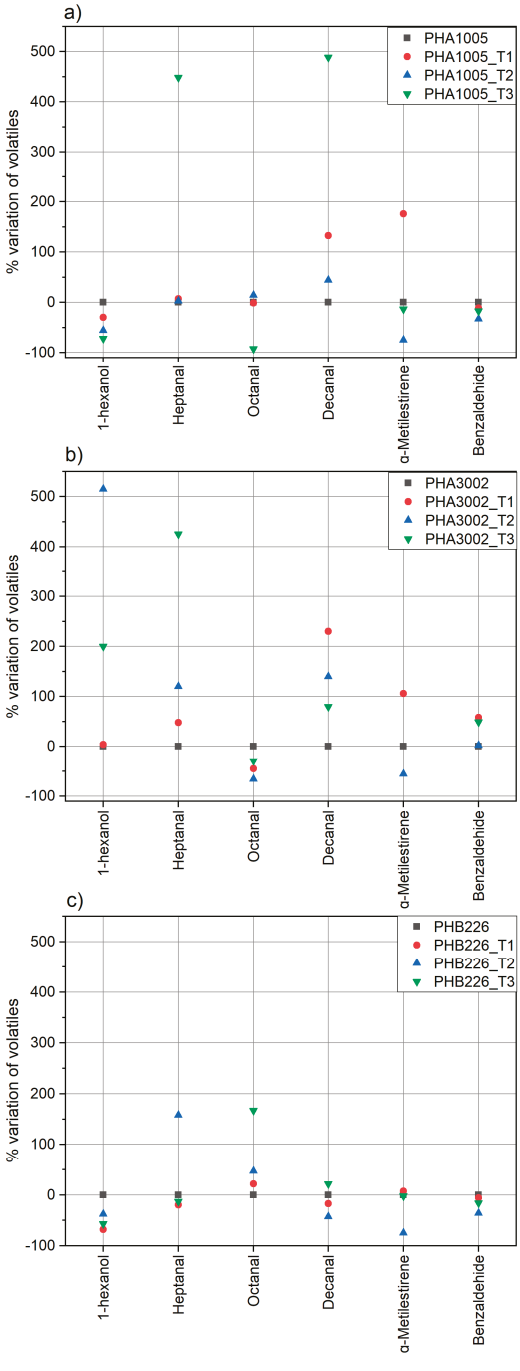

Figure 5. Percentage variation of volatile substances in the samples of study: (**a**) PHA1005, (**b**) PHA3002, (**c**) PHB226.

Table 5. Summary of the organoclay that works best to reduce the release of the volatile compounds studied for each polymer matrix.

Volatile	PHA 1005	PHA 3002	PHB 226
1-Hexanol	T3	T1	T1
Heptanal	T2	T1	T1
Octanal	T3	T2	T1
Decanal	T2	T3	T2
α-Methylstyrene	T2	T3	T2
Benzaldehyde	T2	T2	T2

4. Conclusions

The incorporation of organoclays to PHAs greatly affects the dispersion and integration of the nanoclay in the polymer matrix due to surface modification. SEM micrographs confirm how important is adequate the surface polarity of nanoclays for a particular matrix, having found largest differences between T2 which showed a lack of surface adhesion and voids formation and T3 apparently exhibiting better surface interaction and delamination. There is also a clear difference between micrographs containing T1 and T2, especially for PHB226, where the aminosilane modification clearly accentuates affinity for the PHAs matrices. Moreover, T1 has been demonstrated to be the unique nanoclay really enhancing the thermal stability of the composites developed according to TGA results while T2 maintains the original behaviour and T3 induces a remarkable decrease on T_{onset} and T_{max}.

In addition, TGA analysis has allowed us to identify thermal decomposition peaks for our composites and understand the degradation phases of matrices and the decomposition and volatilization of the organic modifiers employed onto nanoclays. However, the release of volatile compounds coming from matrix aldehydes and ketones at thermal rates between 100 and 220 °C cannot be identified with this technique and therefore the determination of this off-flavour compounds has been optimised by applying headspace analysis. The obtained results from the experimental design demonstrate the suitability of the HS-SPME technique followed by GC-MS to be used in biopolymer analysis to identify and monitor the release of volatile compounds in PHAs matrices.

It has been demonstrated that the reached effect depends on the volatile nature and the affinity of the organoclay with each matrix. On the one hand, for PHB226, T1 seems more suitable for low M_w volatiles whileT2 could be more effective to reduce the released volatiles with higher M_w, which indeed are present in a major proportion. On the other hand, for PHA 1005 compounds, T2 seems to be the most effective to reduce heptanal and decanal and also α-Methylstyrene and benzaldehyde. However, T3 was of great relevance in the reduction of the octanal and 1-hexanol compounds. Finally, for PHA 3002 formulations T1 seems the most effective to reduce 1-hexanol and heptanal (lowest M_w), while T2 would tackle best octanal and benzaldehyde (medium M_w) and T3 would be the most effective for decanal and α-Methylstyrene (highest M_w).

As a general outcome from this commercial PHA off-flavour analysis, if a plastic converter would not desire to tackle a particular subgroup of volatiles, but try to comprise as much of them as possible, T2 might result in the most versatile candidate. However, the compromise with other properties such as mechanical or barrier properties for example for food or cosmetics packaging should also be taken under consideration.

Author Contributions: L.G.-Q. Conceived the work, carried out the experimental work related to materials development, contributed to the scientific discussion and wrote the major part of the manuscript.; A.V. conceived the volatile designed of experiments and carried out the analysis, contributed to the scientific discussion and wrote part of the manuscript; Á.F.C. contributed to scientific discussion and reviewed the manuscript; A.J. contributed to scientific discussion and reviewed the manuscript; M.d.C.G. contributed to scientific discussion and reviewed the manuscript; P.C. designed the methodology, contributed to the interpretation of results and scientific discussion, got funding and reviewed the manuscript.

Funding: The authors gratefully acknowledge the Government of Aragón (DGA) under the project T08_17R (I+AITIIP) for support and financial aid for this publication.

Acknowledgments: The authors acknowledge TOLSA for kindly provide the nanoclays used for this research.

Conflicts of Interest: The authors declare no conflict of interest.

References

1. Research and Markets. Global Polyhydroxyalkanoate (PHA) Market Analysis & Trends—Industry Forecast to 2025. Available online: https://www.researchandmarkets.com/reports/4375504/global-polyhydroxyalkanoate-pha-market-analysis (accessed on 1 August 2017).
2. Wang, S.; Chen, W.; Xiang, H.; Yang, J.; Zhou, Z.; Zhu, M. Modification and Potential Application of Short-Chain-Length Polyhydroxyalkanoate (SCL-PHA). *Polymers* **2016**, *8*, 273. [CrossRef] [PubMed]
3. Pramanik, K.; Patra, J.K. Polyhydroxyalkanoates: Biodegradable Plastics for Environmental Conservation. In *Industrial & Environmental Biotechnology*; Studium Press: New Delhi, India, 2014; Chapter 1.
4. Rehm, B.H.A. Polyester synthases: Natural catalysts for plastics. *Biochem. J.* **2003**, *376*, 15–33. [CrossRef] [PubMed]
5. Sudesh, K.; Iwata, T. Sustainability of Biobased and Biodegradable Plastics. *Clean* **2008**, *36*, 433–442. [CrossRef]
6. Obruca, S.; Sedlacek, P.; Krzyzanek, V.; Mravec, F.; Hrubanova, K.; Samek, O.; Kucera, D.; Benesova, P.; Marova, I. Accumulation of Poly(3-hydroxybutyrate) Helps Bacterial Cells to Survive Freezing. *PLoS ONE* **2016**, *11*, e0157778. [CrossRef] [PubMed]
7. Koller, M.; Braunegg, G. Advanced approaches to produce polyhydroxyalkanoate (PHA) biopolyesters in a sustainable and economic fashion. *EuroBiotech J.* **2018**, *2*, 89–103. [CrossRef]
8. Kabasci, S. *Bio-Based Plastics: Materials and Applications*; John Wiley & Sons Ltd.: Hoboken, NJ, USA, 2014; Chapter 7.3.2, ISBN 9781119994008.
9. Koller, M.; Maršálek, L.; de Sousa Dias, M.M.; Braunegg, G. Producing microbial polyhydroxyalkanoate (PHA) biopolyesters in a sustainable manner. *New Biotechnol.* **2017**, *37*, 24–38. [CrossRef] [PubMed]
10. Ong, S.Y.; Kho, H.-P.; Riedel, S.L.; Kim, S.-W.; Gan, C.-Y.; Taylor, T.D.; Sudesh, K. An integrative study on biologically recovered polyhydroxyalkanoates (PHAs) and simultaneous assessment of gut microbiome in yellow mealworm. *J. Biotechnol.* **2018**, *265*, 31–39. [CrossRef]
11. Brigham, C.J.; Riedel, S.L. The Potential of Polyhydroxyalkanoate Production from Food Wastes. *Appl. Food Biotechnol.* **2018**, *6*, 7–18. [CrossRef]
12. Kunasundari, B.; Sudesh, K. Isolation and recovery of microbial polyhydroxyalkanoates. *Express Polym. Lett.* **2011**, *5*, 620–634. [CrossRef]
13. Jacquel, N.; Lo, C.-W.; Wei, Y.-H.; Wu, H.-S.; Wang, S.S. Isolation and purification of bacterial poly(3-hydroxyalkanoates). *Biochem. Eng. J.* **2008**, *39*, 15–27. [CrossRef]
14. Fung, F.M.; Su, M.; Feng, H.; Li, S.F.Y. Extraction, separation and characterization of endotoxins in water samples using solid phase extraction and capillary electrophoresis-laser induced fluorescence. *Sci. Rep.* **2017**, *7*, 10774. [CrossRef] [PubMed]
15. Hamilton, R.J. Oxidative rancidity as a source of off-flavours. In *Taints and Off-Flavours in Food*; Woodhead Publishing Limited: Cambridge, UK, 2003; pp. 140–158.
16. Koller, M.; Bona, R.; Chiellini, E.; Braunegg, G. Extraction of short-chain-length poly-[(R)-hydroxyalkanoates] (scl-PHA) by the antisolvent acetone under elevated temperature and pressure. *Biotechnol. Lett.* **2013**, *35*, 1023–1028. [CrossRef] [PubMed]
17. Khosravi-Darani, K.; Vasheghani-Farahani, E. Application of supercritical fluid extraction in biotechnology. *Crit. Rev. Biotechnol.* **2005**, *25*, 231–242. [CrossRef] [PubMed]
18. Kokosa, J.M. Recent Trends in Using Single-Drop Microextraction and Related Techniques in Green Analytical Methods. *Trends Anal. Chem.* **2015**, *71*, 194–204. [CrossRef]
19. Barros, P.; Moreira, E.; Elias Pereira, N.; Leite, G.; Moraes Rezende SG, F.; Guedes de Pinho, P. Development and validation of automatic HS-SPME with a gas chromatography-ion trap/mass spectrometry method for analysis of volatiles in wines. *Talanta* **2012**, *101*, 177–186. [CrossRef] [PubMed]
20. Curran, K.; Strlič, M. Polymers and volatiles: Using VOC analysis for the conservation of plastic and rubber objects. *Stud. Conserv.* **2014**, *60*, 1–14. [CrossRef]

21. Vilaplana, F.; Martínez-Sanz, M.; Ribes-Greus, A.; Karlsson, S. Emission pattern of semi-volatile organic compounds from recycled styrenic polymers using headspace solid-phase microextraction gas chromatography–mass spectrometry. *J. Chromatogr. A* **2010**, *1217*, 359–367. [CrossRef]
22. Kaykhaii, M.; Linford, M.R. Application of Microextraction Techniques Including SPME and MESI to the Thermal Degradation of Polymers: A Review. *Crit. Rev. Anal. Chem.* **2016**, *47*, 172–186. [CrossRef]
23. Hashemi, S.H.; Kaykhaii, M.; Khajeh, M. Molecularly Imprinted Polymers for Stir Bar Sorptive Extraction: Synthesis, Characterization, and Application. *Anal. Lett.* **2015**, *48*, 1815–1829. [CrossRef]
24. Wang, S.; Peng, Y. Natural zeolites as effective adsorbents in water and wastewater treatment. *Chem. Eng. J.* **2010**, *156*, 11–24. [CrossRef]
25. Franchini, E. Structuration of Nano-Objects in Epoxy-based Polymer Systems: Nanoparticles & Nanoclusters for Improved Fire Retardant Properties. Ph.D. Thesis, Institut National des Sciences Appliquées de Lyon, Lyon, France, 2008.
26. Volle, N.; Giulieri, F.; Burr, A.; Pagnotta, S.; Chaze, A.M. Controlled interactions between silanol groups at the surface of sepiolite and an acrylate matrix: Consequences on the thermal and mechanical properties. *Mater. Chem. Phys.* **2012**, *134*, 417–424. [CrossRef]
27. Peinado, V.; García, L.; Fernández, A.; Castell, P. Novel lightweight foamed poly(lactic acid) reinforced with different loadings of functionalised Sepiolite. *Compos. Sci. Technol.* **2014**, *101*, 17–23. [CrossRef]
28. Zheng, Y.; Zaoui, A. Mechanical behavior in hydrated Na-montmorillonite clay. *Physica A* **2018**, *505*, 582–590. [CrossRef]
29. Wang, S.; Song, C.; Chen, G.; Guo, T.; Liu, J.; Zhang, B.; Takeuchi, S. Characteristics and biodegradation properties of poly(3-hydroxybutyrate-co-3-hydroxyvalerate)/organophilic montmorillonite (PHBV/OMMT) nanocomposite. *Polym. Degrad. Stab.* **2005**, *87*, 69–76. [CrossRef]
30. García-Quiles, L.; Fernández, A.; Castell, P. Sustainable Materials with Enhanced Mechanical Properties Based on Industrial Polyhydroxyalkanoates Reinforced with Organomodified Sepiolite and Montmorillonite. *Polymers* **2019**, *11*, 696. [CrossRef] [PubMed]
31. Félix, J.S.; Domeño, C.; Nerín, C. Characterization of wood plastic composites made from landfill-derived plastic and sawdust: Volatile compounds and olfactometric analysis. *Waste Manag.* **2013**, *33*, 645–655. [CrossRef]
32. Lattuati-Derieux, A.; Egasse, C.; Thao-Heu, S.; Balcar, N.; Barabant, G.; Lavédrine, B. What do plastics emit? HS-SPME-GC/MS analyses of new standard plastics and plastic objects in museum collections. *J. Cult. Herit.* **2013**, *14*, 238–247. [CrossRef]
33. Espert, A.; de las Heras, L.A.; Karlsson, S. Emission of possible odourous low molecular weight compounds in recycled biofibre/polypropylene composites monitored by head-space SPME-GC–MS. *Polym. Degrad. Stab.* **2005**, *90*, 555–562. [CrossRef]
34. Mahesh, K.R.V.; Murthy, H.N.N.; Kumaraswamy, B.E.; Raghavendra, N.; Sridhar, R.; Krishna, M.; Pattar, N.; Pal, R.; Sherigara, B.S. Synthesis and characterization of organomodified Na-MMT using cation and anion surfactants. *Front. Chem. China* **2011**, *6*, 153–158. [CrossRef]
35. Jalali, A.M.; Taromi, F.A.; Atai, M.; Solhi, L. Effect of reaction conditions on silanisation of sepiolite nanoparticles. *J. Exp. Nanosci.* **2016**, *11*, 1171–1183. [CrossRef]
36. González-Ausejo, J.; Gámez-Pérez, J.; Balart, R.; Lagarón, J.M.; Cabedo, L. Effect of the addition of sepiolite on the morphology and properties of melt compounded PHBV/PLA blends. *Polym. Compos.* 2017. [CrossRef]
37. Wang, H.H.; Zhou, X.R.; Liu, Q.; Chen, G.Q. Biosynthesis of polyhydroxyalkanoates homopolymers by Pseudomonas putida. *Appl. Microbiol. Biotechnol.* **2011**, *89*, 1497–1507. [CrossRef] [PubMed]
38. Wang, X.; Zhang, H.; Liu, M.; Jia, D. Thermal stability of poly(3-hydroxybutyrate-co-4-hydroxybutyrate)/modified montmorillonite bio-nanocomposites. *Polym. Compos.* **2015**, *38*, 673–681. [CrossRef]
39. Tang, D.; Noordover BA, J.; Sablong, R.J.; Koning, C.E. Metal-free synthesis of novel biobased dihydroxyl-terminated aliphatic polyesters as building blocks for thermoplastic polyurethanes. *J. Polym. Sci. A Polym. Chem.* **2011**, *49*, 2959–2968. [CrossRef]
40. Corre, Y.M.; Bruzaud, S.; Audic, J.L.; Grohens, Y. Morphology and functional properties of commercial Polyhydroxyalkanoates: A comprehensive and comparative study. *Polym. Test.* **2012**, *31*, 226–235. [CrossRef]
41. Ipsita, R.; Visakh, P.M. *Polyhydroxyalkanoate (PHA) Based Blends, Composites and Nanocomposites*; Royal Society of Chemistry: Cambridge, UK, 2015.

42. Wypych, G. *Handbook of Nucleating Agents*; Chemtech Publishing: Toronto, ON, Canada, 2016; ISBN 978-1-895198-93-5.
43. Tartaglione, G.; Tabuani, D.; Camino, G. Thermal and morphological characterisation of organically modified sepiolite. *Microporous Mesoporous Mater.* **2008**, *107*, 161–168. [CrossRef]
44. Lvov, Y.; Guo, B.; Fakhrullin, R.F. *Functional Polymer Composites with Nanoclays*; RSC Smart Materials: Cambridge, UK, 2016; ISBN 1782624228.
45. Lemić, J.; Tomašević-Čanović, M.; Djuričić, M.; Stanić, T. Surface modification of sepiolite with quaternary amines. *J. Colloid Interface Sci.* **2005**, *292*, 11–19. [CrossRef]
46. Botana, A.; Mollo, M.; Eisenberg, P.; Torres Sanchez, R.M. Effect of modified montmorillonite on biodegradable PHB nanocomposites. *Appl. Clay Sci.* **2010**, *47*, 263–270. [CrossRef]
47. Cervantes-Uc, J.M.; Cauich-Rodríguez, J.V.; Vázquez-Torres, H.; Garfias-Mesías, L.F.; Paul, D.R. Thermal degradation of commercially available organoclays studied by TGA–FTIR. *Thermochim. Acta* **2007**, *457*, 92–102. [CrossRef]
48. Han, L.; Han, C.; Cao, W.; Wang, X.; Bian, J.; Dong, L. Preparation and characterization of biodegradable poly(3-hydroxybutyrate-co-4-hydroxybutyrate)/silica nanocomposites. *Polym. Eng. Sci.* **2011**, *52*, 250–258. [CrossRef]
49. Hongchao, Z.; Kanishka, B.; Pengqun, K.; Juming, T.; Barbara, R.; Scott, M.; Shyam, S. Effects of Oxygen and Water Vapor Transmission Rates of Polymeric Pouches on Oxidative Changes of Microwave-Sterilized Mashed Potato. *Food Bioprocess Technol.* **2016**, *9*, 341–351. [CrossRef]
50. Wilson, A.S. *Plasticisers: Principles and Practice*; The Institute of Materials: London, UK, 1995.
51. Järnström, H.; Saarela, K.; Kalliokoski PPasanen, A.-L. Comparison of VOC and ammonia emissions from individual PVC materials, adhesives and from complete structures. *Environ. Int.* **2008**, *34*, 420–427. [CrossRef] [PubMed]
52. Ohkado, Y.; Kawamura, Y.; Mutsuga, M.; Tamura, H.-O.; Tanamoto, K. Analysis of residual volatiles in recycled polyethylene terephthalate. *J. Food Hyg. Soc. Jpn.* **2005**, *46*, 13–20. [CrossRef]
53. Hu, M.; Jacobsen, C. *Oxidative Stability and Shelf Life of Foods Containing Oils and Fats*; Subchapter 13.5.5 Aldehyde Scavenging Packaging; Elsevier: Amsterdam, The Netherlands, 2016; ISBN 978-1-63067-056-6.
54. Azarbad, M.H.; Jeleń, H. Determination of Hexanal—An Indicator of Lipid Oxidation by Static Headspace Gas Chromatography (SHS-GC) in Fat-Rich Food Matrices. *Food Anal. Methods* **2014**, *8*, 1727–1733. [CrossRef]

polymers

MDPI

Article

Sustainable Materials with Enhanced Mechanical Properties Based on Industrial Polyhydroxyalkanoates Reinforced with Organomodified Sepiolite and Montmorillonite

Lidia García-Quiles [1,*], Ángel Fernández Cuello [2] and Pere Castell [3,*]

[1] Tecnopackaging, Polígono Industrial Empresarium C/Romero N° 12, 50720 Zaragoza, Spain
[2] University of Zaragoza, Escuela de Ingeniería y Arquitectura, Av. Maria de Luna, 3, 50018 Zaragoza, Spain; afernan@unizar.es
[3] Fundación Aitiip, Polígono Industrial Empresarium C/Romero N° 12, 50720 Zaragoza, Spain
* Correspondence: lgarcia@tecnopackaging.com (L.G.-Q.); pere.castell@aitiip.com (P.C.); Tel.: +34-607-01-88-03 (L.G.-Q.); +34-976-46-45-44 (P.C.)

Received: 21 March 2019; Accepted: 15 April 2019; Published: 16 April 2019

Abstract: Microplastics have become one of the greatest environmental challenges worldwide. To turn this dramatic damage around, EU regulators now want to ensure that plastic itself is fully recyclable or biodegradable. The aim of the present work is to develop a biobased and biodegradable biocomposite based on commercial polyhydroxyalkanoates (PHAs) and nanoclays, with the objective of achieving a reduction of rancid odour while avoiding any loss in thermomechanical properties, thus tackling two key disadvantages of PHAs. This research aims at completely characterising the structural, thermal and mechanical behaviour of the formulations developed, understanding the compatibility mechanisms in order to be able to assess the best commercial combinations for industrial applications in the packaging and automotive sectors. We report the development of nine nanobiocomposite materials based on three types of commercial PHA matrices: a linear poly(3-hydroxybutyrate) (P3HB); two copolymers based on poly(3-hydroxybutyrate)-*co*-poly(4-hydroxybutyrate) (P3HB-*co*-P4HB); and nanoclays, which represent a different polar behaviour. Dispersion achieved is highly relevant compared with literature results. Our findings show impressive mechanical enhancements, in particular for P3HB reinforced with sepiolite modified via aminosilanes.

Keywords: biopolymers; nanoclays; nanobiocomposites; extrusion-compounding; polyhydroxyalkanoates; thermal properties; mechanical properties; differential scanning calorimetry; nuclear magnetic resonance; X-ray diffraction

1. Introduction

At least 8 million tonnes of plastics leak into the ocean each year, which is equivalent to dumping the contents of one bin truck into the ocean per minute. In 2016, 27.1 million tonnes of plastic waste were collected through official schemes in Europe, from which 31.1% of plastic post-consumer waste was recycled, 41.6% was dedicated to energy recovery and 27.3% was landfilled [1]. Moreover, landfill rates are very uneven across Europe. In countries where landfill bans are in effect (Belgium, Luxembourg, Netherlands, Germany, Denmark, Switzerland, Austria, Norway and Sweden), less than 10% of plastic waste is landfilled. In other countries, such as Spain and Greece, a staggering amount of over 50% of all plastic waste still finds its way to landfill [2]. Furthermore, the option of exporting plastic waste to EU or non-EU counties has been foreseen and allowed by the existing EU legislation given that there is evidence that recovery of materials is taking place under conditions that are equivalent to the EU legislation [3]. This situation is starting to change. For decades, China was the world's largest

importer of waste, but this has been changing after Beijing banned 24 types of scraps from entering its borders starting January 2018. This decision has forced other countries, such as Europe, USA and Japan, to improve management of their own waste [4]. The problem is even accentuated when talking about microplastics. It is estimated that between 75,000 and 300,000 tonnes of microplastics are released into the environment each year in the EU [5]. These are reasons why EU regulators now want to ensure that the plastic itself is fully recyclable or biodegradable.

In December 2015, the European Commission adopted an EU Action Plan for a circular economy, and in January 2018, the European Commission published its Communication 'A European Strategy for Plastics in a Circular Economy' as an ambitious step towards making the European plastics system more resource-efficient and to drive the change from a linear to a circular system [5]. A circular economy aims to keep products, components and materials at their highest utility and value at all times, emphasising the benefits of recycling residual waste materials [6]. The New Plastics Economy has three main ambitions:

1. Create an effective after-use plastics economy by improving the economics and uptake of recycling, reuse and controlled biodegradation for targeted applications;
2. Drastically reduce leakage of plastics into natural systems (in particular, the ocean);
3. Decouple plastics from fossil feedstocks by exploring and adopting renewably sourced feedstocks.

Therefore, a new sustainable solution for the plastic sector needs to tackle three pillars: eco-design, functionality and end-of-life. In this sense, various investigations are aimed at decreasing the amounts of plastic waste and manufacturing products with less environmental impact via recycling strategies or via the use of biodegradable materials. Aware of the environmental impacts of the production of synthetic polymers from nonrenewable resources, a promising solution could be the usage of mixtures of biopolymers that gradually replace those synthetic polymers. It is relevant to recall that biopolymers, also referred to in some cases as bioplastics, can be classified into two main groups. When referring to their origin, they can be biobased or fossil-based, and when alluding to end-of-life, they can be biodegradable or nonbiodegradable. Different families and combinations can be found. For example, polylactic acid (PLA) as well as polyhydroxyalkanoates (PHAs) are renewable resource-based biopolyesters, in contrast to polycaprolactone (PCL), polybutylene succinate (PBS) and aliphatic–aromatic polyesters, which are petroleum-based biodegradable polyesters [7–9].

Nowadays, bioplastics represent about one percent of the approximately 320 million tonnes of plastic produced annually [10]. By 2020, biodegradable plastics are expected to represent 18% of bioplastics production and biobased, nonbiodegradable plastics will rise to 82% [11].

The development of new biopolymer materials will require availability of the raw material (second- and third-generation feedstocks), surpassing of market barriers facing economic disadvantages, and additional technological improvements dealing, for example, with higher heat resistance, UV stabilization, controlled barrier properties to water vapour and gases, and better mechanical properties. Blending is a useful strategy to modify material properties for specific applications. In addition to incorporation of fibres or nanoclays, the mentioned technical properties of biopolymers may be improved by chemical and physical crosslinking, or even with the use of surface treatments, such as grafting and coating. The economical barrier is expected to be compensated once disposal costs are taken into consideration and/or production volumes have increased further [12].

Polyhydroxyalkanoates (PHAs) are gaining attention in the biopolymers market due to their high biodegradation rates as well as processing versatility, thus representing a potential sustainable replacement for fossil oil-based commodities. PHAs are most relevant when referring to new biopolymer applications [13]. Polyhydroxyalkanoates (PHA) are polyesters which are intracellularly deposited by bacteria for energy storage. When carbon sources are alternated over time during the bacterial fermentation process, microorganisms synthesize PHA block copolymers. PHA biopolymers are formed mainly from saturated and unsaturated hydroxyalkanoic acids. Each monomer unit harbours a side-chain R group, which is usually a saturated alkyl group. These features give rise to diverse

PHA combinations [14]. PHA biopolyesters include isotactic poly(3-hydroxybutyrate) P3HB, with a high melting point, being very crystalline and brittle; and the poly(3-hydroxybutyrate-*co*-valerate) PHBV copolymer, with a lower crystallinity and lower melting point. More recently, new customised copolymers have been developed by randomly incorporating controlled amounts of flexible linear aliphatic spacers along the main chain; for example, 3-hydroxypropionate (3HP) or 4-hydroxybutyrate (4HB) [15]. The results are semicrystalline copolymer structures designed to have a tailored melting point between 80 °C and 150 °C and that are less susceptible to thermal degradation during processing. Their properties range from brittle thermoplastics to gummy elastomers and can be controlled by the choice of substrate, bacteria and fermentation conditions. These biopolymers have attracted much interest for many new products in the medical and pharmaceutical sectors due to their natural ability to control drug release [16,17] and intrinsic biocompatibility properties [18]. More recently, the material has found new niches in the replacement of conventional oil-based plastic products. Good examples can be found in the food and cosmetic packaging sectors [19], mulch films for agricultural purposes [20], as bio-fuels [21] and even as interior automobile parts. However, PHA biopolymers face a technical barrier which is unique and intrinsic to this biopolyester family and the way it is produced: rancid odour [22]. Lipid residues and endotoxins often remain attached to the biopolymer after extraction. These lipids are oxidised to odourless and flavourless intermediates that could break into molecules giving off-flavours. These conditions are associated with the production of free radicals by autoxidation, which has been recognized as a potential shortcoming of PHA for many applications [23,24]. Different solutions can be approached in order to avoid polymer autoxidation. Most of them deal with the extraction and purification stages of the polymer, but these stages are the most expensive ones, especially if high purity is required. However, the current situation is that nowadays, plastic product converters purchase commercial-grade PHA with unsatisfactory smell, which is a handicap for many potential applications. Our proposed solution approaches the compounding stage of customised blends for industrial applications. It tackles the use of nanoclays with high adsorbance properties which are able to capture volatile compounds responsible for the displeasing fragrance.

Commercial PHAs purchased for plastic parts production are usually blended with other copolyesters and contain small amounts of plasticisers and metal elements, such as Na^{+}, Ca^{2+} and Mg^{2+}. These additives have an effect on the crystallisation, thermal stability [25], mechanical properties [26] and biodegradability of the commercial materials. However, this behaviour is not always functional enough for many industrial applications, and the use of other additives or fillers such as fibres [27–29] or nanoparticles [30,31] is needed. Their use gives rise to thermoplastic nanobiocomposite structures. To enhance the compatibility between the nanoparticle and the polymer is key to better fit the requirements of a certain application, although improving the compatibility of a heterogeneous system is often accompanied by the deterioration of other properties [32,33]. Sepiolite nanoclay fibres form ribbons with inner channels called zeolitic tunnels, offering interesting characteristics such as microporosity and large specific surface area. Due to its natural morphology, sepiolite is considered a good reinforcing agent as well as presenting an outstanding sorption capacity [34]. Moreover, there is much literature demonstrating that its surface functionalisation also helps to improve the transference of properties to the polymeric matrix [35]. In this work, natural sepiolite and sepiolite functionalised via aminosilanes are compared, and with montmorillonite as well. Montmorillonite falls into the smectite group and is largely used for its swelling and adsorption properties [36].

The objective of this research is to develop biobased and biodegradable biocomposites based on commercial PHA and nanoclays, enhancing their thermomechanical properties. This research aims at completely characterising the structural, thermal and mechanical behaviour of the formulations developed and tackles the understanding of the compatibility mechanisms that take place in order to be able to assess the best commercial combinations for industrial applications in the packaging and automotive sectors.

In the present work, three grades of PHAs were reinforced with modified and unmodified sepiolite and montmorillonite kindly provided by TOLSA (Spain). The clays differ in geometries, with sepiolites

being T1 and T2 needles and montmorillonite being T3 fibres formed by sheets. The degree of improvement in the PHAs' properties is a combination of the morphology of the clays, their dispersion in the polymer matrix and their interfacial polymer–clay interactions. The three candidates selected present different behaviours, from polar (T1) and neutral (T2) to nonpolar (T3) features, which directly affect the affinity for the PHA polyesters and therefore affects the matrix's final properties in a different manner.

2. Materials and Methods

2.1. Materials

Three grades of PHAs were used as polymer matrixes: Mirel PHA1005, Mirel PHA3002 (both food contact-grade P3HB-*co*-P4HB grades, purchased from Metabolix USA) and Biomer PHB P226 (isotactic and linear short chain length scl-PHA homopolymer P3HB grade purchased from Biomer, Germany).

Three different modified and unmodified organoclays were kindly provided by TOLSA (hereby referred to as T1, T2 and T3, which have been previously characterised by other studies [34,37–39]), being:

- T1: Modified sepiolite: organically modified through aminosilane groups on the surface;
- T2: Natural sepiolite without modifications on its surface (naturally containing silanol groups, commercially marketed as Pangel 9);
- T3: Natural sodium montmorillonite (Na-MMT) modified with a quaternary ammonium salt; it is an anionic organoclay (highly compatible with nonpolar polymers).

2.2. Nanobiocomposite Preparation

PHA/clay formulations were prepared by extrusion-compounding with a 26-mm twin-screw Coperion ZSK 26 compounder machine (Germany). Twelve different formulations were studied in total, accounting for the three control matrixes plus nine developed materials prepared on the compounder machine by loading them with the three nanoclays at 3 wt.% in all cases (see description in Table 1). The melted polymers and nanoclay powder were mixed at a screw speed of 125 rpm; temperature was increased from 150 °C in the feeding zone up to 165 °C at the nozzle for PHA1005 and PHA3002 (P3HB-*co*-P4HB formulations) and slightly decreased from 140 °C in the feeding zone up to 160 °C at the nozzle when blending PHB226 (P3HB). The compounding was extruded through a 2-mm diameter die for a constant output of 10 kg/h. The extrudate was quenched in a water bath at room temperature, dried and cut into pellets.

Table 1. Summary of material formulations based on poly(3-hydroxybutyrate) (P3HB); poly(3-hydroxybutyrate)-*co*-poly(4-hydroxybutyrate) (P3HB-*co*-P4HB) and nanoclays

Material Formulation	Commercial Matrix Used	Nature of the PHA	Type of Reinforcement (3 wt.%)
PHA1005	PHA1005	P3HB-*co*-P4HB	17% P4HB/P3HB and talc
PHA1005_T1	PHA1005	P3HB-*co*-P4HB	T1: Aminosilane sepiolite
PHA1005_T2	PHA1005	P3HB-*co*-P4HB	T2: Natural sepiolite
PHA1005_T3	PHA1005	P3HB-*co*-P4HB	T3: Sodium montmorillonite: quaternary ammonium salt
PHA3002	PHA3002	P3HB-*co*-P4HB	23.5% P4HB/P3HB and talc
PHA3002_T1	PHA3002	P3HB-*co*-P4HB	T1: Aminosilane sepiolite
PHA3002_T2	PHA3002	P3HB-*co*-P4HB	T2: Natural sepiolite
PHA3002_T3	PHA3002	P3HB-*co*-P4HB	T3: Sodium montmorillonite: quaternary ammonium salt
PHB226	PHB226	P3HB	Traces of PBA (polybutyladipate), plasticiser, and talc found
PHB226_T1	PHB226	P3HB	T1: Aminosilane sepiolite
PHB226_T2	PHB226	P3HB	T2: Natural sepiolite
PHB226_T3	PHB226	P3HB	T3: Sodium montmorillonite: quaternary ammonium salt

Specimens for mechanical and tensile testing were obtained by injection moulding with a JSW 85 EL II electric injection machine (JSW, Tokyo, Japan) following ISO 178 and ISO 527 standards. Temperature profile was increased from 160 °C at the hopper up to 200 °C at the nozzle. Dosage and filling pressure were varied for each formulation injected. A packing pressure of 25% was applied.

2.3. General Characterisation Methods

Mechanical tests were conducted under ambient conditions using a Zwick Roell Z 2.5 (Zwick, Germany). At least five specimens per material were tested, according to ISO 178 and ISO 527 methodology.

Nuclear magnetic resonance (NMR) spectra were measured on a Bruker instrument at 25 °C using 400 MHz for the three neat biopolymers (PHB226, PHA1005 and PHA3002) (Bruker, Karlsruhe, Germany). Samples were dissolved in $CDCl_3$ and washed to clean them up from mineral fillers. ^1H NMR spectra were obtained.

Thermal characterisation was carried out by differential scanning calorimetry (DSC) using a Mettler Toledo 223E (Mettler, Columbus, OH, USA). Dynamic heating was performed from room temperature to 220 °C at a rate of 10 °C/min for 8 mg samples placed into standard 40 µL aluminium crucibles, under a 100 mL/min flow of nitrogen. DSC tests were duplicated to ensure the reproducibility of results.

Energy-dispersive X-ray spectroscopy (EDX) was also used for samples' chemical characterization in a Hitachi S3400N (Hitachi, Tokyo, Japan). The diffraction pattern was determined using a Bruker D8 X-ray diffraction (XRD) equipment using Cu Kα irradiation at 44 kV (Bruker, Karlsruhe, Germany). The diffractogram was carried out between 5° and 80° at a step of 0.5°/min. XRD was used to identify changes in PHA/clay blends' crystalline structure. XRD tests were duplicated to ensure the reproducibility of results.

3. Results and Discussion

3.1. Mechanical Results (Flexural and Tensile)

The mechanical properties of composite materials are always a compromise between stiffness and toughness. These properties are generally mutually exclusive. The elastic modulus (E), tensile strength (σ_M) and elongation at break (ε_B) are useful parameters which describe the mechanical behaviour of the developed materials and are closely related to the internal microstructure. Toughness (U_T) was calculated by integrating the stress–strain curves and obtaining the area under the curves. The mechanical properties determined from uniaxial tensile and flexural tests are summarized in Table 2.

It is well-documented that P3HB seems to be more crystalline, mechanically stiffer, stronger and less ductile than its copolymers [40]. According to Koller et al., pure P3HB presents a tensile strength of 40 MPa and 6% elongation at break, while pure P4HB presents 104 MPa and 1000%, respectively [41]. Cong et al. demonstrated that the addition of a 4HB copolymer at up to 30 wt.% into P3HB causes reductions in the storage modulus, stress at yield and stress at break, while the elongation at yield and at break increases [42]; however, our results show a different situation. It has to be taken into account that even our commercial-grade P3HB (PHB226) may contain small percentages of talc, plasticiser and other polyesters. The presence of these and other additives will be explored and discussed by DSC and NMR analysis. Therefore, the general statements and results obtained by other authors in similar research works where the polymers were synthetised and blended in a laboratory with nanoparticles might not always correspond to others' findings. In addition, NMR results established the molar ratio of the P3HB-*co*-P4HB blends, with PHA3002 being the one containing the highest percentage of P4HB. The amounts of talc that each blend contains highly affects the elongation at break and toughness of the blends, and it is not possible to find a correlation due to its random behaviour.

Table 2. Mechanical properties under tensile and flexural forces: modulus (E), flexural strength (σ_M), elongation at break (ε_B) and toughness (U) for all characterised materials.

Material	E (MPa)	σ_M (MPa)	ε_B (%)	U_T (MPa)	E_f (MPa)	σ_{fM} (MPa)	ε_{fB} (%)	U_{fT} (MPa)
PHB 226	2028 ± 68	21.8 ± 0.5	3.1 ± 0.3	53.9	1316 ± 28	30.2 ± 0.4	4.4 ± 0.2	98.8
PHB 226_T1	2004 ± 66	23.7 ± 0.6	4.6 ± 0.7	83.9	1306 ± 17	30.1 ± 1.0	4.8 ± 0.3	115.8
PHB 226_T2	2435 ± 88	22.1 ± 1.1	1.9 ± 0.3	33.6	1318 ± 68	34.1 ± 0.9	4.7 ± 0.4	111.5
PHB 226_T3	2006 ± 65	22.5 ± 0.3	4.2 ± 0.3	69.9	1871 ± 9	42.3 ± 0.3	3.6 ± 0.1	99.3
PHA 1005	2770 ± 99	22.4 ± 0.7	2.0 ± 0.1	32	1801 ± 39	31.5 ± 0.4	3.9 ± 0.1	92.8
PHA 1005_T1	3411 ± 98	25.2 ± 0.5	1.8 ± 0.1	33.9	2066 ± 71	32.2 ± 0.8	3.2 ± 0.1	71.9
PHA 1005_T2	3420 ± 218	25.9 ± 0.6	1.9 ± 0.2	38.2	2240 ± 88	33.9 ± 1.7	2.7 ± 0.1	60.3
PHA 1005_T3	3755 ± 41	23.8 ± 0.6	1.4 ± 0.1	24.9	2980 ± 90	47.6 ± 2.3	2.6 ± 0.2	81.6
PHA 3002	2263 ± 37	24.7 ± 0.5	2.8 ± 0.1	50	1342 ± 71	33.9 ± 1.5	5.0 ± 0.2	121.9
PHA 3002_T1	1997 ± 48	26.2 ± 0.3	4.1 ± 0.2	84.6	1485 ± 35	34.3 ± 1.1	4.2 ± 0.1	97.6
PHA 3002_T2	2961 ± 87	28.7 ± 0.3	2.9 ± 0.2	65.7	1807 ± 85	43.1 ± 1.1	4.4 ± 0.8	128.9
PHA 3002_T3	2463 ± 115	27.4 ± 0.2	3.3 ± 0.3	68.9	2358 ± 7	57.0 ± 0.7	4.3 ± 0.3	134.1

Our results show that PHA1005 is the stiffest matrix with the highest elastic modulus under tensile and flexural stress, followed by PHA 3002 and finally by PHB226. However, PHB226 presents a high elongation at break, probably due to the PBA, and in consequence, it presents the highest toughness under tensile efforts. PHA3002 maintains an intermediate behaviour under tensile and flexural stresses.

A common behaviour found in many nanobiocomposites when nanoparticles are introduced is an increase in the elastic modulus, a preservation or even a slight increase in the tensile stress and a decrease in elongation at break [43]. Botana et al. demonstrated that the incorporation of small quantities of montmorillonite (2–10% in mass) with a certain degree of exfoliated structure have a great influence on the properties of the final material, such as mechanical strength, stiffness, thermal stability, conductivity and gas barrier properties [44]. Our samples comply partially with this generally observed behaviour, depending on the nanoclay reinforcing the matrix.

In the PHA1005 blends, the three nanoclays generally improved the stiffness of the material (both under flexural and tensile forces), with T3 (montmorillonite) being the one introducing the greatest enhancement. PHA1005_T3 shows a 35% higher Young's modulus and 65% higher flexural modulus than neat PHA1005, although toughness was clearly compromised. Only for PHA1005_T2 was toughness enhanced under tensile forces, by 19%.

PHA3002 T1 (sepiolite modified via aminosilanes) greatly improves elongation at break, by 46%, and the increase in toughness by 69% compared to neat PHA3002 is therefore noticeable (although the elastic modulus is slightly compromised, falling by 13%). The modified surface of T1 may have acted as plasticiser with this matrix, favouring the interphase affinity. When testing the same material, PHA3002_T1, under flexural forces, an opposite behaviour was found, with the flexural modulus being increased and the elongation at break and toughness reduced. The authors consider that the alignment or orientation of the sepiolite ribbons with the flow when extruding the material may have also an important effect on the final strain and toughness. For PHA3002_T2, there was an increase of 31% in the Young's modulus, while the elongation at break was maintained, as for PHA3002, and hence the tenacity was improved. The same tendency of behaviour was found for this material under flexural stress. Finally, a significant improvement was found when adding T3. The exfoliation of the layers (see XRD results) induced mechanical improvements for all parameters under tensile forces and was even more significant under flexural ones. PHA3002_T3 had its flexural modulus increased by 75%. The elongation at break was slightly reduced, but the improvement in stiffness was so high that final toughness was also increased by 10% compares to neat PHA3002.

For PHB226, the greatest improvement in mechanical properties is observed for T1, as it maintains the elastic modulus while substantially improving the elongation at break and therefore toughness. PHB226_T1 is the only material developed for which all the mechanical properties were maintained or increased. Under tensile stress, strain is increased by 48% and toughness by 55%, while under flexural stress, strain is increased by 9% and toughness by 17%. Probably the combination of a good dispersion in the blend, the large surface area of sepiolite and the organic modification of T1 produces a better

interaction and affinity due to the aminosilane modification, which may present a better compatibility with the P3HB matrix.

This behaviour disappears for T2 (sepiolite without the functional modification). Despite the large amount of silanol groups, T2 acts as a filler, enhancing the stiffness of the material by 20% for tensile stress, but reducing elongation at break and toughness considerably. The material has similar mechanical properties to neat PHB226 under flexural stresses. Finally, when T3 is added, the overall stiffness of the material is improved, in particular increasing by 42% under flexural forces, but strain and toughness are compromised. The exfoliation of montmorillonite probably leads to the enhancement in toughness under tensile forces, but this is not as significant as the one produced by T1.

As a global pattern in all nanobiocomposites developed, T1 (modified sepiolite) probably has a better interphase, as elongation at break enhances while flexural modulus is maintained, whereas T2 formulations show higher rigidity and poorer toughness. T3 produces significant overall mechanical improvements, which may be induced due to exfoliation of clay layers leading to an increase of the effective aspect ratio, but probably the nonpolar behaviour of montmorillonite hinders a better polymer–matrix interaction.

Mechanical analysis demonstrates that PHA1005 is the matrix with the least overall improvement in mechanical properties when reinforcing the matrix with organoclays, while PHB226_T1 shows the greatest enhancement (modified sepiolite). However, it has to be taken into account that for all reinforced nanocomposites, there is an optimum load of filler, over which the matrix appears to be oversaturated. The combination of talc plus nanoclay may lead to this point being reached, which produces a loss of mechanical properties, especially regarding elongation at break and toughness. The results obtained for PHA1005 suggest that the material may contain larger amounts of talc than PHA3002.

Czerniecka-Kubicka et al. developed Biomer P3HB samples loaded with modified montmorillonite (cloisite 30B: natural montmorillonite modified with methylbis(2-hydroxyethyl)tallowalkylammonium cations) at 1 wt.%, 2 wt.% and 3 wt.% and evaluated the mechanical properties under flexural stress. The flexural modulus values found for nanocomposite containing 1 wt.% nanoclay increased by approximately 20% in relation to the nonmodified sample. Further increase of nanofiller content caused a decrease in flexural modulus values, but they were still higher than that of neat P3HB [45]. Our findings have shown an increase of 42% in flexural modulus when adding 3 wt.% of montmorillonite to Biomer P3HB (PHB226). The increase in the flexural modulus with PHA1005 and PHA3002 is even higher (65% and 75%, respectively). Therefore, we can confirm that either the dispersion or the surface modification has an extremely important effect on the composite. Dispersion is directly related to the extrusion-compounding process, where the temperature and shear force induced are key parameters in obtaining a homogenous blend without degrading the biopolymer. Compared to Czerniecka-Kubicka et al., our samples were mixed at lower temperatures, but at much higher rotation speeds (inducing higher shear and therefore favouring dispersion and delamination of montmorillonite in this case).

3.2. NMR

The ^{1}H NMR spectra of P3HB (PHB226) and P(3HB-*co*-4HB) (PHA1005 and PHA3002) polymers is shown in Figure 1, with the various peaks labelled for the different protons in the 3HB and 4HB units, as well as for additional polyesters identified (PBA, plasticiser).

Very few articles have been dedicated to understanding the commercial grades of PHAs, which are the real ones that industry is incorporating in our daily products. Some characterisations have been done by Corre et al. [46] for commercial P3HB (PHB226), P3HB-*co*-P4HB (1006, 3002) and P3HB-*co*-3HV (Y1000P), but without explaining their composition in detail or giving further assessment on how to improve their weak properties.

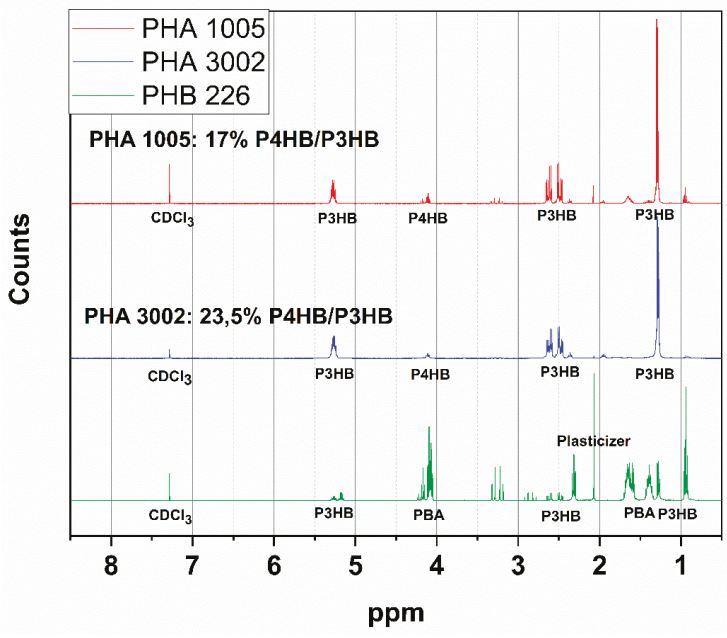

Figure 1. The ^{1}H-NMR spectra of PHB226, PHA1005 and PHA3002.

Modification of PHA with plasticisers and other copolymers is a conventional technique for the improvement of the processability and brittleness of PHA. Nuclear magnetic resonance (NMR) is a useful analytical method to obtain information about the organic chemical structure of our blends.

The ^{1}H NMR spectra of PHB226, PHA1005 and PHA 3002 were obtained. Results revealed the domain structure of P3HB in all samples. Specific peaks associated to P3HB and P4HB [47,48] protons were identified and the molar relation between PH3B and PH4B in PHA1005 and PHA3002 samples was obtained by integrating the peaks. The content found for P4HB corresponds to 23.5 mol % in PHA3002 and 17 mol % in PHA1005.

The presence of peaks different from P3HB were found in PHB226 samples (according to the product datasheet, it is 89.8% biobased P3HB). These are probably related to the addition of another biopolyester used as a plasticiser. Those peaks did not appear for PHA1005 or PHA 3002 polymers. Taking into account the nature of PHB, two candidates have been found to be potential copolymers in the blend: polybutylene adipate (PBA) components and triacetin (or citrate ester) [49,50]. Specific peaks that may be associated to PBA appeared between 1.3 and 1.7 ppm [48]. The presence of PBA is corroborated in DSC results, with the melting peak found at 50°C, which is characteristic of this polyester [51]. Initially, the addition of Polybutyrene adipate terephtalate (PBAT) was considered as it is a frequent additive used in many biopolymer formulations. However, the lack of a single peak at 8 ppm [43] confirms that no terephthalate had been added into any of the formulations. Often, these polyesters are added on purpose as plasticisers, and other times, they may be considered to be impurities from the purification stage of the PHA. It has to be taken into consideration that different batches of these materials may show slight differences due to additive traces used during polymer growth as carbon sources for the strain of microbe. For example, acetic acid, adipic acid, propionic acid or dodecanioic acid are used as precursors in the production of P3HB-*co*-P4HB or PHBHV4HB polymers [52]. The ^{1}H-NMR spectrum of PHB226, PHA1005 and PHA3002 can be found in Figure 1.

3.3. DSC—Differential Scanning Calorimetry

DSC measurements were performed in order to observe the melting behaviour of the crystals and to determine the changes induced in the highly ordered structure. The DSC analysis of the samples was carried out over three cycles, involving a first heating cycle followed by a second cooling cycle and finally a third heating. This method ensures the removal of residual thermal behaviour in the polymers.

According to the literature data, the T_g of PHA biopolymers may vary between −1 and −48 °C, depending on the type and molar fraction of the second monomer (4HB, 3HV, 3HO, 3HHx) [53,54]. The T_g of P3HB has been reported to vary between −3 and 5 °C, and the T_g of P4HB at −46 °C [48]. Our thermograms for the neat matrixes are aligned to those of other neat PHAs reported by Corre et al. [46].

Comparing the T_g of our three raw matrixes, we can observe that the T_g of PHA1005 and the T_g of PHA3002 have almost no deviations around −24°C, which is about 10 °C lower than the T_g of PHB226. This behaviour is expected as the P4HB side groups in PHA1005 and PHA3002 increase the free volume in the molecule, resulting in a decrease of T_g.

The increase in the T_g transition appreciated in the DSC diagram for PHA3002_3T1 should be highlighted, which might be induced by an increase of the amorphous phase in the interphase between the matrix and the nanoclay. For the case of PHA1005 bionanocomposite formulations, it can be observed that the three nanoclays (T1, T2 and T3) induce a decrease of T_g, being especially remarkable in the case of T3. In addition, the transition becomes almost indiscernible, which suggests that nanoclays induce a plasticiser effect in the three cases. Moreover, T_g lowering could result from some interfacial interactions between the clay and the matrix producing disorganized molecular arrangements within the interphase, probably due to an agglomeration of filler, which might become a predominant factor for T_g decrease [55,56]. This tendency in behaviour can be observed for PHB226 too. T1 and T2 produce a clear decrease of T_g. PHB226 is the polymer with the highest crystallinity in comparison with PHA1005 and PHA 3002. Thus, T_g results are difficult to be obtained as the transition is not clear in the DSC diagram due to the very low amorphous range. In the case of T3, it is not possible to find an approximate value. This is an indication about the good dispersion achieved with this nanoclay and is in coherence with the results obtained in XRD.

In Figure 2, we can observe that all diagrams show a clear crystallization peak, which indicates that our compounds undergo some small amount of crystallization while heating. Comparing the three matrixes, it can be corroborated that PHB226 is the one with highest crystallinity, followed by PHA3002 and finally PHA1005. This result is in contradiction to the findings of Bayari et al., who confirmed the fact that the degree of crystallinity of P(3HB-*co*-4HB) copolymers decreased with an increase in the amount of the 4HB content [57]. However, these are based on lab-produced PHA materials, not commercial blends, in which the use of additives tailors the crystallisation rates. Our results agree with the findings shown by Corre et al. [46], in which similar Mirel matrixes (P3HB-*co*-P4HB) under polarized optical microscopy (POM) featured larger spherulites with lower nucleation density than PHB226 (P3HB). The introduction of inorganic nanoparticles to increase the nucleation density and decrease the spherulite size is a common practice in commercial PHAs. Examples of these inorganic particles include tungsten disulphide inorganic nanotubes (INT-WS2), boron nitride (BN), talc ($Mg_3Si_4O_{10}(OH)_2$), hydroxyapatite (HA) and zinc stearate (ZnSt) [58], used as nucleation agents to modify the properties of P3HB-*co*-4HB. Wang et al. [58] suggested that the addition of talc increased the crystallisation degree of P3HB-*co*-4HB, but had little effect on the crystallisation rate. This cheap material is used at the industrial level by commercial material producers and it can be found in our neat PHB226, PHA1005 and PHA3002 matrices (according to EDX results carried out by the authors, in which Mg^{2+} cations and silicon are clearly identified).

The PHA1005 DSC diagram is accompanied by a rise in the cold crystallisation temperature and crystallisation enthalpy, with T1 being the nanoclay that induces the highest augmentation. Crystallization temperature (T_c) increases by almost the same ratio in all cases (3–4%) for PHA3002 formulations when adding any of the three nanoclays with respect to the neat matrix. A similar

tendency is obtained for PHB226 compounds, except for the case of PHB226_T3, which suffers a slight decrease with respect to neat PHB226. High Tc implies that the polymer crystallisation ability of the material is better [29].

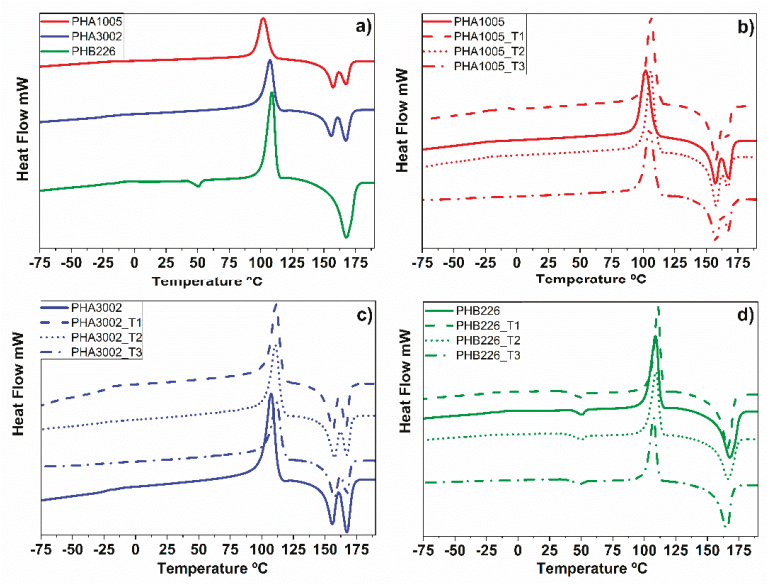

Figure 2. Differential scanning calorimetry (DSC) thermograms. (**a**) Raw matrices: PHA1005, PHA3002 and PHB226; (**b**) PHA 1005 loaded with 3 wt.% T1, T2 and T3; (**c**) PHA 3002 loaded with 3 wt.% T1, T2 and T3; (**d**) PHB 226 loaded with 3 wt.% T1, T2 and T3.

The crystallinity of the samples was calculated for the second heating from the general equation: X_c (%) = ($\Delta H_m/\Delta H°_m$*(1 − w_t))*100, where w_t is the clay fraction and $AH°_m$ is the theoretical melting enthalpy of 100% crystalline PHB polymer, taken as 146 J/g [59].

P3HB chains typically form spherulites that are crystallised from the melt polymer. The nucleation density for P3HB is known to be excessively low, leading to the development of extremely large spherulites which grow radially within P3HB materials. The size varies from several micrometres to a few millimetres, depending on the crystallisation temperature and molecular weight [60]. Lamellar thicknesses in spherulites range from 5 nm to 10 nm, depending on the crystallisation temperature. It is well known that P3HB exhibits two crystal polymorphs: α and β crystals. It is assumed that the β-crystals appear from amorphous chains present between the lamellar crystals of the α-crystal (tie-chain). The β-form is introduced by the orientation of free chains in the amorphous regions between α-form lamellar crystals. The authors understand that these crystals form part of the so-called rigid amorphous phase (RAF) for this particular case of PHA structure. Di Lorenzo et al. assigned a peak around 45 °C to the RAF structure [61]. The presence or absence of this peak depends on the thermal history of the material. Our DSC results corresponds to the second heating, and therefore the thermal history of our matrixes has already been removed and the peak does not appear. However, our XRD results show the presence of β-crystals. The rigid amorphous structure growths during the first stage of cold crystallisation and slows down crystallisation before completion, creating an immobilised amorphous layer that surrounds the crystals. The physical state of the rigid amorphous fraction affects the crystallisation kinetics of P3HB. The crystal dimensions of P3HB and P4HB have been deeply characterised in the literature.

Our DSC results show the two peaks related to the two distinct populations of crystals (P3HB and P4HB) for all composite formulations. To understand the effects induced on crystallinity, it is

important to take into account the differences in the kinetics and crystal formation in the copolymers between P3HB and P4HB, as well as the particular modifications that the nature of each nanoclay (with different polar affinity and structure) is introducing into the system. When adding the nanoclays, different behaviours can be observed according to the interphase created, which is directly related to the dispersion grade and interaction of the nanoclays with each polymer.

According to the literature [62], crystals related to P3HB exhibit a higher T_m than those corresponding to PH4B. Different authors report the Tm for pure 3HB to be 171–175 °C [57], while the Tm for pure 4HB appears at 56–58 °C [38]. The Tm for P3HB reported in the literature ranges between 162 °C and 197 °C [63]. The differences in Tm indicate that the size or thickness of P3HB crystals is greater than those for P4HB. Volova et al. compile quite a lot of information related to thermal behaviour and the structure of the different monomers and polymers that form PHAs, in particular for P3HB, P4HB, PHV and PHH [64].

In this research, PHA1005 and PHA3002 samples showed two endothermic peaks which correspond to the two crystalline phases: the 3HB-rich crystalline microregion at 167 °C and the 4HB-rich crystalline microregion around 157 °C. According to the literature [47], P(3HB-*co*-4HB) crystallises like P(3HB), with the 4HB units acting as defects in the crystal lattice when the 4HB content is less than 30 mol % (which has been confirmed in this study with the NMR results). Thus, the multiple melting behaviour of P(3HB-*co*-4HB) samples corresponding to PHA1005 and PHA3002 originates from microphase separation [65]. Kabe et al. studied the transition of spherulite morphology and measured the radial growth rate of spherulites in the blend of polyesters composed of P(3HB-*co*-3HH) and neat PHB with polarisation optical microscopy. They concluded that the radial growth rate of spherulites of neat P3HB was 0.25 mm/min, and complete crystallisation took about 5 min, while for the copolymer, they were 0.0008 mm/min and 9 h, respectively [66]. Therefore, it might be deduced that P3HB crystals appear to present the fastest radial growth rate.

In addition, PHB226 shows a melting peak at 50 °C, indicating the presence of another polymer or plasticiser, as suspected from the NMR results. Mohanty et al. described the presence of citrate plasticiser in this Biomer grade without providing further information [49]. Other authors consider that the material may contain small amounts of other copolymers, such as PBAT or PLA [48,67,68]. Our characterisation results (NMR and DSC) confirm that the formulation contains small amounts of PBA (with a Tm reported between 50 °C and 60 °C) [69], but not PBAT, as there is no trace of terephthalate. Anyhow, comparing the three neat matrixes, it can be observed that PHB226 presents the highest crystallinity of 79.5%, followed by PHA3002 with 44.2% and PHA1005 with 41.2%. Knowing that PHA3002 contains the highest P4HB/P3HB ratio, the crystallinity of PHA3002 should have been lower than that for PHA1005. However, both materials present high loads of mineral fillers (talc, according to EDX results) that most probably influence the crystallisation of the samples, varying the nucleation points and kinetics. The system becomes even more complex when the nanoclays are introduced. There is a decrease in the melting temperature (Tm) of the nanocomposites compared with pure matrixes, as the presence of the nanoclay seemed to induce crystal defects. This observation suggests the formation of smaller crystals with larger imperfections, which melt at lower temperatures [37].

In the case of the PHA1005 copolyester, when incorporating T1 (sepiolite modified with aminosilanes), an increase in crystallinity is achieved, while when introducing T2 (natural sepiolite), it seems not to affect the crystallisation of the original matrix. On the contrary, the tendency of T3 (Na-montmorillonite) is to decrease crystallinity slightly. For the matrix PHA3002, the introduction of sepiolites (T1 and T2) decreases the crystallinity of the material in a similar rate. Furthermore, when T3 is incorporated, the effect is even more acute, which suggests a global tendency for the rigidisation of the side chains when the nanoclays are dispersed. It can be observed that nanoclays particularly affect the peaks which correspond to a major concentration of P3HB crystals, so these are mostly hindering the rearrangement of short P3HB crystals. This result can be explained according to an induced modification in the crystallisation kinetics.

In PHB226, both Tm and ΔH_m decreases, and so does the global Xc. For both sepiolite nanoclays, a clear difference can be found. The superficial aminosilane groups of T1 seem not to be modified as much as natural sepiolite does, neither in the amount of crystals formed nor in their size. Therefore, the global crystallinity of the polymer is maintained. Some authors have demonstrated that nanoclay surfaces can be useful in providing nucleation points [38]. When PHB crystallises in the presence of the clay mineral particles, crystals could grow on the particle surfaces. In these cases, fillers (such as sepiolite, montmorillonite, cellulose nanowhiskers or fine lignin powder) reduce the energy barrier for polymer crystallisation and increase the nucleating density, originating smaller spherulites in higher number than in neat PHB [56]. We can find a slight decrease in Tm for all nanoclays, indicating a small reduction in size of the crystals formed. In addition, we can observe that T2 (natural sepiolite) may present a worse dispersion inside the blend, favouring the formation of agglomerates and therefore reducing the amount of crystals formed (as ΔH_m decreases with respect to neat PHB226 or PHB226_T1). The discontinuity of the silica sheets on the outer edges in sepiolite fibre leads to the presence of numerous silanol groups (Si–OH) at their external surface, which allows easy functionalisation based on their reaction with coupling agents such as organosilanes [39,70]. In T1 nanoclay, sepiolite has been grafted with aminosilane groups which are very stable, generating an organophilic clay that can be more easily dispersed in low-polarity polymers than unmodified clays [71]. Chemical covalent functionalisation is believed to counteract the stacking forces in the nanoparticles and to lead to debundling [72]. This effect may be caused by the intercalation of the attached moieties that finally results in a more effective dispersion within the polymeric matrix. Therefore, the affinity T1 inside the PHB226 may be scattered enough to keep a similar amount of nucleating points.

Anyhow, the most noticeable drop in T_m and ΔH_m is found for PHB226_T3. The exfoliation of montmorillonite may lead to a very high dispersion of the nanoclay. Exfoliation of T3 has been confirmed by XRD results. A good exfoliation should give rise into an increment in crystallinity, as it favours the creation of nucleation points. Nevertheless, the reaction can be so fast that crystals formed may be irregularly arranged, which increases the amorphous regions (RAF) between lamellae, and hence a decrease of the global crystallinity of the material [66], which means that it may hinder PHB226 chain movements by absorbing PHB226 segments on its surface [73]. Botana et al. studied the kinetics and dispersion of organically modified montmorillonites (among them, Na-montmorillonite) in PHB blends under polarised microscopy. The polarised optical micrographs indicated differences in the spherulite size [44]. In particular, Na-montmorillonite produced a large amount of spherulites, but being smaller in comparison to neat PHB. The appearance of disordered areas surrounding some spherulites corroborate that intercalated/exfoliated montmorillonite produces larger amorphous regions.

3.4. WAX—X-ray Diffraction

The XRD spectra of the samples revealed the crystallisation pattern of our PHA samples, which follows the trend of standard P3HB and P3HB-*co*-P4HB. P3HB exhibits two crystal polymorphs: α and β crystals. Diffraction patterns can be found in Figure 3.

The profile of PHB226 exhibits distinct diffraction peaks patterns of 2θ at 13.58, 17.03, 19.93, 21.5; 22.26, 25.69 and 30.69, corresponding to orthorhombic crystal planes (0,2,0), (1,1,0), (0,2,1), (1,0,1), (1,1,1), (1,2,1) and (0,1,2) [74], respectively. Sharp peaks at 2θ = 13.58 and 17.03 show typical α-crystals, while 2θ = 19.93 reveals that β-crystal structure also appears. This peak is also observed for PHA3002 with lesser intensity than PHB226, while for PHA1005, it disappears. This behaviour suggests that PHA3002 presents higher crystallinity than PHA1005, which is in coherence with the results obtained in DSC. For PHA1005 and PHA3002, a new peak not found for PHB226 is observed at 2θ = 27.13, which is attributed to the crystal plane (0,4,0) [75], indicating a preferential order of the copolymer blend P3HB-*co*-P4HB for this crystal structure.

In the neat polymers (PHB226, PHA1005 and PHB3002), X-ray diffraction patterns show three peaks at 2θ = 9.55, 19.07 and 28.71 that correspond to the addition of talc (usually used by manufacturers

to control the nucleation of the polymer). To corroborate the chemical structure of the original clay included in the neat polymers, EDX was carried out. The results confirmed the incorporation of talc.

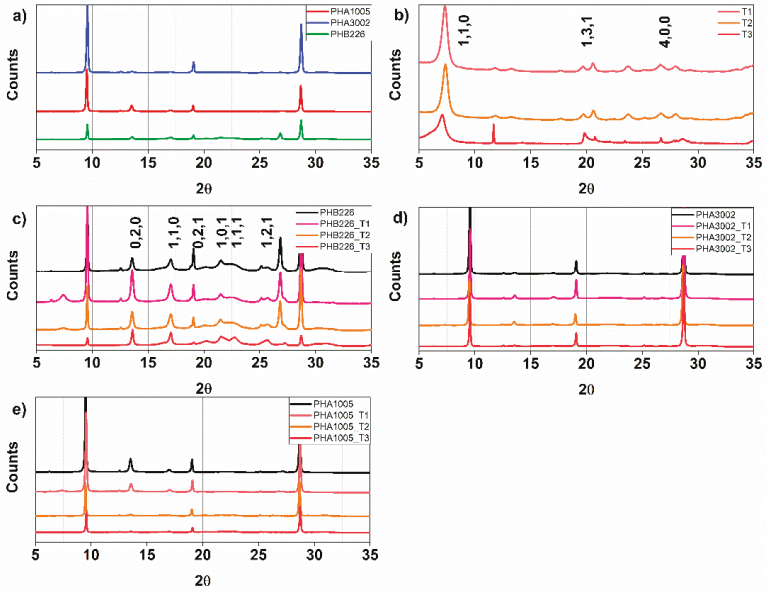

Figure 3. X-Ray diffraction patterns. (**a**) Raw matrixes: PHA1005, PHA3002 and PHB226; (**b**) Nanoclays: T1, T2 and T3; (**c**) Neat PHB226 and loaded with 3 wt.% T1, T2 and T3; (**d**) Neat PHA3002 and loaded with 3 wt.% T1, T2 and T3; (**e**) Neat PHA1005 and loaded with 3 wt.% T1, T2 and T3.

The diffraction patterns of T1 and T2 shows the expected structure for sepiolite organoclays, with the principle peak being at 2θ = 7.29, showing highest intensity. Results agree with those of Penning et al. as the basal interlayer distance of pristine sepiolite seems not to be altered by the silanisation process [76], and as the authors had corroborating calculations for the basal distance for d(1,2,1) and d(1,2,0), respectively (see Table 3). In addition, T3 presents three well-differentiated peaks at 2θ = 14.03, 19.83 and 61.9, which are typical of montmorillonite organoclay. These outcomes agree well with results previously reported in the literature [77–81].

The effects of each nanoclay on PHB226 and therefore on P3HB are different for each case. The peak associated with 2θ = 7.29 suffers from variations when blending the polymers with the nanoclays. T1 presents higher intensity than T2, which indicates that T2 presents a more effective interaction with the polymer. This result may be contradictory to the findings of DSC. At times, the greater the amount of organic modifier in clays, the greater the impediment to debundle (T2) or exfoliate (T3), and this seems to be the behaviour observed between T1 (modified) and T2 (natural). Moreover, for T3, the peak has completely disappeared, which may indicate the complete intercalation or exfoliation of the clay sheets, which was expected due to the laminar structure of this nanoclay. PHB226_T1 presents sharper peaks for 2θ = 13.58 and 17.03 than for PHB226_T2 and PHB226_T3 or even the neat PHB226, suggesting a preferred α-crystal orientation for planes (0,2,0) and (1,1,0) and a more ordered structure, which is aligned to the increase in crystallinity observed in DSC results (raising X_c by 5%). Moreover, a well-defined peak can be observed for the blend PHB226_T3 at 2θ = 19.93, indicating that T3 favours the introduction of the β form, which corroborates the creation of further amorphous regions due to the speeding up of crystallisation kinetics. In addition, the peaks corresponding to talc, 2θ = 19.07 and 28.71, had much lower intensity for PHB226T3, which suggests an intercalation with the talc of the PHB226 blend, producing a high dispersion of these mineral additives.

Table 3. Main crystallographic planes and d-spacing calculated from X-ray diffraction.

Material	D-spacing (Å)								
	(0,2,0)	**(1,1,0)**	**(0,2,1)**	**(1,0,1)**	**(1,1,1)**	**(1,2,1)**	**(1,3,1)**	**(1,9,1)**	**(4,0,0)**
PHB226	6.517	5.204	4.453	4.131	3.991	3.466	-	-	-
PHA1005	6.546	5.216	4.470 *	-	3.995	3.468	-	-	-
PHA3002	6.536	5.204	4.424 *	-	3.484	3.285	-	-	-
T1	-	12.120	-	-	-	-	4.311	2.565	3.344
T2	-	12.012	-	-	-	-	4.307	2.561	3.339
T3	-	12.444	-	-	-	-	4.282	2.565	3.342
PHB226_T1	6.514	5.203	4.439	4.060	3.953	3.463	-	-	3.317
PHB226_T2	6.524	5.203	4.389	4.137	3.976	3.465	-	-	3.320
PHB226_T3	6.505	5.197	4.368	4.118	3.912	3.470	-	-	3.268
PHA1005_T1	6.524	5.197	-	-	-	3.536	-	-	-
PHA1005_T2	6.542	5.227	-	4.118	3.929	3.545	-	-	-
PHA1005_T3	6.514	5.215	-	4.096	3.893	3.534	-	-	-
PHA3002_T1	6.514	5.197	-	-	-	3.534	-	-	3.322
PHA3002_T2	6.552	5.215	-	-	-	3.545	-	-	-
PHA3002_T3	6.524	* disappeared	-	4.104	-	3.534	-	-	-

* Almost not discernible/not found.

A global decrease of crystallisation for both P3HB-*co*-4HB blends (PHA1005 and PHA3002) can be observed, as not as many and such well-defined peaks can be found compared to PHB226 (higher-purity P3HB). Regarding PHA1005, 2θ = 13.58 and 17.03 are attenuated for PHA1005_T1 and are supressed for PHA1005_T2 and PHA1005_T3, indicating again the debundling and exfoliation of T2 and T3, respectively. For PHA3002, the addition of sepiolite T1 and T2 accentuates the α-form crystal formation, as again, the peaks at 2θ = 13.58 and 17.03 appear to sharpen compared to neat PHA3002 and PHA3002_T3. Often, if a peak is shifted to a lower angle or is reduced in intensity, it can be produced by the increase in the interplanar distance. It is usually an indication of good dispersion. The d-spacing calculated from the XRD figures for all samples is listed in Table 3. D-spacing for (P3HB-*co*-P4HB) apparently decreases when 4HB content is increased (PHA3002). These differences in basal distance can be appreciated in Table 3 for all diffracted angles and with particular attention at d(1,1,1) and d(1,2,1).

The basal distance has been increased for the main α-crystal planes in the case of T2 for PHB226 and PHA3002. Disappearance of the associated peak for PHA3002_T3 is also a relevant signal for a new order in the structure, probably induced due to exfoliation.

4. Conclusions

The present work demonstrates an industrial methodology to produce novel nanobiocomposite materials. Nine formulations were developed by adding 3 wt.% of sepiolite (T2), modified sepiolite via aminosilanes (T1) and montmorillonite (T3). Each nanoclay represents a different polar behaviour passing from one extreme to the other (polar, medium polarity and nonpolar). The different nanoclays were compounded into three types of commercial PHA matrixes: PHB226 (P3HB), PHA1005 and PHA3002 (P3HB-*co*-P4HB with different molar ratios of 4HB, being 17% and 23.5%, respectively). Results of NMR and EDX permitted us to better understand the composition of the commercial blends, as these contain talc, plasticisers, and even other polyesters. Therefore, we are dealing with complex quaternary and quinary composites.

For PHA1005 and PHA3002, two characteristic melting zones rich in 4HB and 3HB crystals are found at around 157 °C and 167 °C, respectively. A higher degree of crystallinity is observed for PHA1005 than for PHA3002, which a priori may seem contradictory. However, the results show the importance of nucleation kinetics which greatly affects the crystallisation process, as well as the appearance of RAF zones. The addition of nanoclays decreases Tm, which indicates the formation of smaller crystals. As a general conclusion, although minor exceptions appear, it can be said that T1 increases the Xc of the matrixes, T2 does not seem to modify it and T3 tends to decrease the overall Xc.

From the XRD patterns, we notice the appearance of α and β crystals typical of P3HB, as well as natural peaks proper tosepiolite, talc and montmorillonite. The appearance of β crystals confirms the formation of RAF zones, particularly for PHA1005. In addition, XRD confirms the exfoliation of montmorillonite, as well as the lack of complete debundling of both sepiolites. The grafting of aminosilane groups on top of the sepiolite surface is intended to favour the affinity and compatibility of the clay for the polymer; however, in this case, it acts as an impediment for dispersion. A good interaction between the nanoclay and the polymer is confirmed when mechanical properties are evaluated. The greatest mechanical improvement in terms of higher stiffness and toughness under tensile and flexural forces can be found for PHB226_T1. T3 produces significant overall improvement of the matrixes, but not as much as T1 does, and hence the polar/functional behaviour may predominate over dispersion to achieve good thermomechanical properties in complex polymer systems such as the ones selected. Anyhow, dispersion achieved in T1, T2 and T3 is highly relevant compared with literature results.

Our findings show impressive mechanical enhancements. Therefore, we believe that optimisation of the production parameters of the blend during extrusion compounding is critical to maximise the potential of any nanoparticle in the production of nanobiocomposites (being the lowest temperature as possible, medium to high screw speed and an low shear screw profile).

Author Contributions: L.G.-Q. conceived the work, carried out the experimental work, contributed to the scientific discussion and wrote the manuscript.; A.F.C. contributed to scientific discussion and reviewed the manuscript; P.C. designed the methodology, contributed in the interpretation of results and scientific discussion, obtained funding and reviewed the manuscript.

Funding: The authors gratefully acknowledge the Government of Aragón (DGA) under the project T08_17R (I+AITIIP) for support in financial aid for this publication.

Acknowledgments: The authors acknowledge TOLSA for kindly providing the nanoclays used for this research.

Conflicts of Interest: The authors declare no conflict of interest.

References

1. Plastics Europe, Plastics—the Facts 2018. An analysis of European plastics production, demand and waste data. Available online: https://www.plasticseurope.org/es/resources/publications/619-plastics-facts-2018 (accessed on 1 March 2019).
2. Plastics Europe, Plastics—The Facts 2015. An analysis of European plastics production, demand and waste data. Available online: https://www.plasticseurope.org/93-plastics-facts-2015 (accessed on 1 March 2019).
3. Available online: https://www.cnbc.com/2018/04/16/climate-change-china-bans-import-of-foreign-waste-to-stop-pollution.html (accessed on 1 March 2019).
4. Available online: https://www.reuters.com/article/us-eu-environment/eu-targets-recycling-as-china-bans-plastic-waste-imports-idUSKBN1F51SP (accessed on 1 March 2019).
5. European Commission. *Communication from the Commission to the European Parliament, the Council, the European Economic and Social Committee and the Committee of the Regions*; A European Strategy for Plastics in a Circular Economy; European Commission: Brussels, Belgium, 2018.
6. European Commision. A European Strategy for Plastics in a Circular Economy. 2015. Available online: http://ec.europa.eu/environment/circular-economy/pdf/plastics-strategy-brochure.pdf (accessed on 1 March 2019).
7. Kuang, T.; Ju, J.; Yang, Z.; Geng, L.; Peng, X. A facile approach towards fabrication of lightweight biodegradable poly(butylene succinate)/carbon fiber composite foams with high electrical conductivity and strength. *Compos. Sci. Technol.* **2018**, *159*, 171–179. [CrossRef]
8. Gao, S.; Tang, G.; Hua, D.; Xiong, R.; Han, J.; Jiang, S.; Zhang, Q.; Huang, C. Stimuli-responsive bio-based polymeric systems and their applications. *J. Mater. Chem. B* **2019**, 1–21. [CrossRef]
9. Kuang, T.; Chang, L.; Chen, F.; Sheng, Y.; Fu, D.; Peng, X. Facile preparation of lightweight high-strength biodegradable polymer/multi-walled carbon nanotubes nanocomposite foams for electromagnetic interference shielding. *Carbon* **2016**, *105*, 305–313. [CrossRef]
10. European Bioplastics. Bioplastics Market Data Report. 2016. Available online: https://docs.european-bioplastics.org/publications/EUBP_Bioplastics_market_data_report_2016.pdf (accessed on 1 March 2019).

11. Dreizen, C. 2020 Bioplastics Market Forecast. Sustainable Packaging Coalition (GREENBLUE). 2017. Available online: https://sustainablepackaging.org/2020-bioplastics-market-forecast/ (accessed on 1 March 2019).
12. La Rosa, A.D. *Biopolymers and Biotech Admixtures for Eco-Efficient Construction Materials*, 1st ed.; Woodhead Publishing: Cambridge, UK, 2016; ISBN 9780081002148.
13. Ipsita, R.; Visakh, P.M. Polyhydroxyalkanoate (PHA) Based Blends, Composites and Nanocomposites. *R. Soc. Chem.* **2015**. [CrossRef]
14. Wang, S.; Chen, W.; Xiang, H.; Yang, J.; Zhou, Z.; Zhu, M. Modification and Potential Application of Short-Chain-Length Polyhydroxyalkanoate (SCL-PHA). *Polymers* **2016**, *8*, 273. [CrossRef] [PubMed]
15. Sudesh, K.; Iwata, T. Sustainability of Biobased and Biodegradable Plastics. *Clean* **2008**, *36*, 433–442. [CrossRef]
16. Jirage, A.; Baravkar, V.; Kate, V.; Payghan, S.; Disouza, J. Poly-β-Hydroxybutyrate: Intriguing Biopolymer in Biomedical Applications and Pharma Formulation Trends. *Int. J. Pharm. Biol. Arch.* **2013**, *4*, 1107–1118.
17. Shrivastav, A.; Kim, H.Y.; Kim, Y.R. Advances in the Applications of Polyhydroxyalkanoate Nanoparticles for Novel Drug Delivery System. *Biomed Res. Int.* **2013**, 1–12. [CrossRef] [PubMed]
18. Kok, F.; Hasirci, V. Chapter 15: Polyhydroxybutyrate and Its Copolymers: Applications in the Medical Field. In *Tissue Engineering and Novel Delivery Systems*; Marcel Dekker: New York, NY, USA, 2004.
19. Chaos, A.; Sangroniz, A.; Gonzalez, A.; Iriarte, V.; Sarasua, J.R.; del Río, J.; Etxeberria, A. Tributyl citrate as an effective plasticizer for biodegradable polymers: Effect of the plasticizer on the free volume, transport and mechanical properties. *Polym. Int.* **2018**. [CrossRef]
20. Milani, P.; França, D.; Balieiro, A.G.; Faez, R. Polymers and its applications in agriculture. *Polímeros* **2017**, *27*, 256–266. [CrossRef]
21. Mozejko-Ciesielska, J.; Kiewisz, R. Bacterial polyhydroxyalkanoates: Still fabulous? *Microbiol. Res.* **2016**, *192*, 271–282. [CrossRef]
22. Choi, J.I.; Lee, S.Y. Efficient and economical recovery of poly(3-hydroxybutyrate) from recombinant Escherichia coli by simple digestion with chemicals. *Biotechnol. Bioeng.* **1999**, *62*, 546–553. [CrossRef]
23. Koller, M.; Bona, R.; Chiellini, E.; Braunegg, G. Extraction of short-chain-length poly-[(R)-hydroxyalkanoates] (scl-PHA) by the antisolvent acetone under elevated temperature and pressure. *Biotechnol. Lett.* **2013**, *35*, 1023–1028. [CrossRef]
24. Khosravi-Darani, K.; Vasheghani-Farahani, E. Application of supercritical fluid extraction in biotechnology. *Crit. Rev. Biotechnol.* **2005**, *25*, 1–12. [CrossRef]
25. Peelman, N.; Ragaert, P.; Ragaert, K.; Erkoç, M.; Van Brempt, W.; Faelens, F.; Cardon, L. Heat resistance of biobased materials, evaluation and effect of processing techniques and additives. *Polym. Eng. Sci.* **2017**, *58*, 513–520. [CrossRef]
26. Kai, D.; Chong, H.M.; Chow, L.P.; Jiang, L.; Lin, Q.; Zhang, K.; Loh, X.J. Strong and biocompatible lignin/poly(3-hydroxybutyrate) composite nanofibers. *Compos. Sci. Technol.* **2018**, *158*, 26–33. [CrossRef]
27. Han, H.; Wang, X.; Wu, D. Isothermal Crystallization Kinetics, Morphology, and Mechanical Properties of Biocomposites Based on Poly(3-hydroxybutyrate-*co*-4-hydroxybutyrate) and Recycled Carbon Fiber. *Ind. Eng. Chem. Res.* **2012**, *51*, 14047–14060. [CrossRef]
28. Zini, E.; Focarete, M.L.; Noda, I.; Scandola, M. Bio-composite of bacterial poly(3-hydroxybutyrate-*co*-3-hydroxyhexanoate) reinforced with vegetable fibers. *Compos. Sci. Technol.* **2007**, *67*, 2085–2094. [CrossRef]
29. An, S.; Ma, X. Properties and structure of poly(3-hydroxybutyrate-*co*-4-hydroxybutyrate)/wood fiber biodegradable composites modified with maleic anhydride. *Ind. Crop. Prod.* **2017**, *109*, 882–888. [CrossRef]
30. Al, G.; Aydemir, D.; Kaygin, B.; Ayrilmis, N.; Gunduz, G. Preparation and characterization of biopolymer nanocomposites from cellulose nanofibrils and nanoclays. *J. Compos. Mater.* **2017**, *52*, 689–700. [CrossRef]
31. Larsson, M.; Hetherington, C.J.D.; Wallenberg, R.; Jannasch, P. Effect of hydrophobically modified graphene oxide on the properties of poly(3-hydroxybutyrate-*co*-4-hydroxybutyrate). *Polymer* **2017**, *108*, 66–77. [CrossRef]
32. Bumbudsanpharoke, N.; Ko, S. Nanoclays in Food and Beverage Packaging—Review article. *J. Nanomater.* **2019**, 1–13. [CrossRef]
33. Ramos, Ó.L.; Pereira, R.N.; Cerqueira, M.A.; Martins, J.R.; Teixeira, J.A.; Malcata, F.X.; Vicente, A.A. Bio-Based Nanocomposites for Food Packaging and Their Effect in Food Quality and Safety. *Food Packag. Preserv.* **2018**, 271–306. [CrossRef]

34. Franchini, E. Structuration of Nano-Objects in Epoxy-Based Polymer Systems: Nanoparticles & Nanoclusters for Improved Fire Retardant Properties, Institut National des Sciences Appliquées de Lyon, Lyon. Ph.D. Thesis, INSA Lyon, Villeurbanne, France, 2008.
35. Falco, G.; Giulieri, F.; Volle, N.; Pagnotta, S.; Sbirrazzuoli, N.; Peuvrel Disdier, E.; Mija, A. Self-organization of sepiolite fibbers in a biobased thermoset. *Compos. Sci. Technol.* **2019**, *171*, 226–233. [CrossRef]
36. Zheng, Y.; Zaoui, A. Mechanical behavior in hydrated Na-montmorillonite clay. *Phys. A* **2018**, *505*, 582–590. [CrossRef]
37. Wang, S.; Song, C.; Chen, G.; Guo, T.; Liu, J.; Zhang, B.; Takeuchi, S. Characteristics and biodegradation properties of poly(3-hydroxybutyrate-*co*-3-hydroxyvalerate)/organophilic montmorillonite (PHBV/OMMT) nanocomposite. *Polym. Degrad. Stab.* **2005**, *87*, 69–76. [CrossRef]
38. Peinado, V.; García, L.; Fernández, A.; Castell, P. Novel lightweight foamed poly(lactic acid) reinforced with different loadings of functionalised sepiolite. *Compos. Sci. Technol.* **2014**, *101*, 17–23. [CrossRef]
39. Khandal, D.; Pollet, E.; Avérous, L. Elaboration and behavior of poly(3-hydroxybutyrate-*co*-4-hydroxybutyrate)-nano-biocomposites based on montmorillonite or sepiolite nanoclays. *Eur. Polym. J.* **2016**, *81*, 64–76. [CrossRef]
40. Reinsch, V.; Kelley, S. Crystallization of poly(hydroxybutyrate-cohydroxyvalerate) in wood fiber-reinforced composite. *J. Appl. Sci.* **1997**, *64*, 1785–1796. [CrossRef]
41. Koller, M. Poly(hydroxyalkanoates) for Food Packaging: Application and Attempts towards Implementation. *Appl. Food Biotechnol.* **2014**, *1*, 3–15.
42. Cong, C.; Zhang, S.; Xu, R.; Lu, W.; Yu, D. The Influence of 4HB Content on the Properties of Poly(3-hydroxylbutyrate-*co*-4-hydroxylbutyrate) based on Melt Molded Sheets. *J. Appl. Polym. Sci.* **2008**, *109*, 1962–1967. [CrossRef]
43. Avérous, L. Nano- and Biocomposites. *Mater. Today* **2010**, *13*, 57. [CrossRef]
44. Botana, A.; Mollo, M.; Eisenberg, P.; Torres Sanchez, R.M. Effect of modified montmorillonite on biodegradable PHB nanocomposites. *Appl. Clay Sci.* **2010**, *47*, 263–270. [CrossRef]
45. Czerniecka-Kubicka, A.; Fracz, W.; Jasiorski, M.; Błazejewski, W.; Pilch-Pitera, B.; Pyda, M.; Zarzyka, I. Thermal properties of poly(3-hydroxybutyrate) modified by nanoclay. *J. Therm. Anal. Calorim.* **2017**, *128*, 1513–1526. [CrossRef]
46. Corre, Y.M.; Bruzaud, S.; Audic, J.L.; Grohens, Y. Morphology and functional properties of commercial polyhydroxyalkanoates: A comprehensive and comparative study. *Polym. Test.* **2012**, *31*, 226–235. [CrossRef]
47. Hu, D.; Chung, A.L.; Wu, L.P.; Zhang, X.; Wu, Q.; Chen, J.C.; Chen, G.Q. Biosynthesis and Characterization of Polyhydroxyalkanoate Block Copolymer P3HB-b-P4HB. *Biomacromolecules* **2011**, *12*, 3166–3173. [CrossRef]
48. Wang, H.-H.; Zhou, X.-R.; Liu, Q.; Chen, G.Q. Biosynthesis of polyhydroxyalkanoate homopolymers by Pseudomonas putida. *Appl. Microbiol. Biotechnol.* **2010**, *89*, 1497–1507. [CrossRef]
49. Mohanty, A.K.; Parulekar, Y. Methods of Making Nanocomposites and Compositions of Rubber Toughened Polyhydroxyalkanoates. U.S. Patent US20070015858A1, 2005.
50. Xiao, N.; Chen, Y.; Shen, X.; Zhang, C.; Yano, S.; Gottschaldt, M.; Schubert, U.S.; Kakuchi, T.; Satoh, T. Synthesis of miktoarm star copolymer Ru(II) complexes by click-to-chelate approach. *Polym. J.* **2013**, *45*, 216–225. [CrossRef]
51. Sun, X.; Liu, J.; Takahashi, I.; Yan, S. Melting and β to α transition behavior of β-PBA and the β-PBA/PVPh blend investigated by synchrotron SAXS and WAXD. *RSC Adv.* **2014**, *4*, 39101. [CrossRef]
52. Koller, M.; Maršálek, L.; de Sousa Dias, M.M.; Braunegg, G. Producing microbial polyhydroxyalkanoate (PHA) biopolyesters in a sustainable manner. *New Biotechnol.* **2017**, *37*, 24–38. [CrossRef]
53. Madison, L.L.; Huismann, G.W. Metabolic engineering of poly(3-hydroxyalkanoates): From DNA to plastic. *Microbiol. Mol. Biol. Rev.* **1999**, *63*, 21–53. [PubMed]
54. Sudesh, K.; Abe, H.; Doi, Y. Synthesis, structure and properties of polyhydroxyalkanoates: Biological polyesters. *Prog. Polym. Sci.* **2000**, *25*, 1503–1555. [CrossRef]
55. Utracki, A.L.; Jamieson, A.M. *Polymer Physics: From Suspensions to Nanocomposites and Beyond*; Wiley: Hoboken, NJ, USA, 2010; ISBN 978-0-470-19342-6.
56. Thiré, R.M.; Arruda, L.C.; Barreto, L.S. Morphology and thermal properties of poly(3-hydroxybutyrate-*co*-3-hydroxyvalerate)/attapulgite nanocomposites. *Mater. Res.* **2011**, *14*, 340–344. [CrossRef]

57. Bayarı, S.; Severcan, F. FTIR study of biodegradable biopolymers: P(3HB), P(3HB-*co*-4HB) and P(3HB-*co*-3HV). *J. Mol. Struct.* **2005**, *744–747*, 529–534. [CrossRef]
58. Wang, L.; Wang, X.J.; Zhu, W.F.; Chen, Z.F.; Pan, J.Y.; Xu, K.T. Effect of nucleation agents on the crystallization of poly(3-hydroxybutyrate-*co*-4-hydroxybutyrate) (P3HB4HB). *J. Appl. Polym. Sci.* **2009**, *2*, 1116–1123. [CrossRef]
59. Inoue, Y.; Yoshie, N. Structure and physical properties of bacterially synthesized polyesters. *Prog. Polymer. Sci.* **1992**, *17*, 571–610. [CrossRef]
60. Kumar, S.; Hideki, A. *Practical Guide to Microbial Polyhydroxyalkanoates. Chapter 6: Crystalline and Solid-State Structures of Polyhydroxyalkanoates (PHA)*; Smithers Rapra: Shrewsbury, UK, 2010; pp. 1–160. ISBN 1847351174.
61. Di Lorenzo, M.L.; Gazzano, M.; Righetti, M.C. The Role of the Rigid Amorphous Fraction on Cold Crystallization of Poly(3-hydroxybutyrate). *Macromolecules* **2012**, *45*, 5684–5691. [CrossRef]
62. Zhang, J.; Chu, T.L. Property analysis of biodegradable material P(3HB-*co*-4HB). *Adv. Mater. Res.* **2012**, *380*, 168–172. [CrossRef]
63. Akhtar, S.; Pouton, C.W.; Notarianni, L.J. Crystallization behaviour and drug release from bacterial polyhydroxyalkanoates. *Polymer* **1992**, *33*, 117–126. [CrossRef]
64. Volova, T.G.; Vinogradova, O.N.; Zhila, N.O.; Peterson, I.V.; Kiselev, E.G.; Vasiliev, A.D.; Sukovatiy, A.G.; Shishatskaya, E.I. Properties of a novel quaterpolymer P(3HB/4HB/3HV/3HHx). *Polymer* **2016**, *101*, 67–74. [CrossRef]
65. Kunioka, M.; Tamaki, A.; Doi, Y. Crystalline and Thermal Properties of Bacterial Copolyesters: Poly(3-hydroxybutyrate-*co*-3-hydroxyvalerate) and Poly(3-hydroxybutyrate-*co*-4-hydroxybutyrate). *Macromolecules* **1989**, *22*, 694–697. [CrossRef]
66. Kabe, T.; Sato, T.; Kasuya, K.; Hikima, T.; Takata, M.; Iwata, T. Transition of spherulite morphology in a crystalline/crystalline binary blend of biodegradable microbial polyesters. *Polymer* **2014**, *55*, 271–277. [CrossRef]
67. Alavi, S.; Thomas, S.; Sandeep, K.P.; Kalarikal, N.; Varghese, J.; Yaragalla, S. *Polymers for Packaging Applications*; Appe Academic Press, CRC Press: Boca Raton, FL, USA, 2014; ISBN 9781926895772.
68. Ray, D. *Biocomposites for High-Performance Applications, Current Barriers and Future Needs Towards Industrial Development*; Woodhead Publishing Series in Composites Science and Engineering: Elsevier, Cambridge, UK, 2017; pp. 1–336. ISBN 9780081007945.
69. Penning, J.P.; St John Manley, R. Miscible Blends of Two Crystalline Polymers. 1. Phase Behavior and Miscibility in Blends of Poly(vinylidene fluoride) and Poly(1,4-butylene adipate). *Macromolecules* **1996**, *29*, 77–83. [CrossRef]
70. Ruiz-Hitzky, E.; Aranda, P.; Alvarez, A.; Santarén, J.; Esteban-Cubillo, A. *Developments in Palygorskite-Sepiolite Research. A New Outlook on These Nanomaterials*; Galán, E., Singer, A., Eds.; Elsevier, B.V.: Oxford, UK, 2011; pp. 393–452. ISBN 9780444536082.
71. Ruiz-Hitzky, E.; Van Meerbeek, A. *Handbook of Clay Science*, Development in Clay Science, ed.; Bergaya, F., Theng, B.K.G., Lagaly, G., Eds.; Elsevier: Amsterdam, The Netherlands, 2006; pp. 583–621. ISBN 9780080457635.
72. Lvov, Y.; Guo, B.; Fakhrullin, R.F. Functional Polymer Composites with Nanoclays. *REC Smart Mater.* **2016**. [CrossRef]
73. Karami, S.; Ahmadi, Z.; Nazockdast, H.; Rabolt, J.F.; Noda, I.; Chase, B.D. The effect of well-dispersed nanoclay on isothermal and non-isothermal crystallization kinetics of PHB/LDPE blends. *Mater. Res. Express* **2018**, *5*, 015316. [CrossRef]
74. Bruckner, S.; Meille, S.V.; Malpezzi, L. The Structure of Poly(D-(-)-@-hydroxybutyrate). A Refinement Based on the Rietveld Method. *Macromolecules* **1988**, *21*, 967–972. [CrossRef]
75. Anbukarasu, P.; Sauvageau, D.; Elias, A. Tuning the properties of polyhydroxybutyrate films using acetic acid via solvent casting. *Sci. Rep.* **2015**, *5*, 17884. [CrossRef]
76. Jalali, A.M.; Taromi, F.A.; Atai, M.; Solhi, L. Effect of reaction conditions on silanisation of sepiolite nanoparticles. *J. Exp. Nanosci.* **2016**, *11*, 1171–1183. [CrossRef]
77. Patrício, A.C.L.; da Silva, M.M.; de Sousa, A.K.F.; Mota, M.F.; Freire Rodrigues, M.G. SEM, XRF, XRD, Nitrogen Adsorption, Fosters Swelling and Capacity Adsorption Characterization of Cloisite 30 B. *Mater. Sci. Forum* **2012**, *727–728*, 1591–1595. [CrossRef]

78. Xue, M.-L.; Yu, Y.-L.; Li, P. Preparation, Dispersion, and Crystallization of the Poly(trimethylene terephthalate)/Organically Modified montmorillonite (PTT/MMT) Nanocomposites. *J. Macromol. Sci. Part B* **2010**, *49*, 1105–1116. [CrossRef]
79. Sarier, N.; Onder, E.; Ersoy, S. The modification of Na-montmorillonite by salts of fatty acids: An easy intercalation process. *Colloids Surf. A Physicochem. Eng. Asp.* **2010**, *371*, 40–49. [CrossRef]
80. Høgsaa, B.; Fini, E.H.; Christiansen, J.D.; Hung, A.; Mousavi, M.; Jensen, E.A.; Pahlavan, F.; Pedersen, T.H.; Sanporean, C.G. A Novel Bioresidue to Compatibilize Sodium montmorillonite and Linear Low Density Polyethylene. *Ind. Eng. Chem. Res.* **2018**, *57*, 1213–1224. [CrossRef]
81. Krupskaya, V.V.; Zakusin, S.V.; Tyupina, E.A.; Dorzhieva, O.V.; Zhukhlistov, A.P.; Belousov, P.E.; Timofeeva, M.N. Experimental Study of montmorillonite Structure and Transformation of Its Properties under Treatment with Inorganic Acid Solutions. *Minerals* **2017**, *7*, 49. [CrossRef]

polymers

MDPI

Article

Synthesis and Properties of Tung Oil-Based Unsaturated Co-Ester Resins Bearing Steric Hindrance

Chengguo Liu [1,*], Qiong Wu [1,2], Rongrong An [3], Qianqian Shang [1], Guodong Feng [1], Yun Hu [1], Puyou Jia [1], Yonghong Zhou [1,*] and Wen Lei [2,*]

1 National Engineering Lab for Biomass Chemical Utilization; Key Lab of Chemical Engineering of Forest Products, National Forestry and Grassland Administration; Key Lab of Biomass Energy and Material, Jiangsu Province; Co-Innovation Center of Efficient Processing and Utilization of Forest Resources, Jiangsu Province; Institute of Chemical Industry of Forest Products, Chinese Academy of Forestry, Nanjing 210042, China; wqzjj9394@163.com (Q.W.); Shang_qianqian@126.com (Q.S.); fengguodong21@163.com (G.F.); 15150509893@139.com (Y.H.); jiapuyou@icifp.cn (P.J.)

2 College of Science, Nanjing Forestry University, Nanjing 210037, China

3 College of Geographic and Biologic Information, Nanjing University of Posts and Telecommunications, Nanjing 210023, China; anrongrong@njupt.edu.cn

* Correspondence: liuchengguo@icifp.cn (C.L.); zyh@icifp.cn (Y.Z.); njfuleiwen@163.com (W.L.); Tel./Fax: +86-25-85482520 (C.L.); +86-25-854825777 (Y.Z.); +86-25-85427206 (W.L.)

Received: 31 March 2019; Accepted: 29 April 2019; Published: 7 May 2019

Abstract: New tung oil (TO)-based, unsaturated, co-ester (Co-UE) macromonomers bearing steric hindrance were synthesized by modifying a TO-based maleate (TOPERMA) monomer with an anhydride structure with hydroxyethyl methacrylate (HEMA) and methallyl alcohol (MAA), respectively. The obtained Co-UE monomers (TOPERMA-HEMA and TOPERMA-MAA) were then characterized by ^{1}H NMR and gel permeation chromatography (GPC). For comparison, hydroxyethyl acrylate (HEA)-modified TOPERMA (TOPERMA-HEA) was also synthesized and characterized. Subsequently, the obtained Co-UEs were thermally cured with styrene, and the ultimate properties of the resulting materials were studied. It was found that by introducing the structure of steric hindrance into the TO-based Co-UE monomer, the tensile strength and Young's modulus of the resulting materials were improved. Furthermore, by reducing the length of the flexible chain in the Co-UE monomer, the tensile strength, Young's modulus, and glass transition temperature (T_g) of the resultant materials were also improved. The TOPERMA-MAA resin gave the best performance in these TO-based Co-UE resins, which showed a tensile strength of 32.2 MPa, Young's modulus of 2.38 GPa, and T_g of 130.3 °C. The developed ecofriendly materials show promise in structural plastic applications.

Keywords: tung oil; unsaturated polyester resins; thermosetting polymers; structure–property relationship; structural plastics

1. Introduction

Unsaturated polyester resin (UPR) is one of the most frequently used thermosetting polymers because of its low price, ease of handling, and good balance of mechanical, thermal, electrical, and chemical properties. As the main component of fiber-reinforced plastics (FRPs) and some other composites, UPR has been widely utilized in the areas of transportation, marine applications, pipes and tanks, wind energy, construction, electronics, etc [1–4]. However, due to the uncertainties about petroleum's supply and price in the future as well as environmental problems, substitutes of polymers from natural resources such as carbohydrates, lignin, and natural oils have been intensively explored [5–12]. Among all the bioresources, plant oils are the most common one employed for the

development of UPRs thanks to their abundance and low cost, triglyceride structure suitable for further chemical manipulation, and biodegradability [13,14]. The development of UPRs with plant oils may not only provide a means of sustainable development for the present UPR industry, but also can improve the value of plant oil resources.

Generally, two methods have been reported for chemically converting plant oils to UPRs. The first method is converting plant oils into feedstocks such as diacids and diols, which can generate linear unsaturated polyesters via direct polycondensation [15,16]. In fact, this method is not commonly used, possibly because plant oils are not easily converted into high-purity feedstocks, and the content of the resulting materials is low if only one kind of oil-based feedstock was employed. As a result, the second method, converting plant oils into unsaturated ester (UE) macromonomers or oligomers containing active C=C groups, became popular. By introducing maleic or acrylic moiety, a variety of plant oil-based UE monomers or oligomers were developed [17–26]. However, most of the obtained UEs possessed a low C=C functionality, thus leading to low cross-ink density and inferior performance in stiffness and heat resistance in the resulting materials. For instance, acrylated epoxidized soybean oil (AESO), synthesized through the ring-opening reaction of epoxidized soybean oil with acrylic acid, usually possessed a C=C functionality of 2–4. Consequently, the resultant AESO resin with 40 wt % of styrene only demonstrated a tensile strength of 21 MPa, Young's modulus of 1.6 GPa, and glass transition temperature (T_g) of 65 °C [17]. In order to improve the C=C functionality of AESO, maleic anhydride was used to further react with the generated hydroxyl groups on AESO [22]. The obtained MA-modified AESO (MAESO) could reach a C=C functionality up to 5.9, and the resulting materials with 38 wt % of styrene showed a tensile strength of 41−44 MPa, Young's modulus of 2.2–2.5 GPa, and T_g of 115–130 °C. As the new UE monomer comprised two types of active C=C moieties, it can be named as an unsaturated co-ester (Co-UE). However, up until now, only a few routes were developed to acquire such UE monomers or oligomers.

In our previous work, in an effort to improve the C=C functionality of a tung oil (TO)-based maleate (TOPERMA) monomer bearing an anhydride structure, hydroxyethyl acrylate (HEA) was used to further modify the TOPERMA, and a new TO-based Co-UE macromonomer was obtained [27]. It should be noted that this was the first instance where to a Co-UE monomer was achieved by introducing maleic groups firstly and acrylic groups subsequently onto plant oils. At last, a novel tung oil-based Co-UE monomer (TOPERMA-HEA) was obtained, which had a tensile strength of 36.3 MPa, Young's modulus of 1.70 GPa, and T_g of 127 °C after curing with 40 wt % of styrene. Although the properties of this new, biobased, Co-UE resin were good among all the reported oil-based UE resins, some key properties, like stiffness, were still far inferior to those of petroleum-based UPRs.

In order to achieve better performance of such biobased Co-UE resins, two novel, TO-based, Co-UE macromonomers were synthesized by modifying TOPERMA with hydroxyethyl methacrylate (HEMA) or methallyl alcohol (MAA), as shown in Scheme 1. For comparison, HEA-modified TOPERMA (TOPERMA-HEA) and TOPERMA products were also synthesized. Another important goal for this study is to establish the structure–property relationship for the new, biobased, Co-UE resins. As indicated in Scheme 1, by modifying the types of unsaturated alcohol, two structural factors—steric hindrance (corresponding to the change of R_1) and length of flexible chain (corresponding to the change of R_2)—could be modulated, and their effects on the ultimate properties of the resultant biobased materials were carefully investigated.

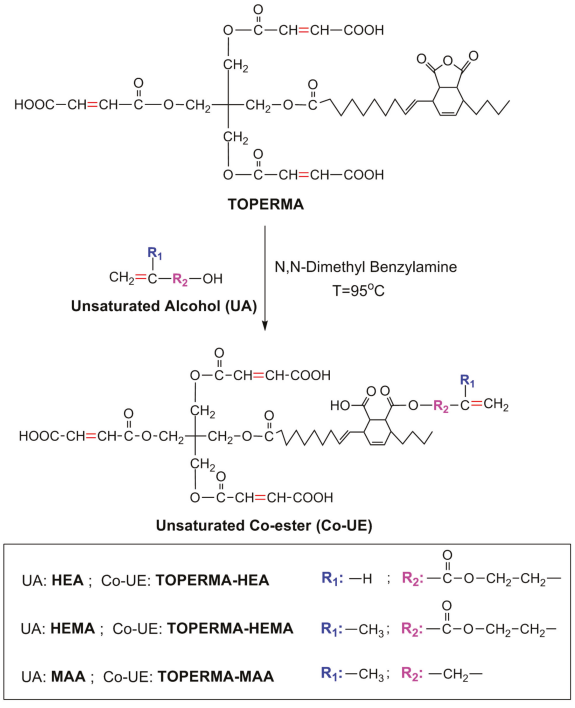

Scheme 1. Synthesis of tung oil-based, unsaturated co-esters (Co-UEs) by modifying tung oil (TO)-based maleate (TOPERMA) with different unsaturated alcohols.

2. Experimental

2.1. Materials

Tung oil (TO) was obtained from Jiangsu Donghu Bioenergy Plant Plantation Co., Ltd. (Yancheng, China), which possessed a yellow color and specific gravity of 0.935−0.940 at 25 °C. The pentaerythritol (PER, ≥98%) and maleic anhydride (MA, ≥99.5%) solid were obtained from Nanjing Chemical Reagent Co., Ltd. (Nanjing, China). The HEA liquid (≥97%) was supplied by Macklin Chemical Reagent Co., Ltd. (Shanghai, China). The HEMA liquid (≥97%) was supplied by Adamas Reagent Co., Ltd. (Shanghai, China). The MAA liquid (≥97%) was supplied by Shanghai Energy Chemical Co., Ltd. (Shanghai, China). Calcium hydroxide ($Ca(OH)_2$, ≥95%) and *N*,*N*-dimethyl benzyl amine (≥98%) were purchased from Tianjin Chemical Reagent Institute Co., Ltd. (Tianjin, China). Hydroquinone (≥99%) and styrene (≥99%) were purchased from Chengdu Kelong Chemical Reagent Co., Ltd. (Chengdu, China). The initiator *tert*-butyl peroxy benzoate (*t*-BPB, ≥ 98%) was obtained from Shanghai Aladdin Chemistry Co., Ltd. (Shanghai, China). The styrene, HEA, HEMA, MAA, and *N*,*N*-dimethyl benzyl amine were all dried by molecular sieves for at least 1 week before use.

2.2. Synthesis of TOPERMA

The TO-based maleate was synthesized according to our previous work [28]. Typically, about 348.8 g of TO, 108.8 g of PER, and 4.6 g of $Ca(OH)_2$ were placed together in a 1 L, four-neck, round-bottom flask equipped with a mechanical stirrer, thermometer, nitrogen (N_2) gas inlet, and refluxing condenser capped with an anhydrous calcium chloride drier. The reaction mixture was heated to about 230 °C by a heating mantle under N_2 atmosphere and agitated at this temperature for 2 h. After 2 h, the mixture was cooled using ice water, and the tung oil pentaerythritol alcoholyis (TOPER)

product was obtained. For the maleinization reaction, 231.1 g of the obtained TOPER product, 176.5 g of MA, and 0.82 g of hydroquinone were added to the same reaction device as that in the alcoholysis process. The mixture was heated to 70 °C by an oil bath and agitated at this temperature until the MA completely melted and mixed with TOPER. After that 4.08 g of *N*,*N*-dimethyl benzylamine was added and the reaction mixture was heated to 95 °C under N_2 atmosphere. The mixture was agitated at this temperature for 5h. Finally, crude, maleinated product (TOPERMA) was obtained. The product was divided into two parts: a small part was purified, while the left large part was employed to further synthesize TO-based Co-UEs. In the purifying process, the product was put into a separating funnel and washed three times with hot saturated sodium chloride (NaCl)/water solution (prepared by blending sodium chloride with boiled water). Subsequently, dichloromethane was added to dissolve the product, and the separated organic layer was dried by anhydrous magnesium sulfate overnight. Finally, the solution was filtered and the solvent was removed by a rotary evaporator. The purified TOPERMA product (with a yield of 66.9%) was a light brown and transparent liquid resin when cooled naturally to room temperature.

2.3. Synthesis of TO-Based Co-UEs

Firstly, around 100 g of the unpurified TOPERMA product was added into a 250 mL, four-neck, round-bottom flask. It should be stated that the unpurified product (~350 g) mentioned above was added into three 250 mL flasks at a time to avoid repeatedly heating the product. Then, about 8.71 g (0.075 mol) of HEA, 9.76 g of HEMA (0.075 mol), or 5.41 g (0.075 mol) of MAA was added to the flask, and the device was also equipped with a mechanical stirrer, thermometer, N_2 gas inlet, and refluxing condenser with an anhydrous calcium chloride drier. The reaction mixture was heated to 95 °C under N_2 atmosphere and agitated at this temperature for 4 h. The obtained products were purified with the same procedure as that of the TOPERMA product. Finally, three TO-based, Co-UE products were obtained, which were all light brown and transparent liquid resins at room temperature. According to the unsaturated alcohols used, the products were labeled as TOPERMA-HEA, TOPERMA-HEMA, and TOPERMA-MAA. The yields of TOPERMA-HEA, TOPERMA-HEMA, and TOPERMA-MAA were 73.0%, 79.3%, and 78.5%, respectively.

2.4. Curing of the TO-Based Resins

All of the obtained TO-based resins were cured following the same procedure. First, the TO-based resin samples were prepared by blending the TO-based macromonomer, styrene (40% of total weight of the macromonomer and styrene), and hydroquinone (0.2% of the total weight of the macromonomer and styrene) for 30 min at room temperature. The obtained samples were then mixed with *t*-BPB initiator (3% of total weight of the macromonomer and styrene) for 30 min, degassed at 40 °C for 10 min, and poured into homemade polytetrafluoroethylene molds (the sketch and description were shown in Figures S1 and S2). Finally, the samples in the molds were thermally cured at 80 °C for 2 h, 120 °C for 2 h, and postcured at 160 °C for 1 h.

2.5. Characterization

2.5.1. Gel Permeation Chromatography (GPC)

The GPC tests of samples were conducted on a high-pressure liquid chromatography (HPLC) system (Waters Corporation, Milford, MA, USA) equipped with a 1515 isocratic HPLC pump, 717 plus automated injector, and column heater. The separating columns were a pair of Styragel HR1 and HR2 (300 mm × 7.8 mm), and the temperature of the columns was 35 °C. The ranges of molar masses for the HR1 and HR2 columns were 100−5000 and 500−20,000, respectively. A Waters 2414 Refractive Index (RI) detector was employed to detect RI signals. Chromatographic-grade tetrahydrofuran (THF) was employed as an eluent with a flow rate of 1.0 mL/min. The samples were dissolved by THF in disposable transparent glass vials with a concentration of 15−25 mg/mL. The relative molar masses

of samples were determined with a standard curve calibrated by a series of narrowly distributed polystyrene standards with a known molar mass of 580−19,600.

2.5.2. Nuclear Magnetic Resonance (NMR)

The ^{1}H NMR spectra of samples were recorded on a DRX-300 Advance NMR spectrometer (Bruker Corporation, Billerica, MA, USA) using $CDCl_3$ as the solvent.

2.5.3. Dynamic Mechanical Analysis (DMA)

The DMA tests of the cured samples were conducted on a Q800 solids analyzer (TA Corporation, New Castle, DE, USA) with a three-point bending geometry and an oscillating frequency of 1 Hz. All the samples were polished carefully to avoid surface defects before the test. The samples with a size of $40 \times 10 \times 4$ mm^3 were examined at a heating rate of 3 °C·min^{-1}.

2.5.4. Thermogravimetric Analysis (TGA)

The TGA tests of the cured samples were carried out on an STA 409PC thermogravimetry instrument (Netzsch Corporation, Selb, Germany) with a heating rate of 15 °C·min^{-1}. Ground samples with a mass of about 10 mg were heated in a range of 35–600 °C under N_2 gas at a flow rate of 100 mL/min.

2.5.5. Mechanical Properties

The tensile tests of the cured samples were evaluated on a SANS7 CMT-4304 universal tester from Shenzhen Xinsansi Jiliang Instrument Corporation (Shenzhen, China) at a crosshead speed of 5.0 mm/min. Dumbbell specimens with a size of $9.53 \times 3.18 \times 3.2$ mm^3 at the narrow middle part and an overall length of 63.5 mm were conducted for the tensile tests. All the specimens were polished to avoid surface defects before the test. For each sample, at least five specimens were tested to determine the average values.

2.5.6. Water Absorption

The cured samples were dried in an oven at 50 °C for 24 h and weighed. Subsequently, the dried samples were immersed into distilled water for 48 h at room temperature. At last, the immersed samples were dried with filter papers and weighed again. For each resin, two samples were tested to determine the average values. The water absorption was calculated based on the following equation:

$$S = \frac{W1 - W0}{W1} \times 100\%$$

where W_0 and W_1 are the weights of the sample before and after being immersed into water, respectively.

3. Results and Discussion

3.1. Characterization of TO-Based Co-UEs

Figure 1 shows the GPC chromatographs of TO-based maleate and Co-UEs. Multi-peaks were observed in the chromatograph of TOPERMA, as the TOPERMA product was composed of mixed TO-based maleates [28]. This phenomenon was also seen in the chromatographs of TO-based Co-UEs. Furthermore, all the chromatographs of TO-based Co-UEs moved to a shorter retention time compared with TOPERMA, indicating the growth of the molar masses for all the Co-UE monomers [29]. Using the calibration curve of polystyrene standards, the molar masses of the TOPERMA and Co-UE monomers were calculated and listed in Table 1. All the TO-based Co-UEs demonstrated higher weight-average and number-average molar masses (M_w and M_n) than TOPERMA, indicating the unsaturated alcohols, including HEA, HEMA, and MAA, were successfully grafted onto TOPERMA.

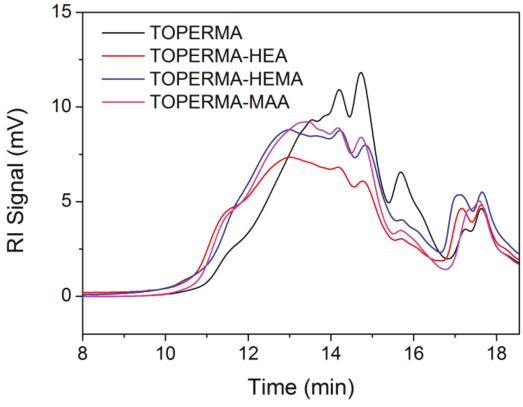

Figure 1. Gel permeation chromatography (GPC) chromatographs of TO-based maleate and Co-UEs.

Table 1. Data of Characterization of TOPERMA and TO-based Co-UE Monomers.

Sample ID	M_w [a] (g/mol)	M_n [b] (g/mol)	D [c]	$N_{C=C}$ [d]
TOPERMA	2247	1043	2.15	1.26
TOPERMA-HEA	3396	1406	2.42	1.62
TOPERMA-HEMA	3099	1298	2.39	1.56
TOPERMA-MAA	3120	1313	2.38	1.61

[a] Weight-average molar mass. [b] Number-average molar mass. [c] Polydispersity index. [d] Introduced C=C functionality per fatty acid.

Figure 2 indicates the ^{1}H NMR spectra of TO-based maleate and Co-UEs. In the spectrum of TOPERMA, the wide peak at 8.6 ppm corresponded to the protons on the carboxyl groups. The peaks at 6.2–6.9 ppm were corresponding to the maleate and fumarate vinyl protons. The multi-peaks at 5.3–5.9 ppm represented the residue protons of TO-conjugated trienes and the protons of the new yielding C=C due to D–A addition. The peaks at 4.0–4.4 ppm were assigned to the methylene protons of the polyol backbones connecting to the ester structure. The low peaks at 3.1–3.5 ppm represented the protons in the structure where MA connected to TO-conjugated triene. The peak at around 0.9 ppm corresponded to the terminal methyl protons of TO fatty acids, which is always taken as a reference to calculate proton amounts because its intensity should not be altered throughout all the reactions. In the spectrum of TOPERMA-HEA, the peak related to the protons on carboxyl groups shifted to 9.2 ppm and widened due to newly generated carboxyl groups. New and low peaks occurred at around 6.1 ppm, which was assigned to two vinyl protons on acrylate [27]. New peaks also appeared at about 5.8 ppm and 4.3–4.5 ppm, corresponding to the left vinyl protons on acrylate and the methylene protons from HEA, respectively. In the spectrum of TOPERMA-HEMA, the peak about the protons on carboxyl groups shifted to 8.9 ppm and also widened. New sharp peaks occurred at around 6.1 ppm, which was assigned to one of the two vinyl protons on methacrylate. New peaks appeared at around 2.0 ppm, which corresponded to the methyl protons on methacrylate. In the spectrum of TOPERMA-MAA, the peak corresponding to the protons on the carboxyl groups shifted to 9.7 ppm. New peaks occurred at around 5.0, 4.6, and 1.8 ppm, which were assigned to the two vinyl protons, methylene protons, and methyl protons on the methallyl groups, respectively. In general, all of these changes indicated that TOPERMA was successfully modified by HEA, HEMA, and MAA, respectively.

Using the peak at around 0.9 ppm as a reference, the proton amounts of the TO-based products can be determined. Combined with the information on the vinyl protons mentioned above, the

introduced C=C functionality per fatty acid ($N_{C=C}$) for each product could be determined by the following equations:

$$N_{C=C}(\text{TOPERMA}) = \frac{1}{2}\left(\frac{A_{6.2-6.9ppm}}{A_{0.9ppm}/3}\right) \quad (1)$$

$$N_{C=C}(\text{TOPERMA-HEA}) = \frac{1}{2}\left(\frac{A_{6.0-6.9ppm}}{A_{0.9ppm}/3}\right) \quad (2)$$

$$N_{C=C}(\text{TOPERMA-HEMA}) = \frac{1}{2}\left(\frac{A_{6.2-6.9ppm}}{A_{0.9ppm}/3}\right) + \frac{A_{6.1ppm}}{A_{0.9ppm}/3} \quad (3)$$

$$N_{C=C}(\text{TOPERMA-MAA}) = \frac{1}{2}\left(\frac{A_{6.2-6.9ppm}}{A_{0.9ppm}/3}\right) + \frac{1}{2}\left(\frac{A_{5.0ppm}}{A_{0.9ppm}/3}\right) \quad (4)$$

The results are summarized in Table 1. Firstly, all the $N_{C=C}$ values of the TO-based Co-UEs were larger than that of TOPERMA, suggesting the successful graft of unsaturated alcohols onto TOPERMA too. The grafted amounts of HEA, HEMA, and MAA were 0.36, 0.30, and 0.35, respectively. Second, the $N_{C=C}$ values for the three TO-based Co-UEs were almost equal to each other, meaning that they are suited to be employed in the study of structure–property relationship for the new Co-UE resins.

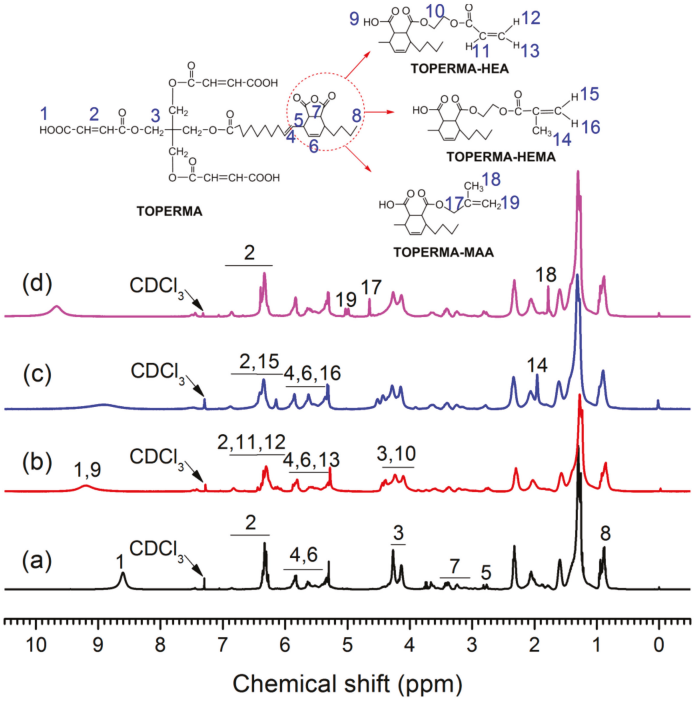

Figure 2. ^{1}H NMR spectra of (**a**) TOPERMA, (**b**) TOPERMA-HEA, (**c**) TOPERMA-HEMA, and (**d**) TOPERMA-MAA.

3.2. Properties of TO-Based Co-UE Resins

3.2.1. Dynamic Mechanical Analysis

Figure 3 shows DMA curves of the cured TO-based maleate and Co-UE resins containing 40 wt% of styrene. The related data, including storage modulus at 25 °C (E'_{25}) and T_g (determined from peak

temperatures of tan δ curves), were summarized in Table 2. Compared with the TOPERMA resin, all the Co-UE resins demonstrated higher values of E'_{25} and T_g, indicating that the incorporation of an unsaturated alcohol structure was beneficial to the improvement of the resin's thermo-mechanical properties. Compared with the TOPERMA-HEA resin, E'_{25} value of the TOPERMA-HEMA resin increased by 0.04 GPa, while the T_g value decreased by 0.8 °C, suggesting that only the stiffness of the resin was improved by the incorporation of steric hindrance. Moreover, compared with the TOPERMA-HEMA resin, the E'_{25} and T_g values of the TOPERMA-MAA resin grew by 0.22 GPa and 5.3 °C, indicating that both the stiffness and heat resistance could be improved by the reduction of the length of the flexible chain.

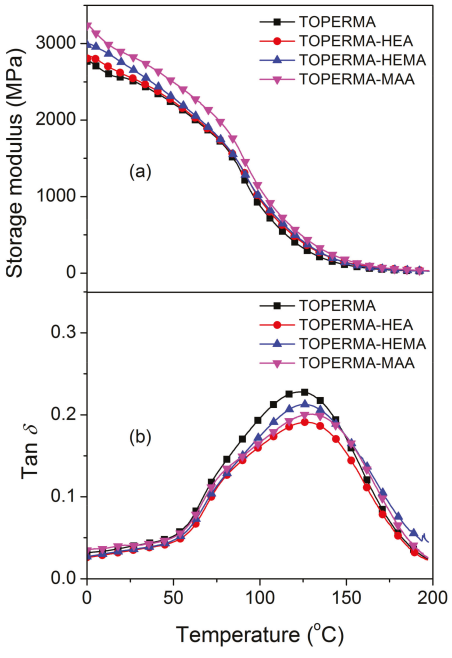

Figure 3. (**a**) Storage modulus and (**b**) loss factor of the cured, TO-based resins.

The thermo-mechanical properties of thermosets usually have a close relationship with crosslink density (ν_e). According to the kinetic theory of rubber elasticity, the experimental ν_e of thermosets can be determined from the rubbery modulus by the following equation [22,27,30]

$$E\prime = 3\nu_e RT \tag{5}$$

where E' represents the storage modulus of crosslinked copolymers in the rubbery plateau region, R is the gas constant, and T is the absolute temperature. In this work, the rubber modulus at T_g + 50 °C was selected for the calculation of ν_e. It was observed that all of the ν_e values of the obtained Co-UE resins were apparently larger than that of the TOPERMA resin. The reason for this lies in how all the Co-UEs had higher C=C functionality than TOPERMAA. In addition, in comparison with the TOPERMA-HEA resin, the drop in T_g for the TOPERMA-HEMA resin was probably attributed to the decrease of ν_e.

Table 2. Dynamic mechanic and thermal properties of the cured TO-based resins.

Samples	E'_{25} [a] (GPa)	T_g [b] (°C)	ν_e [c] (10^3 mol/m^3)	T_5 [d] (°C)	T_{p1} [e] (°C)	T_{p2} [e] (°C)	w_{char} [f] (%)
TOPERMA	2.05	123.1	3.44	384.9	408.0	453.8	9.04
TOPERMA-HEA	2.07	125.8	4.28	380.2	413.0	455.1	8.45
TOPERMA-HEMA	2.11	125.0	3.75	370.8	403.8	442.7	10.2
TOPERMA-MAA	2.33	130.3	3.93	379.5	406.4	452.3	8.36

[a] Storage modulus at 25 °C. [b] Glass transition temperature. [c] Crosslink density. [d] 5% weight loss temperature. [e] Peak temperature at the curves of weight loss rate; two peak values were observed for all the samples. [f] Char yield.

3.2.2. Thermogravimetric Analysis

Figure 4 depicts TGA thermograms and their derivative curves of the cured, TO-based maleate and Co-UE resins. All of the materials were thermally stable below 150 °C and exhibited a three-stage decomposition course [31]. The first stage was within 150−350 °C and can be ascribed to the evaporation and decomposition of soluble components (e.g., unreacted feedstocks) in the bulk materials. The second stage at about 350−500 °C was the fastest, which may result from the degradation and char formation of the crosslinked structures. The final stage (>500 °C) corresponded to the gradual degradation of char residue. The data of the obtained materials, including 5% weight loss temperature (T_5), peak temperature at the curves of weight loss rate (T_p), and char yield (w_{char}), are listed in Table 2. Compared with the TOPERMA resin, the T_5 and T_p values decreased slightly for almost all of the Co-UE resins, which may be ascribed to the flexible components from the unsaturated alcohols. However, the T_p values of the TOPERMA-HEA resin is an exception, which may be attributed to the large growth of ν_e. Compared with the TOPERMA-HEA resin, all of the T_5 and T_p values of the TOPERMA-HEMA resin decreased, which could be caused by the drop of ν_e. Moreover, compared with the TOPERMA-HEMA resin, all of the T_5 and T_p values of the TOPERMA-MAA resin increased, which is possibly ascribed to the reduction of the length of the flexible chain.

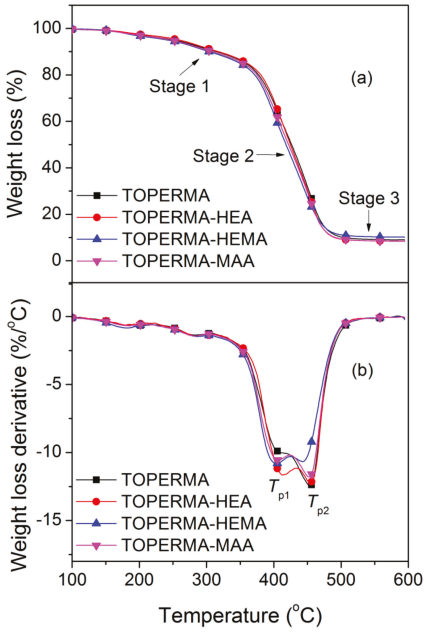

Figure 4. (**a**) TGA curves and (**b**) their derivatives of the cured TO-based resins.

3.2.3. Mechanical Properties

Figure 5 demonstrates the typical tensile stress–strain curves of the cured TO-based maleate and Co-UE resins. The corresponding data, including tensile strength (σ), Young's modulus (E), and tensile breaking strain (ε), are summarized in Table 3. All of the TO-based materials broke without reaching a yielding point, indicating that they were rigid materials. Compared with the TOPERMA resin, the σ and E values for all the Co-UE resins increased, indicating that the stiffness of the new Co-UE resins was improved by the incorporation of unsaturated alcohols. Compared with the TOPERMA-HEA resin, the σ and E values for the TOPERMA-HEMA resin increased by 0.6 MPa and 0.10 GPa, suggesting that the stiffness of the Co-UE resins was improved by the incorporation of steric hindrance. Furthermore, compared with the TOPERMA-HEMA resin, the σ and E values of the TOPERMA-MAA resin increased by 1.3 MPa and 0.26 GPa, which means that the stiffness of the Co-UE resins was also improved by the reduction of the length of the flexible chain. The TOPERMA-MAA resin reached a maximum σ of 32.2 MPa and E of 2.38 GPa among the CO-UE resins, which is probably because it contained both the structures of steric hindrance and shortest length of the flexible chain.

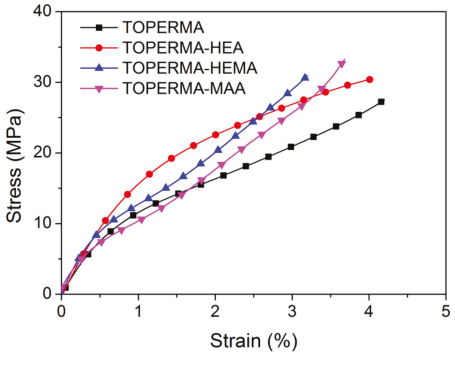

Figure 5. Typical tensile curves of the cured TO-based resins.

Table 3. Mechanical properties of the cured TO-based resins.

Samples	σ [a] (MPa)	E [b] (GPa)	ε [c] (%)
TOPERMA	27.4 ± 2.2	1.91 ± 0.02	4.03 ± 0.29
TOPERMA-HEA	30.3 ± 2.2	2.01 ± 0.06	3.98 ± 0.11
TOPERMA-HEMA	30.9 ± 1.7	2.12 ± 0.03	3.11 ± 0.04
TOPERMA-MAA	32.2 ± 1.0	2.38 ± 0.15	3.79 ± 0.25

[a] Tensile strength. [b] Young's modulus. [c] Tensile breaking strain.

3.2.4. Water Absorption

The values of water absorption for the cured TO-based maleate and Co-UE resins are illustrated in Figure 6. Firstly, all of the materials showed a very low water absorption (<1%), which is probably because TO is a drying oil. Second, all of the TO-based Co-UE resins demonstrated lower water uptakes than the TOPERMA resin, which is possibly attributed to the higher ν_e values of the resulting Co-UE thermosets and the hydrophobic structures from the unsaturated alcohols. In addition, compared with the TOPERMA-HEA resin, the TOPERMA-HEMA and TOPERMA-MAA resins also possessed lower water absorption, indicating that the employment of HEMA and MAA could further increase the hydrophobicity for the Co-UE materials.

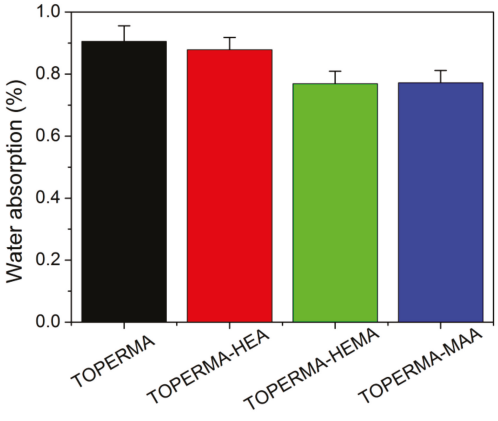

Figure 6. Water absorption of the cured TO-based resins.

4. Conclusions

For plant oil-based UE thermosets, improving their ultimate properties, such as stiffness and T_g, is closely related to their real application in the area of structural plastics. Previous studies have suggested that the development of UE macromonomers or oligomers with high C=C functionality could lead to biobased materials with high crosslink density and good ultimate properties. This work also showed that the developed TO-based, Co-UE resins obviously possessed higher C=C functionality and better performance in stiffness and T_g than the original TO-based maleate resin. However, the previous literature did not show us how to further improve their performance for these new oil-based UE resins. In this work, we successfully found out some new ways to improve their performance. The first way is to incorporate the structure of steric hindrance into the TO-based Co-UE macromonomers. For example, the TOPERMA-HEMA resin showed a tensile strength of 30.9 MPa and Young's modulus of 2.12 GPa, which was 2.0% and 5.4% higher than those of TOPERMA-HEA resin. The second way is to reduce the length of the flexible chain in the Co-UE macromonomers. For instance, the TOPERMA-MAA resin showed a tensile strength of 32.2 MPa, Young's modulus of 2.38 GPa, and T_g of 130.3 °C, which was 4.2%, 12.3%, and 4.2% larger than those of TOPERMA-HEMA resin, respectively. Moreover, a combined effect could be achieved when the two ways were applied simultaneously into modulating the structure of the Co-UE monomer, e.g., the tensile strength and Young's modulus of the TOPERMA-MAA resin increased by 6.3% and 18.4% compared with the TOPERMA-HEA resin. In general, this fundamental research could provide effective guidance for the preparation of plant oil-based UE thermosets with high performance.

Supplementary Materials: The Supporting Information is available free of charge on the MDPI Publications website at http://www.mdpi.com/2073-4360/11/5/826/s1.

Author Contributions: Conceptualization & Data Curation & Writing-Original Draft Preparation, C.L.; Investigation & Data Curation, Q.W.; Data Curation & Formal Analysis, R.A.; Data Curation, Q.S.; Data Curation, G.F.; Data Curation, Y.H.; Data Curation, P.J.; Writing-Review & Editing, Y.Z.; Writing-Review & Editing, W.L.

Funding: This research was funded by the Fundamental Research Funds of CAF [CAFYBB2017QB006] and the Natural Science Foundation of Jiangsu Province [BK20161122].

Acknowledgments: The authors greatly appreciate the Fundamental Research Funds of CAF (CAFYBB2017QB006) and the Natural Science Foundation of Jiangsu Province (BK20161122) for financial support.

Conflicts of Interest: The authors declare no conflict of interest.

References

1. Kandelbauer, A.; Tondi, G.; Zaske, O.C.; Goodman, S.H. Unsaturated polyesters and vinyl esters. In *Handbook of Thermoset Plastics*, 3rd ed.; Dodiuk, H., Goodman, S.H., Eds.; Elsevier: Amsterdam, The Netherlands, 2014; pp. 111–172.
2. Barile, C.; Casavola, C.; De Cillis, F. Mechanical comparison of new composite materials for aerospace applications. *Compos. Part B-Eng.* **2019**, *162*, 122–128.
3. Liu, C.G.; Wang, C.N.; Tang, J.J.; Zhang, J.; Shang, Q.Q.; Hu, Y.; Wang, H.X.; Wu, Q.; Zhou, Y.H.; Lei, W.; et al. High-performance biobased unsaturated polyester nanocomposites with very low loadings of graphene. *Polymers* **2018**, *10*, 1288. [CrossRef] [PubMed]
4. Kandola, B.K.; Ebdon, J.R.; Chowdhury, K.P. Flame retardance and physical properties of novel cured blends of unsaturated polyester and furan resins. *Polymers* **2015**, *7*, 298–315. [CrossRef]
5. Raquez, J.M.; Deleglise, M.; Lacrampe, M.F.; Krawczak, P. Thermosetting (bio)materials derived from renewable resources: A critical review. *Prog. Polym. Sci.* **2010**, *35*, 487–509. [CrossRef]
6. Chen, J.Q.; Tang, C.Q.; Yue, Y.Y.; Qiao, W.C.; Hong, J.G.; Kitaoka, T.; Yang, Z. Highly translucent all wood plastics via heterogeneous esterification in ionic liquid/dimethyl sulfoxide. *Ind. Crop. Prod.* **2017**, *108*, 286–294. [CrossRef]
7. Guo, Y.; Chen, J.Q.; Su, M.; Hong, J.G. Bio-based plastics with highly efficient esterification of lignocellulosic biomass in 1-methylimidazole under mild conditions. *J. Wood Chem. Technol.* **2018**, *38*, 338–349. [CrossRef]
8. Feng, Y.C.; Liang, H.Y.; Yang, Z.M.; Yuan, T.; Luo, Y.; Li, P.W.; Yang, Z.H.; Zhang, C.Q. A solvent-free and scalable method to prepare soybean-oil-based polyols by thiol-ene photo-click reaction and biobased polyurethanes therefrom. *ACS Sustain. Chem. Eng.* **2017**, *5*, 7365–7373.
9. Zhang, C.Q.; Garrison, T.F.; Madbouly, S.A.; Kessler, M.R. Recent advances in vegetable oil-based polymers and their composites. *Prog. Polym. Sci.* **2017**, *71*, 91–143. [CrossRef]
10. Chen, J.Q.; Su, M.; Zhang, X.L.; Chen, R.P.; Hong, J.G.; Yang, L.Y.; Yang, Z. The role of cations in homogeneous succinoylation of mulberry wood cellulose in salt-containing solvents under mild conditions. *Cellulose* **2014**, *21*, 4081–4091. [CrossRef]
11. Huang, C.; Dong, H.; Su, Y.; Wu, Y.; Narron, R.; Yong, Q. Synthesis of carbon quantum dot nanoparticles derived from byproducts in bio-refinery process for cell imaging and in vivo bioimaging. *Nanomaterials* **2019**, *9*, 387. [CrossRef] [PubMed]
12. Huang, C.; Su, Y.; Shi, J.; Yuan, C.; Zhai, S.; Yong, Q. Revealing the effects of centuries of ageing on the chemical structural features of lignin in archaeological fir woods. *New J. Chem.* **2019**, *43*, 3520–3528. [CrossRef]
13. Wool, R.P.; Sun, X.S. *Bio-Based Polymers and Composites*; Elsevier: Amesterdam, The Netherlands, 2005.
14. Liu, W.; Fei, M.-E.; Ban, Y.; Jia, A.; Qiu, R. Preparation and evaluation of green composites from microcrystalline cellulose and a soybean-oil derivative. *Polymers* **2017**, *9*, 541. [CrossRef] [PubMed]
15. Costa, C.; Fonseca, A.C.; Moniz, J.; Godinho, M.; Serra, A.C.; Coelho, J.F.J. Soybean and coconut oil based unsaturated polyester resins: Thermomechanical characterization. *Ind. Crop Prod.* **2016**, *85*, 403–411. [CrossRef]
16. Qin, Y.; Jia, J.; Zhao, L.; Huang, Z.; Zhao, S.; Zhang, G.; Dai, B. Synthesis and characterization of soybean oil based unsaturated polyester resin. In *Biotechnology, Chemical and Materials Engineering, Pts 1-3*; Chen, R., Sung, W.P., Eds.; Trans Tech Publications Ltd.: Zurich, Switzerland, 2012; Volumes 393–395, pp. 349–353.
17. Khot, S.N.; Lascala, J.J.; Can, E.; Morye, S.S.; Williams, G.I.; Palmese, G.R.; Kusefoglu, S.H.; Wool, R.P. Development and application of triglyceride-based polymers and composites. *J. Appl. Polym. Sci.* **2001**, *82*, 703–723. [CrossRef]
18. Can, E.; Kusefoglu, S.; Wool, R.P. Rigid, thermosetting liquid molding resins from renewable resources. I. Synthesis and polymerization of soy oil monoglyceride maleates. *J. Appl. Polym. Sci.* **2001**, *81*, 69–77. [CrossRef]
19. Can, E.; Wool, R.P.; Kusefoglu, S. Soybean and castor oil based monomers: Synthesis and copolymerization with styrene. *J. Appl. Polym. Sci.* **2006**, *102*, 2433–2447. [CrossRef]
20. Eren, T.; Kusefoglu, S.H. Synthesis and polymerization of the acrylamide derivatives of fatty compounds. *J. Appl. Polym. Sci.* **2005**, *97*, 2264–2272. [CrossRef]
21. Eren, T.; Kusefoglu, S.H. Synthesis and polymerization of the bromoacrylated plant oil triglycerides to rigid, flame-retardant polymers. *J. Appl. Polym. Sci.* **2004**, *91*, 2700–2710. [CrossRef]

22. Lu, J.; Khot, S.; Wool, R.P. New sheet molding compound resins from soybean oil. I. Synthesis and characterization. *Polymer* **2005**, *46*, 71–80. [CrossRef]
23. Echeverri, D.A.; Rios, L.A.; Rivas, B.L. Synthesis and copolymerization of thermosetting resins obtained from vegetable oils and biodiesel-derived crude glycerol. *Eur. Polym. J.* **2015**, *67*, 428–438. [CrossRef]
24. Zhang, P.; Zhang, J.W. One-step acrylation of soybean oil (so) for the preparation of so-based macromonomers. *Green Chem.* **2013**, *15*, 641–645. [CrossRef]
25. Liu, C.G.; Dai, Y.; Hu, Y.; Shang, Q.Q.; Feng, G.D.; Zhou, J.; Zhou, Y.H. Highly functional unsaturated ester macromonomer derived from soybean oil: Synthesis and copolymerization with styrene. *ACS Sustain. Chem. Eng.* **2016**, *4*, 4208–4216. [CrossRef]
26. Gomez, C.L.; Echeverri, D.A.; Inciarte, H.C.; Rios, L.A. Efficient processing of bioglycerol to a novel biobased polyunsaturated monomer. *J. Chem. Technol. Biotechnol.* **2019**, *94*, 634–640. [CrossRef]
27. Liu, C.G.; Shang, Q.Q.; Jia, P.Y.; Dai, Y.; Zhou, Y.H.; Liu, Z.S. Tung oil-based unsaturated co-ester macromonomer for thermosetting polymers: Synergetic synthesis and copolymerization with styrene. *ACS Sustain. Chem. Eng.* **2016**, *4*, 3437–3449. [CrossRef]
28. Liu, C.G.; Yang, X.H.; Cui, J.F.; Zhou, Y.H.; Hu, L.H.; Zhang, M.; Liu, H.J. Tung oil based monomer for thermosetting polymers: Synthesis, characterization, and copolymerization with styrene. *Bioresources* **2012**, *7*, 447–463.
29. Liu, C.G.; Zhou, Y.H.; Cheng, R.S. Quantitative characterization of complex formation of a pmma/peg solution by sec-ls. *J. Liq. Chromatogr. Relat. Technol.* **2013**, *36*, 2534–2546.
30. Can, E.; Wool, R.P.; Küsefoğlu, S. Soybean- and castor-oil-based thermosetting polymers: Mechanical properties. *J. Appl. Polym. Sci.* **2006**, *102*, 1497–1504. [CrossRef]
31. Andjelkovic, D.D.; Valverde, M.; Henna, P.; Li, F.; Larock, R.C. Novel thermosets prepared by cationic copolymerization of various vegetable oils—Synthesis and their structure–property relationships. *Polymer* **2005**, *46*, 9674–9685. [CrossRef]

polymers

MDPI

Article

Solvent- and Catalyst-free Synthesis, Hybridization and Characterization of Biobased Nonisocyanate Polyurethane (NIPU)

Xin He, Xiaoling Xu, Qian Wan, Guangxu Bo and Yunjun Yan *

Key Laboratory of Molecular Biophysics of the Ministry of Education, College of Life Science and Technology, Huazhong University of Science and Technology, Wuhan 430074, China; n785888@163.com (X.H.); xuxiaoling@hust.edu.cn (X.X.); m201671694@hust.edu.cn (Q.W.); m201671171@hust.edu.cn (G.B.)

* Correspondence: yanyunjun@hust.edu.cn; Tel.: +86-27-8779-2213

Received: 15 May 2019; Accepted: 6 June 2019; Published: 10 June 2019

Abstract: Nonisocyanate polyurethane (NIPU) is a research hotspot in polyurethane applications because it does not use phosgene. Herein, a novel method of solvent- and catalyst-free synthesis of a hybrid nonisocyanate polyurethane (HNIPU) is proposed. First, four diamines were used to react with ethylene carbonate to obtain four bis(hydroxyethyloxycarbonylamino)alkane (BHA). Then, BHA reacted with dimer acid under condensation in the melt to prepare four nonisocynate polyurethane prepolymers. Further, the HNIPUs were obtained by crosslinking prepolymers and resin epoxy and cured with the program temperature rise. In addition, four amines and two resin epoxies were employed to study the effects and regularity of HNIPUs. According to the results from thermal and dynamic mechanical analyses, those HNIPUs showed a high degree of thermal stability, and the highest 5% weight loss reached about 350 °C. More importantly, the utilization of these green raw materials accords with the concept of sustainable development. Further, the synthetic method and HNIPUs don't need isocyanates, catalysts, or solvents.

Keywords: hybrid nonisocyanate polyurethane; solvent- and catalyst-free; dimer acid; melt condensation

1. Introduction

Owing to their excellent surface protection, chemical and abrasion resistance, mechanical properties, high elasticity, and good biocompatibility, polyurethanes (PUs) have become one of the most versatile polymers, with wide application in many fields, such as furnishing, cars, clothing, shoes, elastomers, coatings, walls, and roofing insulation [1–10]. However, considering the potential harm to the environment and human health by cyanate and phosgene (raw materials for isocyanate), developing non-isocyanate polyurethanes (NIPUs) is a question that needs an immediate answer [9,11,12].

Today, the sustainable development of raw materials is becoming imperative for human beings, as a result of the lack of fossil fuels [13]. The current challenge in the polyurethane industry is to switch from petro-based polyurethane to bio-based PUs or NIPUs [11,14]. In traditional bio-based PUs, vegetable oil was one of the major raw materials because of its convenient designability of double bonds and ester bonds [15,16]. Kong et al. utilized canola, sunflower, and camelina oil to synthesize bio-based polyols, which were the starting materials for the production of PU coating [17]. Wu et al. applied natural *Sapium sebiferum* oil to produce polyol, the hydroxyl value of which reached to 211 mgKOH/g. Finally, the synthesized PU featured good thermal and mechanical properties [18]. Campanella et al. synthesized bio-based polyurethane foams from soybean oil and proved it was feasible [19]. Kirpluks et al. obtained high functional polyols from rapeseed oil, aiming to prepare rigid PU foam thermal insulation material [20]. Vanags et al. used epoxidized tall oil fatty acids to synthesize polyol, which had a high OH value (reaching to 527 ± 2 mg KOH/g) for polyurethane application [21].

Furthermore, dimer acid, derived from fatty acids, was a renewable resource and can be an alternative for PU [22–24]. Although dimer acid is a value-added product, a few conversion technologies have been proposed by researchers. Yao et al. used dimer acid and ethylene glycol to synthesize polyester polyol and then obtained PU via a reaction with isophorone diisocyanate [25]. NIPU can also use these sustainable resources as the main raw materials. Specifically, bio-based cyclic carbonates have been an important research topic, including the epoxidation of vegetable oils, terpenes, or vanillin derivates, or by the glycidylization of bio-polyols followed by carbonation with carbon dioxide [26,27].

Today, many studies of NIPU have been reported, and most of the synthetic methods (as shown in Scheme 1) were ring-opening polymerizations of cyclic carbonates via diamines or multi-amines [28,29]. Therefore, the synthesis of cyclic carbonate oligomers/polymers has represented the majority of research on NIPU preparation [30,31]. However, few studies have been industrialized because of the raw material cost, safety, construction difficulty, and so on. Naturally, searching alternative methods for NIPU preparation has also become an issue worth thoroughly investigating. Among them, the carbamate monomer (bis-hydroxycarbamate), synthesized by a cyclocarbonate and a diamine, is an appropriate option. This way, the carbamate monomer can react with polyol or polyacid to produce NIPU by a polycondensation reaction. Rokicki et al. used bis-hydroxycarbamate, synthesized by ethylene carbonate and diamine (1, 4-diaminobutane or 1, 6-diaminohexane), to react with diol (1, 6-hexanediol or 1, 10-decanediol), and obtained several NIPUs [32]. However, the disadvantages of the synthesized NIPUs by this route cannot be ignored, especially the low glass transition temperature, which is a consequence of the low average molecular weight [3,4,33]. To solve this problem, appropriate catalysts, chain extenders, and crosslinking agents are worthwhile choices.

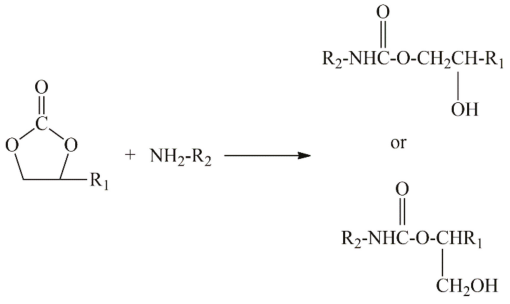

Scheme 1. Ring-opening synthesis of non-isocyanate polyurethanes (NIPU).

Therefore, in this study, for the purposes of renewable and sustainable development, dimer acid (DA) was selected as the biomass with a flexible chain and low glass transition temperature [34,35]. Ethylene carbonate (EC) was chosen as the key component of the urethane group because it can be synthesized by ethylene oxide and carbon dioxide and is also a green raw material [36]. Furthermore, as is known, fixing carbon dioxide is one of the potential ways to resolve the greenhouse gas problem [37,38]. First, a series of bis(hydroxyethyloxycarbonylamino)alkanes (BHAs) were synthesized from several amines and EC, and then the BHAs reacted with the DA to produce an NIPU-prepolymer by melt polycondensation. To solve the problem of low average molecular weight, epoxy resins were employed to crosslink the NIPU-prepolymer with the secondary amine. For characterization of those products, finding out the regularity of the epoxy value and secondary amine for hybrid nonisocyanate polyurethane (HNIPU) and exploring whether them have potential for coating applications, several instruments, including Fourier transform infrared spectroscopy (FTIR), nuclear magnetic resonance (NMR), Fourier transform mass spectrometer (FTMS), Gel permeation chromatography (GPC), thermogravimetric analysis (TGA), differential scanning calorimetry (DSC), dynamic mechanical analysis (DMA), field emission scanning electron microscopy (FSEM), X-ray diffraction (XRD), Atomic force microscope (AFM), water absorption, and swelling, were used in this study.

2. Materials and Methods

2.1. Materials

Ethylene carbonate (EC, 99%), ethanediamine (EDA, 99%), diethylenetriamine (DETA, 100%), triethylenetetramine (TETA, 100%) and tetraethylenepentamine (TEPA, 90%) were purchased from Sinopharm Chemical Reagent Ltd Co. (Shanghai, China). All the materials were analytical reagents and used without any extra processing. Dimer acid (DA, 98%, 9-[(Z)-non-3-enyl]-10-octylnonadecanedioic acid) was bought from Bangcheng Chemical Ltd. Bisphenol-A epoxy resin E-44 (mean epoxy value: 0.44) and Bisphenol-A epoxy resin E-51 (mean epoxy value: 0.51) were obtained from Yueyang Petrochemical Ltd Co. (Yueyang, China).

2.2. Synthesis of BHAs

BHAs were synthesized from EC and four amines (EDA, DETA, TETA, and TEPA) by a ring opening reaction (seen in Scheme 2). A 100.0 g amount of EC was weighed into a 500 mL three-necked round-bottomed flask, and equimolar amine (EDA:34.1 g; DETA: 58.0 g; TETA: 82.2 g; TEPA: 118.2 g) was put into a constant pressure separation funnel. Then, both were kept in a 60 °C oil bath with magnetic stirring, and the amine was added dropwise. The mixture was stirred continuously until no bubbles appeared. Then the temperature was increased to 100 °C and kept for four hours. After cooling to room temperature, the sample was washed three times with acetonitrile and the solution was dumped. Subsequently, the products were dried under a 60 °C vacuum drying oven for a day. On the basis of four amines, the derived BHAs were named BHA-2 (obtained 127.4 g, yield 95%), BHA-23 (obtained 148.5 g, yield 94%), BHA-34 (obtained 174.9 g, yield 96%), and BHA-45 (obtained 207.3, yield 95%). The detailed raw material mass and results of the BHAs are listed in Table 1. BHA-2, BHA-23, and BHA-34 were a light-yellow powder with a little viscidity. BHA-45 was a yellow paste with some viscidity.

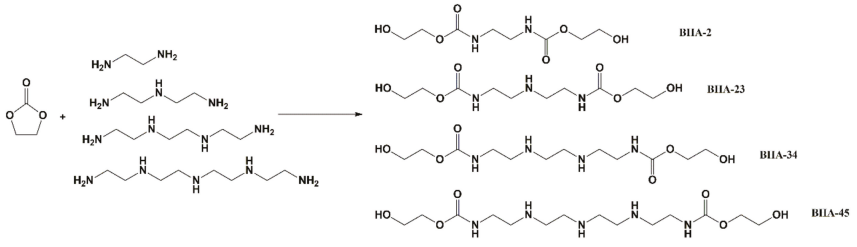

Scheme 2. Synthesis of bis(hydroxyethyloxycarbonylamino)alkanes (BHAs).

Table 1. The raw materials mass and results of the BHAs. EDA, ethanediamine; DETA, diethylenetriamine; TETA, trethylenetriamine; TEPA, diethylenetriamine; EC, Ethylene carbonate.

BHA Type	Amine Type	Mole Ratio (Amine:EC)	Mole Ratio	EC Mass	Amine Mass	BHA Mass	Yield
BHA-2	EDA	1:2	1:1	100.0 g	34.1 g	127.4 g	95%
BHA-23	DETA	1:2	1:1	100.0 g	58.0 g	148.5 g	94%
BHA-34	TETA	1:2	1:1	100.0 g	82.2 g	174.9 g	96%
BHA-45	TEPA	1:2	1:1	100.0 g	118.2 g	207.3 g	95%

2.3. Synthesis of NIPU Prepolymers

As Scheme 3 shows, the reaction is an esterification reaction. After mixing 10.0 g BHA with a little excess of dimer acid (reactant molar ratio = 1:1.05), the reaction was set in a 250 mL three-necked round-bottomed flask with magnetic stirring, and reacted at 180 °C for 4 h under nitrogen blowing. Then, the nitrogen pipe was withdrawn and the reaction was continued with a reduced pressure aimed

at removing the water to promote the esterification reaction. Finally, the samples were poured into a beaker and dried at 60 °C in a vacuum drying oven. Corresponding to the different BHAs, the NIPU prepolymers were named NIPU-2, NIPU-23, NIPU-34, and NIPU-45. The detailed raw material mass and results of the NIPUs are listed in Table 2. NIPU-2, NIPU-23, and NIPU-34 were a brown paste with some viscidity. NIPU-45 was a brown colloid with little viscidity.

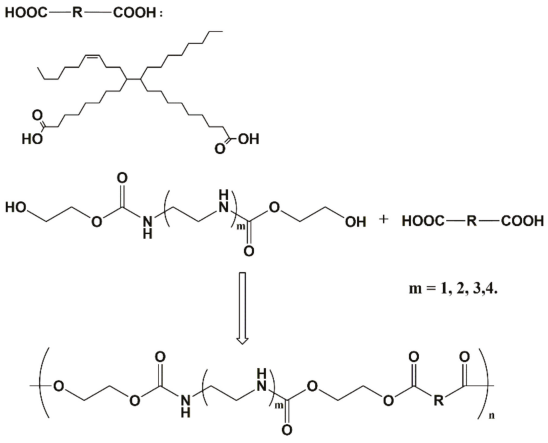

Scheme 3. Synthesis of the NIPU prepolymer.

Table 2. The raw material mass and results of the NIPUs.

NIPU Type	BHA Type	Mole Ratio (BHA:DA)	BHA Mass	DA Mass	NIPU Mass	Yield
NIPU-2	BHA-2	1:1.05	10.0 g	38.9 g	43.3 g	89%
NIPU-23	BHA-23	1:1.05	10.0 g	28.0 g	32.9 g	87%
NIPU-34	BHA-34	1:1.05	10.0 g	17.9 g	25.0 g	90%
NIPU-45	BHA-45	1:1.05	10.0 g	15.7 g	21.8 g	85%

2.4. Synthesis of HNIPUs

To increase the crosslinking degree, epoxy resins were employed to react with the secondary amines, which were produced by the polyethyene polyamine. Therefore, the NIPU-2 was excluded from this step because of the lack of a secondary amine. First, 2.0 g NIPU prepolymer were taken into a flask, and kept in a 60 °C oil bath with magnetic stirring. When the samples reverted to the liquid stage, 1.4 g of epoxy resin was added; then, the mixture was stirred and the bubble was eliminated by vacuum. When the mixture turned to a homogeneous phase it was poured into a teflon mold and kept on a 60 °C vacuum drying oven for 12 h. Subsequently, the temperature was changed to 90 °C and the HNIPUs were cured for 4 h. After naturally cooling to room temperature, bulk specimens were obtained (3.4 g, yield 100%, Scheme 4), packed, and kept for characterization. The detailed raw material mass and results of HNIPUs are listed in Table 3. HNIPU-2344 and HNIPU-2351 were a light-yellow paste with some viscidity. HNIPU-3444 (ϱ = 1.02 g/cm^3), HNIPU-3451 (ϱ = 1.26 g/cm^3), HNIPU-4544 (ϱ = 1.01 g/cm^3), and HNIPU-4551 (ϱ = 1.35 g/cm^3) were yellow elastic with non-viscidity. There were no bubbles in all these samples.

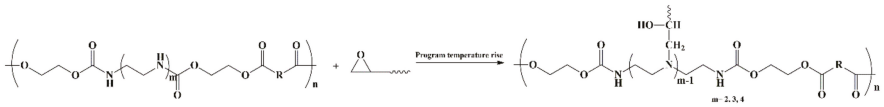

Scheme 4. Synthesis of hybrid nonisocyanate polyurethanes (HNIPUs).

Table 3. The raw materials mass and results of HNIPUs.

HNIPU Type	NIPU Type	EP Type	Mass Ratio (NIPU:EP)	NIPU Mass	EP Mass	HNIPU Mass	Yield
HNIPU-2344	NIPU-23	E44	1:0.7	2.0 g	1.4 g	3.4 g	100%
HNIPU-2351	NIPU-23	E51	1:0.7	2.0 g	1.4 g	3.4 g	100%
HNIPU-3444	NIPU-34	E44	1:0.7	2.0 g	1.4 g	3.4 g	100%
HNIPU-3451	NIPU-34	E51	1:0.7	2.0 g	1.4 g	3.4 g	100%
HNIPU-4544	NIPU-45	E44	1:0.7	2.0 g	1.4 g	3.4 g	100%
HNIPU-4551	NIPU-45	E51	1:0.7	2.0 g	1.4 g	3.4 g	100%

2.5. Characterization

The ^{1}H nuclear magnetic resonance (NMR) spectra of samples were determined by a Bruker AV600 MHz NMR spectrometer (Bruker, Karlsruhe, Germany). BHA-2 was dissolved by dimethylsulfoxide (DMSO) and the other BHAs were dissolved by Deuteroxide (Tetramethylsilane as an internal standard), and all mixtures were injected into 5 mm diameter NMR sample tubes. All of the ^{1}H-NMR spectra were measured at room temperature.

A Bruker Vertex 70 Fourier transform infrared spectroscopy (FTIR) spectrometer (Bruker, Karlsruhe, Germany), equipped with an attenuated total reflection (ATR) accessary, was employed to test the FTIR spectra. Liquid samples were smeared on a KBr tablet, and solid block samples were test by ATR accessary. All samples were scanned from 4000 to 40 cm^{-1} with a resolution of 4 cm^{-1} with 128 scans at room temperature.

A Solari 7.0T high resolution Fourier transform mass spectrometer (FTMS) (Bruker, Karlsruhe, Germany) was employed to determine the mass-to-charge ratios by electrospray ionization (ESI). The BHAs were dissolved into water and injected for characterization.

The weight average molecular weight (*M*w) and polymer dispersity index (PDI = *M*w/*M*n, *M*n was number average molecular weight) were measured by using an SSI Series 1500 Gel permeation chromatography (GPC) instrument (SSI, USA), which was equipped with a refractive index detector and Shodex KF-802.5 chromatogram column. The temperature was set to 40 °C, and tetrahydrofuran (THF) was used as eluent at a flow rate of 1.0 mL/min.

A Pyris 1 thermogravimetric analysis (TGA) instrument (Perkin-Elmer, Waltham, MA, USA) was employed to study the thermostability of samples and performed from room temperature to 600 °C with a heating rate of 10 °C /min in N_2 atmosphere.

The glass transition temperature (T_g) was tested by using a Perkin-Elmer Diamond DSC instrument (Perkin-Elmer, Waltham, MA, USA). The testing conditions included increasing the temperature to 150 °C at a rate of 30 °C /min and keeping it at 150 °C for 2 min to eliminate the thermal history of a sample; then, decreasing the temperature to −50 °C at a rate of 5 °C/min and keeping it at –50 °C for 2 min. Finally, the temperature was increased from −50 to 150 °C at a rate of 10 °C/min. The last heating curve was recorded for analysis. During the test, the N_2 atmosphere was kept stable.

Dynamic mechanical analysis (DMA) was performed on a Perkin-Elmer Diamond DMA instrument (Perkin-Elmer, Waltham, MA, USA). All HNIPUs were cut into a 1 mm × 10 mm × 30 mm rectangular block and heated from −100 °C to 150 °C at a heating rate of 3 °C /min under a N_2 atmosphere with a single cantilever mode in the testing process.

A sirion 200 field emission scanning electron microscopy (FSEM) instrument (FEI, Eindhoven, Netherlands) was employed to observe the morphology of the HNIPUs. All samples were freeze-fractured after a short immersing time in liquid nitrogen and sputter coated with a Au layer.

X-ray diffraction (XRD) was utilized to confirm the crystallization behavior of the samples and characterized by using a x' pert3 powder X-ray diffractometer. A 10 mm × 10 mm flakelet was placed on the instrument with a 2θ range from 5° to 50° at 5 °/min.

An atomic force microscope (AFM) analysis was performed using an SPM9700 AFM instrument (Shimadzu, Kyoto, Japan) with a tapping mode. Samples were cut into flat pieces, and the surface was cleared by absolute ethanol. Then, the samples were dried at 60 °C for 24 h.

The water absorption of all HNIPUs was tested from the weight change of a film sample before and after the immersion in deionized water at room temperature over time. The samples of the HNIPUs were taken out and immediately wiped with filter paper and accurately weighed. The following equation was calculation for water absorption:

$$\text{Water absorption}(\%) = \frac{W_a - Wo}{Wo} \times 100 \quad (1)$$

where W_a and W_o are the weight of samples after and before immersion in deionized water, respectively.

A swelling test was determined by the mass change of a film sample under immersion in dimethylsulfoxide (DMSO) at room temperature. After taking out the sample, a filter paper was used to dry the residual DMSO on the surface and accurately weigh the mass. The swelling was calculated by the following equation:

$$\text{Swelling}(\%) = \frac{W_t - Wo}{Wo} \times 100 \quad (2)$$

where W_t and W_o are after and before immersion in DMSO, respectively.

3. Results and Discussion

3.1. Synthesis of BHAs

Few reports have described the synthesis of BHAs, especially utilizing polyene polyamine. In this section, four BHAs were first obtained via ring opening reaction and confirmed by NMR, FTIR, and FTMS. In Figure 1, because of the different solubility of BHAs, the Figure shows that the dissimilar solvent peak: δ (ppm) = 2.50 (DMSO-d6, solvent peak) and 3.30 ($\underline{H_2}O$, water peak) belonged to Figure 1a; δ (ppm) = 4.70 ($\underline{D_2}O$, solvent peak) belonged to Figure 1b–d. Figure 1 shows the chemical shift of different hydrogen atom, and confirmed successful synthesis of the four BHAs.

Figure 2 shows the FTIR spectra of four BHAs. From the dotted box of **a**, as the interaction of –OH (v, 3400 cm^{-1}) and –NH– (v, 3300 cm^{-1}), the stretching vibration changed with an increasing number of secondary amines, especially BHA-45. The rest of the characteristic peaks are as follows: 2942 cm^{-1} (v_{as}, $–CH_2–$), 2836 cm^{-1} (v, $–CH_2–$), 1695 cm^{-1} (v, C=O), 1540 cm^{-1} (δ, N–H), 1043 cm^{-1} (v, C–OH). The band characteristic for the urethane group was proven to successfully form via 1695 cm^{-1} (v, C=O) and 1540 cm^{-1} (δ, N–H). Further, by contrasting with EC, the vibration peak at 1786 cm^{-1} for BHAs disappeared because of the ring opening of EC.

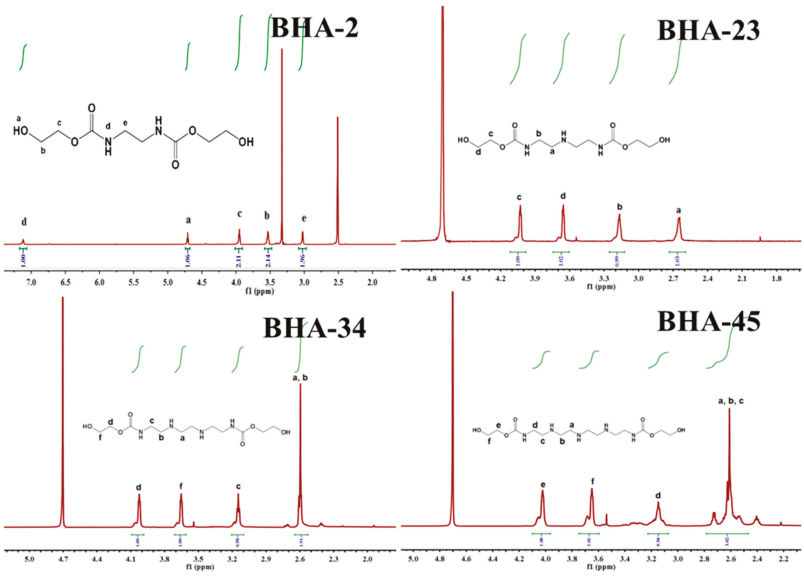

Figure 1. ^{1}H nuclear magnetic resonance (NMR) spectra of four BHAs. (**BHA-2**) ^{1}H NMR (DMSO-d_6): δ (ppm) = 3.03 (–C(O)–NH–C<u>H</u>$_2$–), 7.12 (–C(O)–N<u>H</u>–CH$_2$–), 3.94 (HO–CH$_2$–C<u>H</u>$_2$–O–), 3.54 (HO–C<u>H</u>$_2$–CH$_2$–O–), 4.70 (<u>H</u>O–CH$_2$–CH$_2$–O–). (**BHA-23**) ^{1}H NMR (D_2O): δ (ppm) = 2.64 (–C(O) –NH–CH$_2$–C<u>H</u>$_2$–NH–), 3.17 (–C(O)–NH–C<u>H</u>$_2$–CH$_2$–NH–), 3.65 (HO–CH$_2$–C<u>H</u>$_2$–O–), 4.03 (HO–C<u>H</u>$_2$–CH$_2$–O–). (**BHA-34**) ^{1}H NMR (D_2O): δ (ppm) = 2.59–2.61 (–C(O)–NH–CH$_2$–C<u>H</u>$_2$–NH–C<u>H</u>$_2$–), 3.16 (–C(O)–NH–C<u>H</u>$_2$–CH$_2$–NH–CH$_2$–), 3.65 (HO–CH$_2$–C<u>H</u>$_2$–O–), 4.02 (HO–C<u>H</u>$_2$–CH$_2$–O–). (**BHA-45**) ^{1}H NMR (D_2O): δ (ppm) = 2.46–2.73 (–C(O)–NH–CH$_2$–C<u>H</u>$_2$–NH–C<u>H</u>$_2$–C<u>H</u>$_2$), 3.15 (–C(O)–NH–C<u>H</u>$_2$–CH$_2$–NH–CH$_2$–CH$_2$), 3.66 (HO–CH$_2$–C<u>H</u>$_2$–O–), 4.02 (HO–C<u>H</u>$_2$–CH$_2$–O–).

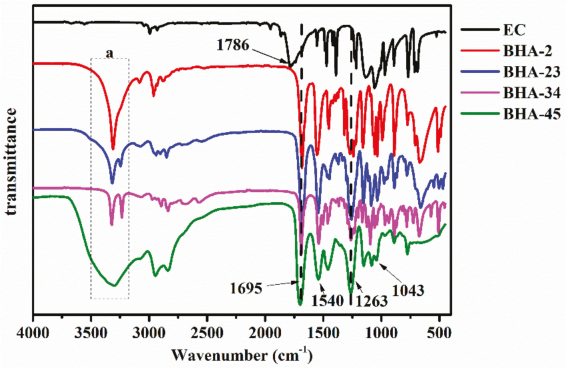

Figure 2. Fourier transform infrared spectroscopy (FTIR) spectra of four BHAs.

Figures S1–S4 show the FTMS spectra of four BHAs, respectively. The corresponding relative molecular mass of BHAs are as follows: BHA-2, 236.10 g/mol; BHA-23, 279.14 g/mol; BHA-34, 322.19 g/mol; BHA-45, 365.23 g/mol. In contrast, the FTMS showed the [M+H], and confirmed the synthesis and purity of the BHAs.

Figure 3 provides the TGA curves of the BHAs. When the temperature exceeded 180 °C, there was a sharp decrease in the weight loss of the four BHAs. Thus, In consideration of the

decomposition and reactivity of the BHAs, 180 °C would be an appropriate temperature for the synthesis of a NIPU-prepolymer.

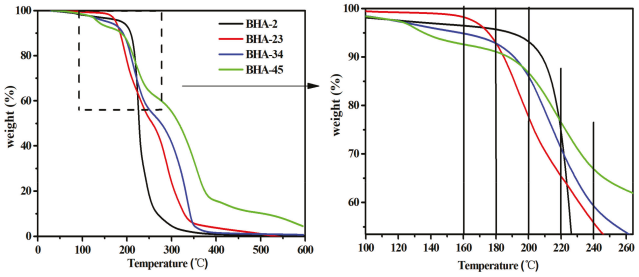

Figure 3. Thermogravimetric analysis (TGA) curves of four BHAs.

3.2. Synthesis of NIPU-prepolymers

Figure 4 shows the FTIR spectra of different NIPU-prepolymers. The main vibration peaks were indicated by arrows: 3303 cm^{-1} (*v*, –NH–), 1741 cm^{-1} (*v*, C=O, from carboxyl groups), 1691 cm^{-1} (*v*, C=O, from urethane groups), 1648 cm^{-1} (*v*, C=O, from ester groups). Compared with Figure 2, a new vibration peak appears at 1648 cm^{-1} in Figure 4 and confirmed the formation of ester groups. The vibration peak at 3303 cm^{-1} increased along with the increase of the secondary amine. The vibration peak at 1741 cm^{-1} proved that the prepolymer was blocked with dimer acid.

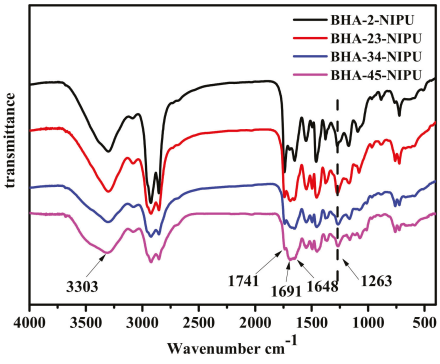

Figure 4. FTIR spectra of four NIPU-prepolymers.

The thermal stability of NIPU-prepolymers was characterized using TGA, and the results are demonstrated in Figure 5 (left). When the secondary amine number increased, the 5% mass decomposition temperature obviously increased, and the highest temperature was about 375 °C. The root of this result might be because the hydrogen bonds were formed between the different N atoms [39]. Further, according to differential thermal gravity (DTG) curves (Figure 5, right), there was only one maximum decomposition rate (at about 460 °C) in the curve, which illustrated that thermal degradation occurred in one step [40]. Moreover, the maximum decomposition rate slightly decreased as the number of secondary amines increased, and possible explanations may be due to the lower bond dissociation energy of C–N (337.7 kJ/mol) than that of C–C (359.2 kJ/mol) [41].

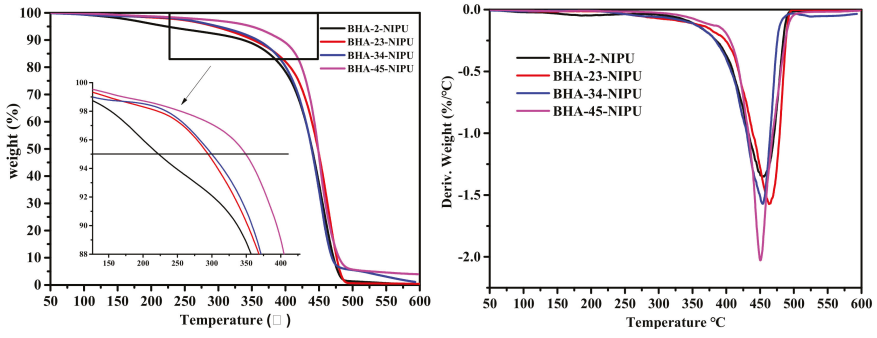

Figure 5. TGA (**left**) and differential thermal gravity (DTG) (**right**) curves of four NIPU-prepolymers.

The glass transition temperatures of the four NIPU-prepolymers were determined by DSC, and the results were displayed in Figure 6. It can be seen that there was only one T_g in every DSC curve, indicating that all NIPU-prepolymers were a homogeneous phase system. The results also showed that all T_g of NIPU-prepolymers were blew zero, and the NIPU-prepolymers formed a viscous flow state, which is ascribed to their low relative molecular weight. In addition, because the significant influence of free hydrogen from the secondary amine number could facilitate the formation of more hydrogen bonds, the T_g of the NIPU-prepolymers increased as the secondary amine number increased.

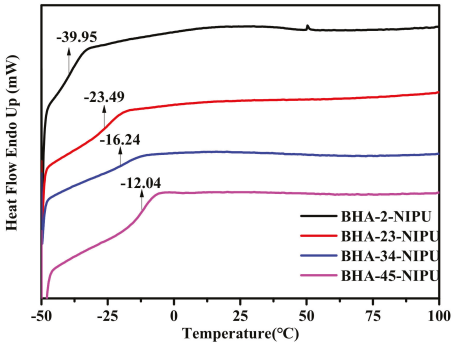

Figure 6. Differential scanning calorimetry (DSC) curves of four NIPU-prepolymer.

Gel permeation chromatography (GPC) was applied to measure the weight average molecular weight (Mw) and polymer dispersity index (PDI), and the results are shown in Figure 7. The Mw of BHA-45-NIPU reached 6460 g/mol, which was the highest. The Mw of BHA-23-NIPU was almost as low as that of BHA-2-NIPU. According to the research, the secondary amine could facilitate polycondensation. One possible reason for this result is that the secondary amine is alkaline and easily reacted with acid as a first process. The trend of PDI also could be explained by the above reason.

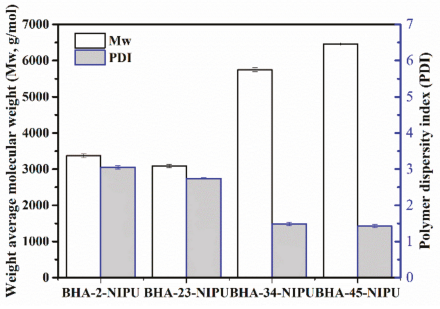

Figure 7. Molecular weight (Mw) and PDI of four NIPU-prepolymers.

3.3. Synthesis of HNIPUs

The main purpose of Figure 8 was to indicate whether the reaction was complete, according to the presence of the peak at 916 cm^{-1} (epoxy group). It can be found that BHA-2344-HNIPU and BHA-2351-HNIPU have residual epoxy groups, mainly because o the low content of secondary amines, which led to lower reaction sites with epoxy groups. In contrast to Figure 4, the band intensity of the vibration peak at 1741 cm^{-1}, which belongs to C=O (carboxyl groups), showed an obviously reduction. This result might boil down to the reaction between the carboxyl groups and the epoxy group. The vibration peaks at 1684 cm^{-1} and 1649 cm^{-1} were attributed to the urethane groups and ester groups, respectively. Compared with Figure 4, the C=O vibration peak at 1691 cm^{-1} shifted to lower wavenumbers of 1684 cm^{-1}, which indicated that the epoxy group provided additional hydrogen bonding for HNIPU [42,43]. Further, Scheme 4 showed the additional hydroxyl groups because of the ring opening of epoxy groups, which could lead to more hydrogen bonding.

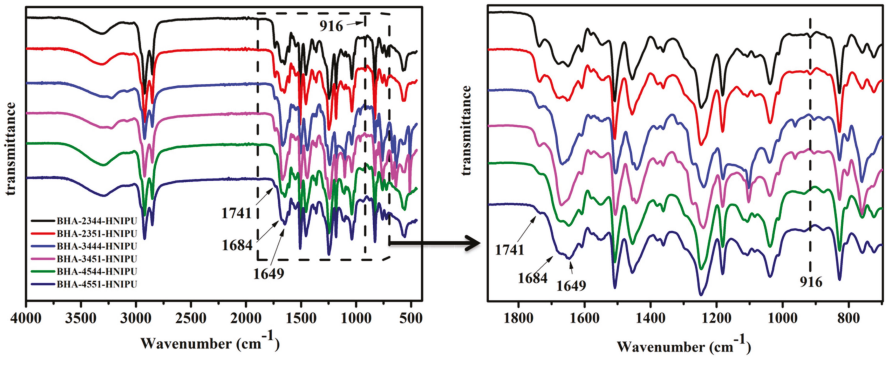

Figure 8. FTIR spectra of HNIPUs.

Figure 9 shows the thermal stability of HNIPUs. According to the partial enlargement of TGA curves, the varied trend affected by secondary amine was consistent with Figure 5, illustrating that thermal stability was mainly affected by the content of the secondary amine. In other words, after reacting with epoxy groups under the condition of the programmed temperature, the chemical bond from the secondary amine still had a good thermal stability and a dominant role. Meanwhile, the E-44 with the lower epoxy value provided better thermal stability than E-51, based on the results of Figure 9 (left). This phenomenon could be explained by the greater number of hydroxyl groups in the structure of E-44, which could influence the hydrogen bond or crosslinking degree. In Figure 9 (right), the BHA-4544-HNIPU clearly had the highest maximum decomposition rate and the BHA-2351-HNIPU had the lowest maximum decomposition rate.

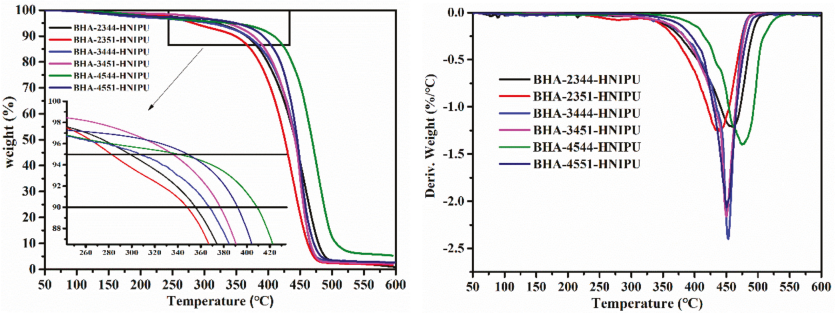

Figure 9. TGA (**left**) and DTG (**right**) curves of HNIPUs.

As the only secondary amine in BHA-23, the crosslinking degree was naturally low in BHA-2344-HNIPU and BHA-2351-HNIPU. Therefore, these two HNIPUs showed a viscous flow state instead of an elastomeric state at room temperature, and this result was represented in Figure 10. The glass transition temperature (T_g) is affected by many different parameters, such as intermolecular interactions, molecular symmetry, chain stiffness, type of aside group, branching/crosslinking density, and molar mass [44]. In this study, we found that secondary amine content played a bigger role in influencing T_g than the epoxy value. The BHA-4551-HNIPU had the highest T_g (34.82 °C) in all HNIPUs. The main reason for this result could be its high crosslinking degree, especially the greater number of sites of crosslinking from the secondary amine.

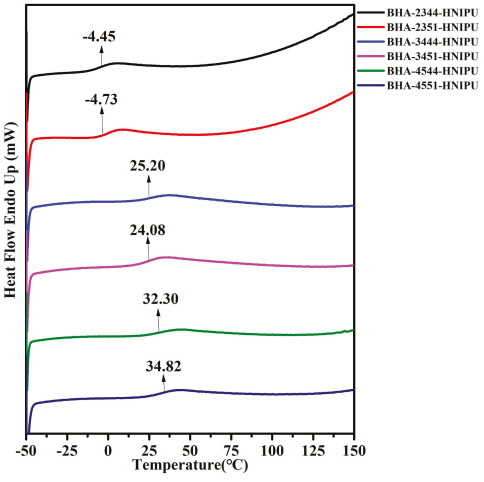

Figure 10. DSC curves of HNIPUs.

Because the DMA tensile mode needs the materials to present an elastomeric state, BHA-2344-HNIPU and BHA-2351-HNIPU, which were a viscous flow state, could not satisfy the testing requirement. Usually, the highest tanδ indicates the T_g, and the results are consistent with that of the DSC (seen in Figure 11). Meanwhile, the regularity of DMA also agrees with the DSC in T_g. The homogeneity of material can be characterized by the tanδ peak: a symmetrical and narrow tanδ reveals a homogeneous material [45]. Consequently, a loss factor tanδ shows that HNIPUs are homogeneous.

The storage modulus E′ was used to illustrate the rigidity of material. The storage modulus of BHA-3444-HNIPU and BHA-3451-HNIPU were higher than those of BHA-4544-HNIPU and

BHA-4551-HNIPU before 13 °C, which could be attributed to the crystallization behavior of these two HNIPUs. However, BHA-4551-HNIPU had the highest storage modulus after 13 °C, and the other three HNIPUs just had a tiny difference. This result shows that the BHA-4551-HNIPU had the best rigidity of all HNIPUs after 13 °C, and demonstrates that the crosslinking degree was important for the storage modulus.

Crosslinking density (ν_e) was calculated by the following equation:

$$\nu_e = \frac{E'_{at\ T\alpha+50}}{3RT_{\alpha+50}} \quad (3)$$

where $E'_{at\ T\alpha+50}$ is the storage modulus at the rubbery region, R is the gas constant, and $T_{\alpha+50}$ (K) is the temperature in the rubbery region (of transition from the vitreous to elastic domain of material determined at the maximum of the tanα curve [45,46]. According to Table 4, the BHA-4551-HNIPU had the highest crosslinking density of all HNIPUs, which was in accordance with the results of TGA and DSC.

Table 4. HNIPU parameters obtained from the DMA.

Sample	T_α (°C)	T_α + 50 (°C)	$E'_{at\ T\alpha+50}$ (MPa)	ν_e (mol/m^3)
BHA-3444-HNIPU	38.04	88.04	7.95	881.30
BHA-3451-HNIPU	32.87	82.87	7.29	821.74
BHA-4544-HNIPU	42.32	92.32	6.35	696.34
BHA-4551-HNIPU	47.50	97.50	8.56	925.33

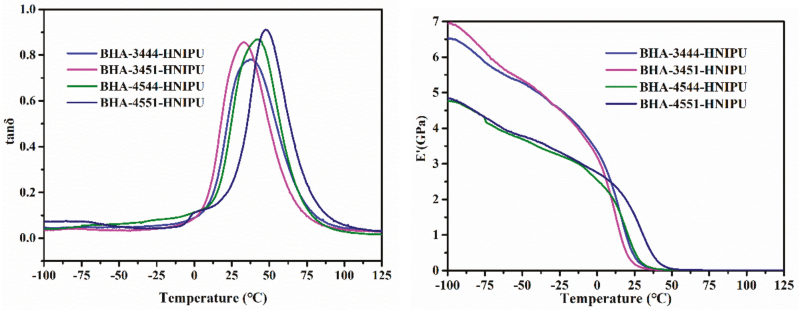

Figure 11. tanδ and E′ of HNIPUs.

The Figure 12 showed surface morphology of the four HNIPUs. It was evident that the materials had a layer structure in Figure 12 of BHA-3444-HNIPU, BHA-3451-HNIPU and BHA-4544-HNIPU. In contrast, BHA-4551-HNIPU had a more continuous surface, and the others had an obviously stratified structure, which confirmed that BHA-4551-HNIPU had a better rigidity than the other HNIPUs. This result was consistent with the DMA test. Moreover, this could make it possible for this material to be applied in coating.

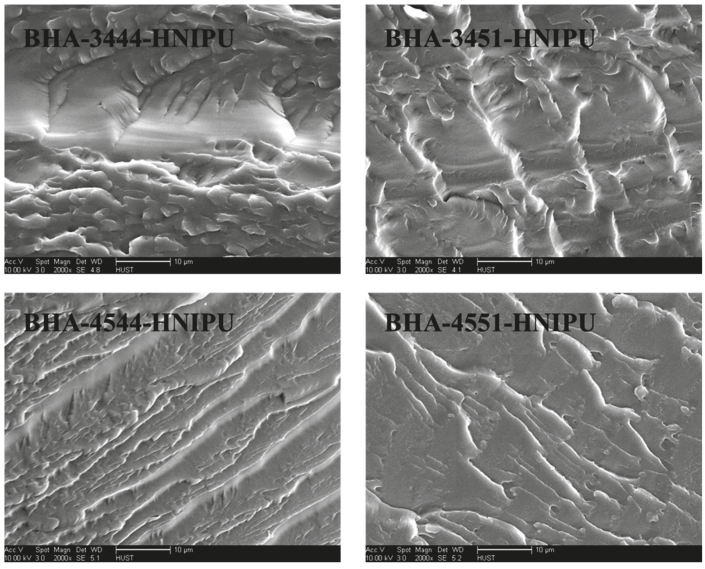

Figure 12. SEM images of HNIPUs.

In order to understand the crystallization behavior of the HNIPUs, XRD analysis was necessarily investigated. As seen in Figure 13, there were no prominent diffraction peaks, and this result indicates that BHA-4544-HNIPU and BHA-4551-HNIPU were structurally amorphous. However, BHA-3444-HNIPU and BHA-3451-HNIPU might form crystallization, which could be explained by the lower secondary amine content and lower crosslinking degree. Therefore, the crystallization behavior of HNIPUs could be tailored based on the secondary content.

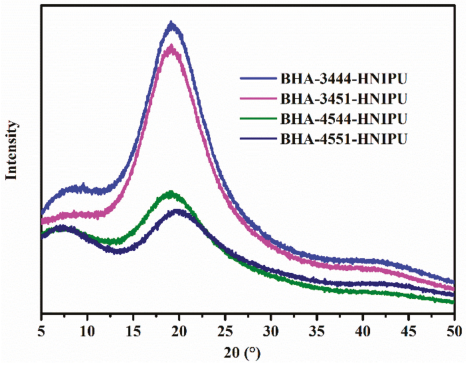

Figure 13. XRD pattern of HNIPUs.

AFM was an appropriate morphological surface characterization method for studying the nanophase separation of HNIPUs. As shown in Figure 14 of BHA-3444-HNIPU, BHA-3451-HNIPU and BHA-4544-HNIPU, the two phases (the bright domain represents the soft segment and the dark domain represents the hard segment) were apparently heterogeneous, especially for BHA-3444-HNIPU and BHA-4544-HNIPU; in other words, the E-44 had a larger impact on nanophase separation than E-51. Furthermore, amine type played a less important role than epoxy value because it could only determine the hard segment, and BHA-4551-HNIPU naturally had the best microphase separation

(seen in Figure 14 of BHA-4551-HNIPU). For this reason, BHA-4551-HNIPU showed wonderful thermodynamic properties as a result of the TGA and DMA shown.

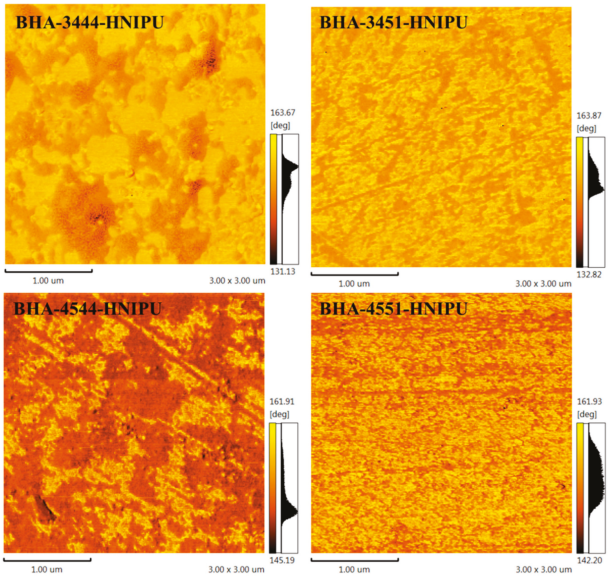

Figure 14. Surface morphology of HNIPUs characterized by AFM phase imaging.

The water absorption of HNIPUs was studied for water tolerance in Figure 15. After 125 h, water absorption of the materials began to stabilize. Theoretically, the higher crosslinking degree could lead to worse water absorption [47], but BHA-3451-HNIPU had the worst water absorption of all HNIPUs. By contrast, E51 could bring a higher epoxy value than E44 and made a higher crosslinking degree. This did lead to a worse water absorption. However, a higher secondary amine could make the HNIPU reserve more water via a hydrogen bond. This hydrogen bond could have a more important role in water absorption than the influence of the epoxy value, so the result showed that BHA-3451-HNIPU had the best water tolerance among all HNIPUs.

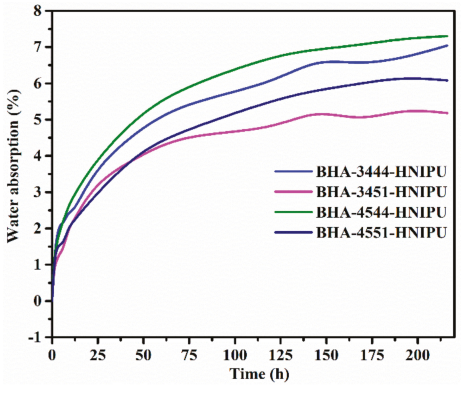

Figure 15. Water absorption of HNIPUs.

Swelling was also an instruction of the crosslinking degree for HNIPUs. In this study, DMSO was chosen as a solvent, which cannot dissolve these polymers and just makes them swell. As Figure 16

shows, BHA-4551-HNIPU had the greatest swelling in these four HNIPUs, which indicates that it has the highest crosslinking degree. Meanwhile, the epoxy value was a more critical influence than the secondary amine content on swelling. In other words, the epoxy value had a noticeable impact on crosslinking degree instead of secondary amine content. The greatest swelling of the HNIPUs was less than 70%, which suggests that its environmental stabilities might be reasonably good.

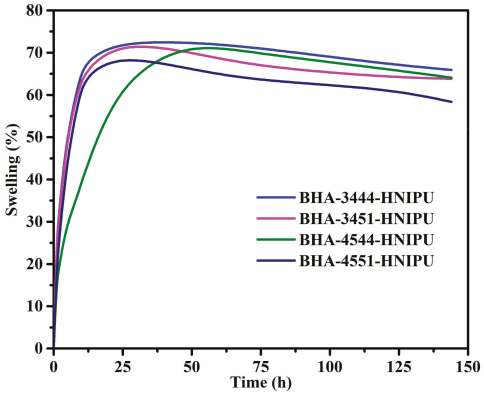

Figure 16. Swelling of HNIPUs.

4. Conclusions

In this study, four BHAs were synthesized as reactants for an NIPU-prepolymer. Then, epoxy resin was selected as the crosslinking agent of NIPU via an environment friendly approach. Accordingly, with crosslinking with epoxy groups, the properties of HNIPUs had been greatly improved on T_g and thermal stability. A series of tests had confirmed the correct chemical constructions of the synthesized products and diverse properties of those samples. Among them, BHA-4551-HNIPU had the highest crosslinking degree in all synthesized HNIPUs, which led to the highest thermal stability with mutually confirmed characterization via TGA, DMA, SEM, and AFM. According to these results, this HNIPU possesses the application potential of heat resistant coatings. Moreover, it was found that the regularity of the crosslinking degree, epoxy value, and secondary amine: epoxy value played a more important role for crosslinking degree than secondary amine content. Meanwhile, it provided an ingenious method to synthesize HNIPU via renewable materials for the polyurethane industry.

Supplementary Materials: The following are available online at http://www.mdpi.com/2073-4360/11/6/1026/s1, Figure S1: FTMS spectrum of BHA-2, Figure S2: FTMS spectrum of BHA-23, Figure S3: FTMS spectrum of BHA-34, and Figure S4: FTMS spectrum of BHA-45

Author Contributions: X.H. and Y.Y. conceived and designed the experiments; X.H. performed the experiments; X.H. and X.X. analyzed the data; X.X., Q.W. and G.B. assisted in part of the experiments and testing. X.H. wrote the paper. X.H. and Y.Y. contributed to the revision and proofreading of the manuscript.

Funding: This study was financially supported by the National Natural Science Foundation of China (Nos: 31070089, 31170078 and J1103514), the National High Technology Research and Development Program of China (Nos: 2011AA02A204, 2013AA065805), the National Natural Science Foundation of Hubei Province (grant Nos: 2015CFA085) and the Fundamental Research Funds for HUST (Nos: 2014NY007, 2017KFXKJC010, 2017KFTSZZ001).

Acknowledgments: This study was financially supported by the National Natural Science Foundation of China (Nos: 31070089, 31170078 and J1103514), the National High Technology Research and Development Program of China (Nos: 2011AA02A204, 2013AA065805), the National Natural Science Foundation of Hubei Province (grant Nos: 2015CFA085) and the Fundamental Research Funds for HUST (Nos: 2014NY007, 2017KFXKJC010, 2017KFTSZZ001). The authors would like to acknowledge the Analytical and Testing Center of HUST for their valuable assistance in FTIR, DSC, TGA and DMA measurements.

Conflicts of Interest: The authors declare no conflict of interest.

References

1. Wu, Z.; Cai, W.; Chen, R.; Qu, J. Synthesis and properties of ambient-curable non-isocyanate polyurethanes. *Prog. Org. Coat.* **2018**, *119*, 116–122. [CrossRef]
2. Cornille, A.; Auvergne, R.; Figovsky, O.; Boutevin, B.; Caillol, S. A perspective approach to sustainable routes for non-isocyanate polyurethanes. *Eur. Polym. J.* **2017**, *87*, 535–552. [CrossRef]
3. Wang, Z.; Zhang, X.; Zhang, L.; Tan, T.; Fong, H. Nonisocyanate Biobased Poly(ester urethanes) with Tunable Properties Synthesized via an Environment-Friendly Route. *ACS Sustain. Chem. Eng.* **2016**, *4*, 2762–2770. [CrossRef]
4. Li, Y.; Li, S.; Zhao, J.; Zhang, Z.; Zhang, J.; Yang, W. Synthesis and characterization of crystallizable aliphatic thermoplastic poly(ester urethane) elastomers through a non-isocyanate route. *Chin. J. Polym. Sci.* **2016**, *34*, 1220–1233. [CrossRef]
5. Jing, Q.; Liu, Q.; Li, L.; Dong, Z.; Silberschmidt, V.V. Effect of graphene-oxide enhancement on large-deflection bending performance of thermoplastic polyurethane elastomer. *Compos. Part B Eng.* **2016**, *89*, 1–8. [CrossRef]
6. Mazari, F.; Chotebor, M.; Naeem, J.; Mazari, A.; Havelka, A. Effect of Perforated Polyurethane Foam on Moisture Permeability for Car Seat Comfort. *Fibres Text. East. Eur.* **2016**, *24*, 165–169. [CrossRef]
7. Kathalewar, M.S.; Joshi, P.B.; Sabnis, A.S.; Malshe, V.C. Non-isocyanate polyurethanes: From chemistry to applications. *RSC Adv.* **2013**, *3*, 4110–4129. [CrossRef]
8. Hamaviriyapornwattana, N.; Sombatsompop, N.; Markpin, T.; Kositchaiyong, A.; Wimolmala, E. Solar reflectance, surface adhesion, and thermal conductivity of wood/natural rubber composite sheet with Tio2/polyurethane topcoat for roofing applications. *J. Vinyl Addit. Technol.* **2012**, *18*, 184–191. [CrossRef]
9. Guan, J.; Song, Y.; Lin, Y.; Yin, X.; Zuo, M.; Zhao, Y.; Tao, X.; Zheng, Q. Progress in Study of Non-Isocyanate Polyurethane. *Ind. Eng. Chem. Res.* **2011**, *50*, 6517–6527. [CrossRef]
10. Ubaghs, L.; Fricke, N.; Keul, H.; Hocker, H. Polyurethanes with pendant hydroxyl groups: Synthesis and characterization. *Macromol. Rapid Comm.* **2004**, *25*, 517–521. [CrossRef]
11. Nohra, B.; Candy, L.; Blanco, J.; Guerin, C.; Raoul, Y.; Mouloungui, Z. From Petrochemical Polyurethanes to Biobased Polyhydroxyurethanes. *Macromolecules* **2013**, *46*, 3771–3792. [CrossRef]
12. Karol, M.H.; Kramarik, J.A. Phenyl isocyanate is a potent chemical sensitizer. *Toxicol. Lett.* **1996**, *89*, 139–146. [CrossRef]
13. Wunschik, D.S.; Ingenbosch, K.N.; Zähres, M.; Horst, J.; Mayer, C.; Jäger, M.; Strehmel, V.; Dornbusch, M.; Hoffmann-Jacobsen, K. Biocatalytic and solvent-free synthesis of a bio-based biscyclocarbonate. *Green Chem.* **2018**, *20*, 4738–4745. [CrossRef]
14. Zhang, K.; Nelson, A.M.; Talley, S.J.; Chen, M.; Margaretta, E.; Hudson, A.G.; Moore, R.B.; Long, T.E. Non-isocyanate poly(amide-hydroxyurethane)s from sustainable resources. *Green Chem.* **2016**, *18*, 4667–4681. [CrossRef]
15. Furtwengler, P.; Avérous, L. Renewable polyols for advanced polyurethane foams from diverse biomass resources. *Polym. Chem.-UK.* **2018**, *9*, 4258–4287. [CrossRef]
16. Noreen, A.; Zia, K.M.; Zuber, M.; Tabasum, S.; Zahoor, A.F. Bio-based polyurethane: An efficient and environment friendly coating systems: A review. *Prog. Org. Coat.* **2016**, *91*, 25–32. [CrossRef]
17. Kong, X.; Liu, G.; Qi, H.; Curtis, J.M. Preparation and characterization of high-solid polyurethane coating systems based on vegetable oil derived polyols. *Prog. Org. Coat.* **2013**, *76*, 1151–1160. [CrossRef]
18. Wu, G.; He, X.; Yan, Y. Lipase-catalyzed modification of natural Sapium sebiferum oil-based polyol for synthesis of polyurethane with improved properties. *RSC Adv.* **2017**, *7*, 1504–1512. [CrossRef]
19. Campanella, A.; Bonnaillie, L.M.; Wool, R.P. Polyurethane foams from soyoil-based polyols. *J. Appl. Polym. Sci.* **2009**, *112*, 2567–2578. [CrossRef]
20. Kirpluks, M.; Kalnbunde, D.; Benes, H.; Cabulis, U. Natural oil based highly functional polyols as feedstock for rigid polyurethane foam thermal insulation. *Ind. Crop. Prod.* **2018**, *122*, 627–636. [CrossRef]
21. Vanags, E.; Kirpluks, M.; Cabulis, U.; Walterova, Z. Highly functional polyol synthesis from epoxidized tall oil fatty acids. *J. Renew. Mater.* **2018**, *6*, 764–771. [CrossRef]
22. Chaudhari, A.; Kulkarni, R.; Mahulikar, P.; Sohn, D.; Gite, V. Development of PU coatings from neem oil based alkyds prepared by the monoglyceride route. *J. Am. Oil Chem. Soc.* **2015**, *92*, 733–741. [CrossRef]
23. Rajput, S.D.; Mahulikar, P.P.; Gite, V.V. Biobased dimer fatty acid containing two pack polyurethane for wood finished coatings. *Prog. Org. Coat.* **2014**, *77*, 38–46. [CrossRef]

24. Li, Y.; Noordover, B.A.J.; van Benthem, R.A.T.M.; Koning, C.E. Chain extension of dimer fatty acid- and sugar-based polyurethanes in aqueous dispersions. *Eur. Polym. J.* **2014**, *52*, 12–22. [CrossRef]
25. Yao, X.; Wu, G.; Xu, L.; Zhang, H.; Yan, Y. Enzyme-catalyzed preparation of dimeric acid polyester polyol from biodiesel and its further use in the synthesis of polyurethane. *RSC Adv.* **2014**, *4*, 31062–31070. [CrossRef]
26. Yu, A.Z.; Setien, R.A.; Sahouani, J.M.; Docken, J.; Webster, D.C. Catalyzed non-isocyanate polyurethane (NIPU) coatings from bio-based poly(cyclic carbonates). *J. Coat. Technol. Res.* **2019**, *16*, 41–57. [CrossRef]
27. Blattmann, H.; Lauth, M.; Mülhaupt, R. Flexible and bio-based nonisocyanate polyurethane (nipu) foams. *Macromol. Mater. Eng.* **2016**, *301*, 944–952. [CrossRef]
28. Haniffa, M.A.C.M.; Ching, Y.C.; Chuah, C.H.; Kuan, Y.C.; Liu, D.; Liou, N. Synthesis, characterization and the solvent effects on interfacial phenomena of jatropha curcas oil based non-isocyanate polyurethane. *Polymers-Basel.* **2017**, *9*, 162. [CrossRef]
29. Bähr, M.; Bitto, A.; Mülhaupt, R. Cyclic limonene dicarbonate as a new monomer for non-isocyanate oligo- and polyurethanes (NIPU) based upon terpenes. *Green Chem.* **2012**, *14*, 1447–1454. [CrossRef]
30. Fache, M.; Darroman, E.; Besse, V.; Auvergne, R.; Caillol, S.; Boutevin, B. Vanillin, a promising biobased building-block for monomer synthesis. *Green Chem.* **2014**, *16*, 1987–1998. [CrossRef]
31. Bhr, M.; Mlhaupt, R. Linseed and soybean oil-based polyurethanes prepared via the non-isocyanate route and catalytic carbon dioxide conversion. *Green Chem.* **2012**, *14*, 483–489. [CrossRef]
32. Rokicki, G.; Piotrowska, A. A new route to polyurethanes from ethylene carbonate, diamines and diols. *Polymer* **2002**, *43*, 2927–2935. [CrossRef]
33. Chattopadhyay, D.K.; Webster, D.C. Thermal stability and flame retardancy of polyurethanes. *Prog. Polym. Sci.* **2009**, *34*, 1068–1133. [CrossRef]
34. Poussard, L.; Mariage, J.; Grignard, B.; Detrembleur, C.; Jérôme, C.; Calberg, C.; Heinrichs, B.; De Winter, J.; Gerbaux, P.; Raquez, J.M.; et al. Non-isocyanate polyurethanes from carbonated soybean oil using monomeric or oligomeric diamines to achieve thermosets or thermoplastics. *Macromolecules* **2016**, *49*, 2162–2171. [CrossRef]
35. Carré, C.; Bonnet, L.; Avérous, L. Solvent- and catalyst-free synthesis of fully biobased nonisocyanate polyurethanes with different macromolecular architectures. *RSC Adv.* **2015**, *5*, 100390–100400. [CrossRef]
36. North, M.; Pasquale, R.; Young, C. Synthesis of cyclic carbonates from epoxides and CO_2. *Green Chem.* **2010**, *12*, 1514–1539. [CrossRef]
37. Sakakura, T.; Kohno, K. The synthesis of organic carbonates from carbon dioxide. *Chem. Commun.* **2009**, 1312–1330. [CrossRef]
38. Xia, H.; Song, M. Preparation and characterization of polyurethane—carbon nanotube composites. *Soft Matter.* **2005**, *1*, 386–394. [CrossRef]
39. Beniah, G.; Uno, B.E.; Lan, T.; Jeon, J.; Heath, W.H.; Scheidt, K.A.; Torkelson, J.M. Tuning nanophase separation behavior in segmented polyhydroxyurethane via judicious choice of soft segment. *Polymer* **2017**, *110*, 218–227. [CrossRef]
40. Asemani, H.; Zareanshahraki, F.; Mannari, V. Design of hybrid nonisocyanate polyurethane coatings for advanced ambient temperature curing applications. *J. Appl. Polym. Sci.* **2019**, *136*, 47266. [CrossRef]
41. Mó, O.; Yáñez, M.; Eckert-Maksić, M.; Maksić, Z.B.; Alkorta, I.; Elguero, J. Periodic Trends in Bond Dissociation Energies. A Theoretical Study. *J. Phys. Chem. A.* **2005**, *109*, 4359–4365. [CrossRef] [PubMed]
42. Ke, J.; Li, X.; Jiang, S.; Liang, C.; Wang, J.; Kang, M.; Li, Q.; Zhao, Y. Promising approaches to improve the performances of hybrid non-isocyanate polyurethane. *Polym. Int.* **2018**, *68*, 651–660. [CrossRef]
43. Jin, K.; Leitsch, E.K.; Chen, X.; Heath, W.H.; Torkelson, J.M. Segmented Thermoplastic Polymers Synthesized by Thiol-Ene Click Chemistry: Examples of Thiol–Norbornene and Thiol—Maleimide Click Reactions. *Macromolecules* **2018**, *51*, 3620–3631. [CrossRef]
44. Aoyagi, N.; Furusho, Y.; Endo, T. Convenient synthesis of cyclic carbonates from CO_2 and epoxides by simple secondary and primary ammonium iodides as metal-free catalysts under mild conditions and its application to synthesis of polymer bearing cyclic carbonate moiety. *J. Polym. Sci. Pol. Chem.* **2013**, *51*, 1230. [CrossRef]
45. Cornille, A.; Michaud, G.; Simon, F.; Fouquay, S.; Auvergne, R.; Boutevin, B.; Caillol, S. Promising mechanical and adhesive properties of isocyanate-free poly(hydroxyurethane). *Eur. Polym. J.* **2016**, *84*, 404–420. [CrossRef]

46. Karami, Z.; Zohuriaan-Mehr, M.J.; Rostami, A. Bio-based thermo-healable non-isocyanate polyurethane DA network in comparison with its epoxy counterpart. *J. CO_2 Utilization* **2017**, *18*, 294–302. [CrossRef]
47. Lee, J.H.; Ju, Y.M.; Kim, D.M. Platelet adhesion onto segmented polyurethane film surfaces modfied by addition and crosslinking of PEO-containing block copolymers. *Biomaterials* **2000**, *21*, 683–691. [CrossRef]

polymers

MDPI

Article

Preparation and Characterization of Low-Molecular-Weight Natural Rubber Latex via Photodegradation Catalyzed by Nano TiO_2

Suhawati Ibrahim [1,2], Nadras Othman [1,*], Srimala Sreekantan [1], Kim Song Tan [2], Zairossani Mohd Nor [2] and Hanafi Ismail [1]

[1] School of Materials and Mineral Resources Engineering, Universiti Sains Malaysia, Engineering Campus, Nibong Tebal 14300, Penang, Malaysia; suhawati@lgm.gov.my (S.I.); srimala@usm.my (S.S.); ihanafi@usm.my (H.I.)

[2] Technology and Engineering Division, Malaysian Rubber Board, Sungai Buloh 47000, Selangor, Malaysia; kstan@lgm.gov.my (K.S.T.); zairossani@lgm.gov.my (Z.M.N.)

* Correspondence: srnadras@usm.my; Tel.: +60-4-5996-177

Received: 14 September 2018; Accepted: 31 October 2018; Published: 1 November 2018

Abstract: Natural rubber is one of the most important renewable biopolymers used in many applications due to its special properties that cannot be easily mimicked by synthetic polymers. To sustain the existence of natural rubber in industries, modifications have been made to its chemical structure from time to time in order to obtain new properties and to enable it to be employed in new applications. The chemical structure of natural rubber can be modified by exposure to ultraviolet light to reduce its molecular weight. Under controlled conditions, the natural rubber chains will be broken by photodegradation to yield low-molecular-weight natural rubber. The aim of this work was to obtain what is known as liquid natural rubber via photodegradation, with titanium dioxide nanocrystals as the catalyst. Titanium dioxide, which was firstly synthesized using the sol–gel method, was confirmed to be in the form of an anatase, with a size of about 10 nm. In this work, the photodegradation was carried out in latex state and yielded low-molecular-weight natural rubber latex of less than 10,000 g/mol. The presence of hydroxyl and carbonyl groups on the liquid natural rubber (LNR) chains was observed, resulting from the breaking of the chains. Scanning electron microscopy of the NR latex particles showed that titanium dioxide nanocrystals were embedded on the latex surface, but then detached during the degradation reaction.

Keywords: photodegradation; liquid natural rubber; UV light; TiO_2 anatase; latex state

1. Introduction

Natural rubber (NR), tapped from the *Hevea brasiliensis* tree, is the biggest bio-based polymer source at present [1]. Several million tons of NR are produced commercially each year as it is an important material in the production of tyres, gloves, liners, tubes, etc. NR currently ranks as the fourth most important natural resource after air, water, and petroleum [2]. As NR is a renewable resource, its applications should not be limited to common products, but can be diversified through modifications to the NR chains to produce new rubbers with new properties. The molecular structure of NR consists of a double bond in its repeating units of *cis*-1,4-isoprene, which can be modified with regard to specific functional groups such as epoxidized natural rubber (ENR) [3], acrylated NR [4], carbonyl telechelic natural rubber (CTNR) [5], and hydroxyl telechelic liquid natural rubber (HTNR) [6,7].

As a natural product, NR has a very high molecular weight, which has always been a hurdle during mixing. An intensive shearing process is needed to break down the molecular weight to a state wherein it is easier for the material to be blended with additives, shaped, and then vulcanized.

Apparently, reducing the molecular weight of NR to obtain what is known as liquid natural rubber (LNR) has solved the mixing problem during compounding. LNR commonly has a molecular weight of less than 20,000 g/mol and is considered as a new material derived from NR. Furthermore, the degradation process also opens up the opportunity to use LNR in various applications such as in binders [8], adhesives [9], coatings [10], processing aids [11,12], compatibilizers [13], and encapsulation of paraffin wax [14], as well as precursors for new materials [15,16] and further modifications [17]. Consequently, reducing the molecular weight has extended the potential and possible applications of NR. Indeed, this old material can change the perception of its conventional use and open up new areas of applications, especially to challenge the properties of synthetic rubber [18]. Therefore, LNR is important for the sustainability of the NR industry, especially in expanding its potential to new areas of applications and new advanced materials. Currently, LNR can be produced by the mechanical, chemical, photochemical, sonication, or thermal degradation of NR, either in a dry, solution, or latex state.

In the photodegradation of NR, TiO_2 has been determined to be an excellent catalyst in the presence of hydrogen peroxide to effectively oxidize the NR chain and scissor via the radical activity of the oxygen–oxygen single bond [19,20]. Hence, it has been shown that the LNR chain has formed hydroxyl and carbonyl groups at its extremities. LNR with a hydroxyl end group becomes attractive when its application can be expanded into new areas such as precursor specialty block polymerization [21,22], high-performance adhesives [9,23], and binders [8]. LNR has the same repeating unit (*cis*-1,4-isoprene) as virgin NR; consequently, they exhibit similar excellent characteristics such as flexibility, elasticity, low temperature, etc.

Due to the increasing demand for a green and environmentally friendly process, the optimization of parameters and conditions for the photodegradation of NR in the latex state is being intensively explored [19,24,25]. Hence, the method of photodegradation developed by Ravindran [20] was duplicated and adopted for implementation in the latex state. Sakdapipanich et al. (2001) exposed NR latex to UV light in the presence of hydrogen peroxide, but no significant degradation was reported. This may have been due to the difficulty for the reagents and UV light to penetrate the membrane of the rubber particles [24]. In a recent work, when NR latex in the presence of hydrogen peroxide was exposed to UV light at an elevated temperature, significant degradation occurred wherein the molecular weight of the NR was reduced [25,26]. The use of TiO_2 as a photocatalyst in the degradation of NR latex was also studied. TiO_2 was assembled as a nanomatrix film to degrade NR latex under UV light in the presence of hydrogen peroxide, and it was reported to have yielded low-molecular-weight NR [19]. Even though the use of assembled nanomatrix TiO_2 films yields a clean LNR, it has a limitation in that it is difficult to maximize the exposure of the film to UV light for optimum absorption and reaction. This problem can be overcome by adding TiO_2 nanocrystals into the bulk latex, but the TiO_2 would remain in the latex solution after the reaction has been completed. However, the remaining TiO_2 nanocrystals in the LNR after the reaction can be useful either as a filler or catalyst for other advanced chemical reactions. TiO_2 is well known as a good inorganic filler as it is chemically stable and biologically benign. The presence of TiO_2 in NR has been found to increase the rate of stress relaxation [27], thermal conductivity, thermal diffusivity [28], UV protection [29], and antimicrobial activities [30] of the NR compound, in addition to its conventional role as an inorganic pigment in rubber products.

In this present work, the synergistic effect of the photodegradation of NR latex under UV light in the presence of hydrogen peroxide and TiO_2 as a photocatalyst was investigated. TiO_2 nanocrystals used in this study were prepared via the sol–gel method, and the effect of an acid catalyst and annealing temperature on the size and structure of the TiO_2 was investigated. The anatase form of TiO_2 was chosen as the photocatalyst in the degradation of NR latex. The reaction was carried out under a controlled temperature to obtain a degraded NR, which was then characterized for its structure and properties. The molecular weights of the NR and LNR were determined by means of gel permeation

chromatography (GPC), whilst the molecular structure was determined using Fourier transform infrared (FTIR) spectroscopy and nuclear magnetic resonance (NMR) spectroscopy.

2. Materials and Methods

2.1. Materials

Titanium (IV) isopropoxide (TTIP), nitric acid (HNO_3), and isopropanol were purchased from Sigma Aldrich (Saint Louis, MO, USA), and all these reagents were used without further purification.

The low-ammonia natural rubber latex (LATZ) used in this work was purchased from Lee Rubber Sdn Bhd (Selangor, Malaysia). Analytical-grade hydrogen peroxide was purchased from Merck (M) Sdn Bhd (Kenilworth, NJ, USA). Methanol, sodium dodecyl sulphate (SDS), and toluene were purchased from Fluka (Loughborough, UK). All the materials were used as received.

2.2. Preparation of TiO_2 via Sol–Gel Method

Solutions of TTIP in isopropanol (solution A) and water in isopropanol (solution B) were prepared. Under vigorous stirring, solution A was added dropwise into solution B. The molar ratio of water/TTIP was fixed at 115, and the pH of solution B was varied from 1 to 7 using HNO_3. The sol obtained was washed thrice and dried overnight in an oven at 60 °C. The TiO_2 was then ground in a mortar and was calcined in a furnace at temperatures between 300 to 700 °C for 2 h.

2.3. Photodegradation of NR Latex

LATZ latex was mixed with 2 phr of SDS, and the required amount of TiO_2. Water was then added to obtain a dry rubber content (DRC) of 10%. The solution was then poured into a reaction flask and was heated to 65 °C before hydrogen peroxide was dropped into the solution. The parameters and temperature used were similar to those used in our previous work [25]. Next, the solution was left under a 30 watt UV light (365 nm) for 48 h. The degraded latex was then coagulated using methanol and washed a few times with water, after which it was dried in a vacuum oven. The purification of the sample was carried out by dissolving the yield in toluene and re-precipitating it in methanol, followed by drying in a vacuum oven until a constant weight was achieved.

2.4. Characterizations

X-ray diffraction (XRD) was used to study the crystallization of TiO_2. The measurement was performed using a Bruker D8 Advance diffractometer (Karlsruhe, Germany) operating in the reflection mode with Cu Kα radiation (35 kV, 30 mA) and a diffracted beam monochromator using a step scan mode with a step of 0.075° (2θ) at 4 s per step. The diffraction patterns of both the anatase and rutile TiO_2 powders were compared with reference to the Join Committee on Powder Diffraction Standards (JCPDS) database.

Transmission electron microscopy (TEM, FEI, Eindhoven, The Netherlands) was used to study the morphology of TiO_2. A sample of the diluted latex containing TiO_2 nanocrystals was first sonicated in an ultrasound bath for 1 h, followed by immediate transfer to a copper grid using a pipette. The copper grid was allowed to dry completely at ambient temperature before being inserted into the TEM, an FEI Tecnai G20. The TEM images were taken at 200 kV at various magnifications. High-resolution TEM (HRTEM) images for the nano TiO_2 where fringes of the crystal could be clearly observed were also recorded using the same instrument. For the LNR, the sample was diluted with toluene, drop cast onto a copper grid, and allowed to dry under ambient temperature before being inserted into the transmission electron microscope.

Viscotek multi-detector gel permeation chromatography (GPC, Malvern, UK) was used to measure the weight-average molecular weight (Mw) and the number-average molecular weight (Mn) of the prepared LNR samples. The measurements were carried out at 30 °C using tetrahydrofuran (THF) as the mobile phase and polyisoprene as the internal standard.

Crosslinking of the sample was studied in terms of the mean gel content. The gel content was determined by dissolving about 2 g of the sample (m_0) in 100 mL of toluene and keeping it for one week in a dark place. The gel fraction was then filtered and dried (m_1) in an oven at 60 °C for 24 h. The percentage ratio of gel and the original sample was estimated to be the gel content, as shown in Equation (1).

$$\text{Gel content } (\%) = \frac{\text{Weight of dried gel}(m_1)}{\text{Weight of sample } (m_0)} \times 100 \quad (1)$$

A Fourier transform infrared (FTIR) spectroscopy analysis was done using a Thermo Nicolet 6700 FTIR spectrometer (Waltham, MA, USA), and the Diamond Attenuated Total Reflectance (DATR) technique was used for the analysis. The sample was analyzed in the transmittance mode within the range of 4000–600 cm^{-1} at a resolution of 4 cm^{-1} and 64 scans per sample.

The ^{1}H and ^{13}C NMR spectra were recorded for a sample that was dissolved in deuterated chloroform and was analyzed using a Bruker 500 spectrometer (Billerica, MA, USA) with TMS as the internal standard at room temperature. The ^{1}H NMR spectrum was measured with 1024 scans at a frequency of 500 MHz, while the ^{13}C spectrum was measured with 16,384 scans at a frequency of 125 MHz and spinning rate of 20 Hz.

The morphology of the natural rubber latex surface was taken on a JOEL FE-SEM JSM 6701F (Tokyo, Japan) that was operated at 2.0 kV. Prior to the observation, the sample was placed onto a specimen stub and was sputter-coated with an ultra-thin layer of platinum, which was approximately 100 Å thick, to reduce charging.

3. Results and Discussion

3.1. Preparation and Characterization of TiO_2 Nanocrystals

TiO_2 synthesized via the sol–gel method will undergo two simultaneous reactions (hydrolysis and condensation) when organometallic precursors react with water. These two reactions are sensitive to many experimental parameters such as raw material concentration, pH, hydrolysis temperature, mixing conditions, annealing time, and annealing temperature [31,32].

3.1.1. Effect of pH

Figure 1 shows the XRD patterns of the TiO_2 powders prepared at pH 1 to 7 and subsequently annealed at 500 °C for 2 h. The samples that were prepared at pH 3, 5, and 7 exhibit peaks at 2θ of 25°, 30°, 37°, 47°, 53°, 55°, and 62°, corresponding to the (101), (121), (004), (200), (105), (211), and (204) planes of the TiO_2 anatase phase. However, for the sample prepared at pH 1, the anatase peaks appeared together with small peaks at 2θ of 27°, 36°, and 56°, indicating the presence of a rutile phase. Nevertheless, these results contradict the results reported by Nolan et al. [33], where it was claimed that reducing the acidity of the sol had resulted in a lowering of the anatase to a rutile transformation temperature. However, this contradiction may be due to differences in the preparation procedures and materials used.

Apparently, the crystallization of TiO_2 is affected by parameters of the treatment process such as the annealing and the atmosphere of the reaction [34,35]. Furthermore, parameters such as the pH of the media, the solvent, precursor concentration, annealing temperature, and annealing time will influence the properties of the TiO_2 obtained. Consequently, the presence of an acid as a hydrolysis catalyst influences both the condensation rate and the structure of the TiO_2 [36].

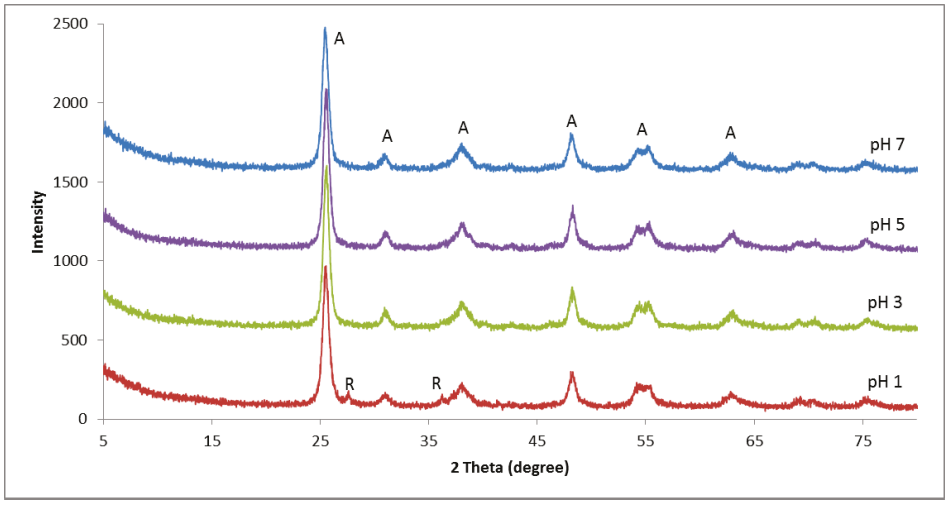

Figure 1. XRD patterns of TiO_2 prepared at various pH, where A and R denote the XRD peaks assigned to the anatase and rutile phases of TiO_2, respectively.

In a sol–gel synthesis, two simultaneous reactions (hydrolysis and condensation) take place when titanium alkoxides are hydrolyzed and subsequently polymerized to form a three-dimensional oxide network, represented schematically as follows:

$$Ti(OR)_4 + 4H_2O \rightarrow Ti(OH)_4 + 4ROH \text{ (hydrolysis)} \quad (2)$$

$$Ti(OH)_4 \rightarrow TiO_2 \cdot nH_2O + (2 - n)H_2O \text{ (condensation)} \quad (3)$$

where R is ethyl, i-propyl, n-butyl, etc. [32]. Due to the high acidity of the tetravalent cation, an unstable hydroxide $Ti(OH)_4$ is formed. Oxolation and olation will then proceed simultaneously during nucleation to form an amorphous oxide, $TiO_2.nH_2O$. The presence of the H^+ ion will catalyze the hydrolysis by protonating the hydroxide group, which then prevents agglomeration from occurring to cause the formation of gel. Generally, inorganic acids such as HCl, HNO_3, and H_2SO_4 are used as acid catalysts. Thus, a low (acidic) pH promotes the formation of an anatase structure, whilst an amorphous structure is obtained at a high (alkaline) pH [32].

Figure 2 shows the TEM micrographs of the TiO_2 nanocrystals prepared at pH 1, 3, 5, and 7. The average sizes were 10.2, 12.0, 13.9, and 15.7 nm for the TiO_2 synthesized at pH 1, pH 3, pH 5, and pH 7, respectively. The size of the TiO_2 nanocrystals prepared at a lower pH was found to be smaller than those prepared at a higher pH. In an acidic medium, the rate of particle formation is slower compared to in neutral and alkaline media [37], especially when the hydrolysis reaction is catalyzed by the presence of protons through protonation of the leaving group [38,39]. In the meantime, the protonation of the OH group in the Ti cluster inhibited nucleophilic attacks on the other clusters that prevented precipitation and led to gelation [38]. Hence, the TiO_2 particles were reported to be smaller in size compared with the particles in the neutral and alkaline media.

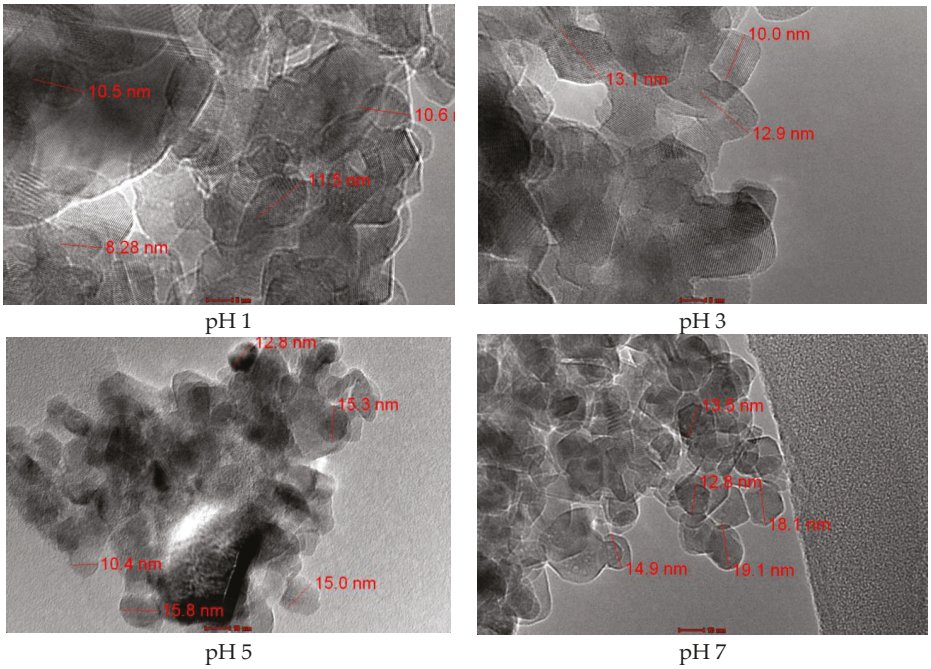

Figure 2. TEM micrographs of TiO_2 nanocrystals prepared by a sol–gel process at pH 1 to 7.

3.1.2. Effect of Annealing Temperature

Figure 3 shows the XRD pattern of the TiO_2 nanocrystals prepared at pH 3 and subsequently annealed at 300 to 700 °C. The TiO_2 nanocrystals annealed at 300, 400, and 500 °C exhibited peaks at 2θ of 25°, 30°, 37°, 47°, 53°, 55°, and 62° corresponding to the (101), (121), (004), (200), (105), (211), and (204) planes of the anatase phase (Figure 3a–c). However, when the annealing temperature was increased to 600 °C, the rutile peaks at 2θ of 27°, 36°, and 56° appeared (Figure 3d). Beyond 700 °C, the anatase phase was completely transformed to the rutile phase (Figure 3e). During the annealing process, the metastable anatase phase was transformed into a thermally stable rutile phase, which was in agreement with another reported work [40].

Among the three polymorphs of TiO_2, the anatase form has been widely used as a popular catalyst due to its various merits, such as optical and electronic properties, high photocatalytic activity, low cost, nontoxicity, and chemical stability [41–43], and it is being widely used in the degradation of organic pollutants [44,45]. Therefore, in this work, the TiO_2 that was prepared in pH 3 and annealed at a temperature of 500 °C for 2 h was used as a catalyst in the photodegradation of NR latex.

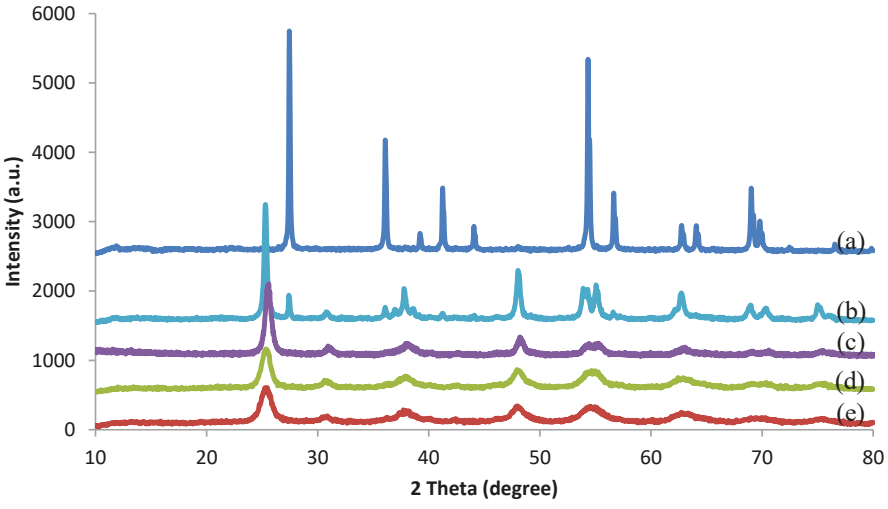

Figure 3. XRD patterns of TiO_2 nanocrystals annealed at various temperatures: (**a**) 700 °C, (**b**) 600 °C, (**c**) 500 °C, (**d**) 400 °C, (**e**) 300 °C.

3.2. Photodegradation of NR Latex

The degradation of NR in the presence of TiO_2 is similar to the decomposition of most other organic materials. The activation of TiO_2 under UV light involves the migration of photon-generated electrons ($e-$) and holes ($h+$) to the surface to serve as redox sources, which then attack the organic material. Furthermore, the use of nano-sized TiO_2 increases the photocatalytic activities toward the latex particles due to higher coalescence with a bigger surface area of TiO_2, by which lower-molecular-weight LNR can be obtained. Among the TiO_2 polymorphs, the anatase structure shows the highest photocatalytic activities possessed by the larger band gap and better surface properties [41].

3.2.1. Effect of TiO_2 Nanocrystals on Photodegradation

Table 1 shows the molecular weights and gel contents of LNRs that were prepared with various amounts of TiO_2 nanocrystals. The molecular weight of NR was found to have been reduced to 18.6×10^3 g/mol after photodegradation without the addition of TiO_2 nanocrystals. In the presence of TiO_2 nanocrystals, the molecular weight was further reduced to 15.8×10^3 and 7.3×10^3 g/mol when 0.4 and 0.8 phr, respectively, of TiO_2 nanocrystals were added. However, when the amount of TiO_2 nanocrystals was increased to more than 0.8 phr, the molecular weight of the LNR was found to increase together with the polydispersity value. The increase was expected due to the presence of a high amount of radical species, which induced side products such as crosslinking and chain reconnecting, as indicated by the increase in the polydispersity and gel content [20,46,47]. This would explain the increase in the gel content and polydispersity of the degraded rubber when the amount of TiO_2 was increased even when the molecular weight decreased. A high amount of TiO_2 nanocrystals would have increased the kinetics of reactions rapidly; hence, more side reactions such as crosslinking and chain connecting occurred. These side reactions would have increased and become uncontrolled due to the simultaneous effect of a high concentration of TiO_2 during exposure to UV light [48].

Table 1. Molecular weights and gel contents of liquid natural rubbers (LNRs) prepared with and without TiO_2.

TiO_2 (phr)	Mn ($\times 10^3$) (g/mol)	Standard Deviation of Mn	Polydispersity	Gel Content (%)	Standard Deviation of Gel Content
NR	549.3	3.20	7.5	19.2	1.69
0	18.6	1.09	5.00	0.09	3.53
0.2	19.1	0.88	3.01	0.24	0.11
0.4	15.8	1.35	3.60	0.49	0.60
0.8	7.3	2.34	8.00	0.57	0.48
1.2	12.7	0.16	6.08	0.69	0.27
1.6	20.1	0.86	5.19	0.93	0.18

3.2.2. FTIR Analysis of LNRs

Figure 4 shows the FTIR spectra of the NR and LNRs that were prepared with various amounts of TiO_2 nanocrystals ranging from 0 to 1.2 phr. Generally, the spectra of the LNRs showed a similar pattern to that of the NR spectrum. However, there was a depletion in the peaks, indicating the breaking of chains, and an increase in some peaks, indicating the presence of terminal groups as a result of the chains breaking.

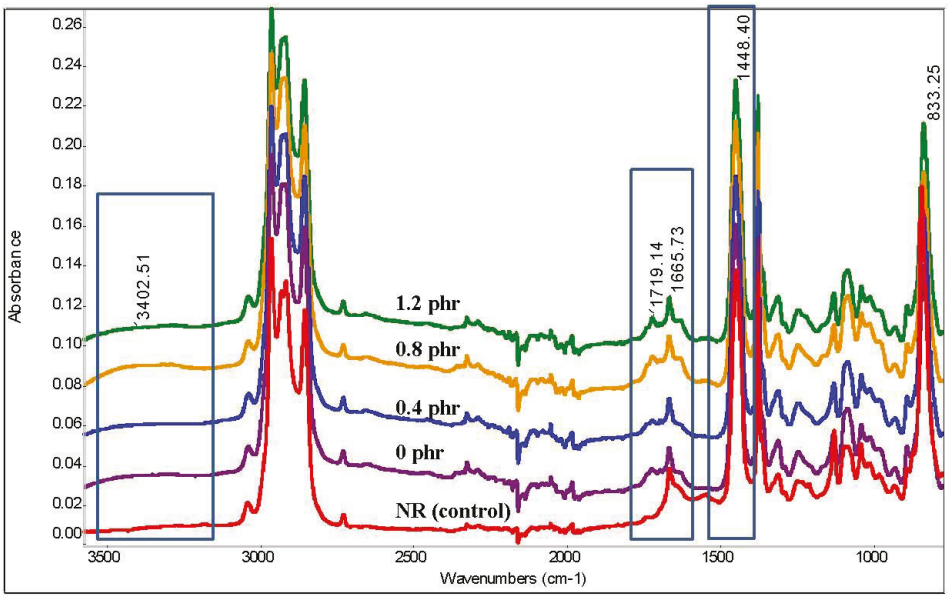

Figure 4. FTIR spectra of NR and LNRs prepared with various amounts of TiO_2.

Table 2 shows the intensity of the IR changes in the respective peaks for the NR and LNRs prepared with and without TiO_2. The calculated values were solely based on the peak areas—as it was difficult to find a reference peak to make a comparison—and the ratio. The peaks at 1660 and 1445 cm^{-1} that correspond to the C=C and C–C bonds are commonly used as a reference, but these have been found to change after degradation. The discussions below refer to the respective peak changes as tabulated in Table 2.

Table 2. Peak areas of IR spectra for NR and LNRs that were prepared with various amount of TiO_2.

Peaks (cm^{-1})	Peak Assignment	Peak Area				
		NR	Amount of TiO_2 (phr)			
			0	0.4	0.8	1.2
3400	C-OH stretching	0.211	0.960	0.694	1.699	0.865
1720	Carbonyl	0.002	0.085	0.056	0.114	0.119
1661	C=C stretching	0.809	0.388	0.325	0.490	0.455
1445	CH_2 bending	3.712	3.446	3.493	3.397	3.455

The peak areas of 1660 and 1445 cm^{-1}, which correspond to the C=C and C–C bonds, decreased after degradation for all the LNR samples. Both groups were expected to be attacked, and hence, the NR chains were broken during degradation. The depletion of the C=C and C–C bonds suggests that both groups were involved in the chain breaking by means of at least two different mechanisms, namely, oxidation at the C=C bond by the oxygen species and the activity of radicals at the C–C bond. Furthermore, both groups were also able to absorb UV light to enter into an excited state, followed by chain breaking [49–51].

The broad peak at 3400 cm^{-1}, which corresponded to the vibrations of the bonded OH group, was increased in the spectra of the LNRs, thereby indicating the presence of OH groups on the LNR chains. Among the samples, the LNR prepared with 0.8 phr of TiO_2 showed the highest peak intensity in this region, thereby indicating the existence of the highest number of OH groups on the LNR chain. A similar pattern was also observed for the weak peak at 1720 cm^{-1} which corresponded to the carbonyl group. As discussed above, this LNR sample showed the lowest molecular weight; hence, a greater number of terminal end groups should have been observed, as indicated in the spectrum. Hydroxyl and carbonyl groups are commonly found in degraded polymers as a result of chain breaking during photodegradation [52,53].

Hydrogen peroxide, on exposure to UV light, decomposes to a hydroxyl radical that is a very reactive species. Its concentration will be higher when this radical is generated in an illumination process, where TiO_2 has been activated after absorbing photons from UV light [54–56], and this relates to the surface area of TiO_2 [43]. This radical is capable of breaking the NR chains by attacking the C–C bond and leaving the hydroxyl as a terminal group [46]. Besides this, hydrogen peroxide is also well known as a strong oxidation agent that is able to oxidize and break the NR chain at the C=C bond, leaving the carbonyl group as a terminal end group [57,58]. At the same time, the C=C bond absorbs UV light to cause photooxidative degradation and break the NR chain, thereby also leaving the carbonyl group as a terminal end group [48]. The presence of nano-sized TiO_2 certainly increases the formation of OH radicals due to a higher surface area.

Figure 5 illustrates the mechanisms that can possibly occur during the degradation of NR under UV light in the presence of TiO_2 as a photocatalyst. The generation of hydroxyl radicals, either from the activities of TiO_2 in an excited state or upon decomposition of hydrogen peroxide under UV light, is depicted in Figure 5a. It is possible that this reactive species attacks the C–C bond of NR, whereby it can easily break up under favorable conditions such as in the presence of free radicals. The protons that are bonded to this alpha carbon ($C_\alpha H_2$–$C_\alpha H_2$) are labile protons due to the *cis* configuration of the isoprenic units. These groups are not in the same plane and provide an unbalanced structure with the pendent methyl groups, resulting in stearic hindrance. In the presence of hydroxyl radicals, the labile protons will be abstracted and inserted into the hydroxyl groups during the chain-breaking process [59,60]. The broken C=C bonds in the NR chains can be oxidized by hydrogen peroxide, which is a strong oxidizing agent, to leave a carbonyl as the end group, as shown in Figure 5b.

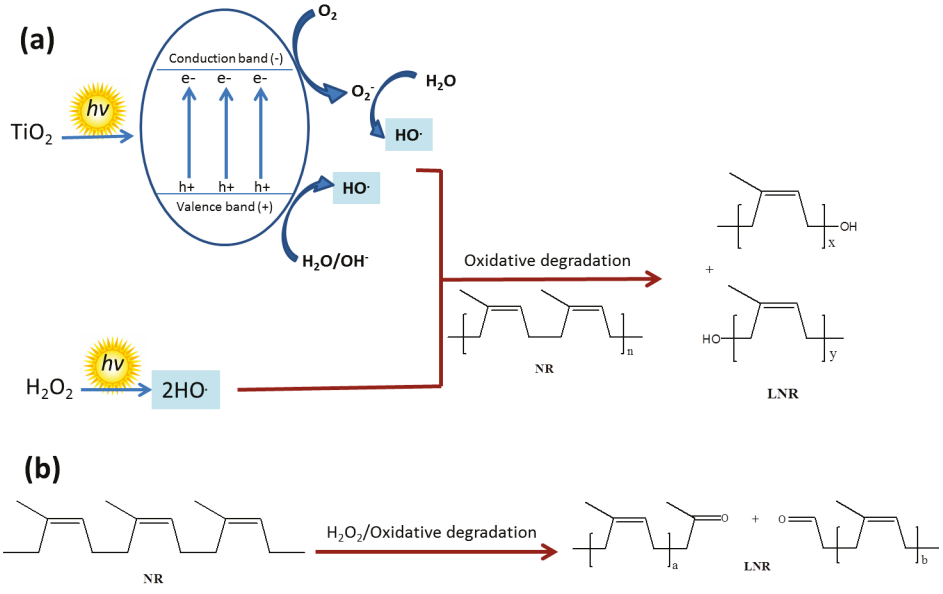

Figure 5. Diagram of oxidative degradation of NR under UV light in the presence of TiO_2 by (**a**) a hydroxyl radical and (**b**) hydrogen peroxide as an oxidizing agent.

3.2.3. NMR Analysis of LNRs

Figure 6 shows the ^{1}H NMR spectrum of LNR which was prepared with 0.8 phr TiO_2 nanocrystals. Typical NR peaks were assigned to the chemical shifts (ppm) 1.68 (–C**H**$_3$), 2.05 (–C**H**$_2$), and 5.13 (=C**H**–) [61]. The small peaks at 3–4 ppm indicated the presence of hydroxyl groups on the LNR chains at different locations. These new small signals at the chemical shifts of 1.28, 3.47, 3.65, and 3.84 ppm could be assigned to methylene protons adjacent to the secondary alcohol, protons of the hydroxyl group, hydroxylated methane protons, and hydroxylated methylene protons, respectively [62,63]. The pattern of this spectrum was similar to that in our previous work for LNR prepared without TiO_2 [26].

The presence of carbonyl groups on the LNR chain was also observed for both aldehyde and ketone groups. The aldehyde group was indicated by the presence of small peaks at the chemical shift of 9.8 ppm for aldehyde protons and 9.38 ppm for α,β-unsaturated aldehyde protons, while the ketone group was detected at the chemical shift of 2.14 ppm for ketone methylic protons and 2.25–2.48 ppm for α,β-unsaturated ketone protons. Since the reaction was carried out under atmospheric air and in latex, reactions involving oxygen could not be avoided and occurred as side reactions. The oxidation reactions by singlet oxygen, radical-induced auto-oxidation from hydrogen peroxide, and hydroperoxide photolysis resulting from UV light led to the formation of by-products such as hydroperoxy, hydroxyl, carbonyl, and epoxide groups [63]. These results were in agreement with reports by previous researchers that the degradation of NR by an oxidizing agent and hydroxyl radical leaves carbonyl and hydroxyl groups as the end groups [26,57,64–66].

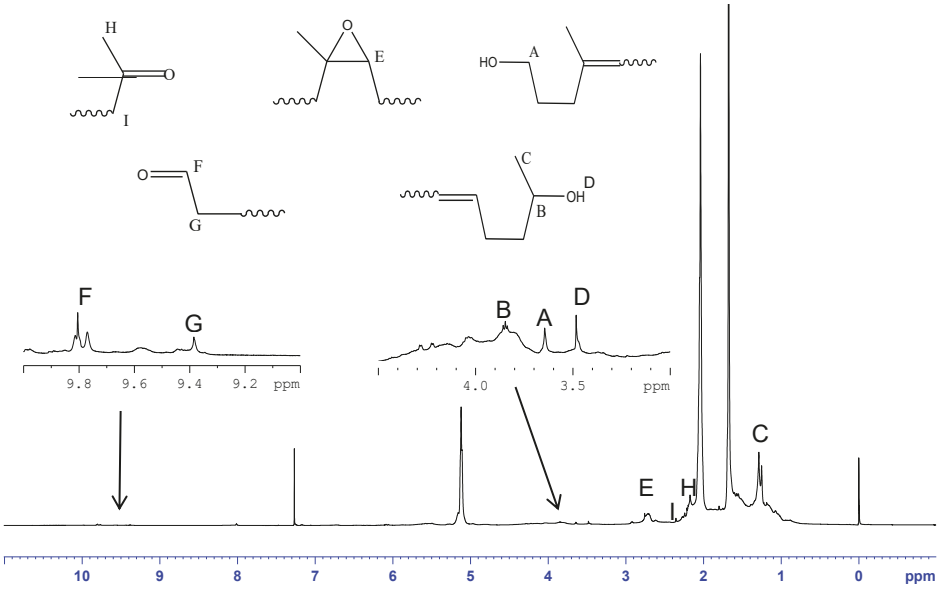

Figure 6. ^{1}H NMR spectrum of LNR prepared with 0.8 phr TiO_2.

Figure 7 shows the LNR spectrum of ^{13}C NMR to confirm its structure and the reactive groups present on its chain. The spectrum indicates the presence of typical peaks of NR at chemical shifts of δ 23.51 ppm (–C($\underline{C}H_3$)=CH–), 26.44 ppm (–C(CH_3)=CH$\underline{C}H_2$), 32.12 ppm (–$\underline{C}H_2$C(CH_3)=CH–), 124.98 ppm (–C(CH_3)=$\underline{C}$H–), and 135.16 ppm (–$\underline{C}$(CH_3)=CH–). Besides this, small peaks corresponding to terminal groups were also observed at chemical shifts of δ 63.30 and 70.60, which were assigned to hydroxylated methylene and tertiary carbon groups, respectively, thereby confirming the presence of the hydroxyl end group. Further, signals were also observed at chemical shifts of δ 60.78 and 64.58 ppm, which were assigned to carbons of the epoxy group. The epoxy groups would come from those naturally existing in NR chains [67] and also from a side reaction of photodegradation [63].

The determination of reactive groups such as hydroxyl and carbonyl groups on the LNR chain is quite challenging as the quantity of these groups is extremely low compared to the whole mass of LNR. In this present work, ^{1}H and ^{13}C NMR showed a reliable signal-to-noise ratio and good resolution to determine and identify the presence of end groups which resulted from chain-breaking during the photodegradation reaction [16].

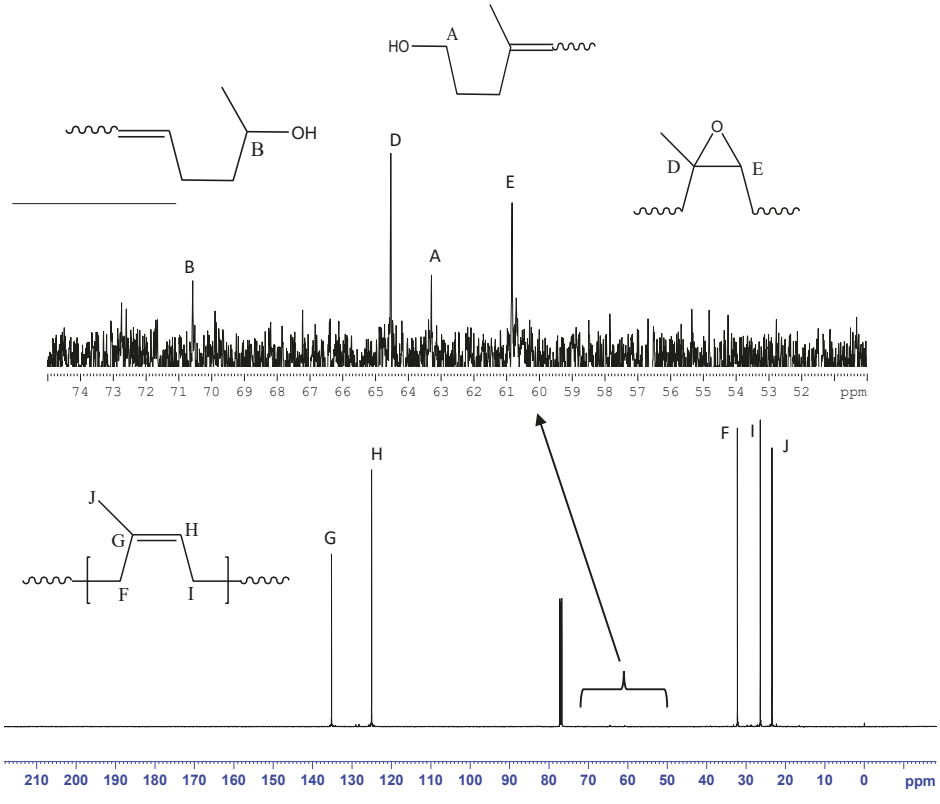

Figure 7. ^{13}C NMR spectrum of LNR that was prepared with 0.8 phr TiO_2.

3.2.4. SEM and TEM Micrographs of Latex Particles

The SEM micrographs of NR latex particles before and after photodegradation are shown in Figure 8a,b, respectively. From the micrographs, it is evident that the latex particles were able to maintain their shape, and no destruction was observed after the photodegradation. Before the photodegradation, TiO_2 nanoparticles could be clearly observed to be embedded on the NR latex particles. The existence of the TiO_2 nanoparticles could be clearly seen in the clusters, which had a size of more than 100 nm. However, the TiO_2 nanoparticles were not dispersed homogeneously on the surface of the particles. Figure 8a shows that the TiO_2 nanoparticles were embedded on certain latex particles only, depending on the introduction of the TiO_2 nanoparticles to the latexes. However, TiO_2 nanoparticles were not observed on the surface of the latex particles after photodegradation, as depicted in Figure 8b. Further analysis using TEM was carried out to confirm the position of TiO_2 on the surface of latex particles.

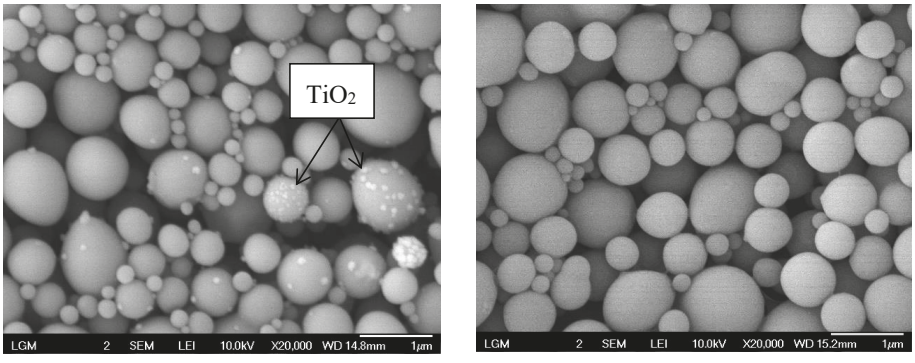

(**a**) (**b**)

Figure 8. SEM micrographs of NR latex particles in the presence of TiO_2 (**a**) before reaction (20 K magnification and (**b**) after reaction (20 K magnification).

Figure 9 shows the TEM micrographs of NR latex particles before (Figure 9a) and after (Figure 9b) photodegradation. The micrograph of the NR latex particles before photodegradation shows that the TiO_2 nanoparticles were located at the outer layer of the latex surface, which was the non-rubber layer of the latex particles. The whiter layer around the latex particles is referred to as the non-rubber layer [68]. Even though the size of the TiO_2 nanoparticles used was about 10 to 15 nm, they were embedded onto the latex surface as aggregates with sizes of about 100 to 140 nm. These aggregates could not penetrate into the latex membrane but instead were embedded on the outer layer or the non-rubber layer only. The TEM result for the sample after photodegradation supported the micrograph obtained from the SEM, where the TiO_2 nanocrystals were not observed on the surface of the LNR latex particles. The desorption of the TiO_2 nanocrystals from the latex surface during photodegradation may have been due to some changes in the composition of the non-rubber layer during the reaction. A further investigation is required to confirm the hypothesis, but it will not be discussed in this paper.

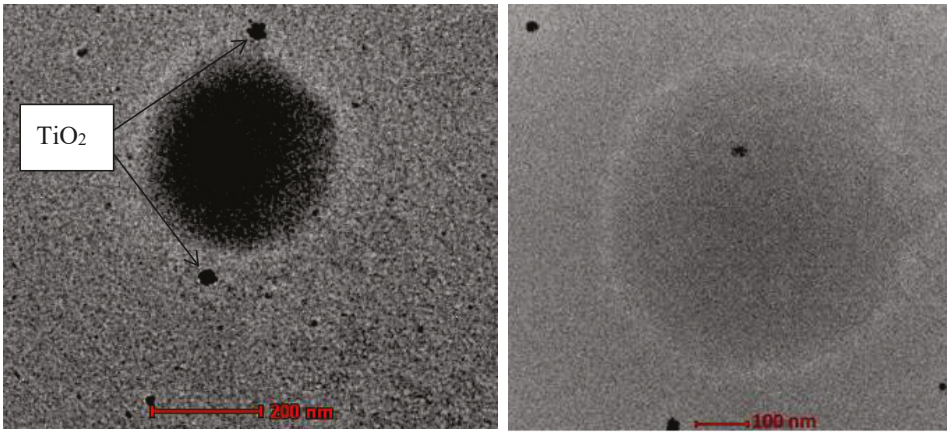

(**a**) (**b**)

Figure 9. TEM micrographs of NR latex particles in the presence of TiO_2 (**a**) before and (**b**) after the reaction.

4. Conclusions

Functionalized LNR was successfully prepared via photodegradation catalyzed by TiO_2 anatase nanocrystals. TiO_2 as a photocatalyst was prepared via the sol–gel method. The presence of TiO_2 increased the efficiency of the photodegradation of NR. The molecular weight of NR was significantly reduced from 549.3×10^3 g/mol to 7.3×10^3 g/mol when 0.8 phr of TiO_2 nanocrystals was used. The LNR obtained was observed to have depleted FTIR signals corresponding to the C–C and C=C bonds compared to the virgin NR, indicating that chain-breaking had occurred in both these groups during the degradation reaction. These sites might have been attacked either by hydroxyl radicals or oxygen species formed from the photocatalytic activities of TiO_2 and hydrogen peroxide under UV light. The broken chains then formed hydroxyl and carbonyl groups at the terminals, where these groups were found to have increased on the LNR chain.

Author Contributions: Conceptualization, S.I., N.O. and Z.M.N.; Methodology, S.I., N.O. and S.S.; Software, S.I.; Validation, S.I., N.O. and S.S.; Formal Analysis, S.I. and K.S.T.; Investigation, S.I.; Resources, S.I.; Data Curation, S.I.; Writing—Original Draft Preparation, S.I.; Writing—Review and Editing, S.I.; Visualization, S.I.; Supervision, N.O., S.S., Z.M.N. and H.I.; Project Administration, S.I.; Funding Acquisition, S.I., and N.O.

Funding: This research was funded by the Malaysian Rubber Board under SEAC grant no. S16FCB0605 and also by Universiti Sains Malaysia under FRGS grant no. 203.PBAHAN.6071350.

Acknowledgments: We gratefully acknowledge the technical and financial support provided by the Malaysian Rubber Board and Universiti Sains Malaysia under the SEAC grant no. S16FCB0605 and FRGS grant no. 203.PBAHAN.6071350.

Conflicts of Interest: The authors declare no conflict of interest.

References

1. Zhang, J.; Wang, R.; Zhang, L. Editorial corner—A personal view status, challenges and future trends of biorubber. *Express Polym. Lett.* **2017**, *11*, 343. [CrossRef]
2. Cornish, K. Biochemistry of natural rubber, a vital raw material, emphasizing biosynthetic rate, molecular weight and compartmentalization, in evolutionarily divergent plant species. *Nat. Prod. Rep.* **2001**, *18*, 182–189. [CrossRef] [PubMed]
3. Heping, Y.; Sidong, L.; Zheng, P. Preparation and study of epoxidized natural rubber. *J. Therm. Anal. Calorim.* **1999**, *58*, 293–299. [CrossRef]
4. Le Xuan, H.; Decker, C. Photocrosslinking of acrylated natural rubber. *J. Polym. Sci. Part A Polym. Chem.* **1993**, *31*, 769–780. [CrossRef]
5. Thitithammawong, A.; Srangkhum, S.; Rungvichaniwat, A. Hydroxytelechelic Natural Rubber from Natural Rubber and Epoxidised Natural Rubber. *J. Rubber Res.* **2011**, *14*, 230–240.
6. Amnuaysin, T.; Buahom, P.; Areerat, S. Preparation of natural rubber-based polyol by oxidative degradation under supercritical carbon dioxide for flexible bio-based polyurethane foams. *J. Cell. Plast.* **2015**, *52*, 585–594. [CrossRef]
7. Hirzin, R.S.F.N.; Azzahari, A.D.; Yahya, R.; Hassan, A.; Tahir, H. The behavior of semi-rigid polyurethane film based on functionalized rubber by one-shot and two-shot method preparation. *J. Mater. Sci.* **2018**, *53*, 13280–13290. [CrossRef]
8. Baharulrazi, N.; Nor, H.M.; Ali, W.K.W. Hydroxyl Terminated Natural Rubber (HTNR) as a Binder in Solid RocketPropellant. *Appl. Mech. Mater.* **2015**, *695*, 174–178. [CrossRef]
9. Klinpituksa, P.; Rungvichaniwat, A.; Saetung, A.; Pilard, J.F.; Campistron, I.; Laguerre, A. Polyurethane Adhesives from Hydroxyl Terminated Natural Rubber. *J. Rubber Res.* **2012**, *15*, 217–229.
10. Kwanming, K.; Klinpituksa, P.; Waehamad, W.-A. Ultraviolet Curing of Acrylated Liquid Natural Rubber for Surface Coating Application. *Songklanakarin J. Sci. Technol.* **2008**, *311*, 49–55.
11. Karnika De Silva, K.G.; Silva, E.; Vitharana, L.P. Depolymerized Natural Rubber as a Processing Aid. *J. Rubber Res. Inst. Sri Lanka* **1996**, *77*, 38–53.
12. Nair, N.R.; Thomas, S.; Mathew, N.M. Liquid Natural Rubber as a Viscosity Modifier in Nitrile Rubber Processing. *Polym. Int.* **1997**, *42*, 289–300. [CrossRef]

13. Dahlan, H.M.; Zaman, M.D.K.; Ibrahim, A. Liquid Natural Rubber (LNR) as a Compatibilizer in NR/LLDPE Blends. *J. Appl. Polym. Sci.* **2000**, *78*, 1776–1782. [CrossRef]
14. Chaiyasat, A.; Waree, C.; Songkhamrod, K.; Sirithip, P.; Voranuch, V.; Chaiyasat, P. Preparation of polydivinylbenzene/natural rubber capsule encapsulating octadecane: Influence of natural rubber molecular weight and content. *Express Polym. Lett.* **2012**, *6*, 70–77. [CrossRef]
15. Panwiriyarat, W.; Tanrattanakul, V.; Pilard, J.F.; Pasetto, P.; Khaokong, C. Effect of the Diisocyanate Structure and the Molecular Weight of Diols on Bio-Based Polyurethanes. *J. Appl. Polym. Sci.* **2013**, *130*, 453–462. [CrossRef]
16. Saetung, A.; Rungvichaniwat, A.; Campistron, I.; Klinpituksa, P.; Laguerre, A.; Phinyocheep, P.; Pilard, J.F. Controlled Degradation of Natural Rubber and Modification of the Obtained Telechelic Oligoisoprenes: Preliminary Study of their Potentiality as Polyurethane Foam Precursors. *J. Appl. Polym. Sci.* **2010**, *117*, 1279–1289. [CrossRef]
17. Kumar, K.D.; Kothandaraman, B. Modification of (DGEBA) epoxy resin with maleated depolymerised natural rubber. *Express Polym. Lett.* **2008**, *2*, 302–311. [CrossRef]
18. Panwiriyarat, W.; Saetung, N.; Badawy, H.; Khaokong, C.; Pasetto, P.; Campistron, I.; Nourry, A.; Pascual, S.; Fontaine, L.; Cutrigth, T.; et al. Natural Rubber: An Old Material for New Applications. In Proceedings of the 182nd Technical Meeting of the ACS Rubber Division, Cincinnati, OH, USA, 9 October 2012.
19. Sakdapipanich, J.; TSuksawad, P.; Insom, K.; Kawahara, S. Preparation of Functionalized Low Molecular Weight Natural Rubber Latex using Solid Nanometric TiO_2 Film as a Photocatalyst. *Rubber Chem. Technol.* **2005**, *72*, 597–605. [CrossRef]
20. Ravindran, T.; Nayar, M.R.G.; Francis, D.J. A novel Method for the Preparation of Hydroxyl Terminated Liquid Natural Rubber. *Macromol. Chem. Rapid Commun* **1986**, *7*, 159–163. [CrossRef]
21. Panwiriyarat, W.; Tanrattanakul, V.; Pilard, J.F.; Pasetto, P.; Khaokong, C. Preparation and Properties of Bio-based Polyurethane Containing Polycaprolactone and Natural Rubber. *J. Polym. Environ.* **2013**, *21*, 807–815. [CrossRef]
22. Gopakumar, S.; Gopinathan Nair, M.R. Determination of Molecular Parameters of NR/PU Block Copolymers by Transport Studies. *Eur. Polym. J.* **2005**, *41*, 2002–2009. [CrossRef]
23. Wayakron Phetphaisit, C.; Bumee, R.; Namahoot, J.; Ruamcharoen, J.; Ruamcharoen, P. Polyurethane Polyester Elastomer: Innovative Environmental Friendly Wood Adhesive from Modified PETs and Hydroxyl Liquid Natural Rubber Polyols. *Int. J. Adhes. Adhes.* **2013**, *41*, 127–131. [CrossRef]
24. Sakdapipanich, J.; Kowitteerawut, T.; Kawahara, S.; Tanaka, Y. Depolymerisation of Highly Purified Natural Rubber. I. Metal-catalysed Oxidation of Deproteinised Natural Rubber. *J. Rubb. Res* **2001**, *4*, 1–10.
25. Ibrahim, S.; Othman, N.; Ismail, H. Degradation of Natural Rubber Latex. In *Natural Rubber: Properties, Behavior and Application*; Hamilton, J.L., Ed.; Nova Science Publishers, Inc.: Hauppauge, NY, USA, 2016; pp. 105–136.
26. Ibrahim, S.; Othman, N.; Mohd Nor, Z.; Ismail, H. Preliminary Study on Photochemical Degradation of Natural Rubber Latex. *Macromol. Symp.* **2017**, *371*, 22–26. [CrossRef]
27. Meera, A.P.; Said, S.; Grohens, Y.; Luyt, A.S.; Thomas, S. Tensile Stress Relaxation Studies of TiO_2 and Nanosilica Filled Natural Rubber Composites. *Ind. Eng. Chem. Res.* **2009**, *48*, 3410–3416. [CrossRef]
28. Meera, A.P.; Tlili, R.; Boudenne, A.; Ibos, L.; Poornima, V.; Thomas, S.; Candau, Y. Thermophysical and Mechanical Properties of TiO_2 and silica Nanoparticle-Filled Natural Rubber Composites. *J. Elastomers Plast.* **2012**, *44*, 369–382. [CrossRef]
29. Seentrakoon, B.; Junhasavasdikul, B.; Chavasiri, W. Enhanced UV-Protection and Antibacterial Properties of Natural Rubber/Rutile-TiO_2 Nanocomposites. *Polym. Degrad. Stab.* **2013**, *98*, 566–578. [CrossRef]
30. Lin, G.; Tian, M.; Lu, Y.L.; Zhang, X.; Zhang, L.Q. Morphology, Antimicrobial and Mechanical Properties of Nano-TiO_2/Rubber Composites Prepared by Direct Blending. *Polym. J.* **2006**, *38*, 498–502. [CrossRef]
31. Mehrizad, A.; Gharbani, P.; Tabatabii, S.M. Synthesis of Nanosized TiO_2 Powder by Sol-Gel Method in Acidic Conditions. *J. Iran. Chem. Res.* **2009**, *2*, 145–149.
32. Lim, C.S.; Ryu, J.H.; Kim, D.-H.; Cho, S.-Y.; Oh, W.-C. Reaction Morphology and the Effect of pH on the Preparation of TiO_2 Nanoparticles by a Sol-Gel Method. *J. Ceram. Process. Res.* **2010**, *11*, 736–741.
33. Nolan, N.T.; Seery, M.K.; Pillai, S.C. Spectroscopic Investigation of the Anatase-to-Rutile Transformation of Sol-Gel Synthesised TiO_2 Photocatalysts Spectroscopic Investigation of the Anatase-to-Rutile Transformation of Sol-Gel-Synthesized. *J. Phys. Chem. C* **2009**, *113*, 16151–16157. [CrossRef]

34. Cenovar, A.; Paunovic, P.; Grozdanov, A.; Makreski, P.; Fidancevska, E. Preparation of Nano-Crystalline TiO_2 by Sol-Gel Method using Titanium Tetraisopropoxide (TTIP) as a Precursor. *Adv. Nat. Sci. Theory Appl.* **2012**, *1*, 133–142.
35. Wetchakun, N.; Phanichphant, S. Effect of Temperature on the Degree of Anatase-Rutile Transformation in Titanium Dioxide Nanoparticles Synthesized by the Modified Sol-Gel Method. *Curr. Appl. Phys.* **2008**, *8*, 343–346. [CrossRef]
36. Sayilkan, F.; Asilturk, M.; Sayilkan, H.; Onal, Y.; Akarsu, M.; Arpaç, E. Characterization of TiO_2 Synthesized in Alcohol by a Sol-Gel Process: The Effects of Annealing Temperature and Acid Catalyst. *Turk. J. Chem.* **2005**, *29*, 697–706.
37. Simonsen, M.E.; Søgaard, E.G. Sol-Gel Reactions of Titanium Alkoxides and Water: Influence of pH and Alkoxy Group on Cluster Formation and Properties of the Resulting Products. *J. Sol-Gel Sci. Technol.* **2010**, *53*, 485–497. [CrossRef]
38. Marchisio, D.L.; Omegna, F.; Barresi, A.A.; Bowen, P. Effect of Mixing and Other Operating Parameters in Sol-Gel Processes. *Ind. Eng. Chem. Res* **2008**, *47*, 7202–7210. [CrossRef]
39. Kallala, M.; Jullien, R.; Cabane, B. Crossover from Gelation to Precipitation. *J. Phys. II* **1992**, *2*, 7–25. [CrossRef]
40. Zhang, H.; Banfield, J.F. Understanding Polymorphic Phase Transformation Behavior during Growth of Nanocrystalline Aggregates: Insights from TiO_2. *J. Phys. Chem. B* **2000**, *104*, 3481–3487. [CrossRef]
41. Luttrell, T.; Halpegamage, S.; Tao, J.; Kramer, A.; Sutter, E.; Batzill, M. Why is Anatase a Better Photocatalyst than Rutile? Model Studies on Epitaxial TiO_2 Films. *Sci. Rep.* **2014**, *4*, 1–8. [CrossRef] [PubMed]
42. Yang, H.; Zhang, K.; Shi, R.; Li, X.; Dong, X.; Yu, Y. Sol-Gel Synthesis of TiO_2 Nanoparticles and Photocatalytic Degradation of Methyl Orange in Aqueous TiO_2 Suspensions. *J. Alloys Compd.* **2006**, *413*, 302–306. [CrossRef]
43. Karami, A. Synthesis of TiO_2 Nano Powder by the Sol-Gel Method and its use as a Photocatalyst. *J. Iran. Chem. Soc.* **2010**, *7*, 154–160. [CrossRef]
44. Wold, A. Photocatalytic Properties of TiO_2. *Chem. Mater.* **1993**, *5*, 280–283. [CrossRef]
45. Diebold, U. The Surface Science of Titanium Dioxide. *Surf. Sci. Rep.* **2003**, *48*, 53–229. [CrossRef]
46. Ravindran, T.; Nayar, M.R.G.; Francis, D.J. Production of Hydroxyl-Terminated Liquid Natural Rubber—Mechanism of Photochemical Depolymerization and Hydroxylation. *J. Appl. Polym. Sci.* **1988**, *35*, 1227–1239. [CrossRef]
47. Tang, D.K.; Ho, S.Y. The Photopolymerization of Isoprene with the Use of Hydrogen Peroxide as Photoinitiator. *J. Polym. Sci. Polym. Chem. Ed.* **1984**, *22*, 1357–1363. [CrossRef]
48. Bussière, P.O.; Gardette, J.L.; Lacoste, J.; Baba, M. Characterization of Photodegradation of Polybutadiene and Polyisoprene: Chronology of Crosslinking and Chain-Scission. *Polym. Degrad. Stab.* **2005**, *88*, 182–188. [CrossRef]
49. Kehlet, C.; Catalano, A.; Dittmer, J. Degradation of Natural Rubber in Works of Art Studied by Unilateral NMR and High Field NMR Spectroscopy. *Polym. Degrad. Stab.* **2014**, *107*, 270–276. [CrossRef]
50. Tasakorn, P.; Amatyakul, W. Photochemical Reduction of Molecular Weight and Number of Double Bonds in Natural Rubber Film. *Korean J. Chem. Eng.* **2008**, *25*, 1532–1538. [CrossRef]
51. Morand, J.L. Chain Scission in the Oxidation of Polyisoprene. *Rubber Chem. Technol.* **1976**, *50*, 373–396. [CrossRef]
52. Ranby, B. Basic Reactions in the Photodegradation of Some Important Polymers. *J. Macromol. Sci. Pure Appl. Chem.* **1993**, *A30*, 583–594. [CrossRef]
53. Nagai, N.; Matsunobe, T.; Imai, T. Infrared Analysis of Depth Profiles in UV-Photochemical Degradation of Polymers. *Polym. Degrad. Stab.* **2005**, *88*, 224–233. [CrossRef]
54. Saquib, M.; Abu Tariq, M.; Haque, M.M.; Muneer, M. Photocatalytic Degradation of Disperse Blue 1 using $UV/TiO_2/H_2O_2$ Process. *J. Environ. Manag.* **2008**, *88*, 300–306. [CrossRef] [PubMed]
55. Boonstra, A.H.; Mutsaers, C.A.H.A. Adsorption of Hydrogen Peroxide on the Surface of Titanium Dioxide. *J. Phys. Chem.* **1975**, *79*, 1940–1943. [CrossRef]
56. Kormann, C.; Bahnemann, D.W.; Hoffmann, M.R. Photocatalytic Production of Hydrogen Peroxides and Organic Peroxides in Aqueous Suspensions of Titanium Dioxide, Zinc Oxide and Desert Sand. *Environ. Sci. Technol.* **1988**, *22*, 798–806. [CrossRef] [PubMed]
57. Ibrahim, S.; Daik, R.; Abdullah, I. Functionalization of Liquid Natural Rubber via Oxidative Degradation of Natural Rubber. *Polymers* **2014**, *6*, 2928–2941. [CrossRef]

58. Chaikumpollert, O.; Sae-Heng, K.; Wakisaka, O.; Mase, A.; Yamamoto, Y.; Kawahara, S. Low Temperature Degradation and Characterization of Natural Rubber. *Polym. Degrad. Stab.* **2011**, *96*, 1989–1995. [CrossRef]
59. Mohd Nor, H.; Ebdon, J.R. Telechelic Liquid Natural Rubber: A Review. *Prog. Polym. Sci.* **1998**, *23*, 143–177. [CrossRef]
60. Tobolsky, A.V.; Mercurio, A. Catalyzed Oxidative Degradation of Natural Rubber Networks. *J. Am. Chem. Soc.* **1959**, *81*, 5539–5540. [CrossRef]
61. Phetphaisit, C.W.; Phinyocheep, P. Kinetics and Parameters Affecting Degradation of Purified Natural Rubber. *J. Appl. Polym. Sci.* **2003**, *90*, 3546–3555. [CrossRef]
62. Rasid, H.M.; Azhar, N.H.A.; Yusoff, S.F.M. Physicochemical Properties of Liquid Natural Rubber Bearing Fluoro Groups for Hydrophobic Surfaces. *J. Polym. Res.* **2017**, *24*, 106. [CrossRef]
63. Hirzin, R.S.F.N.; Azzahari, A.D.; Yahya, R.; Hassan, A. Optimizing the Usability of Unwanted Latex Yield by in Situ Depolymerization and Functionalization. *Ind. Crops Prod.* **2015**, *74*, 773–783. [CrossRef]
64. Tangpakdee, J.; Mizokoshi, M.; Endo, A.; Tanaka, Y. Novel Method for Preparation of Low Molecular Weight Natural Rubber Latex. *Rubber Chem. Technol.* **1998**, *71*, 795–802. [CrossRef]
65. Rooshenass, P.; Yahya, R.; Gan, S.N. Comparison of Three Different Degradation Methods To Produce Liquid Epoxidized Natural Rubber. *Rubber Chem. Technol.* **2016**, *89*, 177–198. [CrossRef]
66. Rooshenass, P. *Investigation of Different Degradation Methods to Prepare Liquid Epoxidized Natural Rubber for Coating Applications*; University of Malaya: Kuala Lumpur, Malaysia, 2017.
67. Thuong, N.T.; Yamamoto, Y.; Nghia, P.T.; Kawahara, S. Analysis of damage in commercial natural rubber through NMR spectroscopy. *Polym. Degrad. Stab.* **2016**, *123*, 155–161. [CrossRef]
68. Sansatsadeekul, J.; Sakdapipanich, J.; Rojruthai, P. Characterization of Associated Proteins and Phospholipids in Natural Rubber Latex. *J. Biosci. Bioeng.* **2011**, *111*, 628–634. [CrossRef] [PubMed]

polymers

MDPI

Article

Recycled Heavy Bio Oil as Performance Enhancer for Rubberized Bituminous Binders

Jiangmiao Yu [1], Zhibin Ren [1], Zheming Gao [2], Qi Wu [3], Zihan Zhu [1] and Huayang Yu [1,*]

[1] School of Civil Engineering and Transportation, South China University of Technology, Wushan Road, Tianhe District, Guangzhou 510000, China; yujm@scut.edu.cn (J.Y.); mszhibinren@mail.scut.edu.cn (Z.R.); 201730187102@mail.scut.edu.cn (Z.Z.)

[2] Sonny Astani Department of Civil and Environmental Engineering, University of Southern California, Los Angeles, CA 90089, USA; zhemingg@usc.edu

[3] Guangdong Province Communications Planning& Design Institute Co., Ltd, Xinghua Road, Tianhe District, Guangzhou 510000, China; wuqi614@126.com

* Correspondence: huayangyu@scut.edu.cn; Tel.: +86-188-9883-7614

Received: 18 March 2019; Accepted: 29 April 2019; Published: 4 May 2019

Abstract: Asphalt rubber (AR) is a sustainable paving material with merits including waste tire consumption, low traffic noise, and enhanced mechanical performance. However, the poor workability and storage stability limited its further application. This study attempted to alleviate these two concerns of AR simultaneously by incorporating heavy bio oil (HBO). To achieve this goal, bio-AR binders with three different mixing sequences were prepared. A series of rheological and chemical tests were conducted. Test results prove that the bio-AR binders exhibited superior rutting and fatigue resistance compared to AR binder. The viscosity values of bio-ARs were closed to AR modified with commercial warm mix additive, which indicates enhancement in workability. Due to the relatively high density of HBO, the density difference between the asphalt liquid phase and crumb rubber in the bio-AR system narrowed, which brought improved storage stability. Among bio-ARs prepared with different mixing sequences, the direct mixing one (ARB) had the most satisfied overall performance. The early incorporation of HBO had limited negative influence on binder performance, but allowed for more energy saving during the bio-AR binder production. Future study will be conducted on performance of bio-AR mixtures and quantitative estimation of its energy saving during the blending and compacting process.

Keywords: asphalt rubber; bio-asphalt; mixing sequence; workability; storage stability

1. Introduction

Asphalt mixture, composed of bituminous binder and mineral aggregates, is the most common paving material for highways and urban roads. The durability of asphalt pavement highly depends on the rheological properties of the bituminous binder. Due to the growing traffic loading and aggravation of axis, incorporating polymer modifiers (e.g., styrene-butadiene-styrene, crumb rubber, polyethylene) in virgin bitumen for superior adhesive and cohesive performance has become a common practice [1–4]. Among the modified bituminous binders, asphalt rubber (AR) is considered a green paving material with attractive engineering and environmental benefits. During its production, certain amount of crumb rubber particles (usually 15–20 wt %) are blended with hot virgin bitumen. Light fractions of bitumen are absorbed by the crumb rubber modifiers (CRM), which leads to the swelling of the crumb rubber [5,6]. AR contributes to the recycling of abundant disposal waste tires in an efficient and economical way [7]. The incorporation of resilient rubber particles also leads to enhanced rutting, fatigue, and low-temperature cracking resistance of asphalt pavement [8–10]. Moreover, the elastic

rubber particles are beneficial for decreasing the traffic noise generated by the tire-road contact and abrasion [11].

Despite the previously mentioned metrics, two main concerns of AR, the poor workability, and storage stability limit its further application. The highly viscous behavior of the AR binder causes the workability concern. In recent years, warm mix asphalt (WMA), which is a clean production technology, has been used with AR to address the workability concern [12]. It is reported that a maximum decrement of 55 °C can be obtained by using chemical WMA additives, which certainly reduces the energy consumption and construction emission for the AR pavement [13]. The storage stability concern of AR is caused by the density difference between the incorporated CRM particles and the liquid bitumen. It is reported that nano-montmorillonite exhibited a significantly positive effect for reducing the segregation of CRM and the bitumen liquid phase of AR when storing in an elevated temperature [14]. However, very few practical approaches have been proposed for the improvement of both workability and storage stability of AR.

Recently, using bio-asphalt from bio-waste to replace part of the petroleum-based bitumen has been a hot topic for pavement researchers. It is reported that the heavy bio-oil can significantly decrease the viscosity of asphalt and bring better workability [15]. The common dosage of bio-oil is usually 20–40% by weight of bio-asphalt [16,17]. However, the bio-asphalt was found to have relatively poorer rutting and fatigue resistance. The bio-asphalt is not quite stable since a certain amount of bio-oil may evaporate during the construction process, which makes the asphalt content in the final asphalt pavement uncontrollable [18]. Considering the low viscosity and suitable density (1.07 g/cm^3) of heavy bio oil (HBO), it is promising to use it as a performance enhancer for the AR binder, which may simultaneously alleviate the workability and storage stability concern of AR. In addition, when used as an additive rather than an alternate of bitumen, the dosage of HBO can be limited to 5–10% by weight of virgin bitumen, which makes the modified binder more stable compared to traditional bio-asphalt materials.

The objective of this study was to evaluate the feasibly of incorporating heavy bio-oil to improve both the workability and storage stability of the AR binder. To achieve this goal, rheological and chemical tests were conducted on modified bitumen. The virgin bitumen, CRM and HBO, were blended by three different mixing sequences. Physical and rheological properties, including penetration, softening point, Superpave rutting/fatigue factors, and low temperature stiffness of asphalt rubber modified with HBO (HBO-AR) binders were characterized. Gel permeation chromatography (GPC) analysis and Fourier Transform Infrared Spectroscopy (FTIR), which characterizes the molecular weight distribution and chemical functional groups respectively, were conducted to reveal the compound modification mechanism of CRM and HBO. This study is anticipated to provide useful information to pavement researchers who are interested in mitigating the workability and storage stability concerns of rubberized asphalt binders.

2. Materials and Methods

2.1. Materials

Pen60/70, which was provided by Guangzhou Xinyue Transportation Technology Co., Ltd., Guangzhou, China, was selected as virgin bitumen to prepare AR and HBO-AR binders. The hot AR binder was prepared by high shear mixing (10,000 rpm) crumb rubber (40 mesh, provided by Huayi Rubber Co., Ltd., Dujiangyan, China) and virgin bitumen for 1 h at 176 °C, which allows the rubber particles to swell and dissolve in bitumen fractions. The CRM content was set as 18 wt % by weight of the hot AR binder, which is consistent with some previous publications [12,19,20].

The HBO additives were provided by a new energy company named Handan Zhenfei Trade Limited Company in the Hebei province, China. It is caramel viscous liquid (containing 3 wt % water) with a density of 1.07 g/cm^3. The mass loss ratio of HBO after rolling thin film oven (RTFO) aging is 41.13%.

Three mixing sequences were applied to prepared rubberized bituminous binder containing HBO. For all warm asphalt rubber (WAR) binders, the HBO or Evotherm-DAT (provided by MeadWestvac Company, Richmond, VA, USA) content was set as 5 wt % by weight of the hot AR binder. Specifically, AR-B refers to the WAR prepared by a conventional sequence, mixing HBO and the hot AR binder for 10 min at 160 °C. ARB was prepared by directly blending the same amount of virgin bitumen, CRM and HBO together at 160 °C for 60 min. BR-A used a pretreatment process in which CRM were soaked into liquid HBO for 48 h. This makes the HBO additive completely absorbed by the CRM particles. After that, the CRM containing HBO (B-CRM) was incorporated to virgin bitumen by 1 hour high shear mixing at 160 °C. For all rubberized binders with HBO, the mass ratio was set as 61:220:1000 for HBO, CRM, and virgin bitumen, respectively. In addition, the WAR binder with Evotherm-DAT (labelled as ER-A) was prepared as a control group to evaluate the performance of the HBO additive. ER-A is prepared by the pretreatment method like BR-A. According to Yu's study, the pretreatment method provides the optimal performance for the WAR binder with Evotherm-DAT [20].

2.2. Testing Program

2.2.1. Standardized Performance Tests

The penetration and softening point test were conducted to evaluate the general performance of test binders. Rotational viscosity was conducted for workability characterization at three different temperatures (135, 160, and 176 °C), using a Brookfield rotational viscometer (AMETEK Brookfield Company, Middleboro, MA, USA) with 20# spindle. A dynamic shear rheometer (DSR, Malvern Kinexus Lab+, Malvern analytical Company, UK) was used to conduct rheological tests.

The high temperature performance of prepared binders was characterized by both the Superpave rutting factor ($G^*/\sin\delta$, for both unaged and RTFO aged samples) and non-recoverable creep compliance (J_{nr}, for RTFO aged samples only). The standard RTFO procedure takes unaged asphalt binder samples in cylindrical glass bottles and places these bottles in a rotating carriage within an oven. The carriage rotates within the oven while the 163 °C temperature ages the samples for an additional 85 min. The $G^*/\sin\delta$ test started at 64 °C, and the temperature was increased automatically to the next PG temperature if the measured rutting factor was larger than the values, i.e., 1.0 kPa for unaged binder and 2.2 kPa for the RTFO binder. J_{nr} was evaluated by the multiple stress creep recover (MSCR) test at 64 °C. During the test, a creep load was applied for 1 s followed by 9 s of a recovery. Each specimen was subjected to 10 cycles with a creep stress of 0.1 kPa, which is followed by 10 cycles with a creep stress of 3.2 kPa.

The fatigue resistance was evaluated by the Superpave fatigue factor ($G^*\sin\delta$) test and linear amplitude sweep (LAS) test with pressurized aging vessel (PAV) aged specimens. During the PAV aging procedure, the RTFO aged asphalt was placed in a chamber with 100 °C and 2.1 MPa for 20 h. The $G^*\sin\delta$ test was started at 25 °C with a decrement of 3 °C until the $G^*\sin\delta$ value was larger than 5000 kPa. The LAS test was started with a frequency sweep followed by a linear amplitude strain sweep to determine the cycles to failure denoted as N_f. The fatigue failure is defined as the 35% reduction of the initial modulus in the LAS test, according to the viscoelastic continuum damage (VECD) model.

The bending beam rheometer (BBR, CANNON Instrument Company, State College, PA, USA) test was conducted for a low temperature performance evaluation. It characterized the stiffness and m-value of the test binder at a PAV aging state. The tests were implemented in a fluid bath with a constant load (980 ± 50 mN) at −12 °C, −18 °C, and −24 °C, respectively.

2.2.2. Frequency Sweep

In addition to the standardized performance tests, the overall rheological performance of test binders was evaluated by master curves of a complex shear modulus (G^*) based on the time-temperature superposition principle. Master curves (reference temperature: 60 °C) were obtained through a series of frequency sweeps at a temperature range from 76 to 4 °C with various frequencies between 0.01

and 30 Hz. The best fit of frequency sweep test data was conducted to obtain a single master curve based on the Williams-Landel-Ferry (WLF) formula (Equation (1) and Equation (2)) and the sigmoidal function (Equation (3)) [21].

$$\log(\mathrm{a(T)}) = \frac{-C_1 \Delta T}{C_2 + \Delta T} \quad (1)$$

where a(T) is the shifting factor at one specific temperature T, ΔT is the different value between the test temperature and reference temperature, and C_1 and C_2 are model constants.

$$\log(\xi) = \log(f) + \log(\mathrm{a(T)}) \quad (2)$$

where ξ is the reduced frequency at reference temperatures and f is the test frequency at specific temperatures.

$$\log(\mathrm{G^*}) = \delta + \frac{\alpha}{1 + e^{\beta + \gamma \log(\xi)}} \quad (3)$$

where β, γ are the shape parameters, α is the span of $\mathrm{G^*}$ values, and δ is the minimum modulus value.

2.2.3. Storage Stability Test

The storage stability was conducted to evaluate the phase separation of modified binders during the storage process at an elevated temperature. A lab-simulated high-temperature storage process was conducted on test binders. About 70 g of hot asphalt binder was first poured into an aluminum tube, which were then vertically stored at 163 °C for 48 h. The tube was then cooled down and cut into three equal parts horizontally. The top and bottom parts were used to identify their difference in property after storage. According to ASTM D36, the storage stability was characterized by the softening point difference between the binders in top and down parts.

2.2.4. Chemical Tests

For a mechanism investigation, Gel Permeation Chromatography (GPC, Agilent 1260, Agilent Technologies Inc., Santa Clara, CA, USA) and Fourier transform infrared spectroscopy (FTIR, VERTEX 70, Bruker, Hamburg, Germany) were performed on prepared binders. The GPC test was conducted to evaluate the effect of crumb rubber and HBO on molecular weight distribution of liquid asphalt fractions, while FTIR tests characterized the chemical bonds and functional groups of test binders.

For GPC tests, the test binders were dissolved in Tetrahydrofuran (THF) solvent and then filtered through a 0.45 μm Polytetrafluoroethylene (PTFE) syringe filter. The insoluble particles were removed by this process, while all the residual fractions can be completely dissolved in THF. By the filtering process, about 18–20 wt % of samples was filtered out. The asphalt-THF solution was drained through columns and allowed to flow at a rate of 0.5 ml/min, and the temperatures of the columns were maintained at 40 °C.

For FTIR tests, the test binder was first pressed to pellets with a thickness of approximately 1 mm, and then placed in a transmission holder and scanned. Infrared spectroscopy ranging from 4000 to 400 $\mathrm{cm^{-1}}$ was obtained by scanning using an FTIR spectrometer.

The detailed information of conducted tests in this study was summarized in Table 1. For all the above-mentioned tests, three replicates were prepared and tested.

Table 1. Details of laboratory tests.

Performance	Experiments	Aging Level	Specification/Standard	Notes
Conventional property	Softening point	Unaged	ASTM D36	N/A
	Penetration		ASTM D5	25 °C
Workability	Rotational viscosity	Unaged	AASHTO T316	135, 160, and 176 °C
Rutting resistance	Rutting factor ($G^*/\sin\delta$)	Unaged & RTFO-aged	AASHTO M320	beginning at 64 °C, 25 mm plate, 2 mm gap
	MSCR	RTFO- aged	AASHTO MP19-10	64 °C, 25-mm plate, 2-mm gap
Fatigue resistance	Fatigue factor ($G^*\sin\delta$)	RTFO- + PAV- aged	AASHTO M320	beginning at 25 °C, 8-mm plate, 2-mm gap
	LAS		AASHTO TP101	25 °C, 8-mm plate, 2-mm gap
Low temperature cracking resistance	BBR	RTFO- + PAV- aged	AASHTO T313	−12, −18, −24 °C
Overall rheological properties	Frequency sweep	Unaged	N/A	4 to 76 °C, 0.01 to 30 Hz
Storage stability	Softening point	unaged	ASTM D36	N/A
Mechanism investigation	FTIR		N/A	N/A
	SEM	unaged	N/A	N/A
	GPC		GPC testing manual	30 °C

3. Results and Discussion

3.1. Penetration and Softening Point

Figure 1a shows the results of penetration and softening point tests. It is observed that CRM led to a lower penetration value and a higher softening point, which indicates that the rubberized binders were stiffer and more stable in an elevated temperature compared to virgin bitumen. The liquid additives, both HBO and Evotherm-DAT, made the rubberized binders softer and more sensitive to temperature variation. The effect of mixing sequence on penetration of the HBO-AR binder was clear. The one with conventional mixing order, AR-B, had even a higher penetration value than Pen60/70. By comparison, BR-A and ARB exhibited similar performance to ER-A, which is the WAR binder with a commercial WMA additive. One possible explanation is that the blending time of the AR binder and HBO additive (10 min) is not enough for a completed reaction among the components. It is also observed that the mass loss of AR-B after RTFO aging was higher than other WAR binders (Figure 1b).

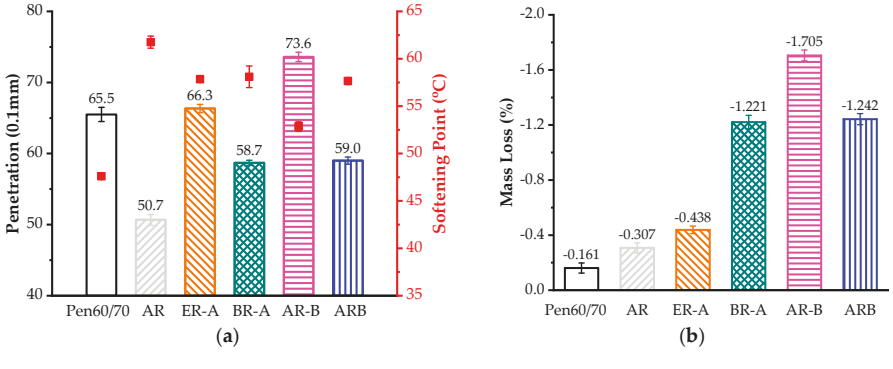

Figure 1. Conventional tests: (**a**) Penetration (histogram) and softening point (scatter diagram). (**b**) Mass loss after short-term aging.

3.2. Workability

Figure 2 shows the rotational viscosity values of test binders at 135, 160, and 176 °C. The poor workability is the most critical concern for rubberized binders. As depicted, the viscosity of AR at

135 °C is almost 25 times that of Pen60/70. With the aid of liquid WMA additives, the WAR binders showed better workability, but the viscosity values were still higher than virgin bitumen. It is observed that HBO-AR binders had superior workability compared to ER-A binder, regardless of the mixing sequence. Consistent with the previous studies [20], the pretreatment sequence led to the poorest workability of HBO-ARs, while specimens prepared with direct mixing and conventional mixing methods had similar viscosity values. According to the AASHTO standard, mixtures with ARB and AR-B can be compacted at 160 °C since their viscosity values were lower than 3000 cP [22].

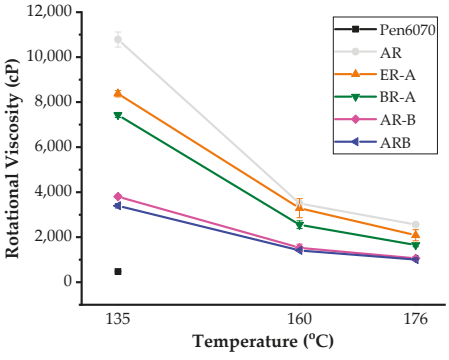

Figure 2. Rotational viscosity test results.

3.3. Rutting Resistance

Figure 3 shows the results of the Superpave rutting factor test. As expected, CRM had a significant effect on enhancing the rutting resistance. In the unaged state, AR had the highest failure temperature. However, after short-term aging, the HBO-ARs showed better rutting performance than AR. Moreover, it is noted that all HBO-ARs outperformed ER-A in terms of rutting resistance. Among the HBO-AR binders prepared with different blending sequences, BR-A had the best high-temperature performance followed by ARB and AR-B.

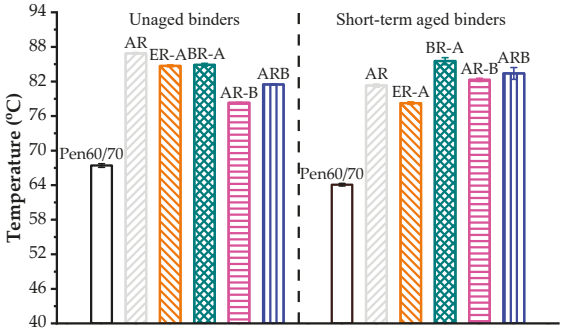

Figure 3. Superpave rutting factor results.

Table 2 presents the MSCR test results. The J_{nr} difference of all modified binders did not meet the requirement of AASHTO TP70-13 i.e., < 75%. This is attributed to the extremely low J_{nr} values at the applied stress of 0.1 kPa [19]. Based on the $J_{nr}3.2$ values, Evotherm-DAT had a negative effect on the rutting resistance while HBO showed a positive influence. Consistent with the results of the Superpave rutting factor test, BR-A exhibited the lowest $J_{nr}3.2$ value, which indicates the best rutting resistance among three HBO-AR binders.

Table 2. MSCR test results.

Sample ID	J_{nr}			% Recovery	
	0.1 kPa (kPa^{-1})	3.2 kPa (kPa^{-1})	J_{nr}% Diff	0.1 kPa (kPa^{-1})	3.2 kPa (kPa^{-1})
Pen60/70	4.514 ± 0.166	5.007 ± 0.154	11.0 ± 0.6	0.7 ± 0.4	−0.5 ± 0.2
AR	0.186 ± 0.015	0.529 ± 0.002	186.4 ± 24.4	72.1 ± 2.0	35.0 ± 0.4
ER-A	0.087 ± 0.026	0.870 ± 0.044	954.5 ± 367.1	89.6 ± 3.3	26.1 ± 0.9
BR-A	0.041 ± 0.002	0.167 ± 0.013	307.2 ± 11.0	86.4 ± 0.8	54.0 ± 1.3
AR-B	0.123 ± 0.036	0.332 ± 0.092	171.7 ± 6.6	76.6 ± 2.9	46.4 ± 5.9
ARB	0.186 ± 0.039	0.399 ± 0.039	117.2 ± 25.1	65.7 ± 4.7	35.4 ± 2.2

The numbers after "±" are standard deviations.

3.4. Fatigue Resistance

Figure 4a shows the fatigue failure temperatures and Figure 4b shows the relationship between the G*sin δ value and the test temperature. AASHTO M320 specified that the fatigue factor, G*sin δ, should be less than 5 MPa to pass a performance grade test at a specific temperature. The higher the fatigue failure temperature is, the poorer the fatigue resistance the test binder has. As depicted in Figure 4a, the failure temperature of AR was 8.9 °C lower than that of Pen60/70, which indicates superior fatigue resistance brought by CRM. The incorporation of Evotherm-DAT further enhanced the fatigue resistance by decreasing the failure temperature by 0.2 °C. By comparison, HBO had a negative effect on the fatigue performance of the rubberized binder. The failure temperature values of HBO-ARs were 1.3–2.2 °C higher than that of AR.

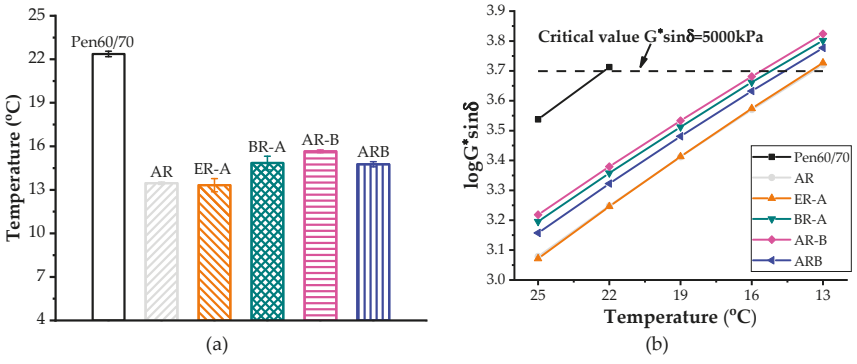

Figure 4. Fatigue performance of asphalt binders: (**a**) failure temperatures and (**b**) logarithm of G*sin δ values.

Figure 5 shows the LAS test results at two applied strains (2.5% and 5%). Higher cycles to fatigue (N_f) refer to better resistance of fatigue cracking. According to Figure 6, the N_f values of AR were more than 11 times of virgin bitumen at 2.5% and 5% strain levels. Inconsistent with Superpave fatigue test results, the HBO-ARs had higher fatigue lives compared to AR based on LAS evaluation. Since previous studies have proven that LAS is a more reliable fatigue characterizing methods for bituminous specimens, it is believed that the HBO additive has a limited negative effect on the fatigue performance of AR [9,23].

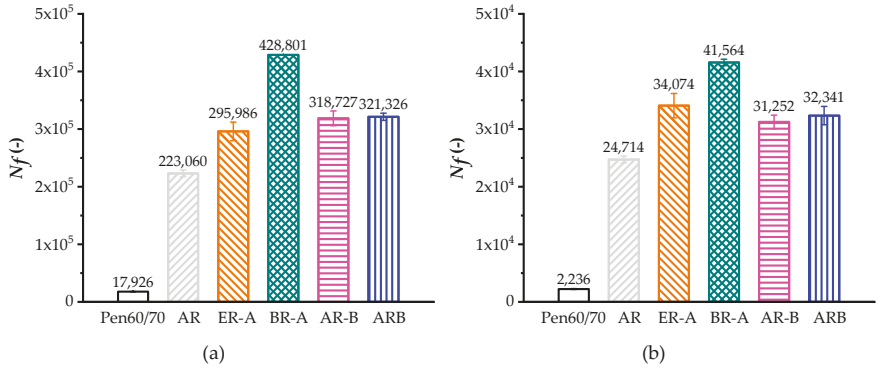

Figure 5. LAS test results: (**a**) applied strain of 2.5% and (**b**) applied strain of 5.0%.

3.5. Low Temperature Cracking Resistance

Table 3 shows the stiffness and m-values of test binders obtained by the BBR test. According to AASHTO T313, at one specific temperature grade, the m-value should be over 0.3, and the stiffness value should be less than 300 MPa. Higher stiffness values result in low-temperature cracking. According to Table 3, it is noted that all rubberized binders had lower stiffness compared to Pen60/70 at a low temperature, which is attributed to the resilient behavior of the CRM particles. According to thermal characterization, the glass transition temperatures of crumb rubber, HBO, and virgin asphalt are approximately −50 °C, −40 °C, and −25 °C (PAV aged binder), respectively. The incorporation of Evotherm-DAT and HBO exhibited a negative effect on the low-temperature performance of AR. Among the HBO-AR binders, the low temperature performance of ARB was slightly better than BR-A and AR-B.

Table 3. BBR test results.

Sample ID	−12 °C		−18 °C		−24 °C	
	Stiffness (MPa)	m-Value (× 10^{-2})	Stiffness (MPa)	m-Value (× 10^{-2})	Stiffness (MPa)	m-Value (× 10^{-2})
Pen60/70	277 ± 4.2	29.1 ± 1.5	534 ± 9.9	20.4 ± 0.6	N/A	N/A
AR	93.6 ± 14.7	37.9 ± 0.8	168 ± 12.7	32.2 ± 1.5	375 ± 24.0	20.4 ± 1.7
ER-A	183 ± 12.7	63.7 ± 18.2	311 ± 4.9	32.8 ± 7.9	484 ± 9.2	19.4 ± 1.8
BR-A	194 ± 17.7	49.2 ± 2.3	271 ± 7.8	24.7 ± 4.3	453 ± 62.9	19.8 ± 1.1
AR-B	112 ± 14.8	32.8 ± 1.1	243 ± 42.4	27.4 ± 2.0	448 ± 24.7	19.1 ± 1.6
ARB	97.0 ± 12.8	34.6 ± 3.8	208 ± 17.0	28.0 ± 3.6	412 ± 13.4	19.4 ± 0.9

The numbers after "±" are standard deviations.

3.6. Overall Rheological Behavior

Master curves were drawn to evaluate the overall rheological properties of asphalt binders at a wide angle of frequencies (10^{-2}–10^{-8} Hz). To obtain the master curves, a series of complex mathematical calculations were conducted. The WLF formula (Equation (1) and Equation (2)) was first substituted into the sigmoidal function (Equation (3)) as Equation (4).

$$\log(G^*) = \delta + \frac{\alpha}{1 + e^{\beta + \gamma(\log(f) + \frac{-C_1 \Delta T}{C_2 + \Delta T})}} \quad (4)$$

Then a nonlinear surface fit was conducted to obtain parameters C_1 and C_2 with $\log(f)$ and ΔT as independent variable using Equation (4). Different loading frequencies were shifted at a given temperature (60 °C) to obtain a single master curve based on Equation (2). Lastly, the fitting master

curves were obtained by a best fit based on Equation (3). The parameters of the WLF formula and sigmoidal function were presented in Table 4.

Table 4. Model parameters of the WLF formula and sigmoidal function.

Parameters	WLF Formula		Sigmoidal Function				
	C_1 (-)	C_2 (-)	δ (Pa)	α (Pa)	B (-)	γ (-)	R^2 @$\|G^*\|$ (-)
Pen60/70	−8.82557	138.09993	−0.55919	8.71694	0.25486	−0.45159	0.99942
AR	−8.26021	136.30605	−0.11497	8.67516	0.18174	-0.32416	0.99930
ER-A	−6.80041	117.83596	−0.44963	9.09011	0.16465	−0.30914	0.99887
CR−A	−8.10492	135.16876	−2.27332	11.3535	−0.14977	−0.24744	0.99926
AR−C	−7.69053	131.04835	−2.8193	11.86402	−0.17005	−0.25139	0.99925
ARC	−8.08466	132.99088	−2.87974	11.86654	−0.25577	−0.25754	0.99912

Figure 6 shows the master curves of G^* of test binders at the reference temperature of 60 °C. Based on sigmoidal function, scatters and smooth curves were obtained in term of the lg|G^*| versus reduced frequency (lgf_r). Based on the time-temperature superposition principle of viscoelastic material, low frequency refers to high temperature and vice versa. As expected, the increased frequency resulted in an increase of complex shear modulus. According to Figure 6b, the moduli of all rubberized binders were lower in high frequencies but higher in low frequencies compared to neat bitumen, which indicates superior performance in both high and low temperatures. Findings obtained from master curves were consistent with the results obtained by the Superpave rutting factor test, the MSCR test, and the BBR test.

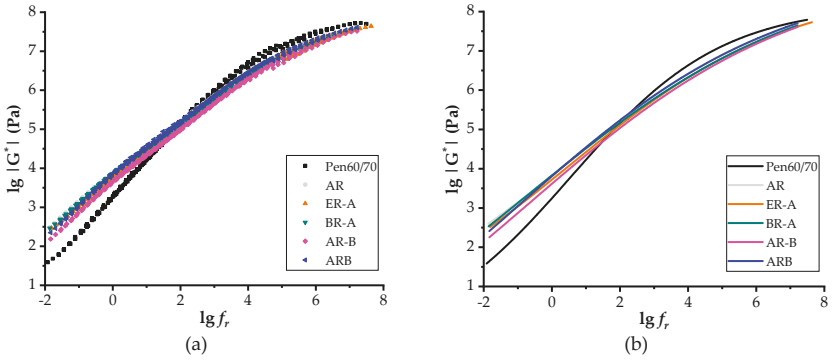

Figure 6. Master curves of test binders: (**a**) scatters of test results and (**b**) sigmoidal fitting curves.

3.7. Storage Stability

Figure 7 show the softening point difference (D-value) of test binders after lab-simulated storage. A smaller D-value refers to better storage stability. According to Figure 7, both AR-B and ARB exhibited better storage stability compared to AR, while BR-A had poorer performance. Since HBO had higher density compared to virgin bitumen, it narrowed the density difference between the bitumen liquid phase and CRM particles in the bio-AR system, which provided resistance to prevent the settling of CRM particles. However, the reason why the poorest storage stability belonged to BR-A still required further investigation.

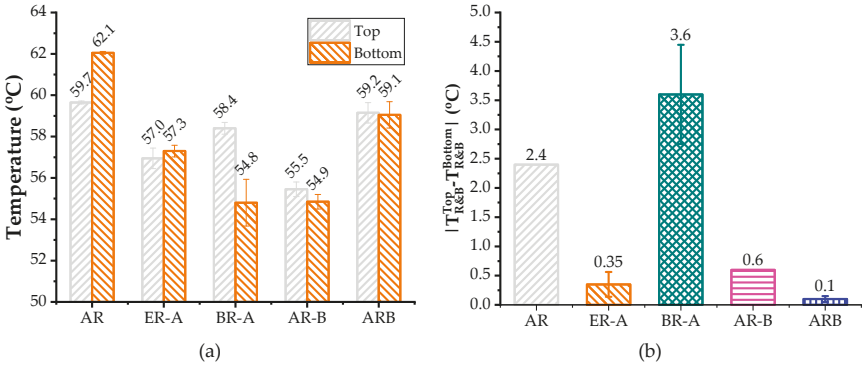

Figure 7. Softening point difference of test binders after storage: (**a**) Softening points of top and bottom sections. (**b**) D-value between top and bottom sections.

3.8. Molecular Weight Distribution

Figure 8 presents the GPC test results of liquid additives and test binders. The elution amount of specific molecular range can be obtained by analyzing the curves' fluctuation of test binders. According to their molecular weight, the constituents of all specimens were classified into several groups [24–27]. As shown in Figure 8, the chromatograms were divided into eight slices based on the selected retention time ranging from 10 to 17.2 min (referring to molecular weight ranges from 48,386 to 245 g/mol). The entire area of eight slices for each specimen was adjusted to 1, and then the area ratio was used to compare their molecular weight distribution. A higher area ratio represents a larger percentage of the specific molecular size. It is shown in Figure 8a that the constituents of Evotherm-DAT gathered from 14.5 to 17.2 min, while those of HBO concentrated in 16.3 to 17.2 min. This indicates that the average molecular weight of HBO was much smaller than that of Evotherm-DAT. As shown in Figure 8b, the highest area ratio of ARB in 16.3 to 17.2 min may lead to the lowest average molecular weight among all binders.

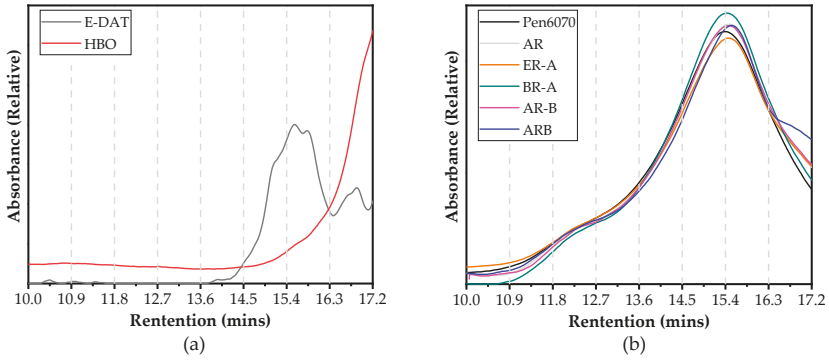

Figure 8. GPC test results: (**a**) chromatograms of Evotherm-DAT and HBO and (**b**) chromatograms of test binders.

Table 5 presents the GPC test results based on numerical statistics analysis. Four different parameters were selected to describe the variations of molecular weight distribution during the modification process, i.e. peak molecular weight (M_p), number-average molecular weight (M_n), weight-average molecular weight (M_w), and polydispersity (PDI = M_w/M_n). It is noted that the PDI values of HBO and Evotherm-DAT were lower than that of asphalt binder samples, which indicates

more concentrated distribution of molecular weight. AR had a lower M_n value but higher M_w value than Pen 60/70, which is likely caused by the modification of CRM dissolved in asphalt fractions. This indicates that the dissolution of CRM varied the molecular weight distribution slightly. Among three preparation procedures, the PDI of AR was 1.8068 and 1.3126 higher than those of BR-A and AR-B, respectively, while 0.2173 was lower than that of ARB. However, the M_w values of all HBO-ARs were lower than those of AR. Therefore, different preparation procedures led to a different molecular weight distribution. Yet, the large molecules' content of all HBO-ARs was lower than that of AR. By contrast, incorporating Evotherm-DAT decreased both M_w and M_n of AR. One possible reason is that the dissolution process of CRM was promoted by the incorporation of Evotherm-DAT, which affected the molecular weight distribution significantly.

Table 5. GPC parameters.

Sample ID	M_p (g/mol)	M_n (g/mol)	M_w (g/mol)	PDI (-)
Pen60/70	917 ± 9	682 ± 27	2371 ± 575	3.4619 ± 0.7065
Evotherm-DAT	882 ± 14	513 ± 16	900 ± 10	1.3722 ± 0.4696
HBO	145 ± 4	193 ± 18	252 ± 40	1.3052 ± 0.0859
AR	866 ± 4	593 ± 13	2864 ± 622	4.8357 ± 0.9078
ER-A	873 ± 5	585 ± 4	2425 ± 737	4.1527 ± 1.2857
BR-A	896 ± 5	658 ± 4	1992 ± 6	3.0289 ± 0.0066
AR-B	877 ± 5	586 ± 12	2059 ± 374	3.5231 ± 0.7112
ARB	836 ± 3	496 ± 9	2535 ± 213	5.053 ± 0.4030

The numbers after "±" are standard deviations.

3.9. Chemical Bonds Variation

Figure 9a–c present the FTIR spectra of virgin bitumen, Evotherm-DAT, and HBO, respectively. These three kinds of materials have similar elementary composition (including carbon, hydrogen, oxygen, nitrogen, and sulfur), but display quite a difference in their functional groups. Evotherm-DAT and HBO show more complex chemical composition compared to neat bitumen [28]. Evotherm-DAT peaked at approximately 3362 cm^{-1} (O-H or N-H stretching vibration of the hydrogen-bonded hydroxyl group and amino groups), 1651 cm^{-1} (C=O stretching vibration of secondary amides), and 1356 cm^{-1} (symmetric SO2 stretching of sulphone group), which indicated the existence of amines, amino ions, and sulfur-containing organics, respectively [29]. As shown in Figure 9c, it is noted that HBO peaked at 3417 cm^{-1} (O-H or N-H stretching vibration of hydrogen-bonded hydroxyl group and amino groups), 3049 cm^{-1} (=CH stretching vibration of the benzene ring), and 1600 cm^{-1} (C=C stretching vibration of the aromatic ring). These absorbance peaks were most likely caused by the presence of phenol, cresol, and xylenol. HBO did not peak at 724 cm^{-1} (–$(CH2)_n$– rocking vibration of alkane groups, n > 4). This may lead to a smaller average molecular weight than neat bitumen and Evotherm–DAT, which is consistent with the results of the GPC test.

Figure 9d–f show the FTIR spectra of CRM, CRM containing Evotherm–DAT (E–CRM) and B–CRM, while Figure 10 show their morphologies in micro scale (scanning electron microscope (SEM) images). E–CRM had a smoother surface than CRM, while B–CRM had no significant variation. As shown in Figure 9e, the spectra of E–CRM included most peaks found in CRM and Evotherm–DAT. However, the peaks occurring at 800 to 1600cm^{-1} showed up in the spectra of E–CEM compared to that of both CRM and Evotherm–DAT. This indicates the decrease of the –COOH group of Evotherm–DAT and the –OH group of rubber caused by a chemical reaction between the two groups. Approximately, it can be seen in Figure 9f that CRM and HBO can find similar peaks with B–CRM. Meanwhile, peaks at 1096 and 1746 cm^{-1} (C–O–C and C=O stretching) were observed in B–CRM, which did not occur in either CRM or HBO. This may demonstrate the chemical reaction between the phenol of HBO and residual acetone of CRM during its regenerative process.

The FTIR spectra of AR were shown in Figure 9g. The major absorption bands of AR occurred at similar locations with those of neat bitumen. However, adding CRM enhanced the absorbance by

700–1700cm^{-1} (mainly C–H stretching) and weakened the absorbance of 1639 cm^{-1} (C=O stretching). One possible reason is that the unsaturated functional groups of CRM and base binder was oxidized by high shear mixing. Therefore, the modification of CRM is not a single physical process. The modification can also result in the variation of functional groups and chemical bonds. As shown in Figure 9h, it is noted that all HBO–ARs and ER–A had very similar spectra of FTIR, which indicates their close chemical components [30].

The mechanism of HBO contributing to the modification of AR can be illustrated as follows. During the modification process through high shear mixing, chemical bonding and physical absorbing may result in redistribution of hydrocarbon chains [31,32]. Then one more compacted and steadier micro structure was obtained. The heavy bio oil, which is mainly composed by aromatics (phenol, cresol, and xylenol), will surround rubber particles. This will promote the devulcanization and depolymerization of crumb rubber [30], and eventually results in superior rheological properties of the modified binder.

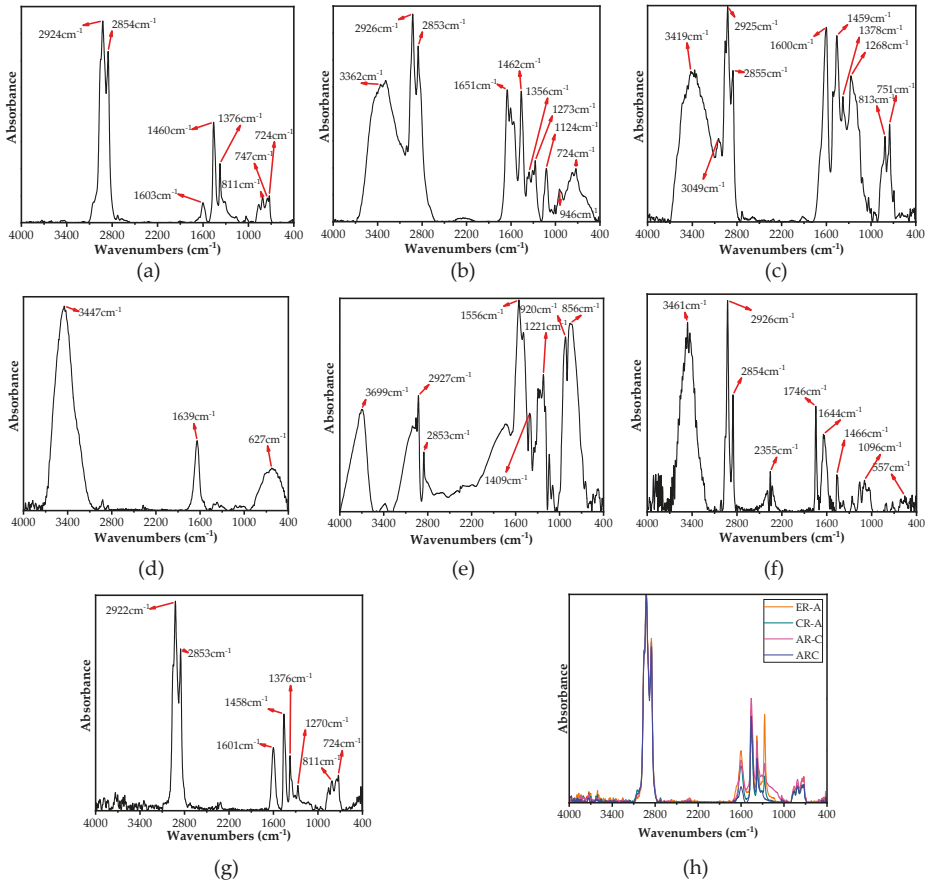

Figure 9. FTIR test results: (**a**) Base binder, (**b**) Evotherm–DAT, (**c**) HBO, (**d**) CRM, (**e**) E–CRM, (**f**) B–CRM, (**g**) AR, and (**h**) Evotherm–DAT and HBO modified binders.

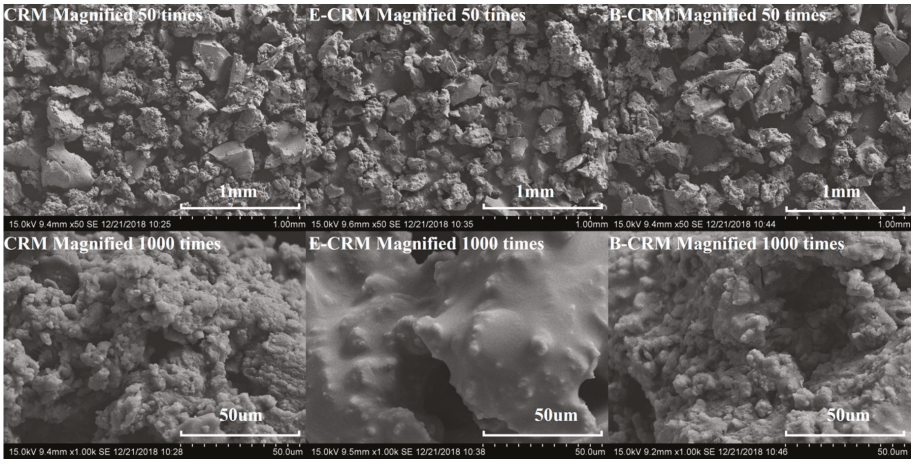

Figure 10. SEM results: variations of CRM before and after soaking in Evotherm–DAT or HBO.

4. Conclusions

This study evaluated the feasibly of using heavy bio–oil to improve both the workability and storage stability of the AR binder. Rheological and chemical tests were conducted to characterize the effects of HBO and its different preparation procedures for modifying AR. According to test results, the findings were obtained as follows.

- Compared to a conventional AR binder, the bio–ARs had superior rutting and fatigue resistance but slightly poorer low temperature performance.
- The bio–ARs exhibited better performance in both workability and storage stability compared to AR. Specifically, the warm mix effect of HBO additive is comparable to the commercial liquid WMA additive.
- The methods that incorporate bio–oil in earlier stages (direct mixing and pretreatment methods) had a very marginal negative effect on the performance of bio–AR. Moreover, they are more sustainable since they reduce both the temperature of the mixing AR binder with aggregate, and that of blending CRM with virgin asphalt.

The findings of this study have proven that HBO is a promising modifier that simultaneously alleviates enhancing the workability and storage stability of AR. Future study will focus on effect of HBO on AR mixtures and quantitative estimation of energy saving during blending and the compacting process.

Author Contributions: Data curation, Z.R. Funding acquisition, H.Y. Investigation, Z.G., Z.R., J.Y., and H.Y. Methodology, Q.W., Z.Z., and H.Y. Supervision, J.Y. Writing—original draft, Z.R. Writing—review & editing, H.Y.

Funding: The National Natural Science Foundation of China [NSFC 51808228] and China Postdoctoral Science Foundation (2018M643089) funded this research. The Fundamental Research Funds for the Central Universities [2018MS92] funded the APC.

Conflicts of Interest: The authors declare no conflict of interest.

References

1. Padhan, R.K.; Sreeram, A. Enhancement of storage stability and rheological properties of polyethylene (PE) modified asphalt using cross linking and reactive polymer based additives. *Constr. Build. Mater.* **2018**, *188*, 772–780. [CrossRef]
2. Zhang, W.; Jia, Z.; Zhang, Y.; Hu, K.; Ding, L.; Wang, F. The effect of direct-to-plant styrene-butadiene-styrene block copolymer components on bitumen modification. *Polymers* **2019**, *11*, 140. [CrossRef]

3. Wang, J.; Yuan, J.; Xiao, F.; Li, Z.; Wang, J.; Xu, Z. Performance investigation and sustainability evaluation of multiple polymer asphalt mixtures in airfield pavement. *J. Clean. Prod.* **2018**, *189*, 67–77. [CrossRef]
4. Li, J.; Han, M.; Muhammad, Y.; Liu, Y.; Su, Z.; Yang, J.; Yang, S.; Duan, S. Preparation and properties of SBS-G-GOS-modified asphalt based on a thiol-ene click reaction in a bituminous environment. *Polymers* **2018**, *10*, 1264. [CrossRef]
5. Wang, S.; Cheng, D.; Xiao, F. Recent developments in the application of chemical approaches to rubberized asphalt. *Constr. Build. Mater.* **2017**, *131*, 101–113. [CrossRef]
6. Yu, H.; Leng, Z.; Gao, Z. Thermal analysis on the component interaction of asphalt binders modified with crumb rubber and warm mix additives. *Constr. Build. Mater.* **2016**, *125*, 168–174. [CrossRef]
7. Farina, A.; Zanetti, M.C.; Santagata, E.; Blengini, G.A. Life cycle assessment applied to bituminous mixtures containing recycled materials: Crumb rubber and reclaimed asphalt pavement. *Resour. Conserv. Recycl.* **2017**, *117*, 204–212. [CrossRef]
8. Xiao, F.; Li, R.; Amirkhanian, S.; Yuan, J. Rutting-resistance investigation of alternative polymerized asphalt mixtures. *J. Mater. Civ. Eng.* **2018**, *30*, 04018116. [CrossRef]
9. Yu, J.; Yu, X.; Gao, Z.; Guo, F.; Wang, D.; Yu, H. Fatigue Resistance Characterization of Warm Asphalt Rubber by Multiple Approaches. *Appl. Sci.* **2018**, *8*, 1495. [CrossRef]
10. Puga, K.L.N.N.; Williams, R.C. Low temperature performance of laboratory produced asphalt rubber (AR) mixes containing polyoctenamer. *Constr. Build. Mater.* **2016**, *112*, 1046–1053. [CrossRef]
11. Eskandarsefat, S.; Sangiorgi, C.; Dondi, G.; Lamperti, R. Recycling asphalt pavement and tire rubber: A full laboratory and field scale study. *Constr. Build. Mater.* **2018**, *176*, 283–294. [CrossRef]
12. Yu, H.; Leng, Z.; Dong, Z.; Tan, Z.; Guo, F.; Yan, J. Workability and mechanical property characterization of asphalt rubber mixtures modified with various warm mix asphalt additives. *Constr. Build. Mater.* **2018**, *175*, 392–401. [CrossRef]
13. Oliveira, J.R.M.; Silva, H.M.R.D.; Abreu, L.P.F.; Fernandes, S.R.M. Use of a warm mix asphalt additive to reduce the production temperatures and to improve the performance of asphalt rubber mixtures. *J. Clean. Prod.* **2013**, *41*, 15–22. [CrossRef]
14. Yu, J.; Ren, Z.; Yu, H.; Wang, D.; Svetlana, S.; Korolev, E.; Gao, Z.; Guo, F. Modification of asphalt rubber with nanoclay towards enhanced storage stability. *Materials* **2018**, *11*, 2093. [CrossRef]
15. Samieadel, A.; Schimmel, K.; Fini, E.H. Comparative life cycle assessment (LCA) of bio-modified binder and conventional asphalt binder. *Clean Technol. Environ. Policy* **2018**, *20*, 191–200. [CrossRef]
16. Dong, Z.; Zhou, T.; Luan, H.; Wang, H.; Xie, N.; Xiao, G.Q. Performance evaluation of bio-based asphalt and asphalt mixture and effects of physical and chemical modification. *Road Mater. Pavement Des.* **2018**. [CrossRef]
17. Sun, D.; Sun, G.; Du, Y.; Zhu, X.; Lu, T.; Pang, Q.; Shi, S.; Dai, Z. Evaluation of optimized bio-asphalt containing high content waste cooking oil residues. *Fuel* **2017**, *202*, 529–540. [CrossRef]
18. Yang, X.; You, Z.; Mills-Beale, J. Asphalt binders blended with a high percentage of biobinders: Aging mechanism using ftir and rheology. *J. Mater. Civ. Eng.* **2015**, *27*, 04014157. [CrossRef]
19. Yu, H.; Leng, Z.; Xiao, F.; Gao, Z. Rheological and chemical characteristics of rubberized binders with non-foaming warm mix additives. *Constr. Build. Mater.* **2016**, *111*, 671–678. [CrossRef]
20. Yu, H.; Leng, Z.; Zhou, Z.; Shih, K.; Xiao, F.; Gao, Z. Optimization of preparation procedure of liquid warm mix additive modified asphalt rubber. *J. Clean. Prod.* **2017**, *141*, 336–345. [CrossRef]
21. Pellinen, T.K.; Witczak, M.W.; Bonaquist, R.F. Asphalt mix master curve construction using sigmoidal fitting function with non-linear least squares optimization. In Proceedings of the 15th ASCE Engineering Mechanics Conference, New York, NY, USA, 2–5 June 2002; Volume 27.
22. American Association of State and Highway Transportation Officials. Grading or verifying the performance grade (PG) of an asphalt binder. In *AASHTO Standard R 29*; American Association of State and Highway Transportation Officials: Washington, DC, USA, 2013.
23. Zhou, F.; Mogawer, W.; Li, H.; Andriescu, A.; Copeland, A. Evaluation of Fatigue Tests for Characterizing Asphalt Binders. *J. Mater. Civ. Eng.* **2013**, *25*, 610–617. [CrossRef]
24. Ding, Y.; Huang, B.; Shu, X. Investigation of functional group distribution of asphalt using liquid chromatography transform and prediction of molecular model. *Fuel* **2018**, *227*, 300–306. [CrossRef]
25. Wang, D.; Li, D.; Yan, J.; Leng, Z.; Wu, Y.; Yu, J.; Yu, H. Rheological and chemical characteristic of warm asphalt rubber binders and their liquid phases. *Constr. Build. Mater.* **2018**, *193*, 547–556. [CrossRef]

26. Yang, S.-H.; Lee, L.-C. Characterizing the chemical and rheological properties of severely aged reclaimed asphalt pavement materials with high recycling rate. *Constr. Build. Mater.* **2016**, *111*, 139–146. [CrossRef]
27. Kim, S.; Lee, S.H.; Kwon, O.; Han, J.Y.; Kim, Y.S.; Kim, K.W. Estimation of service-life reduction of asphalt pavement due to short-term ageing measured by GPC from asphalt mixture. *Road Mater. Pavement Des.* **2016**, *17*, 153–167. [CrossRef]
28. Yang, Z.; Zhang, X.; Zhang, Z.; Zou, B.; Zhu, Z.; Lu, G.; Xu, W.; Yu, J.; Yu, H. Effect of aging on chemical and rheological properties of bitumen. *Polymers* **2018**, *10*, 1345. [CrossRef]
29. Fini, E.H.; Kalberer, E.W.; Shahbazi, A.; Basti, M.; You, Z.; Ozer, H.; Aurangzeb, Q. Chemical characterization of biobinder from swine manure: Sustainable modifier for asphalt binder. *J. Mater. Civ. Eng.* **2011**, *23*, 1506–1513. [CrossRef]
30. Fini, E.H.; Oldham, D.J.; Abu-Lebdeh, T. Synthesis and characterization of biomodified rubber asphalt: Sustainable waste management solution for scrap tire and swine manure. *J. Environ. Eng.* **2013**, *139*, 1454–1461. [CrossRef]
31. Ghavibazoo, A.; Abdelrahman, M. Composition analysis of crumb rubber during interaction with asphalt and effect on properties of binder. *Int. J. Pavement Eng.* **2013**, *14*, 517–530. [CrossRef]
32. Leite, L.F.M.; Constantino, R.S.; Vivoni, A. Rheological studies of asphalt with ground tire rubber. *Road Mater. Pavement Des.* **2011**, *2*, 125–139. [CrossRef]

polymers

MDPI

Article

Pollutant Absorption as a Possible End-Of-Life Solution for Polyphenolic Polymers

Thomas Sepperer, Jonas Neubauer, Jonas Eckardt, Thomas Schnabel, Alexander Petutschnigg and Gianluca Tondi *

Forest Products Technology & Timber Constructions Department, Salzburg University of Applied Sciences, Marktstraße 136a, 5431 Kuchl, Austria; thomas.sepperer@fh-salzburg.ac.at (T.S.); jonas.neubauer@fh-salzburg.ac.at (J.N.); jonas.eckardt@fh-salzburg.ac.at (J.E.); thomas.schnabel@fh-salzburg.ac.at (T.S.); alexander.petutschnigg@fh-salzburg.ac.at (A.P.)
* Correspondence: gianluca.tondi@fh-salzburg.ac.at; Tel.: +43-50-2211-2250

Received: 16 April 2019; Accepted: 17 May 2019; Published: 20 May 2019

Abstract: Tannin- and lignin-furanic foams are natural porous materials that have attracted high interest in the scientific and industrial communities for their high thermal and fire-resistant properties. However, no interesting solutions have been proposed for the management of their end-life as yet. In this study, the phenolic-furanic powders derived from the foams were analyzed for their capacity to remove different pollutants like neutral, cationic, and anionic organic molecules from wastewater. It was observed that the macromolecules produced from initially bigger fractions were more suitable to remove methylene blue and sodium dodecyl sulfate (SDS) while contained absorptions were observed for riboflavin. Acidified tannin powders were also prepared to understand the role of the flavonoid in the absorption mechanism. The latter showed outstanding absorption capacity against all of the tested pollutants, highlighting the key-role of the flavonoid fraction and suggesting the limited contribution of the furanic part. All adsorbents were investigated through FT-IR and solid state ^{13}C-NMR. Finally, the powders were successfully regenerated by simple ethanol washing, showing almost complete absorption recovery.

Keywords: Bio-based foams; wastewater treatments; cationic dyes; anionic surfactants; pollutant adsorbents; tannin polymer; tannin-furanic foam

1. Introduction

Water plays a major role in many industrial activities such as the textile dyeing and washing, chemical manufacturing, and heavy-metal mining [1–5]. During these processes, the water is often contaminated with different pollutants including, but are not limited to, surfactants (e.g., alkylphenol ethoxylates, sodium dodecyl sulfate), heavy metal ions (e.g., lead, copper, mercury), and dyes (methylene blue, amaranth or tartrazine). Therefore, effluents derived from these industries have to be regenerated before the water is reinserted into its natural cycle.

There are several strategies to approach wastewater treatment that range from well-known processes like filtration, flocculation, and decantation to specially designed adsorbents or by-products of the agricultural industry [6–9].

A recent study presented interesting organic hydrogels and inorganic nanocomposites for the removal of methylene blue dyes with very high adsorptions [10–12]. Anionic surfactants are generally removed from wastewater by using anaerobic bacteria [13,14], though cationic polymers have recently also been applied as absorbents [15]. Neutral organic molecules are removed by using active carbons [16,17].

Natural polyphenols such as lignin and tannins are characterized by high numbers of aromatic and hydroxyl groups [18] and their combination with furanic structures [19] could further enhance their capacity to establish tight secondary forces with organic pollutants.

First generation tannin-furanic foams have already been studied for their capacity to absorb pollutants [20–23] and heavy-metals [24,25], but unfortunately contained formaldehyde, which have hindered their development as an insulation material for buildings.

More recently, formaldehyde-free furanic foams made of tannin and lignin have been prepared [26,27]. These products have attracted high scientific and industrial interest due to their completely natural skeletal constitution, their high thermal insulating performance, and their fire and water resistance [28–30]. At present, the major drawbacks for these materials are: (i) the heterogeneous nature of the tannin extract that contains several non-phenolics like sugars and proteins, and (ii) the undefined strategy for the end-life of this material. In recent studies, easy extraction processes for improving the purity of the fraction have been carried out [31,32] and tannin foams based on these extract have also been synthesized [33]. However, regarding the end-life of the product, no alternatives to the partial recycling of the foams have been proposed as yet [34].

The objective of this study was to observe the absorption properties of the polyphenolic-furanic powders derived from the foams against three different classes of pollutants (anionic, cationic, and neutral) in order to find an interesting end-life application for these materials.

2. Materials and Methods

2.1. Chemicals

Mimosa (Acacia mearnsii) tannin powder "Weibull AQ" was supplied by Tanac SA (Montenegro, RS, Brazil). Black liquor was supplied by Lenzing AG (Lenzing, Austria). For the production of the foams, furfuryl alcohol was supplied by Trans Furans Chemicals (Geel, Belgium). Diethylether and sulfuric acid 98% were purchased from Merck (Darmstadt, Germany). The other chemicals used were technical grade acetone, formaldehyde (37%), chloroform, methylene blue, sodium dodecyl sulfate and riboflavin, all purchased from VWR (Darmstadt, Germany) and Roth (Karlsruhe, Germany).

2.2. Adsorbent Preparation

The preparation of the foams was undertaken by homogenizing the tannin (or tannin-black liquor (BL) mixture) with water, furfuryl alcohol (FOH), formaldehyde (37% water solution), and diethylether (DEE). Afterward, sulfuric acid (4 M) was added and the suspension was further stirred to obtain a homogeneous blend that was poured into a wooden mold. The mold was then covered and placed in a laboratory hot press for 5 min at different temperatures for expansion. Table 1 summarizes the produced foams and the exact synthesis procedure can be found in previous studies [27,29,33,34].

Table 1. Formulations used for foam production.

Foam	Tannin [%]	FOH [%]	DEE [%]	H_2O [%]	H_2SO_4 [%]	CH_2O/BL [%]	Temperature [°C]
Standard	41.9	25.9	5.6	8.4	18.2	-	90
Acetone soluble	41.9	25.9	5.6	8.4	18.2	-	90
Acetone insoluble	41.9	25.9	5.6	8.4	18.2	-	90
Tannin-Lignin	29.6	20.7	3.3	-	16.8	29.6	120
Formaldehyde	44.3	27.5	5.9	-	13.4	8.9	45

The foams were successively pulverized using a mortar and pestle and washed with distilled water. Afterward, the powders were dried in a convection oven at 103 °C and finally washed with ethanol to remove all unreacted chemicals. After drying, the powders were sieved and those of a particle size up to 250 μm were used for the adsorption experiments.

Acidified tannin gel was prepared following the procedure described by [5,35,36] with modifications concerning the acid amount and reaction time. In more detail, the tannin gel was synthesized by mixing 20% of tannin powder with 40% water, afterward, 40% of concentrated sulfuric acid (98%) was added and a reflux condenser was attached to the flask. The mixture was kept under magnetic stirring and heated to 100 °C for 2 h. The precipitate was recovered through glass filtering and this acidified tannin gel was used as a flavonoid reference after washing with water and ethanol and final drying at 103 °C.

2.3. Adsorption Experiments

Three different water contaminants were tested: (i) riboflavin, (ii) sodium dodecyl sulfate, and (iii) methylene blue (structures shown in Figure 1). Methylene blue was chosen to represent cationic dyes, particularly since this compound can be hazardous in higher concentrations [7]. The second class of chemicals were anionic surfactants and were represented by sodium dodecyl sulfate, which is harmful to water organisms as it denatures proteins and also causes irritation to humans [37,38]. As a representative for neutral charged components, but also to represent pharmaceuticals, riboflavin was the third tested pollutant. Aqueous solutions containing 20 ppm of the pollutants were prepared to determine the absorption capacity. An equivalent of 1 mg of absorbent was added per 5 mL of the solution and magnetically stirred for 48 h in the dark to avoid photo-degradation of the compounds at ambient temperature. After this period, the adsorption was considered complete and saturation of the adsorbents was expected [21].

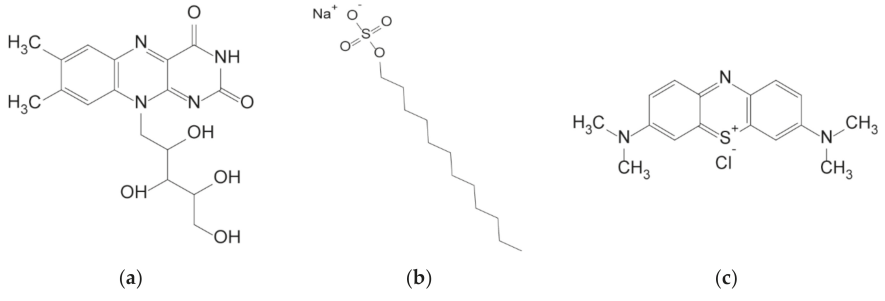

Figure 1. Chemical formula of the three pollutants tested: **(a)** riboflavin; **(b)** SDS; **(c)** methylene blue.

The remaining concentration of riboflavin and methylene blue were determined using a Shimadzu UVmini 1240 UV/vis spectrophotometer (Shimadzu, Kyoto, Japan). After adsorption, the solutions were centrifuged at 3000 rpm for 3 min and the absorption of the supernatant was measured at 450 nm for riboflavin and 656 nm for methylene blue. A multipoint calibration curve for both compounds was created (R^2 = 0.9999).

To determine the remaining SDS concentration, the assay described by [39] was used. Therefore, a 0.5 % methylene blue solution was diluted 100 fold with a pH stable medium (pH 7.2). A total of 0.5 mL of the sample (after adsorption) was mixed with 0.25 mL of the methylene blue solution in a reaction vial. Afterward, 1.5 mL of chloroform was added and vortexed twice for 3 s each. The mixture was then centrifuged at 3000 rpm for 3 min. Then, the chloroform layer was transferred to a quartz cuvette and the absorption was read at 656 nm. All measurements were performed in triplicate.

Furthermore, the adsorption capacity q of each foam was calculated using Equation (1). The results are expressed as mg pollutant absorbance per g adsorbent.

$$q = \frac{(C_0 - C_1) \cdot V}{W} \quad (1)$$

where C_0 and C_1 are the initial and the equilibrium concentration of pollutant (ppm), respectively, and V (mL) and W (mg) are the volume of the solution and the mass of the adsorbent, respectively.

2.4. ATR FT-IR Investigation

The polyphenolic powders (tannin foams, acidified tannin gel, and original tannin powder) were scanned with an FT-IR Frontier (Perkin-Elmer, Waltham, MA, USA) spectrometer coupled with an ATR miracle unit. The spectra were registered in triplicate with 32 scans in the spectral region between 4000 and 600 cm^{-1} with a resolution of 4 cm^{-1}. The spectra were then investigated in the spectral region between 1800 and 600 cm^{-1}, averaged, normalized, and baseline corrected with the software KnowItAll (BioRad, California, USA).

2.5. Solid State ^{13}C-NMR

Spectra of the standard tannin foam, the acidified tannin gel, and the original tannin powder were obtained on a Bruker Avance NEO 500 wide bore system (Bruker BioSpin, Rheinstetten, Germany) at the NMR Center of the Faculty of Chemistry, University of Vienna. A 4 mm triple resonance magic angle spinning (MAS) probe was used with a resonance frequency for ^{13}C at 125.78 MHz and the MAS rotor spinning was set to 14 kHz. Cross polarization (CP) was achieved by a ramped contact pulse with a contact time of 2 ms. During acquisition, ^{1}H was high power decoupled using SPINAL with 64 phase permutations. The chemical shifts for ^{13}C are reported in ppm and are referenced external to adamantane by setting the low field signal to 38.48 ppm.

The data elaboration was done with the software Top-spin 4.0.6 (Bruker) and OriginPro (OriginLab) while the calculations of the theoretical chemical shifts were done with the software NMR-Predict developed by the University of Lausanne (L. Patiny) and the University of del Valle (J. Wist) [40–42].

2.6. Regeneration of the Adsorbents

As methylene blue is particularly well soluble in ethanol and chloroform, a cheap and easy method to regenerate the adsorbents after adsorption was developed. A total of 150 mg of foam powders were washed with 150 mL of ethanol at different temperatures (ambient, 50 °C, and boiling) in a magnetically stirred beaker for 10 min. Afterward, the mixture was filtrated and the foam could be recovered. Furthermore, it is possible to separate the methylene blue from the ethanol at reduced pressure to repurpose the solvent.

The regenerated foams were further tested for their adsorption capacity and the results were compared with the first adsorption cycle.

2.7. Statistical Analysis

ANOVA and Tukey's post hoc test were performed at a significance level of $\alpha = 0.05$ using the IBM SPSS 25 statistics processor to determine significant differences between the adsorbents.

3. Results and Discussion

3.1. Pollutant Removal

Table 2 shows a summary of the removal capacities of the investigated polymer powders.

It was evident that the nature of the pollutant had a major influence in the remediation capacity of the powders: charged pollutants like the anionic surfactant SDS and even more of the cationic dye methylene blue were significantly adsorbed, while the neutral riboflavin was much less adsorbed. This observation confirms the finding of previous research when heavy-metal cations were absorbed [25]. It was also observed that (i) the higher initial molecular mass (acetone insoluble and tannin-lignin) and (ii) the highly cross-linked (formaldehyde) polymers had a positive effect on the absorption of the pollutants.

Table 2. Adsorption capacities [mg/g] of the foams against different pollutants.

Foam	Riboflavin [1]	SDS [1]	Methylene blue [1]
Standard	3.8 ± 0.81 ^{a,b}	24.1 ± 0.31 ^{a}	45.4 ± 0.31 ^{a}
Acetone soluble	4.8 ± 0.88 ^{a,b,c}	20.3 ± 0.34 ^{a}	33.2 ± 1.29 ^{b}
Acetone insoluble	7.6 ± 0.28 ^{c}	32.7 ± 2.05 ^{b}	63.3 ± 2.33 ^{c}
Tannin-Lignin	6.0 ± 1.41 ^{b,c}	32.8 ± 2.46 ^{c}	73.8 ± 2.40 ^{d}
Formaldehyde	2.1 ± 1.48 ^{a}	32.6 ± 2.05 ^{b}	56.9 ± 1.92 ^{e}

[1] Same letters in a column suggest no significant difference at α.

A positive effect of the lignin was observed when compared to the results for adsorption by tannin based polymers in the literature. Similar materials adsorbed roughly 45 mg methylene blue per gram adsorbent and 22 mg SDS per gram of the tannin polymer [21]. The results also exceeded the adsorption capacity of other agricultural by-products like hazelnut shells [43] or spruce wood [7]. However, as soon as the adsorbents are specifically designed for the removal of pollutants, the absorptions skyrocket (e.g., 200 mg/g for the simultaneous removal of methylene blue and oil by polymer membranes [10] or lignin derived activated carbons with 550 mg/g [44]).

The adsorption mechanism of SDS on flavonoids was studied by Liu and Guo where they stated that the more negatively charged B and C ring interacted with the SDS [45]. This finding and the well-known interaction between SDS and proteins can explain the removal of SDS from solution by tannin based polymers. A further aspect to be considered for understanding the adsorption mechanism for methylene blue is the natural electrostatic attraction between the cationic dye and the flavonoid units [9].

Acidified tannin gels were produced and their pollutant absorption capacity were investigated to understand the contribution of tannin in the absorption process. The results of pollutant absorption capacity measured with the same parameters are reported in Figure 2, which highlights that the adsorptions obtained for this powder were much higher than that registered for the polyphenolic-furanic polymers.

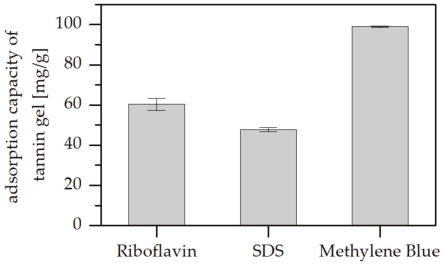

Figure 2. Adsorption capacity of the tannin gel against different pollutants.

These high adsorptions suggest that the major contribution to the absorption process is given by the tannin part, while the furanic moieties of the polymers limit the establishment of secondary forces with the pollutants. These unexpected results further addressed the interest in the chemistry of the adsorbents, therefore a detailed chemical characterization of the powders was carried out.

3.2. Adsorbent Characterization

In Figure 3, the FT-IR spectra of the tannin foam, acidified tannin gel, and tannin powder are presented.

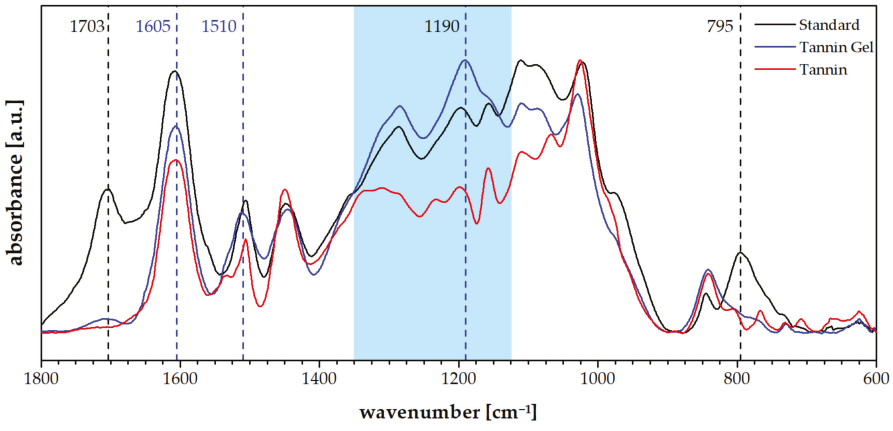

Figure 3. FT-IR spectra of the standard foam (black), the tannin acidified gel (blue), and the tannin extract (red).

The spectra of the tannin gel presented a similar profile to the standard foam except for a decrease in the signals typically due to the furanic moieties like the carbonyl group at 1703 cm^{-1} and the signal at 795 cm^{-1}, which were attributed to furanic C–H bending (out-of-plane) [46]. The tannin gel also presented a very different profile to the tannin powder and particularly, a higher absorption at 1605 and 1510 cm^{-1}, which suggests increased aromatic contribution as well as a general increase in the region between 1350 and 1100 cm^{-1}, which is dominated by C_{arom}–O vibrations [47]. The band at 1190 cm^{-1}, which was higher for the tannin gel than for the foam, and the tannin powder could be attributed to the interflavonoid vibrations [48].

The solid state ^{13}C-NMR analysis of the adsorbing powders and of the tannin powder was performed and is reported in Figure 4.

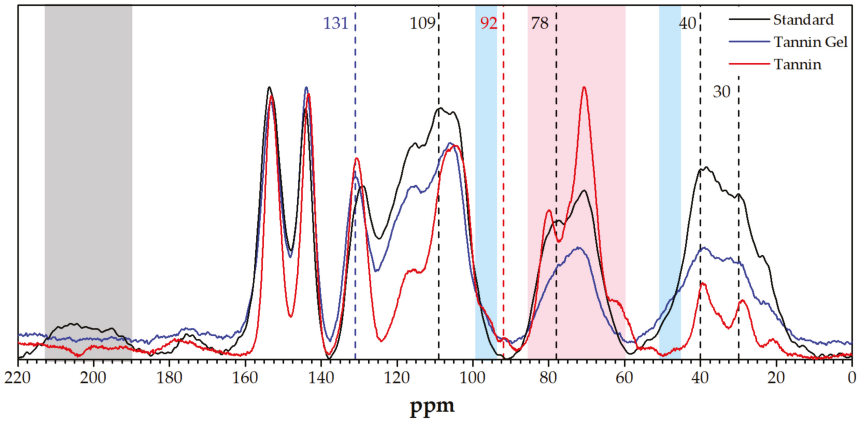

Figure 4. Solid-state ^{13}C-NMR spectra of the standard foam (black), the tannin acidified gel (blue), and the tannin extract (red).

Comparing the spectra of the foam with that of the gel, we observed that the bands attributed to the furanic part decreased in the tannin gel, in particular, the carbonyl signal due to γ-diketons resulting from the furanic ring opening at 210–190 [49] disappeared, the furan band at around 110 ppm

decreased, and the methylene signals between furans at around 30 ppm decreased. Additionally, the signals due to the second polymerization step of furfuryl alcohol decreased, especially the ones at around 80 and 40 ppm (due to furanic ring opening and Diels–Alder rearrangements) [50]. Differences between the tannin gel and the tannin powder could also be highlighted through this technique. In particular, we observed that the region between 85 and 60 ppm dramatically decreased, together with the small peak at 92 ppm. These signals can be attributed to carbohydrates, confirming that in the acidified tannin gel in this fraction was removed (e.g., hydrolyzed and leached out). Furthermore, the signal at 130 ppm was significantly increased together with the shoulder band at 45 ppm, while the shoulder at 97 ppm disappeared. These results suggest that the unreacted C6 and C8 of the tannin were involved in establishing new interflavonoid bonds [51,52].

The two spectroscopic investigations highlighted that tannin gel has a similar chemistry to the tannin foam without furanic contribution and differs from the tannin powder because: (i) the carbohydrate fraction is removed, and (ii) the molecular mass is increased through the establishment of further interflavonoid bonds. The gel is then constituted by higher molecular mass flavonoids, no furanics, and no sugars, which explains its outstanding absorption activity.

3.3. Regeneration

These adsorbing materials have shown an interesting absorption capacity, especially for charged pollutants, therefore their regeneration was considered by washing them with ethanol. Table 3 shows the regeneration of the standard foam after the methylene blue adsorption test at 21, 50, and 79 °C (the boiling point of ethanol).

Table 3. Adsorption capacity of the standard foam washed in ethanol at different temperatures.

Foam Condition	Removal Capacity [mg/g]	Compared to Initial Removal [%]
Fresh	45.38 ± 0.31	-
Washed at 21 °C	44.03 ± 0.21	97.6
Washed at 50 °C	44.96 ± 0.58	99.2
Washed at 79 °C	44.77 ± 0.48	98.7

It can be stated that almost all of the absorbing sites were already free after washing with ethanol at room temperature. This means that the foams can be almost completely regenerated with a contained removal decrease, suggesting that these materials are suitable for several removal cycles.

4. Conclusions

The present study had the objective to understand the possibility of using tannin and tannin-lignin furanic powder as a pollutant adsorbent in wastewater treatments. We discovered that these materials have high affinities for cationic dyes and anionic surfactants, while low absorption was observed for the neutral molecules (riboflavin). The flavonoid backbone of the macromolecule is the moiety that positively contributes to the absorption because acidified tannin gels present much higher absorptions. On the other hand, the furanic part limits the pollutant adsorption because the number of reactive sites on the flavonoids is reduced by the presence of furanic moieties. Furthermore, the higher dimension of the starting building blocks (e.g., lignin containing) and the higher crosslinking degree (e.g., formaldehyde, acidified gel) contribute to increasing the absorption capacity due to the minor chance for the furanic part to hinder the absorption activity of the flavonoids. This finding was also confirmed through spectroscopic analysis of the acidified tannin gels, which highlighted the increase of interflavonoid linkages in the tannin. Notwithstanding the limiting contribution of the furanic part, we can determine that the tannin foams can be used as a pollutant absorbent at the end of their life, especially because the absorbing capacity can be almost completely recovered after simple ethanol bathing.

Author Contributions: Conceptualization, T.S. and G.T.; Resources, T.S., J.N., J.E.; Formal Analysis, T.S.; Investigation, T.S.; Writing—Original Draft Preparation, G.T. and T.S.; Writing—Review and Editing, G.T.; Visualization, T.S.; Supervision, G.T.; Funding Acquisition, G.T., A.P., and T. Sch.

Funding: The authors would like to acknowledge the support from European funding INTERREG Italy–Austria for the project InCIMa ITAT 1023.

Conflicts of Interest: The authors declare no conflict of interest. The funders had no role in the design of the study; in the collection, analyses, or interpretation of data; in the writing of the manuscript, or in the decision to publish the results.

References

1. Pala, A.; Tokat, E. Color removal from cotton textile industry wastewater in an activated sludge system with various additives. *Water Res.* **2002**, *36*, 2920–2925. [CrossRef]
2. Gurung, M.; Adhikari, B.B.; Kawakita, H.; Ohto, K.; Inoue, K.; Alam, S. Recovery of Au(III) by using low cost adsorbent prepared from persimmon tannin extract. *Chem. Eng. J.* **2011**, *174*, 556–563. [CrossRef]
3. Kawakita, H.; Abe, M.; Inoue, J.I.; Ohto, K.; Harada, H.; Inoue, K. Selective gold recovery using orange waste. *Sep. Sci. Technol.* **2009**, *44*, 2797–2805. [CrossRef]
4. Parajuli, D.; Kawakita, H.; Kajiyama, K.; Ohto, K.; Harada, H.; Inoue, K. Recovery of gold from hydrochloric acid by using lemon peel gel. *Sep. Sci. Technol.* **2008**, *43*, 2363–2374. [CrossRef]
5. Parajuli, D.; Kawakita, H.; Inoue, K.; Ohto, K.; Kajiyama, K. Persimmon peel gel for the selective recovery of gold. *Hydrometallurgy* **2007**, *87*, 133–139. [CrossRef]
6. Alila, S.; Boufi, S. Removal of organic pollutants from water by modified cellulose fibres. *Ind. Crops Prod.* **2009**, *30*, 93–104. [CrossRef]
7. Janoš, P.; Coskun, S.; Pilařová, V.; Rejnek, J. Removal of basic (Methylene Blue) and acid (Egacid Orange) dyes from waters by sorption on chemically treated wood shavings. *Bioresour. Technol.* **2009**, *100*, 1450–1453. [CrossRef]
8. Uddin, M.T.; Islam, M.A.; Mahmud, S.; Rukanuzzaman, M. Adsorptive removal of methylene blue by tea waste. *J. Hazard. Mater.* **2009**, *164*, 53–60. [CrossRef]
9. Wang, G.; Chen, Y.; Xu, G.; Pei, Y. Effective removing of methylene blue from aqueous solution by tannins immobilized on cellulose microfibers. *Int. J. Biol. Macromol.* **2019**, *129*, 198–206. [CrossRef]
10. Cao, J.; Zhang, J.; Zhu, Y.; Wang, S.; Wang, X.; Lv, K. Novel Polymer Material for Efficiently Removing Methylene Blue, Cu(II) and Emulsified Oil Droplets from Water Simultaneously. *Polymers (Basel)* **2018**, *10*, 1393. [CrossRef]
11. Yu, K.; Wang, D.; Wang, Q.; Yu, K.; Wang, D.; Wang, Q. Tough and Self-Healable Nanocomposite Hydrogels for Repeatable Water Treatment. *Polymers (Basel)* **2018**, *10*, 880. [CrossRef]
12. Ge, M.; Xi, Z.; Zhu, C.; Liang, G.; Hu, G.; Jamal, L.; Alam S. M., J. Preparation and Characterization of Magadiite–Magnetite Nanocomposite with Its Sorption Performance Analyses on Removal of Methylene Blue from Aqueous Solutions. *Polymers (Basel)* **2019**, *11*, 607. [CrossRef]
13. Delforno, T.P.; Moura, A.G.L.; Okada, D.Y.; Sakamoto, I.K.; Varesche, M.B.A. Microbial diversity and the implications of sulfide levels in an anaerobic reactor used to remove an anionic surfactant from laundry wastewater. *Bioresour. Technol.* **2015**, *192*, 37–45. [CrossRef] [PubMed]
14. Karray, F.; Mezghani, M.; Mhiri, N.; Djelassi, B.; Sayadi, S. Scale-down studies of membrane bioreactor degrading anionic surfactants wastewater: Isolation of new anionic-surfactant degrading bacteria. *Int. Biodeterior. Biodegradation* **2016**, *114*, 14–23. [CrossRef]
15. Hussain, S.; Malik, A.H.; Iyer, P.K. Highly Precise Detection, Discrimination, and Removal of Anionic Surfactants over the Full pH Range via Cationic Conjugated Polymer: An Efficient Strategy to Facilitate Illicit-Drug Analysis. *ACS Appl. Mater. Interfaces* **2015**, *7*, 3189–3198. [CrossRef]
16. Ali, I.; Asim, M.; Khan, T.A. Low cost adsorbents for the removal of organic pollutants from wastewater. *J. Environ. Manage.* **2012**, *113*, 170–183. [CrossRef] [PubMed]
17. Zietzschmann, F.; Stützer, C.; Jekel, M. Granular activated carbon adsorption of organic micro-pollutants in drinking water and treated wastewater—Aligning breakthrough curves and capacities. *Water Res.* **2016**, *92*, 180–187. [CrossRef]
18. Quideau, S.; Deffieux, D.; Douat-Casassus, C.; Pouységu, L. Plant Polyphenols: Chemical Properties, Biological Activities, and Synthesis. *Angew. Chemie Int. Ed.* **2011**, *50*, 586–621. [CrossRef]

19. Pizzi, A.; Tondi, G.; Pasch, H.; Celzard, A. Matrix-assisted laser desorption/ionization time-of-flight structure determination of complex thermoset networks: Polyflavonoid tannin-furanic rigid foams. *J. Appl. Polym. Sci.* **2008**, *110*, 1451–1456. [CrossRef]
20. Sánchez-Martín, J.; Beltrán-Heredia, J.; Carmona-Murillo, C. Adsorbents from Schinopsis balansae: Optimisation of significant variables. *Ind. Crops Prod.* **2011**, *33*, 409–417. [CrossRef]
21. Sánchez-Martín, J.; Beltrán-Heredia, J.; Delgado-Regaña, A.; Rodríguez-González, M.A.; Rubio-Alonso, F. Optimization of tannin rigid foam as adsorbents for wastewater treatment. *Ind. Crops Prod.* **2013**, *49*, 507–514. [CrossRef]
22. Sánchez-Martín, J.; González-Velasco, M.; Beltrán-Heredia, J. Acacia mearnsii de Wild Tannin-Based Flocculant in Surface Water Treatment. *J. Wood Chem. Technol.* **2009**, *29*, 119–135. [CrossRef]
23. Sánchez-Martín, J.; González-Velasco, M.; Beltrán-Heredia, J.; Gragera-Carvajal, J.; Salguero-Fernández, J. Novel tannin-based adsorbent in removing cationic dye (Methylene Blue) from aqueous solution. Kinetics and equilibrium studies. *J. Hazard. Mater.* **2010**, *174*, 9–16. [CrossRef] [PubMed]
24. Inoue, K.; Paudyal, H.; Nakagawa, H.; Kawakita, H.; Ohto, K. Selective adsorption of chromium(VI) from zinc(II) and other metal ions using persimmon waste gel. *Hydrometallurgy* **2010**, *104*, 123–128. [CrossRef]
25. Tondi, G.; Oo, C.W.; Pizzi, A.; Trosa, A.; Thevenon, M.F. Metal adsorption of tannin based rigid foams. *Ind. Crops Prod.* **2009**, *29*, 336–340. [CrossRef]
26. Link, M.; Kolbitsch, C.; Tondi, G.; Ebner, M.; Wieland, S.; Petutschnigg, A. Formaldehyde-free tannin-based foams and their use as lightweight panels. *BioResources* **2011**, *6*, 4218–4228.
27. Tondi, G.; Link, M.; Kolbitsch, C.; Lesacher, R.; Petutschnigg, A. Pilot plant up-scaling of tannin foams. *Ind. Crops Prod.* **2016**, *79*, 211–218. [CrossRef]
28. Grishechko, L.I.; Amaral-Labat, G.; Szczurek, A.; Fierro, V.; Kuznetsov, B.N.; Pizzi, A.; Celzard, A. New tannin–lignin aerogels. *Ind. Crops Prod.* **2013**, *41*, 347–355. [CrossRef]
29. Tondi, G.; Pizzi, A. Tannin-based rigid foams: Characterization and modification. *Ind. Crops Prod.* **2009**, *29*, 356–363. [CrossRef]
30. Kolbitsch, C.; Link, M.; Petutschnigg, A.; Wieland, S.; Tondi, G. Microwave Produced Tannin-furanic Foams. *J. Mater. Sci. Res.* **2012**, *1*. [CrossRef]
31. Sepperer, T.; Petutschnigg, A.; Bogner, B.; Oostingh, G.; Hernandez-Ramos, F.; Labidi, J.; Tondi, G. Purification of industrial tannin extract through simple solid-liquid extractions - submitted. *Ind. Crops Prod.* **2018**.
32. Missio, A.L.; Tischer, B.; dos Santos, P.S.B.; Codevilla, C.; de Menezes, C.R.; Barin, J.S.; Haselein, C.R.; Labidi, J.; Gatto, D.A.; Petutschnigg, A.; et al. Analytical characterization of purified mimosa (*Acacia mearnsii*) industrial tannin extract: Single and sequential fractionation. *Sep. Purif. Technol.* **2017**, *186*, 218–225. [CrossRef]
33. Sepperer, T.; Tondi, G. Tannin-furanic foams from purified extracts. In Proceedings of the 5th International Conference on Processing Technologies for the Forest and Biobased Industries, PTF-BPI, Freising/Munich, Germany, 20–21 September 2018.
34. Tondi, G.; Link, M.; Kolbitsch, C.; Gavino, J.; Luckeneder, P.; Petutschnigg, A.; Herchl, R.; Van Doorslaer, C. Lignin-based Foams: Production Process and Characterization. *BioResources* **2016**, *11*. [CrossRef]
35. Shan, W.; Ren, F.; Zhang, Q.; Wan, L.; Xing, Z.; Lou, Z.; Xiong, Y. Enhanced adsorption capacity and selectivity towards molybdenum in wastewater by a persimmon tannin waste based new adsorbent. *J. Chem. Technol. Biotechnol.* **2015**, *90*, 888–895. [CrossRef]
36. Jiang, X.; Liu, Y.; Wu, Y.; Tan, H.; Meng, F.; Wang, Y.S.; Li, M.; Zhao, L.; Liu, L.; Qian, Y.; et al. Analysis of accumulation patterns and preliminary study on the condensation mechanism of proanthocyanidins in the tea plant [Camellia sinensis]. *Sci. Rep.* **2015**, *5*. [CrossRef]
37. Bhuyan, A.K. On the mechanism of SDS-induced protein denaturation. *Biopolymers* **2010**, *93*, 186–199. [CrossRef] [PubMed]
38. Marrakchi, S.; Maibach, H.I. Sodium Lauryl Sulfate-Induced Irritation in the Human Face: Regional and Age-Related Differences. *Skin Pharmacol. Physiol.* **2006**, *19*, 177–180. [CrossRef]
39. Hayashi, K. A rapid determination of sodium dodecyl sulfate with methylene blue. *Anal. Biochem.* **1975**, *67*, 503–506. [CrossRef]
40. Banfi, D.; Patiny, L. Resurrecting and Processing NMR Spectra On-line. *Chim. Int. J. Chem.* **2008**, *62*, 280–281. [CrossRef]

41. Steinbeck, C.; Krause, S.; Kuhn, S. NMRShiftDBConstructing a Free Chemical Information System with Open-Source Components. *J. Chem. Inf. Comput. Sci.* **2003**, *43*, 1733–1739. [CrossRef]
42. Castillo, A.M.; Patiny, L.; Wist, J. Fast and accurate algorithm for the simulation of NMR spectra of large spin systems. *J. Magn. Reson.* **2011**, *209*, 123–130. [CrossRef]
43. Doğan, M.; Abak, H.; Alkan, M. Adsorption of methylene blue onto hazelnut shell: Kinetics, mechanism and activation parameters. *J. Hazard. Mater.* **2009**, *164*, 172–181. [CrossRef] [PubMed]
44. Lin, J.; Zhao, G. Preparation and characterization of high surface area activated carbon fibers from lignin. *Polymers (Basel)* **2016**, *8*. [CrossRef]
45. Liu, W.; Guo, R. Interaction between flavonoid, quercetin and surfactant aggregates with different charges. *J. Colloid Interface Sci.* **2006**, *302*, 625–632. [CrossRef]
46. Tondi, G.; Link, M.; Oo, C.W.; Petutschnigg, A. A simple approach to distinguish classic and formaldehyde-free tannin based rigid foams by ATR FT-IR. *J. Spectrosc.* **2015**, *2015*. [CrossRef]
47. Tondi, G.; Petutschnigg, A. Middle infrared (ATR FT-MIR) characterization of industrial tannin extracts. *Ind. Crops Prod.* **2015**, *65*, 422–428. [CrossRef]
48. Taylor, P.; Ricci, A.; Olejar, K.J.; Parpinello, G.P.; Kilmartin, P.A. Application of Fourier Transform Infrared (FTIR) Spectroscopy in the Characterization of Tannins. **2015**, *50*, 37–41.
49. Tondi, G. Tannin-Based Copolymer Resins: Synthesis and Characterization by Solid State 13C NMR and FT-IR Spectroscopy. *Polymers (Basel)* **2017**, *9*, 223. [CrossRef]
50. Tondi, G.; Sepperer, T.; Cefarin, N.; Musso, M.; Reyer, A.; Vaccari, L. Multi-technique investigation of poly-furfuryl alcohol - submitted. *Macromolucules* **2019**.
51. Pizzi, A. Tannin based Wood Adhesives Technology. In *Advanced Wood Adhesives Technology*; Decker: New York, NY, USA, 1994; p. 304. ISBN 9780824792664.
52. Pizzi, A.; Stephanou, A. A comparative C13 NMR study of polyflavonoid tannin extracts for phenolic polycondensates. *J. Appl. Polym. Sci.* **1993**, *50*, 2105–2113. [CrossRef]

polymers

MDPI

Article

Core-Shell Structured HMX@Polydopamine Energetic Microspheres: Synergistically Enhanced Mechanical, Thermal, and Safety Performances

Congmei Lin [1,2], Feiyan Gong [1,*], Zhijian Yang [1,*], Xu Zhao [1], Yubin Li [1], Chengcheng Zeng [1], Jiang Li [2] and Shaoyun Guo [2]

[1] Institute of Chemical Material, China Academy of Engineering Physics, Mianyang 621900, China; lincmei2009@caep.cn (C.L.); xuzhao@caep.cn (X.Z.); liyubin030102@caep.cn (Y.L.); zengcc1314@caep.cn (C.Z.)

[2] The State Key Laboratory of Polymer Materials Engineering, Polymer Research Institute of Sichuan University, Chengdu 610065, China; li_jiang@scu.edu.cn (J.L.); nic7702@scu.edu.cn (S.G.)

* Correspondence: freya@caep.cn (F.G.); zhijianyang@caep.cn (Z.Y.)

Received: 25 February 2019; Accepted: 19 March 2019; Published: 26 March 2019

Abstract: The solid–solid phase transition, poor mechanical properties, and high sensitivity has impeded further practical applications of 1,3,5,7-tetranitro-1,3,5,7-tetrazocane (HMX) based polymer bonded explosives (PBXs). To address these issues together, a facile and effective route was employed to achieve a coating of polydopamine (PDA) on the surface of explosive crystals via in situ polymerization of dopamine. Additionally, PBXs based on HMX@PDA microcapsules were prepared with a fluoropolymer as polymer binder. Improved storage modulus, static mechanical strength and toughness, and creep resistance has been achieved in as-prepared PDA modified PBXs. The β-δ phase transition temperature of as-obtained PBXs based on conventional HMX (C-HMX)@PDA was improved by 16.3 °C. The friction sensitivity of the C-HMX based PBXs showed a dramatic drop after the PDA coating. A favorable balance proposed in this paper among thermal stability, mechanical properties, and sensitivity was achieved for C-HMX based PBXs with the incorporation of PDA.

Keywords: bio-inspired interfaces; mechanical properties; thermal stability; sensitivity

1. Introduction

Energetic materials (EMs) contain high chemical energy, in which organic small molecular crystals act as functional materials. For decades, they have attracted increasing interest for their significant applications in both military and civil fields. Among them, 1,3,5,7-tetranitro-1,3,5,7-tetrazocane (HMX) and HMX-based formulations have been extensively studied, due to the high detonation energy and high melting point [1,2]. However, the high sensitivity towards external mechanical stimuli, phase transition under thermal insult, and poor mechanical properties induced by weak adhesive properties with polymer binder are main shortcomings which limit its applications.

Several strategies have been established to desensitize HMX, including preparing HMX with higher crystal quality by recrystallization [3], designing energetic cocrystals [4], synthesizing HMX@insensitive explosive core-shell microparticles [5,6], and coating the HMX crystal with polymers via in situ polymerization [7]. However, the energetic cocrystals and core-shell microparticles which combine the HMX with large amounts of insensitive explosive reduce the energy output. Due to the difficulty in controlling the mass transfer, the polymer binder cannot be completely coated onto explosive crystals at the large-scale production by the in situ polymerization.

Another limitation for the application of HMX energetic crystal is that it undergoes a solid–solid β-δ phase transition under thermal shock, which is harmful for the long-term storage and transportation

of materials. Solid–solid phase transition causes expansion [8] and extensive microstructural damage [9], such as mesoscale evolution of voids and porosity, which tend to act as hot spots under external impact or shock, making the heated HMX based explosives more sensitive [10,11]. So far, coating approaches have been mainly developed to tune the phase transition temperature of the explosives [12]. Additives of TATB and olefin in high concentration can form compact coatings on the HMX crystals to delay the nucleations of δ-HMX and build up a heat conduction obstacle, leading to a higher temperature required for the β-δ phase transition [13]. The phase transition of HMX explosives can be greatly improved after core-shell coating of melamine-formaldehyde resin, with the appreciable increment of more than 16 °C [7]. However, the high concentration of shell materials is necessary to completely coat explosive crystals. In contrast, fewer additives lead to larger free surface area of HMX, which accelerates the phase transition [13]. Furthermore, solid–solid phase transition of explosive crystals depends on the chemical interaction between explosives and binders, which may promote or delay the phase transition [14].

Polymer bonded explosives (PBXs) are typical polymer-based energetic composites with a high loading of solid explosive crystals. The mechanical properties of PBX composites are determined in part by the chemical structure and bonding at the interface between constituents in the microstructure [15]. Mechanical failure paths tend to primarily run around the interface between crystals and the binder matrix and avoid regions of fine filler and binder [16]. This can lead to materials with abundant cracks, which is harmful for the safety and reliability of the explosive. Considerable efforts have been undertaken to increase the interfacial interaction and mechanical properties of HMX and HMX-based composites. A common and convenient method is the addition of neutral polymer bonding agent (NPBA) to achieve interfacial reinforcement [17]. In situ polymerization of hydroxyethyl acrylate-acrylate-acrylonitrile copolymer and isophorone diisocyanate is also applied to the coating on HMX surfaces [18]. It is shown that forming a cross-linked polymeric coating on HMX plays a role for interfacial reinforcement between HMX fillers and polymeric binders, resulting in a 21% increase of the tensile strength. Another technique is the fabrication of core-shell microparticles, such as HMX@nano-TATB composites [19]. It significantly changes the surface morphology of HMX and the interface adhesion state between particles and polymer binder, resulting in the enhancement of mechanical properties. Among them, it is still a big challenge to precisely control the surface structure and morphology for the application of NPBA and in situ polymerization. Besides, the production scale of HMX@nano-TATB core-shell particles is difficult to amplify for engineering applications, due to the extraordinary low solubility of TATB in common solvents.

Up until now, mussel-inspired coating with the in-situ polymerization of dopamine has raised increasing interest and has been frequently used to coat various substrates, such as glass, metal, polymer, and nanocarbon materials [20–28]. Recently, there have been some reports on the application of dopamine chemistry to energetic crystal processing, such as HMX, hexanitrohexaazaisowurtzitane (CL-20), and 1,3,5-triamino-2,4,6-trinitrobenzene (TATB) [29–31]. It has been found that in situ polymerization of dopamine can provide a facile and versatile method for modifying the surfaces of energetic crystals. However, little work has been done to explore the application of well-coated energetic crystals in PBXs and its effects on the comprehensive performance.

The balance among the explosive performances, including the sensitivity, thermal stability, and mechanical properties of the energetic material, is fraught with challenges. Such three performances of PBX often constrain each other, and it is very difficult to synergistically improve. Therefore, novel techniques to acquire better balance and super comprehensive performance should be explored. The strong chemical adhesion to form the robust and compact core-shell structure and high rigidity of polydopamine (PDA) enables it to provide a great potential to efficiently reduce the sensitivity and improve the thermal stability and mechanical properties of energetic materials without a sacrifice of detonation power. In this work, we demonstrate a facile in situ polymerization approach to synthesize core-shell microparticles with a high-energy HMX core and a PDA shell. Then, the polymer binder was added to further coat HMX@PDA microspheres and prepare PBXs. The crystal quality and particle size of HMX crystals are varied to study their effects on the thermal and mechanical behavior of PBXs.

Additionally, the amount of PDA in core-shell microparticles is varied to investigate the dependence of the comprehensive properties on the degree of coating.

2. Experimental Section

2.1. Materials

Three kinds of HMX were used, including a conventional one of industrial grade (C-HMX) and two recrystallized samples with reduced sensitivity (RS-HMX). The C-HMX was purchased (Baiyin Chemical Industry Co., Ltd., Baiyin, China) and used without further purification. RS-HMX with fine and large grains were marked as FRS-HMX and LRS-HMX, respectively. Dopamine and (hydroxymethyl)aminomethane (Tris) were obtained from Sigma-Aldrich (St. Louis, MI, USA) and used as received. Ultrapure water with a resistivity of 18.2 MΩ·cm was prepared with a Milli-Q apparatus (Millipore, Billerica, MA, USA). A vinylidene fluoride (VDF) and chlorotrifluoroethylene (CTFE) copolymer provided by Zhonghao Chenguang Chemical Industry Co., Ltd. (Zigong, China) was used as polymer binders.

2.2. Sample Preparations

The preparation of core-shell structured HMX@PDA and PBX composites are illustrated in Figure 1. The PDA-coated HMX were synthesized as follows: Tris solution (10 mM) was prepared and adjusted to pH of 8.5 by HCl solution. 100 g HMX crystals were added to 3000 mL Tris solution and dispersed under high-intensity ultrasonic irradiation for 5 min. Then, 6 g dopamine was added to the suspension whilst stirring at room temperature. After filtering and washing with a large quantity of ultrapure water several times to remove excessive PDA in the solution, the PDA-coated HMX particles were obtained by drying at 60 °C in a vacuum oven. In this paper, samples were denoted as *x*HMX@PDA-*y*h, where *x* represented the HMX particle type and *y* represented the PDA coating time. For example, C-HMX@PDA-3h represented the matrix was C-HMX and the corresponding PDA coating time was 3 h.

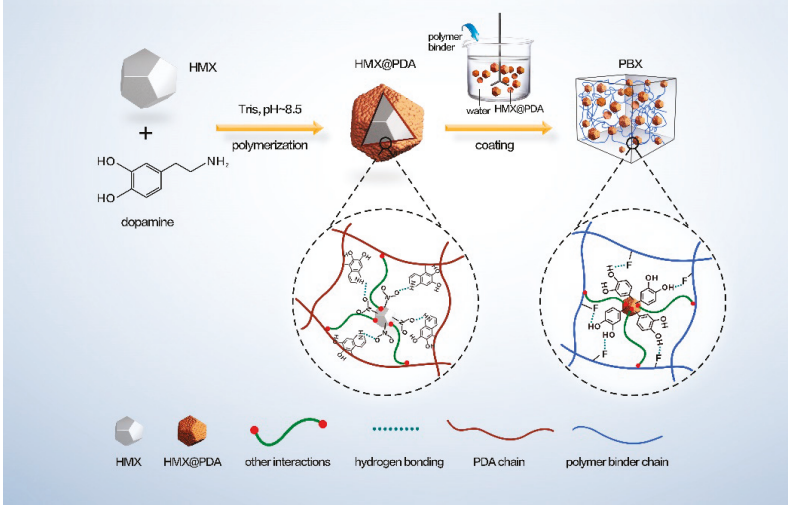

Figure 1. Proposed schematic preparation procedure and enhancement mechanism for polydopamine (PDA) modified polymer bonded explosives (PBXs).

The molding powders of various PBX formulations were prepared by water suspension method. For distinguishing purposes, PBX based on C-HMX, FRS-HMX, and LRS-HMX were labeled as

PBX-C-yh, PBX-F-yh, and PBX-L-yh, respectively, where *y* represented PDA coating time. For instance, PBX-C-3h represented PBX based on the C-HMX with the corresponding PDA coating time of 3 h. The obtained molding powders were then dried in a vacuum oven at 60 °C for 48 h. To test the mechanical and creep properties of the PBXs, the molding powders were pressed in a mold and transformed into explosive pellets with a given geometrical shape.

2.3. Material Characterizations

The coating content of the PDA shell was quantitatively analyzed by a high-performance liquid chromatography (HPLC, Agilent, Santa Clara, CA, USA). The morphologies and structures of various HMX@PDA samples were characterized by matching refractive index (OMMRI), scanning electron microscopy (SEM, Zeiss, Oberkochen, Germany), X-ray photoelectron energy spectrum (XPS, Thermo Fisher Scientific, Waltham, MA, USA), laser particle size analyzer (LPSA, Beckman Coulter, Brea, CA, USA), Fourier-transform infrared spectra (FT-IR, Thermo Fisher Scientific, Waltham, MA, USA), Raman spectra (Renishaw, Gloucestershire, UK), and X-ray diffraction (XRD, Bruker, Karlsruhe, Germany). The thermal properties of the HMX and corresponding PBXs were analyzed by using a differential scanning calorimeter (DSC, Mettler, Zurich, Swiss). The mechanical reinforcement effect of PDA on various HMX and PBX composites was investigated by compressive stiffness tests (CST), dynamic mechanical analysis (DMA), creep, Brazilian, and compression tests. The mechanical sensitivity measurements were conducted according to GJB-772A-97 standard method 601.2 and 602.1 [32]. Detailed characterization methods and processes are shown in Electronic Supplementary Information (ESI).

3. Results and Discussion

3.1. Morphological and Structural Features of Core-Shell HMX@PDA Particles

The morphologies of three HMX raw crystals are exhibited in Figure S1 in ESI. RS-HMX crystals possessed a more regular diamond-like shape, less internal defects, and a narrower particle size distribution than that of C-HMX. The amount of PDA for core-shell HMX@PDA can be tuned by simply varying the coating time (Table S1 in ESI). With increased coating time, the white HMX crystals gradually changed from gray to thick brown with increasing PDA coating amount (Figure S2 in ESI). The average particle size of C-HMX, FRS-HMX, and LRS-HMX was 47.0, 44.8, and 149.1 μm, respectively. Compared with the raw materials, the average particle size for the FRS-HMX@PDA became smaller, suggesting the better dispersion of the particle powders due to the PDA coating.

The surface morphologies of the raw HMX materials and PDA coated HMX crystals were investigated in detail using SEM measurements, as shown in Figure 2. The surface morphologies of the C-HMX and FRS-HMX crystals exhibited ignorable change after PDA modification. It may be attributable to the difference in surface features and specific surface area. However, the color change of C-HMX and FRS-HMX crystals with the polymerization time was similar to that of LRS-HMX@PDA composites (Figure S2 in ESI). The white HMX crystals gradually changed from pale brown to a deep brown with the increase of PDA contents. Furthermore, the resistance ability to electron beams was also gradually increased, as examined by the C-HMX crystals. Neat HMX was sensitive to electron beams and a lot of cracks were observed on the crystal surface. With a uniform and compact PDA coating shell, the amount of cracks on the crystal surface gradually relieved, indicating that the PDA coating could enhance the high power electron beam bombardment resistance of HMX. The influences of electron beam time on the evolution of surface morphology for C-HMX@PDA-9h composites were also investigated and depicted in Figure S3 in ESI. Undistinguishable cracks could be observed after exposing C-HMX@PDA-9h under electron beam for 3 min, which could be possibly attributed to the protection of PDA.

In addition, the surface of LRS-HMX crystals was smooth, while LRS-HMX@PDA was observed as a relatively rough surface made up of compact and continuous PDA shell. It can be seen from

Figure 2 that more PDA particles and a thicker PDA coating layer formed on the LRS-HMX surface with the processing time increasing from 3 to 6 h, building up a uniform and compact shell. Moreover, PDA agglomeration could be obviously observed on the LRS-HMX surface when the reaction time increased to 9 h.

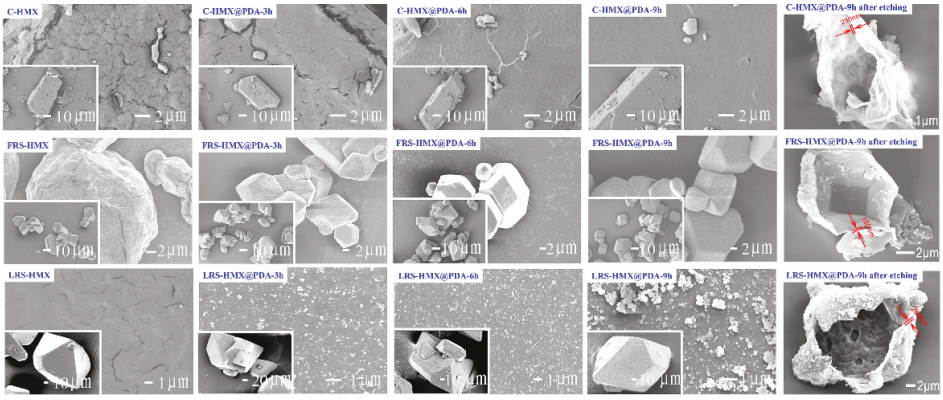

Figure 2. SEM micrographs of the structure morphologies for different HMX and PDA coated specimens.

A core-etching technique was introduced, using acetone as the etching solvent. SEM characterization of the indiscerptible PDA shells was carried out and the results are also shown in Figure 2, exhibiting a hollow PDA shell structure of HMX@PDA after the etching treatment. The PDA shell maintained the shape of the HMX crystal, with the inner surface reflecting the roughness of interface between PDA and HMX. The shape of particles of C-HMX samples was irregular with a rough surface, while a relatively smooth surface for RS-HMX can be obtained. Furthermore, for core-shell samples, the thickness of PDA shell was at nano scale, depending on the HMX matrix.

Element states on the surface of energetic microcapsules could be conducted by XPS analyses [33]. The C 1s, O 1s, and N 1s spectra for FRS-HMX, PDA, and various FRS-HMX@PDA samples are shown in Figure 3. The characteristic peaks of C 1s, O 1s, and N 1s spectra for HMX and PDA were in accordance with the results of the previous reports [5,34]. The corresponding functional groups of PDA coated composites are marked in Figure 3.

According to quantitative analysis, the surface element composition of FRS-HMX, PDA, and FRS-HMX@PDA composites are listed in Table S2 in ESI. The coating efficiency of PDA can be also estimated from XPS results by the change of N/C ratio. The N/C ratio on the surface of FRS-HMX@PDA composites was gradually close to that of PDA, indicating the successful surface modification by PDA. With the increase in polymerization time from 3 to 9 h, the decrease in N/C ratio from 0.485 to 0.287 indicated the gradual deposition of PDA content on the surface of microcapsules. XPS atomic concentration of functional groups in all atoms of HMX, PDA, and HMX@PDA are summarized in Table S3 in ESI. The concentration ratios of C–NH–C group (in PDA)/NO_2 group (in FRS-HMX) from N 1s spectrum were 0.21, 0.40, and 0.58 for FRS-HMX@PDA-3h, FRS-HMX@PDA-6h, FRS-HMX@PDA-9h composites, respectively. The results indicated a successful coating of PDA on the FRS-HMX step by step. Hence, the perfect core-shell structure of HMX@PDA microcapsules was further confirmed by XPS.

The crystal structures were further investigated by Raman spectrum, X-ray diffractometry (XRD) patterns, and Fourier-transform infrared (FT-IR) spectra. After surface modification by dopamine solution, a new absorption signal from Raman spectrum in Figure S4a appeared at 1580–1700 cm^{-1}, which can be attributable to the typical feature of G bands in PDA [35]. In Figure S4b, all diffraction peaks of HMX and HMX/PDA can be indexed to β-HMX (JCPDS card No. 42-1768), indicating the polymorph nature of the crystals did not change. FT-IR results in Figure S4c indicated that the

PDA coated composites displayed a combination of the characteristic peaks of the functional groups in HMX [36] and PDA [37]. In addition, the values of the initial secant modulus (ISM) calculated according to Ref. [38] were dependent on the PDA content (Figure S4d and Table S1 in ESI). Due to the enhancement of the density of cross-linked network, the ISM of these core-shell HMX@PDA composites increased with increasing the content of PDA.

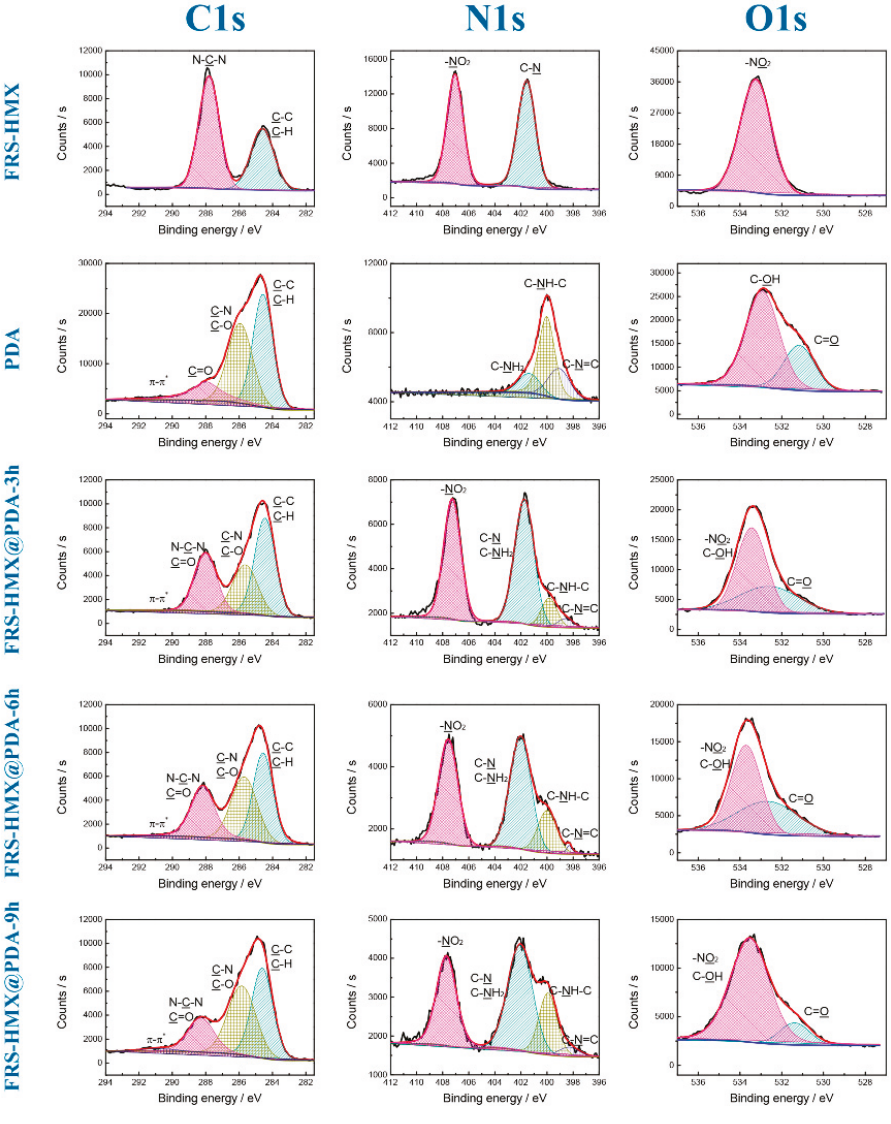

Figure 3. XPS of the uncoated FRS-HMX crystals, PDA, and FRS-HMX@PDA microparticles.

3.2. Detonation Properties of PBXs Based on HMX@Polydopamine

According to the Urizar equation, the detonation velocity of composites explosive (D) could be calculated by:

$$w_i = \frac{V_i}{\sum V_i} \tag{1}$$

$$D = \sum w_i D_i \quad (2)$$

where V_i denotes the volume of component i, w_i is the volume fraction of component i, and D_i is the characteristic detonation velocity of component i, respectively. The characteristic detonation velocity for HMX and insensitive materials (PDA and fluoropolymer) are about 9150 and 5400 m/s, respectively. In order to maintain detonation performance unchanged, the mass fraction of HMX in the formulation remained a certain value of 95%. The calculated theoretical detonation velocity is listed in Table S4. It can be found that the difference of detonation velocity of all the formulations was less than 0.32%.

3.3. Mechanical Properties of PBXs Based on HMX@Polydopamine

Figure S5 reflects the dependence of the dynamic mechanical properties, including storage modulus (E') and loss factor (tan δ) on the temperature for PDA modified PBXs. With the incorporation of PDA, the value of storage modulus was improved due to the enhanced interface. An inflexion, corresponding to the T_g of corresponding fluoropolymer binders [39], could be observed in the loss factor curves between 45–75 °C for the PBXs.

Static compressive and Brazilian tests were also conducted to analyze the effect of PDA modification on the mechanical properties of PBXs. Representative mechanical characteristics were summarized in Figure 4 and Table S4 in ESI, indicating an obvious enhanced mechanical property after PDA modification. Generally, the compressive and tensile strength and elongation at break were higher than the corresponding samples without PDA coating, suggesting a reinforcing and toughening role of PDA in PBX. The compressive fracture energy (W_c) and the tensile fracture energy (W_t), obtained by the integration of the stress–strain curves, could be used to characterize the toughness of explosive materials. PBXs with a PDA polymerization time of 6 h presented optimal mechanical properties. PBX-C-6h, PBX-F-6h, and PBX-L-6h composites showed 40.1%, 17.4%, and 38.4% improvement in W_t compared to the corresponding pristine PBX-C, PBX-F, and PBX-L samples, respectively.

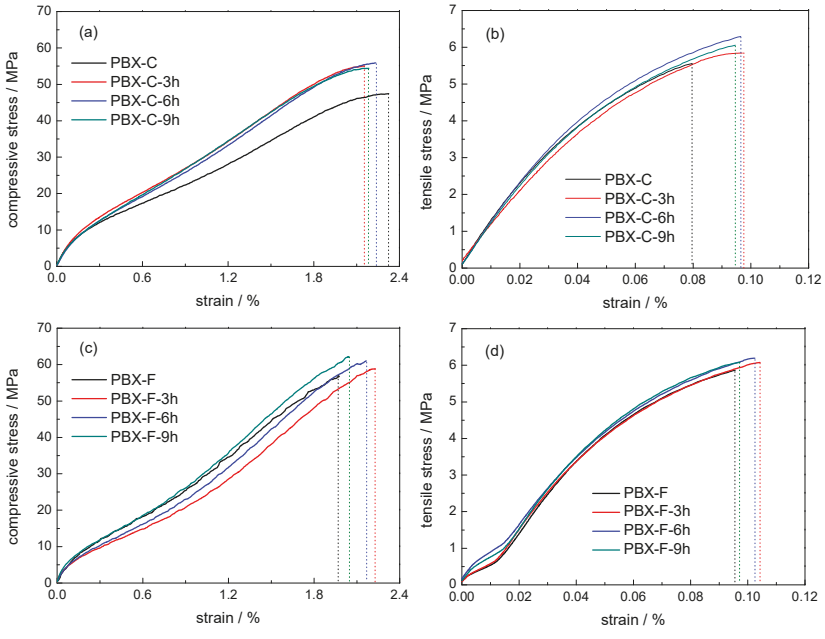

Figure 4. *Cont.*

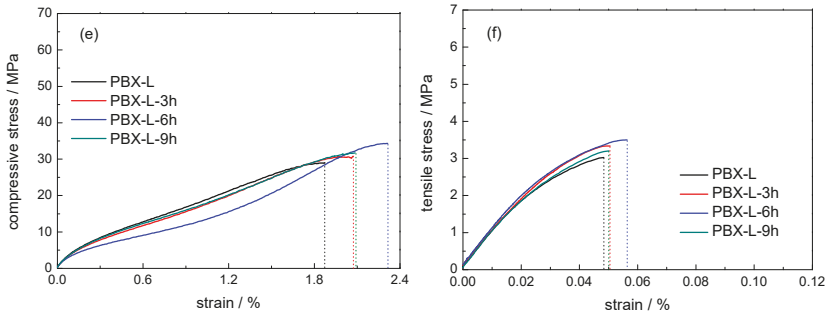

Figure 4. The typical mechanical response at room temperature for PDA modified PBXs: compressive test (**a**,**c**,**e**); Brazilian test (**b**,**d**,**f**).

Consequently, creep analysis was applied to analyze the effects of PDA content on the non-linear viscoelastic properties for PBXs. As shown in Figure 5, the introduction of PDA significantly decreased the creep strain at low temperatures (30 and 45 °C) and prolonged the creep failure time at high temperatures (60 and 80 °C), illustrating the reinforcing effect of PDA on the creep resistance of the materials. Obviously, PBXs with PDA polymerization time of 6 h exhibited an excellent improvement in creep resistance, which agreed with the above dynamic and static mechanical results. It can be associated with the significant improvement interfacial interaction between HMX crystals and polymer binders, achieved by the incorporation of PDA, and thus restriction of the mobility of polymer chains.

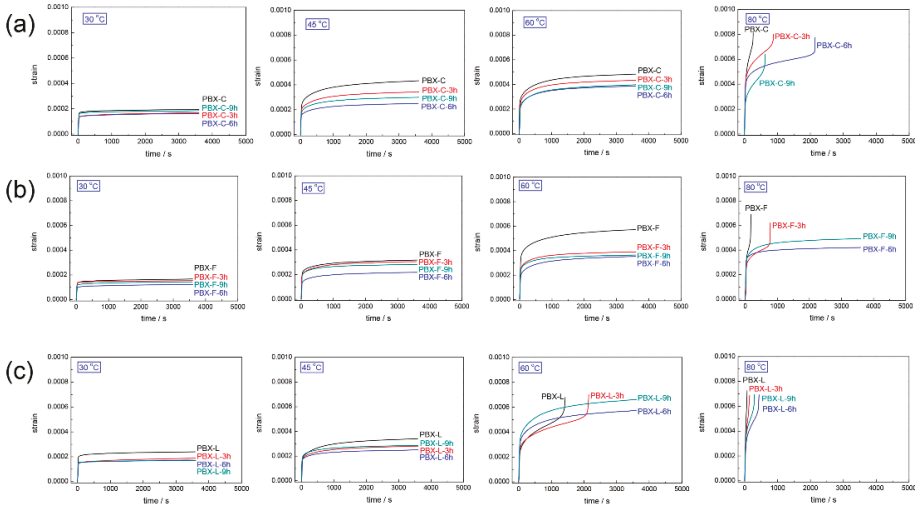

Figure 5. Time-dependent creep strain of PBXs at different temperatures under 4 MPa: (**a**) PDA modified PBX-C, (**b**) PDA modified PBX-F, (**c**) PDA modified PBX-L.

3.4. Mechanism for the Enhancement of Mechanical Properties

To summarize the synthetic procedure of PDA shell and enhancement mechanism in PBXs, a schematic mechanism was proposed in Figure 1. The gradual in situ polymerization of dopamine was coated or deposited on the HMX crystal surface. Sufficient noncovalent interactions, including π–π stacking, charge transfer, and hydrogen bonding between the N–O groups in the HMX molecules and the catechol groups in the PDA chains, were carried out between the PDA and HMX

crystals [32]. Subsequently, the compact and uniform PDA shell was formed to give core-shell energetic microcapsules.

As the polymer binder was added, the PDA layer acted as an interfacial platform to construct a bridge between HMX and fluoropolymer. Sufficient interaction, including hydrogen bonding interactions and other interactions, would be carried out between the PDA molecules and HMX explosives. The supramolecular interactions, such as hydrogen bonding etc., could contribute to and be important interaction mechanisms between PDA and fluoropolymers. The hydrogen bonds with the OH groups as proton donors and F groups in the fluoropolymer chains as proton acceptors constructed a physical cross-linking network [40]. As a result, PDA formed multiple interfacial interactions with HMX crystal and fluoropolymer binders to modify mechanical behavior.

3.5. Thermal Properties of PBXs Based on HMX@Polydopamine

Figure 6 and Table S5 in ESI show the DSC results of PDA modified HMX-based PBXs. The DSC curve of PBX-C displayed an endothermic peak at 201.5 °C and an exothermic peak at 286.4 °C, corresponding to the β-δ phase transition and the thermal decomposition of HMX, respectively. The thermal decomposition temperature of HMX for the PDA modified PBXs was almost the same as that for the original PBX material. Notably, the polymorphic phase transition peaks shifted increasingly to 206.0, 209.0, and 217.8 °C for the PDA modified PBX-C samples with PDA coating for 3, 6, and 9 h.

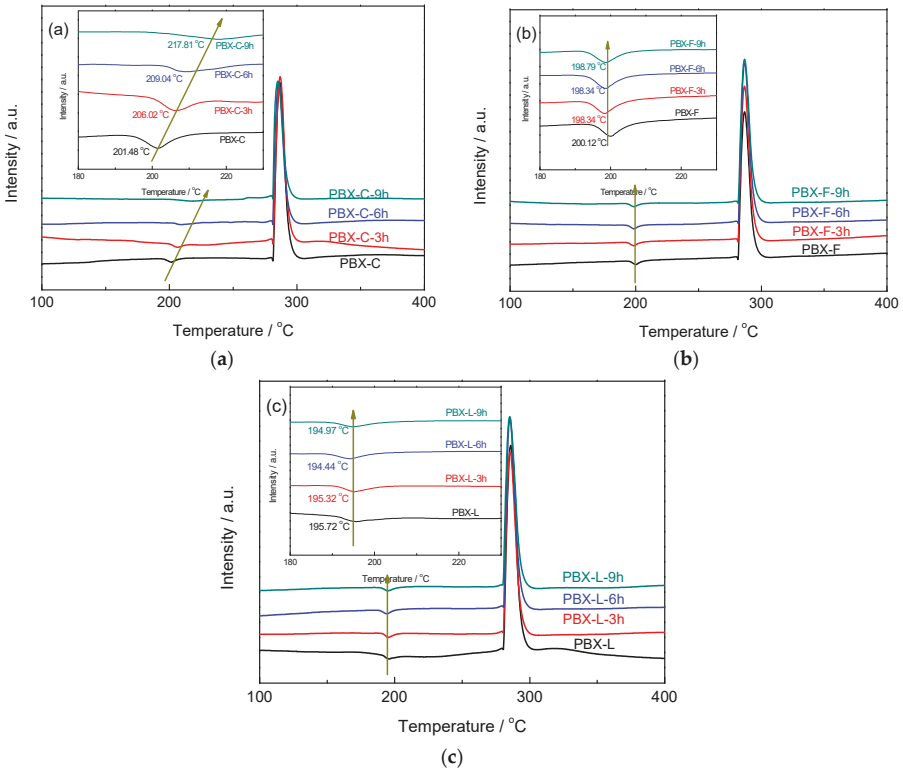

Figure 6. DSC curves of PDA modified PBXs: (**a**) PDA modified PBX-C, (**b**) PDA modified PBX-F, (**c**) PDA modified PBX-L.

The phase transition behavior of core-shell structured HMX@PDA microcapsules without polymer binder were also studied by DSC analysis to further reveal the phase transition mechanism of PDA

modified PBXs. Corresponding results and peak data were demonstrated in Figure S6 and Table S6 in ESI. Compared with the naked C-HMX, the phase transition peak of PBX-C with fluoropolymer as polymer binder showed a slight shift to lower temperature, indicating the unconspicuous role of fluoropolymer towards the phase transition. The phase transition temperature increased with increasing PDA content for core-shell HMX@PDA samples, revealing the enhanced polymorph stability of C-HMX explosives by core-shell coating with PDA. C-HMX@PDA-9h sample exhibited an appreciable increment of temperature peaks by more than 30 °C. Some interesting phenomena were found for PDA modified RS-HMX-based PBXs. Even when the phase transition temperature of HMX for RS-HMX@PDA microcapsules was shifted to ~220 °C, the phase transition temperatures of HMX in PDA modified RS-HMX-based PBXs showed negligible retardation compared with the original RS-HMX-based PBXs.

The difference of coverage degree between the C-HMX@PDA and RS-HMX@PDA composites (Figure 2) could be used to better understand the relationship between the coating structure and thermal phase transition properties of HMX@PDA composites. According to a lattice Monte Carlo simulation, it was found that the morphology of the filler surface was one of the primary factors which influenced the interactions at the interface of polymer matrix-filler particle [41]. PBX was a typical particle-filled polymer-based composite with a high loading of solid explosive crystals. Consequently, the geometry of the energetic crystal surface played a crucial role in determining the interfacial interactions. Besides, compared with the smooth surface of RS-HMX, the rough surface of C-HMX formed an "interlocking block" [40] with PDA to enhance the interfacial interaction.

To further study the relationship between the structure evolvement during the water suspension process and the phase transition of HMX, the effects of solvent, temperature, and stirring on coverage degree of HMX@PDA composites were investigated. As shown in Figure S7 in ESI, after immersion in the ethyl acetate/butyl acetate solvent or water for 1 h or dried in a vacuum oven at 70 °C for 1 h, no distinct difference on the morphology of HMX@PDA composites could be observed, indicating slight influences of solvent, water, and temperature on as-obtained core-shell structure. However, after stirring in the water for 1 h, the surface of HMX@PDA composites cracked. Compared with C-HMX@PDA-9h, stirring could lead to void in the surface of RS-HMX@PDA-9h tending towards both a larger size and higher void concentration. The slight destruction of core-shell structure for C-HMX@PDA-9h after granulation caused the phase transition temperatures of HMX in PBXs to decrease, compared with that of the C-HMX@PDA microcapsules. The high destruction of the core-shell structure during granulation was the main course of no change in the phase transition temperatures of HMX in PDA modified RS-HMX-based PBXs, compared with raw HMX.

3.6. Sensitivity Study of PBXs Based on HMX@Polydopamine

The results of impact and friction sensitivity studies of the PDA modified PBXs are summarized in Table 1. The impact sensitivity of PDA modified PBXs remained consistent with raw PBXs (100%), which can be attributed to the following reasons. Firstly, crystal defects were usually responsible for the impact sensitivity, which was enhanced by the growth of hot-spots that originated from crystal defects during impact and adiabatic compression [42]. PDA coating did not change the amounts of defects. Generally, soft coating was helpful to insensitive design by absorbing the impact energy to reduce hot-spots formation. PDA coating was not soft enough to make a difference. Secondly, heat absorbing materials such as wax can alleviate the hot-spots formation during impact, but PDA was not heat absorbing material. Based on these reasons, PDA coating had no effect on hot-spots formation and impact sensitivity.

As shown in Table 1, the friction sensitivity of PDA modified PBXs varied with the crystal quality and particle size of the HMX crystal, depending on the interfaces interaction intension. The introduction of PDA coating had led to more insensitive composites than the original PBX-C. The friction sensitivity of PBX-C-9h samples decreased to 40%, compared with that of the original PBX-C (84%). The same level of sensitivity had been measured for PBX-F samples with and without PDA coating (about 30%). Similar

results have been found for the PBX-L used in this study, with a friction sensitivity of 100%. In the friction sensitivity test, the ignition mechanism was a viscous heating of explosive material subjected to extreme velocity gradients as the explosive was violently deformed between the rigid surfaces [43]. This viscous heating mechanism depended on the explosive/polymers interfaces interaction intension. A larger surface roughness of C-HMX benefited a stronger PDA coating; as a result, their interfacial interaction intension was higher than that between PDA coating and RS-HMX, with a smaller surface roughness. The SEM images showed that the PDA coating was damaged in the RS-HMX@PDA coating system during the granulation process, while no similar result was observed in the C-HMX@PDA coating system. One can conclude that PDA benefited the C-HMX/fluoropolymer system as a desensitizer, and not for other systems. A similar example was reported by Bazaki [44]. The catalysts they added in ammonium perchlorate (AP) were responsible for the friction sensitivity by accelerating the AP decomposition, but not responsible for the fall hammer sensitivity.

Table 1. Impact and friction sensitivities for conventional HMX/fluoropolymer (PBX-C), PDA modified conventional HMX/fluoropolymer with in situ polymerization of dopamine for 9h (PBX-C-9h), fine and high quality HMX/fluoropolymer (PBX-F) and its coating system (PBX-F-9h), large and high quality HMX/fluoropolymer (PBX-L) and its coating system (PBX-L-9h).

Sample	Impact Sensitivity [%]	Friction Sensitivity [%]
PBX-C	96	84
PBX-C-9h	100	40
PBX-F	100	32
PBX-F-9h	100	28
PBX-L	100	100
PBX-L-9h	92	100

4. Conclusions

In conclusion, PDA coated HMX crystals were synthesized via a facile in situ polymerization of dopamine on the surface of HMX. A compact and uniform PDA coating shell was confirmed by in-depth observation of SEM, XPS, XRD, FT-IR spectra, and Raman spectrum. The core-shell structured HMX@PDA microcapsules were applied to construct PBX with the addition of fluoropolymer. The interface adherence between the HMX crystals and fluoropolymer binder was strengthened with the incorporation of PDA due to the formation of hydrogen bonds and other supramolecular interactions, including π–π stacking and charge transfer. The mechanical properties of as-fabricated HMX@PDA based PBXs showed improved storage modulus, the mechanical strength and toughness, as well as creep resistance. Additionally, the β-δ phase transition temperature of the explosives could be visibly increased by 16.3 °C, attributing to the fact that the rigid PDA shell acted as an armature to protect the HMX crystal. The friction sensitivity could be reduced from 84% to 40% for C-HMX based PBXs with PDA coating. Taking into consideration these results, the preparation of explosive composites with core-shell structure by bio-inspired PDA material provided an effective route for simultaneously boosting mechanical enhancement, thermal stability improvement, and sensitivity reduction of high explosives.

Supplementary Materials: The following are available online at http://www.mdpi.com/2073-4360/11/3/568/s1, Figure S1: OMMRI micrographs of the structure morphologies for different HMX specimens: (a) C-HMX; (b) FRS-HMX; (c) LRS-HMX, Figure S2: Photos of HMX crystals and HMX@PDA composites, Figure S3: The influence of electron beam on the evolution of surface morphology for C-HMX@PDA-9h composites, Figure S4: Characterization of the uncoated HMX crystals and HMX@PDA microparticles: (a) Raman spectra, (b) XRD patterns, (c) FT-IR spectra, and (d) curves of uniaxial stress vs compressive rate, Figure S5: Storage modulus (a) and tanδ (b) as a function of temperature for PDA modified PBXs, Figure S6: DSC curves of HMX@PDA microcapsules, Figure S7: The evolvement in the surface morphology of HMX@PDA microcapsules subjected to solvent, temperature, stirring and water. The solvent was the mixture of ethyl acetate and butyl acetate, and the temperature used is 70 °C, Table S1: The parameters for three types of HMX and HMX@PDA composites, Table S2: Surface element composition of FRS-HMX, PDA, and FRS-HMX @PDA composites as determined by XPS, Table S3: XPS atomic concentration of functional groups in C, O, N atoms of FRS-HMX, PDA, and

FRS-HMX@PDA composites, Table S4: Detonation and mechanical characteristics of the PDA modified PBXs, Table S5: Thermal analysis data of the PDA modified PBXs, Table S6: Thermal analysis data of HMX crystals and HMX@PDA microparticles.

Author Contributions: Conceptualization, J.L. and S.G.; Data curation, Y.L.; Investigation, F.G.; Project administration, Z.Y.; Writing—original draft, C.L.; Writing—review & editing, X.Z. and C.Z.

Funding: This work was supported by the National Natural Science Foundation of China (51703211, 21875232, 21875229, 21875230, 11502243, 11502245, 11702266, 11702267) and the Presidential Foundation of CAEP (YZJJLX2016005).

Conflicts of Interest: The authors declare no conflict of interest.

References

1. Yan, Q.L.; Zeman, S.; Elbeih, A. Recent advances in thermal analysis and stability evaluation of insensitive plastic bonded explosives (PBXs). *Thermochim. Acta* **2012**, *537*, 1–12. [CrossRef]
2. Li, Y.B.; Yang, Z.J.; Zhang, J.H.; Pan, L.P.; Ding, L.; Tian, X.; Zheng, X.; Gong, F.Y. Fabrication and characterization of HMX@TPEE energetic microspheres with reduced sensitivity and superior toughness properties. *Compos. Sci. Technol.* **2017**, *142*, 253–263. [CrossRef]
3. Lin, C.M.; Liu, J.H.; He, G.S.; Yang, Z.J.; Pan, L.P.; Liu, S.J.; Li, J.; Guo, S.Y. Effect of crystal quality and particle size of HMX on the creep resistance for TATB/HMX composites. *Propellants Explos. Pyrotech.* **2017**, *42*, 1410–1417. [CrossRef]
4. Wei, C.X.; Huang, H.; Duan, X.H.; Pei, C.H. Structures and properties prediction of HMX/TATB co-crystal. *Propellants Explos. Pyrotech.* **2011**, *36*, 416–423. [CrossRef]
5. Huang, B.; Hao, X.F.; Zhang, H.B.; Yang, Z.J.; Ma, Z.G.; Li, H.Z.; Nie, F.D.; Huang, H. Ultrasonic approach to the synthesis of HMX@TATB core-shell microparticles with improved mechanical sensitivity. *Ultrason. Sonochem.* **2014**, *21*, 1349–1357. [CrossRef] [PubMed]
6. Ma, Z.G.; Gao, B.; Wu, P.; Shi, J.C.; Qiao, Z.Q.; Yang, Z.J.; Yang, G.C.; Huang, B.; Nie, F.D. Facile, continuous and large-scale production of core-shell HMX@TATB composites with superior mechanical properties by a spray-drying process. *RSC Adv.* **2015**, *5*, 21042–21049. [CrossRef]
7. Yang, Z.J.; Ding, L.; Wu, P.; Liu, Y.G.; Nie, F.D.; Huang, F.L. Fabrication of RDX, HMX and CL-20 based microcapsules via in situ polymerization of melamineformaldehyde resins with reduced sensitivity. *Chem. Eng. J.* **2015**, *268*, 60–66. [CrossRef]
8. Xue, C.; Sun, J.; Kang, B.; Liu, Y.; Liu, X.; Song, G.; Xue, Q. The β-δ phase transition and thermal expansion of octahydro-1,3,5,7-tetranitro-1,3,5,7-tetrazocine. *Propellants Explos. Pyrotech.* **2010**, *35*, 333–338. [CrossRef]
9. Willey, T.M.; Lauderbach, L.; Gagliardi, F.; Buuren, T.; Glascoe, E.A.; Tringe, J.W.; Lee, J.R.I.; Springer, H.K.; Ilavsky, J. Mesoscale evolution of voids and microstructural changes in HMX-based explosives during heating through the β-δ phase transition. *J. Appl. Phys.* **2015**, *118*, 055901. [CrossRef]
10. Risse, B.; Schnell, F.; Spitzer, D. Synthesis and desensitization of nano-beta-HMX. *Propellants Explos. Pyrotech.* **2014**, *39*, 397–401. [CrossRef]
11. Urtiew, P.A.; Forbes, J.W.; Tarver, C.M.; Vandersall, K.S.; Garcia, F.; Greenwood, D.W.; Hsu, P.C.; Maienschein, J.L. Shock sensitivity of LX-04 containing delta phase HMX at elevated temperatures. *AIP Conf. Proc.* **2004**, *706*, 1053–1056.
12. Yang, Z.J.; Li, J.S.; Huang, B.; Liu, S.J.; Huang, Z.; Nie, F.D. Preparation and properties study of core-shell CL-20/TATB composites. *Propellants Explos. Pyrotech.* **2014**, *39*, 51–58. [CrossRef]
13. Dai, X.G.; Xu, J.J.; Wen, Y.S.; Li, Y.B.; Huang, F.L.; Li, M.; Zeng, Q. Delay mechanism of β-δ phase transition of cyclotetramethylene tetranitramine in polymer bonded explosive composites by heat conduction obstacle. *Propellants Explos. Pyrotech.* **2016**, *41*, 637–640. [CrossRef]
14. Guo, C.P.; Wang, D.J.; Gao, B.; Wang, J.; Luo, B.; Yang, G.C.; Nie, F.D. Solid-solid phase transition study of ε-CL-20/binder composites. *RSC Adv.* **2016**, *6*, 859–865. [CrossRef]
15. Yeager, J.D.; Dubey, M.; Wolverton, M.J.; Jablin, M.S.; Majewski, J.; Bahr, D.F.; Hooks, D.E. Examining chemical structure at the interface between a polymer binder and a pharmaceutical crystal with neutron reflectometry. *Polymer* **2011**, *52*, 3762–3768. [CrossRef]
16. Rae, P.J.; Palmer, S.J.P.; Goldrein, H.T.; Field, J.E.; Lewis, A.L. Quasi-static studies of the deformation and failure of PBX-9501. *Proc. R. Soc. A* **2002**, *458*, 2227–2242. [CrossRef]

17. Liu, J.H.; Liu, S.J.; Chen, L.L.; Lin, C.M.; Gong, F.Y.; Nie, F.D. Improving mechanical property of HMX-based PBX with neutral polymer bonding agent. In Proceedings of the 45nd Interational Annual Conference of the Fraunhofer ICT, Karlsruhe, Germany, 24–27 June 2014; pp. 56/1–56/8.
18. Ma, F.G.; Wu, W.H.; Tan, H.M. Coating modification of nirtramine HMX by polymerization and its application. *J. Beijing Inst. Technol.* **2000**, *20*, 389–393.
19. Liu, J.H.; Li, H.Z.; Huang, B.; Ding, L.; Liu, S.J.; Liu, Y.G. The effects of HMX@TATB core-shell composites on the mechanical properties of PBX. *New Trends Res. Energetic Mater. Czech Republic* **2016**, *19*, 154–159.
20. Postma, A.; Yan, Y.; Wang, Y.; Zelikin, A.N.; Tjipto, E.; Carus, F. Self-polymerization of dopamine as a versatile and robust technique to prepare polymer capsules. *Chem. Mater.* **2009**, *21*, 3042–3044. [CrossRef]
21. Zhang, J.; Hwang, J.; Antonietti, M.; Schmidt, B.V.K.J. Water-in-water pickering emulsion stabilized by polydopamine particles and cross-linking. *Biomacromolecules* **2019**, *20*, 204–211. [CrossRef]
22. Shang, K.; Song, S.; Cheng, Y.; Guo, L.; Pei, Y.; Lv, X.; Aastrup, T.; Pei, Z. Fabrication of carbohydrate chips based on polydopamine for real-time determination of carbohydrate–lectin interactions by QCM biosensor. *Polymers* **2018**, *10*, 1275. [CrossRef]
23. Guo, J.; Tardy, B.L.; Christofferson, A.J.; Dai, Y.; Richardson, J.J.; Zhu, W.; Hu, M.; Ju, Y.; Cui, J.; Dagastine, R.R.; et al. Modular assembly of superstructures from polyphenol-functionalized building blocks. *Nat. Nanotechnol.* **2016**, *11*, 1105–1111. [CrossRef] [PubMed]
24. Ran, J.; Wang, C.; Zhang, J.; Wang, W.; Xiao, L.; Jia, S.; Wang, Z.; Wu, W.; Xiao, J. New insight into polydopamine@ZIF-8 nanohybrids: A zinc-releasing container for potential anticancer activity. *Polymers* **2018**, *10*, 476. [CrossRef]
25. Zhao, X.; Wang, H.E.; Chen, X.X.; Cao, J.; Zhao, Y.D.; Neale, Z.G.; Cai, W.; Sui, J.H.; Cao, G.Z. Tubular MoO_2 organized by two-dimensional assemblies for fast and durable alkali-ion storage. *Energy Storage Mater.* **2018**, *11*, 161–169. [CrossRef]
26. Wei, Q.; Zhang, F.; Li, J.; Li, B.; Zhao, C. Oxidant-induced dopamine polymerization for multifunctional coatings. *Polym. Chem.* **2010**, *1*, 1430–1433. [CrossRef]
27. Nie, C.; Yang, Y.; Cheng, C.; Ma, L.; Deng, J.; Wang, L.; Zhao, C. Bioinspired and biocompatible carbon nanotube-Ag nanohybrid coatings for robust antibacterial applications. *Acta Biomater.* **2017**, *51*, 479–494. [CrossRef]
28. Nie, C.; Cheng, C.; Peng, Z.; Ma, L.; He, C.; Xia, Y.; Zhao, C. Mussel-inspired coatings on Ag nanoparticle-conjugated carbon nanotubes: Bactericidal activity and mammal cell toxicity. *J. Mater. Chem. B* **2016**, *4*, 2749–2756. [CrossRef]
29. Gong, F.Y.; Zhang, J.H.; Ding, L.; Yang, Z.J.; Liu, X.B. Mussel-inspired coating of energetic crystals: A compact core-shell structure with highly enhanced thermal stability. *Chem. Eng. J.* **2017**, *309*, 140–150. [CrossRef]
30. Zhu, Q.; Xiao, C.; Li, S.B.; Luo, G. Bioinspired fabrication of insensitive HMX particles with polydopamine coating. *Propellants Explos. Pyrotech.* **2016**, *41*, 1092–1097. [CrossRef]
31. Lin, C.M.; Gong, F.Y.; Yang, Z.J.; Pan, L.P.; Liu, S.J.; Li, J.; Guo, S.Y. Bio-inspired fabrication of core-shell structured TATB/polydopamine microparticles via in situ polymerization with tunable mechanical properties. *Polym. Test.* **2018**, *68*, 126–134. [CrossRef]
32. National Military Standard of China. *Experimental Methods of Sensitivity and Safety*; GJB/772A-97; National Defense Science Technology and Industry Comission Press: Beijing, China, 1997. (In Chinese)
33. Zhao, X.; Cai, W.; Yang, Y.; Song, X.; Neale, Z.; Wang, H.; Sui, J.; Cao, G. $MoSe_2$ nanosheets perpendicularly grown on graphene with Mo-C bonding for Sodium-ion capacitors. *Nano Energy* **2018**, *47*, 224–234. [CrossRef]
34. Zangmeister, R.A.; Morris, T.A.; Tarlov, M.J. Characterization of polydopamine thin films deposited at short times by autoxidation of dopamine. *Langmuir* **2013**, *29*, 8619–8628. [CrossRef]
35. Yu, X.; Fan, H.; Liu, Y.; Shi, Z.; Jin, Z. Characterization of carbonized polydopamine nanoparticles suggests ordered supramolecular structure of polydopamine. *Langmuir* **2014**, *30*, 5497–5505. [CrossRef] [PubMed]
36. Soni, P.; Sarkar, C.; Tewari, R.; Sharma, T.D. HMX polymorphs: Gamma to beta phase transformation. *J. Energy Mater.* **2011**, *29*, 261–279. [CrossRef]
37. Jiang, J.H.; Zhu, L.P.; Zhu, L.J.; Zhu, B.K.; Xu, Y.Y. Surface characteristics of a self-polymerized dopamine coating deposited on hydrophobic polymer films. *Langmuir* **2011**, *27*, 14180–14187. [CrossRef]
38. Li, M.; Huang, M.; Kang, B.; Wen, M.P.; Li, H.Z.; Xu, R. Quality evaluation of RDX crystalline particles by confined quasi-static compression method. *Propellants Explos. Pyrotech.* **2007**, *32*, 401–405.

39. Lin, C.M.; Liu, S.J.; Huang, Z.; He, G.S.; Gong, F.Y.; Liu, Y.G.; Liu, J.H. The dependence of the non-linear creep properties of TATB-based polymer bonded explosives on the molecular structure of the polymer binder: (II) effects of the comonomer ratio in fluoropolymers. *RSC Adv.* **2015**, *5*, 59804–59811. [CrossRef]
40. He, G.S.; Yang, Z.J.; Pan, L.P.; Zhang, J.H.; Liu, S.J.; Yan, Q.L. Bioinspired interfacial reinforcement of polymerbased energetic composites with a high loading of solid explosive crystals. *J. Mater. Chem. A* **2017**, *5*, 13499–13510. [CrossRef]
41. Feng, J.; Venna, S.R.; Hopkinson, D.P. Interactions at the interface of polymer matrix-filler particle composites. *Polymer* **2016**, *103*, 189–195. [CrossRef]
42. Dartyge, B.F. Influence of crystal defects on sensitivity of explosives. In Proceedings of the 10th International Detonation Symposium, Boston, MA, USA, 12–16 June 1993; p. 816.
43. Asay, B.W.; Dickson, P.M.; Henson, B.; Fugard, C.; Funk, D.J.; Idar, D.J. Dynamic measurement of the influence of projectile radius and velocity on strain localization during impact of an energetic material. In Proceedings of the 11th International Detonation Symposium, Snowmass Village, CO, USA, 31 August–4 September 1998; pp. 781–787.
44. Bazaki, H.; Kubota, N. Friction sensitivity mechanism of ammonium perchlorate composite propellants. *Propellants Explos. Pyrotech.* **1991**, *16*, 43–47. [CrossRef]

MDPI
St. Alban-Anlage 66
4052 Basel
Switzerland
Tel. +41 61 683 77 34
Fax +41 61 302 89 18
www.mdpi.com

Actuators Editorial Office
E-mail: actuators@mdpi.com
www.mdpi.com/journal/polymers

MDPI
St. Alban-Anlage 66
4052 Basel
Switzerland

Tel: +41 61 683 77 34
Fax: +41 61 302 89 18

www.mdpi.com

ISBN 978-3-03928-926-4